

Reactions of Nonagermanide Clusters towards Transition Metal and Main Group Element Compounds

Christoph Wallach

Vollständiger Abdruck der von der Fakultät für Chemie der Technischen Universität München zur Erlangung eines
Doktors der Naturwissenschaften (Dr. rer. nat.)
genehmigten Dissertation.

Vorsitz: Prof. Dr. Tom Nilges

Prüfer*innen der Dissertation:

1. Prof. Dr. Thomas F. Fässler
2. Prof. Dr. Shigeyoshi Inoue
3. Prof. Dr. Jonathan Veinot (schriftliche Beurteilung)
apl. Prof. Dr. Wolfgang Eisenreich (mündliche Prüfung)

Die Dissertation wurde am 17.05.2022 bei der Technischen Universität München eingereicht und durch die Fakultät für Chemie am 29.06.2022 angenommen.

Für meine Familie.

Angenehm sind die erledigten Arbeiten.

Marcus Tullius Cicero (106 – 43 v. Chr.)

DANKSAGUNG

Zuallererst gilt mein Dank **Prof. Dr. Thomas F. Fässler** für die Möglichkeit an seinem Lehrstuhl zu promovieren, für die gewährten großen Freiheiten sowie seine kontinuierliche Unterstützung über die gesamte Promotion.

An dem Erfolg der letzten Jahre waren viele weitere Personen maßgeblich beteiligt, denen ich auf diese Weise herzlich danken möchte.

Manuela Donaubauer, für ihr Organisationstalent und ihre Hilfe in allen formellen Angelegenheiten.

Wilhelm Klein, für die zahlreichen Kristallfeinschliffe bis zur vollendeten Verfeinerung _schlussendlichfinalfertigaus.

Tassilo Restle, für seine motivierende Art und Hilfestellungen in allen Angelegenheiten.

Christian Fajman, für fachnahe und -ferne Diskussionen.

Terrance Hadlington, für die richtungsweisenden Diskussionen.

Maria Müller, für die vielen EDX Messungen.

Max Schütz und **Maximilian Muhr**, für die Messung der LIFDI Spektren.

Lukas Niederegger, für die Unterstützung bei den UV-Vis Messungen.

Philip Keil, **Nicole Willeit** und **Kevin Frankiewicz** für die Messung der VT NMRs.

Yasmin Selic und **Prof. Dr. Antti J. Karttunen**, für die Durchführung der theoretischen Berechnungen.

Ulrike Ammari und **Bircan Dilki**, für die Messung der Elementaranalysen.

Annette Schier, für das Korrekturlesen der Manuskripte.

Felix Geitner, **Christian Fajman**, **Tassilo Restle** und **Kerstin Mayer**, für das Korrekturlesen der Dissertationsteile.

Yvonne Anderson und **Dominik Dankert**, für ihre engagierte Arbeit während der Masterarbeit.

Franziska Hnyk, **Dominik Wildegger**, **Johannes Mayr** und **Lukas Eylert** für ihre tatkräftige Unterstützung im Labor während der Forschungspraktika.

Der **Studienstiftung des Deutschen Volkes** danke ich herzlich für die Verleihung eines Promotionsstipendiums, die Organisation vieler interessanter Seminare und das entgegengebrachte Vertrauen.

Bedanken möchte ich mich herzlich bei **Prof. Dr. Jonathan Veinot**, für die Möglichkeit den Forschungsaufenthalt in Kanada zu verwirklichen und die Aufnahme in seine Arbeitsgruppe. Für die große Unterstützung während des Aufenthalts danke ich **Chuyi (Martin) Ni**, **Kevin O'Connor** und **Riley Hooper**. Die Ausflüge durch verschneite Lande werden mir immer im Gedächtnis bleiben, danke fürs spontane Mitkommen an **Elisabeth Groß** und **Anabelle Degg**.

Mein besonderer Dank gilt des Weiteren:

Felix Geitner, für das Lehren der praktischen Fertigkeiten und die vielen angeregten Diskussionen;

Benedikt Witzel, für die Erinnerung an das Leben nach dem Labor;

Kerstin Mayer, für das Aufzeigen der künstlerischen Seite der Chemie;

David Müller, für die musikalischen Feierabende;

Thomas Wylezich, für die Weitergabe der Praktikumsversuche;

Lukas Eylert, für die langjährige Unterstützung als Tutor;

zusammen mit **Renaud Valois**, **Sebastian Geier**, **Alexander Mutschke**, **Tan Trinh**, **Annika Schulz** und **Stefan Strangmüller** für die stimmungsvollen Abende im Kaffeeraum.

Mein Dank gilt auch meinen **Freunden** aus dem Studium für die vielen schönen gemeinsamen Stunden. Ohne euch hätte mir die Zeit nicht annähernd so viel Freude bereitet.

Besonders herzlich möchte ich mich an dieser Stelle bei meinen **Eltern** und meinen Geschwistern **Johanna** und **Benedikt** bedanken. Ihr steht mir stets mit Ratschlägen und unerschütterlicher Unterstützung zur Seite und habt somit im Stillen wesentlich zu dieser Arbeit beigetragen.

Nicht weniger hast du, **Claudia**, stoisch meine schwankenden Launen ertragen und mich immer wieder aufs Neue motiviert. Dafür kann ich dir nicht genug danken.

List of Abbreviations

abbreviation	meaning
[2.2.2]crypt	4,7,13,16,21,24-hexaoxa-1,10-diazabicyclo[8.8.8]hexacosane
18-crown-6	1,4,7,10,13,16-hexaoxacyclooctadecane
2c-2e	two-center-two-electron
A	alkali metal
Å	Ångstrom
<i>a, b, c</i>	lattice parameters
adamantyl	tricyclo[3.3.1.1]decyl
BTS	copper oxide catalyst for gas regeneration
CAAC	cyclic alkyl(amino)carbene
CCDC	Cambridge Crystallographic Data Center
cod	cyclooctadiene
coe	cyclooctene
Cp	cyclopentadienyl
Cp*	1,2,3,4,5-pentamethylcyclopentadienyl
cSt	centi Stokes
Cy	cyclohexyl
d	day
d _x	diagonal
DAB	1,3,2-diazaborolidine
DAB(II)	1,3,2-diazaborole
def	density functional
DFT	density functional theory
Dipp	2,6-di- <i>iso</i> -propylphenyl
dmf	dimethylformamide
dppe	1,2-bis(diphenylphosphino)ethane
<i>E</i>	tetrel element
EDX	energy dispersive X-ray spectroscopy
en	ethylenediamine
equiv.	equivalents
ESI-MS	electro spray ionization mass spectrometry
Et	ethyl
Et ₂ O	diethyl ether
eV	electron volt
g	gram
h _x	height of trigonal prism
h	hour
HOMO	highest occupied molecular orbital
Hz	Hertz
INEPT	insensitive nuclei enhanced by polarisation transfer
^{<i>i</i>} Pr	<i>iso</i> -propyl
K	Kelvin
L	liter
LUMO	lowest unoccupied molecular orbital
<i>m</i>	<i>meta</i>

abbreviation	meaning
m/z	mass-to-charge ratio
Me	methyl
MeCN	acetonitrile
Mes, mesityl	2,4,6-trimethylphenyl
NacNac ^{Mes}	<i>N,N'</i> -bis(2,4,6-trimethylphenyl)- β -diketiminato
MHz	megahertz
mg	milligram
MIC	mesoionic carbene
min	minute
mL	milliliter
ⁿ Bu	<i>n</i> -butyl
NHC	<i>N</i> -heterocyclic carbene
NHC ^{Dipp}	1,3-di(2,6-di- <i>iso</i> -propylphenyl)imidazole-2-ylidene
NHC ^{Pr}	1,3-di(<i>iso</i> -propyl)imidazole-2-ylidene
nm	nanometer
NMR	nuclear magnetic resonance
<i>o</i>	<i>ortho</i>
<i>o</i> -tol	2-methylphenyl
<i>o</i> -xyl	2,6-dimethylphenyl
<i>p</i>	<i>para</i>
PBE0	hybrid DFT-functional according to Perdew, Burke, and Ernzerhof
Ph	phenyl
ppm	parts per million
P-XRD	powder X-ray diffractogram
<i>R</i>	organic ligand
r.t.	room temperature
s	second
SC-XRD	single crystal X-ray diffraction
^t Bu	<i>tert</i> -butyl
thf	tetrahydrofuran
<i>TM</i>	transition metal
tmo	trimethylene oxide
TMS	trimethylsilyl
TZVP	valence triple-zeta polarization
UV-Vis	ultraviolet-visible
<i>V</i>	volume
<i>X</i>	halide
<i>Z</i>	number of formula units per unit cell
α, β, γ	lattice parameters
δ	chemical shift
η	hapticity (coordination number)
θ	Bragg angle
$\tilde{\nu}$	wave number
λ	wavelength
ω	dihedral angle

Abstract

Semiconductors play a vital role in our daily life in the digital age. Almost every electronic device depends on the application of semiconducting materials, and the continuously growing demand for electric power requires the development of highly efficient alternative energy sources and storage capacities. However, the design of novel materials relies on understanding chemical reactions on a molecular level. Here, small-scale model systems represent an inexpensive possibility to investigate physical and chemical properties of a variety of substances. Within the binary solid-state phases $A_{12}Ge_{17}$ and A_4Ge_9 (A = alkali metal) the deltahedral germanium clusters $[Ge_4]^{4-}$ and $[Ge_9]^{4-}$ are contained, which can be seen as synthons at the border of isolated molecules and solid-state-like structures. Within this thesis reactions of the four- and nine-atom clusters with main group element compounds and transition metal complexes are described, yielding functionalized and intermetalloid clusters, respectively.

The first part of this thesis focuses on reactions of the twofold and threefold silylated clusters $[Ge_9\{Si(TMS)_3\}_2]^{2-}$ and $[Ge_9\{Si(TMS)_3\}_3]^-$ with main group element compounds. In comparison to the bare ion $[Ge_9]^{4-}$ the silylated clusters feature an enhanced solubility as well as a decreased reductive potential, thus allowing the generation of stable mixed-substituted clusters.

The reactions of chlorophosphines RR^1PCl (R, R^1 = alkyl, alkenyl, aryl, aminoalkyl) with the twofold and threefold silylated clusters yielded the monoanionic species $[Ge_9\{Si(TMS)_3\}_2PRR^1]^-$ and the charge-neutral cluster $[Ge_9\{Si(TMS)_3\}_3\{P^iBu\{(CH_2)_3CH=CH_2\}\}]$, respectively. In subsequent reactions the anionic cluster species were reacted with silver-carbenes, yielding the adducts $NHC^{Dipp}Ag[Ge_9\{Si(TMS)_3\}_2PRR^1]$ in which the transition metal either coordinates to the $[Ge_9]$ cluster or to the phosphanyl moiety, in dependence of the steric shielding of the organic ligands R and R^1 . Indicative for the latter case is the $^1J(^{31}P-^{107}Ag/^{109}Ag)$ spin-spin coupling observed in the ^{31}P NMR spectra.

Furthermore, the oxidative-coupling of two $[Ge_9\{Si(TMS)_3\}_2]^{2-}$ clusters is reported, yielding the anionic dimer $[Ge_9\{Si(TMS)_3\}_2]_2^{2-}$. Within the reaction the added chloroborane Cy_2BCl acts as an oxide-scavenger as corroborated by the isolation of the boryl ether $Cy_2B-O-BCy_2$.

The boranyl-decoration of the twofold silylated cluster was achieved upon its reaction with chloro-1,3,2-diazaborolidines DAB^R-Cl (R = Me, iPr , o -tol). The formed anionic species $[Ge_9\{Si(TMS)_3\}_2DAB^R]^-$ were crystallized as the copper-carbene adducts. Quantum chemical calculations provide the idea of intramolecular frustrated Lewis acid-base pairs, formed by the attachment of distinct boranyl ligands.

Reactions of the anion $[\text{Ge}_9\{\text{Si}(\text{TMS})_3\}_2]^{2-}$ with bromo-1,3,2-diazaborolidines $\text{DAB}^R\text{-Br}$ ($R = o\text{-tol, Mes, Dipp}$) in cyclic ethers yielded the mixed-substituted clusters $[\text{Ge}_9\{\text{Si}(\text{TMS})_3\}_2(\text{CH}_2)_n\text{O-DAB}^R]^-$ ($n = 3, 4$), comprising incorporated ring-opened ether entities. In dependency of the applied alkali metal counterion the monoanionic clusters reveal a structural isomerism concerning the ligand arrangement at the $[\text{Ge}_9]$ cluster core.

In similar experiments the incorporation of imine moieties was observed upon conducting the reactions in various nitriles $R^i\text{C}\equiv\text{N}$ ($R^i = \text{alkyl, alkenyl, aryl}$). The obtained deep red species $[\text{Ge}_9\{\text{Si}(\text{TMS})_3\}_2\{R^i\text{C}=\text{N}\}\text{-DAB}^R]^-$ form in a frustrated Lewis pair-like reaction. In further experiments the protonation of the incorporated imine moiety was achieved, resulting in the formation of the green-colored zwitterion $[\text{Ge}_9\{\text{Si}(\text{TMS})_3\}_2\{\text{MeC}=\text{N}(\text{H})\}\text{-DAB}(\text{II})^{\text{Dipp}}]$. As corroborated by UV-Vis spectroscopic investigations in combination with quantum chemical calculations, the bathochromic shift is most probably induced by charge-transfer processes between the cluster and the iminium entity.

The second part of this thesis discusses reactions of non-functionalized germanide clusters with organometallic reactants. Reactions of the solid-state precursors $A_4\text{Ge}_9$ and $A_{12}\text{Ge}_{17}$ with zinc organyls in liquid ammonia yielded a series of intermetalloid clusters, such as the dianionic species $[(\eta^3:\eta^3\text{-Ge}_4)(\text{ZnEt})_2]^{2-}$. While the isolated cluster species extend the number of known four- and nine-atom polyanions coordinating to Zn(II) fragments, the characterization of various Zn-amides, which formed as by-products in liquid ammonia, accounts for the detection of intermediates on the way to intermetalloid Ge-Zn clusters.

Transition metal atoms do not only coordinate to the surface of $[\text{Ge}_9]$ clusters, but are also incorporated into the cluster shell, thereby generating so called endohedral clusters. The reaction of K_4Ge_9 with a nickel precursor in ethylenediamine generated the doubly-filled cluster $[\text{Ni}_2@\text{Ge}_{17}]^{4-}$, which in combination with the cobalt-filled ion $[\text{Co}_2@\text{Ge}_{17}]^{6-}$ bridges the gap between known 16- and 18-atom endohedral germanides. The arrangement of the Ge vertex atoms in the obtained polyanions is discussed with respect to structure motifs derived from icosahedra.

Usually, alkali metal counterions balance the negative charge of nonagermanide clusters. However, the counterions can readily be exchanged by reacting the cluster precursors with magnesium organyls, thus obtaining the compounds $[\text{Mg}(\text{NacNac}^{\text{Mes}})(\text{MeCN})_4][\text{Ge}_9\{\text{Si}(\text{TMS})_3\}_3]$ and $[\text{K}[2.2.2]\text{crypt}]_4[\text{Mg}(\text{NacNac}^{\text{Mes}})(\text{NH}_3)_4]_2[\text{Ge}_9\text{-Ge}_9]$ featuring Mg(II) counterions. The presented reactions open the way to the synthesis of compounds which are not accessible through the application of the respective solid-state precursors.

Kurzzusammenfassung

Halbleiter sind in unserem heutigen Leben im Digitalzeitalter unabkömmlich. Halbleitende Materialien finden hierbei in fast allen elektronischen Bauteilen Anwendung, während der Bedarf an hocheffizienten, alternativen Energiequellen und Speichersystemen aufgrund des stetig steigenden Energiebedarfs wächst. Für die Herstellung neuer Materialien ist ein grundlegendes Verständnis der chemischen Vorgänge auf einer molekularen Ebene nötig. Das Studium der chemischen und physikalischen Eigenschaften neuer Substanzen anhand kleiner Modellsysteme bietet hierbei einen kostengünstigen Ausgangspunkt. Die binären Festphasen $A_{12}Ge_{17}$ und A_4Ge_9 ($A = \text{Alkalimetall}$) enthalten die deltaedrischen Cluster $[Ge_4]^{4-}$ und $[Ge_9]^{4-}$, welche als Bausteine zwischen einzelnen isolierten Molekülen und festkörperartigen Strukturen angesehen werden können. In dieser Dissertation werden Reaktionen der vier- und neunatomigen Cluster mit Hauptgruppenelementverbindungen sowie Übergangsmetallkomplexen untersucht, welche in funktionalisierten bzw. intermetalloiden Clustern resultieren.

Der erste Teil der Arbeit behandelt Reaktionen der zweifach- und dreifach-silylierten Cluster $[Ge_9\{Si(TMS)_3\}_2]^{2-}$ und $[Ge_9\{Si(TMS)_3\}_3]^-$ mit Hauptgruppenelementverbindungen. Im Vergleich zu den nicht-funktionalisierten $[Ge_9]$ -Clustern weisen die silylierten Spezies eine höhere Löslichkeit sowie ein geringeres Reduktionspotential auf, was die Herstellung stabiler, gemischt-funktionalisierter Spezies erleichtert.

In Reaktionen der Chlorphosphane $RR^lP(Cl)$ ($R, R^l = \text{Alkyl, Alkenyl, Aryl, Aminoalkyl}$) mit dem zweifach- und dreifach-silylierten Cluster wurden die Anionen $[Ge_9\{Si(TMS)_3\}_2PRR^l]^-$ bzw. der neutrale Cluster $[Ge_9\{Si(TMS)_3\}_3\{P^tBu((CH_2)_3CH=CH_2)\}]$ erhalten. Die anionischen Spezies wurden in weiteren Reaktionen mit Silbercarbenen umgesetzt, wobei die Addukte $NHC^{Dipp}Ag[Ge_9\{Si(TMS)_3\}_2PRR^l]$ erhalten wurden. In den Verbindungen koordiniert das Übergangsmetall in Abhängigkeit von der sterischen Hinderung durch die organischen Reste R und R^l entweder direkt an den $[Ge_9]$ -Cluster oder an die Phosphanylgruppe. Letzterer Fall führt zur Ausbildung von $^1J(^{31}P-^{107}Ag/^{109}Ag)$ Spin-Spin Kopplungen in den ^{31}P NMR Spektren.

Des Weiteren wird die oxidative Kopplung zweier Cluster $[Ge_9\{Si(TMS)_3\}_2]^{2-}$ unter Bildung des Dimers $[Ge_9\{Si(TMS)_3\}_2]^{2-}$ beschrieben. Hierbei dient das zugesetzte Chlorboran Cy_2BCl als Fänger für Oxidionen, was durch die Isolierung des Diboroxans $Cy_2B-O-BCy_2$ bestätigt wurde.

Die Funktionalisierung des zweifach silylierten Clusters mit Boranylliganden wurde durch Reaktionen des Clusters mit Chlor-1,3,2-diazaborolidinen DAB^R-Cl ($R = \text{Me, } ^i\text{Pr, } o\text{-tol}$) erreicht. Die gebildeten Anionen $[Ge_9\{Si(TMS)_3\}_2DAB^R]^-$ wurden als Kupfercarben-Addukte kristallisiert. Quantenchemischen Berechnungen weisen darauf hin, dass die Anbindung bestimmter Boranylliganden prinzipiell zur Ausbildung von frustrierten Lewis Säure-Base Paaren führt.

Die gemischt-substituierten Cluster $[\text{Ge}_9\{\text{Si}(\text{TMS})_3\}_2(\text{CH}_2)_n\text{O-DAB}^R]^-$ ($n = 3, 4$) wurden in Reaktionen des zweifach silylierten Clusters mit Brom-1,3,2-diazaborolidinen $\text{DAB}^R\text{-Br}$ ($R = o\text{-tol, Mes, Dipp}$) in zyklischen Ethern hergestellt und beinhalten Ring-geöffnete Etherfragmente. In Abhängigkeit von den Alkalimetall Gegenionen wurden verschiedene Strukturisomere beobachtet, die sich hinsichtlich der Anordnung der Liganden am $[\text{Ge}_9]$ -Cluster unterscheiden.

In vergleichbaren Experimenten wurde die Inkorporierung von Iminfragmenten beobachtet, wobei die Reaktionen in verschiedenen Nitrilen $R^l\text{C}\equiv\text{N}$ ($R^l = \text{Alkyl, Alkenyl, Aryl}$) durchgeführt wurden. Die erhaltenen roten Cluster $[\text{Ge}_9\{\text{Si}(\text{TMS})_3\}_2\{R^l\text{C}=\text{N}\}\text{-DAB}^R]^-$ bilden sich hierbei nach einem frustrierten Lewis-Paar Mechanismus. Des Weiteren wurde die Iminfunktion protoniert, was in der Bildung des grünen Zwitterions $[\text{Ge}_9\{\text{Si}(\text{TMS})_3\}_2\{\text{MeC}=\text{N}(\text{H})\}\text{-DAB}(\text{II})^{\text{Dipp}}]$ resultierte. UV-Vis spektroskopische Untersuchungen in Kombination mit quantenchemischen Berechnungen deuten darauf hin, dass der bathochrome Effekt durch Ladungsübergänge zwischen dem Cluster und dem Iminiumfragment verursacht wird.

Im zweiten Teil der Arbeit werden Reaktionen nicht-funktionalisierter Germaniumcluster mit Übergangsmetallkomplexen diskutiert. Reaktionen der Festphasen $A_4\text{Ge}_9$ und $A_{12}\text{Ge}_{17}$ mit Zinkorganyle in flüssigem Ammoniak führten zur Bildung einer Reihe intermetalloider Cluster, wie zum Beispiel des Dianions $[(\eta^3:\eta^3\text{-Ge}_4)(\text{ZnEt})_2]^{2-}$. Die Isolierung der verschiedenen Cluster ergänzt die Reihe der bereits bekannten vier- und neunatomigen, $\text{Zn}(\text{II})$ -koordinierten Polyanionen. Des Weiteren wurden verschiedene Zinkamide als Nebenprodukte isoliert, welche als Zwischenstufen auf dem Weg zu intermetalloiden Ge-Zn Clustern betrachtet werden können.

Übergangsmetalle können jedoch nicht nur an den $[\text{Ge}_9]$ -Cluster koordinieren, sondern auch inkorporiert werden. Dies führt zur Bildung sogenannter endohedraler Cluster. Der zweifach gefüllte Cluster $[\text{Ni}_2@\text{Ge}_{17}]^{4-}$ wurde in einer Reaktion von K_4Ge_9 mit einem Nickelorganyl aus Ethylendiamin erhalten und füllt zusammen mit dem Cluster $[\text{Co}_2@\text{Ge}_{17}]^{6-}$ die Lücke zwischen bekannten 16- und 18-atomigen endohedralen Germaniden. Die Anordnung der Gerüstatome in den isolierten Anionen wird im Hinblick auf ikosaedrische Strukturmerkmale diskutiert.

Im Allgemeinen finden Alkalimetalle als Gegenionen zu negativ geladenen, neunatomigen Germaniumclustern Verwendung. Die Gegenionen können jedoch in Reaktionen der Cluster-Präkursoren mit Magnesiumorganyle ausgetauscht werden, wobei die Verbindungen $[\text{Mg}(\text{NacNac}^{\text{Mes}})(\text{MeCN})_4][\text{Ge}_9\{\text{Si}(\text{TMS})_3\}_3]$ und $[\text{K}[2.2.2]\text{crypt}]_4[\text{Mg}(\text{NacNac}^{\text{Mes}})(\text{NH}_3)_4]_2[\text{Ge}_9\text{-Ge}_9]$ erhalten wurden, welche $\text{Mg}(\text{II})$ Ionen enthalten. Die beschriebenen Reaktionen ebnet den Weg zur Herstellung von Clusterverbindungen, die nicht ausgehend von den entsprechenden Festphasen zugänglich sind.

Declaration

The experiments described within this work were performed at the Chair of Inorganic Chemistry with Focus on Novel Materials at the Technical University of Munich between June 2018 and June 2022. This dissertation is written as a publication-based thesis. All manuscripts which were prepared for publication, and manuscripts which were published in peer-reviewed journals are included in Chapter 6. Contributions from co-authors to the presented manuscripts are explicitly stated in Chapter 6 accompanying the corresponding manuscripts. A complete list of these manuscripts containing the bibliographic data for published articles is enclosed in Chapter 7. In the introductory Chapter 1 the relevance of this work for research, a review on relevant literature, the scope, and the outline of this thesis are presented. The results of each manuscript are discussed in Chapter 2, which is divided into the sub-chapters 2.1 (reactions of silylated [Ge₉] clusters) and 2.2 (reactions of bare [Ge₉] clusters). General conclusions are drawn in Chapter 3. Details on the experimental procedures and characterization methods are provided in Chapter 4. A list of cited literature is given in Chapter 5.

TABLE OF CONTENTS

1 INTRODUCTION	1
1.1 Occurrence, Supply and Applications of Elemental Germanium	1
1.1.1 Exploitation of Germanium	1
1.1.2 Properties and Applications of Germanium.....	2
1.2 From Elemental Germanium to Molecular Clusters	4
1.2.1 Bottom-up Route	4
1.2.2 Solid-State Approach.....	5
1.2.3 Structure and Bonding in Tetrel Element <i>Zintl</i> Clusters.....	7
1.3 Reactions of [Ge₄]⁴⁻ and [Ge₉]⁴⁻ Clusters in Solution	9
1.3.1 Reactivity of the Bare [Ge ₄] ⁴⁻ and [Ge ₉] ⁴⁻ Polyanions towards Transition Metal Complexes	10
1.3.1.1 Transition Metal Coordination to Tetrahedral Germanium Clusters	10
1.3.1.2 Transition Metal Coordination to Nine-Atom Germanium Clusters.....	11
1.3.1.3 Formation of Endohedral Germanium Clusters	13
1.3.2 Reactivity of the [Ge ₉] ⁴⁻ Ion towards Main Group Element Compounds	16
1.3.2.1 Oxidative Coupling of [Ge ₉] Clusters	16
1.3.2.2 Addition of Main Group Element Fragments to [Ge ₉] Clusters	17
1.4 Reactions of Silylated [Ge₉] Clusters in Solution	22
1.4.1 Reactivity towards Main Group Element Compounds	22
1.4.1.1 Reactions with Group 14 Element Compounds	22
1.4.1.2 Reactions with Group 15 Element Compounds	24
1.4.2 Reactivity towards Transition Metal Complexes.....	25
1.5 Motivation	27
1.6 Scope and Outline	28
2 RESULTS AND DISCUSSION	31
2.1 Reactions of the Cluster [Ge₉{Si(TMS)₃}₂]²⁻ with Chloro-Phosphines and Halo- Boranes	31
2.1.1 Review of Relevant Literature.....	32
2.1.1.1 Attachment of Functional Groups at Silylated [Ge ₉] Clusters.....	32
2.1.1.2 Principles of Lewis Acid-Base Systems.....	34
2.1.2 Reactions of Silylated [Ge ₉] Clusters towards Chlorophosphines and Chloroboranes.....	35
2.1.3 Intermolecular Frustrated Lewis Pairs of the Cluster [Ge ₉ {Si(TMS) ₃ } ₂] ²⁻ and Bromo-1,3,2-diazaborolidines or Bromo-1,3,2-diazaboroles	42
2.2 Deltahedral [Ge₄]⁴⁻ and [Ge₉]⁴⁻ Anions as Synthons for Intermetalloid Clusters..	53

2.2.1 Review of Relevant Literature.....	54
2.2.1.1 Reactions of Germanide <i>Zintl</i> Clusters with Zinc Organyls.....	54
2.2.1.2 Structure Motifs in Endohedral Tetrel Element Clusters	55
2.2.1.3 Counterion-Exchange at <i>Zintl</i> Clusters.....	56
2.2.2 Synthesis and Characterization of Intermetalloid Germanide Clusters.....	58
2.2.2.1 Investigations on Potential Intermediates and Reaction Paths Yielding Tetrel Element-Zinc Clusters.....	59
2.2.2.2 Synthesis and Structural Characterization of the Endohedral Ions $[TM_2@Ge_{17}]^{n-}$ ($TM = Co, n = 6$; $TM = Ni, n = 4$).....	61
2.2.2.3 Synthesis of Germanide <i>Zintl</i> Clusters Comprising Mg^{2+} Counterions	63
3 CONCLUSIONS	65
4 EXPERIMENTAL SECTION	68
4.1 General Procedures and Equipment	68
4.2 List of Lubricants, Solvents, Chemicals, and Reactants	69
4.2.1 Lubricants.....	69
4.2.2 Solvents	69
4.2.3 Chemicals.....	69
4.2.4 Reactants	72
4.3 Synthesis of Solid-State Precursors	74
4.3.1 Preparation of A_4Ge_9 ($A = K-Cs$).....	74
4.3.2 Preparation of $K_{12}Ge_{17}$	74
4.4 Filtration Techniques.....	77
4.4.1 Whatman Filtration at the Schlenk Line	77
4.4.2 Filtration Using a Schlenk Frit with Glass Filter.....	77
4.4.3 Filtration through Syringe Filters in the Glove Box	77
4.5 Condensation of Liquid Ammonia	78
4.6 Selection and Dissection of Single Crystals for Structure Determination.....	79
4.6.1 Isolation of Single Crystals at Room Temperature	79
4.6.2 Isolation of Single Crystals at Low Temperature	79
4.7 Characterization Methods	81
4.7.1 Nuclear Magnetic Resonance Spectroscopy (NMR).....	81
4.7.2 Raman Spectroscopy	81
4.7.3 Electrospray Ionization Mass Spectrometry (ESI-MS)	81
4.7.4 Liquid Injection Field Desorption Ionization Mass Spectrometry (LIFDI-MS).....	82
4.7.5 UV-Vis Spectroscopy.....	82
4.7.6 Powder X-Ray Diffractometry (P-XRD).....	82

4.7.7 Single Crystal X-Ray Diffraction Analysis (SC-XRD).....	83
4.7.8 Energy Dispersive X-Ray Analysis (EDX).....	83
4.7.9 Elemental Analysis (EA).....	83
4.7.10 Quantum Chemical Calculations.....	84
5 REFERENCES.....	85
6 PUBLICATIONS AND MANUSCRIPTS.....	95
6.1 Enhancing the Variability of [Ge ₉] Cluster Chemistry through Phosphine Functionalization.....	95
6.2 Oxidative Coupling of Silylated Nonagermanide Clusters.....	182
6.3 Boranyl-Functionalized [Ge ₉] Clusters: Providing the Idea of Intramolecular Ge/B Frustrated Lewis Pairs.....	201
6.4 Crystal Structure of (1,4,7,10,13,16-hexaoxacyclooctadecane- <i>k</i> ⁶ O ₆) potassium (2-methylphenylamino)ethyl-2-methylphenylamide ammoniate (1/3.5), [K(18-crown-6)] (o-CH ₃ C ₆ H ₄)NH(CH ₂) ₂ N(o-CH ₃ C ₆ H ₄) · 3.5 NH ₃ , C ₂₈ H _{53.5} KN _{5.5} O ₆	234
6.5 FLP-type Nitrile Activation and Cyclic Ether Ring-Opening by Halo Borane Nonagermanide-Cluster Lewis Acid–Base Pairs.....	246
6.6 Counterion Related Structural Isomerism in the Nonagermanide Clusters A[Ge ₉ {Si(TMS) ₃ } ₂ (CH ₂) ₄ O-DAB ^{Mes}] (A = K, Cs).....	314
6.7 Charge-Transfer Processes in Functionalized [Ge ₉] Clusters Based on the Reversible Formation of a Zwitterion.....	348
6.8 Intermediates and Products of the Reaction of Zn(II) Organyls with Tetrel Element <i>Zintl</i> Ions: Cluster Extension Versus Complexation.....	422
6.9 Filled Trivacant Icosahedra as Building Fragments in 17-atom Endohedral Germanides [TM ₂ @Ge ₁₇] ⁿ⁻ (TM = Co, Ni).....	446
6.10 Nonagermanide <i>Zintl</i> Clusters with Mg ²⁺ Counter Ions.....	476
6.11 Crystal Structure of <i>N</i> ² , <i>N</i> ⁴ -dimesitylpentane-2,4-diamine, C ₂₃ H ₃₄ N ₂	494
7 COMPLETE LIST OF PUBLICATIONS.....	501

1 INTRODUCTION

1.1 Occurrence, Supply and Applications of Elemental Germanium

1.1.1 Exploitation of Germanium

The element germanium was first isolated by Clemens Winkler (1838-1904) upon reduction of GeS_2 , which naturally occurs in the minerals argyrodite Ag_8GeS_6 and germanite $\text{Cu}_6\text{FeGe}_2\text{S}_8$.^[1] The natural abundance of Ge in the earth's crust is low with approximately 0.00014 wt %, while its lighter homologue Si occurs with 29.5 wt % in the upper continental crust.^[2] Ge does not exist in its native state in nature, and the retrieval of pure Ge is a challenging process involving multiple steps. Flue gasses of the Zn producing industry or coal burning are commonly used as a starting material for the extraction of Ge due to the relative high concentration of GeO_2 in the dust. The recovery of Ge from flue gasses of the Zn manufacturing process initiates with the extraction of the Ge and Zn oxides from the crude flue gasses by the addition of sulfuric acid. Upon increasing the pH value the oxides are reformed, and subsequently transferred into the chlorides GeCl_4 and ZnCl_2 using hydrochloric acid. The volatile Ge-halide is distilled off and hydrolyzed to yield pure GeO_2 , which then is reduced to elemental Ge in a H_2 gas stream. Finally, zone melting leads to single crystalline, elemental Ge.^[1] The close relation between the Zn- and the Ge-producing industry is reflected in similar trends concerning the world production capacity over time (Figure 1). Today, the biggest supplier of Ge is China with a share of 66 % of the worldwide production of 130 t in the year 2020.^[3] Despite the fluctuating price per unit, the capacity in the production of Ge shows an increasing trend over the last three decades (Figure 1b), closely related to the designation of Ge as an element of strategic value.^[4-5]

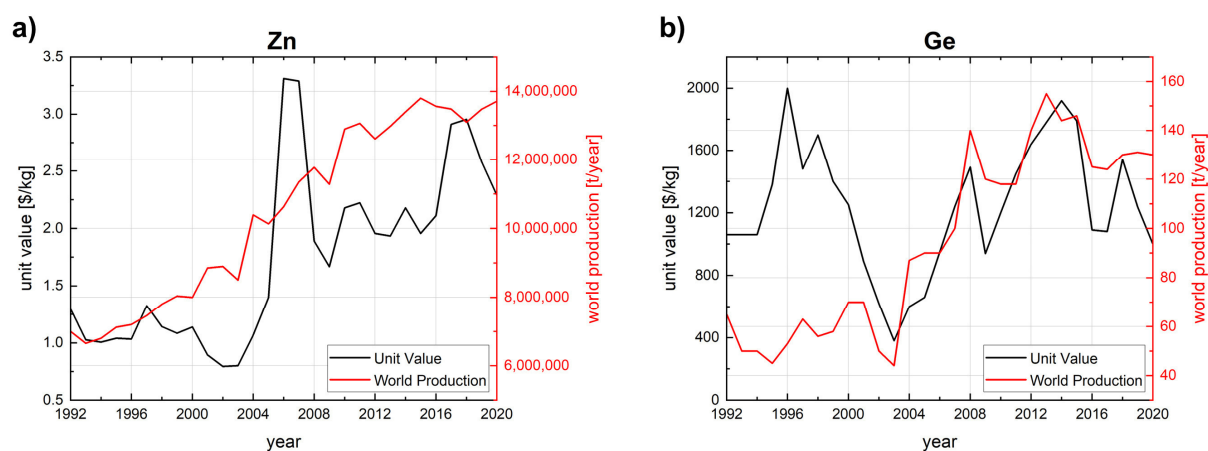


Figure 1. World production (t/year; red graph) of a) Zn and b) Ge and the corresponding development of the unit value (\$/kg; black graph) in the years 1992-2020.^[3-4, 6-8]

Today, sustainable chemistry has become a meaningful field of research and the recovery of elements from decommissioned devices is of great interest, concerning the avoidance of environmental pollution, for example upon open-pit mining. Also recycling Ge scrap is of interest as the world production capacity of this semiconductor is limited and the reward is high. Consequently, today about 30 % of the total Ge amount consumed per year is recovered from discarded products.^[3] Working-up Ge-containing waste is a multistep process, which is highly dependent on the composition of the recycling feed material. In order to separate Ge from other elements various methods like solvent extraction, ion-exchange, or chelation are applied. However, due to the low quantity of Ge in many products, the recycling of this element is a demanding process including the usage of aggressive chemicals and the formation of by-products.^[9-11]

1.1.2 Properties and Applications of Germanium

Due to its semiconducting character and high electron mobility α -Ge (indirect band gap: 0.67 eV)^[1] was used to fashion the first transistors and found application as substrate in GaAs and GaInP III-V photovoltaic cells for satellites.^[12-14] The offered high efficiency is beneficial for the design of powerful, low-weight modules for use in outer space.^[12-13] Furthermore, optical lenses, prisms and windows are produced from Ge and GeO₂ as both are transparent to infrared irradiation. Thus, many optical devices like IR spectrometers or night vision tools rely on the utilization of this specific element.^[1, 15] The oxide GeO₂ is known as a fertile catalyst in the production of polyethylene terephthalate, producing polymers of outstanding white color and stability towards hydrolysis.^[16-17] Even though Ge increases the hardness of certain alloys, its high production costs prohibit the element to be widely used in metallurgical applications.^[15] However, it is of interest concerning scientific aspects. Exemplarily, the intermixing of Ge and Si leads to solid solutions of the general composition Ge_{1-x}Si_x.^[18-19] On a nanoscale level this blending is used to create Ge/Si-based composite materials as thin films or nanocrystals, which show a tunable composition in combination with interesting properties regarding their application in telecommunication, as transistors, and detectors.^[20-23] Upon shrinking down Ge to the nanometer size-regime an adjustable photoluminescence of the particles is observed which is absent in bulk Ge, causing the particles to be of interest for the design of light emitting devices.^[24-25] With respect to the energy transition from fossil fuels to renewable power sources the demand for highly efficient energy accumulators is continuously growing. Here, investigations also focus on Ge as potential anode material in alkali metal ion batteries.^[26-31]

All application areas listed above as well as the demand for developing new technologies and materials fighting climate change require knowledge about the reactivity of the pure element Ge itself. Therefore, basic research is a necessity to explore the versatile chemical behavior

of the semiconductor Ge towards a range of substances. Investigations on a molecular level are of special interest as only little amounts of the element are required, and oftentimes small particles show different physical properties than the element in bulk. As a molecular model system for the pure element nano-particles might be utilized, however their preparation often suffers from a broad size distribution as well as difficulties in describing the resulting materials on an atomic level.^[32] As an alternative, within this work the *Zintl* cluster anion $[\text{Ge}_9]^{4-}$ is used as a precursor to investigate targeted reactions of Ge with transition metal complexes and main group element compounds. The utilized nonagermanide clusters resemble pre-formed, three-dimensional building blocks, which are prepared in a reliable, straightforward way. Thus, they reveal a suitable basis for the synthesis of functionalized, extended, or net-like structures. The obtained products are characterized by single crystal structure determination, revealing the deepest possible insight into the connectivity of single atoms. Furthermore, consecutive reactions corroborate the controllable reactivity of the synthesized polyanions, paving the way for potential future applications.

1.2 From Elemental Germanium to Molecular Clusters

The discovery of three-dimensional aggregates of (semi)metals featuring metal-metal bonds and triangular or polyhedral structure motifs, including non-classical bonds between the atoms, prompted the nomenclature of the respective atom arrangements as clusters.^[33-34] Besides transition metal-based molecules also main group elements like Ge are prone to arrange accordingly.^[35-39] Within this thesis, especially reactions with clusters made of this tetrel element are investigated. Two major paths towards such clusters exist, which split into a bottom-up synthesis path utilizing molecular precursors, and a solid-state route starting directly from the elements. The two methods in principal, as well as the resulting clusters will be described in the following sections.

1.2.1 Bottom-up Route

So called bottom-up synthesis protocols reveal a prosperous route towards Ge-rich clusters. The different synthetic approaches lead to a great number of ions and compounds, which can formally be divided into electron deficient *Zintl* ions, clusters comprising unsubstituted vertex atoms, and all saturated, electron-precise cage compounds. In case the cluster features a higher number of vertex atoms than ligands, and the oxidation state of the cage-forming atoms lies between 0 and +1, such species are referred to as “metalloid” clusters.^[35, 40] The analogous term is applicable for similar compounds of the heavier homologue Sn, whereas Si-rich clusters are usually referred to as “siliconoids”, irrespective of the formal oxidation state of the Si vertices.^[37, 41-42] A prerequisite for the latter terminus are unsubstituted cluster atoms solely bonded to further vertices pointing into one theoretical half-sphere around the “naked” cage atom (purple atoms in Figure 2). These so called “hemispheroidal” cluster vertices comprise the formal oxidation state 0, and thus are seen as model systems for the description of bulk element surfaces.^[37]

An important synthesis method towards homonuclear Ge clusters is the disproportionation of metastable Ge(I) halides with main group element compounds. Via this method clusters like $[\text{Ge}_9\{\text{Si}(\text{TMS})_3\}_3]^-$ (Figure 2a),^[43] $[\text{Ge}_{14}\{E(\text{TMS})_3\}_5]^{3-}$ ($E = \text{Si}, \text{Ge}$; Figure 2b),^[44-45] $[\text{Ge}_{14}\text{Br}_8(\text{PEt}_3)_4]$,^[46-47] or the cubane $[\text{Ge}_8\{2,6\text{-}(t\text{BuO})_2\text{C}_6\text{H}_3\}_6]$ (Figure 2c)^[48] are accessible. Further routes towards molecular clusters are the reductive elimination including the cleavage of leaving groups, and the reductive coupling of $R_n\text{GeX}_{4-n}$ species ($R = \text{organic ligand}$, $X = \text{halide}$) in the presence of GeX_2 salts.^[49] Respective examples are the syntheses of the clusters $[\text{Ge}_{10}\{\text{Si}^i\text{Bu}_3\}_6]^+$ ^[50] as well as $[\text{Ge}_6\{\text{N}(\text{TMS})\text{Dipp}\}_4]$,^[51] and $[\text{Ge}_6\{\text{CH}(\text{TMS})_2\}_6]$ (Figure 2d).^[52] Additionally, the propellane $[\text{Ge}_5\text{Mes}_6]$ ^[53] is formed by reductive coupling. Intriguingly, also heteronuclear propellanes like $[\text{Ge}_2\text{Si}_3\text{Mes}_6]$ (Figure 2e),^[54] $[\text{Ge}_2\{\text{SnClR}\}_3]$

($R = 2,6\text{-dimesitylphenyl}$),^[55] or $[\text{Si}R_2\text{Ge}_4R'_4]$ ^[56] ($R = \text{}^t\text{Bu}$, $R' = \text{SiMe}^t\text{Bu}_2$) are accessible, the latter species of which dimerizes upon photolysis. Via the application of a reactive diselenide to GeCl_2 in the presence of a reducing agent the digermatetrasilane-analogue of hexasilabenzene, $[\text{Ge}_2\text{Si}_4R_6]$ ($R = 2,4,6\text{-}^i\text{Pr}_3\text{C}_6\text{H}_2$), is prepared (Figure 2f).^[57]

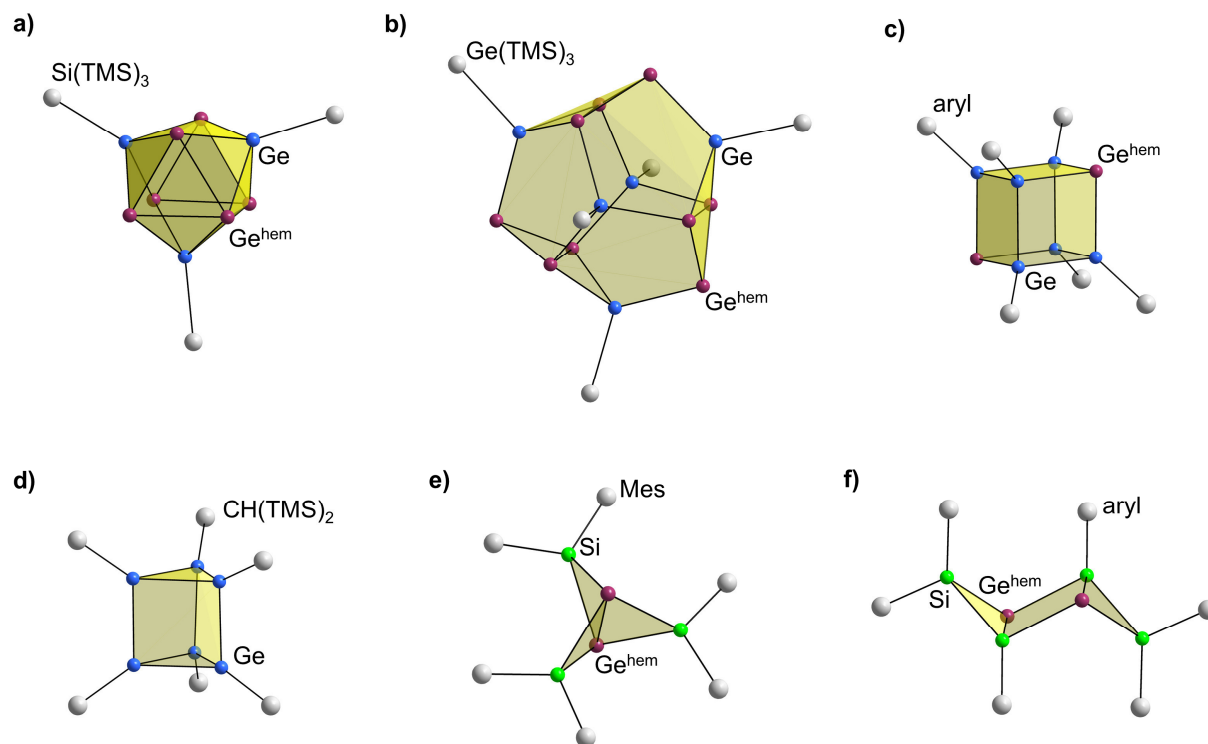


Figure 2. Various clusters obtained from bottom-up synthesis approaches. a) The metalloid *Zintl* cluster ion $[\text{Ge}_9\{\text{Si}(\text{TMS})_3\}_3]^{3-}$; ^[43] b) the extended metalloid cluster $[\text{Ge}_{14}\{\text{Ge}(\text{TMS})_3\}_5]^{3-}$; ^[44] c) the cubane $[\text{Ge}_8(\text{aryl})_6]$ ($\text{aryl} = \{2,6\text{-}(\text{}^t\text{BuO})_2\text{C}_6\text{H}_3\}$); ^[48] d) the fully saturated cage $[\text{Ge}_8\{\text{CH}(\text{TMS})_2\}_6]$; ^[52] e) the heteronuclear propellane $[\text{Ge}_2\text{Si}_3\text{Mes}_6]$; ^[54] f) the hexasilabenzene-analogue $[\text{Ge}_2\text{Si}_4(\text{aryl})_6]$ ($\text{aryl} = 2,4,6\text{-}^i\text{Pr}_3\text{C}_6\text{H}_2$). ^[57] Hemispheroidal vertex atoms Ge^{hem} are shown in purple.

1.2.2 Solid-State Approach

Intermetallic compounds consisting of an electropositive element (alkali or alkaline earth metal) as well as an electronegative counterpart (elements of groups 14-16) are referred to as *Zintl* phases and oftentimes contain molecular clusters (*Zintl* ions).^[1] Such solid-state materials are usually prepared by reacting the elements in inert containers at high temperatures, which guarantees high yields and purities of the obtained products. The structures of the obtained compounds can be described using an ionic bonding concept including a charge separation between the two elements. Thus, according to the *Zintl-Klemm* concept, the element accepting the valence electrons adopts structure motifs observed for isoelectronic, charge-neutral compounds of the adjacent higher group of the periodic table.^[58-60] The bonding situation is evaluated by applying the 8- N rule ($N =$ number of valence electrons). As an example, layers of threefold bonded formal “ Ge^- ” ions exist in CaGe_2 in analogy to grey arsenic,^[1, 61] while CaGe (“ Ge^{2-} ”) exhibits zigzag chains as found in the hexagonal modification of Se or Te.^[1, 62] Further

formal “Ge²⁻” entities are observed in the dumbbell of [Ge₂]⁴⁻ (Li₃NaGe₂),^[63] which resembles molecular oxygen. Intriguingly, the highly charged motif [Ge₂]⁶⁻ (“Ge³⁻”, BaMg₂Ge₂) forms the tetrel element analogue to molecular bromine.^[64] Consequently, in Ca₂Ge (“Ge⁴⁻”) isolated Ge atoms are surrounded by a matrix of cations, mimicking inert gas behavior.^[65] Even more complicated structures such as the butterfly-like arrangement of Ge vertices in [Ge₄]⁶⁻ (Ba₃Ge₄) can be explained following the 8-*N* rule, as a combination of two three-valent (“Ge⁻”) and two two-valent (“Ge²⁻”) Ge atoms.^[66]

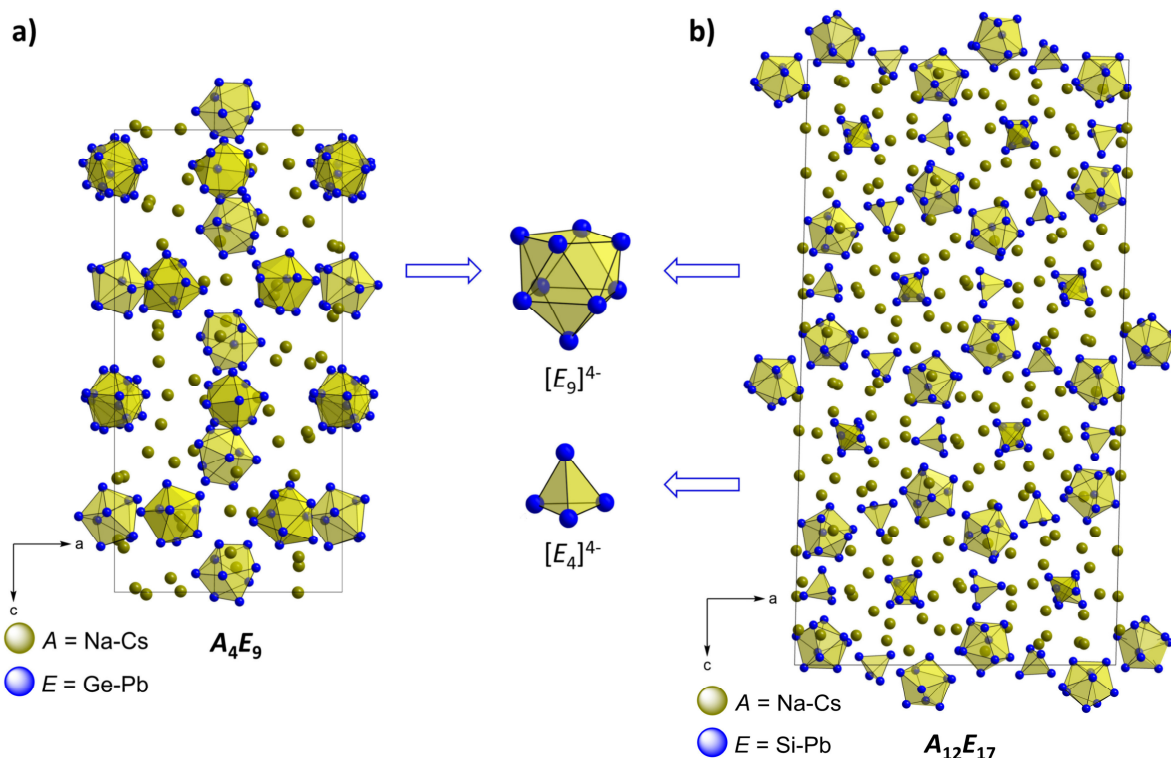


Figure 3. Different cluster types in the solid-state phases a) A_4E_9 and b) $A_{12}E_{17}$ containing either solely $[E_9]^{4-}$ anions or the anions $[E_4]^{4-}$ and $[E_9]^{4-}$ in a 2:1 ratio, respectively. For the illustration the crystallographic data of a) Cs₄Ge₉^[67] and b) Na₁₂Ge₁₇^[68] were used.

The obtained polyanionic structures of the electronegative elements in such phases are versatile and further dumbbells (such as in Li₃NaGe₂)^[63, 69-70] and rings (like in Li₁₂Ge₇)^[71-75] are reported among others.^[76-77] Prominent examples for solid-state phases containing isolated, three-dimensional clusters are the compounds A_4E_9 (A = Na-Cs, E = Ge-Pb; Figure 3a)^[67, 78-84] and $A_{12}E_{17}$ (A = Na-Cs, E = Si-Pb; Figure 3b).^[82, 84-86] They contain either solely the *Zintl* clusters $[E_9]^{4-}$ or a 2:1 ratio of the clusters $[E_4]^{4-}$ and $[E_9]^{4-}$, respectively. Since the polyanionic clusters are directly obtained from fusing the pure elements at elevated temperature, only cages of a defined composition are formed, avoiding the need for further purification steps. In the solid phases A_4E_9 and $A_{12}E_{17}$, the deltahedral clusters are embedded into a matrix of alkali metal cations (“metal scissors”)^[87-89] and can be transferred into solution without any change in composition by dissolving the phases in highly polar solvents like liquid ammonia or

ethylenediamine.^[90-95] The high charge-per-atom ratio of the anions $[E_9]^{4-}$ causes the clusters to act as escharotic, pre-formed building blocks in subsequent reactions. However, the even higher charge-per-atom ratio in $[E_4]^{4-}$ anions at the same time limits a controllable chemistry to a certain extent.

1.2.3 Structure and Bonding in Tetrel Element *Zintl* Clusters

By applying the 8-*N* rule the structure of the $[E_4]^{4-}$ polyanions ("*E*⁻") can be predicted to a tetrahedral atom arrangement in analogy to white phosphorous. However, the geometry of the nine-atom tetrel element clusters cannot be solely explained by this simple rule. In lieu, a correlation between *Zintl* clusters and borane cage compounds was drawn by applying the *Wade-Mingos* concepts.^[96-100] In typical boranes each B atom contributes two electrons for the bonding within the cluster, while each vertex atom is saturated with a hydrogen atom (Figure 4a). Similar conditions are estimated for the bonding within isolobal $[E_9]$ polyanions, with the exception that the vertex atoms exhibit a lone pair instead of an *E*-H termination (Figure 4b). Thus, the $[E_9]^{4-}$ clusters might be described as a nine-fold Lewis base. The structures of the cage compounds can be predicted by counting the skeletal electrons in the respective cluster. In the anion $[Ge_9]^{4-}$ the electrons sum up to $9 \cdot 2 + 4 = 22$, which equals $2(n + 2)$ electrons (*n* = number of cluster vertex atoms), and thus results in a *nido*-cluster adopting the shape of a mono-capped square antiprism (C_{4v} -symmetric, Figure 4b). An analogous calculation reveals 12 skeletal electrons for $[Ge_4]^{4-}$ corresponding to a *nido*-cluster.

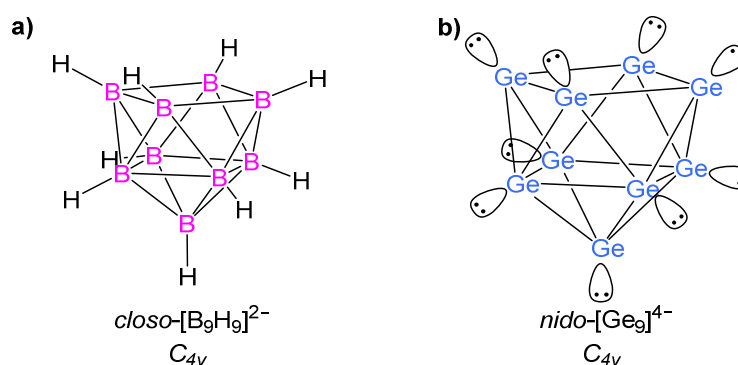


Figure 4. Correlation between a) the borane cluster $[B_9H_9]^{2-}$ with hydrogen terminated vertex atoms^[101-102] and b) the *Zintl* cluster $[Ge_9]^{4-}$ with emphasis on the free electron pairs at each vertex atom, forming a nine-fold Lewis base.

The nine-atom tetrel element *Zintl* clusters are electronically flexible systems, and in solution a dynamic equilibrium between clusters in different oxidation states and solvated electrons exists, leading to variously charged species $[Ge_n]^{n-}$ (*n* = 2, 3, 4).^[103-104] This fluctuating process causes highly redox-active solutions. Furthermore, the symmetry of the polyanions is influenced due to changes in the total number of electrons per cluster. While the C_{4v} -symmetric

nido-[Ge₉]⁴⁻ anion (22 skeletal electrons) adopts the shape of a mono-capped square antiprism, with the diagonals d_1 and d_2 being almost equal in length (Figure 5a), the *closo*-[Ge₉]²⁻ anion (20 skeletal electrons) features a D_{3h} -symmetric cage (Figure 5b).^[67, 84, 94-95, 105-106] In the latter case all prisms heights h_1 - h_3 are equal. In the threefold negatively charged paramagnetic cluster [Ge₉]³⁻ one of the prism heights is elongated leading to an approximately C_{2v} -symmetric cluster comprising a distorted tricapped trigonal prism.^[107-108] The clusters obtaining the two border symmetries C_{4v} and D_{3h} differ only slightly in energy (< 0.05 eV), explaining the readily occurring interconversion of one species into another.^[109-110]

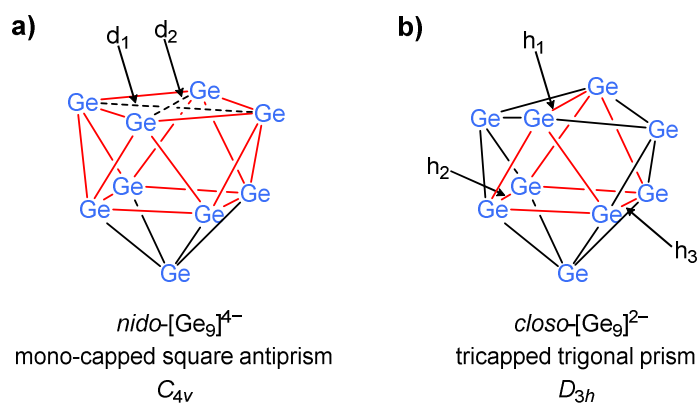


Figure 5. Structure variation in [Ge₉]ⁿ⁻ ($n = 2, 4$) cluster anions. a) Mono-capped square antiprism of the *nido*-[Ge₉]⁴⁻ anion featuring C_{4v} symmetry; b) tricapped trigonal prism of the *closo*-[Ge₉]²⁻ anion featuring D_{3h} symmetry. The square antiprism and the trigonal prism are indicated by red lines.^[67, 84, 94-95, 105-106]

1.3 Reactions of $[\text{Ge}_4]^{4-}$ and $[\text{Ge}_9]^{4-}$ Clusters in Solution

Over the last three decades a rewarding chemistry evolved regarding the fourfold-negatively charged clusters $[\text{E}_4]^{4-}$ and $[\text{E}_9]^{4-}$ ($\text{E} = \text{Si-Pb}$). However, the following chapters will mainly focus on reactions and structures reported for Ge-containing four- and nine-atom *Zintl* clusters. While the reactivity of the tetrahedral cages is almost exclusively limited to a coordination of transition metals (*TM*), the nine-atom clusters show a diverse chemistry. Figure 6 summarizes the most important reactive sites at $[\text{Ge}_9]$ clusters in a generalized, schematic way.

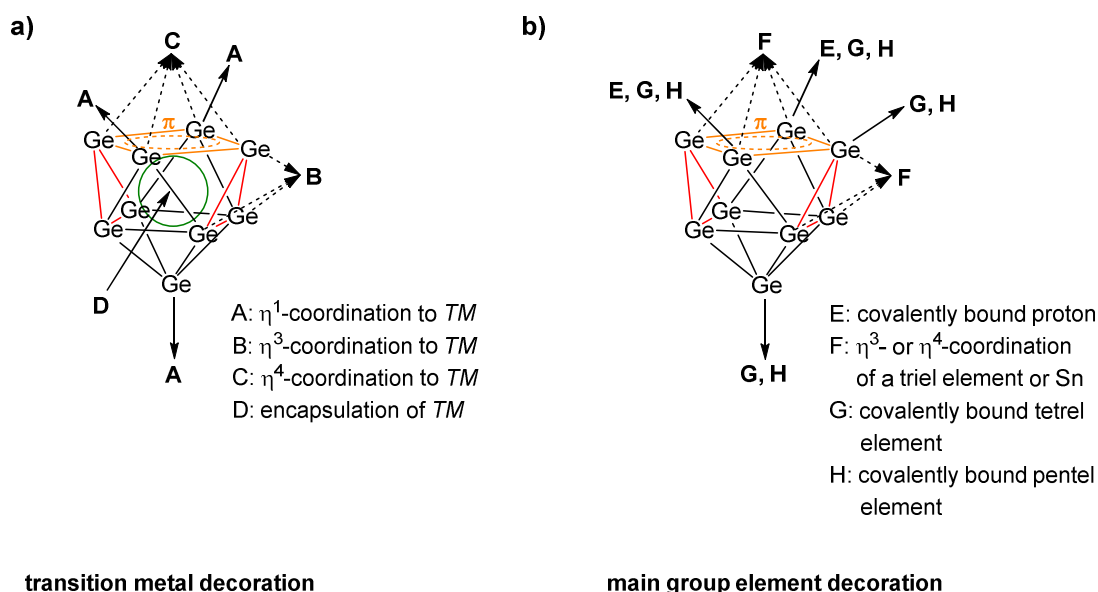


Figure 6. Reactive sites at the $[\text{Ge}_9]$ cluster resulting in a) an interaction of the cage with transition metal complexes or b) a main group element substitution. In both cases the formation of 2c-2e and multi-center bonds is observed.

Detailed information on the respective reactions will be provided in the following chapters reviewing relevant literature. The consecutive Chapter 1.3.1 focuses on the reactions of the bare clusters $[\text{Ge}_4]^{4-}$ and $[\text{Ge}_9]^{4-}$ towards organometallic precursors, covering the coordination of the polyanions to transition metals and the encapsulation of transition metals within the cluster core. The second Chapter 1.3.2 reviews the reactivity of $[\text{Ge}_9]^{4-}$ clusters towards main group element-based fragments, including the oxidative coupling of $[\text{Ge}_9]$ entities and the stabilization of the nine-atom clusters with group 13-15 element substituents. Concluding, the Chapter 1.4 summarizes the chemistry of silylated $[\text{Ge}_9]$ clusters, comprising the generation of mixed-functionalized clusters and the attachment of transition metal-based moieties.

1.3.1 Reactivity of the Bare $[\text{Ge}_4]^{4-}$ and $[\text{Ge}_9]^{4-}$ Polyanions towards Transition Metal Complexes

1.3.1.1 Transition Metal Coordination to Tetrahedral Germanium Clusters

The cluster $[\text{Ge}_4]^{4-}$ features an increased charge-per-atom ratio in comparison to the nine-atom analogue. Due to the high negative cluster charge the chemistry of these anions is limited to reactions in highly polar solvents, and to reactants withstanding their immense reductive potential. The standard reaction protocol involves dissolving the tetrahedra-containing solid-state phase in the presence of a transition metal complex as well as a sequestering agent in liquid ammonia. After prolonged crystallization times, single crystalline products may be obtained, which can be classified in **A** isolated tetrahedra with a coordinating organometallic fragment as well as **B** transition metal bridged tetrahedra. As models for the first type **A** the polyanionic species $[(\eta^3:\eta^3\text{-Ge}_4)(\text{CuMes})_2]^{4-}$ (Figure 7a),^[111] the mixed tetrel element cluster $[(\eta^3:\eta^3\text{-(Si}_{4-x}\text{Ge}_x))(\text{CuMes})_2]^{4-}$,^[112] and the protonated complex ion $[(\mu_2\text{-H})(\eta^2\text{-Ge}_4)\text{ZnPh}_2]^{3-}$ can be listed.^[113] Interconnected tetrahedral clusters of type **B** were isolated in $[(\eta^2\text{-(Si}_{4-x}\text{Ge}_x))\text{Zn}\{\eta^2\text{-(Si}_{4-x}\text{Ge}_x)\}]^{6-}$ (Figure 7b).^[114] Up to this date, the supertetrahedral clusters $[(\eta^2:\eta^2:\eta^2\text{-Ge}_4)_4\text{TM}_6]^{4-}$ [$\text{TM} = \text{Zn}$ (Figure 7c), Cd]^[115] present the largest cluster assemblies yielded from $[\text{Ge}_4]$ units, and resemble outstanding examples for the versatile products obtained upon utilizing molecular precursors as building blocks. Furthermore, specific solid-state compounds comprise interconnected tetrel element tetrahedra as reported for the phases Cs_6ZnGe_8 and $\text{K}_{14}\text{ZnGe}_{16}$ containing the intermetalloid clusters $[(\eta^3\text{-Ge}_4)\text{Zn}(\eta^3\text{-Ge}_4)]^{6-}$ ^[116] and its structural isomer $[(\eta^2\text{-Ge}_4)\text{Zn}(\eta^3\text{-Ge}_4)]^{6-}$,^[111] respectively. Moreover, an infinite $\infty^1\{\text{Au}[(\eta^2\text{-Ge}_4)]\}^{3-}$ chain of gold-interconnected Ge tetrahedra was discovered in the phase A_3AuGe_4 ($\text{A} = \text{K-Cs}$).^[117]

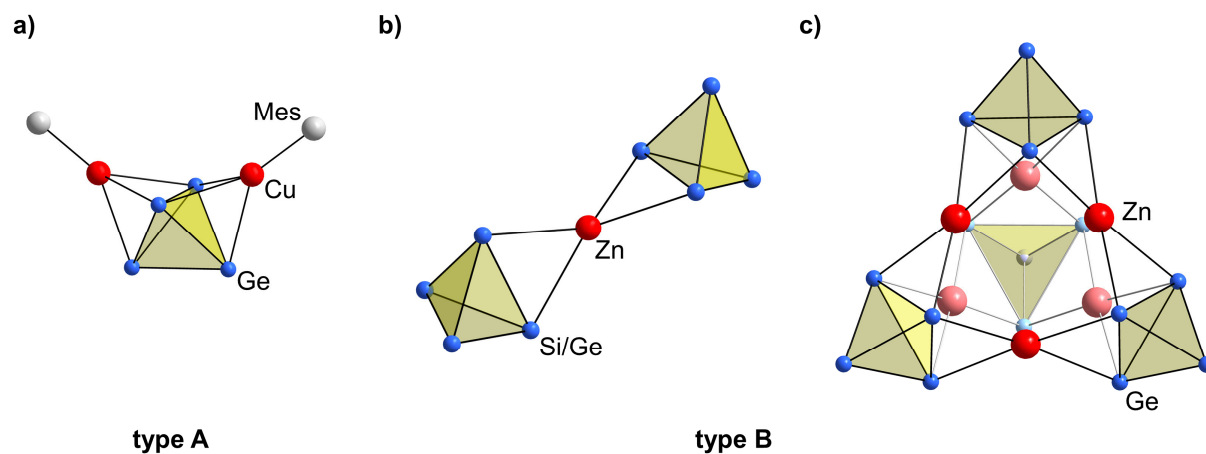


Figure 7. Structures of the transition metal-coordinated tetrahedral clusters a) $[(\eta^3:\eta^3\text{-Ge}_4)(\text{CuMes})_2]^{4-}$,^[111] b) $[(\eta^2\text{-(Si}_{4-x}\text{Ge}_x))\text{Zn}\{\eta^2\text{-(Si}_{4-x}\text{Ge}_x)\}]^{6-}$,^[114] c) $[(\eta^2:\eta^2:\eta^2\text{-Ge}_4)_4\text{Zn}_6]^{4-}$.^[115] In c) atoms and bonds behind the paper plane are presented in desaturated color for a clearer view of the structure.

1.3.1.2 Transition Metal Coordination to Nine-Atom Germanium Clusters

The chemistry of non-functionalized $[\text{Ge}_9]^{4-}$ anions towards transition metal complexes can be summarized in a straightforward way by dividing the corresponding reaction products into three categories, which are **A** the complexation of the tetrel element cluster by an organometallic fragment, **B** the interconnection of two nine-atom clusters by one or more *TM* atoms, and **C** the formation of extended cluster spheres through oxidation and their stabilization by coordinated Ge and *TM* atoms. Two major reaction types dominate in **A** and **B** which are firstly ligand exchange reactions, including the cleavage of weakly bound organic ligands, and secondly metathesis reactions, in case negatively charged leaving groups like halides are abundant in the organometallic precursor.

The pseudo-square plane of the $[\text{Ge}_9]^{4-}$ cluster equals six electron donors like the cyclopentadienyl anion or benzene, and thus is a preferred site for the coordination of transition metal complexes regarding class **A**.^[118] The η^4 -coordination of organometallic fragments resembles an extension of the cluster by one vertex atom, and ten-atom cluster species such as $[(\eta^4\text{-E}_9)\text{TML}]^{3-}$ ($\text{TML} = \text{NiCO}$;^[119] CuP^iPr_3 , CuPCy_3 ;^[120] Zn^iPr , ZnPh , ZnMes ;^[118, 121] PdPPh_3 ;^[122] Figure 8a) form. However, in some cases organometallic moieties coordinate to single cluster vertices mimicking the covalent substitution of the cluster with main group element-based fragments, as discussed in the forthcoming Chapter 1.3.2. Respective examples are the charge-neutral compound $[(\eta^1\text{-Ge}_9)\{\text{Zn}(\text{NH}_3)_3\}_2]$,^[123] and the carbonyl complexes $[(\eta^1\text{-Ge}_9)\{\text{TM}(\text{CO})_5\}_3]^{4-}$ ($\text{TM} = \text{Cr}, \text{Mo}, \text{W}$; Figure 8b)^[124] as well as $[(\eta^1:\eta^1:\eta^5\text{-Ge}_9)\{\text{Cr}(\text{CO})_5\}_2\{\text{Cr}(\text{CO})_3\}]^{4-}$.^[125] In the latter ion mixed coordination modes of the chromium carbonyls are found, which is also observed for Cu in the dimer $[\{\text{Mes}(\eta^1:\eta^4\text{-Ge}_9)\text{Cu}\}_2]^{4-}$ (Figure 8c).^[126] These examples nicely illustrate the versatile chemistry of transition metals towards $[\text{Ge}_9]$ clusters.

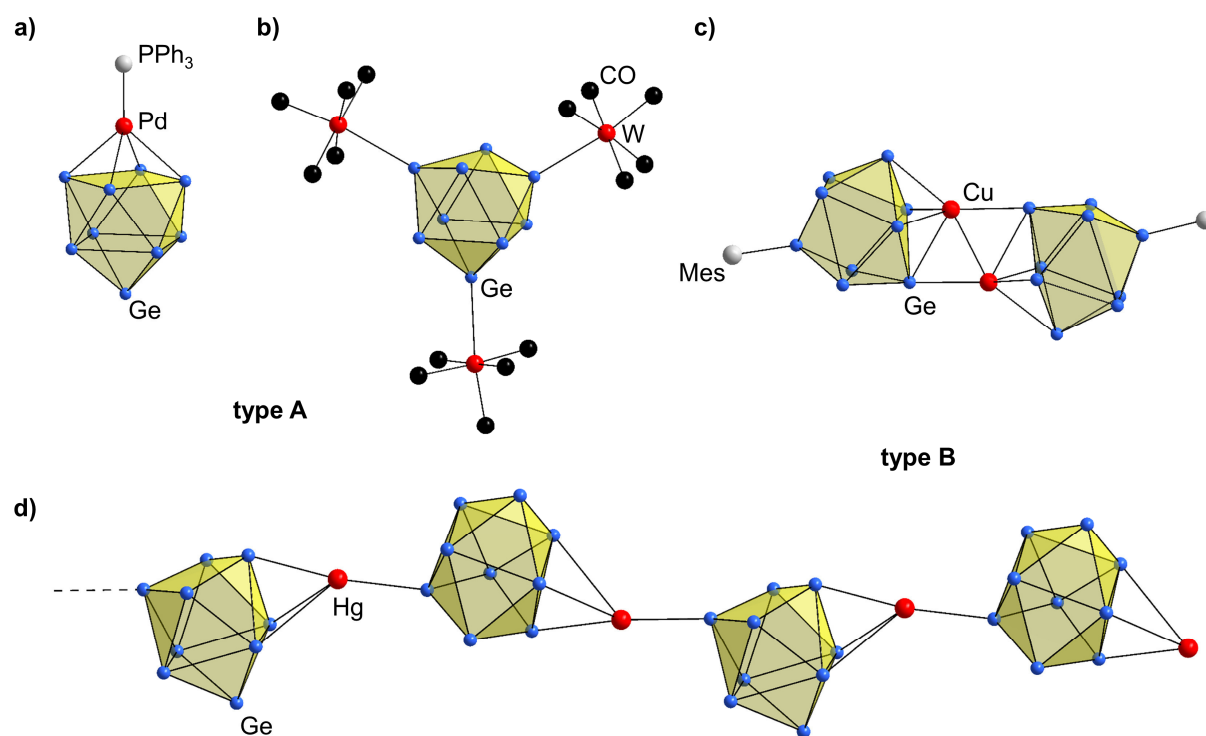


Figure 8. Structures of *TM*-coordinated [Ge₉] clusters. a) The ten vertex atom cluster $[(\eta^4\text{-Ge}_9)\text{Pd}(\text{PPh}_3)]^{3-}$; [122] b) the carbonyl complex-coordinated cluster $[(\eta^1\text{-Ge}_9)\{\text{W}(\text{CO})_5\}_3]^{4-}$; [124] c) the mixed-coordinated ion $[\{\text{Mes}(\eta^1:\eta^4\text{-Ge}_9)\text{Cu}\}_2]^{4-}$; [126] d) the polymer chain of ${}_{\infty}^1\{\text{Hg}(\eta^3:\eta^1\text{-Ge}_9)\}^{2-}$. [127] In a) the PPh₃ ligand is illustrated as a grey sphere, and in b) the carbonyl ligands are indicated as black spheres for clarity.

The aforementioned Cu-species, as well as oligomeric species such as $[(\eta^4\text{-Ge}_9)\text{Cu}(\eta^1\text{-Ge}_9)]^{7-}$, [120] $[(\eta^3\text{-Ge}_9)\text{Cd}(\eta^3\text{-Ge}_9)]^{6-}$, [128] $[(\eta^4\text{-Ge}_9)\text{Zn}(\eta^1:\eta^1\text{-Ge}_9)\text{Zn}(\eta^4\text{-Ge}_9)]^{8-}$, [129] ${}_{\infty}^1\{\text{Zn}(\eta^4:\eta^1\text{-Ge}_9)\}^{2-}$, [129] ${}_{\infty}^1\{\text{Zn}(\eta^3:\eta^3\text{-Ge}_9)\}^{2-}$, [130] and ${}_{\infty}^1\{\text{Hg}(\eta^3:\eta^1\text{-Ge}_9)\}^{2-}$ (Figure 8d) [127] populate the field of *TM*-interconnected cage compounds in the category **B**. Furthermore, a rare dumbbell of Zn(I) was isolated in the ion $[(\eta^4\text{-Ge}_9)\text{Zn}\text{-Zn}(\eta^4\text{-Ge}_9)]^{6-}$. [129] Illustrations of the Zn-comprising clusters are shown in Figure 29 in Chapter 2.2.1.1.

The stabilizing nature of *TM* atoms was already pointed out regarding the formation of the supertetrahedral clusters $[(\eta^2:\eta^2:\eta^2\text{-Ge}_4)_4\text{TM}_6]^{4-}$ (*TM* = Zn, Cd; Chapter 1.3.1.1). [115] They do also facilitate the formation of extended clusters based on [Ge₉] entities according to type **C**, such as in the polyanions $[\text{Au}_3\text{Ge}_{18}]^{5-}$, [131] $[\text{Au}_3\text{Ge}_{45}]^{9-}$ (Figure 9a), [132] $[(\eta^3\text{-Ge}_9)_2\{\text{Ge}(\text{PdPPh}_3)_3\}]^{4-}$ (Figure 9b), [133] and $[(\eta^3\text{-Ge}_9)_2\{\text{Ge}(\text{Ni}(\text{CO})_2)_3\}]^{4-}$ (Figure 9c). [128] Within the latter ions not only transition metals interconnect the [Ge₉] cluster entities, but also Ge atoms in the formal oxidation state 0 are participating in the formation of the structure. Due to the fact that the reported reactions can hardly be monitored *in situ*, studies rely mostly on the isolation of cluster intermediates or cleaved organic ligands. [134] However, there is still a lack of resilient evidence for a general understanding of the reactions occurring in solution, which requires continuous investigations.

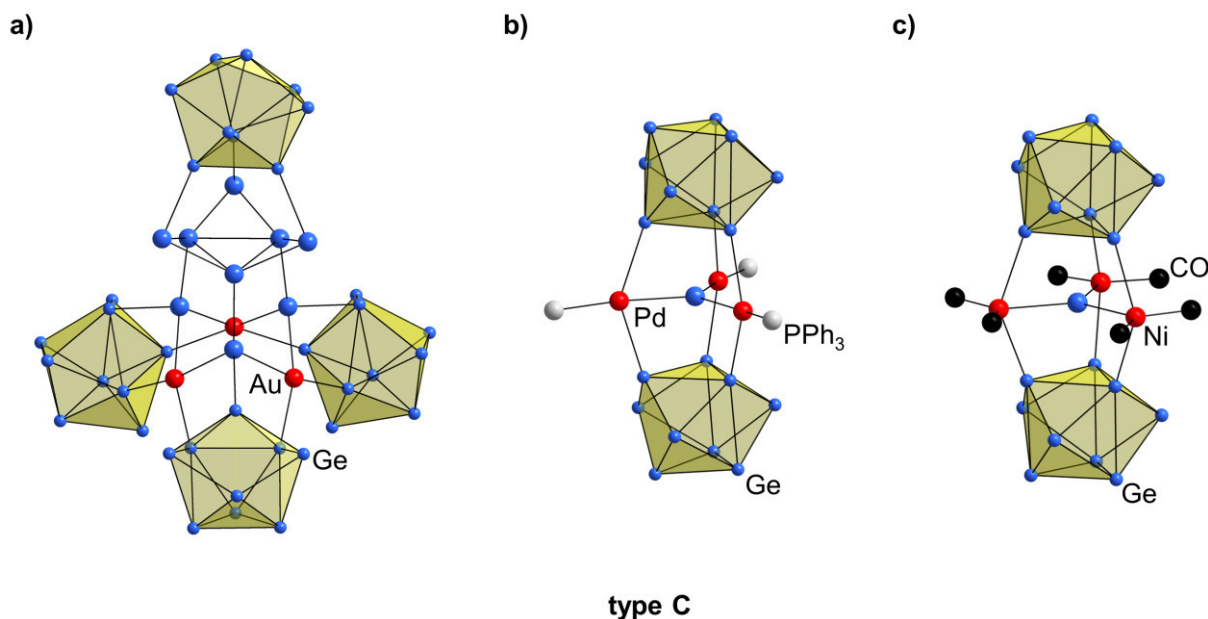


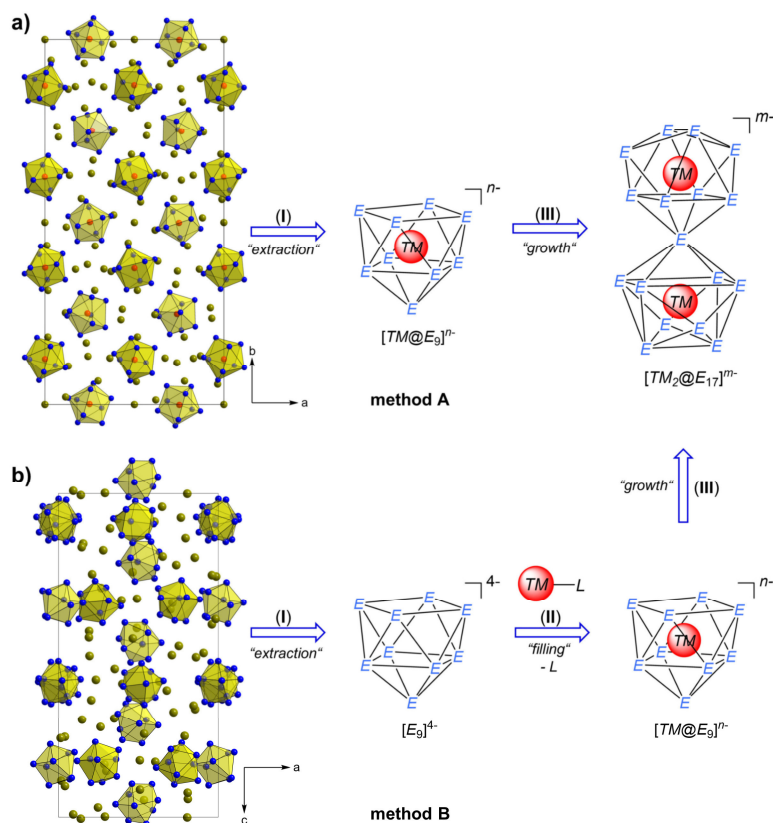
Figure 9. Extended $[\text{Ge}_9]$ cluster aggregates stabilized by transition metals and Ge atoms. a) $[\text{Au}_3\text{Ge}_{45}]^{9-}$,^[132] b) $[(\eta^3\text{-Ge}_9)_2\{\text{Ge}(\text{PdPPh}_3)_3\}]^{4-}$,^[133] c) $[(\eta^3\text{-Ge}_9)_2\{\text{Ge}(\text{Ni}(\text{CO})_2)_3\}]^{4-}$.^[128] In b) PPh_3 groups are indicated as grey spheres, in c) carbonyl ligands are illustrated as black spheres, and in b) and c) the interactions between the central Ge atom and the triangular cluster faces are neglected for clarity.

1.3.1.3 Formation of Endohedral Germanium Clusters

In the previous chapter the coordination of transition metals to $[\text{Ge}_9]$ cages was discussed, leading to coordination complexes or extended clusters with the *TM* acting as additional vertex atom in some cases. However, the empty shell of tetrel elements in the polyanions $[\text{E}_9]^{4-}$ ($E = \text{Ge-Pb}$) encloses a cavity of approximately 30 \AA^3 , which is big enough to host *TM* atoms as guests ($\text{Ge} = 22.1 \text{ \AA}^3$, $\text{Sn} = 32.6 \text{ \AA}^3$, $\text{Pb} = 37.5 \text{ \AA}^3$).^[89] Until today, no nonasilicide cluster with encapsulated *TM* was reported, which is correlated with the small internal cluster volume ($\text{Si} = 18.4 \text{ \AA}^3$),^[82, 86, 135-136] and only a few species are reported for slightly larger germanides. The filled, so called endohedral clusters of Ge to Pb coined the definition of intermetalloid clusters.^[38, 137] A common feature of such molecules is the d^{10} electron configuration of the guest atoms, which therefore adopt oxidation states from -II (Ru) to +I (coinage metals).^[89, 138-140] Formally, no significant electron transfer between the transition metal and the cluster shell is observed, however the provided d orbitals provoke a stabilization of the whole cluster.^[89, 141-142] As key aspects the electrostatic attraction between the *TM* atom and the surrounding cluster shell, as well as an interaction of the transition metal's d orbitals with the cluster are discussed.^[142]

Filled group 14 element anions are accessible in two distinct synthesis methods: **A** the endohedral species are formed in solid-state reactions and subsequently extracted

(Scheme 1a);^[88, 140, 143-145] and **B** pre-formed empty $[E_9]^{4-}$ clusters are filled in solution-based experiments by a reaction with a transition metal complex (Scheme 1b).^[138, 146]



Scheme 1. Schematic representation of the two methods **A** and **B** accessing endohedral clusters by a) the extraction of filled clusters from solid-state phases, and b) the extraction of empty nine-atom clusters from the phases A_4E_9 , and subsequent reactions with *TM* complexes. (I) extraction of the clusters into solution; (II) filling of empty $[E_9]^{4-}$ clusters using *TM* precursors; (III) fragmentation reactions leading to endohedral clusters of higher nuclearity. For the illustration the crystallographic data of a) $K_{5-x}Co_{1-x}Sn_9$ ^[144] and b) Cs_4Ge_9 ^[67] were used.

While an exhaustive overview on endohedral stannides and plumbides is provided in a recent review article,^[89] this chapter mainly focuses on filled germanides. The solid-state phases comprising filled cluster entities illustrated in Scheme 1a are usually prepared by alloying the tetrel element and transition metal in a first step, and subsequently reacting this alloy with alkali metals at high temperatures. However, solely few Sn-based phases featuring endohedral clusters are known in neat solids.^[88, 140, 143, 145] The presence of filled $[Co@Ge_9]^{5-}$ clusters (Figure 10a) in the solid-state was monitored in one single Ge-containing phase of nominal composition “ $K_5Co_{1.2}Ge_9$ ” via Raman spectroscopy.^[140, 147] The latter anion is readily extracted by the addition of liquid ammonia (Scheme 1-I, “extraction”) and potentially prone to undergo reactions leading to extended endohedral species as observed for the analogous Sn species (Scheme 1-III, “growth”).^[140, 143-144] Indeed, just recently the edge-shared doubly filled cluster $[Co_2@(Ge_{17}Ni)]^{4-}$ has been obtained utilizing the aforementioned solid-state precursor.^[148]

In contrast, by following the wet-chemical approach depicted in Scheme 1b various endohedral germanides are accessible by dissolving K_4Ge_9 in ethylenediamine (Scheme 1-I, “extraction”) and adding *TM* compounds to the reaction. Exemplarily, the reaction of the polyanion $[Ge_9]^{4-}$ with $Ni(cod)_2$ yields the cluster $[Ni@Ge_9]^{3-}$ (Scheme 1-II, “filling”).^[119, 146] If the stoichiometry of the reactants is adjusted, the extended cluster $[(Ni@Ge_9)Ni(Ni@Ge_9)]^{4-}$ arises comprising a linear Ni-Ni-Ni strand enfolded into two $[Ge_9]$ entities (Scheme 1-III, “growth”).^[146] However, still there remain uncertainties on the exact mechanisms occurring upon cluster extension in solution, and studies mainly rely on the isolation of intermediate species.^[89] Potentially, the process of cluster-filling starts from the transition metal complex coordinating a pseudo-square plane of the nine-atom cage, followed by a subsequent ligand cleavage, and a migration of the metal into the cluster core.^[120, 134, 138, 149] However, on the way to the endohedral Ge clusters $[TM@Ge_{10}]^{3-}$ ($TM = Fe$,^[150] Co ,^[151-152] Figure 10b), $[TM@Ge_{12}]^{3-}$ ($TM = Co$; Figure 10c,^[152] Ru ^[153]), and doubly-filled cages such as $[TM_2@Ge_{16}]^{4-}$ ($TM = Fe$,^[154] Co ^[155-156]) as well as $[Pd_2@Ge_{18}]^{4-}$ ^[157] (Figure 10d and e) also fragmentation reactions of the cluster precursor need to take place, which have not been understood so far. Furthermore, all of the above mentioned species were obtained by reacting the unfilled nine-atom Ge cluster with *TM* complexes in ethylenediamine, with the polar solvent ascribed an active, but uncertain role in cluster extension processes.^[150, 158-159] In addition, many endohedral structures comprise motifs derived from icosahedra, thus hinting for a preferential, spherical atom arrangement surrounding the central *TM* atom (orange ellipses in Figure 10c-e).^[89, 134, 139, 160]

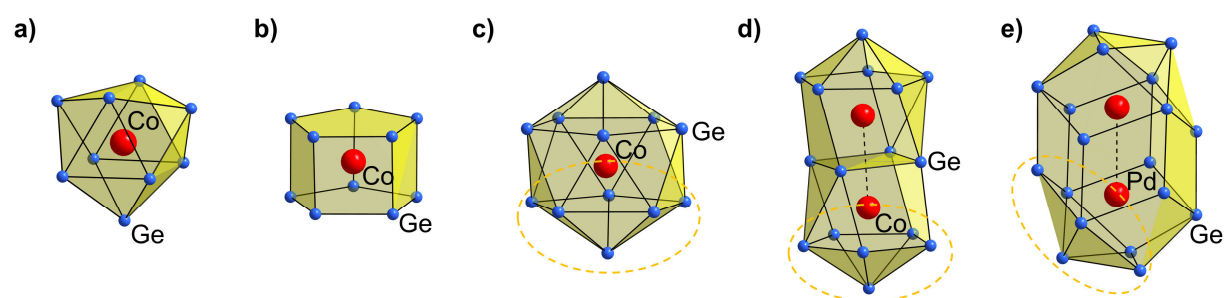


Figure 10. Structures of the endohedral Ge clusters a) $[Co@Ge_9]^{5-}$,^[140] b) $[Co@Ge_{10}]^{3-}$,^[151] c) $[Co@Ge_{12}]^{4-}$,^[152] d) $[Co_2@Ge_{16}]^{4-}$,^[156] e) $[Pd_2@Ge_{18}]^{4-}$.^[157] The transition metal dumbbells in d) and e) are indicated by dashed lines (d: Co-Co = 3.1 Å; e: Pd-Pd = 2.8 Å). The reoccurring icosahedral building fragment in c)-e) is indicated by a dashed orange ellipse.

More exotic endohedral clusters comprise an incorporated guest atom as well as an additional *TM* vertex atom. As key examples the anionic species $[Ni@\{Ge_9(NiL)\}]^{n-}$ ($L = CO$,^[119] PPh_3 ,^[161] $n = 2$; $L = en, C\equiv CPh$,^[119] $n = 3$) might be listed, in combination with the palladium-analogue $[Ni@\{Ge_9(PdPPh_3)\}]^{2-}$,^[122] which forms in a stepwise reaction comprising the intermediate species $[Ge_9Pd(PPh_3)]^{3-}$.

1.3.2 Reactivity of the $[\text{Ge}_9]^{4-}$ Ion towards Main Group Element Compounds

1.3.2.1 Oxidative Coupling of $[\text{Ge}_9]$ Clusters

As described in the previous Chapter 1.2.3 the tetrel element clusters reveal a distinct redox activity in solution and the isolation of diamagnetic $[\text{Ge}_9]^{2-}$ [105, 162] as well as paramagnetic $[\text{Ge}_9]^{3-}$ [163-168] ions accounts for the potential to oxidize the fourfold negatively charged clusters in highly polar solvents. The preferred adopted charge of the cluster is also related to the application and the amount of sequestering agents such as 18-crown-6 or [2.2.2]crypt. These reactants are added to the reaction to enhance the solubility of the cluster-bearing solid-state phases and support the crystallization. Such reactants form coordination complexes with the alkali metal ions and increase their effective ion radius to a size in the range of the polyanionic clusters.^[104] If an excess of the organic molecules is added, lower negative charges become more likely due to steric reasons.^[103-105]

Oxidative processes in solution are not only limited to yield nine-atom clusters of varying charge, but an abundance of oxidatively coupled Ge clusters has been described. Within these polyanions two or more clusters are interconnected by the formation of Ge-Ge *exo*-bonds. Besides the smallest isolated dimeric unit $[\text{Ge}_9\text{-Ge}_9]^{6-}$ [95, 147, 166, 169-174] (Figure 11a), also the trimeric and tetrameric anions $[\text{Ge}_9=\text{Ge}_9=\text{Ge}_9]^{6-}$ [175-177] (Figure 11b) and $[\text{Ge}_9=\text{Ge}_9=\text{Ge}_9=\text{Ge}_9]^{8-}$ [173, 178-179] (Figure 11c) were reported, respectively, featuring two cluster-interconnecting bonds. In addition, a one-dimensional polymer of the formula $\infty^1\{[\text{Ge}_9]^{2-}\}$ [180-181] (Figure 11d) was characterized by single crystal diffraction. While the dimeric and polymeric moieties feature classical 2c-2e bonds (average Ge-Ge inter-cluster bond length: 2.486 Å), the trimer and tetramer show a more complex bonding situation including a delocalization of the bonds, and a thereof resulting elongation of the average Ge-Ge inter-cluster bond length (2.595 Å). In specific cases the oxidation is guided by the addition of reactants as reported for the reaction of $\text{K}_{12}\text{Ge}_{17}$ with $\text{Co}(\text{dppe})\text{Cl}_2$, yielding a rod-like $[\text{Ge}_{24}]^{4-}$ cluster comprising formally two $[\text{Ge}_9]$ and one interconnecting $[\text{Ge}_6]$ unit (Figure 11e).^[182] As mentioned in Chapter 1.3.1.2 the structure of oxidatively-grown clusters might be further supported by *TM* atoms such as in $[\text{Au}_3\text{Ge}_{45}]^{9-}$.^[132] However, until this day, it is not fully understood which steps are involved in the oxidative linking of clusters. A recent study draws a correlation between the concentration of the dianionic cluster $[\text{Ge}_9]^{2-}$ in solution and the formation of the trimeric species.^[175]

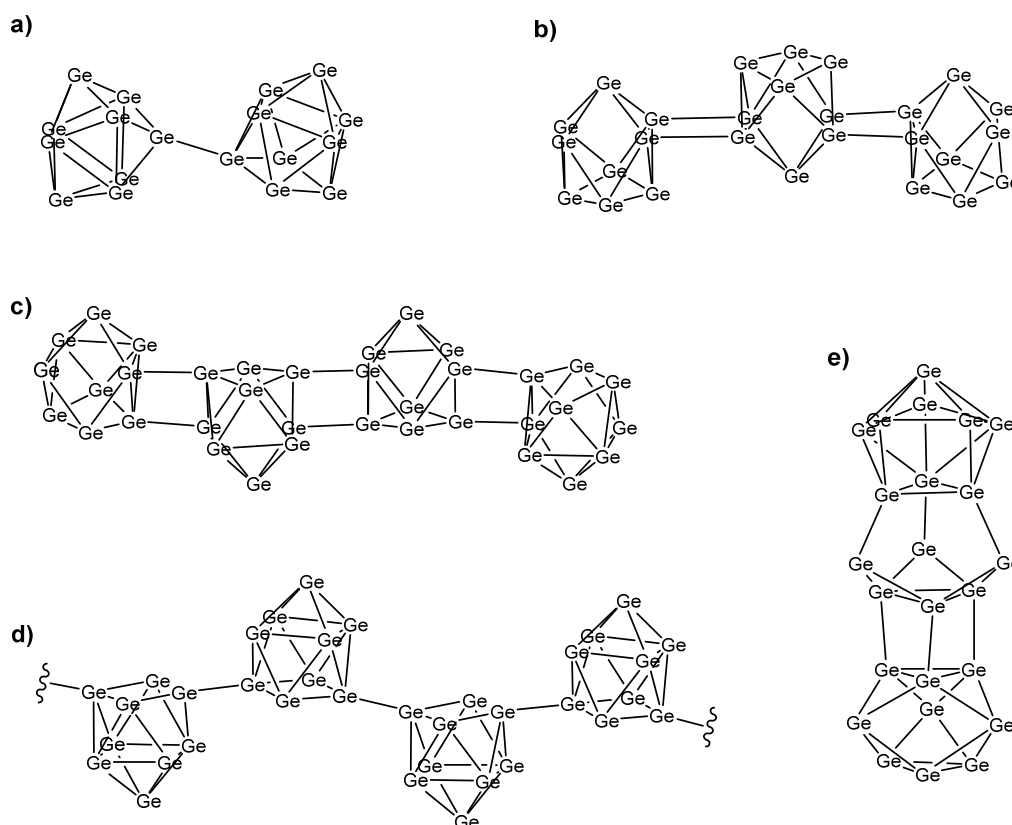


Figure 11. Schematic structures of oxidatively-coupled germanides containing $[\text{Ge}_9]$ building motifs. a) $[\text{Ge}_9\text{-Ge}_9]^{6-}$;[183] b) $[\text{Ge}_9\text{=Ge}_9\text{=Ge}_9]^{6-}$;[177] c) $[\text{Ge}_9\text{=Ge}_9\text{=Ge}_9\text{=Ge}_9]^{8-}$;[179] d) ${}^1_{\infty}\{[\text{Ge}_9]^{2-}\}$;[181] e) $[\text{Ge}_{24}]^{4-}$;[182]

1.3.2.2 Addition of Main Group Element Fragments to $[\text{Ge}_9]$ Clusters

Protonation of the $[\text{Ge}_9]$ cluster

The formation of *exo*-cluster bonds in oxidatively coupled $[\text{Ge}_9]$ oligomers led to the assumption that the nine-atom cluster might be a reactive species towards main group element compounds.[184] Indeed, only recently the protonated clusters $[\text{HGe}_9]^{3-}$ [185] as well as the mixed tetrel element cluster $[\text{H}_2(\text{Si}/\text{Ge})_9]^{2-}$ [186] were reported (among protonated siliconoids),[186-188] featuring protons as the smallest possible substituents. The protons most probably are provided by the applied solvents acting as Brønsted acids. Even though protons are scarcely detectable in X-ray diffraction experiments, their presence is evidenced by geometrical changes in the cluster shape. Evaluating these modifications represents a first qualitative proof of a potential protonation. The protonation of the $[\text{Ge}_9]^{4-}$ cluster ion (C_{4v} symmetry, Figure 12a) leads to a compression of the hydrogen-bearing corner of the cluster and a resulting shortening of the bonds between the protonated Ge atom and its direct neighbors in the formerly pseudo-square plane (Figure 12b). By contrast, the remaining Ge-Ge bonds of the square surface are elongated resulting in an overall C_s -symmetric cluster.[79, 185] Even though the hydrogen atoms

are localized at certain vertex atoms in the solid-state structures, NMR spectroscopic investigations of the protonated silicon and tin congeners revealed a dynamic behavior in solution, accounting for a fast scrambling of the proton across the cluster surface.^[187-189]

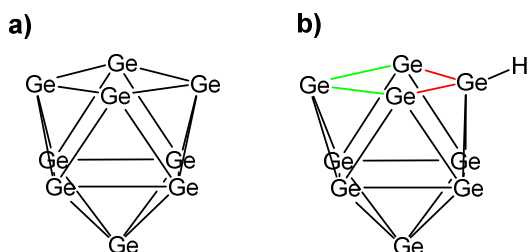


Figure 12. Illustration of changes in the geometry of the $[\text{Ge}_9]$ cluster upon protonation. a) Structure of the C_{4v} -symmetric $[\text{Ge}_9]^{4-}$ ion;^[79] b) structure of the protonated cluster $[\text{HGe}_9]^{3-}$ showing C_s symmetry and a compression of one of the cluster corners.^[185] Elongated Ge-Ge bonds are indicated in green color, shortened bonds are highlighted in red.

Reactivity towards group 13 element compounds

Considering the $[\text{Ge}_9]^{4-}$ cluster as a Lewis base (Chapter 1.2.3), its reactivity towards Lewis acidic centers was anticipated. Indeed, structures containing the heavy group 13 metals Ga-Tl were isolated: Besides the incorporation of a formal $[\text{Ga}_2]^{4+}$ unit in the cluster $[(\eta^4\text{-Ge}_9)\text{Ga-Ga}(\eta^4\text{-Ge}_9)]^{4-}$,^[190] also the ten-vertex atom *closo*-cluster $[(\eta^4\text{-Ge}_9)\text{Tl}]^{3-}$ is accessible (Figure 13a).^[191] The combination of the nine-atom cluster with indium organyls resulted in various species. While triphenylindium doubly coordinates the tetrel element cluster in the ion $[(\eta^1\text{-Ge}_9)(\text{InPh}_3)_2]^{4-}$, a single indium atom bridges two cluster moieties in the cluster $[(\eta^3\text{-Ge}_9)\text{In}(\eta^3\text{-Ge}_9)]^{5-}$.^[128, 192] A combined coordination to and linkage of two $[\text{Ge}_9]$ entities by indium is manifested in the ion $[(\eta^2\text{-Ge}_9)(\eta^2\text{-Ge}_9)\text{InPh}]^{4-}$ (Figure 13b).^[192] The versatile behavior of electron deficient group 13 elements towards $[\text{Ge}_9]$ clusters indicates that only the edge of this field of chemistry has been scratched, and holds promise for further interesting reactions to be discovered.

Reactivity towards group 14 element compounds

Regarding the chemistry of tetrel element compounds towards $[\text{Ge}_9]^{4-}$ ions, a multitude of clusters bearing organic substituents was reported. In a typical reaction alkylchlorides $R\text{Cl}$ [$R = \text{tBu}$,^[193] $\text{CH}_2\text{-CH}(\text{CH}_2)_2$ ^[194]] are added to ethylenediamine solutions of the binary solid-state phase K_4Ge_9 , forming alkylated clusters of the type $[\text{Ge}_9R_2]^{2-}$ or dimeric species $[R\text{-Ge}_9\text{-Ge}_9\text{-R}]^{4-}$.^[193-194] In addition, the aryl substituent Mes might be attached at the $[\text{Ge}_9]^{4-}$

cluster by a ligand transfer from Ag_4Mes_4 .^[195] Through the application of alkynes like TMS-C≡C-TMS functional vinyl groups are bound to the cluster. The resulting species either reveal a decoration with vinyl groups as observed in $[\text{Ge}_9(\text{CH}=\text{CH}_2)]^{3-}$,^[195] $[\text{Ge}_9(\text{CH}=\text{CHCH}_2\text{NH}_2)_2]^{2-}$ (Figure 13c),^[196] or $[\text{Ge}_9(\text{CH}=\text{CH}_2)]_2^{4-}$ ^[197] (among others),^[194, 198-199] or so called *Zintl* triads are formed. These triads contain three building blocks, namely an interconnecting, conjugated hydrocarbon chain and two nine-atom Ge cages. Examples are reported in anions such as $[\text{Ge}_9-(\text{CH}=\text{CH}-\text{CH}=\text{CH})-\text{Ge}_9]^{6-}$ ^[200] and $[\text{R}-\text{Ge}_9-(\text{CH}=\text{CH}-\text{CH}=\text{CH})-\text{Ge}_9-\text{R}]^{4-}$ ($\text{R} = \text{CH}=\text{CH}_2$,^[201] $\text{C}(\text{CH}_3)=\text{CH}-\text{CH}=\text{N}(\text{CH}_2)_2\text{NH}_2$ ^[201-202]).

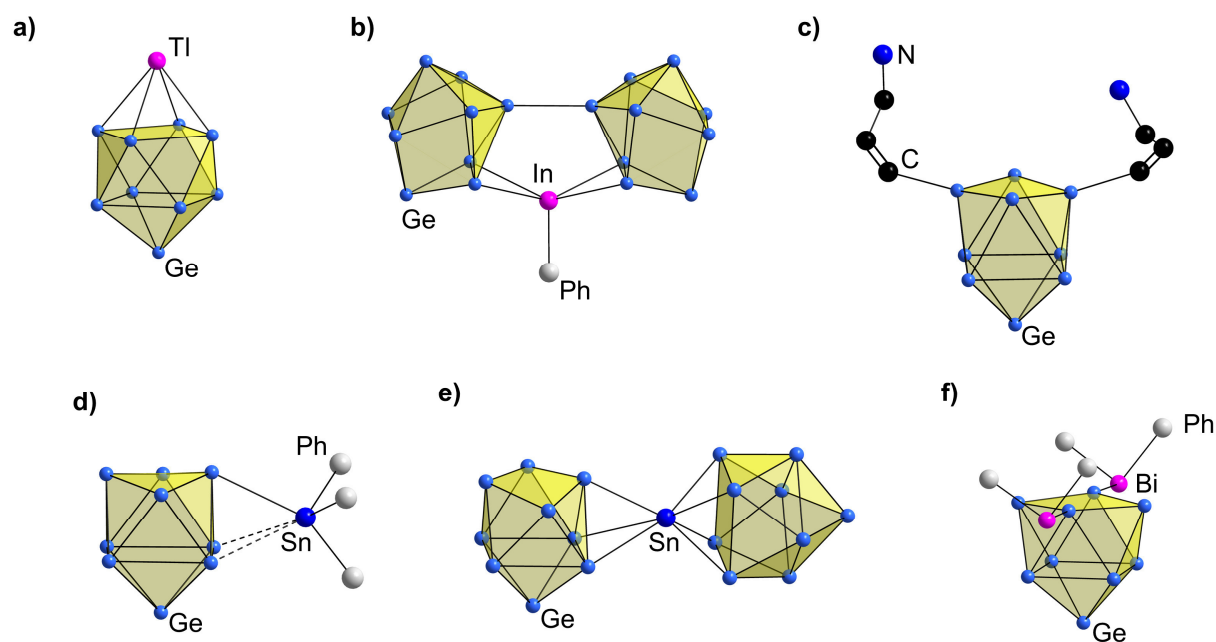


Figure 13. Varying bonding modes in main group element fragment-decorated $[\text{Ge}_9]$ cages. Structure of a) $[(\eta^4-\text{Ge}_9)\text{TI}]^{3-}$ with an additional TI vertex atom;^[191] b) $[(\eta^2-\text{Ge}_9)(\eta^2-\text{Ge}_9)\text{InPh}]^{4-}$ with a doubly η^2 -coordinating InPh moiety;^[192] c) the doubly-vinylated cluster $[\text{Ge}_9(\text{CH}=\text{CHCH}_2\text{NH}_2)_2]^{2-}$;^[196] d) $[\text{Ge}_9(\text{SnCy}_3)]^{3-}$ showing a partial multicenter bond to the Sn organyl;^[103] e) the Sn-bridged dimer $[(\eta^3-\text{Ge}_9)\text{Sn}(\eta^4-\text{Ge}_9)]^{4-}$;^[203] f) $[\text{Ph}_2\text{Bi}-\text{Ge}_9-\text{BiPh}_2]^{2-}$ featuring 2c-2e bonds.^[184] In b), d), and f) phenyl groups are indicated as grey spheres, in c) hydrogen atoms are omitted for clarity.

In contrast to triel elements, organic substituents bind to the cluster under formation of classical 2c-2e bonds, pointing radially away from the center of the cluster. However, deviations from this rule are observed for stannide substituents which show shorter distances to more than one cage vertex atom, thus resulting in Ge-Sn bonds featuring a partial multicenter character.^[103, 204] As key example, the ion $[\text{Ge}_9(\text{SnPh}_3)]^{3-}$ might be used, in which the $[\text{SnPh}_3]^+$ fragment is tilted towards a triangular face of the $[\text{Ge}_9]$ cluster (Figure 13d).^[103] True multicenter bonds are observed in the Sn-bridged dimer $[(\eta^3-\text{Ge}_9)\text{Sn}(\eta^4-\text{Ge}_9)]^{4-}$ (Figure 13e).^[203] The structure of the latter cluster can be described as a *closo*- $[\text{Ge}_9\text{Sn}]^{2-}$ cluster, which donates two electrons to a triangular surface of a second $[\text{Ge}_9]^{2-}$ anion.^[203]

Even though several main group element decorated $[\text{Ge}_9]$ clusters were described, the synthesis of the species mentioned beforehand suffers oftentimes from low yields and a low

controllability, thus limiting any subsequent chemistry. By contrast, the silylation of the $[\text{Ge}_9]$ core proved to be a promising starting point for further reactions. Two or three silyl groups can be introduced to the cluster, thus reducing the negative charge to minus 2 or 1, respectively. At the same time, the solubility of the cage compounds increases. Thus, the salt metathesis of K_4Ge_9 and $(\text{TMS})_3\text{SiCl}$ in MeCN, under the formation of equimolar amounts of KCl, is a reliable way to yield the twofold and threefold silylated clusters $[\text{Ge}_9\{\text{Si}(\text{TMS})_3\}_2]^{2-}$ (Figure 14a)^[205] and $[\text{Ge}_9\{\text{Si}(\text{TMS})_3\}_3]^-$ (Figure 14b),^[206] respectively. The degree of silylation is audited by the applied stoichiometry of the reactants. The reduced cluster charge is concomitant with a reduced reductive nature, however the clusters still possess unsubstituted reactive sites. Due to the lower steric shielding of the twofold silylated cluster, this species is exhaustively used as a fruitful precursor for the synthesis of mixed-substituted clusters (Chapter 1.4.1). The potential of the stabilization through silylation was transferred to elusive $[\text{Si}_9]^{4-}$ clusters obtained in the solid state phase $\text{K}_{12}\text{Si}_{17}$, enabling the syntheses of the clusters $[\text{Si}_9\{\text{R}\}_3]^-$ and $[\text{Si}_9\{\text{R}\}_2]^{2-}$ [$\text{R} = \text{Si}(\text{TMS})_3$, $\text{Si}^t\text{Bu}_2\text{H}$; Figure 14a].^[207-208] In a similar reaction of ${}^i\text{Pr}_3\text{SnCl}$ and K_4Ge_9 the threefold stannylated cluster $[\text{Ge}_9\{\text{Sn}^i\text{Pr}_3\}_3]^-$ was formed.^[209-210]

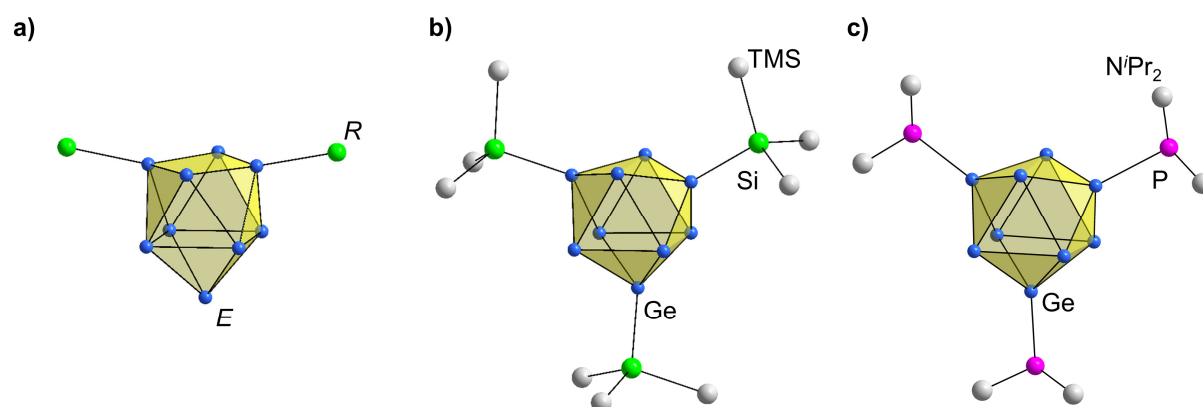


Figure 14. Structures of the multiple-functionalized clusters a) $[\text{E}_9\{\text{R}\}_2]^{2-}$ [$\text{E} = \text{Si}$, $\text{R} = \text{Si}^t\text{Bu}_2\text{H}$, $\text{Si}(\text{TMS})_3$; $\text{E} = \text{Ge}$, $\text{R} = \text{Si}(\text{TMS})_3$].^[205, 207-208] b) $[\text{Ge}_9\{\text{Si}(\text{TMS})_3\}_3]^-$.^[206] c) $[\text{Ge}_9\{\text{P}(\text{N}^i\text{Pr}_2)_2\}_3]^-$.^[211] TMS and N^iPr_2 groups are indicated as grey spheres.

Reactivity towards group 15 element compounds

In analogy to halosilanes, chlorophosphines such as RR^iPCl ($\text{R} = \text{N}^i\text{Pr}_2$; $\text{R}^i = {}^t\text{Bu}$, N^iPr_2) are utilized to yield the triply phosphanylated anions $[\text{Ge}_9\{\text{PRR}^i\}_3]^-$ starting from pristine $[\text{Ge}_9]^{4-}$ clusters (Figure 14c).^[211-212] Notably, the attachment of phosphanyl groups does not only account for a stabilizing effect, but also for the introduction of further Lewis basic groups to the cluster, broadening its chemical reactivity. Even though few further examples for reactions of group 15 element compounds and the polyanion $[\text{Ge}_9]^{4-}$ have been reported, it was the anionic cluster $[\text{Ph}_2\text{Bi}-\text{Ge}_9-\text{BiPh}_2]^{2-}$ in which covalent interactions between main group element

fragments and nine-atom tetrel element clusters extracted from binary solids were reported for the first time (Figure 13f).^[184] Shortly after, these findings were expanded by the isolation of the ions $[\text{Ph-Ge}_9\text{-SbPh}_2]^{2-}$ and $[\text{Ph}_2\text{Sb-Ge}_9\text{-Ge}_9\text{-SbPh}_2]^{4-}$.^[213]

1.4 Reactions of Silylated [Ge₉] Clusters in Solution

Due to the straightforward procedure and high yields, the silylation of [E₉]⁴⁻ clusters became the functionalization method of choice. Since silylated [Si₉] clusters can only be obtained with sequestered alkali metal counterions, which is due to the reaction protocol comprising a pre-extraction of K₁₂Si₁₇ in liquid ammonia, the subsequent chemistry of the siliconoid species is limited.^[207-208] Therefore, the chemistry of silyl fragment-bearing [Ge₉] clusters, has been investigated to a greater extent. Such clusters are either obtained by the disproportionation of metastable Ge(I) halides in the presence of reactants like LiSi(TMS)₃,^[43] or silyl groups are attached at [Ge₉]⁴⁻ clusters contained in the solid-state phase K₄Ge₉ via salt metathesis reactions utilizing chlorosilanes.^[205-206] Generally, both the twofold and threefold silylated clusters [Ge₉{Si(TMS)₃}₂]²⁻ and [Ge₉{Si(TMS)₃}₃]⁻, respectively, are escharotic species towards main group element compounds. The existence of two comparable silylated clusters, varying with respect to the cluster charge and steric crowding, offers the choice to select the most suitable cluster precursor for each reaction.

1.4.1 Reactivity towards Main Group Element Compounds

1.4.1.1 Reactions with Group 14 Element Compounds

In analogy to the silylation reaction described in more detail in Chapter 1.3.2.2, the attachment of further ligands relies on salt metathesis reactions. Amongst them, the reaction of EtBr with the threefold and twofold silylated nonagermanide cluster led to the formation of the neutral species [Ge₉{Si(TMS)₃}₃Et]^[214-216] (Figure 15a) and the mixed substituted cluster [Ge₉{Si(TMS)₃}Et]²⁻,^[217] respectively. In the latter ion one hypersilyl group was cleaved upon crystallization. Additionally, the introduction of functional alkene moieties was achieved in the compounds [Ge₉{Si(TMS)₃}₃R] [R = CH=CH₂, (CH)₃CH=CH₂].^[218] Further reactions of the cluster [Ge₉{Si(TMS)₃}₃]⁻ with various acyl chlorides RC(=O)Cl (R = Me, ⁱPr, Ph, ^tBu) yielded the complex compounds [Ge₉{Si(TMS)₃}₃{C(=O)R}] (Figure 15b), and for R = ^tBu a subsequent decarbonylation to [Ge₉{Si(TMS)₃}₃^tBu] occurred.^[219]

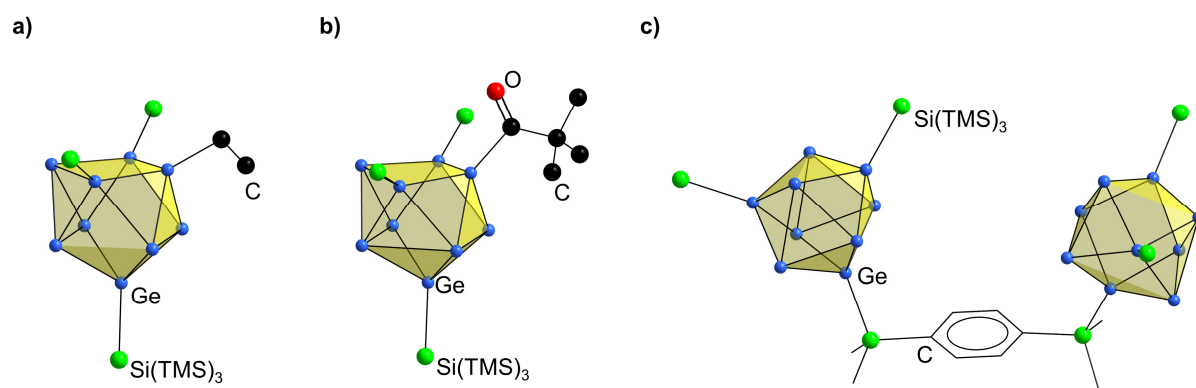


Figure 15. Structures of mixed-substituted, silylated $[\text{Ge}_9]$ clusters. a) $[\text{Ge}_9\{\text{Si}(\text{TMS})_3\}_3\text{Et}]^{2-}$;^[216] b) $[\text{Ge}_9\{\text{Si}(\text{TMS})_3\}_3\{\text{C}(=\text{O})^t\text{Bu}\}]^{2-}$;^[219] c) $[\{\text{Si}(\text{TMS})_3\}_2\text{Ge}_9\text{-SiMe}_2\text{-C}_6\text{H}_4\text{-SiMe}_2\text{-Ge}_9\{\text{Si}(\text{TMS})_3\}_2]^{2-}$.^[220] In a-c) hydrogen atoms at the organic ligands are omitted, and hypersilyl groups are indicated as green spheres for clarity. In c) hydrocarbons are indicated as wire-sticks.

Due to the successful application of the silylated clusters $[\text{Ge}_9\{\text{Si}(\text{TMS})_3\}_2]^{2-}$ and $[\text{Ge}_9\{\text{Si}(\text{TMS})_3\}_3]^-$ in subsequent reactions, further studies focused on altering the silyl fragments to increase the variability of the cluster precursors. Resulting species such as $[\text{Ge}_9\{\text{Si}R_3\}_3]^-$ ($R = \text{Et}$, ^iPr , ^tBu ,^[221] Ph ^[222]) and $[\text{Ge}_9\{\text{Si}(\text{H}^t\text{Bu}_2)\}_3]^-$ ^[223] show a decreased steric shielding compared to three $[\text{Si}(\text{TMS})_3]^+$ fragments, and might allow reactions which otherwise would get hampered by the steric crowding at the $[\text{Ge}_9]$ core. Furthermore, mixed silylated species were prepared by silylation of the Ge atom capping the antiprism in the C_{2v} -symmetric anion $[\text{Ge}_9\{\text{Si}(\text{TMS})_3\}_2]^{2-}$, yielding the ions $[\text{Ge}_9\{\text{Si}(\text{TMS})_3\}_2\{\text{Si}R_3\}]^-$ ($R = ^i\text{Pr}$,^[223] Ph ^[224]). By applying the rigid dichlorosilane $\text{ClSiMe}_2\text{-C}_6\text{H}_4\text{-SiMe}_2\text{Cl}$ as reactant, two $[\text{Ge}_9\{\text{Si}(\text{TMS})_3\}_2]^{2-}$ anions were interconnected via a classical silylation reaction (Figure 15c).^[220] Furthermore, functional alkene moieties were introduced by utilizing the chlorides Ph_2RSiCl [$R = \text{CH}=\text{CH}_2$, $(\text{CH}_2)_3\text{CH}=\text{CH}_2$].^[172, 225] The introduced olefin groups are seen as anchor groups for a potential immobilization of the clusters on surfaces.^[172, 225]

In addition to Si-based fragments, heavier tetrel element halides are suitable precursors for a functionalization of silylated $[\text{Ge}_9]$ clusters, yielding species like $[\text{Ge}_9\{\text{Si}(\text{TMS})_3\}_2\{\text{Ge}(\text{TMS})_3\}]^-$ ^[226] and $[\text{Ge}_9\{\text{Si}(\text{TMS})_3\}_3\{\text{Sn}R_3\}]$ ($R = \text{Ph}$,^[227] ^nBu ^[216]). In the latter compounds the central Sn atom of the organometallic fragment exhibits a partial multicenter bond to a triangular face of the $[\text{Ge}_9]$ cluster, in analogy to the stannylated cluster $[\text{Ge}_9(\text{SnPh}_3)]^{3-}$ (Figure 13d).^[103, 216, 227]

1.4.1.2 Reactions with Group 15 Element Compounds

The impact of the different steric shielding and cluster charge of the twofold, respectively threefold silylated $[\text{Ge}_9]$ cluster became obvious regarding phosphanylation reactions. While the crowded anion $[\text{Ge}_9\{\text{Si}(\text{TMS})_3\}_3]^-$ solely reacts with small chlorophosphines $R_2\text{PCl}$ ($R = i\text{Pr}$, Cy ; Figure 16a),^[228] the higher reductive power of the dianion reduces the latter phosphines immediately to $R_2\text{P-PR}_2$. However, upon increasing the steric demand of the phosphine's organic substituents they become stable against reduction, and bind to a vacant position of the dianionic cluster yielding the functionalized species $[\text{Ge}_9\{\text{Si}(\text{TMS})_3\}_2(\text{PR}_2)]^-$ ($R = \text{alkyl}$, aminoalkyl, aryl).^[212, 228-229] A summary of the introduced phosphanyl groups can be found in Figure 16b.

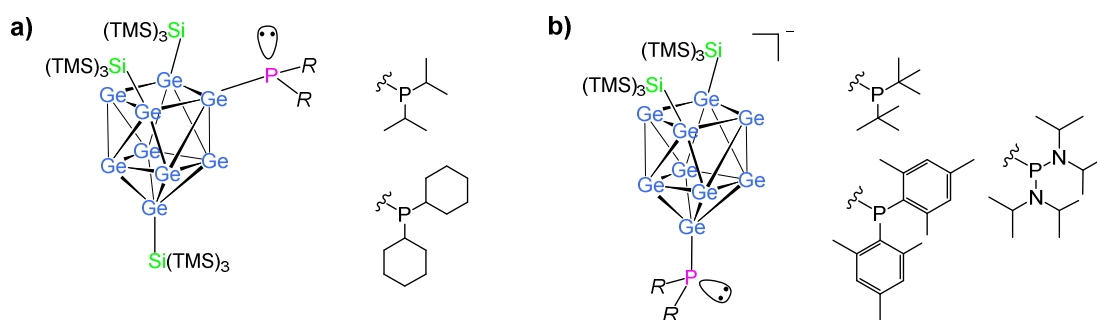


Figure 16. Overview on the variable phosphanylation of silylated $[\text{Ge}_9]$ clusters. a) Attachment of sterically less hindered phosphanyl fragments at the sterically crowded cluster $[\text{Ge}_9\{\text{Si}(\text{TMS})_3\}_3]^-$;^[228] b) attachment of sterically hindered phosphanyl entities at the dianionic cluster $[\text{Ge}_9\{\text{Si}(\text{TMS})_3\}_2]^{2-}$.^[212, 228-229]

An intriguing aspect of the introduction of phosphanyl groups to the $[\text{Ge}_9]$ cluster is that the P atom features Lewis basic properties due to its lone pair. The successful attachment of electron-rich groups at the cluster core raises the question whether also electrophilic fragments could be attached at the silylated cluster to design Lewis acid-base pairs. However, so far only one such species has been reported, which is the silylated thallium-homologue to the cluster $[(\eta^4\text{-Ge}_9)\text{Tl}]^{3-}$ (Figure 13a),^[191] namely $[(\eta^4\text{-Ge}_9\{\text{Si}(\text{TMS})_3\}_3)\text{Tl}]$.^[216]

1.4.2 Reactivity towards Transition Metal Complexes

Reactions of transition metal complexes R_xTM or $RTMX$ (R = organic ligand; X = halide) towards silylated $[Ge_9]$ clusters rely on ligand exchange, salt metathesis, as well as redox reactions, and might be divided into five sub-categories with respect to the formed products. These types are **A** a η^1 -coordination of an organometallic fragment to the cluster via a lone pair, **B** a η^3 -coordination of the TM to a triangular cluster face, **C** a coordination of the TM complex to a square plane, **D** an incorporation of the TM as an additional vertex atom (η^5 -coordination), and **E** a formation of extended clusters through the application of TM reactants. For each case an exemplarily cluster is presented in Figure 17.

Certain transition metal complexes form a η^1 -coordination to silylated clusters according to type **A**. Respective examples are $[\{\eta^1-Ge_9\{Si(TMS)_3\}_3\}\{Ti(MeCN)Cp_2\}]$, $[\{\eta^1-Ge_9\{Si(TMS)_3\}_2\}_2\{TiCp_2\}]^{3-}$,^[230] $[\{\eta^1-Ge_9\{Si(TMS)_3\}_3\}\{Cr(CO)_5\}]^-$ (Figure 17a),^[231] $[\{\eta^1-Ge_9\{Si(TMS)_3\}_3\}\{FeCp(CO)_2\}]$,^[232] and $[\{\eta^1-Ge_9\{Si(TMS)_3\}_2\}_4Zn]^{6-}$.^[123] These cage compounds are accessible by reacting the twofold or threefold silylated clusters with the TM complexes $[Cp_2TiCl]_2$, $Cr(CO)_5(coe)$, $BrFeCp(CO)_2$, and $ZnCp^*_2$, respectively.

Regarding type **B**, several clusters featuring an electrostatic interaction between a triangular face of the $[Ge_9]$ cluster and the transition metal are reported. Reactions of the threefold silylated cluster with the organometallic precursors $(dppe)NiCl_2$,^[233] $(P^iPr_3)CuCl$,^[222] *carbene-TMCl* ($TM = Cu-Au$, *carbene* = NHC;^[234] $TM = Cu$, *carbene* = CAAC, MIC^[235]), $(PR_3)AuCl$,^[236] and $ZnCp^*_2$ ^[222] yield the respective species $[\{\eta^3-Ge_9\{Si(TMS)_3\}_3\}TMR]$. In case the TM complex bears proper leaving groups, the interconnection of two silylated clusters via a central TM becomes feasible. Thus, the reaction of $Pd(PPh_3)_4$ ^[237] and $Ni(cod)_2$ ^[238] with the threefold silylated $[Ge_9]$ cluster yields the species $[TM\{\eta^3-Ge_9\{Si(TMS)_3\}_2\}]^{n-}$ ($n = 2$; Figure 17b). Similar reaction products form with the TM halides $TMCl_2$ ($n = 0$; $TM = Mn$,^[233] Zn , Cd , Hg ^[239]) or the organometallic complexes R_xTMX ($n = 1$; $TM = Cu$,^[240] Ag ,^[234, 240] Au ^[240-241]). A scarce mixed transition metal-decorated cluster was described for $[RZn(\eta^3:\eta^3-Ge_9R_3)Pt(\eta^3:\eta^3-Ge_9R_3)ZnR]$ [$R = Si(TMS)_3$], which comprises two platinum-bridged, Zn-coordinated $[Ge_9\{Si(TMS)_3\}_3]$ clusters.^[242] Furthermore, multiply TM -decorated clusters are found in $[\{\eta^3:\eta^3-Ge_9\{Si(TMS)_3\}_3\}\{Ni(dppe)\}_2]^+$,^[233] $[\{\eta^3-Ge_9\{Si(TMS)_3\}_2\}(Cu-carbene)_2]$ (*carbene* = NHC,^[243] CAAC^[235]), and $[\{\eta^4:\eta^3:\eta^3-Ge_9\{Si(TMS)_3\}_3\}\{(cod)Rh\}\{(cod)Ni\}_2]$.^[244]

The latter compound at the same time is an example for the type **C**, a coordination of a TM complex to a square plane. An analogous coordination of a Cu-comprising fragment to the nonagermanide cluster was reported for the reaction of the twofold- and threefold silylated $[Ge_9]$ clusters with the carbenes $NHC^R CuCl$ ($R = ^iPr$, Dipp; Figure 17c).^[245]

Exemplarily for category **D**, an extension of the threefold silylated $[\text{Ge}_9]$ cluster is reported for its reaction with $\text{Cr}(\text{CO})_3(\text{MeCN})_3$ yielding the *closo*-cluster $[\{\eta^5\text{-Ge}_9\{\text{Si}(\text{TMS})_3\}_3\}\{\text{Cr}(\text{CO})_3\}]^-$ (Figure 17d), which structure can be described as a distorted bicapped square antiprism.^[231] Most probably, the η^1 -coordinated cluster species is formed in a first step, followed by a subsequent ligand cleavage, and a partial rearrangement of the Ge vertex atoms.^[231, 246] A similar cluster geometry is observed in the compounds $[\{\eta^5\text{-Ge}_9\{\text{Si}(\text{TMS})_3\}_3\}\{\text{TM}(\text{PPh}_3)\}\text{Et}]$ ($\text{TM} = \text{Ni},^{[214]} \text{Pd},^{[215]} \text{Pt}^{[214]}$), which arise from the reaction of the charge-neutral species $[\text{Ge}_9\{\text{Si}(\text{TMS})_3\}_3\text{Et}]$ with organometallic precursors.

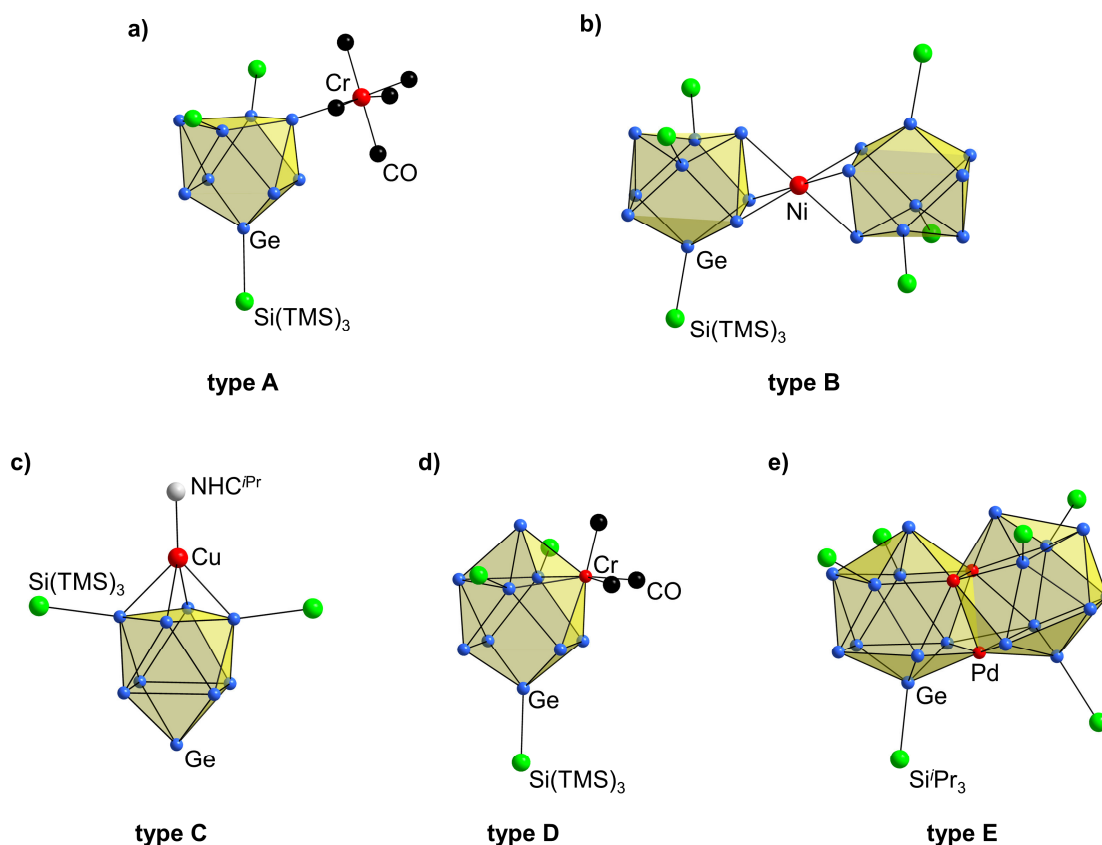


Figure 17. Selected structures formed upon the reaction of silylated $[\text{Ge}_9]$ clusters with transition metal complexes. a) η^1 -coordination of Cr in $[\{\eta^1\text{-Ge}_9\{\text{Si}(\text{TMS})_3\}_3\}\{\text{Cr}(\text{CO})_3\}]^-$;^[231] b) $[\text{Ni}\{\eta^3\text{-Ge}_9\{\text{Si}(\text{TMS})_3\}_2\}]^{2-}$ featuring two silylated clusters linked by a central Ni atom;^[238] c) the η^4 -coordination complex $[\{\eta^4\text{-Ge}_9\{\text{Si}(\text{TMS})_3\}_2\}\{\text{CuNHC}^{\text{Pr}}\}]^-$;^[245] d) the ten-atom *closo*-cluster $[\{\eta^5\text{-Ge}_9\{\text{Si}(\text{TMS})_3\}_3\}\{\text{Cr}(\text{CO})_3\}]^-$;^[231] e) the fused silylated $[\text{Ge}_9]$ cluster $[\text{Pd}_3\text{Ge}_{18}\{\text{Si}^{\text{Pr}}\}_6]^{2-}$ featuring a Pd_3 triangle.^[210] For clarity reasons in a)-e) hypersilyl groups are illustrated as green spheres, the carbonyl groups are drawn as black spheres, and the NHC ligand is shown as a grey sphere.

In contrast to the multitude of structures described before, solely few reports on the formation of extended silylated clusters of type **E** exist. Exemplarily, the dianion $[\text{Pd}_3\text{Ge}_{18}\{\text{E}^{\text{Pr}}\}_6]^{2-}$ ($\text{E} = \text{Si}, \text{Sn}$; Figure 17e) was yielded upon reacting the threefold substituted $[\text{Ge}_9]$ clusters with $\text{Pd}(\text{PPh}_3)_4$. In dependency of the central atoms E the substituents either show an eclipsed ($\text{E} = \text{Si}$) or staggered ($\text{E} = \text{Sn}$) arrangement around the cluster.^[209-210] Furthermore, the charge-neutral metalloid cluster $[\text{Ge}_{18}\{\text{Si}(\text{TMS})_3\}_6]$ was prepared by an oxidative fusion of two threefold silylated clusters in the presence of an Fe(II) source.^[247]

1.5 Motivation

Finding answers to global challenges like the climate change demands for the development of new technologies. However, for the potential development of novel materials or applications an understanding of the processes and chemical reactions occurring on a molecular level is essential. Thus, model systems are needed, which can be manufactured in a reproducible way and are easy to fully characterize. This thesis focuses on the reactivity of germanium, which is studied using molecular $[\text{Ge}_9]$ clusters as models. These clusters resemble pre-formed, three-dimensional atom arrangements and are obtained from the solid-state phase K_4Ge_9 . As outlined in the previous sections, the bare $[\text{Ge}_9]^{4-}$ clusters are valuable building blocks for the synthesis of novel (extended) structures. However, still there remains a lack of understanding concerning the reaction conditions and mechanisms yielding such molecules. To address these open questions, a part of this thesis focuses on the isolation and characterization of intermetalloid cluster compounds, obtained from reactions in highly polar solvents. By taking a close look at the isolated structures, common building motifs as well as possible intermediates are identified, which allow a better understanding of the underlying processes in solution.

Conveniently, the high negative charge of the $[\text{Ge}_9]^{4-}$ cluster can be tailored by silylating the cluster core, thus allowing for an *in-situ* reaction monitoring of the more soluble silylated clusters. Thus, investigations on the reactions of the twofold silylated cluster with main group element compounds form the focal point of this thesis. An interesting aspect is the introduction of triel or pentel element-based fragments to the cluster, as such elements are frequently used as dopants in semiconducting materials relying on group 14 elements.^[248] At the same time, the introduction of group 13 and 15 element-based fragments accounts for the introduction of Lewis acidic as well as basic groups, respectively. Due to its lone pairs at unsubstituted vertex atoms the $[\text{Ge}_9]$ cluster itself might be regarded as a manifold Lewis base, and the design of potentially reactive Lewis acid-base pairs becomes conceivable. Those systems are known to interact with a plethora of molecules in a predictable fashion. Thus, the $[\text{Ge}_9]$ clusters become reactive species in a reaction system consisting of multiple molecules, possibly allowing for an alternative way of attaching new substituents at the cluster. This is of special concern as the potential introduction of, for example, unsaturated moieties adjacent to the cluster might affect its interaction with visible light. A targeted tuning of the optical properties might be an interesting aspect in view of designing cluster-based, light harvesting materials.

1.6 Scope and Outline

Within this thesis, the reactivity of the cluster $[\text{Ge}_9]^{4-}$ towards transition metal complexes as well as main group element fragments is investigated. General information on elemental Ge as well as a review of the relevant literature is provided in the **Chapter 1**.

The discussion of the results is enclosed in **Chapter 2**, which is divided into further sub-chapters.

In **Chapter 2.1** the functionalization of the twofold silylated cluster $[\text{Ge}_9\{\text{Si}(\text{TMS})_3\}_2]^{2-}$ with group 13, 14 and 15 element fragments is outlined, covering the lion's share of this work. In the beginning of this section a review of the relevant literature is provided (**2.1.1**). In the following sub-chapter **2.1.2** reactions of silylated $[\text{Ge}_9]$ clusters towards chlorophosphines and chloroboranes are discussed. Here, the first section focuses on the introduction of phosphanyl fragments $[\text{PRR}^l]^+$ ($R, R^l = \text{alkyl, alkenyl, aryl, aminoalkyl}$) of varying steric demand to the ion $[\text{Ge}_9\{\text{Si}(\text{TMS})_3\}_2]^{2-}$. The emphasis is set on the subsequent coordination of the Lewis basic P atom to Ag-carbenes, which is investigated by $^1J(^{31}\text{P}-^{107}\text{Ag}/^{109}\text{Ag})$ spin-spin coupling experiments. Subsequently, the oxidative coupling of two doubly silylated $[\text{Ge}_9]$ clusters is described, which is mediated by the electrophilic alkyl chloroborane $\text{C}_2\text{H}_5\text{BCl}$, which acts as an oxide-scavenger in the redox process. The reaction of the cluster $[\text{Ge}_9\{\text{Si}(\text{TMS})_3\}_2]^{2-}$ with chloro-1,3,2-diazaborolidines $\text{DAB}^R\text{-Cl}$ leads to the attachment of boranyl fragments $[\text{DAB}^R]^+$ at the cluster, which is discussed with respect to the formation of intramolecular frustrated Lewis acid-base pairs.

In the consecutive chapter **2.1.3** reactions of the intermolecular frustrated Lewis acid-base-like system $\text{DAB}^R\text{-Br}/[\text{Ge}_9\{\text{Si}(\text{TMS})_3\}_2]^{2-}$ are investigated. It is shown that the system is capable of ring-opening cyclic ethers like thf and incorporating the resulting solvent molecule fragments between the cluster and the borane entity by the formation of Ge-C and B-O bonds, respectively. Further studies focus on the influence of the type of the alkali metal counter cation A^+ on the substitution pattern of the $[\text{Ge}_9]$ core in the solid-state. In the following section the observed reactions are transferred to various nitriles, which leads to the interlinking of the cluster and boranyl moiety by imine fragments. The functionality of the imine fragment is proven by a reversible protonation of the N atom leading to a zwitterionic species, which is investigated in UV-Vis measurements and by quantum chemical calculations.

Chapter 2.2 describes the synthesis and chemistry of novel intermetalloid clusters, starting with a review of relevant literature (**2.2.1**). Subsequently, insights into the reactions of the *Zintl* phase $\text{K}_{12}\text{Ge}_{17}$ with organo-Zn complexes in liquid ammonia are provided, including the isolation of the anion $[\text{Ge}_4(\text{ZnEt})_2]^{2-}$ (**2.2.2.1**). The study discusses potential reaction paths in the solvent, which are derived from the isolation of various Zn-amides and other by-products.

Furthermore, the syntheses of 17-atom endohedral Ge clusters $[TM_2@Ge_{17}]^{n-}$ ($TM = Co, Ni$) is presented (2.2.2.2). They bridge the gap between the literature-known filled 16- and 18-atom germanide clusters, and the structures are discussed with respect to their icosahedral building fragments. In the consecutive section ion-exchange reactions are described, focusing on the introduction of Mg^{2+} counter cations to bare as well as threefold silylated $[Ge_9]$ clusters (2.2.2.3).

An illustration of the Scope and Outline of **Chapter 2** is provided in Scheme 2.

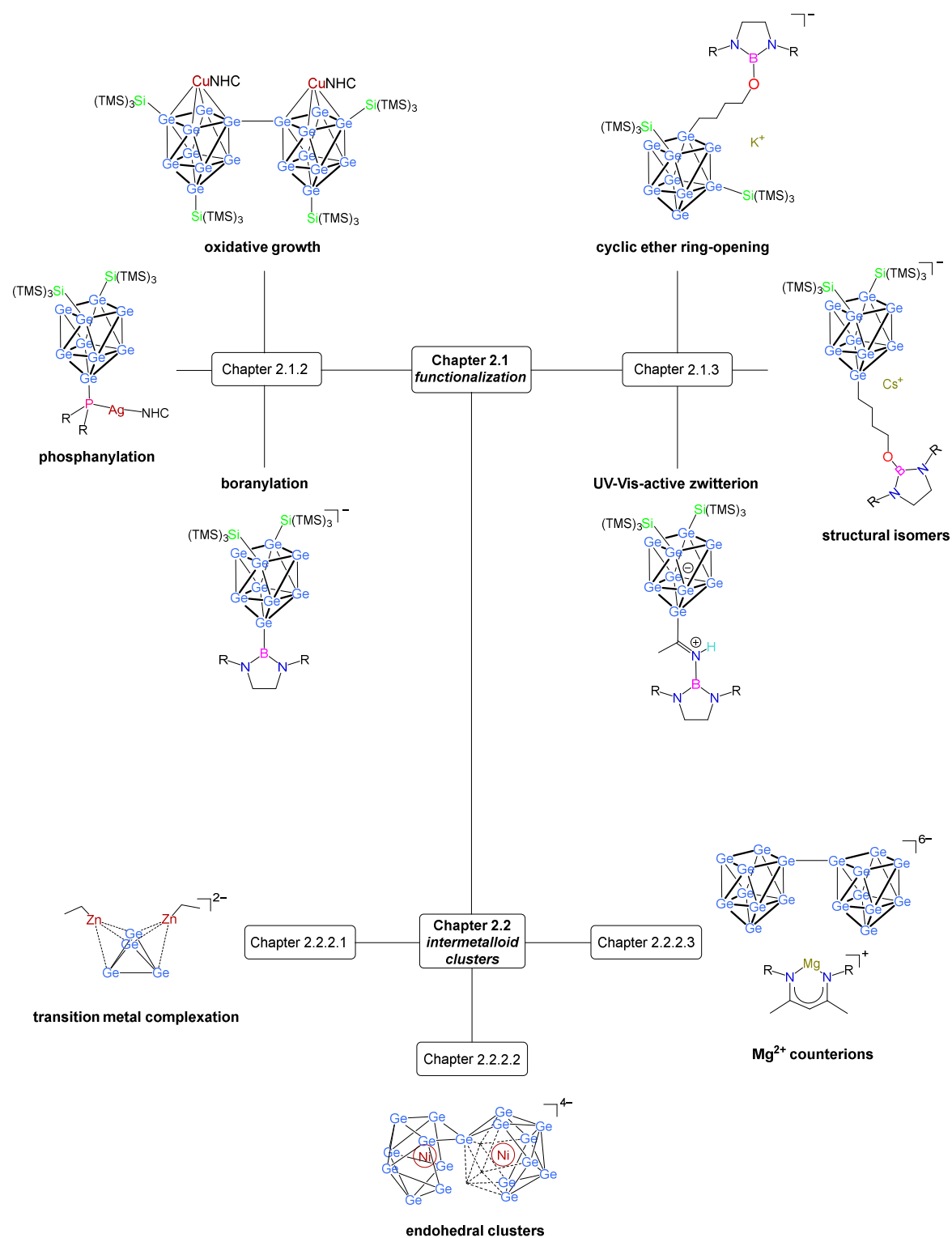
In **Chapter 3** the relevance of the obtained results is discussed, and prospects for further investigations are provided.

In **Chapter 4** the experimental details are listed, giving an overview on the utilized starting materials and chemicals, the applied working techniques, used characterization methods, and the performed quantum chemical calculations.

Chapter 5 lists the references referred to in the previous chapters.

The publications and manuscripts for publication are enclosed in **Chapter 6**, including detailed authors' contributions to the corresponding manuscripts.

Chapter 7 provides a list summarizing all peer-reviewed publications and manuscripts prepared for publication.



Scheme 2. Illustrated Outline and Scope of Chapter 2 summarizing the most important reaction products.

2 RESULTS AND DISCUSSION

The following sub-chapters discuss and summarize the results obtained for reactions of molecular $[\text{Ge}_9]$ clusters with transition metal complexes as well as main group element compounds. Details on the general experimental procedures are provided in Chapter 4, while further detailed information can be excerpted from the corresponding manuscripts and the accompanying supporting information attached in Chapter 6.

2.1 Reactions of the Cluster $[\text{Ge}_9\{\text{Si}(\text{TMS})_3\}_2]^{2-}$ with Chloro-Phosphines and Halo-Boranes

The isolation of the doubly substituted cluster ion $[\text{Ph}_2\text{Bi-Ge}_9\text{-BiPh}_2]^{2-}$ in the year 2002,^[184] in which covalent interactions between tetrel element *Zintl* clusters and main group element entities were reported for the first time, formed the basis for an emerging chemistry in this field. However, it took about one decade to elaborate an efficient and reliable synthesis strategy to yield main group element fragment substituted $[\text{Ge}_9]$ clusters.^[206] Meanwhile, the application of silylated $[\text{Ge}_9]$ clusters as a source for soluble molecular clusters is basis for most follow-up reactions in this particular field of chemistry. Exemplarily, the clusters can be interconnected to form extended structures,^[123, 220] or find application as substrate for catalytically active transition metal species.^[244] Furthermore, silylated $[\text{Ge}_9]$ anions were decorated with additional main group element fragments featuring functional groups such as alkene^[218, 225] or phosphanyl moieties.^[228-229] While unsaturated groups might allow an immobilization of the cluster on surfaces, the attachment of Lewis basic phosphanyl moieties accounts for the introduction of electron-donating groups at the cluster, which can address electrophilic organometallic fragments. In view of the cluster as a manifold Lewis base itself it seems likely that it could interact with Lewis acidic counterparts. To validate this hypothesis, the doubly silylated cluster $[\text{Ge}_9\{\text{Si}(\text{TMS})_3\}_2]^{2-}$ was reacted with several halogenated alkylboranes and halo-1,3,2-diazaborolidines, the results of which are discussed in the forthcoming chapters.

In the following chapters, synthesized compounds are successively numbered. The suffix “a” in the compound number refers to an anionic species, while counterions follow beyond as element symbols, if applicable.

2.1.1 Review of Relevant Literature

2.1.1.1 Attachment of Functional Groups at Silylated $[\text{Ge}_9]$ Clusters

The silylation of $[\text{Ge}_9]^{4-}$ clusters with hypersilyl chloride $(\text{TMS})_3\text{SiCl}$ yielding the cluster ions $[\text{Ge}_9\{\text{Si}(\text{TMS})_3\}_2]^{2-}$ and $[\text{Ge}_9\{\text{Si}(\text{TMS})_3\}_3]^-$ became the method of choice for the stabilization of the bare nonagermanide cages.^[205-206] The obtained anions are stable and well soluble synthons for the generation of mixed-functionalized clusters, thus overcoming the restrictions of the low solubility and high reductive potential of the unsubstituted cluster anions. An important step towards the functionalization of $[\text{Ge}_9]$ clusters was taken upon introducing main group element-based fragments comprising unsaturated hydrocarbon chains to the cluster core. Here, two different paths evolved comprising the reaction of a doubly silylated $[\text{Ge}_9]$ cluster with the properly modified chlorosilane $\text{Ph}_2\{(\text{CH}_2)_3\text{CH}=\text{CH}_2\}\text{SiCl}$ in a salt metathesis reaction,^[225] and the $\text{S}_{\text{N}}2$ -like reaction of the threefold silylated cluster with pentenyl bromide.^[218] The alkenyl moieties in the resulting molecules $[\text{Ge}_9\{\text{Si}(\text{TMS})_3\}_2\{\text{SiPh}_2\{(\text{CH}_2)_3\text{CH}=\text{CH}_2\}\}]^-$ (Figure 18a) and $[\text{Ge}_9\{\text{Si}(\text{TMS})_3\}_3\{(\text{CH}_2)_3\text{CH}=\text{CH}_2\}]^-$ (Figure 18b) are anticipated to act as anchor groups for the potential immobilization of the clusters on surfaces or the interconnection of different cluster species.^[172] However, until this date a double bond could not be chemically addressed.

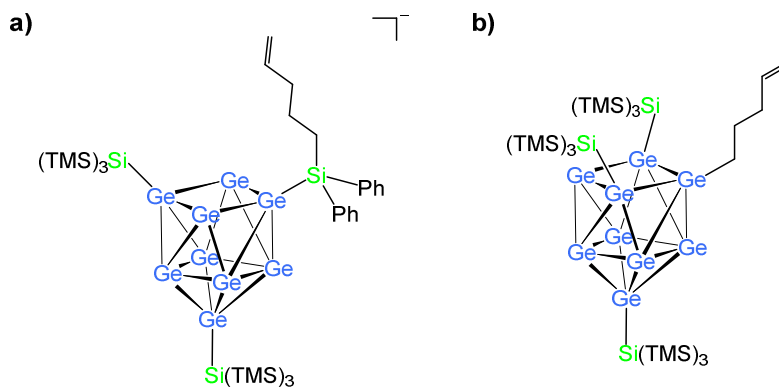


Figure 18. Representation of the alkenyl-bearing species a) $[\text{Ge}_9\{\text{Si}(\text{TMS})_3\}_2\{\text{SiPh}_2\{(\text{CH}_2)_3\text{CH}=\text{CH}_2\}\}]^-$;^[225] b) $[\text{Ge}_9\{\text{Si}(\text{TMS})_3\}_3\{(\text{CH}_2)_3\text{CH}=\text{CH}_2\}]^-$.^[218]

Generally, the introduction of functional groups to the $[\text{Ge}_9]$ cluster core is not limited to the hydrocarbon chain, but also attached main group elements themselves may act as reactive centers. The reaction of two- and threefold silylated nonagermanide clusters with chlorophosphines $R_2\text{PCl}$ yielded phosphanyl-decorated molecules as depicted in Figure 16.^[228] The attachment of a phosphorous atom featuring a free electron pair, and thus Lewis basic properties, allows for subsequent reactions at the pentel element. A consequent proof of reactivity is to offer Lewis acidic reagents such as the N-heterocyclic coinage metal-carbene complex $\text{NHC}^{\text{Dipp}}\text{TMCl}$ ($\text{TM} = \text{Cu-Au}$) to the cluster. Indeed, a direct coordination of the

$[\text{NHC}^{\text{Dipp}}\text{TM}]^+$ fragment to the P atom was reported for small organic ligands at the central pentel element ($R = \text{tBu}$; Figure 19a).^[228] The resulting charge-neutral molecules were described as zwitterionic species. In contrast, the utilization of sterically demanding substituents ($R = \text{N}^i\text{Pr}_2, \text{Mes}$) prohibited such an interaction, leading to a coordination of the coinage metal entity to a triangular face of the cluster (Figure 19b).^[212, 229]

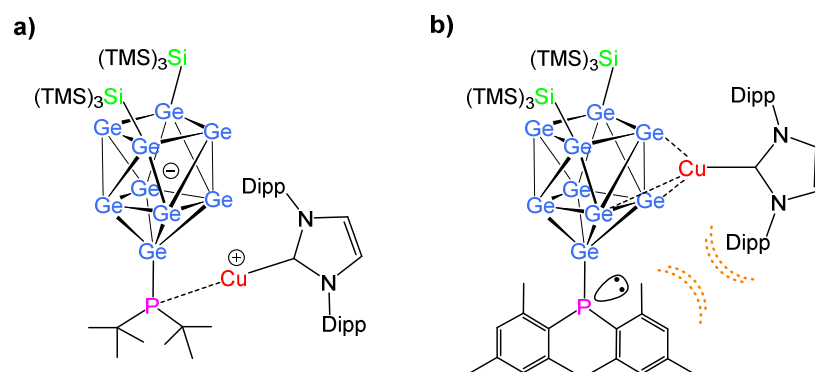
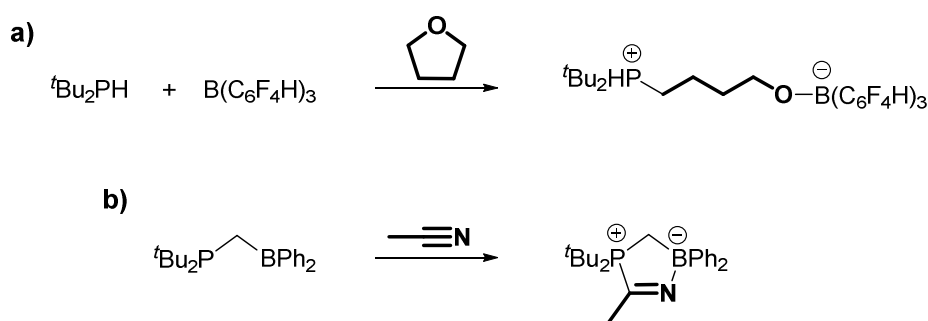


Figure 19. Different coordination modes of a Lewis acidic $[\text{NHC}^{\text{Dipp}}\text{Cu}]^+$ fragment to the monoanionic cluster $[\text{Ge}_9\{\text{Si}(\text{TMS})_3\}_2\text{PR}_2]^-$ ($R = \text{tBu}, \text{Mes}$). a) Direct coordination of the Lewis acidic entity to the nucleophilic P atom for the small organic ligand tBu, causing the formation of a zwitterionic species;^[228] b) coordination of the Cu-carbene to a triangular face of the $[\text{Ge}_9]$ cluster for the aromatic Mes ligand due to steric repulsion (indicated by dashed orange lines).^[212, 229]

While the attachment of nucleophilic moieties to the $[\text{Ge}_9]$ cluster is a rare example for the introduction of reactive ligands to the cluster, at the same time the question arises whether Lewis acidic moieties could react with the sevenfold Lewis base $[\text{Ge}_9\{\text{Si}(\text{TMS})_3\}_2]^{2-}$ in a controlled manner. However, so far solely the TI-capped threefold silylated cluster has been isolated,^[216] while preliminary studies focusing on the application of electron deficient boranyls did not lead to unequivocal results.^[212] One prospect of generating cluster species with discrete Ge-B *exo*-bonds is the potential formation of Lewis acid-base pairs, which might show interesting properties concerning their reactivity.

2.1.1.2 Principles of Lewis Acid-Base Systems

A century ago, G. N. Lewis expanded the typical proton-centered acid-base concept of Brønsted by observing that also other electron pair acceptors than H^+ ions are prone to interact with electron pair donors.^[249-250] Thus, today the terms Lewis acid and Lewis base refer to electron accepting and electron donating entities, respectively. The interaction of the energetically low-lying LUMO at the acceptor and high-lying HOMO at the donor allows for the formation of a covalent bond between the centers, yielding a Lewis acid-base adduct.^[251] However, an adduct formation can be precluded by choosing sterically demanding ligands at the respective centers. As key example, no reaction between PMe_3 and $B(C_6F_5)_3$ in solution is observed.^[252] Such sterically hindered reaction systems are referred to frustrated Lewis pairs (FLP).^[253] Besides the aforementioned intermolecular B/P system also intramolecular FLPs such as $Mes_2P-(CH_2)_2-B(C_6F_5)_2$ exist, combining spatially separated Lewis-active centers in one single molecule.^[253] Even though FLPs cannot form classical Lewis acid-base adducts, they tend to react with a number of substances ranging from gasses like H_2 , NO , or CO_2 to olefins, isocyanates, and nitriles (among others).^[251, 254-255] In several cases FLPs are capable of interacting with solvent molecules, exemplarily leading to a cyclic ether ring-opening (Scheme 3a)^[256] or the insertion of imine entities between the active centers (Scheme 3b).^[257]



Scheme 3. Reactions of B/P FLP systems leading to a) a cyclic ether ring-opening reaction mediated by an intermolecular FLP,^[256] and b) a cyclization upon imine insertion at an intramolecular FLP.^[257] The incorporated organic fragments of the initially utilized molecules thf and MeCN are illustrated with bold lines for clarity.

The application of transition metal-free FLP systems is of special interest regarding the high production costs of alternative metal catalysts as well as in terms of the production of heavy metal-free pharmaceuticals.^[254, 258] Over the years, multiple element combinations have been tested for their activity in FLP-based reactions, however no B/Ge system has been reported so far. The only example given is a bis-amido germylene acid-base pair, which forms an adduct in the ground state and thus is not considered as a typical FLP, even though a C=O bond activation of ketones is described.^[259] An attachment of boranyl groups at a $[Ge_9]$ cage would potentially generate a FLP as the cluster core features several lone pair-bearing vertex atoms. These electron pairs are embedded into a rather rigid shell, thus most likely preventing an instantaneous adduct formation.

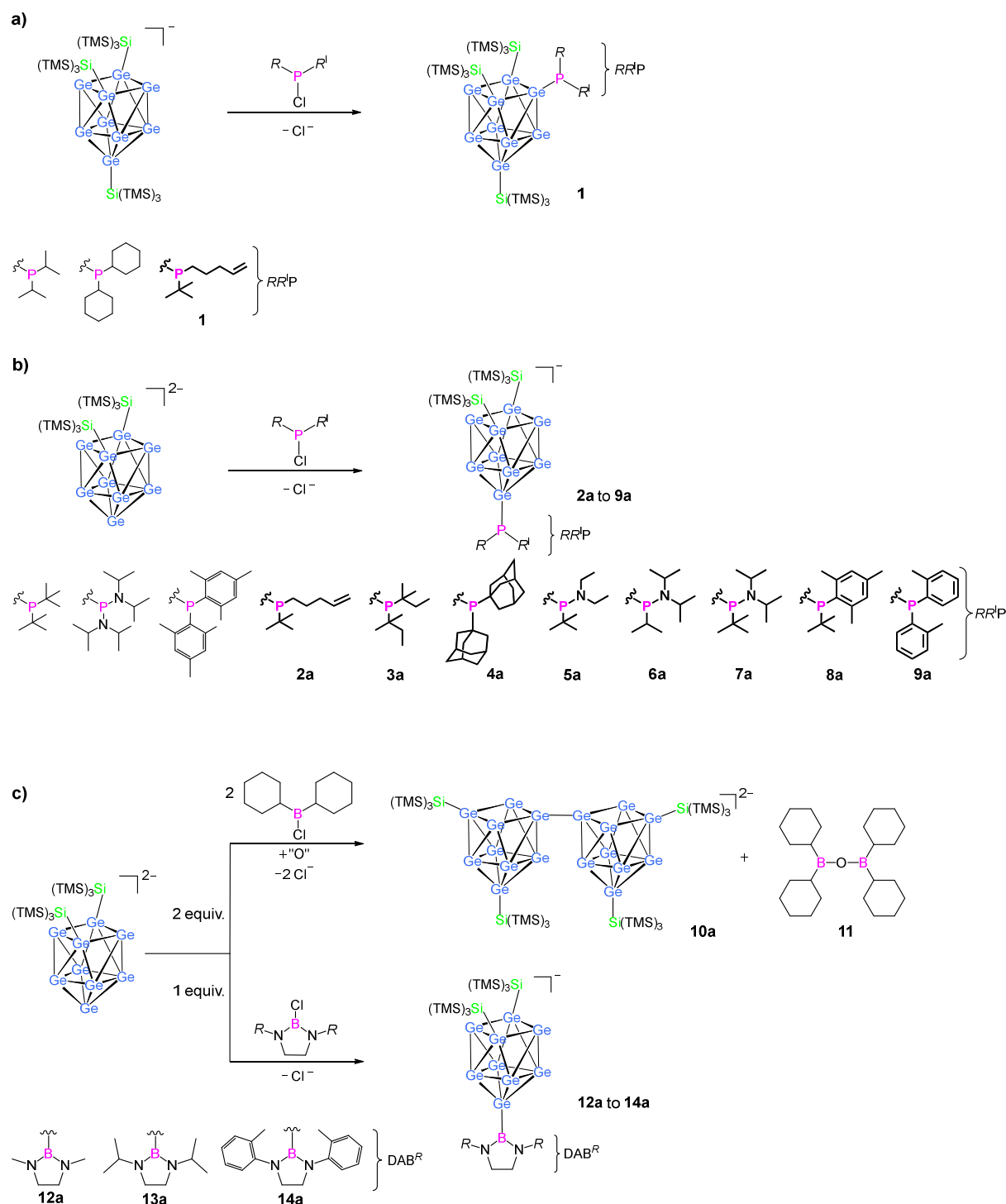
2.1.2 Reactions of Silylated [Ge₉] Clusters towards Chlorophosphines and Chloroboranes

- Chapter 6.1:** C. Wallach,[‡] F. S. Geitner,[‡] W. Klein and T. F. Fässler, Enhancing the Variability of [Ge₉] Cluster Chemistry through Phosphine Functionalization, *Chem. Eur. J.* **2019**, *25*, 12349.
- Chapter 6.2:** C. Wallach, W. Klein and T. F. Fässler, Oxidative Coupling of Silylated Nonagermanide Clusters, *Chem. Commun.* **2022**, *58*, 5486.
- Chapter 6.3:** C. Wallach,[‡] F. S. Geitner,[‡] A. J. Karttunen and T. F. Fässler, Boranyl-Functionalized [Ge₉] Clusters: Providing the Idea of Intramolecular Ge/B Frustrated Lewis Pairs, *Angew. Chem. Int. Ed.* **2021**, *60*, 2648.
- Chapter 6.4:** C. Wallach, W. Klein and T. F. Fässler, Crystal Structure of (1,4,7,10,13,16-hexaoxacyclooctadecane-κ⁶O₆) potassium (2-methylphenylamino)ethyl-2-methylphenylamide ammoniate (1/3.5), [K(18-crown-6)](o-CH₃C₆H₄)NH(CH₂)₂N(o-CH₃C₆H₄) · 3.5 NH₃, C₂₈H_{53.5}KN_{5.5}O₆, single crystal structure communication submitted for publication in *Z. Kristallogr., New Cryst. Struct.*

[‡]: authors contributed equally to this work.

Within this chapter the results of the reactions of silylated [Ge₉] clusters with chlorophosphines as well as chloroboranes are summarized. The attachment of phosphanyl fragments bearing an alkene moiety accounts for an alternative way to introduce functional groups to the cluster, and indirect insights into the molecular structure of the species NHC^{Dipp}Ag[Ge₉{Si(TMS)₃}₂PRR^l] (*R*, *R*^l = alkyl, alkenyl, aryl, aminoalkyl) were obtained via ³¹P-^{107/109}Ag spin-spin coupling NMR spectroscopic investigations. In comparable reactions chloroboranes of differing Lewis acidity were reacted with the twofold silylated cluster. While reactions with the highly Lewis acidic chloroborane Cy₂BCl led to an oxidative coupling of two silylated clusters yielding the dimer [Ge₉{Si(TMS)₃}₂]₂²⁻, the application of electron-rich N-heterocyclic chloro-1,3,2-diazaborolidines DAB^R-Cl (*R* = alkyl, aryl) caused a direct boranyl-substitution of the [Ge₉] core in the cluster [Ge₉{Si(TMS)₃}₂DAB^R]⁻.

A schematic representation of the performed experiments and the obtained cluster species is provided in Scheme 4.^[260]



Scheme 4. Summary of the reactions of silylated $[\text{Ge}_9]$ clusters towards chlorophosphines and chloroboranes. a) Formation of the alkenyl-substituted cluster $[\text{Ge}_9\{\text{Si}(\text{TMS})_3\}_3\{\text{P}^i\text{Bu}\{(\text{CH}_2)_3\text{CH}=\text{CH}_2\}\}]^-$ (**1**); b) synthesis of variously phosphanylated monoanionic clusters $[\text{Ge}_9\{\text{Si}(\text{TMS})_3\}_3\{\text{P}^i\text{RR}'\}]^-$ (**2a to 9a**); c) formation of the dimer $[\text{Ge}_9\{\text{Si}(\text{TMS})_3\}_2]^{2-}$ (**10a**) and the boryl ether $\text{Cy}_2\text{B}-\text{O}-\text{BCy}_2$ (**11**), as well as the boranyl-functionalized clusters $[\text{Ge}_9\{\text{Si}(\text{TMS})_3\}_2\text{DAB}^R]^-$ (**12a to 14a**). In a) and b) newly introduced phosphanyl fragments are highlighted in bold, in contrast to fragments which have already been published.^[212, 228-229, 260]

Reactions towards chlorophosphines

Phosphanyl moieties attached at the $[\text{Ge}_9]$ cluster can be regarded as functional groups due to their Lewis basic properties. Chlorophosphines $\text{RR}'\text{PCI}$ are readily prepared by the reaction of RPCI_2 with e.g. a Grignard solution $\text{R}'\text{MgX}$ ($\text{X} = \text{Cl}, \text{Br}$).^[261-262] The successful synthesis of the novel chlorophosphine ${}^t\text{Bu}\{(\text{CH}_2)_3\text{CH}=\text{CH}_2\}\text{PCI}$ allowed the phosphanyl-functionalization of the threefold silylated cluster, yielding the alkenyl-decorated species $[\text{Ge}_9\{\text{Si}(\text{TMS})_3\}_3\{\text{P}{}^t\text{Bu}\{(\text{CH}_2)_3\text{CH}=\text{CH}_2\}\}]$ (**1**, Scheme 4a).^[260] Thus, an alternative route to the previously reported introduction of unsaturated hydrocarbon chains using chlorosilanes or bromoalkenes (Chapter 2.1.1.1) is presented.^[218, 225] The molecular structure of compound **1** was determined by single crystal diffraction analysis. The $[\text{Ge}_9]$ core in **1** is best described as a slightly distorted C_{2v} -symmetric mono-capped square antiprism, which comprises one hypersilyl group at the capping Ge atom as well as two further $[\text{Si}(\text{TMS})_3]^+$ fragments at the open square plane of the cluster, to which also the phosphanyl fragment is bound (Figure 20a).

In a similar manner the twofold silylated cluster reacts with chlorophosphines forming the phosphanyl-substituted monoanions $[\text{Ge}_9\{\text{Si}(\text{TMS})_3\}_2\text{PRR}'^-]$ (**2a** to **9a**, Scheme 4b). The attachment of a P-comprising fragment to the silylated $[\text{Ge}_9]$ cluster was spectroscopically evidenced by a shift of the silyl group protons from formerly $\delta = 0.17$ ppm ($\text{thf-}d_8$) for the twofold silylated cluster to approximately $\delta = 0.25$ ppm for anions **2a** to **9a**. Furthermore, all synthesized monoanions in Scheme 4b were characterized by ESI-MS, and Figure 20b exemplarily shows the mass spectrum of the cluster **2a**.

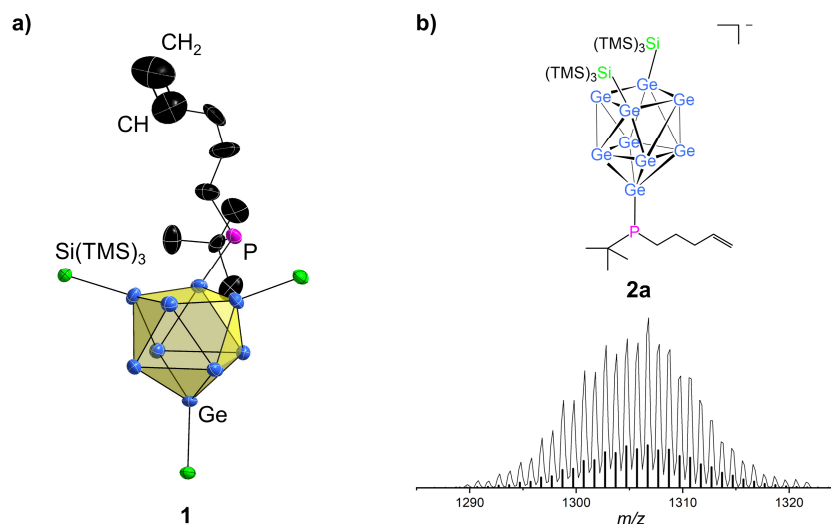
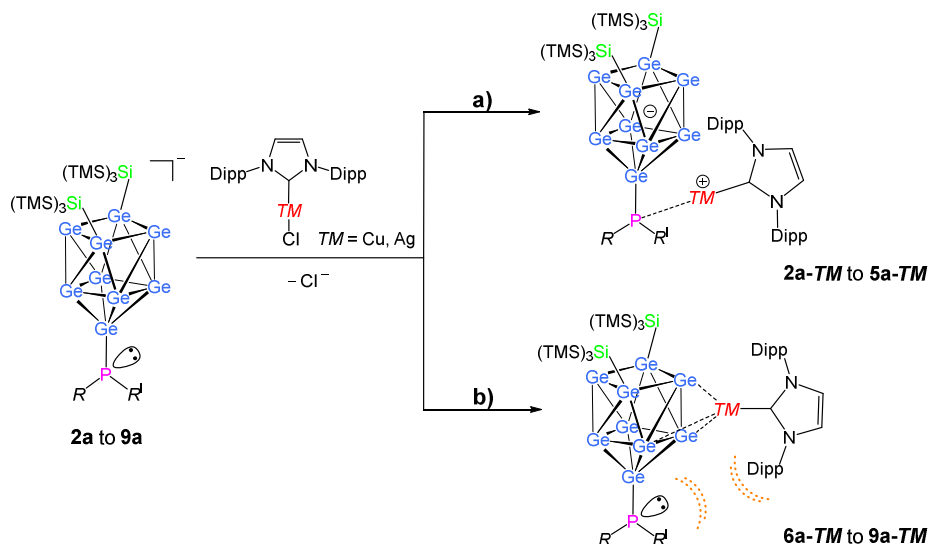


Figure 20. a) Molecular structure of compound **1**. All ellipsoids are presented at a 50 % probability level. Solely the central Si atoms of the hypersilyl groups are shown, while hydrogen atoms are omitted. b) Schematic illustration of the ion **2a** with the corresponding ESI-MS spectrum (m/z 1306.8, negative-ion mode). The calculated isotope pattern is presented as black bars.

As outlined before, the Lewis basic P center at the cluster is prone to interact with electrophilic coinage metal NHC-complexes. Therefore, anions **2a** to **9a** were transferred into the coinage metal-carbene adducts by reacting them with the precursor $\text{NHC}^{\text{Dipp}}\text{TMCl}$ ($\text{TM} = \text{Cu}, \text{Ag}$) according to Scheme 5, yielding the adducts **2a-TM** to **9a-TM**.^[260] In analogy to the literature, sterically less hindered phosphanyl groups allow a direct coordination of the TM to the P atom, while bigger ligands result in a η^3 -coordination of the TM to the $[\text{Ge}_9]$ cluster.^[228-229]



Scheme 5. Formation of the coinage metal-carbene adducts **2a-TM** to **9a-TM** in dependency of the steric impact of the organic ligand at the P atom: a) direct coordination of the TM to the P atom for small ligands R ; b) coordination of the TM to a trigonal cluster face for sterically demanding ligands R .

The formed Cu- and Ag-carbene adducts were characterized by NMR spectroscopy (^1H , ^{13}C , ^{29}Si , ^{31}P), and the observation of $^1J(^{31}\text{P}-^{107}\text{Ag}/^{109}\text{Ag})$ spin-spin coupling in **2a-Ag** to **5a-Ag** indirectly allows to derive the coordination type of the TM to the monoanionic cluster (Table 1). In contrast, compounds **6a-Ag** to **9a-Ag** show singlets in the ^{31}P NMR spectra. Another hint to the substitution pattern can be obtained from the shift of the TMS group protons in the ^1H NMR spectra. While a coordination of the TM -carbene to the phosphine hardly influences the bound silyl groups of the monoanions ($\delta \approx 0.25$ ppm), a distinct up-field shift is monitored for a coordination of the TM -carbene to a triangular cluster face (Table 1).

Table 1. Summary of $^1J(^{31}\text{P}-^{107}\text{Ag}/^{109}\text{Ag})$ spin-spin coupling constants and ^1H NMR shifts (thf-d_8) of the TMS group protons of the compounds **2a-Ag** to **9a-Ag**.

	2a-Ag	3a-Ag	4a-Ag	5a-Ag	6a-Ag	7a-Ag	8a-Ag	9a-Ag
$^1J(\text{P-Ag})$ [Hz]	258.7	406.0	422.5	207.8	-	-	-	-
^1H NMR shift of TMS [ppm]	0.23	0.27	0.28	0.21	0.17	0.17	0.17	0.18

Reactions towards chloroboranes

Inspired by the versatile chemistry of chlorophosphines, the reactivity of analogous alkyl chloroboranes towards the twofold silylated cluster was investigated (Scheme 4c). The highly electrophilic alkyl chloroborane Cy_2BCl was added to a toluene solution of the cluster $[\text{Ge}_9\{\text{Si}(\text{TMS})_3\}_2]^{2-}$ causing its dimerization yielding the dianion $[\text{Ge}_9\{\text{Si}(\text{TMS})_3\}_2]_2^{2-}$ (**10a**). Anion **10a** was monitored by ESI-MS spectroscopy (monoanion, m/z 2336.0) and in the solid-state in the Cu-carbene adduct $\{\text{NHC}^{\text{iPr}}\text{Cu}[\text{Ge}_9\{\text{Si}(\text{TMS})_3\}_2]\}_2$ (**10a-Cu^{iPr}**; Figure 21a). The Cu-carbene adduct was prepared to enhance the crystallization of the ion **10a**, which is an oftentimes applied method.^[211, 221, 228-229, 243, 245] Compound **10a-Cu^{iPr}** comprises two $\{\text{NHC}^{\text{iPr}}\text{Cu}[\text{Ge}_9\{\text{Si}(\text{TMS})_3\}_2]\}$ fragments interconnected via an *exo*-Ge-Ge bond, which causes a Raman band at $\tilde{\nu} = 283 \text{ cm}^{-1}$ (single crystalline sample, Figure 21b).^[263] The *exo*-bond is 2.4259(8) Å long, which is in agreement to values observed for non-functionalized $[\text{Ge}_9]$ dimers and polymers.^[95, 169-171, 183, 264] The shape of the $[\text{Ge}_9]$ clusters is best described as slightly distorted C_{2v} -symmetric mono-capped square antiprisms, which are substituted by two hypersilyl groups and an additional cluster entity. The $[\text{NHC}^{\text{iPr}}\text{Cu}]^+$ fragment η^4 -coordinates to the pseudo-square plane of the antiprism as described before.^[245]

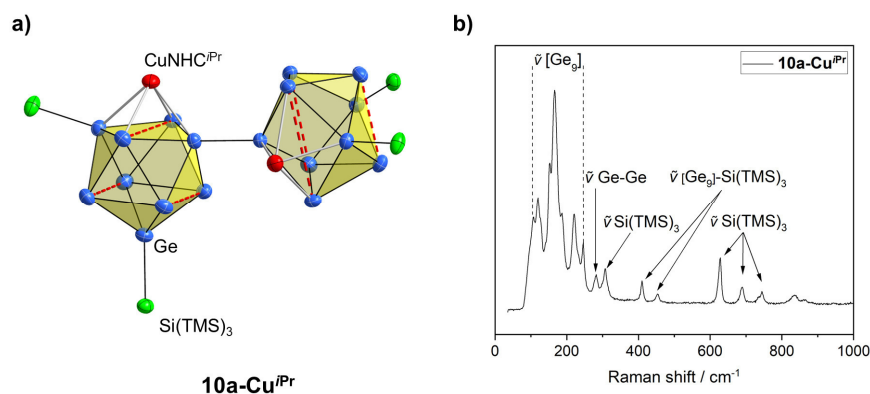


Figure 21. a) Molecular structure of **10a-Cu^{iPr}**. All ellipsoids are presented at a 50 % probability level. For clarity, solely the central Si atoms of the hypersilyl groups are shown and the carbene ligands as well as hydrogen atoms are omitted. Trigonal prism bases are indicated by dashed red lines. b) Raman spectrum of a single crystal of **10a-Cu^{iPr}** (excitation: 785 nm, 1s/frame, power: 1 mW on sample).

The oxidative coupling of two silylated clusters most probably is mediated by the chloroborane Cy_2BCl , which acts as an oxide-scavenger in the reaction. This hypothesis was corroborated by the isolation of the side product $\text{Cy}_2\text{B-O-BCy}_2$ (**11**), which was characterized by ^{11}B NMR spectroscopy and single crystal diffraction analysis in accordance to published data.^[265-266] However, neither could the source of oxygen be unequivocally identified, nor did the addition of stoichiometric amounts of water or the utilization of oxygenated solvents lead to increased yields of anion **10a**. Remarkably, the formation of compound **11** is also observed for the substitution of the silylated cluster by K_4Ge_9 or KC_8 . Thus, the formation of KCl is supposed to be an important driver during the reaction.

In reactions of the twofold silylated cluster with the less Lewis-acidic N-heterocyclic chloro-1,3,2-diazaborolidines $\text{DAB}^R\text{-Cl}$ ($R = \text{Me}, ^i\text{Pr}, o\text{-tol}$) a boranyl-functionalization of the $[\text{Ge}_9]$ cluster was achieved. The synthesized monoanions $[\text{Ge}_9\{\text{Si}(\text{TMS})_3\}_2\text{DAB}^R]^-$ (**12a** to **14a**) reveal covalent Ge-B *exo*-bonds (Scheme 4c). The controlled reactivity of the $\text{DAB}^R\text{-Cl}$ precursors most probably is due to π -backbonding induced by the N atoms in proximity to the central B atom, thereby decreasing its electrophilicity.^[267] Reactions with the bulky diazaborolidine $\text{DAB}^{\text{Mes}}\text{-Cl}$ did not lead to any observable reaction of the precursors even at elevated temperature, thus hinting for a steric limitation of the reaction. The clusters **12a** to **14a** were characterized by NMR spectroscopy and ESI-MS spectrometry. The anions were transferred into the Cu-carbene adducts for crystallization, however according to ^1H NMR spectroscopic data the reaction of **12a** with $\text{NHC}^{\text{Dipp}}\text{CuCl}$ yields the doubly Cu-coordinated complex $[\text{NHC}^{\text{Dipp}}\text{Cu}]_2[\text{Ge}_9\{\text{Si}(\text{TMS})_3\}_2]$ upon cleaving the boranyl ligand.^[243] Nevertheless, single crystals of $\text{NHC}^{\text{Dipp}}\text{Cu}[\text{Ge}_9\{\text{Si}(\text{TMS})_3\}_2\text{DAB}^R]$ (**13a-Cu** and **14a-Cu**; Figure 22) were obtained. The structure determination corroborated the covalent attachment of boranyl groups at the $[\text{Ge}_9]$ cluster. The Ge-B bond lengths are 2.063(5) Å and 2.055(5) Å, respectively, in agreement to published data.^[268-270] The shape of the $[\text{Ge}_9]$ clusters is best described as slightly distorted tricapped trigonal prisms, with each capping Ge vertex bearing either a hypersilyl ligand or the attached boranyl moiety.

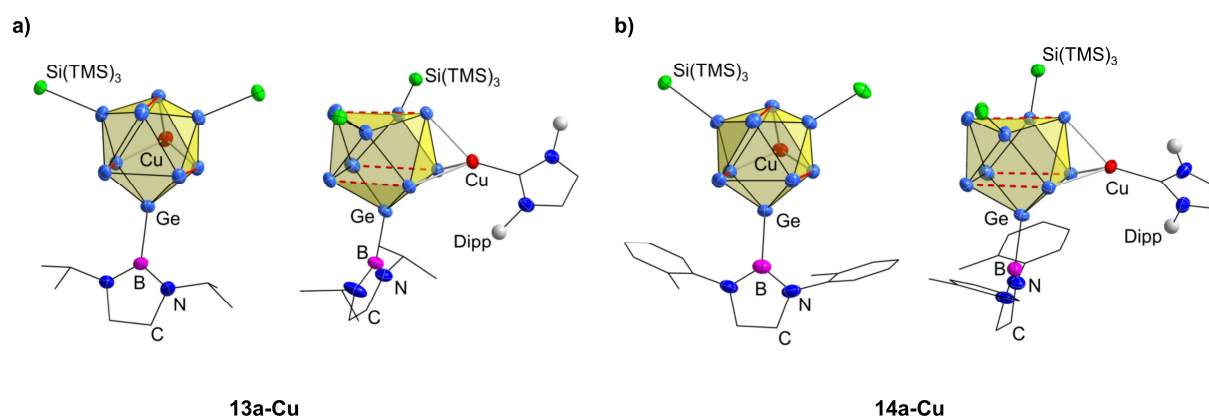


Figure 22. Molecular structures of a) **13a-Cu** and b) **14a-Cu** in two perspectives tilted by approximately 90°. All ellipsoids are presented at a 50 % probability level. For clarity, only the central Si atoms of the hypersilyl groups are shown, hydrocarbon fragments are presented as wire-sticks, and hydrogen atoms are omitted. The NHC^{Dipp} ligands are either completely omitted or the Dipp wingtip substituents are illustrated by grey spheres. Trigonal prism bases are indicated by red dashed lines.

Quantum chemical calculations for the anions **13a** and **14a** reveal that the HOMO and the LUMO both are located at the $[\text{Ge}_9]$ cluster core with an energy gap of 3.8 eV (Figure 23a). Boron-centered orbitals appear above LUMO+4. For the hypothetical anion with the stronger Lewis acidic group $[\text{Cy}_2\text{B}]^+$ the LUMO is however boron-centered, and the HOMO-LUMO gap shrinks to 3.4 eV (Figure 23b). However, since the application of Cy_2BCl to the twofold silylated cluster mediates its dimerization, an experimental preparation of the latter species was not

possible. According to the calculations, the generation of intramolecular frustrated Lewis acid-base pairs consisting of a $[\text{Ge}_9]$ moiety and a boranyl substituent in principle is possible. Nevertheless, it requires a well-balanced choice of the boranyl ligand to achieve a boron-centered LUMO, while the accompanied electrophilicity of the reactant should not induce side-reactions.

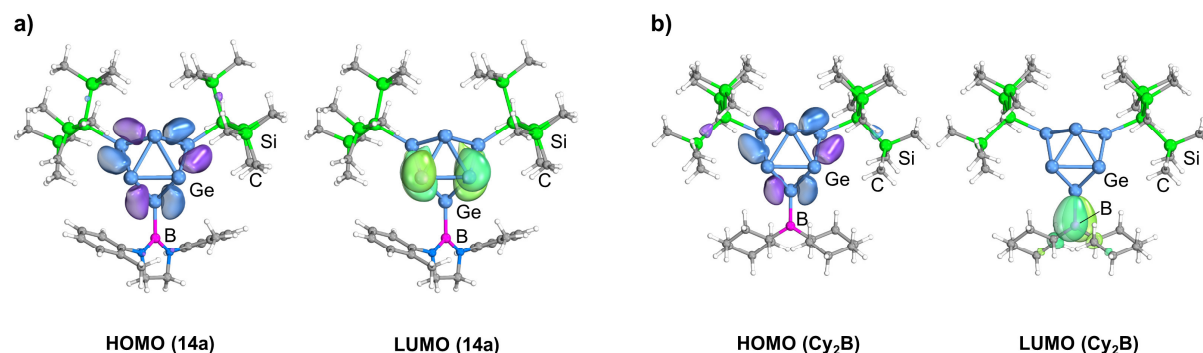


Figure 23. HOMO and LUMO of a) the anion **14a** and b) the theoretical species $[\text{Ge}_9\{\text{Si}(\text{TMS})_3\}_2\text{BCy}_2]^-$. Molecular orbital plots are illustrated in such way that 50 % of the density is enclosed within the isosurface, corresponding to an isovalue of 0.04 a.u.

Due to the successful formation of Ge-B single bonds a multiple boranyl-decoration of the $[\text{Ge}_9]$ cluster becomes feasible starting from the bare $[\text{Ge}_9]^{4-}$ ions. A variety of halo-1,3,2-diazaborolidines was tested aiming for a functionalization of the bare nonagermanide cluster. Even though no substituted cluster species could be isolated from the experiments, the amide $[\text{K}(\text{18-crown-6})](\text{o-CH}_3\text{C}_6\text{H}_4)\text{NH}(\text{CH}_2)_2\text{N}(\text{o-CH}_3\text{C}_6\text{H}_4) \cdot 3.5 \text{NH}_3$ was obtained from the reaction of K_4Ge_9 and a halo-diazaborolidine featuring *o*-tol wingtip substituents in liquid ammonia. Most probably the amide formed from contained trace impurities of the amine N^1, N^2 -di(*o*- $\text{CH}_3\text{C}_6\text{H}_4$)ethylene-1,2-diamine, which serves as reactant in the synthesis of the respective halo-diazaborolidine. Generally, amide formation is an oftentimes observed process in polar solvents like liquid ammonia or ethylenediamine (Chapter 2.2.2.1).^[118, 121, 134, 213, 271] A detailed presentation of the amide's crystal structure is enclosed in Chapter 6.4.

2.1.3 Intermolecular Frustrated Lewis Pairs of the Cluster $[\text{Ge}_9\{\text{Si}(\text{TMS})_3\}_2]^{2-}$ and Bromo-1,3,2-diazaborolidines or Bromo-1,3,2-diazaboroles

- Chapter 6.5:** C. Wallach,[‡] F. S. Geitner [‡] and T. F. Fässler, FLP-type Nitrile Activation and Cyclic Ether Ring-Opening by Halo-Borane Nonagermanide-Cluster Lewis Acid–Base Pairs, *Chem. Sci.* **2021**, *12*, 6969.
- Chapter 6.6:** C. Wallach,[‡] D. M. Dankert [‡] and T. F. Fässler, Counterion Related Structural Isomerism in the Nonagermanide Clusters $A[\text{Ge}_9\{\text{Si}(\text{TMS})_3\}_2(\text{CH}_2)_4\text{O-DAB}^{\text{Mes}}]$ ($A = \text{K}, \text{Cs}$), manuscript for publication.
- Chapter 6.7:** C. Wallach, Y. Selic, F. S. Geitner, W. Klein, A. J. Karttunen and T. F. Fässler, Charge-Transfer Processes in Functionalized $[\text{Ge}_9]$ Clusters Based on the Reversible Formation of a Zwitterion, manuscript for publication.

[‡]: authors contributed equally to this work.

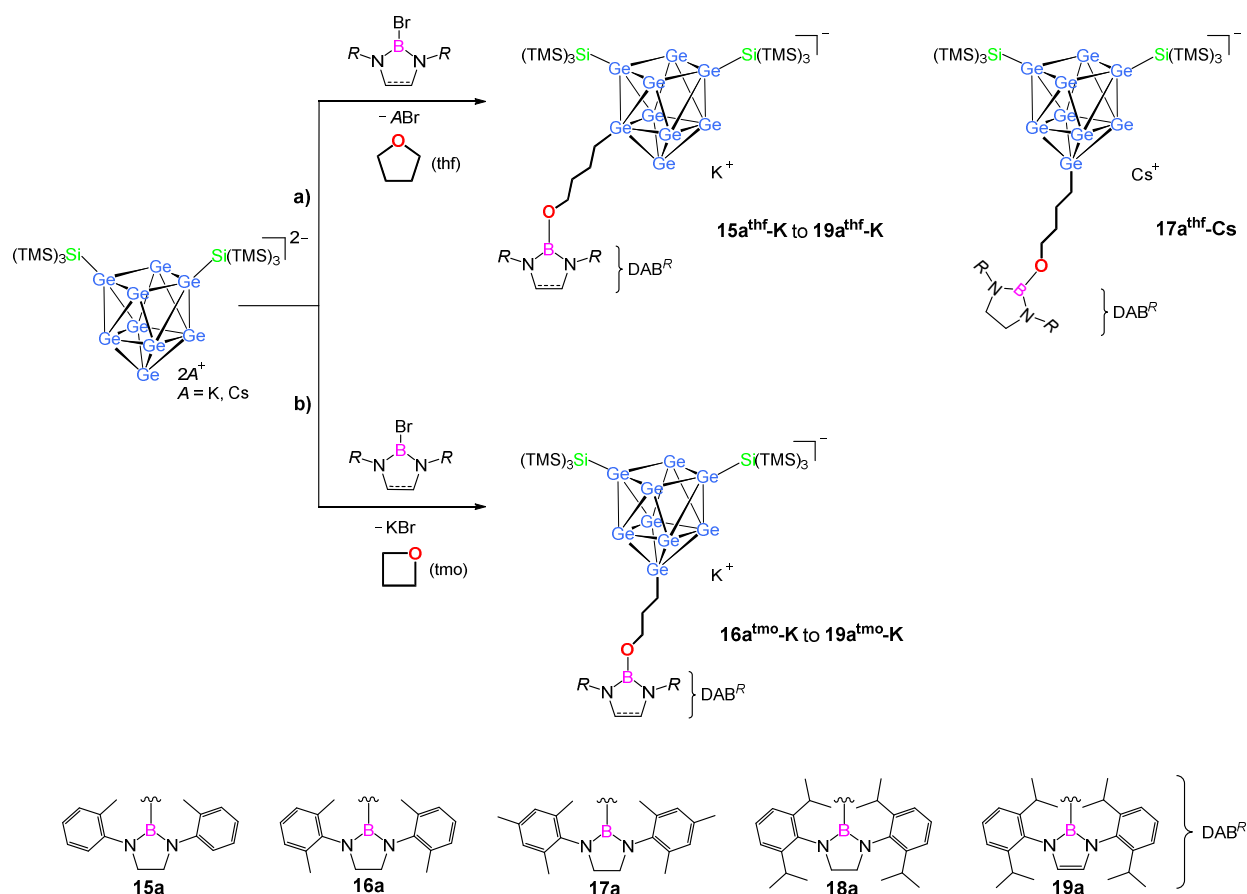
The reactions of the cluster $[\text{Ge}_9\{\text{Si}(\text{TMS})_3\}_2]^{2-}$ with alkylated chloroboranes and chloro-1,3,2-diazaborolidines discussed so far revealed that the electrophilicity of the boron center is a decisive factor for the formation of either oxidatively-coupled clusters or boranyl-decorated clusters, respectively. While the variation of organic substituents at the B atom from pure hydrocarbon fragments to amine entities implies a significant change in the electronic properties due to the introduction of backdonating atoms, a more subtle way is exchanging the type of halide. As a general means to evaluate the Lewis acidity of haloboranes the principle of hard and soft acids and bases (HSAB) can be applied.^[272-273] Consequently, chloro-1,3,2-diazaborolidines show a reduced electrophilicity of the boron center in comparison to the respective bromo-species, since the orbital overlap between the empty orbital at the B atom and the filled bromide orbitals is reduced. A relative quantification of this trend is possible by determining the acceptor number according to the *Gutmann-Beckett* method, which relies on measuring the ³¹P NMR shift of $\text{Et}_3\text{P}=\text{O}$ upon addition of a Lewis acid, validating the HSAB concept.^[274-276]

Within the following section reactions of the twofold silylated cluster towards bromo-1,3,2-diazaborolidines $\text{DAB}^R\text{-Br}$ and the bromo-1,3,2-diazaborole $\text{DAB}(\text{II})^{\text{Dipp}}\text{-Br}$ [(II): unsaturated backbone] are described. The two molecules form intermolecular frustrated Lewis pairs, leading to the incorporation of solvent molecule fragments between the cluster and the boranyl species. Thus, ring-opened fragments of cyclic ethers like tmo or thf ($n = 3$ or 4) were integrated in the monoanionic species $[\text{Ge}_9\{\text{Si}(\text{TMS})_3\}_2(\text{CH}_2)_n\text{O-DAB}^R]^-$ ($R = o\text{-tol}, o\text{-xyl}, \text{Mes}$,

Dipp), whereas the application of various nitriles led to the formation of imine-bearing ions $[\text{Ge}_9\{\text{Si}(\text{TMS})_3\}_2\{\text{R}'\text{C}=\text{N}\}\text{-DAB}^{\text{R}}]^-$ $[\text{DAB}(\text{II})^{\text{Dipp}}]$; $\text{R} = o\text{-tol, Mes}$; $\text{R}' = \text{alkyl, alkenyl, aryl}$]. In comprehensive studies the influence of the alkali metal counterion on the arrangement of substituents at the $[\text{Ge}_9]$ cluster was investigated, uncovering two structural isomers of $\text{A}[\text{Ge}_9\{\text{Si}(\text{TMS})_3\}_2(\text{CH}_2)_4\text{O-DAB}^{\text{Mes}}]$ ($\text{A} = \text{K, Cs}$). Furthermore, the introduced imine moieties are prone to protonation yielding the intensively green colored zwitterionic complex $[\text{Ge}_9\{\text{Si}(\text{TMS})_3\}_2\{\text{MeC}=\text{N}(\text{H})\}\text{-DAB}(\text{II})^{\text{Dipp}}]$, which was analyzed by UV-Vis measurements and quantum chemical calculations.

Cyclic ether ring-opening

A schematic representation of the performed experiments yielding cluster species with incorporated ring-opened ether fragments is provided in Scheme 6.

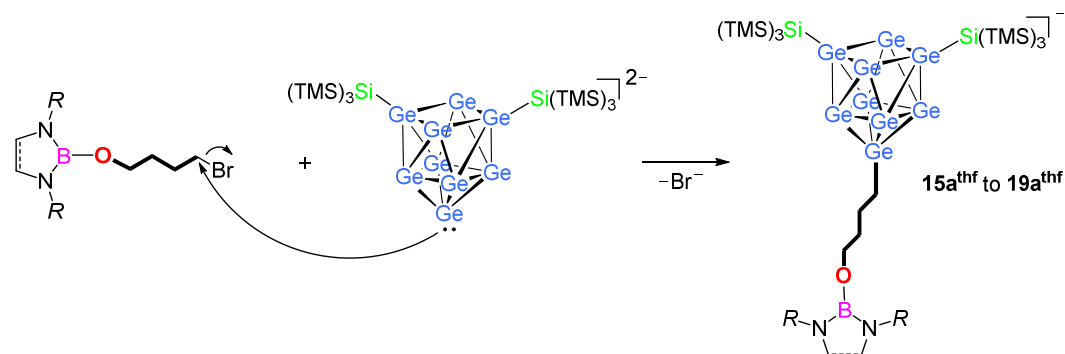


Scheme 6. Summary of the reactions of the twofold silylated $[\text{Ge}_9]$ cluster towards bromoboranes in cyclic ethers. a) Formation of the clusters $A[\text{Ge}_9\{\text{Si}(\text{TMS})_3\}_2(\text{CH}_2)_2\text{O-DAB}^R]$ (**15a^{thf-K}** to **19a^{thf-K}** and **17a^{thf-Cs}**) comprising a ring-opened tetrahydrofuran (thf) moiety and different counter cations; b) formation of the clusters $K[\text{Ge}_9\{\text{Si}(\text{TMS})_3\}_2(\text{CH}_2)_3\text{O-DAB}^R]$ (**16a^{tmo-K}** to **19a^{tmo-K}**) comprising a ring-opened trimethylene oxide (tmo) moiety.

Reactions of the precursor $A_2[\text{Ge}_9\{\text{Si}(\text{TMS})_3\}_2]$ ($A = \text{K}, \text{Cs}$) with bromo-1,3,2-diazaborolidines $\text{DAB}^R\text{-Br}$ or the bromo-1,3,2-diazaborole $\text{DAB}(\text{II})^{\text{Dipp}}\text{-Br}$ in the cyclic ethers tetrahydrofurane (thf, Scheme 6a) or trimethylene oxide (tmo, Scheme 6b) yield cluster species with incorporated ring-opened ether fragments. A variety of wingtip substituents at the heterocyclic ring was tested, resulting in the formation of the compounds $A[\text{Ge}_9\{\text{Si}(\text{TMS})_3\}_2(\text{CH}_2)_4\text{O-DAB}^R]$ (**15a^{thf-K}** to **19a^{thf-K}** and **17a^{thf-Cs}**) and $K[\text{Ge}_9\{\text{Si}(\text{TMS})_3\}_2(\text{CH}_2)_3\text{O-DAB}^R]$ (**16a^{tmo-K}** to **19a^{tmo-K}**) for reactions performed in thf and tmo, respectively.

Reactivity tests of the used bromoboranes towards thf in absence of any cluster species yielded the ring-opened species $\text{DAB}^R\text{-O}(\text{CH}_2)_4\text{-Br}$ according to ^1H and ^{11}B NMR spectroscopic investigations. Cyclic ether ring-opening reactions have been reported for boron-containing species before, which most likely rely on the formation of a four-membered cyclic transition

state, and a subsequent σ -bond metathesis reaction.^[277-279] Consequently, the formation of the cluster species in Scheme 6 is best described as a nucleophilic attack of the cluster at the electrophilic carbon atom adjacent to the bromine atom, following a S_N2 -like protocol (Scheme 7). Reactions with the acyclic borane $(i\text{Pr}_2\text{N})_2\text{B-Br}$ in thf yield analogous products according to ESI-MS analysis.



Scheme 7. Generalized reaction scheme for the formation of cluster species featuring incorporated ring-opened thf moieties.

The synthesized cluster compounds were characterized by a combination of single crystal X-ray diffraction analysis, NMR spectroscopy, and mass spectrometry. The incorporation of ether fragments is well observable in ESI-MS measurements by using deuterated solvents in the reaction protocol. Exemplarily, the m/z ratio of the monoanion 17a^{thf} is shifted by 8 masses upon conducting the reaction in $\text{thf-}d_8$ (Figure 24). A comprehensive overview of the applied methods is provided in Table 2.

Table 2. Summary of the characterization methods used to analyse the cluster species with incorporated ring-opened thf and tmo moieties.

	15a^{thf}	16a^{thf}	17a^{thf}	17a^{thf}	18a^{thf}	19a^{thf}
NMR	✓	-	✓	✓	-	✓
ESI-MS (thf)	✓	✓	✓	✓	✓	✓
ESI-MS (thf- d_8)	✓	-	✓	-	✓	✓
SC-XRD	-	-	✓ (-K)	✓ (-Cs)	-	✓ (-K)
	-	16a^{tmo}	17a^{tmo}	-	18a^{tmo}	19a^{tmo}
NMR	-	-	✓	-	-	-
ESI-MS	-	✓	✓	-	✓	✓
SC-XRD	-	-	✓ (-K)	-	-	-

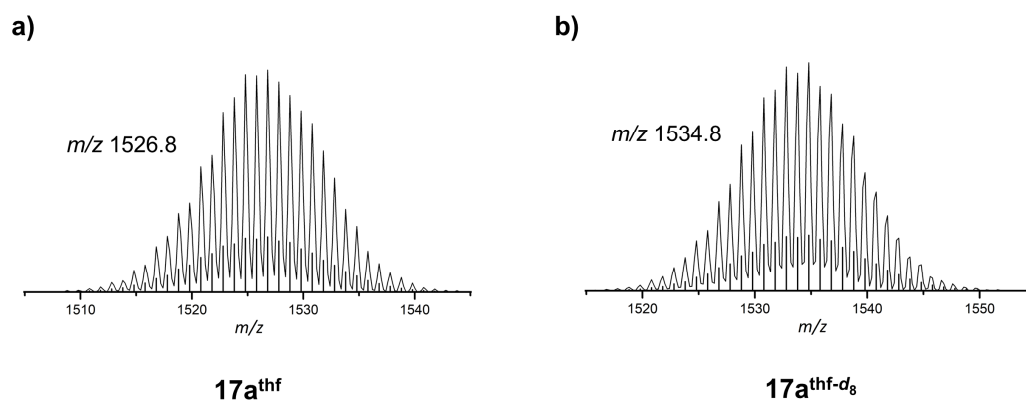


Figure 24. ESI-MS spectra of the monoanion $17a^{thf}$ prepared in a) thf or b) deuterated thf- d_8 . The mass peaks are observed at m/z 1526.8 and m/z 1534.8, respectively. The calculated isotope pattern is presented as black bars.

Concentrated toluene solutions of the compounds $17a^{thf-K}$, $17a^{thf-Cs}$, $19a^{thf-K}$, and $17a^{tmo-K}$ were stored at $-40\text{ }^{\circ}\text{C}$ yielding single crystals suitable for X-ray diffraction analysis. While in each compound the $[\text{Ge}_9]$ cluster is substituted by two hypersilyl groups and an organic fragment, the ligands are attached at different cluster vertices with respect to the trigonal prism. The $[\text{Ge}_9]$ clusters in the respective species feature C_s symmetry due to varying heights of the trigonal prism. Usually, the ligands bind to the three Ge vertex atoms capping the trigonal prism bases.^[206, 211, 223-225, 228] Thus, the compounds $17a^{thf-Cs}$ and $17a^{tmo-K}$ comprise the most common, symmetric ligand arrangement at the nonagermanide cluster (Figure 25b and d). In contrast, the $[\text{Ge}_9]$ cluster in compounds $17a^{thf-K}$ and $19a^{thf-K}$ is substituted in an asymmetric manner with one hypersilyl group and the hydrocarbon chain binding to capping Ge vertices, while the second hypersilyl ligand is attached at a Ge atom of the trigonal prism base (Figure 25a and c). Even though structural isomerism at $[\text{Ge}_9]$ clusters has been described before,^[214-215, 245] no such ligand arrangement has been reported so far. Intriguingly, the alkali metals in the thf-comprising species feature almost the same coordination sphere of one O atom, one aromatic ring, and several Ge contacts. Thus, the isomerization cannot be explained in a straightforward way. Furthermore, variable temperature ^1H NMR spectroscopic studies revealed that both clusters $17a^{thf-K}$ and $17a^{thf-Cs}$ feature a symmetric substitution in solution, since solely one signal set was observed in a temperature range from $-90\text{ }^{\circ}\text{C}$ to $60\text{ }^{\circ}\text{C}$. Consequently, the isomerization should occur during the crystallization process, with the chain length of the incorporated ether fragment as well as the counter cation playing vital, however yet unknown roles. In further studies the alkali metal counterions were sequestered during the reaction using [2.2.2]crypt and 18-crown-6, however the obtained reaction products were invariant to the adjusted reaction protocol. Quantum chemical calculations might be applied to compare the energies of the different species, thus aiding a more comprehensive understanding of the influence of the applied alkali metal and the hydrocarbon chain length on the substitution pattern.

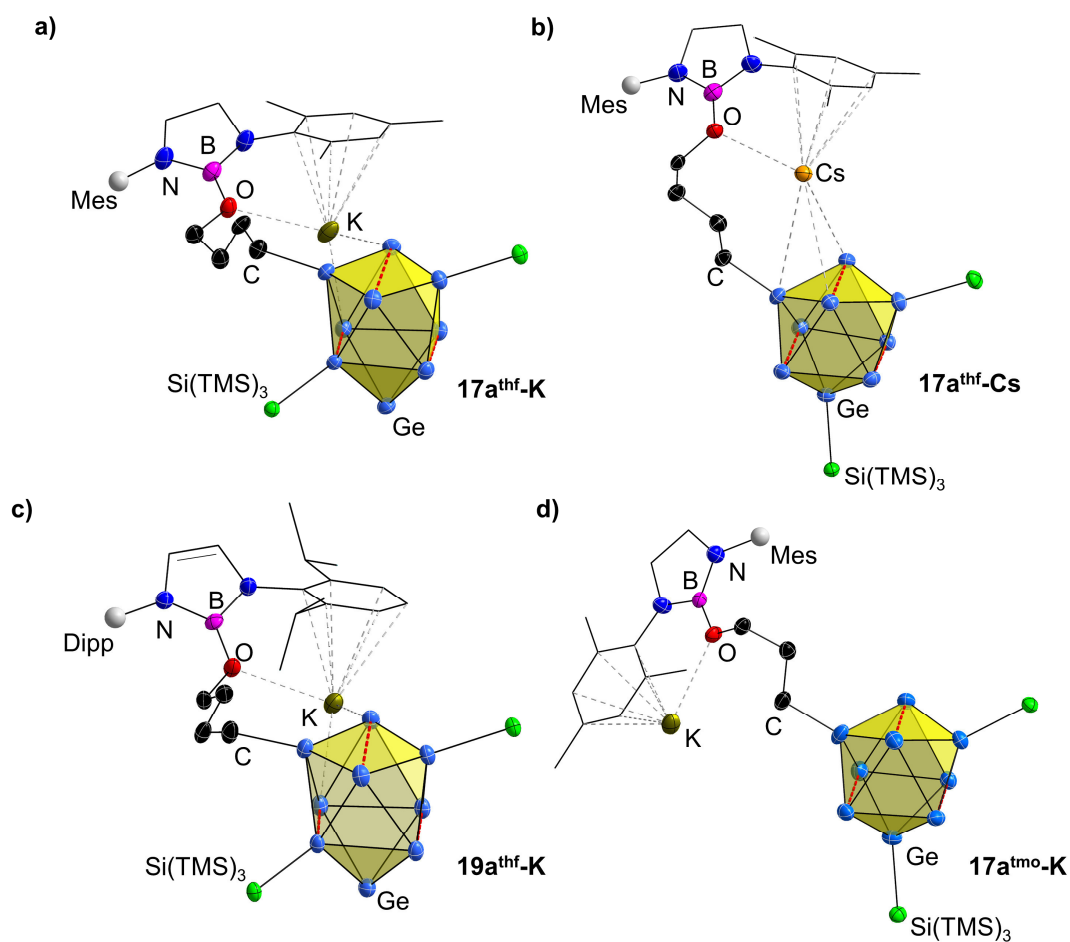
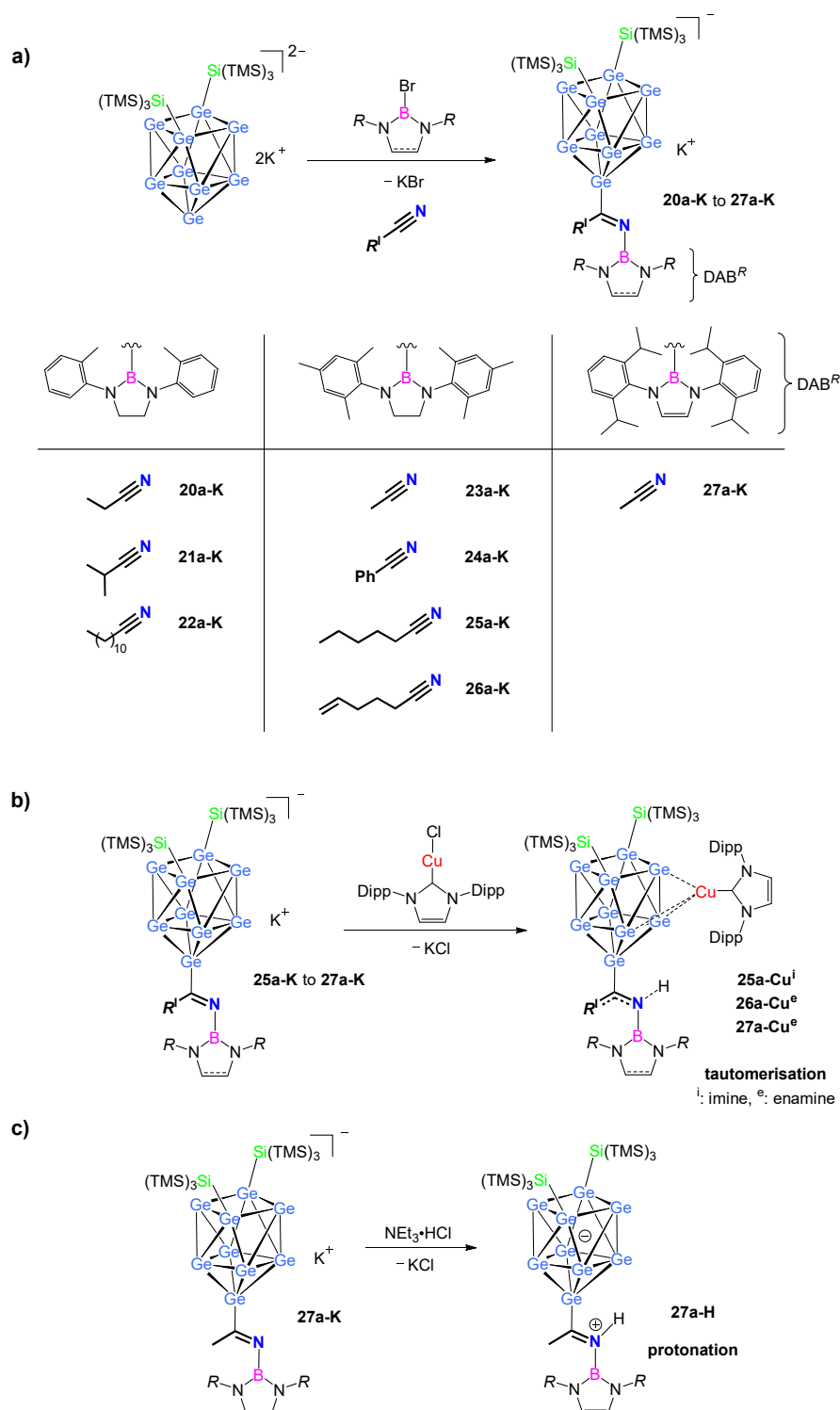


Figure 25. Molecular structures of clusters comprising ring-opened ether fragments: a) **17a^{thf}-K**; b) **17a^{thf}-Cs**; c) **19a^{thf}-K**; d) **17a^{tmo}-K**. All ellipsoids are presented at a 50% probability level. In each figure the wingtip substituent not coordinating to the alkali metal ion is illustrated as a grey sphere. Solely the central Si atoms of the hypersilyl groups are shown and hydrogen atoms are omitted. The backbone of the DAB fragments and the wingtip substituents coordinating the alkali metal ion are shown as wire-sticks. Trigonal prism bases are indicated by red dashed lines.

Frustrated Lewis pair-like nitrile activation

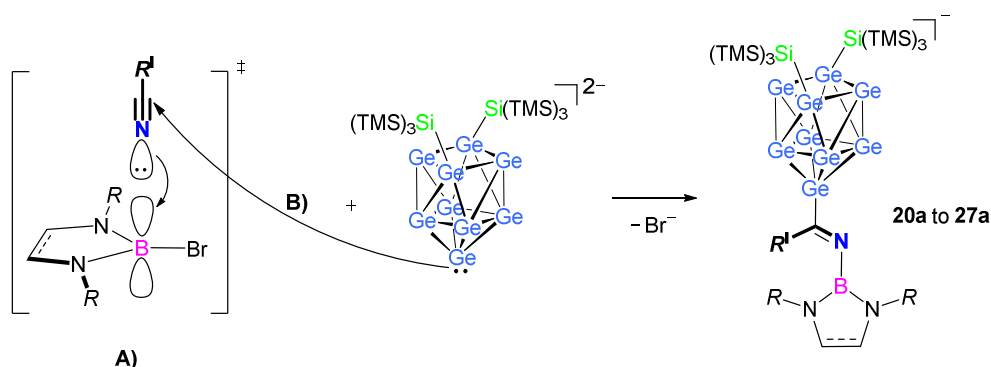
The nitrile incorporation between the twofold silylated cluster and bromoboranes was investigated. An overview of the performed experiments is provided in Scheme 8.



Scheme 8. Summary of the reactions of the twofold silylated $[\text{Ge}_9]$ cluster towards bromoboranes in various nitriles. a) Formation of the clusters $\text{K}[\text{Ge}_9\{\text{Si}(\text{TMS})_3\}_2\{\text{R}'\text{C}=\text{N}\}\text{-DAB}^{\text{R}}]$ (**20a-K** to **27a-K**; R' = alkyl, alkenyl, aryl; R = *o*-tol, Mes, Dipp) comprising an incorporated imine moiety; b) formation of the Cu-carbene adducts $\text{NHC}^{\text{Dipp}}\text{Cu}[\text{Ge}_9\{\text{Si}(\text{TMS})_3\}_2\{\text{R}'\text{CN}\}\text{-DAB}^{\text{R}}]$ (**25a-Cu^I**, **26a-Cu^E**, **27a-Cu^E**) featuring an imine-enamine tautomerism; c) protonation of the imine moiety in **27a-K** yielding the zwitterionic compound **27a-H**, $[\text{Ge}_9\{\text{Si}(\text{TMS})_3\}_2\{\text{MeC}=\text{N}(\text{H})\}\text{-DAB}(\text{II})^{\text{Dipp}}]$.

Reactions of the precursor $\text{K}_2[\text{Ge}_9\{\text{Si}(\text{TMS})_3\}_2]$ with bromo-1,3,2-diazaborolidines $\text{DAB}^R\text{-Br}$ ($R = o\text{-tol, Mes}$) or the bromo-1,3,2-diazaborole $\text{DAB(II)}^{\text{Dipp}}\text{-Br}$ in various nitriles yielded cluster species, which comprise incorporated imine fragments. Several nitriles $R'\text{C}\equiv\text{N}$ featuring alkyl, alkenyl, and aryl side chains were tested towards their reactivity leading to the formation of the compounds $\text{K}[\text{Ge}_9\{\text{Si}(\text{TMS})_3\}_2\{R'\text{C}=\text{N}\}\text{-DAB}^R]$ (**20a-K** to **27a-K**, Scheme 8a).

In contrast to the $\text{S}_{\text{N}}2$ -like mechanism observed for the incorporation of ring-opened ether fragments, the reactions with nitriles follow a frustrated Lewis acid-base-like mechanism. Indeed, no reaction between the nitrile and the bromoboranes is observed in absence of any cluster species even at elevated temperature. Only upon adding the twofold silylated cluster to a solution of the bromoborane in the nitrile a reaction initiates, accounting for a concerted reaction mechanism. Most probably, the reaction comprises a coordination of the nitrile's nucleophilic N atom to the electrophilic B center (non-isolable transition state, Scheme 9A), and an immediately following attack of the nucleophilic cluster at the electrophilic carbon atom in α -position to the terminal N atom (Scheme 9B). Similar findings have been reported for the cyclo-addition of nitriles to the geminal FLP $t\text{Bu}_2\text{P-CH}_2\text{-BPh}_2$ based on quantum chemical calculations.^[257, 280] Reactions with the acyclic borane $(i\text{Pr}_2\text{N})_2\text{B-Br}$ in MeCN yield analogous products according to ESI-MS analysis.



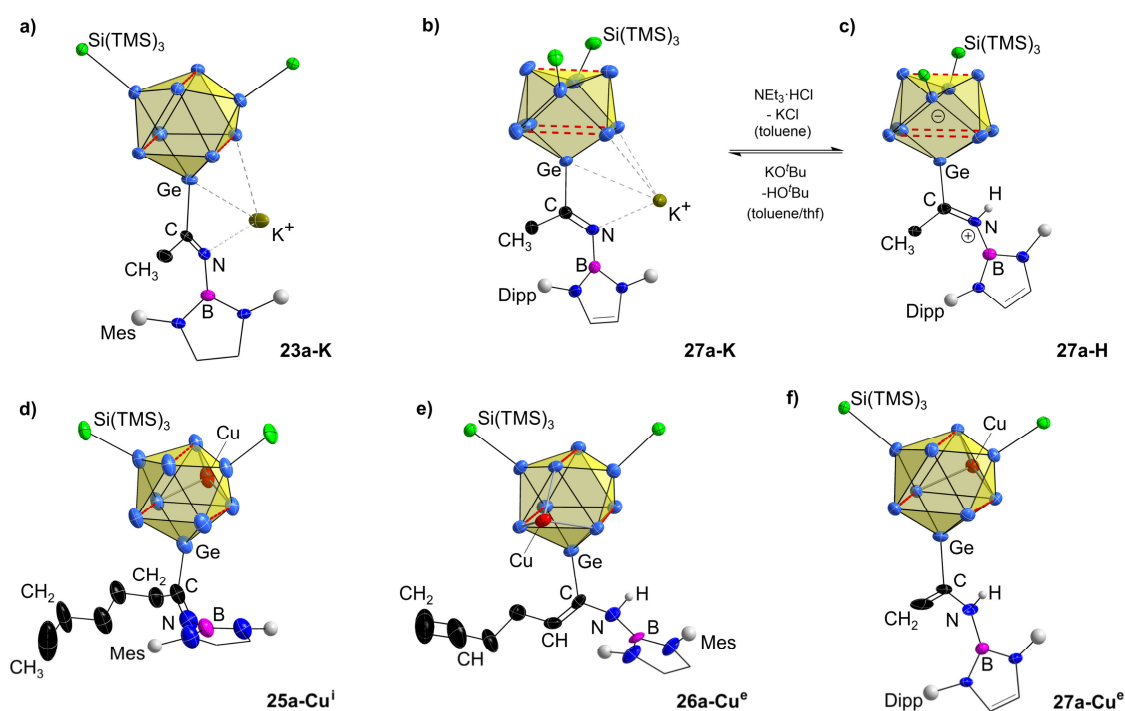
Scheme 9. Proposed reaction path for the formation of the species **20a** to **27a**.^[257, 280] A) coordination of the nucleophilic terminal N atom of the nitrile to the electrophilic boron center forming a non-isolable transition state; B) nucleophilic attack of the cluster at the electrophilic carbon atom adjacent to the N atom under bromide-cleavage.

While the anions **20a**, **21a**, **22a**, and **24a** were characterized by ESI-MS only, single crystals of compounds **23a-K** and **27a-K** were obtained, allowing a complete structure determination of the contained anions **23a** and **27a**. Furthermore, the anions **25a** to **27a** were transferred into the Cu-carbene adducts $\text{NHC}^{\text{Dipp}}\text{Cu}[\text{Ge}_9\{\text{Si}(\text{TMS})_3\}_2\{R'\text{CN}\}\text{-DAB}^R]$ (**25a-Cuⁱ**, **26a-Cu^e**, **27a-Cu^e**; Scheme 8b), which were crystallized and thoroughly characterized by SC-XRD as well as LIFDI-MS measurements. The same methods were applied to compound **27a-H**, $[\text{Ge}_9\{\text{Si}(\text{TMS})_3\}_2\{\text{MeC}=\text{N}(\text{H})\}\text{-DAB(II)}^{\text{Dipp}}]$, which forms upon protonating the imine function in anion **27a** with $\text{NEt}_3\cdot\text{HCl}$ (Scheme 8c). The applied characterization methods are summarized in Table 3.

Table 3. Summary of the characterization methods used to analyse the cluster species with incorporated imine moieties.

	20a	21a	22a	23a	24a	25a	25a-Cu ^I	26a	26a-Cu ^E	27a	27a-Cu ^E	27a-H
NMR	-	-	-	✓	-	-	✓	-	✓	✓	✓	✓
MS (ESI/LIFDI)	✓	✓	✓	✓	✓	✓	✓	✓	✓	✓	✓	✓
SC-XRD	-	-	-	✓ (-K)	-	-	✓	-	✓	✓ (-K)	✓	✓
UV-Vis	-	-	-	-	-	-	-	-	-	✓	-	✓

Repetitive structure motifs are observed in compounds **23a-K**, **27a-K**, **27a-H**, as well as **25a-Cu^I**, **26a-Cu^E**, and **27a-Cu^E** (Figure 26). Each [Ge₉] cluster is substituted at Ge atoms capping the trigonal prism by two hypersilyl groups and an organic ligand comprising the incorporated former nitrile. The protonated iminium entity in **27a-H** was clearly detected in the difference Fourier electron density map. Thus, the cluster is best described as a zwitterion with the negative charge distributed over the [Ge₉] cluster (Figure 26c). In the Cu-containing complexes the *TM* η³-coordinates the cluster as described before. Intriguingly, in the compounds **26a-Cu^E** and **27a-Cu^E** an imine-enamine tautomerism is observed (Figure 26e and f). However, this structural feature is most probably limited to the solid-state, according to NMR studies. The enamine-character of the two latter compounds was derived from shortened C=C *versus* elongated C-N bond lengths in comparison to compound **25a-Cu^I** (imine entity).

**Figure 26.** Molecular structures of clusters comprising incorporated imine or enamine fragments: a) **23a-K**; b) **27a-K**; c) **27a-H**; d) **25a-Cu^I**; e) **26a-Cu^E**; f) **27a-Cu^E**. The reversible transformation of **27a-K** in **27a-H** is indicated. All ellipsoids are presented at a 50 % probability level. Solely the central Si atoms of the hypersilyl groups are shown, hydrogen atoms are omitted, and the wingtip substituents are illustrated as grey spheres. The backbone of the DAB fragments is shown as wire-sticks. Trigonal prism bases are indicated by red dashed lines.

UV-Vis spectroscopy and quantum chemical calculations for compound **27a-H**

Via the presented nitrile-route in principle up to two functional groups can be introduced to the [Ge₉] cluster. On the one side allows the variability of the organic entity R^1 of the nitrile the introduction of functional groups such as alkenyl entities, on the other side the imine (or enamine) moiety is a functional group itself. As described in Scheme 8c, and corroborated by the isolation of single crystals of **27a-K** and **27a-H** (Figure 26b and c), the imine entity is readily protonated by applying the soft acid $\text{NEt}_3\cdot\text{HCl}$. In contrast to the red potassium salt, the cluster **27a-H** forms intensively fir-green colored solutions. The iminium entity was not only substantiated by single crystal diffraction analysis, but also by the presence of iminium protons in the ^1H NMR spectrum as well as by a combined ESI-MS / LIFDI-MS study revealing a mass difference of exactly one hydrogen atom between the monoanionic cluster **27a** and compound **27a-H**. Furthermore, the intensively colored clusters were investigated by UV-Vis absorption measurements as depicted in Figure 27 [note: absorption bands at $\lambda = 210$ nm in a) and 310 nm in b) are artefacts caused by the solvent]. The reversibility of the protonation was proven by time-dependent UV-Vis investigations monitoring the decay of the absorption band at $\lambda = 671$ nm upon adding KO^tBu to the cluster solution. The obtained results were supported by NMR spectroscopic investigations revealing a fading iminium proton signal.

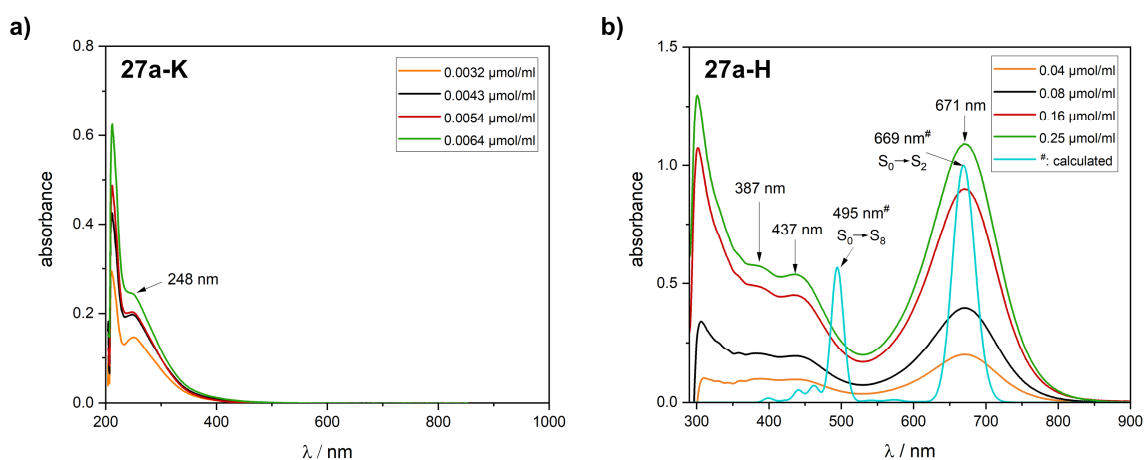


Figure 27. UV-Vis absorption spectra of a) **27a-K** (thf) and b) **27a-H** (toluene). In b) the calculated absorption spectrum obtained at DFT-BP86/TZVP level of theory is presented as turquoise graph, revealing maxima at $\lambda = 495$ nm (transition $S_0 \rightarrow S_8$, 2.14 eV) and $\lambda = 669$ nm (transition $S_0 \rightarrow S_2$, 1.85 eV).^[281-285] For the illustration the vertical excitation energies of the 30 lowest-energy singlet excited states were used (shortest calculated wavelength: 396 nm).

The results of time-dependent DFT calculations^[281-285] for compound **27a-H** are in accordance with the experimentally obtained data, revealing absorption maxima at $\lambda = 669$ nm (transition $S_0 \rightarrow S_2$) and $\lambda = 495$ nm (transition $S_0 \rightarrow S_8$, Figure 27b, turquoise graph). Typically, time-dependent DFT methods suffer larger errors with an increasing charge-transfer contribution, thus explaining the deviation of the calculated absorption band at $\lambda = 495$ nm.^[286]

According to the molecular orbital analysis the HOMO is located at the $[\text{Ge}_9]$ cluster and the covalently connected carbon atom, while the LUMO forms the anti-bonding π^* orbital of the C=N double bond of the imine moiety (Figure 28a and b). The HOMO-LUMO gap was calculated to 1.40 eV. Most probably, the green color of compound **27a-H** is caused by a charge-transfer between the cluster and the iminium entity. This hypothesis is supported by the calculation of the change in the electron density during the excitation $S_0 \rightarrow S_2$ (Figure 28c). During the excitation a decreasing electron density at the $[\text{Ge}_9]$ cluster (yellow color) is monitored, while the electron density at the adjacent carbon atom of the imine moiety increases (red color). A potential explanation for the observed shift in the electron density is the description of the participating molecule fragment using a mesomeric structure with the positive charge located at the central carbon atom (Figure 28d). Thus, the excitation induces an electron density transfer to the electrophilic carbon atom.

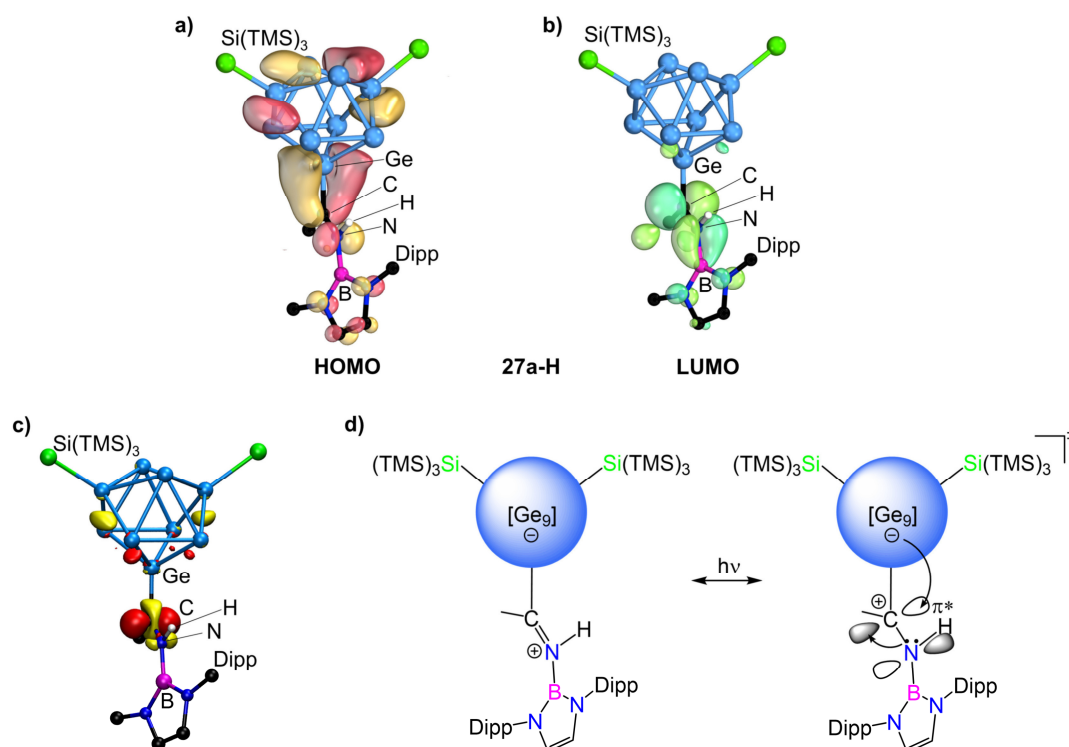


Figure 28. Molecular orbitals of **27a-H** calculated at the DFT-BP86/TZVP level of theory:^[281-285] a) HOMO; b) LUMO. Molecular orbital plots are illustrated in such way that 50 % of the density is enclosed within the isosurface (approximate isovalue of 0.04 a.u.). c) Electron density difference plots for the $S_0 \rightarrow S_2$ excitation of **27a-H**. During the excitation yellow color corresponds to a decreasing electron density and red color corresponds to increasing electron density (approximate isovalue of 0.002 a.u.). d) Proposed mesomeric structure of **27a-H** explaining the observed electron density transfer.

2.2 Deltahedral $[\text{Ge}_4]^{4-}$ and $[\text{Ge}_9]^{4-}$ Anions as Synthons for Intermetalloid Clusters

Reactions with organometallic complexes are one major pillar on which the field of deltahedral *Zintl* cluster chemistry is based. Owing to the immense number of isolated structures reported in the literature, in the introductory Chapter 1.3.1 solely the most prominent examples containing Ge as cluster-forming element are listed. While comprehensive overviews including the chemistry of Sn and Pb analogues are provided elsewhere,^[89, 287-290] publications on the detection of novel intermetalloid clusters and their related chemistry appear on a regular basis, thus accounting for the timelessness and boundlessness of the research field.^[291] Within such reports, a major focus lies on the identification of suitable organometallic reactants and reaction parameters allowing the targeted and reproducible synthesis of extended clusters, which goes along with the aim to clarify the occurring cluster-formation mechanisms on a molecular level. Recently, the fabrication of structures like nano-rods^[129-130] or catalysts^[292] has caught attention, opening the way for potential future applications of the respective materials. Nevertheless, mechanistic insights into the processes occurring in solution are rare, thus requiring persisting research efforts. To challenge this issue, within this thesis reactivity studies of germanide clusters towards organometallic complexes in polar solvents such as liquid ammonia as well as ethylenediamine (en) are described. Here, one focus lies on monitoring potential reaction paths in these media, while another key aspect is isolating and characterizing novel intermetalloid clusters. Several transition metal-coordinated, endohedral, and counterion-exchanged clusters were identified, which are presented in the following sub-chapters.

2.2.1 Review of Relevant Literature

2.2.1.1 Reactions of Germanide *Zintl* Clusters with Zinc Organyls

Chemical manipulations using the bare $[\text{Ge}_4]^{4-}$ and $[\text{Ge}_9]^{4-}$ clusters are usually conducted in polar solvents in the presence of sequestering agents. Even though distinct characterization methods like NMR spectroscopy in liquid ammonia exist,^[293-296] these techniques are technically challenging limiting their common applicability. Thus, the *in-situ* monitoring of reaction steps and the identification of intermediates is mostly limited to the isolation of single crystals. By the comparison of structurally characterized species potential reaction paths can be derived. Exemplarily, the anion $[(\eta^4\text{-Ge}_9)\text{Zn}(\eta^1:\eta^1\text{-Ge}_9)\text{Zn}(\eta^4\text{-Ge}_9)]^{8-}$ (Figure 29b)^[129] might form stepwise via the formation of the doubly Zn-coordinated cluster $[(\eta^1\text{-Ge}_9)\{\text{Zn}(\text{NH}_3)_3\}_2]$ (Figure 29a),^[123] and a subsequent exchange of its NH_3 ligands by two $[\text{Ge}_9]^{4-}$ moieties. A second possible reaction path is the substitution of the organic ligands at two $[(\eta^4\text{-Ge}_9)\text{ZnR}]^{3-}$ ($R = \text{Ph}$,^[118] Mes,^[121] ^{*i*}Pr^[121]; Figure 29d) clusters by a bridging $[\text{Ge}_9]^{4-}$ anion.

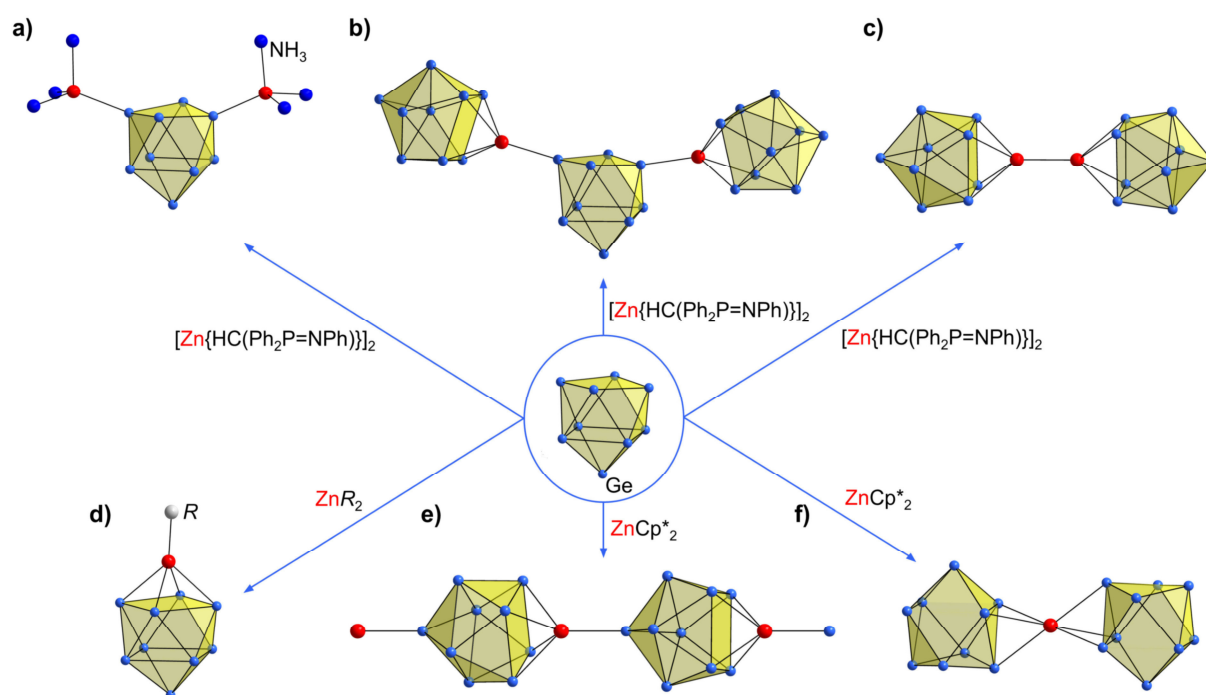


Figure 29. Molecular structures of Zn-coordinated clusters a) $[(\eta^1\text{-Ge}_9)\{\text{Zn}(\text{NH}_3)_3\}_2]$;^[123] b) $[(\eta^4\text{-Ge}_9)\text{Zn}(\eta^1:\eta^1\text{-Ge}_9)\text{Zn}(\eta^4\text{-Ge}_9)]^{8-}$;^[129] c) $[(\eta^4\text{-Ge}_9)\text{Zn-Zn}(\eta^4\text{-Ge}_9)]^{6-}$;^[129] d) $[(\eta^4\text{-Ge}_9)\text{ZnR}]^{3-}$ ($R = \text{Ph}$,^[118] Mes,^[121] ^{*i*}Pr^[121]); e) $\frac{1}{\infty} [\text{Zn}(\eta^4:\eta^1\text{-Ge}_9)]^{2-}$;^[129] f) $[(\eta^3\text{-Ge}_9)\text{Zn}(\eta^3\text{-Ge}_9)]^{6-}$.^[203] Light blue and red spheres represent Ge and Zn atoms, respectively, dark blue and grey spheres NH_3 molecules and organic ligands.

As depicted in Figure 29, the chemistry of Zn organyls towards $[\text{Ge}_9]^{4-}$ anions is very versatile. In reactions of $[\text{Ge}_9]^{4-}$ clusters towards Zn(I) reagents either a formal retention of the Zn-Zn single bond in the polyanion $[(\eta^4\text{-Ge}_9)\text{Zn-Zn}(\eta^4\text{-Ge}_9)]^{6-}$ is observed (Figure 29c),^[129] or the Zn(I) precursor disproportionates leading to Zn(II)-coordinated clusters (Figure 29a and b). These observations account for redox processes in solution, which are not fully understood

yet.^[123, 129] The utilization of Zn(II) precursors usually results in transition metal bridged anions such as $\frac{1}{\infty} \{Zn(\eta^4:\eta^1-Ge_9)\}^{2-}$ (Figure 29e)^[129] and $[(\eta^3-Ge_9)Zn(\eta^3-Ge_9)]^{6-}$ (Figure 29f),^[203] in which the Zn ion adopts different coordination modes. The structural isomer of the former polymer, $\frac{1}{\infty} \{Zn(\eta^3:\eta^3-Ge_9)\}^{2-}$, was obtained upon exchanging $ZnCp^*_2$ by the Zn(I) organyl $[Zn(NacNac^{Mes})]_2$.^[130]

As outlined, Zn-based precursors reveal a very versatile chemistry towards bare germanide clusters, yielding fascinating structures. Besides the oxidation state of the Zn center and the attached ligands, also the applied solvent is considered as an important reaction parameter. As key example, amide formation was observed in some of the aforementioned reactions, caused most likely by the deprotonation of liquid ammonia or ethylenediamine by negatively charged organic fragments R^- , which were cleaved from the ZnR_2 precursors.^[118, 121, 134, 213, 271] However, the role of these small anions in the course of the reactions remains ambiguous.

2.2.1.2 Structure Motifs in Endohedral Tetrel Element Clusters

While the Zn-comprising fragments in the latter chapter coordinate to the surface of the germanide clusters, some *TM* can be incorporated into the cluster core. Even though no experimental proof for the incorporation of Zn atoms in germanide clusters has been reported, its encapsulation was anticipated by calculations.^[297-298] In recent years, compounds featuring core-shell-like building principles have been developed, holding promise for the development of drug delivery systems,^[299] sensors,^[300] and catalysts.^[301] However, the targeted synthesis of onion-like structured materials is a challenging process, involving issues such as island formation or an unfavored intermixing of components.^[302-304]

On an atomic level endohedral *Zintl* clusters (Chapter 1.3.1.3) can be described as core-shell molecules, with the inner sphere consisting of solely one atom.^[89] While deltahedral transition metal-free tetrel element clusters featuring up to ten vertex atoms were reported,^[305-307] the addition of an interstitial *TM* atom allows the formation of extended clusters. Here, the encapsulated *TM* is believed to provision additional orbitals for the cluster stabilization.^[138, 157] Exemplarily, besides filled (distorted) icosahedra of Ge, Sn, and Pb, also extended clusters such as $[TM_2@Ge_{16}]^{4-}$ ($TM = Fe$,^[154] Co ^[155-156]), $[Pd_2@E_{18}]^{4-}$ ($E = Ge$,^[157] Sn ^[308-310]), and $[Rh_3@Sn_{24}]^{5-}$ ^[311] exist, comprising fused, multiple-filled shells of tetrel elements. In addition, a series of doubly filled 17-atom Sn clusters was identified. Here, two $[TM@Sn_9]^{n-}$ entities ($TM = Co$,^[143-144] Ni ,^[312-313] Rh ,^[311] Pt ^[159]) are interlinked by a shared Sn vertex atom (Figure 30c). So far, no such germanide analogue has been reported.^[147, 314]

Despite the structural characterization of many endohedral cluster species, rare evidence on the formation mechanisms occurring in solution has been provided. It is assumed that the formation of filled and extended intermetalloid clusters is a multi-step process, involving a coordination of organometallic fragments to the cluster precursors, a subsequent ligand cleavage, as well as fragmentation and assembling steps.^[89, 134, 290] A key example for the latter processes is the formation of the doubly filled dimer $[\text{Co}_2@\text{Sn}_{17}]^{5-}$ from an ethylenediamine extract of the solid-state phase $\text{K}_{4.79}\text{Co}_{0.79}\text{Sn}_9$ containing $[\text{Co}@\text{Sn}_9]^{4-}$ clusters.^[143] Even though filled $[\text{Ni}@\text{Sn}_9]^{4-}$ anions were described in $\text{Na}_{12}\text{Ni}_{1-x}\text{Sn}_{17}$,^[145] no such germanium-based solid containing filled germanide clusters is known.

The oftentimes occurring icosahedral building fragments in endohedral clusters can be classified according to the nomenclature of *Alvarez*.^[315] Exemplarily, the centered vacant icosahedral fragment $[\text{TM}@\text{E}_8]$ (cvIC-8, Figure 30d) was monitored in clusters such as $[\text{Ni}_2@\text{Sn}_{17}]^{4-}$ (Figure 30c),^[312] as well as in the fragmentation products $[\text{CpTi}(\eta^4\text{-Sn}_8)]^{3-}$ (Figure 30a) and $[\{\text{Cp}_2\text{Ti}\}_2\{\text{CpTi}\}\text{TiSn}_{15}]^{n-}$ ($n = 4, 5$; Figure 30b). The latter species form in reactions of $[\text{Sn}_9]^{4-}$ clusters with titanium organyls.^[134] Generally, an icosahedral atom arrangement with approximately equal distances of the *TM* to each cluster vertex seems favourable.^[141]

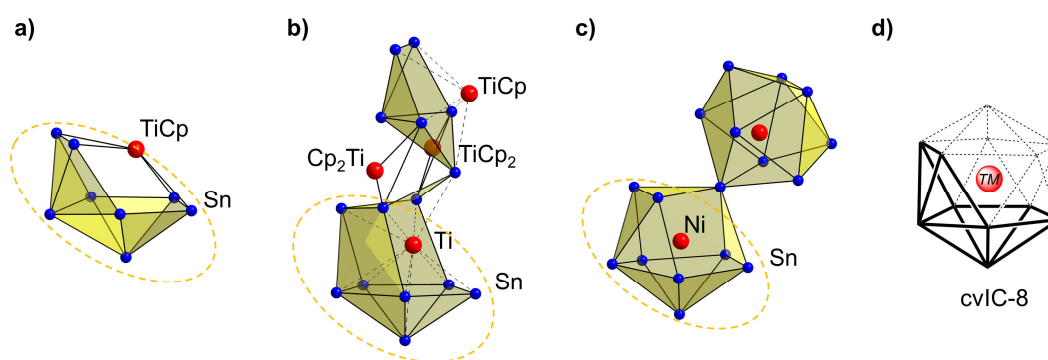


Figure 30. Icosahedral fragments in the molecular structures of a) $[\text{CpTi}(\eta^4\text{-Sn}_8)]^{3-}$; b) $[\{\text{Cp}_2\text{Ti}\}_2\{\text{CpTi}\}\text{TiSn}_{15}]^{n-}$ ($n = 4, 5$);^[134] c) $[\text{Ni}_2@\text{Sn}_{17}]^{4-}$.^[312] Repetitive $[\text{Sn}_8]$ structure motifs in a)-c) are indicated by dashed orange ellipses. d) Illustration of a centered vacant icosahedron according to the nomenclature of *Alvarez*.^[315]

2.2.1.3 Counterion-Exchange at *Zintl* Clusters

The major share of isolated and structurally characterized nonagermanide *Zintl* clusters features K^+ counterions,^[290] while the Zn-coordinated cluster $[(\eta^1\text{-Ge}_9)\{\text{Zn}(\text{NH}_3)_3\}_2]$ ^[123] is one of the few exceptions. However, also binary phases such as $A_4\text{Ge}_9$ and $A_{12}\text{Ge}_{17}$ ($A = \text{Na}$,^[68, 78, 82, 84] Rb ,^[84] Cs ^[67, 84]) are known, opening a straightforward way to alter the counterions in the obtained reaction products. Nevertheless, the lithium-containing phases remain elusive, most likely due to the size-mismatch between the small alkali metal cation and

the bulky nine-atom cluster. Nevertheless, the Li^+ counterion-comprising $[\text{Sn}_9]^{4-}$ and $[\text{Pb}_9]^{4-}$ clusters are accessible by reducing elemental tin and lead with lithium in liquid ammonia.^[90] Another possibility is exchanging the counterions of the respective potassium-containing compounds by Li^+ ions in solution, which can be achieved by the application of ion-exchange resins to liquid ammonia extracts of the K-based solid-state phases. Though, this protocol is limited to the production of Li_4Sn_9 so far.^[147] A targeted exchange of counterions is of interest, as it opens a forthright way to the characterization and comparison of several closely-related compounds differing solely concerning their counterions. By this way, insights into the role of the cations regarding the reactivity of the clusters or the arrangement of substituents at the cluster core might be obtained.

2.2.2 Synthesis and Characterization of Intermetalloid Germanide Clusters

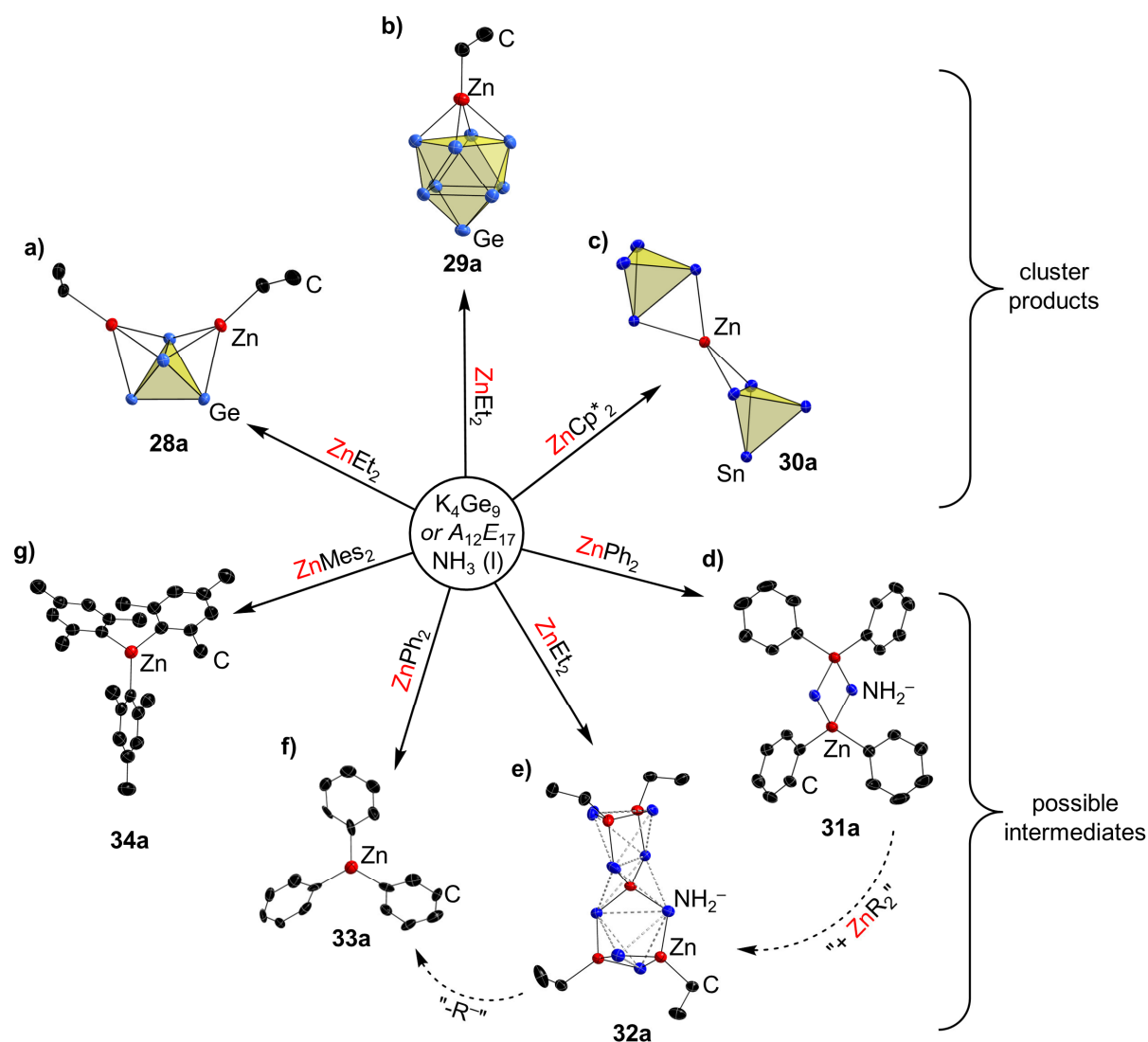
- Chapter 6.8:** C. Wallach,[‡] K. Mayer,[‡] T. Henneberger, W. Klein and T. F. Fässler, Intermediates and Products of the Reaction of Zn(II) Organyls with Tetrel Element *Zintl* Ions: Cluster Extension Versus Complexation, *Dalton Trans.* **2020**, 49, 6191.
- Chapter 6.9:** C. Wallach, Y. Selic, B. J. L. Witzel, W. Klein and T. F. Fässler, Filled Trivacant Icosahedra as Building Fragments in 17-atom Endohedral Germanides $[TM_2@Ge_{17}]^{n-}$ ($TM = Co, Ni$), *Dalton Trans.* **2021**, 50, 13671.
- Chapter 6.10:** C. Wallach, W. Klein and T. F. Fässler, Nonagermanide *Zintl* Clusters with Mg^{2+} Counterions, *Z. Anorg. Allg. Chem.* **2022**, accepted article, DOI: 10.1002/zaac.202200065.
- Chapter 6.11:** C. Wallach, W. Klein and T. F. Fässler, Crystal Structure of N^2, N^4 -dimesitylpentane-2,4-diamine, $C_{23}H_{34}N_2$, single crystal structure communication submitted for publication in *Z. Kristallogr., New Cryst. Struct.*

[‡]: authors contributed equally to this work.

Within this chapter reactions of the bare ions $[Ge_4]^{4-}$ and $[Ge_9]^{4-}$ with various organometallic complexes are described. The focus of the conducted experiments is the identification of potential intermediates and repetitive structural building fragments in different isolated clusters. However, also the structures of germanium-free by-products are investigated to obtain insights into reaction processes occurring in solution. Since harsh reaction conditions are applied to obtain intermetalloid clusters, oftentimes the isolation of single crystalline product species and intermediates provides the only possibility to elaborate potential reaction paths. In the following chapter Zn-coordinated germanium tetrahedra as well as nine-atom clusters are described, which were isolated in combination with several Zn amides from reactions of the solid-state precursors K_4Ge_9 and $K_{12}Ge_{17}$ from liquid ammonia.^[172, 316-317] Most probably, the formation of amides plays a key role in the generation of the isolated intermetalloid clusters. Furthermore, the endohedral 17-atom germanides $[TM_2@Ge_{17}]^{n-}$ ($TM = Co, Ni$) were obtained either by reacting the solid-state phase of nominal composition “ $K_5Co_{1.2}Ge_9$ ” with a titanium complex in liquid ammonia,^[147, 314] or by filling and fusing empty $[Ge_9]^{4-}$ ions by the addition of $Ni(cod)_2$ to an ethylenediamine solution of K_4Ge_9 , respectively. Both filled cluster anions are discussed with respect to their building principles, which resemble an atom arrangement in analogy to icosahedra. In further experiments the potassium counterion-exchange at bare $[Ge_9]^{4-}$ clusters as well as at the silylated species $K[Ge_9\{Si(TMS)_3\}_3]$ is described, achieved by the application of magnesium organyls.

2.2.2.1 Investigations on Potential Intermediates and Reaction Paths Yielding Tetrel Element-Zinc Clusters

Reactions of deltahedral *Zintl* clusters with organozinc precursors in liquid ammonia led to the formation of various intermetalloid clusters and Zn complexes, an overview of which is provided in Scheme 10.^[172, 316-317]



Scheme 10. Molecular structures of the polyanions obtained from reactions of zinc organyls with K_4Ge_9 and $A_{12}E_{17}$ ($A = K, Rb$; $E = Si-Sn$) in liquid ammonia. a) $[(\eta^3:\eta^3-Ge_4)(ZnEt)_2]^{2-}$ (**28a**); b) $[(\eta^4-Ge_9)(ZnEt)]^{3-}$ (**29a**); c) $[(\eta^2-Sn_4)Zn(\eta^2-Sn_4)]^{6-}$ (**30a**);^[172, 316] d) $[(ZnPh)_2(\mu_2-NH_2)_2]^{2-}$ (**31a**); e) $\{[Zn(\mu_2-NH_2)_4][ZnEt)_2(\mu_2-NH_2)_2]^{2-}$ (**32a**); f) $[ZnPh_3]^-$ (**33a**); g) $[ZnMes_3]^-$ (**34a**).^[317] All ellipsoids are shown at a 50 % probability level. Hydrogen atoms, counterions, and co-crystallizing solvent molecules are omitted for clarity. In e) tetrahedral motifs spanned by amide ions are indicated by dashed grey lines.

Anions **28a** to **34a** were isolated from liquid ammonia solutions upon dissolving the solid-state phases K_4Ge_9 or $A_{12}E_{17}$ ($A = K, Rb$; $E = Si-Sn$) in the presence of ZnR_2 species and the sequestering agents [2.2.2]crypt or 18-crown-6 (Scheme 10). Single crystalline material containing these anions was collected from the flask after storing the reactions several months at $-70^\circ C$. Anion **28a** was obtained in the salt $[K[2.2.2]crypt]_2[(\eta^3:\eta^3-Ge_4)(ZnEt)_2] \cdot 2NH_3$. The

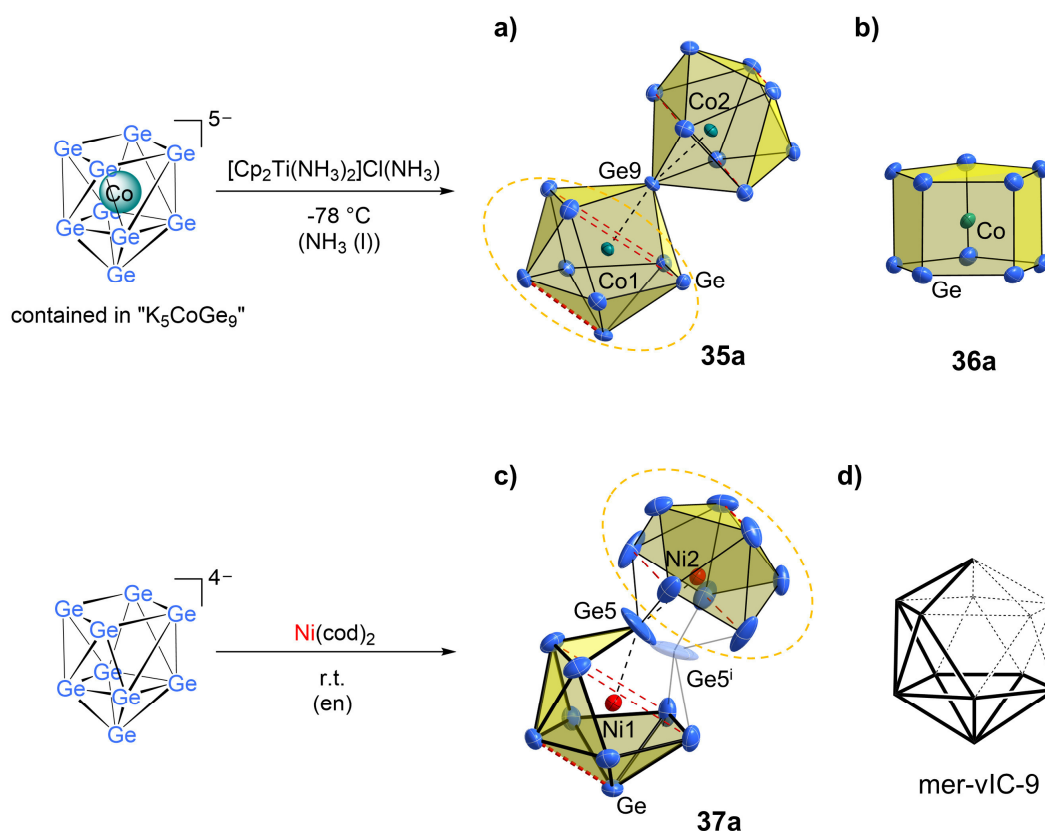
cluster comprises two $[\text{ZnEt}]^+$ entities coordinating to two opposed triangular surfaces of the tetrahedron, resulting in a seesaw-like structure (Scheme 10a). A comparable structural motif has been reported for the related anion $[(\eta^3\text{-}\eta^3\text{-Ge}_4)(\text{CuMes})_2]^{4-}$.^[111] In addition, the same *TM* fragment η^4 -coordinates a nonagermanide cluster in the compound $[\text{K}[2.2.2]\text{crypt}]_3[(\eta^4\text{-Ge}_9)(\text{ZnEt})] \cdot 7.4\text{NH}_3$ comprising anion **29a** (Scheme 10b). The resulting ten-atom *closo*-cluster can either be described as a bicapped square antiprism, or as a coordination complex of Zn and the square plane of the $[\text{Ge}_9]$ cage, which acts as a 6-electron donor and allows the transition metal to reach 18 valence electrons.^[118] The anions **28a** and **29a** are relatively stable in solution, corroborated by the detection of the mono-anionic species in ESI-MS measurements. A complete exchange of the $[\text{Cp}^*]^-$ ligands at the Zn atom by Sn tetrahedra was observed in anion **30a** (Scheme 10c), which was isolated in the compound $[\text{K}]_6[(\eta^2\text{-Sn}_4)\text{Zn}(\eta^2\text{-Sn}_4)] \cdot 16\text{NH}_3$. Anion **30a** is a structural isomer and heavier homologue to the previously reported clusters $[(\eta^3\text{-Sn}_4)\text{Zn}(\eta^2\text{-Sn}_4)]^{6-}$ ^[294] and $[\{\eta^2\text{-(Si/Ge)}_4\}\text{Zn}\{\eta^2\text{-(Si/Ge)}_4\}]^{6-}$, respectively.^[114]

In further experiments cluster-free Zn complexes were isolated. Among these were the amides **31a** and **32a** (Scheme 10d and e), which crystallized in the compounds $[\text{K}(18\text{-crown-6})]_2[(\text{ZnPh}_2)_2(\mu_2\text{-NH}_2)_2] \cdot 8\text{NH}_3$ and $[\text{K}(18\text{-crown-6})]_2\{[\text{Zn}(\mu_2\text{-NH}_2)_4][(\text{ZnEt})_2(\mu_2\text{-NH}_2)_2]_2\} \cdot 5\text{NH}_3$, respectively. While the species **31a** consists of two charge-neutral ZnPh_2 fragments interconnected by two amide ions, in the complex anion **32a** a central Zn^{2+} cation and four $[\text{ZnEt}]^+$ entities are interconnected by eight amide ions. These form three edge-sharing tetrahedra, the outer ones of which being capped with two organozinc fragments each. The central tetrahedron encapsulates a Zn^{2+} ion. The Zn^{2+} ion and the $[\text{ZnEt}]^+$ fragments can be seen as “activated” species of the ZnR_2 precursors. Even though the source of the amide ions cannot be identified unequivocally, previous investigations regarding amide-formation referred to the existence of solvated electrons in the cluster containing reaction solutions.^[103-104] These electrons most probably initiate a reductive cleavage of an organic ligand of the Zn complex. The formed anions R^- abstract a proton from the solvent yielding NH_2^- ions.^[118, 121] This assumption is corroborated by the isolation of the anionic Zn complexes **33a** and **34a** (Scheme 10f and g) in the compounds $[\text{K}_{0.8}\text{Rb}_{0.2}(18\text{-crown-6})][\text{ZnPh}_3]$ and $[\text{K}(18\text{-crown-6})][\text{ZnMes}_3] \cdot \text{NH}_3 \cdot 2\text{thf}$, respectively. The organozinc complexes can be described as traps for cleaved organic ligands R^- .

Although the molecules described in this section were neither derived from the same organozinc precursor nor from one single reaction, the isolation of several anionic clusters **28a** to **30a** and by-products **31a** to **34a** containing Zn^{2+} ions, $[\text{ZnR}]^+$ fragments, and cleaved R^- ligands hints towards stepwise reactions on the way to intermetaloid clusters. The formation of such cluster species is most probably induced by the formation of intermediate Zn amides.

2.2.2.2 Synthesis and Structural Characterization of the Endohedral Ions $[TM_2@Ge_{17}]^{n-}$ ($TM = Co, n = 6$; $TM = Ni, n = 4$)

As outlined in Chapter 1.3.1.3 endohedral clusters are obtained either by solid-state reactions, followed by an extraction of the filled clusters, or empty clusters are reacted with organometallic complexes in solution to yield an incorporation of the transition metal. Both reaction protocols were applied as illustrated in Scheme 11.^[147, 314]



Scheme 11. Synthesis and molecular structures of the polyanions a) $[Co_2@Ge_{17}]^{6-}$ (**35a**); b) $[Co_2@Ge_{10}]^{3-}$ (**36a**);^[147, 314] c) $[Ni_2@Ge_{17}]^{4-}$ (**37a**). The quotation marks indicate the nominal composition of the solid-state phase. All ellipsoids are presented at a 50 % probability level. In c) the split atom $Ge5^i$ is indicated transparently [symmetry operation (i): $1-x, y, 0.5-z$]. Co-crystallizing solvent molecules and cations are omitted. In a) and c) the reoccurring $[Ge_8]$ tubs are indicated by dashed orange ellipsis, and trigonal prism bases as red dashed lines. In d) an additional atom arrangement derived from an icosahedron is schematically presented.^[315] The analogous structure feature in anion **37a** is indicated in bold.

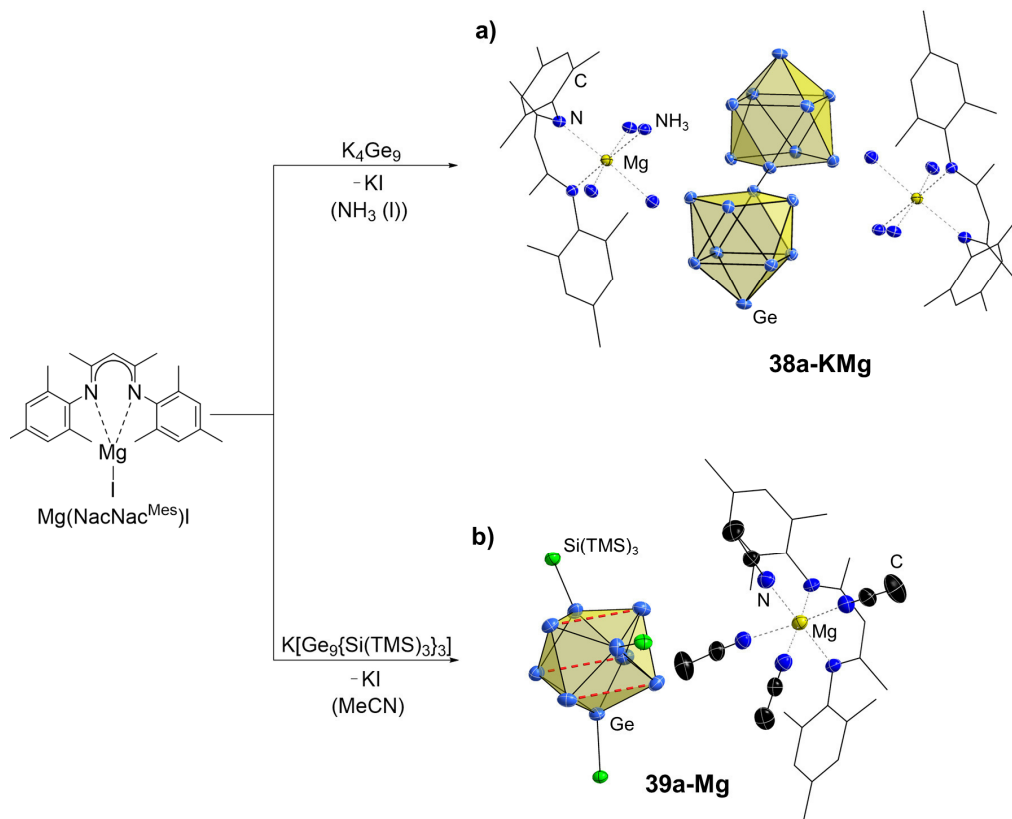
According to Raman spectroscopic investigations the solid-state phase of nominal composition $K_5Co_{1.2}Ge_9$ comprises filled $[Co@Ge_9]^{5-}$ clusters, which can be extracted using liquid ammonia.^[140] In previous studies, titanium organyls revealed a variable reactivity towards tetrel element *Zintl* clusters,^[134] thus the organometallic complex $[Cp_2Ti(NH_3)_2]Cl(NH_3)$ was added to the liquid ammonia extract of the cobalt-containing solid-state phase. From the reaction mixture the anions $[Co_2@Ge_{17}]^{6-}$ (**35a**) and $[Co_2@Ge_{10}]^{3-}$ (**36a**, Scheme 11a and b) were isolated in the compounds $[K([2.2.2]crypt)]_2K_4[Co_2@Ge_{17}] \cdot 15NH_3$ and $[K(2.2.2-crypt)]_3[Co@Ge_{10}] \cdot 9NH_3$, respectively. The latter ion has previously been isolated and

characterized from ethylenediamine, thus it is not extensively discussed at this point.^[151-152] So far, the structure motif of two fused cobalt-filled [Ge₉] clusters comprising a shared Ge vertex in **35a** has solely been observed in the corresponding *TM*-filled stannides.^[143-144, 159, 311-312] The corresponding Ni-congener [Ni₂@Ge₁₇]⁴⁻ (**37a**, Scheme 11c) was prepared by reacting finely grounded K₄Ge₉ with Ni(cod)₂ in ethylenediamine. The utilized Ni complex is a common precursor for the generation of intermetalloid clusters.^[119, 313, 318]

Even though the two doubly filled clusters **35a** and **37a** feature the same number of vertices, their structures differ from each other. The anion **35a** can either be described as two [Co@Ge₉] entities which are linked via the shared Ge₉ atom, or as two [Ge₈] tubs which encapsulate an almost linear Co1-Ge9-Co2 strand, which is also accordingly found in the published ion [Ni₂@Sn₁₇]⁴⁻.^[312] In contrast, the cage-interconnecting Ge₅ atom in the Ni-containing cluster **37a** splits in two positions Ge₅ and Ge₅ⁱ (Scheme 11c). The deviation of Ge₅ from an ideal centered position causes a strongly bent angle Ni1-Ge5-Ni2, and the formation of two distinct coordination polyhedra encapsulating the Ni atoms. The cluster can be described as a [Ge₈] tub which is interconnected to a trivacant icosahedral entity termed mer-vIC-9 (Scheme 11c and d).^[315] While anion **37a** was monitored in ESI-MS measurements, quantum chemical calculations corroborated the determined structures of the endohedral 17-atom clusters **35a** and **37a** to be true local minima.

2.2.2.3 Synthesis of Germanide *Zintl* Clusters Comprising Mg²⁺ Counterions

In analogy to the reactions of nonagermanide clusters with organozinc complexes, magnesium organyls were reacted with the precursor K₄Ge₉ as well as with the threefold silylated cluster K[Ge₉{Si(TMS)₃}₃]. The most important results are summarized in Scheme 12.



Scheme 12. Synthesis and molecular structures of the Mg-comprising clusters a) [K[2.2.2]crypt]₄[Mg(NacNac^{Mes})(NH₃)₄]₂[Ge₉-Ge₉]·32.58NH₃ (**38a-KMg**); b) [Mg(NacNac^{Mes})(MeCN)₄][Ge₉{Si(TMS)₃}₃]·MeCN (**39a-Mg**). All ellipsoids are presented at a 50 % probability level and co-crystallizing solvent molecules as well as hydrogen atoms are omitted for clarity. In a) and b) the carbon atoms of the [NacNac^{Mes}]⁻ ligands are shown as wire-sticks for clarity. In a) the four [K[2.2.2]crypt]⁺ counterions are neglected for clarity, and in b) solely the central Si atoms of the hypersilyl groups are shown.

The reaction of K₄Ge₉ with the precursor Mg(NacNac^{Mes})I in liquid ammonia yielded compound **38a-KMg**, [K[2.2.2]crypt]₄[Mg(NacNac^{Mes})(NH₃)₄]₂[Ge₉-Ge₉]·32.58NH₃, in which two of the six K⁺ counterions were exchanged by [Mg(NacNac^{Mes})(NH₃)₄]⁺ complexes. The isolated compound comprises a [Ge₉-Ge₉]⁶⁻ unit featuring a Ge-Ge *exo*-bond, and the structure and geometry of the dimer is in agreement with previously reported species (Scheme 12a).^[170-171, 183, 264] The Mg²⁺ ion is embedded into a slightly distorted octahedral sphere of N atoms, formed by the organic ligand and four coordinating NH₃ molecules. However, due to the spatial separation of the Mg²⁺ ion to any Ge vertex, no direct interactions between the cluster and the counterion are observed as for the comparable Zn-comprising species discussed in Chapter 2.2.1.1.

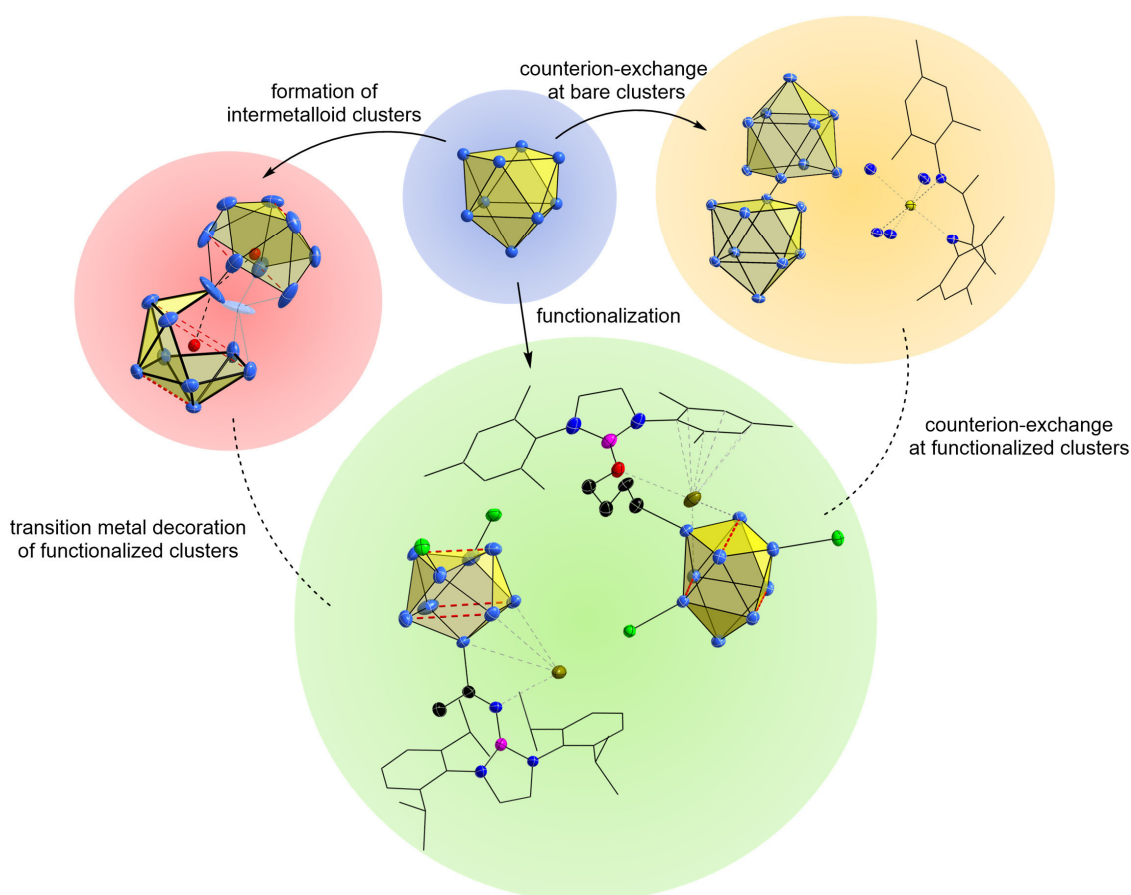
A complete ion-exchange of K^+ by Mg^{2+} was achieved by reacting the threefold silylated cluster with $Mg(NacNac^{Mes})I$. The formed species **39a-Mg**, $[Mg(NacNac^{Mes})(MeCN)_4][Ge_9\{Si(TMS)_3\}_3] \cdot MeCN$ (Scheme 12b), comprises an unaltered $[Ge_9\{Si(TMS)_3\}_3]^-$ cluster,^[206] which co-crystallizes with the cationic Mg complex featuring an octahedral coordination sphere in analogy to **38a-KMg**. Again, any direct interactions between the cluster and the organo-magnesium fragment can be excluded. Even though the Mg^{2+} ions do not directly interact with the $[Ge_9]$ clusters, a straightforward way was established to (partially) exchange the cluster's counterions by the application of organometallic halides. A reactivity test of compound **39a-Mg** towards the N-heterocyclic carbene $NHC^{Dipp}CuCl$ was performed, yielding the Cu-carbene adduct $NHC^{Dipp}Cu[Ge_9\{Si(TMS)_3\}_3]$,^[234] which also forms upon utilizing the K-containing precursor $K[Ge_9\{Si(TMS)_3\}_3]$. Thus, the influence of the counterion on the reactivity of the cluster in subsequent reactions seems to play a minor role.

In further studies the reactivity of the Mg(I) complex $[Mg(NacNac^{Mes})]_2$ towards liquid ammonia solutions containing dissolved germanide clusters was tested. Even though deep red solutions were obtained, no single crystalline material comprising germanide clusters could be isolated from the reddish precipitates. Instead, a rapid color change of the reaction solution and of isolated solid material to brown-green was observed upon opening the reaction flask, indicating the presence of highly sensitive species. Nevertheless, colorless to light-yellow crystals of the by-products $[K(18\text{-crown-6})][NacNac^{Mes}] \cdot 3NH_3$ and $[K[2.2.2]crypt][NacNac^{Mes}] \cdot NH_3$ were isolated. The capture of cleaved $[NacNac^{Mes}]^-$ ligands accounts for reactions taking place in solution, however potentially formed Ge species remained elusive.

During the synthesis of the precursor $NacNac^{Mes}H$ few crystals of the fully reduced congener N^2, N^4 -dimesitylpentane-2,4-diamine were obtained, whose crystal structure is comprehensively discussed in Chapter 6.11.

3 CONCLUSIONS

Within this thesis reactions of bare and silylated germanium clusters towards main group element compounds and transition metal complexes are discussed. A generalized overview of the performed reactions and cross-relations is provided in Scheme 13, including exemplarily structures of isolated compounds.



Scheme 13. Generalized overview of reactions discussed in this thesis. For each reaction type one exemplary molecular structure is presented. Dashed lines resemble cross-relations between the different fields.

The performed experiments can be divided into major fields: functionalization of the [Ge₉] cluster core with main group element fragments, formation of intermetalloid clusters, and counterion-exchange at [Ge₉] clusters. However, cross relations between the fields exist. As key example, functionalized nonagermanide clusters react with *TM* complexes yielding the respective coinage metal-carbene adducts, as described in several cases. A second cross-relation applies to the counterion-exchange, since the substitution of K⁺ ions by Mg²⁺ can either be performed starting from the bare [Ge₉] clusters or from a cluster species which was functionalized with silyl groups in a first instance. Closely related is the exchange of counterions in the solid-state precursor, allowing for instance the synthesis of Cs⁺-comprising functionalized clusters. Cross-relations are indicated by dashed lines in Scheme 13.

In the first section of this thesis reactions of the twofold silylated cluster with chlorophosphines and chloroboranes are described. In case of the chlorophosphines, various phosphanylated species were obtained which showed a subsequent reactivity towards coinage metal-carbene compounds due to their Lewis basic character. Since the silylated $[\text{Ge}_9]$ cluster is described as a Lewis base itself, the major focus of this thesis is investigating reactions of the cluster towards electrophilic halo-boranes. The applied boranes can be roughly sorted according to their Lewis acidity: $\text{Cy}_2\text{BCl} > \text{DAB}^{\text{R}}\text{-Br} > \text{DAB}^{\text{R}}\text{-Cl}$. Most intriguingly, even small variations in the chemical composition of the respective boranes lead to severe changes in their reactivity towards the cluster precursor.

The alkyl chloroborane Cy_2BCl acts as an oxide-scavenger in the oxidative coupling of two twofold silylated clusters under the formation of a Ge-Ge single bond between the cluster entities. Even though a plethora of oligomeric clusters comprising bare $[\text{Ge}_9]$ motifs as building blocks has been reported,^[95, 147, 166, 169-174, 180-181] the oxidation agents yielding such species have not unequivocally been identified. The presented results illustrate that parameters like trace amounts of oxygen or water, which cannot be removed from the system even under a most careful handling of the reactants, can play a vital role in *Zintl* cluster chemistry. According to the described observations it is feasible that the intentional application of suitable oxidation agents could be a potential strategy towards developing targeted routes for the bottom-up synthesis of extended, oxidatively-coupled tetrel element clusters.

In reactions of the twofold silylated cluster with the less electrophilic bromo-1,3,2-diazaborolidines $\text{DAB}^{\text{R}}\text{-Br}$ an alternative way of attaching ligands at the $[\text{Ge}_9]$ cluster was introduced. The incorporation of ring-opened ether fragments between the silylated cluster and the boranyl fragment is based on a $\text{S}_{\text{N}}2$ -like reaction mechanism, which is an oftentimes observed reaction type in this field of chemistry. However, the interlinking of the cluster and boranyl entity by an imine moiety clearly is due to a frustrated Lewis acid-base-like reactivity. Via this method up to two functional groups, which are the imine moiety as well as an olefin group, were introduced to the $[\text{Ge}_9]$ core. The described reaction protocol could in principle be transferred to other boron-free Lewis acids, thus immobilizing various types of acidic centers in close proximity to the $[\text{Ge}_9]$ cluster. Furthermore, the straightforward protonation of the imine moiety led to an intense color change of the compound from red to green, thus accounting for an alteration of the electronic situation, which was investigated in more detail using a quantum chemical approach. The tailorable interaction of the cluster with visible light is a first step on the way to the design of antenna molecules, which could potentially find application in light harvesting devices.

The application of the least Lewis acidic chloro-1,3,2-diazaborolidines led to the formation of boranyl-decorated silylated $[\text{Ge}_9]$ clusters. The respective species were obtained in a reliable

reaction protocol, and quantum chemical calculations revealed that the attachment of specific boranyl ligands generates intramolecular frustrated Lewis pairs. However, the calculated species remained elusive on an experimental level. The combined results reveal that the design and choice of the applied borane reactants is a balancing act between their reactivity and stability, with small deviations in the electrophilicity imposing a significant influence on the occurring reactions.

The second part of this thesis focuses on the formation of various intermetalloid germanide clusters. By reacting solid-state phases containing $[E_4]^{4-}$ ($E = \text{Ge}, \text{Sn}$) and $[\text{Ge}_9]^{4-}$ ions with organozinc complexes, a series of Zn-coordinated clusters and by-products was identified. By screening the isolated structures for cross-relations, a formation path for the generation of tetrel element-Zn clusters was proposed: the reductive cleavage of R^- ions from the ZnR_2 precursor initiates an amide formation with the reaction medium liquid ammonia.^[118, 121] The amide anions react with the Zn precursors forming “activated” Zn species, which contain bare Zn^{2+} ions or $[\text{ZnR}]^+$ fragments. Subsequently, these reactants are available for reactions with the polyanionic clusters. The presented results allow a better understanding of the processes occurring in solution, which in the future might lead to improved synthesis protocols in the hardly controllable medium liquid ammonia. Thus, the generation of extended intermetalloid clusters at the border of isolated molecules and solid-state-like structures might become feasible.

In a similar direction points the isolation and characterization of the 17-atom endohedral species $[\text{Co}_2@\text{Ge}_{17}]^{6-}$ and $[\text{Ni}_2@\text{Ge}_{17}]^{4-}$. The clusters do not only bridge the gap between known endohedral 16- and 18-atom germanides, but also nicely illustrate that two congeners of a similar sum formula do not necessarily obtain the same structure. Both anions feature $[\text{Ge}_8]$ tubs as building fragments, which is an oftentimes observed feature in endohedral clusters. The development of a targeted and reliable synthesis strategy yielding such cluster fragments could pave the way to the synthesis of endohedral species of defined compositions, which might find application as synthons in catalytic reactions.^[292]

Reactions of Mg(II) compounds with bare and silylated $[\text{Ge}_9]$ clusters uncovered a straightforward way to (partially) exchange the counter ions at the respective clusters. It can be assumed that further organometallic alkaline earth metal complexes are feasible to act in an analogous way, which allows the systematic characterization of a row of substances deviating concerning their counterions. The exchange of the ions might impact the reactivity or solubility of the respective compounds. Furthermore, the solution-based ion-exchange allows the synthesis of clusters which would otherwise not be accessible due to the absence of the respective solid-state precursors.

4 EXPERIMENTAL SECTION

4.1 General Procedures and Equipment

All manipulations were conducted under the exclusion of moisture and oxygen if not stated otherwise. Therefore, experiments were performed using standard Schlenk line techniques and an Ar-filled glove box (*MBraun MB 200B*, mean O₂ value < 0.1 ppm, mean H₂O value < 0.1 ppm). The Ar gas used for operating the Schlenk line and the liquid ammonia device was purified from trace amounts of oxygen and moisture by passing it over columns filled with a heated BTS catalyst (70 °C), silica gel ("orange gel" indicator), as well as P₂O₅ (H₂O indicator). Furthermore, the Schlenk line was equipped with a mercury overpressure release vent and a *RZ 5* rotary vane pump (*Vacuubrand*), reaching an average pressure of 5·10⁻³ mbar (*Pfeiffer Vacuum Single Gauge*). Reactions were performed in Schlenk tubes (volume: 20 mL to 200 mL) or Schlenk flasks (volume: 100 mL to 1000 mL) made of borosilicate glass. The flasks were sealed either with rubber septa or glass stoppers, the latter of which were lubricated using high-vacuum resistant grease. All reaction containers were heated prior to usage under dynamic vacuum at 650 °C using a heat gun (*Steinel*). The procedure was repeated three times, and after each cycle the flasks were purged with Ar after cooling down to r.t. Glass ware was cleaned in a KOH/isopropanol bath (100 g/L) over night, and subsequently rinsed three times with deionized water. Further technical equipment like Teflon-coated magnetic stirring bars, spatula, Teflon tubings, syringe filters, *Whatman* filters, metal cannulas, NMR tubes, *Pasteur* pipettes, storage containers, agate mortars, tantalum ampoules, and steel autoclaves were stored in a drying oven (*Binder ED115*) at 120 °C for at least one hour before using it. All consumables were purchased from *VWR*. Experiments were stirred using a magnetic stirrer *RCT basic* (*IKA Labortechnik*) equipped with an integrated heating plate and a temperature sensor *ETS-D4* (*IKA Labortechnik*). Oil baths were used for performing experiments at elevated temperature or distillations, while cooling was achieved using a water/ice bath (0 °C) or an isopropanol/dry ice bath (-78 °C). Solid and liquid reactants were weighed in using an analytical scale *Entris 2241-1S* or *TE214S* (*Sartorius*) in the glove box. Solvents were transferred between flasks either by using a syringe and a rubber septum or a Teflon tube. In the latter case, both flasks were sealed with rubber septa which were punctured with the tubing. The septum of one flask was equipped with an additional steel cannula to allow a pressure compensation, and the solvent was passed over by applying an Ar overpressure to the storage flask.

4.2 List of Lubricants, Solvents, Chemicals, and Reactants

4.2.1 Lubricants

In Table 4 the lubricants used for sealing glass ware as well as oils for selecting single crystals and operating the vacuum pumps are listed.

Table 4. List of used lubricants.

grease/oil	supplier	usage
high vacuum grease	<i>Dow Corning</i>	Schlenk flask
PTFE grease	<i>Carl Roth</i>	Schlenk flask
Ramsay grease soft	<i>Leybonol</i>	Schlenk line
Lithilen grease	<i>Leybonol</i>	Schlenk flasks containing liquid ammonia and ethylenediamine
perfluoroalkylether oil, viscosity: 1800 cSt	<i>ABCR</i>	single crystal selection at r.t.
perfluoroalkylether oil Galden LS230	<i>Solvay Speciality Polymers Italy SpA</i>	single crystal selection at -40 °C
P3 PK 001 108-T	<i>Pfeiffer Vacuum GmbH</i>	vacuum pump of Schlenk line
Vorpumpenöl MW-95V	<i>Sindlhauser Materials</i>	vacuum pump of NH ₃ (l) Schlenk line

4.2.2 Solvents

The solvents MeCN, thf, hexane, and toluene were obtained from a solvent purification system *MB-SPS (MBraun)* equipped with columns containing molecular sieves (3 Å and 4 Å), and subsequently were stored over molecular sieves (3 Å, *VWR*). Beforehand, the sieves were activated under dynamic vacuum at 500 °C for 12 hours. Et₂O was dried over Na/benzophenone, ethanol was stirred over Na/diethyl phthalate, and ethylenediamine was dehydrated over CaH₂ prior to distilling all the respective solvents. Liquid ammonia was dried at least for one hour over sodium metal before usage.

4.2.3 Chemicals

Unless otherwise stated all commercially available chemicals were used without further purification. Chemicals were stored either on the bench at r.t., in an Ar-filled glove box, in a fridge at 6 °C (*Lovibond EX490*), or in a freezer at -32 °C (*Liebherr GN2613*). Table 5 gives a summary on the used basic chemicals.

4 Experimental Section

Table 5. List of purchased chemicals used within this work.

substance	sum formula	physical state	supplier	purity [%]	storage
[18]-crown-6	C ₁₂ H ₂₄ O ₆	solid	Merck	>99	glove box
[2.2.2]crypt	C ₁₈ H ₃₆ N ₂ O ₆	solid	Acros Organics	98	glove box
1,10-phenanthroline	C ₁₂ H ₈ N ₂	solid	Sigma Aldrich	>99	bench
2,4,6-trimethylaniline	C ₉ H ₁₃ N	liquid	Alfa Aesar	98	bench
2,4,6-trimethylphenyl bromide	C ₉ H ₁₁ Br	liquid	Alfa Aesar	99	6 °C
2,6-di(<i>iso</i> -propyl)aniline	C ₁₂ H ₁₉ N	liquid	Merck	92	bench
2,6-dimethylaniline	C ₈ H ₁₁ N	liquid	Acros Organics	99	bench
2-methylaniline	C ₇ H ₉ N	liquid	Sigma Aldrich	>99	bench
5-bromopentene	C ₅ H ₉ Br	liquid	Sigma Aldrich	95	6 °C
5-hexenenitrile	C ₆ H ₉ N	liquid	Acros Organics	95	glove box
acetonitrile	C ₂ H ₃ N	liquid	Sigma Aldrich	99.9	bench
acetonitrile- <i>d</i> ₃	CD ₃ CN	liquid	Sigma Aldrich	99.8	glove box
acetylacetone	C ₅ H ₈ O ₂	liquid	Merck	>99	bench
acrylonitrile	C ₃ H ₃ N	liquid	Sigma Aldrich	99	glove box
ammonia	NH ₃	gas	Westfalen AG	99.999	gas cylinder
ammonium chloride	NH ₄ Cl	solid	Grüssing GmbH	99.5	bench
argon	Ar	gas	Westfalen AG	99.998	gas cylinder
benzene	C ₆ H ₆	liquid	Sigma Aldrich	99.8	bench
benzene- <i>d</i> ₆	C ₆ D ₆	liquid	Sigma Aldrich	99.5	glove box
benzonitrile	C ₇ H ₅ N	liquid	Sigma Aldrich	>99	glove box
benzophenone	C ₁₃ H ₁₀ O	liquid	Sigma Aldrich	99	bench
boron tribromide	BBr ₃	liquid	Sigma Aldrich	1M in hexane	6 °C
boron trichloride	BCl ₃	liquid	Alfa Aesar	1M in hexane	6 °C
cesium	Cs	solid	Prof. F. Kraus	-	glove box
calcium hydride	CaH ₂	solid	Merck	>97	bench
chloroform- <i>d</i> ₁	CDCl ₃	liquid	Sigma Aldrich	99.8	glove box
chlorotris(trimethylsilyl)silane	C ₉ H ₂₇ ClSi ₄	solid	TCI	95	glove box
copper(I) chloride	CuCl	solid	Alfa Aesar	97	glove box
di(1-adamantyl)chlorophosphine	C ₂₀ H ₃₀ PCl	solid	Sigma Aldrich	97	glove box
diatomaceous earth	SiO ₂ /Al ₂ O ₃	solid	Carl Roth	-	bench
dichloromethane	CH ₂ Cl ₂	liquid	Brenntag	-	bench
dicyclohexylchloroborane	C ₁₂ H ₂₂ BCl	liquid	Sigma Aldrich	1M in hexane	glove box
di(cyclooctadiene)nickel(0)	C ₁₆ H ₂₄ Ni	solid	Sigma Aldrich	-	-32 °C
diethylaminodichlorophosphine	C ₄ H ₁₀ NOPCl ₂	liquid	Alfa Aesar	97	glove box
diethyl ether	C ₄ H ₁₀ O	liquid	Brenntag	-	bench
diethylzinc	C ₄ H ₁₀ Zn	liquid	Sigma Aldrich	1M in hexane	6 °C
diethyl phthalate	C ₁₂ H ₁₄ O ₄	solid	Sigma Aldrich	99	bench
di(<i>iso</i> -propyl)amine	C ₆ H ₁₅ N	liquid	Sigma Aldrich	99	bench
di(<i>iso</i> -propyl)ethylamine	C ₈ H ₁₉ N	liquid	Sigma Aldrich	>99	bench
dimethylformamide	C ₃ H ₇ NO	liquid	Sigma Aldrich	99.8	glove box
di(<i>ortho</i> -tolyl)chlorophosphine	C ₁₄ H ₁₄ PCl	solid	Alfa Aesar	98	glove box
dioxane	C ₄ H ₈ O ₂	liquid	Acros Organics	>99.8	glove box

substance	sum formula	physical state	supplier	purity [%]	storage
diphenylzinc	C ₁₂ H ₁₀ Zn	solid	ABCR	98	glove box
dodecanenitrile	C ₁₂ H ₂₃ N	liquid	<i>Sigma Aldrich</i>	99	glove box
ethylacetate	C ₄ H ₈ O ₂	liquid	VWR	99.9	bench
ethylenediamine	C ₂ H ₈ N ₂	liquid	<i>Merck</i>	-	glove box
germanium	Ge	solid	<i>Evochem</i>	99.999	glove box
glyoxal	C ₂ H ₂ O ₂	liquid	<i>Merck</i>	40 % in water	bench
hexanenitrile	C ₆ H ₁₁ N	liquid	<i>Sigma Aldrich</i>	98	glove box
hydrochloric acid	HCl	liquid	<i>Sigma Aldrich</i>	37 % solution	bench
iodine	I ₂	solid	VWR	99.8	glove box
iodomethane	CH ₃ I	liquid	<i>Alfa Aesar</i>	99	bench
<i>iso</i> -butyronitrile	C ₄ H ₇ N	liquid	<i>Sigma Aldrich</i>	99	glove box
<i>iso</i> -propylmagnesium chloride	C ₃ H ₇ BrMg	liquid	<i>Acros Organics</i>	2M in thf	bench
lithium granula	Li	solid	<i>Rockwood Lithium</i>	97	glove box
lithium chloride	LiCl	solid	<i>Sigma Aldrich</i>	99.9	glove box
magnesium sulfate	MgSO ₄	solid	VWR	99.8	bench
magnesium turnings	Mg	solid	<i>ChemPur</i>	99.9	bench
menthol	C ₁₀ H ₂₀ O	solid	<i>Sigma Aldrich</i>	99	bench
methanol	CH ₄ O	liquid	VWR	99.5	bench
methylithium	CH ₃ Li	liquid	<i>Sigma Aldrich</i>	1.6M in Et ₂ O	6 °C
nitrogen	N ₂	liquid	<i>Air Liquide</i>	-	dewar
<i>N,N'</i> -di(<i>iso</i> -propyl)ethylenediamine	C ₈ H ₂₀ N ₂	liquid	<i>Sigma Aldrich</i>	99	bench
<i>N,N'</i> -dimethylethylenediamine	C ₄ H ₁₂ N ₂	liquid	<i>Sigma Aldrich</i>	98	bench
<i>n</i> -hexane	C ₆ H ₁₂	liquid	<i>Brenntag</i>	-	bench
<i>n</i> -pentane	C ₅ H ₁₂	liquid	<i>Brenntag</i>	-	bench
oxygen	O ₂	gas	<i>Westfalen AG</i>	99.999	gas cylinder
paraformaldehyde	OH(CH ₂ O) _{<i>n</i>} H (<i>n</i> = 8-100)	solid	<i>Merck</i>	>95	bench
phosphorus trichloride	PCl ₃	liquid	<i>Merck</i>	>99	glove box
potassium	K	solid	<i>ChemPur</i>	98	glove box
potassium hydride	KH	solid	<i>Merck</i>	35 wt% in oil	bench
potassium hydroxide	KOH	solid	<i>Sigma Aldrich</i>	>85	bench
potassium <i>tert</i> -butoxide	C ₄ H ₉ OK	solid	<i>Sigma Aldrich</i>	>98	glove box
propionitrile	C ₃ H ₅ N	liquid	<i>Sigma Aldrich</i>	99	glove box
<i>p</i> -toluenesulfonic acid	C ₇ H ₈ O ₃ S	solid	<i>Merck</i>	>98	bench
pyridine- <i>d</i> ₅	C ₅ D ₅ N	liquid	<i>Sigma Aldrich</i>	>99.5	glove box
rubidium	Rb	solid	Prof. F. Kraus	-	glove box
silver(I) oxide	Ag ₂ O	solid	<i>Merck</i>	99	bench
sodium	Na	solid	<i>ChemPur</i>	99	glove box
<i>tert</i> -butyldichlorophosphine	C ₄ H ₉ PCl ₂	liquid	<i>Alfa Aesar</i>	98	glove box
<i>tert</i> -butyl methyl ether	C ₅ H ₁₂ O	liquid	<i>Sigma Aldrich</i>	99.8	bench
tetrahydrofuran	C ₄ H ₈ O	liquid	<i>Sigma Aldrich</i>	99.9	bench
tetrahydrofuran- <i>d</i> ₈	C ₄ D ₈ O	liquid	<i>Sigma Aldrich</i>	99.5	glove box
toluene	C ₇ H ₈	liquid	<i>Brenntag</i>	-	bench
toluene- <i>d</i> ₈	C ₇ D ₈	liquid	<i>Sigma Aldrich</i>	99	glove box

substance	sum formula	physical state	supplier	purity [%]	storage
triethylamine	C ₆ H ₁₅ N	liquid	VWR	99	bench
triethylamine hydrochloride	C ₆ H ₁₆ NCl	solid	Sigma Aldrich	99	glove box
trimethylene oxide	C ₃ H ₆ O	liquid	Acros Organics	97	6 °C
trimethylsilyl chloride	C ₃ H ₉ SiCl	liquid	Sigma Aldrich	>99	bench
zinc chloride	ZnCl ₂	solid	Alfa Aesar	98	glove box

4.2.4 Reactants

Table 6 summarizes the synthesized reactants used within this thesis. In case the preparation of the respective reactant involved multiple steps solely the final product is given. All reactants were stored at r.t. in an Ar-filled glove box.

Table 6. List of reactants used in this thesis. a: for synthesis of chlorophosphines see Reference [260]. ‡

reactant	sum formula	physical state	preparation
A ₄ Ge ₉ (A = K-Cs)	A ₄ Ge ₉ (A = K-Cs)	solid	Chapter 4.3.1
DAB ^{Dipp} -Br	C ₂₆ H ₃₈ BN ₂ Br	solid	[319]
DAB(II) ^{Dipp} -Br	C ₂₆ H ₃₆ BN ₂ Br	solid	[319]
DAB ^{iPr} -Cl	C ₈ H ₁₈ BN ₂ Cl	liquid	[320]
DAB ^{Me} -Cl	C ₄ H ₁₀ BN ₂ Cl	liquid	[320]
DAB ^{Mes} -Br	C ₂₀ H ₂₆ BN ₂ Br	solid	[319]
DAB ^{Mes} -Cl	C ₂₀ H ₂₆ BN ₂ Cl	solid	[319]
DAB ^{o-tol} -Br	C ₁₆ H ₁₈ BN ₂ Br	solid	[319]
DAB ^{o-tol} -Cl	C ₁₆ H ₁₈ BN ₂ Cl	solid	[319]
DAB ^{o-xy} -Br	C ₁₈ H ₂₂ BN ₂ Br	solid	[319]
(ⁱ Pr ₂ N) ₂ BBr	C ₁₂ H ₂₈ BN ₂ Br	liquid	[321]
(ⁱ Pr ₂ N) ₂ BCl	C ₁₂ H ₂₈ BN ₂ Cl	liquid	[321]
ⁱ Pr(N ⁱ Pr ₂)PCl ^a	C ₉ H ₂₁ PNCl	liquid	[322]
ⁱ Pr ^t BuPCl ^a	C ₇ H ₁₆ PCl	liquid	[262]
K ₁₂ Ge ₁₇	K ₁₂ Ge ₁₇	solid	Chapter 4.3.2
K ₂ [Ge ₉ {Si(TMS) ₃ } ₂]	K ₂ Ge ₉ Si ₈ C ₁₈ H ₅₄	solid	[205]
K[Ge ₉ {Si(TMS) ₃ } ₃]	KGe ₉ Si ₁₂ C ₂₇ H ₈₁	solid	[206]
Mg(NacNac ^{Mes})I	C ₂₃ H ₂₉ MgN ₂ I	solid	[323-324]
NHC ^{Dipp} AgCl	C ₂₇ H ₃₆ AgN ₂ Cl	solid	[325-327]
NHC ^{Dipp} CuCl	C ₂₇ H ₃₆ CuN ₂ Cl	solid	[326-327]
NHC ^{iPr} CuCl	C ₉ H ₁₆ CuN ₂ Cl	solid	[326-327]
^t BuMesPCl ^a	C ₁₃ H ₂₀ PCl	solid	[328]
^t Bu(NEt ₂)PCl ^a	C ₈ H ₁₉ PNCl	liquid	[262]
^t Bu(N ⁱ Pr ₂)PCl ^a	C ₁₀ H ₂₃ PNCl	liquid	[322]
^t Bu{(CH ₂) ₃ CH=CH ₂ }PCl ^a	C ₉ H ₁₈ PCl	liquid	[329]
ZnCp* ₂	C ₂₀ H ₃₀ Zn	solid	[330]

‡: The corresponding alkyl, alkenyl, aminoalkyl, and aryl substituted chlorophosphines were prepared during my Master's thesis.

Table 7 summarizes reactants that were synthesized and generously provided for usage by colleagues at the Technical University of Munich (Prof. Fässler and Prof. Inoue), and by Prof. Jones, Monash University, Australia. All samples were stored at r.t. in an Ar-filled glove box.

Table 7. List of reactants used in this thesis provided by colleagues.

reactant	sum formula	physical state	producer	chair
(1,1-dimethylpropyl) ₂ PCl	C ₁₀ H ₂₂ PCl	liquid	Dr. Felix Geitner	Prof. Fässler
(C ₆ F ₅) ₂ PCl	C ₁₂ F ₁₀ PCl	liquid	Dr. Felix Geitner	Prof. Fässler
[Cp ₂ Ti(NH ₃) ₂]Cl(NH ₃)	C ₁₀ H ₁₉ N ₃ TiCl	solid	Dr. Felix Geitner	Prof. Fässler
ⁱ Pr(N ⁱ Pr ₂)PCl	C ₉ H ₂₁ PNCI	liquid	Dr. Felix Geitner	Prof. Fässler
KC ₈	KC ₈	solid	M. Sc. Yasmin Selic	Prof. Fässler
"K ₅ Co _{1.2} Ge ₉ "	K ₅ Co _{1.2} Ge ₉	solid	Dr. Benedikt Witzel	Prof. Fässler
Mes ₂ BBr	C ₁₈ H ₂₂ BBr	liquid	Dr. Daniel Franz	Prof. Inoue
[NacNac ^{Mes} Mg] ₂	C ₄₆ H ₅₈ N ₄ Mg ₂	solid	–	Prof. Jones
^t Bu(N ⁱ Pr ₂)PCl	C ₁₀ H ₂₃ PNCI	liquid	Dr. Felix Geitner	Prof. Fässler
ZnMes ₂	C ₁₈ H ₂₂ Zn	solid	Dr. Thomas Henneberger	Prof. Fässler

4.3 Synthesis of Solid-State Precursors

The solid-state phases K_4Ge_9 , Rb_4Ge_9 , Cs_4Ge_9 , and $K_{12}Ge_{17}$ were prepared according to modified literature procedures.^[79, 82, 84]

4.3.1 Preparation of A_4Ge_9 ($A = K-Cs$)

Elemental A (K: 1.052 g; Rb: 2.286 g; Cs: 3.575 g; 26.9 mmol, 1 equiv.) was weighed into a stainless-steel tube, and subsequently finely grounded Ge powder (3.999 g, 55.1 mmol, 2.1 equiv.) was added. Afterwards, the steel tube was inserted into a stainless-steel autoclave which was closed with a screw cap (Figure 31a). The autoclave was set in a corundum tube (length: 60 cm, diameter: 3.8 cm, wall thickness: 0.5 cm), which was evacuated and purged with Ar before. The tube was sealed with a glass cap featuring a connected rubber balloon for pressure regulation. After a repeated flushing of the corundum tube with Ar it was vertically placed into a tube furnace *Loba 1200-42-600-1-OW* (*HTM Reetz GmbH*).

4.3.2 Preparation of $K_{12}Ge_{17}$

A tantalum ampoule (Figure 31b) was rinsed stepwise in acetone, acetic acid, deionized water, and again acetone in an ultra-sonication bath (30 min each). Afterwards, the bottom of the ampoule was welded on the tantalum tube (length: 60 mm, diameter: 10 mm, wall thickness: 0.5 mm) by using an electric arc furnace *MAM 1* (*Edmund Bühler*) in the glove box. Elemental K (1.146 g, 29.3 mmol, 1 equiv.) was weighed into the ampoule, and subsequently finely grounded Ge powder (3.018 g, 41.5 mmol, 1.4 equiv.) was added. The reaction container was sealed by welding a tantalum lid on top of it using the arc furnace. The ampoule was inserted in a quartz glass tube, which was sealed with a glass cap and evacuated afterwards. The tube was vertically inserted into a tube furnace *Loba 1200-42-600-1-OW* (*HTM Reetz GmbH*).

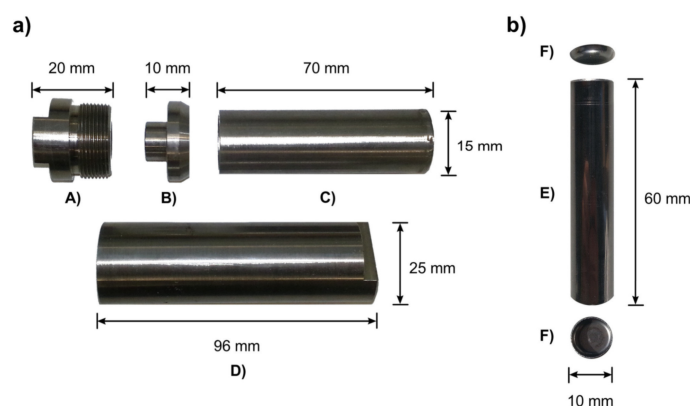
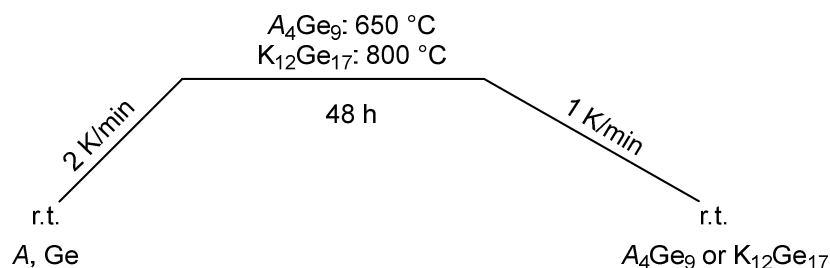


Figure 31. Components of a) the stainless-steel autoclave (A-D) and b) the tantalum ampoule (E, F) for the synthesis of A_4Ge_9 and $K_{12}Ge_{17}$, respectively. A) screw cap with thread, B) stamp, C) reaction tube, D) steel autoclave with inner thread; E) tantalum ampoule, F) tantalum lids.

Using an automatic temperature control system *S 14083* (*Eurotherm Deutschland GmbH*) the reaction containers were heated with a rate of 2 K/min to 650 °C or 800 °C for A_4Ge_9 or $K_{12}Ge_{17}$, respectively (Scheme 14). The temperature was kept for 48 h before the samples were cooled down to r.t. at a rate of 1 K/min.



Scheme 14. Temperature program for the synthesis of the *Zintl* phases A_4Ge_9 and $K_{12}Ge_{17}$.

Subsequently, the reaction containers were transferred into the glove box and the obtained solid products were removed from the autoclaves by scratching with a spatula. With the help of an agate mortar the *Zintl* phases were finely grounded, and a sample was filled into a Mark capillary (*Hilgenberg GmbH*, diameter: 0.5 mm, wall thickness: 0.01 mm, length: 80 mm), which was sealed with some molten wax (*Max Wax* pen). For determining the phase purity, a powder X-ray diffractogram was collected. The theoretical powder patterns for A_4Ge_9 (Figure 32a-c) were calculated using the single crystal data of the respective solid-state phases and the program *WinXPOW* (*STOE*).^[67, 79] A theoretical pattern for $K_{12}Ge_{17}$ was simulated with the program *Diamond* (*Crystal Impact GbR*) by using the single crystal data of $K_{12}Si_{17}$ and replacing Si with Ge (Figure 32d).^[82]

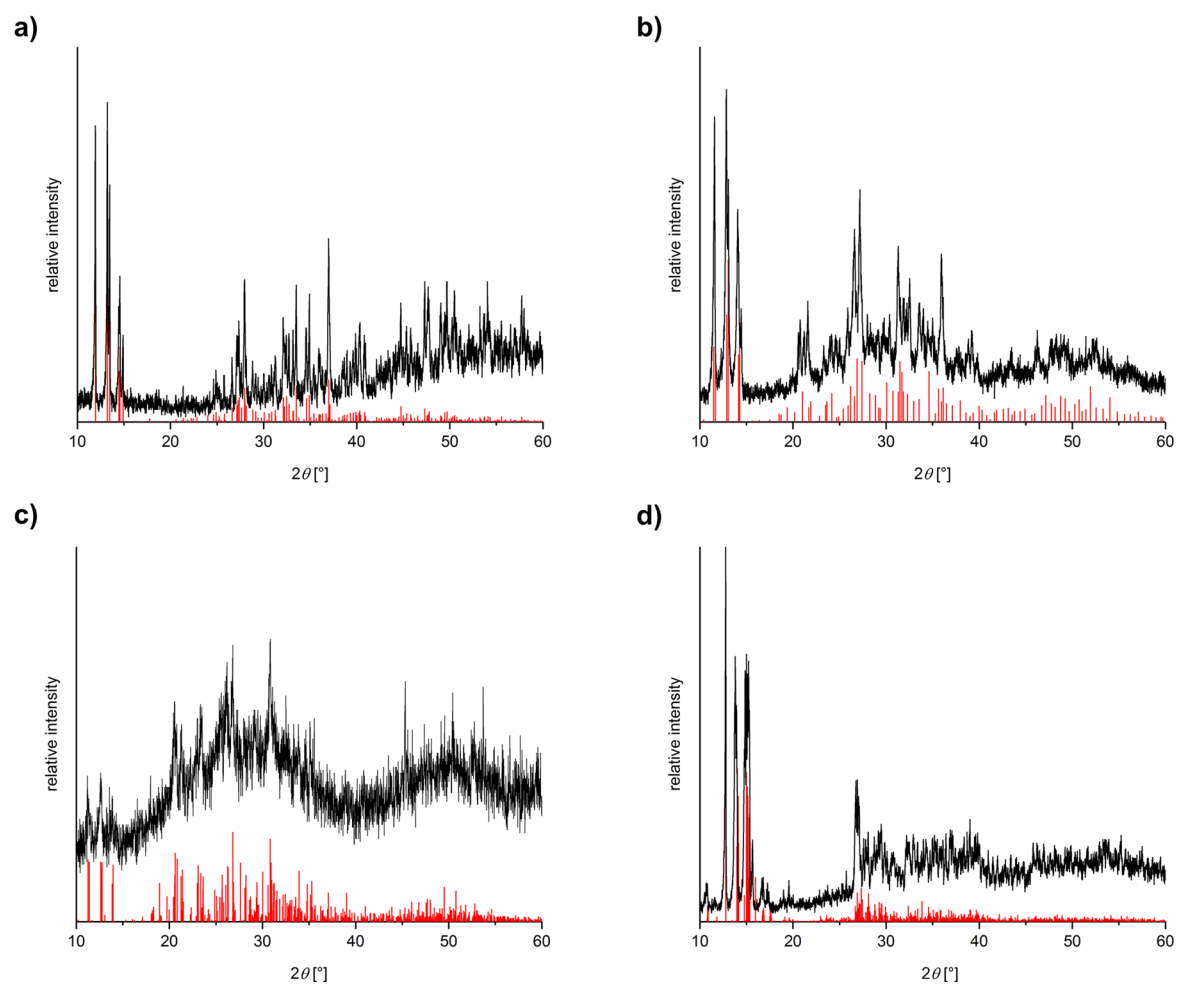


Figure 32. Powder X-ray diffractograms of a) K_4Ge_9 ; b) Rb_4Ge_9 ; c) Cs_4Ge_9 ; d) $K_{12}Ge_{17}$ in the region of 10° to 60° 2θ . The collected data is presented as black graphs, the calculated reflexes are presented as red columns. For the calculation of the theoretical diffraction patterns the crystal structure data of A_4Ge_9 ^[67, 79] and $K_{12}Si_{17}$ ^[82] were used.

4.4 Filtration Techniques

4.4.1 Whatman Filtration at the Schlenk Line

A *Whatman* glass filter (*Whatman GD 1UM*) was wrapped around a Teflon tubing (*VWR*, diameter: 1 mm or 4 mm) and fixed with 10 cm of Teflon tape (*VWR*). Afterwards, the filter was dried for 2 hours in the drying oven. Subsequently, the reaction flask and the collecting flask were interconnected with the filtration unit, which was led through rubber septa. An Ar overpressure was applied to the Schlenk flask containing the suspension, causing a transfer of the neat filtrate through the filter into the empty flask. To allow a pressure compensation the septum of the collecting flask was punctured with a steel cannula. The filtration technique is best suited for volumes between 2 mL to 5 mL and a coarse precipitate.

4.4.2 Filtration Using a Schlenk Frit with Glass Filter

A Schlenk frit with incorporated glass filter was equipped with a 1 cm thick layer of diatomaceous earth (*Carl Roth*), and excessively dried under dynamic vacuum at 650 °C. Subsequently, the reaction flask was connected to the frit and the whole apparatus was slowly turned upside-down. At the collecting flask a static vacuum was applied leading to an enhanced filtration performance. The filtration technique is best suited for volumes greater than 50 mL and a fine precipitate.

4.4.3 Filtration through Syringe Filters in the Glove Box

In the glove box a syringe filter with PTFE membrane (*VWR*, diameter: 25mm, pore size: 0.25 µm) was connected to a syringe containing the suspension. The stamp of the syringe was pressed down and the filtrate was collected in a flask. The filtration technique is best suited for volumes between 5 mL to 20 mL and a fine precipitate.

4.5 Condensation of Liquid Ammonia

As stated in the introduction, the highly charged Ge clusters dissolve in polar solvents like liquid ammonia. Figure 33 gives a schematic illustration of the experimental setup for the condensation of gaseous ammonia. A NH_3 gas cylinder was connected to a Schlenk line which was entirely made of glass. The whole Schlenk line was three times evacuated to a pressure below $8 \cdot 10^{-4}$ mbar, and subsequently flushed with Ar. A dewar containing dry ice and isopropanol was attached to one of the cooling traps, and the gaseous ammonia was condensed into the trap under a static vacuum. The cooling trap itself contained a piece of sodium metal (3 g) to remove any water traces from the condensed ammonia. An indicator for water-free liquid ammonia is the blue color of the solvent, resulting from the formation of solvated electrons.^[1] The solvent was stored at least one hour over the alkali metal before usage.

All solid reactants were weighed into a Schlenk flask in the glove box, and the sealed flask was connected to the Schlenk line by flushing the interconnecting glass newels several times with Ar. The reaction flasks were placed in a dry ice/isopropanol bath, a static vacuum was applied to the whole Schlenk apparatus, and all vents to the cooling trap containing liquid ammonia were opened. In a last step, the dewar was removed from the cooling trap and approximately 3 mL to 5 mL ammonia was transferred via the gas phase (static vacuum) into the cooled connected reaction flasks. The experiments were stored in a freezer at either -40 °C (*Elcold UNI31/EL31L*) or -70 °C (*Thermo Electron Corporation ULT 1790-3-V34*) to allow a slow crystallization process. It is important to handle flasks containing liquid ammonia under permanent cooling below -34 °C to prevent a rapid and potential harmful evaporation of the solvent.^[331]

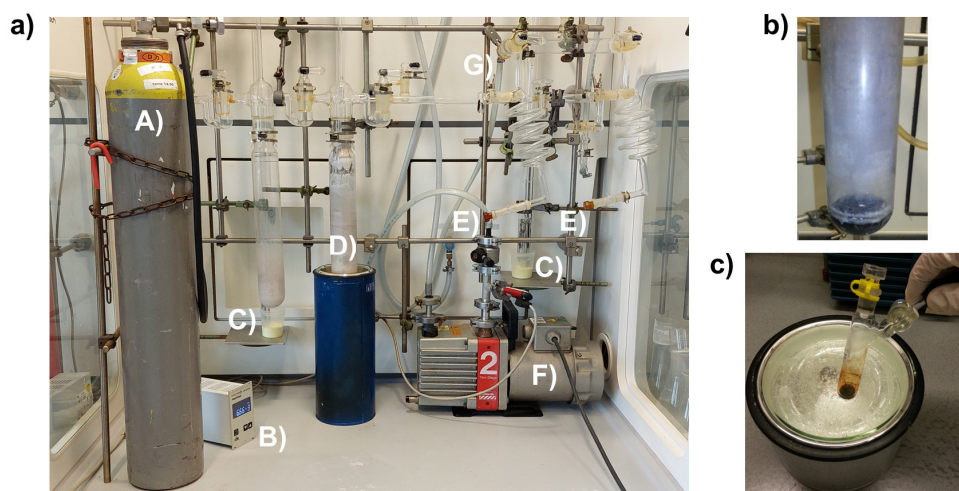


Figure 33. a) Experimental setup for the condensation of gaseous ammonia. A) NH_3 gas cylinder, B) pressure gauge, C) mercury overpressure releases, D) cooling trap containing Na metal and condensed ammonia, E) glass newel featuring an adapter for Schlenk tubes, F) vacuum pump, G) Ar supply; b) cooling trap containing Na metal and condensed ammonia; c) Schlenk flask containing a red solution of K_4Ge_9 in liquid ammonia.

4.6 Selection and Dissection of Single Crystals for Structure Determination

4.6.1 Isolation of Single Crystals at Room Temperature

Crystallization experiments which were stored at r.t. were monitored for the formation of crystalline material at regular time intervals. If solid components were observed, the Schlenk tube was transferred into the glove box. Under the inert atmosphere the crystals were transferred onto a microscope plate with perfluoralkylether oil (*ABCR*, viscosity: 1800 cSt). With the help of an integrated microscope (*Leica MZ6*) and a light source (*Leica KL1500LCD*) crystals suitable for single crystal diffraction were selected. The crystals were mounted on glass capillaries (diameter 0.3 mm, length 2 cm) through adhesion, which were then fixated with wax in brass tubes (diameter 3 mm, length 3 cm). The selected crystals were transferred to the diffractometer in an Ar-filled glass cap.

4.6.2 Isolation of Single Crystals at Low Temperature

Crystallization experiments which were stored at -40 °C or -70 °C (especially valid for liquid ammonia) were carefully monitored for the formation of crystalline material on a regular basis. If crystals were observed, the Schlenk tube was transferred into a dewar containing an isopropanol/dry ice bath. For the selection of single crystals a cooling table was used, which was designed according to the setup of Kottke and Stalke (Figure 34).^[332] The installation consisted of a small Schlenk line featuring an Ar supply and a vacuum source. Perfluoralkylether oil (*Galden LS230*) was dispersed on a microscope plate, which was subsequently cooled to approximately -40 °C. The cooling was achieved by a dewar filled with liquid nitrogen, which was positioned below the glass plate, as well as a cold stream of nitrogen gas applied from above. The gaseous stream was cooled down by leading it through a copper newel in a liquid nitrogen filled dewar. Solids were extracted from the reaction vessel using a spatula and transferred into the cold oil. Crystals suitable for single crystal diffraction were selected under a microscope (*Leica M80*) and mounted on the glass loop of the crystal cap (*Hampton research*). The crystal cap was transferred under liquid nitrogen to the diffractometer using a metal pincer.

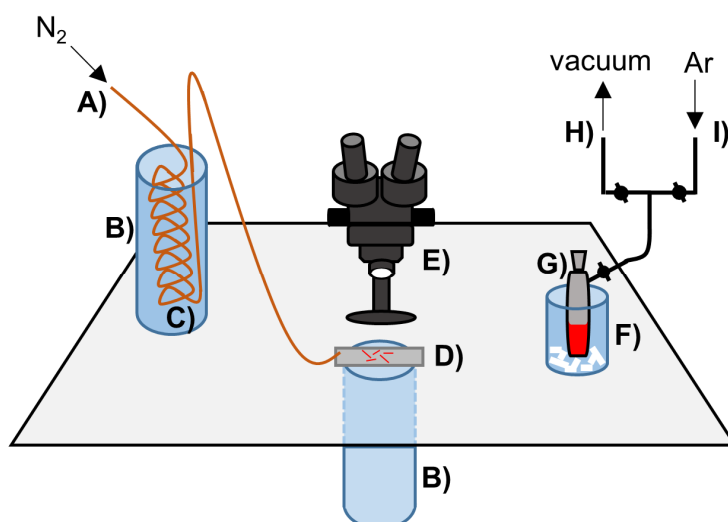


Figure 34. Schematic illustration of the experimental setup for selecting single crystals at low temperature using a cooling table.^[332] A) N_2 supply, B) dewar containing liquid nitrogen, C) copper newel, D) glass plate with oil and crystalline material, E) microscope with light source, F) dewar containing dry ice and isopropanol, G) Schlenk flask, H) connection to a vacuum pump, I) Ar supply.

4.7 Characterization Methods

4.7.1 Nuclear Magnetic Resonance Spectroscopy (NMR)

NMR spectra at ambient temperature were measured on a *Bruker Avance Ultrashield 400 MHz* spectrometer and a *Bruker Ultrashield Plus 500 MHz* spectrometer. Variable temperature measurements were carried out using a *Bruker DRX 400 MHz spectrometer*. ^1H and ^{13}C NMR spectra were calibrated using the residual proton or carbon signal of the used deuterated solvents. Chemical shifts are reported in ppm (parts per million) relative to SiMe_4 , with the solvent peaks serving as internal reference.^[333] The samples were prepared in an Ar-filled glove box in air-tight *J-Young* tubes equipped with a Teflon screw cap (*Deutero*). Signal multiplicities are abbreviated as follows: singlet (s), doublet (d), triplet (t), heptet (hept), multiplet (m), broad signal (br). Spectra were plotted using *MestReNova 12 (Mestrelab Research)*.

4.7.2 Raman Spectroscopy

Raman spectra were acquired on an *inVia Raman microscope RE04 (Renishaw)* equipped with a CCD detector. For the sample preparation the compound (powder or single crystal) was transferred into a Mark capillary (*Hilgenberg GmbH*, diameter: 0.3 mm, wall thickness: 0.01 mm, length: 80 mm), which was sealed with a small piece of wax (*Max Wax pen*). Data evaluation was performed using the program *WiRe 4.2 (Renishaw)*, and spectra were plotted using *Excel (Microsoft 365)* and *OriginPro 2021 (OriginLab)*. Details on the parameters of the measurements can be found in the respective manuscripts.

4.7.3 Electrospray Ionization Mass Spectrometry (ESI-MS)

ESI-MS spectra were acquired in the negative-ion mode on a *Bruker Daltronic HCT mass spectrometer* (injection speed: 300 $\mu\text{L/h}$, dry gas temperature 300 $^\circ\text{C}$) using varying capillary voltages (1500 V to 4000 V). For the sample preparation approximately 20 μmol of the compound was dissolved and filtered using a syringe filter. The sample solution was taken up in a *Hamilton* syringe (*VWR*) and transferred to the ESI-MS device. Data evaluation, including the calculation of the theoretical isotope pattern, was performed with the program *Compass Data Analysis 4.0 SP 5 (Bruker)*, and spectra were plotted using *Excel (Microsoft 365)* and *OriginPro 2021 (OriginLab)*.

4.7.4 Liquid Injection Field Desorption Ionization Mass Spectrometry (LIFDI-MS)

An *Exactive PlusOrbitrap* system (*Thermo Fisher Scientific*) equipped with an ion source from *Linden CMS GmbH* was used for the acquisition of LIFDI-MS spectra.^[334] For the sample preparation the compound was dissolved in toluene and filtered through a syringe filter in the glove box. The solution was applied on a graphite-dendrite coated tungsten wire and an ionization voltage of 10 kV was adjusted. The resulting radical cations were observed in the positive-ion mode. Data evaluation was performed with the program *Thermo Exactive Plus 2.9 SP3* (*Thermo Fisher Scientific*). Spectra were plotted using *Excel (Microsoft 365)* and *OriginPro 2021 (OriginLab)*. The theoretical isotope pattern was calculated using the website *enviPat Web 2.4*.^[335]

4.7.5 UV-Vis Spectroscopy

Data acquisition was performed using a *Cary 60 UV-visible spectrophotometer (Agilent Technologies)*. For the sample preparation a standard solution of the respective compound was prepared, and a *Hamilton* syringe (*VWR*) was used to dilute defined volumes of the standard to an exact total volume of 3 mL. Spectra were recorded in rubber septum-sealed quartz glass cuvettes (*STARNA GmbH*, diameter: 12.5 mm, height: 45 mm, volume: 3.5 ml, beam path: 10 mm) with a step size of 1 nm in the range of 200 nm to 900 nm. An automatic baseline correction was performed by recording the absorption data of the pure solvent. Kinetic studies were performed using an integrated magnetic stirrer and a stirring bar inside the cuvette (2500 rpm). The sample was excited using a defined wavelength, the second reactant was added through a rubber septum, and the absorption was measured as a function of time every 0.0125 s. Data evaluation was performed using the programs *Cary WinUV Scan Application* and *Cary WinUV Kinetics Application (Agilent Technologies)*. Spectra were plotted using *Excel (Microsoft 365)* and *OriginPro 2021 (OriginLab)*.

4.7.6 Powder X-Ray Diffractometry (P-XRD)

Powder diffraction data were acquired with Cu K α_1 radiation ($\lambda = 1.54056 \text{ \AA}$) using a *STOE STADI P* diffractometer equipped with a Ge monochromator, a Cu collimator (slit diameter: 0.3 mm), and a *MYTHEN 1K* detector (*DECTRIS*). For the sample preparation the solid-state phases were finely grounded and filled into Mark capillaries (*Hilgenberg GmbH*, diameter: 0.3 mm, wall thickness: 0.01 mm, length: 80 mm), which were sealed with some molten wax (*Max Wax* pen). Measurements were performed in the Debye-Sherrer geometry and data evaluation was performed using the program *WinXPOW (STOE)*. Spectra were plotted using *OriginPro 2021 (OriginLab)*.

4.7.7 Single Crystal X-Ray Diffraction Analysis (SC-XRD)

Single crystal selection and dissection was performed according to Chapter 4.6. Subsequently, the crystal cap or the brass tube with the attached crystal was mounted to the goniometer head under a stream of cold N₂ gas (150 K). The single crystal diffraction data were collected using a *StadiVari* diffractometer (STOE) equipped with a *PILATUS 300K* detector (DECTRIS) and a Mo K α_1 radiation source ($\lambda = 0.71073 \text{ \AA}$). Fast SC-XRD measurements (30 min) were performed in a first step to examine the lattice parameters of the compound. The parameters were compared to the chair-internal database and the database *ConQuest* (*The Cambridge Crystallographic Data Center*) before the measurement was started. An optimized run list for an extended measurement was calculated using the program *X-Area* (STOE & Cie GmbH). The same program was used for the data evaluation comprising the determination of the unit cell, the reflex integration, and a first internal refinement. The single crystal structures were determined by direct methods using the program *SHELXTL* and *SHELXS-2014*. Structure refinements were performed by full-matrix least-squares calculations against F^2 (*SHELXL-2014*).^[336-337] A riding model was used to calculate and refine the positions of hydrogen atoms. Other elements than hydrogen were refined with anisotropic displacement parameters. The electron density of heavily distorted solvent molecules was eliminated by using the PLATON squeeze function.^[338] While the initial structure refinement was performed by myself, Dr. Wilhelm Klein (Prof. Fässler, TUM) provided help in case of any crystallographic problems and finalized the structure refinements for publications. The crystallographic information files (cif) of most of the structures discussed within this thesis may be obtained from the *Cambridge Structural Database* following the link www.ccdc.cam.ac.uk/data_request/cif.

4.7.8 Energy Dispersive X-Ray Analysis (EDX)

Energy dispersive X-ray spectra were acquired using a *TM-1000 tabletop scanning electron microscope* (Hitachi). For the sample preparation the compound (powder or single crystal) was applied onto a carbon sticky tape (*PLANO GmbH*) in the glove box and the sample was transferred to the EDX device in a closed glass.

4.7.9 Elemental Analysis (EA)

Elemental analysis was performed in the micro-analytical laboratory of the Chemistry Department of the Technical University of Munich. For the determination of the C, H, and N content a combustion analyser (*HEKAtech EURO EA*) was used.

4.7.10 Quantum Chemical Calculations

Quantum chemical calculations were performed with the *TURBOMOLE* program package^[339] using either the BP86^[281, 284] or the PBE0^[340-342] hybrid density functional method and polarized triple- ζ -valence Karlsruhe basis sets (def2-TZVP for B, K, N, Si, Ge and Ni and def-TZVP for C and H).^[285] If applicable, a *COSMO* solvent field was applied to counter the anionic charge.^[343] Excited states were calculated using time-dependent DFT (TD-DFT).^[282-283] Multipole-accelerated resolution-of-the-identity technique was used to speed up the calculations.^[342, 344-345] As initial data sets the atomic coordinates of the single crystal structure data were used. Results were visualized using the programs *VMD*^[346] and *IboView*.^[347]

5 REFERENCES

- [1] A. F. Holleman, E. Wiberg and N. Wiberg, *Lehrbuch der anorganischen Chemie*, vol. 102, Walter de Gruyter GmbH & Co KG, Berlin, New York, **2008**, DOI 10.1515/9783110177701.
- [2] A. Yaroshevsky, *Geochem. Int.* **2006**, *44*, 48.
- [3] U.S. Geological Survey, *Mineral commodity summaries 2021*, **2021**, DOI 10.3133/mcs2021.
- [4] National Minerals Information Center, *Historical Statistics for Mineral and Material Commodities in the United States*, **2018**, <https://www.usgs.gov/centers/nmic/historical-statistics-mineral-and-material-commodities-united-states>, accessed 28th February 2022.
- [5] D. C. Curtolo, S. Friedrich and B. Friedrich, *J. Cryst. Process Technol.* **2017**, *7*, 65.
- [6] Statista, *Refinery production of germanium worldwide in 2020 by country*, <https://www.statista.com/statistics/1062116/global-germanium-production-by-country/>, accessed 28th February 2022.
- [7] Statista, *Global production of zinc metal from 2004 to 2020*, <https://www.statista.com/statistics/264878/world-production-of-zinc-metal/>, accessed 04th May 2022.
- [8] Statista, *London Metal Exchange zinc price from 2004 to 2021*, <https://www.statista.com/statistics/242291/global-zinc-price/>, accessed 04th May 2022.
- [9] T. Jiang, T. Zhang and Z. Liu, *ACS Sustain. Chem. Eng.* **2020**, *8*, 18545.
- [10] M. Patel and A. K. Karamalidis, *Sep. Purif. Technol.* **2021**, *275*, 118981.
- [11] J. Tao, Z. Tao and L. Zhihong, *J. Clean. Prod.* **2021**, *294*, 126217.
- [12] M. A. Green, K. Emery, Y. Hishikawa and W. Warta, *Prog. Photovolt. Res. Appl.* **2010**, *18*, 144.
- [13] P. A. Iles, *Prog. Photovolt. Res. Appl.* **2000**, *8*, 39.
- [14] H. G. Grimmeiss, *Semiconductors* **1999**, *33*, 939.
- [15] R. Moskalyk, *Miner. Eng.* **2004**, *17*, 393.
- [16] L. Finelli, C. Lorenzetti, M. Messori, L. Sisti and M. Vannini, *J. Appl. Polym. Sci.* **2004**, *92*, 1887.
- [17] W. A. MacDonald, *Polym. Int.* **2002**, *51*, 923.
- [18] E. Kasper, *J. Cryst. Growth* **1995**, *150*, 921.
- [19] E. Kasper, A. Schuh, G. Bauer, B. Holländer and H. Kibbel, *J. Cryst. Growth* **1995**, *157*, 68.
- [20] K. Hammani, M. A. Ettabib, A. Bogris, A. Kapsalis, D. Syvridis, M. Brun, P. Labeye, S. Nicoletti, D. J. Richardson and P. Petropoulos, *Opt. Express* **2013**, *21*, 16690.
- [21] E. Kasper, J. Eberhardt, H. Jorke, J.-F. Luy, H. Kibbel, M. Dashiell, O. Schmidt and M. Stoffel, *Solid-State Electron.* **2004**, *48*, 837.
- [22] A. Yakimov, V. Kirienko, V. Armbrister and A. Dvurechenskii, *Nanoscale Res. Lett.* **2013**, *8*, 1.
- [23] I. Stavarache, L. Nedelcu, V. Teodorescu, V. Maraloiu, I. Dascalescu and M. Ciurea, *GeSi Nanocrystals in SiO₂ Matrix with Extended Photoresponse in Near Infrared; in: 2018 International Semiconductor Conference*, Institute of Electrical and Electronic Engineers, Sinaia, Romania, **2018**, DOI 10.1109/SMICND.2018.8539745.
- [24] Y. Kanemitsu, *Silicon and germanium nanoparticles; in: Semiconductors and Semimetals*, vol. 49, Academic Press - Elsevier, Cambridge, Massachusetts, **1997**, DOI 10.1016/S0080-8784(08)62503-X.
- [25] N. Shirahata, D. Hirakawa, Y. Masuda and Y. Sakka, *Langmuir* **2013**, *29*, 7401.
- [26] P. R. Abel, Y.-M. Lin, T. de Souza, C.-Y. Chou, A. Gupta, J. B. Goodenough, G. S. Hwang, A. Heller and C. B. Mullins, *J. Phys. Chem. C* **2013**, *117*, 18885.
- [27] X. Li, Z. Yang, Y. Fu, L. Qiao, D. Li, H. Yue and D. He, *ACS Nano* **2015**, *9*, 1858.
- [28] J. Liang, X. Li, Z. Hou, T. Zhang, Y. Zhu, X. Yan and Y. Qian, *Chem. Mater.* **2015**, *27*, 4156.
- [29] M. H. Park, K. Kim, J. Kim and J. Cho, *Adv. Mater.* **2010**, *22*, 415.

- [30] S. Geier, R. Jung, K. Peters, H. A. Gasteiger, D. Fattakhova-Rohlfing and T. F. Fässler, *Sustain. Energy Fuels* **2018**, *2*, 85.
- [31] S. Geier, T. Kratky, S. Günther, and T. F. Fässler, *Z. Anorg. Allg. Chem.*, **2022**, DOI 10.1002/zaac.202100362.
- [32] C. Schöttle, *Nanopartikel unedler Metalle*, Cuvillier Verlag, Göttingen, **2016**, ISBN 9783736982222.
- [33] F. Cotton, *Q. Rev. Chem. Soc.* **1966**, *20*, 389.
- [34] F. A. Cotton, *Inorg. Chem.* **1964**, *3*, 1217.
- [35] A. Schnepf, *Chem. Soc. Rev.* **2007**, *36*, 745.
- [36] A. Schnepf, *New J. Chem.* **2010**, *34*, 2079.
- [37] Y. Heider and D. Scheschkewitz, *Chem. Rev.* **2021**, *121*, 9674.
- [38] T. F. Fässler, *Zintl phases: principles and recent developments; in: Structure and Bonding*, vol. 139, Springer, Berlin, Heidelberg, **2011**, DOI 10.1007/978-3-642-21150-8.
- [39] S. Dehnen and J. F. Corrigan, *Clusters-contemporary insight in structure and bonding; in: Structure and Bonding*, vol. 174, Springer, Berlin, Heidelberg, **2017**, DOI 10.1007/978-3-319-52296-8.
- [40] A. Schnepf, G. Stösser and H. Schnöckel, *J. Am. Chem. Soc.* **2000**, *122*, 9178.
- [41] K. Abersfelder, A. Russell, H. S. Rzepa, A. J. White, P. R. Haycock and D. Scheschkewitz, *J. Am. Chem. Soc.* **2012**, *134*, 16008.
- [42] Y. Heider and D. Scheschkewitz, *Dalton Trans.* **2018**, *47*, 7104.
- [43] A. Schnepf, *Angew. Chem. Int. Ed.* **2003**, *42*, 2624.
- [44] C. Schenk and A. Schnepf, *Chem. Commun.* **2008**, 4643.
- [45] C. Schenk, A. Kracke, K. Fink, A. Kubas, W. Klopper, M. Neumaier, H. Schnöckel and A. Schnepf, *J. Am. Chem. Soc.* **2011**, *133*, 2518.
- [46] T. Kunz, C. Schrenk and A. Schnepf, *Angew. Chem. Int. Ed.* **2018**, *57*, 4088.
- [47] T. Kunz, V. Graf, C. Schrenk and A. Schnepf, *Inorg. Chem.* **2021**, *60*, 15364.
- [48] A. Schnepf and C. Drost, *Dalton Trans.* **2005**, 3277.
- [49] A. Schnepf, *Coord. Chem. Rev.* **2006**, *250*, 2758.
- [50] A. Sekiguchi, Y. Ishida, Y. Kabe and M. Ichinohe, *J. Am. Chem. Soc.* **2002**, *124*, 8776.
- [51] J. Helmer, A. Hepp and F. Lips, *Dalton Trans.* **2020**, *49*, 11843.
- [52] A. Sekiguchi, C. Kabuto and H. Sakurai, *Angew. Chem.* **1989**, *101*, 97.
- [53] D. Nied, W. Klopper and F. Breher, *Angew. Chem. Int. Ed.* **2009**, *48*, 1411.
- [54] D. Nied, P. Oña-Burgos, W. Klopper and F. Breher, *Organometallics* **2011**, *30*, 1419.
- [55] A. Richards, M. Brynda and P. Power, *Organometallics* **2004**, *23*, 4009.
- [56] Y. Ito, V. Y. Lee, H. Gornitzka, C. Goedecke, G. Frenking and A. Sekiguchi, *J. Am. Chem. Soc.* **2013**, *135*, 6770.
- [57] A. Jana, V. Huch, M. Repisky, R. J. Berger and D. Scheschkewitz, *Angew. Chem. Int. Ed.* **2014**, *53*, 3514.
- [58] W. Klemm, *Proc. Chem. Soc. Lond.* **1958**, 329.
- [59] W. Klemm and E. Busmann, *Z. Anorg. Allg. Chem.* **1963**, *319*, 297.
- [60] E. Zintl, *Angew. Chem.* **1939**, *52*, 1.
- [61] H. Schäfer, *J. Solid State Chem.* **2007**, *180*, 1575.
- [62] P. Eckerlin, H. Meyer and E. Wölfel, *Z. Anorg. Allg. Chem.* **1955**, *281*, 322.
- [63] L. M. Scherf, A. J. Karttunen, O. Pecher, P. C. Magusin, C. P. Grey and T. F. Fässler, *Angew. Chem. Int. Ed.* **2016**, *55*, 1075.
- [64] B. Eisenmann and H. Schäfer, *Z. Anorg. Allg. Chem.* **1974**, *403*, 163.
- [65] P. Eckerlin and E. Wölfel, *Z. Anorg. Allg. Chem.* **1955**, *280*, 321.
- [66] F. Zürcher and R. Nesper, *Angew. Chem. Int. Ed.* **1998**, *37*, 3314.
- [67] V. Queneau and S. C. Sevov, *Angew. Chem. Int. Ed.* **1997**, *36*, 1754.
- [68] W. Carrillo-Cabrera, R. Cardoso Gil, M. Somer, Ö. Persil and H. Von Schnering, *Z. Anorg. Allg. Chem.* **2003**, *629*, 601.
- [69] W. Schnelle, A. Ormeci, A. Wosylus, K. Meier, Y. Grin and U. Schwarz, *Inorg. Chem.* **2012**, *51*, 5509.
- [70] L. Siggelkow, V. Hlukhyy and T. F. Fässler, *J. Solid State Chem.* **2012**, *191*, 76.
- [71] S. Dupke, T. Langer, R. Pöttgen, M. Winter and H. Eckert, *Solid State Nucl. Magn. Reson.* **2012**, *42*, 17.

- [72] R. Nesper, J. Curda and H. Von Schnering, *J. Solid State Chem.* **1986**, *62*, 199.
- [73] I. Todorov and S. C. Sevov, *Inorg. Chem.* **2004**, *43*, 6490.
- [74] O. Yañez, V. Garcia, J. Garza, W. Orellana, A. Vásquez-Espinal and W. Tiznado, *Chem. Eur. J.* **2019**, *25*, 2467.
- [75] I. Todorov and S. C. Sevov, *Inorg. Chem.* **2006**, *45*, 4478.
- [76] R. Nesper, A. Currao and S. Wengert, *Chem. Eur. J.* **1998**, *4*, 2251.
- [77] U. Aydemir, A. Ormeci, H. Borrmann, B. Böhme, F. Zürcher, B. Uslu, T. Goebel, W. Schnelle, P. Simon and W. Carrillo-Cabrera, *Z. Anorg. Allg. Chem.* **2008**, *634*, 1651.
- [78] A. M. Guloy, R. Ramlau, Z. Tang, W. Schnelle, M. Baitinger and Y. Grin, *Nature* **2006**, *443*, 320.
- [79] S. Ponou and T. F. Fässler, *Z. Anorg. Allg. Chem.* **2007**, *633*, 393.
- [80] V. Queneau and S. C. Sevov, *Inorg. Chem.* **1998**, *37*, 1358.
- [81] C. Hoch, M. Wendorff and C. Roehr, *Acta Crystallogr. Sect. C: Cryst. Struct. Commun.* **2002**, *58*, i45.
- [82] C. Hoch, M. Wendorff and C. Röhr, *J. Alloys Compd.* **2003**, *361*, 206.
- [83] S. Bobev and S. C. Sevov, *Polyhedron* **2002**, *21*, 641.
- [84] H. Von Schnering, M. Baitinger, U. Bolle, W. Carrillo-Cabrera, J. Curda, Y. Grin, F. Heinemann, J. Llanos, K. Peters and A. Schmeding, *Z. Anorg. Allg. Chem.* **1997**, *623*, 1037.
- [85] J. D. Corbett, *Angew. Chem. Int. Ed.* **2000**, *39*, 670.
- [86] V. Quéneau, E. Todorov and S. C. Sevov, *J. Am. Chem. Soc.* **1998**, *120*, 3263.
- [87] Y. Wang, Q. Qin, R. Sang and L. Xu, *Dalton Trans.* **2015**, *44*, 18316.
- [88] M. Boyko, V. Hlukhyy, H. Jin, J. Dums and T. F. Fässler, *Z. Anorg. Allg. Chem.* **2020**, *646*, 1575.
- [89] W. Klein, A. Schier and T. F. Fässler, *Molecules Meet Solids: From Wade–Mingos Clusters to Intermetalloid Clusters; in: Structure and Bonding*, vol. 188, Springer, Berlin, Heidelberg, **2021**, DOI 10.1007/430_2021_82.
- [90] N. Korber and A. Fleischmann, *J. Chem. Soc., Dalton Trans.* **2001**, 383.
- [91] C. B. Benda, T. Henneberger, W. Klein and T. F. Fässler, *Z. Anorg. Allg. Chem.* **2017**, *643*, 146.
- [92] R. Hauptmann and T. F. Fässler, *Z. Kristallogr., New Cryst. Struct.* **2003**, *218*, 490.
- [93] L. Yong, S. D. Hoffmann and T. F. Fässler, *Inorg. Chim. Acta* **2006**, *359*, 4774.
- [94] M. Somer, W. Carrillo-Cabrera, E. M. Peters, K. Peters and H. Von Schnering, *Z. Anorg. Allg. Chem.* **1998**, *624*, 1915.
- [95] C. Suchentrunk, J. Daniels, M. Somer, W. Carrillo-Cabrera and N. Korber, *Z. Naturforsch. B* **2005**, *60*, 277.
- [96] D. Michael, P. Mingos and R. L. Johnston, *Theoretical models of cluster bonding; in: Structure and Bonding*, vol. 68, Springer, Berlin, Heidelberg, **1987**, DOI 10.1007/3-540-18058-3_2.
- [97] D. M. P. Mingos, *Acc. Chem. Res.* **1984**, *17*, 311.
- [98] K. Wade, *J. Chem. Soc. D, Chem. Commun.* **1971**, 792.
- [99] K. Wade, *Nat. Phys. Sci.* **1972**, *240*, 71.
- [100] K. Wade, *Adv. Inorg. Chem. Radiochem.* **1976**, *18*, 1.
- [101] F. Klanberg and E. Muetterties, *Inorg. Chem.* **1966**, *5*, 1955.
- [102] A. Y. Bykov, A. Zhdanov, K. Y. Zhizhin and N. Kuznetsov, *Russ. J. Inorg. Chem.* **2016**, *61*, 1629.
- [103] A. Ugrinov and S. C. Sevov, *Chem. Eur. J.* **2004**, *10*, 3727.
- [104] S. C. Sevov and J. M. Goicoechea, *Organometallics* **2006**, *25*, 5678.
- [105] C. H. Belin, J. D. Corbett and A. Cisar, *J. Am. Chem. Soc.* **1977**, *99*, 7163.
- [106] W. Carrillo-Cabrera, U. Aydemir, M. Somer, A. Kircali, T. F. Fässler and S. D. Hoffmann, *Z. Anorg. Allg. Chem.* **2007**, *633*, 1575.
- [107] T. F. Fässler, *Coord. Chem. Rev.* **2001**, *215*, 347.
- [108] S. Scharfe, F. Kraus, S. Stegmaier, A. Schier and T. F. Fässler, *Angew. Chem. Int. Ed.* **2011**, *50*, 3630.
- [109] H. Von Schnering, M. Somer, M. Kaupp, W. Carrillo-Cabrera, M. Baitinger, A. Schmeding and Y. Grin, *Angew. Chem. Int. Ed.* **1998**, *37*, 2359.
- [110] J. Rosdahl, T. F. Fässler and L. Kloo, *Eur. J. Inorg. Chem.* **2005**, *2005*, 2888.

- [111] S. Stegmaier, M. Waibel, A. Henze, L.-A. Jantke, A. J. Karttunen and T. F. Fässler, *J. Am. Chem. Soc.* **2012**, *134*, 14450.
- [112] M. Waibel, G. Raudaschl-Sieber and T. F. Fässler, *Chem. Eur. J.* **2011**, *17*, 13391.
- [113] T. Henneberger, W. Klein, J. V. Dums and T. F. Fässler, *Chem. Commun.* **2018**, *54*, 12381.
- [114] M. Waibel, T. Henneberger, L.-A. Jantke and T. F. Fässler, *Chem. Commun.* **2012**, *48*, 8676.
- [115] H. L. Xu, I. A. Popov, N. V. Tkachenko, Z. C. Wang, A. Muñoz-Castro, A. I. Boldyrev and Z. M. Sun, *Angew. Chem. Int. Ed.* **2020**, *59*, 17286.
- [116] V. Queneau and S. C. Sevov, *J. Am. Chem. Soc.* **1997**, *119*, 8109.
- [117] U. Zachwieja and J. Wlodarski, *Z. Anorg. Allg. Chem.* **2004**, *630*, 993.
- [118] J. M. Goicoechea and S. C. Sevov, *Organometallics* **2006**, *25*, 4530.
- [119] J. M. Goicoechea and S. C. Sevov, *J. Am. Chem. Soc.* **2006**, *128*, 4155.
- [120] S. Scharfe and T. F. Fässler, *Eur. J. Inorg. Chem.* **2010**, *2010*, 1207.
- [121] B. Zhou, M. S. Denning, C. Jones and J. M. Goicoechea, *Dalton Trans.* **2009**, 1571.
- [122] Z.-M. Sun, Y.-F. Zhao, J. Li and L.-S. Wang, *J. Cluster Sci.* **2009**, *20*, 601.
- [123] K. Mayer, W. Klein and T. F. Fässler, *Chem. Commun.* **2019**, *55*, 12156.
- [124] L. Wang, Y. Wang, Z. Li, H. Ruan and L. Xu, *Dalton Trans.* **2017**, *46*, 6839.
- [125] Y.-S. Huang, D. Chen, J. Zhu and Z.-M. Sun, *Chin. Chem. Lett.* **2022**, *33*, 2139.
- [126] Z.-C. Wang, N. V. Tkachenko, L. Qiao, E. Matito, A. Muñoz-Castro, A. I. Boldyrev and Z.-M. Sun, *Chem. Commun.* **2020**, *56*, 6583.
- [127] A. Nienhaus, R. Hauptmann and T. F. Fässler, *Angew. Chem. Int. Ed.* **2002**, *41*, 3213.
- [128] L. Lin, Y. Wang and L. Xu, *Organometallics* **2022**, *41*, 450.
- [129] K. Mayer, L. A. Jantke, S. Schulz and T. F. Fässler, *Angew. Chem. Int. Ed.* **2017**, *56*, 2350.
- [130] C. B. Benda, R. Schäper, S. Schulz and T. F. Fässler, *Eur. J. Inorg. Chem.* **2013**, *2013*, 5964.
- [131] A. Spiekermann, S. D. Hoffmann, F. Kraus and T. F. Fässler, *Angew. Chem. Int. Ed.* **2007**, *46*, 1638.
- [132] A. Spiekermann, S. D. Hoffmann, T. F. Fässler, I. Krossing and U. Preiss, *Angew. Chem. Int. Ed.* **2007**, *46*, 5310.
- [133] H.-L. Xu, N. V. Tkachenko, Z.-C. Wang, W.-X. Chen, L. Qiao, A. Muñoz-Castro, A. I. Boldyrev and Z.-M. Sun, *Nat. Commun.* **2020**, *11*, 5286.
- [134] C. B. Benda, M. Waibel and T. F. Fässler, *Angew. Chem. Int. Ed.* **2015**, *54*, 522.
- [135] K. Momma and F. Izumi, *J. Appl. Crystallogr.* **2011**, *44*, 1272.
- [136] The cluster volume was calculated using the single crystal data of the compound $K_{12}Si_{17}$ and the program *VESTA (JP-Minerals)*.
- [137] T. F. Fässler and S. D. Hoffmann, *Angew. Chem. Int. Ed.* **2004**, *43*, 6242.
- [138] S. Scharfe, T. F. Fässler, S. Stegmaier, S. D. Hoffmann and K. Ruhland, *Chem. Eur. J.* **2008**, *14*, 4479.
- [139] C.-C. Shu, H. W. Morgan, L. Qiao, J. E. McGrady and Z.-M. Sun, *Nat. Commun.* **2020**, *11*, 3477.
- [140] B. J. Witzel, W. Klein, J. V. Dums, M. Boyko and T. F. Fässler, *Angew. Chem. Int. Ed.* **2019**, *58*, 12908.
- [141] J. E. McGrady, F. Weigend and S. Dehnen, *Chem. Soc. Rev.* **2022**, *51*, 628.
- [142] X. Zhao, G. Pei, S. Xu, C. Kong, Z. Yang and T. Yang, *Phys. Chem. Chem. Phys.* **2021**, *23*, 20654.
- [143] H. He, W. Klein, L. A. Jantke and T. F. Fässler, *Z. Anorg. Allg. Chem.* **2014**, *640*, 2864.
- [144] V. Hlukhyy, H. He, L. A. Jantke and T. F. Fässler, *Chem. Eur. J.* **2012**, *18*, 12000.
- [145] V. Hlukhyy, S. Stegmaier, L. van Wüllen and T. F. Fässler, *Chem. Eur. J.* **2014**, *20*, 12157.
- [146] J. M. Goicoechea and S. C. Sevov, *Angew. Chem. Int. Ed.* **2005**, *44*, 4026.
- [147] B. J. L. Witzel, PhD Thesis, Technical University of Munich, **2020**, <http://nbn-resolving.de/urn/resolver.pl?urn:nbn:de:bvb:91-diss-20200214-1534198-1-0>, accessed 27th March 2022.
- [148] H.-L. Xu, L. Qiao and Z.-M. Sun, *Chem. Commun.* **2022**, *58*, 3190.

- [149] J. Q. Wang, S. Stegmaier, B. Wahl and T. F. Fässler, *Chem. Eur. J.* **2010**, *16*, 1793.
- [150] B. Zhou, M. S. Denning, D. L. Kays and J. M. Goicoechea, *J. Am. Chem. Soc.* **2009**, *131*, 2802.
- [151] J. Q. Wang, S. Stegmaier and T. F. Fässler, *Angew. Chem. Int. Ed.* **2009**, *48*, 1998.
- [152] C. Liu, L. J. Li, I. A. Popov, R. J. Wilson, C. Q. Xu, J. Li, A. I. Boldyrev and Z. M. Sun, *Chin. J. Chem.* **2018**, *36*, 1165.
- [153] G. Espinoza-Quintero, J. C. Duckworth, W. K. Myers, J. E. McGrady and J. M. Goicoechea, *J. Am. Chem. Soc.* **2014**, *136*, 1210.
- [154] H. W. Morgan, K.-S. Csizi, Y.-S. Huang, Z.-M. Sun and J. E. McGrady, *J. Phys. Chem. A* **2021**, *125*, 4578.
- [155] X. Jin, G. Espinoza-Quintero, B. Below, V. Arcisauskaite, J. M. Goicoechea and J. E. McGrady, *J. Organomet. Chem.* **2015**, *792*, 149.
- [156] C. Liu, I. A. Popov, L. J. Li, N. Li, A. I. Boldyrev and Z. M. Sun, *Chem. Eur. J.* **2018**, *24*, 699.
- [157] J. M. Goicoechea and S. C. Sevov, *J. Am. Chem. Soc.* **2005**, *127*, 7676.
- [158] B. Kesanli, J. Fettingner, D. R. Gardner and B. Eichhorn, *J. Am. Chem. Soc.* **2002**, *124*, 4779.
- [159] B. Kesanli, J. E. Halsig, P. Zavalij, J. C. Fettingner, Y.-F. Lam and B. W. Eichhorn, *J. Am. Chem. Soc.* **2007**, *129*, 4567.
- [160] M. Schütz, C. Gemel, W. Klein, R. A. Fischer and T. F. Fässler, *Chem. Soc. Rev.* **2021**, *50*, 8496.
- [161] E. N. Esenturk, J. Fettingner and B. Eichhorn, *Polyhedron* **2006**, *25*, 521.
- [162] J. Åkerstedt, S. Ponou, L. Kloo and S. Lidin, *Eur. J. Inorg. Chem.* **2011**, *2011*, 3999.
- [163] V. Angilella and C. Belin, *J. Chem. Soc., Faraday Trans.* **1991**, *87*, 203.
- [164] C. Belin, H. Mercier and V. Angilella, *New J. Chem.* **1991**, *15*, 931.
- [165] T. F. Fässler and M. Hunziker, *Inorg. Chem.* **1994**, *33*, 5380.
- [166] T. F. Fässler and U. Schütz, *Inorg. Chem.* **1999**, *38*, 1866.
- [167] T. F. Fässler, M. Hunziker, M. E. Spahr, H. Lueken and H. Schilder, *Z. Anorg. Allg. Chem.* **2000**, *626*, 692.
- [168] C. Suchentrunk and N. Korber, *Inorg. Chim. Acta* **2006**, *359*, 267.
- [169] R. Hauptmann and T. F. Fässler, *Z. Kristallogr., New Cryst. Struct.* **2003**, *218*, 461.
- [170] R. Hauptmann and T. F. Fässler, *Z. Anorg. Allg. Chem.* **2003**, *629*, 2266.
- [171] L. Xu and S. C. Sevov, *J. Am. Chem. Soc.* **1999**, *121*, 9245.
- [172] K. Mayer, PhD Thesis, Technical University of Munich, **2018**, <http://nbn-resolving.de/urn/resolver.pl?urn:nbn:de:bvb:91-diss-20180822-1446349-0-7>, accessed 27th March 2022.
- [173] K. Mayer, W. Klein, S. Geier and T. F. Fässler, *Z. Anorg. Allg. Chem.* **2021**, *647*, 377.
- [174] K. Mayer, M. Giebel, M. M. Bentlohner, W. Klein and T. F. Fässler, *Z. Kristallogr., New Cryst. Struct.* **2015**, *230*, 286.
- [175] S. Frischhut, J. G. Machado de Carvalho, A. J. Karttunen and T. F. Fässler, *Z. Anorg. Allg. Chem.* **2018**, *644*, 1337.
- [176] L. Yong, S. D. Hoffmann and T. F. Fässler, *Z. Anorg. Allg. Chem.* **2005**, *631*, 1149.
- [177] A. Ugrinov and S. C. Sevov, *J. Am. Chem. Soc.* **2002**, *124*, 10990.
- [178] L. Yong, S. D. Hoffmann and T. F. Fässler, *Z. Anorg. Allg. Chem.* **2004**, *630*, 1977.
- [179] A. Ugrinov and S. C. Sevov, *Inorg. Chem.* **2003**, *42*, 5789.
- [180] C. Downie, J.-G. Mao, H. Parmar and A. M. Guloy, *Inorg. Chem.* **2004**, *43*, 1992.
- [181] C. Downie, Z. Tang and A. M. Guloy, *Angew. Chem. Int. Ed.* **2000**, *39*, 337.
- [182] H.-L. Xu, N. V. Tkachenko, D. W. Szczepanik, I. A. Popov, A. Muñoz-Castro, A. I. Boldyrev and Z.-M. Sun, *Nat. Commun.* **2022**, *13*, 2149.
- [183] S. Scharfe and T. F. Fässler, *Z. Anorg. Allg. Chem.* **2011**, *637*, 901.
- [184] A. Ugrinov and S. C. Sevov, *J. Am. Chem. Soc.* **2002**, *124*, 2442.
- [185] C. Lorenz and N. Korber, *Crystals* **2018**, *8*, 374.
- [186] T. Henneberger, W. Klein and T. F. Fässler, *Z. Anorg. Allg. Chem.* **2018**, *644*, 1018.
- [187] C. Lorenz, F. Hastreiter, J. Hioe, N. Lokesh, S. Gärtner, N. Korber and R. M. Gschwind, *Angew. Chem. Int. Ed.* **2018**, *57*, 12956.

- [188] L. J. Schiegerl, A. J. Karttunen, J. Tillmann, S. Geier, G. Raudaschl-Sieber, M. Waibel and T. F. Fässler, *Angew. Chem. Int. Ed.* **2018**, *57*, 12950.
- [189] F. S. Kocak, D. O. Downing, P. Zavalij, Y.-F. Lam, A. N. Vedernikov and B. Eichhorn, *J. Am. Chem. Soc.* **2012**, *134*, 9733.
- [190] C. Fischer, PhD Thesis, Technical University of Munich, **2020**, <http://nbn-resolving.de/urn/resolver.pl?urn:nbn:de:bvb:91-diss-20201125-1575114-1-2>, accessed 27th March 2022.
- [191] D. Rios, M. M. Gillett-Kunnath, J. D. Taylor, A. G. Oliver and S. C. Sevov, *Inorg. Chem.* **2011**, *50*, 2373.
- [192] D. F. Hansen, B. Zhou and J. M. Goicoechea, *J. Organomet. Chem.* **2012**, *721*, 53.
- [193] M. W. Hull, A. Ugrinov, I. Petrov and S. C. Sevov, *Inorg. Chem.* **2007**, *46*, 2704.
- [194] M. W. Hull and S. C. Sevov, *J. Am. Chem. Soc.* **2009**, *131*, 9026.
- [195] C. B. Benda, J. Q. Wang, B. Wahl and T. F. Fässler, *Eur. J. Inorg. Chem.* **2011**, *2011*, 4262.
- [196] M. W. Hull and S. C. Sevov, *Chem. Commun.* **2012**, *48*, 7720.
- [197] C. B. Benda, H. He, W. Klein, M. Somer and T. F. Fässler, *Z. Anorg. Allg. Chem.* **2015**, *641*, 1080.
- [198] D. J. Chapman and S. C. Sevov, *Inorg. Chem.* **2008**, *47*, 6009.
- [199] M. W. Hull and S. C. Sevov, *J. Organomet. Chem.* **2012**, *721*, 85.
- [200] M. M. Bentlohner, S. Frischhut and T. F. Fässler, *Chem. Eur. J.* **2017**, *23*, 17089.
- [201] S. Frischhut, M. M. Bentlohner, W. Klein and T. F. Fässler, *Inorg. Chem.* **2017**, *56*, 10691.
- [202] M. M. Bentlohner, W. Klein, Z. H. Fard, L. A. Jantke and T. F. Fässler, *Angew. Chem. Int. Ed.* **2015**, *54*, 3748.
- [203] M. M. Bentlohner, L. A. Jantke, T. Henneberger, C. Fischer, K. Mayer, W. Klein and T. F. Fässler, *Chem. Eur. J.* **2016**, *22*, 13946.
- [204] F. S. Kocak, P. Y. Zavalij, Y.-F. Lam and B. W. Eichhorn, *Chem. Commun.* **2009**, 4197.
- [205] O. Kysliak and A. Schnepf, *Dalton Trans.* **2016**, *45*, 2404.
- [206] F. Li and S. C. Sevov, *Inorg. Chem.* **2012**, *51*, 2706.
- [207] L. J. Schiegerl, A. J. Karttunen, W. Klein and T. F. Fässler, *Chem. Eur. J.* **2018**, *24*, 19171.
- [208] L. J. Schiegerl, A. J. Karttunen, W. Klein and T. F. Fässler, *Chem. Sci.* **2019**, *10*, 9130.
- [209] L. G. Perla and S. C. Sevov, *J. Am. Chem. Soc.* **2016**, *138*, 9795.
- [210] L. G. Perla, A. Muñoz-Castro and S. C. Sevov, *J. Am. Chem. Soc.* **2017**, *139*, 15176.
- [211] F. S. Geitner, W. Klein and T. F. Fässler, *Angew. Chem. Int. Ed.* **2018**, *57*, 14509.
- [212] F. S. Geitner, PhD Thesis, Technical University of Munich, **2018**, <http://nbn-resolving.de/urn/resolver.pl?urn:nbn:de:bvb:91-diss-20181122-1454192-1-7>, accessed 27th March 2022.
- [213] A. Ugrinov and S. C. Sevov, *J. Am. Chem. Soc.* **2003**, *125*, 14059.
- [214] S. Frischhut, F. Kaiser, W. Klein, M. Drees, F. E. Kühn and T. F. Fässler, *Organometallics* **2018**, *37*, 4560.
- [215] F. Li, A. Muñoz-Castro and S. C. Sevov, *Angew. Chem. Int. Ed.* **2016**, *55*, 8630.
- [216] F. Li and S. C. Sevov, *J. Am. Chem. Soc.* **2014**, *136*, 12056.
- [217] S. Frischhut, W. Klein and T. F. Fässler, *C. R. Chim.* **2018**, *21*, 932.
- [218] S. Frischhut and T. F. Fässler, *Dalton Trans.* **2018**, *47*, 3223.
- [219] S. Frischhut, W. Klein, M. Drees and T. F. Fässler, *Chem. Eur. J.* **2018**, *24*, 9009.
- [220] O. Kysliak, C. Schrenk and A. Schnepf, *Inorg. Chem.* **2017**, *56*, 9693.
- [221] L. J. Schiegerl, F. S. Geitner, C. Fischer, W. Klein and T. F. Fässler, *Z. Anorg. Allg. Chem.* **2016**, *642*, 1419.
- [222] K. Mayer, L. J. Schiegerl and T. F. Fässler, *Chem. Eur. J.* **2016**, *22*, 18794.
- [223] O. Kysliak, T. Kunz and A. Schnepf, *Eur. J. Inorg. Chem.* **2017**, *2017*, 805.
- [224] O. Kysliak, C. Schrenk and A. Schnepf, *Inorg. Chem.* **2015**, *54*, 7083.
- [225] K. Mayer, L. J. Schiegerl, T. Kratky, S. Günther and T. F. Fässler, *Chem. Commun.* **2017**, *53*, 11798.
- [226] O. Kysliak and A. Schnepf, *Z. Anorg. Allg. Chem.* **2019**, *645*, 335.
- [227] F. Li, A. Muñoz-Castro and S. C. Sevov, *Angew. Chem. Int. Ed.* **2012**, *51*, 8581.
- [228] F. S. Geitner, J. V. Dums and T. F. Fässler, *J. Am. Chem. Soc.* **2017**, *139*, 11933.

- [229] F. S. Geitner, C. Wallach and T. F. Fässler, *Chem. Eur. J.* **2018**, *24*, 4103.
- [230] F. S. Geitner, W. Klein, O. Storcheva, T. D. Tilley and T. F. Fässler, *Inorg. Chem.* **2019**, *58*, 13293.
- [231] C. Schenk and A. Schnepf, *Chem. Commun.* **2009**, 3208.
- [232] N. C. Michenfelder, C. Gienger, A. Schnepf and A.-N. Unterreiner, *Dalton Trans.* **2019**, *48*, 15577.
- [233] O. Kysliak, C. Schrenk and A. Schnepf, *Chem. Eur. J.* **2016**, *22*, 18787.
- [234] F. S. Geitner and T. F. Fässler, *Eur. J. Inorg. Chem.* **2016**, *2016*, 2688.
- [235] L. J. Schiegerl, M. Melaimi, D. R. Tolentino, W. Klein, G. Bertrand and T. F. Fässler, *Inorg. Chem.* **2019**, *58*, 3256.
- [236] C. Gienger and A. Schnepf, *Z. Anorg. Allg. Chem.* **2021**, *647*, 1695.
- [237] F. Li and S. C. Sevov, *Inorg. Chem.* **2015**, *54*, 8121.
- [238] O. P. Townrow, A. S. Weller and J. M. Goicoechea, *Chem. Commun.* **2021**, *57*, 7132.
- [239] F. Henke, C. Schenk and A. Schnepf, *Dalton Trans.* **2009**, 9141.
- [240] C. Schenk, F. Henke, G. Santiso-Quiñones, I. Krossing and A. Schnepf, *Dalton Trans.* **2008**, 4436.
- [241] C. Schenk and A. Schnepf, *Angew. Chem. Int. Ed.* **2007**, *46*, 5314.
- [242] O. Kysliak, D. D. Nguyen, A. Z. Clayborne and A. Schnepf, *Inorg. Chem.* **2018**, *57*, 12603.
- [243] F. S. Geitner, M. A. Giebel, A. Pöthig and T. F. Fässler, *Molecules* **2017**, *22*, 1204.
- [244] O. P. Townrow, C. Chung, S. A. Macgregor, A. S. Weller and J. M. Goicoechea, *J. Am. Chem. Soc.* **2020**, *142*, 18330.
- [245] F. S. Geitner and T. F. Fässler, *Inorg. Chem.* **2020**, *59*, 15218.
- [246] F. Henke, C. Schenk and A. Schnepf, *Dalton Trans.* **2011**, *40*, 6704.
- [247] O. Kysliak, C. Schrenk and A. Schnepf, *Angew. Chem. Int. Ed.* **2016**, *55*, 3216.
- [248] R. P. Huebener, *Conductors, Semiconductors, Superconductors; in: Undergraduate Lecture Notes in Physics*, Springer, Berlin, Heidelberg, **2019**, DOI 10.1007/978-3-030-31420-0.
- [249] J. N. Brønsted, *Recl. Trav. Chim. Pays-Bas.* **1923**, *42*, 718.
- [250] G. N. Lewis, *Valence and the Structure of Atoms and Molecules; in: American Chemical Monograph Series*, the Chemical Catalog Company Inc., New York, **1923**, DOI 10.1002/jctb.5000430107.
- [251] D. W. Stephan and G. Erker, *Angew. Chem. Int. Ed.* **2010**, *49*, 46.
- [252] G. C. Welch and D. W. Stephan, *J. Am. Chem. Soc.* **2007**, *129*, 1880.
- [253] J. S. McCahill, G. C. Welch and D. W. Stephan, *Angew. Chem. Int. Ed.* **2007**, *46*, 4968.
- [254] D. W. Stephan, *J. Am. Chem. Soc.* **2015**, *137*, 10018.
- [255] D. W. Stephan, *Science* **2016**, *354*, aaf7229.
- [256] B. Birkmann, T. Voss, S. J. Geier, M. Ullrich, G. Kehr, G. Erker and D. W. Stephan, *Organometallics* **2010**, *29*, 5310.
- [257] E. R. Habraken, L. C. Mens, M. Nieger, M. Lutz, A. W. Ehlers and J. C. Slootweg, *Dalton Trans.* **2017**, *46*, 12284.
- [258] D. W. Stephan, *Acc. Chem. Res.* **2015**, *48*, 306.
- [259] J. Li, B. Li, R. Liu, L. Jiang, H. Zhu, H. W. Roesky, S. Dutta, D. Koley, W. Liu and Q. Ye, *Chem. Eur. J.* **2016**, *22*, 14499.
- [260] The corresponding alkyl, alkenyl, aminoalkyl, and aryl substituted chlorophosphines were prepared during my Master's thesis. During the Master's thesis also the compound $[\text{Ge}_3\{\text{Si}(\text{TMS})_3\}_3\{\text{P}^t\text{Bu}\{(\text{CH}_2)_3\text{CH}=\text{CH}_2\}}]$ was characterized, and reactions with the carbene $\text{NHC}^{\text{Dipp}}\text{CuCl}$ were conducted. Within the PhD project the reaction system was extended to Ag-carbenes, and the ^{31}P - $^{107}\text{Ag}/^{109}\text{Ag}$ spin-spin coupling was investigated using ^{31}P NMR measurements, allowing for an indirect determination of the coordination pattern.
- [261] A. J. Rucklidge, G. E. Morris, A. M. Slawin and D. J. Cole-Hamilton, *Helv. Chim. Acta* **2006**, *89*, 1783.
- [262] O. J. Scherer and W. Gick, *Chem. Ber.* **1970**, *103*, 71.
- [263] V. Volodin, M. Efremov, A. Deryabin and L. Sokolov, *Semiconductors* **2006**, *40*, 1314.
- [264] A. Nienhaus, S. D. Hoffmann and T. F. Fässler, *Z. Anorg. Allg. Chem.* **2006**, *632*, 1752.
- [265] S. S. Barnes, C. M. Vogels, A. Decken and S. A. Westcott, *Dalton Trans.* **2011**, *40*, 4707.
- [266] B. Wrackmeyer and O. L. Tok, *Z. Naturforsch. B* **2006**, *61*, 949.

- [267] C. K. Narula and H. Noeth, *Inorg. Chem.* **1984**, *23*, 4147.
- [268] T. Gädt, J.-A. Dimmer, S. Fleischhauer, A. Frank, C. Nickl, T. Wütz, K. Eichele and L. Wesemann, *Dalton Trans.* **2015**, *44*, 4726.
- [269] A. V. Protchenko, K. H. Birjukumar, D. Dange, A. D. Schwarz, D. Vidovic, C. Jones, N. Kaltsoyannis, P. Mountford and S. Aldridge, *J. Am. Chem. Soc.* **2012**, *134*, 6500.
- [270] Y. Wang, M. Karni, S. Yao, Y. Apeloig and M. Driess, *J. Am. Chem. Soc.* **2018**, *141*, 1655.
- [271] C. B. Benda, M. Waibel, T. Köchner and T. F. Fässler, *Chem. Eur. J.* **2014**, *20*, 16738.
- [272] R. G. Pearson, *J. Am. Chem. Soc.* **1963**, *85*, 3533.
- [273] R. G. Pearson, *Coord. Chem. Rev.* **1990**, *100*, 403.
- [274] M. A. Beckett, G. C. Strickland, J. R. Holland and K. S. Varma, *Polymer* **1996**, *37*, 4629.
- [275] V. Gutmann, *Coord. Chem. Rev.* **1976**, *18*, 225.
- [276] I. B. Sivaev and V. I. Bregadze, *Coord. Chem. Rev.* **2014**, *270*, 75.
- [277] C. Bonnier and T. P. Bender, *Molecules* **2015**, *20*, 18237.
- [278] H. C. Brown, P. V. Ramachandran and J. Chandrasekharan, *Heteroat. Chem.* **1995**, *6*, 117.
- [279] J. B. Heilmann, Y. Qin, F. Jäkle, H.-W. Lerner and M. Wagner, *Inorg. Chim. Acta* **2006**, *359*, 4802.
- [280] D. H. Boom, A. R. Jupp, M. Nieger, A. W. Ehlers and J. C. Slootweg, *Chem. Eur. J.* **2019**, *25*, 13299.
- [281] A. D. Becke, *Phys. Rev. A* **1988**, *38*, 3098.
- [282] F. Furche and R. Ahlrichs, *J. Phys. Chem.* **2002**, *117*, 7433.
- [283] F. Furche and D. Rappoport, *Density Functional Methods for Excited States: Equilibrium Structure and Electronic Spectra*; in: *Computational Photochemistry*, vol. 16, Elsevier: Amsterdam, The Netherlands, **2005**, ISBN: 9780080455198.
- [284] J. P. Perdew, *Phys. Rev. B* **1986**, *33*, 8822.
- [285] F. Weigend and R. Ahlrichs, *Phys. Chem. Chem. Phys.* **2005**, *7*, 3297.
- [286] A. Dreuw and M. Head-Gordon, *Chem. Rev.* **2005**, *105*, 4009.
- [287] K. Mayer, J. Weßing, T. F. Fässler and R. A. Fischer, *Angew. Chem. Int. Ed.* **2018**, *57*, 14372.
- [288] B. Weinert, S. Mitzinger and S. Dehnen, *Chem. Eur. J.* **2018**, *24*, 8470.
- [289] C. Liu and Z.-M. Sun, *Coord. Chem. Rev.* **2019**, *382*, 32.
- [290] R. J. Wilson, N. Lichtenberger, B. Weinert and S. Dehnen, *Chem. Rev.* **2019**, *119*, 8506.
- [291] Y. Wang, J. E. McGrady and Z.-M. Sun, *Acc. Chem. Res.* **2021**, *54*, 1506.
- [292] Y. Wang, C. Zhang, X. Wang, J. Guo, Z.-M. Sun and H. Zhang, *ACS Catal.* **2020**, *10*, 7808.
- [293] V. Streitferdt, S. M. Tiefenthaler, I. G. Shenderovich, S. Gärtner, N. Korber and R. M. Gschwind, *Eur. J. Inorg. Chem.* **2021**, *2021*, 3684.
- [294] F. Fendt, C. Koch, S. Gärtner and N. Korber, *Dalton Trans.* **2013**, *42*, 15548.
- [295] F. Hastreiter, C. Lorenz, J. Hioe, S. Gärtner, N. Lokesh, N. Korber and R. M. Gschwind, *Angew. Chem. Int. Ed.* **2019**, *58*, 3133.
- [296] S. M. Tiefenthaler, J. Baumann, S. Gaertner, N. Korber, V. Streitferdt and R. M. Gschwind, *Z. Anorg. Allg. Chem.* **2020**, *646*, 1595.
- [297] V. Kumar and Y. Kawazoe, *Appl. Phys. Lett.* **2002**, *80*, 859.
- [298] V. Kumar and Y. Kawazoe, *Appl. Phys. Lett.* **2003**, *83*, 2677.
- [299] R. Misra, *Mater. Technol.* **2010**, *25*, 118.
- [300] Y. Su, H. Guo, Z. Wang, Y. Long, W. Li and Y. Tu, *Sens. Actuators B: Chem.* **2018**, *255*, 2510.
- [301] J. Guo, L. Shi, J. Zhao, Y. Wang, K. Tang, W. Zhang, C. Xie and X. Yuan, *Appl. Catal. B: Environ.* **2018**, *224*, 692.
- [302] J. Wan, Y. Luo, Z. Jiang, G. Jin, J. Liu, K. L. Wang, X. Liao and J. Zou, *Appl. Phys. Lett.* **2001**, *79*, 1980.
- [303] V. Van Tran, T. L. Nguyen, J.-Y. Moon and Y.-C. Lee, *Chem. Eng. J.* **2019**, *368*, 88.
- [304] Y.-W. Mo, D. Savage, B. Swartzentruber and M. G. Lagally, *Phys. Rev. Lett.* **1990**, *65*, 1020.
- [305] D. Rios and S. C. Sevov, *Inorg. Chem.* **2010**, *49*, 6396.

- [306] M. M. Bentlohner, C. Fischer and T. F. Fässler, *Chem. Commun.* **2016**, 52, 9841.
- [307] A. Spiekermann, S. D. Hoffmann and T. F. Fässler, *Angew. Chem. Int. Ed.* **2006**, 45, 3459.
- [308] Z.-M. Sun, H. Xiao, J. Li and L.-S. Wang, *J. Am. Chem. Soc.* **2007**, 129, 9560.
- [309] F. S. Kocak, P. Zavalij, Y.-F. Lam and B. W. Eichhorn, *Inorg. Chem.* **2008**, 47, 3515.
- [310] F. K. Sheong, W.-J. Chen, J.-X. Zhang, Y. Li and Z. Lin, *Dalton Trans.* **2017**, 46, 2214.
- [311] C. Liu, X. Jin, L. Li, J. Xu, J. E. McGrady and Z.-M. Sun, *Chem. Sci.* **2019**, 10, 4394.
- [312] E. N. Esenturk, J. C. Fettinger and B. W. Eichhorn, *J. Am. Chem. Soc.* **2006**, 128, 12.
- [313] M. M. Gillett-Kunnath, J. I. Paik, S. M. Jensen, J. D. Taylor and S. C. Sevov, *Inorg. Chem.* **2011**, 50, 11695.
- [314] The filled anions $[\text{Co}_2@\text{Ge}_{17}]^{6-}$ and $[\text{Co}@\text{Ge}_{10}]^{3-}$ were reported in the PhD Thesis of B. J. L. Witzel, Technical University of Munich, **2020**. The structures were not published elsewhere before.
- [315] A. Ruiz-Martínez, D. Casanova and S. Alvarez, *Dalton Trans.* **2008**, 2583.
- [316] The anions $[(\eta^2\text{-Sn}_4)\text{Zn}(\eta^2\text{-Sn}_4)]^{6-}$ and $[(\eta^4\text{-Ge}_9)(\text{ZnEt})]^{3-}$ were reported in the PhD Thesis of K. Mayer, Technical University of Munich, **2018**. The structures were not published elsewhere before.
- [317] The anions $[(\text{ZnPh}_2)_2(\mu_2\text{-NH}_2)_2]^{2-}$, $[\text{ZnPh}_3]^-$, and $[\text{ZnMes}_3]^-$ were reported in the PhD Thesis of T. Henneberger, Technical University of Munich, **2019**, <http://nbn-resolving.de/urn/resolver.pl?urn:nbn:de:bvb:91-diss-20191219-1509766-0-4>, accessed 27th March 2022. The structures were not published elsewhere before.
- [318] C. Zhang, H. W. Morgan, Z.-C. Wang, C. Liu, Z.-M. Sun and J. E. McGrady, *Dalton Trans.* **2019**, 48, 15888.
- [319] Y. Segawa, Y. Suzuki, M. Yamashita and K. Nozaki, *J. Am. Chem. Soc.* **2008**, 130, 16069.
- [320] C. Kleeberg, *Dalton Trans.* **2013**, 42, 8276.
- [321] P. Chavant and M. Vaultier, *J. Organomet. Chem.* **1993**, 455, 37.
- [322] B. Wrackmeyer, C. Köhler, W. Milius, J. M. Grevy, Z. García-Hernández and R. Contreras, *Heteroat. Chem.* **2002**, 13, 667.
- [323] S. P. Green, C. Jones and A. Stasch, *Science* **2007**, 318, 1754.
- [324] J. Prust, K. Most, I. Müller, E. Alexopoulos, A. Stasch, I. Usón and H. W. Roesky, *Z. Anorg. Allg. Chem.* **2001**, 627, 2032.
- [325] P. De Fremont, N. M. Scott, E. D. Stevens, T. Ramnial, O. C. Lightbody, C. L. Macdonald, J. A. Clyburne, C. D. Abernethy and S. P. Nolan, *Organometallics* **2005**, 24, 6301.
- [326] L. Hintermann, *Beilstein J. Org. Chem.* **2007**, 3, 22.
- [327] O. Santoro, A. Collado, A. M. Slawin, S. P. Nolan and C. S. Cazin, *Chem. Commun.* **2013**, 49, 10483.
- [328] W. McFarlane and C. T. Regius, *Polyhedron* **1997**, 16, 1855.
- [329] C. Wallach, F. S. Geitner, W. Klein and T. F. Fässler, *Chem. Eur. J.* **2019**, 25, 12349.
- [330] R. Blom, J. Boersma, P. Budzelaar, B. Fischer, A. Haaland, H. Volden and J. Weidlein, *Acta Chem. Scand. A* **1986**, 40, 113.
- [331] U. Böhme, *Inertgastechnik: Arbeiten unter Schutzgas in der Chemie*, Walter de Gruyter GmbH & Co KG, Berlin, Boston, **2020**, DOI 10.1515/9783110627046.
- [332] T. Kottke and D. Stalke, *J. Appl. Crystallogr.* **1993**, 26, 615.
- [333] G. R. Fulmer, A. J. Miller, N. H. Sherden, H. E. Gottlieb, A. Nudelman, B. M. Stoltz, J. E. Bercaw and K. I. Goldberg, *Organometallics* **2010**, 29, 2176.
- [334] M. Muhr, P. HeiB, M. Schütz, R. Bühler, C. Gemel, M. H. Linden, H. B. Linden and R. A. Fischer, *Dalton Trans.* **2021**, 50, 9031.
- [335] <https://www.envipat.eawag.ch/>, enviPat Web 2.4, accessed 15th February 2022.
- [336] G. M. Sheldrick, *Acta Crystallogr. Sect. A: Found. Crystallogr.* **2008**, 64, 112.
- [337] G. M. Sheldrick, *Acta Crystallogr. Sect. C: Struct. Chem.* **2015**, 71, 3.
- [338] A. L. Spek, *Acta Crystallogr. Sect. D: Biol. Crystallogr.* **2009**, 65, 148.
- [339] TURBOMOLE V7.3 2018, a development of University of Karlsruhe and Forschungszentrum Karlsruhe GmbH, 1989-2007; TURBOMOLE GmbH, since 2007; available from www.turbomole.com, accessed 3rd March 2022.
- [340] J. P. Perdew, M. Ernzerhof and K. Burke, *J. Phys. Chem.* **1996**, 105, 9982.

- [341] C. Adamo and V. Barone, *J. Phys. Chem.* **1999**, *110*, 6158.
[342] F. Weigend, *Phys. Chem. Chem. Phys.* **2006**, *8*, 1057.
[343] A. Klamt and G. Schüürmann, *J. Chem. Soc., Perkin Trans. 2* **1993**, 799.
[344] K. Eichkorn, O. Treutler, H. Öhm, M. Häser and R. Ahlrichs, *Chem. Phys. Lett.* **1995**, *240*, 283.
[345] M. Sierka, A. Hogekamp and R. Ahlrichs, *J. Phys. Chem.* **2003**, *118*, 9136.
[346] W. Humphrey, A. Dalke and K. Schulten, *J. Mol. Graph.* **1996**, *14*, 33.
[347] G. Knizia and J. E. Klein, *Angew. Chem. Int. Ed.* **2015**, *54*, 5518.

6 PUBLICATIONS AND MANUSCRIPTS

6.1 Enhancing the Variability of [Ge₉] Cluster Chemistry through Phosphine Functionalization

C. Wallach,[‡] F. S. Geitner,[‡] W. Klein and T. F. Fässler

[‡]: authors contributed equally to this work.

Published in: *Chemistry-A European Journal* **2019**, 25, 12349.

© Wiley-VCH GmbH, Weinheim 2019, reprint licence ID: 5307460986845 (CCC RightsLink[®]).

Access online via: <https://chemistry-europe.onlinelibrary.wiley.com/doi/abs/10.1002/chem.201901673>.

Contents and Contributions

The reactivity of a series of chlorophosphines $RR^lP\text{Cl}$ ($R, R^l = \text{alkyl, alkenyl, aminoalkyl, aryl}$) is tested towards the silylated clusters $[\text{Ge}_9\{\text{Si}(\text{TMS})_3\}_2]^{2-}$ and $[\text{Ge}_9\{\text{Si}(\text{TMS})_3\}_3]^-$. In the course of the experiments, a novel chlorophosphine, ${}^t\text{Bu}\{(\text{CH}_2)_3\text{CH}=\text{CH}_2\}\text{P}\text{Cl}$ (**1**), was synthesized comprising an unsaturated hydrocarbon chain. Its reaction with the threefold silylated cluster yielded the compound $[\text{Ge}_9\{\text{Si}(\text{TMS})_3\}_3\text{P}{}^t\text{Bu}\{(\text{CH}_2)_3\text{CH}=\text{CH}_2\}]$ (**2**), which was thoroughly characterized by spectroscopic methods as well as single crystal X-ray diffraction analysis. Reactions of the twofold silylated cluster with $RR^lP\text{Cl}$ led to the formation of the monoanionic species $[\text{Ge}_9\{\text{Si}(\text{TMS})_3\}_2\text{PRR}^l]^-$ (**3a** to **11a**), which were analyzed by NMR spectroscopy as well as ESI-MS analysis. The anions **3a** to **11a** still comprise reactive sites at the $[\text{Ge}_9]$ cluster as well as the Lewis basic P atom. Thus, N-heterocyclic carbenes $\text{NHC}^{\text{DiPP}}\text{MCl}$ ($M = \text{Cu, Ag}$) were reacted with the monoanions, leading to the formation of the species **3-MNHC**^{DiPP} to **11-MNHC**^{DiPP}. In dependency of the steric impact of the organic ligands at the phosphine the transition metal either coordinates to a triangular face of the $[\text{Ge}_9]$ cluster (high steric shielding) or the metal directly coordinates to the Lewis basic P atom (low steric shielding). Consequently, the evaluation of the ${}^{31}\text{P}$ NMR spectra revealed a singlet or a doublet caused by ${}^1J({}^{31}\text{P}-{}^{107}\text{Ag}/{}^{109}\text{Ag})$ spin-spin coupling, respectively. The spectroscopic data indirectly allow to distinguish between the different coordination modes the coinage metal carbene adopts towards the phosphanyl-substituted cluster.

The experimental work was done in two periods: a) the preparation of compounds **1** and **2** as well as the preparation of various chlorophosphines, anions **3a** to **11a**, and their reaction towards the carbene $\text{NHC}^{\text{Dipp}}\text{Cu-Cl}$ (**3a-CuNHC^{Dipp}** to **11a-CuNHC^{Dipp}**) was performed as part of my Master's thesis, which was supervised by Dr. Felix S. Geitner. b) Reactions of the monoanions **3a** to **11a** towards the carbene $\text{NHC}^{\text{Dipp}}\text{Ag-Cl}$ were investigated during my PhD project, including the acquisition of the spectroscopic data (**3a-AgNHC^{Dipp}** to **11a-AgNHC^{Dipp}**). All experimental work was performed by me. Dr. Felix S. Geitner selected a suitable single crystal of compound **2** and performed the initial structure refinement. Dr. Wilhelm Klein finalized the single crystal structure refinement for publication. Elemental analysis data were acquired by Ulrike Ammari and Bircan Dilki in the microanalytical laboratory of the Chemistry Department of the Technical University of Munich. Dr. Kerstin Mayer and Dr. Felix S. Geitner partially supported the ESI-MS measurements. A first version of the manuscript was prepared by Dr. Felix S. Geitner and was included in his PhD thesis. During my PhD project I synthesized the Ag-carbene complexes and collected the NMR spectroscopic data. Furthermore, I rewrote the manuscript refocusing on the P-Ag spin-spin coupling, and included the additional data, figures and tables. Dr. Felix S. Geitner and Dr. Annette Schier proof-read the final version of the manuscript. The publication of the manuscript was managed by Prof. Dr. Thomas F. Fässler, the peer-review process including corrections was a joined task accomplished by Prof. Dr. Thomas F. Fässler and me.

■ [Ge₉] Cluster Chemistry | Hot Paper |● Enhancing the Variability of [Ge₉] Cluster Chemistry through Phosphine FunctionalizationChristoph Wallach,⁺[a] Felix S. Geitner,⁺[a, b] Wilhelm Klein,^[a] and Thomas F. Fässler^{*[a]}

Abstract: The synthetic approach towards molecules that contain Ge atoms with oxidation state 0, and which are exclusively connected to other Ge atoms, is explored by using anionic clusters extracted from binary solids. Besides providing a novel variable method for the introduction of alkenyl moieties to [Ge₉] cluster compounds, this work expands the spectrum of mixed-functionalized [Ge₉] cluster anions, which are suitable for the straightforward synthesis of zwitterionic compounds upon coordination to metal cations. In detail, the synthesis of a series of mixed-functionalized [Ge₉] clusters is reported, including [Ge₉{Si(TMS)₃}₃PRR¹] (R = *t*Bu, R¹ = (CH₂)₃CH=CH₂; **2**) and [Ge₉{Si(TMS)₃}₂PRR¹]⁻ (R and R¹: alkyl, alkenyl, aryl, aminoalkyl; **3 a** to **11 a**, TMS: (trimethyl)silyl). In **2**

and **3 a**, pentenyl functionalization of the [Ge₉] clusters was achieved by reaction of the novel chlorophosphine *t*Bu{(CH₂)₃CH=CH₂}PCl (**1**) with silylated [Ge₉] clusters. Furthermore, the reactivity of the cluster anions **3 a** to **11 a** towards NHC^{Dipp}MCl (NHC^{Dipp} = 1,3-di(2,6-diisopropylphenyl)imidazolyldine; M = Cu, Ag) showed a dependency on the steric demand of the phosphine either zwitterions (**3**-MNHC^{Dipp} to **7**-MNHC^{Dipp}) featuring P–M interactions are formed, or Ge–M coordination (**8**-MNHC^{Dipp} to **11**-MNHC^{Dipp}) occurs. For M = Ag, the formation of zwitterionic complexes was unequivocally proven by NMR investigations showing ¹J(³¹P–¹⁰⁷Ag/¹⁰⁹Ag) spin-spin coupling.

Introduction

Molecular cluster species of silicon and germanium resemble the structural and electronic properties of nano-scale particles as well as of silicon and germanium surfaces. They typically contain one or more unsubstituted Si or Ge atoms, which in addition are exclusively bound to atoms of the same type.^[1] Such clusters that consequently contain Si and Ge atoms in oxidation state 0 have received considerable attention in recent years.^[2]

Lately, the protonated molecular deltahedral Si and Ge clusters [H₂Si₉]²⁻,^[3] [HSi₉]³⁻,^[4] [HGe₉]³⁻,^[5] [HGe₄ZnPh₂]⁴⁻,^[6] as well as [H₂(Si/Ge)₉]²⁻^[4b] have been obtained, closing the structural gap to hydrogen-terminated Si and Ge particles and surfaces. A major breakthrough for the synthesis of nine-atom clusters containing up to seven uncoordinated Si or Ge atoms was achieved some years ago through the co-condensation of meta-

stable Ge^I salts with Li[Si(TMS)₃].^[7] Subsequently, more straightforward methods for the synthesis of such species were found in the silylation reactions of [Ge₉]⁴⁻^[8] and recently [Si₉]⁴⁻^[9] as well as by the multiple phosphine functionalization of [Ge₉]⁴⁻ *Zintl* anions.^[10]

The precursor *Zintl* phases K₁₂Si₁₇, K₄Ge₉, and K₁₂Ge₁₇ contain nine-atom silicide and germanide clusters and are easily accessible from the elements in quantitative yield by solid-state reactions. With respect to their straightforward synthesis and their interesting electronic properties (fourfold negative charge, however, their shape can be explained by the Wade–Mingos rules for electron-deficient cage compounds), the included [Si₉] and [Ge₉] clusters are not only of interest regarding the synthesis of nanostructured materials but are also interesting ligands with respect to organometallic chemistry.^[11] Whereas only one example has been reported for [Si₉] clusters so far,^[9] the chemistry of the related [Ge₉] clusters has been explored in more detail and allows for a more precise decoration of the clusters. [Ge₉] cages bearing multiple organic or main group element substituents are interesting owing to their decreased charge, which makes them soluble in standard solvents (MeCN and THF) and decreases their reductive nature at the same time. Examples for such [Ge₉] cages were originally found in the bis-vinylated species [Ge₉{CH=CH₂}₂]²⁻^[12] or the tris-silylated cluster [Ge₉{Si(TMS)₃}₃]⁻,^[7,8a] however, only for the latter species a prosperous subsequent chemistry evolved, introducing the tris-silylated [Ge₉] cluster to organic^[1b,13] and main group element compounds^[13,14] or transition metal complexes.^[15] Subsequently, further silylated [Ge₉] cluster species bearing various silyl substituents were reported,^[15i,j,16] the

[a] C. Wallach,⁺ Dr. F. S. Geitner,⁺ Dr. W. Klein, Prof. Dr. T. F. Fässler
Department Chemie
Technische Universität München
Lichtenbergstraße 4
85747 Garching b. München (Germany)
E-mail: thomas.faessler@lrz.tum.de

[b] Dr. F. S. Geitner⁺
WACKER Institute for Silicon Chemistry
Technische Universität München
Lichtenbergstraße 4, 85747 Garching b. München (Germany)

[*] These authors contributed equally to this work.

Supporting information and the ORCID identification number(s) for the author(s) of this article can be found under:
<https://doi.org/10.1002/chem.201901673>

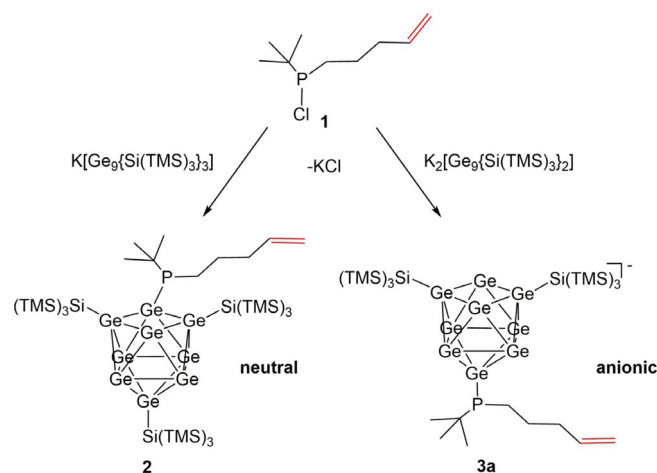
number of the silyl substituents was varied (twofold substituted cluster $[\text{Ge}_9\{\text{Si}(\text{TMS})_3\}_2]^{2-}$),^[8b] and tris-stannyl decoration of $[\text{Ge}_9]$ was achieved.^[17] However, the reactivity of these cluster species was limited to the $[\text{Ge}_9]$ cluster core owing to the inert nature of the attached silyl or stannyl groups. Thus, for a further expansion of the $[\text{Ge}_9]$ clusters chemistry, the introduction of functional and potentially reactive groups to the $[\text{Ge}_9]$ core was necessary. In previous studies, we already achieved the introduction of $[\text{PR}_2]^+$ ($\text{R} = \text{alkyl, aryl, aminoalkyl}$) groups to tris- and bis-silylated $[\text{Ge}_9]$ clusters, leading to neutral species $[\text{Ge}_9\{\text{Si}(\text{TMS})_3\}_3\text{PR}_2]$ ($\text{R} = i\text{Pr, Cy}$) or anionic clusters $[\text{Ge}_9\{\text{Si}(\text{TMS})_3\}_2\text{PR}_2]^-$ ($\text{R} = t\text{Bu, Mes, NiPr}_2$), respectively. In subsequent reactions with the Lewis acidic copper N-heterocyclic carbene (NHC) complex $\text{NHC}^{\text{Dipp}}\text{CuCl}$ we found that the anionic species can interact with $[\text{NHC}^{\text{Dipp}}\text{Cu}]^+$ either via the $[\text{Ge}_9]$ cluster core, giving $[\text{Ge}_9]$ cluster Cu-NHC compounds $(\text{NHC}^{\text{Dipp}}\text{Cu})[\text{Ge}_9\{\text{Si}(\text{TMS})_3\}_3\text{PR}_2]$ ($\text{R} = \text{Mes, NiPr}_2$), or with the lone pair situated at the phosphorous atom under formation of the zwitterionic compound $[(\text{Ge}_9\{\text{Si}(\text{TMS})_3\}_2\text{Bu}_2\text{P})(\text{CuNHC}^{\text{Dipp}})]$. In this context, the steric impact of the phosphine substituents appears to be the decisive factor for the course of the reaction (smaller substituents: P-Cu; larger substituents: Ge-Cu). According to these findings, anionic mixed-functionalized clusters $[\text{Ge}_9\{\text{Si}(\text{TMS})_3\}_2\text{PR}_2]^-$ can either be described as phosphine-substituted $[\text{Ge}_9]$ clusters ($\text{R} = \text{Mes, NiPr}_2$) or as $[\text{Ge}_9]$ cluster-substituted phosphines ($\text{R} = t\text{Bu}$). The latter species allows for the straightforward synthesis of zwitterionic compounds upon coordination to a transition metal cation, which might be of interest regarding catalytic applications.^[18]

In further attempts to obtain $[\text{Ge}_9]$ clusters with functional ligands, pre-silylated $[\text{Ge}_9]$ cages were decorated with alkenyl moieties leading to neutral compounds $[\text{Ge}_9\{\text{Si}(\text{TMS})_3\}_3\{(\text{CH}_2)_n\text{CH}=\text{CH}_2\}]$ ($n = 1, 3$),^[1b] or alkenyl-functionalized silyl groups were introduced at bis-silylated clusters yielding $[\text{Ge}_9\{\text{Si}(\text{TMS})_3\}_2\{\text{SiPh}_2(\text{CH}_2)_n\text{CH}=\text{CH}_2\}]^-$ ($n = 0, 3$) and at bare $[\text{Ge}_9]^{4-}$ clusters resulting in $[\text{Ge}_9\{\text{SiPh}_2(\text{CH}_2)_n\text{CH}=\text{CH}_2\}_3]^-$ ($n = 0, 3$).^[19] Alkenyl substituents may be used as anchor groups with respect to the attachment of $[\text{Ge}_9]$ -rich clusters at nanoparticles and other surfaces or for the linkage of the clusters to build up nanostructured materials. The requirements for optimal anchor groups are an easy, straightforward introduction at the $[\text{Ge}_9]$ clusters, a variable applicability (e.g., for bis- and tris-silylated cluster compounds), and an exposed position of the reactive terminal double bond upon the attachment to the $[\text{Ge}_9]$ cluster. Alkenyl-functionalized phosphine groups fulfil most of the demands for such an anchor group (easy and variable introduction). To assure an exposed nature of the reactive double bond, a functionalized chlorophosphine with a long alkenyl chain is needed. However, reports on alkenyl-functionalized chlorophosphines are very rare, and all reported molecules were only substituted with short alkenyl chains.^[20] Therefore, we investigated the synthesis of a novel chlorophosphine comprising a pentenyl group and examined its reactivity towards variously silylated $[\text{Ge}_9]$ clusters. Furthermore, we synthesized a series of novel mixed-functionalized cluster anions $[\text{Ge}_9\{\text{Si}(\text{TMS})_3\}_2\text{PRR}']^-$ (R and $\text{R}' = \text{alkyl, aryl, aminoalkyl}$) and tested their suitability as ligands for the straightforward syn-

thesis of zwitterionic compounds upon reaction with $\text{NHC}^{\text{Dipp}}\text{MCl}$ ($\text{M} = \text{Cu, Ag}$).

Results and Discussion

The pentenyl-functionalized chlorophosphine $t\text{Bu}\{(\text{CH}_2)_3\text{CH}=\text{CH}_2\}\text{P}(\text{Cl})$ (**1**) was obtained by the reaction of a freshly prepared 5-bromomagnesium pentene Grignard solution with $t\text{BuP}(\text{Cl})_2$ in diethyl ether. To assure the mono alkenylation of $t\text{BuP}(\text{Cl})_2$, a slight excess (1.25 equiv) of the dichlorophosphine was used. Purification of **1** was achieved by vacuum distillation, giving compound **1** as a colorless liquid in medium yield. In the next step, we reacted compound **1** with the tris-silylated cluster $[\text{Ge}_9\{\text{Si}(\text{TMS})_3\}_3]^-$ and the bis-silylated cluster $[\text{Ge}_9\{\text{Si}(\text{TMS})_3\}_2]^{2-}$ (Scheme 1). For reactions of **1** with $[\text{Ge}_9\{\text{Si}(\text{TMS})_3\}_3]^-$, the silylat-



Scheme 1. Reactions of the pentenyl-functionalized chlorophosphine **1** with the tris-silylated cluster $[\text{Ge}_9\{\text{Si}(\text{TMS})_3\}_3]^-$ (left) or the bis-silylated cluster $[\text{Ge}_9\{\text{Si}(\text{TMS})_3\}_2]^{2-}$ (right) yielding neutral species **2** or anion **3a**, both carrying a pentenyl anchor group attached to the $[\text{Ge}_9]$ cluster via the phosphine moiety.

ed cluster was dissolved in toluene, and a toluene solution of **1** was added. The resulting deep-red reaction mixture was stirred at room temperature for 1 h before the solvent was removed in vacuo, and the remaining brownish solid was washed with MeCN to remove excess reactants. The ^1H NMR spectra of the crude product suggested the attachment of a $[t\text{Bu}\{(\text{CH}_2)_3\text{CH}=\text{CH}_2\}\text{P}]^+$ moiety to $[\text{Ge}_9\{\text{Si}(\text{TMS})_3\}_3]^-$ according to the observed signal ratio. Subsequently, the solid was dissolved in toluene, filtered to remove insoluble materials, and stored in a freezer at -40°C , yielding orange, block-shaped crystals. The single-crystal data confirmed the attachment of the pentenyl-functionalized phosphine moiety at the $[\text{Ge}_9]$ cluster and formation of the neutral compound $[\text{Ge}_9\{\text{Si}(\text{TMS})_3\}_3\text{PtBu}\{(\text{CH}_2)_3\text{CH}=\text{CH}_2\}]$ (**2**). Compound **2** crystallizes in the triclinic space group $P\bar{1}$, with two formula units in the unit cell. The shape of the $[\text{Ge}_9]$ cluster core can be described as a slightly distorted capped square antiprism (C_{4v} symmetry). The Ge-Ge distances range between 2.4715(6) Å (Ge1-Ge2) and 3.1642(6) Å (Ge5-Ge8) with the shortest distances in the

open square and the longest distances in the Ge-capped square. The hypersilyl groups are attached at two opposite Ge vertices (Ge2 and Ge4) within the open square of the cluster and at the capping Ge atom (Ge9) with distances between 2.374 Å (Ge9–Si9) and 2.404 Å (Ge2–Si1), which are in the range of previously reported data.^[15g,18]

The phosphine group in **2** is disordered (Figure 1 c) and attached to a further Ge vertex within the open square of the [Ge₉] cluster. The two individuals with occurrences of 56.9% (P1A) and respectively 43.1% (P1B) show Ge–P distances of 2.362(2) Å (Ge1–P1A) or 2.337(2) Å (Ge1–P1B), which are also in the range of reported Ge–P single bonds (Figure 1).^[18a,21] The observed disorder probably results from the pyramidal inversion of the ligands bound to the P atom (P1A: Ge1, C28A, C32A; P1B: Ge1, C28B, C32B). Both individuals of the disordered phosphine moiety point radially away from the center of the [Ge₉] cluster as shown by the angles Ge3–Ge1–P1A of 137.76(5)° and Ge3–Ge1–P1B of 137.61(8)°.

The functional pentenyl group has an exposed position and is not encumbered by any other ligands (space filling model), which might allow for further reactions at the alkenyl site (Figure 1, Supporting Information). Reactions of **1** with the bis-

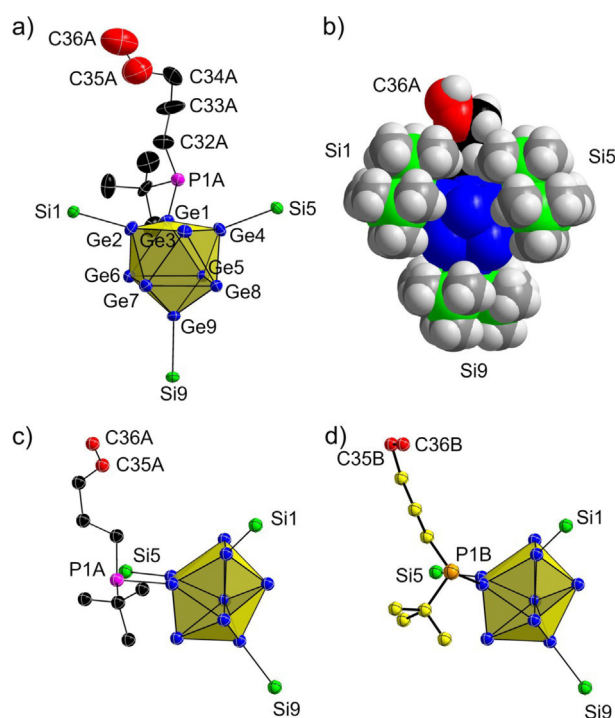


Figure 1. a) Molecular structure of the major individual of compound **2**, showing the slightly distorted C_{4v} -symmetric shape of the [Ge₉] cluster core and the attachment of all ligands through two center–two electron (2c–2e) *exo* bonds. All ellipsoids are shown at the 50% probability level. b) Space filling model of compound **2**, showing the exposed nature of the double bond of the pentenyl group. c) and d) represent the disordered phosphine moiety of compound **2** in isotropical atom presentation, with c) being the individual of major occurrence. Color code: Ge: blue; Si: green; P_{major individual}: purple; P_{minor individual}: orange; C_{major individual}: black; C_{minor individual}: yellow; C–double bond: red; C–TMS: dark gray; H: light gray. For clarity, in figures a), c), and d) the TMS groups of the hypersilyl groups as well as all protons are omitted; in a) and b) only the major individual of the disordered phosphine group is shown. Selected distances of **2** are provided in the Supporting Information.

silylated cluster [Ge₉{Si(TMS)₃}₂]^{2–} were carried out in MeCN. Addition of a solution of **1** in MeCN to an acetonitrile solution containing the anion [Ge₉{Si(TMS)₃}₂]^{2–} resulted in a deep-red reaction mixture, which was stirred at room temperature for 1 h, before it was filtered to remove all solids, and then the solvent was removed in vacuo. The NMR examination of the obtained brownish solid revealed the formation of the mixed-functionalized anion [Ge₉{Si(TMS)₃}₂PtBu{(CH₂)₅CH=CH₂}][–] (**3a**) according to the observed signal ratio. In ESI-MS examinations, the molecule peak of **3a** was monitored at *m/z*: 1306.8 (Figure 2). Hence, the pentenyl-functionalized chlorophosphine

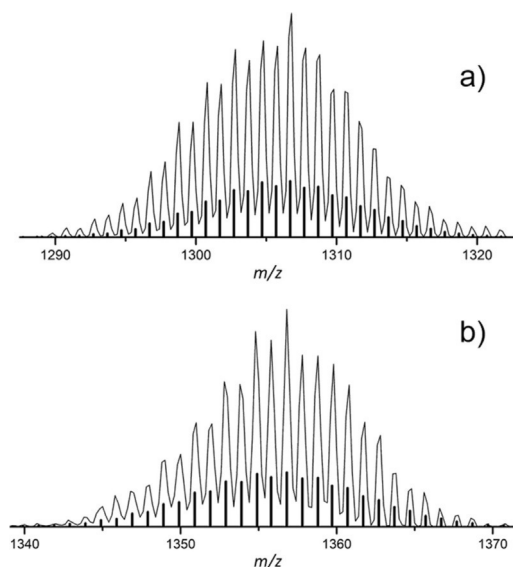


Figure 2. ESI-MS spectra of the anions a) **3a** and b) **10a**. Spectrum a) was recorded from THF solution in the negative ion mode (3500 V, 300 °C) showing the signal of the molecule peak of **3a** at *m/z*: 1306.8. Spectrum b) was obtained from THF solution in negative ion mode (3500 V, 300 °C) showing the molecule peak of **10a** at *m/z*: 1356.8. Calculated patterns are presented as black bars. All other ESI-MS spectra are provided in the Supporting Information.

1 was qualified as a suitable precursor for the introduction of pentenyl anchor groups at variously silylated [Ge₉] clusters with varying charge and steric shielding of the [Ge₉] cluster core. In further investigations, a series of mixed-functionalized [Ge₉] anions [Ge₉{Si(TMS)₃}₂PRR¹][–] (**4a**: R: *i*Pr, R¹: *t*Bu; **5a**: R: *t*Bu, R¹: NEt₂; **6a**: R=R¹: 1,1-dimethylpropyl; **7a**: R=R¹: 1-adamantyl; **8a**: R: *i*Pr, R¹: NiPr₂; **9a**: R: *t*Bu, R¹: NiPr₂; **10a**: R: *t*Bu, R¹: Mes; **11a**: R=R¹: *o*-tolyl) was synthesized and their suitability to give zwitterionic compounds by reaction with NHC^{Dipp}AgCl was tested (for NMR spectra, see the Supporting Information, Table 2). The formation of the zwitterions (P–Ag interactions) can be seen by the occurrence of ¹J(³¹P–¹⁰⁷Ag/¹⁰⁹Ag) spin-spin coupling by ³¹P NMR spectroscopy. Moreover, the respective copper compounds with an analogous interaction between the cluster anions and [Cu–NHC^{Dipp}]⁺ were prepared. The anionic clusters **4a–11a** were obtained by the reaction of the bis-silylated cages [Ge₉{Si(TMS)₃}₂]^{2–} with the respective chlorophosphines RR¹PCl in acetonitrile, yielding the crude products as brownish solids in medium to good yield after filtration of

the reaction mixtures and removal of the solvent in vacuo (in analogy to **3a**).

The anions were characterized by NMR (^1H , ^{31}P , ^{29}Si , ^{13}C) and ESI-MS investigations (monitoring of molecule peaks). All NMR and ESI-MS spectra are presented in the Supporting Information. Interestingly, the reactions of the electron-poor chlorophosphine $(\text{C}_6\text{F}_5)_2\text{P}(\text{Cl})$, which is of similar bulkiness to $t\text{Bu}_2\text{P}(\text{Cl})$, with $[\text{Ge}_9(\text{Si}(\text{TMS})_3)_2]^{2-}$ were not successful and resulted in unidentified products. This indicates that a certain basicity of the applied chlorophosphines is mandatory for the successful synthesis of mixed-functionalized $[\text{Ge}_9]$ clusters (all other tested chlorophosphines had increased donor strength according to the Tolman electronic parameter).^[22] Reactions of **3a** to **11a** with $\text{NHC}^{\text{Dipp}}\text{MCl}$ ($\text{M}=\text{Cu}$, Ag) were carried out by adding MeCN solutions of $\text{NHC}^{\text{Dipp}}\text{MCl}$ to freshly prepared solutions containing the respective anions **3a** to **11a** in MeCN, which resulted in the immediate formation of brownish precipitates. The supernatant solutions were filtered off, the residues were washed with MeCN, and the resulting red to brown solids were examined by NMR spectroscopy, proving the attachment of $[\text{NHC}^{\text{Dipp}}\text{M}]^+$ to the anions **3a** to **11a** under formation of the neutral compounds **3-MNHC}^{\text{Dipp}} to **11-MNHC}^{\text{Dipp}}. An indication whether a zwitterionic compound with P–M interactions or a $[\text{Ge}_9]$ cluster M–NHC compound (Ge–M interactions) has been formed, is given by the chemical shift of the methyl protons of the silyl groups, which is very sensitive with regard to the number of substituents directly bound to the $[\text{Ge}_9]$ cluster core. If a zwitterionic compound is formed, the silyl group signal is not significantly shifted. By contrast, the addition of the $[\text{NHC}^{\text{Dipp}}\text{M}]^+$ ($\text{M}=\text{Cu}$, Ag) fragment to the $[\text{Ge}_9]$ core, which****

increases the number of ligands at the cluster, leads to a significant high-field shift of the respective signals (Table S2, Table S3 in the Supporting Information). This correlation has been observed from the NMR data of similar phosphine-functionalized $[\text{Ge}_9]$ units, which have been structurally characterized by single-crystal X-ray diffraction, and additionally by ESI-MS and elemental analyses.^[18] As an example, the ^1H NMR signal of the silyl group of the anion **3a** shows only a small shift from 0.26 to 0.23 ppm upon addition of the $[\text{Ag-NHC}^{\text{Dipp}}]^+$ fragment, giving the zwitterionic **3-AgNHC}^{\text{Dipp}} (Table S2, Figure S10 in the Supporting Information). By contrast, a non-negligible shift of -0.08 ppm is observed for the respective signal of **8a** upon the formation of neutral **8-AgNHC}^{\text{Dipp}}. In all cases, the coordination of M^+ to a triangular face of the cluster results in a shift to 0.17 or 0.18 ppm, whereas for P–Ag interactions, a fluctuation within ± 0.04 ppm around 0.25 ppm is observed. Comparable correlations are observed for Cu^+ containing complexes (Table S3, Figure S11 in the Supporting Information).****

Results of the $^1J(^{31}\text{P}-^{107}\text{Ag}/^{109}\text{Ag})$ spin-spin coupling experiments in solution unambiguously confirmed the results derived from the ^1H NMR spectra concerning the interactions between the cluster anions and the $[\text{NHC}^{\text{Dipp}}\text{M}]^+$ units. ^{31}P NMR investigations of solutions of **3-AgNHC}^{\text{Dipp}} to **7-AgNHC}^{\text{Dipp}} showed doublets with $^1J(^{31}\text{P}-^{107}\text{Ag}/^{109}\text{Ag})$ coupling constants ranging from 207.8 to 486.2 Hz (Table 1, Table 2), which are in accordance with previously reported values.^[23] By contrast, solutions of complexes **8-AgNHC}^{\text{Dipp}} to **11-AgNHC}^{\text{Dipp}} exhibited singlet ^{31}P NMR signals proving the absence of Ag–P bonds.********

Table 1. ^{31}P NMR shifts of mixed-functionalized cluster anions $[\text{Ge}_9(\text{Si}(\text{TMS})_3)_2\text{PRR}]^-$ (**3a** to **11a**) and respective zwitterionic compounds **3-AgNHC}^{\text{Dipp}} to **7-AgNHC}^{\text{Dipp}} (left) or $[\text{Ge}_9]$ cluster Ag-NHC compounds **8-AgNHC}^{\text{Dipp}} to **11-AgNHC}^{\text{Dipp}} (right). $^1J(^{31}\text{P}-^{107}\text{Ag}/^{109}\text{Ag})$ spin-spin coupling constants (Hz) are reported for **3-AgNHC}^{\text{Dipp}} to **7-AgNHC}^{\text{Dipp}}.************

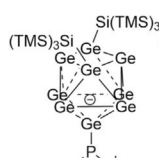
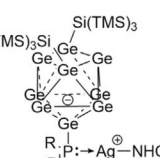
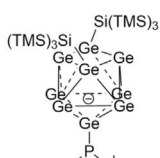
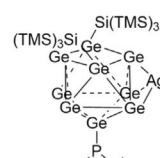
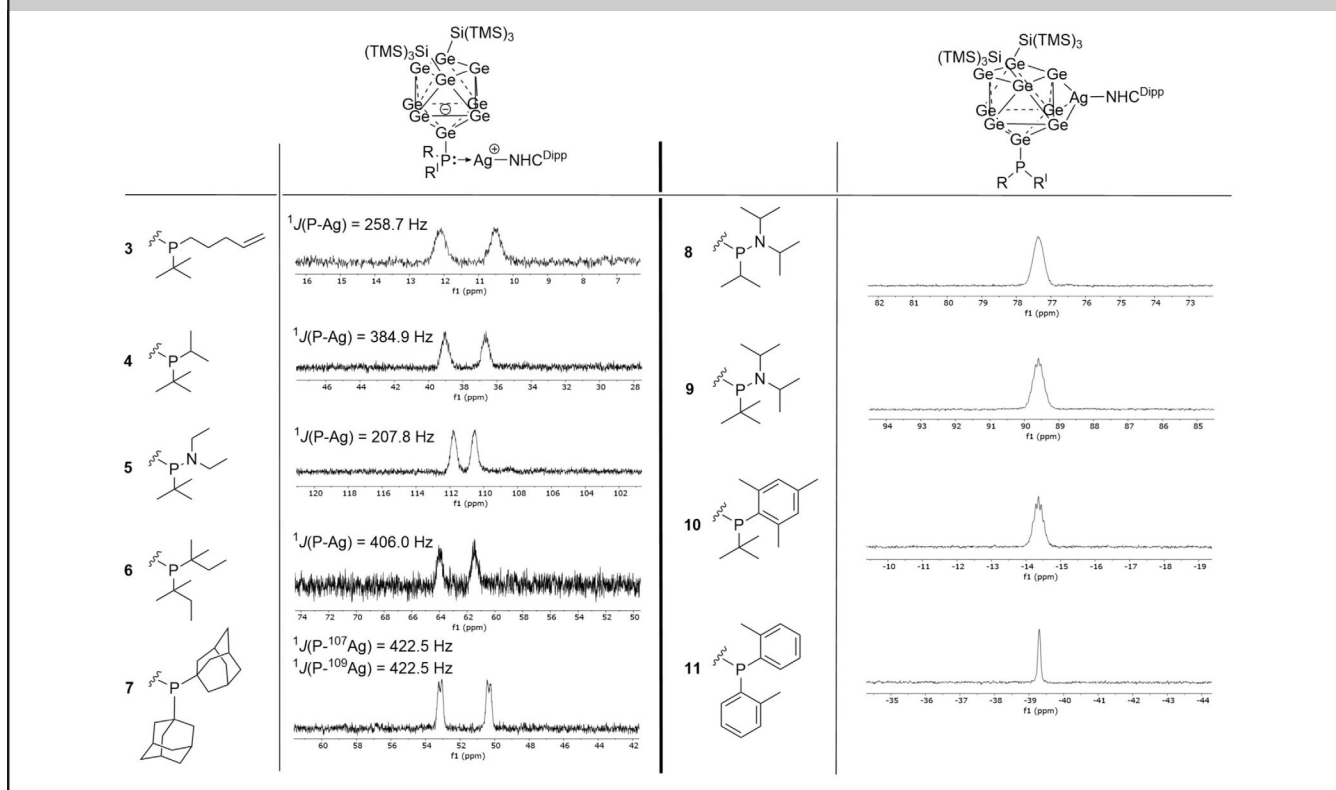
					
	[ppm]	doublet, [ppm]	$^1J(^{31}\text{P}-^{107}\text{Ag}/^{109}\text{Ag})$ [Hz]	[ppm]	singlet, [ppm]
3	4.11 3a	11.32 3-AgNHC}^{\text{Dipp}}	258.7	8	69.83 8-AgNHC}^{\text{Dipp}}
4	35.55 4a	37.83 4-AgNHC}^{\text{Dipp}}	384.9	9	83.12 9-AgNHC}^{\text{Dipp}}
5	110.04 5a	111.15 5-AgNHC}^{\text{Dipp}}	207.8	10	-19.40 10-AgNHC}^{\text{Dipp}}
6	52.93 6a	62.81 6-AgNHC}^{\text{Dipp}}	405.5	11	-41.66 11-AgNHC}^{\text{Dipp}}
7	57.32 7a	51.73 7-AgNHC}^{\text{Dipp}}	$^1J(^{31}\text{P}-^{107}\text{Ag}) = 422.5$ $^1J(^{31}\text{P}-^{109}\text{Ag}) = 486.2$		77.38 8-AgNHC}^{\text{Dipp}}
					89.59 9-AgNHC}^{\text{Dipp}}
					-14.36 10-AgNHC}^{\text{Dipp}}
					-39.30 11-AgNHC}^{\text{Dipp}}

Table 2. ^{31}P NMR spectra of compounds **3**- $\text{AgNHC}^{\text{Dipp}}$ to **11**- $\text{AgNHC}^{\text{Dipp}}$ in THF-d_3 allowing for the determination of the interaction (P–Ag or Ge–Ag) between the mixed-functionalized cluster anions **3a** to **11a** and the $[\text{NHC}^{\text{Dipp}}\text{Ag}]^+$ moiety, by using the presence of $^1J(^{31}\text{P},^{107}\text{Ag}/^{109}\text{Ag})$ spin-spin coupling as an indicator.

Owing to ^{31}P - ^1H spin-spin coupling, the ^{31}P signals show a slightly visible additional splitting (Table 2). Accordingly, the anions **3a** to **7a** are better described as phosphines carrying a $[\text{Ge}_9]$ cluster substituent (no significant shift of the silyl groups' signal upon coordination of $[\text{NHC}^{\text{Dipp}}\text{M}]^+$ for $\text{M}=\text{Cu}, \text{Ag}$ as well as the occurrence of spin-spin coupling for $\text{M}=\text{Ag}$), which are suitable ligands for the synthesis of the zwitterionic compounds $[(\text{Ge}_9\{\text{Si}(\text{TMS})_3\}_2)\text{RR}'\text{P}](\text{MNHC}^{\text{Dipp}})$ **3**- $\text{MNHC}^{\text{Dipp}}$ to **7**- $\text{MNHC}^{\text{Dipp}}$ comprising P–M interactions. By contrast, anions **8a** to **11a** can be described as phosphine-substituted Ge clusters as the $[\text{Ge}_9]$ cluster core directly interacts with the $[\text{NHC}^{\text{Dipp}}\text{M}]^+$ moiety (indicated by the high-field shift of the silyl groups' signals upon coordination of $[\text{NHC}^{\text{Dipp}}\text{M}]^+$ ($\text{M}=\text{Cu}, \text{Ag}$) and the absence of spin-spin coupling for $\text{M}=\text{Ag}$), under formation of Ge cluster compounds $(\text{NHC}^{\text{Dipp}}\text{M})[\text{Ge}_9\{\text{Si}(\text{TMS})_3\}_2\text{PRR}']$ **8**- $\text{MNHC}^{\text{Dipp}}$ to **11**- $\text{MNHC}^{\text{Dipp}}$ (Table 1, Table 2).

Hence, mixed-functionalized $[\text{Ge}_9]$ cluster anions with phosphine groups bearing one *tert*-butyl group and another smaller ligand (**3a** to **5a**), as well as phosphine moieties with slightly larger 1,1-dimethylpropyl (**6a**) or 1-adamanyl groups (**7a**), if compared with $[\text{tBu}_2\text{P}]^+$,^[22,24] are suitable precursors for the straightforward synthesis of zwitterionic compounds upon coordination to a transition metal cation. By contrast, more bulky substituents such as NiPr_2 or Mes do not allow for P–M interactions even with the second substituent at phosphorus being a smaller *tert*-butyl (**9a**, **10a**) or *iso*-propyl group (**8a**). Similar re-

activity is observed upon introduction of a $[(o\text{-tolyl})_2\text{P}]^+$ unit (**11a**).

Electronic effects seem to not be a decisive factor for the formation of either a zwitterionic or a neutral compound, as the aminoalkyl phosphines **8a** and **9a** only differ from **5a** by an enlarged alkyl group. However, this small steric deviation enables a nucleophilic attack of the phosphine's lone pair of **5a** at the ML^+ fragments. These findings confirm that the steric effect of the phosphines' substituents dominates the electronic factors with respect to the coordination of M^+ to the P atom and in consequence the formation of zwitterionic organometallic complexes.

Conclusion

In this work, we report the synthesis of a novel pentenyl-functionalized chlorophosphine (**1**), which allows for the introduction of an exposed alkenyl anchor group at variously silylated $[\text{Ge}_9]$ clusters via the phosphine moiety. The products were either the uncharged compound $[\text{Ge}_9\{\text{Si}(\text{TMS})_3\}_2\text{PRR}']$, **2**, or the anionic species $[\text{Ge}_9\{\text{Si}(\text{TMS})_3\}_2\text{PRR}']^-$, **3a** ($\text{R}=\text{tBu}$; $\text{R}'=(\text{CH}_2)_3\text{CH}=\text{CH}_2$). Moreover, a series of mixed-functionalized anions $[\text{Ge}_9\{\text{Si}(\text{TMS})_3\}_2\text{PRR}']^-$ (**4a** to **11a**) was synthesized, and the reactivity of the anions **3a** to **11a** towards $\text{NHC}^{\text{Dipp}}\text{MCl}$ ($\text{M}=\text{Cu}, \text{Ag}$) was tested. The anions **3a** to **7a** reacted as Ge cluster-substituted phosphines and are suitable ligands for the formation of zwitterionic compounds **3**- $\text{MNHC}^{\text{Dipp}}$ to

7-MNHC^{Dipp} (P–M interactions). By contrast, anions **8a–11a** can be regarded as phosphine-substituted Ge clusters, which form neutral [Ge₉] cluster M–NHC compounds **8-MNHC^{Dipp}** to **11-MNHC^{Dipp}** (Ge–M interactions). Besides expanding the spectrum of mixed-functionalized [Ge₉] clusters suitable for the synthesis of zwitterionic compounds upon coordination of a coinage metal cation (**3a** to **7a**), the obtained results confirm that the steric impact of the phosphine substituents rather than the phosphines' electronic properties is the decisive factor for the formation of mixed-functionalized [Ge₉] clusters.

Experimental Section

General

All manipulations were performed under oxygen-free, dry conditions under argon atmosphere by using standard Schlenk or glove-box techniques. Glassware was dried prior to use by heating it in vacuo. The solvents used were obtained from an MBraun Grubbs apparatus. All other commercially available chemicals were used without further purification. K₄Ge₉ was prepared by fusion of stoichiometric amounts of the elements in stainless-steel tubes at 650 °C. The silylated cluster compounds K[Ge₉{Si(TMS)₃}₃] and K₂[Ge₉{Si(TMS)₃}₂]^[8b], the chlorophosphines MesPCl₂^[25], *i*Pr*t*BuPCl₂^[26], *t*Bu(NEt₂)PCl₂^[27], (1,1-dimethylpropyl)₂PCl₂^[28], *i*Pr(NiPr₂)PCl₂^[29], *t*Bu(NiPr₂)PCl₂^[29], *t*BuMesPCl₂^[30], (C₆F₅)₂PCl₂^[31], the imidazolium salt NHC^{Dipp}·HCl, and the corresponding coinage metal complexes NHC^{Dipp}MCl (M = Cu, Ag) were synthesized according to modified literature procedures.^[32]

Single-crystal structure determination

The air- and moisture-sensitive crystals of **2** were transferred from the mother liquor into cooled perfluoroalkyl ether oil under a cold stream of N₂ gas. For diffraction data collection, the single crystals were fixed on a glass capillary and positioned in a 150 K cold N₂ gas stream by using the crystal cap system. Data collection was performed with a STOE StadiVari (MoK_α radiation) diffractometer equipped with a DECTRIS PILATUS 300 K detector. The structure was solved by direct methods (SHELXS-2014) and refined by full-matrix least-squares calculations against F² (SHELXL-2014).^[33] The positions of the hydrogen atoms were calculated and refined by using a riding model. Unless stated otherwise, all non-hydrogen atoms were treated with anisotropic displacement parameters. The supplementary crystallographic data for this paper have been deposited with the Cambridge Structural database and are available free of charge via www.ccdc.cam.ac.uk/data_request/cif. The crystallographic data for compound **2** is summarized in Table 3. In compound **2**, the phosphine group attached to the cluster is disordered and was refined on split positions. The carbon atoms 32A/B or 36A/B were refined with identical room coordinates and the carbon atoms C28A/B, C32A/B, C34A/B, C36A/B were refined with identical anisotropic vibrational parameters. Furthermore, some of the carbon atoms of the phosphine moiety were treated with ISOR restraints (C29A, C35A/B, C36A/B).

NMR spectroscopy

NMR spectra were measured with a Bruker Avance Ultrashield 400 MHz spectrometer. The ¹H spectra were calibrated by using the residual proton signal of the used deuterated solvents. Chemical shifts are reported in parts per million (ppm) relative to TMS,

Table 3. Crystallographic data of compound **2**.

Compound	2
formula	C ₃₆ H ₉₉ Ge ₉ Si ₁₂ P
F _w [g mol ⁻¹]	1552.86
space group	P $\bar{1}$
a [Å]	9.7899(5)
b [Å]	14.9782(5)
c [Å]	25.002(1)
α [°]	80.934(3)
β [°]	83.629(3)
γ [°]	84.714(3)
V [Å ³]	3587.5(3)
Z	2
T [K]	123
λ [Å]	MoK _α
ρ _{calcd} [g cm ⁻³]	1.440
μ [mm ⁻¹]	3.960
collected reflections	56768
independent reflections	14066
R _{int} /R _σ	0.0568/0.0383
parameters/restraints	618/40
R ₁ [I > 2 σ(I)/all data]	0.0396/0.0566
wR ₂ [I > 2 σ(I)/all data]	0.0937/0.1041
goodness of fit	1.043
max./min. diff. electron density [e Å ⁻³]	0.93/−0.74
CCDC	1831874

with the solvent peaks serving as internal reference.^[34] Abbreviations for signal multiplicities are: singlet (s), doublet (d), triplet (t), heptet (hept). ²⁹Si NMR spectra were obtained with the ²⁹Si-INEPT-RD method (RD: refocused with decoupling). In some of the ¹³C NMR spectra, the methyl groups of the Dipp substituents of the NHC ligand overlapped with the THF solvent signal and could therefore not be properly assigned. The carbene carbon signals as well as the methyl carbon signals of the NHC's iso-propyl groups could not be monitored in any of the ¹³C NMR spectra of compounds **3-MNHC^{Dipp}** to **11-MNHC^{Dipp}**. In the ²⁹Si-INEPT RD spectra of compounds **8-CuNHC^{Dipp}** and **9-CuNHC^{Dipp}**, the Si_{Ge9} signal could not be detected. All recorded NMR spectra are provided in the Supporting Information.

Electrospray ionization mass spectrometry (ESI-MS)

ESI-MS analyses were performed with a Bruker Daltonic HCT mass spectrometer (dry gas temperature: 300 °C; injection speed: 240 μL h⁻¹), and the data evaluation was carried out by using the Bruker Compass Data Analysis 4.0 SP 5 program (Bruker). Spectra were plotted by using OriginPro2016G (Origin Lab) and Excel 2016 (Microsoft). All obtained ESI-MS spectra are provided in the Supporting Information.

Elemental analyses (EA)

Elemental analyses were carried out at the microanalytical laboratory of the Chemistry Department of Technische Universität München. Analyses of C, H, N were performed with a combustion analyzer (elementar vario EL, Bruker).

Syntheses

tBu{(CH₂)₃CH=CH₂}PCl (1): 5-Bromopentene (5.0 g, 33.5 mmol, 1 equiv) was added dropwise to a suspension of magnesium shavings (4.0 g, 164.0 mmol, 4.9 equiv) in Et₂O (50 mL) under constant reflux, and two grains of iodine were added for activation. After

complete addition of the halide, the mixture was heated at reflux for a further 3.5 h. The concentration of the obtained Grignard solution was determined to be 0.6 mol L^{-1} by titration of menthol using 1,10-phenanthroline as indicator. Subsequently, the Grignard solution (30 mL, 18.1 mmol, 1 equiv) was dropwise added to a solution of $t\text{BuPCl}_2$ (3.60 g, 22.6 mmol, 1.25 equiv) in Et_2O (50 mL) at -78°C , before the cooling was removed and the reaction solution was allowed to warm to room temperature. Addition of hexane (30 mL) led to the formation of a colorless precipitate, and the resulting suspension was stirred at room temperature overnight. The mixture was filtered to remove all solids, and the solvent was removed in vacuo to yield the crude product. Purification was achieved by vacuum distillation (9×10^{-3} mbar, 41°C), yielding **1** as a colorless liquid (0.90 g, 23%). $^1\text{H NMR}$ (400 MHz, 298 K , CDCl_3): $\delta = 5.84\text{--}5.75$ (m, 1H, CH_{db}), $5.07\text{--}4.08$ (m, 2H, $\text{CH}_{2(\text{db})}$), $2.23\text{--}1.18$ (m, 2H, CH_2), $1.87\text{--}1.56$ (m, 4H, CH_2), 1.16 ppm (d, $^3J_{\text{HP}} = 13.0$ Hz, 9H, Me_{tBu}); $^{13}\text{C NMR}$ (101 MHz, 298 K , CDCl_3): $\delta = 137.99$ (s, CH_{db}), 115.47 (s, $\text{CH}_{2(\text{db})}$), 34.83 (m, CH_2), 32.54 (d, $^1J_{\text{CP}} = 28.6$ Hz, C_{tBu}), 29.57 (d, $^1J_{\text{CP}} = 35.2$ Hz, CH_2), 26.10 (d, $^2J_{\text{CP}} = 16.8$ Hz, Me_{tBu}), 25.46 (d, $^2J_{\text{CP}} = 16.8$ Hz, Me_{tBu}), 24.72 ppm (d, $^2J_{\text{CP}} = 16.0$ Hz, CH_2); $^{31}\text{P NMR}$ (162 MHz, 298 K , CDCl_3): $\delta = 128.41$ ppm (m, P_{Ge9}).

[Ge₉{Si(TMS)₃}₃PrBu{(CH₂)₃CH=CH₂}] (2): K[Ge₉{Si(TMS)₃}₃] (70 mg, 0.049 mmol, 1 equiv) was dissolved in toluene (1 mL), and a toluene solution (1 mL) of $t\text{Bu}[(\text{CH}_2)_3\text{CH}=\text{CH}_2]\text{PCl}$ (10.6 mg, 0.049 mmol, 1 equiv) was added, yielding a deep-red reaction mixture. After stirring at room temperature for 1 h, the solvent was removed under reduced pressure, and the remaining dark-brown solid was washed with acetonitrile (3×2 mL). Subsequently, the solid was dissolved in toluene (1 mL), filtered to remove insoluble materials, and stored in a freezer at -40°C , yielding the product as orange crystals (25.9 mg, 35%). $^1\text{H NMR}$ (400 MHz, 298 K , C_6D_6): $\delta = 5.94\text{--}5.84$ (m, 1H, CH_{db}), $5.20\text{--}5.07$ (m, 2H, $\text{CH}_{2(\text{db})}$), $2.28\text{--}2.19$ (m, 2H, CH_2), $2.19\text{--}2.10$ (m, 2H, CH_2), $1.95\text{--}1.82$ (m, 2H, CH_2), 1.34 (d, $^3J_{\text{HP}} = 11.4$ Hz, 9H, Me_{tBu}), 0.47 ppm (s, 81H, Me_{TMS}); $^{13}\text{C NMR}$ (101 MHz, 298 K , C_6D_6): $\delta = 138.38$ (s, CH_{db}), 115.53 (s, $\text{CH}_{2(\text{db})}$), 36.05 (d, $^1J_{\text{CP}} = 13.0$ Hz, CH_2), 31.46 (d, $^2J_{\text{CP}} = 13.9$ Hz, Me_{tBu}), 30.26 (d, $^3J_{\text{CP}} = 21.9$ Hz, CH_2), 28.78 (d, $^1J_{\text{CP}} = 30.0$ Hz, C_{tBu}), 27.93 (d, $^2J_{\text{CP}} = 30.1$ Hz, CH_2), 3.10 ppm (s, Me_{TMS}); $^{29}\text{Si-INEPT NMR}$ (79 MHz, 298 K , C_6D_6): $\delta = -8.31$ (s, Si_{TMS}), -102.52 ppm (s, Si_{Ge9}); $^{31}\text{P NMR}$ (162 MHz, 298 K , C_6D_6): $\delta = 19.46$ ppm (m, P_{Ge9}); elemental analysis calcd (%) for $\text{Ge}_9\text{Si}_{12}\text{P}_1\text{C}_{36}\text{H}_{99}$: C 27.83, H 6.42; found: C 27.84, H 6.43.

General procedure for the syntheses of [Ge₉{Si(TMS)₃}₂PRR']⁻ (**3a to 11a**)

$\text{K}_2[\text{Ge}_9\{\text{Si}(\text{TMS})_3\}_2]$ was dissolved in MeCN, and the respective chlorophosphine dissolved in MeCN was added. The resulting mixtures were stirred at room temperature for 1 h, before the solutions were filtered to remove all solids, and the solvents were removed in vacuo to yield the crude compounds **3a–11a** as brownish solids.

General procedure for the syntheses of [(Ge₉{Si(TMS)₃}₂)RR']⁻[(MNHCD^{Dipp}) (3-MNHCD^{Dipp} to 7-MNHCD^{Dipp}) and (NHC^{Dipp}M)[Ge₉{Si(TMS)₃}₂PRR'] (8-MNHCD^{Dipp} to 11-MNHCD^{Dipp}) (M = Cu, Ag)

$\text{K}_2[\text{Ge}_9\{\text{Si}(\text{TMS})_3\}_2]$ was dissolved in MeCN, and the respective chlorophosphine dissolved in MeCN was added. The resulting mixtures were stirred at room temperature for 1 h, before a solution of $\text{NHC}^{\text{Dipp}}\text{MCl}$ in MeCN was added dropwise, resulting in the formation of red to brown precipitates. The supernatant solutions (slightly orange) were filtered, and the solids were washed with acetoni-

trile. Subsequently, the solids were dissolved in toluene and filtered to remove insoluble materials, before the solvent was removed to yield the crude products as red to brown solids.

All experimental details can be found in the Supporting Information.

Acknowledgments

This work was financially supported by Deutsche Forschungsgemeinschaft (DFG) within the International Research Training Group 2022 (ATUMS), Bavarian Ministry of Economic Affairs, Regional Development and Energy "Solar Technologies go Hybrid", through the TUM International Graduate School of Science and Engineering (IGSSE) and Wacker Chemie AG. C.W. and F.S.G. thank Dr. Kerstin Mayer for support with ESI-MS measurements. Furthermore, C.W. and F.S.G. thank the TUM Graduate School for support.

Conflict of interest

The authors declare no conflict of interest.

Keywords: alkenyl · anchor group · mixed functionalization · phosphine · zwitterion

- [1] a) K. Abersfelder, A. J. White, H. S. Rzepa, D. Scheschke, *Science* **2010**, *327*, 564; b) S. Frischhut, T. F. Fässler, *Dalton Trans.* **2018**, *47*, 3223; c) T. Iwamoto, N. Akasaka, S. Ishida, *Nat. Commun.* **2014**, *5*, 5353; d) C. Schenk, A. Kracke, K. Fink, A. Kubas, W. Klopfer, M. Neumaier, H. Schnöckel, A. Schnepf, *J. Am. Chem. Soc.* **2011**, *133*, 2518; e) C. Schenk, A. Schnepf, *Chem. Commun.* **2008**, 4643; f) D. Scheschke, *Angew. Chem. Int. Ed.* **2005**, *44*, 2954; *Angew. Chem.* **2005**, *117*, 3014; g) A. Sekiguchi, Y. Ishida, Y. Kabe, M. Ichinohe, *J. Am. Chem. Soc.* **2002**, *124*, 8776; h) K. I. Leszczynska, V. Huch, C. Präsang, J. Schwabedissen, R. J. Berger, D. Scheschke, *Angew. Chem. Int. Ed.* **2005**, *58*, 5124; *Angew. Chem.* **2019**, *131*, 5178.
- [2] a) Y. Heider, D. Scheschke, *Dalton Trans.* **2018**, *47*, 7104; b) A. Schnepf, *New J. Chem.* **2010**, *34*, 2079.
- [3] L. J. Schiegerl, A. J. Karttunen, J. Tillmann, S. Geier, G. Raudaschl-Sieber, M. Waibel, T. F. Fässler, *Angew. Chem. Int. Ed.* **2018**, *57*, 12950; *Angew. Chem.* **2018**, *130*, 13132.
- [4] a) C. Lorenz, F. Hastreiter, J. Hioe, N. Lokesh, S. Gärtner, N. Korber, R. M. Gschwind, *Angew. Chem. Int. Ed.* **2018**, *57*, 12956; *Angew. Chem.* **2018**, *130*, 13138; b) T. Henneberger, W. Klein, T. F. Fässler, *Z. Anorg. Allg. Chem.* **2018**, *644*, 1018.
- [5] C. Lorenz, N. Korber, *Crystals* **2018**, *8*, 374.
- [6] T. Henneberger, W. Klein, J. V. Dums, T. F. Fässler, *Chem. Commun.* **2018**, *54*, 12381.
- [7] A. Schnepf, *Angew. Chem. Int. Ed.* **2003**, *42*, 2624; *Angew. Chem.* **2003**, *115*, 2728.
- [8] a) F. Li, S. C. Sevov, *Inorg. Chem.* **2012**, *51*, 2706; b) O. Kysliak, A. Schnepf, *Dalton Trans.* **2016**, *45*, 2404.
- [9] L. J. Schiegerl, A. J. Karttunen, W. Klein, T. F. Fässler, *Chem. Eur. J.* **2018**, *24*, 19171.
- [10] F. S. Geitner, W. Klein, T. F. Fässler, *Angew. Chem. Int. Ed.* **2018**, *57*, 14509; *Angew. Chem.* **2018**, *130*, 14717.
- [11] a) J. D. Corbett, *Chem. Rev.* **1985**, *85*, 383; b) T. F. Fässler, S. D. Hoffmann, *Angew. Chem. Int. Ed.* **2004**, *43*, 6242; *Angew. Chem.* **2004**, *116*, 6400; c) S. C. Sevov, J. M. Goicoechea, *Organometallics* **2006**, *25*, 5678; d) S. Scharfe, F. Kraus, S. Stegmaier, A. Schier, T. F. Fässler, *Angew. Chem. Int. Ed.* **2011**, *50*, 3630; *Angew. Chem.* **2011**, *123*, 3712.
- [12] a) M. W. Hull, S. C. Sevov, *Inorg. Chem.* **2007**, *46*, 10953; b) C. B. Benda, J.-Q. Wang, B. Wahl, T. F. Fässler, *Eur. J. Inorg. Chem.* **2011**, 4262.

- [13] F. Li, S. C. Sevov, *J. Am. Chem. Soc.* **2014**, *136*, 12056.
- [14] F. Li, A. Muñoz-Castro, S. C. Sevov, *Angew. Chem. Int. Ed.* **2012**, *51*, 8581; *Angew. Chem.* **2012**, *124*, 8709.
- [15] a) C. Schenk, A. Schnepf, *Angew. Chem. Int. Ed.* **2007**, *46*, 5314; *Angew. Chem.* **2007**, *119*, 5408; b) C. Schenk, F. Henke, G. Santiso-Quinones, I. Krossing, A. Schnepf, *Dalton Trans.* **2008**, 4436; c) F. Henke, C. Schenk, A. Schnepf, *Dalton Trans.* **2009**, 9141; d) C. Schenk, A. Schnepf, *Chem. Commun.* **2009**, 3208; e) F. Henke, C. Schenk, A. Schnepf, *Dalton Trans.* **2011**, *40*, 6704; f) F. Li, S. C. Sevov, *Inorg. Chem.* **2015**, *54*, 8121; g) F. S. Geitner, T. F. Fässler, *Eur. J. Inorg. Chem.* **2016**, 2688; h) O. Kysliak, C. Schrenk, A. Schnepf, *Chem. Eur. J.* **2016**, *22*, 18787; i) K. Mayer, L. J. Schiegerl, T. F. Fässler, *Chem. Eur. J.* **2016**, *22*, 18794; j) L. J. Schiegerl, F. S. Geitner, C. Fischer, W. Klein, T. F. Fässler, *Z. Anorg. Allg. Chem.* **2016**, *642*, 1419.
- [16] a) O. Kysliak, C. Schrenk, A. Schnepf, *Inorg. Chem.* **2015**, *54*, 7083; b) O. Kysliak, T. Kunz, A. Schnepf, *Eur. J. Inorg. Chem.* **2017**, 805.
- [17] a) L. G. Perla, S. C. Sevov, *J. Am. Chem. Soc.* **2016**, *138*, 9795; b) L. G. Perla, A. Muñoz-Castro, S. C. Sevov, *J. Am. Chem. Soc.* **2017**, *139*, 15176.
- [18] a) F. S. Geitner, J. V. Dums, T. F. Fässler, *J. Am. Chem. Soc.* **2017**, *139*, 11933; b) F. S. Geitner, C. Wallach, T. F. Fässler, *Chem. Eur. J.* **2018**, *24*, 4103.
- [19] K. Mayer, L. J. Schiegerl, T. Kratky, S. Günther, T. F. Fässler, *Chem. Commun.* **2017**, *53*, 11798.
- [20] a) F. Mercier, C. Hugel-Le Goff, F. Mathey, *Organometallics* **1988**, *7*, 955; b) S. Haber, P. Le Floch, F. Mathey, *J. Chem. Soc. Chem. Commun.* **1992**, 1799.
- [21] K. Izod, D. G. Rayner, S. M. El-Hamruni, R. W. Harrington, U. Baisch, *Angew. Chem. Int. Ed.* **2014**, *53*, 3636; *Angew. Chem.* **2014**, *126*, 3710.
- [22] C. A. Tolman, *Chem. Rev.* **1977**, *77*, 313.
- [23] S. Socol, J. Verkade, *Inorg. Chem.* **1984**, *23*, 3487.
- [24] a) H. Clavier, S. P. Nolan, *Chem. Commun.* **2010**, *46*, 841; b) B. P. Carrow, L. Chen, *Synlett* **2017**, *28*, 280.
- [25] S. T. Liddle, K. Izod, *Organometallics* **2004**, *23*, 5550.
- [26] A. J. Rucklidge, G. E. Morris, A. M. Z. Slawin, D. J. Cole-Hamilton, *Helv. Chim. Acta* **2006**, *89*, 1783.
- [27] O. J. Scherer, W. Gick, *Chem. Ber.* **1970**, *103*, 71.
- [28] P. C. Crofts, D. M. Parker, *J. Chem. Soc. C* **1970**, 2529.
- [29] B. Wrackmeyer, C. Köhler, W. Milius, J. M. Grevy, Z. García-Hernández, R. Contreras, *Heteroat. Chem.* **2002**, *13*, 667.
- [30] W. McFarlane, C. T. Regius, *Polyhedron* **1997**, *16*, 1855.
- [31] O. G. M. Fild, I. Hollenberg, *Z. Naturforsch. B* **1966**, *21*, 920.
- [32] a) L. Hintermann, *Beilstein J. Org. Chem.* **2007**, *3*, 22; b) O. Santoro, A. Collado, A. M. Z. Slawin, S. P. Nolan, C. S. J. Cazin, *Chem. Commun.* **2013**, *49*, 10483; c) P. De Frémont, N. M. Scott, E. D. Stevens, T. Ramnial, O. C. Lightbody, C. L. B. Macdonald, J. A. C. Clyburne, C. D. Abernethy, S. P. Nolan, *Organometallics* **2005**, *24*, 6301.
- [33] G. Sheldrick, *Acta Crystallogr. Sect. C* **2015**, *71*, 3.
- [34] G. R. Fulmer, A. J. M. Miller, N. H. Sherden, H. E. Gottlieb, A. Nudelman, B. M. Stoltz, J. E. Bercaw, K. I. Goldberg, *Organometallics* **2010**, *29*, 2176.

Manuscript received: April 10, 2019

Accepted manuscript online: June 23, 2019

Version of record online: August 2, 2019

CHEMISTRY

A **European** Journal

Supporting Information

Enhancing the Variability of [Ge₉] Cluster Chemistry through Phosphine Functionalization

Christoph Wallach^{+, [a]} Felix S. Geitner^{+, [a, b]} Wilhelm Klein,^[a] and Thomas F. Fässler^{*[a]}

chem_201901673_sm_miscellaneous_information.pdf

Supporting Information

Content

Experimental details	2
Crystallographic data	7
NMR spectra.....	9
ESI-MS spectra	69

Experimental details

[Ge₉{Si(TMS)₃}₂P^tBu{(CH₂)₃CH=CH₂}]⁻ (3a): K₂[Ge₉{Si(TMS)₃}₂] (100 mg, 0.082 mmol, 1 eq.) and ^tBu(CH₂)₃CH=CH₂PCl (20.5 mg, 0.107 mmol, 1.3 eq.) in MeCN (2 + 1 mL). The crude product was obtained as a brown solid (72 mg, 65 %). **¹H NMR** (400 MHz, thf-*d*₈, 298 K): δ [ppm] = 7.26 – 7.07 (m, 1H, CH_{db}), 5.91 – 5.68 (m, 2H, CH_{2(db)}), 2.26 – 2.11 (m, 2H, CH₂), 2.10 – 2.01 (m, 2H, CH₂), 1.71 – 1.63 (m, 2H, CH₂), 1.14 (d, ³J_{HP} = 11.4 Hz, 9H, Me_{tBu}), 0.26 (s, 54H, Me_{TMS}). **¹³C NMR** (101 MHz, thf-*d*₈, 298 K): δ [ppm] = 139.23 (s, CH_{db}), 115.28 (s, CH_{2(db)}), 36.67 (s, CH₂), 36.01 (s, CH₂), 31.07 (s, C_{tBu}), 29.47 (s, Me_{tBu}), 19.24 (d, ¹J_{CP}, CH₂), 3.20 (s, Me_{TMS}). **²⁹Si-INEPT NMR** (79 MHz, thf-*d*₈, 298 K): δ [ppm] = -11.32 (s, Si_{TMS}), -109.61 (s, Si_{Ge9}). **³¹P NMR** (400 MHz, thf-*d*₈, 298 K): δ [ppm] = 4.11 (m, P_{Ge9}). **ESI-MS:** (negative ion mode, 3500 V, 300 °C): *m/z* 1306.8 [Ge₉{Si(TMS)₃}₂P^tBu{(CH₂)₃CH=CH₂}]⁻.

[(Ge₉{Si(TMS)₃}₂)^tBu(CH₂)₃CH=CH₂P](AgNHC^{DiPP}) (3-AgNHC^{DiPP}): K₂[Ge₉{Si(TMS)₃}₂] (40.0 mg, 0.033 mmol, 1 eq.) and ^tBu(CH₂)₃CH=CH₂PCl (6.9 mg, 0.036 mmol, 1.1 eq.) in MeCN (2 + 1 mL). NHC^{DiPP}AgCl (21 mg, 0.039 mmol, 1.2 eq.) in MeCN (2 mL). The crude product was obtained as a pale brown solid (23 mg, 39 %). **¹H NMR** (400 MHz, thf-*d*₈, 298 K): δ [ppm] = 7.63 (s, 2H, CH_{Im}), 7.48 (s, 2H, CH_{Ph(p)}), 7.39 (s, 4H, CH_{Ph(m)}), 5.73 – 5.61 (m, 1H, CH_{db}), 4.98 – 4.85 (m, 2H, CH_{2db}), 2.83 – 2.67 (m, 4H, CH_{tPr}), 2.00 – 1.90 (m, 6H, CH₂), 1.45 (s, 12H, Me_{tPr}), 1.22 (s, 12H, Me_{tPr}), 0.93 (d, ³J_{HP} = 13.7 Hz, 9H, Me_{tBu}), 0.23 (s, 54H, Me_{TMS}). **¹³C NMR** (101 MHz, thf-*d*₈, 298 K): δ [ppm] = 146.26 (s, C_{Ph(o)}), 139.31 (s, CH_{db}), 135.97 (s, C_{PhN}), 131.61 (s, CH_{Ph(p)}), 126.38 (s, CH_{Ph(m)}), 125.29 (s, CH_{Im}), 115.10 (s, CH_{2db}), 36.21 (s, CH₂), 30.22 (s, CH_{tPr}), 30.11 (s, Me_{tBu}), 29.79 (s, CH₂), 29.54 (s, CH₂), 26.26 (s, C_{tBu}), 24.20 (s, CH_{3tPr}), 3.12 (s, Me_{TMS}). **²⁹Si-INEPT NMR** (79 MHz, thf-*d*₈, 298 K): δ [ppm] = -9.28 (s, Si_{TMS}), -105.59 (s, Si_{Ge9}). **³¹P NMR** (162 MHz, thf-*d*₈, 298 K): δ [ppm] = 11.32 (d, ¹J_{PAg} = 258.7 Hz, P_{Ge9}).

[(Ge₉{Si(TMS)₃}₂)^tBu(CH₂)₃CH=CH₂P](CuNHC^{DiPP}) (3-CuNHC^{DiPP}): K₂[Ge₉{Si(TMS)₃}₂] (100 mg, 0.082 mmol, 1 eq.) and ^tBu(CH₂)₃CH=CH₂PCl (20.5 mg, 0.107 mmol, 1.3 eq.) in MeCN (2 + 1 mL). NHC^{DiPP}CuCl (39.6 mg, 0.082 mmol, 1 eq.) in MeCN (2 mL). The crude product was obtained as a dark brown solid (75 mg, 52 %). **¹H NMR** (400 MHz, thf-*d*₈, 298 K): δ [ppm] = 7.56 (s, 2H, CH_{Im}), 7.47 (s, 2H, CH_{Ph(p)}), 7.39 (s, 4H, CH_{Ph(m)}), 5.74 – 5.57 (m, 1H, CH_{db}), 4.98 – 4.85 (m, 2H, CH_{2db}), 2.87 – 2.72 (m, 4H, CH_{tPr}), 2.01 – 1.87 (m, 6H, CH₂), 1.46 (s, 12H, Me_{tPr}), 1.21 (s, 12H, Me_{tPr}), 0.83 (d, ³J_{HP} = 12.1 Hz, 9H, Me_{tBu}), 0.25 (s, 54H, Me_{TMS}). **¹³C NMR** (101 MHz, thf-*d*₈, 298 K): δ [ppm] = 146.34 (s, C_{Ph(o)}), 139.09 (s, CH_{db}), 136.30 (s, C_{PhN}), 131.63 (s, CH_{Ph(p)}), 125.37 (s, CH_{Ph(m)}), 125.08 (s, CH_{Im}), 115.24 (s, CH_{2db}), 36.48 (s, CH₂), 30.18 (s, CH_{tPr}), 29.83 (s, Me_{tBu}), 29.67 (s, CH₂), 29.49 (s, CH₂), 26.19 (s, C_{tBu}), 3.14 (s, Me_{TMS}). **²⁹Si-INEPT NMR** (79 MHz, thf-*d*₈, 298 K): δ [ppm] = -11.02 (s, Si_{TMS}), -107.01 (s, Si_{Ge9}). **³¹P NMR** (162 MHz, thf-*d*₈, 298 K): δ [ppm] = 8.33 (m, P_{Ge9}).

[Ge₉{Si(TMS)₃}₂P^tPr^tBu]⁻ (4a): K₂[Ge₉{Si(TMS)₃}₂] (36.8 mg, 0.030 mmol, 1 eq.) and ^tPr^tBuPCl (7.4 mg, 0.033 mmol, 1.1 eq.) in MeCN (1 + 1 mL). The crude product was obtained as a brown solid (29 mg, 74 %). **¹H NMR** (400 MHz, 298 K, thf-*d*₈): δ [ppm] = 2.00 (hept, 1H, CH_{tPr}), 1.24 – 1.07 (m, 6H, Me_{tPr}), 1.20 (d, ³J_{HP} = 11.0 Hz, 9H, Me_{tBu}), 0.26 (s, 54H, Me_{TMS}). **¹³C NMR** (101 MHz, thf-*d*₈, 298 K): δ [ppm] = 32.40 (s, CH_{tPr}), 29.89 (s, Me_{tBu}), 27.40 (s, Me_{tPr}), 26.52 (d, ¹J_{CP} = 10.8 Hz, C_{tBu}), 3.18 (s, Me_{TMS}). **²⁹Si-INEPT NMR** (79 MHz, thf-*d*₈, 298 K): δ [ppm] = -11.53 (s, Si_{TMS}), -109.67 (s, Si_{Ge9}). **³¹P NMR** (162 MHz, 298 K, thf-*d*₈): δ [ppm] = 35.55 (m, P_{Ge9}). **ESI-MS** (negative ion mode, 3500 V, 300 °C): *m/z* 1280.8 [Ge₉{Si(TMS)₃}₂P^tPr^tBu]⁻.

[(Ge₉{Si(TMS)₃}₂)^tPr^tBuP](AgNHC^{DiPP}) (4-AgNHC^{DiPP}): K₂[Ge₉{Si(TMS)₃}₂] (40.0 mg, 0.033 mmol, 1 eq.) and ^tPr^tBuPCl (7.4 mg, 0.033 mmol, 1 eq.) in MeCN (1 + 1 mL). NHC^{DiPP}AgCl (20.8 mg, 0.039 mmol, 1.2 eq.) in MeCN (1 mL). The crude product was obtained as a bright brown solid (17 mg, 29 %). **¹H NMR** (400 MHz, thf-*d*₈, 298 K): δ [ppm] = 7.68 (s, 2H, CH_{Im}), 7.53 – 7.43 (m, 2H, CH_{Ph(p)}), 7.42 – 7.34 (m, 4H, CH_{Ph(m)}), 2.76 (s, 4H, CH_{tPr}), 2.44 – 2.28 (m, 1H, CH_{tPr}), 1.45 (s, 12H, Me_{tPr}), 1.19 (s, 12H, Me_{tPr}), 0.98 – 0.73 (m, 15H, Me_{tPr} and Me_{tBu}), 0.26 (s, 54H, Me_{TMS}). **¹³C NMR** (101 MHz, thf-*d*₈, 298 K): δ [ppm] = 146.56 (s, C_{Ph(m)}), 136.66 (s, C_{PhN}), 131.60 (s, CH_{Ph(p)}), 125.34 (s, CH_{Ph(o)}), 125.27 (s, CH_{Im}), 31.32 (s, Me_{tPr}), 31.24 (Me_{tBu}), 29.78 (s, CH_{tPr}), 3.10 (Me_{TMS}). **²⁹Si-INEPT NMR** (79 MHz, thf-*d*₈, 298 K): δ [ppm] = -9.25 (s, Si_{TMS}), -105.76 (s, Si_{Ge9}). **³¹P NMR** (162 MHz, thf-*d*₈, 298 K): δ [ppm] = 37.83 (d, ¹J_{PAg} = 384.9 Hz, P_{Ge9}).

[(Ge₉{Si(TMS)₃}₂)^tPr^tBuP](CuNHC^{DiPP}) (4-CuNHC^{DiPP}): K₂[Ge₉{Si(TMS)₃}₂] (36.8 mg, 0.030 mmol, 1 eq.) and ^tPr^tBuPCl (7.4 mg, 0.033 mmol, 1.1 eq.) in MeCN (1 + 1 mL). NHC^{DiPP}CuCl (14.6 mg, 0.030 mmol, 1 eq.) in MeCN (1 mL). The crude product was obtained as a bright brown solid (35.1 mg, 67 %). **¹H NMR** (400 MHz, thf-*d*₈, 298 K): δ [ppm] = 7.59 (s, 2H, CH_{Im}), 7.51 – 7.46 (m, 2H, CH_{Ph(p)}), 7.42 – 7.35 (m, 4H, CH_{Ph(m)}), 2.86 (hept, ³J_{HH} = 6.9 Hz, 2H, CH_{tPr}), 2.78 (hept, ³J_{HH} = 6.9 Hz, 2H, CH_{tPr}), 1.45 (dd, ³J_{HH} = 6.9 Hz, 12H, Me_{tPr}), 1.19 (dd, ³J_{HH} = 6.9 Hz, 12H, Me_{tPr}), 0.91 (dd, ³J_{HH} = 6.8 Hz, 6H, Me_{tPr}), 0.79 (d, ³J_{HP} = 6.8 Hz, 9H, Me_{tBu}), 0.27 (s, 54H, Me_{TMS}). **¹³C NMR** (101

MHz, thf- d_6 , 298 K): δ [ppm] = 146.43 (s, $C_{Ph(m)}$), 136.66 (s, C_{PhN}), 131.58 (s, $CH_{Ph(p)}$), 125.48 (s, $CH_{Ph(o)}$), 125.36 (s, CH_{Im}), 31.47 (s, Me_{Pr}), 31.40 (Me_{tBu}), 29.81 (s, CH_{Pr}), 3.12 (Me_{TMS}). **^{29}Si -INEPT NMR** (79 MHz, thf- d_6 , 298 K): δ [ppm] = -9.14 (s, Si_{TMS}), -105.28 (s, Si_{Ge9}). **^{31}P NMR** (162 MHz, thf- d_6 , 298 K): δ [ppm] = 32.97 (m, P_{Ge9}).

[$Ge_9\{Si(TMS)_3\}_2P^tBu(NEt_2)^-$ (5a): $K_2[Ge_9\{Si(TMS)_3\}_2]$ (44.2 mg, 0.036 mmol, 1 eq.) and $tBu(NEt_2)PCl$ (6.8 mg, 0.047 mmol, 1.3 eq.) in MeCN (1 + 1 mL). The crude product was obtained as a brown solid (24 mg, 50 %). **1H NMR** (400 MHz, thf- d_6 , 298 K): δ [ppm] = 3.05 – 2.94 (m, 2H, $CH_2(NEt_2)$), 2.93 – 2.82 (m, 2H, $CH_2(NEt_2)$), 1.14 (d, $^3J_{HP}$ = 13.0 Hz, 9H, Me_{tBu}), 0.97 (t, $^3J_{HH}$ = 7.1 Hz, 6H, $Me_{(NEt_2)}$), 0.25 (s, 54H, Me_{TMS}). **^{13}C NMR** (101 MHz, thf- d_6 , 298 K): δ [ppm] = 50.58 (s, $CH_2(NEt_2)$), 34.97 (d, $^1J_{CP}$ = 30.9 Hz, C_{tBu}), 30.05 (s, Me_{tBu}), 15.39 (s, $Me_{(NEt_2)}$), 3.22 (s, Me_{TMS}). **^{29}Si -INEPT NMR** (79 MHz, thf- d_6 , 298 K): δ [ppm] = -11.38 (s, Si_{TMS}), -109.96 (s, Si_{Ge9}). **^{31}P NMR** (162 MHz, thf- d_6 , 298 K): δ [ppm] = 110.04 (m, P_{Ge9}). **ESI-MS** (negative ion mode, 4000 V, 300 °C): m/z 1309.7 [$Ge_9\{Si(TMS)_3\}_2P^tBu(NEt_2)^-$].

[($Ge_9\{Si(TMS)_3\}_2$) $tBu(NEt_2)P(AgNHC^{Dipp})$ (5-AgNHC^{Dipp}): $K_2[Ge_9\{Si(TMS)_3\}_2]$ (40.0 mg, 0.033 mmol, 1 eq.) and $tBu(NEt_2)PCl$ (6.4 mg, 0.033 mmol, 1 eq.) in MeCN (1 + 1 mL). $NHC^{Dipp}AgCl$ (20.8 mg, 0.039 mmol, 1.2 eq.) in MeCN (1 mL). The crude product was obtained as a red solid (15 mg, 26 %). **1H NMR** (400 MHz, thf- d_6 , 298 K): δ [ppm] = 7.60 (s, 2H, CH_{Im}), 7.52 – 7.45 (m, 2H, $CH_{Ph(p)}$), 7.40 – 7.35 (m, 4H, $CH_{Ph(m)}$), 2.89 (hept, $^3J_{HH}$ = 6.8 Hz, 2H, $CH_2(NEt_2)$), 2.85 – 2.72 (m, 6H, CH_{Pr} and $CH_2(NEt_2)$), 1.49 (dd, $^3J_{HH}$ = 6.8 Hz, 12H, Me_{Pr}), 1.22 (dd, $^3J_{HH}$ = 6.8 Hz, 12H, Me_{Pr}), 0.98 (d, 9H, $^3J_{HP}$ = 14.8 Hz, Me_{tBu}), 0.91 (t, 6H, $^3J_{HH}$ = 6.8 Hz, $Me_{(NEt_2)}$), 0.21 (s, 54H, CH_3 TMS). **^{13}C NMR** (101 MHz, thf- d_6 , 298 K): δ [ppm] = 146.26 (s, $C_{Ph(o)}$), 136.57 (s, $CH_{Ph(p)}$), 131.38 (s, C_{PhN}), 125.24 (s, $CH_{Ph(m)}$), 124.97 (s, CH_{Im}), 49.66 (s, $CH_2(NEt_2)$), 29.78 (s, CH_{Pr}), 29.54 (s, Me_{tBu}), 14.68 (s, $Me_{(NEt_2)}$), 3.16 (s, Me_{TMS}). **^{29}Si -INEPT NMR** (79 MHz, thf- d_6 , 298 K): δ [ppm] = -9.36 (s, Si_{TMS}), -105.78 (s, Si_{Ge9}). **^{31}P NMR** (162 MHz, thf- d_6 , 298 K): δ [ppm] = 111.15 (d, $^1J_{PAg}$ = 207.8 Hz, P_{Ge9}). **EA:** anal. calcd. for $Ge_9Si_8N_3P_1AgC_{53}H_{109}$: C, 35.25; H, 6.08; N, 2.33; found: C, 35.29; H, 6.09; N, 2.27.

[($Ge_9\{Si(TMS)_3\}_2$) $tBu(NEt_2)P(CuNHC^{Dipp})$ (5-CuNHC^{Dipp}): $K_2[Ge_9\{Si(TMS)_3\}_2]$ (44.2 mg, 0.036 mmol, 1 eq.) and $tBu(NEt_2)PCl$ (6.8 mg, 0.047 mmol, 1.3 eq.) in MeCN (1 + 1 mL). $NHC^{Dipp}CuCl$ (17.5 mg, 0.036 mmol, 1 eq.) in MeCN (1 mL). The crude product was obtained as a red solid (23.1 mg, 36 %). **1H NMR** (400 MHz, thf- d_6 , 298 K): δ [ppm] = 7.51 (s, 2H, CH_{Im}), 7.48 – 7.44 (m, 2H, $CH_{Ph(p)}$), 7.40 – 7.50 (m, 4H, $CH_{Ph(m)}$), 2.89 (hept, $^3J_{HH}$ = 6.8 Hz, 4H, CH_{Pr}), 2.82 – 2.72 (m, 4H, $CH_2(NEt_2)$), 1.50 (dd, $^3J_{HH}$ = 6.8 Hz, 12H, Me_{Pr}), 1.19 (dd, $^3J_{HH}$ = 6.8 Hz, 12H, Me_{Pr}), 0.91 (s, 6H, $Me_{(NEt_2)}$), 0.89 – 0.84 (m, 9H, Me_{tBu}), 0.23 (s, 54H, CH_3 TMS). **^{13}C NMR** (101 MHz, thf- d_6 , 298 K): δ [ppm] = 146.33 (s, $C_{Ph(o)}$), 136.56 (s, $CH_{Ph(p)}$), 131.38 (s, C_{PhN}), 125.34 (s, $CH_{Ph(m)}$), 125.01 (s, CH_{Im}), 49.05 (s, $CH_2(NEt_2)$), 36.98 (s, C_{tBu}), 29.80 (s, CH_{Pr}), 29.47 (s, Me_{tBu}), 14.60 (s, $Me_{(NEt_2)}$), 3.19 (s, Me_{TMS}). **^{29}Si -INEPT NMR** (79 MHz, thf- d_6 , 298 K): δ [ppm] = -11.13 (s, Si_{TMS}), -106.74 (s, Si_{Ge9}). **^{31}P NMR** (162 MHz, thf- d_6 , 298 K): δ [ppm] = 108.78 (m, P_{Ge9}). **EA:** anal. calcd. for $Ge_9Si_8N_3P_1CuC_{53}H_{109}$: C, 36.14; H, 6.24; N, 2.39; found: C, 36.26; H, 6.32; N, 2.43.

[$Ge_9\{Si(TMS)_3\}_2P(1,1\text{-dimethylpropyl})_2^-$ (6a): $K_2[Ge_9\{Si(TMS)_3\}_2]$ (61.3 mg, 0.050 mmol, 1 eq.) and (1,1-dimethylpropyl) $_2PCl$ (12.0 mg, 0.050 mmol, 1 eq.) in MeCN (1 + 1 mL). The crude product was obtained as a brown solid (32 mg, 47 %). **1H NMR** (400 MHz, thf- d_6 , 298 K): δ [ppm] = 1.91 – 1.83 (m, 2H, CH_{Amyl}), 1.59 – 1.45 (m, 4H, $CH_2(Amyl)$), 1.26 (d, $^3J_{HP}$ = 4.5 Hz, 6H, $Me_{Amyl\text{-sidechain}}$), 1.23 (d, $^3J_{HP}$ = 4.5 Hz, 6H, $Me_{Amyl\text{-sidechain}}$), 0.83 (t, $^3J_{HH}$ = 7.4 Hz, 6H, Me_{Amyl}), 0.25 (s, 54H, Me_{TMS}). **^{13}C NMR** (101 MHz, thf- d_6 , 298 K): δ [ppm] = 38.17 (s, $CH_2(Amyl)$), 36.12 (d, $^1J_{CP}$ = 38.9 Hz, C_{Amyl}), 31.00 (s, Me_{Amyl}), 29.93 (s, Me_{Amyl}), 9.60 (s, $Me_{Amyl\text{-sidechain}}$), 3.19 (Me_{TMS}). **^{29}Si -INEPT NMR** (79 MHz, thf- d_6 , 298 K): δ [ppm] = -9.50 (s, Si_{TMS}), -108.11 (s, Si_{Ge9}). **^{31}P NMR** (162 MHz, thf- d_6 , 298 K): δ [ppm] = 52.93 (m, P_{Ge9}). **ESI-MS:** (negative ion mode, 3000 V, 300 °C): m/z 1322.8 [$Ge_9\{Si(TMS)_3\}_2P(1,1\text{-dimethylpropyl})_2^-$].

[($Ge_9\{Si(TMS)_3\}_2$)(1,1-dimethylpropyl) $_2P]Ag(NHC^{Dipp})$ (6-AgNHC^{Dipp}): $K_2[Ge_9\{Si(TMS)_3\}_2]$ (40.0 mg, 0.033 mmol, 1 eq.) and (1,1-dimethylpropyl) $_2PCl$ (8.3 mg, 0.033 mmol, 1 eq.) in MeCN (1 + 1 mL). $NHC^{Dipp}AgCl$ (20.8 mg, 0.039 mmol, 1.2 eq.) in MeCN (2 mL). The crude product was obtained as a brown solid (8 mg, 13 %). **1H -NMR** (400 MHz, thf- d_6 , 298 K): δ [ppm] = 7.73 – 7.68 (s, 2H, CH_{Im}), 7.52 – 7.47 (m, 2H, $CH_{Ph(p)}$), 7.41 – 7.36 (m, 4H, $CH_{Ph(m)}$), 2.79 (hept, $^3J_{HH}$ = 6.8 Hz, 4H, CH_{Pr}), 1.48 (d, $^3J_{HH}$ = 6.8 Hz, 12H, Me_{Pr}), 1.49 – 1.36 (m, 10H, $CH_2(Amyl)/Me_{Amyl}$), 1.23 (d, $^3J_{HH}$ = 6.8 Hz, 12H, Me_{Pr}), 0.92 (d, $^3J_{HP}$ = 14.6 Hz, 12H, $Me_{Amyl\text{-sidechain}}$), 0.27 (s, 54H, Me_{TMS}). **^{13}C -NMR** (101 MHz, thf- d_6 , 298 K): δ [ppm] = 146.52 (s, $C_{Ph(o)}$), 136.79 (s, C_{PhN}), 131.65 (s, $CH_{Ph(p)}$), 125.53 (s, CH_{Im}), 125.29 (s, $CH_{Ph(m)}$), 38.03 (s, C_{Amyl}), 36.83 (s, $CH_2(Amyl)$), 29.81 (s, CH_{Pr}), 28.31 ($Me_{Amyl\text{-sidechain}}$), 8.62 (s, Me_{Amyl}), 3.10 (Me_{TMS}). **^{29}Si -INEPT NMR** (79 MHz, thf- d_6 , 298 K): δ [ppm] = -9.24 (s, Si_{TMS}), -106.06 (s, Si_{Ge9}). **^{31}P -NMR** (162 MHz, thf- d_6 , 298 K): δ [ppm] = 62.81 (d, $^1J_{PAg}$ = 405.5 Hz, P_{Ge9}).

[($Ge_9\{Si(TMS)_3\}_2$)(1,1-dimethylpropyl) $_2P]Cu(NHC^{Dipp})$ (6-CuNHC^{Dipp}): $K_2[Ge_9\{Si(TMS)_3\}_2]$ (61.3 mg, 0.050 mmol, 1 eq.) and (1,1-dimethylpropyl) $_2PCl$ (12.0 mg, 0.050 mmol, 1 eq.) in MeCN (1 + 1 mL). $NHC^{Dipp}CuCl$ (24.3 mg, 0.050 mmol, 1 eq.) in MeCN (1 mL). The crude product was obtained as a brown solid (27.3 mg, 32 %). **1H -NMR** (400 MHz, thf- d_6 , 298 K): δ [ppm] = 7.61 (s, 2H, CH_{Im}), 7.51 – 7.47 (m, 2H, $CH_{Ph(p)}$), 7.40 – 7.38 (m, 4H,

CH_{Ph(m)}), 2.89 (hept, ³J_{HH} = 6.8 Hz, 4H, CH_{Pr}), 1.49 (d, ³J_{HH} = 6.8 Hz, 12H, Me_{Pr}), 1.36 (m, 10H, CH_{2(Amyl)/Me_{Amyl}}), 1.19 (d, ³J_{HH} = 6.8 Hz, 12H, Me_{Pr}), 0.90 (d, ³J_{HP} = 14.5 Hz, 12H, Me_{Amyl-sidechain}), 0.27 (s, 54H, Me_{TMS}). **¹³C-NMR** (101 MHz, thf-*d*₈, 298 K): δ [ppm] = 146.34 (s, C_{Ph(o)}), 136.77 (s, C_{PhN}), 131.56 (s, CH_{Ph(ρ)}), 125.62 (s, CH_{Im}), 125.40 (s, CH_{Ph(m)}), 37.93 (s, C_{Amyl}), 36.83 (s, CH_{2(Amyl)}), 29.86 (s, CH_{Pr}), 28.56 (Me_{Amyl-sidechain}), 8.60 (Me_{Amyl}), 3.12 (Me_{TMS}). **²⁹Si-INEPT** (79 MHz, thf-*d*₈, 298 K): δ [ppm] = -11.00 (s, Si_{TMS}), -107.54 (s, Si_{Ge9}). **³¹P-NMR** (162 MHz, thf-*d*₈, 298 K): δ [ppm] = 60.18 (m, P_{Ge9}).

[Ge₉{Si(TMS)₃}₂P(1-adamantyl)₂]⁻ (7a): K₂[Ge₉{Si(TMS)₃}₂] (61.3 mg, 0.050 mmol, 1 eq.) and (1-adamantyl)₂PCl (16.9 mg, 0.050 mmol, 1 eq.) in MeCN (1 + 1 mL). The crude product was obtained as a brown solid (58 mg, 78 %) **¹H NMR** (400 MHz, thf-*d*₈, 298 K): δ [ppm] = 2.17 – 1.88 (m, 20H, CH/CH_{2(adamantyl)}), 1.69 (s, 4H, CH/CH_{2(adamantyl)}), 1.61 – 1.54 (m, 6H, CH/CH_{2(adamantyl)}), 0.26 (s, 54H, Me_{TMS}). **¹³C NMR** (101 MHz, thf-*d*₈, 298 K): δ [ppm] = 45.05, 37.97, 37.76, 37.62, 37.57, 37.39 (s, CH_{2/CH_{adamantyl}}), 3.16 (s, Me_{TMS}). **³¹P NMR** (162 MHz, thf-*d*₈, 298 K): δ [ppm] = 57.32 (m, P_{Ge9}). **²⁹Si-INEPT NMR** (79 MHz, thf-*d*₈, 298 K): δ [ppm] = -11.53 (s, Si_{TMS}), -110.03 (s, Si_{Ge9}). **ESI-MS:** (negative ion mode, 4000 V, 300 °C): *m/z* 1450.8 [Ge₉{Si(TMS)₃}₂P(1-adamantyl)₂]⁻.

[(Ge₉{Si(TMS)₃}₂(1-adamantyl)₂P]Ag(NHC^{Dipp}) (7-AgNHC^{Dipp}): K₂[Ge₉{Si(TMS)₃}₂] (40.0 mg, 0.033 mmol, 1 eq.) and (1-adamantyl)₂PCl (11.0 mg, 0.033 mmol, 1 eq.) in MeCN (1 + 1 mL). NHC^{Dipp}AgCl (20.8 mg, 0.039 mmol, 1.2 eq.) in MeCN (2 mL). The crude product was obtained as a bright brown solid (15 mg, 23 %). **¹H NMR** (400 MHz, thf-*d*₈, 298 K): δ [ppm] = 7.69 (s, 2H, CH_{Im}), 7.54 – 7.45 (m, 2H, CH_{Ph(ρ)}), 7.43 – 7.35 (m, 4H, CH_{Ph(m)}), 2.82 (s, 4H, CH_{Pr}), 2.07 – 1.40 (m, 30H, CH/CH_{2(adamantyl)}), 1.51 (s, 12H, Me_{Pr}), 1.22 (s, 12H, Me_{Pr}), 0.28 (s, 54H, Me_{TMS}). **¹³C NMR** (101 MHz, thf-*d*₈, 298 K): δ [ppm] = 146.55 (s, C_{Ph(o)}), 136.93 (s, C_{PhN}), 131.63 (s, CH_{Ph(ρ)}), 125.75 (s, CH_{Im}), 125.36 (s, CH_{Ph(m)}), 44.30, 38.60, 37.14, 29.84 (C/CH/CH_{2(adamantyl)}), 30.04 (CH_{Pr}), 29.55 (CH_{2(adamantyl)}), 3.09 (Me_{TMS}). **²⁹Si-INEPT NMR** (79 MHz, thf-*d*₈, 298 K): δ [ppm] = -9.22 (s, Si_{TMS}), -106.32 (s, Si_{Ge9}). **³¹P NMR** (162 MHz, thf-*d*₈, 298 K): δ [ppm] = 51.73 (d, ¹J_{P-107Ag} = 422.5 Hz, P_{Ge9}, ¹J_{P-109Ag} = 486.2 Hz, P_{Ge9}).

[(Ge₉{Si(TMS)₃}₂(1-adamantyl)₂P]Cu(NHC^{Dipp}) (7-CuNHC^{Dipp}): K₂[Ge₉{Si(TMS)₃}₂] (61.3 mg, 0.050 mmol, 1 eq.) and (1-adamantyl)₂PCl (16.9 mg, 0.050 mmol, 1 eq.) in MeCN (1 + 1 mL). NHC^{Dipp}CuCl (24.3 mg, 0.050 mmol, 1 eq.) in MeCN (1 mL). The crude product was obtained as a bright brown solid (62 mg, 66 %). **¹H NMR** (400 MHz, thf-*d*₈, 298 K): δ [ppm] = 7.59 (s, 2H, CH_{Im}), 7.52 – 7.48 (m, 2H, CH_{Ph(ρ)}), 7.43 – 7.39 (m, 4H, CH_{Ph(m)}), 2.91 (hept, ³J_{HH} = 6.8 Hz, 4H, CH_{Pr}), 2.02 – 1.44 (m, 30H, CH/CH_{2(adamantyl)}), 1.51 (d, ³J_{HH} = 6.8 Hz, 12H, Me_{Pr}), 1.20 (d, ³J_{HH} = 6.8 Hz, 12H, Me_{Pr}), 0.28 (s, 54H, Me_{TMS}). **¹³C NMR** (101 MHz, thf-*d*₈, 298 K): δ [ppm] = 146.43 (s, C_{Ph(o)}), 137.04 (s, C_{PhN}), 131.68 (s, CH_{Ph(ρ)}), 125.95 (s, CH_{Im}), 125.52 (s, CH_{Ph(m)}), 44.49, 38.79, 37.68, 37.15 (C/CH/CH_{2(adamantyl)}), 30.02 (CH_{Pr}), 29.93 (CH_{2(adamantyl)}), 3.39 (Me_{TMS}). **²⁹Si-INEPT NMR** (79 MHz, thf-*d*₈, 298 K): δ [ppm] = -10.99 (s, Si_{TMS}), -107.74 (s, Si_{Ge9}). **³¹P NMR** (162 MHz, thf-*d*₈, 298 K): δ [ppm] = 48.76 (m, P_{Ge9}).

[Ge₉{Si(TMS)₃}₂P^{Pr}(N^{Pr}Pr₂)]⁻ (8a): K₂[Ge₉{Si(TMS)₃}₂] (73.6 mg, 0.060 mmol, 1 eq.) and ⁱPr(N^{Pr}Pr₂)PCl (13.6 mg, 0.066 mmol, 1.1 eq.) in MeCN (1.5 + 1 mL). The crude product was obtained as a brown solid (54 mg, 60 %). **¹H NMR** (400 MHz, thf-*d*₈, 298 K): δ [ppm] = 3.56 – 3.36 (m, 2H, CH_{NPr}), 2.09 – 2.01 (m, 1H, CH_{PPr}), 1.18 (d, ³J_{HH} = 6.8 Hz, 6H, Me_{NPr}), 1.12 (d, ³J_{HH} = 6.9 Hz, 3H, Me_{PPr}), 1.06 (d, ³J_{HH} = 6.9 Hz, 3H, Me_{PPr}), 1.02 (d, ³J_{HH} = 6.8 Hz, 6H, Me_{NPr}), 0.25 (s, 54H, Me_{TMS}). **¹³C NMR** (101 MHz, thf-*d*₈, 298 K): δ [ppm] = 32.24 (d, ¹J_{CP} = 24.1 CH_{Pr}), 22.76 (d, ²J_{CP} = 14.7 Hz, Me_{Pr}), 21.87 (d, ³J_{CP} = 28.9 Hz, Me_{NPr2}), 3.22 (s, Me_{TMS}). **²⁹Si-INEPT** (79 MHz, thf-*d*₈, 298 K): δ [ppm] = -9.57 (s, Si_{TMS}), -108.08 (s, Si_{Ge9}). **³¹P NMR** (162 MHz, thf-*d*₈, 298 K): δ [ppm] = 69.83 (m, P_{Ge9}). **ESI-MS:** (negative ion mode, 3500 V, 300 °C): *m/z* 1323.8. [Ge₉{Si(TMS)₃}₂P^{Pr}(N^{Pr}Pr₂)]⁻.

(NHC^{Dipp}Ag)[Ge₉{Si(TMS)₃}₂P^{Pr}(N^{Pr}Pr₂)] (8-AgNHC^{Dipp}): K₂[Ge₉{Si(TMS)₃}₂] (40.0 mg, 0.033 mmol, 1 eq.) and ⁱPr(N^{Pr}Pr₂)PCl (6.8 mg, 0.033 mmol, 1 eq.) in MeCN (1 + 1 mL). NHC^{Dipp}AgCl (20.8 mg, 0.039 mmol, 1.2 eq.) in MeCN (2 mL). The crude product was obtained as an orange solid (14 mg, 53 %). **¹H NMR** (400 MHz, thf-*d*₈, 298 K): δ [ppm] = 7.54 – 7.51 (m, 2H, CH_{Ph(ρ)}), 7.50 – 7.44 (m, 2H, CH_{Im}), 7.40 – 7.33 (m, 4H, CH_{Ph(m)}), 3.49 – 3.38 (m, 2H, CH_{NPr2}), 2.89 – 2.77 (m, 4H, CH_{NHC(Pr)}), 2.25 – 2.16 (m, 1H, CH_{PPr}), 1.55 – 1.57 (m, 12H, Me_{NHC(Pr)}), 1.23 (d, ³J_{HH} = 6.8 Hz, 12H, Me_{NHC(Pr)}), 1.20 – 1.10 (m, 18H, Me_{NPr2} and Me_{PPr}), 0.17 (s, 54H, Me_{TMS}). **¹³C NMR** (101 MHz, thf-*d*₈, 298 K): δ [ppm] = 146.48 (s, C_{Ph(o)}), 136.45 (s, CH_{Ph(ρ)}), 131.23 (s, C_{PhN}), 125.13 (s, C_{Ph(m)}), 124.57 (s, CH_{Im}), 31.72 (s, CH_{Pr/NPr}), 29.77 (s, CH_{NHC(Pr)}), 22.56 (s, Me_{PPr}), 21.20 (s, Me_{NPr}), 3.18 (Me_{TMS}). **²⁹Si-INEPT NMR** (79 MHz, thf-*d*₈, 298 K): δ [ppm] = -9.49 (s, Si_{TMS}), -105.61 (s, Si_{Ge9}). **³¹P NMR** (162 MHz, thf-*d*₈, 298 K): δ [ppm] = 77.38 (s, P_{Ge9}).

(NHC^{Dipp}Cu)[Ge₉{Si(TMS)₃}₂P^{Pr}(N^{Pr}Pr₂)] (8-CuNHC^{Dipp}): K₂[Ge₉{Si(TMS)₃}₂] (73.6 mg, 0.060 mmol, 1 eq.) and ⁱPr(N^{Pr}Pr₂)PCl (13.6 mg, 0.066 mmol, 1.1 eq.) in MeCN (1.5 + 1 mL). NHC^{Dipp}CuCl (29.2 mg, 0.060 mmol, 1 eq.) in MeCN (1.5 mL). The crude product was obtained as an orange solid (57.0 mg, 53 %). **¹H NMR** (400 MHz, thf-*d*₈,

298 K): δ [ppm] = 7.48 – 7.44 (m, 2H, CH_{Ph(p)}), 7.39 (s, 2H, CH_{Im}), 7.38 – 7.34 (m, 4H, CH_{Ph(m)}), 3.52 – 3.38 (m, 2H, CH_{NiPr₂}), 2.95 – 2.85 (m, 4H, CH_{NHC(iPr)}), 2.28 – 2.17 (m, 1H, CH_{PiPr}), 1.54 (dd, ³J_{HH} = 6.8 Hz, 12H, Me_{NHC(iPr)}), 1.22 – 1.16 (m, 24H, Me_{NHC(iPr)/NiPr₂}), 1.14 (d, 6H, Me_{PiPr}), 0.19 (s, 54H, Me_{TMS}). ¹³C NMR (101 MHz, thf-*d*₈, 298 K): δ [ppm] = 146.29 (s, C_{Ph(o)}), 136.41 (s, CH_{Ph(p)}), 131.21 (s, C_{PhN}), 125.23 (s, C_{Ph(m)}), 124.16 (s, CH_{Im}), 29.81 (s, CH_{NHC(iPr)}), 22.60 (s, Me_{PiPr}), 3.25 (Me_{TMS}). ²⁹Si-INEPT NMR (79 MHz, thf-*d*₈, 298 K): δ [ppm] = -9.49 (s, Si_{TMS}). ³¹P NMR (162 MHz, thf-*d*₈, 298 K): δ [ppm] = 76.49 (m, P_{Ge9}).

[Ge₉{Si(TMS)₃}₂PⁱBu(NⁱPr₂)]⁻ (9a): K₂[Ge₉{Si(TMS)₃}₂] (44.2 mg, 0.036 mmol, 1 eq.) and ⁱBu(NⁱPr₂)PCI (8.8 mg, 0.040 mmol, 1.1 eq.) in MeCN (1 + 1 mL). The crude product was obtained as a brown solid (39 mg, 78 %). ¹H NMR (400 MHz, thf-*d*₈, 298 K): δ [ppm] = 3.09 (brs, 1H, CH_{PiPr}), 1.18 – 1.02 (m, 12H, Me_{PiPr}), 1.12 (d, ³J_{HP} = 13.3 Hz, 9H, Me_{iBu}), 0.25 (s, 54H, Me_{TMS}). ¹³C NMR (101 MHz, thf-*d*₈, 298 K): δ [ppm] = 35.15 (d, ¹J_{CP} = 32.4 Hz, C_{iBu}), 30.86 (d, ²J_{CP} = 17.4 Hz, Me_{iBu}), 30.68 (s, Me_{NiPr₂}), 3.22 (s, Me_{TMS}). ²⁹Si-INEPT NMR (79 MHz, thf-*d*₈, 298 K): δ [ppm] = -9.59 (s, Si_{TMS}), -108.11 (s, Ge₉). ³¹P NMR (162 MHz, thf-*d*₈, 298 K): δ [ppm] = 83.12 (m, P_{Ge9}). **ESI-MS:** (negative ion mode, 3000 V, 300 °C): *m/z* 1337.8 [Ge₉{Si(TMS)₃}₂PⁱBu(NⁱPr₂)]⁻.

NHC^{Dipp}Ag[Ge₉{Si(TMS)₃}₂PⁱBu(NⁱPr₂)] (9-AgNHC^{Dipp}): K₂[Ge₉{Si(TMS)₃}₂] (40.0 mg, 0.033 mmol, 1 eq.) and ⁱBu(NⁱPr₂)PCI (7.3 mg, 0.033 mmol, 1.1 eq.) in MeCN (1 + 1 mL). NHC^{Dipp}AgCl (20.8 mg, 0.039 mmol, 1.2 eq.) in MeCN (2 mL). The crude product was obtained as a red solid (10 mg, 16 %). ¹H NMR (400 MHz, thf-*d*₈, 298 K): δ [ppm] = 7.54 – 7.50 (m, 2H, CH_{Ph(p)}), 7.49 – 7.43 (m, 2H, CH_{Im}), 7.40 – 7.34 (m, 4H, CH_{Ph(m)}), 2.83 (hept, ³J_{HH} = 6.8 Hz, 4H, CH_{NHC(iPr)}), 1.54 (d, ³J_{HH} = 6.8 Hz, 6H, Me_{NHC(iPr)}), 1.49 (d, ³J_{HH} = 6.8 Hz, 6H, Me_{NHC(iPr)}), 1.21 (d, ³J_{HH} = 6.8 Hz, 12H, Me_{NHC(iPr)}), 1.18 – 1.09 (m, 21H, Me_{NiPr₂/iBu}), 0.17 (s, 54H, Me_{TMS}). ¹³C NMR (101 MHz, thf-*d*₈, 298 K): δ [ppm] = 146.37 (s, C_{Ph(o)}), 136.46 (s, CH_{Ph(p)}), 131.26 (s, C_{PhN}), 125.18 (s, CH_{Ph(m)}), 124.70 (s, CH_{Im}), 36.06 (s, CH_{NiPr₂}), 30.78 (s CH_{NHC(iPr)}), 29.75 (Me_{iBu}), 3.21 (Me_{TMS}). ²⁹Si-INEPT NMR (79 MHz, thf-*d*₈, 298 K): δ [ppm] = -9.51 (s, Si_{TMS}), -105.45 (s, Si_{Ge9}). ³¹P NMR (162 MHz, thf-*d*₈, 298 K): δ [ppm] = 89.59 (s, P_{Ge9}).

NHC^{Dipp}Cu[Ge₉{Si(TMS)₃}₂PⁱBu(NⁱPr₂)] (9-CuNHC^{Dipp}): K₂[Ge₉{Si(TMS)₃}₂] (44.2 mg, 0.036 mmol, 1 eq.) and ⁱBu(NⁱPr₂)PCI (8.8 mg, 0.040 mmol, 1.1 eq.) in MeCN (1 + 1 mL). NHC^{Dipp}CuCl (17.5 mg, 0.036 mmol, 1 eq.) in MeCN (1 mL). The crude product was obtained as a red solid (42.9 mg, 67 %). ¹H NMR (400 MHz, thf-*d*₈, 298 K): δ [ppm] = 7.46 – 7.42 (m, 2H, CH_{Ph(p)}), 7.38 (s, 2H, CH_{Im}), 7.37 – 7.34 (m, 4H, CH_{Ph(m)}), 2.91 (hept, ³J_{HH} = 6.8 Hz, 4H, CH_{NHC(iPr)}), 1.57 (d, ³J_{HH} = 6.8 Hz, 6H, Me_{NHC(iPr)}), 1.50 (d, ³J_{HH} = 6.8 Hz, 6H, Me_{NHC(iPr)}), 1.19 (dd, ³J_{HH} = 6.8 Hz, 12H, Me_{NHC(iPr)}), 1.15 – 1.11 (m, 21H, Me_{NiPr₂/iBu}), 0.19 (s, 54H, Me_{TMS}). ¹³C NMR (101 MHz, thf-*d*₈, 298 K): δ [ppm] = 146.34 (s, C_{Ph(o)}), 136.95 (s, CH_{Ph(p)}), 131.23 (s, C_{PhN}), 125.36 (s, CH_{Ph(m)}), 124.35 (s, CH_{Im}), 30.77 (s CH_{NHC(iPr)}), 29.82 (Me_{iBu}), 3.31 (Me_{TMS}). ²⁹Si-INEPT NMR (79 MHz, thf-*d*₈, 298 K): δ [ppm] = -9.52 (s, Si_{TMS}). ³¹P NMR (162 MHz, thf-*d*₈, 298 K): δ [ppm] = 88.11 (m, P_{Ge9}).

[Ge₉{Si(TMS)₃}₂PⁱBu(Mes)]⁻ (10a): K₂[Ge₉{Si(TMS)₃}₂] (44.2 mg, 0.036 mmol, 1 eq.) and ⁱBu(Mes)PCI (14.3 mg, 0.054 mmol, 1.5 eq.) in MeCN (1 + 1 mL). The crude product was obtained as a brown solid (35 mg, 69 %). ¹H NMR (400 MHz, thf-*d*₈, 298 K): δ [ppm] = 6.73 (m, 2H, CH_{Mes}), 2.56 – 2.46 (m, 6H, Me_{Mes}), 2.15 (s, 3H, Me_{Mes}), 1.07 (d, ³J_{HP} = 12.5 Hz, 9H, Me_{iBu}), 0.25 (s, 54H, Me_{TMS}). ¹³C-NMR (101 MHz, thf-*d*₈, 298 K): δ [ppm] = 145.95 (s, C_{Ph(p)}), 137.34 (s, C_{Ph(o)}), 134.35 (s, C_{Ph(p)}), 130.06 (s, CH_{Ph}), 33.39 (s, C_{iBu}), 32.27 (s, Me_{iBu}), 31.22 (s, Me_(o)), 21.09 (s, Me_(p)), 3.20 (s, Me_{TMS}). ²⁹Si-INEPT (79 MHz, thf-*d*₈, 298 K): δ [ppm] = -11.31 (s, Si_{TMS}), -109.41 (s, Si_{Ge9}). ³¹P-NMR (162 MHz, thf-*d*₈, 298 K): δ [ppm] = -19.40 (m, P_{Ge9}). **ESI-MS:** (negative ion mode, 3500 V, 300 °C): *m/z* 1356.8 [Ge₉{Si(TMS)₃}₂PⁱBu(Mes)]⁻.

NHC^{Dipp}Ag[Ge₉{Si(TMS)₃}₂PⁱBu(Mes)] (10-AgNHC^{Dipp}): K₂[Ge₉{Si(TMS)₃}₂] (40.0 mg, 0.033 mmol, 1 eq.) and ⁱBu(Mes)PCI (7.9 mg, 0.033 mmol, 1 eq.) in MeCN (1 + 1 mL). NHC^{Dipp}AgCl (20.8 mg, 0.039 mmol, 1.2 eq.) in MeCN (2 mL). The crude product was obtained as a bright red solid (9 mg, 15 %). ¹H NMR (400 MHz, thf-*d*₈, 298 K): δ [ppm] = 7.55 – 7.52 (m, 2H, CH_{Ph(p)}), 7.46 – 7.40 (m, 2H, CH_{Im}), 7.37 – 7.33 (m, 2H, CH_{Ph(m)}), 7.27 – 7.22 (m, 2H, CH_{Ph(m)}), 6.90 – 6.84 (m, 2H, CH_{Mes}), 2.80 (hept, ³J_{HH} = 6.8 Hz, 4H, CH_{PiPr}), 2.71 – 2.65 (m, 6H, Me_{Mes}), 2.22 (s, 3H, Me_{Mes}), 1.47 (d, ³J_{HH} = 6.8 Hz, 12H, Me_{PiPr}), 1.21 (t, ³J_{HP} = 7.1 Hz, 12H, Me_{PiPr}), 1.16 (d, ³J_{HP} = 7.1 Hz Me_{iBu}), 0.17 (s, 54H, Me_{TMS}). ¹³C NMR (101 MHz, thf-*d*₈, 298 K): δ [ppm] = 146.43 (s, C_{Ph(o)}), 138.80 (s, C_{Ph}), 136.43 (s, C_{Mes(o)}), 131.27 (s, CH_{Ph(p)}), 130.43 (s, CH_{Mes}), 129.57 (s, C_{MesP}), 129.51 (s, C_{Mes(p)}), 125.21 (s, CH_{Im}), 124.55 (s, CH_{Ph(m)}), 34.48 (s, C_{iBu}), 32.32 (Me_{iBu}), 29.77 (CH_{PiPr}), 21.06 (s, Me_{Mes(o)}), 3.19 (Me_{TMS}). ²⁹Si-INEPT (79 MHz, thf-*d*₈, 298 K): δ [ppm] = -9.40 (s Si_{TMS}), -104.87 (s, Si_{Ge9}). ³¹P NMR (162 MHz, thf-*d*₈, 298 K): δ [ppm] = -14.36 (s, P_{Ge9}). **EA:** anal. calcd. for Ge₉Si₈N₂P₁AgC₅₈H₁₁₀: C, 37.60; H, 5.98; N, 1.51; found: C, 37.91; H, 6.10; N, 1.56.

NHC^{Dipp}Cu[Ge₉{Si(TMS)₃}₂PⁱBu(Mes)] (10-CuNHC^{Dipp}): K₂[Ge₉{Si(TMS)₃}₂] (44.2 mg, 0.036 mmol, 1 eq.) and ⁱBu(Mes)PCI (14.3 mg, 0.054 mmol, 1.5 eq.) in MeCN (1 + 1 mL). NHC^{Dipp}CuCl (17.5 mg, 0.036 mmol, 1 eq.) in MeCN (1 mL). The crude product was obtained as a bright red solid (41.0 mg, 61 %). ¹H NMR (400 MHz, thf-*d*₈, 298 K): δ [ppm] = 7.42 – 7.37 (m, 4H, CH_{Ph(m)}), 7.37 – 7.32 (m, 2H, CH_{Im}), 7.29 – 7.21 (m, 2H, CH_{Ph(p)}), 6.92 –

6.85 (m, 2H, CH_{Mes}), 2.89 (hept, ³J_{HH} = 6.8 Hz, 4H, CH_{Pr}), 2.76 – 2.64 (m, 6H, Me_{Mes}), 2.23 (s, 3H, Me_{Mes}), 1.50 (d, ³J_{HH} = 6.8 Hz, 12H, Me_{Pr}), 1.19 (s, 3H, Me_{tBu}), 1.16 (d, ³J_{HH} = 6.8 Hz, 12H, Me_{Pr}), 1.09 – 1.14 (brs, 6H, Me_{tBu}), 0.19 (s, 54H, Me_{TMS}). **¹³C NMR** (101 MHz, thf-*d*₈, 298 K): δ [ppm] = 146.19 (s, C_{Ph(o)}), 138.84 (s, C_{PhN}), 136.38 (s, C_{Mes(o)}), 131.23 (s, CH_{Ph(ρ)}), 130.46 (s, CH_{Mes}), 129.63 (s, C_{MesP}), 129.50 (s, C_{Mes(ρ)}), 125.31 (s, CH_{Im}), 124.19 (s, CH_{Ph(m)}), 34.50 (s, C_{tBu}), 32.09 (Me_{tBu}), 29.80 (CH_{Pr}), 21.05 (s, Me_{Mes(o)}), 3.28 (Me_{TMS}). **²⁹Si-INEPT** (79 MHz, thf-*d*₈, 298 K): δ [ppm] = -11.22 (s Si_{TMS}), -105.12 (s, Si_{Ge9}). **³¹P NMR** (162 MHz, thf-*d*₈, 298 K): δ [ppm] = -14.77 (m, P_{Ge9}). **EA:** anal. calcd. for Ge₉Si₈N₂P₇CuC₅₈H₁₁₀: C, 38.52; H, 6.13; N, 1.55; found: C, 40.29; H, 6.34; N, 1.57. The deviation of C and H content is probably caused by remaining toluene.

[Ge₉{Si(TMS)₃}₂P(*o*-tolyl)₂]⁻ (11a): K₂[Ge₉{Si(TMS)₃}₂] (73.6 mg, 0.060 mmol, 1 eq.) and (*o*-tolyl)₂PCl (14.9 mg, 0.060 mmol, 1 eq.) in MeCN (1.5 + 1 mL). The crude product was obtained as a brown solid (38 mg, 45 %). **¹H NMR** (400 MHz, thf-*d*₈, 298 K): δ [ppm] = 6.94 – 6.87 (m, 8H, CH_{*o*-tolyl}), 2.20 (s, 6H, Me_{*o*-tolyl}), 0.27 (s, 54H, Me_{TMS}). **¹³C NMR** (101 MHz, thf-*d*₈, 298 K): δ [ppm] = 143.05, 141.35, 136.45, 129.62, 127.24, 125.77 (s, C_{Ph/CHPh}), 22.54 (d, ³J_{CP} = 19.9 Hz, Me_{Ph}), 3.18 (s, Me_{TMS}). **²⁹Si-INEPT** (79 MHz, thf-*d*₈, 298 K): δ [ppm] = -9.29 (s Si_{TMS}), -107.67 (s, Si_{Ge9}). **³¹P NMR** (162 MHz, thf-*d*₈, 298 K): δ [ppm] = -41.66 (m, P_{Ge9}). **ESI-MS:** (negative ion mode, 4000 V, 300 °C): *m/z* 1362.8 [Ge₉{Si(TMS)₃}₂P(*o*-tolyl)₂]⁻.

NHC^{Dipp}Ag[Ge₉{Si(TMS)₃}₂P(*o*-tolyl)₂] (11-AgNHC^{Dipp}): K₂[Ge₉{Si(TMS)₃}₂] (40.0 mg, 0.033 mmol, 1 eq.) and (*o*-tolyl)₂PCl (8.1 mg, 0.033 mmol, 1 eq.) in MeCN (1 + 1 mL). NHC^{Dipp}AgCl (20.8 mg, 0.039 mmol, 1.2 eq.) in MeCN (2 mL) The crude product was obtained as a brown solid (7 mg, 11 %). **¹H NMR** (400 MHz, thf-*d*₈, 298 K): δ [ppm] = 7.64 – 7.59 (m, 2H, CH_{Ph(m)}), 7.55 (s, 2H, CH_{Im}), 7.27 (s, 2H, CH_{*o*-tolyl(ρ)}), 7.25 (s, 2H, CH_{*o*-tolyl(m)}), 7.17 – 7.03 (m, 6H, CH_{Ph(m)/*o*-tolyl(o)/*o*-tolyl(m)}), 6.01 – 6.95 (m, 2H, CH_{Ph(ρ)}), 2.78 (hept, ³J_{HH} = 6.8 Hz, 4H, CH_{Pr}), 2.39 (s, 6H, Me_{*o*-tolyl}), 1.44 (d, ³J_{HH} = 6.8 Hz, 12H, Me_{Pr}), 1.18 (d, ³J_{HH} = 6.8 Hz, 12H, Me_{Pr}), 0.18 (s, 54H, Me_{TMS}). **¹³C NMR** (101 MHz, thf-*d*₈, 298 K): δ [ppm] = 146.43 (s, C_{PhN}), 142.14 (s, C_{*o*-tolyl(P)}), 140.14 (s, C_{*o*-tolyl(o)}), 136.47 (s, CH_{Ph(m)}), 131.21 (s, CH_{*o*-tolyl(m)}), 130.37 (s, CH_{*o*-tolyl(o)}), 128.52 (s, CH_{Ph(m)}), 126.36 (s, CH_{Ph(ρ)}), 125.13 (s, CH_{*o*-tolyl(ρ/m)}), 124.35 (s, CH_{Im}), 29.73 (s, CH_{Pr}), 22.46 (s, Me_{*o*-tolyl}), 3.11 (Me_{TMS}). **²⁹Si-INEPT NMR** (79 MHz, thf-*d*₈, 298 K): δ [ppm] = -9.28 (s, Si_{TMS}), -105.68 (s, Si_{Ge9}). **³¹P NMR** (162 MHz, thf-*d*₈, 298 K): δ [ppm] = -39.30 (s, P_{Ge9}).

NHC^{Dipp}Cu[Ge₉{Si(TMS)₃}₂P(*o*-tolyl)₂] (11-CuNHC^{Dipp}): K₂[Ge₉{Si(TMS)₃}₂] (73.6 mg, 0.060 mmol, 1 eq.) and (*o*-tolyl)₂PCl (14.9 mg, 0.060 mmol, 1 eq.) in MeCN (1.5 + 1 mL). NHC^{Dipp}CuCl (29.2 mg, 0.060 mmol, 1 eq.) in MeCN (1.5 mL) The crude product was obtained as a brown solid (40.1 mg, 37 %). **¹H NMR** (400 MHz, thf-*d*₈, 298 K): δ [ppm] = 7.61 – 7.56 (m, 2H, CH_{Ph(m)}), 7.41 (s, 2H, CH_{Im}), 7.27 (s, 2H, CH_{*o*-tolyl(ρ)}), 7.25 (s, 2H, CH_{*o*-tolyl(m)}), 7.16 – 7.05 (m, 6H, CH_{Ph(m)/*o*-tolyl(o)/*o*-tolyl(m)}), 6.99 – 6.94 (m, 2H, CH_{Ph(ρ)}), 2.88 (hept, ³J_{HH} = 6.8 Hz, 4H, CH_{Pr}), 2.39 (s, 6H, Me_{*o*-tolyl}), 1.50 (d, ³J_{HH} = 6.8 Hz, 12H, Me_{Pr}), 1.15 (d, ³J_{HH} = 6.8 Hz, 12H, Me_{Pr}), 0.19 (s, 54H, Me_{TMS}). **¹³C NMR** (101 MHz, thf-*d*₈, 298 K): δ [ppm] = 146.16 (s, C_{PhN}), 142.01 (s, C_{*o*-tolyl(P)}), 140.51 (s, C_{*o*-tolyl(o)}), 136.49 (s, CH_{Ph(m)}), 131.16 (s, CH_{*o*-tolyl(m)}), 130.37 (s, CH_{*o*-tolyl(o)}), 128.54 (s, CH_{Ph(m)}), 126.34 (s, CH_{Ph(ρ)}), 125.19 (s, CH_{*o*-tolyl(ρ/m)}), 123.90 (s, CH_{Im}), 29.77 (s, CH_{Pr}), 22.65 (s, Me_{*o*-tolyl}), 3.15 (Me_{TMS}). **²⁹Si-INEPT NMR** (79 MHz, thf-*d*₈, 298 K): δ [ppm] = -9.28 (s, Si_{TMS}), -104.48 (s, Si_{Ge9}). **³¹P NMR** (162 MHz, thf-*d*₈, 298 K): δ [ppm] = -37.15 (m, P_{Ge9}).

Crystallographic data

Table S1: Selected distances in compound **2**.

bonds	distance [Å]	bonds	distance [Å]
Ge1-Ge2	2.4715(6)	Ge1-P1A	2.362(2)
Ge1-Ge4	2.4760(6)	P1A-C32A	1.788(6)
Ge1-Ge5	2.6043(5)	P1A-C28A	1.86(2)
Ge1-Ge6	2.6059(6)	C28A-C29A	1.49(3)
Ge1-Ge3	3.6324(6)	C28A-C30A	1.59(3)
Ge2-Ge7	2.5307(6)	C28A-C31A	1.50(1)
Ge2-Ge3	2.5908(6)	C32A-C33A	1.521(8)
Ge2-Ge6	2.6832(6)	C33A-C34A	1.536(9)
Ge2-Ge4	3.5112(6)	C34A-C35A	1.501(9)
Ge3-Ge4	2.5799(6)	C35A-C36A	1.328(9)
Ge3-Ge8	2.6458(6)		
Ge3-Ge7	2.6645(6)	Ge1-P1B	2.337(2)
Ge4-Ge8	2.5305(6)	P1B-C32B	1.827(6)
Ge4-Ge5	2.6713(6)	P1B-C28B	1.87(3)
Ge5-Ge9	2.5048(6)	C28B-C30B	1.45(5)
Ge5-Ge6	2.9186(6)	C28B-C31B	1.57(2)
Ge5-Ge8	3.1642(6)	C28B-C32B	1.51(4)
Ge6-Ge9	2.5220(6)	C32B-C33B	1.485(8)
Ge6-Ge7	3.0469(6)	C33B-C34B	1.52(1)
Ge7-Ge9	2.5354(6)	C34B-C35B	1.52(1)
Ge7-Ge8	2.7862(6)	C35B-C36B	1.339(9)
Ge8-Ge9	2.5339(6)		
Ge2-Si1	2.404(1)		
Ge4-Si5	2.390(1)		
Ge9-Si9	2.374(1)		

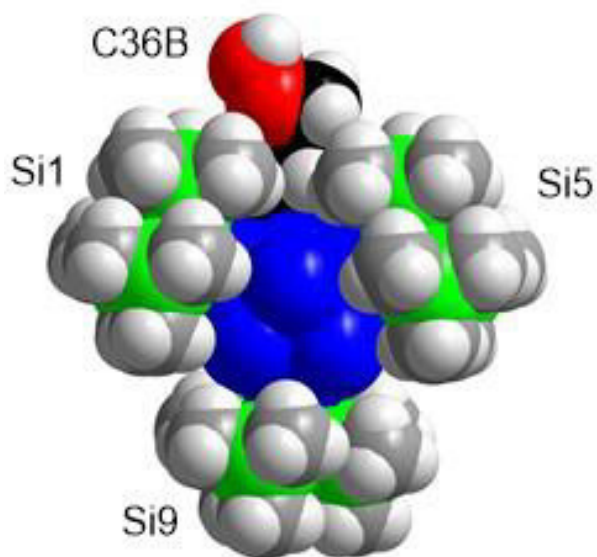


Figure S1: Space filling model of compound **2** (with minor phosphine individual), showing the exposed nature of the double bond of the pentenyl group. Hydrocarbon chain is shown in black, and the carbon atoms connected by the double bond (C35B and C36B) are presented in red. The respective picture of the major individual is provided in the manuscript.

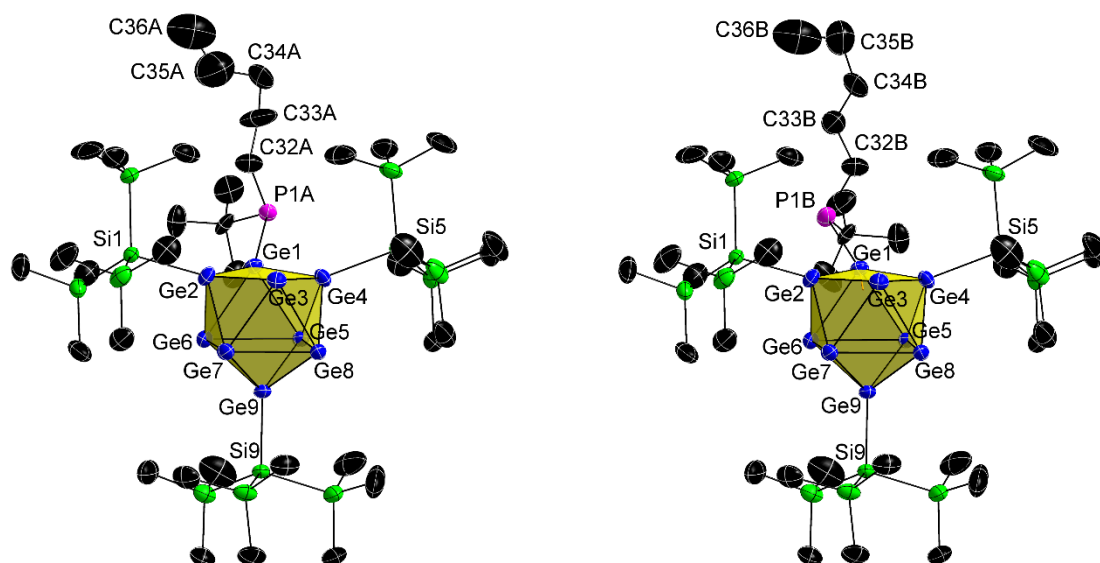


Figure S2: Full ellipsoid plots of compound **2**. Ellipsoids are shown at a 50 % probability level. Compound **2** with the major individual of the disordered phosphine group (left) and with the minor individual of the phosphine group (right). For clarity all protons are omitted.

NMR spectra

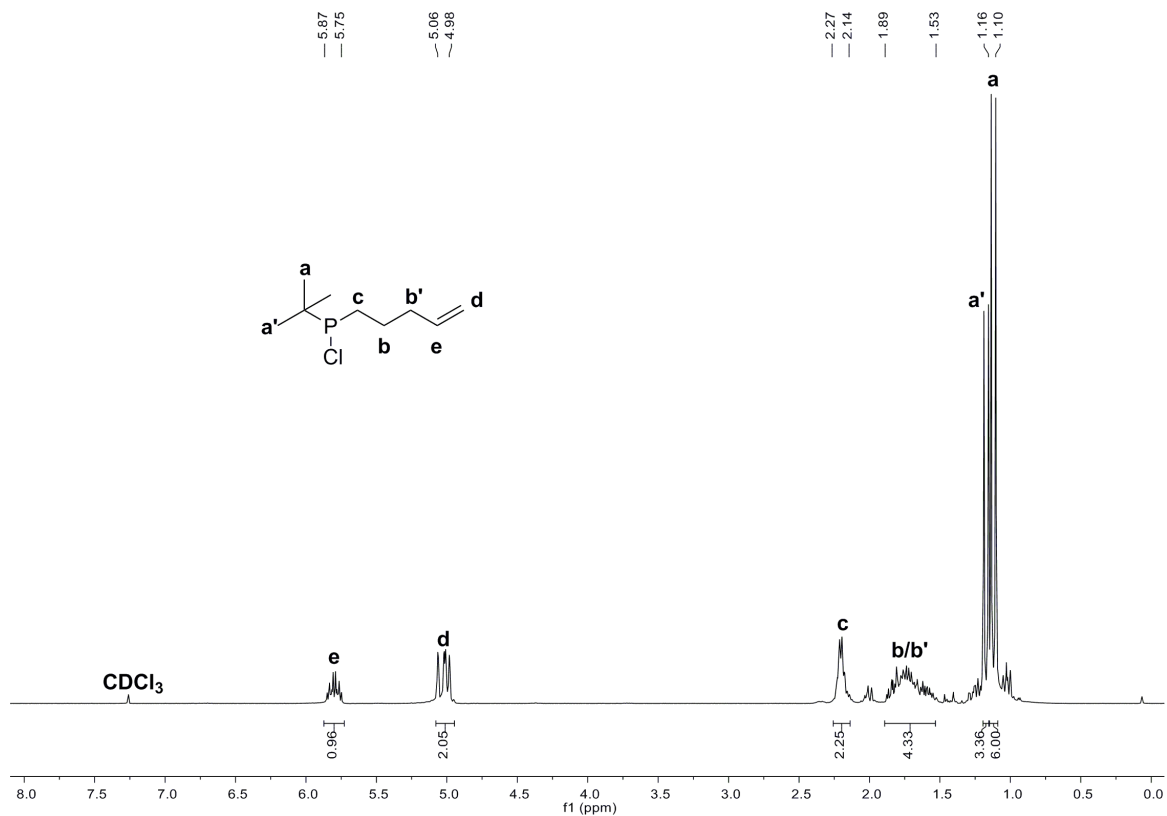


Figure S3: ¹H NMR spectrum of compound 1 in CDCl₃.

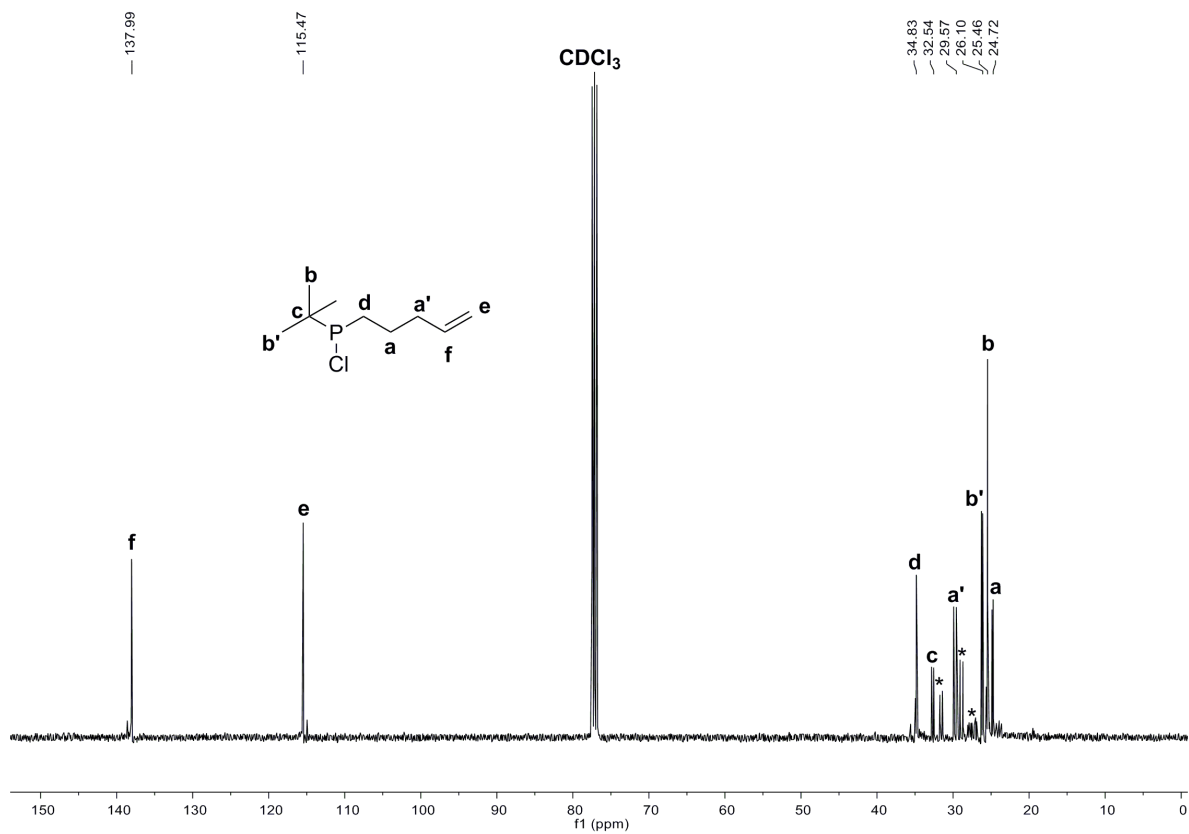


Figure S4: ¹³C NMR spectrum of compound 1 in CDCl₃ (signals marked with * belong to unidentified impurities).

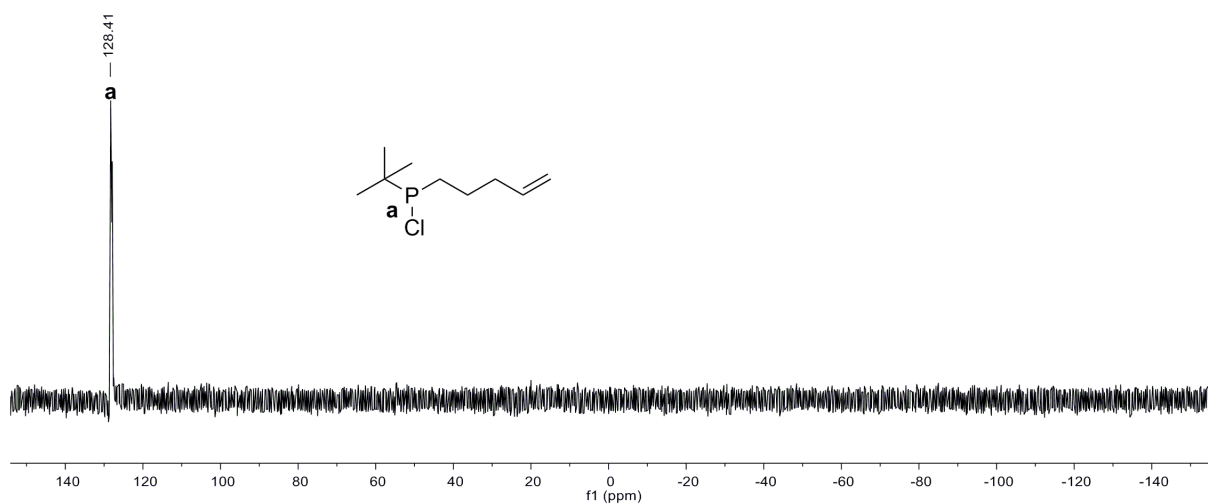


Figure S5: ^{31}P NMR spectrum of compound **1** in CDCl_3 .

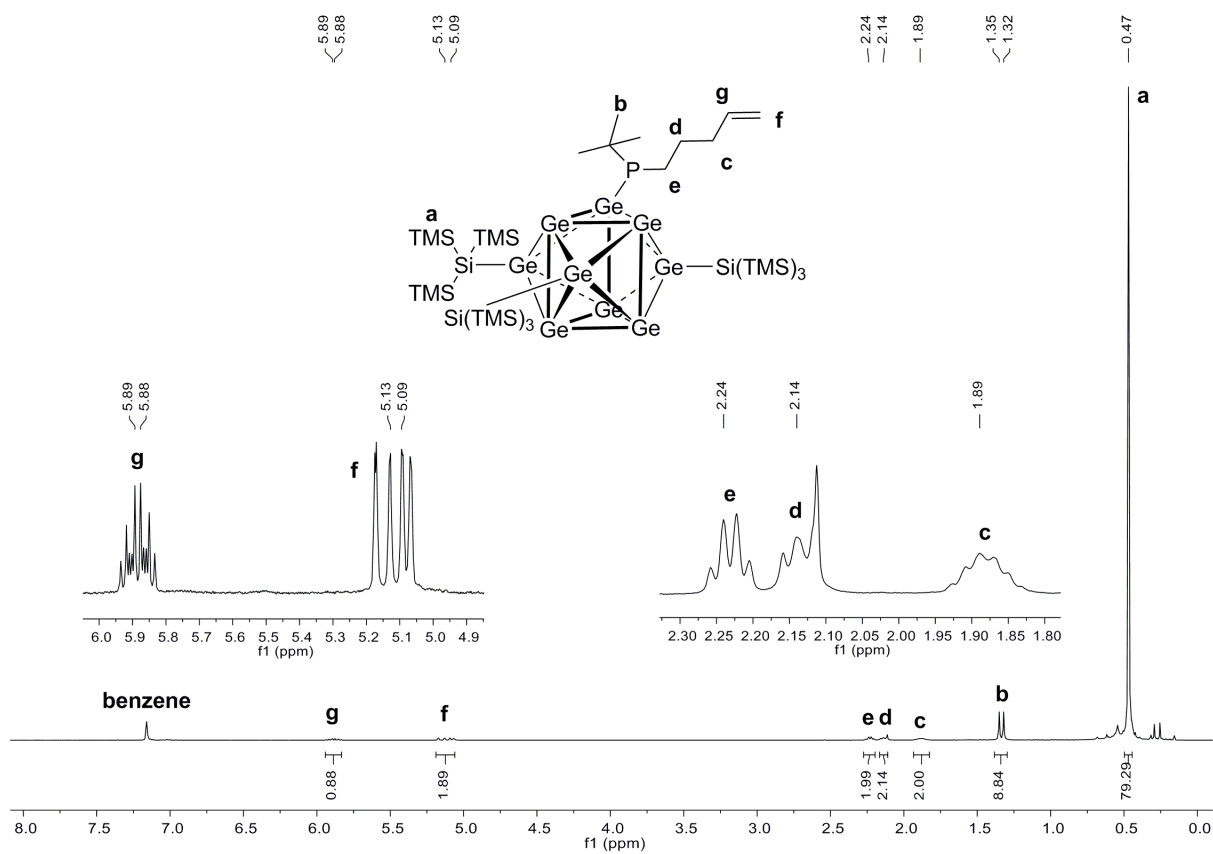


Figure S6: ^1H NMR spectrum of compound **2** in C_6D_6 .

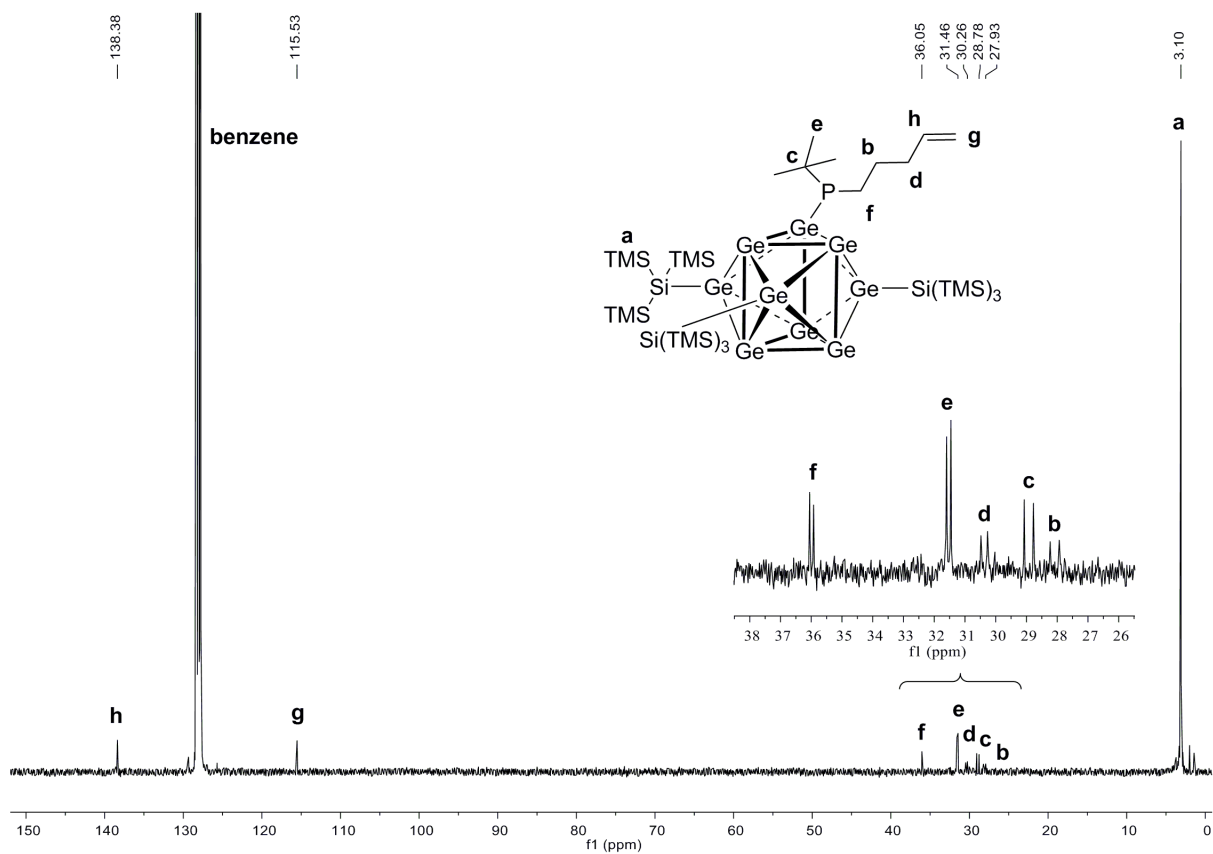


Figure S7: ^{13}C spectrum NMR of compound **2** in C_6D_6 .

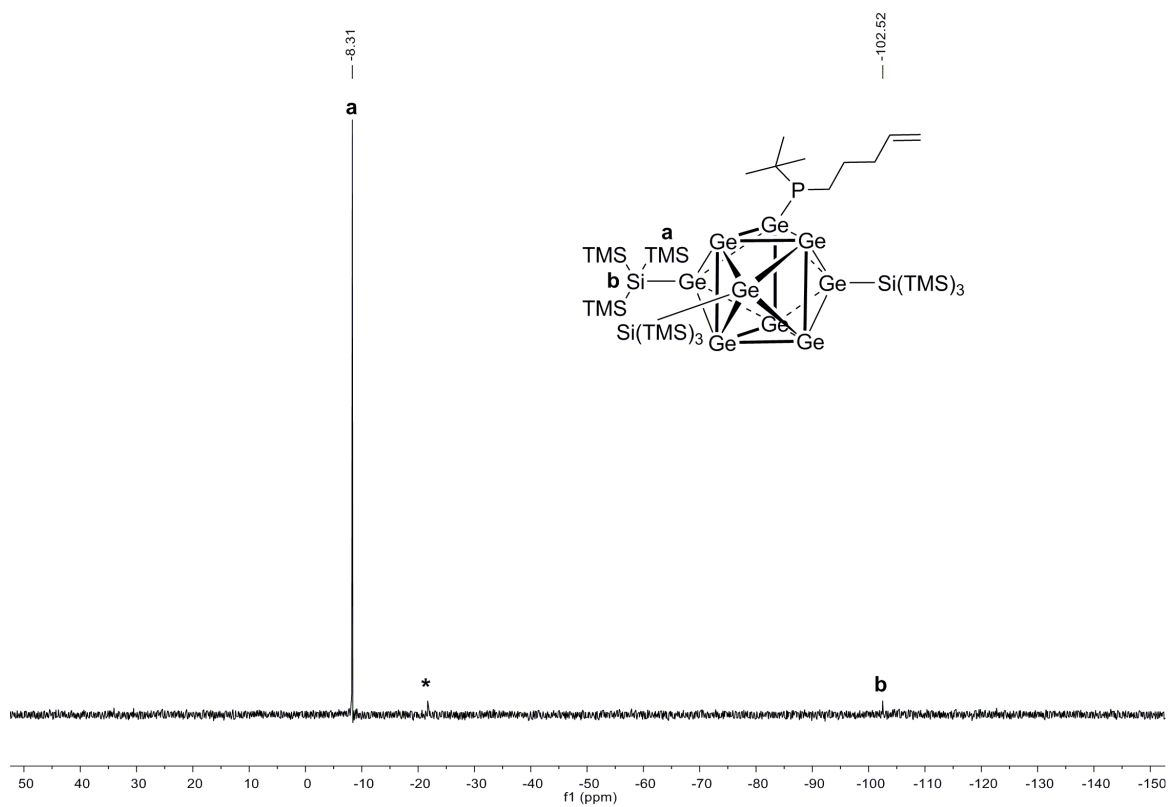


Figure S8: ^{29}Si -INEPT-RD NMR spectrum of compound **2** in C_6D_6 (signal marked with * belongs to unidentified impurity).

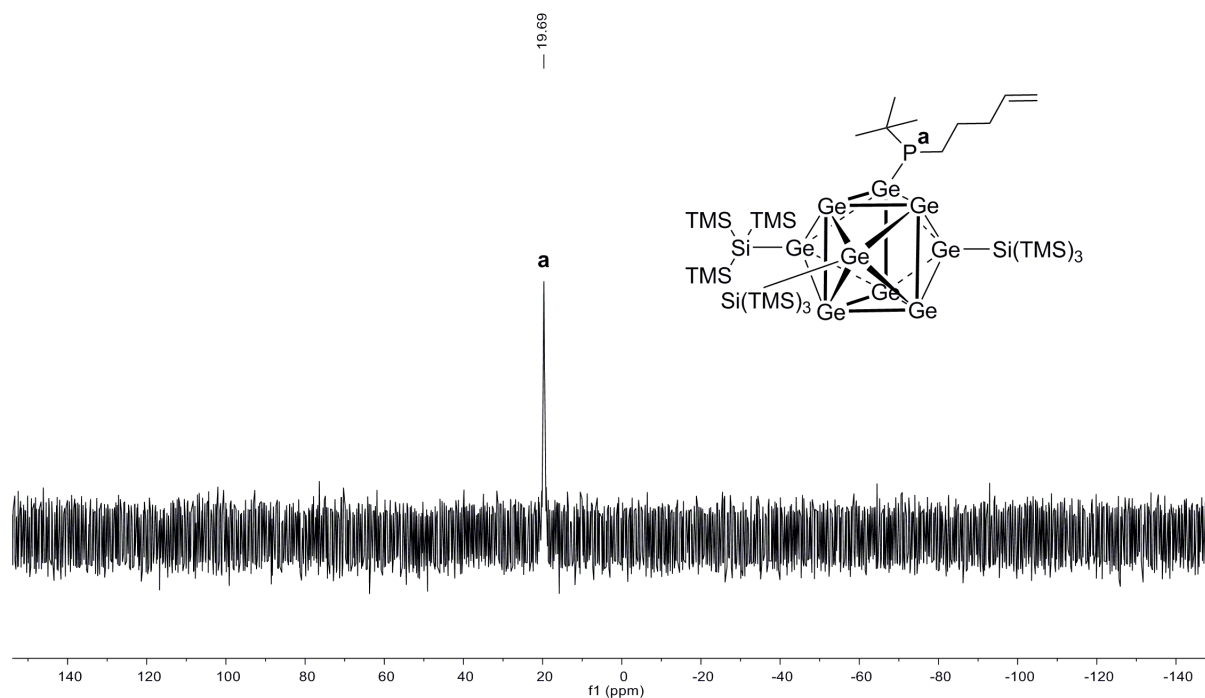
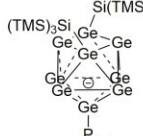
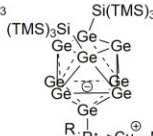
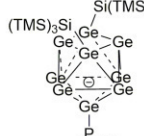
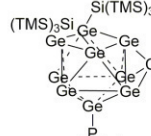
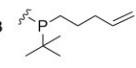
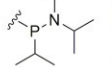
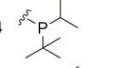
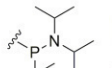
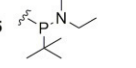
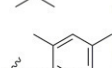
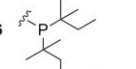
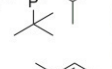
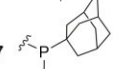


Figure S9: ^{31}P NMR spectrum of compound **2** in C_6D_6 .

Table S2: ^1H NMR shifts of the methyl protons of the silyl groups of the mixed-functionalized cluster anions $[\text{Ge}_9\{\text{Si}(\text{TMS})_3\}_2\text{PRR}]^-$ (**3a – 11a**) and the respective zwitterionic compounds **3-AgNHC^{Dipp}** – **7-AgNHC^{Dipp}** (left) or *Zintl* cluster Ag-NHC compounds **8-AgNHC^{Dipp}** – **11-AgNHC^{Dipp}** (right). The change of the shift value Δshift upon coordination of $[\text{NHC}^{\text{Dipp}}\text{Ag}]^+$ to the cluster anions allows for determination of the coordination mode.

			Δshift			Δshift
	[ppm]	[ppm]			[ppm]	
3	0.26 3a	0.23 3-AgNHC^{Dipp}	-0.03	8	0.25 8a	0.17 8-AgNHC^{Dipp} -0.08
4	0.26 4a	0.26 4-AgNHC^{Dipp}	0.00	9	0.25 9a	0.17 9-AgNHC^{Dipp} -0.08
5	0.25 5a	0.21 5-AgNHC^{Dipp}	-0.04	10	0.25 10a	0.17 10-AgNHC^{Dipp} -0.08
6	0.25 6a	0.27 6-AgNHC^{Dipp}	0.02	11	0.27 11a	0.18 11-AgNHC^{Dipp} -0.09
7	0.26 7a	0.28 7-AgNHC^{Dipp}	0.02			

Table S3: ^1H NMR shifts of the methyl protons of the silyl groups of the mixed-functionalized cluster anions $[\text{Ge}_9\{\text{Si}(\text{TMS})_3\}_2\text{PRR}]^-$ (**3a** – **11a**) and the respective zwitterionic compounds **3-CuNHC^{Dipp}** – **7-CuNHC^{Dipp}** (left) or *Zintl* cluster Cu-NHC compounds **8-CuNHC^{Dipp}** – **11-CuNHC^{Dipp}** (right). The change of the shift value Δshift upon coordination of $[\text{NHC}^{\text{Dipp}}\text{Cu}]^+$ to the cluster anions allows for determination of the coordination mode.

							
	[ppm]	[ppm]	Δshift	[ppm]	[ppm]	Δshift	
3 	0.26 3a	0.25 3-CuNHC^{Dipp}	-0.01	8 	0.25 8a	0.19 8-CuNHC^{Dipp}	-0.06
4 	0.26 4a	0.27 4-CuNHC^{Dipp}	0.01	9 	0.25 9a	0.19 9-CuNHC^{Dipp}	-0.06
5 	0.25 5a	0.23 5-CuNHC^{Dipp}	-0.02	10 	0.25 10a	0.19 10-CuNHC^{Dipp}	-0.06
6 	0.25 6a	0.27 6-CuNHC^{Dipp}	0.02	11 	0.25 11a	0.19 11-CuNHC^{Dipp}	-0.06
7 	0.26 7a	0.28 7-CuNHC^{Dipp}	0.02				

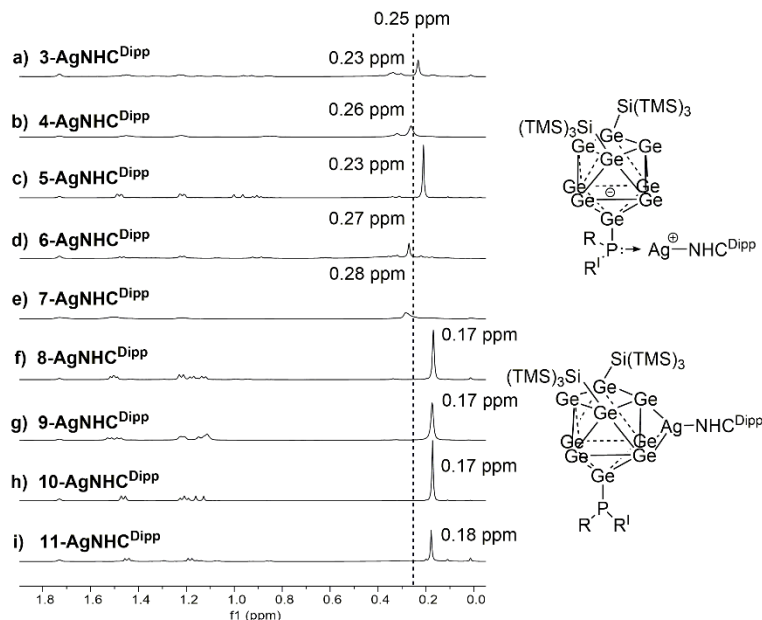


Figure S10: Selected areas of the ^1H NMR spectra of compounds **3-AgNHC^{Dipp}** – **11-AgNHC^{Dipp}** in $\text{thf-}d_8$ allowing for the determination of the interaction (P-Ag or Ge-Ag) between the mixed-functionalized cluster anions **3a-11a** and the $[\text{NHC}^{\text{Dipp}}\text{Ag}]^+$ moiety, using the shift of the silyl groups' methyl proton signals as indicator. Dashed line is positioned at a chemical shift value of 0.25 ppm.

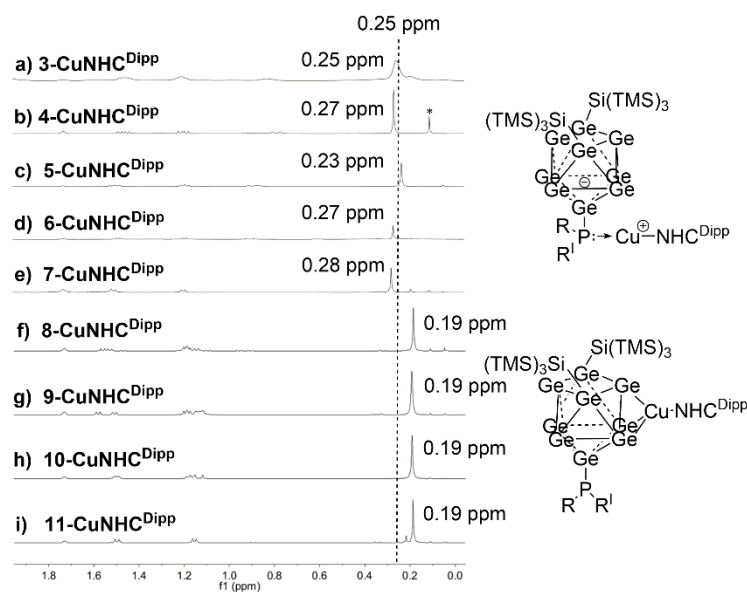


Figure S11: Selected areas of the ^1H NMR spectra of compounds **3-CuNHC^{Dipp}** – **11-CuNHC^{Dipp}** in $\text{thf-}d_8$ allowing for the determination of the interaction (P-Cu or Ge-Cu) between the mixed-functionalized cluster anions **3a-11a** and the $[\text{NHC}^{\text{Dipp}}\text{Cu}]^+$ moiety, using the shift of the silyl groups' methyl proton signals as indicator. Dashed line is positioned at a chemical shift value of 0.25 ppm. Asterisk signal belongs to silicon grease impurity.

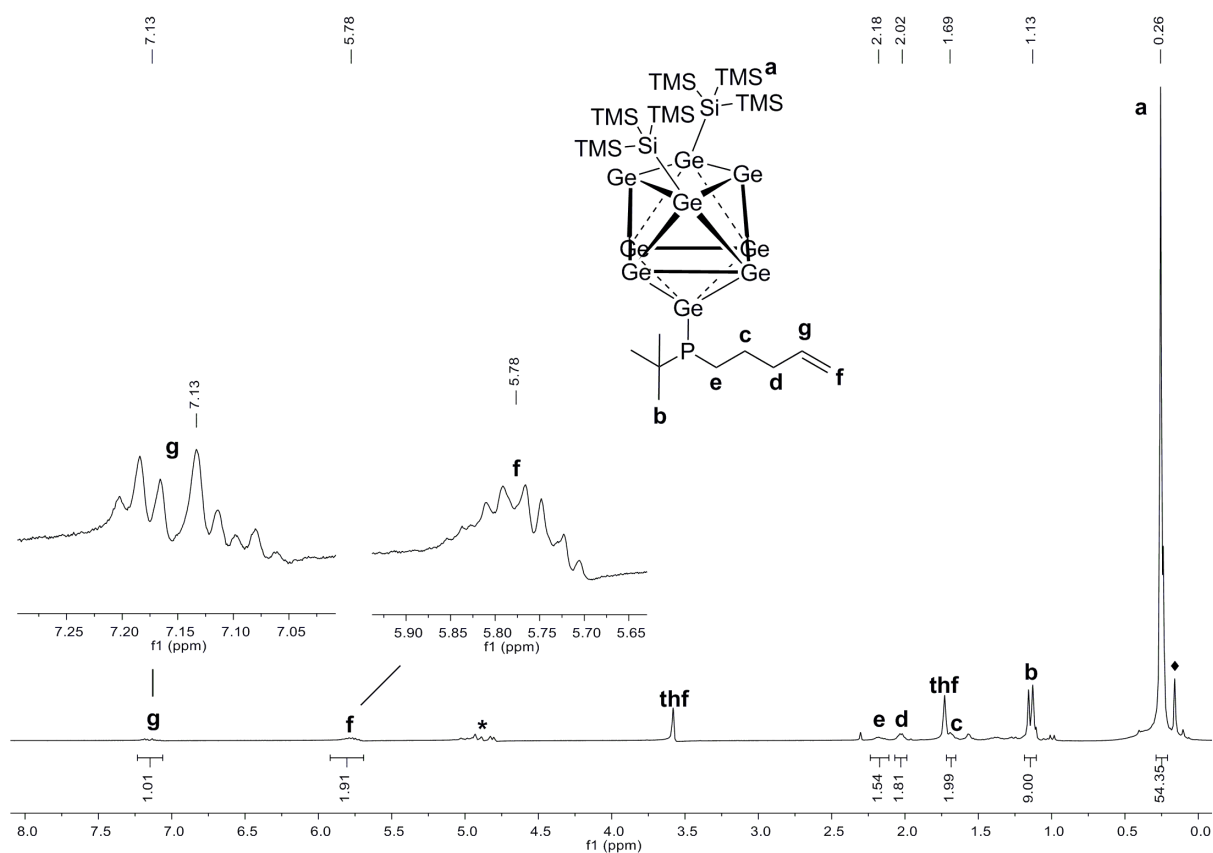


Figure S12: ^1H NMR spectrum of compound **3a** in $\text{thf-}d_8$ (signal marked with * belongs to an unidentified impurity, signal marked with \blacklozenge belongs to silicon grease).

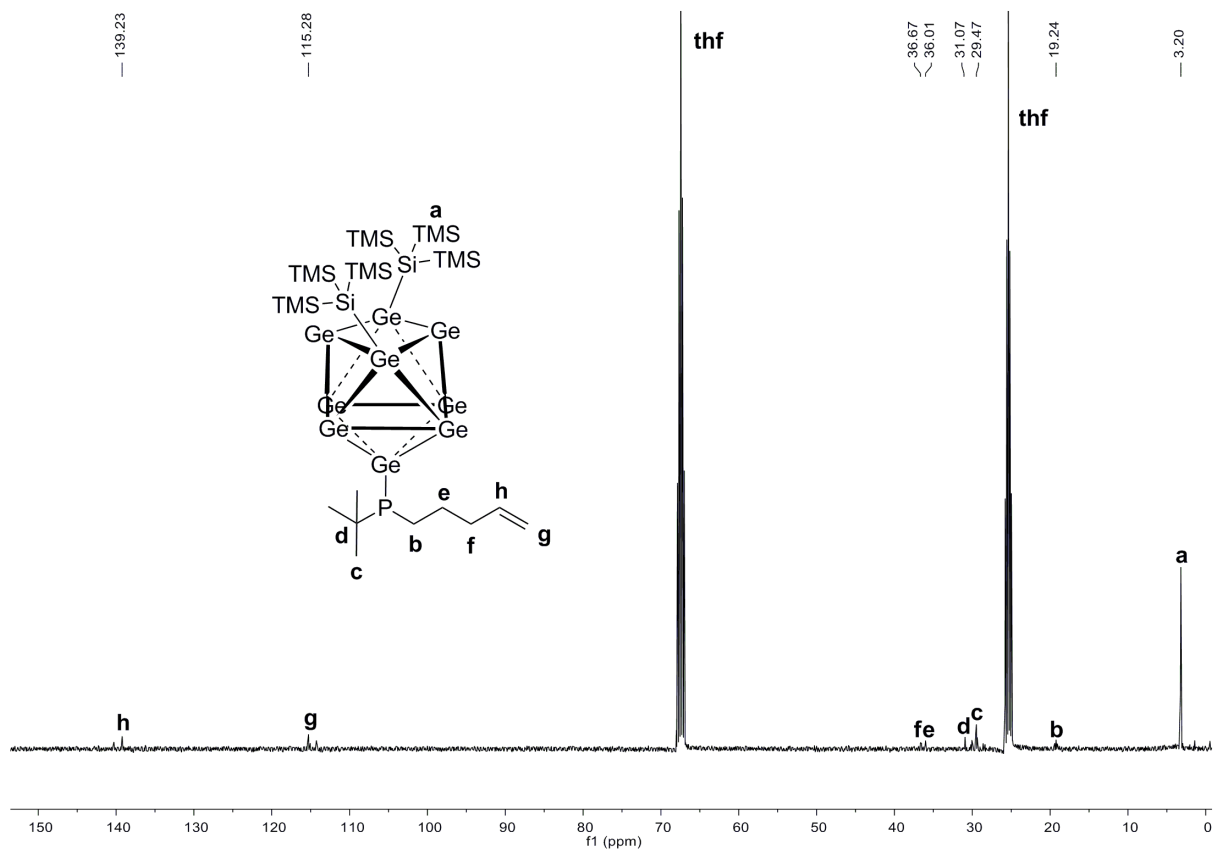


Figure S13: ^{13}C NMR spectrum of compound **3a** in $\text{thf-}d_8$.

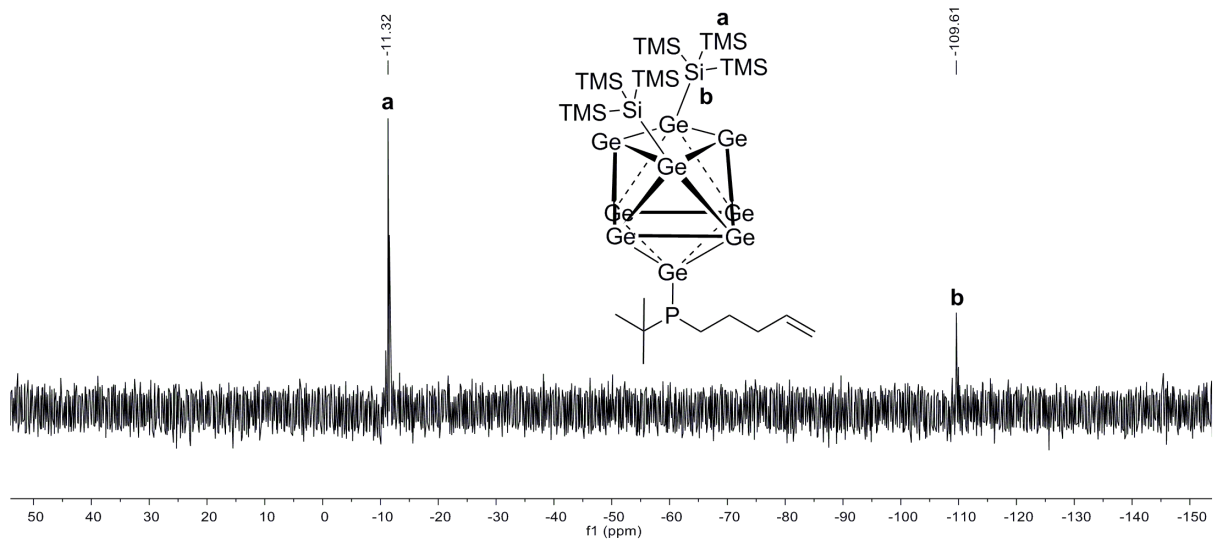


Figure S14: ^{29}Si -INEPT-RD NMR spectrum of compound **3a** in $\text{thf-}d_8$.

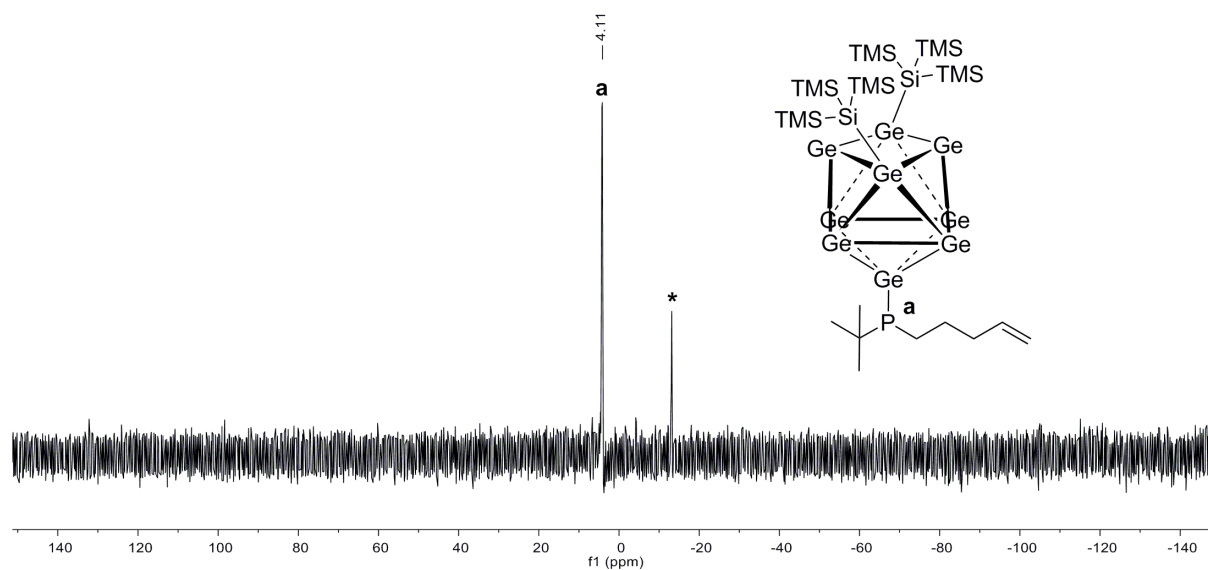


Figure S15: ^{31}P NMR spectrum of compound **3a** in $\text{thf-}d_8$ (signal marked with * belongs to an unidentified impurity).

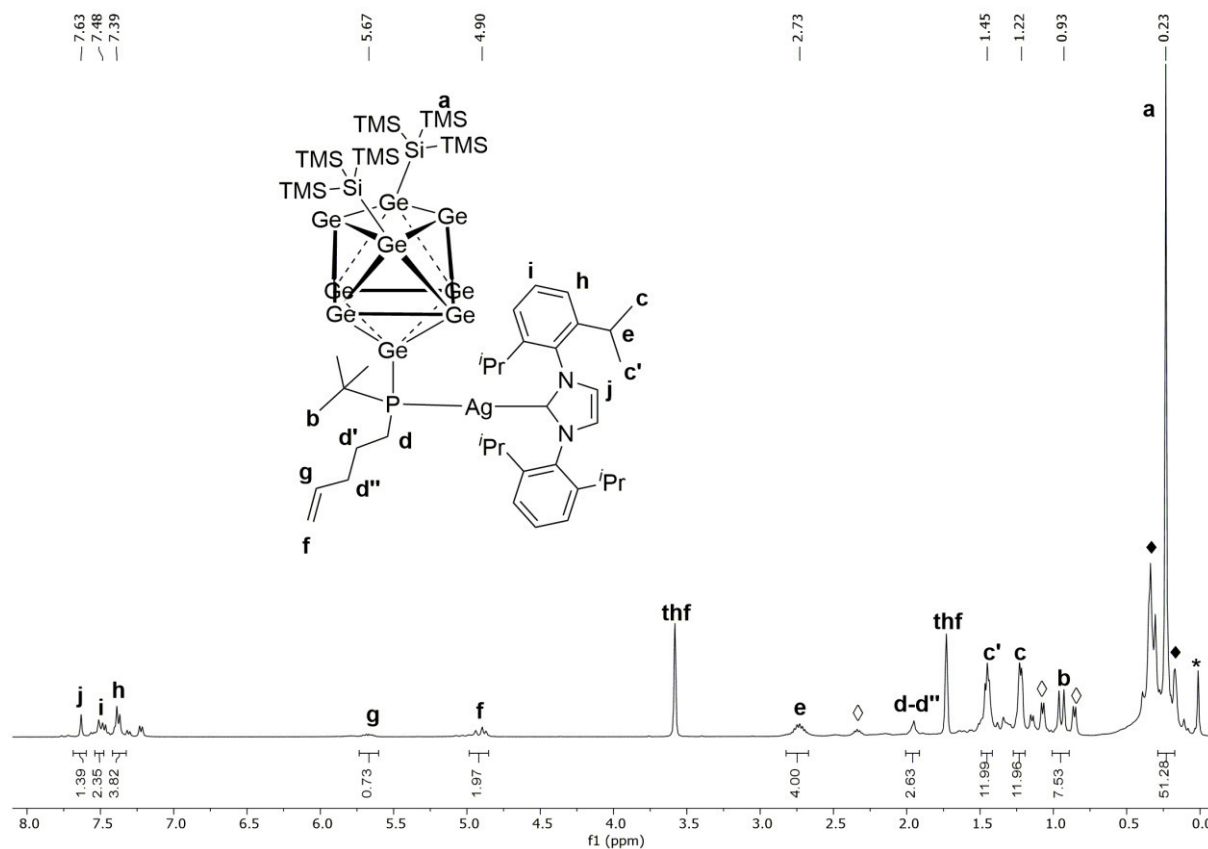


Figure S16: ^1H NMR spectrum of compound **3-AgNHC^{Dipp}** in $\text{thf-}d_8$ (signals marked with * belongs to silicon grease, \blacklozenge to unidentified impurities and \diamond to free $\text{NHC}^{\text{Dipp}}\text{AgCl}$).

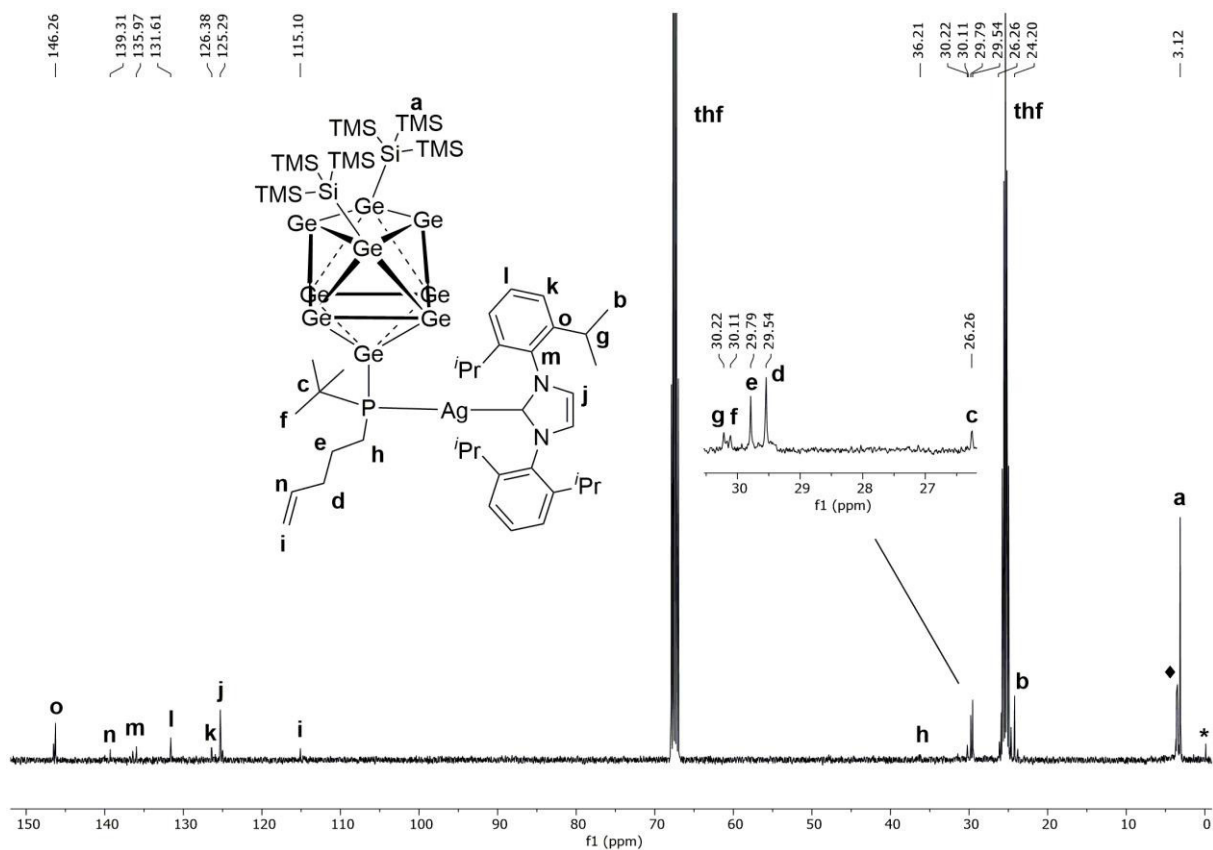


Figure S17: ^{13}C NMR spectrum of compound **3-AgNHC^{DIPP}** in $\text{thf-}d_8$ (signals marked with * belongs to silicon grease, ♦ to an unidentified impurity).

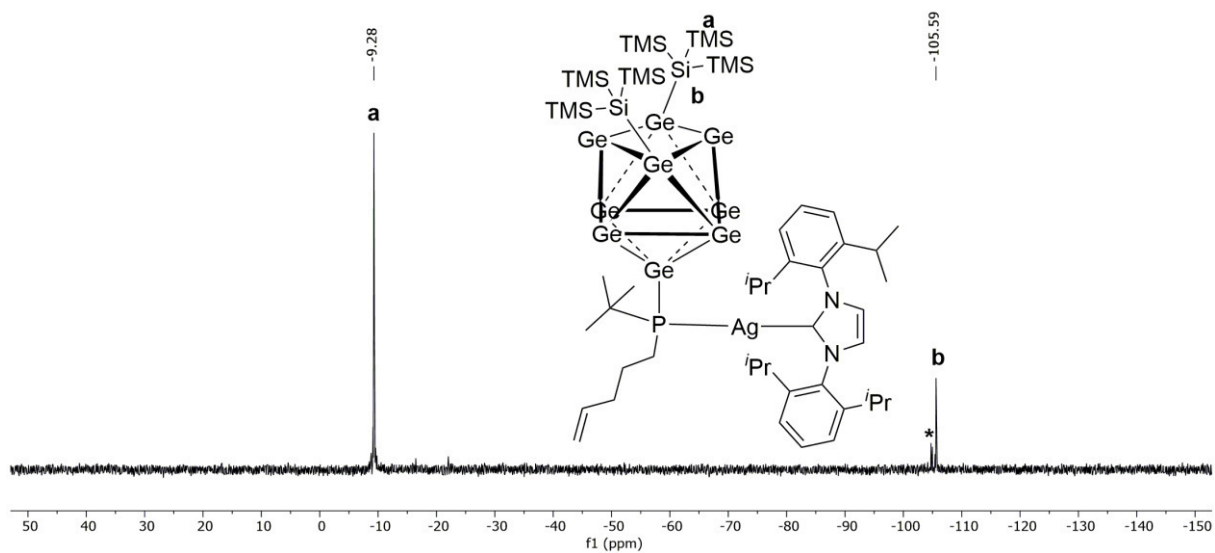


Figure S18: ^{29}Si -INEPT-RD NMR spectrum of compound **3-AgNHC^{DIPP}** in $\text{thf-}d_8$ (signal marked with * belongs to an unidentified impurity).

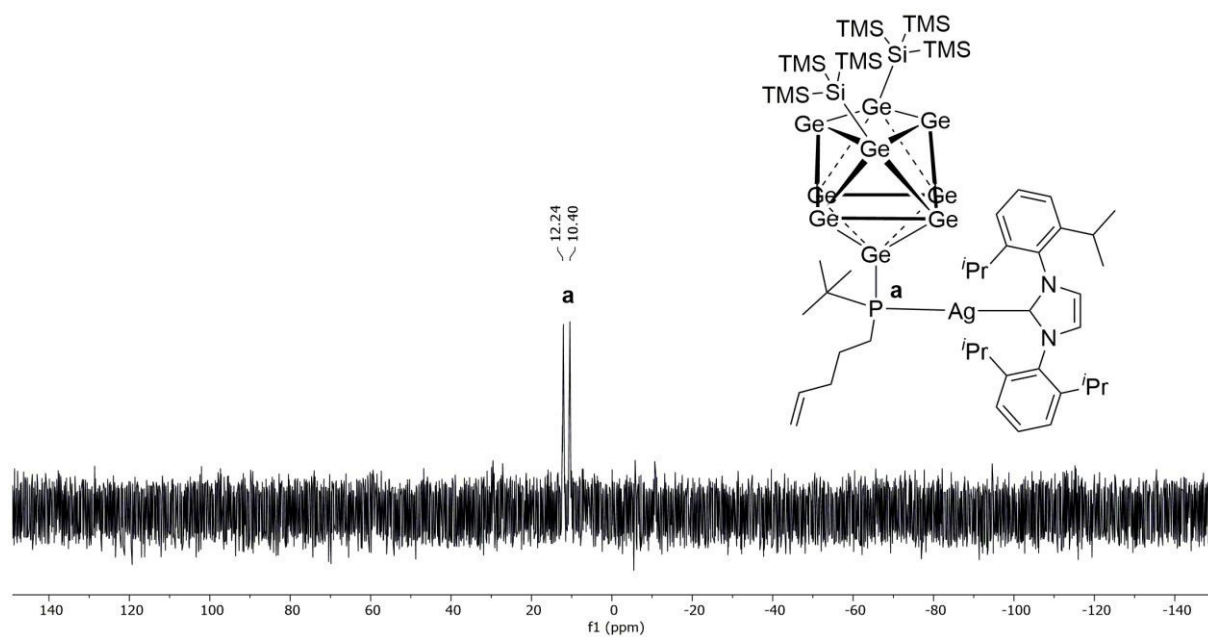


Figure S19: ^{31}P NMR spectrum of compound **3-AgNHC^{Dipp}** in $\text{thf-}d_8$.

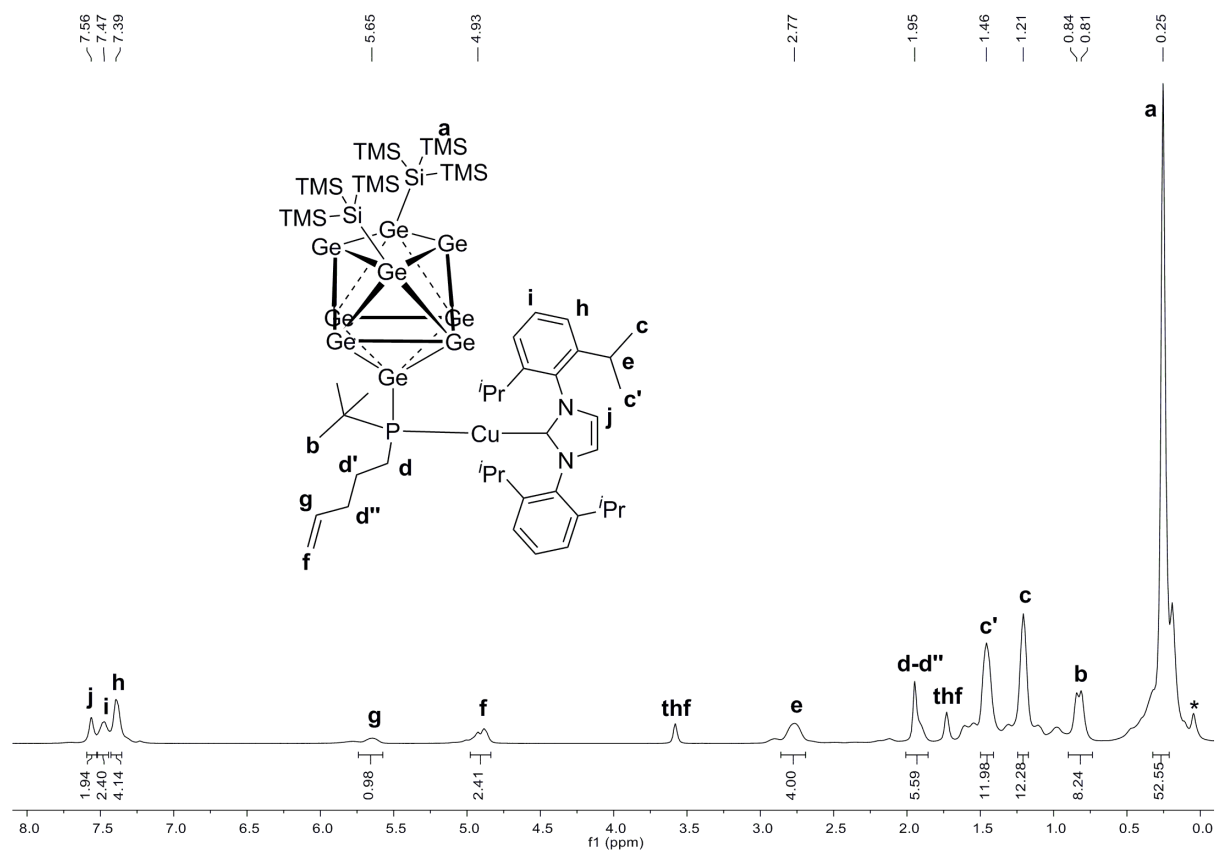


Figure S20: ^1H NMR spectrum of compound **3-CuNHC^{Dipp}** in $\text{thf-}d_8$ (signal marked with * belongs to silicon grease).

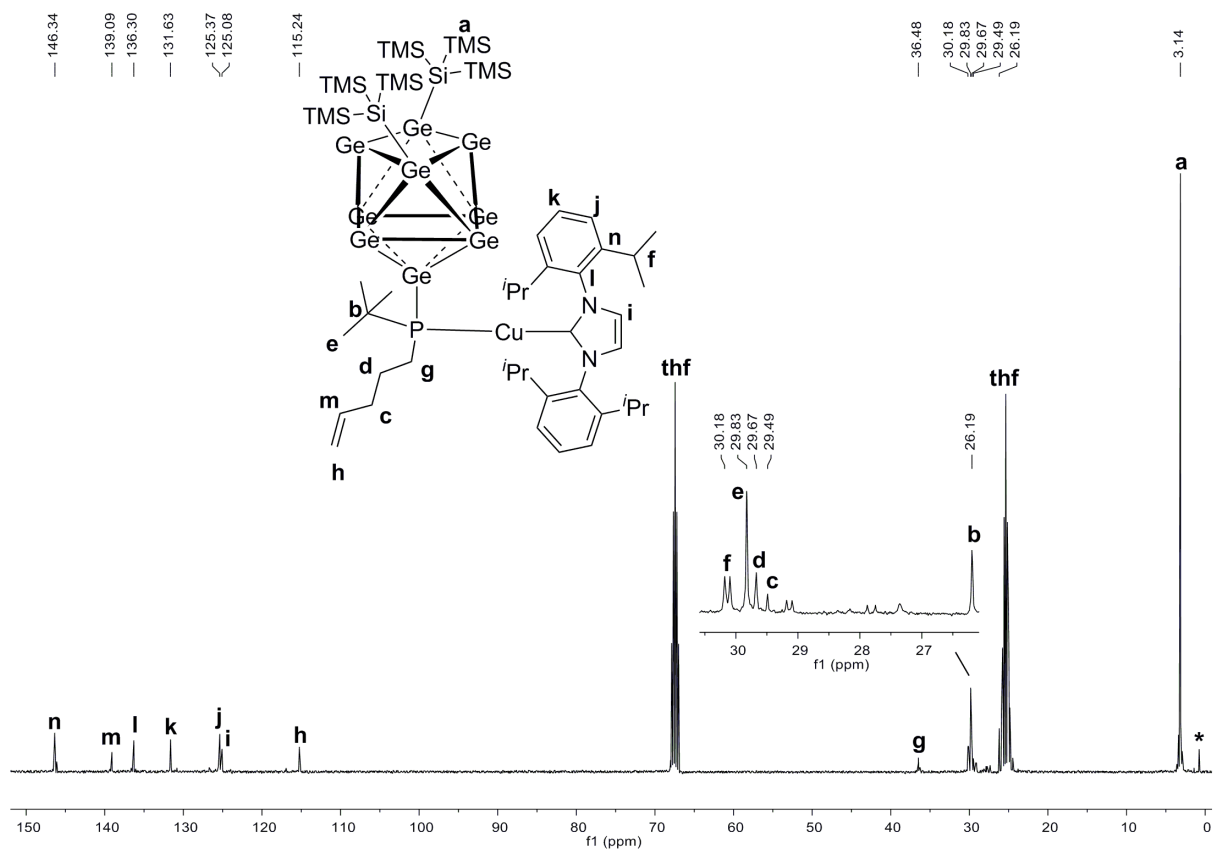


Figure S21: ^{13}C NMR spectrum of compound **3-CuNHC^{DIPP}** in $\text{thf-}d_8$ (signal marked with * belongs to silicon grease).

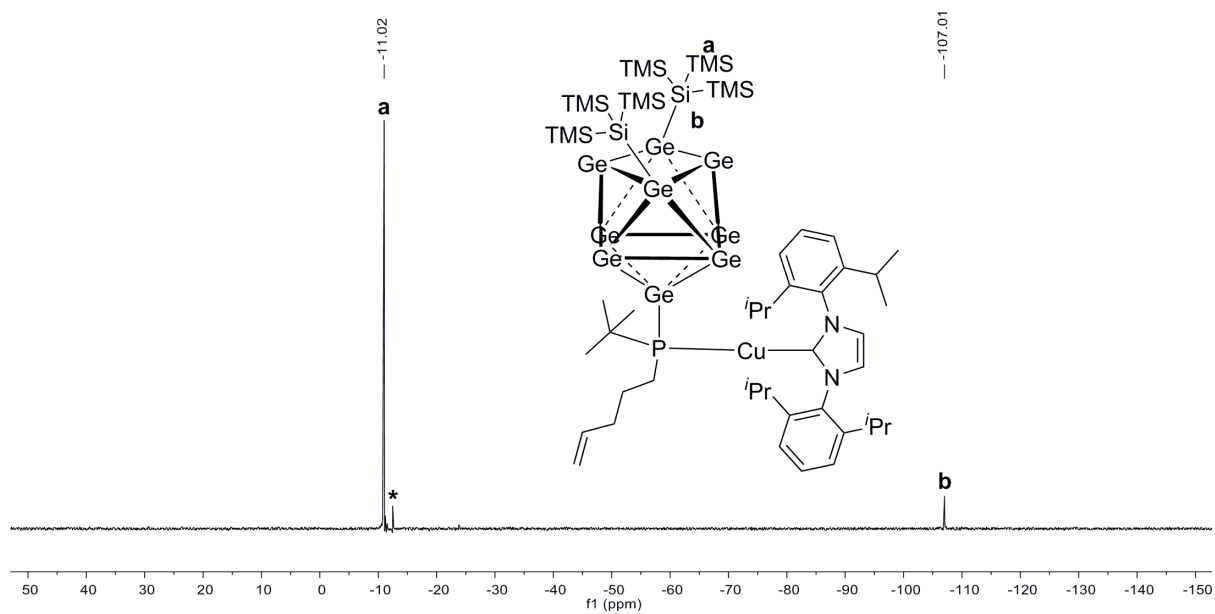


Figure S22: ^{29}Si -INEPT-RD NMR spectrum of compound **3-CuNHC^{DIPP}** in $\text{thf-}d_8$ (signal marked with * belongs to an unidentified impurity).

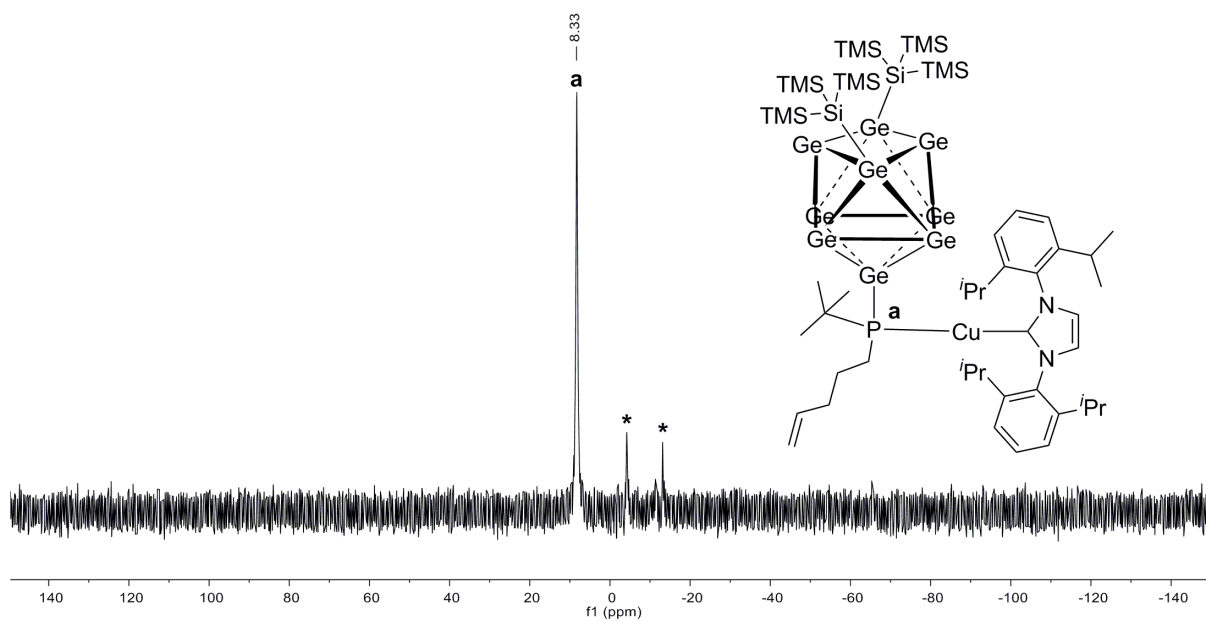


Figure S23: ^{31}P NMR spectrum of compound **3-CuNHC^{DIPP}** in $\text{thf-}d_8$ (signals marked with * belong to an unidentified impurities).

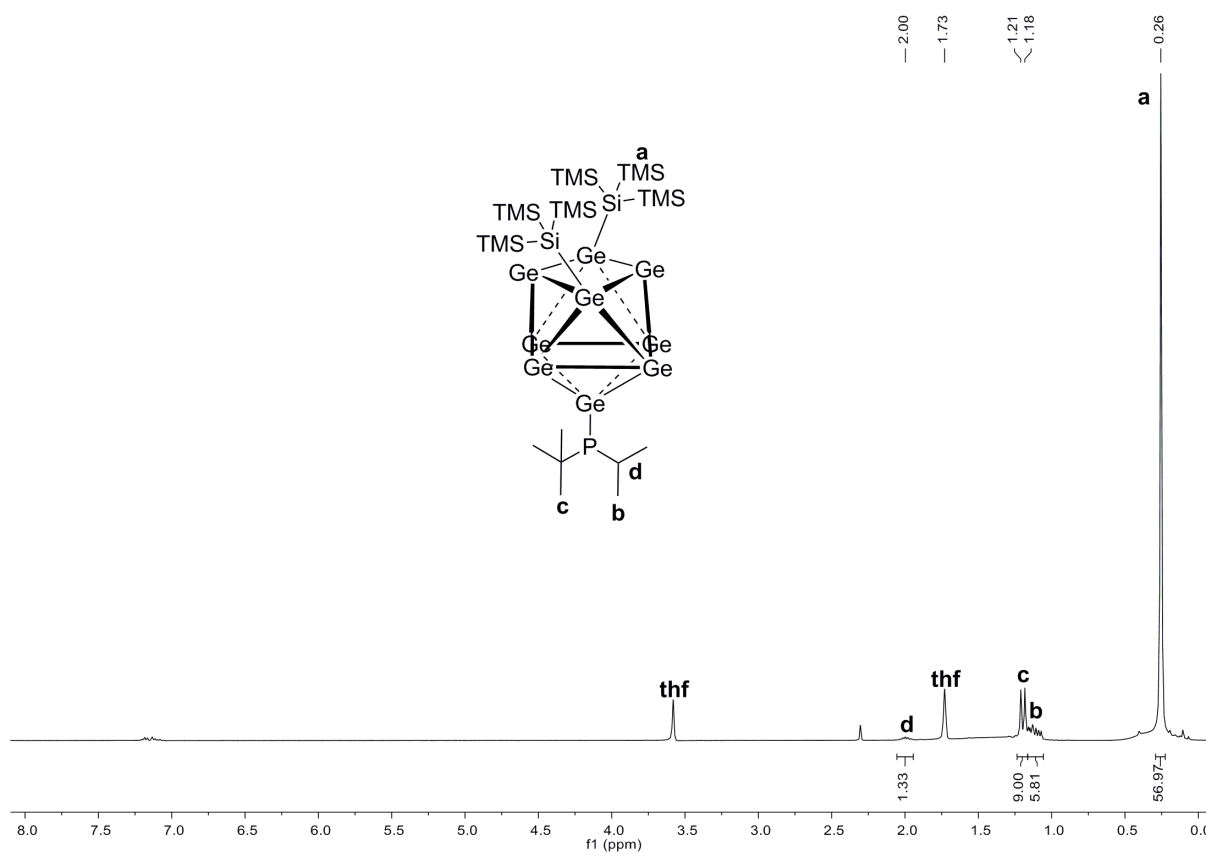


Figure S24: ^1H NMR spectrum of compound **4a** in $\text{thf-}d_8$.

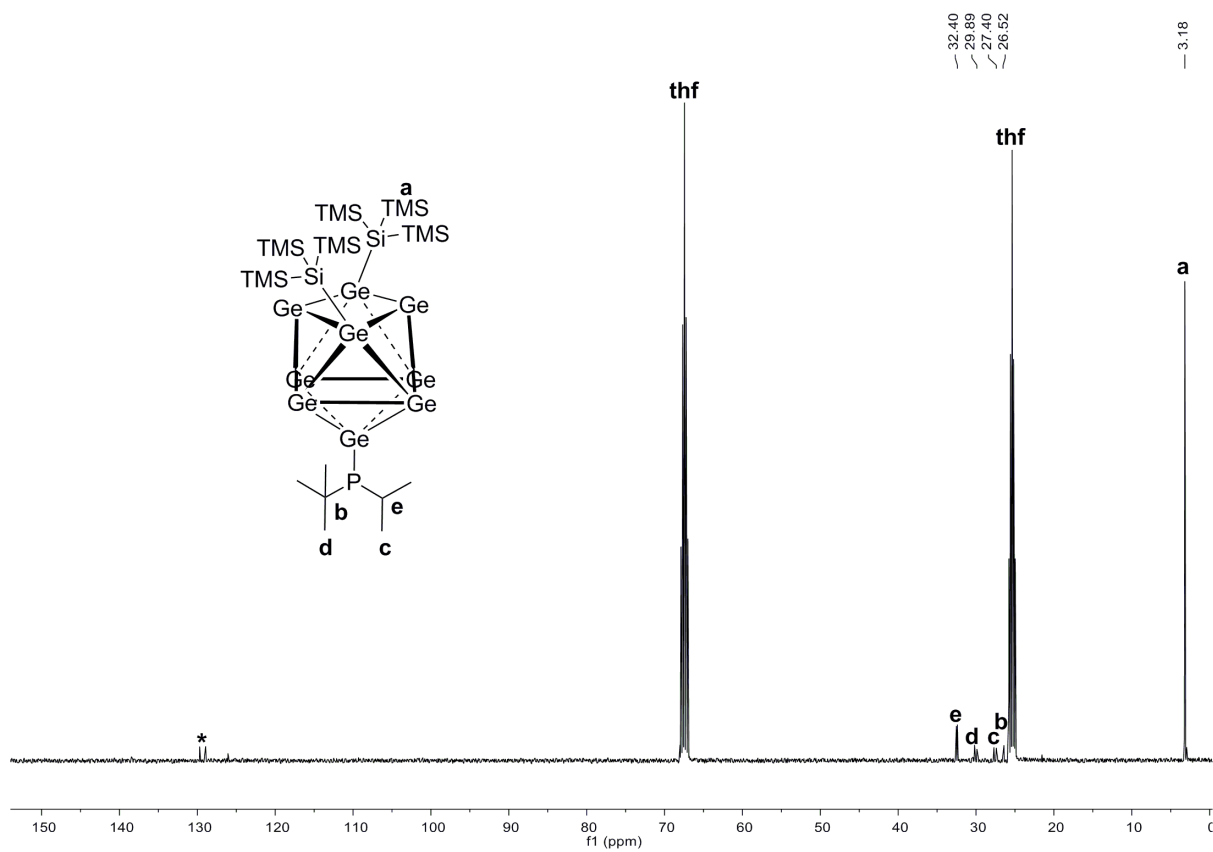


Figure S25: ^{13}C NMR spectrum of compound **4a** in $\text{thf-}d_8$.

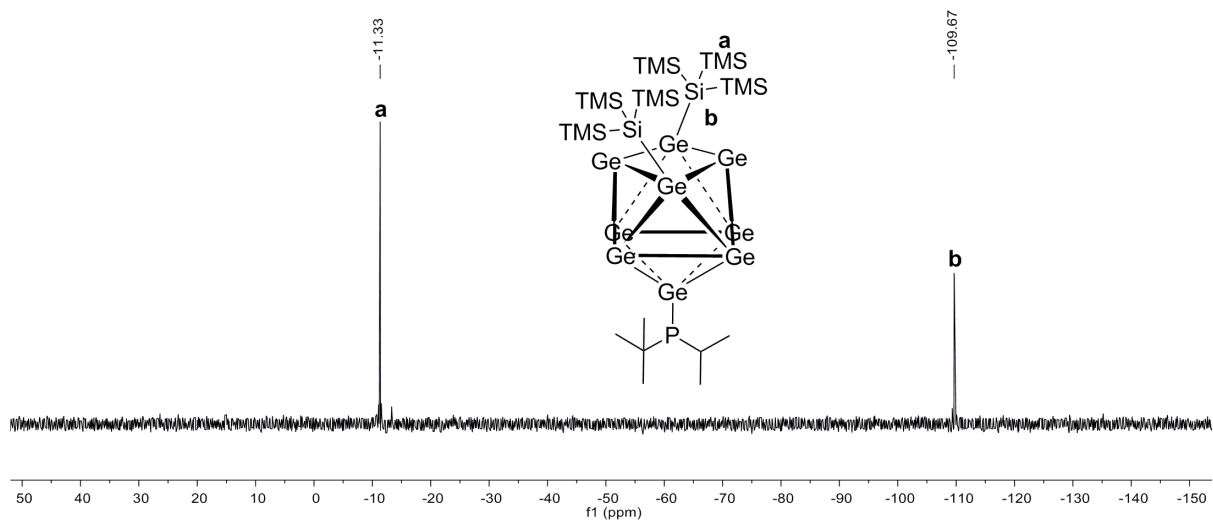


Figure S26: ^{29}Si -INEPT-RD NMR spectrum of compound **4a** in $\text{thf-}d_8$.

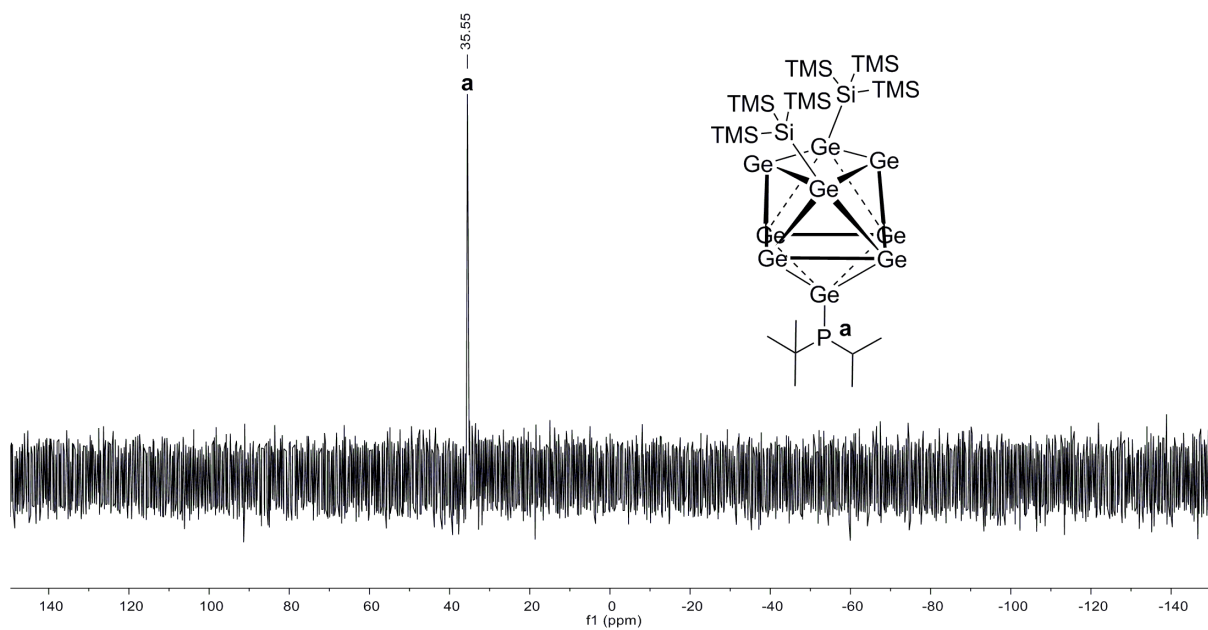


Figure S27: ^{31}P NMR spectrum of compound **4a** in $\text{thf-}d_8$.

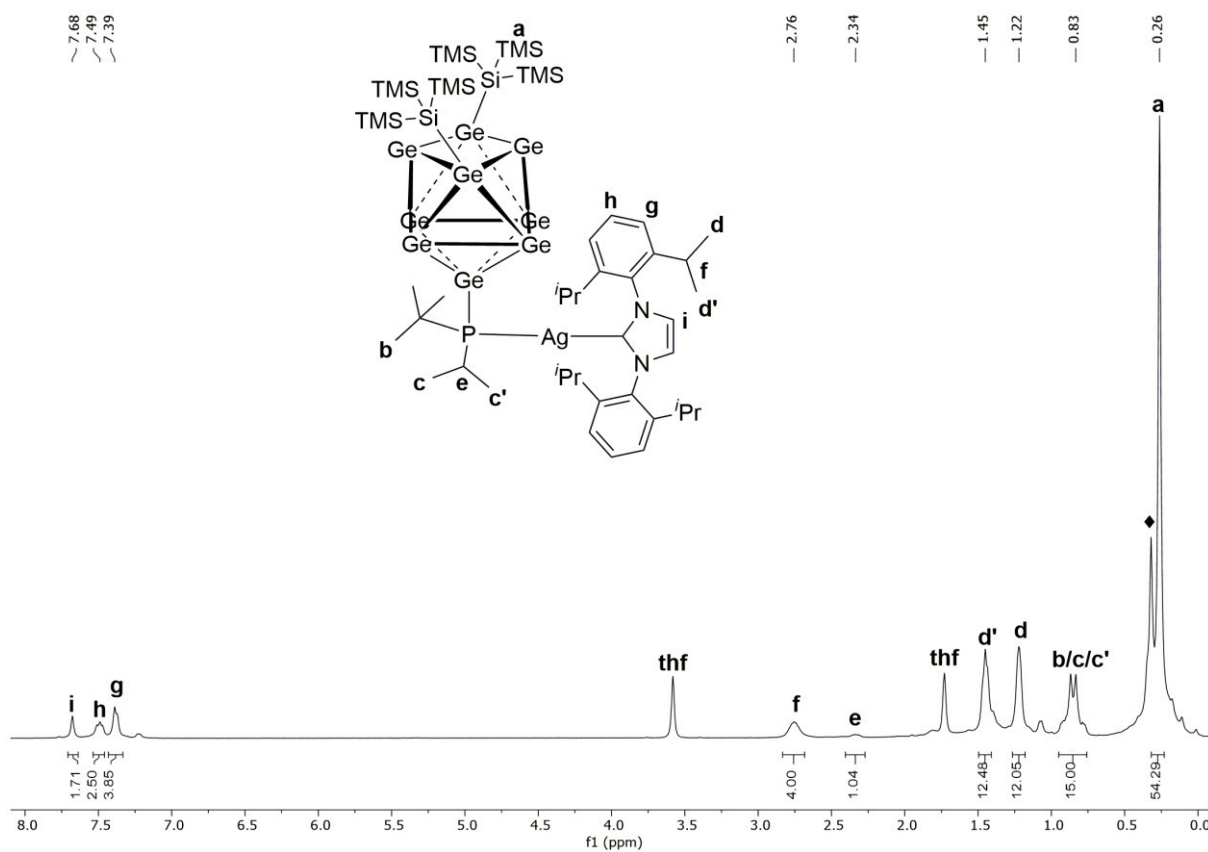


Figure S28: ^1H NMR spectrum of compound **4-AgNHC^{Dipp}** in $\text{thf-}d_8$ (signal marked with \blacklozenge belongs to an unidentified impurity).

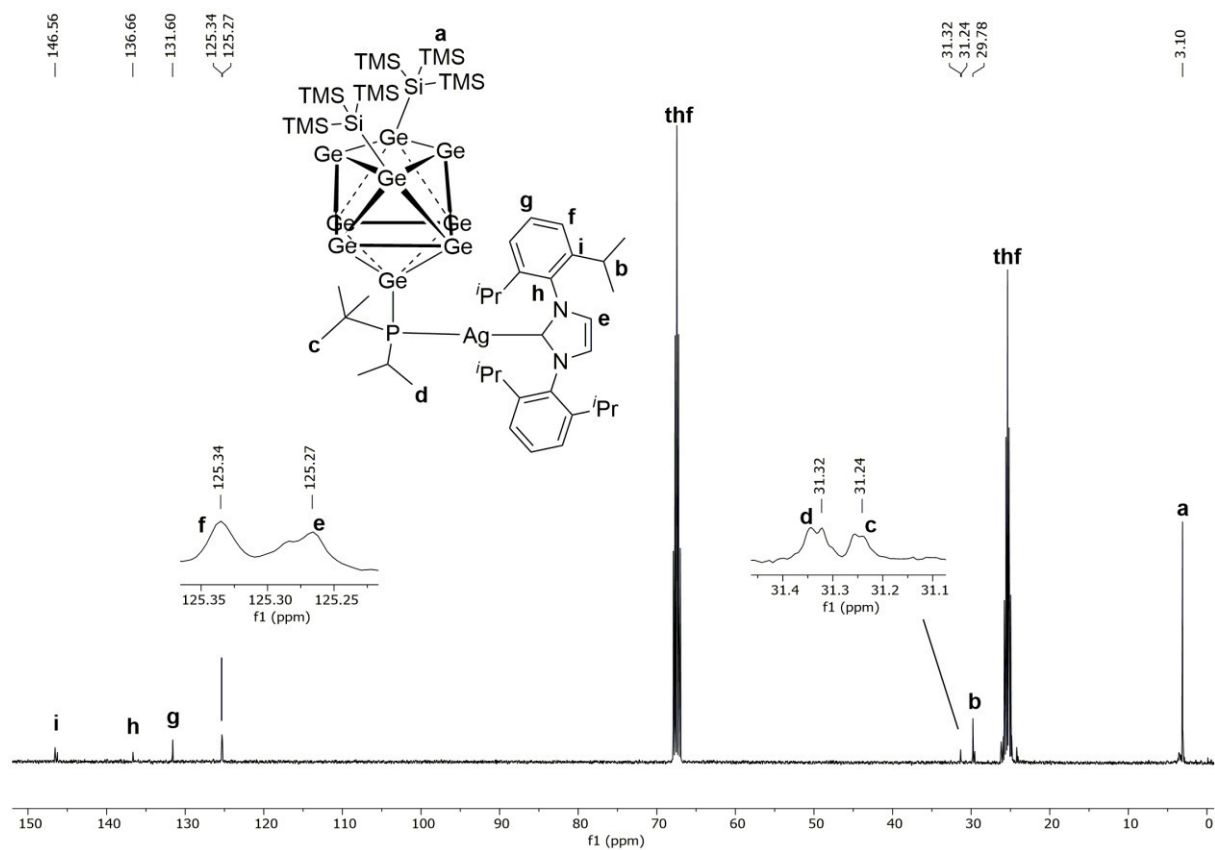


Figure S29: ¹³C NMR spectrum of compound **4-AgNHC^{Dipp}** in thf-*d*₈.

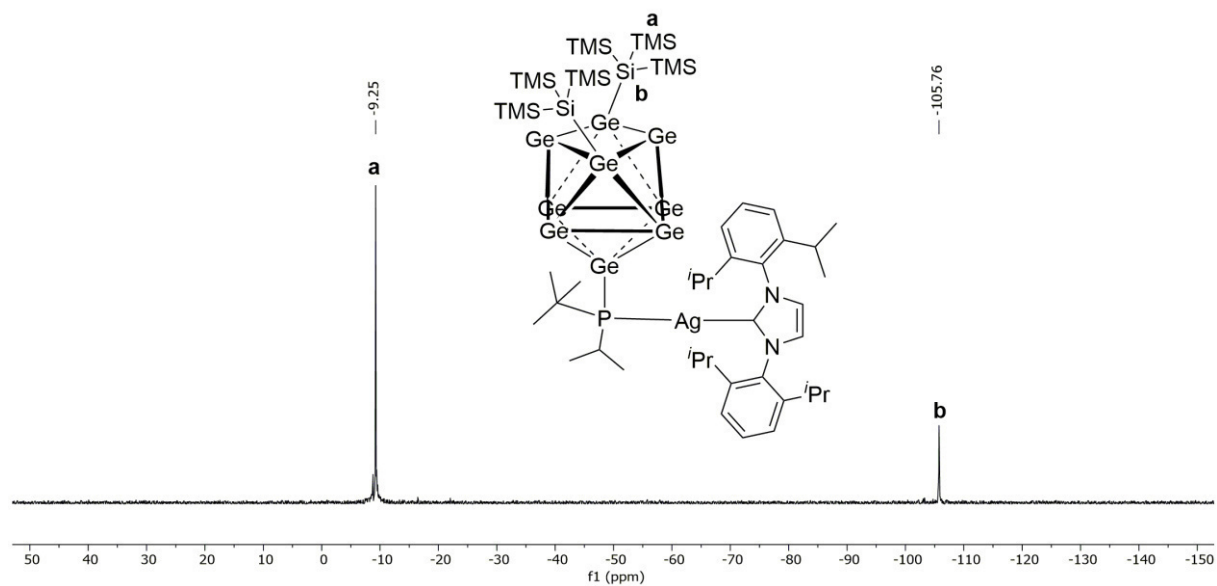


Figure S30: ²⁹Si-INEPT-RD NMR spectrum of compound **4-AgNHC^{Dipp}** in thf-*d*₈.

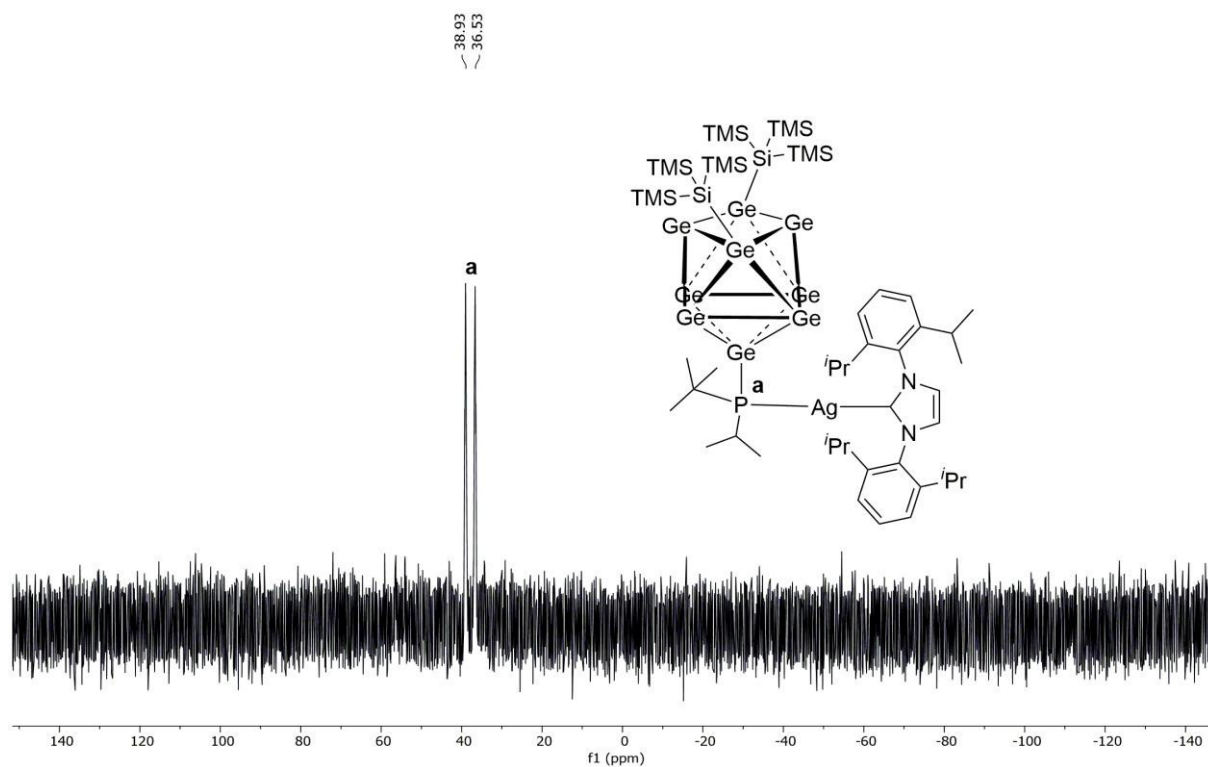


Figure S31: ^{31}P NMR spectrum of compound **4-AgNHC^{Dipp}** in $\text{thf-}d_8$.

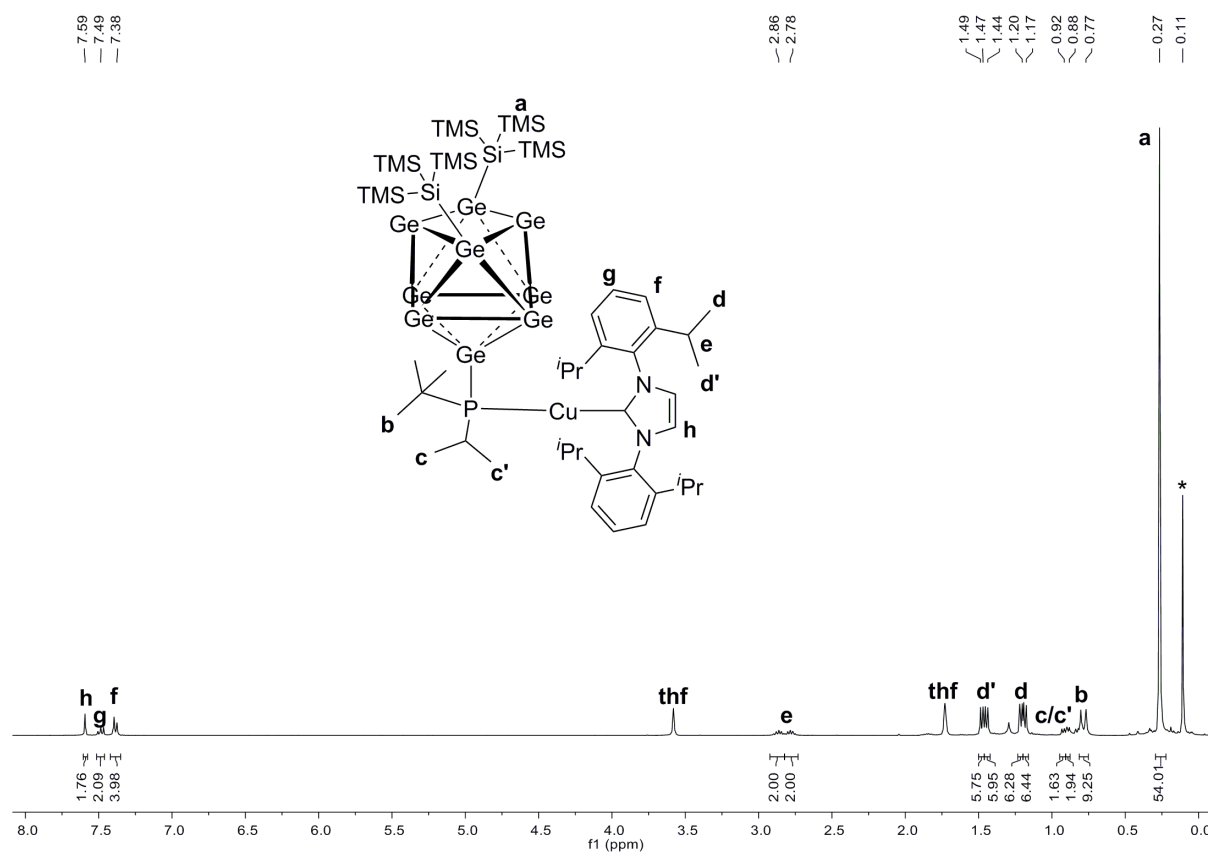


Figure S32: ^1H NMR spectrum of compound **4-CuNHC^{Dipp}** in $\text{thf-}d_8$ (signal marked with * belongs to silicon grease).

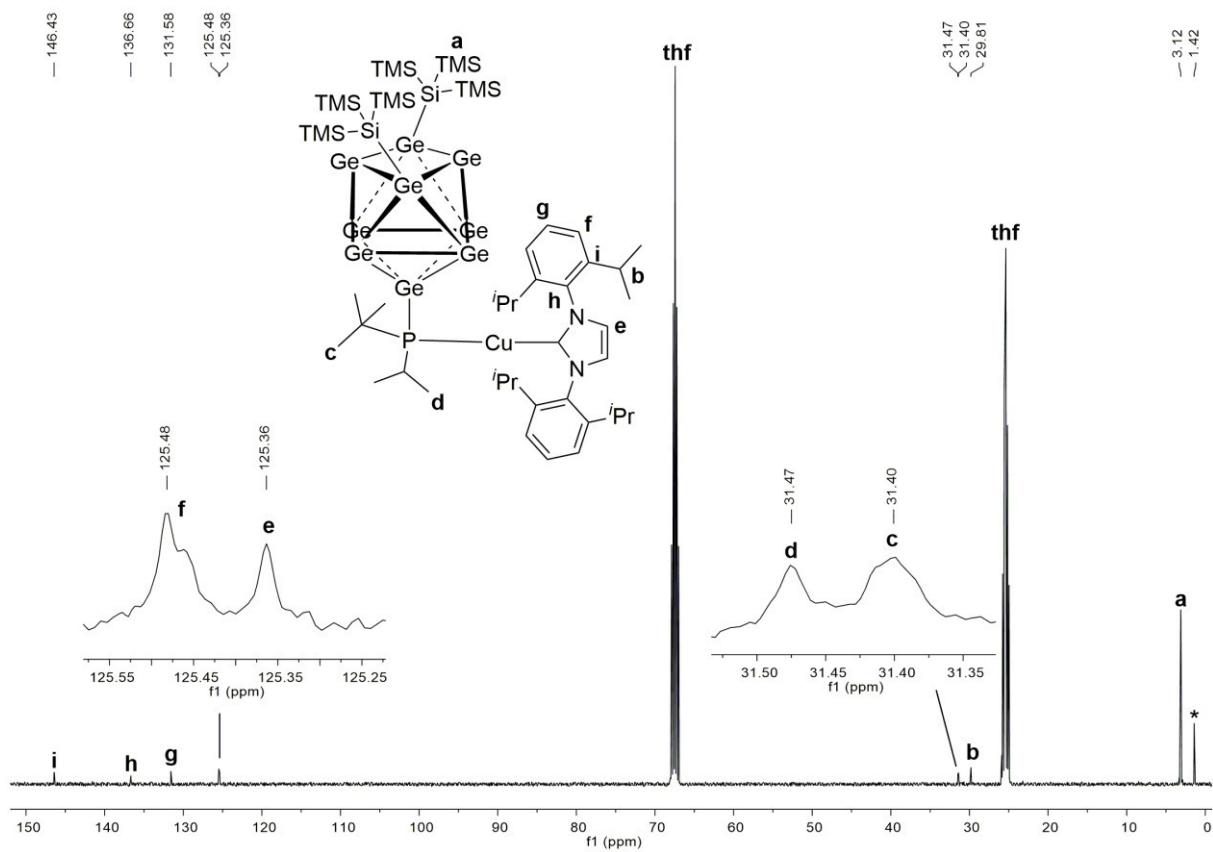


Figure S33: ^{13}C NMR spectrum of compound **4-CuNHC^{Dipp}** in $\text{thf-}d_8$ (signal marked with * belongs to silicon grease).

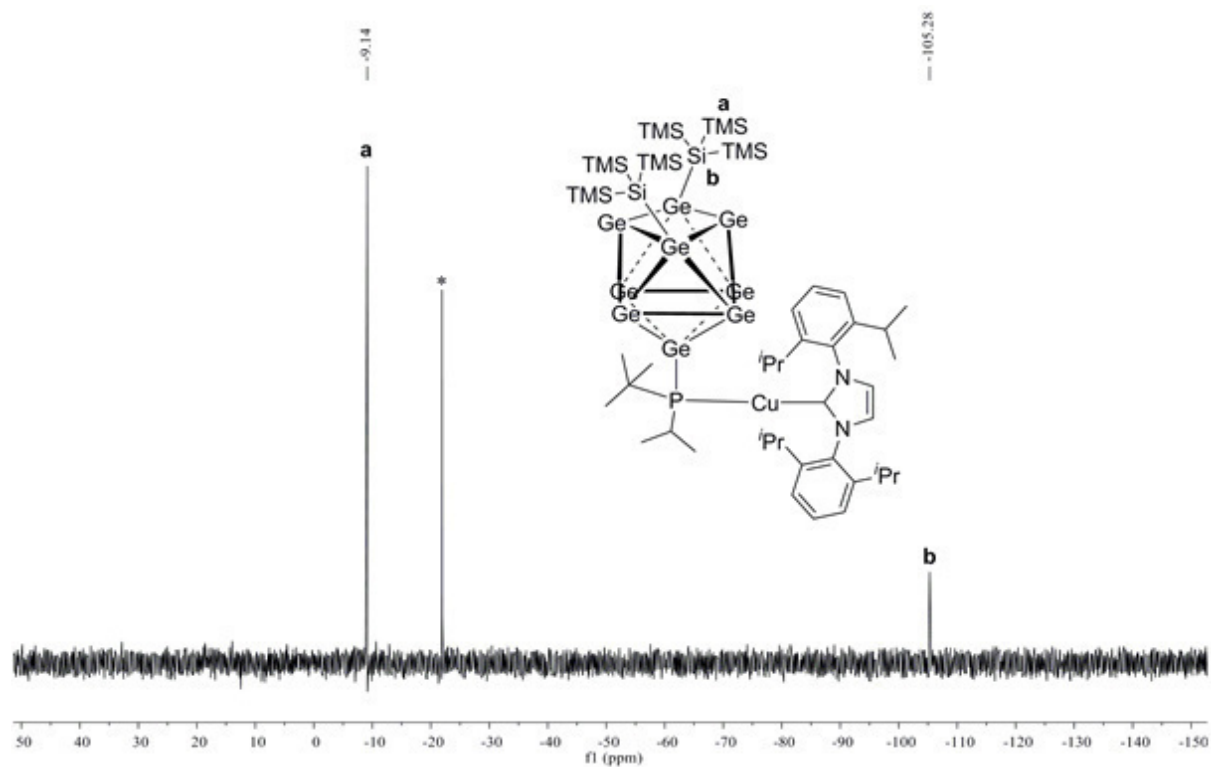


Figure S34: ^{29}Si -INEPT-RD NMR spectrum of compound **4-CuNHC^{Dipp}** in $\text{thf-}d_8$ (signal marked with * belongs to silicon grease).

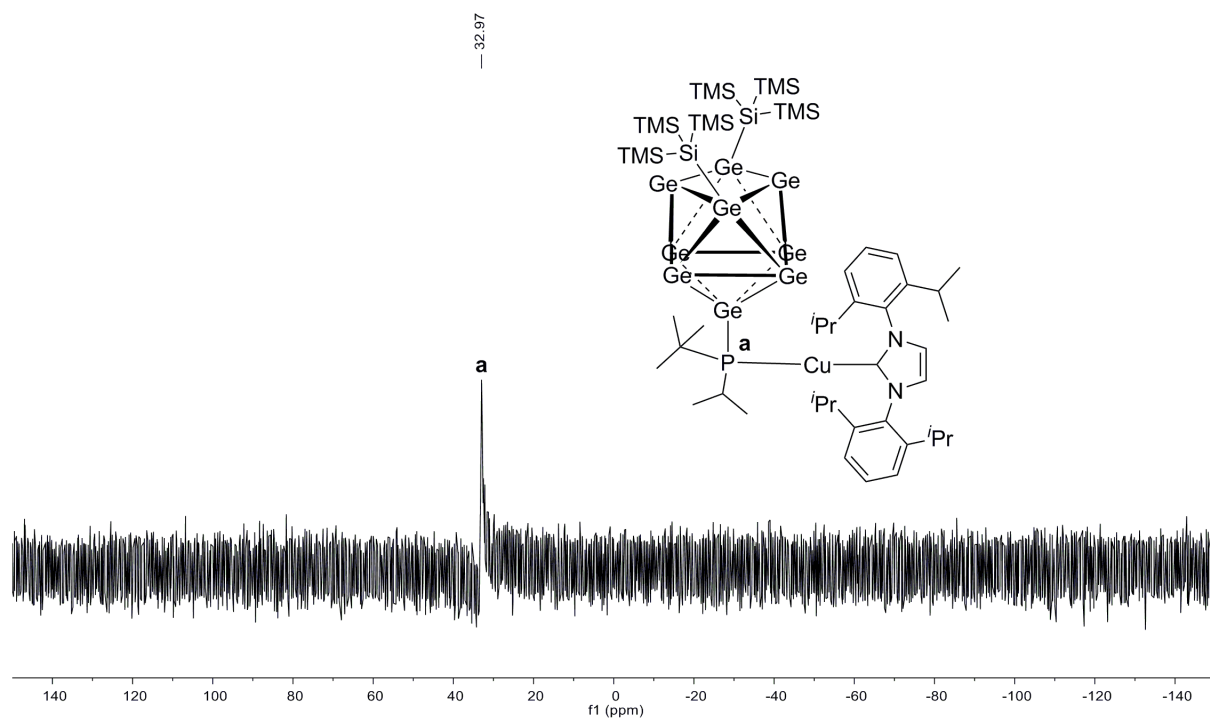


Figure S35: ^{31}P NMR spectrum of compound **4-CuNHC^{DIPP}** in $\text{thf-}d_8$.

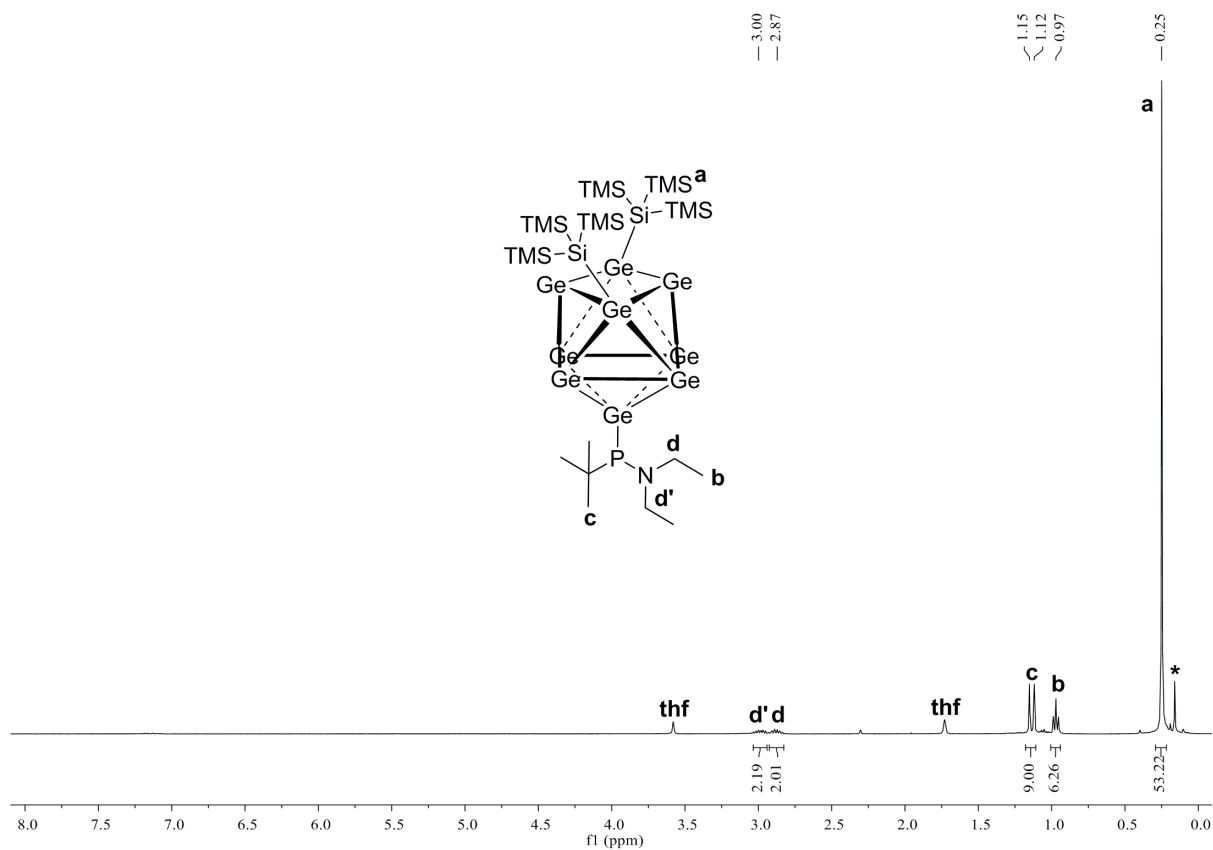


Figure S36: ¹H NMR spectrum of compound **5a** in thf-*d*₈ (signal marked with * belongs to unidentified impurity).

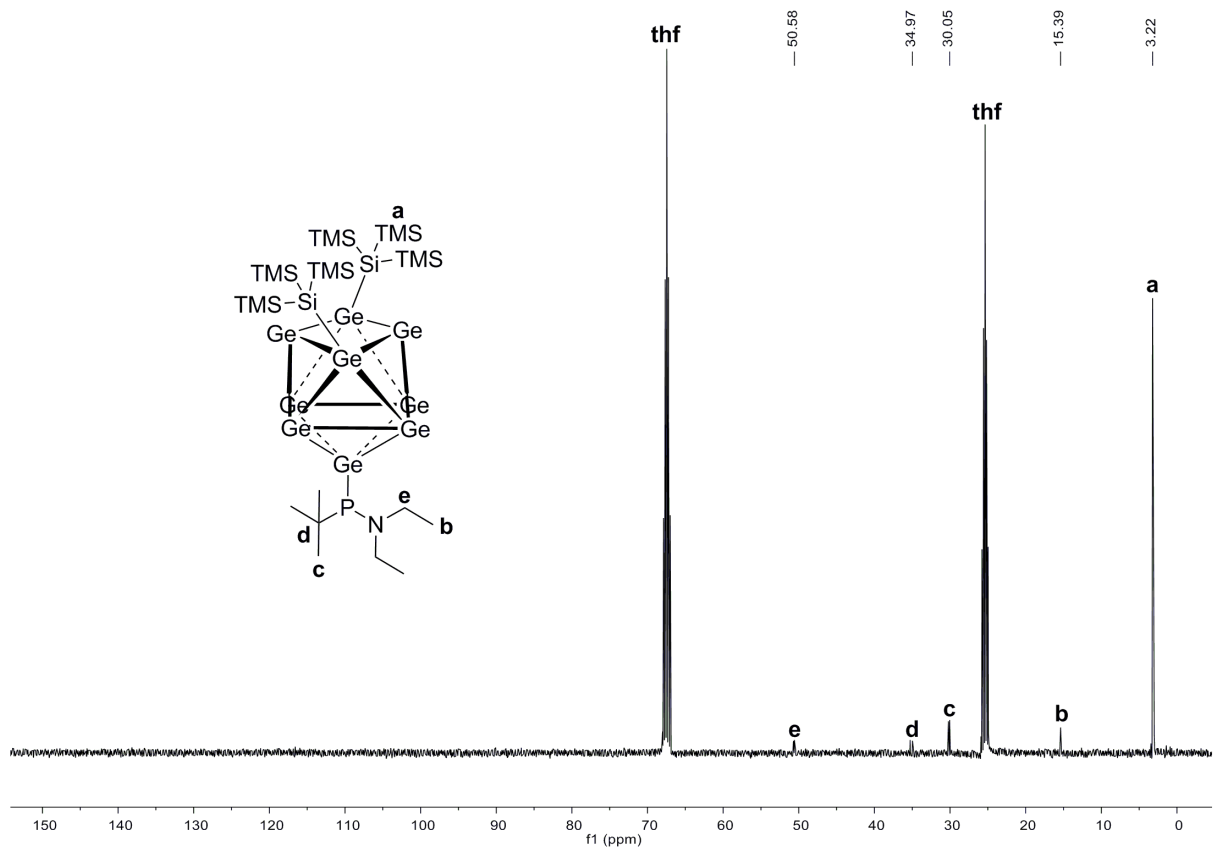


Figure S37: ¹³C NMR spectrum of compound **5a** in thf-*d*₈.

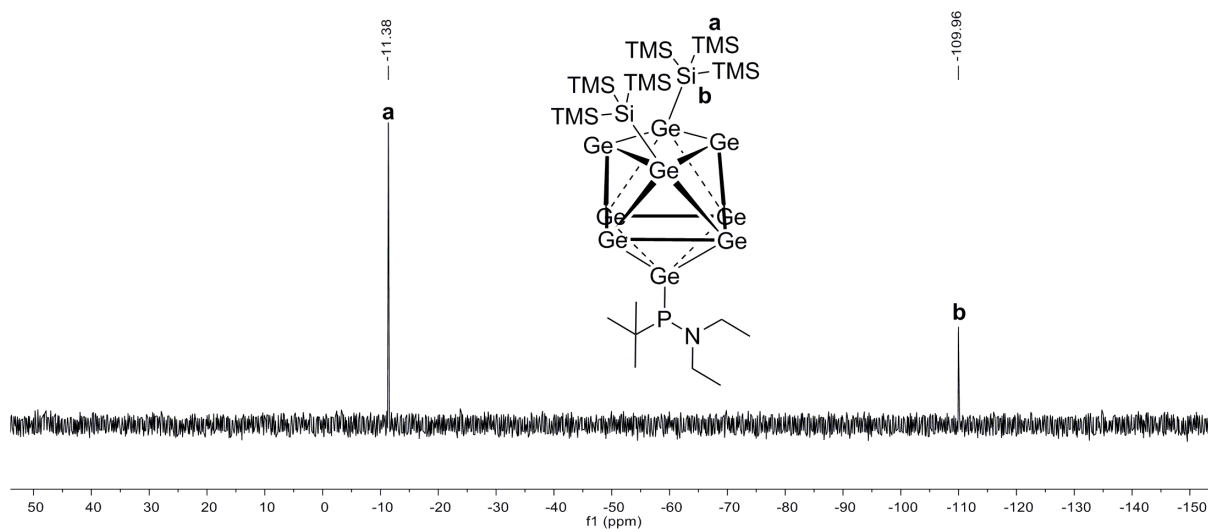


Figure S38: ^{29}Si -INEPT-RD NMR spectrum of compound **5a** in $\text{thf-}d_8$.

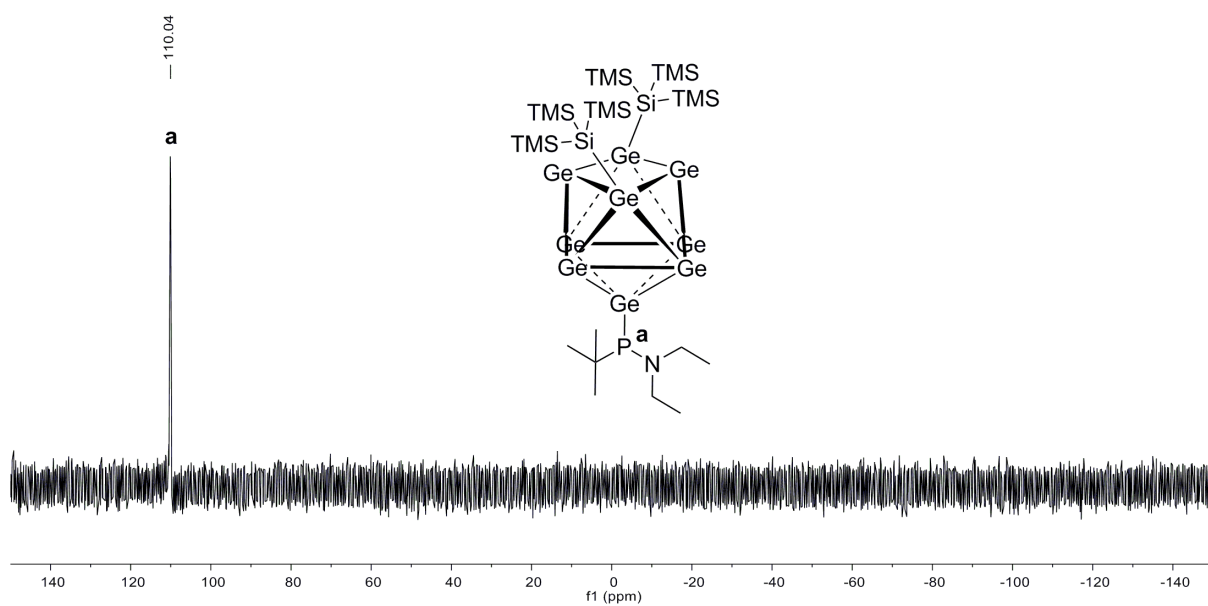


Figure S39: ^{31}P NMR spectrum of compound **5a** in $\text{thf-}d_8$.

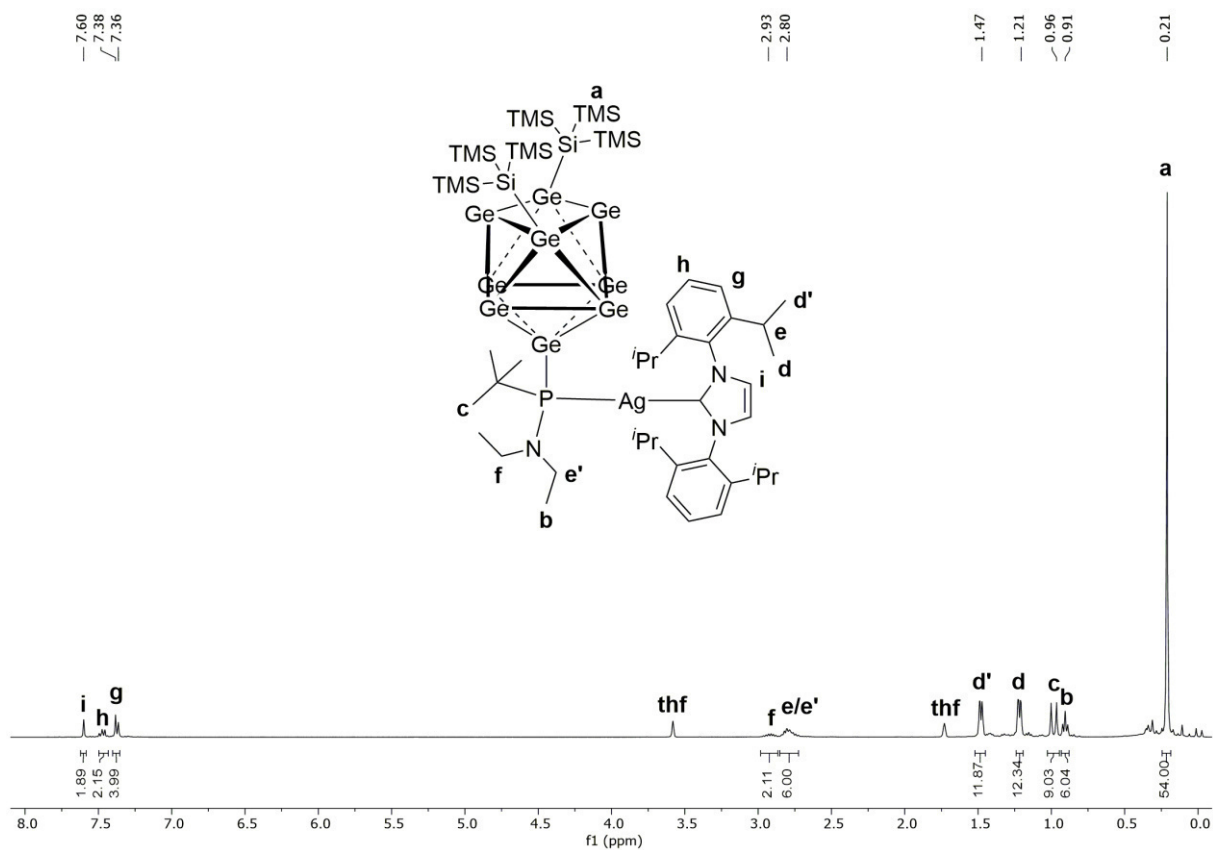


Figure S40: ¹H NMR spectrum of compound **5-AgNHC^{Dipp}** in thf-*d*₈.

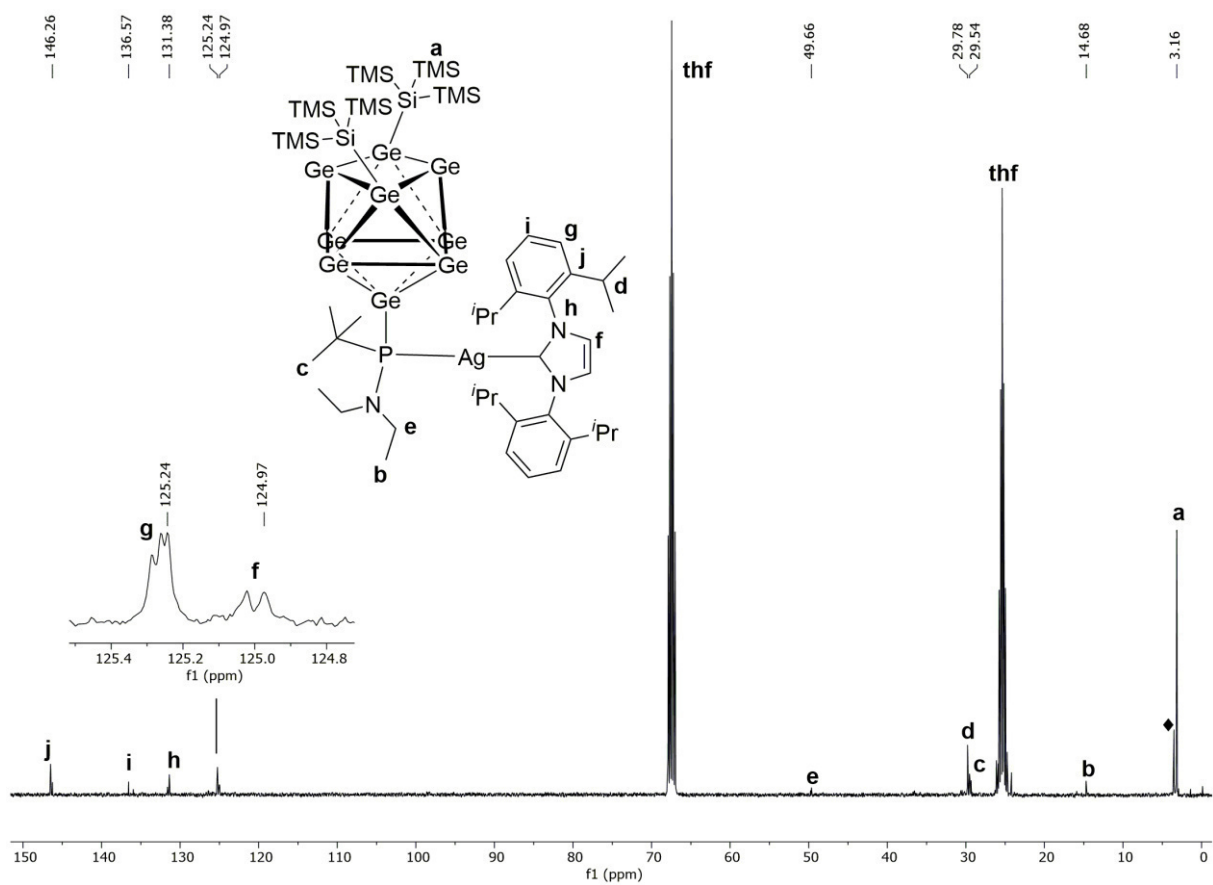


Figure S41: ¹³C NMR spectrum of compound **5-AgNHC^{Dipp}** in thf-*d*₈.

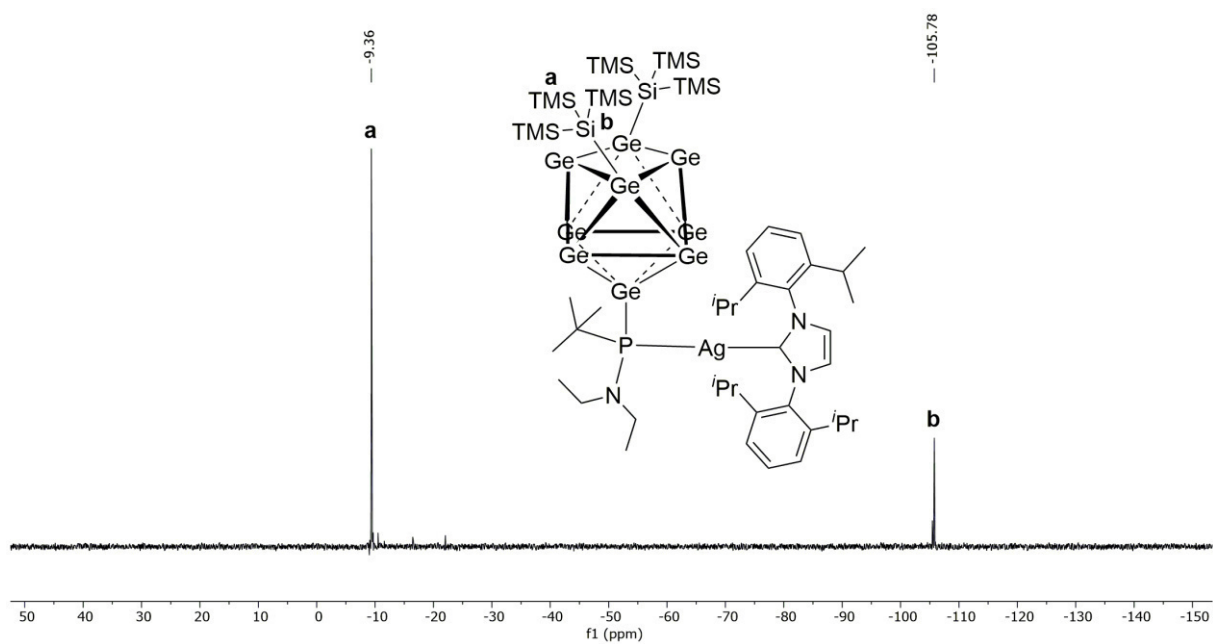


Figure S42: ^{29}Si -INEPT-RD NMR spectrum of compound **5-AgNHC^{Dipp}** in $\text{thf-}d_8$.

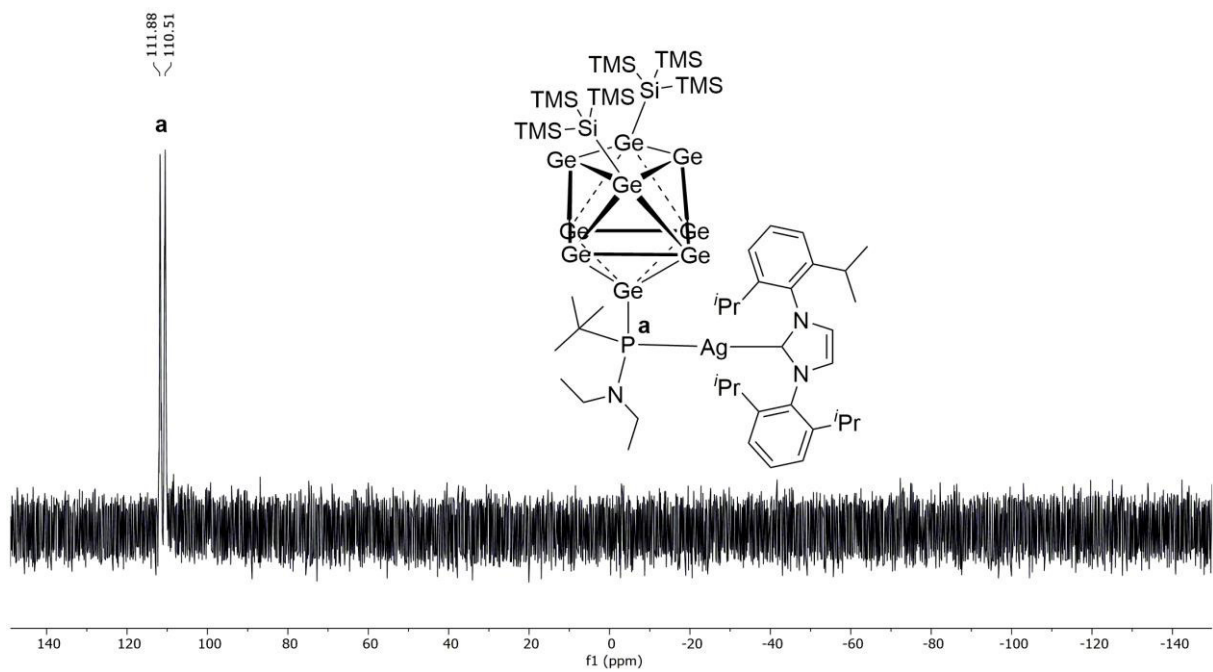


Figure S43: ^{31}P NMR spectrum of compound **5-AgNHC^{Dipp}** in $\text{thf-}d_8$.

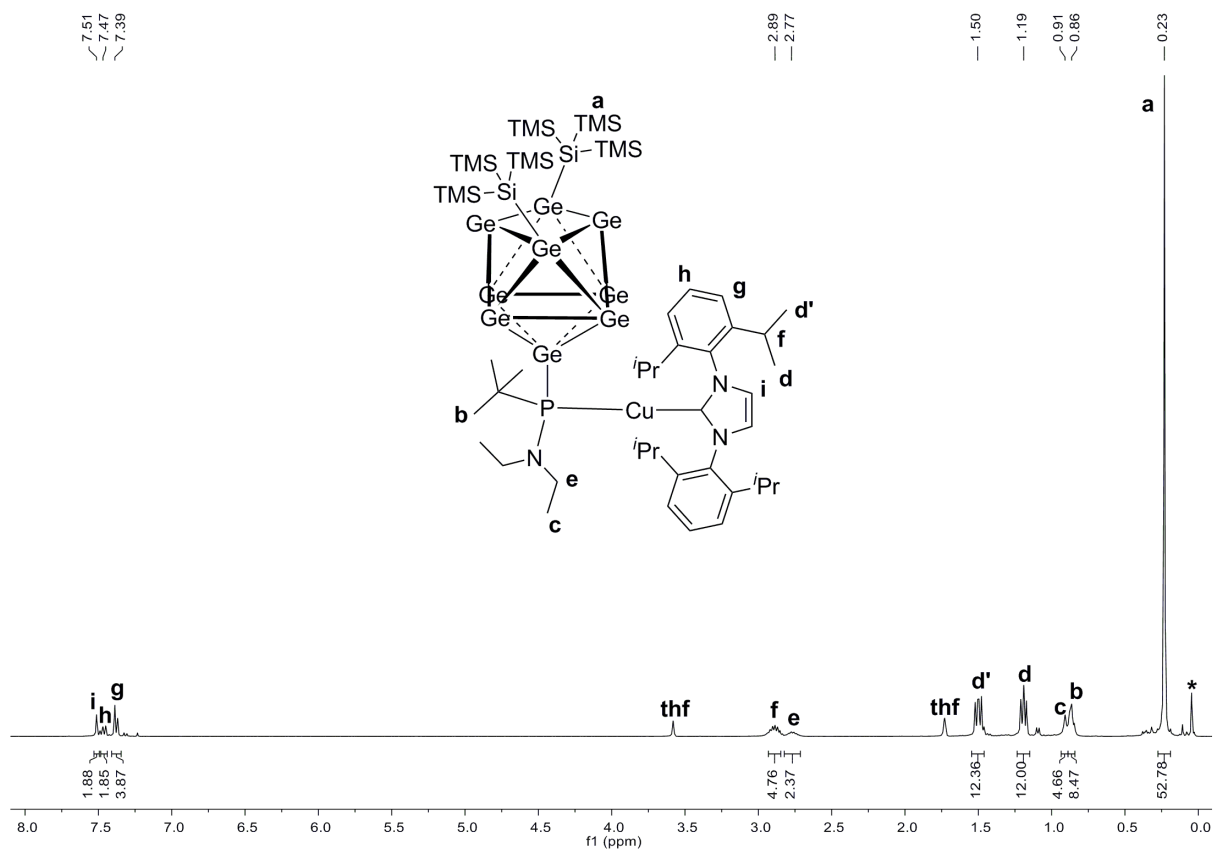


Figure S44: ¹H NMR spectrum of compound **5-CuNHC^{DiPP}** in thf-*d*₈ (signal marked with * belongs to an unidentified impurity).

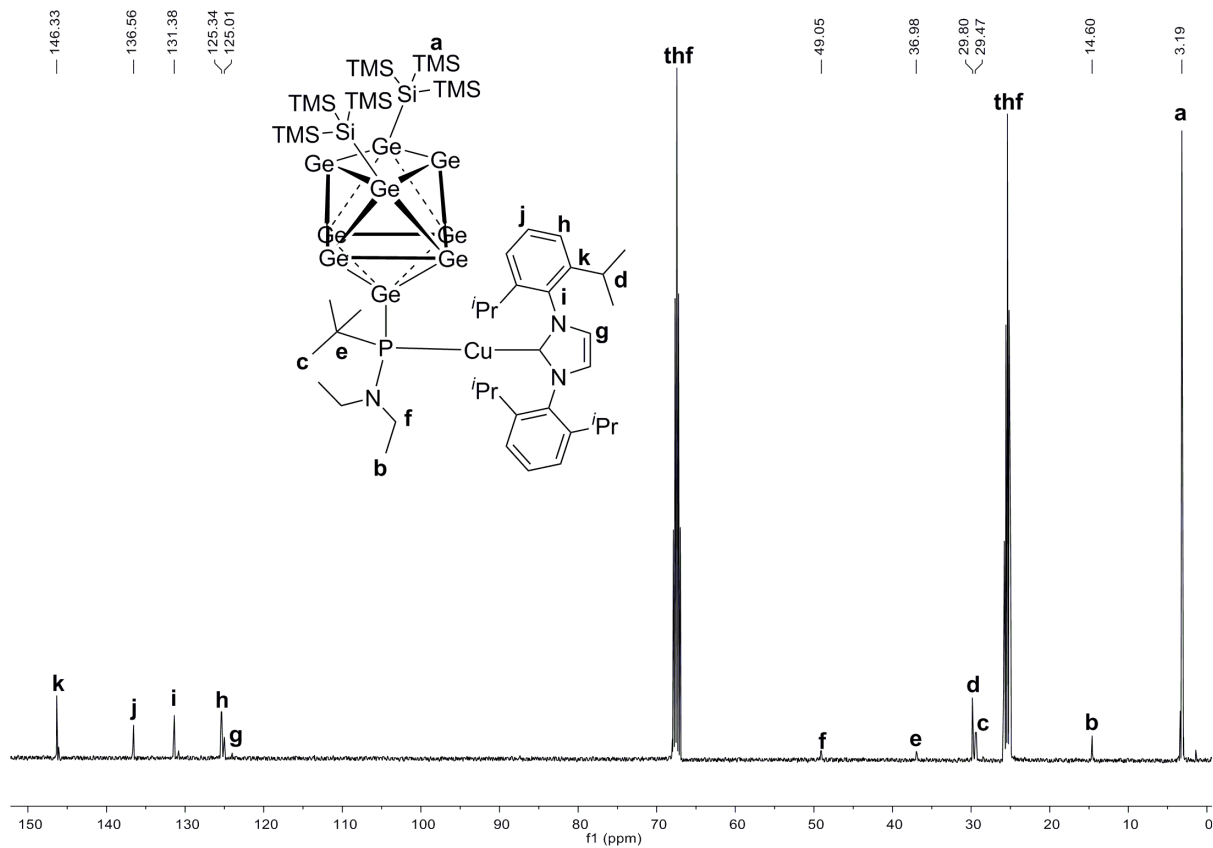
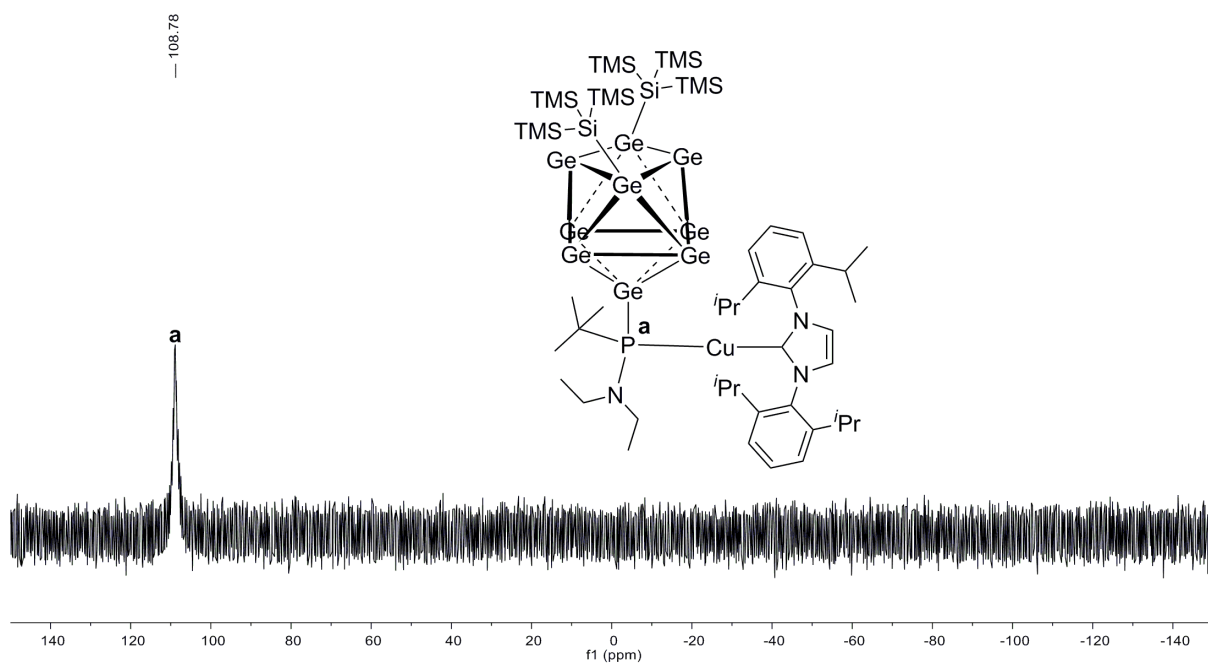
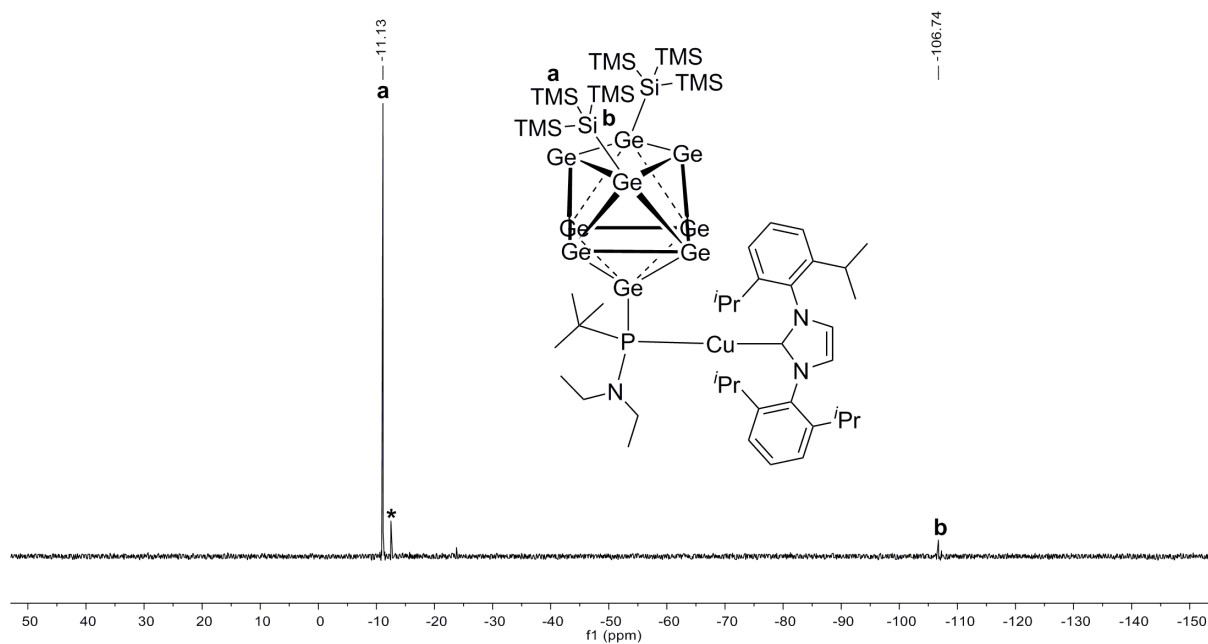


Figure S45: ¹³C NMR spectrum of compound **5-CuNHC^{DiPP}** in thf-*d*₈.



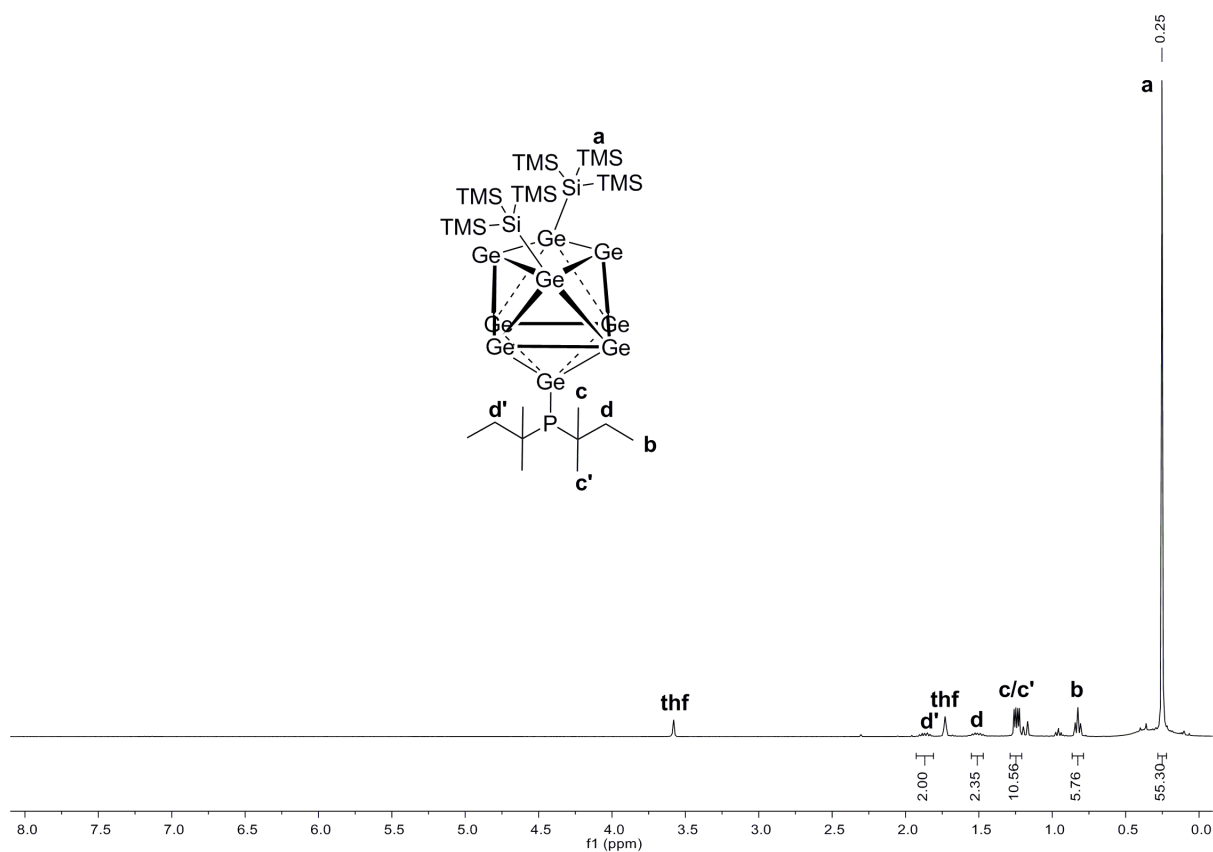


Figure S48: ^1H NMR spectrum of compound **6a** in thf-d_8 .

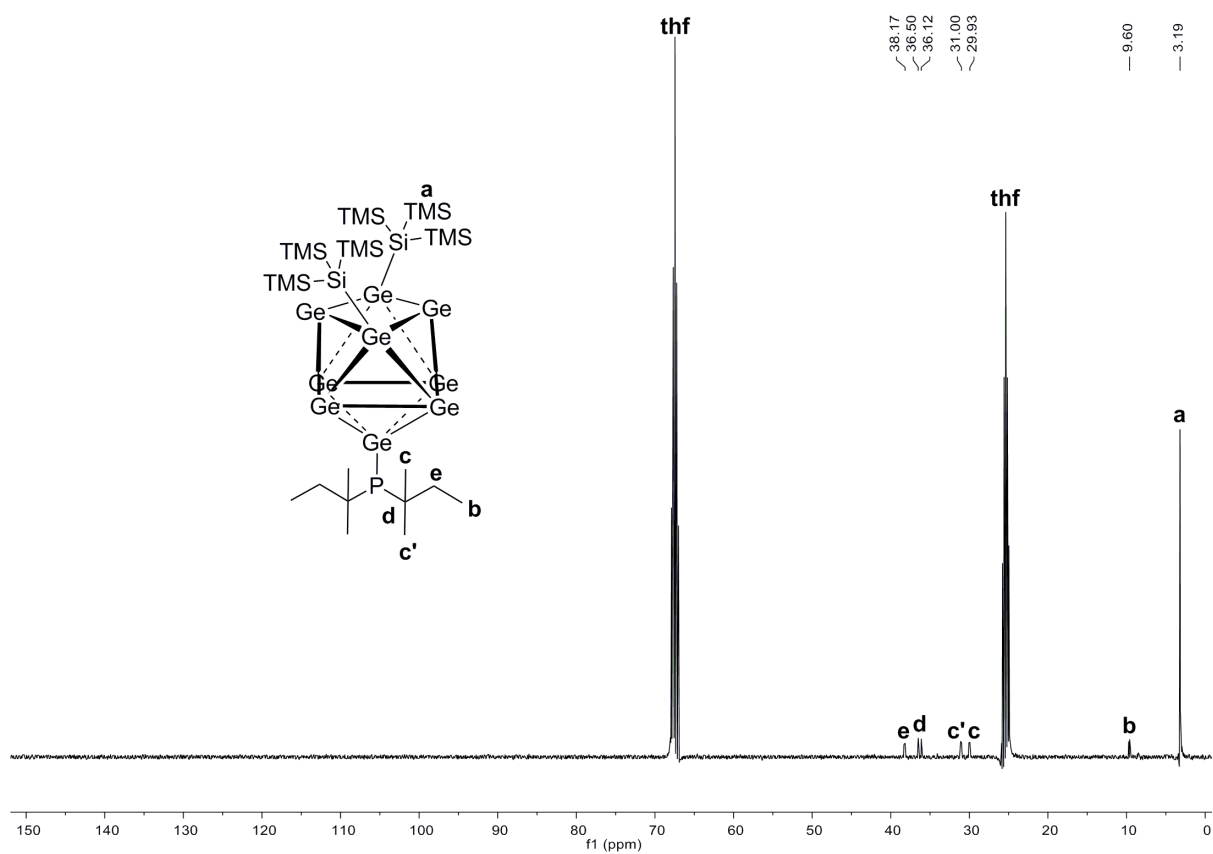


Figure S49: ^{13}C NMR spectrum of compound **6a** in thf-d_8 .

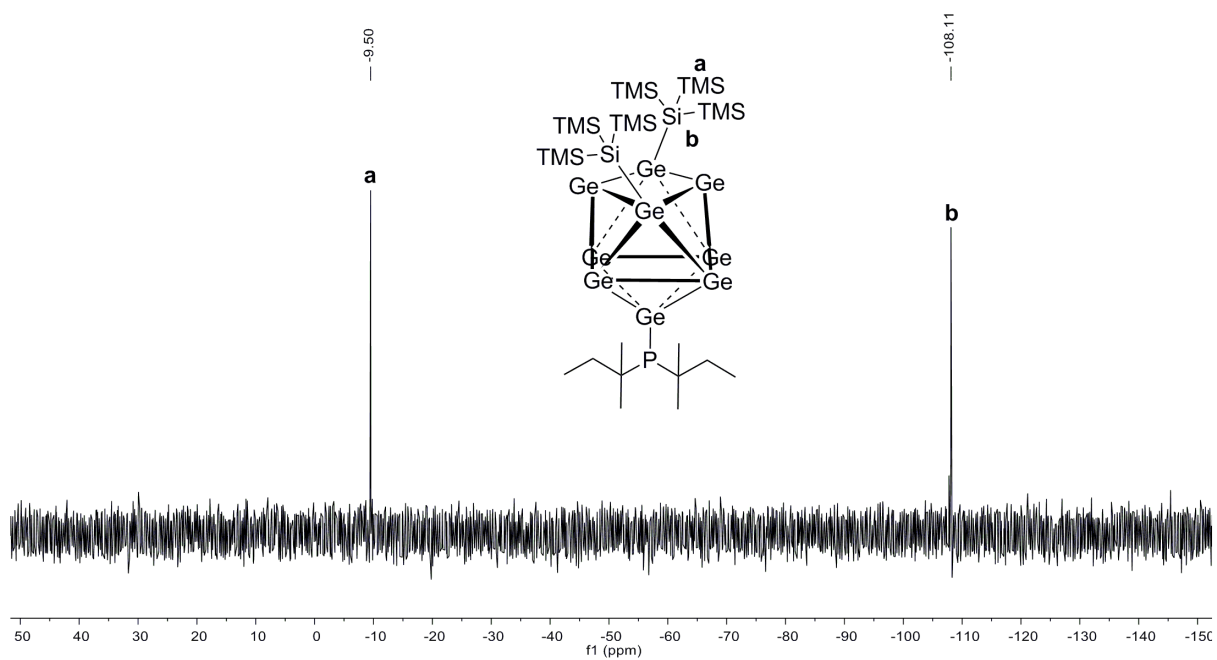


Figure S50: ^{29}Si -INEPT-RD NMR spectrum of compound **6a** in $\text{thf-}d_8$.

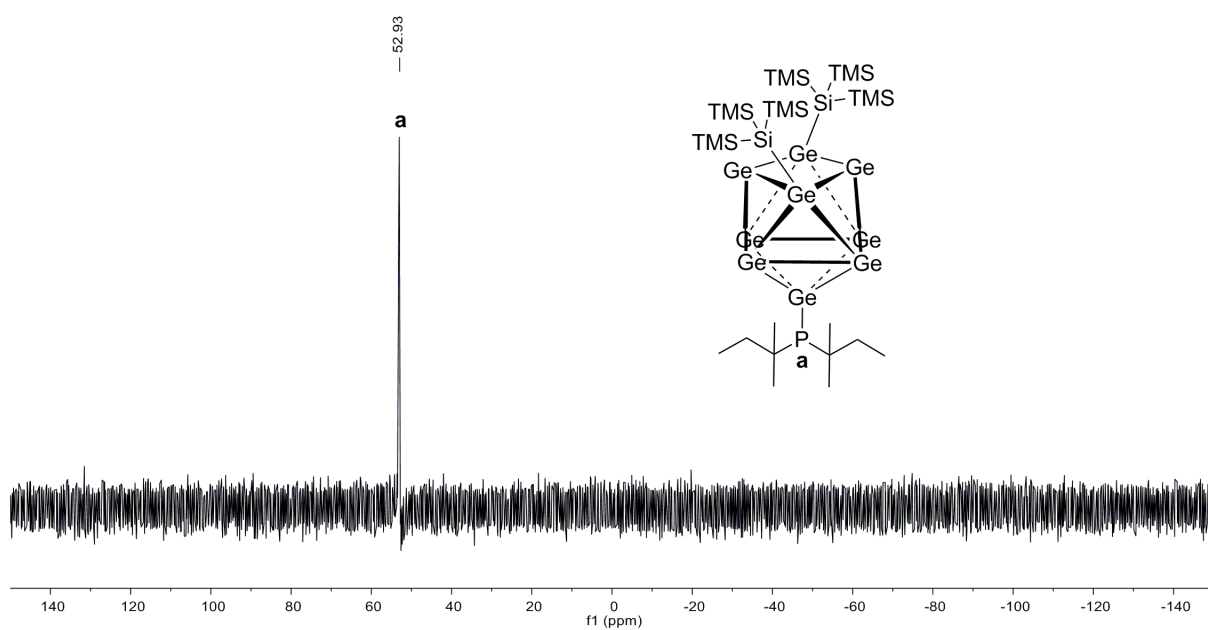


Figure S51: ^{31}P NMR spectrum of compound **6a** in $\text{thf-}d_8$

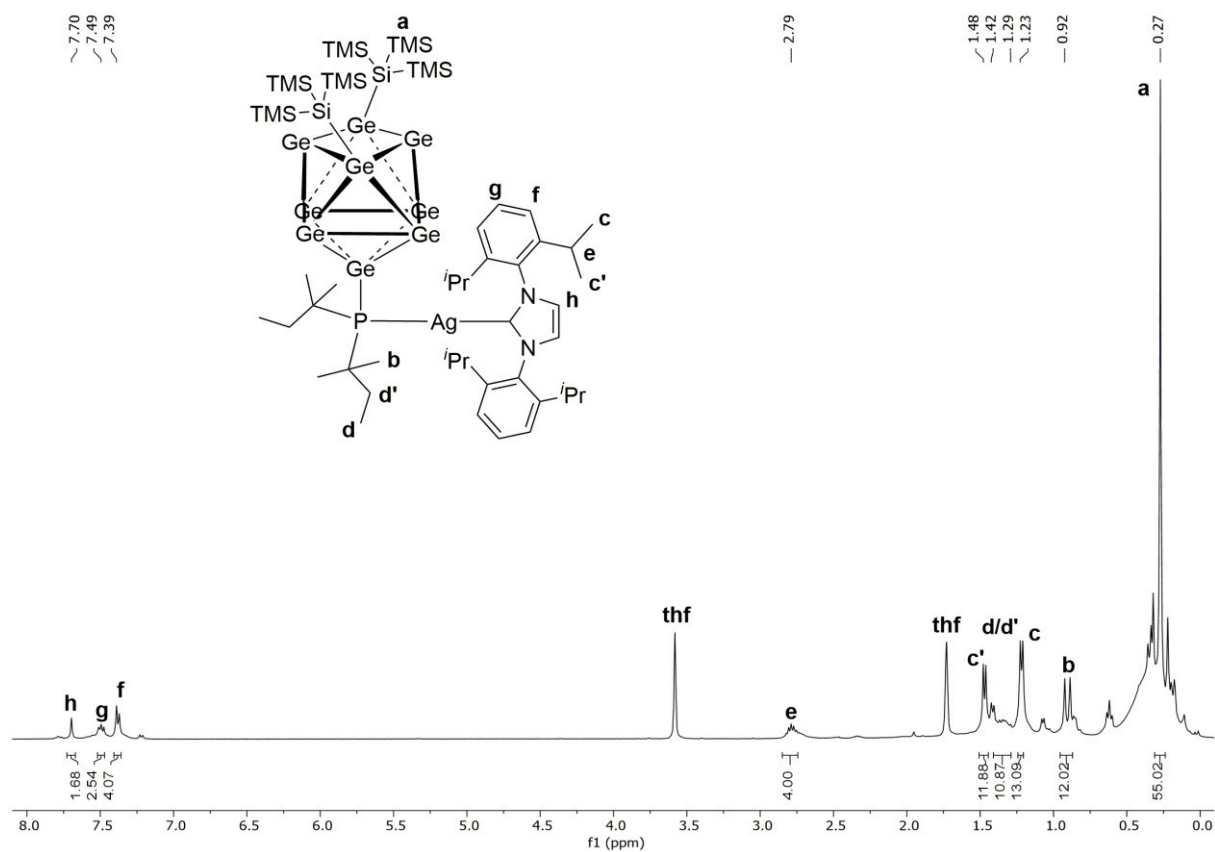


Figure S52: ¹H NMR spectrum of compound **6-AgNHC^{Dipp}** in thf-*d*₈.

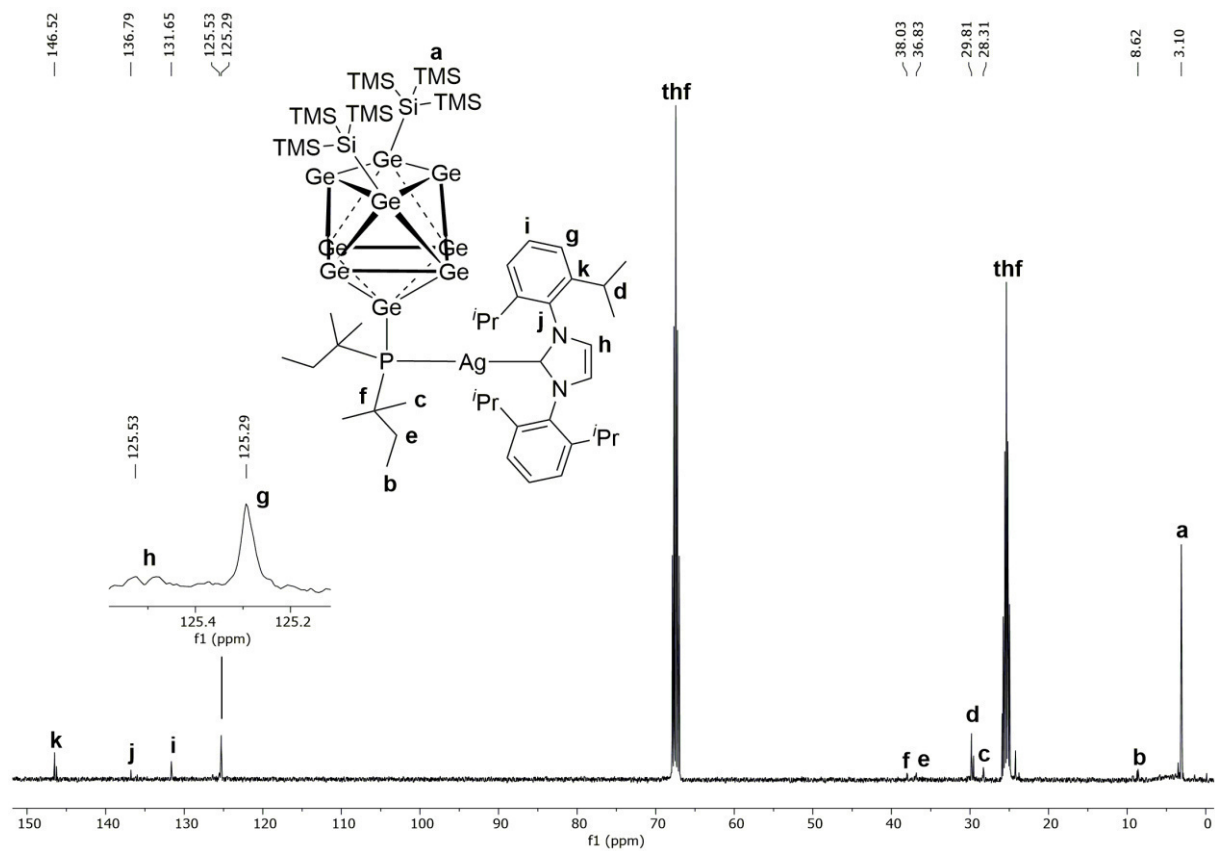


Figure S53: ¹³C NMR spectrum of compound **6-AgNHC^{Dipp}** in thf-*d*₈.

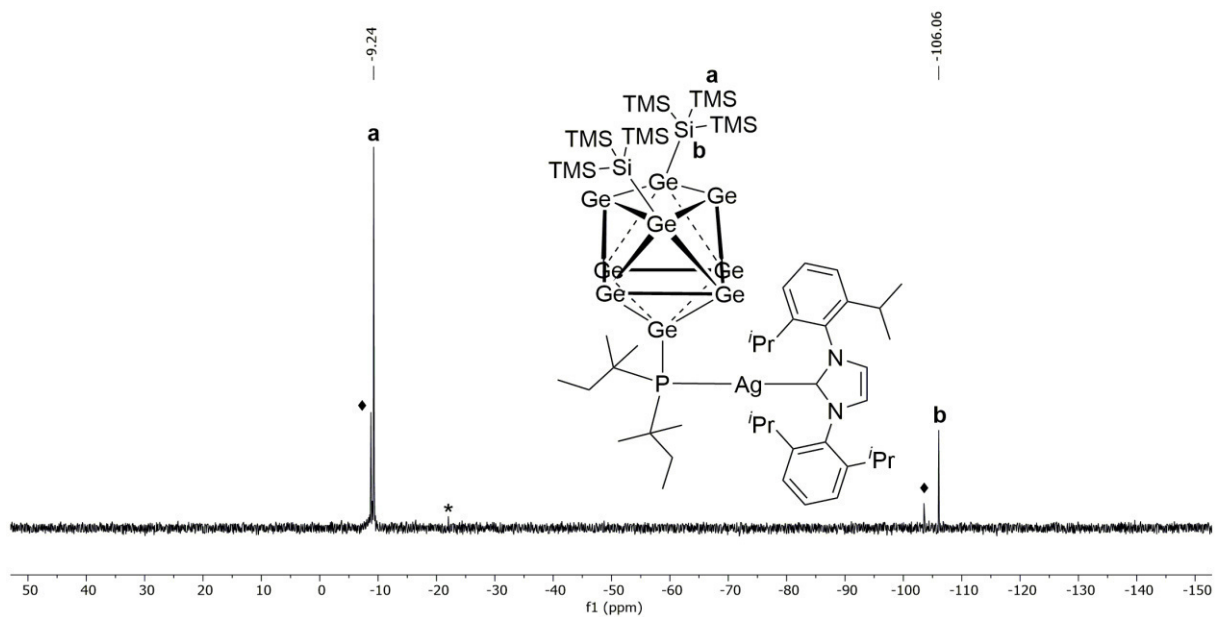


Figure S54: ^{29}Si -INEPT-RD NMR spectrum of compound **6-AgNHC^{DIPP}** in $\text{thf-}d_8$ (signal marked with * belongs to silicon grease, signals marked with ♦ belong to unidentified impurities.)

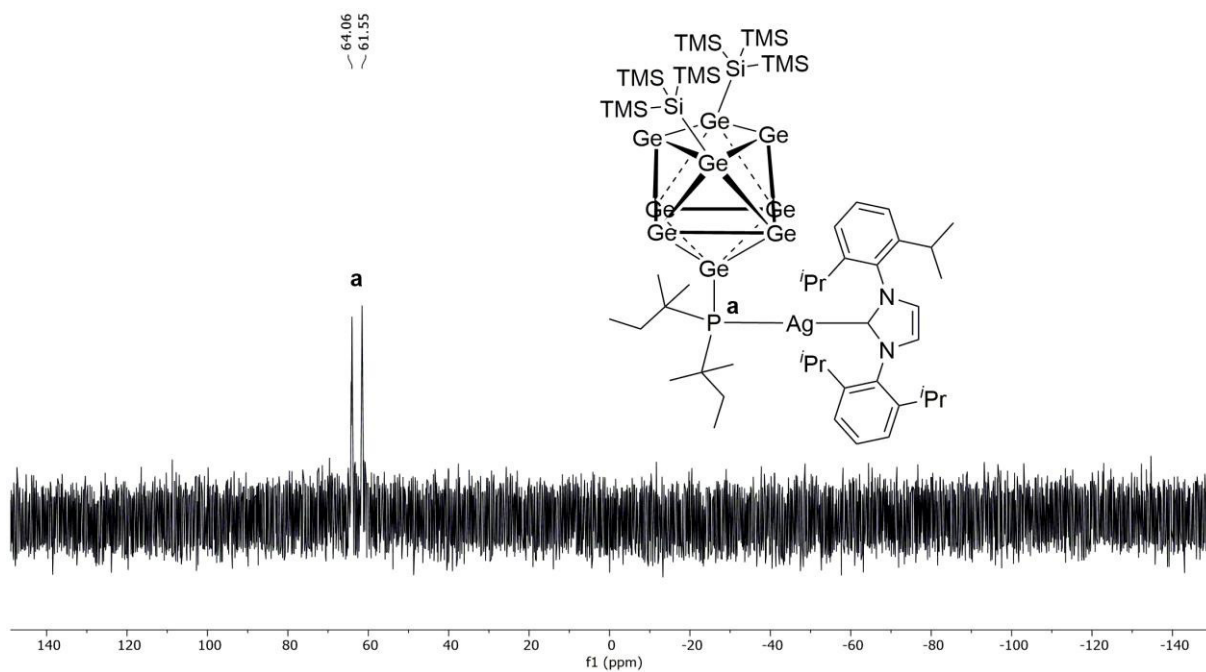


Figure S55: ^{31}P NMR spectrum of compound **6-AgNHC^{DIPP}** in $\text{thf-}d_8$.

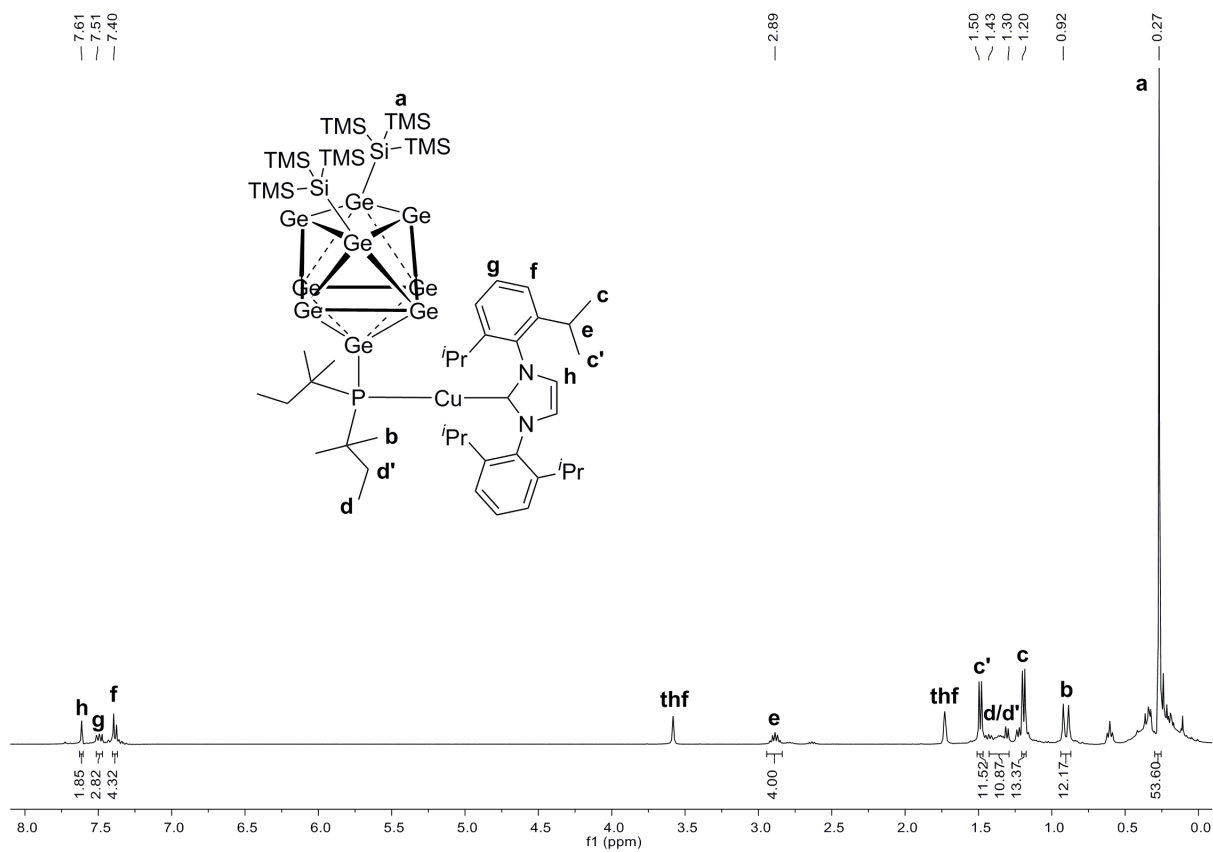


Figure S56: ¹H NMR spectrum of compound **6-CuNHC^{Dipp}** in thf-*d*₈.

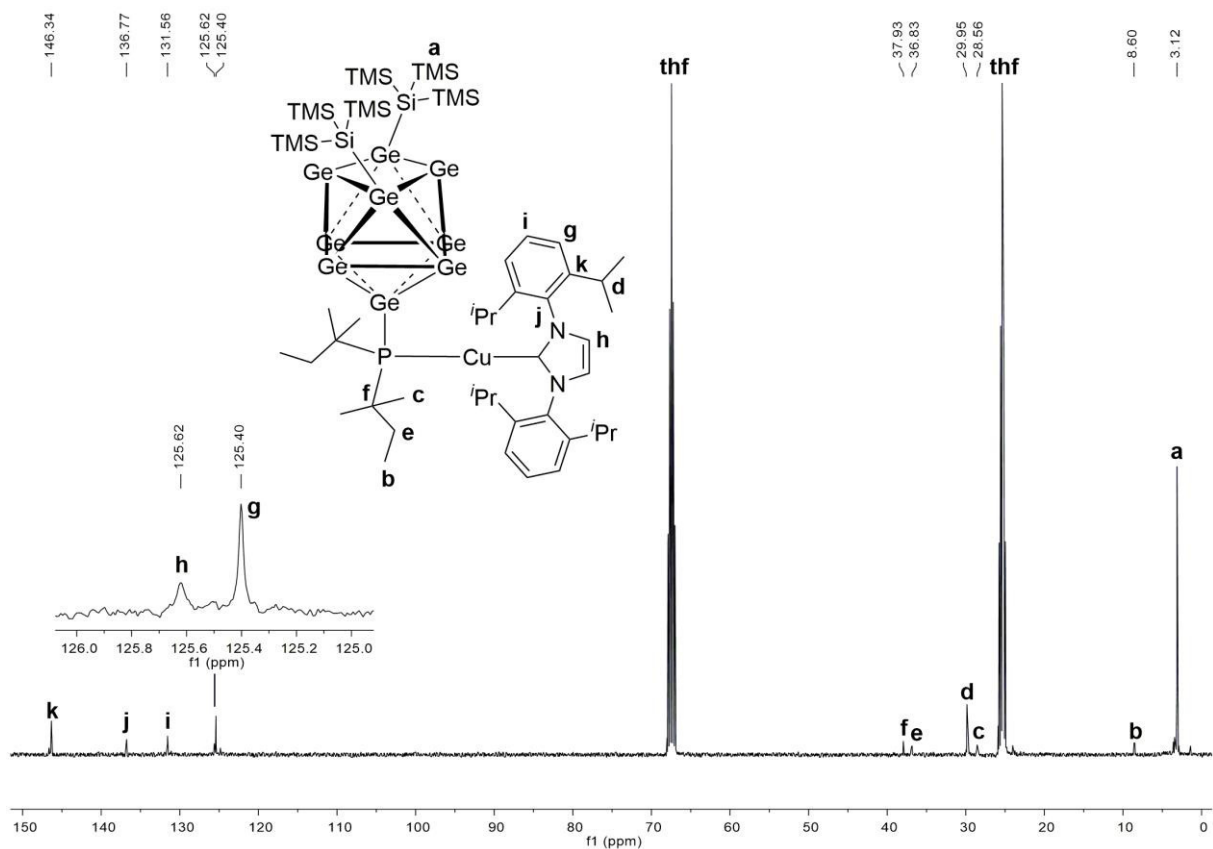


Figure S57: ¹³C NMR spectrum of compound **6-CuNHC^{Dipp}** in thf-*d*₈.

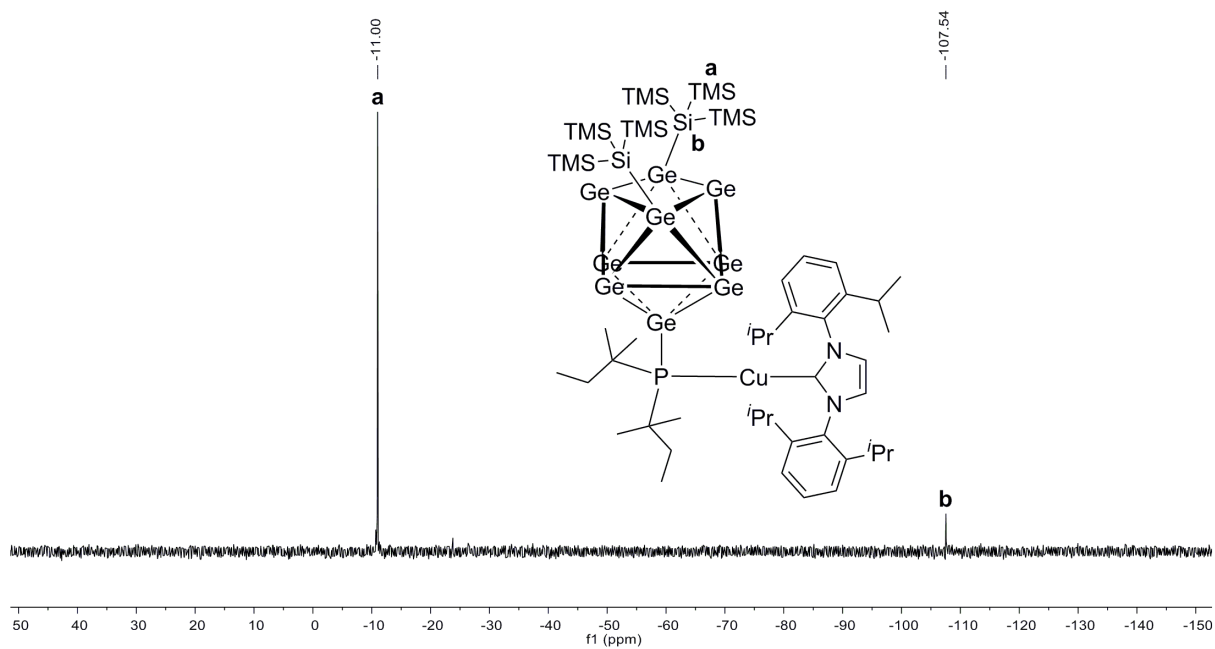


Figure S58: ^{29}Si -INEPT-RD NMR spectrum of compound **6-CuNHC^{Dipp}** in $\text{thf-}d_8$.

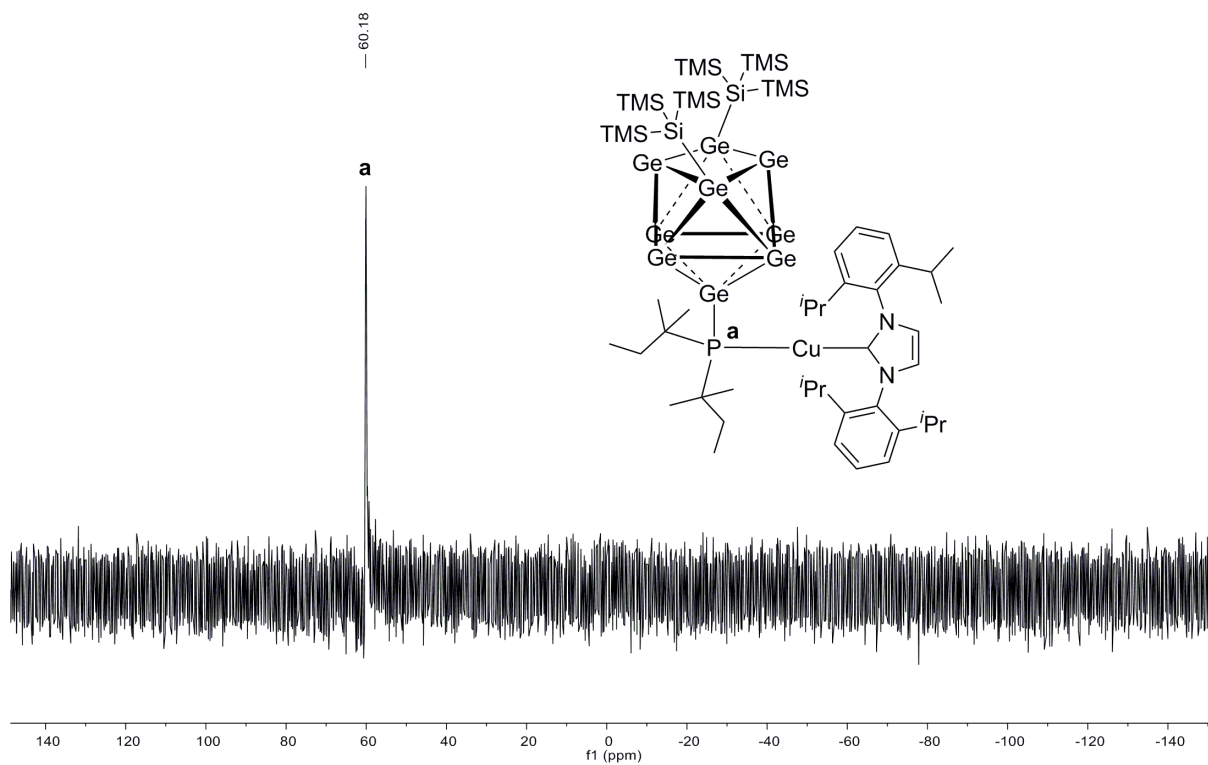


Figure S59: ^{31}P NMR spectrum of compound **6-CuNHC^{Dipp}** in $\text{thf-}d_8$.

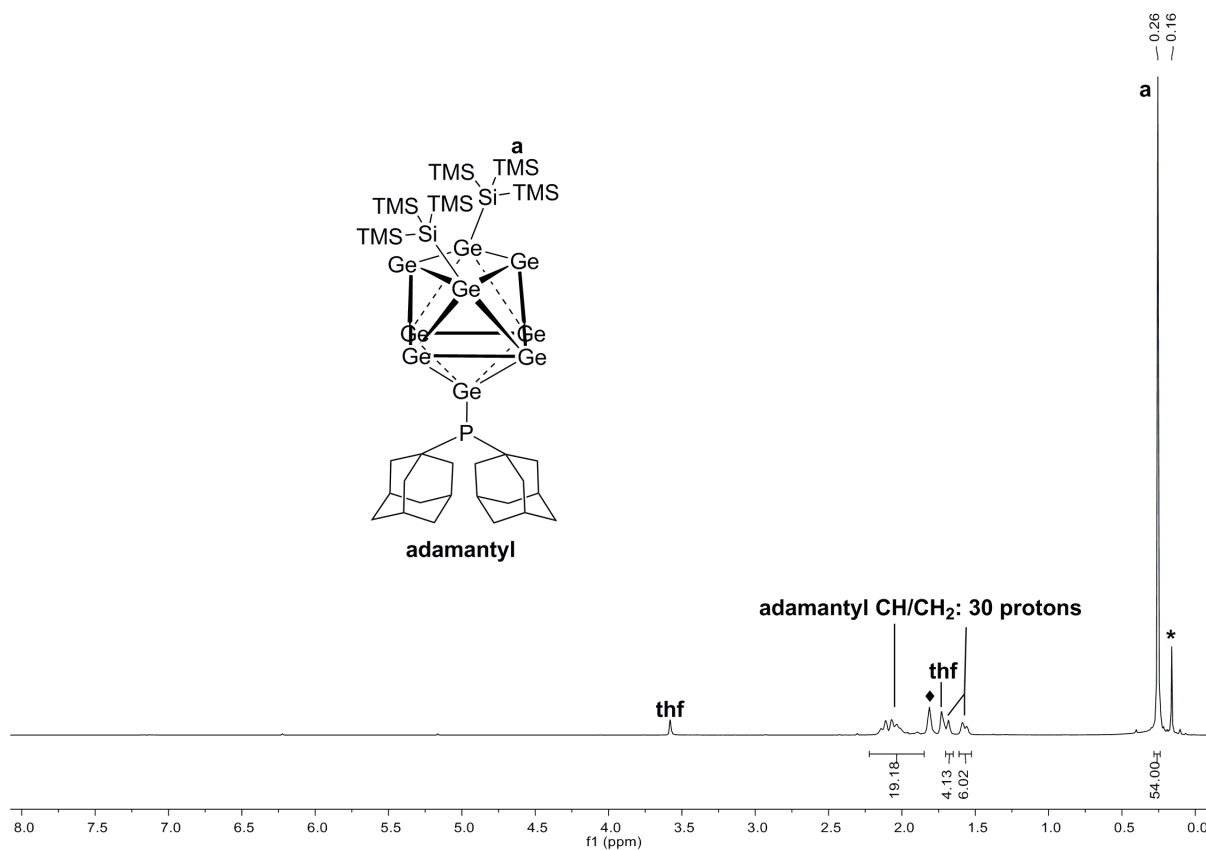


Figure S60: ^1H NMR spectrum of compound **7a** in $\text{thf-}d_8$ (signal marked with * belongs to bis-silylated cluster $[\text{Ge}_9\{\text{Si}(\text{TMS})_3\}_2]^{2-}$, signal marked with \blacklozenge belongs to an unidentified impurity).

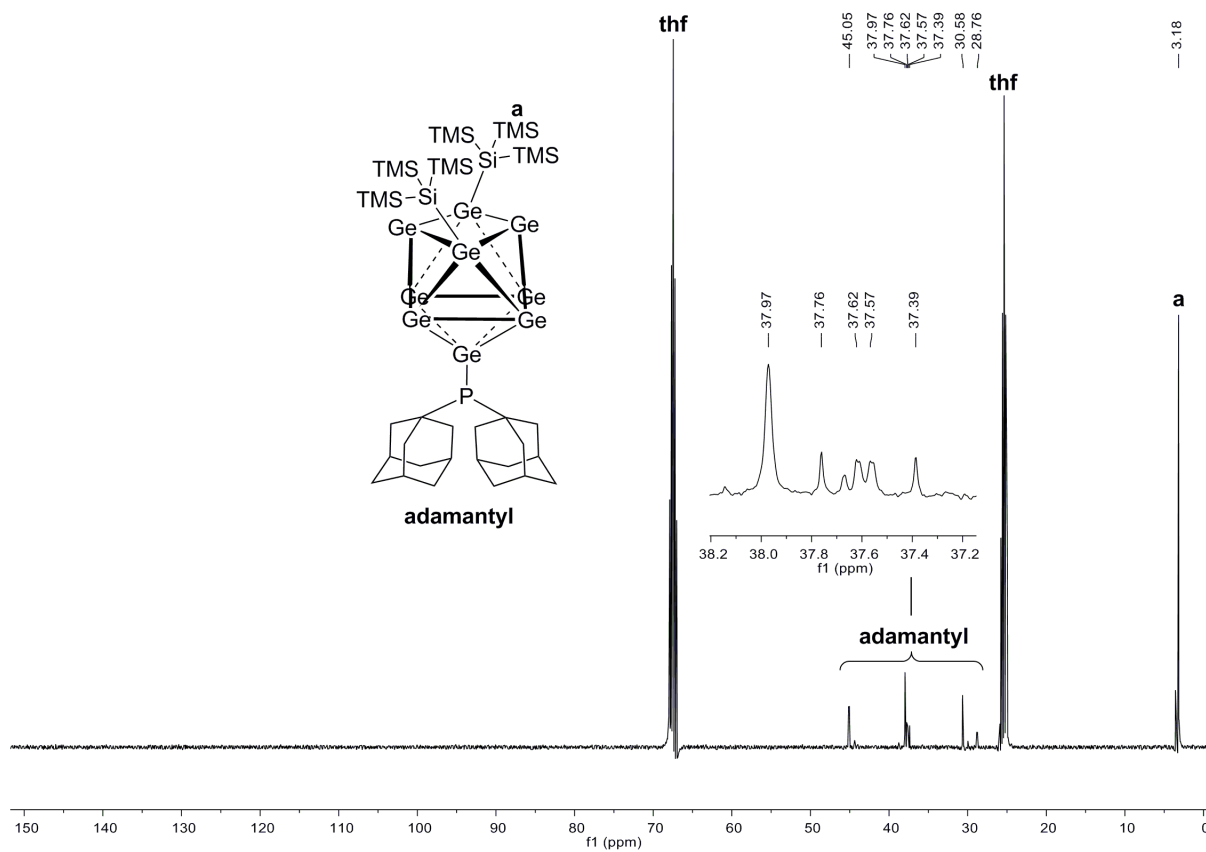


Figure S61: ^{13}C NMR spectrum of compound **7a** in $\text{thf-}d_8$.

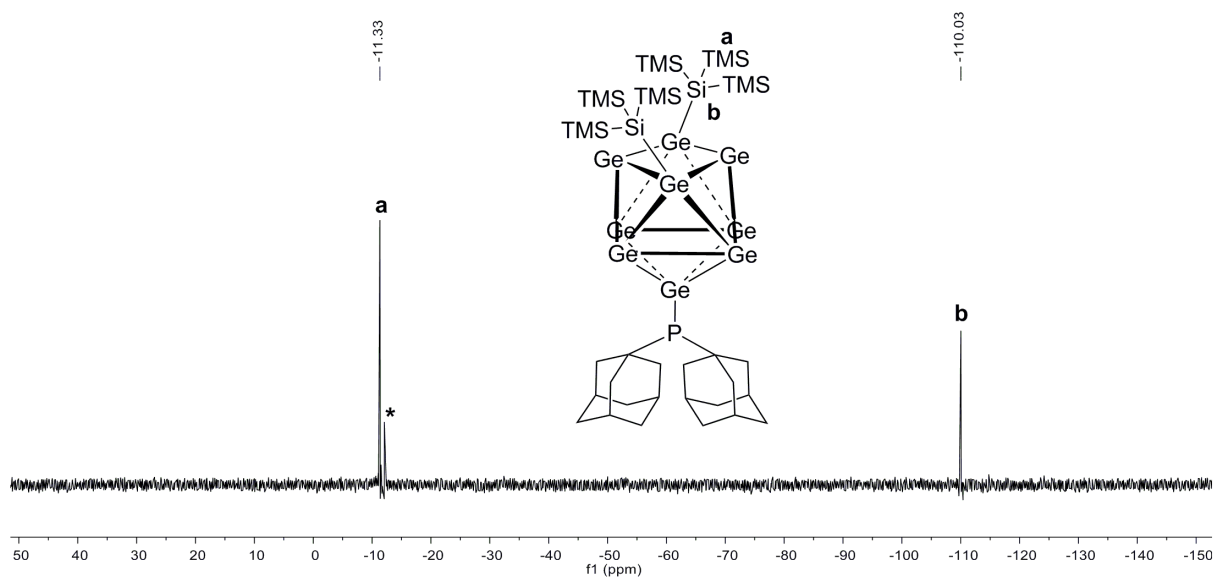


Figure S62: ^{29}Si -INEPT-RD NMR spectrum of compound **7a** in $\text{thf-}d_8$ (signal marked with * belongs to an unidentified impurity).

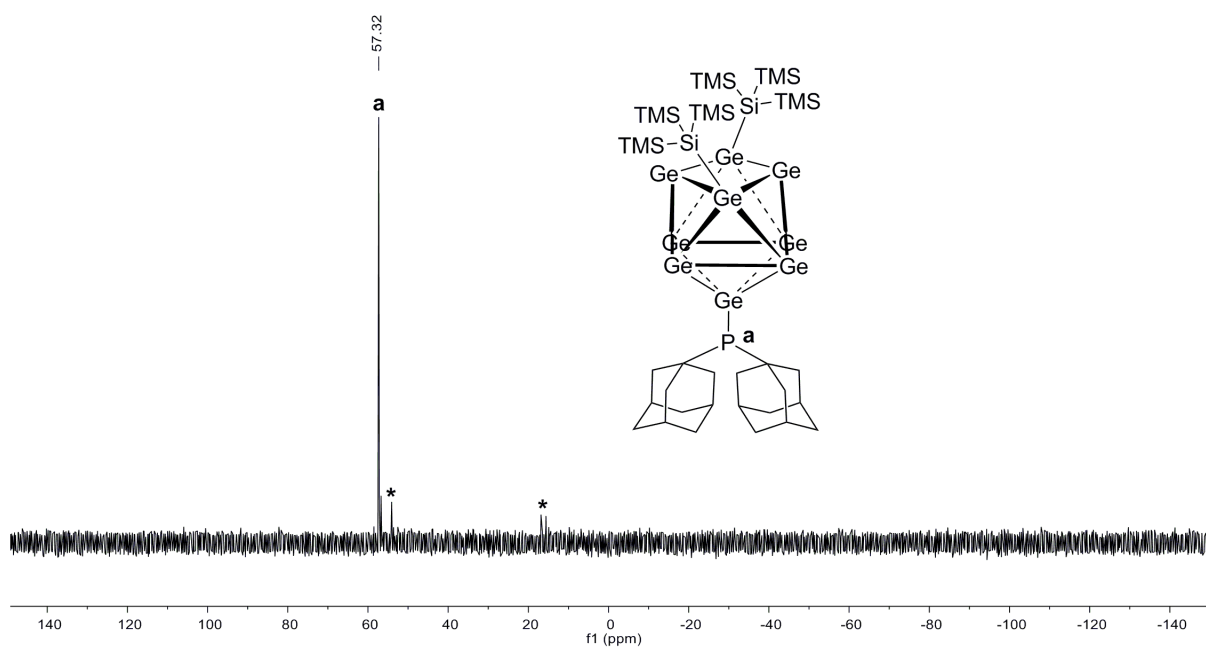


Figure S63: ^{31}P NMR spectrum of compound **7a** in $\text{thf-}d_8$ (signals marked with * belong to unidentified impurities).

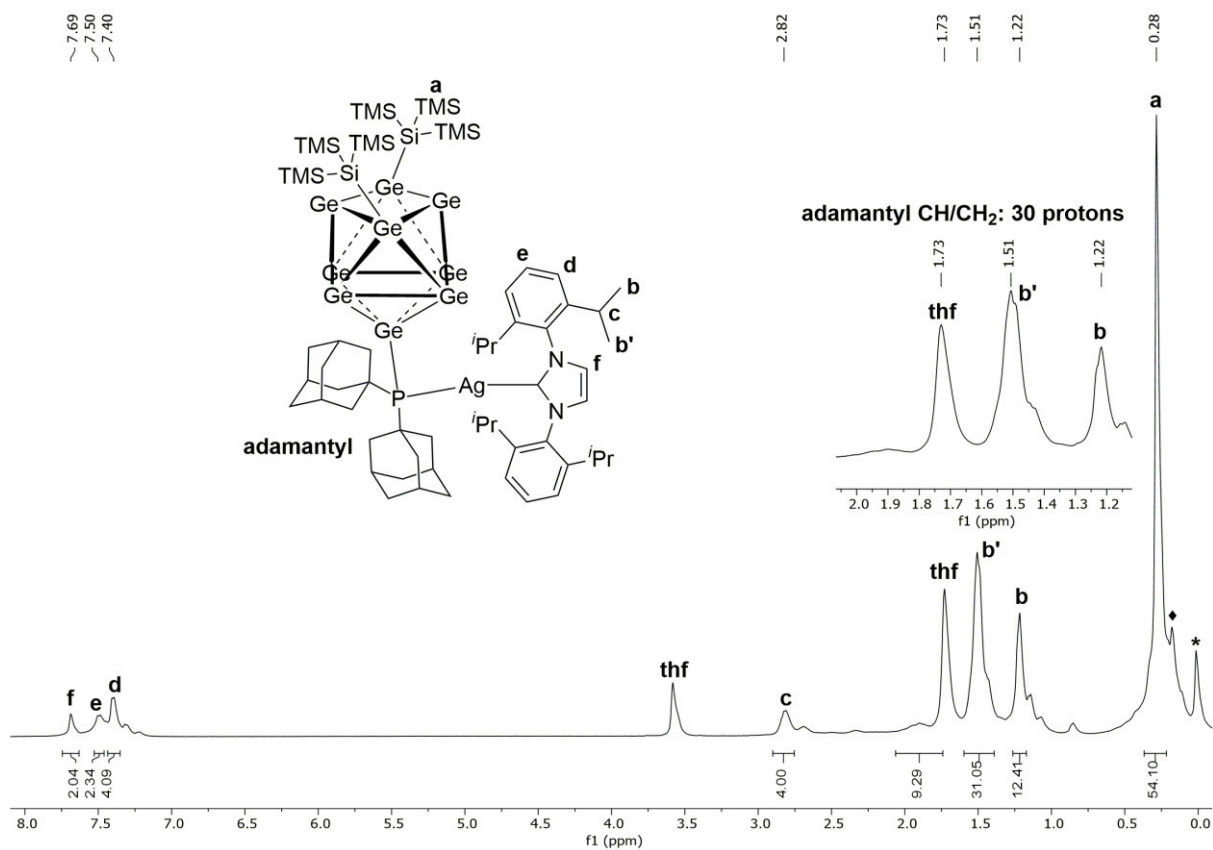


Figure S64: ¹H NMR spectrum of compound **7-AgNHC^{Dipp}** in *thf-d₈* (signal marked with ♦ belongs to an unidentified impurity, signal marked with * belongs to silicon grease).

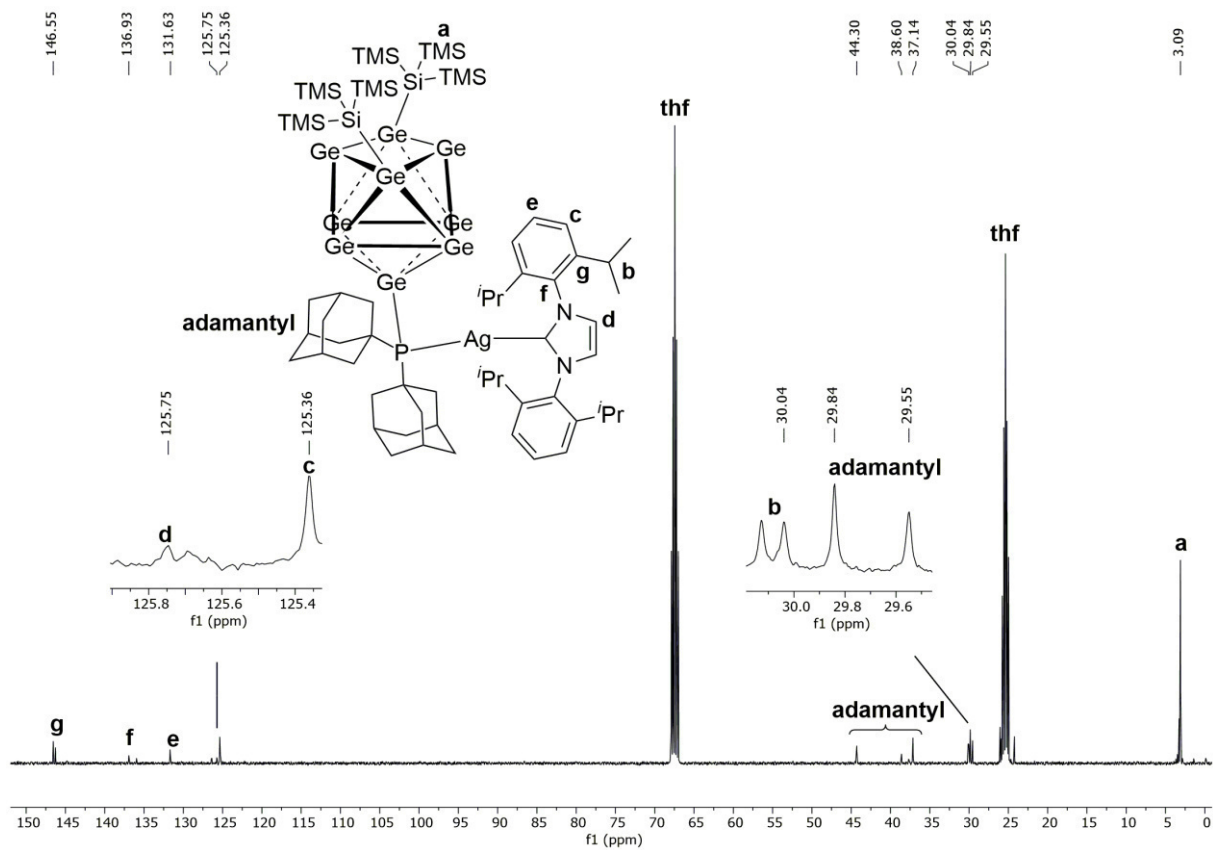


Figure S65: ¹³C NMR spectrum of compound **7-AgNHC^{Dipp}** in *thf-d₈*.

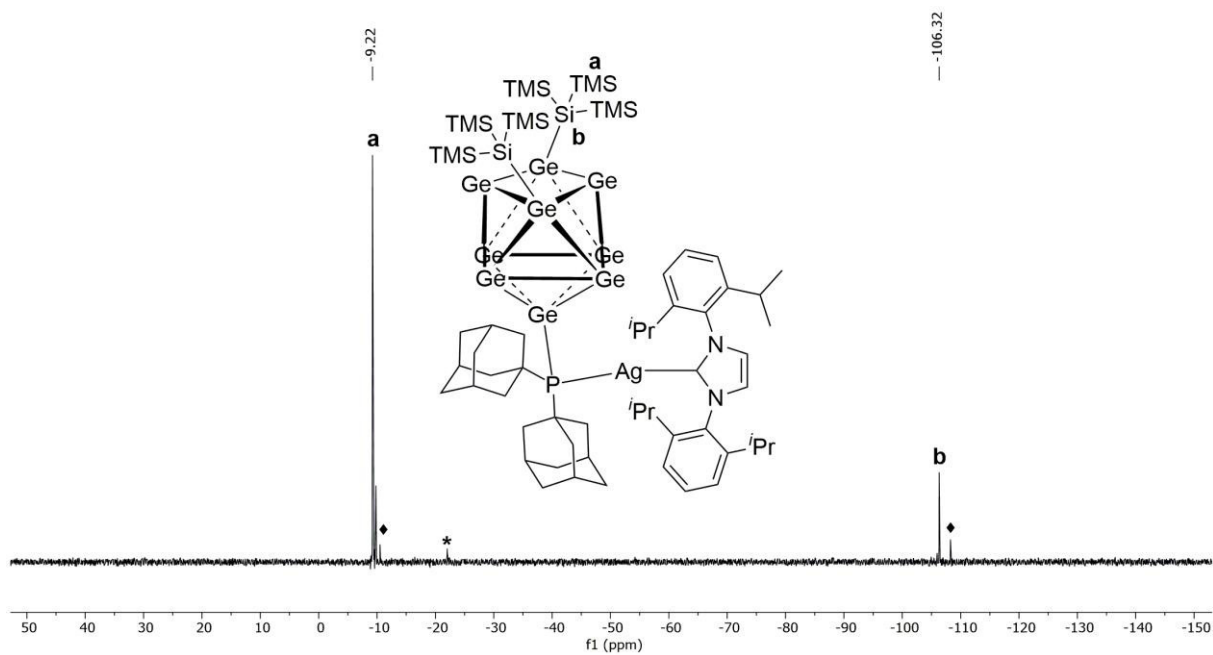


Figure S66: ^{29}Si -INEPT-RD NMR spectrum of compound **7-AgNHC^{DIPP}** in $\text{thf-}d_8$ (signal marked with ♦ belongs to an unidentified impurity, signal marked with * belongs to silicon grease).

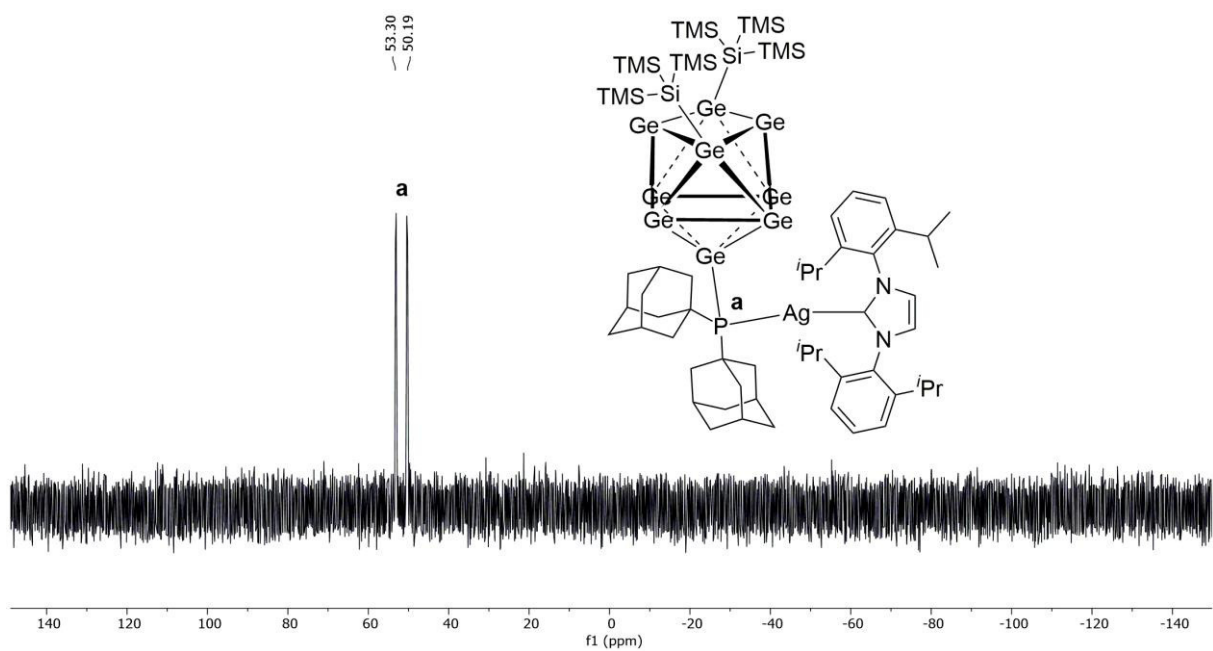


Figure S67: ^{31}P NMR spectrum of compound **7-AgNHC^{DIPP}** in $\text{thf-}d_8$.

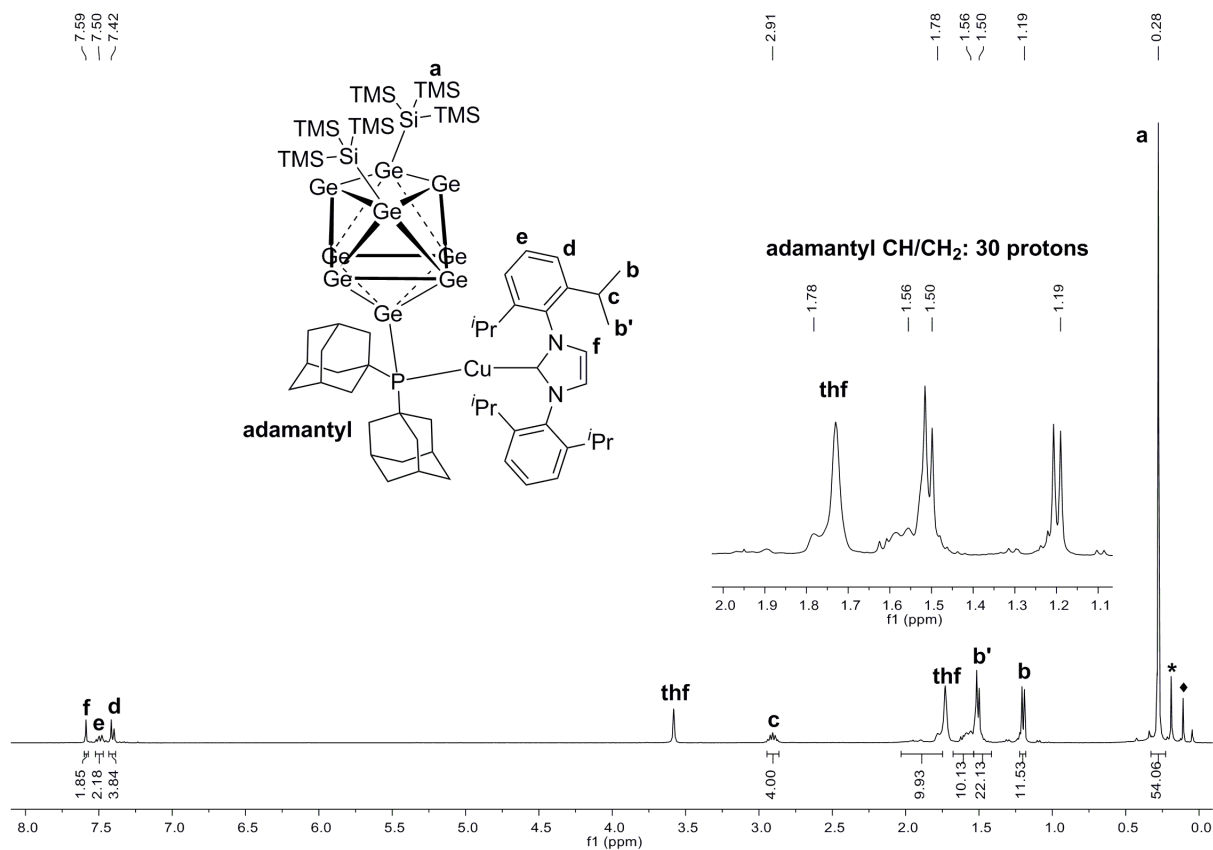


Figure S68: ¹H NMR spectrum of compound **7-CuNHC^{Dipp}** in *thf-d*₈ (signal marked with * belongs to an unidentified impurity, signal marked with ♦ belongs to silicon grease).

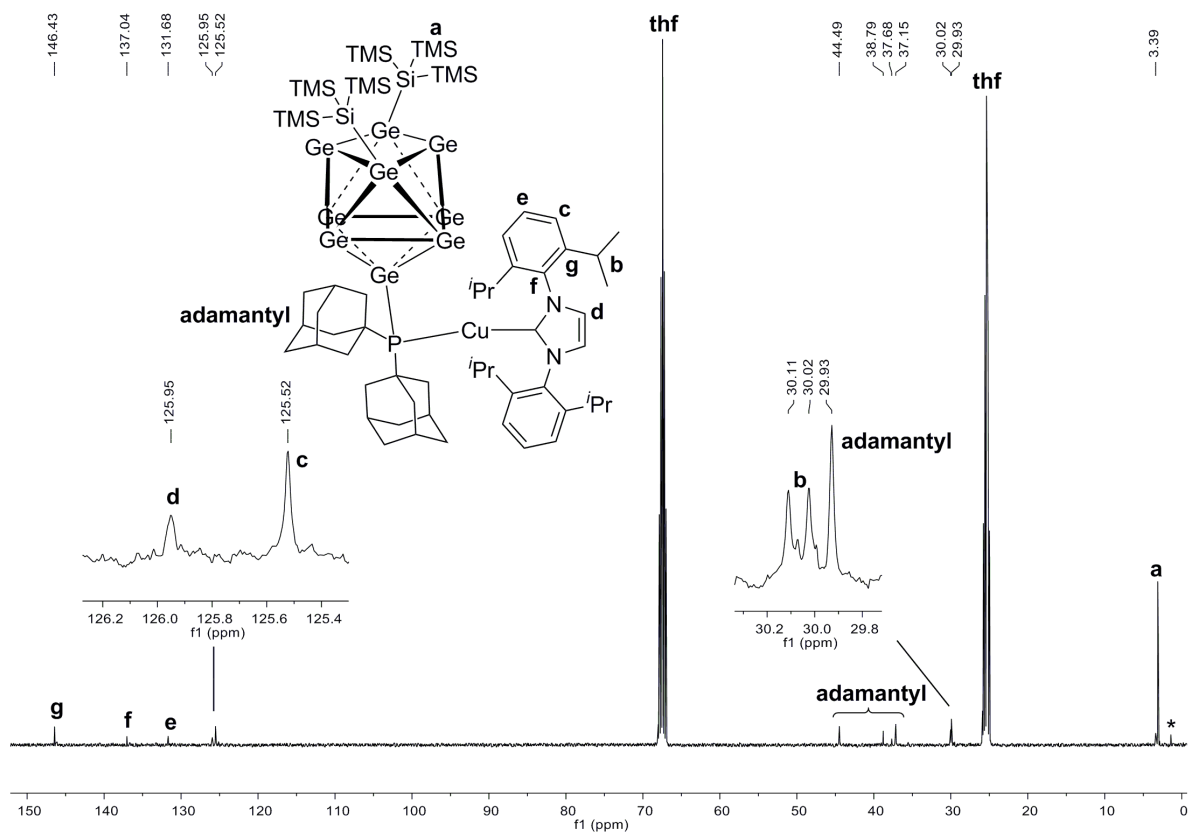


Figure S69: ¹³C NMR spectrum of compound **7-CuNHC^{Dipp}** in *thf-d*₈ (signal marked with * belongs to silicon grease).

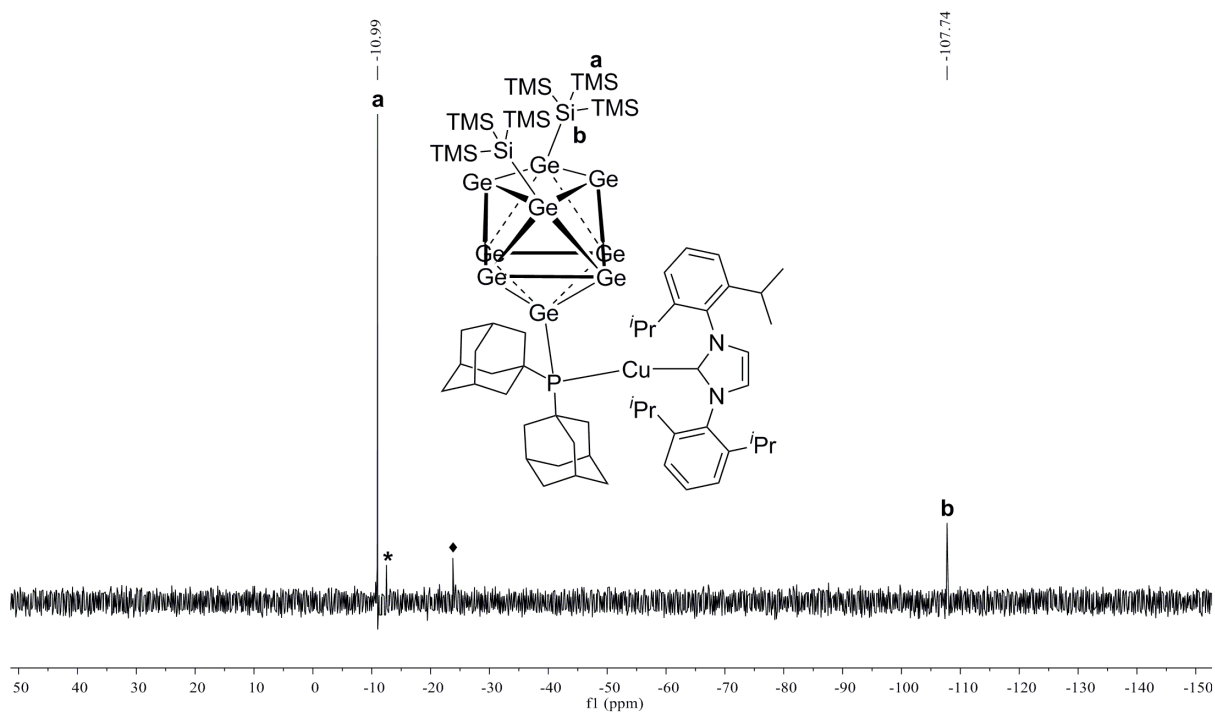


Figure S70: ^{29}Si -INEPT-RD NMR spectrum of compound **7-CuNHC^{Dipp}** in $\text{thf-}d_8$ (signal marked with * belongs to an unidentified impurity, signal marked with \blacklozenge belongs to silicon grease).

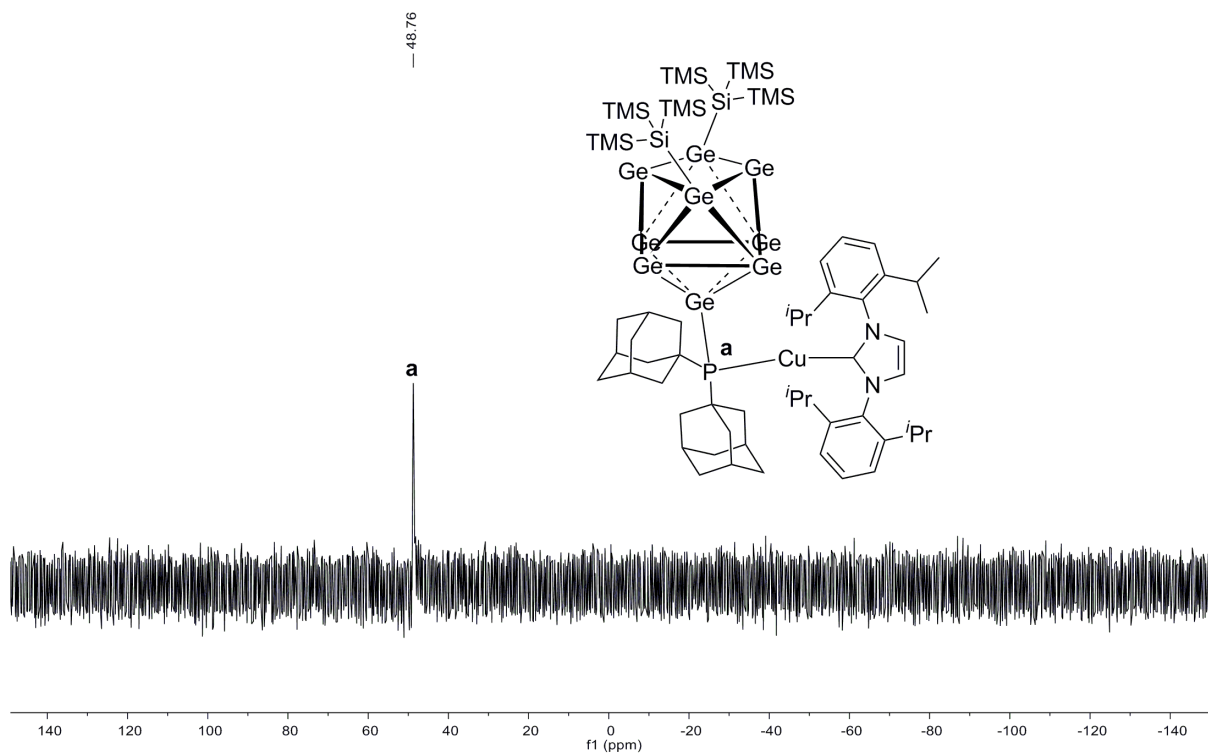


Figure S71: ^{31}P NMR spectrum of compound **7-CuNHC^{Dipp}** in $\text{thf-}d_8$.

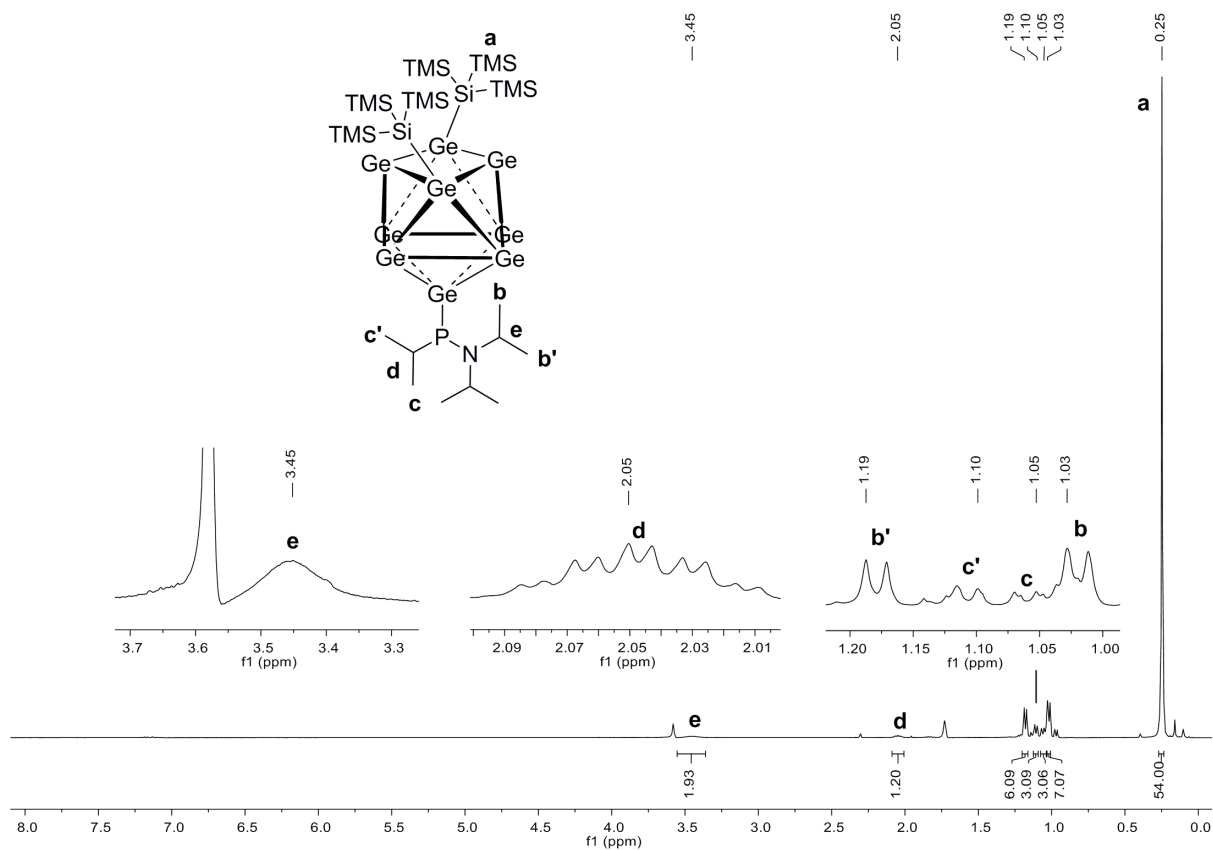


Figure S72: ^1H NMR spectrum of compound **8a** in $\text{thf-}d_8$.

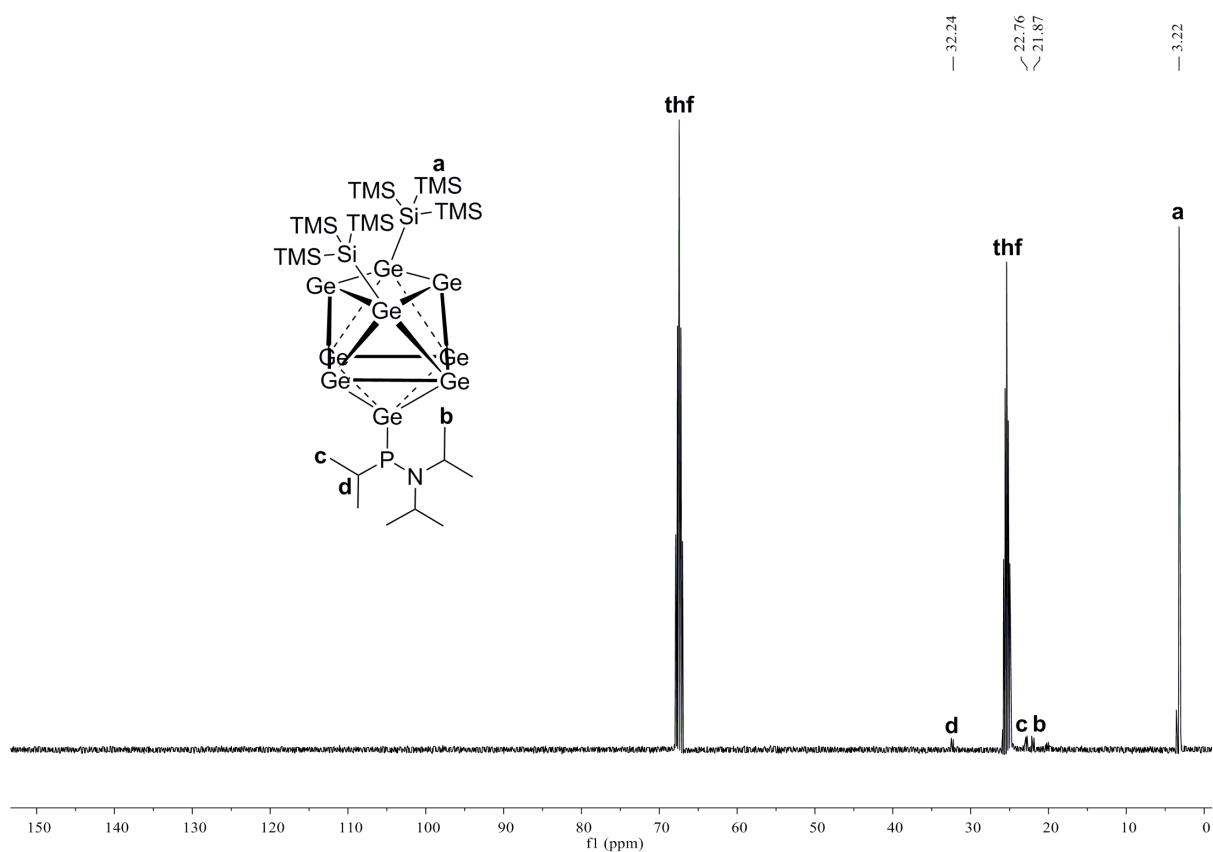
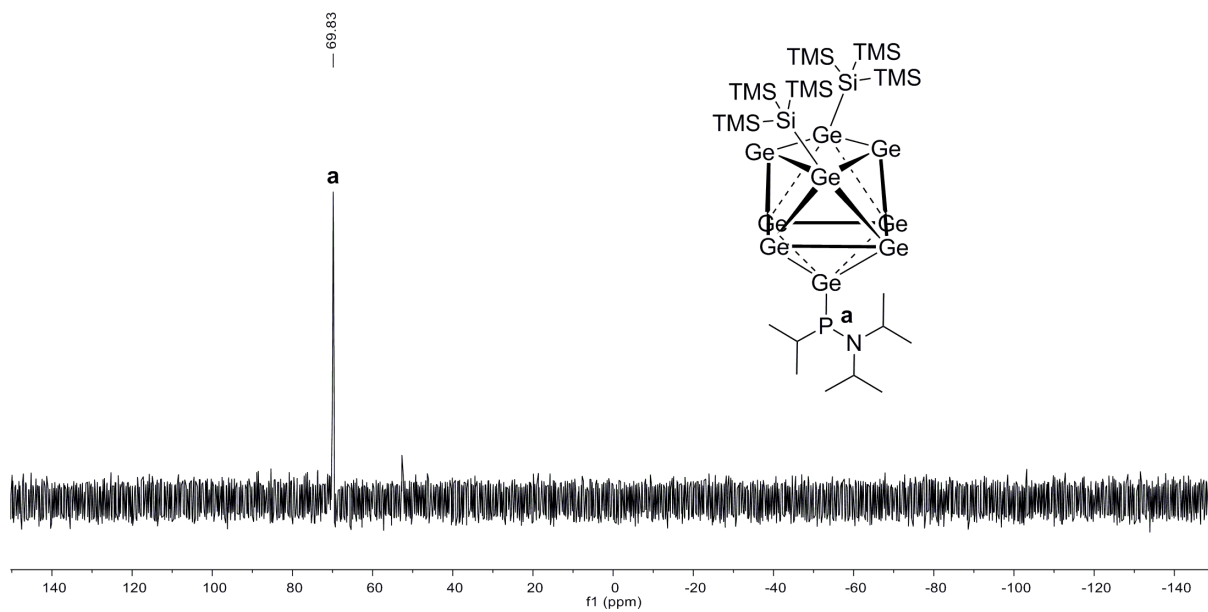
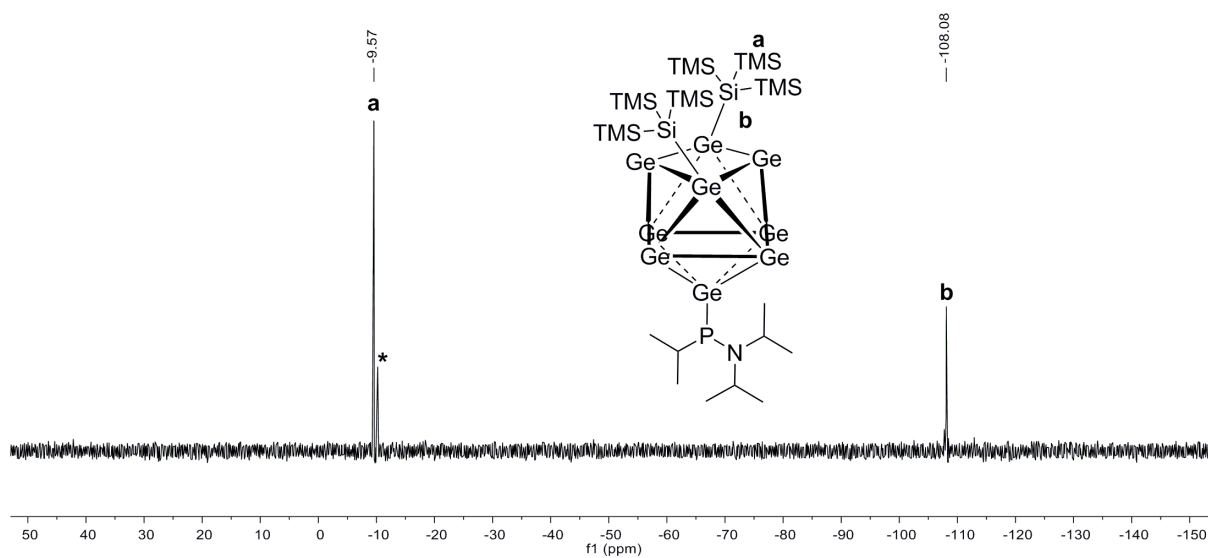


Figure S73: ^{13}C NMR spectrum of compound **8a** in $\text{thf-}d_8$.



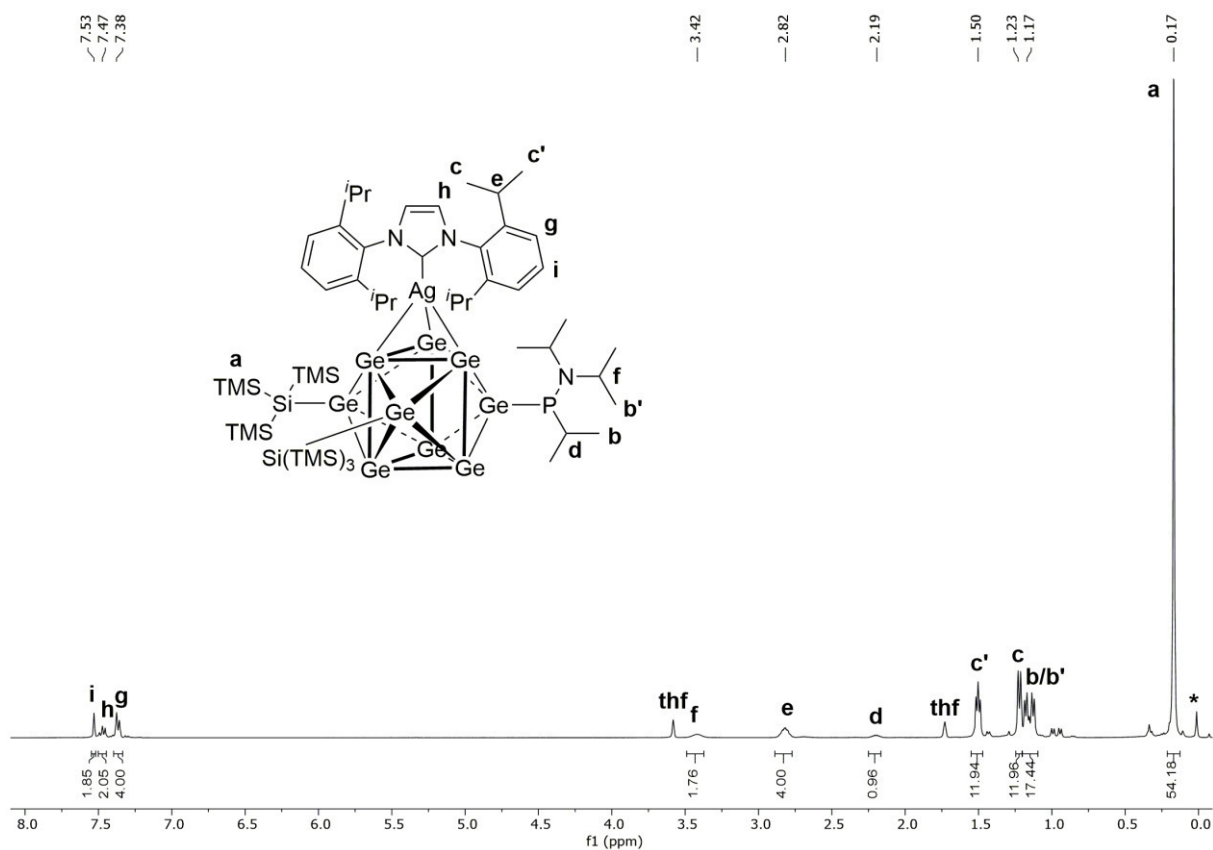


Figure S76: ¹H NMR spectrum of compound **8-AgNHC^{Dipp}** in thf-*d*₈ (signal marked with * belongs to silicon grease).

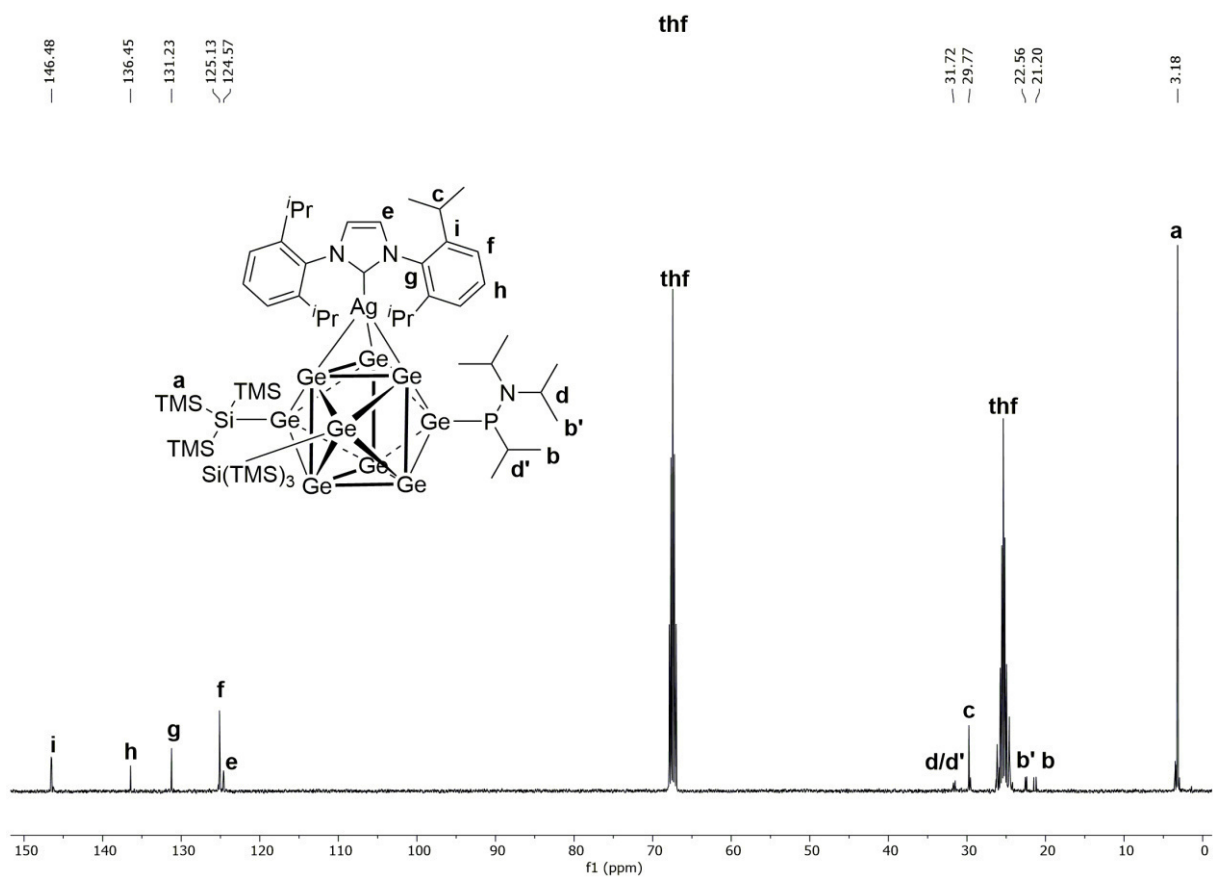
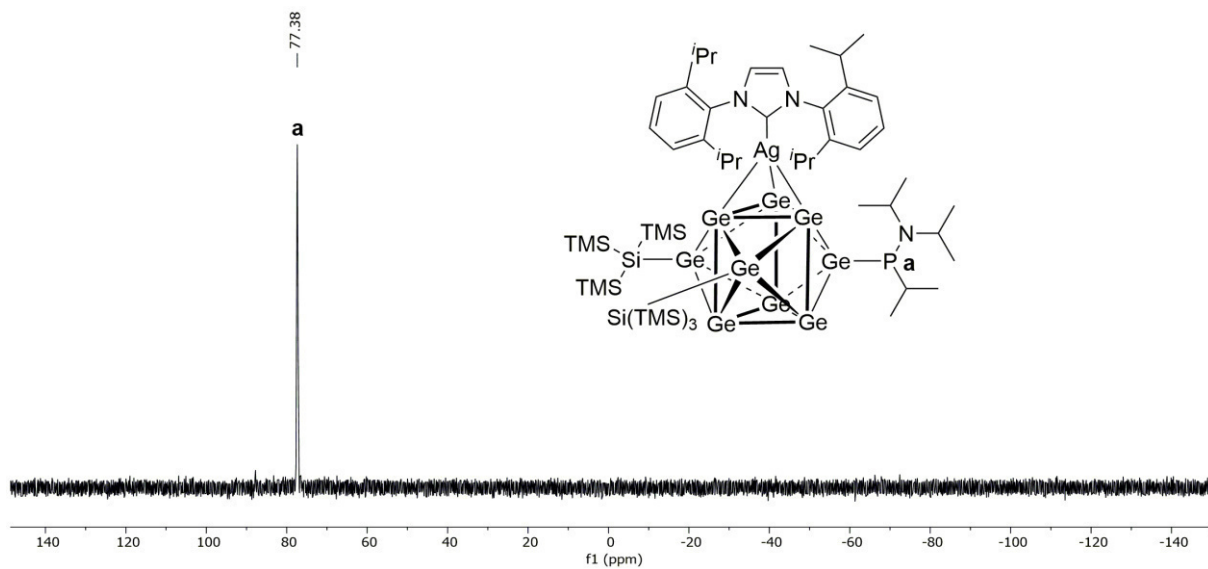
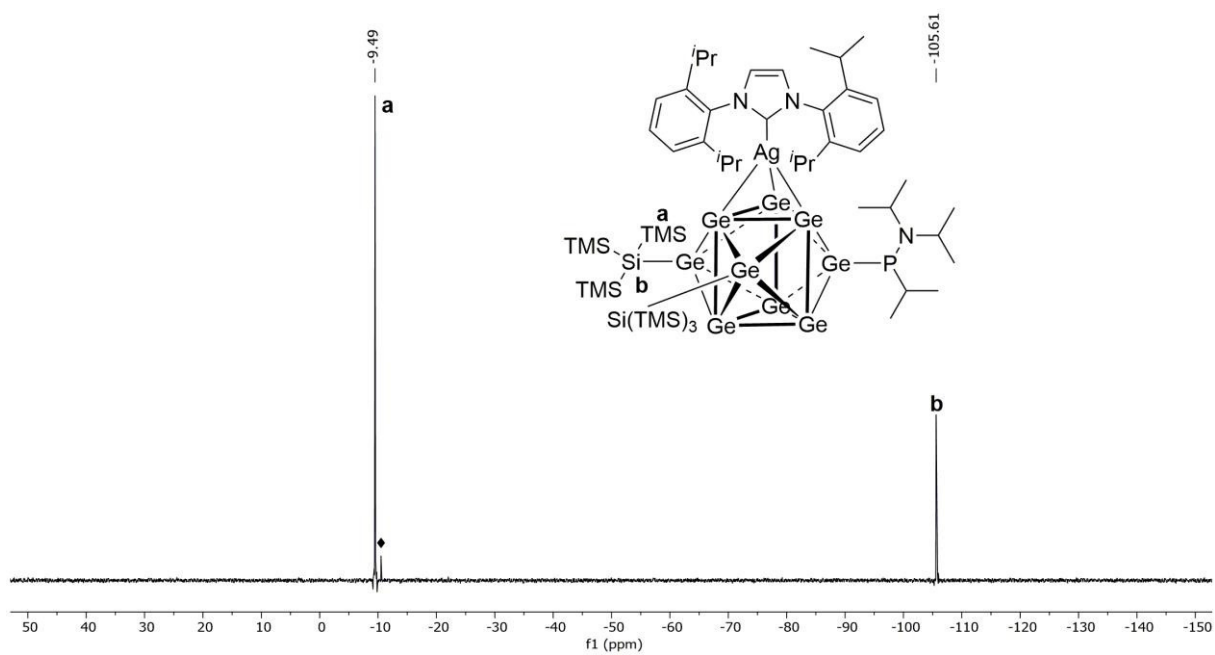


Figure S77: ¹³C NMR spectrum of compound **8-AgNHC^{Dipp}** in thf-*d*₈.



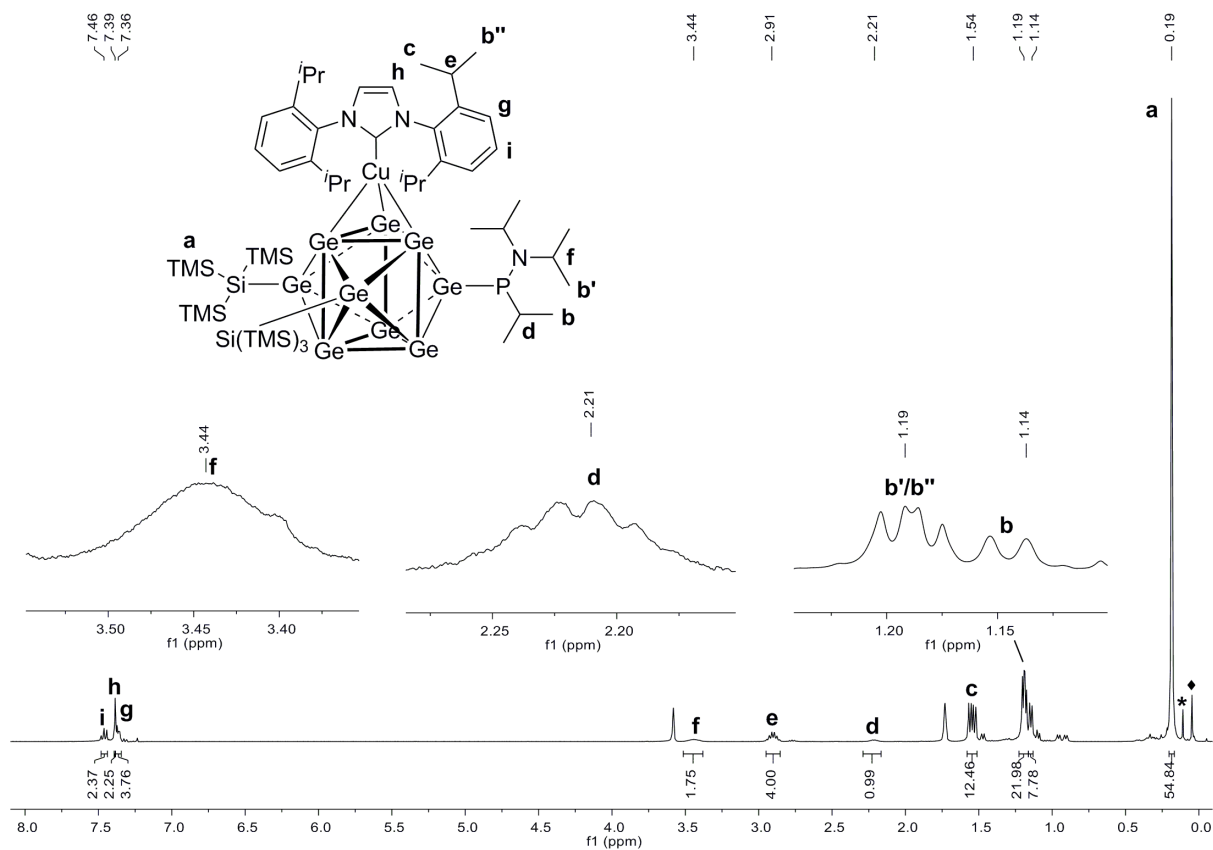


Figure S80: ¹H NMR spectrum of compound **8-CuNHC^{Dipp}** in thf-*d*₈ (signal marked with * belongs to an unidentified impurity, signal marked with ♦ belongs to silicon grease).

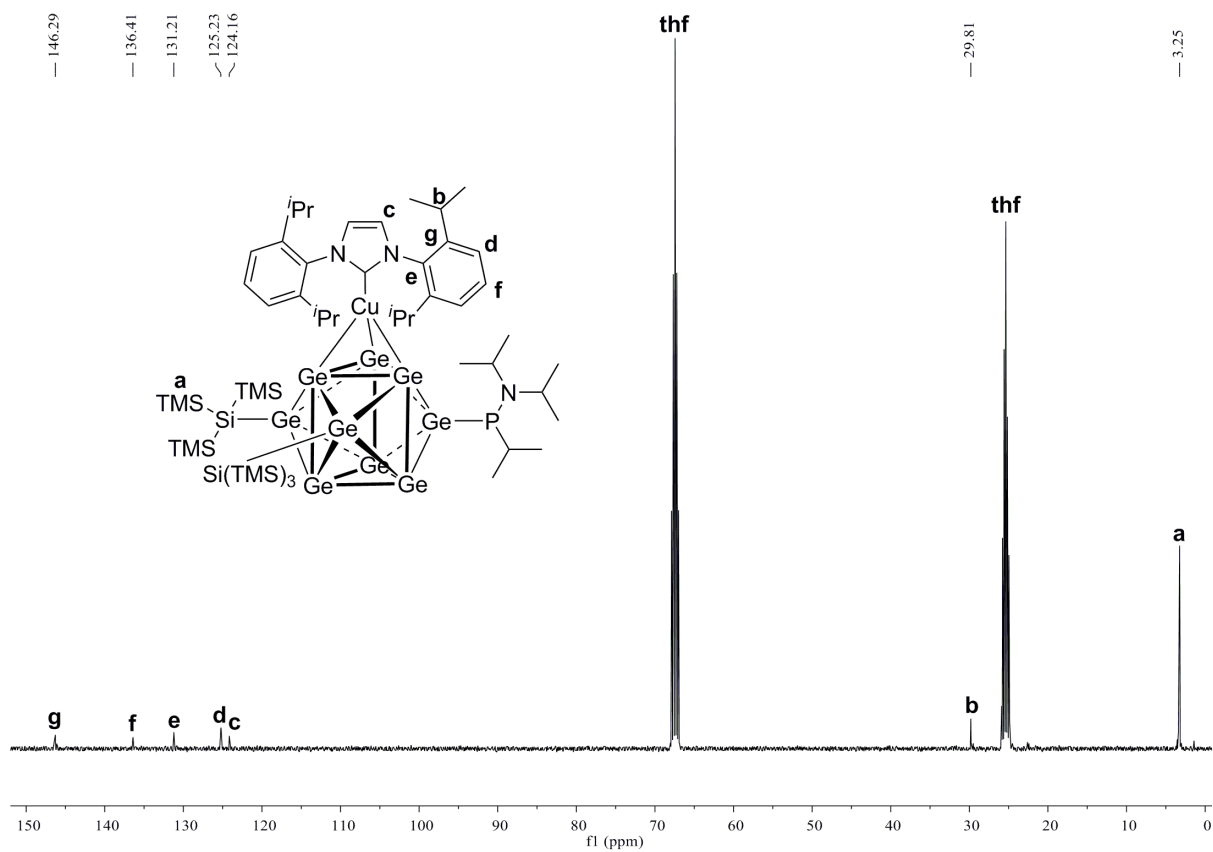


Figure S81: ¹³C NMR spectrum of compound **8-CuNHC^{Dipp}** in thf-*d*₈.

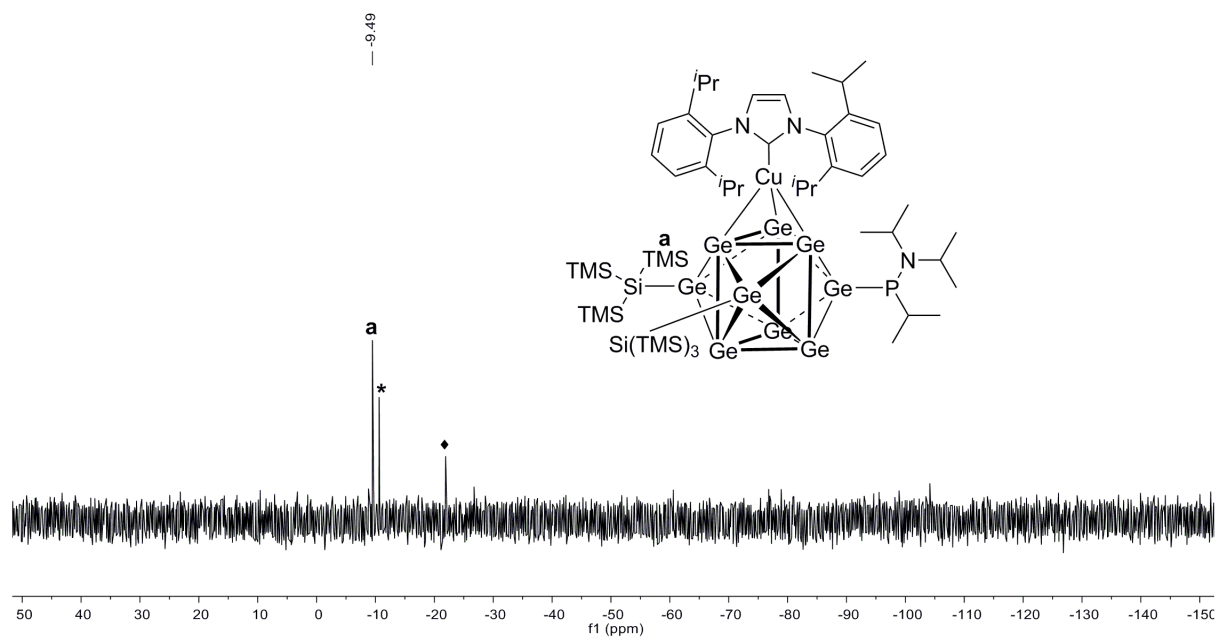


Figure S82: ^{29}Si -INEPT-RD NMR spectrum of compound **8-CuNHC^{DIPP}** in $\text{thf-}d_8$ (signal marked with * belongs to an unidentified impurity, signal marked with ♦ belongs to silicon grease). The signal of $\text{Si}_{\text{Ge}9}$ could not be detected for unknown reasons.

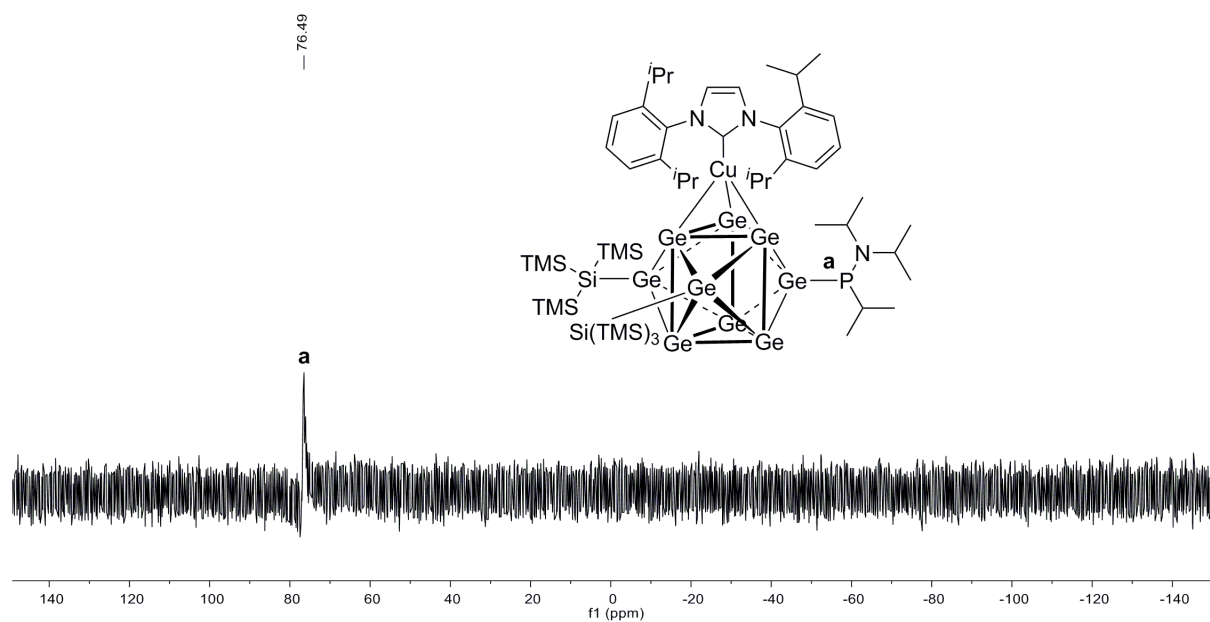


Figure S83: ^{31}P NMR spectrum of compound **8-CuNHC^{DIPP}** in $\text{thf-}d_8$.

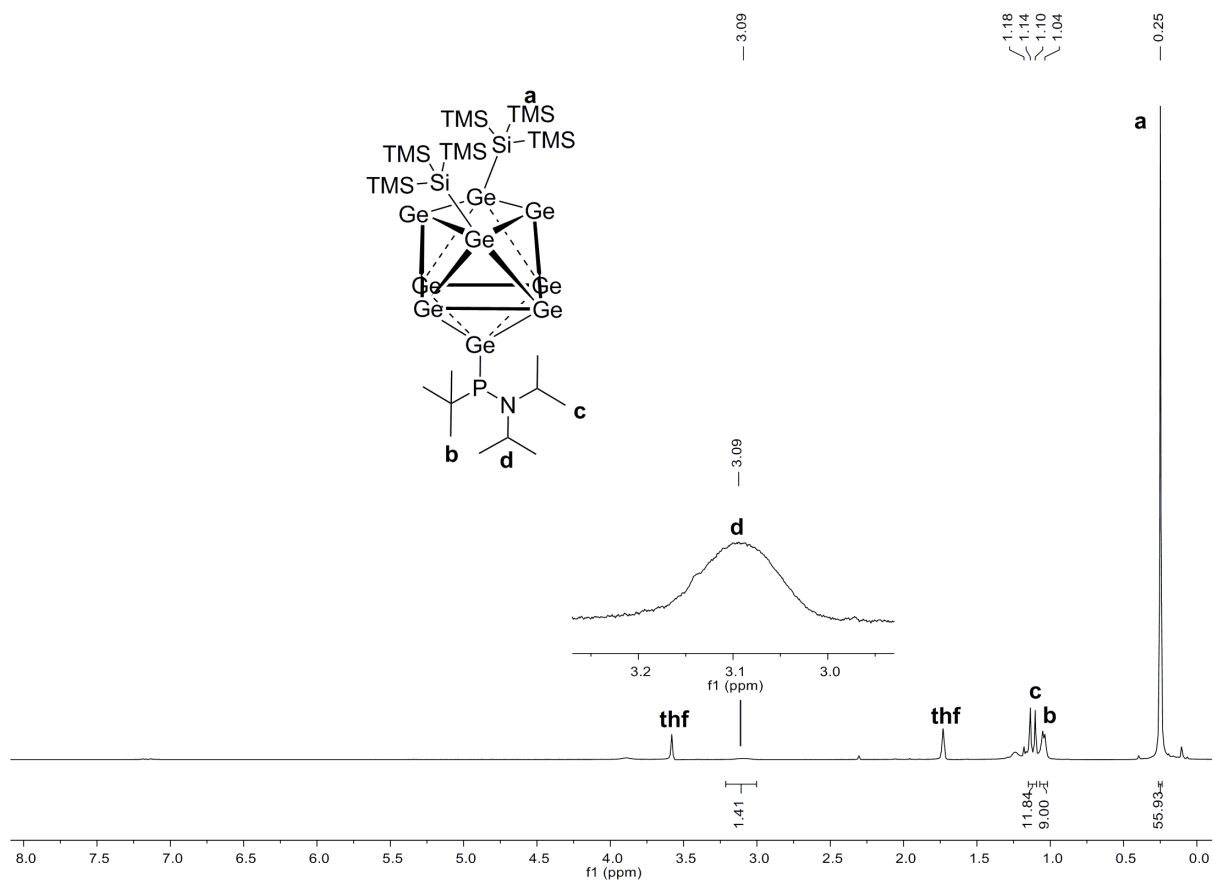


Figure S84: ^1H NMR spectrum of compound **9a** in $\text{thf-}d_8$.

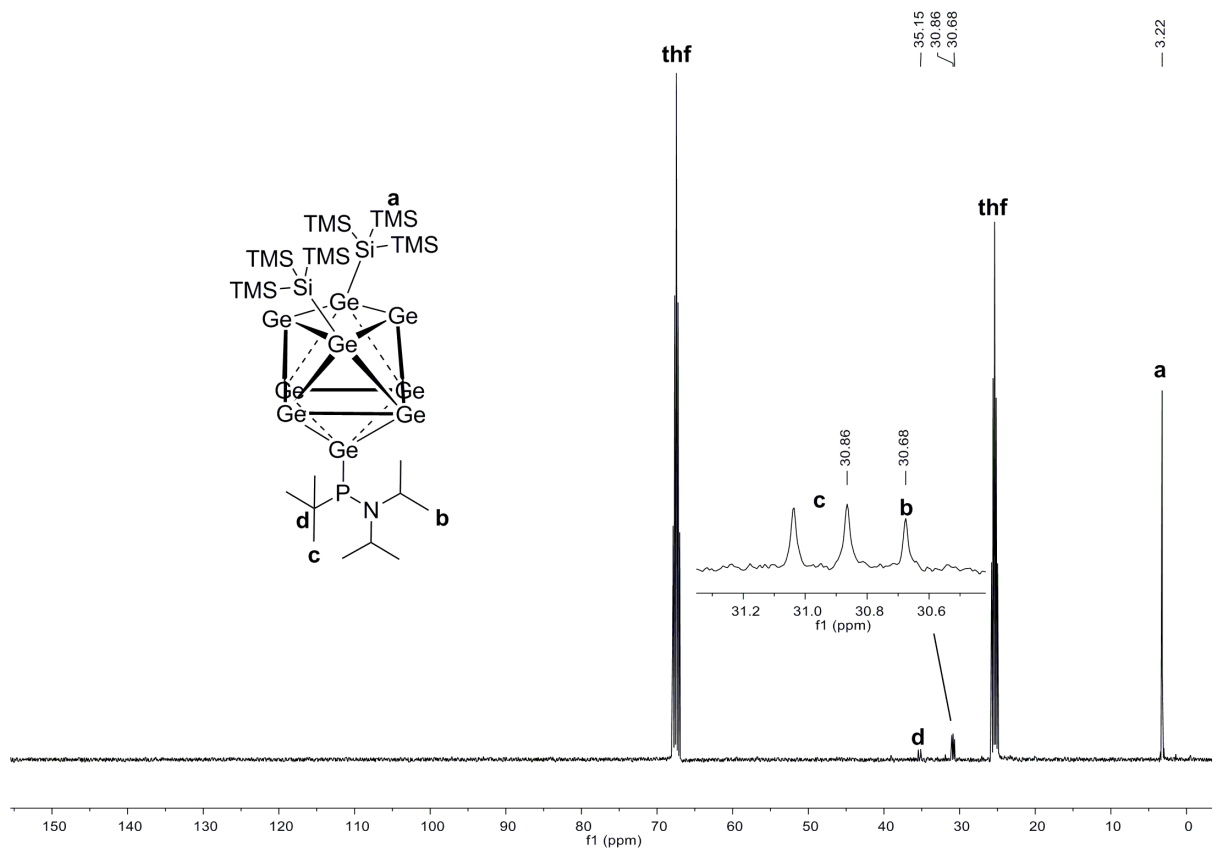


Figure S85: ^{13}C NMR spectrum of compound **9a** in $\text{thf-}d_8$.

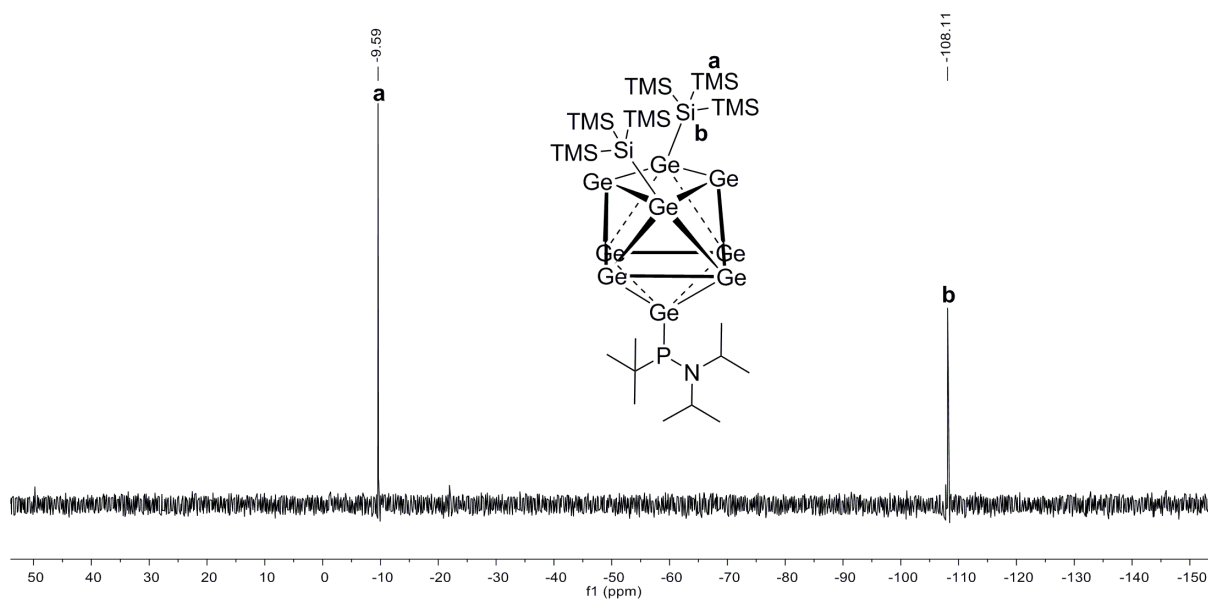


Figure S86: ^{29}Si -INEPT-RD NMR spectrum of compound **9a** in $\text{thf-}d_8$.

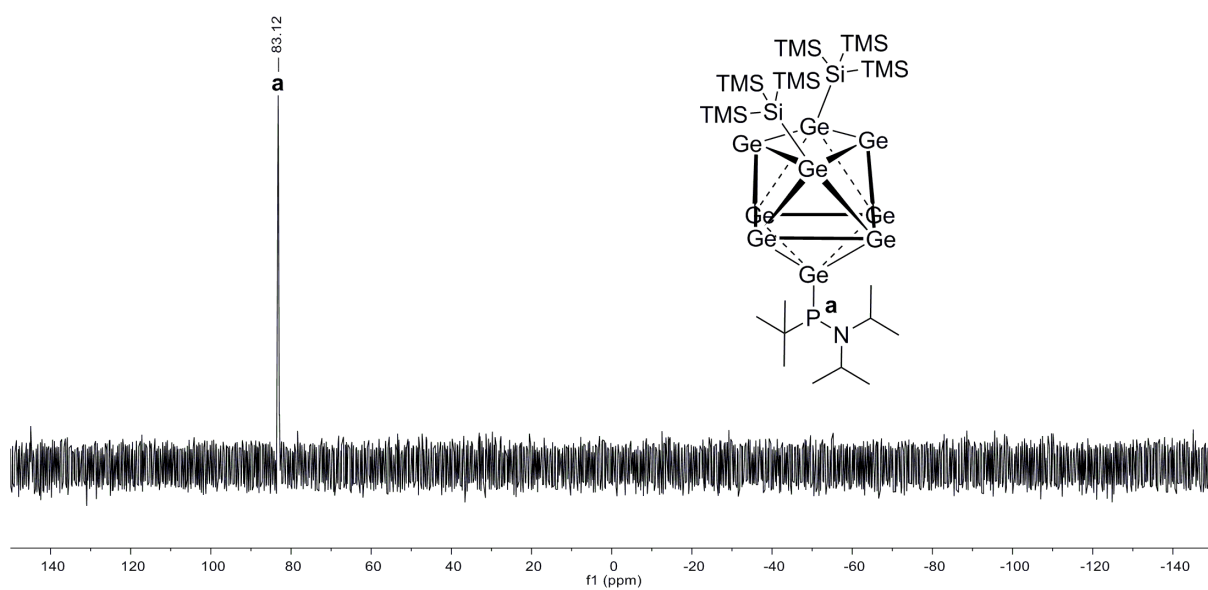


Figure S87: ^{31}P NMR spectrum of compound **9a** in $\text{thf-}d_8$.

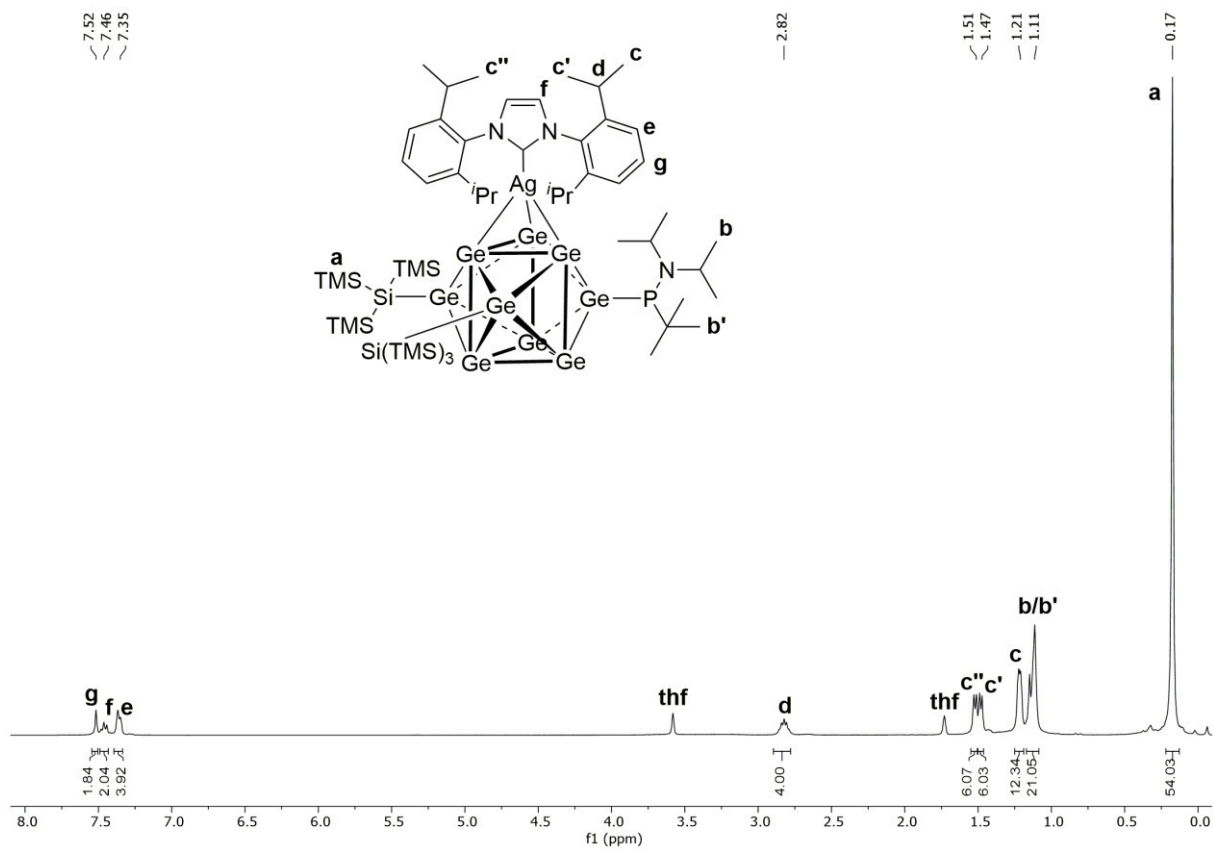


Figure S88: ¹H NMR spectrum of compound **9-AgNHC^{Dipp}** in thf-*d*₈.

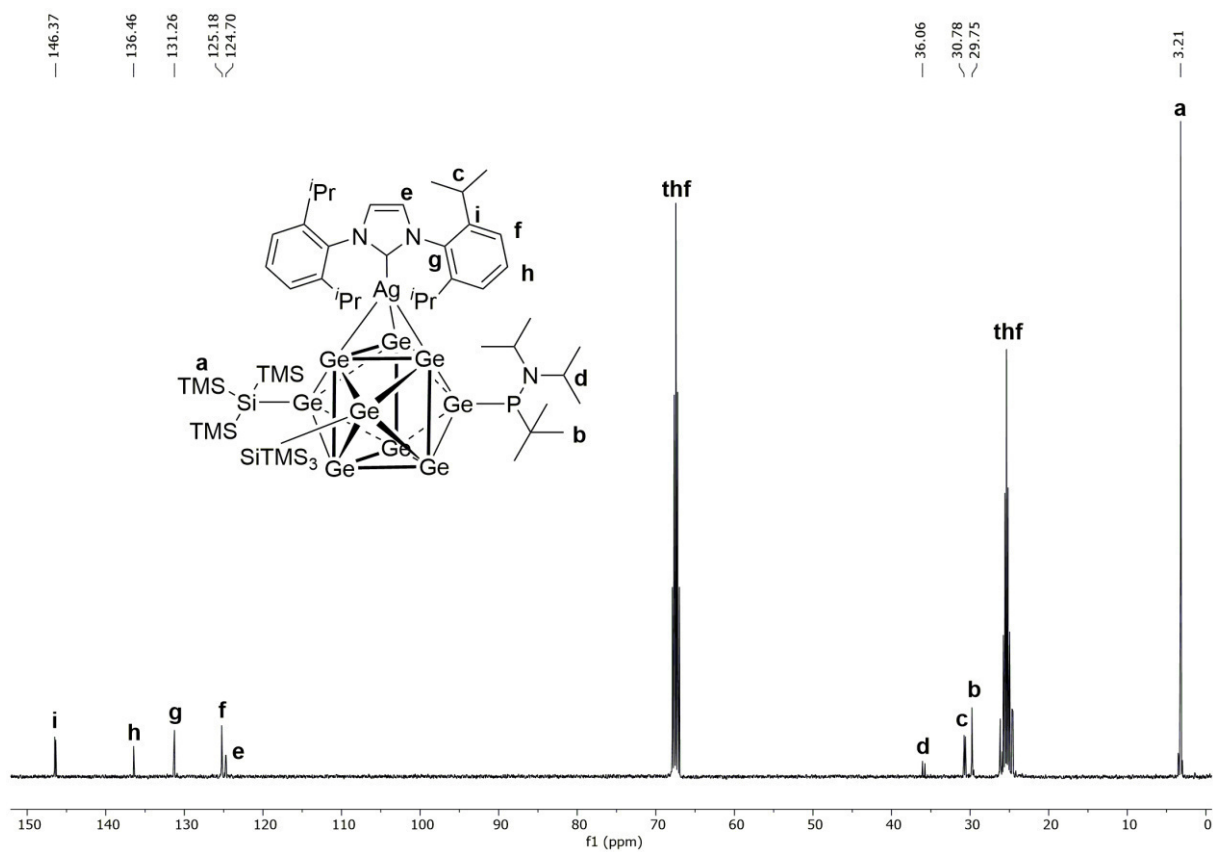


Figure S89: ¹³C NMR spectrum of compound **9-AgNHC^{Dipp}** in thf-*d*₈.

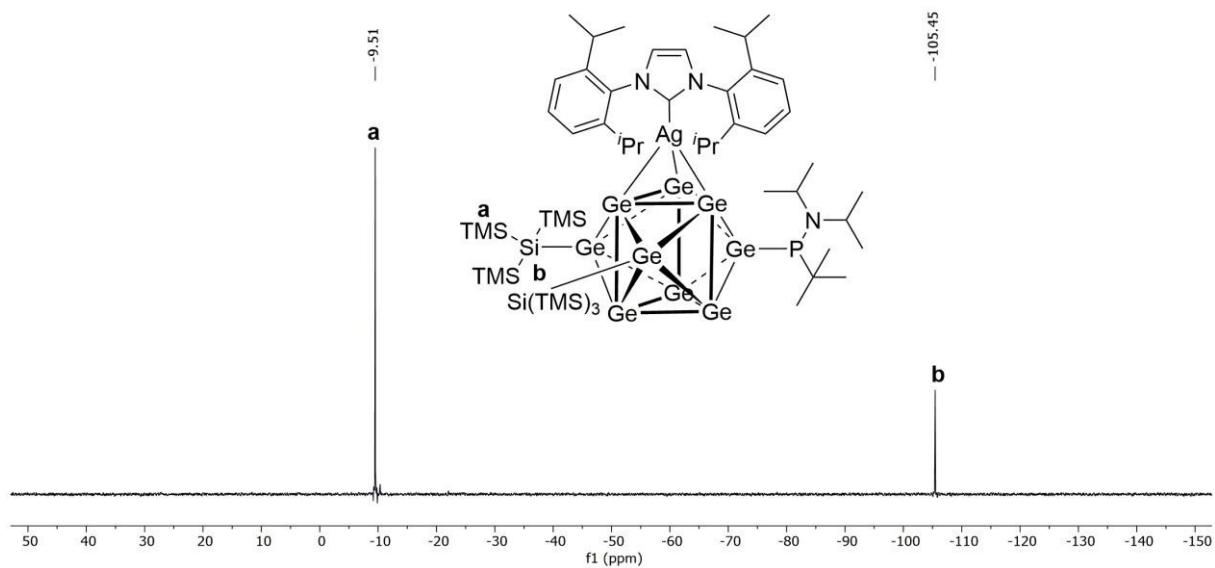


Figure S90: ^{29}Si -INEPT-RD NMR spectrum of compound **9-AgNHC^{Dipp}** in $\text{thf-}d_8$.

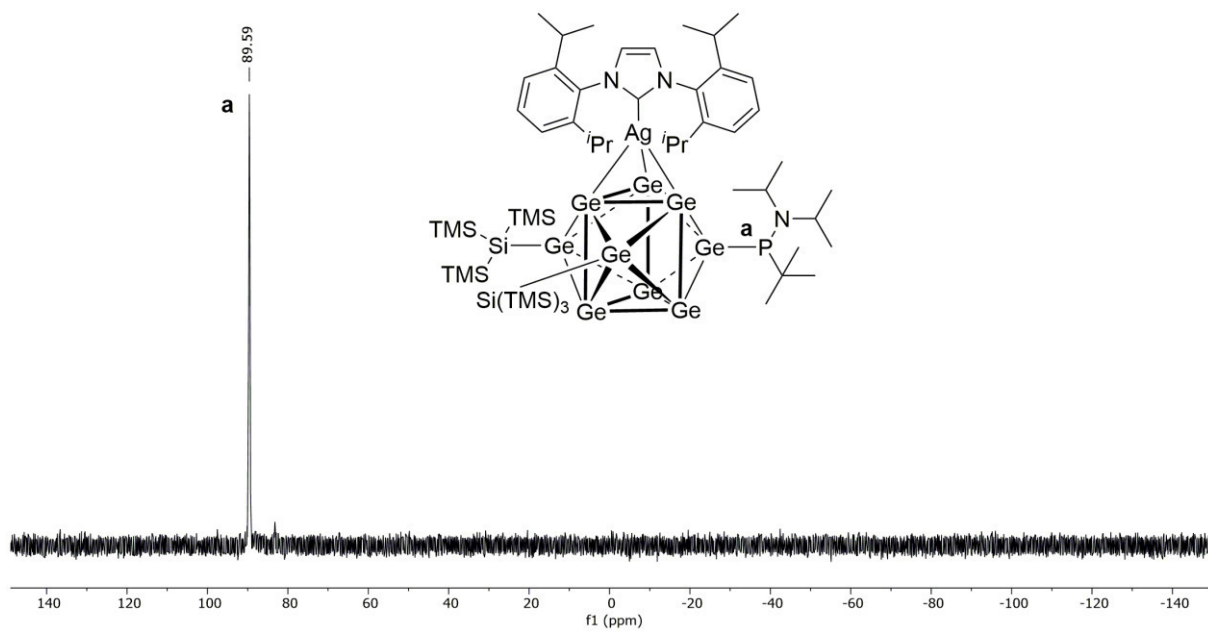


Figure S91: ^{31}P NMR spectrum of compound **9-AgNHC^{Dipp}** in $\text{thf-}d_8$.

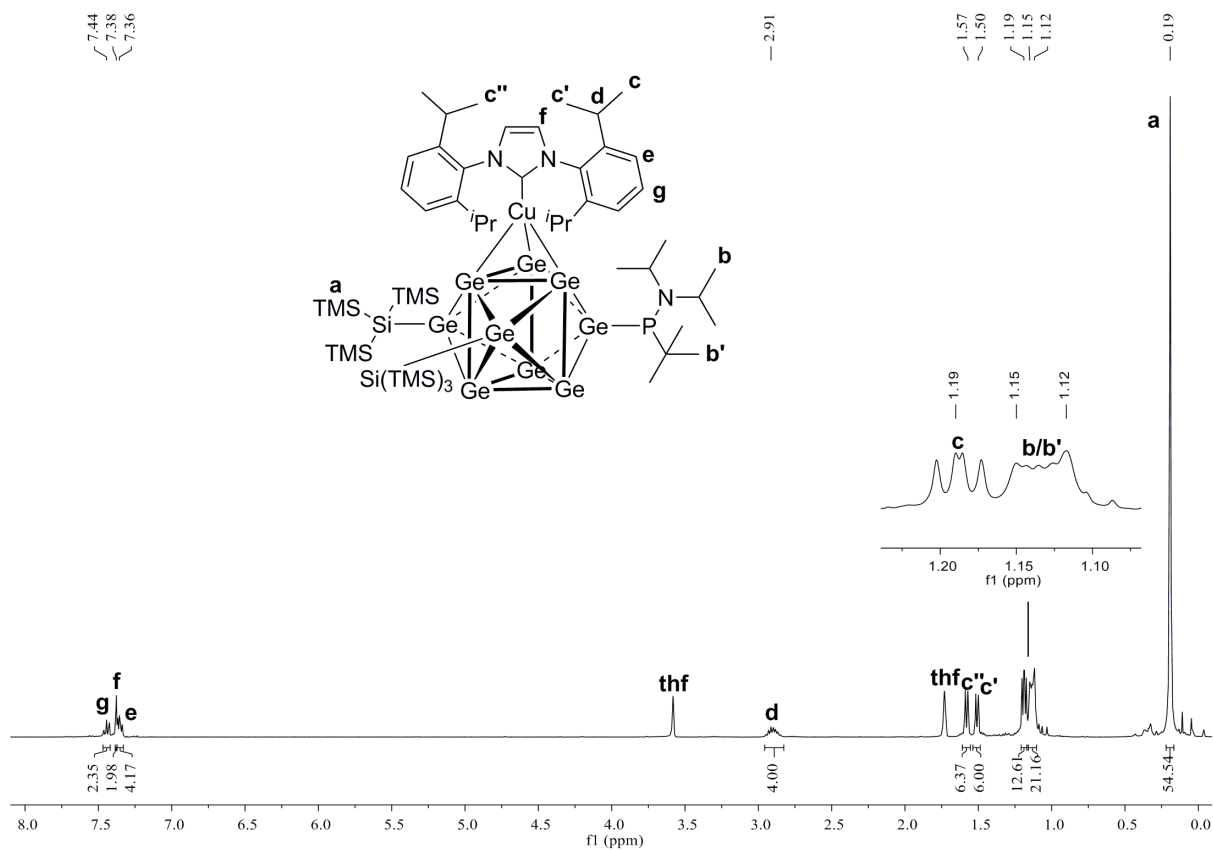


Figure S92: ¹H NMR spectrum of compound **9-CuNHC^{Dipp}** in thf-*d*₈.

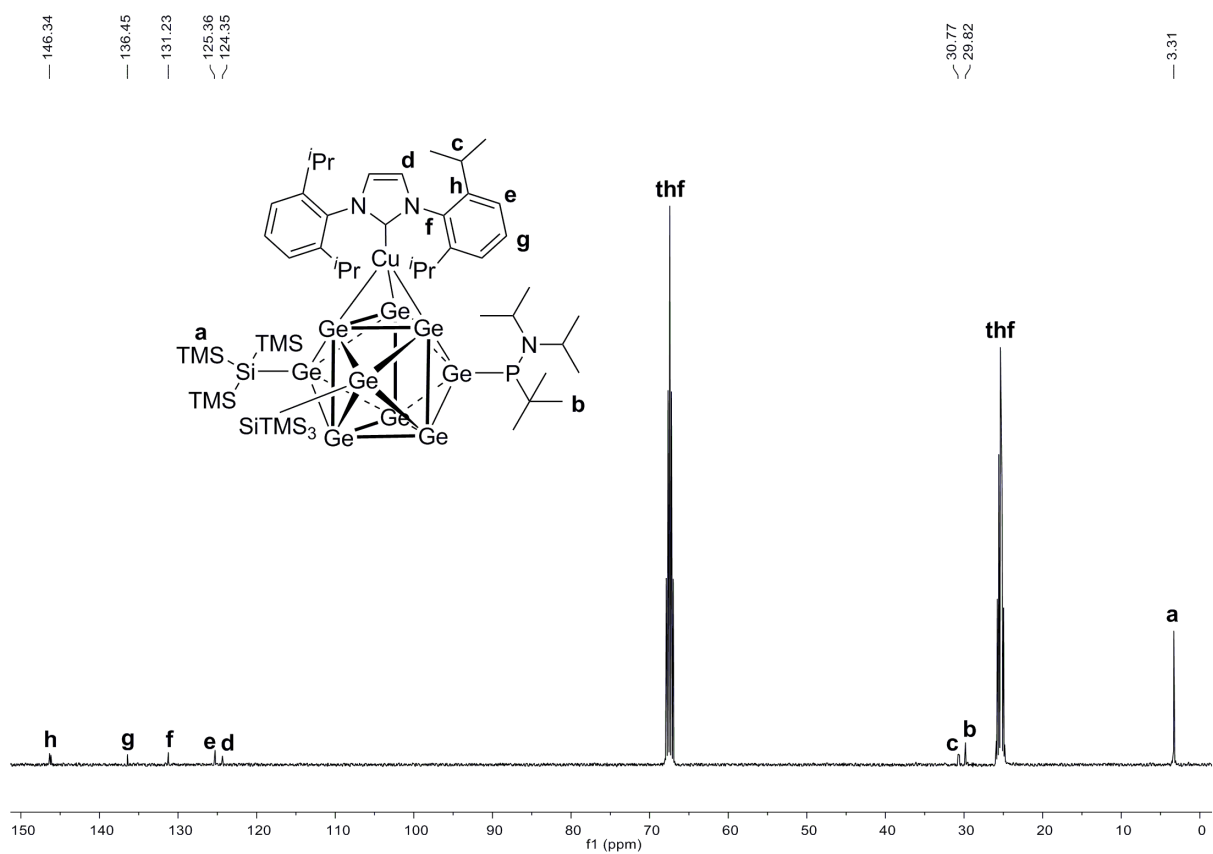
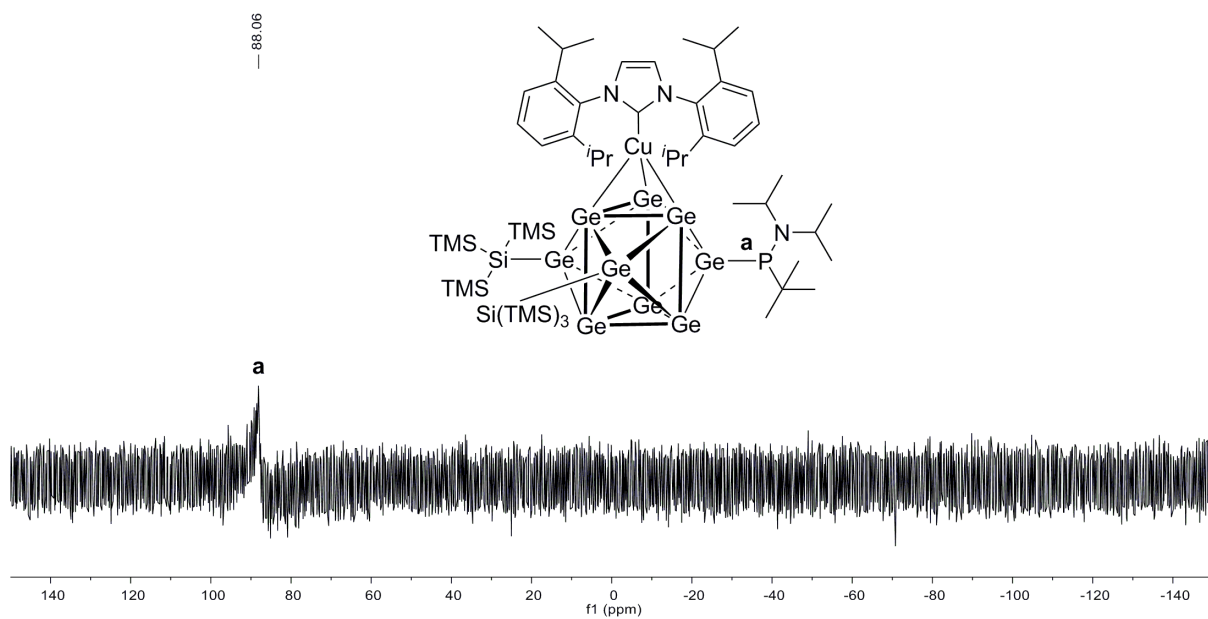
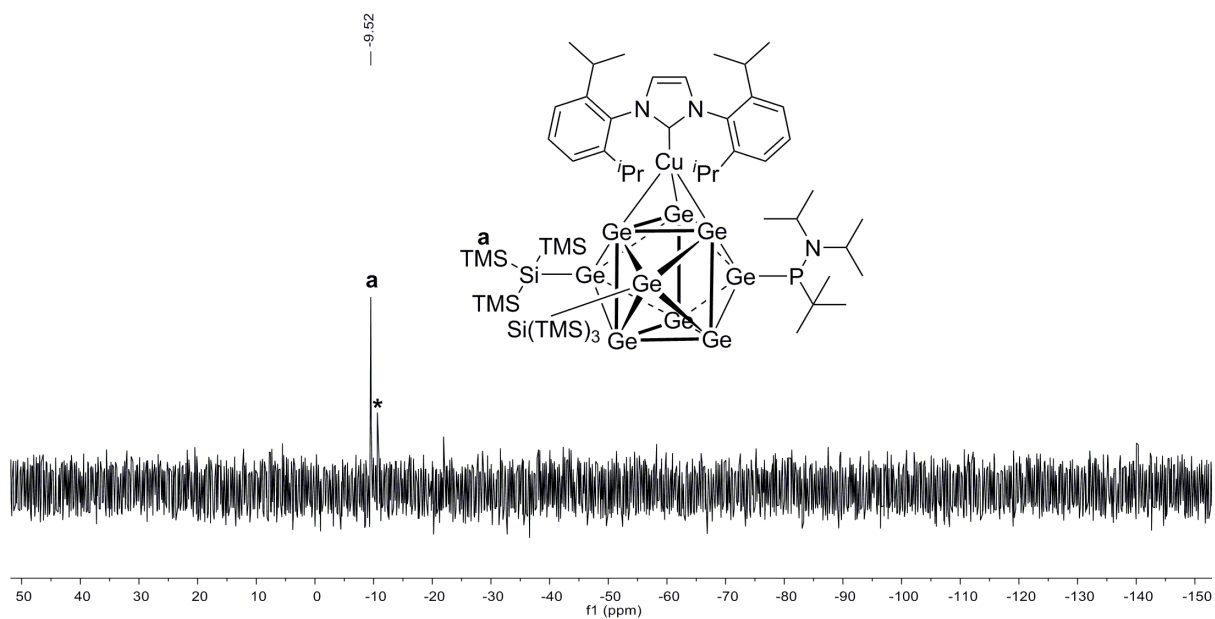


Figure S93: ¹³C NMR spectrum of compound **9-CuNHC^{Dipp}** in thf-*d*₈.



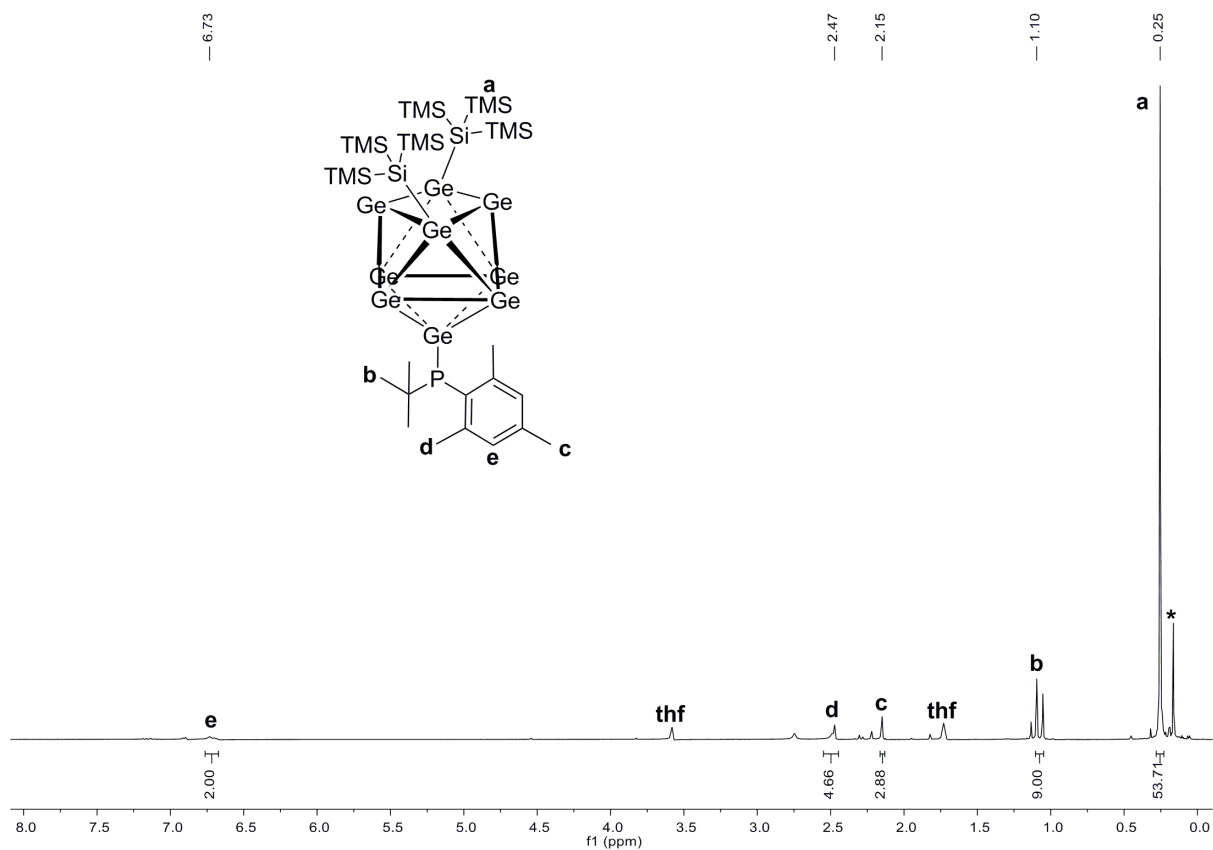


Figure S96: ^1H NMR spectrum of compound **10a** in $\text{thf-}d_8$ (signal marked with * belongs to unidentified impurity).

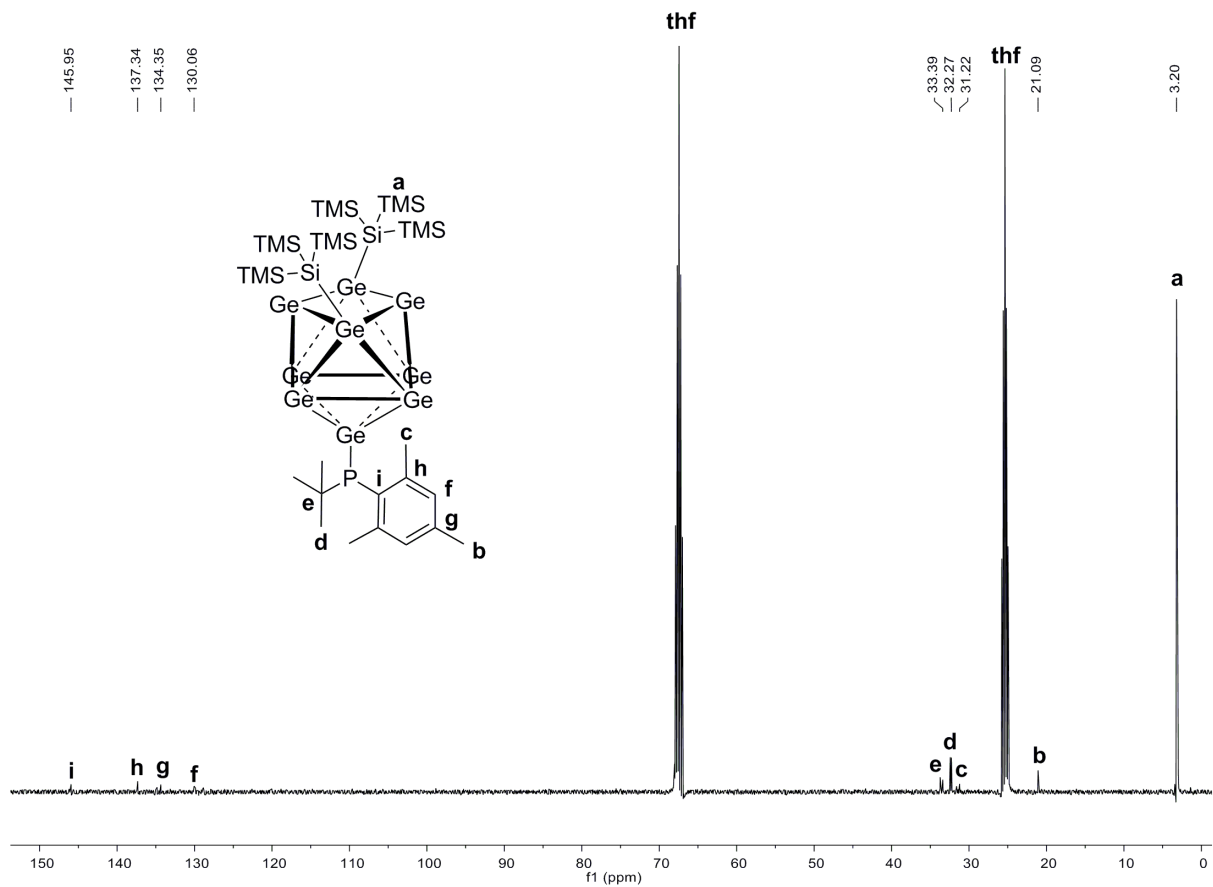


Figure S97: ^{13}C NMR spectrum of compound **10a** in $\text{thf-}d_8$.

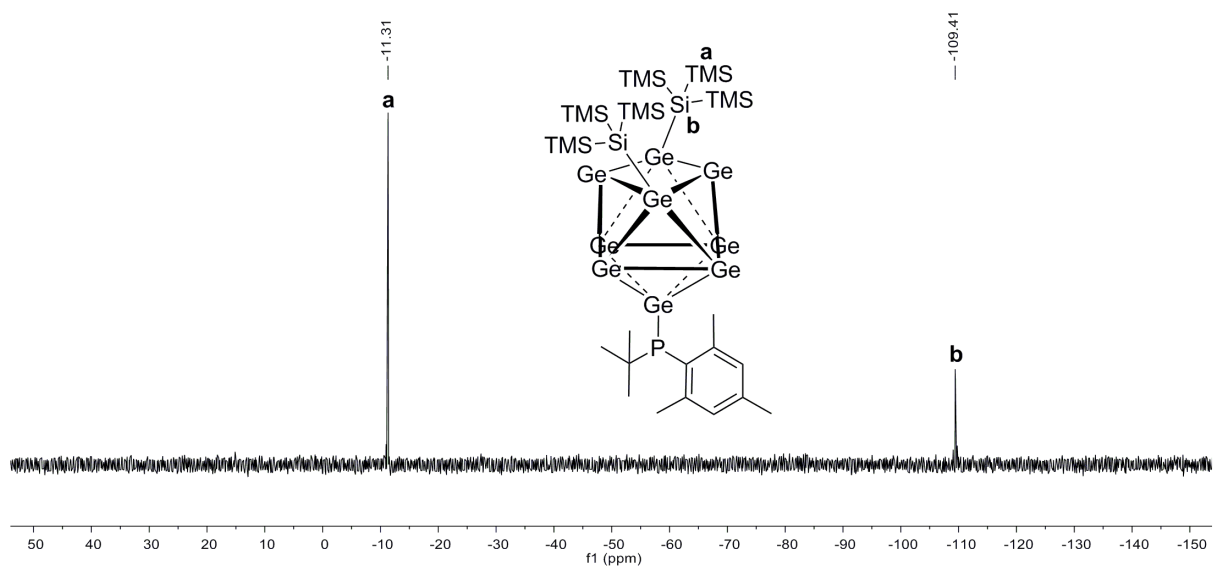


Figure S98: ^{29}Si -INEPT-RD NMR spectrum of compound **10a** in $\text{thf-}d_8$.

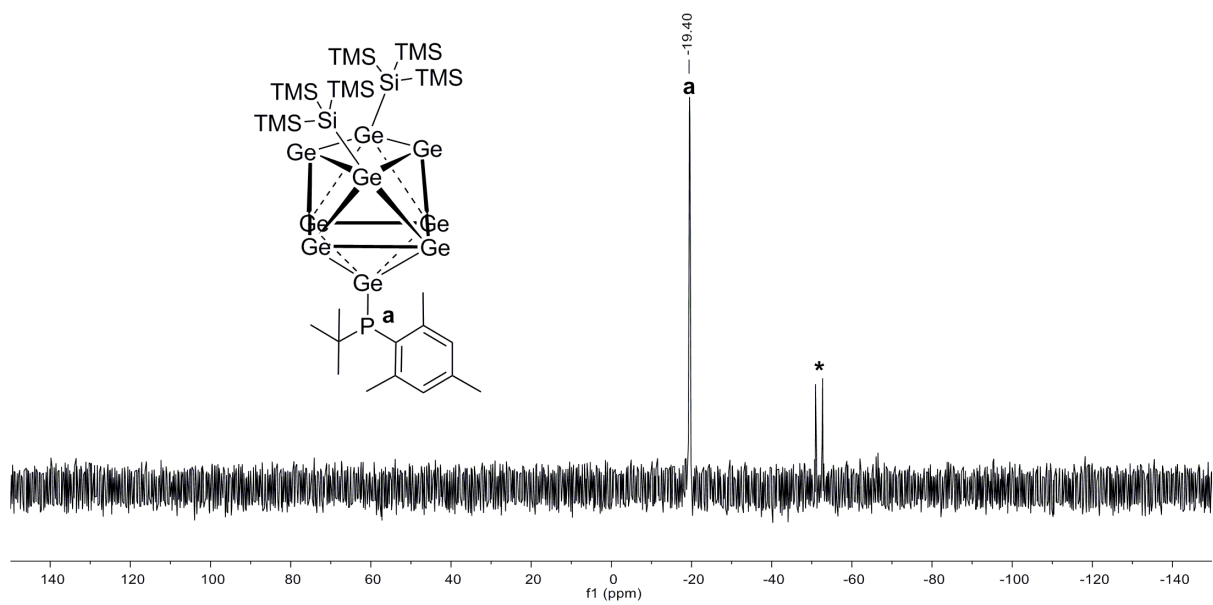


Figure S99: ^{31}P NMR spectrum of compound **10a** in $\text{thf-}d_8$ (signals marked with * belong to unidentified impurities).

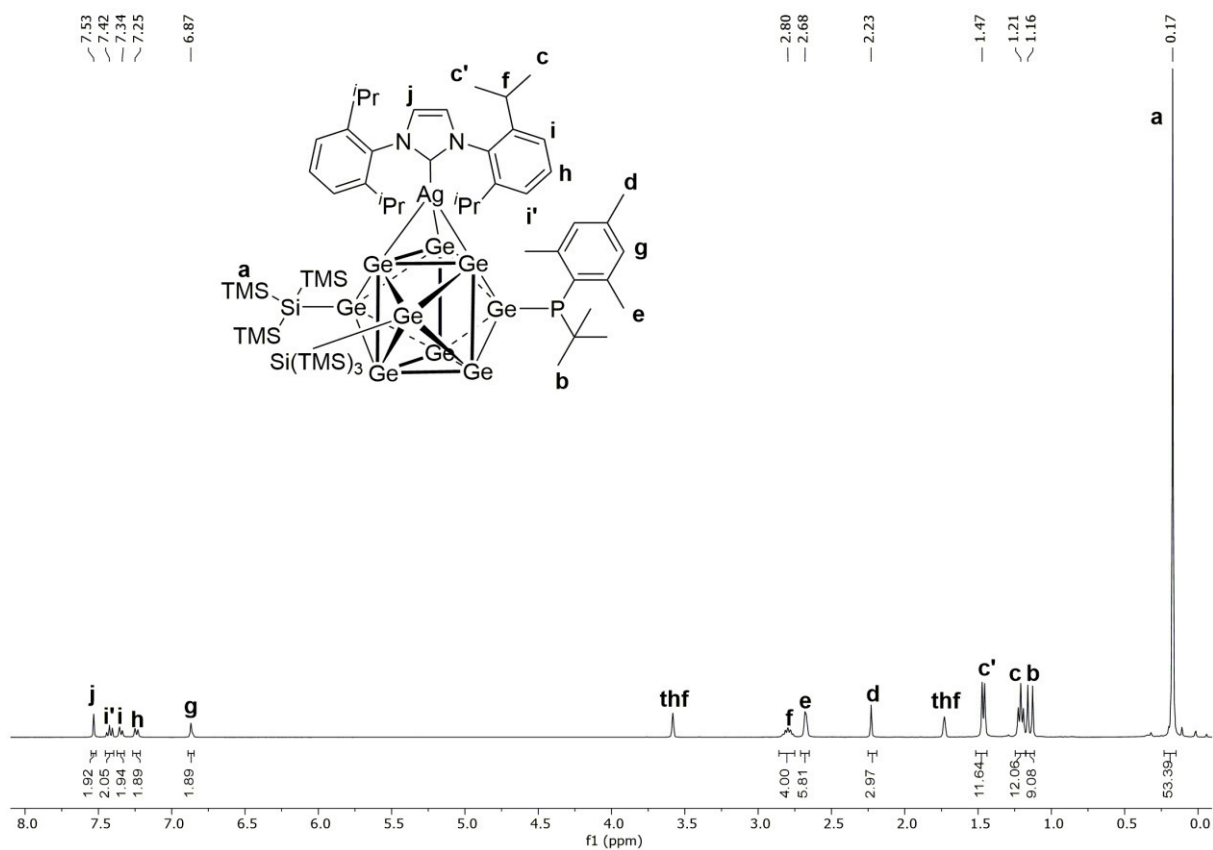


Figure S100: ¹H NMR spectrum of compound **10-AgNHC^{Dipp}** in thf-*d*₈.

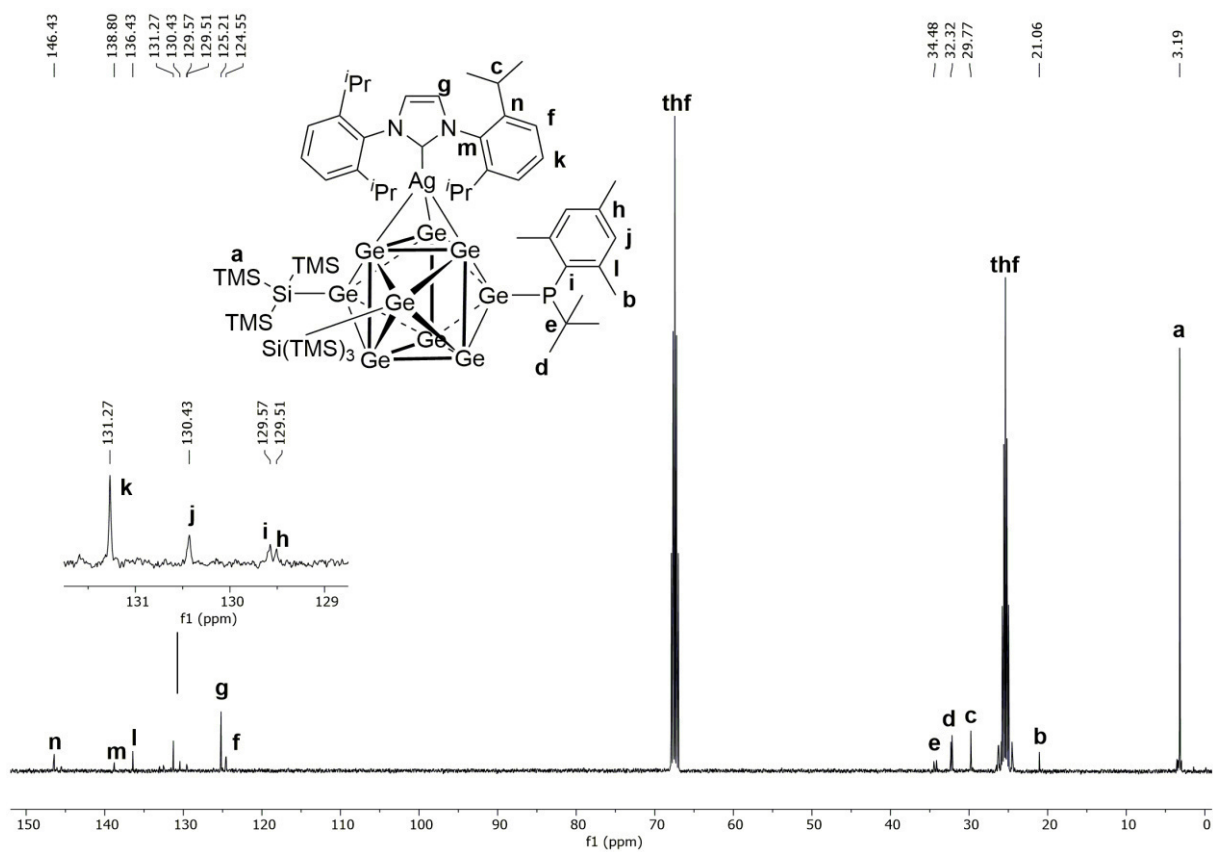


Figure S101: ¹³C NMR spectrum of compound **10-AgNHC^{Dipp}** in thf-*d*₈.

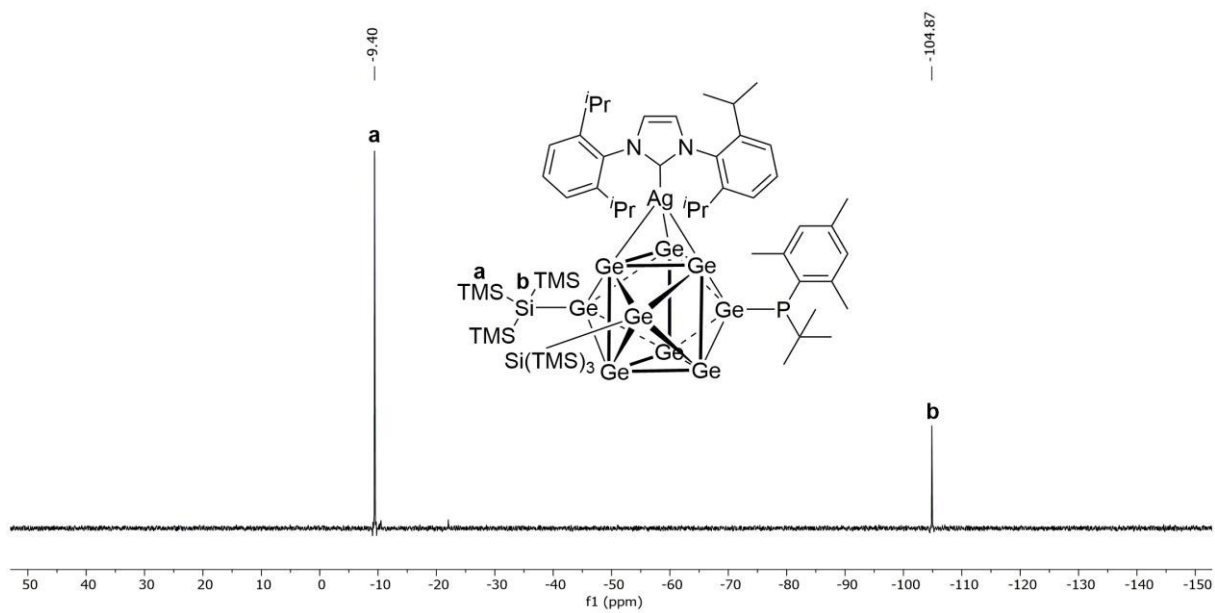


Figure S102: ^{29}Si -INEPT-RD NMR spectrum of compound **10-AgNHC^{Dipp}** in $\text{thf-}d_8$.

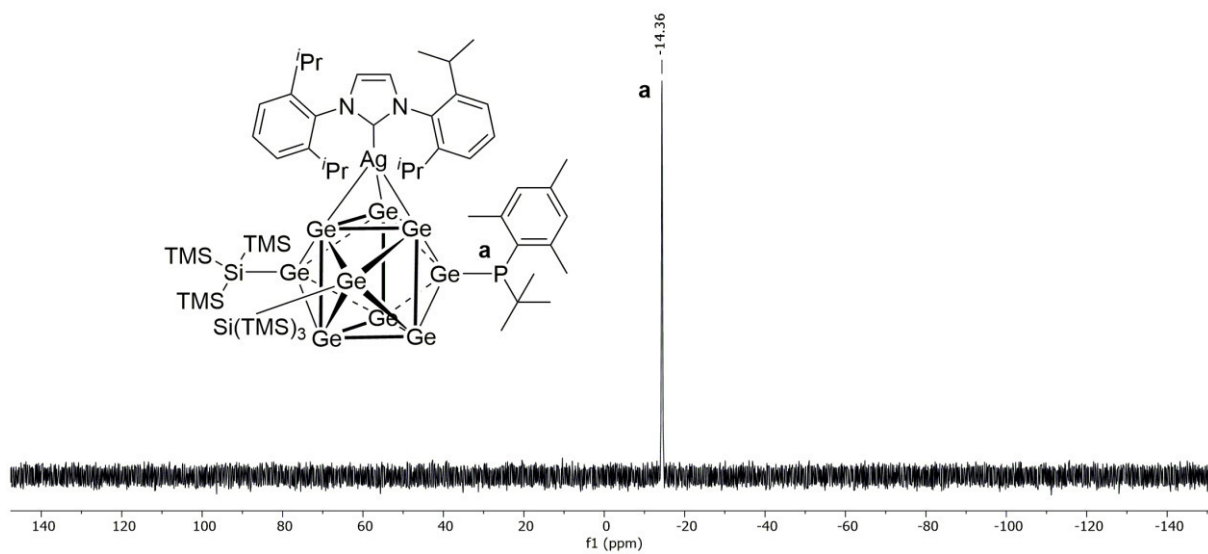


Figure S103: ^{31}P NMR spectrum of compound **10-AgNHC^{Dipp}** in $\text{thf-}d_8$.

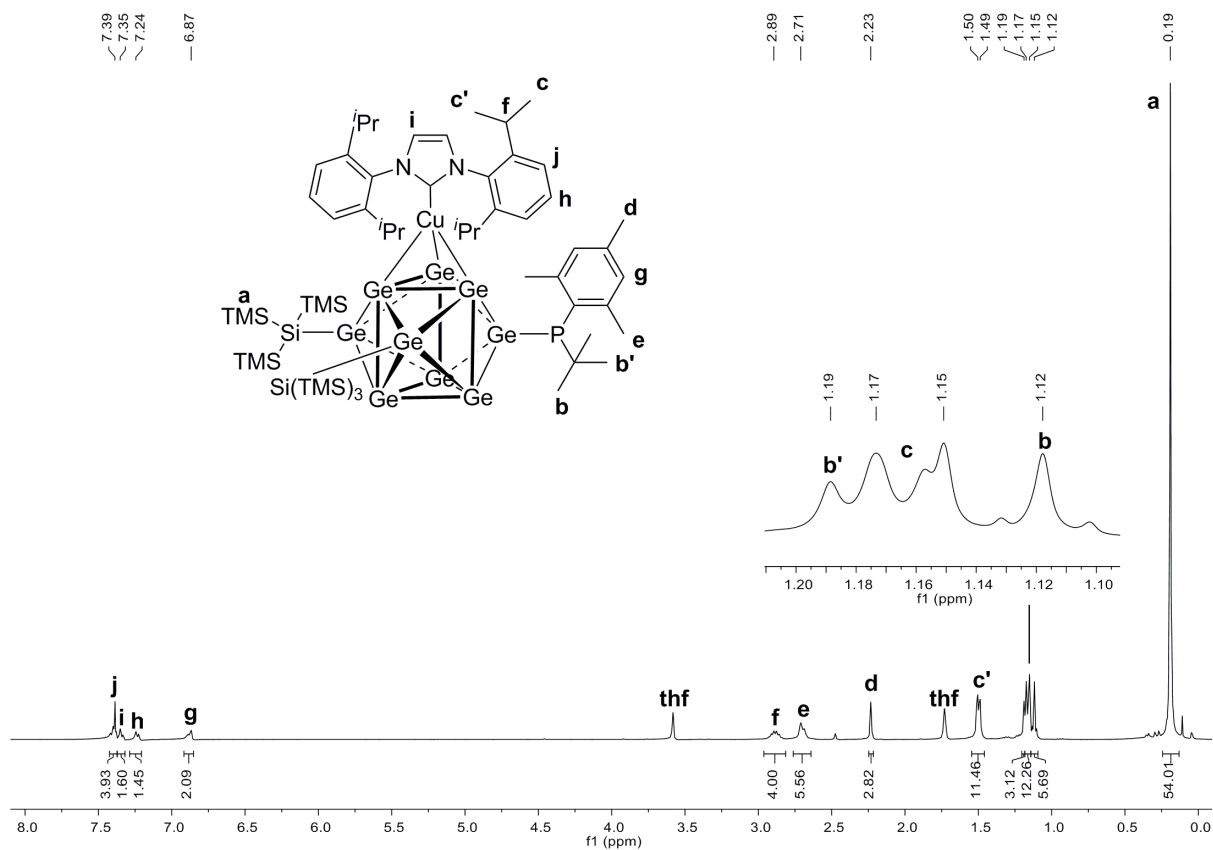


Figure S104: ¹H NMR spectrum of compound **10-CuNHC^{Dipp}** in thf-*d*₈.

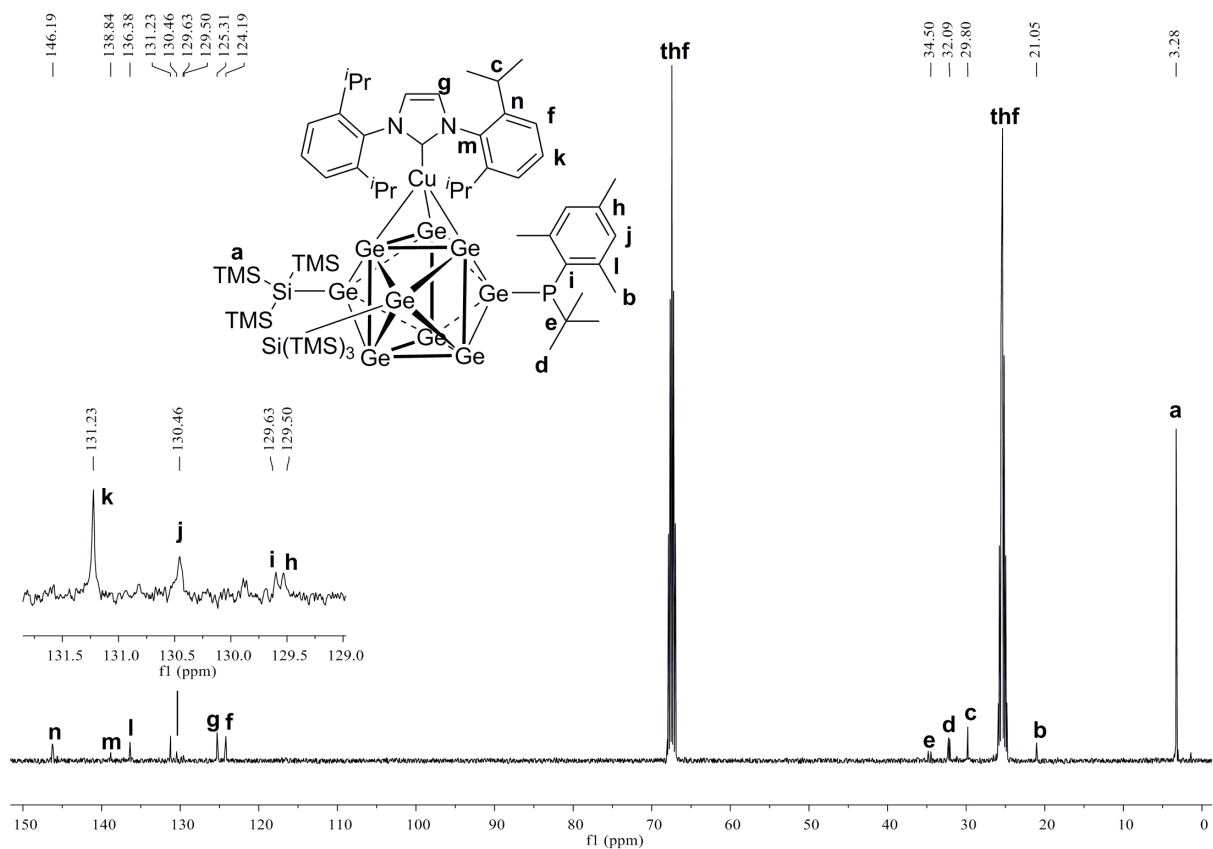


Figure S105: ¹³C NMR spectrum of compound **10-CuNHC^{Dipp}** in thf-*d*₈.

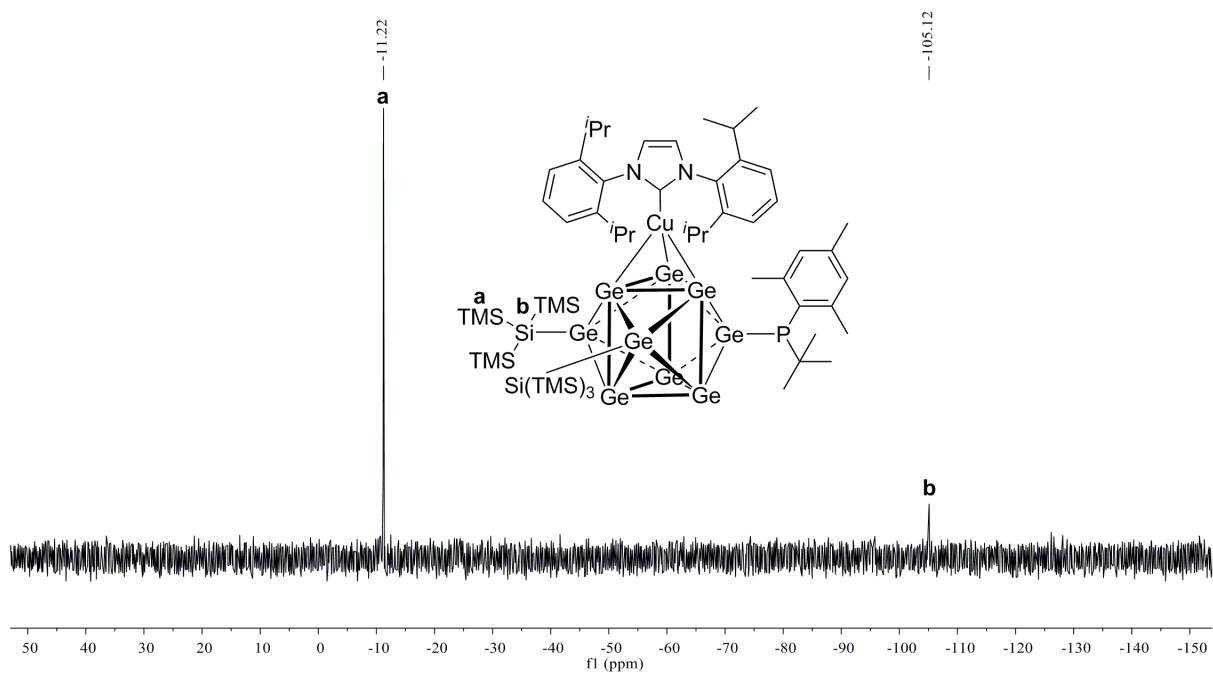


Figure S106: ^{29}Si -INEPT-RD NMR spectrum of compound **10-CuNHC^{Dipp}** in $\text{thf-}d_8$.

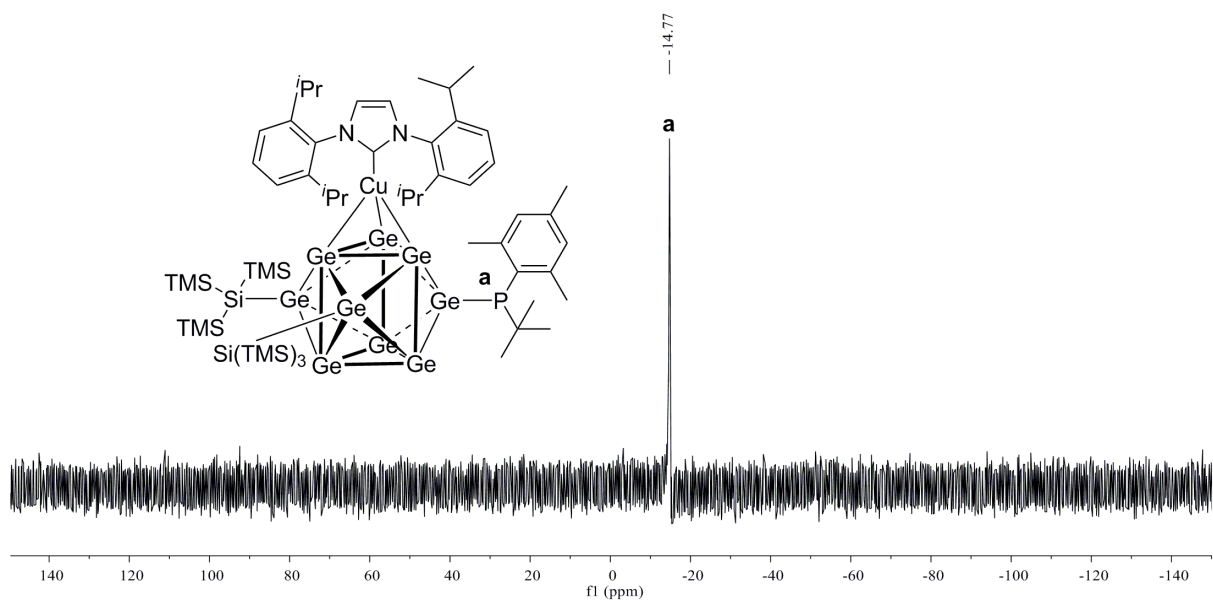


Figure S107: ^{31}P NMR spectrum of compound **10-CuNHC^{Dipp}** in $\text{thf-}d_8$.

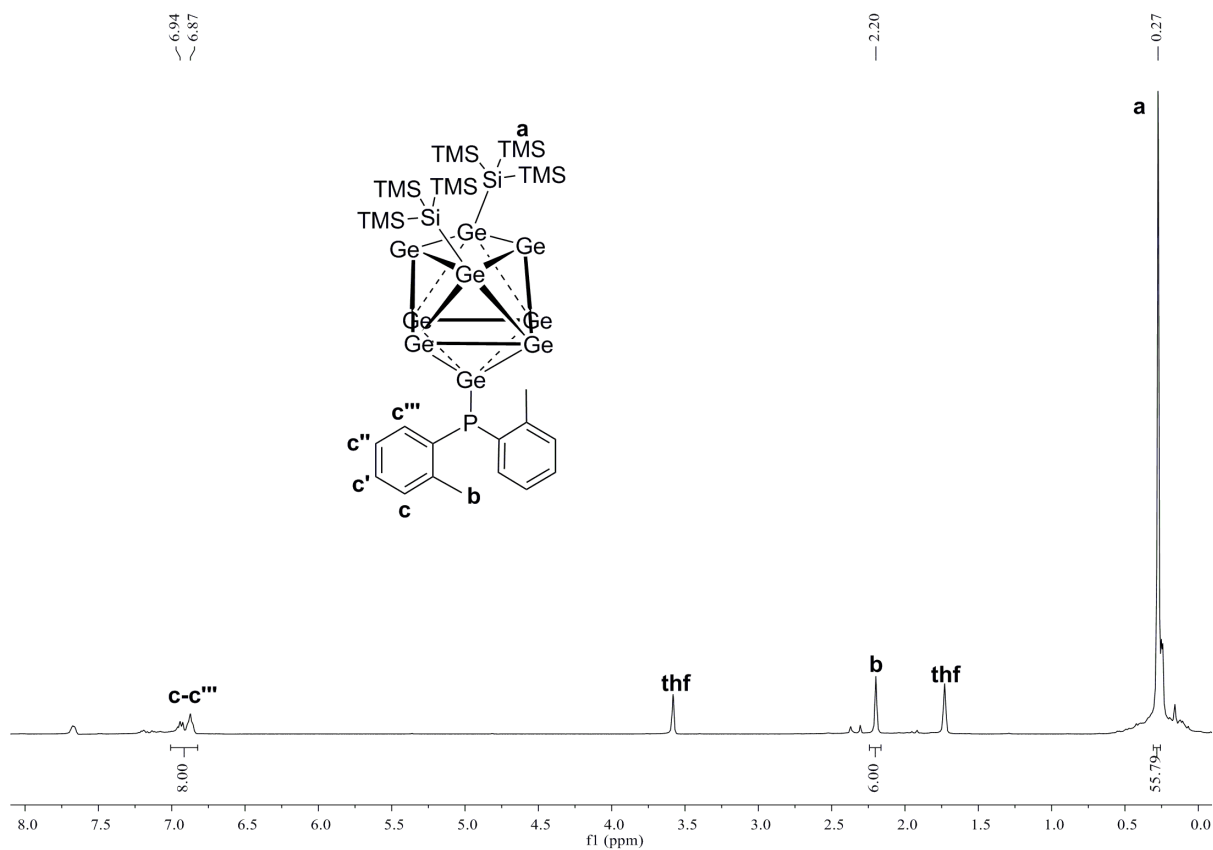


Figure S108: ¹H NMR spectrum of compound **11a** in thf-*d*₈.

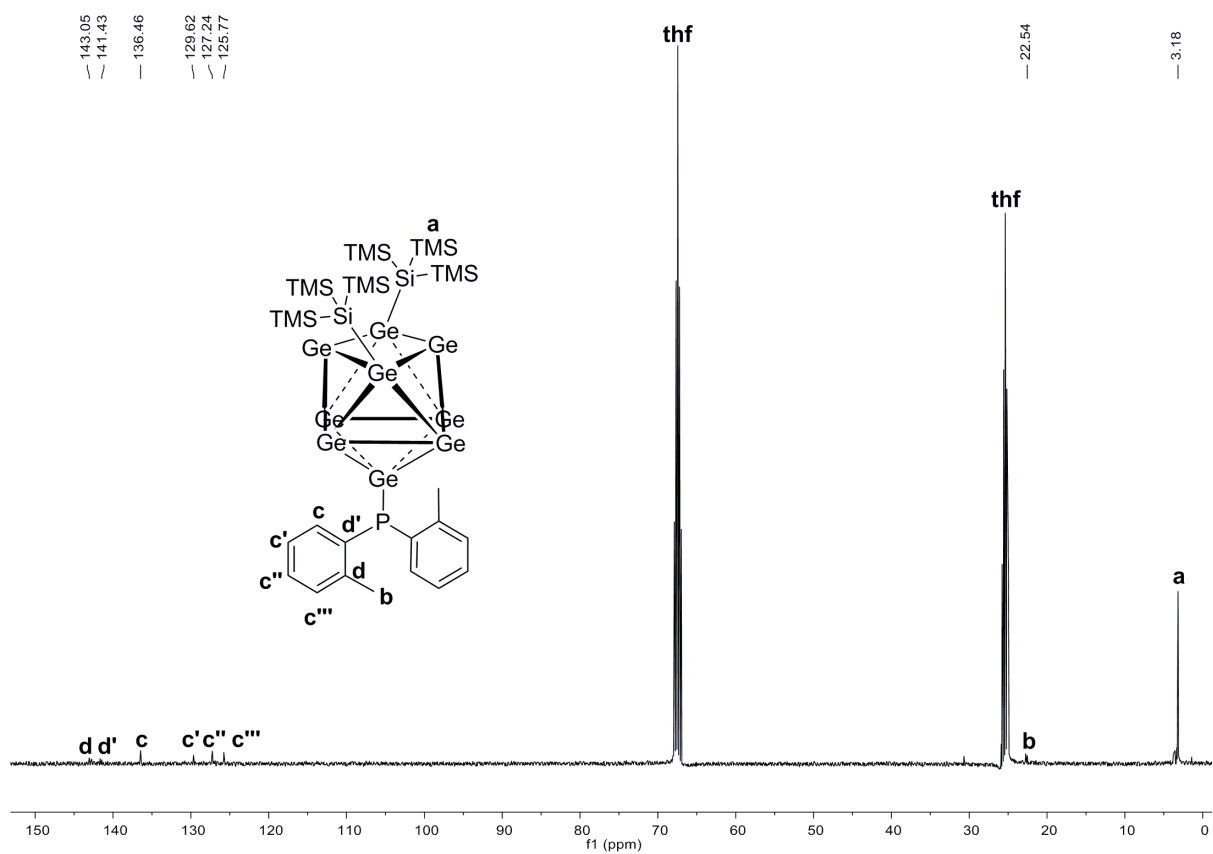


Figure S109: ¹³C NMR spectrum of compound **11a** in thf-*d*₈.

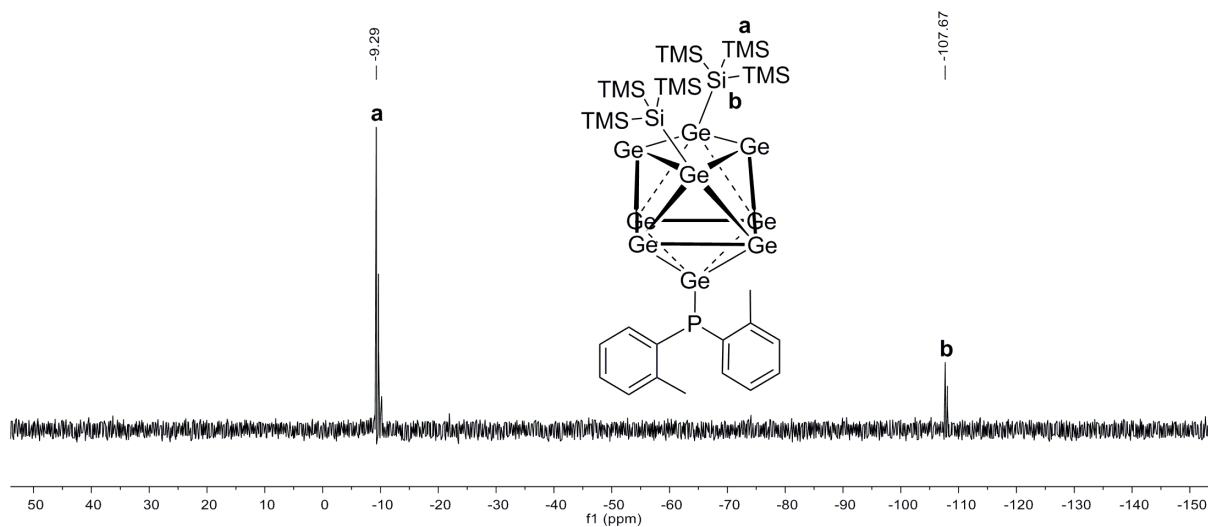


Figure S110: ^{29}Si -INEPT-RD NMR spectrum of compound **11a** in $\text{thf-}d_8$.

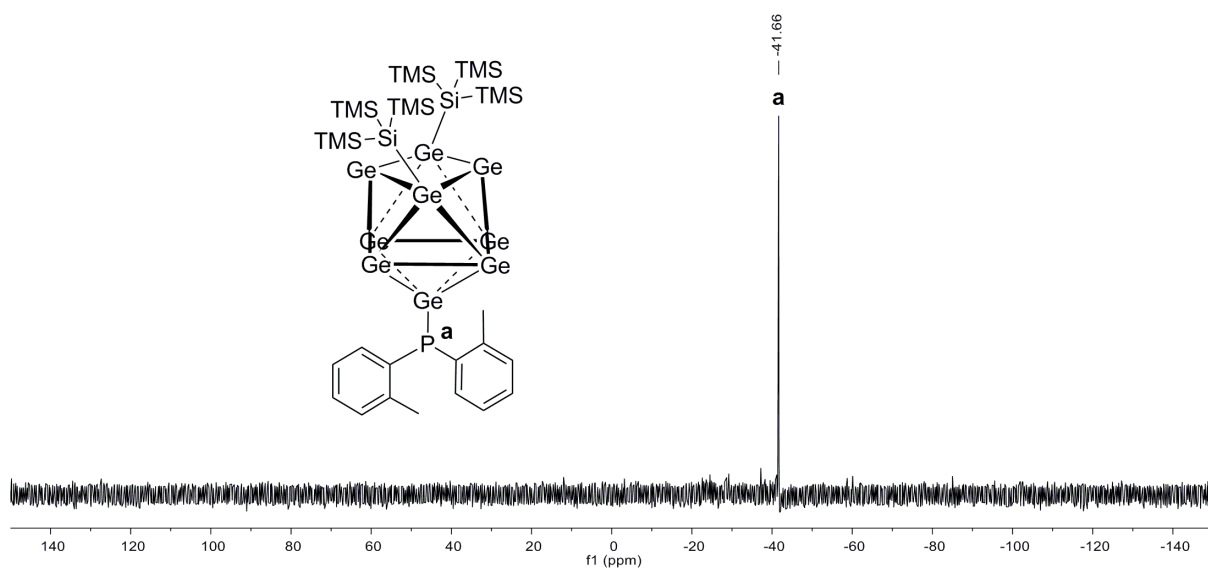


Figure S111: ^{31}P NMR spectrum of compound **11a** in $\text{thf-}d_8$.

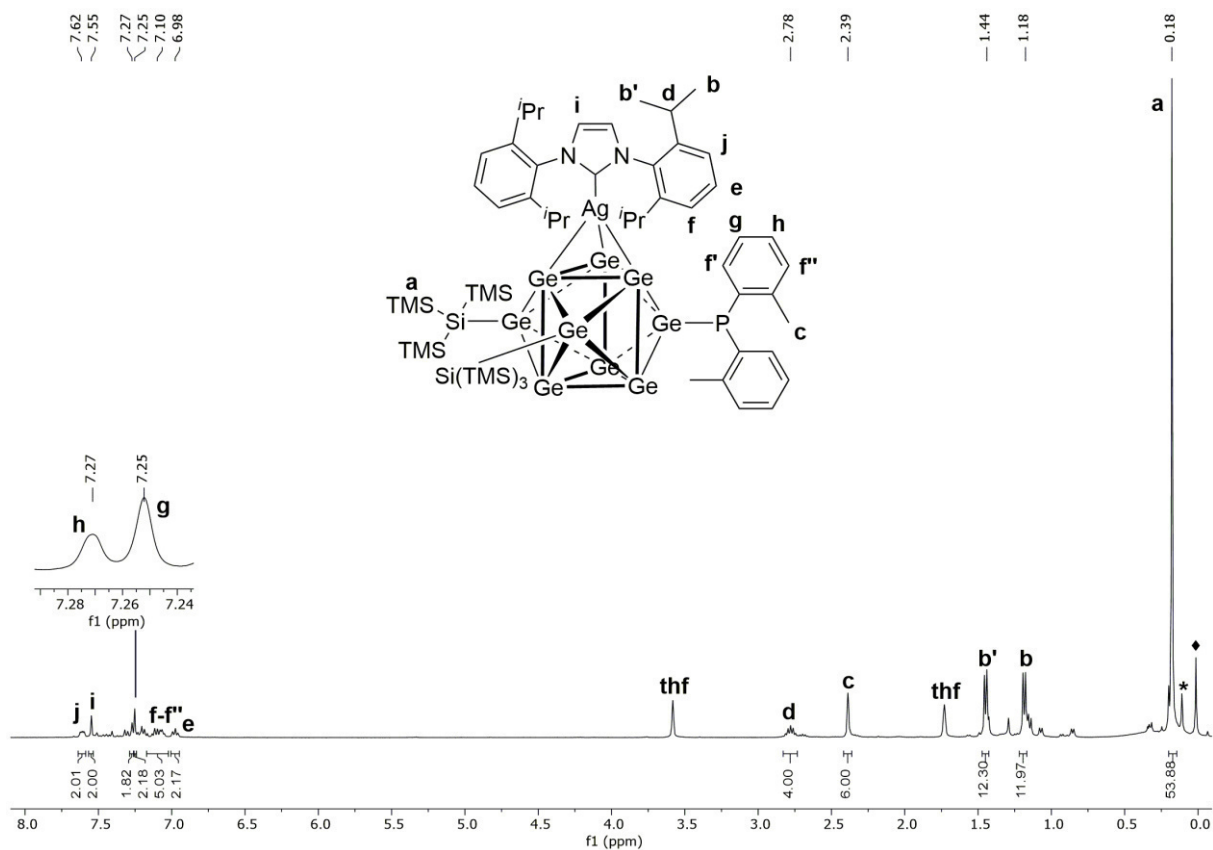


Figure S112: ¹H NMR spectrum of compound **11-AgNHC^{Dipp}** in thf-*d*₈ (signal marked with * belongs to silicon grease, signal marked with ◊ belongs to an unidentified impurity).

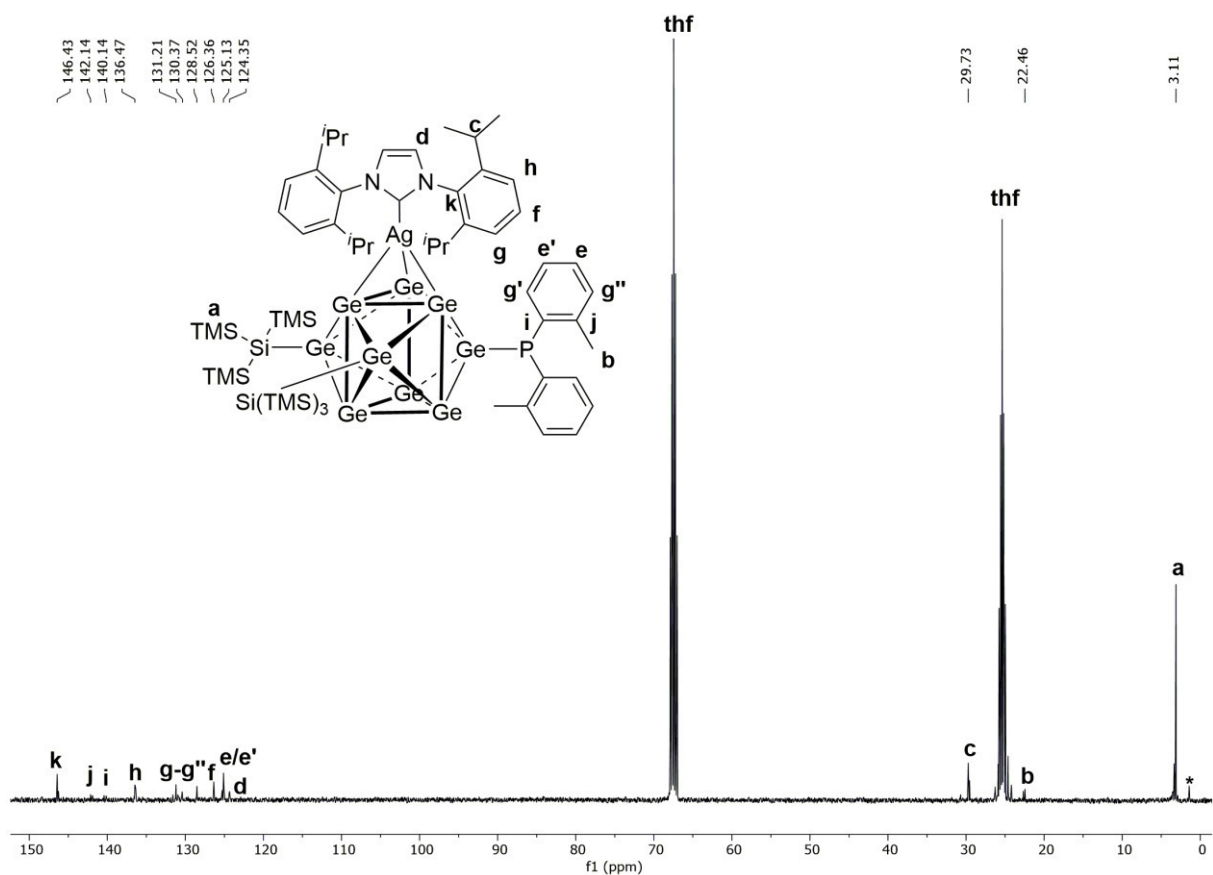


Figure S113: ¹³C NMR spectrum of compound **11-AgNHC^{Dipp}** in thf-*d*₈.

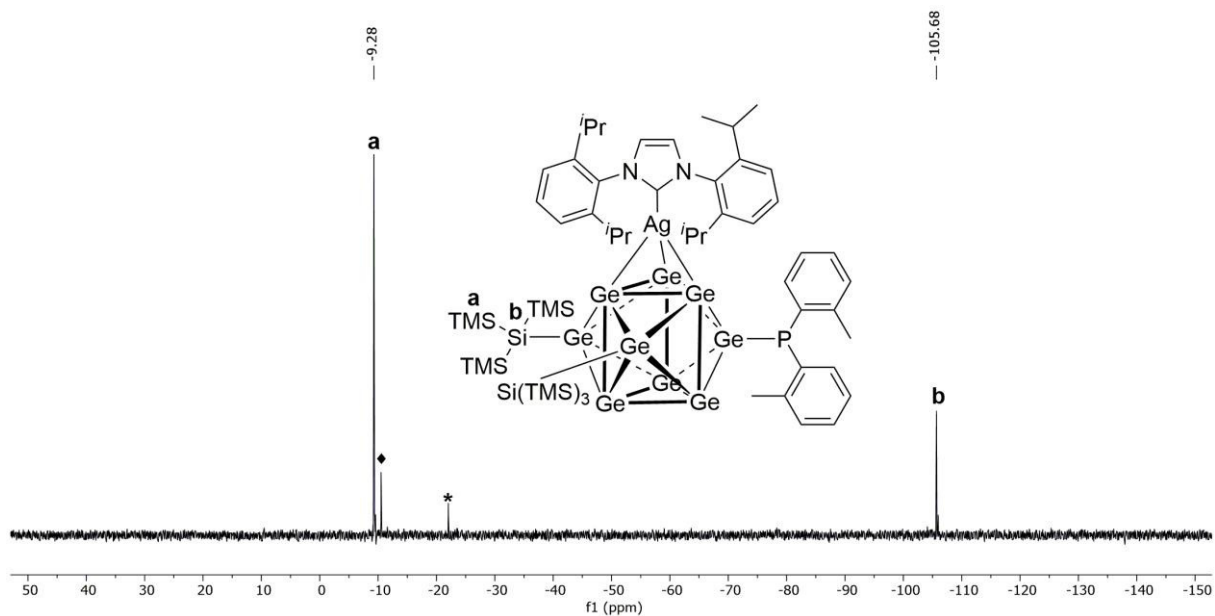


Figure S114: ^{29}Si -INEPT-RD NMR spectrum of compound **11-AgNHC^{Dipp}** in $\text{thf-}d_8$ (signal marked with ♦ belongs to an unidentified impurity, signal marked with * belongs to silicon grease).

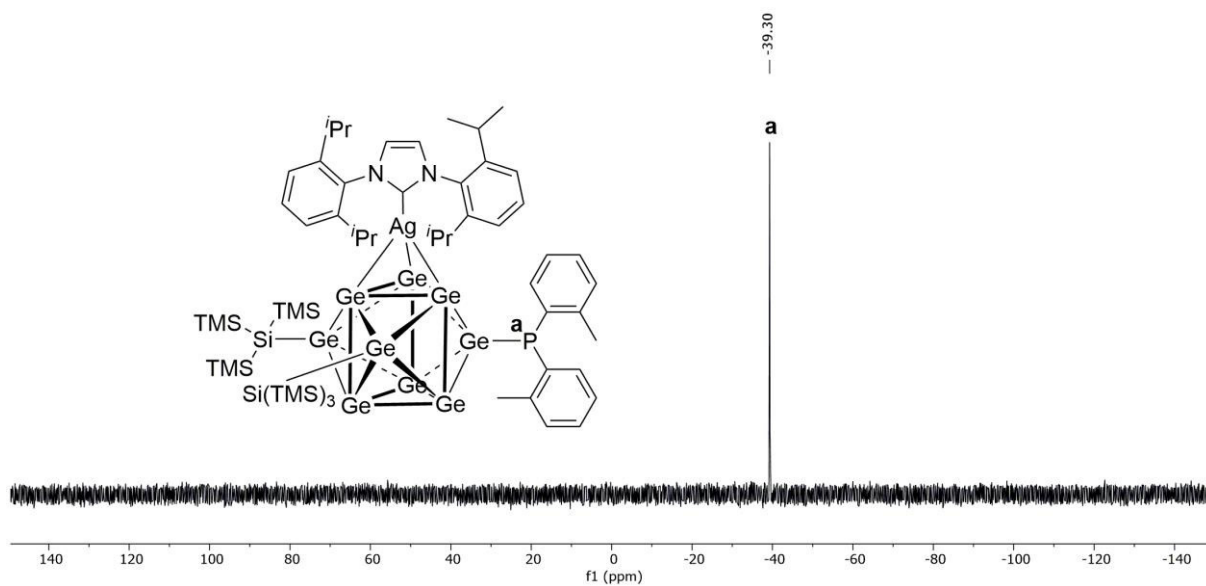


Figure S115: ^{31}P NMR spectrum of compound **11-AgNHC^{Dipp}** in $\text{thf-}d_8$.

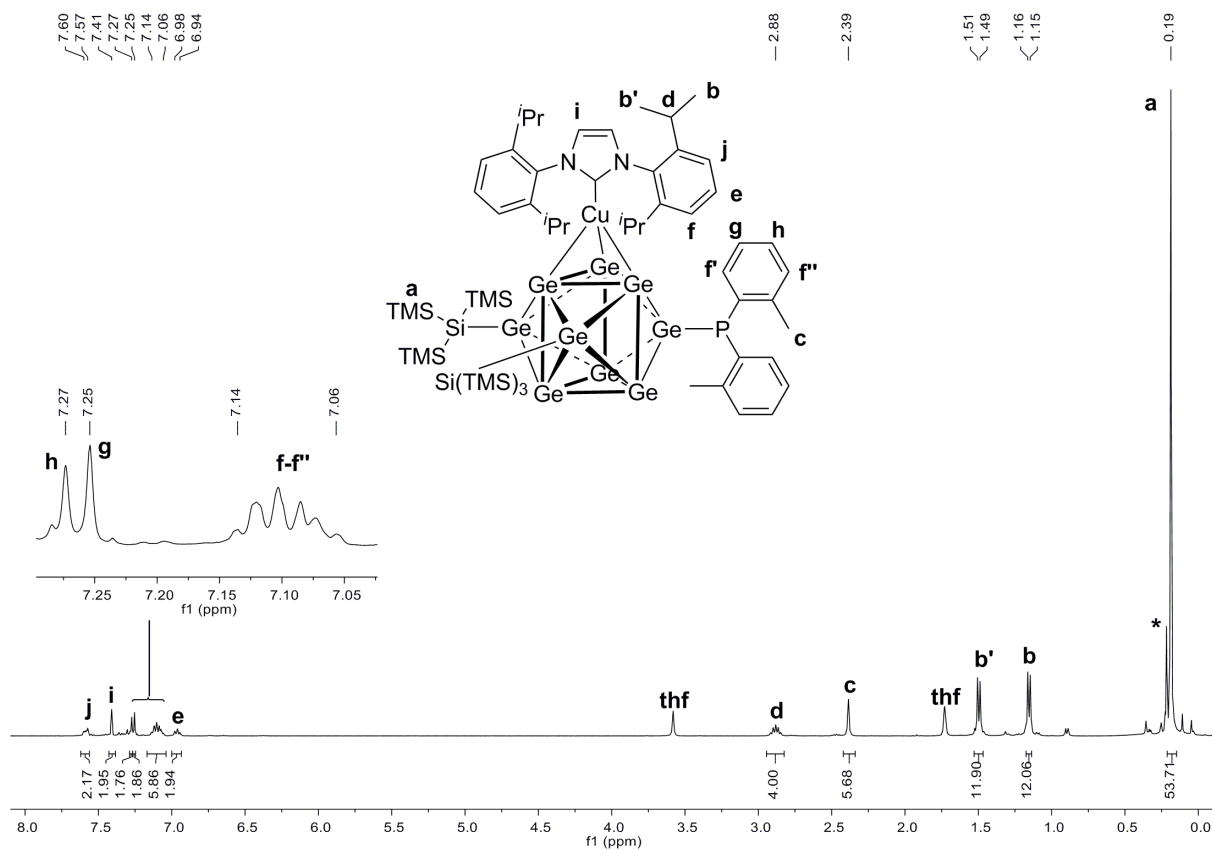


Figure S116: ¹H NMR spectrum of compound **11-CuNHC^{Dipp}** in thf-*d*₈ (signal marked with * belongs to an unidentified impurity).

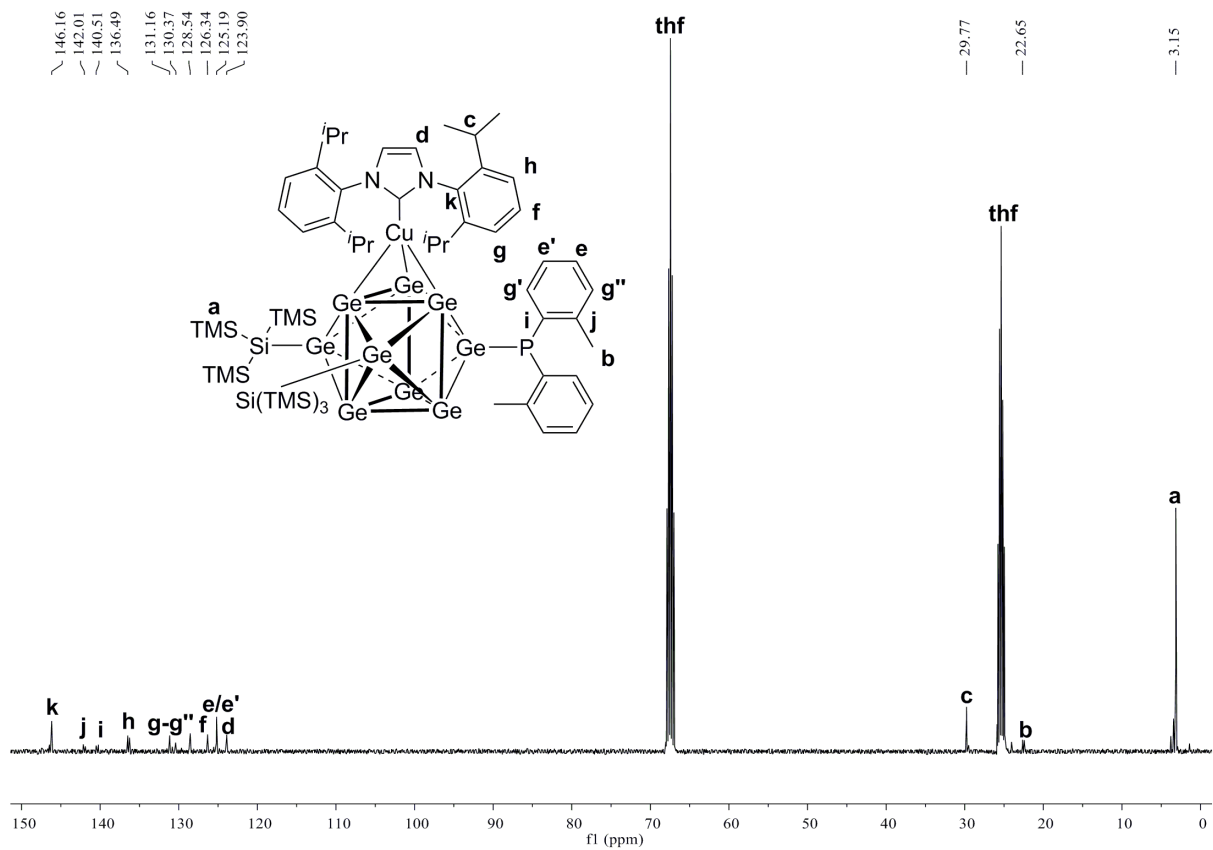


Figure S117: ¹³C NMR spectrum of compound **11-CuNHC^{Dipp}** in thf-*d*₈.

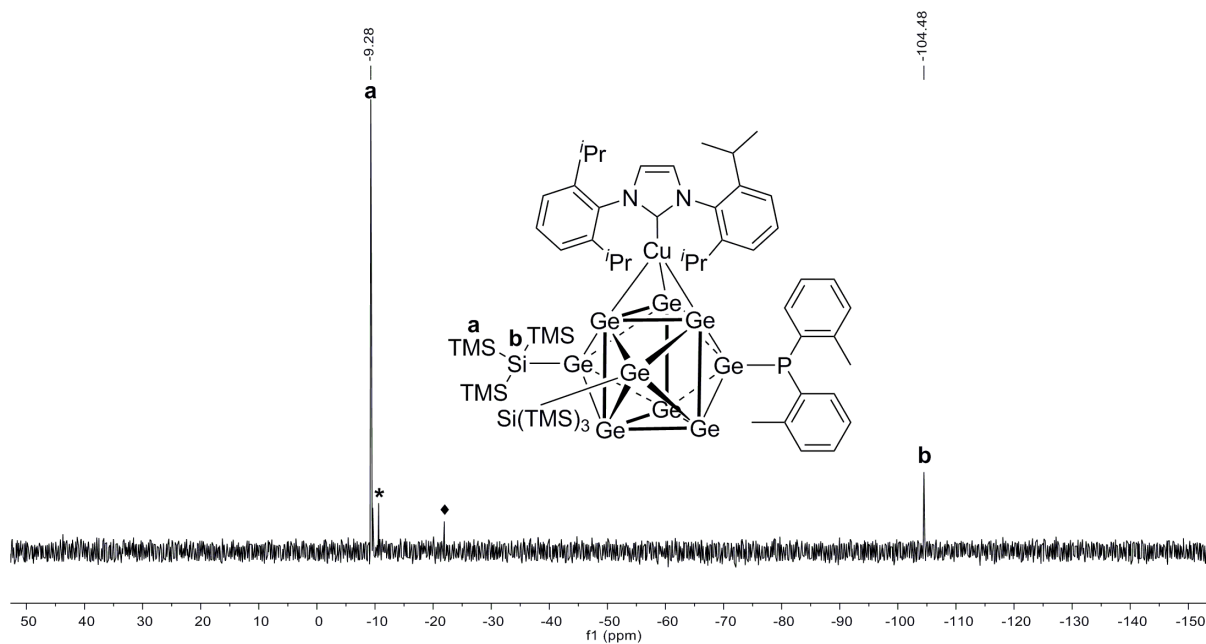


Figure S118: ^{29}Si -INEPT-RD NMR spectrum of compound **11-CuNHC^{Dipp}** in $\text{thf-}d_8$ (signal marked with * belongs to an unidentified impurity, signal marked with \blacklozenge belongs to silicon grease).

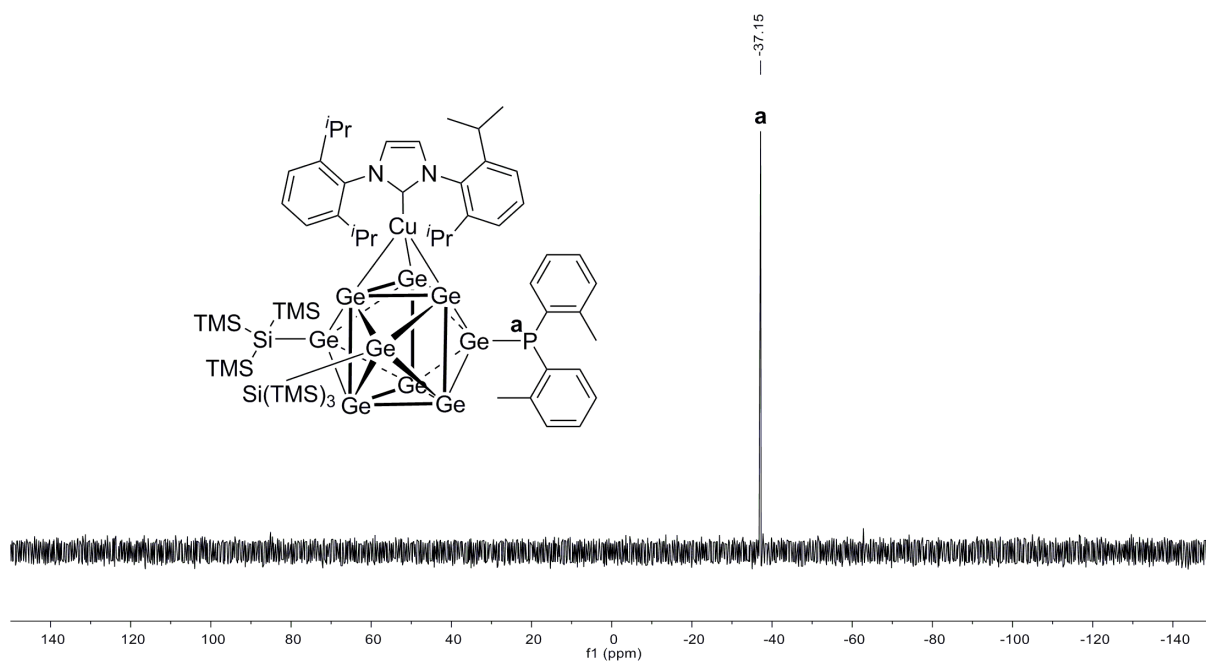


Figure S119: ^{31}P NMR spectrum of compound **11-CuNHC^{Dipp}** in $\text{thf-}d_8$.

ESI-MS spectra

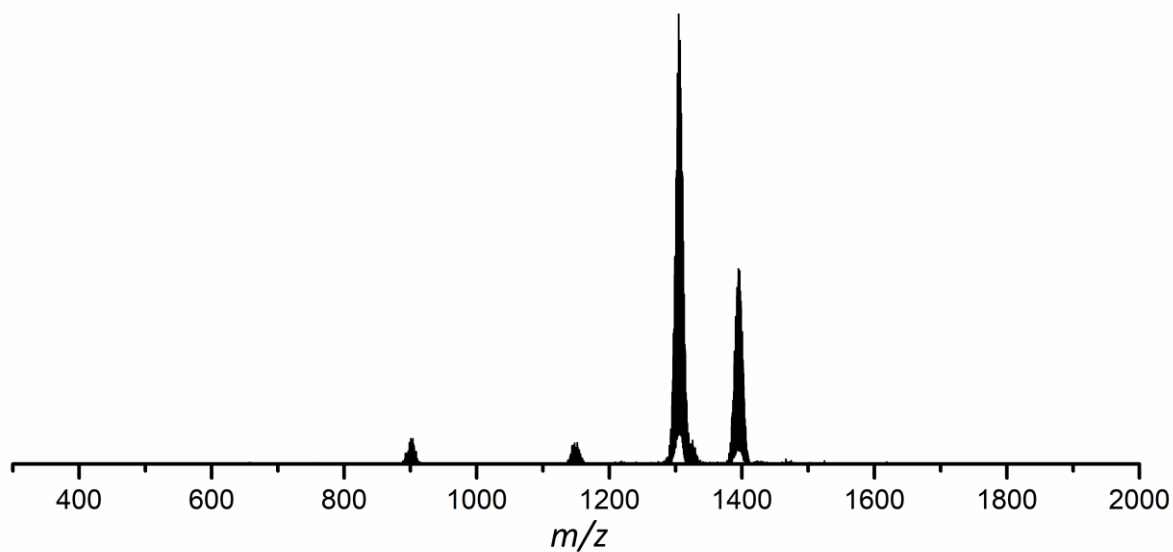


Figure S120: Overview ESI-MS (negative ion mode, 3500 V, 300 °C) obtained from a thf solution of compound **3a**, showing the molecule peak at m/z 1306.8 [$\text{Ge}_9\{\text{Si}(\text{TMS})_3\}_2\text{P}^i\text{Bu}(\text{CH}_2)_3\text{CH}=\text{CH}_2$]. Besides the molecule peak a signal at m/z 1396.4 is detected, which can be assigned to the tris-silylated cluster [$\text{Ge}_9\{\text{Si}(\text{TMS})_3\}_3$] formed during the ionization process (the signals of the species are not present in NMR spectra of **3a**). A detailed view of the signal of anion **3a** is shown in the manuscript.

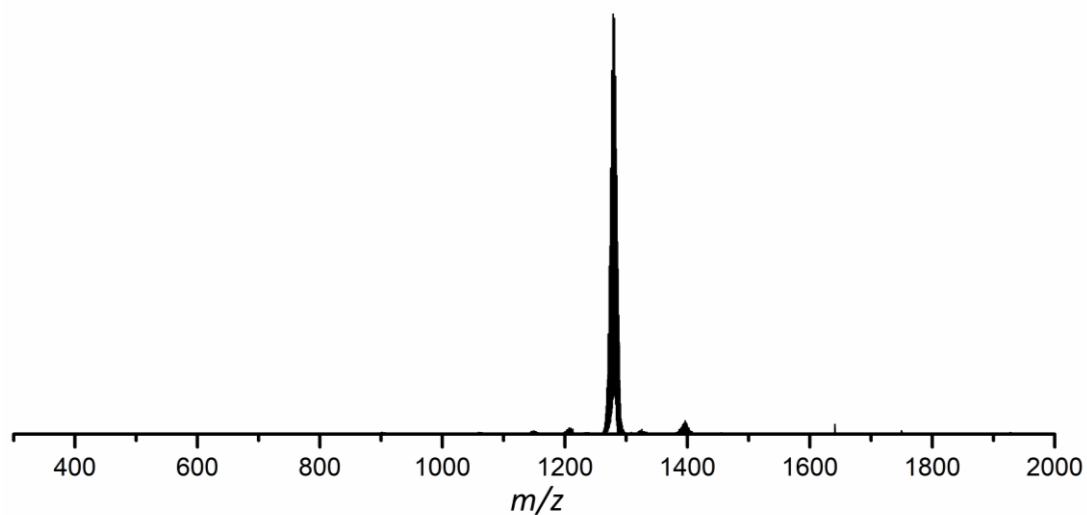


Figure S121: Overview ESI-MS (negative ion mode, 3500 V, 300 °C) obtained from a thf solution of compound **4a**, showing the molecule peak at m/z 1280.8 [$\text{Ge}_9\{\text{Si}(\text{TMS})_3\}_2\text{P}^i\text{Pr}^i\text{Bu}$].

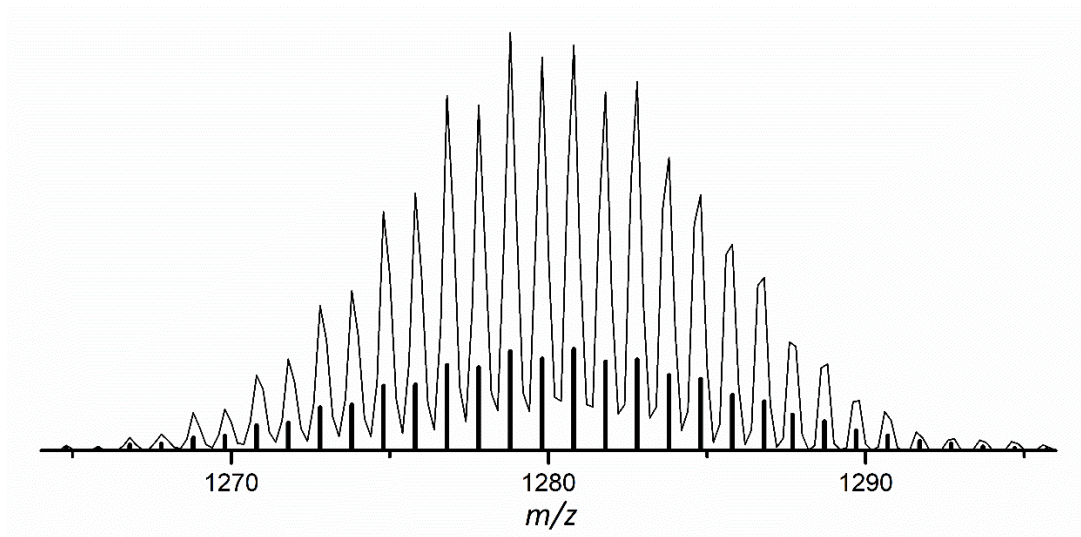


Figure S122: Detailed view of the ESI-MS signal (negative ion mode, 3500 V, 300 °C) of $[\text{Ge}_9\{\text{Si}(\text{TMS})_3\}_2\text{P}^i\text{Pr}^t\text{Bu}]^-$ (**4a**) at m/z 1280.8 obtained from a thf solution. The calculated pattern is shown as black bars.

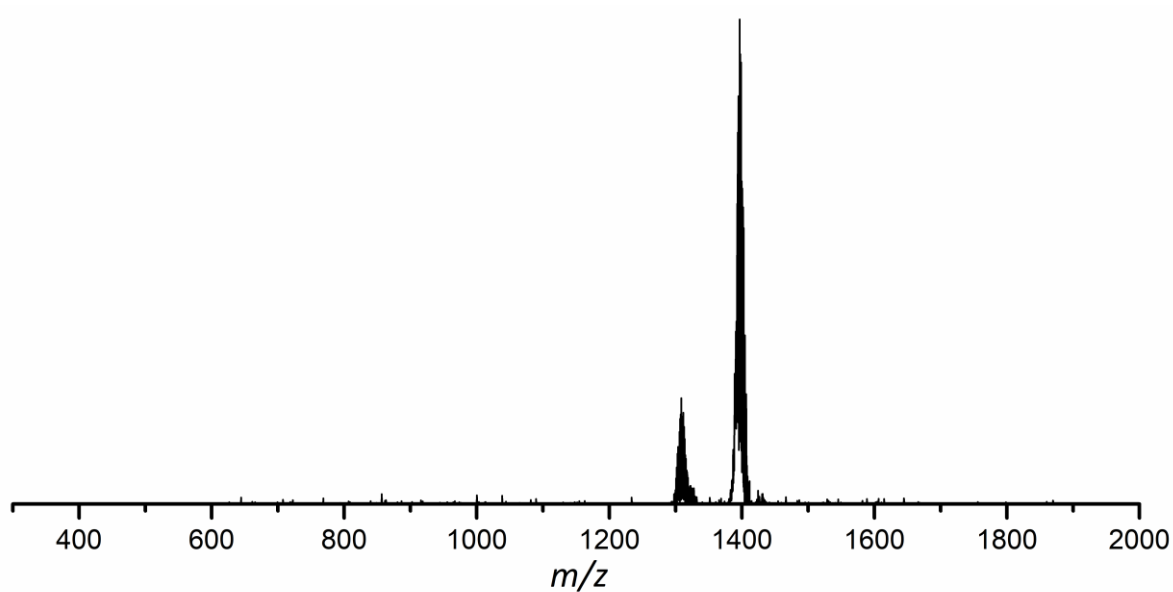


Figure S123: Overview ESI-MS (negative ion mode, 4000 V, 300 °C) obtained from a thf solution of compound **5a**, showing the molecule peak at m/z 1309.7 $[\text{Ge}_9\{\text{Si}(\text{TMS})_3\}_2\text{P}^i\text{Bu}(\text{NEt}_2)]^-$. Besides the molecule peak a signal at m/z 1396.4 is detected, which can be assigned to tris-silylated cluster $[\text{Ge}_9\{\text{Si}(\text{TMS})_3\}_3]^-$ formed during the ionization process (the signals of the species are not present in NMR spectra of **5a**).

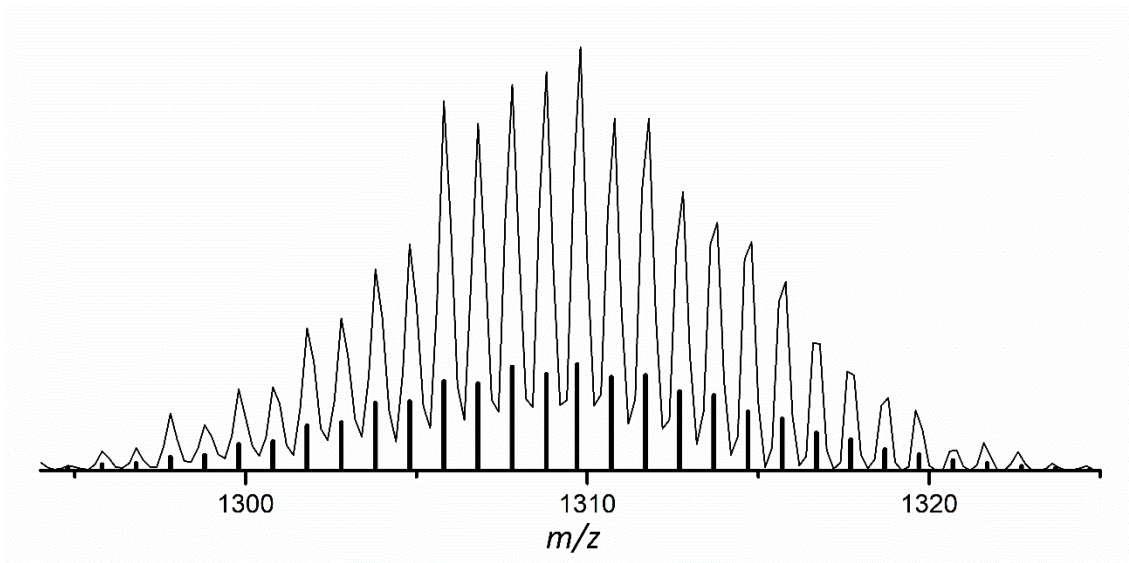


Figure S124: Detail view of ESI-MS signal (negative ion mode, 4000 V, 300 °C) of $[\text{Ge}_9\{\text{Si}(\text{TMS})_3\}_2\text{P}^t\text{Bu}(\text{NEt}_2)]^-$ (**5a**) at m/z 1309.7 obtained from a thf solution. The calculated pattern is shown as black bars.

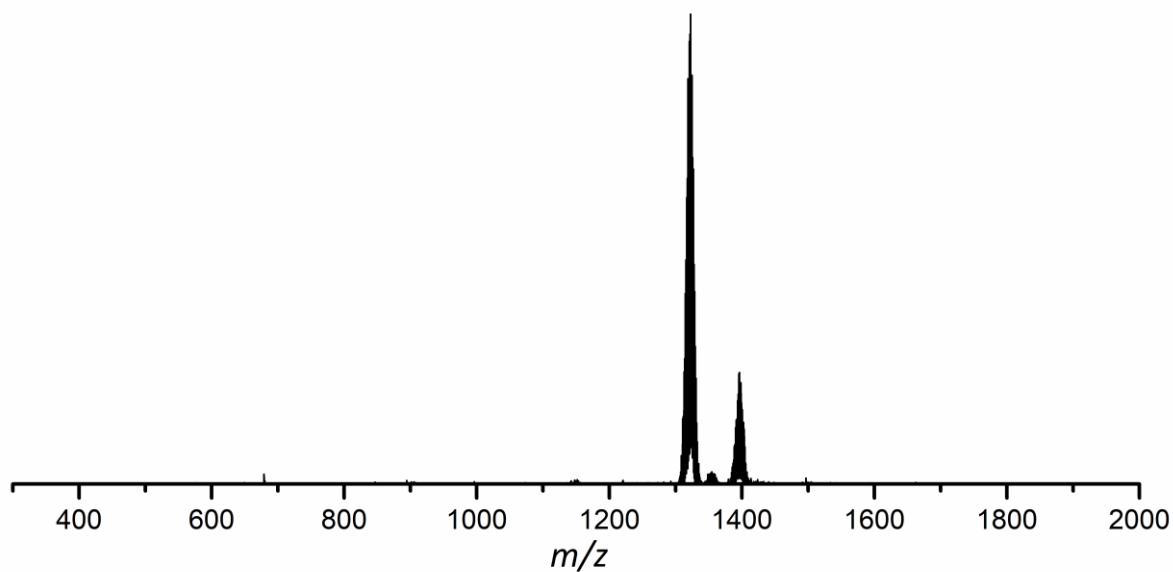


Figure S125: Overview ESI-MS (negative ion mode, 3000 V, 300 °C) obtained from a thf solution of compound **6a**, showing the molecule peak at m/z 1322.8 $[\text{Ge}_9\{\text{Si}(\text{TMS})_3\}_2\text{P}(1,1\text{-dimethylpropyl})_2]^-$. Besides the molecule peak a signal at m/z 1396.4 is detected, which can be assigned to the tris-silylated cluster $[\text{Ge}_9\{\text{Si}(\text{TMS})_3\}_3]^-$ formed during the ionization process (the signals of this species is not present in NMR spectra of **6a**).

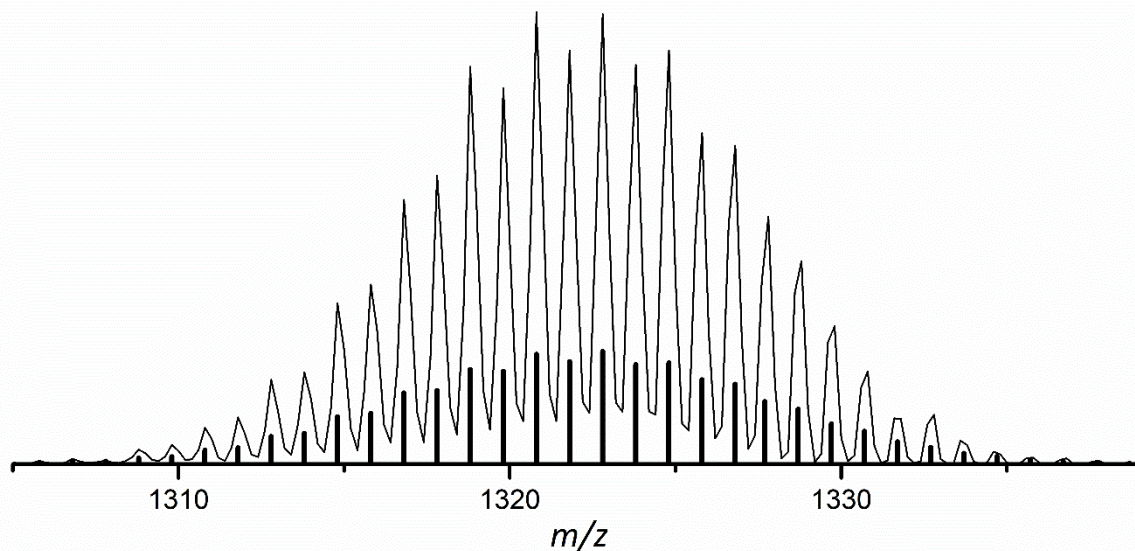


Figure S126: Detail view of ESI-MS signal (negative ion mode, 3000 V, 300 °C) of $[\text{Ge}_9(\text{Si}(\text{TMS})_3)_2\text{P}(1,1\text{-dimethylpropyl})_2]$ (**6a**) at m/z 1322.8 obtained from a thf solution. The calculated pattern is represented as black bars.

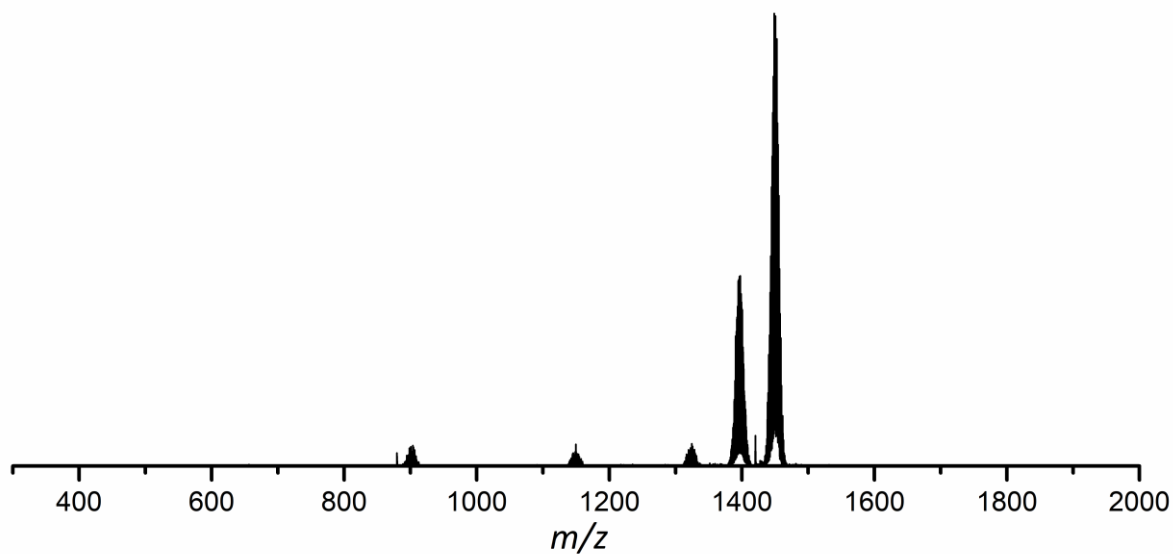


Figure S127: Overview ESI-MS (negative ion mode, 4000 V, 300 °C) obtained from a thf solution of compound **7a**, showing the molecule peak at m/z 1450.8 $[\text{Ge}_9(\text{Si}(\text{TMS})_3)_2\text{P}(1\text{-adamantyl})_2]$. Besides the molecule peak a signal at m/z 1396.4 is detected, which can be assigned to the tris-silylated cluster $[\text{Ge}_9(\text{Si}(\text{TMS})_3)_3]$ formed during the ionization process (the signals of this species are not present in NMR spectra of **7a**).

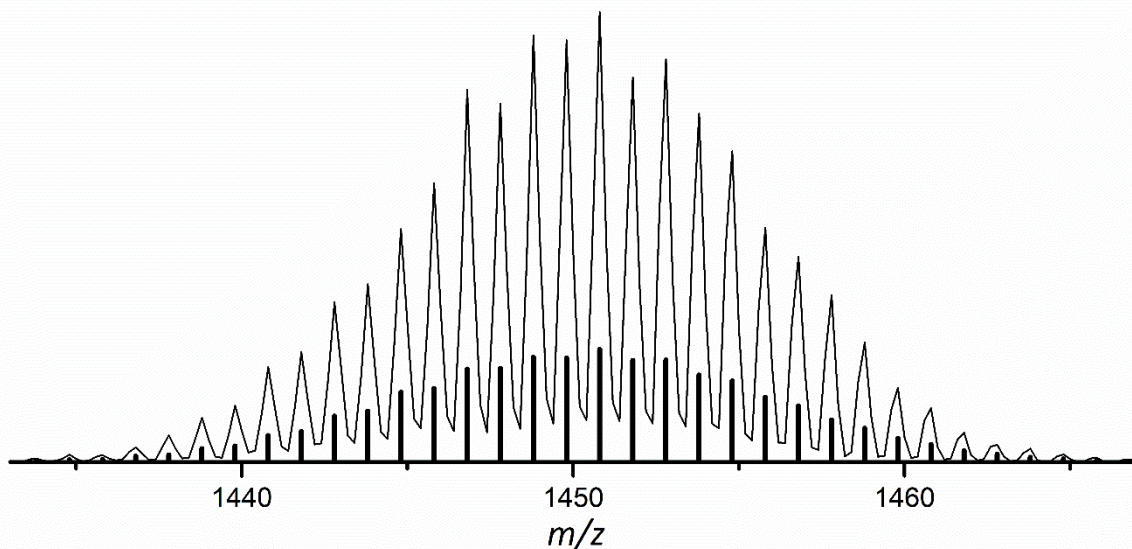


Figure S128: Detail view of ESI-MS signal (negative ion mode, 4000 V, 300 °C) of $[\text{Ge}_9\{\text{Si}(\text{TMS})_3\}_2\text{P}(1\text{-adamantyl})_2]^-$ (**7a**) at m/z 1450.8 obtained from a thf solution. The calculated pattern is represented as black bars.

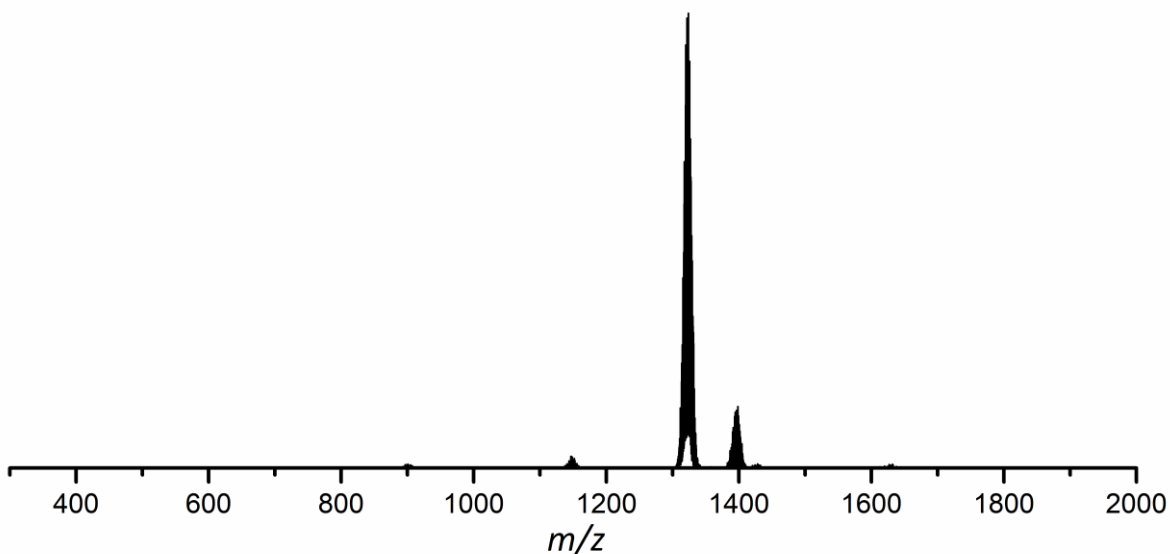


Figure S129: Overview ESI-MS (negative ion mode, 3500 V, 300 °C) obtained from a thf solution of compound **8a**, showing the molecule peak at m/z 1323.8 $[\text{Ge}_9\{\text{Si}(\text{TMS})_3\}_2\text{P}^i\text{Pr}(\text{N}^i\text{Pr}_2)]^-$. Besides the molecule peak a signal at m/z 1396.4 is detected, which can be assigned to the tris-silylated cluster $[\text{Ge}_9\{\text{Si}(\text{TMS})_3\}_3]^-$ formed during the ionization process (the signals of this species are not present in NMR spectra of **8a**).

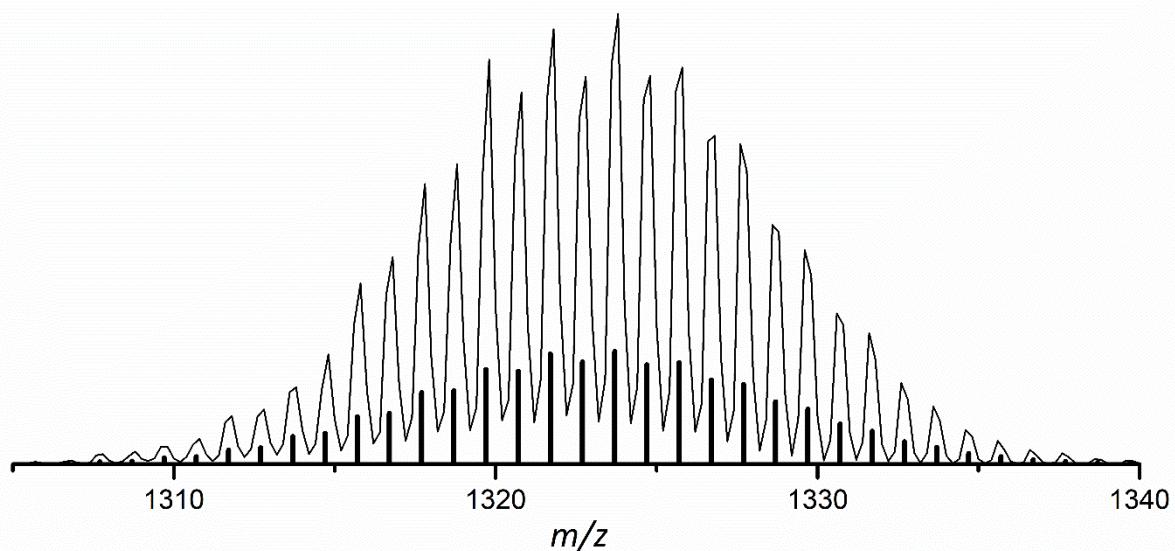


Figure S130: Detailed view of the ESI-MS signal (negative ion mode, 3500 V, 300 °C) of $[\text{Ge}_9\{\text{Si}(\text{TMS})_3\}_2\text{P}^i\text{Pr}(\text{N}^i\text{Pr}_2)]^-$ (**8a**) at m/z 1323.8 obtained from a thf solution. The calculated pattern is represented as black bars.

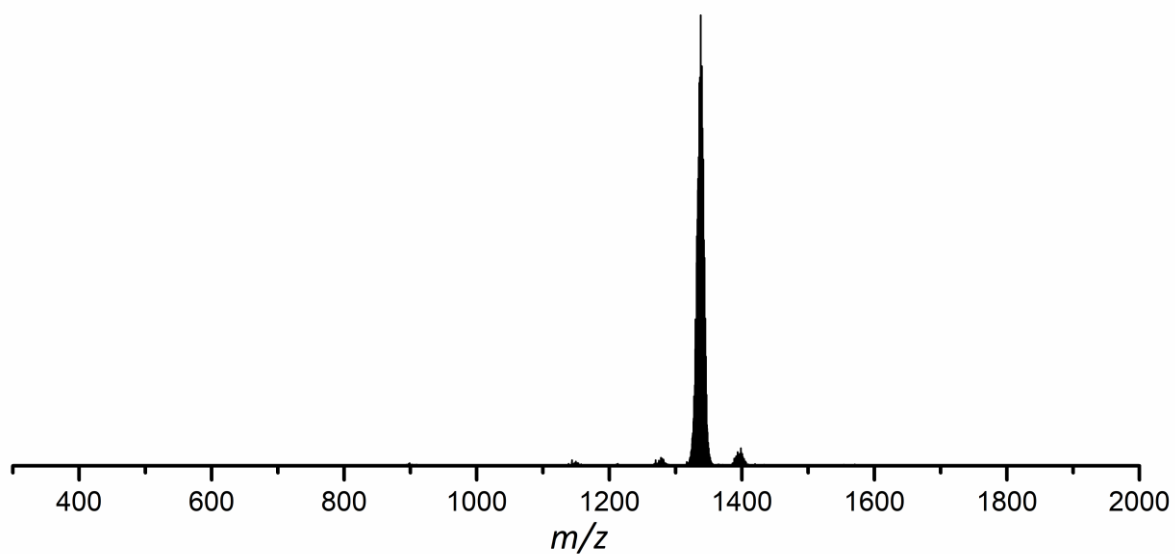


Figure S131: Overview ESI-MS (negative ion mode, 3000 V, 300 °C) obtained from a thf solution of compound **9a**, showing the molecule peak at m/z 1337.8 $[\text{Ge}_9\{\text{Si}(\text{TMS})_3\}_2\text{P}^i\text{Bu}(\text{N}^i\text{Pr}_2)]^-$.

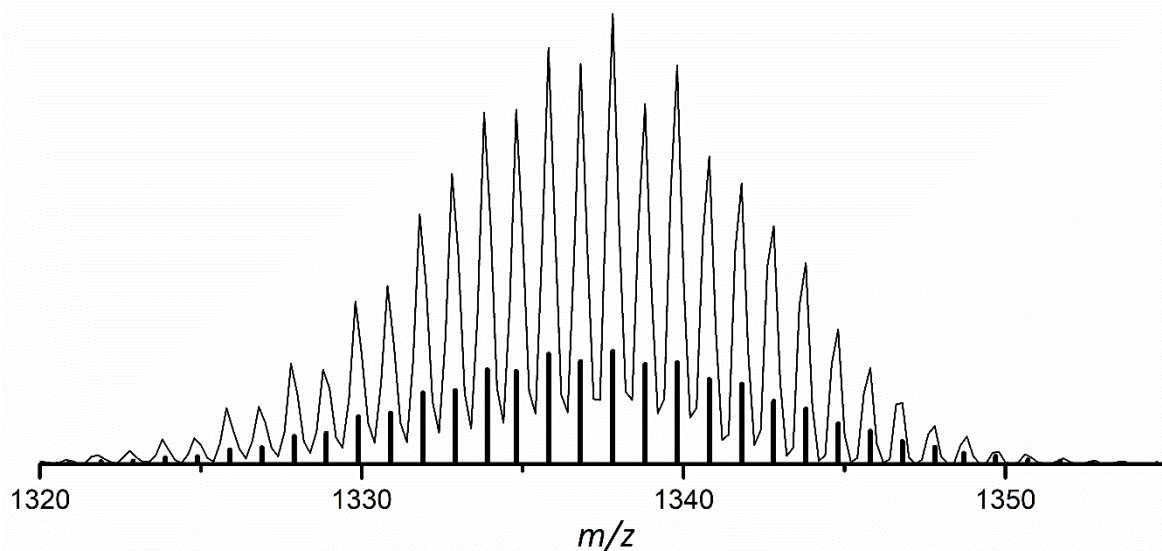


Figure S132: Detailed view of the ESI-MS signal (negative ion mode, 3000 V, 300 °C) of $[\text{Ge}_9(\text{Si}(\text{TMS})_3)_2\text{P}'\text{Bu}(\text{N}'\text{Pr}_2)]^-$ (**9a**) at m/z 1337.8 obtained from a thf solution. The calculated pattern is represented as black bars.

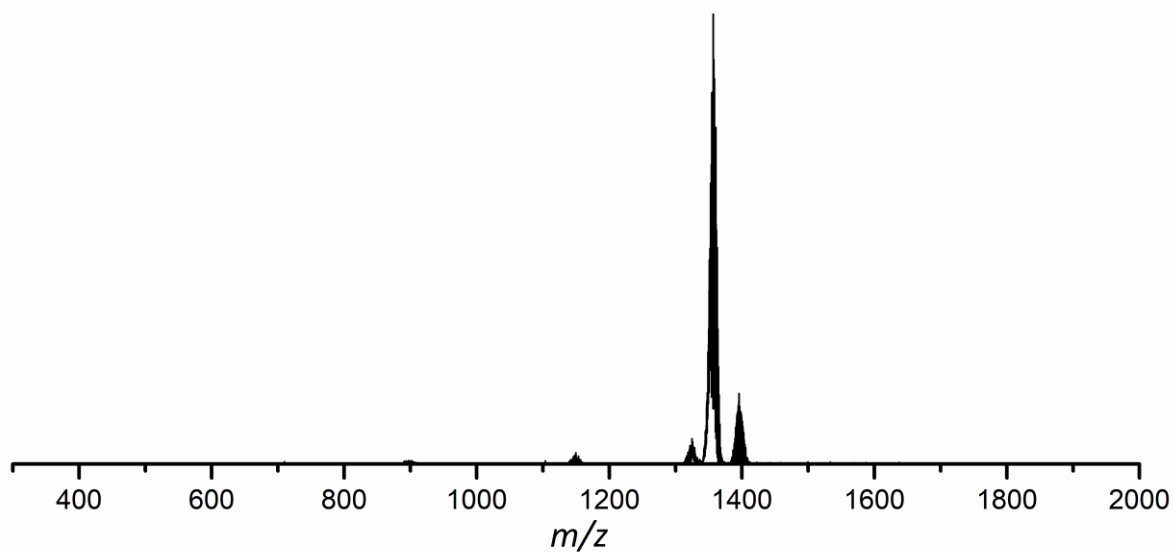


Figure S133: Overview ESI-MS (negative ion mode, 3500 V, 300 °C) obtained from a thf solution of compound **10a**, showing the molecule peak at m/z 1356.8 $[\text{Ge}_9(\text{Si}(\text{TMS})_3)_2\text{P}'\text{Bu}(\text{Mes})]^-$. Besides the molecule peak a signal at m/z 1396.4 is detected, which can be assigned to the tris-silylated cluster $[\text{Ge}_9(\text{Si}(\text{TMS})_3)_3]^-$ formed during the ionization process (the signals of this species are not present in NMR spectra of **10a**). The detailed view of the mixed-functionalized cluster's signal is given in the manuscript.

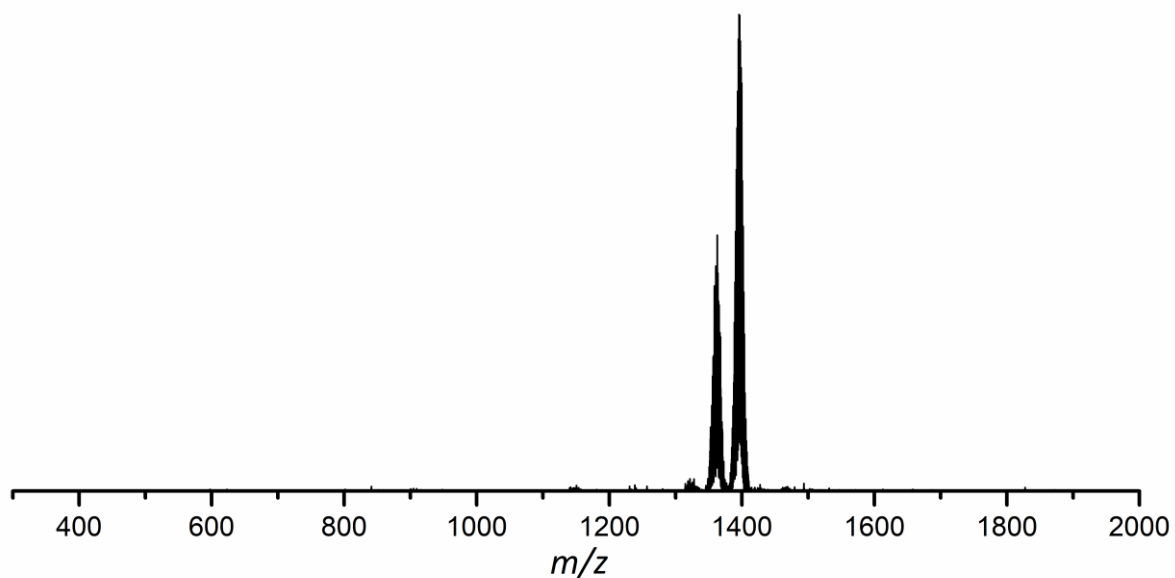


Figure S134: Overview ESI-MS (negative ion mode, 4000 V, 300 °C) obtained from a thf solution of compound **11a**, showing the molecule peak at m/z 1362.8 $[\text{Ge}_9\{\text{Si}(\text{TMS})_3\}_2\text{P}(\text{o-tolyl})_2]^-$. Besides the molecule peak a signal at m/z 1396.4 is detected, which can be assigned to the tris-silylated cluster $[\text{Ge}_9\{\text{Si}(\text{TMS})_3\}_3]^-$ formed during the ionization process (the signals of this species are not present in NMR spectra of **11a**).

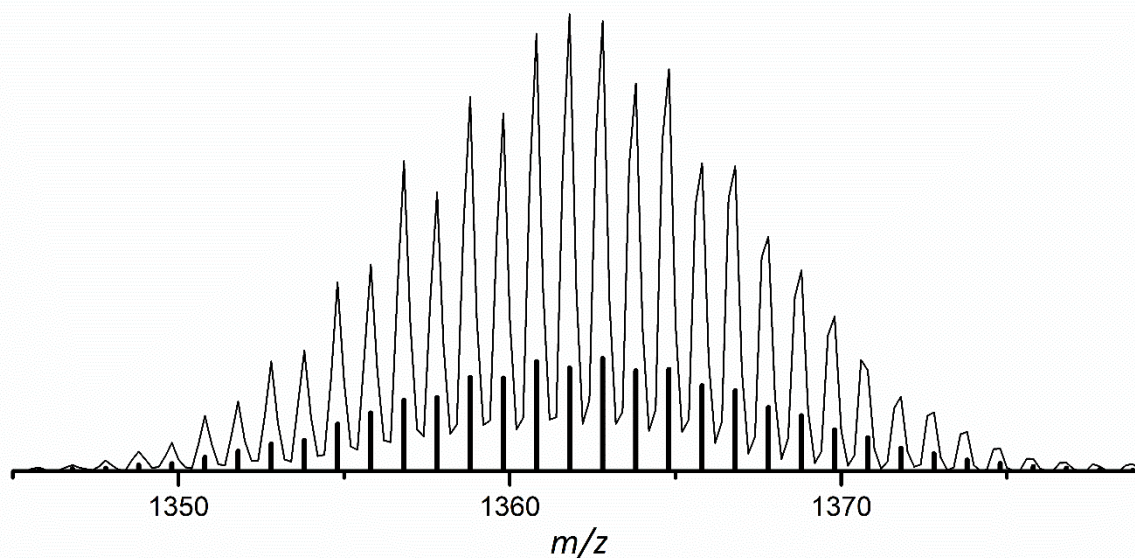


Figure S135: Detailed view of the ESI-MS signal (negative ion mode, 4000 V, 300 °C) of $[\text{Ge}_9\{\text{Si}(\text{TMS})_3\}_2\text{P}(\text{o-tolyl})_2]^-$ (**11a**) at m/z 1362.8 obtained from a thf solution. The calculated pattern is represented as black bars.

6.2 Oxidative Coupling of Silylated Nonagermanide Clusters

C. Wallach, W. Klein and T. F. Fässler

Published in: *Chemical Communications* **2022**, 58, 5486.

© The Royal Society of Chemistry 2022. Reproduced with permission from the Royal Society of Chemistry.

Access online via: <https://pubs.rsc.org/en/content/articlelanding/2022/cc/d2cc01250b>.

Contents and Contributions

The oxidative coupling of two $[\text{Ge}_9\{\text{Si}(\text{TMS})_3\}_2]^{2-}$ clusters in the presence of the borane Cy_2BCl is reported, yielding the dimeric anion $[\text{Ge}_9\{\text{Si}(\text{TMS})_3\}_2]^{2-}$ (**1a**). Anion **1a** was crystallized as the Cu-carbene adduct $\{\text{NHC}^{\text{Pr}}\text{Cu}[\text{Ge}_9\{\text{Si}(\text{TMS})_3\}_2]\}_2$ (**2**). The interconnecting *exo* Ge-Ge bond could not only be traced in the single crystal structure, but also in Raman experiments revealing an additional band at $\tilde{\nu} = 283 \text{ cm}^{-1}$ in comparison to the monomeric compound $\text{NHC}^{\text{Pr}}\text{Cu}[\text{Ge}_9\{\text{Si}(\text{TMS})_3\}_3]$ (**3**). Furthermore, the reaction protocol was successfully reproduced using the sterically more demanding Cu-carbene fragment $[\text{NHC}^{\text{Dipp}}\text{Cu}]^+$ (**4**). Most probably, the oxidative coupling is mediated by trace amounts of oxygen or water and the borane acting as an oxide-scavenger. This assumption is corroborated by the isolation of the boryl ether $\text{Cy}_2\text{B-O-BCy}_2$, which was obtained as a by-product.

The preparation of compounds **1** to **4** was done by me. Furthermore, I measured and evaluated the NMR spectra, the ESI-MS spectrum, and the Raman spectrum. The LIFDI-MS spectrum was acquired by M. Sc. Maximilian Muhr (Prof. Fischer, TUM), I evaluated and plotted the collected data. The elemental analysis was performed by Ulrike Ammari and Bircan Dilki in the microanalytical laboratory of the Chemistry Department of the Technical University of Munich. The single crystal of **2** was selected and measured by me, including the initial structure refinement. Dr. Wilhelm Klein finalized the single crystal structure refinement for publication. The manuscript was authored by me, including the creation of figures, tables, and schemes. Dr. Wilhelm Klein and Dr. Annette Schier proof-read the manuscript. The publication of the manuscript was managed by Prof. Dr. Thomas F. Fässler, the peer-review process including corrections was a joined task accomplished by Prof. Thomas F. Fässler, Dr. Wilhelm Klein and me.


 Cite this: *Chem. Commun.*, 2022, 58, 5486

 Received 3rd March 2022,
 Accepted 29th March 2022

DOI: 10.1039/d2cc01250b

rsc.li/chemcomm

Oxidative coupling of silylated nonagermanide clusters†

 Christoph Wallach, Wilhelm Klein  and Thomas F. Fässler *

Polyhedral main group element clusters of tetrel elements are discussed as suitable building units to form atom-precise nanostructures. Herein we report the oxidative coupling of two $[\text{Ge}_9\{\text{Si}(\text{TMS})_3\}_2]^{2-}$ clusters (TMS = trimethylsilyl) resulting in the dimeric cluster $[\text{Ge}_9\{\text{Si}(\text{TMS})_3\}_2]^{2-}$. The dimer is structurally characterized as the $[\text{NHC}^{\text{iPr}}\text{Cu}]^+$ adduct $\{\text{NHC}^{\text{iPr}}\text{Cu}[\text{Ge}_9\{\text{Si}(\text{TMS})_3\}_2]_2\} [\text{NHC}^{\text{iPr}} = 1,3\text{-di(isopropyl)imidazolylidene}]$. The linkage of two molecular $[\text{Ge}_9\{\text{Si}(\text{TMS})_3\}_2]^{2-}$ anions under formation of an *exo* Ge–Ge bond occurs in the presence of Cy_2BCl (Cy = cyclohexyl) and is mediated by trace amounts of oxygen as indicated by the isolation of the by-product $\text{Cy}_2\text{B-O-BCy}_2$.

Tetrel element clusters have been subject to intensive investigations within the last years, and great efforts have been made to synthesize extended clusters at the border of isolated molecules and solid-state-like structures. Preferably molecules with low-valent Si and Ge atoms are used for the formation of larger clusters.^{1–3} As key examples, clusters like $[\text{Ge}_9\{\text{Si}(\text{TMS})_3\}_3]^-$,⁴ $[\text{Ge}_{14}\{E(\text{TMS})_3\}_5]^{3-}$ ($E = \text{Si}, \text{Ge}$),^{5,6} $[\text{Ge}_{14}\text{Br}_8(\text{PEt}_3)_4]$,⁷ $[\text{Sn}_9\{\text{Si}(\text{TMS})_3\}_2]^{2-}$,⁸ $[\text{Sn}_{10}\{\text{Si}(\text{TMS})_3\}_5]^-$,⁹ and $[\text{Sn}_{10}\{\text{Si}(\text{TMS})_3\}_6]^{10}$ can be mentioned, which arise upon the disproportionation reaction of molecular germanium(II) and tin(II) halides, respectively. The reductive elimination of leaving groups, as well as the reductive coupling of EX_2 salts with organo-halides R_xEX_y ($R = \text{organic ligand}, E = \text{tetrel element}, X = \text{halide}$) are further paths to clusters such as $[\text{Ge}_{10}\{\text{Si}^t\text{Bu}_3\}_6]^+$,¹¹ $[\text{Ge}_6\{\text{N}(\text{TMS})\text{Dipp}\}_4]$ [Dipp = 2,6-di(isopropyl)phenyl],¹² $[\text{Ge}_4\text{Sn}_2\text{R}_2]$ [$R = (2,6\text{-Pr}_2\text{C}_6\text{H}_3)_2\text{C}_6\text{H}_3$],¹³ and the propellane $[\text{Ge}_5\text{Me}_6]$.¹⁴ However, the products of such reactions are usually hard to predict. As a well predictable exception, molecules containing Si and Ge atoms with low oxidation states, as for example the highly reactive disilenide $\text{Tip}_2\text{Si}=\text{SiLiTip}$ [Tip = 2,4,6-tri(isopropyl)phenyl], can be used as the basis for the multistep synthesis of the siliconoid cluster $\text{LiSi}_6\text{Tip}_5$,¹⁵ which subsequently

led to the extended compound $\text{Si}_8\text{Tip}_5\text{Cp}^*$ in a two-step, atom-precise synthesis.¹⁶ Furthermore, the photolysis of the mixed tetrel element cluster $[\text{SiR}_2\text{Ge}_4\text{R}'_4]$ ($R = {}^t\text{Bu}, R' = \text{SiMe}^t\text{Bu}_2$) induced the interlinking of two propellane molecules *via* a central Ge atom in $[\{\text{SiR}_2\text{Ge}_4\text{R}'_2\}_2\text{Ge}]$, featuring an extended cluster with outstanding geometry.¹⁷

An alternative approach to increase the size of molecular compounds is the coupling of pre-formed building blocks. The solid-state phase K_4Ge_9 comprises $[\text{Ge}_9]^{4-}$ clusters, which are transferable into solution without any structural change.^{18,19} The fourfold negatively charged clusters are highly redox-active species,^{20,21} and numerous structures featuring interconnected $[\text{Ge}_9]^{n-}$ units such as dimers $[\text{Ge}_9\text{---}\text{Ge}_9]^{6-}$,^{19,22–29} trimers $[\text{Ge}_9\text{---}\text{Ge}_9\text{---}\text{Ge}_9]^{6-}$,^{30,31} tetramers $[\text{Ge}_9\text{---}\text{Ge}_9\text{---}\text{Ge}_9\text{---}\text{Ge}_9]^{8-}$,^{29,32,33} and polymeric $\infty^1\{[\text{Ge}_9]^{2-}\}^{34,35}$ chains have been described. However, the oxidized cluster species have been obtained only in low yields and from highly polar solvents like ethylenediamine, and the oxidation agents have not been unequivocally identified.

In order to enhance the solubility of the $[\text{Ge}_9]^{4-}$ ion, silyl groups are attached at the cluster unit leading to the most prominent species $[\text{Ge}_9\{\text{Si}(\text{TMS})_3\}_2]^{2-}$ ³⁶ and $[\text{Ge}_9\{\text{Si}(\text{TMS})_3\}_3]^-$.³⁷ In contrast to the numerous oligomers consisting of coupled bare $[\text{Ge}_9]^{n-}$ units, larger cluster species arising from the direct fusion of silylated $[\text{Ge}_9]$ clusters are rare. To the best of our knowledge the oxidation of two $[\text{Ge}_9\{\text{Si}(\text{TMS})_3\}_3]^-$ units in the presence of an Fe(II) salt under formation of small amounts of $[\text{Ge}_{18}\{\text{Si}(\text{TMS})_3\}_6]$ represents the only reported example. In this case, however, the original cluster shape is not retained.³⁸ Though, coupling of two silylated clusters has been achieved through a bridging silyl ligand, resulting in $[\{\text{Si}(\text{TMS})_3\}_2\text{Ge}_9\text{---}\text{SiMe}_2(\text{C}_6\text{H}_4)\text{---}\text{SiMe}_2\text{---}\text{Ge}_9\{\text{Si}(\text{TMS})_3\}_2]^{2-}$.³⁹

We recently investigated the functionalization of the dianionic cluster $[\text{Ge}_9\{\text{Si}(\text{TMS})_3\}_2]^{2-}$ with N-heterocyclic chloroboranes, leading to the formation of Ge–B *exo*-bonds.⁴⁰ Intriguingly, the electronic saturation at the boron center seems to play a crucial role here, since in case of the electron-poor alkyl borane Cy_2BCl such a bond formation could not be observed. However, the reaction of stoichiometric amounts of $[\text{Ge}_9\{\text{Si}(\text{TMS})_3\}_2]^{2-}$ and Cy_2BCl in dioxane yielded

Department Chemie, Technische Universität München, Lichtenbergstraße 4, 85747 Garching, Germany. E-mail: thomas.faessler@lrz.tum.de

† Electronic supplementary information (ESI) available: Details on the experimental procedures, crystallographic details, NMR spectra, LIFDI MS spectrum. CCDC 2129082. For ESI and crystallographic data in CIF or other electronic format see DOI: <https://doi.org/10.1039/d2cc01250b>

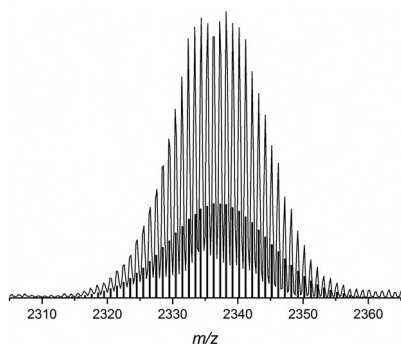


Fig. 1 ESI-MS peak corresponding to the $[\text{Ge}_9\{\text{Si}(\text{TMS})_3\}_2]^-$ dimer at m/z 2336.0. Measurements were carried out in diluted MeCN solution (negative-ion mode, 3500 V, 300 °C). The calculated isotope pattern is presented as black bars.

a deep red solution, indicative of the presence of cluster species. ESI-MS measurements of the dried reaction residue in MeCN revealed a mass peak at m/z 2336.0 fitting the calculated isotope distribution of the oxidatively coupled cluster anion $[\text{Ge}_9\{\text{Si}(\text{TMS})_3\}_2]^-$ (Fig. 1). The detection of mono-anionic species in ESI-MS spectra is frequently observed for polyanionic *Zintl* clusters.⁴¹

The ^1H NMR spectrum of the re-dissolved reaction residue shows a characteristic shift of the silyl protons at 0.22 ppm in CD_3CN , which significantly deviates from the shift of the monomeric reactant $[\text{Ge}_9\{\text{Si}(\text{TMS})_3\}_2]^{2-}$ observed at 0.12 ppm in the same solvent (NMR spectra are provided in the Supporting Information). In the ^{11}B NMR spectrum an up-field shift from formerly 76.5 ppm ($\text{C}_2\text{D}_2\text{Cl}_4$, C_6D_6) to 52 ppm is observed. Crystals of the corresponding salt $\text{K}_2[\text{Ge}_9\{\text{Si}(\text{TMS})_3\}_2]$ (**1**) could not be obtained due to the repetitive formation of oily residues upon concentration of the reaction solution. Furthermore,

sequestering of the K^+ ions by 18-crown-6 or [2.2.2]cryptand also did not lead to the formation of single crystalline material. In previous studies we observed that the addition of N-heterocyclic carbenes $\text{NHC}^R\text{Cu-Cl}$ to monoanionic $[\text{Ge}_9]$ cluster species results in NHC^RCu -cluster complexes, which tend to crystallize more easily. Consequently, a solution of the carbene $\text{NHC}^{\text{iPr}}\text{Cu-Cl}$ was added to a MeCN solution of **1** at 0 °C causing the formation of a light-brown precipitate. After work-up, a few single crystals of $\{\text{NHC}^{\text{iPr}}\text{Cu}[\text{Ge}_9\{\text{Si}(\text{TMS})_3\}_2]\}_2 \cdot 2 \text{Et}_2\text{O}$, **2**, grew from a concentrated diethyl ether solution. Compound **2** crystallizes in the monoclinic space group $I2/c$ and comprises an 18-atom Ge cluster (**1a**), which consists of two $[\text{Ge}_9\{\text{Si}(\text{TMS})_3\}_2]^-$ moieties that are interconnected by a Ge–Ge single bond (Fig. 2; see also Table S1 (ESI[†]) and CCDC 2129082).

The linking Ge1–Ge1 bond has a length of 2.4259(8) Å in agreement with a single bond according to the sum of the covalent radii of Ge (2.42 Å).⁴² Comparable values were reported for $[\text{Ge}_9\text{-Ge}_9]^{6-}$ dimers,^{19,22–26} while trimeric and tetrameric $[\text{Ge}_9]$ units feature slightly longer Ge–Ge *exo*-bonds.^{29–33} The two $[\text{Ge}_9]$ units are best described as distorted, mono-capped square antiprisms with one prism height Ge2–Ge4 [4.0500(8) Å] being significantly elongated compared to the two others [Ge5–Ge6: 3.1989(8) Å; Ge7–Ge8: 3.1254(8) Å], thus resulting in approximately C_{2v} -symmetric cluster fragments. The two Ge cages are tilted towards each other spanning a dihedral angle of the two planes Ge1 to Ge4 of 75.4°. Thus, the orientation of the two $[\text{Ge}_9]$ subunits towards each other deviates from the arrangement of cluster cores in non-functionalized $[\text{Ge}_9\text{-Ge}_9]^{6-}$ dimers, which is most probably a result of the steric influence of the attached groups. Ge–Ge, Ge–Si and Ge–Cu bond lengths agree with previously published data (Table S2, ESI[†]).^{22,35,43–45} All substituted Ge vertex atoms form 2c–2e bonds to the attached hypersilyl groups as well as to the second cluster entity. Thus, the cluster anion might alternatively be described

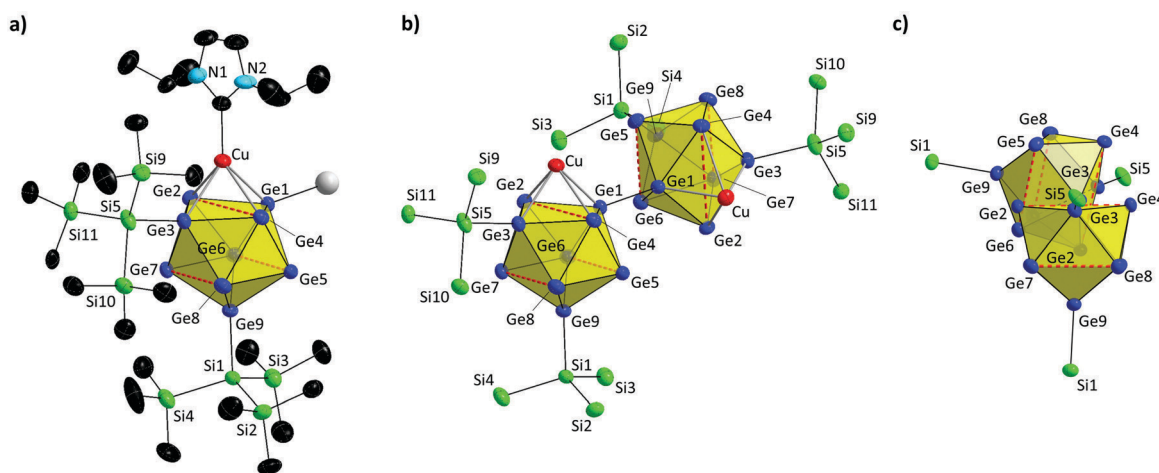


Fig. 2 Molecular structure of the dimer $\{\text{NHC}^{\text{iPr}}\text{Cu}[\text{Ge}_9\{\text{Si}(\text{TMS})_3\}_2]\}_2 \cdot 2 \text{Et}_2\text{O}$, **2**. Representation of (a) one cluster monomer of the dimer and (b) the silylated $[\text{Ge}_9\text{-Ge}_9]$ cluster unit with attached $[\text{NHC}^{\text{iPr}}\text{Cu}]^+$ groups; (c) view along the Ge1–Ge1 bond vector. For clarity reasons, in (a) the second cluster half is indicated by a grey sphere attached to Ge1, in (b) the $\text{NHC}^{\text{iPr}}\text{Cu}$ ligands as well as the carbon atoms are omitted, and in (c) only the central Si atoms of the hypersilyl groups are shown while the $[\text{NHC}^{\text{iPr}}\text{Cu}]^+$ ligands are not shown. In (a–c) hydrogen atoms and the co-crystallizing Et_2O molecules are omitted, and solely the major-occupied TMS groups at Si5 are drawn. All ellipsoids are presented at a 50% probability level. Prism heights are indicated by dashed red lines. Crystallographic details are presented in Table S1 (ESI[†]).

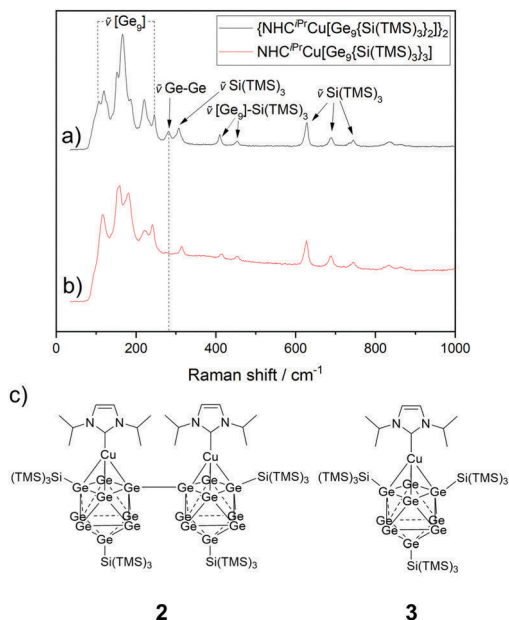


Fig. 3 Raman spectrum of (a) a single crystal of compound **2** (black graph) in comparison to (b) the spectrum of $\text{NHC}^{\text{iPr}}\text{Cu}[\text{Ge}_9\{\text{Si}(\text{TMS})_3\}_3]$ (**3**, powder, red graph);⁴⁵ (c) schematic illustration of compounds **2** and **3**.

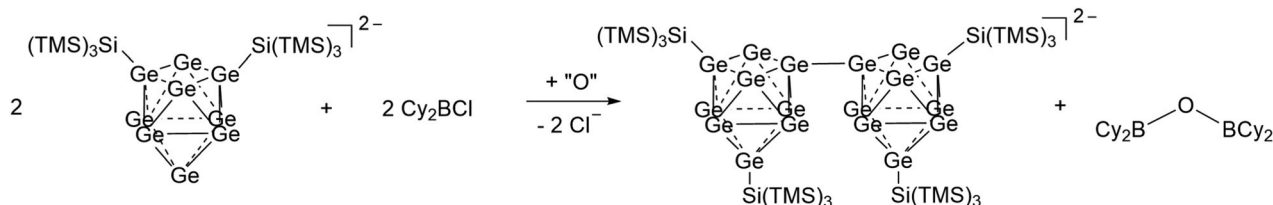
as a threefold substituted cluster, featuring two silyl groups plus another cluster as the additional third ligand. The Cu-carbene fragments are η^4 -coordinated to the pseudo-square planes Ge1 to Ge4, as described before.⁴⁵ The trimethylsilyl groups bound to the central Si5 atom are disordered and were refined on split positions with site occupation factors of 0.534 and 0.466, respectively (Fig. S1, ESI[†]).

The Raman spectrum recorded from the single crystal used for the structure determination is shown in Fig. 3. Beside signals reminiscent to the monomeric compound $\text{NHC}^{\text{iPr}}\text{Cu}[\text{Ge}_9\{\text{Si}(\text{TMS})_3\}_3]$, **3**,⁴⁵ compound **2** exhibits an additional signal at $\tilde{\nu} = 283 \text{ cm}^{-1}$ which can be attributed to the cluster-connecting Ge-Ge bond.⁴⁶ Signals in the region $\tilde{\nu} = 380 - 420 \text{ cm}^{-1}$ are in the range of Si-Ge vibrations.^{46,47} Unfortunately, even though compound **2** had repetitively formed in different experiments, only very few crystals could be isolated. Thus, the NMR spectra and elemental analysis had to be carried out with the crude reaction product, which still contained inseparable impurities.

By contrast, the reaction of a solution of **1a** in MeCN with the sterically more demanding $\text{NHC}^{\text{DiPP}}\text{Cu-Cl}$ carbene [$\text{NHC}^{\text{DiPP}} = 1,3$ -bis(2,6-diisopropylphenyl)imidazolyldiene] leads, according to NMR

spectroscopic and elemental analysis data, to an analytically pure polycrystalline powder of $\{\text{NHC}^{\text{DiPP}}\text{Cu}[\text{Ge}_9\{\text{Si}(\text{TMS})_3\}_3]_2\}_2$ (**4**). Unit cell parameters of **4** obtained from single crystals are provided in the Supporting Information. However, these crystals were too small to permit a full structure determination, particularly in combination with large unit cell parameters for this structure, but the isolation of the two comparable species **2** and **4** accounts for the reproducibility of the reaction protocol.

The ^{11}B NMR spectrum of the reaction solution leading to **1a** showed a signal at 52 ppm, and, in order to shed light on a possible formation path of **1a**, we tried to isolate the boron-containing by-product in this solution. In reactions of solid K_4Ge_9 and Cy_2BCl in dioxane we had observed an analogous signal and obtained a colorless oil after work-up. The advantage of utilizing K_4Ge_9 instead of $[\text{Ge}_9\{\text{Si}(\text{TMS})_3\}_2]^{2-}$ is that solid K_4Ge_9 is prepared from the elements in a one-step synthesis, providing high yields. Thus, we conducted the reaction with the chloroborane using large amounts of the reactants and were able to crystallize the oily residue from hexane at $-40 \text{ }^\circ\text{C}$. Inspection of the light-yellow crystals revealed the lattice parameters previously obtained for $\text{Cy}_2\text{B-O-BCy}_2$ isolated from the reaction of Cy_2BH and H_2O .⁴⁸ Furthermore, the observed ^{11}B NMR shift matches with the shift of the closely related boryl ether $\text{Me}_2\text{B-O-BMe}_2$ (52 ppm).⁴⁹ Additionally, the mass peak of the ionization product $[\text{Cy}_2\text{B-O-BCy}]^+$ was detected in LIFDI-MS measurements (Fig. S12, ESI[†]). These observations suggest that the presence of the chloroborane is essential in mediating the oxidative coupling process, most probably by accumulating oxide and transferring its halide to the potassium counter cation of the $[\text{Ge}_9]$ cluster, which is summarized in Scheme 1. In order to search for the origin of the oxygen source, the solvent dioxane was replaced by dry and degassed toluene to exclude the solvent as possible oxygen source. As a blank test, the borane Cy_2BCl was stirred over night in toluene, and it remained unchanged (^{11}B NMR: 76 ppm in C_6D_6). However, as soon as K_4Ge_9 or $\text{K}_2[\text{Ge}_9\{\text{Si}(\text{TMS})_3\}_2]$ is present in the reaction mixture, the formation of the boryl ether $\text{Cy}_2\text{B-O-BCy}_2$ is observed (^{11}B NMR: 52 ppm in C_6D_6). Furthermore, the formation of the ion **1a** from toluene was proven by ESI-MS measurements and ^1H NMR spectroscopic investigations. So far, we cannot prove whether the oxygen stems from accidental remains of H_2O or O_2 in the solvent or if small amounts of the gas are passed over to the reaction *via* the supernatant gas phase. Experiments in which stoichiometric amounts of H_2O or oxygenated toluene were applied did not lead to enhanced yields of **1a**, but to the formation of by-products. However,



Scheme 1 Proposed reaction scheme for the formation of the anion **1a** and the boryl ether $\text{Cy}_2\text{B-O-BCy}_2$.

the simultaneous presence of a K-containing species and the borane is needed to initiate any reaction since the boryl ether is also formed when KC_8 is used instead of a cluster compound. Thus, the oxophilicity of boron as well as the formation of insoluble KCl most probably are the main driving forces for the observed oxidative coupling of the silylated clusters.

Oxidative coupling reactions under formation of Ge–Ge *exo*-bonds have frequently been reported for bare $[\text{Ge}_9]$ clusters without addition of a specific oxidizing agent.^{23,29,31,35} We report here on the formation and the crystal structure of the first cluster dimer $\{\text{NHC}^{\text{IPr}}\text{Cu}[\text{Ge}_9\{\text{Si}(\text{TMS})_3\}_2]\}_2 \cdot 2 \text{Et}_2\text{O}$ (**2**) comprising two silylated $[\text{Ge}_9]$ units linked by a Ge–Ge *exo*-cluster bond. The formation of **2** corresponds to an oxidative coupling of two $[\text{Ge}_9\{\text{Si}(\text{TMS})_3\}_2]^{2-}$ ions, relying on the presence of the borane C_y_2BCl . The isolation of the boryl ether $\text{C}_y_2\text{B-O-BC}_y_2$ as a by-product of the reaction hints for the role of C_y_2BCl as an oxide-scavenger in this redox process. Due to the negative charge of the ion $[\text{Ge}_9\{\text{Si}(\text{TMS})_3\}_2]^{2-}$ (**1a**) further cluster growth through oxidative coupling is conceivable. Since the approach of silylating clusters was recently transferred to nonasilicide clusters $[\text{Si}_9]^{4-}$ yielding the stabilized species $[\text{Si}_9\{R\}_2]^{2-}$ and $[\text{Si}_9\{R\}_3]^-$ ($R = \text{Si}(\text{TMS})_3, \text{Si}^t\text{Bu}_2\text{H}$),^{50,51} oxidative coupling reactions for the formation of siliconoid clusters¹ also become feasible.

CW performed the experimental work and authored the manuscript. WK refined the crystal structure data. TFF supervised the project.

CW thanks the Deutsche Forschungsgemeinschaft (DFG, German Research Foundation, project number 245845833) within IRTG 2022 – Alberta Technical University of Munich School for Functional Hybrid Materials (ATUMS) for funding. Furthermore, CW thanks the Studienstiftung des Deutschen Volkes for granting a PhD scholarship. MSc Maximilian Muhr (Prof. Fischer, TUM) is acknowledged for the acquisition of the LIFDI-MS spectra.

Conflicts of interest

There are no conflicts to declare.

Notes and references

- Y. Heider and D. Scheschke, *Chem. Rev.*, 2021, **121**, 9674.
- W. Klein, A. Schier and T. F. Fässler, *Structure and Bonding*, Springer, Berlin, Heidelberg, 2021, DOI: [10.1007/430_2021_82](https://doi.org/10.1007/430_2021_82).
- R. J. Wilson, N. Lichtenberger, B. Weinert and S. Dehnen, *Chem. Rev.*, 2019, **119**, 8506.
- A. Schnepf, *Angew. Chem., Int. Ed.*, 2003, **42**, 2624.
- C. Schenk and A. Schnepf, *Chem. Commun.*, 2008, 4643.
- C. Schenk, A. Kracke, K. Fink, A. Kubas, W. Klopfer, M. Neumaier, H. Schnöckel and A. Schnepf, *J. Am. Chem. Soc.*, 2011, **133**, 2518.
- T. Kunz, C. Schrenk and A. Schnepf, *Angew. Chem., Int. Ed.*, 2018, **57**, 4088.
- C. Schrenk, F. Winter, R. Pöttgen and A. Schnepf, *Inorg. Chem.*, 2012, **51**, 8583.
- C. Schrenk, J. Helmlinger and A. Schnepf, *Z. Anorg. Allg. Chem.*, 2012, **638**, 589.
- C. Schrenk, I. Schellenberg, R. Pöttgen and A. Schnepf, *Dalton Trans.*, 2010, **39**, 1872.
- A. Sekiguchi, Y. Ishida, Y. Kabe and M. Ichinohe, *J. Am. Chem. Soc.*, 2002, **124**, 8776.
- J. Helmer, A. Hepp and F. Lips, *Dalton Trans.*, 2020, **49**, 11843.
- A. F. Richards, H. Hope and P. P. Power, *Angew. Chem., Int. Ed.*, 2003, **42**, 4071.
- D. Nied, W. Klopfer and F. Breher, *Angew. Chem., Int. Ed.*, 2009, **48**, 1411.
- K. Abersfelder, A. J. White, H. S. Rzepa and D. Scheschke, *Science*, 2010, **327**, 564.
- K. I. Leszczyńska, V. Huch, C. Präsang, J. Schwabedissen, R. J. Berger and D. Scheschke, *Angew. Chem., Int. Ed.*, 2019, **58**, 5124.
- Y. Ito, V. Y. Lee, H. Gornitzka, C. Goedecke, G. Frenking and A. Sekiguchi, *J. Am. Chem. Soc.*, 2013, **135**, 6770.
- S. Ponou and T. F. Fässler, *Z. Anorg. Allg. Chem.*, 2007, **633**, 393.
- C. Suchentrunk, J. Daniels, M. Somer, W. Carrillo-Cabrera and N. Korber, *Z. Naturforsch. B*, 2005, **60**, 277.
- A. Ugrinov and S. C. Sevov, *J. Am. Chem. Soc.*, 2003, **125**, 14059.
- A. Ugrinov and S. C. Sevov, *Chem. – Eur. J.*, 2004, **10**, 3727.
- L. Xu and S. C. Sevov, *J. Am. Chem. Soc.*, 1999, **121**, 9245.
- R. Hauptmann and T. F. Fässler, *Z. Anorg. Allg. Chem.*, 2003, **629**, 2266.
- R. Hauptmann and T. Fässler, *Z. Kristallogr. – New Cryst. Struct.*, 2003, **218**, 461.
- A. Nienhaus, S. D. Hoffmann and T. F. Fässler, *Z. Anorg. Allg. Chem.*, 2006, **632**, 1752.
- S. Scharfe and T. F. Fässler, *Z. Anorg. Allg. Chem.*, 2011, **637**, 901.
- K. Mayer, M. Giebel, M. M. Bentlohner, W. Klein and T. F. Fässler, *Z. Kristallogr. – New Cryst. Struct.*, 2015, **230**, 286.
- T. F. Fässler and U. Schütz, *Inorg. Chem.*, 1999, **38**, 1866.
- K. Mayer, W. Klein, S. Geier and T. F. Fässler, *Z. Anorg. Allg. Chem.*, 2021, **647**, 377.
- A. Ugrinov and S. C. Sevov, *J. Am. Chem. Soc.*, 2002, **124**, 10990.
- L. Yong, S. D. Hoffmann and T. F. Fässler, *Z. Anorg. Allg. Chem.*, 2005, **631**, 1149.
- L. Yong, S. D. Hoffmann and T. F. Fässler, *Z. Anorg. Allg. Chem.*, 2004, **630**, 1977.
- A. Ugrinov and S. C. Sevov, *Inorg. Chem.*, 2003, **42**, 5789.
- C. Downie, J.-G. Mao, H. Parmar and A. M. Guloy, *Inorg. Chem.*, 2004, **43**, 1992.
- C. Downie, Z. Tang and A. M. Guloy, *Angew. Chem., Int. Ed.*, 2000, **39**, 337.
- O. Kysliak and A. Schnepf, *Dalton Trans.*, 2016, **45**, 2404.
- F. Li and S. C. Sevov, *Inorg. Chem.*, 2012, **51**, 2706.
- O. Kysliak, C. Schrenk and A. Schnepf, *Angew. Chem., Int. Ed.*, 2016, **55**, 3216.
- O. Kysliak, C. Schrenk and A. Schnepf, *Inorg. Chem.*, 2017, **56**, 9693.
- C. Wallach, F. S. Geitner, A. J. Karttunen and T. F. Fässler, *Angew. Chem., Int. Ed.*, 2021, **60**, 2648.
- F. Li and S. C. Sevov, *Inorg. Chem.*, 2015, **54**, 8121.
- P. Pyykkö and M. Atsumi, *Chem. – Eur. J.*, 2009, **15**, 186.
- F. S. Geitner and T. F. Fässler, *Eur. J. Inorg. Chem.*, 2016, 2688.
- F. S. Geitner, M. A. Giebel, A. Pöthig and T. F. Fässler, *Molecules*, 2017, **22**, 1204.
- F. S. Geitner and T. F. Fässler, *Inorg. Chem.*, 2020, **59**, 15218.
- V. Volodin, M. Efmov, A. Deryabin and L. Sokolov, *Semiconductors*, 2006, **40**, 1314.
- C. Fischer, W. Klein, L. A. Jantke, L. J. Schiegerl and T. F. Fässler, *Z. Anorg. Allg. Chem.*, 2016, **642**, 1314.
- S. S. Barnes, C. M. Vogels, A. Decken and S. A. Westcott, *Dalton Trans.*, 2011, **40**, 4707.
- B. Wrackmeyer and O. L. Tok, *Z. Naturforsch., B: J. Chem. Sci.*, 2006, **61**, 949.
- L. J. Schiegerl, A. J. Karttunen, W. Klein and T. F. Fässler, *Chem. – Eur. J.*, 2018, **24**, 19171.
- L. J. Schiegerl, A. J. Karttunen, W. Klein and T. F. Fässler, *Chem. Sci.*, 2019, **10**, 9130.

Oxidative Coupling of Silylated Nonagermanide Clusters

Christoph Wallach, Dr. Wilhelm Klein, Prof. Dr. Thomas F. Fässler

e-mail: thomas.faessler@lrz.tum.de

Supporting information

1. Experimental details	S1
2. Crystallographic details	S5
3. NMR spectra.....	S7
4. LIFDI-MS spectrum	S12
5. References	S13

1. Experimental details

General

All experiments were performed under oxygen-free, dry conditions under argon atmosphere using standard Schlenk or glove box techniques. Glassware was dried prior to usage by repetitively heating it *in vacuo*. The solvents used were obtained from an MBraun Grubbs apparatus. Diethylether was dried prior to usage over Na/benzophenone. Toluene was degassed by three cycles of freeze-pumping after distilling it over Na/benzophenone. The 1M solution of Cy_2BCl in hexane (*Sigma Aldrich*) was degassed by three cycles of freeze-pumping, and anhydrous 1,4-dioxane (stored over molecular sieve) was purchased (*Sigma Aldrich*). All other commercially available chemicals were used without further purification. K_4Ge_9 was prepared by fusion of stoichiometric amounts of the elements in stainless-steel tubes at 650 °C. The bis-silylated $[Ge_9]$ cluster $K_2[Ge_9\{Si(TMS)_3\}_2]$ and the $NHC^R Cu-Cl$ carbenes were prepared according to modified literature procedures.^[1-3]

Single crystal structure determination

The air- and moisture-sensitive crystal of **2** was transferred from the mother liquor into perfluoroalkyl ether oil in an Ar-filled glove box. A glass capillary was used for fixing the crystal, which was subsequently positioned in a 150 K cold N_2 gas stream for data collection. Data collection was performed with a STOE StadiVari diffractometer ($MoK\alpha$ radiation) equipped with a DECTRIS PILATUS 300K detector. The structure was solved by Direct Methods (SHELXS-97)^[4] and refined by full-matrix least-squares calculations against F^2 (SHELXL-2018).^[5] A riding model was used to calculate and refine the positions of the hydrogen atoms. All non-hydrogen atoms were refined by applying anisotropic displacement parameters. The electron density of the disordered diethyl ether molecules was treated with the Platon Squeeze option.^[6] Further information of the crystal structure investigation may be obtained from the joint CCDC/FIZ Karlsruhe online deposition service: <https://www.ccdc.cam.ac.uk/structures/?> by quoting the deposition number CCDC-2129082.

NMR spectroscopy

NMR spectra were measured on a Bruker Avance Ultrashield 400 MHz and a Bruker Ultrashield Plus 500 MHz spectrometer. The 1H NMR and ^{13}C NMR spectra were calibrated using the residual signals of the used deuterated solvents. Chemical shifts are reported in parts per million (ppm) relative to TMS, with the solvent peaks serving as internal reference.^[7] Abbreviations for signal multiplicities are: singlet (s), doublet (d), heptet (hept), broad signal (br).

Electrospray ionization (ESI) mass spectrometry

ESI-MS analyses were performed on a Bruker Daltonic HCT mass spectrometer (dry gas temperature: 300 °C; injection speed: 300 μ L/h), and the data evaluation was carried out using the Bruker Compass Data Analysis 4.0 SP 5 program (Bruker). Spectra were plotted using OriginPro2021 (Origin Lab) and Excel (Microsoft Office 365).

Liquid injection field desorption ionization (LIFDI) mass spectrometry

LIFDI-MS measurements were performed using an ExactiveTM PlusOrbitrap system from the Thermo Scientific Company and a Micromass LCT-QTOF-Micro mass spectrometer at the chair of Inorganic and Metal-Organic Chemistry (Prof. Fischer, TUM). The samples were dissolved in toluene and applied on a graphite dendrite-coated tungsten wire. As ionization voltage 10 kV were adjusted. Data were acquired in the positive ion mode (radical cations)^[8] and spectra were plotted using OriginPro2021 (Origin Lab) and Excel (Microsoft Office 365). The theoretical isotope distribution was calculated using the web-tool enviPat Web 2.4 (<https://www.envipat.eawag.ch/>).

Raman spectroscopy

Raman spectra were acquired using an inVia Raman microscope RE04 (Renishaw) equipped with a CCD detector. Data were plotted using the programs WiRe 4.2 (Renishaw), Excel (Microsoft Office 365), and OriginPro2021 (OriginLab). The cluster $\text{NHC}^{\text{Pr}}\text{Cu}[\text{Ge}_9\{\text{Si}(\text{TMS})_3\}_3]$ (**3**) was prepared for comparison according to literature procedures.^[9] Spectra were recorded with a laser wavelength of 785 nm with a total laser power of 0.5 % (laser power on sample: approximately 1 mW) and an exposure time of 1s/frame. For each measurement 100 frames were accumulated.

Syntheses of compounds 1, 2 and 4

Synthesis of $\text{K}_2[\text{Ge}_9\{\text{Si}(\text{TMS})_3\}_2]$ (**1**)

To a solution of $\text{K}_2[\text{Ge}_9\{\text{Si}(\text{TMS})_3\}_2]$ (92 mg, 75 μ mol, 1 equiv.) in dioxane (2 mL) a 1M solution of C_{72}BCl in hexane (75 μ l, 75 μ mol, 1 equiv.) is added via a Hamilton syringe in the glove box. After five minutes, a color change from milky-brown to deep red is observed. The reaction mixture is stirred at r.t. over night. Subsequently, the solvent is removed under reduced pressure, and the solid residue is re-dissolved in toluene and filtered using a syringe filter to remove any insoluble salts. After removing the solvent under reduced pressure, the residue (23 mg, 9 μ mol, 24 % yield concerning $[\text{Ge}_9]$) is used to acquire ESI-MS and NMR spectra. Due to a repetitively occurring mass gain on the scale (scaling is only possible under a non-inert atmosphere), no reliable elemental analysis could be obtained.

¹H NMR (500 MHz, 298 K, CD₃CN): δ [ppm] = 0.22 (s, 54H, CH₃ TMS). **¹³C NMR** (126 MHz, 298 K, CD₃CN): δ [ppm] = 3.03 (s, CH₃ TMS). **²⁹Si-INEPT NMR** (99 MHz, 298 K, CD₃CN): δ [ppm] = -9.51 (s, Si_{TMS}), -107.10 (s, Si_{Ge9}). **ESI-MS**: *m/z* 2336.0 ([Ge₉{Si(TMS)₃}₂]²⁻).

Synthesis of {NHC^{iPr}Cu[Ge₉{Si(TMS)₃}₂]}₂ (**2**)

To a solution of K₂[Ge₉{Si(TMS)₃}₂] (92 mg, 75 μmol, 1 equiv.) in dioxane (2 mL) a 1M solution of Cy₂BCl in hexane (75 μL, 75 μmol, 1 equiv.) is added via a Hamilton syringe in the glove box. After five minutes, a color change from milky-brown to deep red is observed. The reaction mixture is stirred at r.t. overnight. Subsequently, the solvent is removed under reduced pressure, and the solid residue is redissolved in MeCN. The resulting suspension is filtered to remove solids using a syringe filter. A MeCN solution of NHC^{iPr}Cu-Cl (18.8 mg, 75 μmol, 1 equiv.) is added to the MeCN solution containing **1** at 0 °C, and the formation of a light-brown precipitate is observed. The solvent is removed from the suspension under vacuum, and the residue is washed three times with MeCN (3 mL) at 0 °C. Subsequently, the crude product is dissolved in Et₂O (3 mL), filtered, concentrated, and left at r.t. for crystallization. After three days, the formation of a dark precipitate is observed which contains single crystals of **2** suitable for single crystal diffraction (yield: approximately 10 crystals). Due to the low crystalline yield, the NMR measurements and the elemental analysis were performed with the crude product after washing with MeCN.

¹H NMR (400 MHz, 298 K, thf-*d*₈): δ [ppm] = 7.15 (s, 4H, CH_{NHC}), 5.43 (hept, ³J_{H-H} = 7.0 Hz, 4H, CH_{iPr}), 1.46 (d, ³J_{H-H} = 7.0 Hz, 24H, CH₃), 0.32 (s, 108H, CH₃ TMS). **¹³C NMR** (100 MHz, 298 K, thf-*d*₈): δ [ppm] = 116.07 (s, CH_{NHC}), 52.81 (s, CH_{iPr}), 29.05 (s, CH₃), 28.62 (s, CH₃), 2.97 (s, CH₃ TMS). **²⁹Si-INEPT NMR** (79 MHz, 298 K, thf-*d*₈): δ [ppm] = -11.07 (s, Si_{TMS}), -107.43 (s, Si_{Ge9}). **Elemental analysis** for C₅₄H₁₄₀Cu₂Ge₁₈N₄Si₁₆ **calcd**: C, 23.76; H, 5.17; N, 2.05; **found**: C, 24.91; H, 5.17; N, 1.84.

Synthesis of {NHC^{Dipp}Cu[Ge₉{Si(TMS)₃}₂]}₂ (**4**)

The same procedure as for the preparation of **2** is applied using NHC^{Dipp}Cu-Cl (36.4 mg, 75 μmol, 1 equiv.). After washing the precipitate with MeCN, an analytically pure dark-brown powder is obtained (19 mg, 6 μmol, 16 % yield concerning [Ge₉]).

¹H NMR (400 MHz, 298 K, thf-*d*₈): δ [ppm] = 7.57 (s, 4H, CH_(p)), 7.47 (s, 4H, CH_(m)), 7.45 (s, 4H, CH_(m)), 7.40 (s, 4H, CH_{NHC}), 2.92 (hept, ³J_{H-H} = 6.8 Hz, 8H, CH_{iPr}), 1.61 (d, ³J_{H-H} = 6.8 Hz, 24H, CH₃), 1.20 (d, ³J_{H-H} = 6.8 Hz, 24H, CH₃), 0.19 (s, 108H, CH₃ TMS). **¹³C NMR** (100 MHz, 298 K, thf-*d*₈): δ [ppm] = 146.36 (s, C_(o)), 136.40 (s, C_N), 131.59 (s, CH_(p)), 125.62 (s, CH_(m)), 123.98 (s, CH_{NHC}), 29.92 (s, CH_{iPr}), 26.84 (s, CH₃), 3.44 (s, CH₃ TMS). **²⁹Si-INEPT NMR** (79 MHz, 298 K, thf-*d*₈): δ [ppm] = -9.51 (s, Si_{TMS}), -103.36 (s, Si_{Ge9}). **Elemental analysis** for C₉₀H₁₈₀Cu₂Ge₁₈N₄Si₁₆ **calcd**: C, 33.76; H, 5.67; N, 1.75; **found**: C, 33.78; H, 5.69; N, 1.75. **Proposed unit cell**: *a*: 26.1 Å, *b*: 41.2 Å, *c*: 52.1 Å, *α*: 90.7°, *β*: 90.7°, *γ*: 90.1°, *V*: 55995 Å³.

Formation of $\text{Cy}_2\text{B-O-BCy}_2$

Solid K_4Ge_9 (100 mg, 123 μmol , 1 equiv.) is weighed in into a Schlenk flask and dioxane or toluene (1 mL) is added. To the resulting suspension a 1M solution of Cy_2BCl in hexane (123 μl , 123 μmol , 1 equiv.) is added. The reaction mixture is stirred over night, filtered (yellow filtrate), and the solvent is removed under reduced pressure. The remaining oily residue is re-dissolved in hexane (2 mL), and the solution is filtered. Subsequently, the volume is reduced to a third of its original amount, and the flask is stored at $-40\text{ }^\circ\text{C}$ for crystallization. After two days the formation of colorless to light-yellow crystals of $\text{Cy}_2\text{B-O-BCy}_2$ (8 mg, 21.6 μmol , 35 % yield concerning Cy_2BCl) is observed. **Determined unit cell:** a : 10.22 Å, b : 12.05 Å, c : 19.76 Å, α : 89.1°, β : 78.3°, γ : 87.3°, V : 2379 Å³ (in analogy to literature values).^[10]

Pure Cy_2BCl : $^{11}\text{B NMR}$ (128 MHz, 298 K, C_6D_6): δ [ppm] = 76.7 ppm.

Blind test (no K_4Ge_9): $^{11}\text{B NMR}$ (128 MHz, 298 K, C_6D_6): δ [ppm] = 76.4 ppm.

K_4Ge_9 : $^{11}\text{B NMR}$ (128 MHz, 298 K, C_6D_6): δ [ppm] = 52.3 ppm.

KC_8 instead of K_4Ge_9 : $^{11}\text{B NMR}$ (128 MHz, 298 K, C_6D_6): δ [ppm] = 49.9 ppm.

2. Crystallographic details

Table S1. Crystallographic data of compound **2**.

compound	2
formula	C ₅₄ H ₁₄₄ Cu ₂ Ge ₁₈ N ₄ Si ₁₆ · 2 C ₄ H ₁₀ O
fw [g·mol ⁻¹]	2733.57
space group	<i>I</i> 2/ <i>c</i>
<i>a</i> [Å]	16.6540(4)
<i>b</i> [Å]	27.2393(8)
<i>c</i> [Å]	27.6288(6)
α [deg]	90
β [deg]	103.416(2)
γ [deg]	90
<i>V</i> [Å ³]	12191.6(5)
<i>Z</i>	4
<i>T</i> [K]	150(2)
λ [Å]	0.71073
ρ_{calcd} [g·cm ⁻³]	1.487
μ [mm ⁻¹]	4.887
collected reflections	122568
indep. reflections	11984
<i>R</i> _{int} / <i>R</i> _σ	0.0973/0.0354
parameters / restraints	564/0
<i>R</i> ₁ [<i>I</i> > 2 σ (<i>I</i>) / all data]	0.0311/ 0.0546
<i>wR</i> ₂ [<i>I</i> > 2 σ (<i>I</i>) / all data]	0.0689/0.0818
goodness of fit	1.134
max./min. diff. el. density [e·Å ⁻³]	0.626/-0.484
depository no.	CCDC-2129082

Table S2. Selected interatomic distances in compound **2**.

atoms	distance [Å]	atoms	distance [Å]
Ge1-Ge1	2.4259(8)	Ge1-Cu	2.4511(7)
Ge1-Ge2	2.6786(6)	Ge2-Cu	2.5392(6)
Ge1-Ge4	2.6187(6)	Ge3-Cu	2.4790(6)
Ge1-Ge5	2.5570(6)	Ge4-Cu	2.6188(7)
Ge1-Ge6	2.5747(6)		
Ge2-Ge3	2.7100(6)	Cu-C1	1.955(4)
Ge2-Ge6	2.5947(6)		
Ge2-Ge7	2.6168(6)		
Ge3-Ge4	2.6517(6)		
Ge3-Ge7	2.5705(6)		
Ge3-Ge8	2.5769(7)		
Ge4-Ge5	2.6339(6)		
Ge4-Ge8	2.6259(6)		
Ge5-Ge8	2.7867(6)		
Ge5-Ge9	2.5429(6)		
Ge6-Ge7	2.8403(6)		
Ge6-Ge9	2.5192(6)		
Ge8-Ge9	2.5424(6)		
Ge3-Si5	2.417(1)		
Ge9-Si1	2.381(1)		

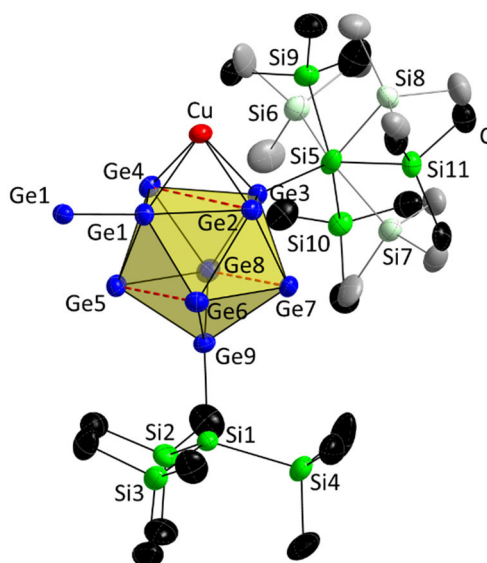


Figure S1. Representation of one cluster monomer of **2** with emphasis on the split positions of the trimethylsilyl-groups at Si5. Major species site occupation factor: 0.543, minor species: 0.466. Color code: Si_{major}: deep green; C_{major}: black; Si_{minor}: light green; C_{minor}: grey. All ellipsoids are presented at a 50 % probability level. The NHC ligand is omitted for clarity. Prism heights are indicated by dashed red lines.

3. NMR spectra

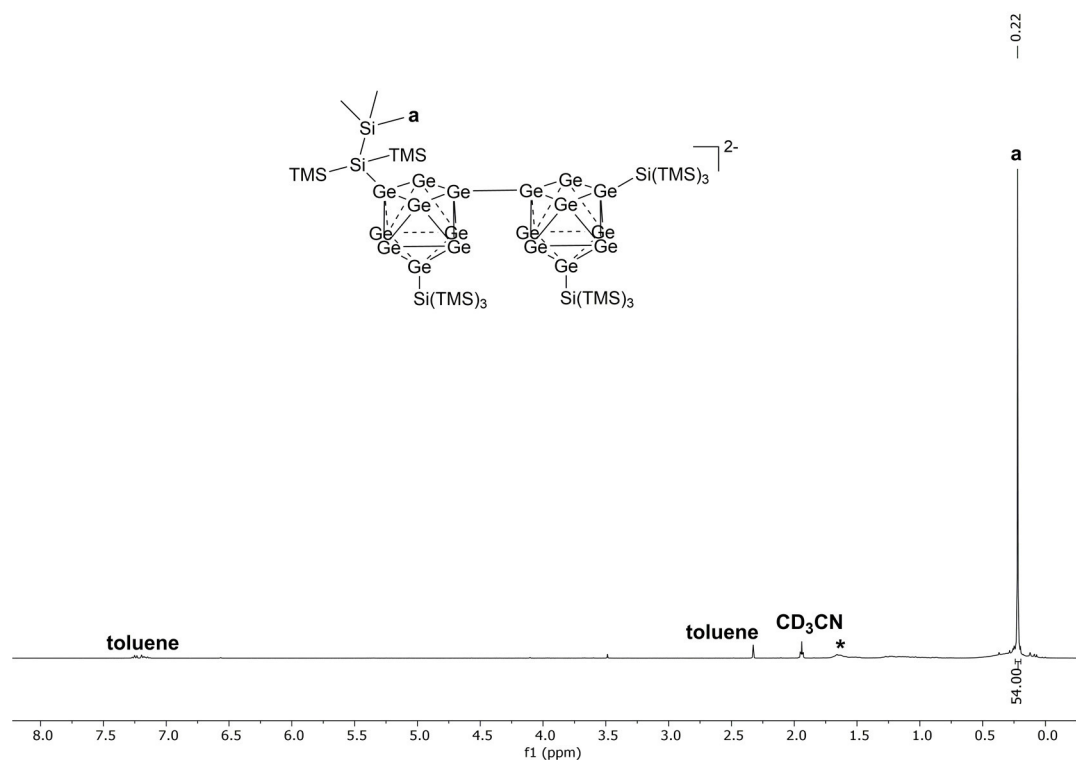


Figure S2. ^1H NMR spectrum (CD_3CN) of $\text{K}_2[\text{Ge}_9\{\text{Si}(\text{TMS})_3\}_2]_2$ (1). Asterisked impurities are assigned to the cyclohexyl groups of trace amounts of $\text{Cy}_2\text{B-O-BCy}_2$.

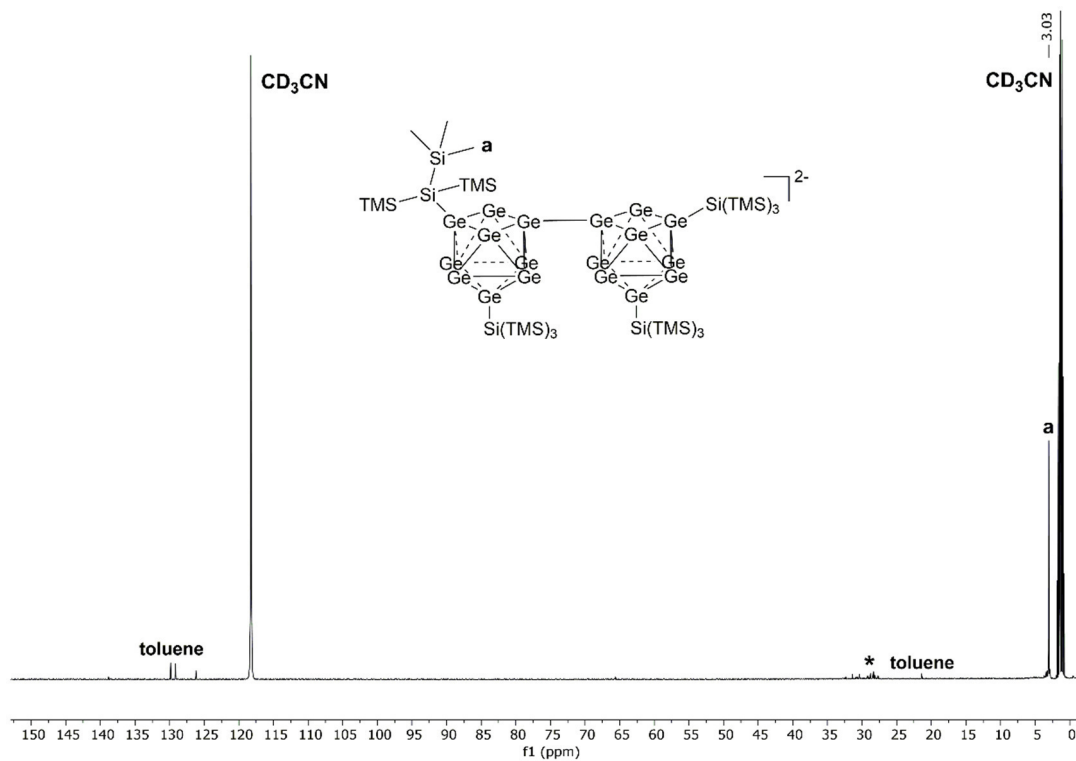


Figure S3. ^{13}C NMR spectrum (CD_3CN) of $\text{K}_2[\text{Ge}_9\{\text{Si}(\text{TMS})_3\}_2]_2$ (1). Asterisked impurities most probably arise from the cyclohexyl groups of trace amounts of $\text{Cy}_2\text{B-O-BCy}_2$.

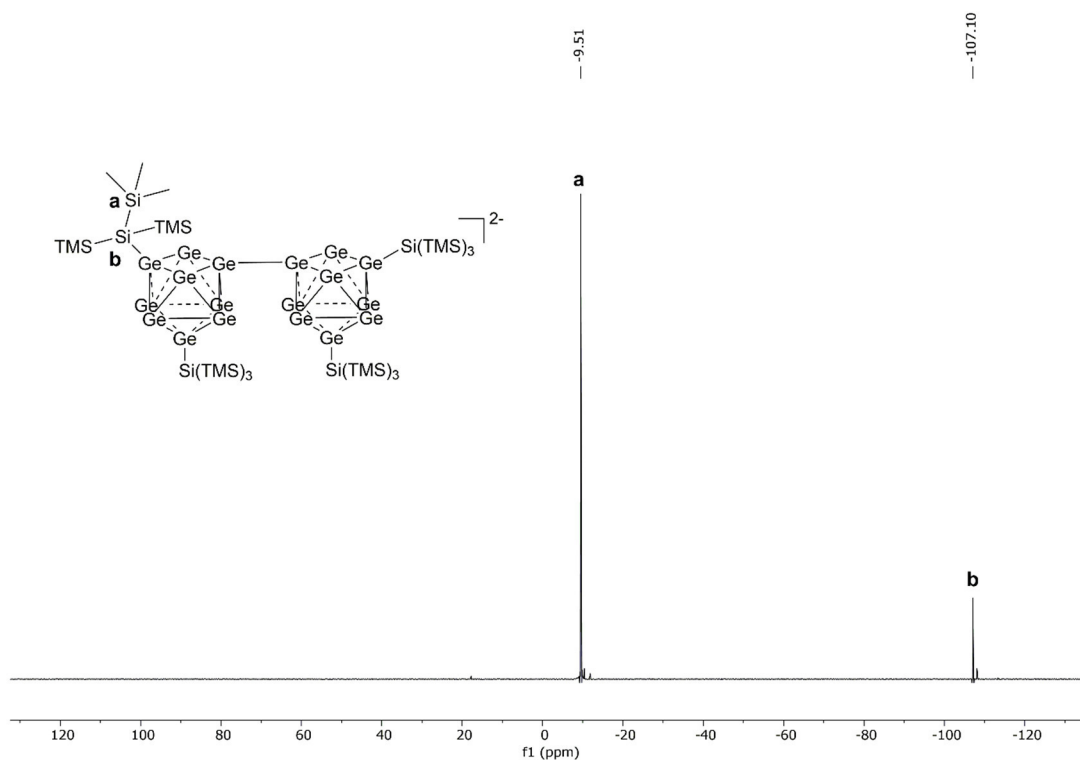


Figure S4. ^{29}Si INEPT spectrum (CD_3CN) of $\text{K}_2[\text{Ge}_9\{\text{Si}(\text{TMS})_3\}_2]_2$ (**1**).

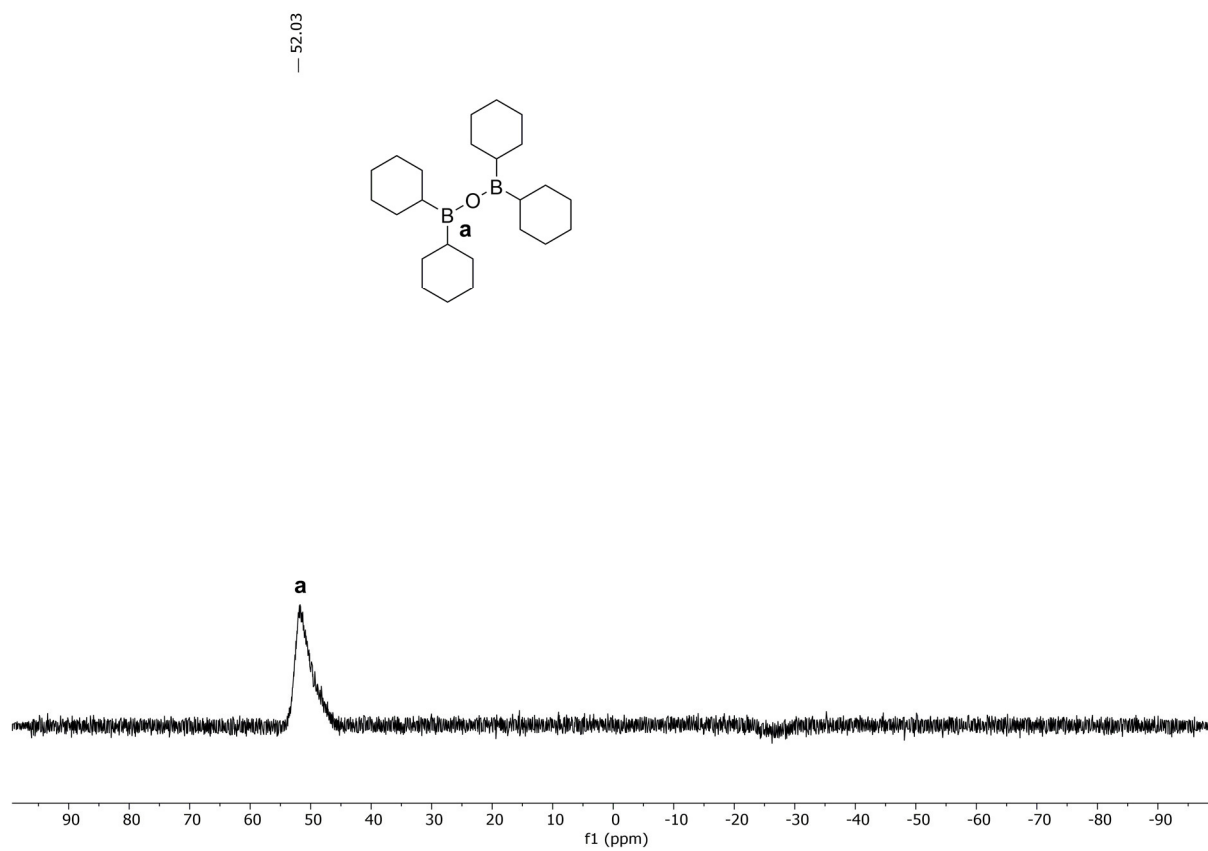


Figure S5. ^{11}B NMR spectrum (CD_3CN) of the reaction solution containing $\text{K}_2[\text{Ge}_9\{\text{Si}(\text{TMS})_3\}_2]_2$ (**1**) showing the signal of the molecule $\text{Cy}_2\text{B-O-BCy}_2$.

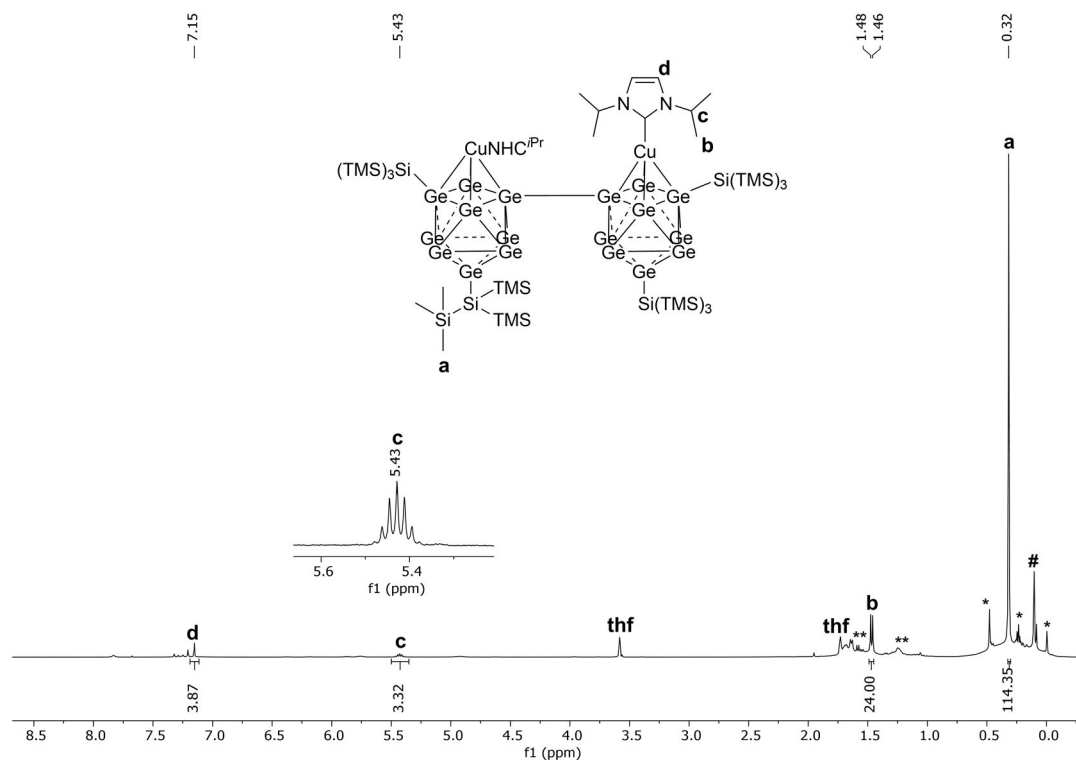


Figure S6. ^1H NMR spectrum ($\text{thf-}d_8$) of $\{\text{NHC}^{\text{iPr}}\text{Cu}[\text{Ge}_9\{\text{Si}(\text{TMS})_3\}_2]\}_2$ (**2**). Double-asterisked impurities are caused by cyclohexyl groups of trace amounts of $\text{Cy}_2\text{B-O-BCy}_2$; asterisked signals are caused by unidentified impurities; signal marked with # is caused by silicon grease.

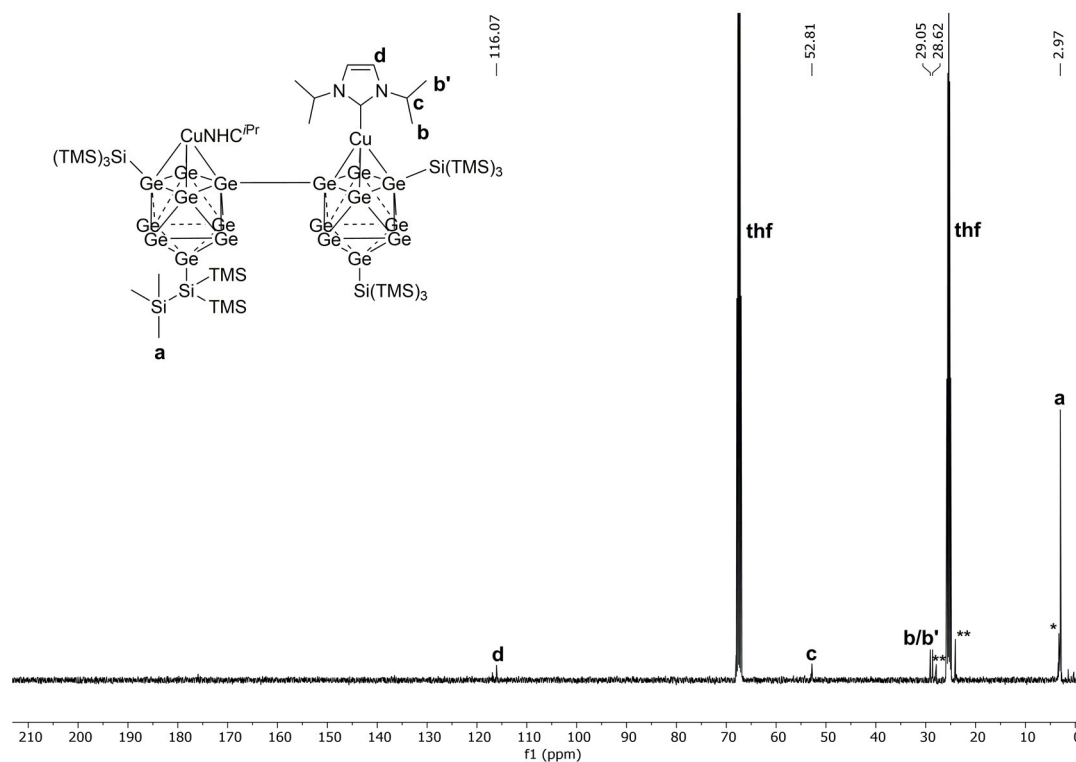


Figure S7. ^{13}C NMR spectrum ($\text{thf-}d_8$) of $\{\text{NHC}^{\text{iPr}}\text{Cu}[\text{Ge}_9\{\text{Si}(\text{TMS})_3\}_2]\}_2$ (**2**). Double-asterisked impurities are caused by cyclohexyl groups of trace amounts of $\text{Cy}_2\text{B-O-BCy}_2$; asterisked signal is caused by an unidentified impurity.

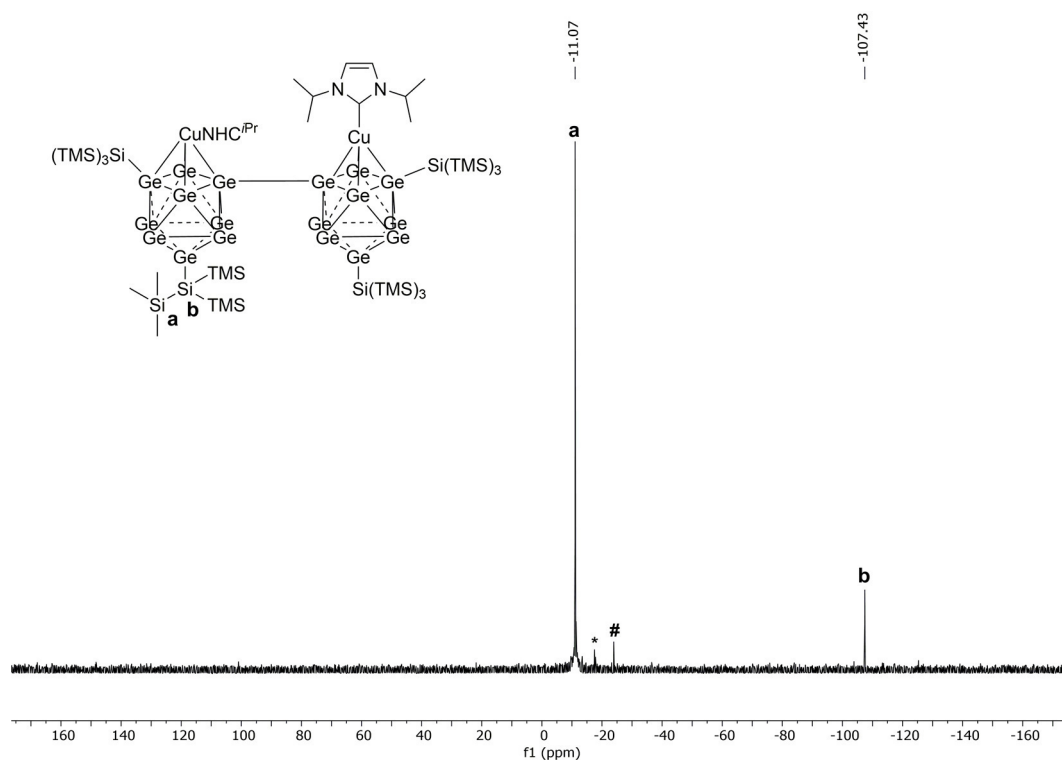


Figure S8. ^{29}Si INEPT spectrum ($\text{thf-}d_8$) of $\{\text{NHC}^{i\text{Pr}}\text{Cu}[\text{Ge}_9\{\text{Si}(\text{TMS})_3\}_2]\}_2$ (**2**). Asterisked signal is caused by an unidentified impurity; the signal marked with # is caused by silicon grease.

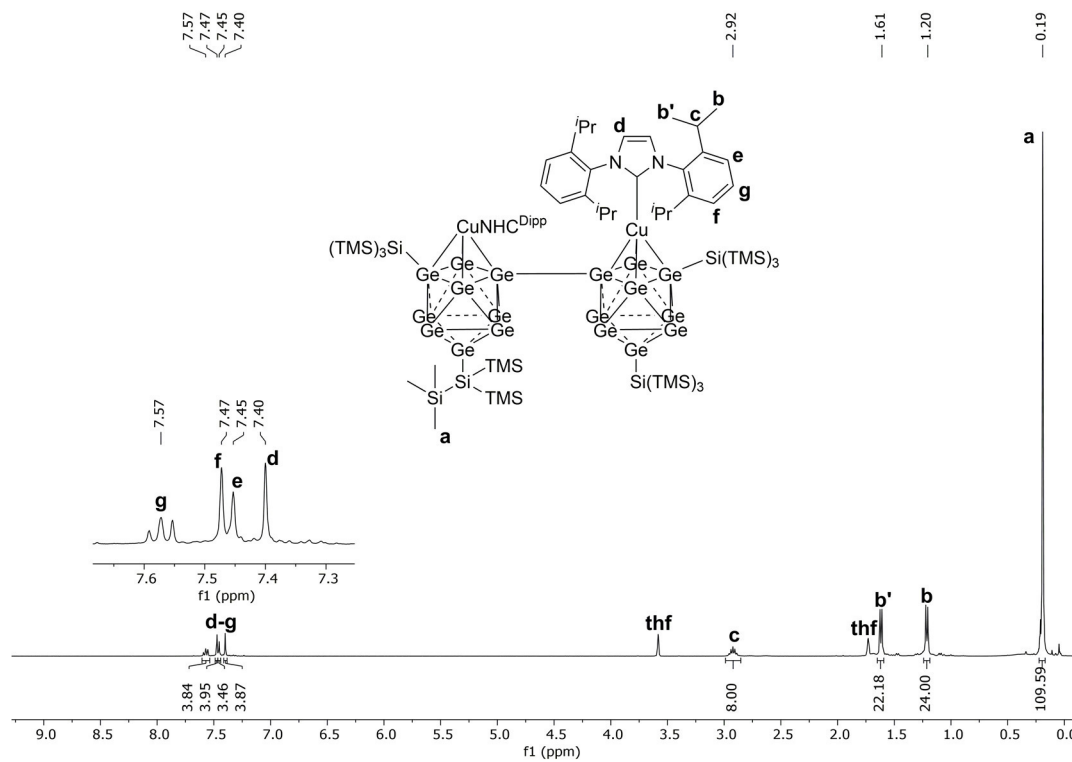


Figure S9. ^1H NMR spectrum ($\text{thf-}d_8$) of $\{\text{NHC}^{\text{Dipp}}\text{Cu}[\text{Ge}_9\{\text{Si}(\text{TMS})_3\}_2]\}_2$ (**4**).

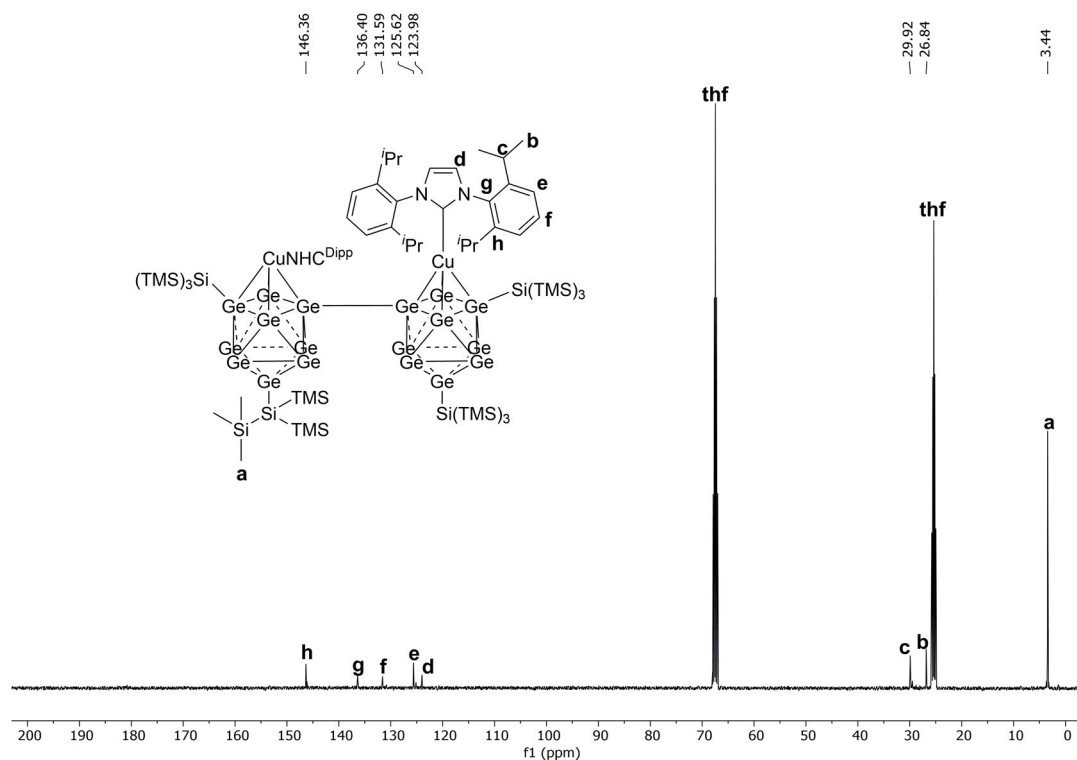


Figure S10. ^{13}C NMR spectrum ($\text{thf-}d_8$) of $\{\text{NHC}^{\text{Dipp}}\text{Cu}[\text{Ge}_9\{\text{Si}(\text{TMS})_3\}_2]\}_2$ (**4**).

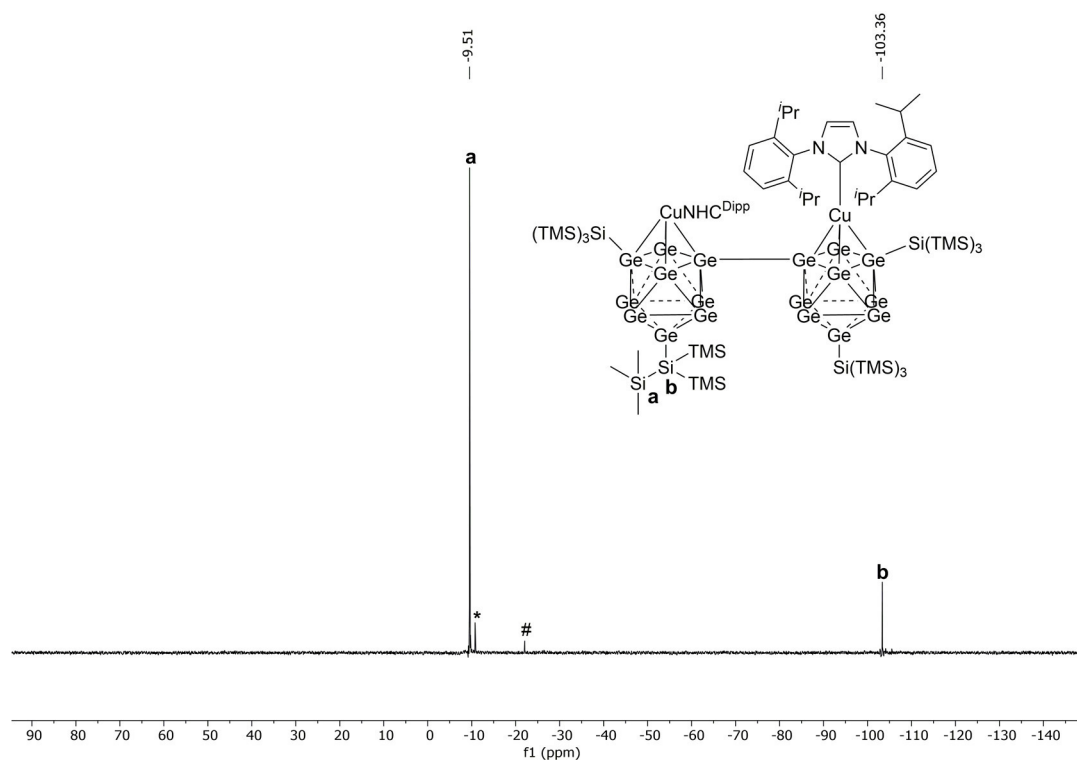


Figure S11. ^{29}Si INEPT spectrum ($\text{thf-}d_8$) of $\{\text{NHC}^{\text{Dipp}}\text{Cu}[\text{Ge}_9\{\text{Si}(\text{TMS})_3\}_2]\}_2$ (**4**). Asterisked signal is caused by an unidentified impurity; the signal marked with # is caused by silicon grease.

4. LIFDI-MS spectrum

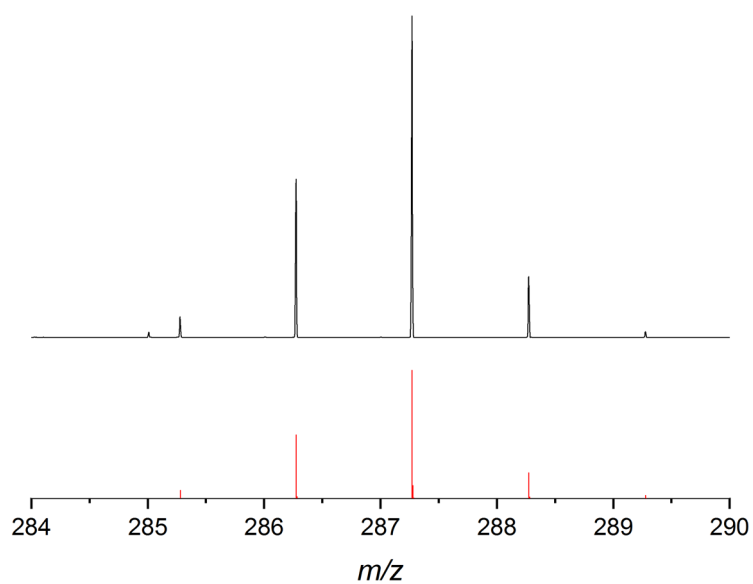


Figure S12. LIFDI-MS spectrum of the ionization product $[\text{C}_2\text{B-O-BCy}]^+$ at m/z 287.27 formed during the ionization of $\text{C}_2\text{B-O-BCy}_2$. The calculated isotope pattern is presented as red bars.

5. References

- [1] O. Kysliak and A. Schnepf, *Dalton Trans.* 2016, **45**, 2404.
- [2] L. Hintermann, *Beilstein J. Org. Chem.* 2007, **3**, 22.
- [3] O. Santoro, A. Collado, A. M. Slawin, S. P. Nolan and C. S. Cazin, *Chem. Commun.* 2013, **49**, 10483.
- [4] G. M. Sheldrick, *Acta Crystallogr., Sect. A: Found. Crystallogr. A* 2008, **64**, 112.
- [5] G. M. Sheldrick, *Acta Crystallogr., Sec. C: Struct. Chem.* 2015, **71**, 3.
- [6] A. Spek, *Acta Crystallogr., Sect. D: Biol. Crystallogr.* 2009, **65**, 148.
- [7] G. R. Fulmer, A. J. M. Miller, N. H. Sherden, H. E. Gottlieb, A. Nudelman, B. M. Stoltz, J. E. Bercaw and K. I. Goldberg, *Organometallics* 2010, **29**, 2176.
- [8] M. Muhr, P. Heiß, M. Schütz, R. Bühler, C. Gemel, M. H. Linden, H. B. Linden and R. A. Fischer, *Dalton Trans.* 2021, **50**, 9031.
- [9] F. S. Geitner and T. F. Fässler, *Inorg. Chem.* 2020, **59**, 15218.
- [10] S. S. Barnes, C. M. Vogels, A. Decken and S. A. Westcott, *Dalton Trans.* 2011, **40**, 4707.

6.3 Boranyl-Functionalized [Ge₉] Clusters: Providing the Idea of Intramolecular Ge/B Frustrated Lewis Pairs

C. Wallach,[‡] F. S. Geitner,[‡] A. J. Karttunen and T. F. Fässler

[‡]: authors contributed equally to this work.

Published in: *Angewandte Chemie International Edition* **2021**, *60*, 2648.

© Wiley-VCH GmbH, Weinheim 2021, reprint license ID: 5307461252344 (CCC RightsLink[®]), open-access article, unchanged reprinted version licensed under the terms of a Creative Commons Attribution-Non Commercial 3.0 Unported License.

Access online *via*: <https://onlinelibrary.wiley.com/doi/full/10.1002/anie.202012336>.

Contents and Contributions

Reactions of the twofold silylated cluster [Ge₉{Si(TMS)₃}₂]²⁻ with N-heterocyclic chloro-1,3,2-diazaborolidines DAB^R-Cl (*R* = Me, ^{*i*}Pr, *o*-tol) yielded the boranyl-functionalized cluster species [Ge₉{Si(TMS)₃}₂DAB^R]⁻ [*R* = Me (**1a**), ^{*i*}Pr (**2a**), *o*-tol (**3a**)]. The anions were characterized by NMR spectroscopy as well as ESI-MS measurements. Anions **2a** and **3a** were transferred into the Cu-carbene adducts NHC^{Dipp}Cu[Ge₉{Si(TMS)₃}₂DAB^R], **2a-Cu** and **3a-Cu**, which were successfully crystallized. The obtained anions are the first examples for covalent interactions between [Ge₉] clusters and triel element-based compounds. Intriguingly, the attachment of boranyl groups at the cluster can in principle be described as the formation of an intramolecular frustrated Lewis acid-base pair, with the boron-comprising entity acting as a Lewis acid, and the cluster revealing properties of a manifold Lewis base. This assumption was corroborated by quantum chemical calculations for the theoretical anionic molecule [Ge₉{Si(TMS)₃}₂BCy₂]⁻ (**4a**).

Anions **1a** to **3a** were prepared by me and transferred into the Cu-carbene adducts **2a-Cu** and **3a-Cu** for crystallization by Dr. Felix S. Geitner. The single crystal of **2a-Cu** was selected, measured, and refined by Dr. Felix S. Geitner, the crystal of **3a-Cu** by me. The quantum chemical calculations were done by Prof. Dr. Antti J. Karttunen (Aalto University, Finland), including the design of the graphic representation of the molecular orbital figures. Elemental analysis data were acquired by Ulrike Ammari and Bircan Dilki in the microanalytical laboratory of the Chemistry Department of the Technical University of Munich. A first preliminary draft of the manuscript was authored by Dr. Felix S. Geitner and me in collaboration. Later, I restructured and rewrote the manuscript for the final publication. Dr. Felix S. Geitner and Dr. Annette Schier proof-read the final version of the manuscript. Dr. Felix S. Geitner compiled

data for the Supporting Information, which were collected in cooperation. The publication of the manuscript was managed by Prof. Dr. Thomas F. Fässler, the peer-review process including corrections was a joined task accomplished by Prof. Dr. Thomas F. Fässler, Prof. Antti J. Karttunen and me.

Frustrated Lewis Pairs

Boranyl-Functionalized [Ge₉] Clusters: Providing the Idea of Intramolecular Ge/B Frustrated Lewis PairsChristoph Wallach[†], Felix S. Geitner[†], Antti J. Karttunen, and Thomas F. Fässler*

Dedicated to Professor Herbert W. Roesky on the Occasion of his 85th Birthday

Abstract: The unique three-dimensional structure of spherical, homoatomic nine-atom germanium clusters opens various possibilities for the spatial arrangement of functional groups. Ligands comprising lone pairs have recently been introduced in the cluster sphere, and we now report the addition of a boranyl group to the cluster featuring a Ge–B *exo*-cluster bond. The reaction of the twofold-silylated cluster [Ge₉{Si(TMS)₃}₂]²⁻ (TMS = trimethylsilyl) with 2-chloro-1,3,2-diazaborolidines DAB^R-Cl leads to the first boranyl-functionalized [Ge₉] clusters [Ge₉{Si(TMS)₃}₂DAB^R]⁻ (R = methyl (**1a**), isopropyl (**2a**), ortho-tolyl (**3a**)). The anions **2a** and **3a** were structurally characterized as [NHC^{Dipp}Cu]⁺ complexes (NHC^{Dipp} = 1,3-di(2,6-diisopropylphenyl)imidazolylidene) through single crystal X-ray structure determination. Quantum-chemical calculations manifest the frustrated Lewis pair (FLP) character of the boranyl-functionalized cluster [Ge₉{Si(TMS)₃}₂BCy₂]⁻ (**4a**).

By fusion of stoichiometric amounts of the elements, the tetrel *Zintl* phase K₄Ge₉ containing soluble [Ge₉]⁴⁻ ions is easily accessible. These clusters have shown great potential to react with main group and transition metal compounds.^[1] The silylation of [Ge₉] through a heterogeneous reaction of K₄Ge₉ with chloro-tris(trimethylsilyl)silane in MeCN has proven to be a straightforward way to reduce the fourfold negative cluster charge thereby enhancing the stability and solubility of the clusters. By variation of the stoichiometry of the reaction, either bis-silylated [Ge₉{Si(TMS)₃}₂]²⁻ or tris-silylated [Ge₉{Si(TMS)₃}₃]⁻ (TMS: trimethylsilyl) species are accessible in high yields.^[2] Furthermore, various tris-silylated clusters have been prepared with silyl groups of different bulkiness.^[3] In

similar reactions the tris-stannylated cluster [Ge₉(SnⁱPr₃)₃]⁻ can also be obtained.^[4] Recently, also ligands with donor functions have been introduced to the sphere of the [Ge₉] clusters allowing for subsequent reactions with Lewis acids, leading to charge-neutral zwitterionic cluster compounds [Ge₉{Si(TMS)₃}₂(^tBu₂P)]M(NHC^{Dipp}) (M: Cu, Ag, Au).^[5] Up to three ligands with Lewis base groups can be introduced in form of the tris-phosphanyl-functionalized clusters [Ge₉(PRR¹)₃]⁻ (R: NⁱPr₂; R¹: NⁱPr₂; ^tBu).^[6] These clusters still possess six or seven unsubstituted cluster vertices with low oxidation state,^[7] and are thus prone to undergo subsequent reactions.

Owing to the shielding of the [Ge₉] core, reactions of the tris-silylated cluster are limited to the introduction of less bulky main group element ligands, yielding uncharged cluster compounds with Ge–C, Ge–P and Ge–Sn *exo*-cluster bonds such as [Ge₉{Si(TMS)₃}₃R] [R: Et,^[8] (CO)^tBu,^[9] ^tBu,^[9] {(CH₂)_nCH=CH₂} (n: 1, 3)^[7c], [Ge₉{Si(TMS)₃}₃(PRR¹)] (R = R¹: ⁱPr, Cy,^[5] R: ^tBu, R¹: {(CH₂)₃CH=CH₂}^[10]), and [Ge₉{Si(TMS)₃}₃SnR₃] (R: ^tBu,^[8] Ph^[11]). Except for the Sn-containing species, which (partially) show multicenter Ge–Sn bonds, all main group element fragments are attached to the [Ge₉] entity via 2-center-2-electron (2c-2e) bonds pointing radially away from the center of the cluster. The Lewis basic property of the [Ge₉] core is manifested in various isolated transition metal decorated clusters such as [Ge₉{Si(TMS)₃}₃TiCp₂(MeCN)], [Cp₂Ti(η¹-Ge₉{Si(TMS)₃}₂)₂]³⁻,^[12] [Ge₉{Si(TMS)₃}₃-Cr(CO)₅]⁻^[13] as well as [Zn(η¹-Ge₉{Si(TMS)₃}₂)₄]⁶⁻.^[14]

Because of the decreased shielding of the [Ge₉] cluster core, the di-anion [Ge₉{Si(TMS)₃}₂]²⁻ is an attractive candidate for subsequent reactions. Upon addition of further halo-silanes, mixed-substituted [Ge₉] clusters of the general composition [Ge₉{Si(TMS)₃}₂R]⁻ [R: Si(TMS)₂SiPh₃,^[2a] Si(TMS)₂Si(ⁱPr)₃,^[3b] SiPh₂{(CH₂)_nCH=CH₂}^[16] (n = 1, 3)] are formed. Using a rigid bis-halo-silane, a connection of two clusters to the anion [[Si(SiMe₃)₃]₂Ge₉-SiMe₂-(C₆H₄)-SiMe₂-Ge₉{Si(SiMe₃)₃}₂]²⁻ is achieved.^[17] Comparable to the reactions reported for the tris-silylated species, alkyl-, germanyl- or phosphanyl-decorated anions [Ge₉{Si(TMS)₃}₃Et]²⁻ (one Si(TMS)₃ group is cleaved upon crystallization),^[18] [Ge₉{Si(TMS)₃}₂Ge(TMS)₃]⁻^[19] or [Ge₉{Si(TMS)₃}₂(PRR¹)]⁻ (R, R¹: alkyl, aryl, aminoalkyl)^[5,10,20] can be synthesized, revealing the prosperous chemistry of [Ge₉{Si(TMS)₃}₂]²⁻ with halo-main group element compounds.

We have shown that ligands with free electron lone pairs such as phosphanyl groups (Scheme 1, **A**) allow for the attachment of Lewis acidic organometallic fragments,^[5,10,20] and now focused on the introduction of electron acceptor

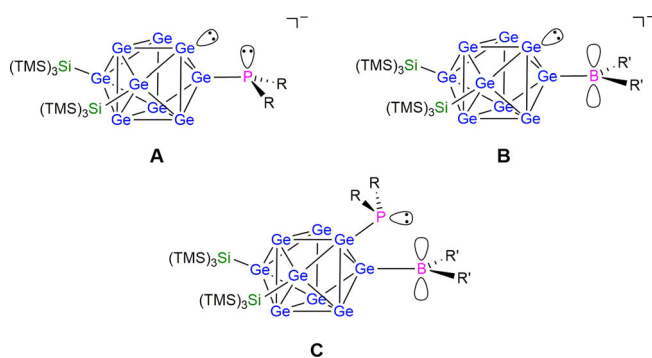
[*] M. Sc. C. Wallach,^[†] Dr. F. S. Geitner,^[†] Prof. Dr. T. F. Fässler
Department Chemie, Technische Universität München
Lichtenbergstraße 4, 85747 Garching b. München (Germany)
E-mail: thomas.faessler@lrz.tum.de

Prof. Dr. A. J. Karttunen
Department of Chemistry and Materials Science, Aalto University
00076 Aalto (Finland)

[†] These authors contributed equally to this work.

Supporting information and the ORCID identification number(s) for the author(s) of this article can be found under:
<https://doi.org/10.1002/anie.202012336>.

© 2020 The Authors. Angewandte Chemie International Edition published by Wiley-VCH GmbH. This is an open access article under the terms of the Creative Commons Attribution Non-Commercial NoDerivs License, which permits use and distribution in any medium, provided the original work is properly cited, the use is non-commercial and no modifications or adaptations are made.



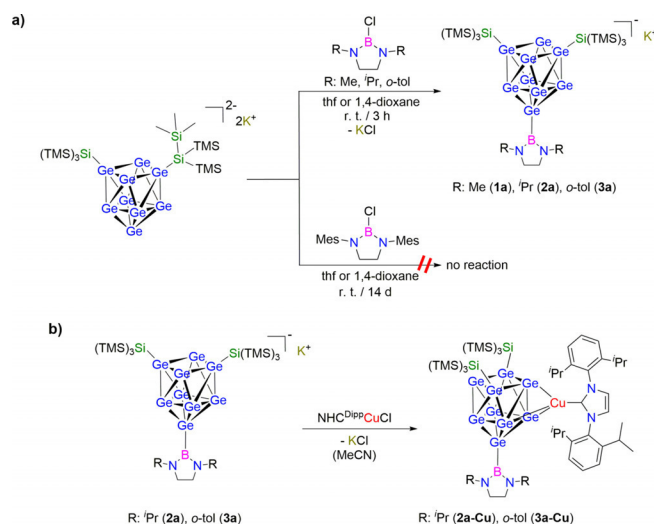
Scheme 1. Different Lewis basic sites at $[\text{Ge}_9]$ occurring in reported **A**^[5,10,20] and boranyl-functionalized $[\text{Ge}_9]$ cluster **B** with FLP character according to quantum-chemical calculations. The lone pair of only one Ge atom is shown. **C** shows a potential mixed-functionalized $[\text{Ge}_9]$ core featuring both Lewis acidic and basic moieties.

functions to the sphere of the $[\text{Ge}_9]$ cluster (Scheme 1, **B**). Scheschkewitz and *co-workers* recently reported on the grafting of silicoindols of general composition Si_6R_6 with $[\text{BH}_3]^-$ fragments,^[21] as well as p-doping such clusters by a formal exchange of one Si vertex by a boranyl group.^[22] These clusters exhibit unsubstituted vertices and thus are conceptually related to *Zintl* ions.^[21b] For several reasons we particularly suspected halo-boranes, 1,3,2-diazaborolidines (DABs), as promising candidates for this venture. Due to the straightforward preparation of 2-halo-DABs from BX_3 (X : Cl, Br) and diamines, the wingtip substituents can easily be tuned concerning their bulkiness. Furthermore, the electron deficiency of the boron center is compensated by π -donation of the lone pairs of adjacent N atoms into the boron p_z orbital, thereby enhancing the stability of the compounds. These species have been established as ligands in complex chemistry reported for the shell-structured ion $[\text{In}_{68}[\text{DAB}^{\text{Dipp}}]_{12}]^-$ ^[23] or in lanthanide boranyl compounds.^[24] Furthermore, diazaboroles act as σ -donor ligands and have recently been used to prepare new types of low-valent group 14 element (Si,^[25] Ge,^[25,26] Sn,^[25,26,27] Pb^[28]) compounds. Such species are prone to activate small molecules via oxidative addition (e.g. H_2 or further nonpolar $E\text{--H}$ bonds; E : B, Si, N, O), and also insertion reactions into the Ge--B bond (e.g. phenylacetylene and diphenylacetylene) have been reported.^[26c,e,27a] Within this work we investigated reactions of the negatively charged germanide cluster $[\text{Ge}_9\{\text{Si}(\text{TMS})_3\}_2]^{2-}$ towards DABs, focusing on the generation of a hitherto

unreported boranyl-functionalized cluster species revealing unprotected Ge atoms in negative oxidation states.

Treatment of solid $\text{K}_2[\text{Ge}_9\{\text{Si}(\text{TMS})_3\}_2]$ with THF or 1,4-dioxane solutions of $\text{DAB}^{\text{R}}\text{--Cl}$ (R : Me, ⁱPr, *o*-tol, Mes = 2,4,6-trimethylbenzene) yielded deep red reaction mixtures, which were stirred for 3–5 h at room temperature. Subsequently, the mixtures were filtered, and the solvent was removed in vacuo. The remaining oily solids were treated with hexane, which was then removed in vacuo to eliminate traces of remaining solvents (this procedure was repeated twice). The brown (R : Me, Mes) or ochre (R : ⁱPr, *o*-tol) residues were investigated by NMR spectroscopy.

¹H NMR examinations indicated the formation of $[\text{Ge}_9\{\text{Si}(\text{TMS})_3\}_2\text{DAB}^{\text{R}}]^-$ [R : Me (**1a**), ⁱPr (**2a**) and *o*-tol (**3a**)] by the downfield shift of the cluster's silyl group protons and the 1:2 ratio of signals assigned to the boranyl moiety and the cluster's silyl protons. The formation of **1a–3a** (Scheme 2a) was confirmed by further NMR experiments (¹¹B, ¹³C and ²⁹Si). In the ¹¹B NMR spectra a significant downfield shift of the product signal from approx. 27 ppm (thf-*d*₈) ($\text{DAB}^{\text{R}}\text{--Cl}$; R : Me, ⁱPr, *o*-tol) to 43.31 ppm (**1a**), 41.90 ppm (**2a**) and 42.92 ppm (**3a**) was observed. Moreover, anions **1a–3a** were detected in ESI MS experiments at m/z 1246.6 (**1a**), m/z 1302.6 (**2a**) and m/z 1398.7 (**3a**) in the negative-ion mode (Figure 1).



Scheme 2. a) Overview on the reactivity of $\text{K}_2[\text{Ge}_9\{\text{Si}(\text{TMS})_3\}_2]$ towards $\text{DAB}^{\text{R}}\text{--Cl}$ (R : Me, ⁱPr, *o*-tol, Mes); b) formation of **2a-Cu** and **3a-Cu** upon addition of $\text{NHC}^{\text{Dipp}}\text{CuCl}$ to **2a** and **3a**, respectively.

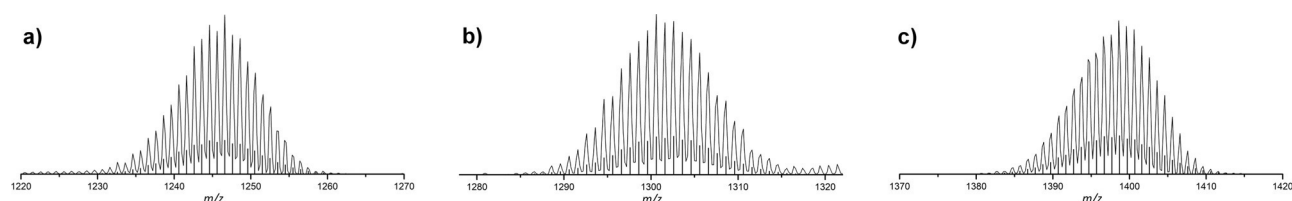


Figure 1. Selected areas of ESI MS spectra of anions **1a–3a**. Spectra were recorded from diluted THF solutions of the samples in the negative-ion mode (3500 V, 300 °C). Calculated isotope patterns are represented as black bars. a) molecule peak of **1a** $[\text{Ge}_9\{\text{Si}(\text{TMS})_3\}_2\text{DAB}^{\text{Me}}]^-$ at m/z 1246.6; b) molecule peak of **2a** $[\text{Ge}_9\{\text{Si}(\text{TMS})_3\}_2\text{DAB}^{\text{iPr}}]^-$ at m/z 1302.6; c) molecule peak of **3a** $[\text{Ge}_9\{\text{Si}(\text{TMS})_3\}_2\text{DAB}^{\text{o-tol}}]^-$ at m/z 1398.7. The respective overview spectra can be found in the Supporting Information.

For crystallization, the crude solids **1a-K** to **3a-K** containing the K^+ -salt of **1a** to **3a** were dissolved in toluene and filtered. Unfortunately, the purification of **1a-K** and **2a-K** has not been successful to date, but $[Ge_9\{Si(TMS)_3\}_2DAB^{o-tol}]K$ (**3a-K**) was obtained as an ochre, polycrystalline powder from concentrated toluene solutions. In analogous reactions of $K_2[Ge_9\{Si(TMS)_3\}_2]$ with $DAB^{Mes}-Cl$ no conversion of the reactants was observed (14 d at room temperature and at elevated temperature; Scheme 2a). Since the DAB^{Mes} ligand has a higher steric demand, we assume that there is a steric limitation for the introduction of boranyl moieties at $[Ge_9]$.

In previous studies we found that neutral species with a $[NHC^{Dipp}Cu]^+$ moiety as the fourth substituent crystallized much more easily than the respective anionic species.^[6,20] Since the isolation of single-crystalline material suitable for structure determination was not possible from the isolated solids, we carried out subsequent reactions of **1a-K** to **3a-K** with $NHC^{Dipp}CuCl$ (Scheme 2b). **1a-K** to **3a-K** were dissolved in MeCN and the resulting dark red solutions were treated dropwise with MeCN solutions of the Cu-NHC complex, immediately resulting in the precipitation of brown (**1a-Cu**) or reddish (**2a-Cu**, **3a-Cu**) solids. In order to assure complete conversion, the mixtures were stirred at room temperature for further 30 min, before the supernatant red solutions were filtered, and the residues were washed with MeCN. 1H NMR examinations of the solids indicated the addition of $[NHC^{Dipp}Cu]^+$ to **2a** and **3a** under formation of $NHC^{Dipp}Cu[Ge_9\{Si(TMS)_3\}_2DAB^R]$ [$R: Pr$ (**2a-Cu**) and $o-tol$ (**3a-Cu**)]. By contrast, the product resulting from the reaction of **1a** with $NHC^{Dipp}CuCl$ was identified as the previously published species $(NHC^{Dipp}Cu)_2[Ge_9\{Si(TMS)_3\}_2]$ comprising two $[NHC^{Dipp}Cu]^+$ moieties.^[29] The Ge–B bond cleavage upon the reaction with the Cu-NHC complex hints for an increased lability of DAB moieties with smaller wingtip substituents. Crude materials of **2a-Cu** and **3a-Cu** were dissolved in toluene and filtered to remove remaining solids. The samples were stored in a freezer at $-40^\circ C$ for crystallization yielding red block-shaped single crystals of **2a-Cu** and **3a-Cu** suitable for single crystal X-ray diffraction. The isolated materials were further characterized by elemental analysis and NMR spectroscopy (1H , ^{11}B , ^{13}C and ^{29}Si). Compounds **2a-Cu** and **3a-Cu** crystallize in the monoclinic space groups $P2_1/n$ and $I2/a$, respectively, and show functionalized clusters and $[NHC^{Dipp}Cu]^+$ moieties in a 1:1 ratio. The shapes of the $[Ge_9]$ cluster cores are best described as slightly distorted, tricapped trigonal prisms (their heights are emphasized by fragmented thick lines between the eclipsed triangles Ge1 to Ge3 and Ge7 to Ge9, Figure 2), with one prism height [$d(Ge1-Ge7) = 3.584(1) \text{ \AA}$ (**2a-Cu**) and $d(Ge1-Ge7) = 3.682(1) \text{ \AA}$ (**3a-Cu**)] being significantly longer compared to the others [$3.164(2) \text{ \AA}$ (Ge2–Ge8) and $3.283(1) \text{ \AA}$ (Ge3–Ge9) in **2a-Cu** and $3.147(1) \text{ \AA}$ (Ge3–Ge9) and $3.166(1) \text{ \AA}$ (Ge2–Ge8) in **3a-Cu**], resulting in C_{2v} -symmetry. The three substituents (two silyl groups and the DAB moiety) bind to three capping Ge atoms (Ge4, Ge5 and Ge6; Figure 2). All Ge–Ge and Ge–Si distances are in the typical range of known functionalized $[Ge_9]$ cluster species.^[2,30] The DAB ligands in **2a-Cu** and **3a-Cu** bind to the $[Ge_9]$ cluster through *exo*-cluster single bonds between one cluster vertex atom and the B atom, with Ge–B

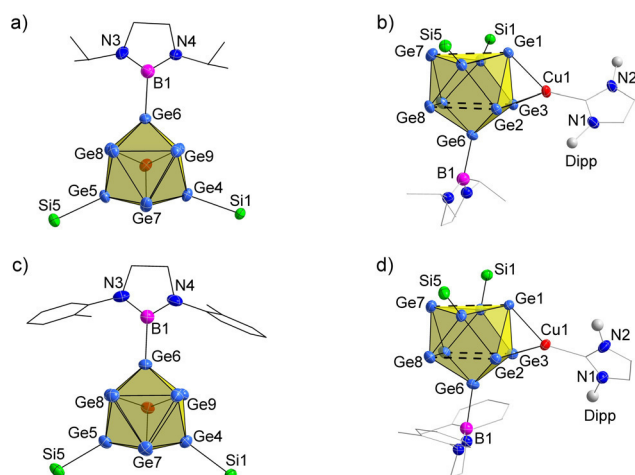


Figure 2. Molecular structures of compounds **2a-Cu** (a,b) and **3a-Cu** (c,d). Ellipsoids are shown at a 50% probability level. a) Front view on compound **2a-Cu** with the two silyl groups and the DAB ligand bonding to the capping Ge atoms of the tricapped trigonal prism. b) Side view on **2a-Cu** showing C_{2v} symmetric shape of $[Ge_9]$ core (prism heights are indicated by thick fragmented lines) and coordination of $[NHC^{Dipp}Cu]^+$ moiety via one of the trigonal prism bases. c) and d) analogue pictures for compound **3a-Cu**. In all pictures protons as well as toluene solvent molecules are omitted. Moreover, TMS groups of silyl substituents (a–d) as well as the NHC^{Dipp} ligand are omitted and carbon atoms of DAB ligands are shown as black (a,c) or grey (b,d) wire sticks for clarity. For the same reason the Dipp wingtips in b) and d) are indicated as grey spheres.

distances of $2.063(5) \text{ \AA}$ and $2.055(5) \text{ \AA}$, respectively. The bond lengths are in the range of previously reported Ge–B bonds in germaborates,^[31] germacarboranes^[32] or germynes.^[25,26b,c,e,33] The $[NHC^{Dipp}Cu]^+$ fragment coordinates one of the trigonal bases of the prism in an η^3 -fashion with Ge–Cu distances known for analogous complexes.^[6,20,29,34]

The anions **1a–3a** and compounds **2a-Cu** and **3a-Cu** are the first examples of boranyl-functionalized $[Ge_9]$ clusters. In general, group 13 element decoration of silylated $[Ge_9]$ species is rather rare if compared to the plethora of examples for group 14 (C-, Si-, Ge-, Sn-based) and group 15 (P) element substituted $[Ge_9]$ clusters. $[Ge_9\{Si(TMS)_3\}_3Tl]$ is the only known example of a triel derivative, however, the Tl atom is included as an additional cluster vertex.^[8]

The most interesting aspect about the anions **1a–3a** is the targeted introduction of boranyl groups to the $[Ge_9]$ core, which is an important step on the way to the possible formation of intramolecular frustrated Lewis acid base pairs (FLPs). The FLP is formed by the combination of an electron-deficient electrophilic boranyl ligand and the $[Ge_9]$ cluster core comprising electron lone pairs at each ligand-free Ge vertex atom with Lewis base properties (Scheme 1, **B**).

In order to obtain a deeper understanding of the electronic situation we carried out quantum-chemical calculations at the DFT-PBE0/TZVP level of theory^[35] using the TURBOMOLE program package.^[36] As an initial structure model for the $[Ge_9]$ cluster the single crystal data of compounds **2a-Cu** and **3a-Cu** were used, the $[NHC-Cu]^+$ fragments were deleted, and a COSMO solvent field was applied to counter the anionic charge.^[37] As depicted in

Figure 3 the HOMO and LUMO of **2a** are located at the $[\text{Ge}_9]$ cluster, and it is not until LUMO + 4 that the LUMO becomes boron-centered (for more MO diagrams see Supporting Information). Similar findings were obtained for anion **3a**. The calculated HOMO–LUMO gaps are 3.8 eV for anions **1a–3a**, which is in a similar range as reported for 1,3,2,5-diazadiborinines (up to 3.7 eV), which are capable of activating small molecules like CO_2 , ketones and alkenes.^[38] In order to investigate the impact of the ligand design on the localization of the HOMO and LUMO, further theoretical studies were carried out, in which the diazaborolidine ligand is substituted by a $-\text{BCy}_2$ group ($[\text{Ge}_9\{\text{Si}(\text{TMS})_3\}_2\text{BCy}_2]^-$, **4a**). Indeed, we observed a shift in the localization of the LUMO, which as for a FLP required becomes boron-based, and the HOMO–LUMO gap decreases to 3.4 eV. This arrangement of orbitals could be favorable to facilitate interactions with small molecules in a frustrated Lewis acid–base type manner, with the cluster acting as the Lewis base (HOMO) and the boranyl ligand as the Lewis acid (LUMO). Interestingly, also the

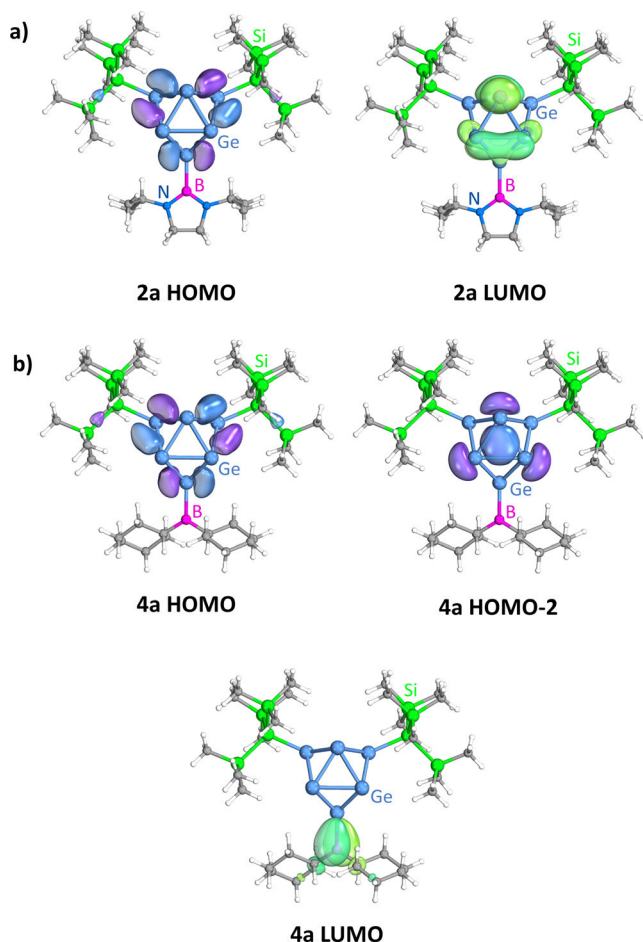


Figure 3. Selected molecular orbitals of a) the anion $[\text{Ge}_9\{\text{Si}(\text{TMS})_3\}_2\text{DAB}^{\text{Pr}}]^-$ (**2a**) and b) the theoretical anion $[\text{Ge}_9\{\text{Si}(\text{TMS})_3\}_2\text{BCy}_2]^-$ (**4a**). The calculations were carried out on the DFT-PBE0/TZVP level of theory, using the single crystal structure data of **2a-Cu** and **3a-Cu** with deleted $[\text{NHC-Cu}]^+$ fragments as a starting point. Orbital figures are drawn so that 50% of the density is enclosed within the isosurface, corresponding to approximately 0.04 a.u. isovalue.

HOMO-2 of **4a**, which is energetically only 0.5 eV lower in energy than the HOMO, allows for another spatial orientation to interact with a Lewis acid. Investigations on the targeted synthesis of **4a** and other derivatives are ongoing. We found for example that the sterically more demanding arylborane Mes_2BBr remained unreactive in dioxane solution.

At this point it has to be mentioned that Roesky et al. previously reported an intramolecular Ge/B Lewis pair which, however, showed Ge–B interactions in the ground state (no FLP).^[33b] Due to their unique reactivity, FLPs have recently gained a lot of attention with respect to the activation of small molecules (CO_2 , H_2), and have also been applied as metal-free hydrogenation catalysts for imines or enamines.^[39] Furthermore, phosphine-borane based FLPs have been reported to insert sterically demanding azides.^[40] These reports hold promise for further investigations at the here presented systems. The unique three-dimensional structure of the $[\text{Ge}_9]$ core opens further possibilities for the spatial arrangement of Lewis-acid Lewis-base pairs. In this context we are currently investigating the addition of a phosphanyl group adjacent to a boranyl group (Scheme 1, C).

In summary we report on the synthesis of the first boranyl functionalized $[\text{Ge}_9]$ clusters $[\text{Ge}_9\{\text{Si}(\text{TMS})_3\}_2\text{DAB}^{\text{R}}]^-$ [R: Me (**1a**), *i*Pr (**2a**), *o*-tol (**3a**)]. The addition of a DAB ligand to the $[\text{Ge}_9]$ core is limited by steric factors (no reaction of bulky $\text{DAB}^{\text{Mes}}\text{-Cl}$). Subsequent reactions with $\text{NHC}^{\text{Dipp}}\text{CuCl}$ led to the formation of $\text{NHC}^{\text{Dipp}}\text{Cu}[\text{Ge}_9\{\text{Si}(\text{TMS})_3\}_2\text{DAB}^{\text{R}}]^-$ [R: *i*Pr (**2a-Cu**) and *o*-tol (**3a-Cu**)]. The structural characterization is in accordance with the spectroscopic data and confirms the presence of a localized Ge–B *exo*-cluster bond. Moreover, Ge–B bond cleavage during the analogous reaction with **1a** reveals an increased lability for DAB ligands with small wingtips (cleavage of DAB^{Me}). Molecular orbital analyses for the anions **1a–3a** using DFT calculations show $[\text{Ge}_9]$ based HOMOs and LUMOs. The isolation of the anions **1a–3a** clearly accounts for the possibility of introducing boranyl moieties to the cluster core. Moreover, quantum-chemical calculations reveal the possibility of altering the position of the LUMO by changing the boranyl group to $-\text{BCy}_2$ (**4a**), which might open the way to $[\text{Ge}_9]$ cluster-based FLP systems. Cyclic-ether ring opening and FLP-type nitrile activation of halo-borane nonagermanide-cluster Lewis acid-base-pairs will be reported in a forthcoming paper.^[41]

Acknowledgements

We thank the Deutsche Forschungsgemeinschaft (DFG, German Research Foundation) (project number 245845833) within International Research Training Group IRTG 2022—Alberta Technical University of Munich School for Functional Hybrid Materials (ATUMS) and the Bavarian Ministry of Economic Affairs, Regional Development and Energy within the project “SolarTechnologies go Hybrid” for funding. Support within TUM IGSSE is greatly appreciated. C. W. also thanks the Studienstiftung des Deutschen Volkes for granting a PhD scholarship. A. J. K. acknowledges funding from the Academy of Finland (grant 317273) and computational resources from CSC—the Finnish IT Center for

Science. Open access funding enabled and organized by Projekt DEAL.

Conflict of interest

The authors declare no conflict of interest.

Keywords: boranes · cluster compounds · germanium · Lewis base · Zintl cluster

- [1] a) S. C. Sevov, J. M. Goicoechea, *Organometallics* **2006**, *25*, 5678–5692; b) S. Scharfe, F. Kraus, S. Stegmaier, A. Schier, T. F. Fässler, *Angew. Chem. Int. Ed.* **2011**, *50*, 3630–3670; *Angew. Chem.* **2011**, *123*, 3712–3754; c) K. Mayer, J. Weßing, T. F. Fässler, R. A. Fischer, *Angew. Chem. Int. Ed.* **2018**, *57*, 14372–14393; *Angew. Chem.* **2018**, *130*, 14570–14593; d) B. Weinert, S. Mitzinger, S. Dehnen, *Chem. Eur. J.* **2018**, *24*, 8470–8490; e) C. Liu, Z.-M. Sun, *Coord. Chem. Rev.* **2019**, *382*, 32–56; f) R. J. Wilson, N. Lichtenberger, B. Weinert, S. Dehnen, *Chem. Rev.* **2019**, *119*, 8506–8554.
- [2] a) O. Kysliak, A. Schnepf, *Dalton Trans.* **2016**, *45*, 2404–2408; b) F. Li, S. C. Sevov, *Inorg. Chem.* **2012**, *51*, 2706–2708.
- [3] a) L. J. Schiegerl, F. S. Geitner, C. Fischer, W. Klein, T. F. Fässler, *Z. Anorg. Allg. Chem.* **2016**, *642*, 1419–1426; b) O. Kysliak, T. Kunz, A. Schnepf, *Eur. J. Inorg. Chem.* **2017**, 805–810; c) O. Kysliak, C. Schrenk, A. Schnepf, *Inorg. Chem.* **2015**, *54*, 7083–7088.
- [4] a) L. G. Perla, A. Muñoz-Castro, S. C. Sevov, *J. Am. Chem. Soc.* **2017**, *139*, 15176–15181; b) L. G. Perla, S. C. Sevov, *J. Am. Chem. Soc.* **2016**, *138*, 9795–9798.
- [5] F. S. Geitner, J. V. Dums, T. F. Fässler, *J. Am. Chem. Soc.* **2017**, *139*, 11933–11940.
- [6] F. S. Geitner, W. Klein, T. F. Fässler, *Angew. Chem. Int. Ed.* **2018**, *57*, 14509–14513; *Angew. Chem.* **2018**, *130*, 14717–14721.
- [7] a) F. S. Geitner, T. F. Fässler, *Chem. Commun.* **2017**, 53, 12974–12977; b) L. J. Schiegerl, A. J. Karttunen, W. Klein, T. F. Fässler, *Chem. Eur. J.* **2018**, *24*, 19171–19174; c) S. Frischhut, T. F. Fässler, *Dalton Trans.* **2018**, *47*, 3223–3226.
- [8] F. Li, S. C. Sevov, *J. Am. Chem. Soc.* **2014**, *136*, 12056–12063.
- [9] S. Frischhut, W. Klein, M. Drees, T. F. Fässler, *Chem. Eur. J.* **2018**, *24*, 9009–9014.
- [10] C. Wallach, F. S. Geitner, W. Klein, T. F. Fässler, *Chem. Eur. J.* **2019**, *25*, 12349–12356.
- [11] F. F. Li, A. Muñoz-Castro, S. C. Sevov, *Angew. Chem. Int. Ed.* **2012**, *51*, 8581–8584; *Angew. Chem.* **2012**, *124*, 8709–8712.
- [12] F. S. Geitner, W. Klein, O. Storcheva, T. D. Tilley, T. F. Fässler, *Inorg. Chem.* **2019**, *58*, 13293–13298.
- [13] C. Schenk, A. Schnepf, *Chem. Commun.* **2009**, 3208–3210.
- [14] K. Mayer, W. Klein, T. F. Fässler, *Chem. Commun.* **2019**, 55, 12156–12159.
- [15] N. C. Michenfelder, C. Gienger, A. Schnepf, A.-N. Unterreiner, *Dalton Trans.* **2019**, *48*, 15577–15582.
- [16] K. Mayer, L. J. Schiegerl, T. Kratky, S. Günther, T. F. Fässler, *Chem. Commun.* **2017**, 53, 11798–11801.
- [17] O. Kysliak, C. Schrenk, A. Schnepf, *Inorg. Chem.* **2017**, *56*, 9693–9697.
- [18] S. Frischhut, W. Klein, T. F. Fässler, *C. R. Chim.* **2018**, *21*, 932–937.
- [19] O. Kysliak, A. Schnepf, *Z. Anorg. Allg. Chem.* **2019**, *645*, 335–339.
- [20] F. S. Geitner, C. Wallach, T. F. Fässler, *Chem. Eur. J.* **2018**, *24*, 4103–4110.
- [21] a) Y. Heider, N. E. Poitiers, P. Willmes, K. I. Leszczyńska, V. Huch, D. Scheschkewitz, *Chem. Sci.* **2019**, *10*, 4523–4530; b) P. Willmes, K. Leszczyńska, Y. Heider, K. Abersfelder, M. Zimmer, V. Huch, D. Scheschkewitz, *Angew. Chem. Int. Ed.* **2016**, *55*, 2907–2910; *Angew. Chem.* **2016**, *128*, 2959–2963.
- [22] Y. Heider, P. Willmes, V. Huch, M. Zimmer, D. Scheschkewitz, *J. Am. Chem. Soc.* **2019**, *141*, 19498–19504.
- [23] A. V. Protchenko, J. Urbano, J. A. Abdalla, J. Campos, D. Vidovic, A. D. Schwarz, M. P. Blake, P. Mountford, C. Jones, S. Aldridge, *Angew. Chem. Int. Ed.* **2017**, *56*, 15098–15102; *Angew. Chem.* **2017**, *129*, 15294–15298.
- [24] a) Y. Segawa, Y. Suzuki, M. Yamashita, K. Nozaki, *J. Am. Chem. Soc.* **2008**, *130*, 16069–16079; b) L. M. Saleh, K. H. Birj Kumar, A. V. Protchenko, A. D. Schwarz, S. Aldridge, C. Jones, N. Kaltsoyannis, P. Mountford, *J. Am. Chem. Soc.* **2011**, *133*, 3836–3839.
- [25] A. V. Protchenko, K. H. Birj Kumar, D. Dange, A. D. Schwarz, D. Vidovic, C. Jones, N. Kaltsoyannis, P. Mountford, S. Aldridge, *J. Am. Chem. Soc.* **2012**, *134*, 6500–6503.
- [26] a) A. Rit, J. Campos, H. Niu, S. Aldridge, *Nat. Chem.* **2016**, *8*, 1022; b) M. Usher, A. V. Protchenko, A. Rit, J. Campos, E. L. Kolychev, R. Tirfoin, S. Aldridge, *Chem. Eur. J.* **2016**, *22*, 11685–11698; c) A. V. Protchenko, M. P. Blake, A. D. Schwarz, C. Jones, P. Mountford, S. Aldridge, *Organometallics* **2015**, *34*, 2126–2129; d) Z. Dong, H. H. Cramer, M. Schmidtmann, L. A. Paul, I. Siewert, T. Müller, *J. Am. Chem. Soc.* **2018**, *140*, 15419–15424; e) R. J. Mangan, A. Rit, C. P. Sindlinger, R. Tirfoin, J. Campos, J. Hicks, K. E. Christensen, H. Niu, S. Aldridge, *Chem. Eur. J.* **2020**, *26*, 306–315.
- [27] a) A. V. Protchenko, J. I. Bates, L. M. Saleh, M. P. Blake, A. D. Schwarz, E. L. Kolychev, A. L. Thompson, C. Jones, P. Mountford, S. Aldridge, *J. Am. Chem. Soc.* **2016**, *138*, 4555–4564; b) A. V. Protchenko, D. Dange, M. P. Blake, A. D. Schwarz, C. Jones, P. Mountford, S. Aldridge, *J. Am. Chem. Soc.* **2014**, *136*, 10902–10905.
- [28] A. V. Protchenko, D. Dange, A. D. Schwarz, C. Y. Tang, N. Phillips, P. Mountford, C. Jones, S. Aldridge, *Chem. Commun.* **2014**, 50, 3841–3844.
- [29] F. S. Geitner, M. A. Giebel, A. Pöthig, T. F. Fässler, *Molecules* **2017**, *22*, 1204.
- [30] A. Schnepf, *Angew. Chem. Int. Ed.* **2003**, *42*, 2624–2625; *Angew. Chem.* **2003**, *115*, 2728–2729.
- [31] T. Gädt, J.-A. Dimmer, S. Fleischhauer, A. Frank, C. Nickl, T. Wütz, K. Eichele, L. Wesemann, *Dalton Trans.* **2015**, *44*, 4726–4731.
- [32] N. S. Hosmane, J. Yang, K.-J. Lu, H. Zhang, U. Siriwardane, M. S. Islam, J. L. Thomas, J. A. Maguire, *Organometallics* **1998**, *17*, 2784–2796.
- [33] a) Y. Wang, M. Karni, S. Yao, Y. Apeloig, M. Driess, *J. Am. Chem. Soc.* **2018**, *41*, 1655–1664; b) J. Li, B. Li, R. Liu, L. Jiang, H. Zhu, H. W. Roesky, S. Dutta, D. Koley, W. Liu, Q. Ye, *Chem. Eur. J.* **2016**, *22*, 14499–14503.
- [34] F. S. Geitner, T. F. Fässler, *Eur. J. Inorg. Chem.* **2016**, 2688–2691.
- [35] a) C. Adamo, V. Barone, *J. Chem. Phys.* **1999**, *110*, 6158–6170; b) J. P. Perdew, K. Burke, M. Ernzerhof, *Phys. Rev. Lett.* **1996**, *77*, 3865; c) F. Weigend, R. Ahlrichs, *Phys. Chem. Chem. Phys.* **2005**, *7*, 3297–3305.
- [36] TURBOMOLE V7.3 2018, a development of University of Karlsruhe and Forschungszentrum Karlsruhe GmbH, **1989–2007**, TURBOMOLE GmbH, since 2007; available from www.turbomole.com.
- [37] A. Klamt, G. Schüürmann, *J. Chem. Soc. Perkin Trans. 2* **1993**, *5*, 799–805.
- [38] a) Y. Su, Y. Li, R. Ganguly, R. Kinjo, *Angew. Chem. Int. Ed.* **2018**, *57*, 7846–7849; *Angew. Chem.* **2018**, *130*, 7972–7975; b) D. Wu, R. Wang, Y. Li, R. Ganguly, H. Hirao, R. Kinjo, *Chem* **2017**, *3*, 134–151; c) D. Wu, L. Kong, Y. Li, R. Ganguly, R. Kinjo, *Nat. Commun.* **2015**, *6*, 1–6; d) D. Wu, R. Ganguly, Y. Li, S. N. Hoo, H. Hirao, R. Kinjo, *Chem. Sci.* **2015**, *6*, 7150–7155.

- [39] a) D. W. Stephan, G. Erker, *Angew. Chem. Int. Ed.* **2010**, *49*, 46–76; *Angew. Chem.* **2010**, *122*, 50–81; b) D. W. Stephan, *J. Am. Chem. Soc.* **2015**, *137*, 10018–10032; c) D. W. Stephan, *Science* **2016**, *354*, aaf7229; d) Z. Huang, S. Wang, R. D. Dewhurst, N. V. Ignat'ev, M. Finze, H. Braunschweig, *Angew. Chem. Int. Ed.* **2020**, *59*, 8800–8816; *Angew. Chem.* **2020**, *132*, 8882–8900.
- [40] a) C. M. Mömning, G. Kehr, B. Wibbeling, R. Fröhlich, G. Erker, *Dalton Trans.* **2010**, *39*, 7556–7564; b) A. Stute, L. Heletta, R. Fröhlich, C. G. Daniliuc, G. Kehr, G. Erker, *Chem. Commun.* **2012**, *48*, 11739–11741; c) L. M. Elmer, G. Kehr, C. G. Daniliuc, M. Siedow, H. Eckert, M. Tesch, A. Studer, K. Williams, T. H. Warren, G. Erker, *Chem. Eur. J.* **2017**, *23*, 6056–6068; d) D. H. Boom, A. R. Jupp, M. Nieger, A. W. Ehlers, J. C. Sootweg, *Chem. Eur. J.* **2019**, *25*, 13299–13308.
- [41] F. S. Geitner, C. Wallach, T. F. Fässler, submitted for publication.

Manuscript received: September 10, 2020
Revised manuscript received: October 3, 2020
Accepted manuscript online: October 14, 2020
Version of record online: December 1, 2020

Supporting Information

**Boranyl-Functionalized [Ge₉] Clusters: Providing the Idea of
Intramolecular Ge/B Frustrated Lewis Pairs**

*Christoph Wallach⁺, Felix S. Geitner⁺, Antti J. Karttunen, and Thomas F. Fässler**

anie_202012336_sm_miscellaneous_information.pdf

Content

1. General information	1
2. Syntheses	2
3. Results and Discussion	4
3.1 Crystallographic data	4
3.2 NMR spectra	7
3.3 ESI MS spectra	18
3.4 Quantum chemical calculations at DFT-PBE0/TZVP level of theory	20
4. References	23

1. General information

All manipulations were performed under oxygen-free, dry conditions under argon atmosphere using standard Schlenk or glove box techniques. Glassware was dried prior to use by heating it *in vacuo*. The solvents used were obtained from an MBraun Grubbs apparatus. All other commercially available chemicals were used without further purification. K_4Ge_9 was prepared by fusion of stoichiometric amounts of the elements in stainless-steel tubes at 650 °C. The bis-silylated $[Ge_9]$ clusters $[Ge_9\{Si(TMS)_3\}_2]^{2-}$,^[1] the chloro-diazaborolidines DAB^R-Cl (DAB = 2-chloro-1,3,2-diazaborolidine; R = Me,^[2] ⁱPr,^[2] *o*-tol,^[3] Mes^[3]), as well as the imidazolium salt NHC^{Dipp}·HCl (NHC^{Dipp} = 1,3-di(2,6-diisopropylphenyl)imidazolylidene)^[4] and the respective copper NHC complex NHC^{Dipp}CuCl^[5] were prepared according to modified literature procedures.

Single crystal structure determination

The air- and moisture-sensitive crystals of **2a-Cu** and **3a-Cu** were transferred from the mother liquor into perfluoroalkyl ether oil in an argon filled glove box. For diffraction data collection, the single crystals were fixed on a glass capillary and positioned in a 150 K cold N₂ gas stream. Data collection was performed with a STOE StadiVari diffractometer (MoK α radiation) equipped with a DECTRIS PILATUS 300K detector. Structures were solved by Direct Methods (SHELXS-97)^[6] and refined by full-matrix least-squares calculations against F^2 (SHELXL-2018).^[7] The positions of the hydrogen atoms were calculated and refined using a riding model. Unless stated otherwise, all non-hydrogen atoms were treated with anisotropic displacement parameters. The supplementary crystallographic data for this paper have been deposited with the Cambridge Structural database and are available free of charge via www.ccdc.cam.ac.uk/data_request/cif. The crystallographic data for compounds **2a-Cu** and **3a-Cu** are summarized in Table S1. In compound **3a-Cu** the electron density of disordered co-crystallized toluene molecules was taken care of by the PLATON SQUEEZE function.^[8]

NMR spectroscopy

NMR spectra were measured on a Bruker Avance Ultrashield 400 MHz spectrometer. The ¹H NMR spectra were calibrated using the residual proton signal of the used deuterated solvents. Chemical shifts are reported in parts per million (ppm) relative to TMS, with the solvent peaks serving as internal reference.^[9] Abbreviations for signal multiplicities are: singlet (s), doublet (d), triplet (t), heptet (hept), broad signal (brs).

Electrospray ionization mass spectroscopy

ESI MS analyses were performed on a Bruker Daltonic HCT mass spectrometer (injection speed: 240 μ L/h), and the data evaluation was carried out using the Bruker Compass Data Analysis 4.0 SP 5 program (Bruker). Spectra were plotted with OriginPro2016G (Origin Lab) and Excel 2016 (Microsoft).

Quantum-chemical calculations

Calculations were carried out with the TURBOMOLE program package, using the PBE0 hybrid density functional method and polarized triple- ζ -valence Karlsruhe basis sets (DFT-PBE0/TZVP with def2-TZVP on Ge and Si, def-TZVP on other atoms).^[10] Multipole-accelerated resolution-of-the-identity technique was used to speed up the calculations.^[11] *m*4 integration grid was used for the numerical integration of the exchange-correlation functional. As initial structures the crystal structure data of compounds **2a-Cu** and **3a-Cu** were used. The structures were fully optimized without any symmetry constraints. To simulate the anionic nature of the clusters the [Cu-NHC]⁺ ligand was deleted and a COSMO solvent field was applied to counter the anionic charge.^[12] The molecular orbitals were illustrated using Iboview.^[13]

2. Syntheses

K[Ge₉{Si(TMS)₃}₂DAB^{Me}]⁻ (1a-K):

In a typical experiment K₂[Ge₉{Si(TMS)₃}₂] (92 mg, 0.075 mmol, 1 equiv.) was weighted in a Schlenk tube in the glove box and a solution of DAB^{Me}-Cl (9.9 mg, 0.075 mmol, 1 equiv.) in thf (3 mL) was added, resulting in a deep red solution. After stirring for 3 h at room temperature, the solvent was removed in vacuo yielding a brown solid. The solid was treated with hexane (2 · 3mL) which was subsequently removed in vacuo (procedure in order to get rid of residual thf). The obtained brown solid was dissolved in toluene (6 mL), the resulting dark brown solution was filtered, and the solvent of the filtrate was removed to obtain the crude product as a brown oily solid (41 mg, 0.032 mmol, 43% yield). Further purification to obtain an analytical pure product by recrystallization has not been successful to date. **¹H NMR (400 MHz, 298 K, thf-*d*₈):** δ [ppm] = 3.13 (s, 4H, CH₂(Bb)), 2.78 (s, 6H, Me), 0.25 (s, 54H, Me_{TMS}). **¹³C NMR (101 MHz, 298 K, thf-*d*₈):** δ [ppm] = 53.46 (s, Me), 38.34 (s, CH₂(Bb)), 3.26 (s, Me_{TMS}). **²⁹Si-INEPT NMR (79 MHz, 298 K, thf-*d*₈):** δ [ppm] = -9.82 (s, Si_{TMS}), -108.11 (s, Si_{Ge9}). **¹¹B NMR (128 MHz, 298 K, thf-*d*₈):** δ [ppm] = 43.41 (brs, B_{Ge9}). **ESI MS (3500 V, 300 °C):** *m/z* 1246.6 [Ge₉{Si(TMS)₃}₂DAB^{Me}]⁻.

K[Ge₉{Si(TMS)₃}₂DAB^{IPr}]⁻ (2a-K):

In a typical experiment K₂[Ge₉{Si(TMS)₃}₂] (92 mg, 0.075 mmol, 1 equiv.) was weighted in a Schlenk tube in the glove box and a solution of DAB^{IPr}-Cl (14.1 mg, 0.075 mmol, 1 equiv.) in dioxane or thf (3 mL) was added, leading to a deep red solution. After stirring for 5 h at room temperature, the solvent was removed in vacuo yielding a brownish solid. Subsequent dissolution in toluene (18 mL) gave a dark red solution, which was filtered to remove remaining solids. Removal of toluene in vacuo and treatment of the obtained oily solid with hexane (2 · 6 mL; addition and evaporation) yielded the crude product as brown solid (50 mg, 0.037 mmol, 50% yield). Purification to obtain an analytical pure product by recrystallization has not been successful to date. **¹H NMR (400 MHz, 298 K, thf-*d*₈):** δ [ppm] = 4.37 (hept, ³J_{HH} = 6.8 Hz, 2H, CH_{IPr}), 3.13 (s, 4H, CH₂(Bb)), 1.02 (d, ³J_{HH} = 6.8 Hz, 12H, Me_{IPr}), 0.25 (s, 54H, Me_{TMS}). **¹³C NMR (101 MHz, 298 K, thf-*d*₈):** δ [ppm] = 48.00 (s, CH_{IPr}), 42.50 (s, CH₂(Bb)), 21.95 (s, Me_{IPr}), 3.28 (s, Me_{TMS}). **²⁹Si-INEPT NMR (79 MHz, 298 K, thf-*d*₈):** δ [ppm] = -9.85 (s, Si_{TMS}), -108.28 (s, Si_{Ge9}). **¹¹B NMR (128 MHz, 298 K, thf-*d*₈):** δ [ppm] = 41.90 (brs, B_{Ge9}). **ESI MS (3500 V, 300 °C):** *m/z* 1302.6 [Ge₉{Si(TMS)₃}₂DAB^{IPr}]⁻.

K[Ge₉{Si(TMS)₃}₂DAB^{o-tol}]⁻ (3a-K):

In a typical experiment equimolar amounts of K₂[Ge₉{Si(TMS)₃}₂] (92 mg, 0.075 mmol, 1 equiv.) and DAB^{o-tol}-Cl (21.3 mg, 0.075 mmol, 1 equiv.) were weighted in a Schlenk tube in the glove box and dioxane or thf (3 mL) was added to obtain a deep red solution. After stirring for 5 h at room temperature, the solvent was removed in vacuo, and a yellow-brownish solid was obtained. Subsequent dissolution in toluene (18 mL) gave a dark red solution, which was filtered to remove remaining solids. Upon concentration the product precipitated as a microcrystalline ochre solid from the solution. The mother liquor was filtered off, and the solid was dried in vacuo to yield the product as an ochre microcrystalline powder (72 mg, 0.050 mmol, 67% yield). **¹H NMR (400 MHz, 298 K, thf-*d*₈):** δ [ppm] = 7.16-7.11 (m, 2H, CH_{Ph}), 7.08-7.04 (m, 2H, CH_{Ph}), 7.01-6.90 (m, 4H, CH_{Ph}), 3.65 (s, 4H, CH₂(Bb)), 2.35 (s, 6H, Me), 0.18 (s, 54H, Me_{TMS}). **¹³C NMR (101 MHz, 298 K, thf-*d*₈):** δ [ppm] = 147.03 (s, C_{Ph(N)}), 137.19 (s, C_{Ph(Me)}), 131.38 (s, CH_{Ph}), 130.60 (s, CH_{Ph}), 127.08 (s, CH_{Ph}), 125.66 (s, CH_{Ph}), 53.93 (s, CH₂(Bb)), 20.14 (s, Me), 3.28 (s, Me_{TMS}). **²⁹Si-INEPT NMR (79 MHz, 298 K, thf-*d*₈):** δ [ppm] = -9.99 (s, Si_{TMS}), -108.80 (s, Si_{Ge9}). **¹¹B NMR (128 MHz, 298 K, thf-*d*₈):** δ [ppm] = 42.92 (brs, B_{Ge9}). **Elemental analysis:** anal. calcd. for Ge₉Si₈BC₃₄H₇₂N₂K: C, 28.41; H, 5.05; N, 1.95; found: C, 27.53; H, 4.87; N, 2.02. **ESI MS (3500 V, 300 °C):** *m/z* 1398.7 [Ge₉{Si(TMS)₃}₂DAB^{o-tol}]⁻.

NHC^{Dipp}Cu[Ge₉{Si(TMS)₃}₂DAB^{Pr}] (2a-Cu):

In a typical experiment K₂[Ge₉{Si(TMS)₃}₂] (92 mg, 0.075 mmol, 1 equiv.) was weighted in into a Schlenk tube in the glove box and a solution of DAB^{Pr}-Cl (14.1 mg, 0.075 mmol, 1 equiv.) in dioxane (3 mL) was added, leading to a deep red solution. After stirring for 5 h at room temperature, the solvent was removed in vacuo to leave a brownish solid. The solid was dissolved in 1.5 mL MeCN and an acetonitrile solution of NHC^{Dipp}CuCl (36.5 mg, 0.075 mmol, 1 equiv.) was added dropwise, instantly leading to the precipitation of a reddish solid. After stirring for 15 min at r. t., the slightly red supernatant solution was filtered off, and the solid was washed with MeCN (2 mL) before it was dried in vacuo. Subsequently, the residue was dissolved in toluene (3 mL), and the deep red solution was filtered to remove remaining solids and then was stored in a freezer at -40 °C for crystallization. The product was obtained as red block-shaped crystals (49 mg, 0.028 mmol, 37%). **¹H NMR (400 MHz, 298 K, C₆D₆):** δ [ppm] = 7.36-7.30 (m, 2H, CH_{Ph}), 7.27-7.23 (m, 4H, CH_{Ph}), 6.25 (s, 2H, CH_{Im}), 4.40 (hept, ³J_{HH} = 6.8 Hz, 2H, CH_{IPr(B)}), 3.20 (s, 4H, CH_{2(Bb)}), 2.82 (hept, ³J_{HH} = 7.2 Hz, 4H, CH_{IPr}), 1.61 (d, ³J_{HH} = 7.2 Hz, 12H, Me_{IPr}), 1.22 (d, ³J_{HH} = 6.8 Hz, 12H, Me_{IPr(B)}), 1.11 (d, ³J_{HH} = 7.2 Hz, 12H, Me_{IPr}), 0.41 (s, 54H, Me_{TMS}). **¹³C NMR (101 MHz, 298 K, C₆D₆):** δ [ppm] = 145.40 (s, C_{Ph(N)-Dipp}), 135.50 (s, CH_{Ph(p)}), 130.63 (s, C_{Ph(IPr)}), 124.88 (s, CH_{Ph(m)}), 122.24 (s, CH_{Im}), 47.82 (CH_{IPr(B)}), 42.41 (s, CH_{2(Bb)}), 29.12 (s, CH_{IPr(NHC)}), 25.62 (s, Me_{IPr}), 24.63 (s, Me_{IPr}), 22.32 (Me_{IPr(NHC)}), 3.20 (s, Me_{TMS}). **²⁹Si-INEPT NMR (79 MHz, 298 K, C₆D₆):** δ [ppm] = -9.56 (s, Si_{TMS}), -104.67 (s, Si_{Ge9}). **¹¹B NMR (128 MHz, 298 K, thf-d₈):** δ [ppm] = 23.82 (brs, B_{Ge9}). **Elemental analysis:** anal. calcd. for Ge₉Si₈BC₅₃H₁₀₇N₄Cu: C, 36.31; H, 6.15; N, 3.20; found: C, 37.17; H, 6.37; N, 3.24.

NHC^{Dipp}Cu[Ge₉{Si(TMS)₃}₂DAB^{o-tol}] (3a-Cu):

In a typical experiment equimolar amounts of K₂[Ge₉{Si(TMS)₃}₂] (92 mg, 0.075 mmol, 1 equiv.) and DAB^{o-tol}-Cl (21.3 mg, 0.075 mmol, 1 equiv.) were weighted in into a Schlenk tube in the glove box, and dioxane (3 mL) was added to obtain a deep red solution. After stirring for 5 h at room temperature, the solvent was removed in vacuo, yielding a yellow-brownish solid. The solid was dissolved in 1.5 mL MeCN, and an acetonitrile solution of NHC^{Dipp}CuCl (36.5 mg, 0.075 mmol, 1 equiv.) was added dropwise, instantly leading to the precipitation of a red solid. The slightly red supernatant solution was filtered off, and the solid was washed with MeCN (2 mL) before it was dried in vacuo. Subsequently the residue was dissolved in toluene (3 mL), and the deep red solution was filtered to remove remaining solids before the solution was stored in a freezer at -40 °C for crystallization. The product was obtained as red block-shaped crystals (56 mg, 0.030 mmol, 40%). **¹H NMR (400 MHz, 298 K, C₆D₆):** δ [ppm] = 7.49-7.46 (m, 2H, CH_{Ph}), 7.38-7.34 (m, 2H, CH_{Ph}), 7.27-7.24 (m, 4H, CH_{Ph}), 7.22-7.19 (m, 2H, CH_{Ph}), 7.14-7.11 (m, 4H, CH_{Ph}), 6.24 (s, 2H, CH_{Im}), 3.89 (s, 4H, CH_{2(Bb)}), 2.82 (hept, ³J_{HH} = 6.9 Hz, 4H, CH_{IPr}), 2.48 (s, 6H, Me_{o-tol}), 1.64 (d, ³J_{HH} = 6.9 Hz, 12H, Me_{IPr}), 1.13 (d, ³J_{HH} = 6.9 Hz, 12H, Me_{IPr}), 0.38 (s, 54H, Me_{TMS}). **¹³C NMR (101 MHz, 298 K, C₆D₆):** δ [ppm] = 145.45 (s, C_{Ph(N)-o-tol}), 145.18 (s, C_{Ph(N)-Dipp}), 136.08 (s, CH_{Ph}), 135.52 (s, CH_{Ph}), 131.32 (C_{Ph(IPr)}), 130.77 (s, (C_{Ph}(Me)), 130.71 (s, CH_{Ph}), 126.77 (s, CH_{Ph}), 126.20 (s, CH_{Ph}), 124.82 (s, CH_{Ph}), 122.21 (s, CH_{Im}), 53.12 (s, CH_{2(Bb)}), 29.10 (s, CH_{IPr}), 25.78 (s, Me_{IPr}), 24.65 (s, Me_{IPr}), 19.68 (Me_{o-tol}), 3.27 (s, Me_{TMS}). **²⁹Si-INEPT NMR (79 MHz, 298 K, C₆D₆):** δ [ppm] = -9.72 (s, Si_{TMS}), -104.65 (s, Si_{Ge9}). **¹¹B NMR (128 MHz, 298 K, thf-d₈):** δ [ppm] = 23.36 (brs, B_{Ge9}). **Elemental analysis:** anal. calcd. for Ge₉Si₈BC₆₁H₁₀₉N₄Cu · 0.33 tol : C, 40.42; H, 5.98; N, 2.98; found: C, 40.53; H, 5.95; N, 2.89 (toluene content was calculated according to NMR spectrum of the respective sample, Figure S19).

3. Results and Discussion

3.1 Crystallographic data

Table S1. Crystallographic data for compounds **2a-Cu** and **3a-Cu**.

Compound	2a-Cu	3a-Cu
formula	Ge ₉ Si ₈ BC ₅₃ H ₁₀₈ N ₄ Cu · 1 tol	Ge ₉ Si ₈ BC ₆₁ H ₁₀₈ N ₄ Cu · 1.5 tol
fw [g·mol ⁻¹]	1845.94	1988.10
space group	<i>P2₁/n</i>	<i>I2/a</i>
<i>a</i> [Å]	20.5298(9)	26.8283(8)
<i>b</i> [Å]	20.9024(7)	25.2020(5)
<i>c</i> [Å]	20.5938(8)	26.9602(7)
α [deg]	90	90
β [deg]	102.548(3)	90.959(2)
γ [deg]	90	90
<i>V</i> [Å ³]	8626.2(6)	18226.0(8)
<i>Z</i>	4	8
<i>T</i> [K]	150	150
λ [Å]	Mo <i>K</i> α	Mo <i>K</i> α
ρ_{calcd} [g·cm ⁻³]	1.421	1.348
μ [mm ⁻¹]	3.474	3.289
collected reflections	188759	222615
independent reflections	16949	17896
<i>R</i> _{int} / <i>R</i> _{σ}	0.0756/0.0529	0.1076/0.0705
parameters / restraints	779/24	785/0
<i>R</i> ₁ [<i>I</i> > 2 σ (<i>I</i>) / all data]	0.0366/0.0740	0.0394/0.0843
<i>wR</i> ₂ [<i>I</i> > 2 σ (<i>I</i>) / all data]	0.0701/0.0804	0.0672/0.0778
goodness of fit	0.978	0.917
max./min. diff. el. density [e / Å ³]	0.95/-0.67	0.67/-0.43
CCDC	1993869	1993870

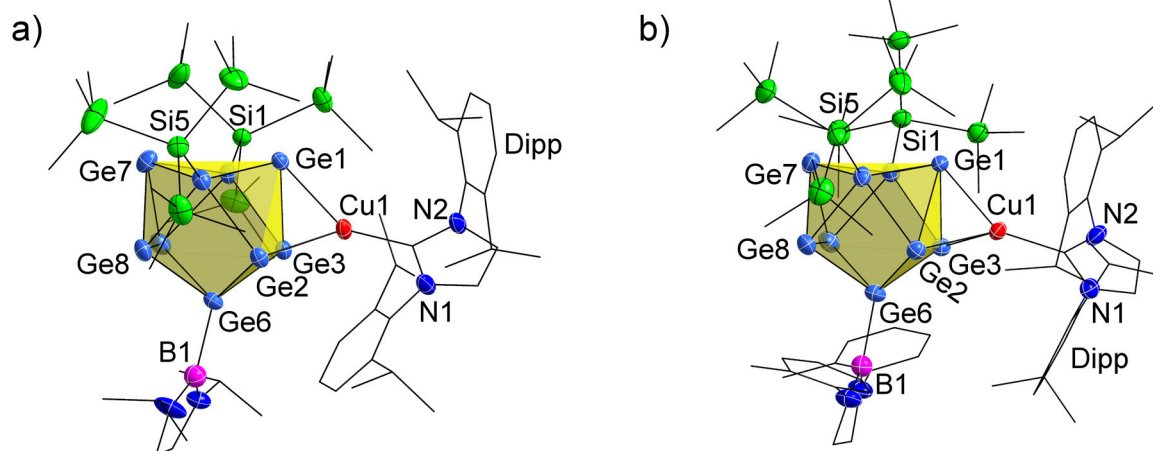


Figure S1. Structures of compounds **2a-Cu** (a) and **3a-Cu** (b). For clarity reasons, protons and co-crystallized toluene molecules are omitted, and all carbon atoms are depicted as black wire sticks. Different views on compounds **2a-Cu** and **3a-Cu** can be found in the manuscript (Figure 2).

Table S2. Selected bond lengths in compound **2a-Cu**.

bond	distance [Å]
Ge1-Ge2	2.8957(6)
Ge1-Ge3	2.8266(6)
Ge1-Ge4	2.5071(6)
Ge1-Ge5	2.5164(6)
Ge2-Ge5	2.5363(6)
Ge2-Ge6	2.4978(6)
Ge3-Ge4	2.5171(6)
Ge3-Ge6	2.4943(6)
Ge4-Ge7	2.5598(6)
Ge4-Ge9	2.5804(6)
Ge5-Ge7	2.5673(6)
Ge5-Ge8	2.5430(6)
Ge6-Ge8	2.5306(6)
Ge6-Ge9	2.5638(6)
Ge7-Ge8	2.6536(7)
Ge7-Ge9	2.5977(7)
Ge8-Ge9	2.6739(6)
Ge1-Cu1	2.4628(6)
Ge2-Cu1	2.5716(6)
Ge3-Cu1	2.4914(6)
Ge4-Si1	2.384(1)
Ge5-Si5	2.385 (1)
Ge6-B1	2.063(5)
Ge1-Ge7	3.584(1)
Ge2-Ge8	3.164(1)
Ge3-Ge9	3.283(2)

Table S3. Selected bond lengths in compound **3a-Cu**.

bond	distance [Å]
Ge1-Ge2	2.8220(6)
Ge1-Ge3	2.8534(6)
Ge1-Ge4	2.5139(6)
Ge1-Ge5	2.5199(7)
Ge2-Ge5	2.5229(6)
Ge2-Ge6	2.4921(6)
Ge3-Ge4	2.5138(6)
Ge3-Ge6	2.4968(7)
Ge4-Ge7	2.5552(7)
Ge4-Ge9	2.5690(7)
Ge5-Ge7	2.5632(7)
Ge5-Ge8	2.5547(6)
Ge6-Ge8	2.5417(7)
Ge6-Ge9	2.5413(7)
Ge7-Ge8	2.6124(7)
Ge7-Ge9	2.6187(7)
Ge8-Ge9	2.7396(7)
Ge1-Cu1	2.4716(6)
Ge2-Cu1	2.5586(7)
Ge3-Cu1	2.5405(7)
Ge4-Si1	2.377(1)
Ge5-Si5	2.385(1)
Ge6-B1	2.055(5)
Ge1-Ge7	3.682(1)
Ge2-Ge8	3.166(1)
Ge3-Ge9	3.147(1)

3.2 NMR spectra

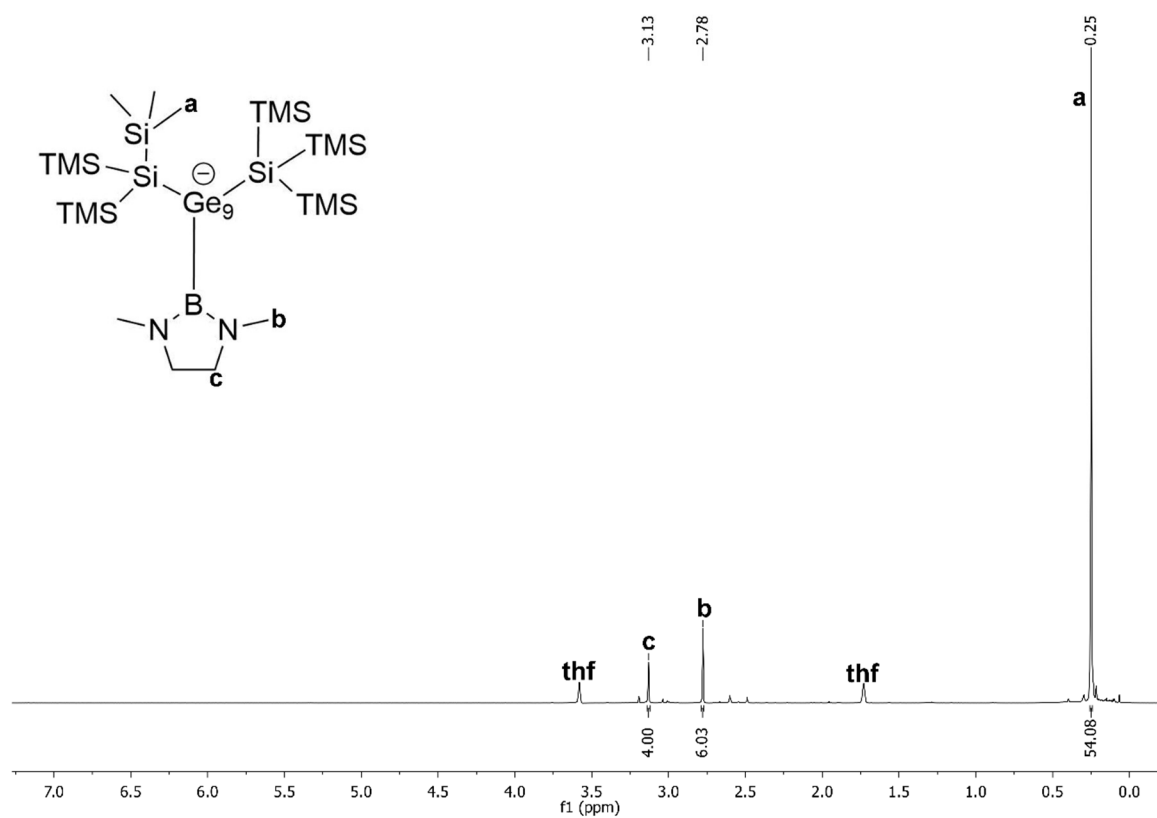


Figure S2. ¹H NMR spectrum of **1a-K** acquired in thf-d₈.

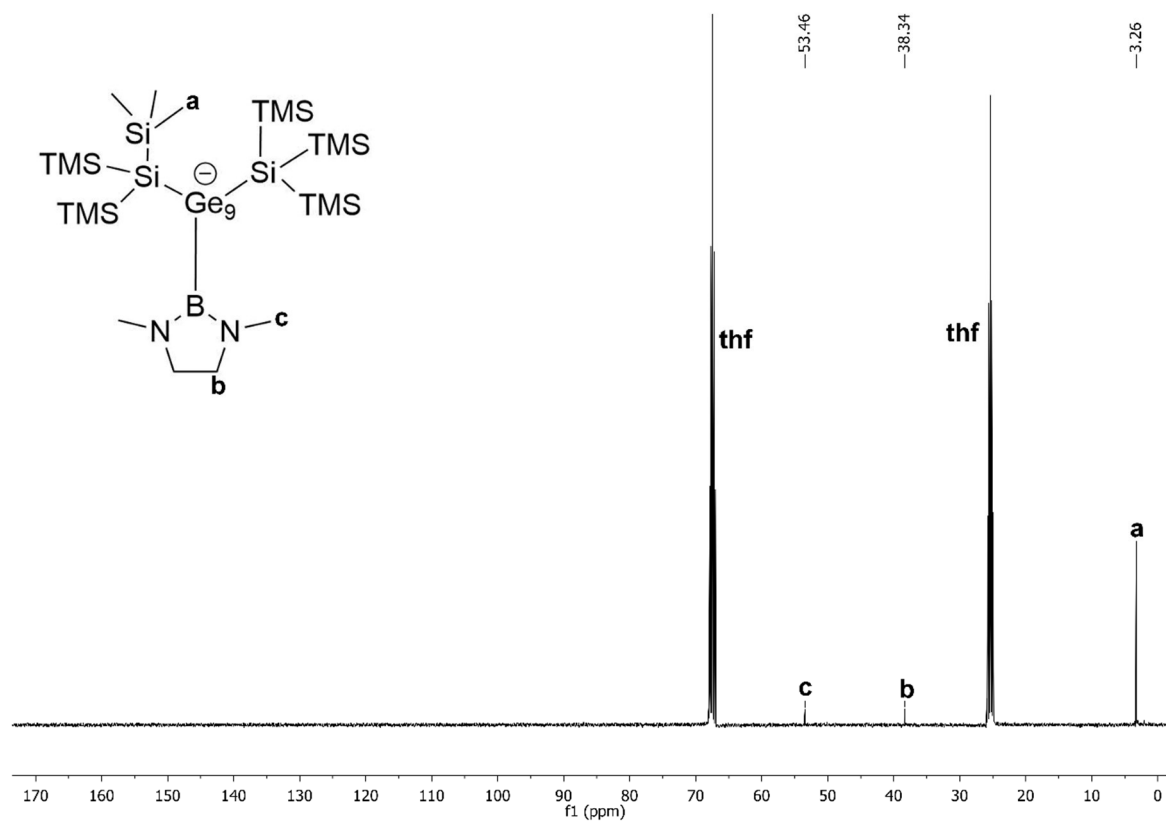


Figure S3. ¹³C NMR spectrum of **1a-K** acquired in thf-d₈.

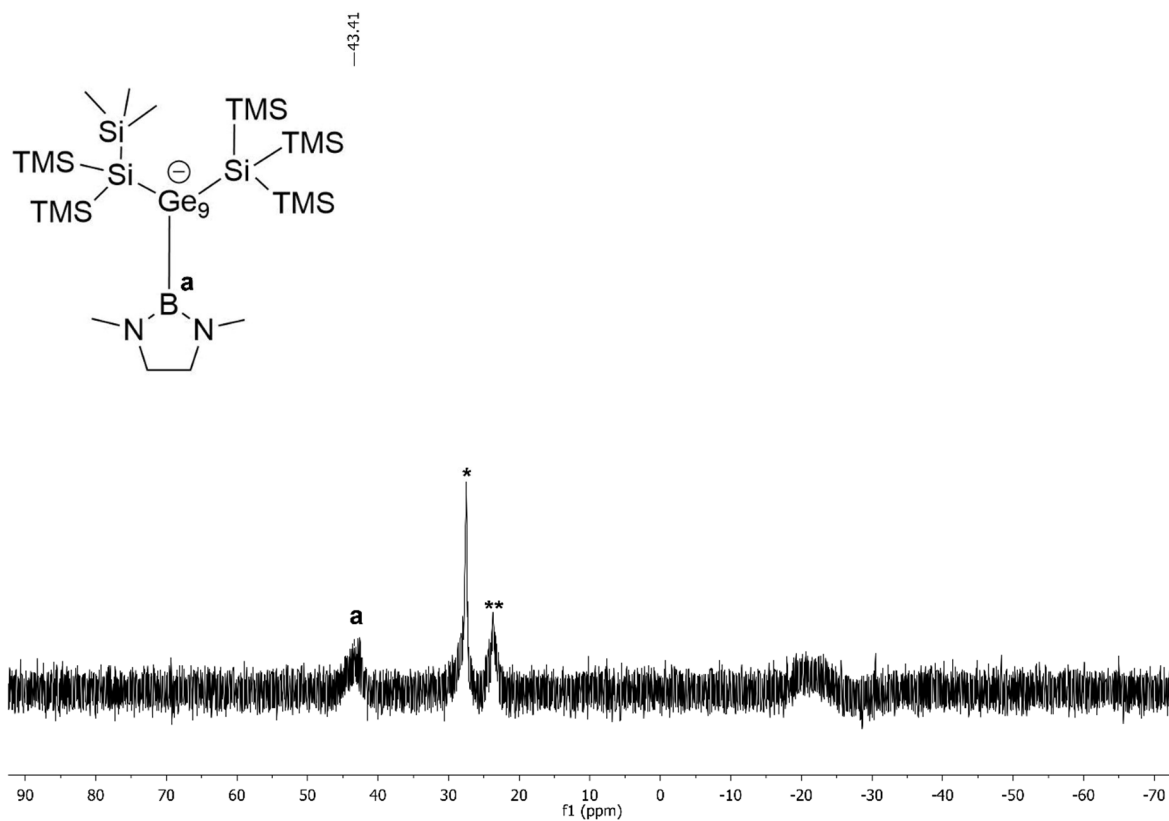


Figure S4. ^{11}B NMR spectrum of **1a-K** acquired in $\text{thf-}d_8$. * excessive reactant; ** unknown side product.

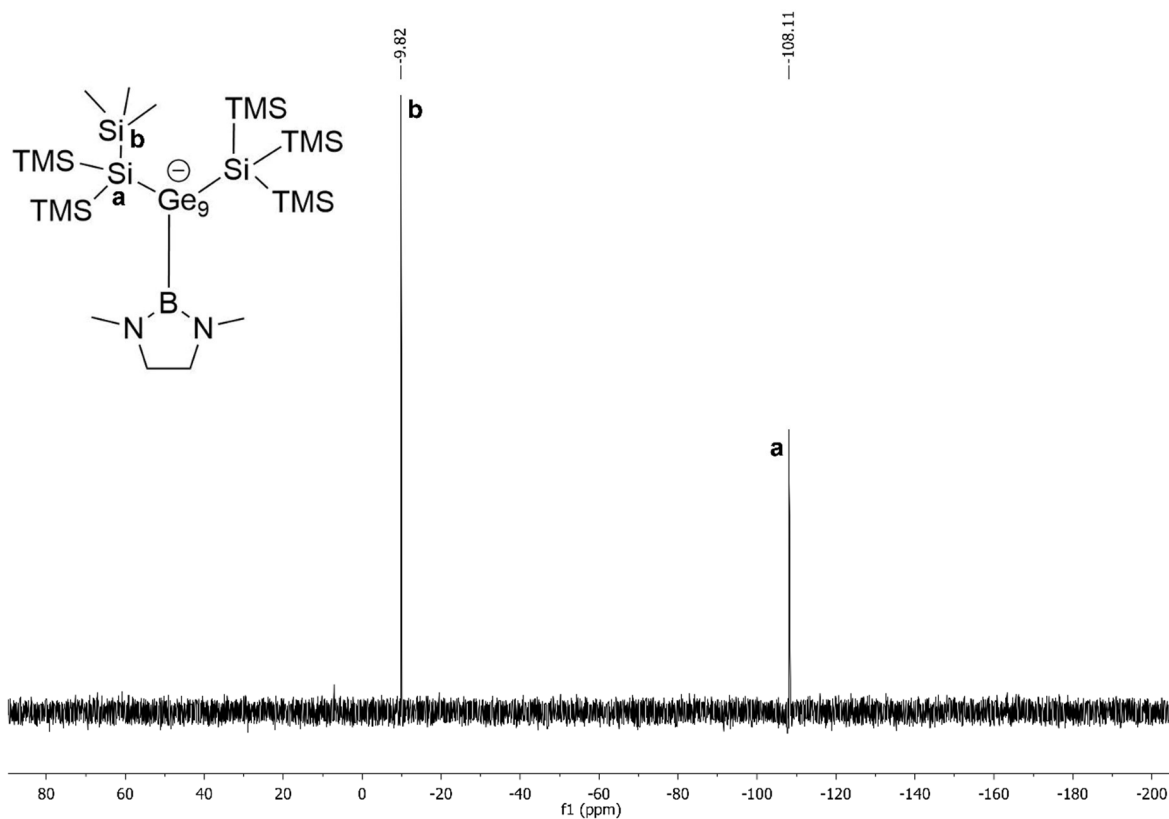


Figure S5. ^{29}Si -INEPT NMR of **1a-K** spectrum acquired in $\text{thf-}d_8$.

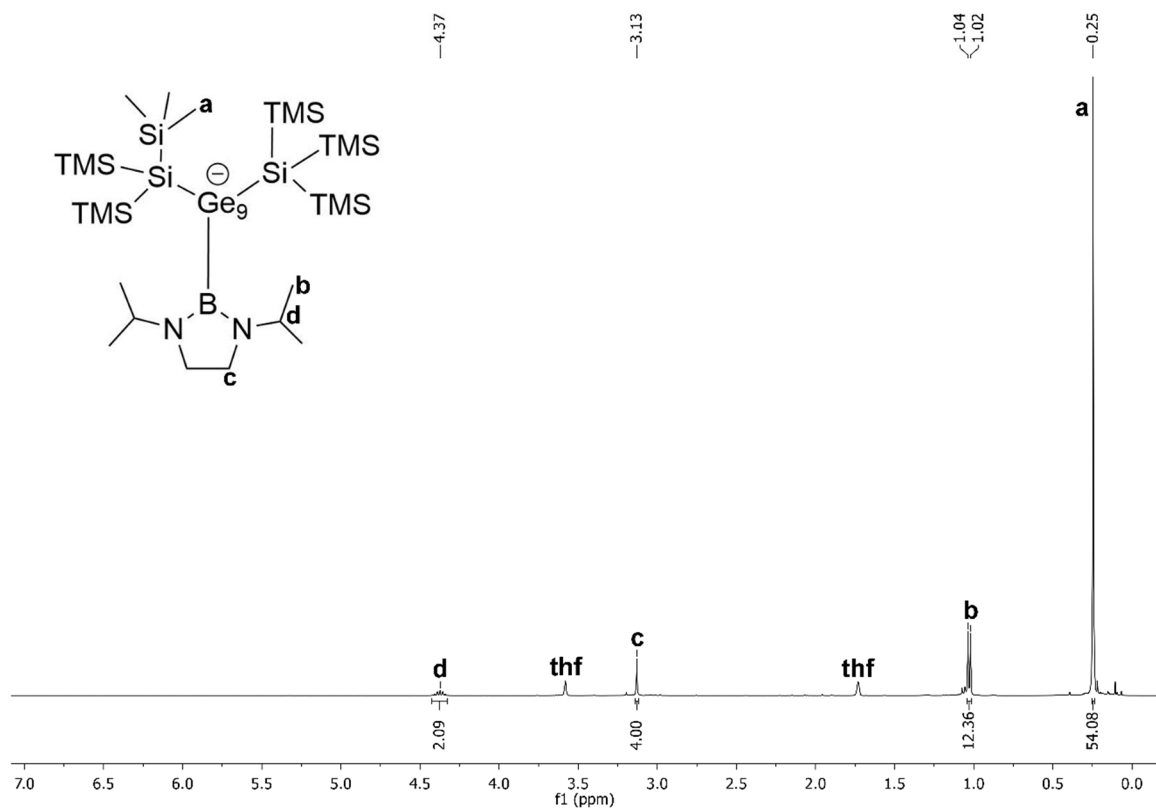


Figure S6. ^1H NMR spectrum of **2a-K** acquired in $\text{thf-}d_8$.

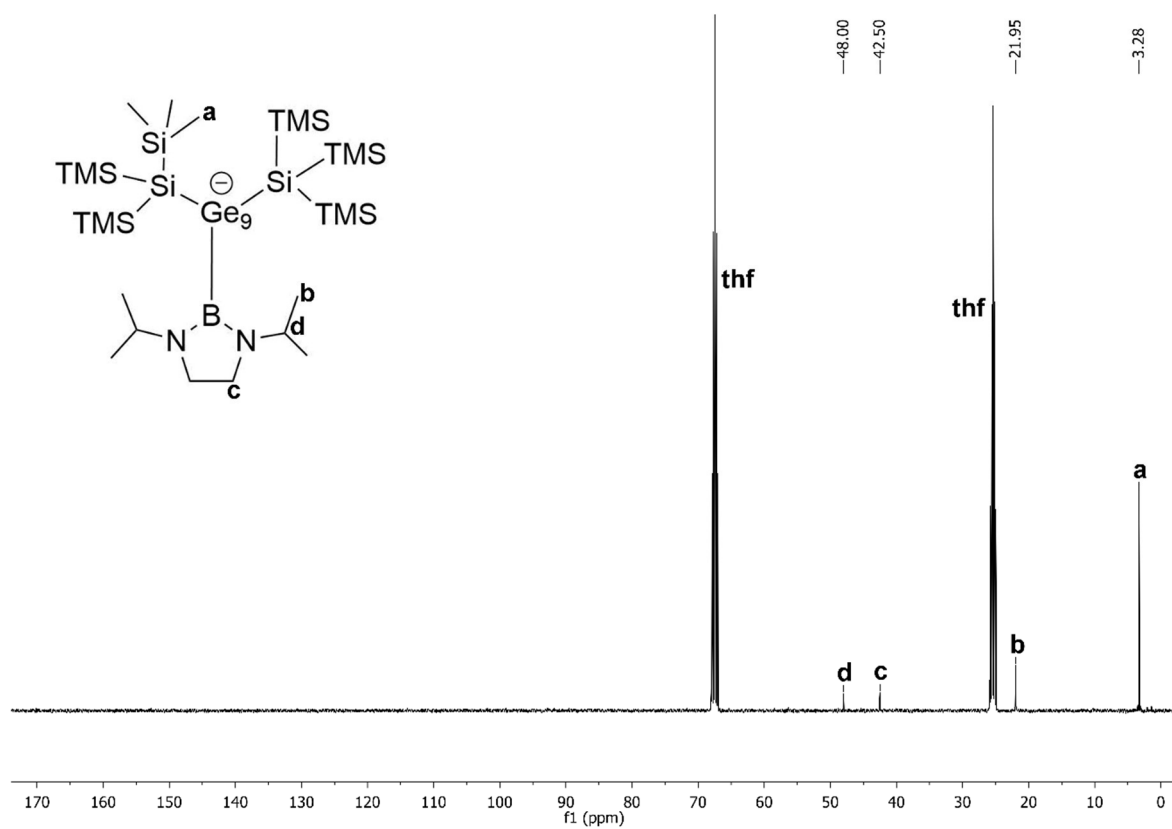


Figure S7. ^{13}C NMR spectrum of **2a-K** acquired in $\text{thf-}d_8$.

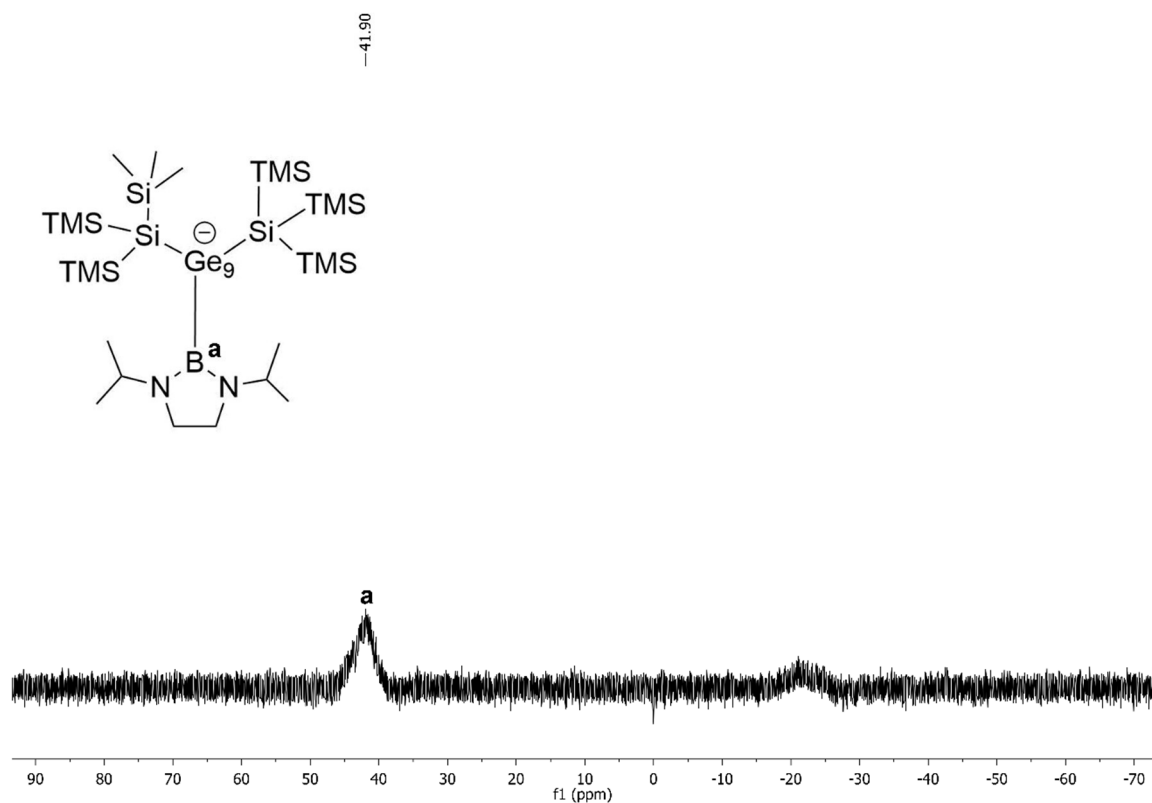


Figure S8. ^{11}B NMR spectrum of **2a-K** acquired in $\text{thf-}d_8$. Unassigned impurity.

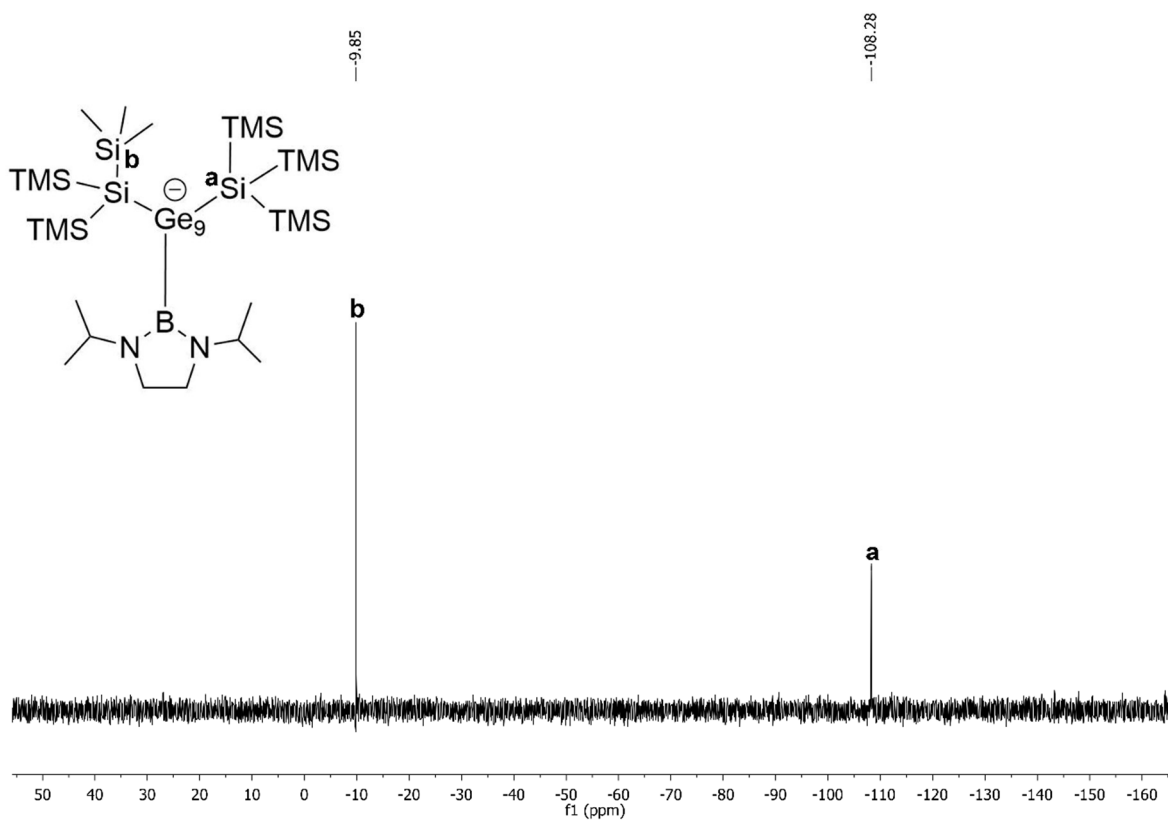


Figure S9. ^{29}Si -INEPT NMR spectrum of **2a-K** acquired in $\text{thf-}d_8$.

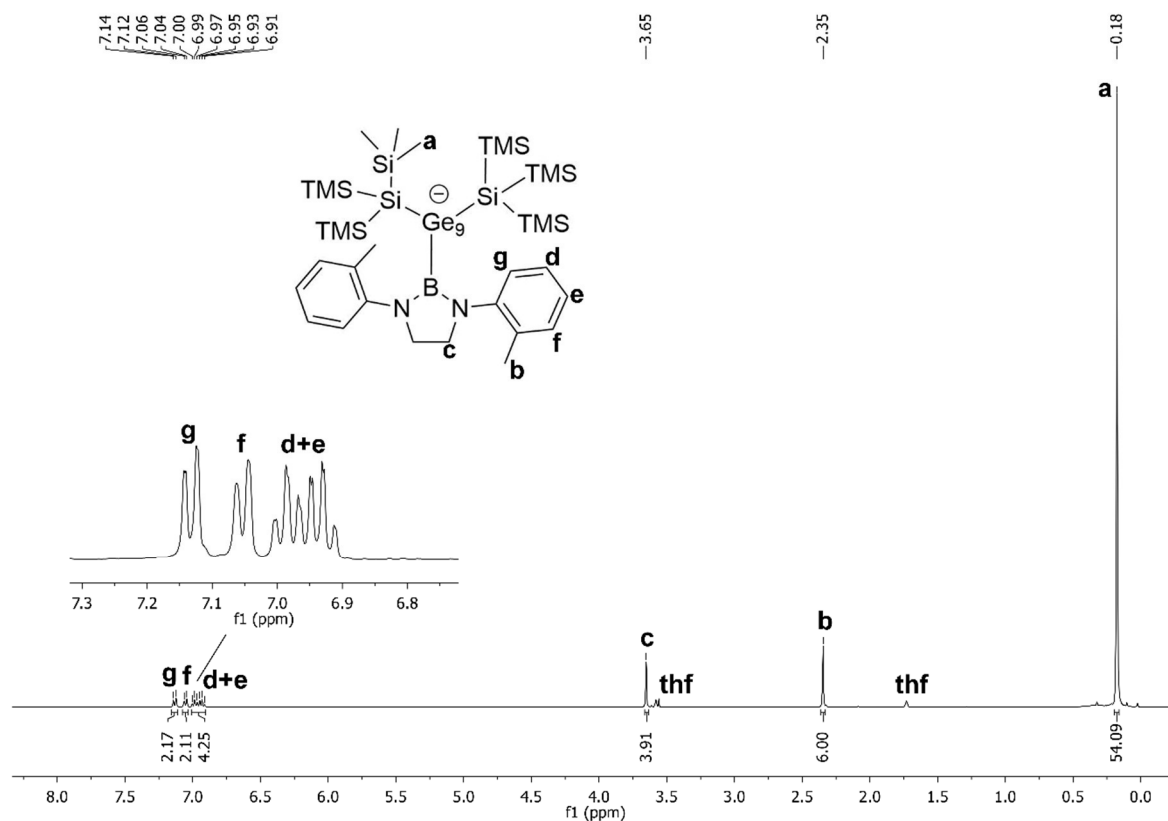


Figure S10. ¹H NMR spectrum of **3a-K** acquired in thf-*d*₈.

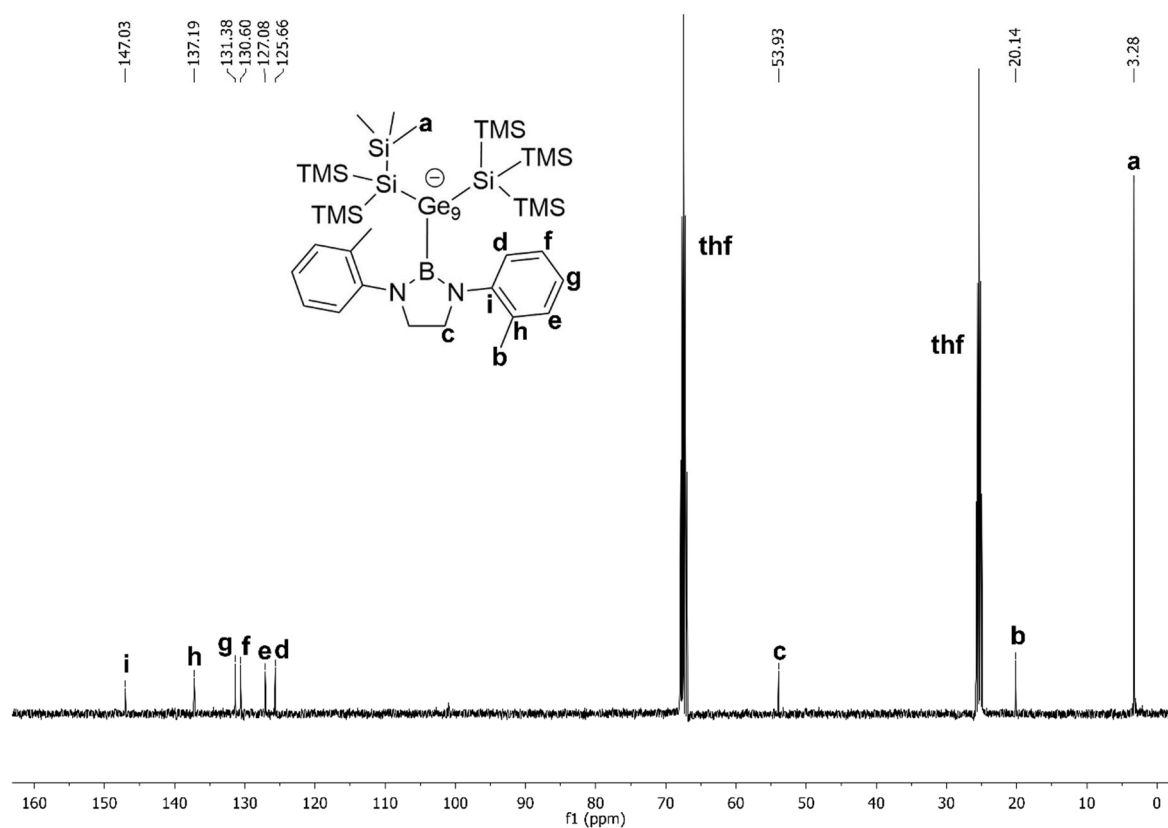


Figure S11. ¹³C NMR spectrum of **3a-K** acquired in thf-*d*₈.

-42.92

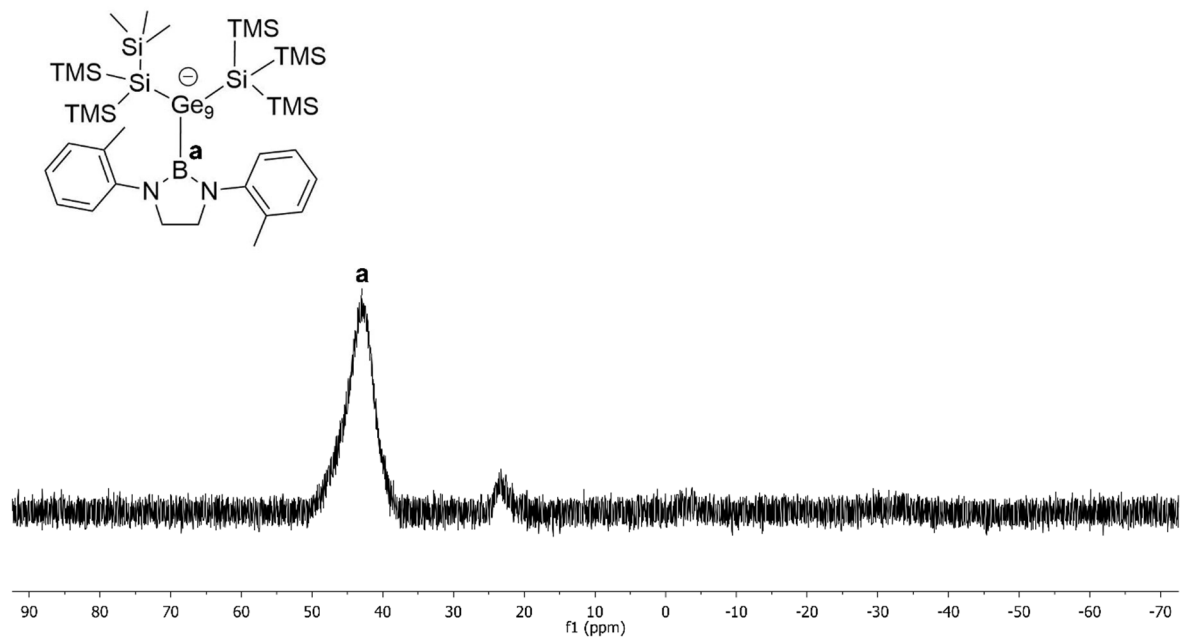


Figure S12. ^{11}B NMR spectrum of **3a-K** acquired in thf-d_8 .

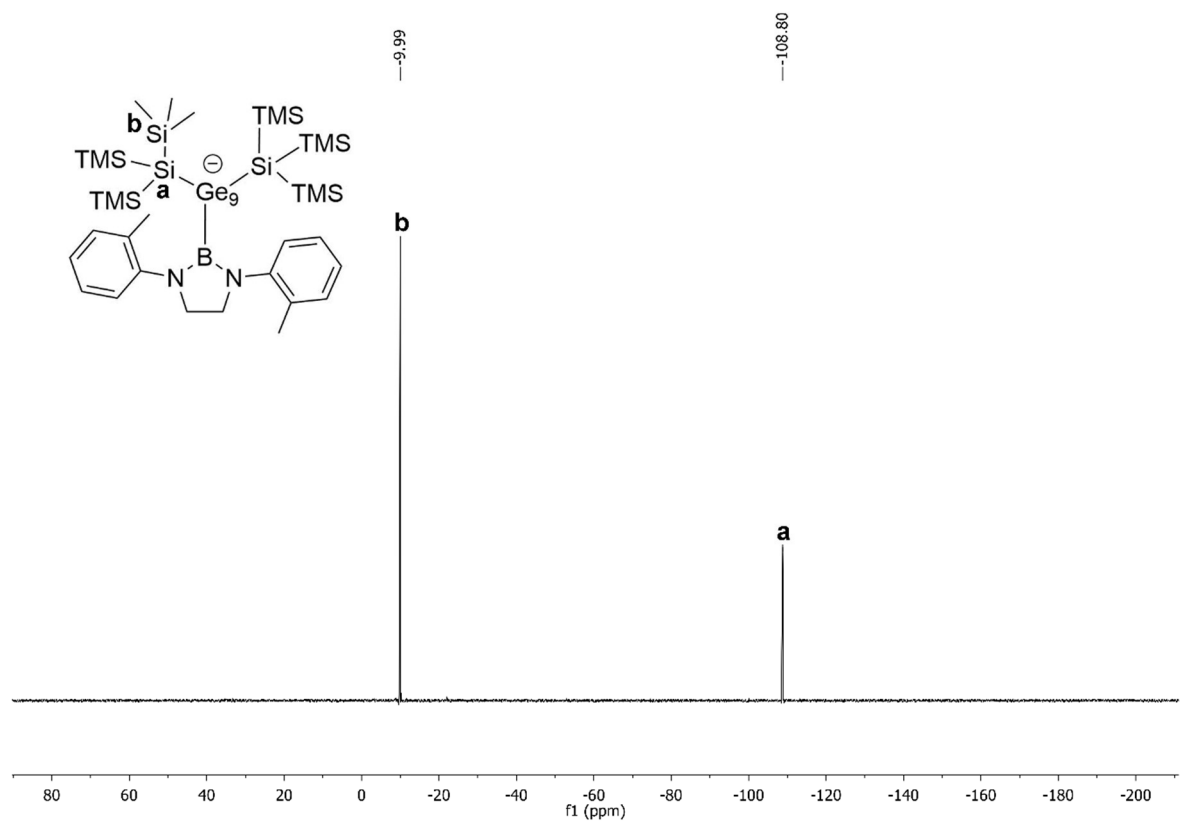


Figure S13. ^{29}Si -INEPT NMR spectrum of **3a-K** acquired in thf-d_8 .

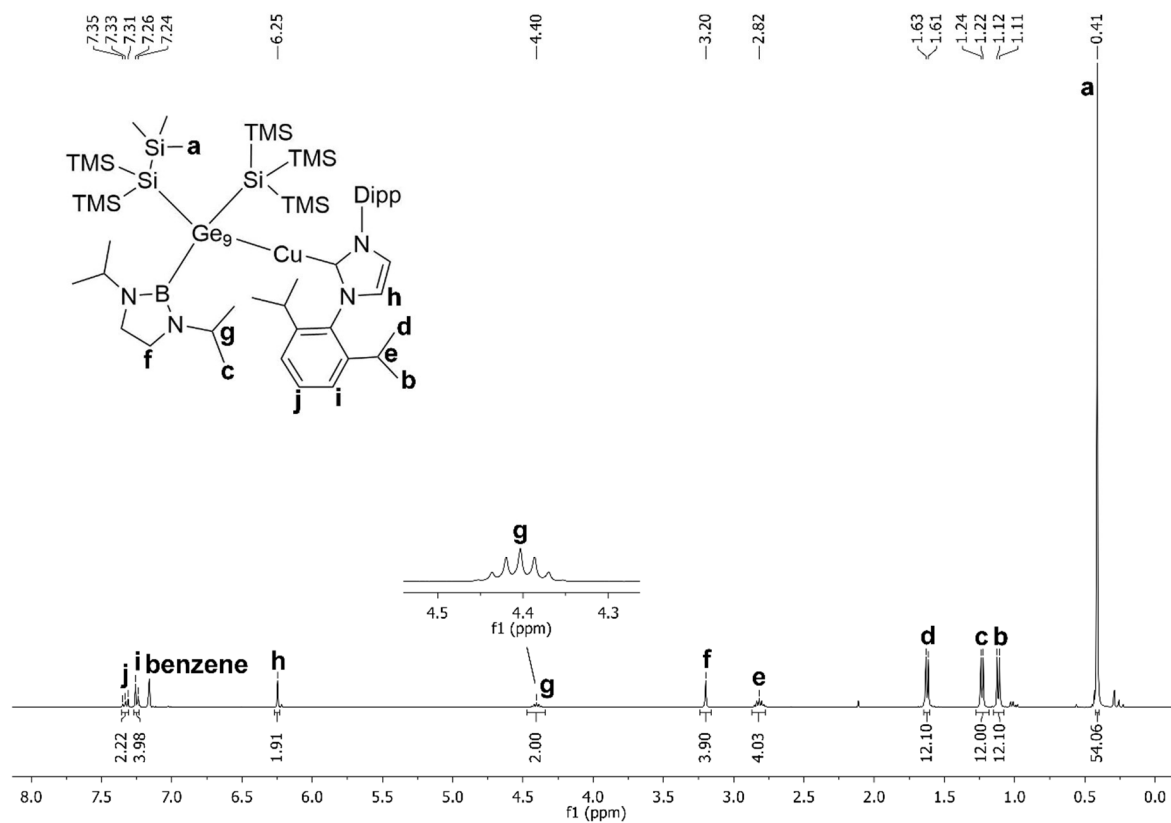


Figure S14. ^1H NMR spectrum of **2a-Cu** acquired in C_6D_6 .

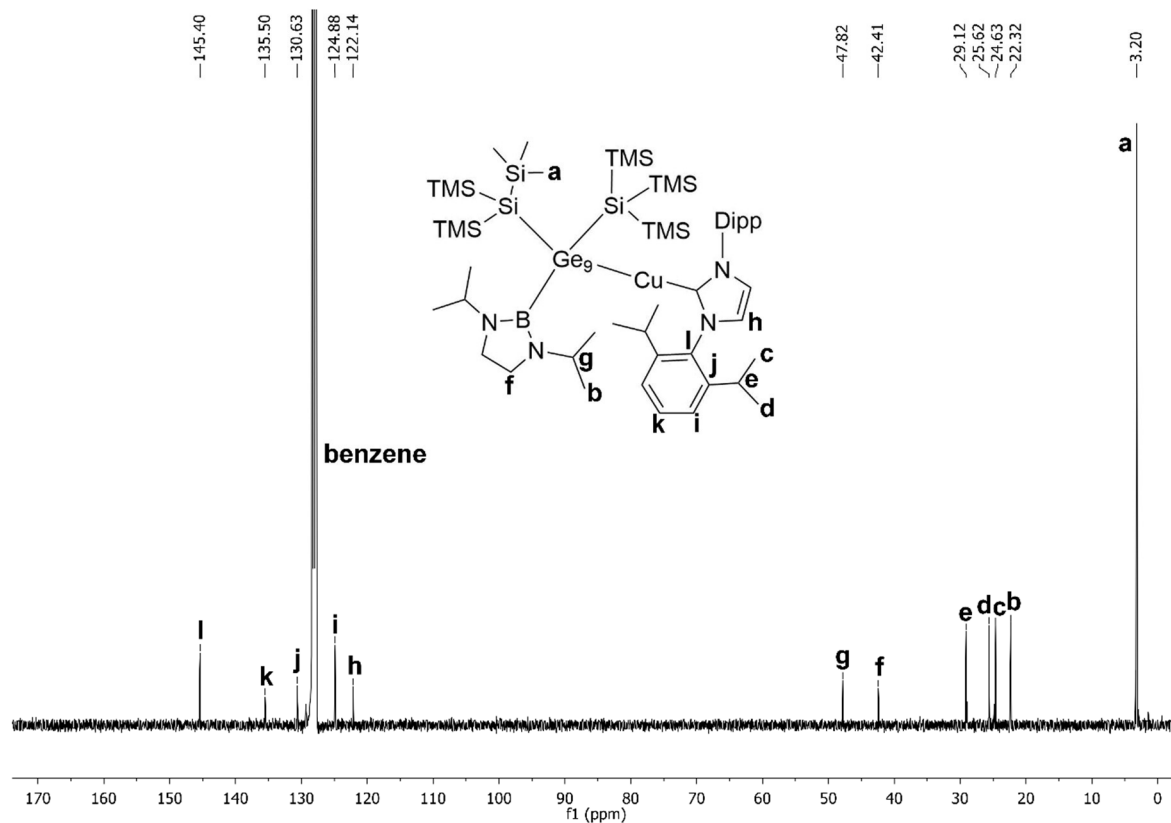


Figure S15. ^{13}C NMR spectrum of **2a-Cu** acquired in C_6D_6 .

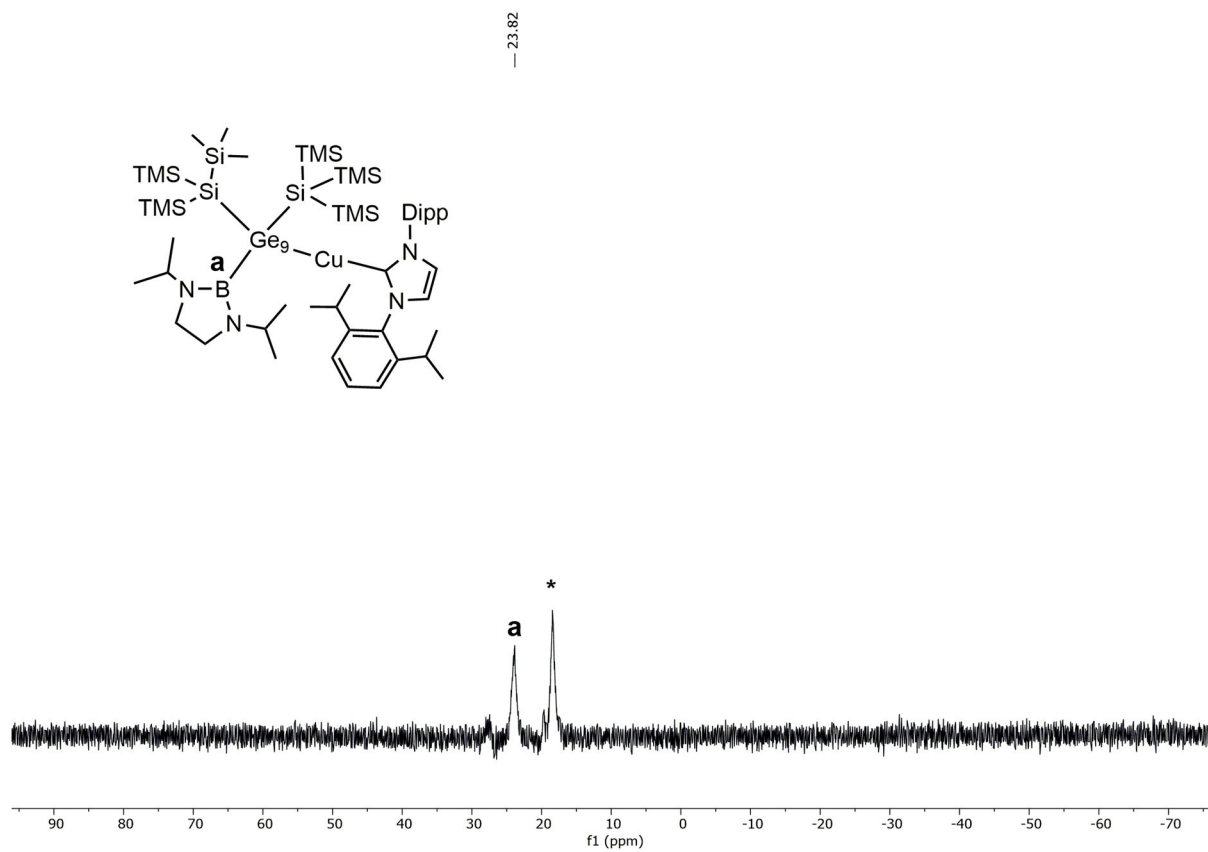


Figure S16. ^{11}B NMR spectrum of **2a-Cu** acquired in thf-d_8 . *: unknown side product.

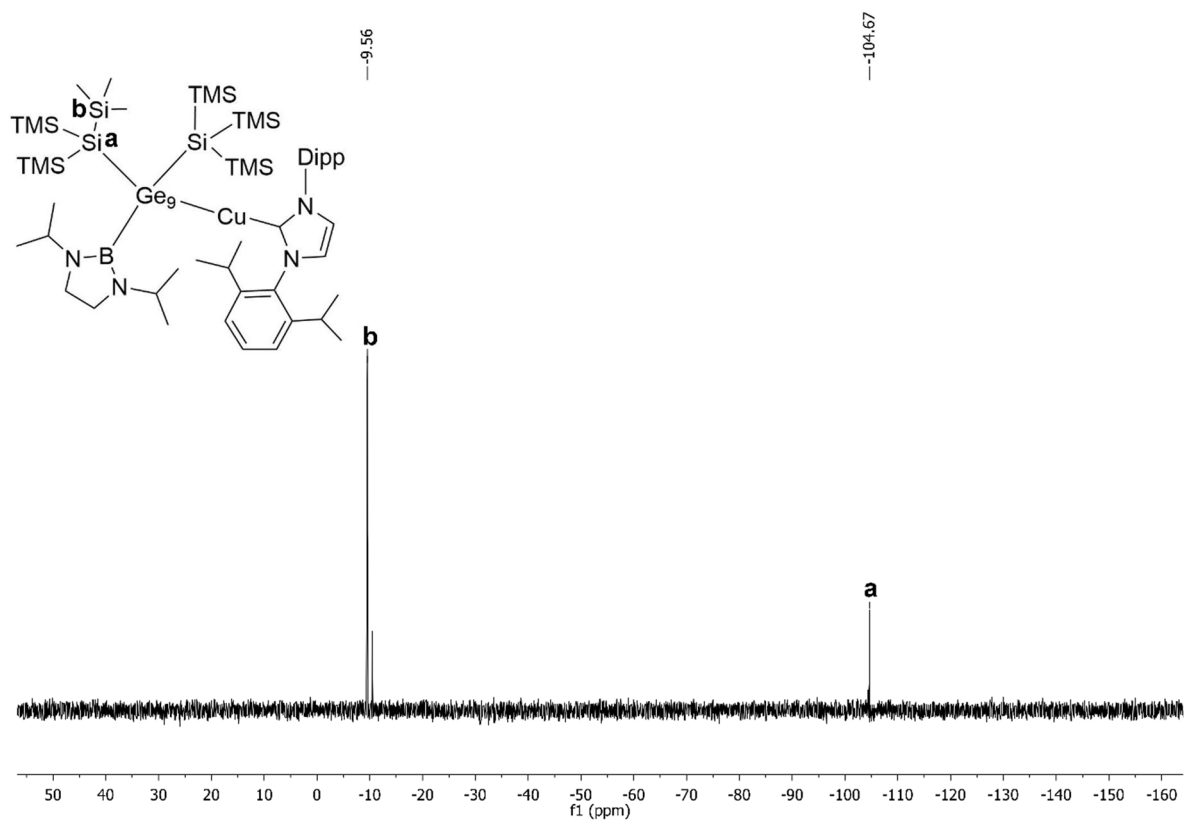


Figure S17. ^{29}Si -INEPT NMR spectrum of **2a-Cu** acquired in C_6D_6 .

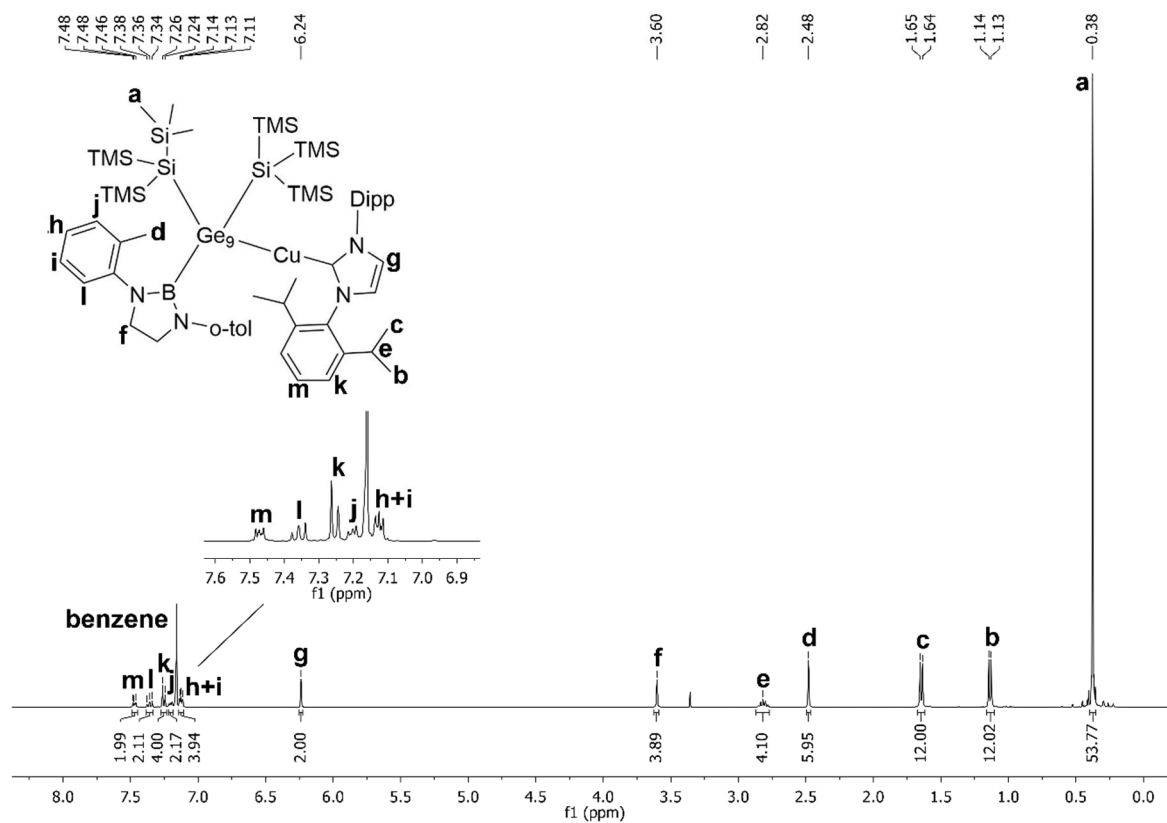


Figure S18. ^1H NMR spectrum of **3a-Cu** acquired in C_6D_6 .

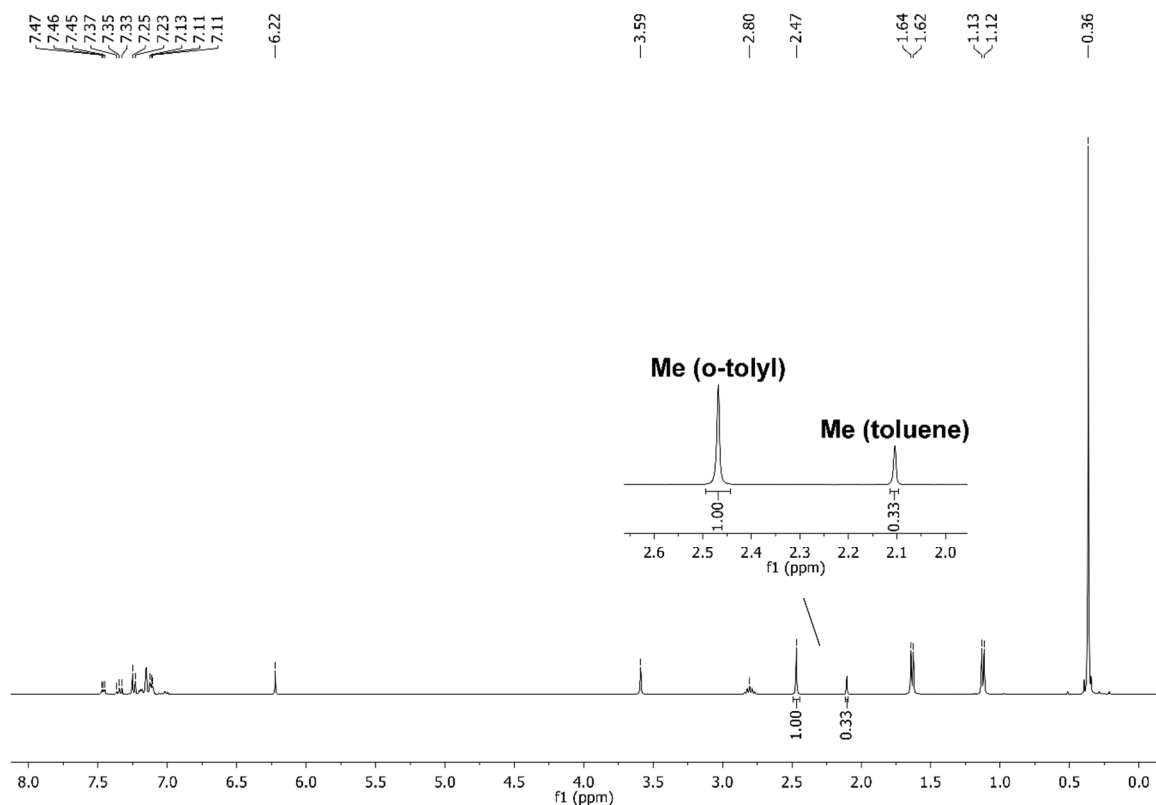


Figure S19. ^1H NMR spectrum of the elemental analysis sample of **3a-Cu** acquired in C_6D_6 . For signal assignment see Figure S18.

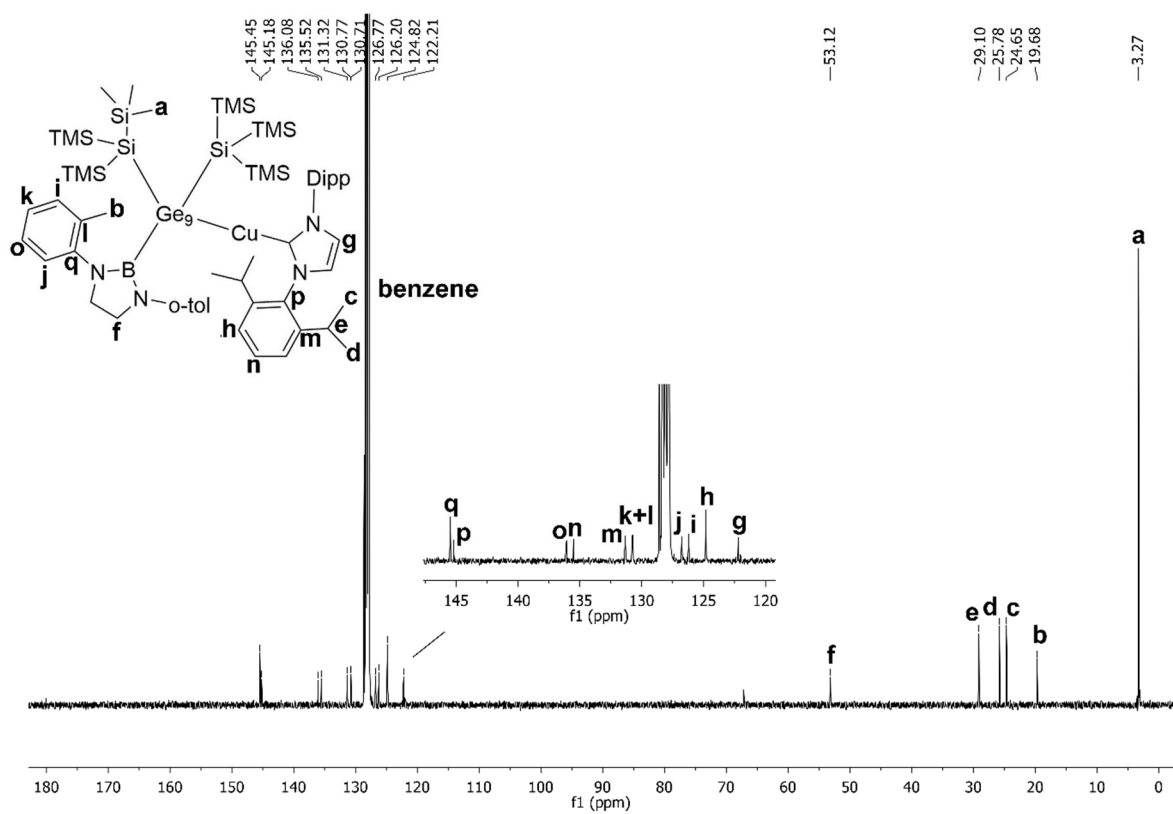


Figure S20. ^{13}C NMR spectrum of **3a-Cu** acquired in C_6D_6 .

—23.36

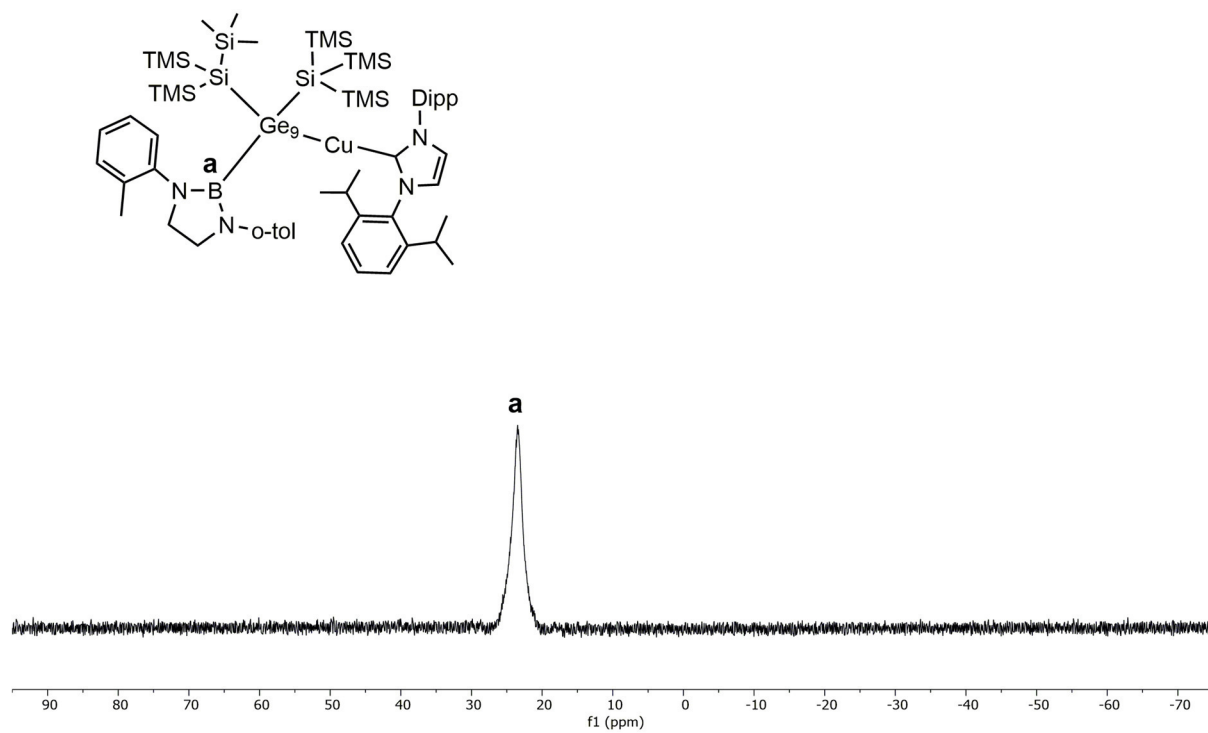


Figure S21. ^{11}B NMR spectrum of **3a-Cu** acquired in thf-d_8 .

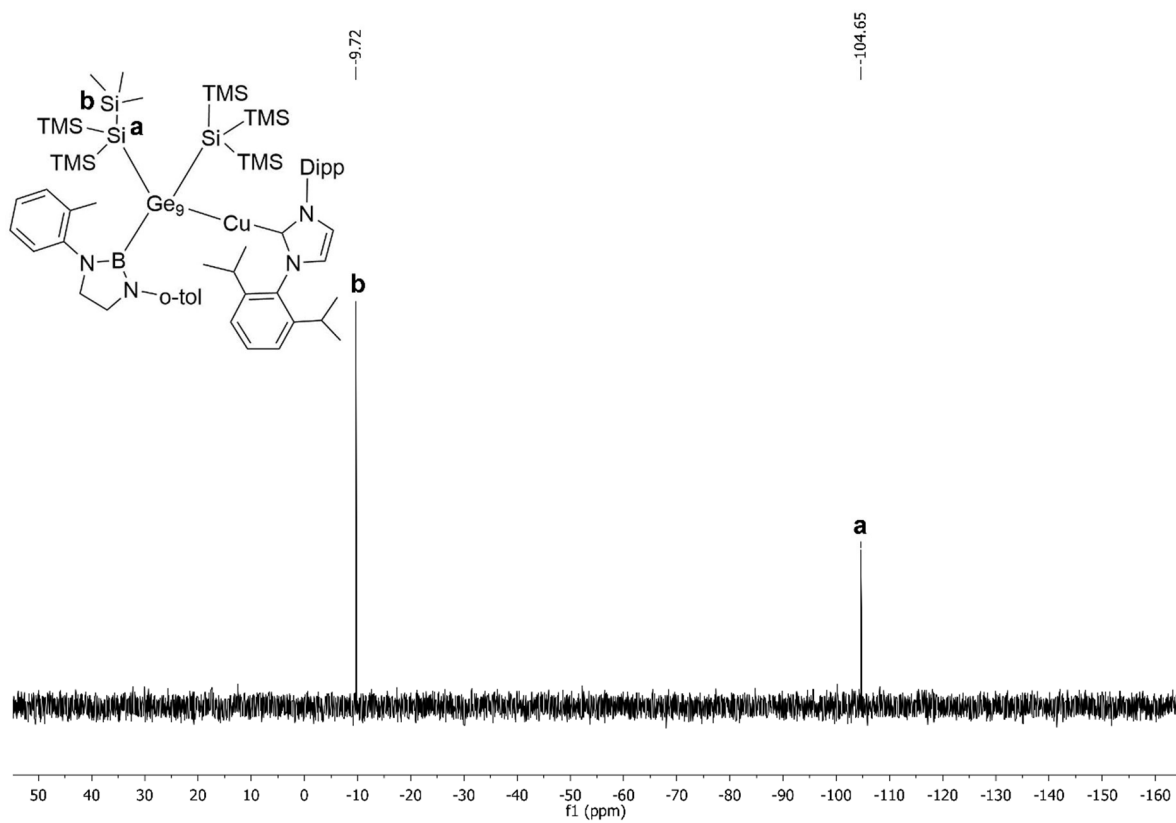


Figure S22. ^{29}Si -INEPT NMR spectrum of **3a-Cu** acquired in C_6D_6 .

3.3 ESI MS spectra

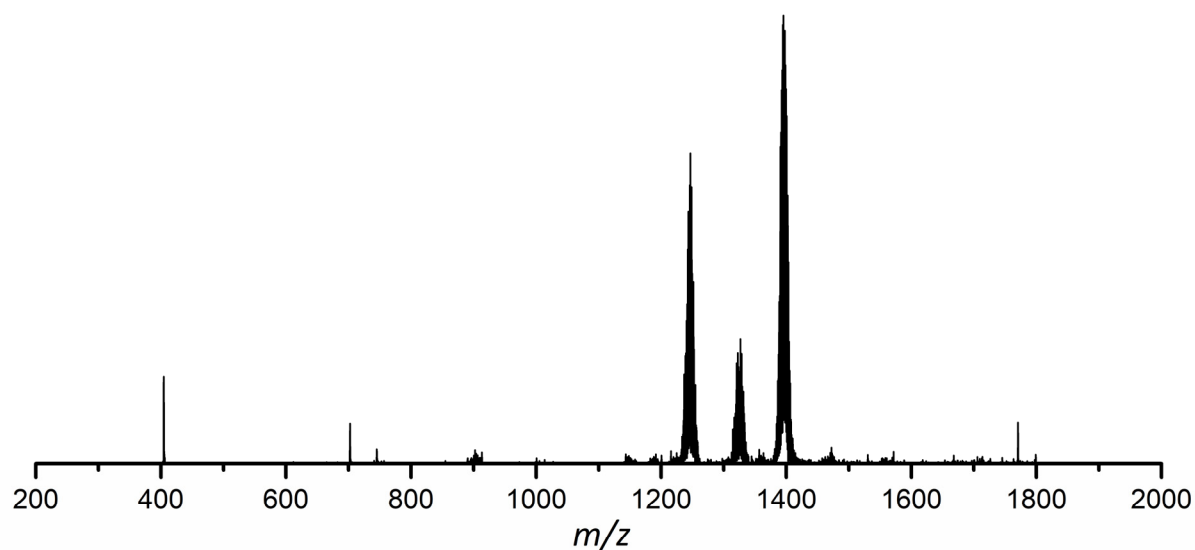


Figure S23. ESI MS spectrum (negative-ion mode, 3500 V, 300 °C) obtained upon examination of a thf solution of $[\text{Ge}_9\{\text{Si}(\text{TMS})_3\}_2\text{DAB}^{\text{Me}}]^-$ **1a** in thf. Besides the signal at m/z 1246.6 (**1a**), two further signals at m/z 1396 $\{[\text{Ge}_9\{\text{Si}(\text{TMS})_3\}_3]^-$ and m/z 1322 (unidentified species) are observed as side products. A detailed view of the signal of anion **1a** is provided in the manuscript (Figure 1).

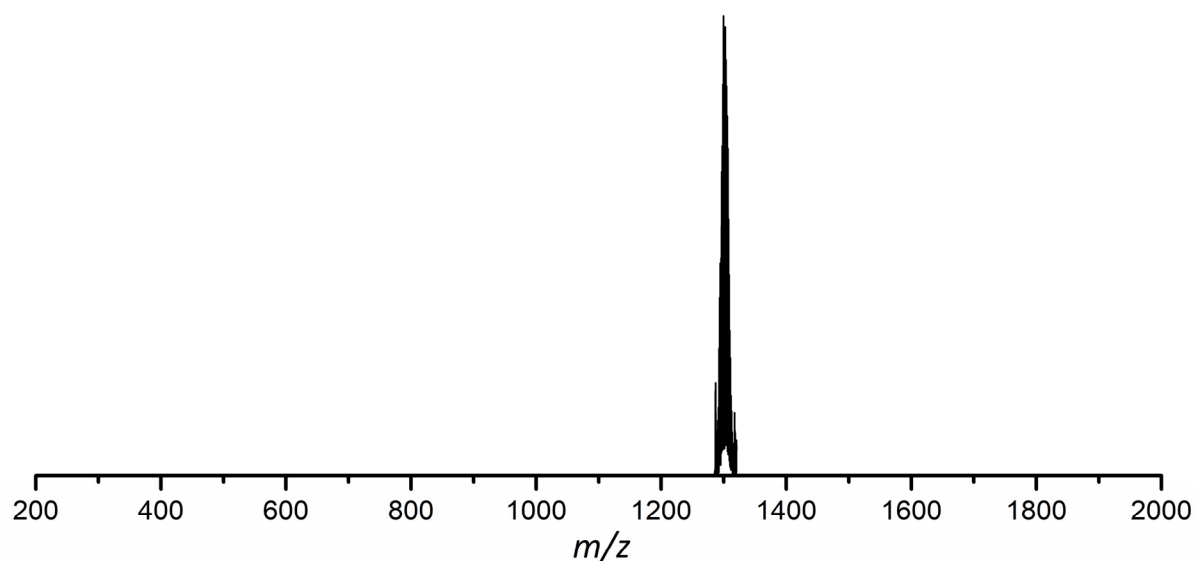


Figure S24. ESI MS spectrum (negative-ion mode, 3500 V, 300 °C) obtained upon examination of a thf solution of $[\text{Ge}_9\{\text{Si}(\text{TMS})_3\}_2\text{DAB}^{\text{Pr}}]^-$ **2a** in thf (m/z 1302.6). A detailed view of the signal of anion **2a** is provided in the manuscript (Figure 1).

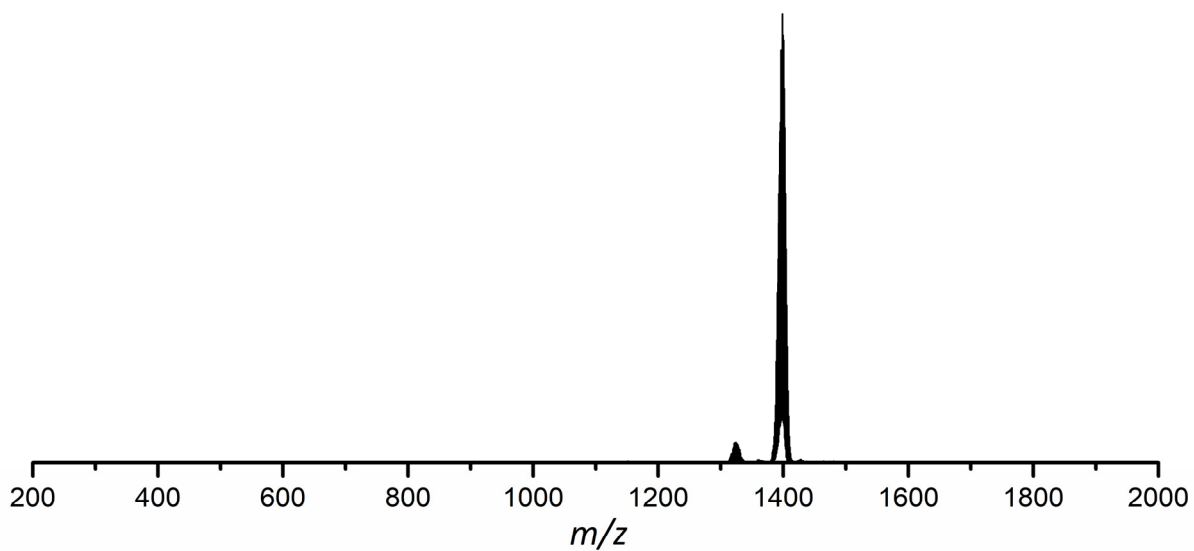


Figure S25. ESI MS spectrum (negative-ion mode, 3500 V, 300 °C) obtained upon examination of a thf solution of $[\text{Ge}_9\{\text{Si}(\text{TMS})_3\}_2\text{DAB}^{9-10}]^-$ **3a** in thf (m/z 1398.7). A detailed view of the signal of anion **3a** is provided in the manuscript (Figure 1).

3.4 Quantum chemical calculations at DFT-PBE0/TZVP level of theory

Table S4. Molecular orbital energies of anion **1a**.

Orbital	Energy [eV] (position)
HOMO-LUMO gap	3.8
LUMO+4	-0.160 (DAB)
LUMO+3	-0.493 ([Ge ₉])
LUMO+2	-0.638 ([Ge ₉])
LUMO+1	-0.689 ([Ge ₉])
LUMO	-0.810 ([Ge ₉])
HOMO	-4.610 ([Ge ₉])

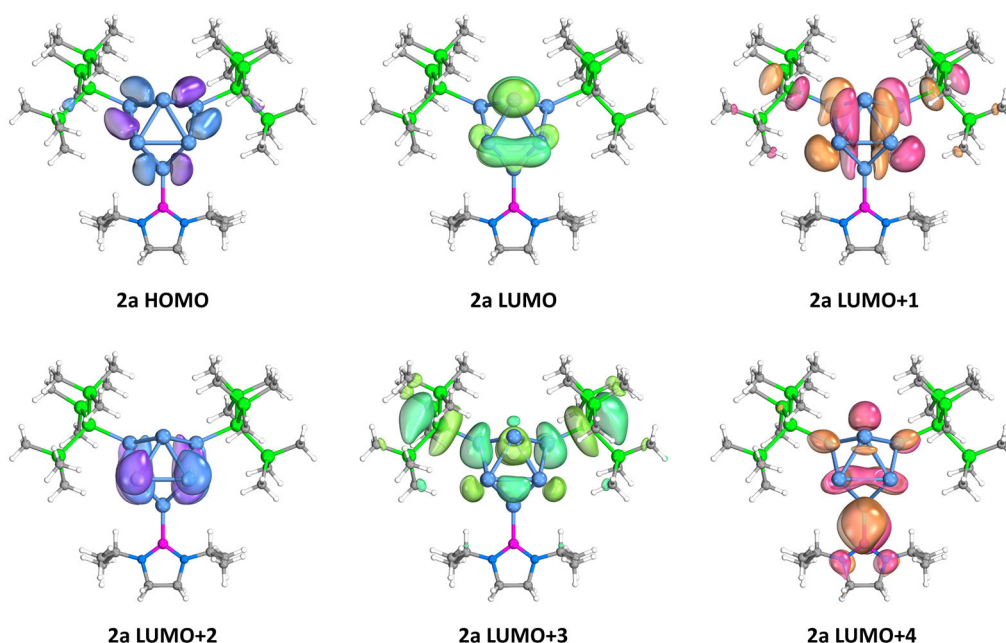


Figure S26. Molecular orbitals at anion **2a**. Orbital figures are drawn in such way that 50% of the density is enclosed within the isosurface, corresponding to approximately 0.04 a.u. isovalue.

Table S5. Molecular orbital energies of anion **2a**.

Orbital	Energy [eV] (position)
HOMO-LUMO gap	3.8
LUMO+4	-0.098 (DAB)
LUMO+3	-0.456 ([Ge ₉])
LUMO+2	-0.618 ([Ge ₉])
LUMO+1	-0.640 ([Ge ₉])
LUMO	-0.778 ([Ge ₉])
HOMO	-4.577 ([Ge ₉])

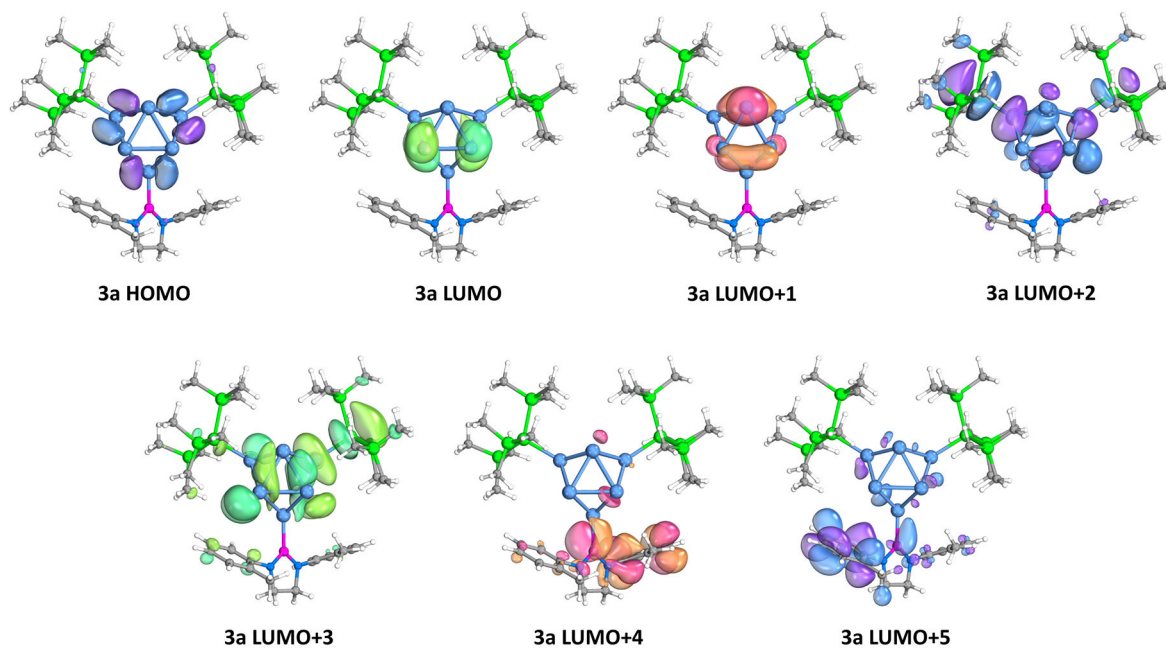


Figure S27. Molecular orbitals at anion **3a**. Orbital figures are drawn in such way that 50% of the density is enclosed within the isosurface, corresponding to approximately 0.04 a.u. isovalue.

Table S6. Molecular orbital energies of anion **3a**.

Orbital	Energy [eV] (position)
HOMO-LUMO gap	3.8
LUMO+5	-0.113 (DAB)
LUMO+4	-0.202 (DAB)
LUMO+3	-0.476 ([Ge ₉])
LUMO+2	-0.489 ([Ge ₉])
LUMO+1	-0.656 ([Ge ₉])
LUMO	-0.742 ([Ge ₉])
HOMO	-4.516 ([Ge ₉])

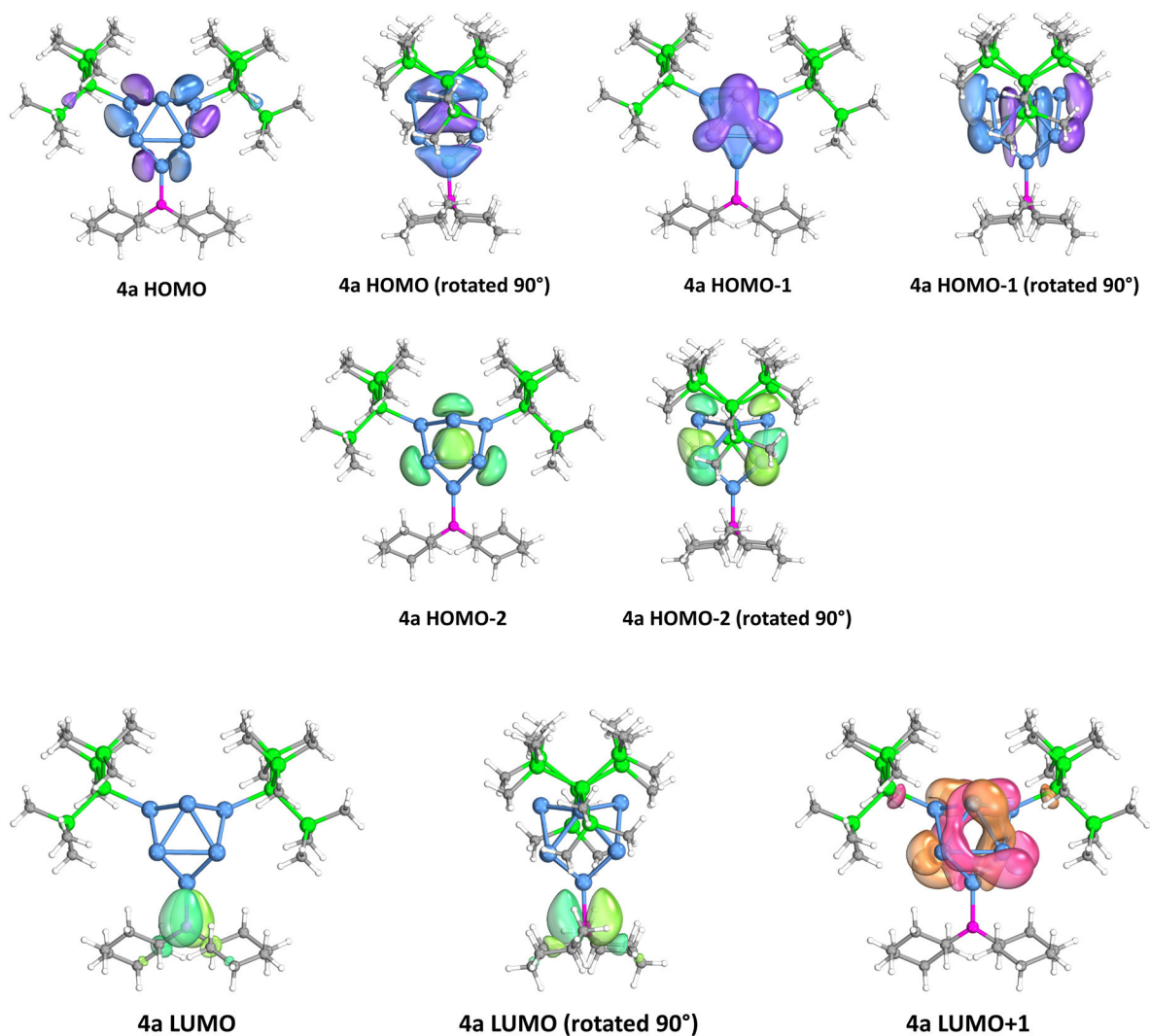


Figure S28. Molecular orbitals at the theoretical anion **4a**. Orbital figures are drawn in such way that 50% of the density is enclosed within the isosurface, corresponding to approximately 0.04 a.u. isovalue.

Table S7. Molecular orbital energies of the theoretical anion **4a**.

Orbital	Energy [eV] (position)
HOMO-LUMO gap	3.4
LUMO+2	-0.693 ([Ge ₉])
LUMO+1	-0.706 ([Ge ₉])
LUMO	-1.197 (B)
HOMO	-4.567 ([Ge ₉])
HOMO-1	-4.873 ([Ge ₉])
HOMO-2	-5.042 ([Ge ₉])

4. References

1. O. Kysliak, A. Schnepf, *Dalton Trans.* **2016**, 45, 2404-2408.
2. C. Kleeberg, *Dalton Trans.* **2013**, 42, 8276-8287.
3. Y. Segawa, Y. Suzuki, M. Yamashita, K. Nozaki, *J. Am. Chem. Soc.* **2008**, 130, 16069-16079.
4. L. Hintermann, *Beilstein J. Org. Chem.* **2007**, 3, 22.
5. O. Santoro, A. Collado, A. M. Z. Slawin, S. P. Nolan, C. S. J. Cazin, *Chem. Commun.* **2013**, 49, 10483-10485.
6. G. M. Sheldrick, *SHELXL-97*, Program for Crystal Structure Refinement, Göttingen, **1997**.
7. G. Sheldrick, *Acta Crystallogr., Sect. C: Struct. Chem.* **2015**, 71, 3-8.
8. A. Spek, *Acta Crystallogr., Sect. D: Struct. Biol.* **2009**, 65, 148-155.
9. G. R. Fulmer, A. J. M. Miller, N. H. Sherden, H. E. Gottlieb, A. Nudelman, B. M. Stoltz, J. E. Bercaw, K. I. Goldberg, *Organometallics* **2010**, 29, 2176-2179.
10. a) C. Adamo, V. Barone, *J. Chem. Phys.* **1999**, 110, 6158-6170; b) J. P. Perdew, K. Burke, M. Ernzerhof, *Phys. Rev. Lett.* **1996**, 77, 3865; c) F. Weigend, R. Ahlrichs, *Phys. Chem. Chem. Phys.* **2005**, 7, 3297-3305; d) TURBOMOLE V7.3 2018, a development of University of Karlsruhe and Forschungszentrum Karlsruhe GmbH, 1989-2007, TURBOMOLE GmbH, since 2007; available from www.turbomole.com.
11. a) K. Eichkorn, O. Treutler, H. Öhm, M. Häser, R. Ahlrichs, *Chem. Phys. Lett.* **1995**, 240, 283-290; b) M. Sierka, A. Hogekamp, R. Ahlrichs, *J. Chem. Phys.* **2003**, 118, 9136-9148; c) F. Weigend, *Phys. Chem. Chem. Phys.* **2006**, 8, 1057-1065.
12. A. Klamt, G. Schüürmann, *J. Chem. Soc. Perkin Trans. 2* **1993**, 5, 799-805.
13. G. Knizia, J. E. Klein, *Angew. Chem. Int. Ed.* **2015**, 54, 5518-5522; *Angew. Chem.* **2015**, 127, 5609-5613.

6.4 Crystal Structure of (1,4,7,10,13,16-hexaoxacyclooctadecane- $\kappa^6\text{O}_6$) potassium (2-methylphenylamino)ethyl-2-methylphenylamide ammoniate (1/3.5), $[\text{K}(\text{18-crown-6})](\text{o-CH}_3\text{C}_6\text{H}_4)\text{NH}(\text{CH}_2)_2\text{N}(\text{o-CH}_3\text{C}_6\text{H}_4) \cdot 3.5 \text{NH}_3$, $\text{C}_{28}\text{H}_{53.5}\text{KN}_{5.5}\text{O}_6$

Christoph Wallach, Wilhelm Klein and Thomas F. Fässler

Crystal structure communication submitted for publication in: *Z. Kristallogr., New Cryst. Struct.*

Contents and Contributions

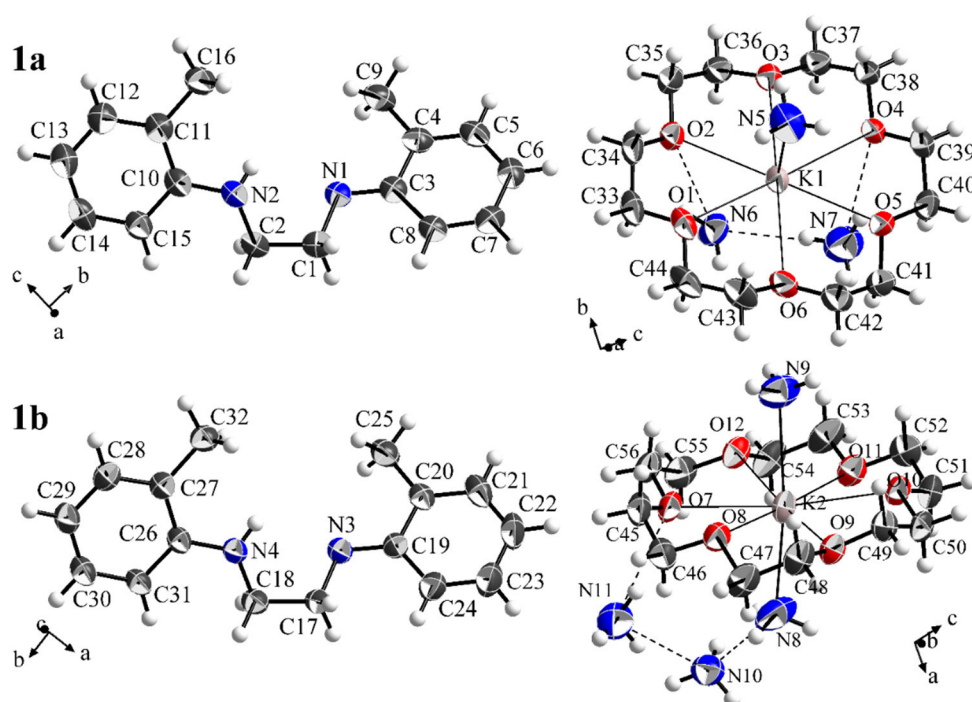
The single crystal structure of the compound $[\text{K}(\text{18-crown-6})](\text{o-CH}_3\text{C}_6\text{H}_4)\text{NH}(\text{CH}_2)_2\text{N}(\text{o-CH}_3\text{C}_6\text{H}_4) \cdot 3.5 \text{NH}_3$ is reported. The compound was obtained as a by-product of the reaction of the bromo-1,3,2-diazaborolidine $\text{DAB}^{\text{o-tol}}\text{-Br}$ with K_4Ge_9 in liquid ammonia in the presence of 18-crown-6 as sequestering agent. The synthesis and single crystal selection was performed by me. Dr. Wilhelm Klein refined the single crystal structure data. The manuscript for publication was written by me and submitted for publication by Dr. Wilhelm Klein.

Crystal Structure of (1,4,7,10,13,16-hexaoxacyclooctadecane- $\kappa^6\text{O}_6$) potassium (2-methylphenylamino)ethyl-2-methylphenylamide ammoniate (1/3.5), $[\text{K}(18\text{-crown-6})](\text{o-CH}_3\text{C}_6\text{H}_4)\text{NH}(\text{CH}_2)_2\text{N}(\text{o-CH}_3\text{C}_6\text{H}_4) \cdot 3.5 \text{NH}_3$, $\text{C}_{28}\text{H}_{53.5}\text{KN}_{5.5}\text{O}_6$

Christoph Wallach, Wilhelm Klein and Thomas F. Fässler

Technische Universität München
Department Chemie, Lichtenbergstr. 4
85747 Garching, Germany

e-mail: thomas.faessler@lrz.tum.de



Abstract

$\text{C}_{28}\text{H}_{53.5}\text{KN}_{5.5}\text{O}_6$, monoclinic, Pc (no. 7), $a = 18.7986(12) \text{ \AA}$, $b = 8.3431(6) \text{ \AA}$, $c = 22.4638(16) \text{ \AA}$, $\alpha = 90^\circ$, $\beta = 100.554(5)^\circ$, $\gamma = 90^\circ$, $V = 3463.6(4) \text{ \AA}^3$, $Z = 4$, $R_{\text{gt}}(F) = 0.0712$, $wR_{\text{ref}}(F^2) = 0.2229$, $T = 150 \text{ K}$.

Table 1. Data collection and handling.

Crystal:	Yellow sphere, 0.2 × 0.2 × 0.1 mm
Wavelength:	Mo K α radiation (0.71073 Å)
μ :	0.197 mm ⁻¹
Diffractometer, scan mode:	STOE StadiVari, ω
$2\theta_{\max}$:	52°
$N(hkl)_{\text{measured}}$, $N(hkl)_{\text{unique}}$	40821, 13144
Criterion for I_{obs} , $N(hkl)_{\text{gt}}$:	$I_{\text{obs}} > 2 \sigma(I_{\text{obs}})$, 10077
$N(\text{param})_{\text{refined}}$:	750
Programs:	X-Area, ^[1] SHELXS, ^[2] SHELXL-2014, ^[3] Diamond ^[4]

Source of material

The title compound was obtained as an unintended side product from a synthesis aiming at functionalized *Zintl* cluster compounds.^[5] All reactions were performed under the exclusion of oxygen and moisture using standard Schlenk line and glove box techniques. Glyoxal (*Merck*), BBr₃ (*Sigma Aldrich*) and *o*-methylanilin (*Sigma Aldrich*) were used without further purification. 1,4,7,10,13,16-hexaoxa-cyclooctadecane (18-crown-6; *Merck*) was purified by sublimation. 2-bromo-1,3-di-*o*-tolyl-1,3,2-diazaborolidine (DAB^{*o*-tol}-Br) was prepared according to a published procedure.^[5-6] K₄Ge₉ was prepared by fusing stoichiometric amounts of the elements in stainless-steel tubes at 650 °C. Liquid ammonia was dried over sodium metal for two hours prior to condensing it onto the reaction mixture. K₄Ge₉ (80 mg, 98.7 μmol , 1 equiv.), DAB^{*o*-tol}-Br (32.5 mg, 98.7 μmol , 1 equiv.), and 18-crown-6 (47.0 mg, 177.7 μmol , 1.8 equiv.) were weighed into a Schlenk tube and liquid ammonia (2 mL) was condensed onto the reactants, causing the formation of a red solution. Yellow spherical crystals of the title compound were isolated from the reaction mixture after 9 months. An exact yield could not be determined due to the experimental setup.

Experimental details

A single crystal was selected under a microscope equipped with a light source using a cooling table.^[7] Subsequently, the crystal was transferred under liquid nitrogen to the diffractometer (*STOE StadiVari*) equipped with a *PILATUS 300K* detector (*DECTRIS*) and a Mo K α radiation source ($\lambda = 0.71073$ Å). For the data collection the crystal was cooled in a 150 K cold stream of dry nitrogen. The single crystal structure was determined by direct methods using the program *SHELXS-97*.^[2] Structure refinements were performed by full-matrix least-squares calculations against F^2 (*SHELXL-2014*).^[3] A riding model was used to calculate and refine the hydrogen atoms, except for the hydrogen atoms at N2 and N4 which were located from the difference Fourier map and were refined with independent positional and isotropic displacement parameters. No similar strong residual electron densities could be detected at

N1 and N3. Other elements than hydrogen were refined with anisotropic displacement parameters.

Discussion

The title compound (**1**) consists of an ion pair of the cationic coordination complex $[K(18\text{-crown-6})]^+$ and the $[(o\text{-CH}_3\text{C}_6\text{H}_4)\text{NH}(\text{CH}_2)_2\text{N}(o\text{-CH}_3\text{C}_6\text{H}_4)]^-$ anion, and crystallizes including 3.5 molecules of ammonia per formula unit. **1** crystallizes in the monoclinic space group Pc with 4 formula units per unit cell, the asymmetric unit is formed by two formula units. The anion is the amide of N^1, N^2 -di($o\text{-CH}_3\text{C}_6\text{H}_4$)ethylene-1,2-diamine, which serves as reactant in the synthesis of the bromo-1,3,2-diazaborolidine $\text{DAB}^{o\text{-tol}}\text{-Br}$.^[6] Most probably, trace amounts of N^1, N^2 -di($o\text{-CH}_3\text{C}_6\text{H}_4$)ethylene-1,2-diamine remained in the synthesized precursor $\text{DAB}^{o\text{-tol}}\text{-Br}$, which were transferred into the reaction mixture in liquid ammonia by weighing in the precursor. Even though an exact formation mechanism for the generation of the amide cannot be determined, the generation of amides in liquid ammonia or ethylenediamine is an oftentimes described process.^[8-11]

The two crystallographically independent anions (**1a**, **1b**) are quite similarly species. The interatomic distances of the central ethanediamine groups [C1-C2 1.517(11) Å, C17-C18 1.531(10) Å, C1-N1 1.451(9) Å, C3-N3 1.459(8) Å, C2-N2 1.461(10) Å, C18-N4 1.464(9) Å] clearly indicate single bonds. Also, the torsion angles of the two amine substituents around the C1-C2 and C17-C18 bonds of ethane of 55.6° and 54.9°, respectively, are in the expected range for this. In contrast, the N-C bonds to the aryl groups of 1.343(9) Å (N1-C3), 1.403(9) Å (N2-C10), 1.353(9) Å (N3-C19), and 1.390(9) Å (N4-C26) are significantly shorter, also shorter than those in related compounds such as *o*-methylaniline (N-C 1.447 Å),^[12] suggesting a partial double bond character, which is even slightly stronger expressed for the negatively charged N atom. This is supported by the torsion angles of the substituents of the N-C(aryl) bond, which are nearly planar around the amide N atom at 179.3° (**1a**) and 179.5° (**1b**), and deviate only slightly from planarity even with a protonated N atom [156.9° (**1a**) and 166.5° (**1b**)]. The relative inclination of the planes of the aromatic rings is 33.7° (**1a**) and 41.3° (**1b**).

The potassium cations are coordinated by [18]crown-6 molecules and are located in the molecular plane. The mean interatomic distances K-O, C-O, and C-C were determined to 2.814 Å, 1.431 Å, and 1.506 Å, respectively. Additionally, there are ammonia molecules on both sides of the crown ether ring planes, which partly coordinate the cations. For K2, two NH_3 molecules are observed at distances of 2.852(9) Å (N8) and 2.871(9) Å (N9), forming an almost linear $\text{H}_3\text{N-K-NH}_3$ unit with an angle of 168.6(3)°. K1 is coordinated by an NH_3 molecule at 2.851(8) Å, while on the opposite side of the molecule there are NH_3 molecules at a greater distance from the K^+ ion, which form hydrogen bonds to oxygen atoms of the crown ether

molecule.^[13] The longish anions are arranged with their major extension roughly along the crystallographic *c* (**1a**) or *a* axis (**1b**) and stacked in the *b* direction, respectively. The cation complexes and the solvent molecules are located in the channels parallel to *b* formed in this way.

Table 2. Fractional atomic coordinates and equivalent isotropic displacement parameters (Å²). Hydrogen atoms are not included.

	<i>x</i>	<i>y</i>	<i>z</i>	<i>U</i> _{eq}
N1	0.0377(3)	0.7889(7)	0.1739(3)	0.0422(12)
C1	0.0781(4)	0.6477(9)	0.1624(3)	0.0474(16)
C2	0.0683(4)	0.5156(8)	0.2067(3)	0.0459(15)
N2	0.0892(3)	0.5747(8)	0.2686(3)	0.0451(13)
C3	0.0432(3)	0.9153(8)	0.1380(3)	0.0402(14)
C4	0.0050(4)	1.0635(9)	0.1467(3)	0.0472(16)
C5	0.0092(4)	1.1952(9)	0.1101(3)	0.0480(16)
C6	0.0492(4)	1.1947(9)	0.0638(3)	0.0520(17)
C7	0.0872(4)	1.0581(10)	0.0546(3)	0.0501(17)
C8	0.0843(3)	0.9210(8)	0.0900(3)	0.0444(15)
C9	-0.0393(5)	1.0667(10)	0.1956(4)	0.059(2)
C10	0.0796(4)	0.4788(8)	0.3179(3)	0.0448(15)
C11	0.0742(3)	0.5489(9)	0.3738(3)	0.0461(15)
C12	0.0652(4)	0.4476(10)	0.4214(4)	0.0545(18)
C13	0.0620(5)	0.2828(10)	0.4155(4)	0.0589(19)
C14	0.0691(4)	0.2147(9)	0.3614(4)	0.0560(19)
C15	0.0769(4)	0.3102(9)	0.3124(4)	0.0497(16)
C16	0.0758(5)	0.7287(9)	0.3804(4)	0.0568(19)
N3	0.5433(3)	0.1425(7)	0.1096(3)	0.0415(12)
C17	0.5542(4)	0.2994(8)	0.0840(3)	0.0426(14)
C18	0.4921(4)	0.4121(8)	0.0912(3)	0.0458(15)
N4	0.4243(3)	0.3337(7)	0.0639(3)	0.0435(13)
C19	0.5945(3)	0.0323(8)	0.1040(3)	0.0423(14)
C20	0.5888(4)	-0.1278(8)	0.1273(3)	0.0426(14)
C21	0.6411(5)	-0.2421(10)	0.1236(4)	0.0558(18)
C22	0.7006(5)	-0.2101(11)	0.0989(5)	0.068(2)
C23	0.7090(4)	-0.0556(12)	0.0758(5)	0.068(2)
C24	0.6566(4)	0.0612(10)	0.0765(4)	0.0539(18)
C25	0.5251(4)	-0.1643(9)	0.1570(4)	0.0557(18)
C26	0.3578(4)	0.4100(8)	0.0596(3)	0.0410(14)
C27	0.2938(4)	0.3162(8)	0.0449(3)	0.0425(14)
C28	0.2276(4)	0.3958(10)	0.0356(3)	0.0515(17)
C29	0.2218(4)	0.5615(9)	0.0416(4)	0.0539(18)
C30	0.2843(4)	0.6516(9)	0.0581(4)	0.0525(17)
C31	0.3521(4)	0.5769(8)	0.0674(3)	0.0451(15)
C32	0.2985(4)	0.1345(9)	0.0411(3)	0.0501(16)

Table 2 continued

K1	0.36436(7)	0.21464(19)	0.32711(7)	0.0464(4)
O1	0.2405(3)	0.1667(7)	0.2405(2)	0.0561(13)
O2	0.3322(3)	0.4312(6)	0.2290(2)	0.0510(12)
O3	0.4354(2)	0.5128(6)	0.3322(2)	0.0459(11)
O4	0.4864(2)	0.2713(6)	0.4198(2)	0.0447(11)
O5	0.3968(3)	-0.0033(6)	0.4244(2)	0.0469(11)
O6	0.2963(3)	-0.0873(6)	0.3183(2)	0.0516(12)
C33	0.2344(4)	0.2585(12)	0.1868(4)	0.060(2)
C34	0.2570(4)	0.4279(11)	0.2027(4)	0.059(2)
C35	0.3594(5)	0.5892(10)	0.2397(4)	0.060(2)
C36	0.4361(5)	0.5814(9)	0.2742(4)	0.0563(18)
C37	0.5048(4)	0.5150(9)	0.3708(4)	0.0546(18)
C38	0.4989(4)	0.4388(9)	0.4301(4)	0.0508(17)
C39	0.4814(4)	0.1898(9)	0.4748(3)	0.0510(17)
C40	0.4673(4)	0.0143(10)	0.4617(4)	0.0546(18)
C41	0.3819(5)	-0.1664(9)	0.4057(4)	0.0571(19)
C42	0.3044(5)	-0.1755(10)	0.3736(4)	0.061(2)
C43	0.2227(4)	-0.0832(12)	0.2878(4)	0.063(2)
C44	0.2183(4)	0.0027(12)	0.2285(4)	0.067(2)
N5	0.2640(4)	0.3465(12)	0.3948(4)	0.080(2)
N6	0.4340(4)	0.1482(9)	0.2097(3)	0.0642(18)
N7	0.5315(6)	-0.0043(13)	0.3260(5)	0.098(3)
K2	0.78874(8)	0.29735(19)	0.38429(7)	0.0499(4)
O7	0.7129(3)	0.2303(7)	0.2689(2)	0.0539(12)
O8	0.8028(3)	-0.0090(7)	0.3326(2)	0.0550(12)
O9	0.8911(3)	0.0873(6)	0.4417(2)	0.0494(11)
O10	0.8481(3)	0.3504(6)	0.5069(2)	0.0507(12)
O11	0.7696(3)	0.5970(6)	0.4397(3)	0.0574(13)
O12	0.6743(3)	0.5073(6)	0.3320(2)	0.0545(12)
C45	0.7085(5)	0.0657(11)	0.2523(4)	0.061(2)
C46	0.7824(5)	-0.0086(11)	0.2680(4)	0.062(2)
C47	0.8761(5)	-0.0672(12)	0.3506(5)	0.070(2)
C48	0.8910(5)	-0.0722(10)	0.4191(4)	0.064(2)
C49	0.9022(4)	0.0896(10)	0.5060(3)	0.0552(19)
C50	0.9141(4)	0.2596(12)	0.5280(4)	0.060(2)
C51	0.8576(4)	0.5139(10)	0.5244(4)	0.0576(19)
C52	0.7858(5)	0.5990(10)	0.5049(4)	0.062(2)
C53	0.7044(5)	0.6816(11)	0.4166(5)	0.072(3)
C54	0.6902(5)	0.6696(10)	0.3485(5)	0.069(2)
C55	0.6578(5)	0.4885(12)	0.2670(4)	0.066(2)
C56	0.6450(4)	0.3130(12)	0.2523(4)	0.062(2)
N8	0.8899(4)	0.4399(14)	0.3199(5)	0.101(3)
N9	0.6663(4)	0.1920(12)	0.4337(4)	0.087(3)
N10	0.8830(4)	0.6655(9)	0.2025(4)	0.0683(19)

Table 2 continued

N11	0.7914(5)	0.3377(13)	0.1559(4)	0.094(3)
-----	-----------	------------	-----------	----------

Table 3. Anisotropic atomic displacement parameters (\AA^2).

	U^{11}	U^{22}	U^{33}	U^{12}	U^{13}	U^{23}
N1	0.042(3)	0.042(3)	0.040(3)	-0.002(2)	0.000(2)	0.003(2)
C1	0.039(3)	0.052(4)	0.048(4)	-0.006(3)	0.002(3)	0.005(3)
C2	0.042(3)	0.039(3)	0.056(4)	-0.006(3)	0.007(3)	0.000(3)
N2	0.045(3)	0.037(3)	0.051(3)	-0.001(3)	0.004(2)	0.000(3)
C3	0.031(3)	0.044(3)	0.040(3)	-0.003(3)	-0.006(2)	-0.002(3)
C4	0.042(3)	0.049(4)	0.048(4)	-0.011(3)	0.001(3)	-0.006(3)
C5	0.044(3)	0.044(4)	0.051(4)	-0.009(3)	-0.004(3)	-0.002(3)
C6	0.052(4)	0.050(4)	0.048(4)	0.003(3)	-0.006(3)	-0.010(3)
C7	0.042(3)	0.061(5)	0.047(4)	-0.008(3)	0.006(3)	-0.013(3)
C8	0.038(3)	0.044(4)	0.048(4)	-0.004(3)	-0.002(3)	0.001(3)
C9	0.062(5)	0.043(4)	0.075(5)	-0.009(4)	0.017(4)	0.002(3)
C10	0.035(3)	0.042(4)	0.054(4)	0.003(3)	0.001(3)	0.002(3)
C11	0.034(3)	0.049(4)	0.053(4)	0.001(3)	-0.001(3)	-0.001(3)
C12	0.049(4)	0.060(5)	0.052(4)	0.001(3)	0.002(3)	-0.006(3)
C13	0.054(4)	0.055(5)	0.064(5)	0.012(4)	0.003(4)	-0.003(4)
C14	0.053(4)	0.040(4)	0.074(5)	0.010(4)	0.009(4)	0.002(3)
C15	0.050(4)	0.043(4)	0.053(4)	0.003(3)	0.002(3)	0.003(3)
C16	0.062(5)	0.049(4)	0.056(4)	-0.008(3)	0.002(4)	-0.005(4)
N3	0.038(3)	0.039(3)	0.043(3)	0.002(2)	-0.005(2)	0.002(2)
C17	0.039(3)	0.038(3)	0.047(4)	0.005(3)	-0.002(3)	-0.002(3)
C18	0.043(3)	0.041(4)	0.049(4)	0.001(3)	-0.002(3)	-0.002(3)
N4	0.038(3)	0.036(3)	0.053(3)	0.000(3)	-0.001(2)	0.001(2)
C19	0.035(3)	0.042(3)	0.045(4)	-0.006(3)	-0.005(3)	0.000(3)
C20	0.047(4)	0.039(3)	0.039(3)	-0.007(3)	-0.002(3)	0.001(3)
C21	0.065(5)	0.045(4)	0.051(4)	-0.002(3)	-0.005(3)	0.014(4)
C22	0.052(4)	0.066(6)	0.082(6)	-0.009(5)	0.004(4)	0.024(4)
C23	0.046(4)	0.074(6)	0.084(6)	-0.014(5)	0.013(4)	0.009(4)
C24	0.043(4)	0.057(5)	0.061(5)	0.005(4)	0.007(3)	0.002(3)
C25	0.061(4)	0.041(4)	0.063(5)	0.002(3)	0.005(4)	0.001(3)
C26	0.044(3)	0.037(3)	0.039(3)	0.004(3)	0.002(3)	0.006(3)
C27	0.044(3)	0.044(4)	0.038(3)	0.001(3)	0.003(3)	0.002(3)
C28	0.041(4)	0.059(5)	0.053(4)	0.001(3)	0.002(3)	0.001(3)
C29	0.049(4)	0.047(4)	0.060(5)	0.009(3)	-0.003(3)	0.012(3)
C30	0.058(4)	0.039(4)	0.058(4)	0.001(3)	0.007(3)	0.010(3)

Table 3 continued

C31	0.052(4)	0.033(3)	0.048(4)	0.002(3)	0.003(3)	0.003(3)
C32	0.045(4)	0.049(4)	0.053(4)	-0.004(3)	0.001(3)	-0.004(3)
K1	0.0431(7)	0.0475(8)	0.0431(8)	0.0017(6)	-0.0066(6)	-0.0022(6)
O1	0.043(3)	0.076(4)	0.043(3)	-0.013(3)	-0.006(2)	0.003(2)
O2	0.051(3)	0.051(3)	0.047(3)	0.000(2)	-0.001(2)	0.014(2)
O3	0.044(2)	0.044(3)	0.048(3)	0.002(2)	0.003(2)	0.000(2)
O4	0.045(2)	0.043(3)	0.042(2)	-0.004(2)	-0.003(2)	0.000(2)
O5	0.049(3)	0.037(2)	0.051(3)	0.001(2)	-0.001(2)	0.004(2)
O6	0.047(3)	0.053(3)	0.052(3)	-0.007(2)	0.003(2)	-0.014(2)
C33	0.045(4)	0.083(6)	0.044(4)	-0.002(4)	-0.009(3)	0.016(4)
C34	0.053(4)	0.075(6)	0.044(4)	0.002(4)	-0.007(3)	0.028(4)
C35	0.084(6)	0.047(4)	0.046(4)	0.005(3)	0.005(4)	0.015(4)
C36	0.071(5)	0.045(4)	0.054(4)	0.002(3)	0.013(4)	-0.009(4)
C37	0.041(4)	0.044(4)	0.075(5)	-0.004(4)	0.001(3)	-0.006(3)
C38	0.048(4)	0.041(4)	0.056(4)	-0.006(3)	-0.009(3)	0.001(3)
C39	0.047(4)	0.057(4)	0.043(4)	-0.003(3)	-0.006(3)	0.000(3)
C40	0.046(4)	0.054(4)	0.058(5)	0.009(4)	-0.006(3)	0.003(3)
C41	0.073(5)	0.043(4)	0.055(4)	0.000(3)	0.012(4)	0.003(4)
C42	0.078(6)	0.056(5)	0.051(4)	-0.004(4)	0.015(4)	-0.018(4)
C43	0.047(4)	0.075(6)	0.067(5)	-0.015(4)	0.009(4)	-0.018(4)
C44	0.043(4)	0.087(6)	0.063(5)	-0.026(5)	-0.008(3)	-0.012(4)
N5	0.062(4)	0.107(7)	0.076(5)	-0.007(5)	0.021(4)	-0.002(4)
N6	0.062(4)	0.061(4)	0.068(4)	0.007(3)	0.007(3)	0.021(3)
N7	0.128(9)	0.081(6)	0.091(7)	0.002(5)	0.032(6)	0.001(6)
K2	0.0481(8)	0.0501(9)	0.0451(8)	0.0021(7)	-0.0082(6)	0.0032(7)
O7	0.044(3)	0.065(3)	0.046(3)	0.000(2)	-0.009(2)	-0.006(2)
O8	0.047(3)	0.061(3)	0.055(3)	-0.006(3)	0.004(2)	0.003(2)
O9	0.046(2)	0.047(3)	0.051(3)	0.003(2)	-0.003(2)	0.002(2)
O10	0.039(2)	0.056(3)	0.052(3)	-0.005(2)	-0.004(2)	0.007(2)
O11	0.050(3)	0.051(3)	0.068(3)	-0.002(3)	0.001(2)	0.005(2)
O12	0.047(3)	0.053(3)	0.057(3)	0.012(2)	-0.007(2)	0.002(2)
C45	0.068(5)	0.065(5)	0.046(4)	-0.009(4)	-0.002(4)	-0.018(4)
C46	0.074(5)	0.063(5)	0.049(4)	-0.006(4)	0.012(4)	-0.008(4)
C47	0.054(5)	0.060(5)	0.092(7)	-0.016(5)	0.002(4)	0.009(4)
C48	0.054(4)	0.054(5)	0.076(6)	0.001(4)	-0.007(4)	0.013(4)
C49	0.051(4)	0.067(5)	0.043(4)	0.010(4)	-0.005(3)	0.008(4)
C50	0.039(4)	0.088(6)	0.044(4)	-0.004(4)	-0.011(3)	0.014(4)
C51	0.057(4)	0.059(5)	0.051(4)	-0.007(4)	-0.006(3)	-0.007(4)
C52	0.066(5)	0.048(4)	0.074(6)	-0.010(4)	0.015(4)	0.003(4)

Table 3 continued

C53	0.049(4)	0.052(5)	0.109(8)	-0.008(5)	-0.002(5)	0.012(4)
C54	0.056(4)	0.051(4)	0.089(7)	0.017(4)	-0.017(4)	0.001(4)
C55	0.053(4)	0.079(6)	0.062(5)	0.027(4)	-0.004(4)	0.007(4)
C56	0.041(4)	0.088(6)	0.050(4)	0.009(4)	-0.010(3)	0.003(4)
N8	0.050(4)	0.134(9)	0.113(8)	0.034(7)	0.001(4)	-0.006(5)
N9	0.060(5)	0.103(7)	0.099(7)	0.028(5)	0.012(4)	0.015(4)
N10	0.065(4)	0.070(5)	0.073(5)	-0.005(4)	0.018(4)	0.000(4)
N11	0.098(6)	0.104(7)	0.080(6)	0.012(5)	0.019(5)	-0.043(5)

Table 4. Geometric parameters (Å, °).

Atoms	Distances	Atoms	Distances
N1—C3	1.343(9)	C26—C27	1.423(10)
N1—C1	1.451(9)	K1—N6	3.201(7)
C1—C2	1.517(11)	O1—C33	1.416(10)
C2—N2	1.461(10)	O1—C44	1.441(11)
N2—C10	1.403(9)	O2—C35	1.418(10)
N2—H2	0.80(9)	O2—C34	1.429(9)
C3—C8	1.437(10)	O3—C36	1.426(9)
C3—C4	1.461(10)	O3—C37	1.427(9)
C4—C5	1.382(11)	O4—C39	1.427(9)
C4—C9	1.495(11)	O4—C38	1.429(8)
C5—C6	1.392(11)	O5—C41	1.437(9)
C6—C7	1.380(11)	O5—C40	1.440(9)
C7—C8	1.400(11)	O6—C43	1.426(9)
C10—C11	1.406(11)	O6—C42	1.429(10)
C10—C15	1.412(10)	C33—C34	1.500(13)
C11—C12	1.398(11)	C35—C36	1.509(12)
C11—C16	1.507(10)	C37—C38	1.499(12)
C12—C13	1.382(12)	C39—C40	1.508(11)
C13—C14	1.370(13)	C41—C42	1.504(12)
C14—C15	1.389(12)	C43—C44	1.502(14)
N3—C19	1.353(9)	K2—O9	2.743(5)
N3—C17	1.459(8)	K2—O7	2.777(5)
C17—C18	1.531(10)	K2—O10	2.810(5)
C18—N4	1.464(9)	K2—O8	2.840(6)
N4—C26	1.390(9)	K2—O11	2.845(6)
N4—H4	0.87(10)	K2—N8	2.852(9)
C19—C24	1.439(10)	K2—O12	2.855(5)
C19—C20	1.446(10)	K2—N9	2.871(9)
C20—C21	1.383(10)	O7—C45	1.422(10)
C20—C25	1.505(11)	O7—C56	1.439(9)
C21—C22	1.363(13)	O8—C46	1.432(10)
C22—C23	1.408(14)	O8—C47	1.446(10)

Table 4 continued

C23—C24	1.388(11)	O9—C49	1.421(9)
C26—C31	1.410(9)	O9—C48	1.424(10)
C27—C28	1.392(10)	O10—C51	1.422(10)
C27—C32	1.522(10)	O10—C50	1.457(9)
C28—C29	1.395(11)	O11—C53	1.427(9)
C29—C30	1.388(11)	O11—C52	1.440(11)
C30—C31	1.399(10)	O12—C54	1.421(11)
K1—O1	2.777(5)	O12—C55	1.443(10)
K1—O3	2.816(5)	C45—C46	1.504(13)
K1—O6	2.816(5)	C47—C48	1.514(14)
K1—O5	2.823(5)	C49—C50	1.505(13)
K1—O2	2.829(5)	C51—C52	1.516(12)
K1—O4	2.842(5)	C53—C54	1.506(15)
K1—N5	2.851(8)	C55—C56	1.510(14)

Atoms	Angles [°]	Atoms	Angles [°]
C3—N1—C1	115.4(6)	C33—O1—K1	116.5(5)
N1—C1—C2	110.1(6)	C44—O1—K1	116.4(4)
N2—C2—C1	109.6(6)	C35—O2—C34	112.7(6)
C10—N2—C2	120.5(6)	C35—O2—K1	116.3(4)
N1—C3—C8	126.0(6)	C34—O2—K1	111.3(5)
N1—C3—C4	119.3(6)	C36—O3—C37	112.9(6)
C8—C3—C4	114.7(6)	C36—O3—K1	113.6(4)
C5—C4—C3	120.7(6)	C37—O3—K1	114.2(4)
C5—C4—C9	121.5(7)	C39—O4—C38	111.2(5)
C3—C4—C9	117.8(7)	C39—O4—K1	112.5(4)
C4—C5—C6	122.7(7)	C38—O4—K1	111.6(4)
C7—C6—C5	118.6(7)	C41—O5—C40	112.1(6)
C6—C7—C8	121.0(7)	C41—O5—K1	112.3(4)
C7—C8—C3	122.4(6)	C40—O5—K1	115.5(4)
N2—C10—C11	120.5(6)	C43—O6—C42	111.7(6)
N2—C10—C15	120.5(7)	C43—O6—K1	113.6(5)
C11—C10—C15	119.0(7)	C42—O6—K1	115.1(4)
C12—C11—C10	118.1(7)	O1—C33—C34	109.4(6)
C12—C11—C16	122.0(7)	O2—C34—C33	109.4(6)
C10—C11—C16	119.9(7)	O2—C35—C36	109.1(6)
C13—C12—C11	122.5(8)	O3—C36—C35	108.7(6)
C14—C13—C12	119.2(8)	O3—C37—C38	109.0(6)
C13—C14—C15	120.4(7)	O4—C38—C37	108.0(6)
C14—C15—C10	120.7(8)	O4—C39—C40	109.4(6)
C19—N3—C17	114.8(6)	O5—C40—C39	108.8(6)
N3—C17—C18	110.1(6)	O5—C41—C42	108.0(6)
N4—C18—C17	107.7(6)	O6—C42—C41	109.3(6)
C26—N4—C18	121.8(6)	O6—C43—C44	109.1(6)

Table 4 continued			
N3—C19—C24	125.0(7)	O1—C44—C43	108.7(7)
N3—C19—C20	119.6(6)	O9—K2—O7	120.41(17)
C24—C19—C20	115.5(6)	O9—K2—O10	61.41(15)
C21—C20—C19	120.9(7)	O7—K2—O10	171.96(17)
C21—C20—C25	121.3(7)	O9—K2—O8	60.49(15)
C19—C20—C25	117.7(6)	O7—K2—O8	60.48(16)
C22—C21—C20	122.4(8)	O10—K2—O8	119.50(16)
C21—C22—C23	119.0(7)	O9—K2—O11	119.33(16)
C24—C23—C22	120.7(8)	O7—K2—O11	120.05(17)
C23—C24—C19	121.4(8)	O10—K2—O11	59.50(16)
N4—C26—C31	122.1(6)	O8—K2—O11	177.01(18)
N4—C26—C27	118.4(6)	O9—K2—N8	91.7(2)
C31—C26—C27	119.4(6)	O7—K2—N8	83.5(2)
C28—C27—C26	117.8(6)	O10—K2—N8	104.4(2)
C28—C27—C32	121.8(6)	O8—K2—N8	92.7(3)
C26—C27—C32	120.4(6)	O11—K2—N8	90.3(3)
C27—C28—C29	122.9(7)	O9—K2—O12	174.89(17)
C30—C29—C28	119.0(7)	O7—K2—O12	61.30(17)
C29—C30—C31	120.2(7)	O10—K2—O12	116.16(16)
C30—C31—C26	120.6(7)	O8—K2—O12	120.22(17)
O1—K1—O3	119.13(17)	O11—K2—O12	59.65(16)
O1—K1—O6	60.64(17)	N8—K2—O12	93.3(2)
O3—K1—O6	177.69(16)	O9—K2—N9	99.5(2)
O1—K1—O5	118.98(17)	O7—K2—N9	89.3(2)
O3—K1—O5	120.24(15)	O10—K2—N9	82.6(2)
O6—K1—O5	60.62(15)	O8—K2—N9	91.4(3)
O1—K1—O2	60.91(17)	O11—K2—N9	85.7(3)
O3—K1—O2	59.98(15)	N8—K2—N9	168.6(3)
O6—K1—O2	119.14(16)	O12—K2—N9	75.5(2)
O5—K1—O2	179.56(16)	C45—O7—C56	112.9(6)
O1—K1—O4	176.92(16)	C45—O7—K2	115.8(4)
O3—K1—O4	60.64(14)	C56—O7—K2	115.1(5)
O6—K1—O4	119.73(15)	C46—O8—C47	110.4(6)
O5—K1—O4	60.56(14)	C46—O8—K2	112.6(5)
O2—K1—O4	119.58(15)	C47—O8—K2	110.1(5)
O1—K1—N5	83.0(2)	C49—O9—C48	111.4(6)
O3—K1—N5	89.6(2)	C49—O9—K2	115.4(4)
O6—K1—N5	92.6(2)	C48—O9—K2	118.4(4)
O5—K1—N5	84.6(2)	C51—O10—C50	110.7(6)
O2—K1—N5	95.8(2)	C51—O10—K2	115.4(4)
O4—K1—N5	94.0(2)	C50—O10—K2	113.5(4)
O1—K1—N6	79.33(17)	C53—O11—C52	111.9(7)
O3—K1—N6	85.63(18)	C53—O11—K2	116.4(5)
O6—K1—N6	92.08(18)	C52—O11—K2	115.8(4)

Table 4 continued

O5—K1—N6	117.63(17)	C54—O12—C55	111.3(6)
O2—K1—N6	61.94(16)	C54—O12—K2	111.7(4)
O4—K1—N6	103.62(17)	C55—O12—K2	110.8(5)
N5—K1—N6	156.4(2)	O7—C45—C46	109.2(6)
C33—O1—C44	112.3(6)		

Acknowledgements

CW thanks the Deutsche Forschungsgemeinschaft (DFG, German Research Foundation, project number 245845833) within the International Research Training Group IRTG 2022 (ATUMS) for funding. Furthermore, CW thanks the Studienstiftung des Deutschen Volkes for granting a PhD scholarship.

References

- [1] Stoe & Cie GmbH: X-Area, Version 1.76. Stoe & Cie GmbH, Darmstadt, Germany **2017**.
- [2] G. M. Sheldrick, *A short history of SHELX*, *Acta Crystallogr. Sect. A: Found. Crystallogr.* **2008**, *64*, 112.
- [3] G. M. Sheldrick, *Crystal structure refinement with SHELXL*, *Acta Crystallogr. Sect. C: Struct. Chem.* **2015**, *71*, 3.
- [4] K. Brandenburg, Diamond Version 3.2k, Crystal Impact GbR, Bonn, 2014.
- [5] C. Wallach, F. S. Geitner and T. F. Fässler, *FLP-type nitrile activation and cyclic ether ring-opening by halo-borane nonagermanide-cluster Lewis acid–base pairs*, *Chem. Sci.* **2021**, *12*, 6969.
- [6] Y. Segawa, Y. Suzuki, M. Yamashita and K. Nozaki, *Chemistry of boryllithium: synthesis, structure, and reactivity*, *J. Am. Chem. Soc.* **2008**, *130*, 16069.
- [7] T. Kottke and D. Stalke, *Crystal handling at low temperatures*, *J. Appl. Crystallogr.* **1993**, *26*, 615.
- [8] J. M. Goicoechea and S. C. Sevov, *Organozinc Derivatives of Deltahedral Zintl Ions: Synthesis and Characterization of closo-[E₉Zn(C₆H₅)]³⁻ (E = Si, Ge, Sn, Pb)*, *Organometallics* **2006**, *25*, 4530.
- [9] B. Zhou, M. S. Denning, C. Jones and J. M. Goicoechea, *Reductive cleavage of Zn–C bonds by group 14 Zintl anions: synthesis and characterisation of [E₉ZnR]³⁻ (E = Ge, Sn, Pb; R = Mes, ⁱPr)*, *Dalton Trans.* **2009**, 1571.
- [10] A. Ugrinov and S. C. Sevov, *Derivatization of Deltahedral Zintl Ions by Nucleophilic Addition: [Ph–Ge₉–SbPh₂]²⁻ and [Ph₂Sb–Ge₉–Ge₉–SbPh₂]⁴⁻*, *J. Am. Chem. Soc.* **2003**, *125*, 14059.
- [11] C. Wallach, K. Mayer, T. Henneberger, W. Klein and T. Fässler, *Intermediates and products of the reaction of Zn (II) organyls with tetrel element Zintl ions: cluster extension versus complexation*, *Dalton Trans.* **2020**, *49*, 6191.
- [12] S. Nishikiori and T. Iwamoto, *Crystal structure of the Hofmann-dma type clathrate*, *J. Struct. Chem.* **1999**, *40*, 726.
- [13] T. Henneberger, W. Klein and T. F. Fässler, *Crystal structure of (1,4,7,10,13,16-hexaoxacyclooctadecane-κ⁶O₆)1,2,3,4,5-pentamethyl-cyclopenta-2,4-dien-1-yl(potassium, rubidium)—ammonia(1/2)*, *[K_{0.3}Rb_{0.7}(18-crown-6)]Cp*·2NH₃, C₂₂H₄₅K_{0.3}N₂O₆Rb_{0.7}*, *Z. Kristallogr., New Cryst. Struct.* **2019**, *234*, 1241.

6.5 FLP-type Nitrile Activation and Cyclic Ether Ring-Opening by Halo Borane Nonagermanide-Cluster Lewis Acid–Base Pairs

C. Wallach,[‡] F. S. Geitner,[‡] and T. F. Fässler

[‡]: authors contributed equally to this work.

Published in: *Chemical Science* **2021**, *12*, 6969.

© The Royal Society of Chemistry 2021, unchanged reprinted version licensed under the terms of a Creative Commons Attribution-Non Commercial 3.0 Unported License. Reproduced with permission from the Royal Society of Chemistry.

Access online *via*: <https://pubs.rsc.org/en/content/articlehtml/2021/sc/d1sc00811k>.

Contents and Contributions

The reaction of the twofold silylated cluster $[\text{Ge}_9\{\text{Si}(\text{TMS})_3\}_2]^{2-}$ with bromo-1,3,2-diazaborolidines $\text{DAB}^{\text{Mes}}\text{-Br}$ or the bromo-1,3,2-diazaborole $\text{DAB}(\text{II})^{\text{Dipp}}\text{-Br}$ in the cyclic ethers trimethylene oxide or tetrahydrofuran ($n = 3$ or 4 , respectively) yielded the monoanionic species $[\text{Ge}_9\{\text{Si}(\text{TMS})_3\}_2(\text{CH}_2)_n\text{O-DAB}^{\text{R}}]^-$ (**2a** to **5a**). Further organic wingtip substituents at the $\text{DAB}^{\text{R}}\text{-Br}$ precursors were tested ($R = o\text{-tol}$, $o\text{-xyl}$, Dipp), as well as the acyclic bromo-borane $(\text{N}^i\text{Pr}_2)_2\text{B-Br}$ revealing the same reactivity. The formed anions were investigated by ESI-MS analysis and the anions **3a** to **5a** were crystallized as the potassium salts $[\text{DAB}(\text{II})^{\text{Dipp}}, n = 4$ (**4a**); $R = \text{Mes}$, $n = 4$ (**3a**), $n = 3$ (**5a**)]. Further ESI-MS studies were conducted using deuterated tetrahydrofuran as solvent, and indeed the mass peaks of the respective monoanionic species shifted to higher values. To obtain insights into the reactions leading to the incorporation of ring-opened ether fragments, all bromo-boranes were reacted with thf in absence of any cluster species, and the formation of the ring-opened molecules $\text{DAB}^{\text{R}}\text{-O}(\text{CH}_2)_4\text{-Br}$ was observed in ^1H NMR spectroscopic investigations. Consequently, the observed reactions can be explained as a two-step mechanism, involving the formation of ring-opened bromides and a subsequent $\text{S}_{\text{N}}2$ -like attack of the cluster. In contrast, the bromo-boranes reveal no reactivity towards other polar molecules like acetonitrile. However, upon adding the twofold silylated cluster to a mixture of the bromo-diazaborolidine $\text{DAB}^{\text{Mes}}\text{-Br}$ and acetonitrile, the formation of the species $[\text{Ge}_9\{\text{Si}(\text{TMS})_3\}_2\{\text{MeC=N}\}\text{DAB}^{\text{Mes}}]^-$ (**6a**) was observed. The incorporation of an imine entity was further proven by single crystal structure analysis as well as in ESI-MS deuteration experiments. Due to the inertness of the bromo-diazaborolidine towards the nitrile, the incorporation of the imine is supposed to follow a frustrated Lewis acid-base-like mechanism, with the cluster acting as Lewis base and the borane as Lewis acid.

The experimental work was equally divided between Dr. Felix S. Geitner and me, including the acquisition and evaluation of spectroscopic and mass spectrometric (deuteration) data. Single crystals were grown, and the single crystal structures were refined by Dr. Felix S. Geitner (**3a**, **4a**, **6a**) and me (**5a**). Reactivity tests of the bromo-boranes towards tetrahydrofuran and acetonitrile in absence of any cluster species were done by me. Elemental analysis data were acquired by Ulrike Ammari and Bircan Dilki in the microanalytical laboratory of the Chemistry Department of the Technical University of Munich. Variable-temperature NMR data were acquired by M. Sc. Kevin Frankiewicz. A first version of the manuscript was authored in cooperation of Dr. Felix S. Geitner and me, after its initial rejection I restructured the manuscript and rewrote parts of it. Dr. Felix S. Geitner and Dr. Annette Schier proof-read the final version of the manuscript. The publication of the manuscript was managed by Prof. Dr. Thomas F. Fässler, the peer-review process including corrections was a joined task accomplished by Prof. Dr. Thomas F. Fässler and me.

Cite this: *Chem. Sci.*, 2021, 12, 6969

All publication charges for this article have been paid for by the Royal Society of Chemistry

FLP-type nitrile activation and cyclic ether ring-opening by halo-borane nonagermanide-cluster Lewis acid–base pairs†

Christoph Wallach,‡ Felix S. Geitner‡ and Thomas F. Fässler *

Even though homoatomic nine-atom germanium clusters are known for two decades, their chemical properties are still rarely investigated. We now discovered that Zintl ion main group-element clusters possess a reactive lone pair of electrons, and we show a new pathway to bind ligands with functional groups to the $[\text{Ge}_9]$ cluster core through Ge–C bond formation. We report on the reactivity of $[\text{Ge}_9\{\text{Si}(\text{TMS})_3\}_2]^{2-}$ (TMS = trimethylsilyl) towards a series of Lewis acidic bromo-boranes. The reaction of $[\text{Ge}_9\{\text{Si}(\text{TMS})_3\}_2]^{2-}$ and $\text{DAB}^{\text{o-tol}}-\text{Br}$ (DAB = 1,3,2-diazaborolidine; o-tol = 2-methylphenyl) resulted, depending on the reaction protocol, either in the formation of $[\text{Ge}_9\{\text{Si}(\text{TMS})_3\}_2\text{DAB}^{\text{o-tol}}]^-$ (**1a**) with direct Ge–B interactions, or in $[\text{Ge}_9\{\text{Si}(\text{TMS})_3\}_2(\text{CH}_2)_4\text{O}-\text{DAB}^{\text{o-tol}}]^-$ (**2a**) featuring a ring-opened thf moiety. Ring opening reactions occur for all bulkier $\text{DAB}^{\text{R}}-\text{Br}$ [R: o-xyl (2,6-dimethylphenyl), Mes (2,4,6-trimethylphenyl), Dipp (2,6-diisopropylphenyl)], $\text{DAB}^{(\text{t})\text{DIPP}}-\text{Br}$ and acyclic $(\text{Pr}_2\text{N})_2\text{BBr}$ without Ge–B bond formation as shown for the structural characterization of the ring-opened products of thf (**3**, **4**) and trimethylene oxide (**5**). In contrast to thf, the activation of CH_3CN requires the simultaneous presence of Lewis-acid and Lewis-basic reactants allowing the formation of $[\text{Ge}_9\{\text{Si}(\text{TMS})_3\}_2\text{CH}_3\text{C}\equiv\text{N}-\text{DAB}^{\text{Mes}}]^-$ (**6a**). Within the presented compounds, **3** and **4** show an unusual substitution pattern of the three ligands at the $[\text{Ge}_9]$ core in the solid state. The $[\text{Ge}_9]$ cluster/borane systems correspond to intermolecular frustrated Lewis pairs (FLPs), in which the $[\text{Ge}_9]$ cluster with several lone pairs represents the Lewis base, and the borane is the Lewis acid.

Received 9th February 2021

Accepted 2nd April 2021

DOI: 10.1039/d1sc00811k

rsc.li/chemical-science

Introduction

Main group element compounds and especially frustrated Lewis pairs (FLPs) have recently emerged in the field of small molecule activation. FLPs rely on a spatial separation of the Lewis-acidic and -basic sites preventing adduct formation and are known to interact with a plethora of different molecules including gasses, unsaturated systems or solvent molecules featuring polarizable bonds.^{1–4} For the latter, as examples the main group assisted opening of cyclic ethers^{5–9} or the reaction with nitriles,^{10–15} which is often accompanied by ring formation, can be quoted.

Recently, the idea that transition-metal free $[\text{Ge}_9]$ clusters might serve as Lewis base in Ge/boron based FLPs was put to

front¹⁶ and metal-functionalized $[\text{Ge}_9]$ -Zintl clusters have been employed as homogeneous catalysts, in which the Ge atoms serve as a “support” for the catalytically active transition metal.¹⁷ Homoatomic anionic nine-atom germanium clusters offer indeed a framework for a spatial arrangement of various functional groups and possess at least six Ge atoms with lone pairs pointing to the outside of the cage, resembling an overall six-fold Lewis base. Nonagermanide clusters are accessible in high yields and purity *via* fusion of stoichiometric amounts of K and Ge forming the Zintl phase K_4Ge_9 ^{18,19} containing discrete, extractable $[\text{Ge}_9]^{4-}$ anions.^{20–23} In heterogeneous reactions organic main group element fragments are bound to the $[\text{Ge}_9]$ core enhancing its solubility and stability. Thus, by treatment of solid K_4Ge_9 with stoichiometric amounts of an acetonitrile solution of chloro-tris(trimethylsilyl)silane the two- and three-fold silylated clusters $[\text{Ge}_9\{\text{Si}(\text{TMS})_3\}_2]^{2-}$ ²⁴ and $[\text{Ge}_9\{\text{Si}(\text{TMS})_3\}_3]^-$ ²⁵ are obtained, respectively. The transfer of this method to elusive $[\text{Si}_9]$ clusters in the phase $\text{K}_{12}\text{Si}_{17}$ yielding $[\text{Si}_9\{\text{SiR}_3\}_2]^{2-}$, $[\text{Si}_9\{\text{SiR}_3\}_3]^-$ (R = TMS, ^tBu₂H),^{26,27} $[\text{Si}_9\text{H}_2]^{2-}$,²⁸ and $[\text{Si}_9\text{H}]^{3-}$ ^{29,30} shows the huge potential of this synthetic protocol using polar intermetallic compounds (Zintl phases) as precursors.

The addition of functional groups such as silyl fragments^{24,31–35} to bare $[\text{Ge}_9]$ allowed for a stabilization and

Department Chemie, Technische Universität München, Lichtenbergstraße 4, 85747 Garching b. München, Germany. E-mail: thomas.faessler@lrz.tum.de

† Electronic supplementary information (ESI) available: Experimental details, crystallographic data of compounds **3–6**; selected bond lengths of compounds **3–6**; NMR spectra of **1–6** (¹H, ¹³C, ¹¹B, ²⁹Si; including VT NMR spectra of **3**); synthesis procedure for $\text{DAB}^{\text{R}}-\text{O}-(\text{CH}_2)_4-\text{Br}$ and $(\text{Pr}_2\text{N})_2\text{B}-\text{O}-(\text{CH}_2)_4-\text{Br}$ together with corresponding ¹H and ¹¹B NMR spectra; details on ESI MS sample preparation and spectra. CCDC 1993875–1993878. For ESI and crystallographic data in CIF or other electronic format see DOI: 10.1039/d1sc00811k

‡ Authors contributed equally to this work.



enhanced solubility of the cluster. Thus, mixed substituted clusters featuring various group 14 element fragments became accessible.^{36–41} However, the attachment of phosphanyl-moieties^{42–45} to $[\text{Ge}_9]$ showed that the clusters can be decorated with more interesting Lewis basic functional groups. Similarly of interest is the addition of a ligand comprising an electron-deficient boranyl moiety by our group.

The boranyl functionalization of $[\text{Ge}_9]$ clusters was achieved by the reaction of $[\text{Ge}_9\{\text{Si}(\text{TMS})_3\}_2]^{2-}$ with the heterocyclic chloro-boranes $\text{DAB}^{\text{R}}\text{-Cl}$ (R: Me, *i*Pr, *o*-tol; DAB: 1,3,2-diazaborolidine) yielding the anions $[\text{Ge}_9\{\text{Si}(\text{TMS})_3\}_2\text{DAB}^{\text{R}}]^-$, thus introducing Lewis acidic moieties to the cluster. In fact, quantum chemical calculations corroborated the anion $[\text{Ge}_9\{\text{Si}(\text{TMS})_3\}_2\text{BCy}_2]^-$ (Cy: cyclohexyl) to be an intramolecular frustrated Lewis acid–base pair (FLP), and its reactivity towards small molecules has been anticipated.¹⁶ Within the system B/Ge, a bis-amido germylene-based Lewis acid/base-related pair is the only reported example, to the best of our knowledge. Since a Ge–B adduct is formed in the ground state, it does not correspond to a typical FLP, but nevertheless, a cleavage of the C=O bond of ketones or isocyanates has been observed.⁴⁶

Triggered by the variety of reactions reported for FLP systems and on the basis of our recent achievements in combining boranes and $[\text{Ge}_9]$ clusters, we now investigated the reactivity of $[\text{Ge}_9\{\text{Si}(\text{TMS})_3\}_2]^{2-}$ as an appropriate Lewis base in combination with sterically hindered boron-based electrophiles, focusing on the reactivity towards molecules with polar groups. As boranes we applied the cyclic species $\text{DAB}^{\text{R}}\text{-Br}$ (R: *i*Pr, *o*-tol, *o*-xyl, Mes, Dipp) and $\text{DAB}(\text{ii})^{\text{DIPP}}\text{-Br}$ [(ii): unsaturated backbone] as well as acyclic (*i*Pr₂N)₂BBr, which (according to the acceptor number (AN) determined by the Gutmann–Beckett method) show an increased electrophilicity compared to the chloro-species used for the synthesis of the reported boranyl-functionalized clusters, thus featuring prerequisites for the formation of (reactive) FLPs.^{16,47–49} Within the presented reactions the transition metal-free Zintl ions can be regarded as an active component in small molecule activation.

Results and discussion

Ring-opening of tetrahydrofuran

The reaction of equimolar amounts of $[\text{Ge}_9\{\text{Si}(\text{TMS})_3\}_2]^{2-}$ and $\text{DAB}^{\text{o-tol}}\text{-Br}$ in 1,4-dioxane selectively yields anionic $[\text{Ge}_9\{\text{Si}(\text{TMS})_3\}_2\text{DAB}^{\text{o-tol}}]^-$ (**1a**). Besides the respective peak at m/z 1398.7 observed in the mass spectrum (Fig. S46[†]), the NMR data are congruent to the reaction product featuring a Ge–B bond as already reported for the reaction with $\text{DAB}^{\text{o-tol}}\text{-Cl}$ (Fig. 1a).¹⁶

In thf as solvent for the reaction, the ¹H NMR spectrum of the solid residue shows the presence of two distinct species, which are identified as anions **1a** and $[\text{Ge}_9\{\text{Si}(\text{TMS})_3\}_2(\text{CH}_2)_4\text{O-DAB}^{\text{o-tol}}]^-$, **2a** ($\delta = 0.24$ ppm, thf-*d*₈) in a 60 : 40 ratio (Fig. 1b). This ratio changes to 15 : 85 performing the reaction at 35 °C. At higher temperature we observe formation of $[\text{Ge}_9\{\text{Si}(\text{TMS})_3\}_3]^-$. To selectively yield anion **2a**, the bromo-borane is dissolved in thf in a first step and the bis-silylated cluster is added in a subsequent step leading to one single peak at m/z 1470.8

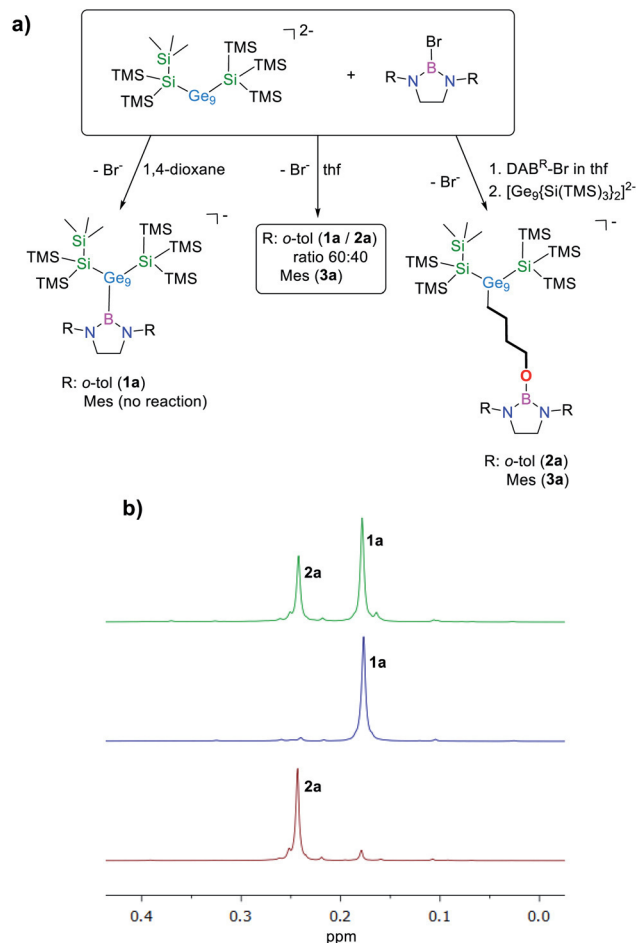


Fig. 1 (a) Reactivity of $[\text{Ge}_9\{\text{Si}(\text{TMS})_3\}_2]^{2-}$ towards $\text{DAB}^{\text{R}}\text{-Br}$ (R: *o*-tol, Mes) depending on the reaction conditions. (b) Selected areas of the ¹H NMR spectra of mixtures of **1a** and **2a** (top), pure **1a** (middle) and pure **2a** (bottom). All spectra were acquired in thf-*d*₈.

(Fig. S49[†]) in the ESI MS and the observation of one signal set in the ¹H NMR spectrum.

After redissolving the residues of analogous reactions performed in deuterated thf, an ESI mass peak at m/z 1478.8 (**2a-d**₈) is observed, indicative of the formation of the thf ring-opened species in which a $-(\text{CD}_2)_4\text{O}-$ moiety is attached to the $[\text{Ge}_9]$ cluster ion (Fig. S51[†]). It is noteworthy that pure **1a** does not react with thf under ring-opening. Using the sterically more hindered borane $\text{DAB}^{\text{Mes}}\text{-Br}$ resulted in a complete conversion of the reactants to one single species within 3 h at room temperature in thf, as shown by ¹H NMR investigations. Recrystallization of the crude product from toluene at -40 °C yielded red crystals suitable for single crystal X-ray diffraction, which were identified as $\text{K}[\text{Ge}_9\{\text{Si}(\text{TMS})_3\}_2(\text{CH}_2)_4\text{O-DAB}^{\text{Mes}}]^-$, **3** (Fig. 2a and 3a).

The anion **3a** originates from thf ring-opening and insertion between the cluster and the boranyl ligand through Ge–C and B–O bond formation, respectively. The formation is confirmed by ESI MS spectra obtained from the intermediate solid products of the reaction using thf and thf-*d*₈ as solvents, resulting in



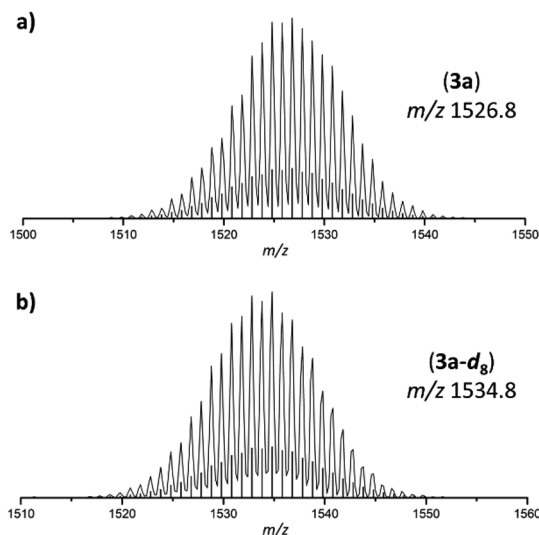


Fig. 2 Selected areas of ESI MS spectra (thf, negative-ion mode, 3500 V, 300 °C) of **3a** and **3a-d₈**. (a) Molecule peak of $[\text{Ge}_9\{\text{Si}(\text{TMS})_3\}_2(\text{CH}_2)_4\text{O}-\text{DAB}^{\text{Mes}}]^-$ (**3a**) at m/z 1526.8; (b) molecule peak of $[\text{Ge}_9\{\text{Si}(\text{TMS})_3\}_2(\text{CD}_2)_4\text{O}-\text{DAB}^{\text{Mes}}]^-$ (**3a-d₈**) at m/z 1534.8. Calculated isotope patterns are shown as black bars. Overview spectra are provided in the ESI.†

mass peaks at m/z 1526.8 (**3a**; Fig. 2a) and m/z 1534.8 (**3a-d₈**, Fig. 2b), respectively.

Similar reactions of $[\text{Ge}_9\{\text{Si}(\text{TMS})_3\}_2]^{2-}$ with $\text{DAB}(\text{II})^{\text{Dipp}}-\text{Br}$ yielded the respective anion $[\text{Ge}_9\{\text{Si}(\text{TMS})_3\}_2(\text{CH}_2)_4\text{O}-$

$\text{DAB}(\text{II})^{\text{Dipp}}]^-$ (**4a**), with observed molecule peaks at m/z 1608.8 (**4a**, Fig. S57†) and m/z 1616.8 (**4a-d₈**, Fig. S59†). Full conversion of the reactants occurs upon stirring the reaction mixture for three weeks at 35 °C (at r. t. no reaction is observed at all due to the increased steric demand of the Dipp rest if compared to a Mes group).⁵⁰ A more convenient access to **4a** was found by heating a solution of $\text{DAB}(\text{II})^{\text{Dipp}}-\text{Br}$ in thf to 70 °C for 2 days, followed by the addition of $[\text{Ge}_9\{\text{Si}(\text{TMS})_3\}_2]^{2-}$. Compound **4**, $\text{K}[\text{Ge}_9\{\text{Si}(\text{TMS})_3\}_2(\text{CH}_2)_4\text{O}-\text{DAB}(\text{II})^{\text{Dipp}}]$, was obtained by recrystallization of the crude material from toluene solution at -40 °C.

Compounds **3** and **4** crystallize in the triclinic space group $P\bar{1}$. In both compounds the bis-silylated clusters carry an additional ligand that comprises a ring-opened thf molecule which is further attached to the boranyl group through the oxygen atom. The $[\text{Ge}_9]$ cluster cores are best described as distorted tricapped trigonal prisms with three different prism heights (Ge2-Ge4, Ge5-Ge6 and Ge7-Ge8) and thus C_s symmetry (Fig. 3a, b and d). All three substituents (one alkyl group and two silyl groups) form classical 2-center-2-electron (2c-2e) *exo*-bonds to single Ge vertices of the $[\text{Ge}_9]$ cluster cores, with Ge-Ge, Ge-Si and Ge-C distances being in accordance with reported values (Table 1).^{24,25,51-53} The alkyl group $-(\text{CH}_2)_4\text{O}-$ and one of the silyl groups (Si1-Si4) are attached at Ge atoms capping the trigonal prism,^{25,34,43,44} whereas the second silyl group (Si5-Si8) does not bind to the third capping atom Ge9, but to Ge5 instead, which is an atom of the trigonal prism base. This feature deviates from the typical substitution pattern in $[\text{Ge}_9]$ clusters presented in Fig. 3e. Isomerization with

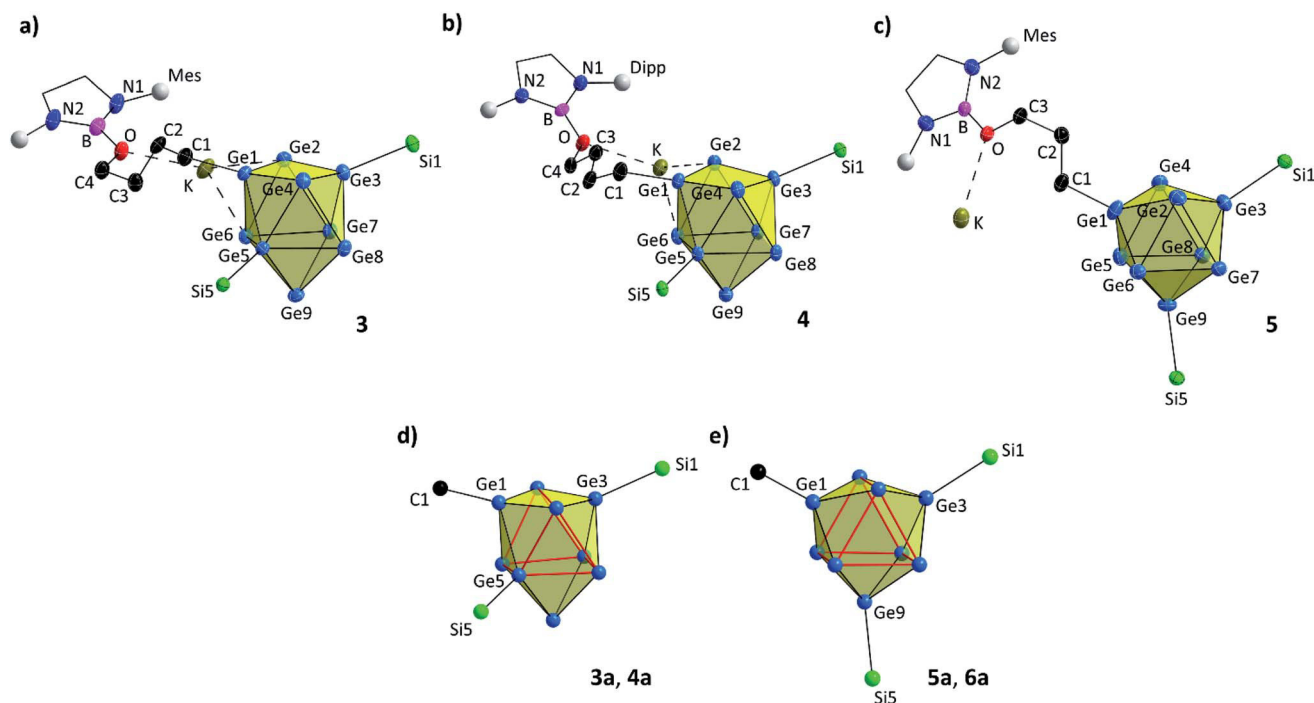


Fig. 3 Molecular structures of compounds **3**–**5** with uncommon (in **3** and **4**) and common (in **5**) substitution patterns of the $[\text{Ge}_9]$ core. All ellipsoids are shown at a 50% probability level. For clarity protons, co-crystallized solvent molecules and TMS groups are omitted. Mes and Dipp fragments are shown as grey spheres, and carbon atoms of DAB and $\text{DAB}(\text{II})$ moieties are presented as black wire sticks. (a) Molecular structure of **3** with $-(\text{CH}_2)_4\text{O}-$ moiety; (b) molecular structure of **4** with $-(\text{CH}_2)_4\text{O}-$ moiety; (c) molecular structure of **5** with $-(\text{CH}_2)_3\text{O}-$ moiety; emphasis on (d) less common and (e) common substitution isomer of the $[\text{Ge}_9]$ core in the anions **3a**–**6a** (trigonal prisms are indicated by bold red lines). Selected bond lengths and crystallographic data of **3**–**5** are presented in the ESI.†



Table 1 Selected bond lengths and prism heights h (both in Å) in compounds 3–6. Additional bond lengths are presented in the ESI

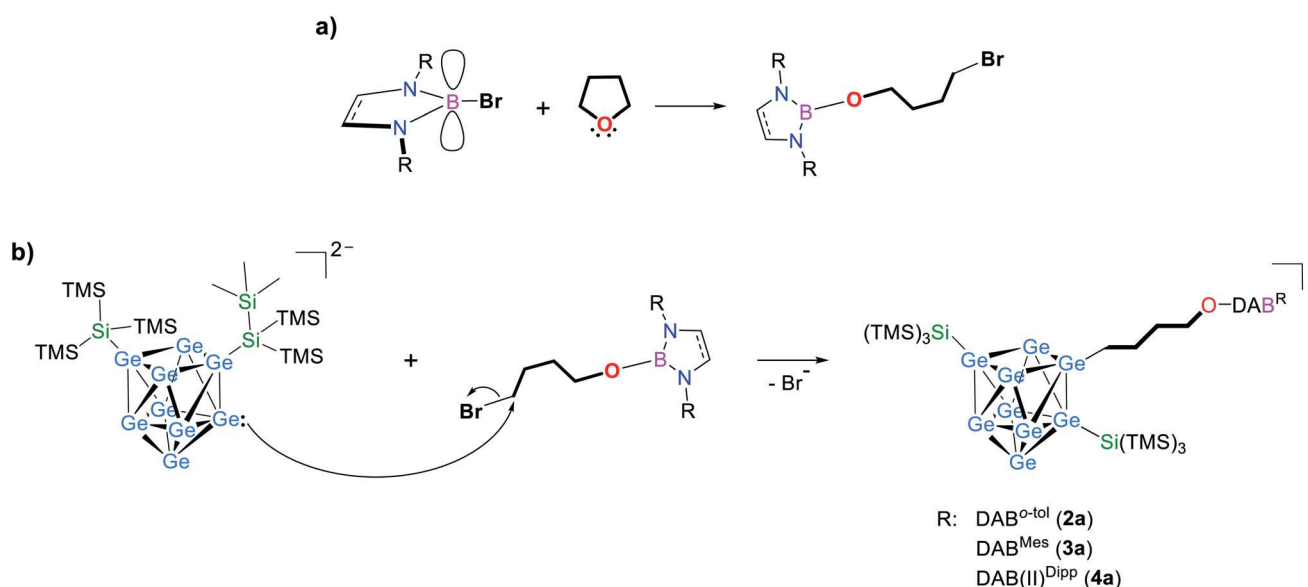
	3	4	5	6
h_1	3.976(1)	3.918(1)	3.429(1)	3.370(1)
h_2	2.759(2)	2.815(2)	3.525(1)	3.663(1)
h_3	2.932(1)	2.934(1)	3.295(1)	3.201(1)
$h_{\text{long}}/h_{\text{short}}$	1.44	1.39	1.07	1.14
Ge–Ge _{short}	2.5038(8) (Ge1–Ge2)	2.5046(8) (Ge1–Ge2)	2.5031(9) (Ge6–Ge9)	2.5128(7) (Ge3–Ge7)
Ge–Ge _{long}	2.9322(8) (Ge7–Ge8)	2.9324(8) (Ge7–Ge8)	2.715(1) (Ge4–Ge8)	2.7396(7) (Ge4–Ge8)
Ge1–C1	1.995(5)	2.007(5)	1.984(6)	1.997(4)
Ge3–Si1	2.396(2)	2.392(2)	2.381(2)	2.369(1)
Ge5–Si5 or Ge9–Si5	2.395(2)	2.403(2)	2.383(2)	2.381(1)

respect to the ligand arrangement has been observed before.^{54–56} However, NMR investigations of **3** in solution suggest a symmetrically decorated [Ge₉] cage with chemically and magnetically identical silyl groups (Fig. S32[†]). Even upon cooling of the NMR sample to $-90\text{ }^\circ\text{C}$ no splitting of the main signal could be observed, nevertheless a minor species (approx. 5%) showing a signal splitting could be monitored reaching its coalescence at $70\text{ }^\circ\text{C}$. Due to the low concentration we believe the latter signal is caused by an impurity. The asymmetric substitution in **3** and **4** could result from packing effects, and thus a rearrangement of the [Ge₉] cluster substituents or cluster vertex atoms might occur during crystallization.

The charge balancing potassium cations of **3a** and **4a** coordinate to two Ge vertices of the [Ge₉] unit and to the oxygen atom of the ring-opened ether (Fig. 3a and b). An influence of the K⁺ cations on the course of the reaction was ruled out, since similar experiments, in which the cations were sequestered by 18-crown-6 or [2.2.2]-cryptand gave the same products. However, the coordination could play a role concerning which possible ligand arrangement at the [Ge₉] clusters is found in crystals of **3** and **4**.

These species resemble intermolecular frustrated Lewis pairs (FLPs) consisting of the bis-silylated [Ge₉] cluster (Lewis base) and the bromo-borane (Lewis acid). The formation of **3** and **4** reveals a new and very promising route to attach further ligands at the silylated [Ge₉] cluster. Currently, the formation of [Ge₉]–C bonds is limited to vinylation reactions, and a direct alkylation of the [Ge₉] cluster using alkyl-halides or acyl-chlorides^{36,39} suffering either from low yields or limitation to neutral cluster species.³⁸


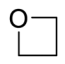
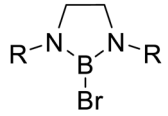
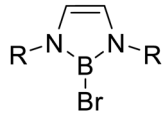
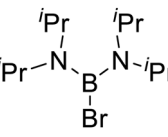
The cleavage of endocyclic C–O bonds has been reported for boron based Lewis acids^{57,58} as well as for non-electron-deficient boron subphthalocyanine, proposing the formation of a four-membered ring intermediate and subsequent σ -bond metathesis.^{59,60} Therefore we tested the reactivity of the boranes DAB^R–Br towards thf in the absence of any cluster species. Indeed, NMR investigations (¹H, ¹¹B; Fig. S5 to S16[†]) of the residues obtained by stirring DAB^R–Br (R: *o*-tol; Mes) or DAB^(II)Dipp–Br in thf at room temperature or $70\text{ }^\circ\text{C}$, respectively, revealed thf ring-opening under formation of DAB^R–O–(CH₂)₄–Br. As observed for anions **2a** to **5a** the ¹¹B NMR shifts for the ring-opened species are only slightly up-field shifted if compared to the



Scheme 1 Possible formation path for compounds **2**–**4** through (a) reaction of DAB^R–Br (R: *o*-tol, Mes) and DAB^(II)Dipp–Br with thf yielding ring-opened DAB^R–(CH₂)₄O–Br and (b) subsequent reaction with [Ge₉(Si(TMS)₃)₂]²⁻. Detailed reaction parameters are provided in the ESI.[†]



Table 2 Insertion of ring-opened ethers between $[\text{Ge}_9\{\text{Si}(\text{TMS})_3\}_2]^{2-}$ and the respective borane, based on ESI MS studies (spectra presented in the ESI)

Reactant/solvent		
	R: <i>o</i> -tol (2) <i>o</i> -xyl Mes (3) Dipp(4)	R: <i>o</i> -xyl Mes (5) Dipp
	R: Dipp	R: Dipp
	Insertion observed	No insertion observed

DAB-reactants, indicating a similar chemical shielding of B. Upon the addition of $[\text{Ge}_9\{\text{Si}(\text{TMS})_3\}_2]^{2-}$ species **2a** to **4a** are formed (Scheme 1), as shown by ESI MS experiments. Reactions with the less hindered $\text{DAB}^{o\text{-xyl}}\text{-Br}$, $\text{DAB}^{\text{Dipp}}\text{-Br}$ (saturated backbone) and acyclic $(i\text{Pr}_2\text{N})_2\text{BBr}$ led to the corresponding ring-opened products (Table 2), whereas in reactions with the analogous chloro-boranes $\text{DAB}^{\text{R}}\text{-Cl}$ no ring opening of thf was observed (with and without $[\text{Ge}_9\{\text{Si}(\text{TMS})_3\}_2]^{2-}$), which we assign to the lower Lewis acidity^{47–49} of the chloro-borane, and Cl^- being a worse leaving group than Br^- .⁶¹

Ring-opening of trimethylene oxide

The reaction of $[\text{Ge}_9\{\text{Si}(\text{TMS})_3\}_2]^{2-}$ with $\text{DAB}^{\text{Mes}}\text{-Br}$ in tmo (trimethylene oxide) accordingly leads to the formation of $[\text{Ge}_9\{\text{Si}(\text{TMS})_3\}_2(\text{CH}_2)_3\text{O-DAB}^{\text{Mes}}]^-$ (**5a**). Isolation of single crystals allowed the structural characterization and revealed the formation of $\text{K}[\text{Ge}_9\{\text{Si}(\text{TMS})_3\}_2(\text{CH}_2)_3\text{O-DAB}^{\text{Mes}}]$ (**5**). ESI MS data of **5a** (m/z 1512.8, Fig. S61†), and NMR spectroscopic investigations corroborate the structure in solution. Compound **5** crystallizes in the triclinic space group $P\bar{1}$. The $[\text{Ge}_9]$ cluster core can be best described as a tricapped trigonal prism with three different prim heights and C_s symmetry. All Ge–Ge, Ge–Si and Ge–C distances are in the range of the bond lengths observed in **3** and **4** (Table 1). In contrast to the asymmetric substitution pattern of the $[\text{Ge}_9]$ cluster in **3** and **4**, the three substituents in **5** bind to the capping Ge atoms of the tricapped trigonal prismatic $[\text{Ge}_9]$ core, as typically observed for tris-substituted $[\text{Ge}_9]$ species (Fig. 3c and e).^{25,34,43,44} Apparently, the slightly shorter alkyl chain changes the favoured structure in the solid state, and the potassium counter ion coordinates solely to the oxygen atom of the alkyl substituents and not to Ge vertices of the $[\text{Ge}_9]$ cluster.

Reactions of $[\text{Ge}_9\{\text{Si}(\text{TMS})_3\}_2]^{2-}$ with further bromo-boranes in tmo resulted in the formation of analogous species, which were characterized by ESI MS only (the spectra are shown in the ESI†). However, no selective ring-opening reaction could be

observed for the reaction of tmo and various boranes $\text{DAB}^{\text{R}}\text{-Br}$, instead the formation of various unidentified products was observed in the NMR spectra. This indicates that a targeted opening of tmo is only feasible if Lewis basic and acidic moieties are simultaneously present. The results of these experiments show that the insertion of different cyclic ethers between the di-anionic cluster and several bromo-boranes corresponds to an easy route for Ge–C bond formation in $[\text{Ge}_9]$ cluster chemistry (Table 2). Additional NMR spectra (^1H , ^{11}B , ^{13}C , ^{29}Si) of compounds **2** to **5** are provided in the ESI.†

Activation of CH_3CN

In contrast to thf the activation of CH_3CN requires the simultaneous presence of Lewis-acid and Lewis-basic reactants. A

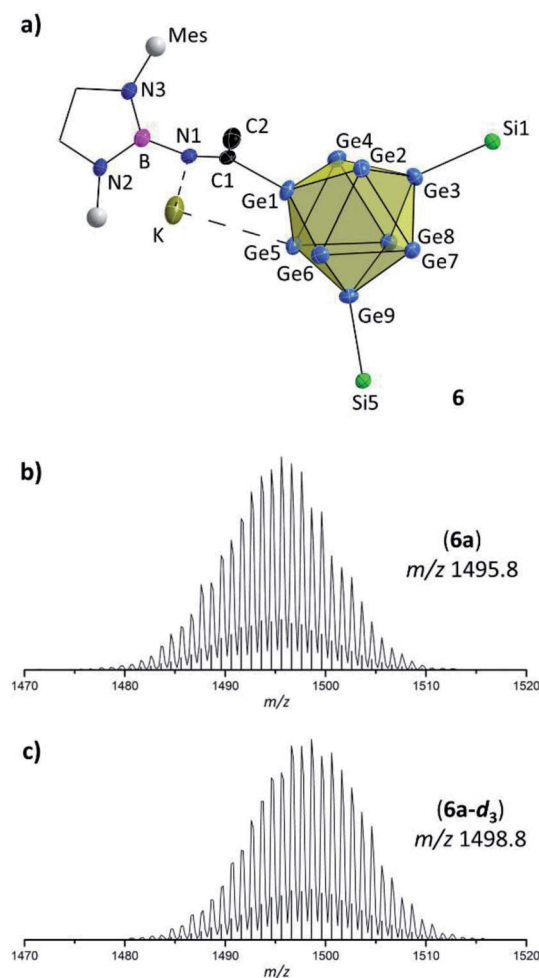
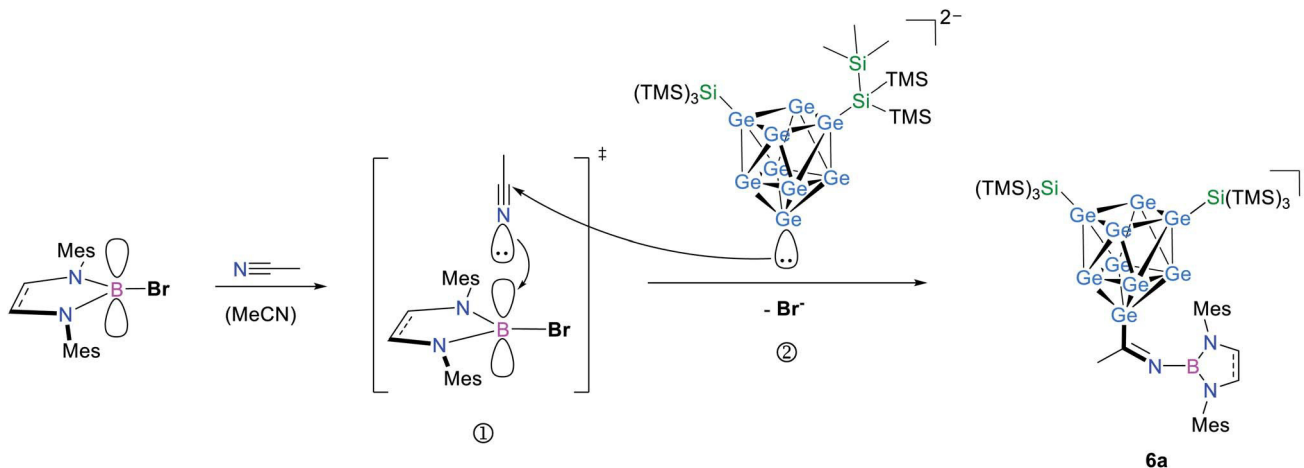


Fig. 4 (a) Molecular structure of compound **6** with $-(\text{CH}_2)_3\text{CN}$ -moiety. All ellipsoids are shown at a 50% probability level. For clarity protons, co-crystallized solvent molecules and TMS groups are omitted. Mes fragments are indicated by grey spheres, and carbon atoms of the DAB moiety are presented as black wire sticks; (b) and (c) selected areas of ESI MS spectra (MeCN, negative-ion mode, 3500 V, 300 °C) of **6a** and **6a-d₃**; (b) molecule peak of $[\text{Ge}_9\{\text{Si}(\text{TMS})_3\}_2\text{CH}_2\text{C}\equiv\text{N-DAB}^{\text{Mes}}]^-$ (**6a**) at m/z 1495.8; (c) molecule peak of $[\text{Ge}_9\{\text{Si}(\text{TMS})_3\}_2\text{CD}_3\text{C}\equiv\text{N-DAB}^{\text{Mes}}]^-$ (**6a-d₃**) at m/z 1498.8. Calculated isotope patterns are shown as black bars. Overview spectra are given in the ESI.†





Scheme 2 Possible reaction path in analogy to the literature for the formation of **6a** through an intermediate activation of acetonitrile by the Lewis acid (①), subsequent attack of $[\text{Ge}_9\{\text{Si}(\text{TMS})_3\}_2]^{2-}$ at the electrophilic C atom of the acetonitrile molecule (②) and product formation under cleavage of Br^- .^{12,62}

reaction of the nitrile was only observed in the presence of $[\text{Ge}_9\{\text{Si}(\text{TMS})_3\}_2]^{2-}$ and $\text{DAB}^{\text{Mes}}\text{-Br}$ in acetonitrile solution, resulting in the anion $[\text{Ge}_9\{\text{Si}(\text{TMS})_3\}_2\text{CH}_3\text{C}=\text{N-DAB}^{\text{Mes}}]^-$ (**6a**, Fig. 4a). By contrast, stirring acetonitrile solutions of $\text{DAB}^{\text{Mes}}\text{-Br}$ at r. t. or at 70 °C overnight did not lead to any reaction, as shown by NMR spectroscopy (Fig. S19 and S20†). However, upon the addition of $[\text{Ge}_9\{\text{Si}(\text{TMS})_3\}_2]^{2-}$, compound **6** is rapidly formed, as indicated by a shift of the silyl group protons from 0.16 ppm (bis-silylated $[\text{Ge}_9]$ cluster) to 0.25 ppm in the ¹H NMR spectrum, a ¹¹B shift from 26 ppm to 18 ppm indicating an increased shielding of B and ESI MS investigations (**6a** at *m/z* 1495.8, **6a-d**₃ at *m/z* 1498.8; Fig. 4b and c).

Hence, in contrast to the reactions with the cyclic ether thf, for which a ring opening reaction is already observed in the presence of the respective bromo-borane, MeCN insertion exclusively occurs in the presence of a Lewis acid–base pair (Scheme 2). Recrystallization of the crude product from toluene at room temperature yielded orange needles suitable for single crystal X-ray diffraction of $\text{K}[\text{Ge}_9\{\text{Si}(\text{TMS})_3\}_2\text{CH}_3\text{C}=\text{N-DAB}^{\text{Mes}}]$ (**6**). Compound **6** crystallizes in the monoclinic space group *P2*₁. The $[\text{Ge}_9]$ core has the shape of a tricapped trigonal prism with one prism height significantly elongated compared to the two others, resulting in *C*_{2v} symmetry (Table 1). As observed in **5**, the three substituents (one imine ligand and two silyl groups) bind to the capping Ge atoms of the cluster. The short bond *d*(C1–N1): 1.273(6) Å and the distorted trigonal planar coordination of C1 by Ge1, N1 and C2 [angles range between 114.2° (Ge1–C1–C2) and 124.4° (N1–C1–C2)] confirm the C=N double bond.¹² The potassium counter ion is coordinated by the imine nitrogen atom N1 and one Ge vertex atom (Ge5) of the $[\text{Ge}_9]$ cluster core. Analogous ESI MS experiments for the boranes $\text{DAB}^{\text{R}}\text{-Br}$ (R: *o*-xyl, Dipp), $\text{DAB}(\text{n})^{\text{Dipp}}\text{-Br}$ and $(\text{Pr}_2\text{N})_2\text{B-Br}$ indicated insertion of the nitrile moiety between cluster and boranyl ligand only under simultaneous presence of both reactants. The results can be understood in terms of previous publications, which suggest a step-wise reaction path for the cyclo-addition of nitriles or azides to the intramolecular, geminal FLP ^tBu₂P–CH₂–BPh₂.^{12,62}

According to quantum chemical calculations the nitrile activation is initiated by the coordination of the terminal N atom of MeCN to the electrophilic boron center (intermediate), followed by the nucleophilic attack of the phosphorus' lone pair at the electrophilic C atom of the nitrile. In analogy, we assume that the $[\text{Ge}_9\{\text{Si}(\text{TMS})_3\}_2]^{2-}/\text{DAB}$ system forms a transition state (Scheme 2), and the reaction occurs according to a frustrated Lewis acid–base-type displacement reaction. These results are further corroborated by the observation that mixtures of $[\text{Ge}_9\{\text{Si}(\text{TMS})_3\}_2]^{2-}$ and the acyclic chloro-borane (^tPr₂N)₂B–Cl readily react with MeCN under formation of $[\text{Ge}_9\{\text{Si}(\text{TMS})_3\}\text{CH}_3\text{C}=\text{N-B}(\text{N}^i\text{Pr}_2)_2]^-$ (chloro-boranes are less

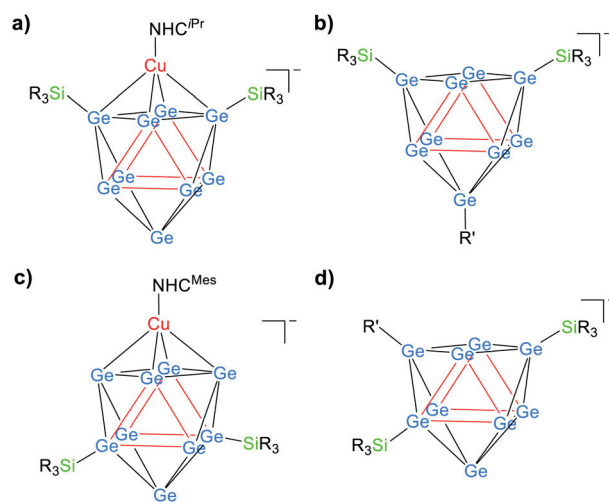


Fig. 5 Different substitution isomers of $[\text{Ge}_9]$. Common substitution pattern with (a) two *exo*-bonded silyl groups at Ge atoms capping the trigonal prism;^{24,36,55} and (b) three ligands capping the trigonal prism.^{25,34,35,43,44,65} Novel substitution isomers with (c) two silyl groups⁵⁵ and (d) three ligands binding to different cluster vertices (this manuscript). Trigonal prisms are indicated by red lines. NHC^{Pr} : 1,3-bis(isopropyl)imidazolyliene; NHC^{Mes} : 1,3-bis(2,4,6-trimethylphenyl)imidazolyliene.



Lewis acidic than their bromo-congeners), whereas this cluster/borane pair does not open cyclic ethers. This contrasts the findings made for analogous mixtures of $[\text{Ge}_9\{\text{Si}(\text{TMS})_3\}_2]^{2-}$ and cyclic $\text{DAB}^{\text{R}}\text{-Cl}$ (R: *o*-tol, Mes), which do not react with MeCN. The difference in the reactivity of the respective cyclic and acyclic chloro-boranes can be explained by the significantly increased Lewis acidity of the acyclic ($^i\text{Pr}_2\text{N}$) $_2\text{B-Cl}$ compared to that of the cyclic $\text{DAB}^{\text{R}}\text{-Cl}$ (R: *o*-tol, Mes) system. This is caused by a decreased electron density donation to the empty B p_z -type orbital due to the low barrier of the torsion about the B–N bond in the acyclic molecule.^{63,64} Therefore, the Lewis acidity can be estimated to follow the sequence $\text{DAB}^{\text{R}}\text{-Br} > (\text{N}^i\text{Pr}_2)_2\text{-BCl} > \text{DAB}^{\text{R}}\text{-Cl}$.

Conclusions

We reported on the reactivity of $[\text{Ge}_9\{\text{Si}(\text{TMS})_3\}_2]^{2-}$ towards several bromo boranes $\text{DAB}^{\text{R}}\text{-Br}$. The reactions of the bisilylated $[\text{Ge}_9]$ cluster with $\text{DAB}^{\text{R}}\text{-Br}$ reveal the tunability of this system, yielding either selectively the anion **1a** with direct Ge–B bond formation, or a participation of solvent molecules in the reaction. Anion **2a** is formed *via* the intermediate $\text{DAB}^{\text{R}}\text{-O}(\text{CH}_2)_4\text{-Br}$, which subsequently reacts with $[\text{Ge}_9\{\text{Si}(\text{TMS})_3\}_2]^{2-}$. Moreover, we found that boranes with sterically demanding ligands such as $\text{DAB}^{\text{R}}\text{-Br}$ (R: *o*-xyl, Mes, Dipp), $\text{DAB}(\text{ii})^{\text{Dipp}}\text{-Br}$ or ($^i\text{Pr}_2\text{N}$) $_2\text{B-Br}$, which cannot bind to $[\text{Ge}_9\{\text{Si}(\text{TMS})_3\}_2]^{2-}$, can also give species analogous to **2a** by ring opening of thf or tmo. By contrast, the insertion of CH_3CN takes place in analogy to a frustrated Lewis acid–base concept, since a reaction is observed only in the presence of both reactants $[\text{Ge}_9\{\text{Si}(\text{TMS})_3\}_2]^{2-}$ (Lewis base) and $\text{DAB}^{\text{R}}\text{-Br}$ (R: *o*-xyl, Mes, Dipp), $\text{DAB}(\text{ii})^{\text{Dipp}}\text{-Br}$ or ($^i\text{Pr}_2\text{N}$) $_2\text{B-Br}$ (Lewis acid).

The structures of compounds **3** to **6** reveal another interesting aspect of the substitution pattern in spherical homoatomic germanium clusters: compounds **3** and **4** show an unusual substitution pattern of the $[\text{Ge}_9]$ cores in the solid state (Fig. 5), which is different from that in solution, indicating a rearrangement of the substituents upon crystallization.

To the best of our knowledge these systems are the first examples for intermolecular Ge/B frustrated Lewis acid–base pairs comprising nine-atom germanide clusters capable of reacting with small molecules. Currently, further investigations on the activation of small molecules by these germanide cluster/bromo-borane systems are carried out in our laboratories.

Author contributions

The experimental work was performed equally by C. W. and F. S. G. The manuscript was authored by C. W., F. S. G. and T. F. F.

Conflicts of interest

There are no conflicts to declare.

Acknowledgements

C. W. thanks the Deutsche Forschungsgemeinschaft (DFG, German Research Foundation) for funding (project number 245845833) within the International Research Training Group IRTG 2022 – Alberta Technical University of Munich School for Functional Hybrid Materials (ATUMS). Support within TUM IGSSE is greatly appreciated. C. W. also thanks the Studienstiftung des Deutschen Volkes for granting a PhD scholarship. This work was financially supported by the Bavarian Ministry of Economic Affairs, Regional Development and Energy “SolarTechnologies go Hybrid”. The authors acknowledge Kevin Frankiewicz for the acquisition of variable temperature NMR data.

References

- 1 P. P. Power, *Nature*, 2010, **463**, 171.
- 2 D. W. Stephan, *Science*, 2016, **354**, aaf7229.
- 3 D. W. Stephan, *Acc. Chem. Res.*, 2015, **48**, 306.
- 4 D. W. Stephan and G. Erker, *Angew. Chem., Int. Ed.*, 2010, **49**, 46.
- 5 B. Birkmann, T. Voss, S. J. Geier, M. Ullrich, G. Kehr, G. Erker and D. W. Stephan, *Organometallics*, 2010, **29**, 5310.
- 6 S. Fantasia, J. M. Welch and A. Togni, *J. Org. Chem.*, 2010, **75**, 1779.
- 7 T. Krachko, E. Nicolas, A. W. Ehlers, M. Nieger and J. C. Sloutweg, *Chem.–Eur. J.*, 2018, **24**, 12669.
- 8 G. C. Welch, J. D. Masuda and D. W. Stephan, *Inorg. Chem.*, 2006, **45**, 478.
- 9 G. Wittig and A. Rückert, *Justus Liebigs Ann. Chem.*, 1950, **566**, 101.
- 10 K. Samigullin, I. Georg, M. Bolte, H. W. Lerner and M. Wagner, *Chem.–Eur. J.*, 2016, **22**, 3478.
- 11 L. M. Elmer, G. Kehr, C. G. Daniliuc, M. Siedow, H. Eckert, M. Tesch, A. Studer, K. Williams, T. H. Warren and G. Erker, *Chem.–Eur. J.*, 2017, **23**, 6056.
- 12 E. R. Habraken, L. C. Mens, M. Nieger, M. Lutz, A. W. Ehlers and J. C. Sloutweg, *Dalton Trans.*, 2017, **46**, 12284.
- 13 Z. Jian, G. Kehr, C. G. Daniliuc, B. Wibbeling and G. Erker, *Dalton Trans.*, 2017, **46**, 11715.
- 14 L. Keweloh, N. Aders, A. Hepp, D. Pleschka, E.-U. Würthwein and W. Uhl, *Dalton Trans.*, 2018, **47**, 8402.
- 15 J. Li, C. Mück-Lichtenfeld, C. G. Daniliuc, G. Kehr and G. Erker, *Angew. Chem., Int. Ed.*, 2020, **59**, 12477.
- 16 C. Wallach, F. S. Geitner, A. J. Karttunen and T. F. Fässler, *Angew. Chem., Int. Ed.*, 2021, **60**, 2648.
- 17 O. P. Townrow, C. Chung, S. A. Macgregor, A. S. Weller and J. M. Goicoechea, *J. Am. Chem. Soc.*, 2020, **142**, 18330.
- 18 S. Ponou and T. F. Fässler, *Z. Anorg. Allg. Chem.*, 2007, **633**, 393.
- 19 H. Von Schnering, M. Baitinger, U. Bolle, W. Carrillo-Cabrera, J. Curda, Y. Grin, F. Heinemann, J. Llanos, K. Peters and A. Schmeding, *Z. Anorg. Allg. Chem.*, 1997, **623**, 1037.
- 20 W. Carrillo-Cabrera, U. Aydemir, M. Somer, A. Kircali, T. F. Fässler and S. D. Hoffmann, *Z. Anorg. Allg. Chem.*, 2007, **633**, 1575.



- 21 C. Downie, J.-G. Mao and A. M. Guloy, *Inorg. Chem.*, 2001, **40**, 4721.
- 22 M. Somer, W. Carrillo-Cabrera, E. M. Peters, K. Peters and H. G. v. Schnering, *Z. Anorg. Allg. Chem.*, 1998, **624**, 1915.
- 23 C. Suchentrunk, J. Daniels, M. Somer, W. Carrillo-Cabrera and N. Korber, *Z. Naturforsch., B: J. Chem. Sci.*, 2005, **60**, 277.
- 24 O. Kysliak and A. Schnepf, *Dalton Trans.*, 2016, **45**, 2404.
- 25 F. Li and S. C. Sevov, *Inorg. Chem.*, 2012, **51**, 2706.
- 26 L. J. Schiegerl, A. J. Karttunen, W. Klein and T. F. Fässler, *Chem.–Eur. J.*, 2018, **24**, 19171.
- 27 L. J. Schiegerl, A. J. Karttunen, W. Klein and T. F. Fässler, *Chem. Sci.*, 2019, **10**, 9130.
- 28 L. J. Schiegerl, A. J. Karttunen, J. Tillmann, S. Geier, G. Raudaschl-Sieber, M. Waibel and T. F. Fässler, *Angew. Chem., Int. Ed.*, 2018, **57**, 12950.
- 29 C. Lorenz, F. Hastreiter, J. Hioe, N. Lokesh, S. Gärtner, N. Korber and R. M. Gschwind, *Angew. Chem., Int. Ed.*, 2018, **57**, 12956.
- 30 T. Henneberger, W. Klein and T. F. Fässler, *Z. Anorg. Allg. Chem.*, 2018, **644**, 1018.
- 31 K. Mayer, L. J. Schiegerl and T. F. Fässler, *Chem.–Eur. J.*, 2016, **22**, 18794.
- 32 O. Kysliak, C. Schrenk and A. Schnepf, *Inorg. Chem.*, 2015, **54**, 7083.
- 33 L. J. Schiegerl, F. S. Geitner, C. Fischer, W. Klein and T. F. Fässler, *Z. Anorg. Allg. Chem.*, 2016, **642**, 1419.
- 34 O. Kysliak, T. Kunz and A. Schnepf, *Eur. J. Inorg. Chem.*, 2017, **2017**, 805.
- 35 K. Mayer, L. Schiegerl, T. Kratky, S. Günther and T. Fässler, *Chem. Commun.*, 2017, **53**, 11798.
- 36 S. Frischhut, W. Klein and T. F. Fässler, *C. R. Chim.*, 2018, **21**, 932.
- 37 S. Frischhut and T. F. Fässler, *Dalton Trans.*, 2018, **47**, 3223.
- 38 F. Li and S. C. Sevov, *J. Am. Chem. Soc.*, 2014, **136**, 12056.
- 39 S. Frischhut, W. Klein, M. Drees and T. F. Fässler, *Chem.–Eur. J.*, 2018, **24**, 9009.
- 40 F. Li, A. Muñoz-Castro and S. C. Sevov, *Angew. Chem., Int. Ed.*, 2012, **51**, 8581.
- 41 O. Kysliak and A. Schnepf, *Z. Anorg. Allg. Chem.*, 2019, **645**, 335.
- 42 F. S. Geitner, W. Klein and T. F. Fässler, *Angew. Chem., Int. Ed.*, 2018, **57**, 14509.
- 43 F. S. Geitner, J. V. Dums and T. F. Fässler, *J. Am. Chem. Soc.*, 2017, **139**, 11933.
- 44 F. S. Geitner, C. Wallach and T. F. Fässler, *Chem.–Eur. J.*, 2018, **24**, 4103.
- 45 C. Wallach, F. S. Geitner, W. Klein and T. F. Fässler, *Chem.–Eur. J.*, 2019, **25**, 12349.
- 46 J. Li, B. Li, R. Liu, L. Jiang, H. Zhu, H. W. Roesky, S. Dutta, D. Koley, W. Liu and Q. Ye, *Chem.–Eur. J.*, 2016, **22**, 14499.
- 47 V. Gutmann, *Coord. Chem. Rev.*, 1976, **18**, 225.
- 48 M. A. Beckett, G. C. Strickland, J. R. Holland and K. S. Varma, *Polymer*, 1996, **37**, 4629.
- 49 I. B. Sivaev and V. I. Bregadze, *Coord. Chem. Rev.*, 2014, **270**, 75.
- 50 H. Clavier and S. P. Nolan, *Chem. Commun.*, 2010, **46**, 841.
- 51 A. Schnepf, *Angew. Chem., Int. Ed.*, 2003, **42**, 2624.
- 52 M. W. Hull and S. C. Sevov, *J. Am. Chem. Soc.*, 2009, **131**, 9026.
- 53 M. W. Hull, A. Ugrinov, I. Petrov and S. C. Sevov, *Inorg. Chem.*, 2007, **46**, 2704.
- 54 S. Frischhut, F. Kaiser, W. Klein, M. Drees, F. E. Kühn and T. F. Fässler, *Organometallics*, 2018, **37**, 4560.
- 55 F. S. Geitner and T. F. Fässler, *Inorg. Chem.*, 2020, **59**, 15218.
- 56 F. Li, A. Muñoz-Castro and S. C. Sevov, *Angew. Chem., Int. Ed.*, 2016, **55**, 8630.
- 57 H. C. Brown, P. V. Ramachandran and J. Chandrasekharan, *Heteroat. Chem.*, 1995, **6**, 117.
- 58 J. B. Heilmann, Y. Qin, F. Jäkle, H.-W. Lerner and M. Wagner, *Inorg. Chim. Acta*, 2006, **359**, 4802.
- 59 C. Bonnier and T. P. Bender, *Molecules*, 2015, **20**, 18237.
- 60 J. Guilleme, L. Martinez-Fernandez, D. Gonzalez-Rodriguez, I. Corral, M. Yanez and T. Torres, *J. Am. Chem. Soc.*, 2014, **136**, 14289.
- 61 M. B. Smith, *March's Advanced Organic Chemistry: Reactions, Mechanisms, and Structure*, John Wiley & Sons, Hoboken, New Jersey, Vol. 8, 2020, pp. 778–779.
- 62 D. H. Boom, A. R. Jupp, M. Nieger, A. W. Ehlers and J. C. Slootweg, *Chem.–Eur. J.*, 2019, **25**, 13299.
- 63 R. W. Alder, P. R. Allen, M. Murray and A. G. Orpen, *Angew. Chem., Int. Ed.*, 1996, **35**, 1121.
- 64 L. M. Slaughter, *ACS Catal.*, 2012, **2**, 1802.
- 65 O. Kysliak, C. Schrenk and A. Schnepf, *Inorg. Chem.*, 2017, **56**, 9693.



FLP-type Nitrile Activation and Cyclic Ether Ring Opening by Halo-Borane Nonagermanide-Cluster Lewis Acid-Base-Pairs

Supporting Information

Content

Experimental details	S1
Activation of thf with DAB ^R -Br and (iPr ₂ N) ₂ B-Br	S4
Reactivity of DAB ^{Mes} -Br towards MeCN	S5
ESI MS sample preparation	S5
Crystallographic data of compounds 3 – 6	S6
NMR spectra	S11
ESI MS spectra	S31
References	S57

Experimental details

General. All manipulations were performed under oxygen-free, dry conditions under argon atmosphere using standard Schlenk or glove box techniques. Glassware was dried prior to use by heating it *in vacuo*. The solvents used were obtained from an MBraun Grubbs apparatus. All other commercially available chemicals were used without further purification. K_4Ge_9 was prepared by fusion of stoichiometric amounts of the elements in stainless-steel tubes at 650 °C. The silylated $[Ge_9]$ clusters $[Ge_9\{Si(TMS)_3\}_2]^{2-}$,¹ the halo-diazaborolidines DAB^R-Br ($DAB = 2\text{-bromo-1,3,2-diazaborolidine}$; $R = o\text{-tol. } o\text{-xyl, Mes, Dipp}$),² 2-bromo-1,3,2-diazaborole $DAB(II)^{Dipp}\text{-Br}$,² and $(iPr_2N)_2B\text{-X}$ ($X: Cl, Br$) were synthesized according to modified literature procedures.³

Single crystal structure determination. The air- and moisture-sensitive crystals of **3** to **6** were transferred from the mother liquor into perfluoroalkyl ether oil under inert gas atmosphere in a glove box. For diffraction data collection, the single crystals were fixed on a glass capillary and positioned in a 150 K cold N_2 gas stream using the crystal cap system. Data collection was performed with a STOE StadiVari diffractometer ($MoK\alpha$ radiation) equipped with a DECTRIS PILATUS 300K detector. Structures were solved by Direct Methods (SHELXS-97) and refined by full-matrix least-squares calculations against F^2 (SHELXL-2014 or SHELXL-2018).⁴ The positions of the hydrogen atoms were calculated and refined using a riding model. Unless stated otherwise, all non-hydrogen atoms were treated with anisotropic displacement parameters. The supplementary crystallographic data for this paper have been deposited with the Cambridge Structural database and are available free of charge via www.ccdc.cam.ac.uk/data_request/cif. The crystallographic data for compounds **3** to **6** are summarized in Table S3. In compound **4** disordered solvent molecules have been taken care of by the Platon squeeze function.⁵

NMR spectroscopy. NMR spectra were measured on a Bruker Avance Ultrashield 400 MHz spectrometer. Chemical shifts are reported in parts per million (ppm) relative to TMS, with the solvent peaks serving as internal reference.⁶ Abbreviations for signal multiplicities are: singlet (s), doublet (d), triplet (t), heptet (hept), broad signal (brs).

Elemental analysis. Elemental analyses were carried out in the microanalytical laboratory of the Chemistry Department of Technische Universität München. Analyses of C, H, N were performed in a combustion analyzer (EURO EA, HEKA tech).

Electron Spray Ionization Mass Spectrometry (ESI MS). Sample preparation was performed under inert conditions using a glove box. Data collection was performed using a Bruker Daltronic HTC mass spectrometer (dry gas temperature: 300 °C; injection speed 240 μ l/h), and the data were processed using the Bruker Compass Data Analysis 4.0 SP 5 program (Bruker). The spectra were plotted using Excel 2016 (Microsoft) and OriginPro2016G (Origin Lab). Simulated spectra are always shown as black bars.

Syntheses.

$K[Ge_9\{Si(TMS)_3\}_2DAB^{o\text{-tol}}]$ (1**):** In a typical experiment equimolar amounts of $K_2[Ge_9\{Si(TMS)_3\}_2]$ (92 mg, 0.075 mmol, 1 equiv.) and $DAB^{o\text{-tol}}\text{-Br}$ (24.7 mg, 0.075 mmol, 1 equiv.) were weighted into a Schlenk tube in the glove box, and dioxane (3 mL) was added to obtain a deep red solution. After stirring for 5 h at room temperature, the solvent was removed *in vacuo* yielding an ochre solid. Subsequent dissolution in toluene (15 mL) gave a dark red solution, which was filtered. Upon concentration, the product precipitated as microcrystalline solid from the solution. The mother liquor was filtered-off, and the solid was dried *in vacuo* to yield the product as a dark yellow microcrystalline powder (65 mg, 0.045 mmol,

60 % yield). **¹H NMR** (400 MHz, 298 K, thf-*d*₈): δ [ppm] = 7.16-7.11 (m, 2H, CH_{Ph}), 7.08-7.04 (m, 2H, CH_{Ph}), 7.01-6.90 (m, 4H, CH_{Ph}), 3.65 (s, 4H, CH_{2(Bb)}), 2.35 (s, 6H, Me), 0.18 (s, 54H, Me_{TMS}). **¹³C NMR** (101 MHz, 298 K, thf-*d*₈): δ [ppm] = 147.03 (s, C_{Ph(N)}), 137.19 (s, C_{Ph(Me)}), 131.38 (s, CH_{Ph}), 130.60 (s, CH_{Ph}), 127.08 (s, CH_{Ph}), 125.66 (s, CH_{Ph}), 53.93 (s, CH_{2(Bb)}), 20.14 (s, Me), 3.28 (s, Me_{TMS}). **²⁹Si-INEPT NMR** (79 MHz, 298 K, thf-*d*₈): δ [ppm] = -9.99 (s, Si_{TMS}), -108.80 (s, Si_{Ge9}). **¹¹B NMR** (128 MHz, 298 K, thf-*d*₈): δ [ppm] = 42.92 (brs, B_{Ge9}). **Elemental analysis:** anal. calcd. for Ge₉Si₈BC₃₄H₇₂N₂K: C, 28.41; H, 5.05; N, 1.95; found: C, 27.53; H, 4.87; N, 2.02. **ESI MS:** *m/z* 1398.7 [Ge₉{Si(TMS)₃}₂DAB^{o-tol}].

K[Ge₉{Si(TMS)₃}₂(CH₂)₄O-DAB^{o-tol}] (2): In a typical experiment DAB^{o-tol}-Br (24.7 mg, 0.075 mmol, 1 equiv.) was weighted into a Schlenk tube in the glove box, and thf (1.5 mL) was added to obtain a colorless solution, which was stirred for 2 h at room temperature, before equimolar amounts of K₂[Ge₉{Si(TMS)₃}₂] (92 mg, 0.075 mmol, 1 equiv.) were added, and then the solution was stirred for another 3 h at room temperature. Subsequently, the solvent was removed *in vacuo*, and hexane (2 · 5 mL) was added to the residue and removed *in vacuo*. Thereafter, the residue was dissolved in toluene (3 mL) and filtered. Removal of toluene yielded the product as a dark-brown oily solid. Purification by recrystallization from toluene solution was not successful so far. **¹H NMR** (400 MHz, 298 K, thf-*d*₈): δ [ppm] = 7.22-7.18 (m, 2H, CH_{Ph}), 7.15-7.09 (m, 4H, CH_{Ph}), 6.95-6.91 (m, 2H, CH_{Ph}), 3.61 (s, 4H, CH_{2(Bb)}), 3.25-3.22 (m, 2H, CH₂-O), 2.34 (s, 6H, Me), 1.25-1.20 (m, 4H, CH₂), 1.12-1.07 (m, 2H, CH₂-Ge), 0.24 (s, 54H, Me_{TMS}). **¹³C NMR** (101 MHz, 298 K, thf-*d*₈): Due to the presence of impurities a reliable assignment of the signals was not possible. **²⁹Si-INEPT NMR** (79 MHz, 298 K, thf-*d*₈): δ [ppm] = -9.65 (s, Si_{TMS}), -108.65 (s, Si_{Ge9}). **¹¹B NMR** (128 MHz, 298 K, thf-*d*₈): δ [ppm] = 23.14 (brs, B_O). **ESI MS:** *m/z* 1470.8 [Ge₉{Si(TMS)₃}₂(CH₂)₄O-DAB^{o-tol}], 1478.8 [Ge₉{Si(TMS)₃}₂(CD₂)₄O-DAB^{o-tol}].

Synthesis of K[Ge₉{Si(TMS)₃}₂(CH₂)₄O-DAB^{Mes}] (3): In a typical experiment equimolar amounts of K₂[Ge₉{Si(TMS)₃}₂] (92 mg, 0.075 mmol, 1 equiv.) and DAB^{Mes}-Br (29 mg, 0.075 mmol, 1 equiv.) were weighted into a glass vial in the glove box, and thf (3 mL) was added to obtain a deep red solution. After stirring for 3 h at room temperature, the solvent was removed *in vacuo* yielding a brown oil. Addition and subsequent removal of hexane (2 · 4 mL) yielded a brownish/red solid. Dissolution in toluene (3 mL) gave a dark red solution, which was filtered and concentrated to one third of its original volume. Placement in a freezer at -40 °C yielded the product as a red microcrystalline powder (45 mg, 0.028 mmol, 38 % yield). **¹H NMR** (400 MHz, 298 K, thf-*d*₈): δ [ppm] = 6.84 (s, 4H, CH_{Ph}), 3.42 (s, 4H, CH_{2(Bb)}), 3.14 (m, 2H, CH₂-O), 2.30 (s, 12H, Me_(o)), 2.23 (s, 6H Me_(p)), 1.19-1.14 (m, 4H, CH₂), 1.09-1.03 (m, 2H, CH₂-Ge), 0.24 (s, 54H, Me_{TMS}). **¹³C NMR** (101 MHz, 298 K, thf-*d*₈): δ [ppm] = 140.98 (s, C_{Ph(N)}), 137.09 (s, C_{Ph(o)}), 134.91 (s, C_{Ph(p)}), 129.65 (s, CH_{Ph}), 64.32 (s, CH₂-O), 49.34 (s, CH_{2(Bb)}), 36.66 (s, CH₂), 31.79 (s, CH₂), 21.37 (s, Me_{Ph(p)}), 18.75 (s, Me_{Ph(o)}), 11.14 (s, CH₂-Ge) 3.23 (s, Me_{TMS}). **²⁹Si-INEPT NMR** (79 MHz, 298 K, thf-*d*₈): δ [ppm] = -9.67 (s, Si_{TMS}), -108.69 (s, Si_{Ge9}). **¹¹B NMR** (128 MHz, 298 K, thf-*d*₈): δ [ppm] = 23.82 (brs, B_O). **Elemental analysis:** anal. calcd. for Ge₉Si₈BC₄₂H₈₈N₂OK: C, 32.22; H, 5.67; N, 1.79; found: C, 32.25; H, 5.40, N, 1.78. **ESI MS:** *m/z* 1526.8 [Ge₉{Si(TMS)₃}₂(CH₂)₄O-DAB^{Mes}] or 1534.8 [Ge₉{Si(TMS)₃}₂(CD₂)₄O-DAB^{Mes}].

Synthesis of K[Ge₉{Si(TMS)₃}₂(CH₂)₄O-DAB(II)^{Dipp}] (4): In a typical experiment equimolar amounts of K₂[Ge₉{Si(TMS)₃}₂] (92 mg, 0.075 mmol, 1 equiv.) and DAB(II)^{Dipp}-Br (35 mg, 0.075 mmol, 1 equiv.) were weighted into a Schlenk tube in the glove box, and thf (2 mL) was added to obtain a deep red solution. After stirring for three weeks at 35 °C, the solvent was removed *in vacuo*, yielding a brown oil. Addition and subsequent removal of hexane (3 · 6 mL) yielded a brown solid. Dissolution in toluene (2 mL) gave a dark red solution, which was filtered. The solution was concentrated to half of its original volume and stored in a freezer at -40 °C for crystallization, yielding the product as red block-shaped crystals (18.5 mg, 0.011 mmol, 15 % yield). **¹H NMR** (400 MHz, 298 K, thf-*d*₈): δ [ppm] = 7.23-7.18 (s, 2H, CH_{Ph(p)}), 7.16-7.13 (m, 4H, CH_{Ph(m)}), 5.87 (s, 2H, CH_{Bb}), 3.25-3.16 (m, 6H, CH_{IPr} + CH₂-O), 1.22 (d, ³J_{HH} = 6.8 Hz, 12H, Me_{IPr}), 1.18 (d, ³J_{HH} = 6.8 Hz, 12H, Me_{IPr}), 1.16-1.14 (m, 4H, CH₂), 1.07-1.03 (m, 2H, CH₂-Ge), 0.22 (s, 54H, Me_{TMS}). **¹³C NMR** (101 MHz, 298 K, thf-*d*₈): δ [ppm] = 147.24 (s, C_{Ph(N)}), 139.49 (s, CH_{Ph(p)}),

127.84 (s, C_{Ph(iPr)}), 123.82 (s, CH_{Ph(m)}), 117.57 (s, CH_{Bb}), 65.47 (s, CH_{2-O}), 36.43 (s, CH₂), 31.57 (s, CH₂), 29.28 (s, CH_{iPr}), 26.43 (s, Me_{iPr}), 24.46 (s, Me_{iPr}), 11.17 (s, CH_{2-Ge}), 3.23 (s, Me_{TMS}). **²⁹Si-INEPT NMR** (79 MHz, 298 K, thf-*d*₈): δ [ppm] = -9.67 (s, Si_{TMS}), -108.72 (s, Si_{Ge9}). **¹¹B NMR** (128 MHz, 298 K, thf-*d*₈): δ [ppm] = 20.66 (brs, B_O). **ESI MS**: *m/z* 1608.8 [Ge₉{Si(TMS)₃}₂(CH₂)₄O-DAB(II)^{Dipp}]⁻ or *m/z* 1616.8 [Ge₉{Si(TMS)₃}₂(CD₂)₄O-DAB(II)^{Dipp}]⁻.

Synthesis of K[Ge₉{Si(TMS)₃}₂(CH₂)₃O-DAB^{Mes}] (5): In a typical experiment equimolar amounts of K₂[Ge₉{Si(TMS)₃}₂] (123 mg, 0.100 mmol, 1 equiv.) and DAB^{Mes}-Br (38.5 mg, 0.100 mmol, 1 equiv.) were weighted into a Schlenk tube in the glove box, and trimethyleneoxide (1.5 mL) was added to obtain a deep red solution. After stirring for 3.5 h at room temperature, the solvent was removed *in vacuo* yielding a brown oil. Addition and subsequent removal of hexane (4 · 4 mL) yielded a brown solid. Dissolution in toluene (2 · 5 mL) gave a dark red solution, which was filtered and concentrated to half of its original volume, before it was placed in a freezer at -40 °C. Overnight a brown oil separated from the solution, which was removed by filtering-off the supernatant solution. The latter was placed in the freezer at -40 °C again, yielding orange block-shaped crystals of the product (26 mg, 0.017 mmol, 17 %). **¹H NMR** (400 MHz, 298 K, thf-*d*₈): δ [ppm] = 6.82 (s, 4H, CH_{Ph}), 3.40 (s, 4H, CH_{2(Bb)}), 3.04 (t, ³J_{HH} = 7.0 Hz, 2H, CH_{2-O}), 2.29 (s, 12H, Me_(o)), 2.21 (s, 6H Me_(p)), 1.39-1.29 (m, 2H, CH₂), 0.83-0.77 (m, 2H, CH_{2-Ge}), 0.23 (s, 54H, Me_{TMS}). **¹³C NMR** (101 MHz, 298 K, thf-*d*₈): δ [ppm] = 140.98 (s, C_{Ph(N)}), 138.46 (s, C_{Ph(o)}), 134.79 (s, C_{Ph(p)}), 129.63 (s, CH_{Ph}), 68.59 (s, CH_{2-O}), 49.35 (s, CH_{2(Bb)}), 38.73 (s, CH₂), 31.33 (s, CH₂), 21.54 (s, Me_{Ph(p)}), 18.81 (s, Me_{Ph(o)}), 6.87 (s, CH_{2-Ge}) 3.23 (s, Me_{TMS}). **²⁹Si-INEPT NMR** (79 MHz, 298 K, thf-*d*₈): δ [ppm] = -9.66 (s, Si_{TMS}), -108.69 (s, Si_{Ge9}). **¹¹B NMR** (128 MHz, 298 K, thf-*d*₈): δ [ppm] = 23.06 (brs, B_O). **Elemental analysis**: anal. calcd. for Ge₉Si₈BC₄₁H₈₆N₂OK · 0.9 tol: C, 34.62; H, 5.75; N, 1.72; found: C, 34.25; H, 5.68, N, 1.71 (toluene content of the microcrystalline solid was determined by ¹H NMR spectroscopy). **ESI MS**: *m/z* 1512.8 [Ge₉{Si(TMS)₃}₂(CH₂)₃O-DAB^{Mes}]⁻.

Synthesis of K[Ge₉{Si(TMS)₃}₂CH₃C=N-DAB^{Mes}] (6): In a typical experiment equimolar amounts of K₂[Ge₉{Si(TMS)₃}₂] (92 mg, 0.075 mmol, 1 equiv.) and DAB^{Mes}-Br (38.5 mg, 0.100 mmol, 1 equiv.) were weighted into a Schlenk tube in the glove box, and MeCN (3 mL) was added. After stirring for 5 h at room temperature, the solvent was removed *in vacuo* yielding a brown oil. Addition and subsequent removal of hexane (2 · 5 mL) yielded a brown solid. Dissolution in toluene (2 mL) gave a dark red solution, which was filtered. The solution was concentrated to half of its original volume and stored at room temperature yielding orange needle-shaped crystals. The supernatant solution was filtered-off, and the solid was washed with hexane (5 · 2 mL) and dried *in vacuo* (49 mg, 0.032 mmol, 43 %). **¹H NMR** (400 MHz, 298 K, thf-*d*₈): δ [ppm] = 6.74 (s, 4H, CH_{Ph}), 3.49 (s, 4H, CH_{2(Bb)}), 2.32 (s, 12H, Me_(o)), 2.20 (s, 6H Me_(p)), 1.78 (s, 3H, Me_{MeCN}), 0.25 (s, 54H, Me_{TMS}). **¹³C NMR** (101 MHz, 298 K, thf-*d*₈): δ [ppm] = 141.07 (s, C_{Ph(N)}), 137.22 (s, C_{Ph(o)}), 134.08 (s, C_{Ph(p)}), 129.59 (s, CH_{Ph}), 50.21 (s, CH_{2(Bb)}), 20.08 (s, Me_{Ph(o)}), 19.29 (s, Me_{Ph(p)}), 3.24 (s, Me_{TMS}). Signal of C=N could not be detected probably due to low concentration of sample. **²⁹Si-INEPT NMR** (79 MHz, 298 K, thf-*d*₈): δ [ppm] = -9.53 (s, Si_{TMS}), -107.27 (s, Si_{Ge9}). **¹¹B NMR** (128 MHz, 298 K, thf-*d*₈): δ [ppm] = 18.38 (brs, B_O). **Elemental analysis**: anal. calcd. for Ge₉Si₈BC₄₀H₈₃N₃K: C, 31.31; H, 5.45; N, 2.74; found: C, 31.90; H, 5.41; N, 2.71. **ESI MS**: *m/z* 1495.7 [Ge₉{Si(TMS)₃}₂(CH₃)C=N-BN^{Mes}]⁻, 1498.7 [Ge₉{Si(TMS)₃}₂(CD₃)C=N-BN^{Mes}]⁻.

Activation of thf with DAB^R-Br and (*i*Pr₂N)₂B-Br

In a typical experiment 100 μmol of the diazaborolidine DAB^R-Br, DAB(II)^{Dipp}-Br or (*i*Pr₂N)₂B-Br was weighted into a Schlenk tube, and thf (2 mL) was added. After the reaction time (Table S1) the solvent was removed *in vacuo* yielding a colorless or light brown (DAB^{Dipp}-Br and DAB(II)^{Dipp}-Br) oil, which was dissolved in C₆D₆ and investigated by NMR spectroscopy (¹H, ¹¹B). Respective NMR spectra are presented below (see Figures S5-S16).

Table S1. Reaction conditions for thf ring-opening reactions induced by different bromo-boranes.

	[mg]	reaction time [h]	temperature
(<i>i</i> Pr ₂ N) ₂ B-Br	29.1	3	r.t.
DAB ^{o-tol} -Br	32.9	1	r.t.
DAB ^{o-xyI} -Br	35.7	3	r.t.
DAB ^{Mes} -Br	38.5	3	r.t.
DAB ^{Dipp} -Br	46.9	69	70 °C
DAB(II) ^{Dipp} -Br	46.7	69	70 °C

(*i*Pr₂N)₂B-O-(CH₂)₄-Br

¹H NMR (400 MHz, 298 K, C₆D₆): δ [ppm] = 3.63 (t, ³J_{HH} = 6.7 Hz, 2H, CH₂-O), 3.34 (hept, ³J_{HH} = 6.6 Hz, 4H, CH_{IPr}), 3.03 (t, ³J_{HH} = 6.7 Hz, 2H, CH₂-Br), 1.81-1.73 (m, 2H, CH₂), 1.56-1.49 (m, 2H, CH₂), 1.13 (d, ³J_{HH} = 6.6 Hz, 24H, CH_{3IPr}). ¹¹B NMR (128 MHz, 298 K, C₆D₆): δ [ppm] = 26.00 (brs).

DAB^{o-tol}-O-(CH₂)₄-Br

¹H NMR (400 MHz, 298 K, C₆D₆): δ [ppm] = 7.14-7.06 (m, 4H, CH_{Ph}), 7.00-6.96 (m, 2H, CH_{Ph}), 6.79-6.73 (m, 2H, CH_{Ph}), 3.34 (s, 4H, CH_{2(Bb)}), 3.26 (t, ³J_{HH} = 6.8 Hz, 2H, CH₂-O), 2.72 (t, ³J_{HH} = 6.8 Hz, 2H, CH₂-Br), 2.36 (s, 6H, Me), 1.38-1.29 (m, 2H, CH₂), 1.13-1.04 (m, 2H, CH₂). ¹¹B NMR (128 MHz, 298 K, C₆D₆): δ [ppm] = 23.71 (brs).

DAB^{o-xyI}-O-(CH₂)₄-Br

¹H NMR (400 MHz, 298 K, C₆D₆): δ [ppm] = 7.04-6.97 (m, 6H, CH_{Ph}), 3.26 (s, 4H, CH_(Bb)), 3.19 (t, ³J_{HH} = 6.9 Hz, 2H, CH₂-O), 2.67 (t, ³J_{HH} = 6.9 Hz, 2H, CH₂-Br), 2.37 (s, 12H, CH_{3(o)}), 1.35-1.27 (m, 2H, CH₂), 1.05-0.98 (m, 2H, CH₂). ¹¹B NMR (128 MHz, 298 K, C₆D₆): δ [ppm] = 23.42 (brs).

DAB^{Mes}-O-(CH₂)₄-Br

¹H NMR (400 MHz, 298 K, C₆D₆): δ [ppm] = 6.85 (s, 4H, CH_{Ph}), 3.31 (s, 4H, CH_{2(Bb)}), 3.26 (t, ³J_{HH} = 6.8 Hz, 2H, CH₂-O), 2.69 (t, ³J_{HH} = 6.8 Hz, 2H, CH₂-Br), 2.39 (s, 12H, Me_(o)), 2.16 (s, 6H, Me_(p)), 1.41-1.32 (m, 2H, CH₂), 1.10-1.01 (m, 2H, CH₂). ¹¹B NMR (128 MHz, 298 K, C₆D₆): δ [ppm] = 23.58 (brs).

DAB^{Dipp}-O-(CH₂)₄-Br

¹H NMR (400 MHz, 298 K, C₆D₆): δ [ppm] = 7.21-7.17 (m, 4H, CH_(m)), 7.16-7.13 (m, 2H, CH_(p)), 3.61 (hept, ³J_{HH} = 6.8 Hz, 4H, CH_{IPr}), 3.43 (s, 4H, CH_(Bb)), 3.29 (t, ³J_{HH} = 6.9 Hz, 2H, CH₂-O), 2.67 (t, ³J_{HH} = 6.9 Hz, 2H, CH₂-Br), 1.37 (d, ³J_{HH} = 6.9 Hz, 12H, CH_{3IPr}), 1.33 (d, ³J_{HH} = 6.9 Hz, 12H, CH_{3IPr}), 1.27-1.23 (m, 2H, CH₂), 1.11-1.03 (m, 2H, CH₂). ¹¹B NMR (128 MHz, 298 K, C₆D₆): δ [ppm] = 23.69 (brs).

DAB(II)^{Dipp}-O-(CH₂)₄-Br

¹H NMR (400 MHz, 298 K, CDCl₃): δ [ppm] = 7.44-7.28 (m, 4H, CH_(m)), 7.24 (s, 2H, CH_(p)), 5.98 (s, 2H, CH_(Bb)), 3.39 (t, ³J_{HH} = 6.2 Hz, 2H, CH₂-O), 3.29-3.21 (m, 4H, CH_{IPr}), 3.20-3.16 (m, CH₂-Br, 2H), 1.66 (pent, ³J_{HH} = 7.0 Hz, 2H, CH₂), 1.44-1.38 (m, 2H, CH₂), 1.29 (d, ³J_{HH} = 5.2 Hz, 12H, CH_{3IPr}), 1.28 (d, ³J_{HH} = 5.2 Hz, 12H, CH_{3IPr}). ¹¹B NMR (128 MHz, 298 K, CDCl₃): δ [ppm] = 20.94 (brs).

Reactivity of DAB^{Mes}-Br towards MeCN

In a typical experiment 100 μmol of the diazaborolidine DAB^{Mes}-Br was weighted into a Schlenk tube, and MeCN (2 mL) was added. After the reaction time (Table S2), the solvent was removed *in vacuo*, yielding a colorless solid, which was dissolved in C₆D₆ and investigated by NMR spectroscopy (¹H, ¹¹B). Furthermore, 100 μmol of the diazaborolidine DAB^{Mes}-Br and 100 μmol MeCN were combined in a *J-Young* NMR tube, and the reaction was monitored directly in C₆D₆. Respective NMR spectra (including the spectrum of pure reactant DAB^{Mes}-Br) are presented below (see Figures S17-S20).

Table S2. Reaction conditions for investigating the reactivity of DAB^{Mes}-Br towards MeCN.

	[mg]	reaction time [h]	temperature
DAB ^{Mes} -Br	38.5	16	r.t.
DAB ^{Mes} -Br	38.5	16	70 °C

DAB^{Mes}-Br

¹H NMR (400 MHz, 298 K, C₆D₆): δ [ppm] = 6.83 (s, 4H, CH_{Ph}), 3.31 (s, 4H, CH_{2(Bb)}), 2.33 (s, 12H, Me_(o)), 2.14 (s, 6H, Me_(p)). **¹¹B NMR** (128 MHz, 298 K, C₆D₆): δ [ppm] = 25.97 (brs).

The residues of the reaction of DAB^{Mes}-Br with MeCN at r. t. or 70 °C as well as the *in situ* investigation of the borane and MeCN in C₆D₆ show no additional or shifted signals in the NMR spectra, manifesting that no reaction occurs (in absence of [Ge₉] cluster; Figures S19 and S20).

ESI MS sample preparation

Insertion of tetrahydrofuran (thf) and trimethyleneoxide (tmo)

Equimolar amounts of K₂[Ge₉{Si(TMS)₃}₂] and DAB^{o-xyI}-Br or (*i*-Pr₂N)₂B-Br (0.020 mmol) were weighted into a glass vial in the glove box, and thf / thf-*d*₈ or tmo (0.5 mL) was added to obtain a deep red solution. The mixture was stirred for 3 h at room temperature, before it was transferred to a Schlenk tube, and the solvent was removed *in vacuo*. Subsequently, the obtained residues were diluted with thf and investigated by ESI MS. The respective spectra are presented below.

Equimolar amounts of K₂[Ge₉{Si(TMS)₃}₂] and DAB(II)^{Dipp}-Br or DAB^{Dipp}-Br (0.020 mmol) were dissolved in thf / thf-*d*₈ or tmo (0.5 mL) and stirred at 35 °C for 3 weeks. Alternatively, a solution of the respective bromo-borane in thf can be heated to 60 °C for 2 d before K₂[Ge₉{Si(TMS)₃}₂] is added. In this case complete conversion of the reactants occurs overnight. Subsequently, the solvent was removed *in vacuo*, and the obtained residues were diluted with thf and investigated by ESI MS. The respective spectra are presented below.

Activation of acetonitrile

Equimolar amounts of K₂[Ge₉{Si(TMS)₃}₂] and DAB^{o-xyI}-Br or (*i*-Pr₂N)₂B-Br (0.020 mmol) were weighted into a glass vial in the glove box, and MeCN / MeCN-*d*₃ (0.5 mL) was added to obtain a deep red solution. The mixture was stirred for 3 h at room temperature, before it was transferred to a Schlenk tube, and the solvent was removed *in vacuo*. Subsequently, the obtained residues were diluted with MeCN and investigated by ESI MS. The respective spectra are presented below.

Equimolar amounts of K₂[Ge₉{Si(TMS)₃}₂] and DAB(II)^{Dipp}-Br or DAB^{Dipp}-Br (0.020 mmol) were dissolved in MeCN / MeCN-*d*₃ (0.5 mL) and stirred at 40 °C for 4 d. Subsequently, the solvent was removed *in vacuo*, and the obtained residues were diluted with MeCN and investigated by ESI MS. The respective spectra are presented below.

Crystallographic data of compounds 3 – 6

Table S3. Crystallographic data of compounds 3 - 6.

Compound	3	4	5	6
formula	Ge ₉ Si ₈ BC ₄₂ H ₈₈ N ₂ OK · 1.5tol	Ge ₉ Si ₈ BC ₄₈ H ₉₈ N ₂ OK · 2tol	Ge ₉ Si ₈ BC ₄₈ H ₉₄ N ₂ OK	Ge ₉ Si ₈ BC ₄₀ H ₈₃ N ₃ K · 1tol
fw [g·mol ⁻¹]	1703.28	1831.49	1643.19	1626.16
space group	<i>P</i> $\bar{1}$	<i>P</i> $\bar{1}$	<i>P</i> $\bar{1}$	<i>P2</i> ₁
<i>a</i> [Å]	14.7094(7)	16.402(1)	14.666(1)	13.7573(4)
<i>b</i> [Å]	16.9327(6)	16.841(1)	15.460(2)	9.2613(3)
<i>c</i> [Å]	18.7377(9)	17.542(1)	18.062(2)	28.424(1)
α [deg]	65.966(3)	92.419(6)	65.417(7)	90
β [deg]	67.528(4)	107.892(5)	82.365(7)	94.438(3)
γ [deg]	88.951(3)	102.920(6)	88.648(8)	90
<i>V</i> [Å ³]	3886.2(3)	4462.2(6)	3688.9(6)	3610.6(2)
<i>Z</i>	2	2	2	2
<i>T</i> [K]	150	150	150	150
λ [Å]	Mo <i>K</i> α	Mo <i>K</i> α	Mo <i>K</i> α	Mo <i>K</i> α
ρ_{calcd} [g·cm ⁻³]	1.456	1.363	1.479	1.496
μ [mm ⁻¹]	3.638	3.174	3.830	3.911
collected reflections	74106	96277	77184	78148
indep. reflections	15237	17531	14484	14199
<i>R</i> _{int} / <i>R</i> _{σ}	0.0695/0.0482	0.0848/0.1019	0.0878/0.0599	0.0405/0.0258
parameters / restraints	682/6	785/0	656/0	648/1
<i>R</i> ₁ [<i>I</i> > 2 σ (<i>I</i>) / all data]	0.0435/0.0836	0.0443/0.1025	0.0475/0.0915	0.0253/0.0296
<i>wR</i> ₂ [<i>I</i> > 2 σ (<i>I</i>) / all data]	0.0880/0.1113	0.0727/0.0871	0.0937/0.1195	0.0556/0.0574
goodness of fit	1.115	0.901	1.084	1.031
max./min. diff. el. density [e · Å ⁻³]	1.45/-1.26	0.78/-0.61	0.81/-0.89	0.43/-0.36
CCDC	1993875	1993876	1993877	1993878

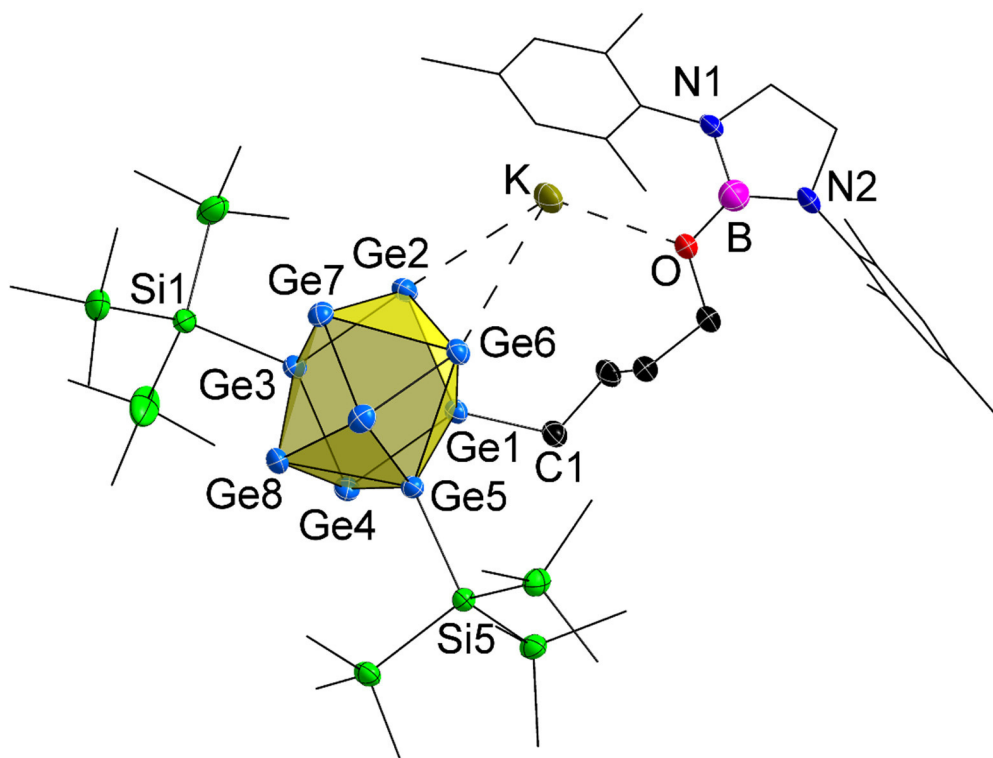


Figure S1. Molecular structure of compound **3**. All ellipsoids are shown at a 50 % probability level. For clarity, protons and co-crystallized solvent molecules are omitted. Carbon atoms of silyl groups and of the DAB^{Mes} moiety are presented as black wire sticks. For crystallographic data and selected bond lengths of **3** see Tables S3 and S4.

Table S4. Selected bond lengths in compound **3**.

bond	distance [Å]
Ge1-Ge2	2.5038(8)
Ge1-Ge4	2.5675(7)
Ge1-Ge5	2.5339(8)
Ge1-Ge6	2.7612(8)
Ge2-Ge3	2.5503(8)
Ge2-Ge6	2.6985(9)
Ge2-Ge7	2.6740(8)
Ge3-Ge4	2.5460(8)
Ge3-Ge7	2.6127(8)
Ge3-Ge8	2.5899(8)
Ge4-Ge5	2.6750(8)
Ge4-Ge8	2.7432(8)
Ge5-Ge6	2.7587(8)
Ge5-Ge8	2.6063(8)
Ge5-Ge9	2.5437(8)
Ge6-Ge7	2.6926(8)
Ge6-Ge9	2.6077(8)
Ge7-Ge8	2.9322(8)
Ge7-Ge9	2.5900(9)
Ge8-Ge9	2.6804(9)
Ge1-C1	1.995(5)
Ge3-Si1	2.396(2)
Ge5-Si5	2.395(2)
Ge2-Ge4	3.976(1)
Ge5-Ge6	2.759(2)
Ge7-Ge8	2.932(1)

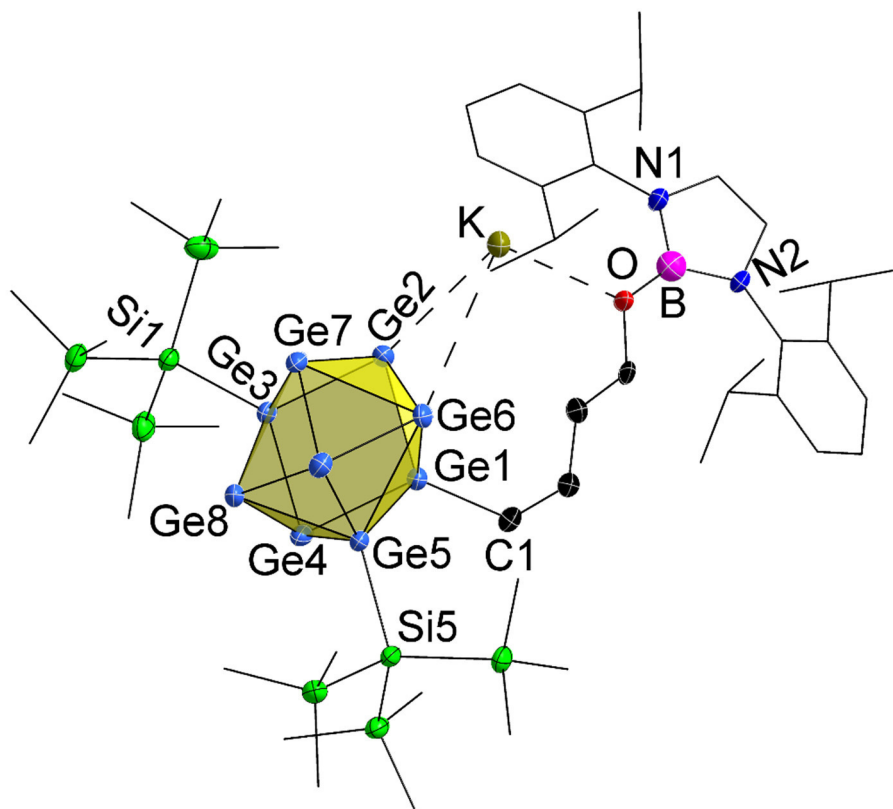


Figure S2. Molecular structure of compound **4**. All ellipsoids are shown at a 50 % probability level. For clarity, protons and co-crystallized solvent molecules are omitted. Carbon atoms of silyl groups and the DAB(II)^{Dipp} moiety are presented as black wire sticks. For crystallographic data and selected bond lengths of **4** see Tables S3 and S5.

Table S5. Selected bond lengths in compound **4**.

bond	distance [Å]
Ge1-Ge2	2.5046(8)
Ge1-Ge4	2.5577(8)
Ge1-Ge5	2.5334(8)
Ge1-Ge6	2.7429(9)
Ge2-Ge3	2.5394(7)
Ge2-Ge6	2.6699(8)
Ge2-Ge7	2.6825(9)
Ge3-Ge4	2.5361(8)
Ge3-Ge7	2.6202(8)
Ge3-Ge8	2.5758(8)
Ge4-Ge5	2.6690(8)
Ge4-Ge8	2.7555(9)
Ge5-Ge6	2.8140(8)
Ge5-Ge8	2.6048(7)
Ge5-Ge9	2.5188(8)
Ge6-Ge7	2.6876(7)
Ge6-Ge9	2.6027(8)
Ge7-Ge8	2.9324(8)
Ge7-Ge9	2.5919(8)
Ge8-Ge9	2.6825(8)
Ge1-C1	2.007(5)
Ge3-Si1	2.392(1)
Ge5-Si5	2.403(2)
Ge2-Ge4	3.918(1)
Ge5-Ge6	2.815(2)
Ge7-Ge8	2.934(1)

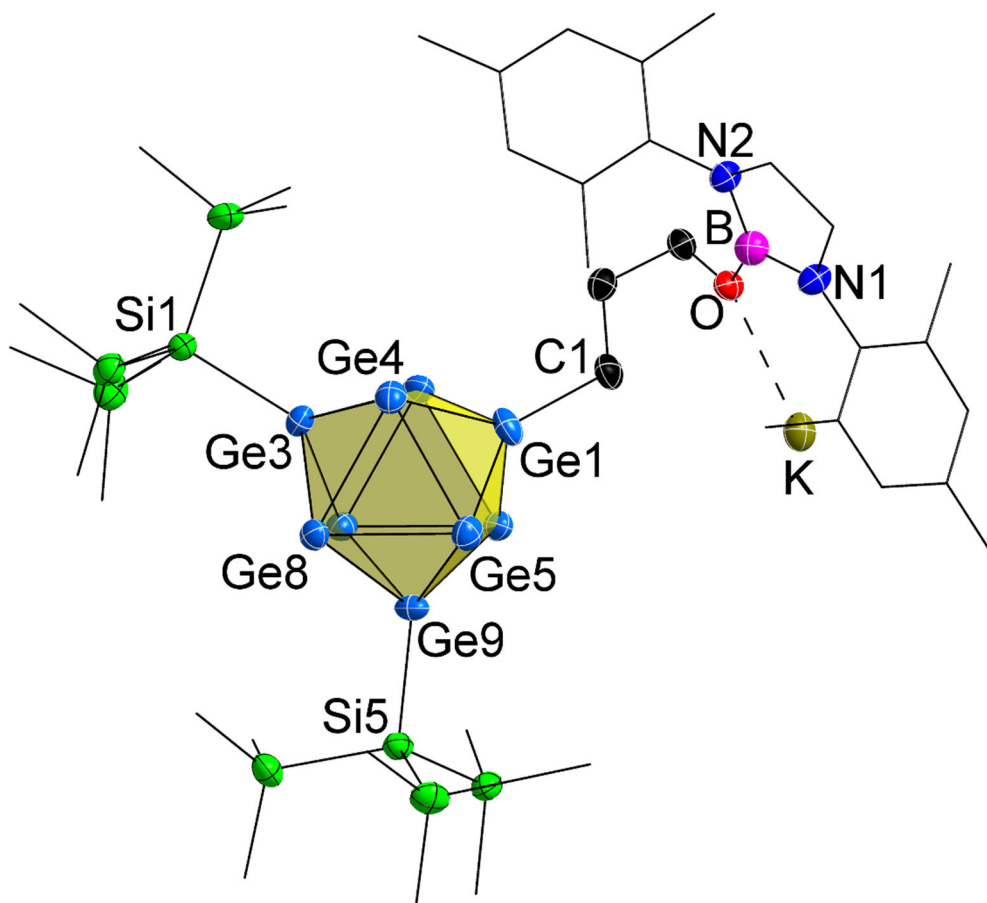


Figure S3. Molecular structure of compound **5**. All ellipsoids are shown at a 50 % probability level. For clarity, protons and co-crystallized solvent molecules are omitted. Carbon atoms of silyl groups and the DAB^{Mes} moiety are presented as black wire sticks. For crystallographic data and selected bond lengths of **5** see Tables S3 and S6.

Table S6. Selected bond lengths in compound **5**.

bond	distance [Å]
Ge1-Ge2	2.528(1)
Ge1-Ge4	2.5237(9)
Ge1-Ge5	2.524(1)
Ge1-Ge6	2.519(1)
Ge2-Ge3	2.5074(9)
Ge2-Ge6	2.692(1)
Ge2-Ge7	2.692(1)
Ge3-Ge4	2.5516(9)
Ge3-Ge7	2.5473(9)
Ge3-Ge8	2.5326(9)
Ge4-Ge5	2.665(1)
Ge4-Ge8	2.715(1)
Ge5-Ge8	2.6612(9)
Ge5-Ge9	2.555(1)
Ge6-Ge7	2.6825(9)
Ge6-Ge9	2.5031(9)
Ge7-Ge9	2.5563(9)
Ge8-Ge9	2.5518(9)
Ge1-C1	1.984(6)
Ge3-Si1	2.381(2)
Ge9-Si5	2.383(2)
Ge2-Ge4	3.429(1)
Ge5-Ge6	3.525(1)
Ge7-Ge8	3.295(1)

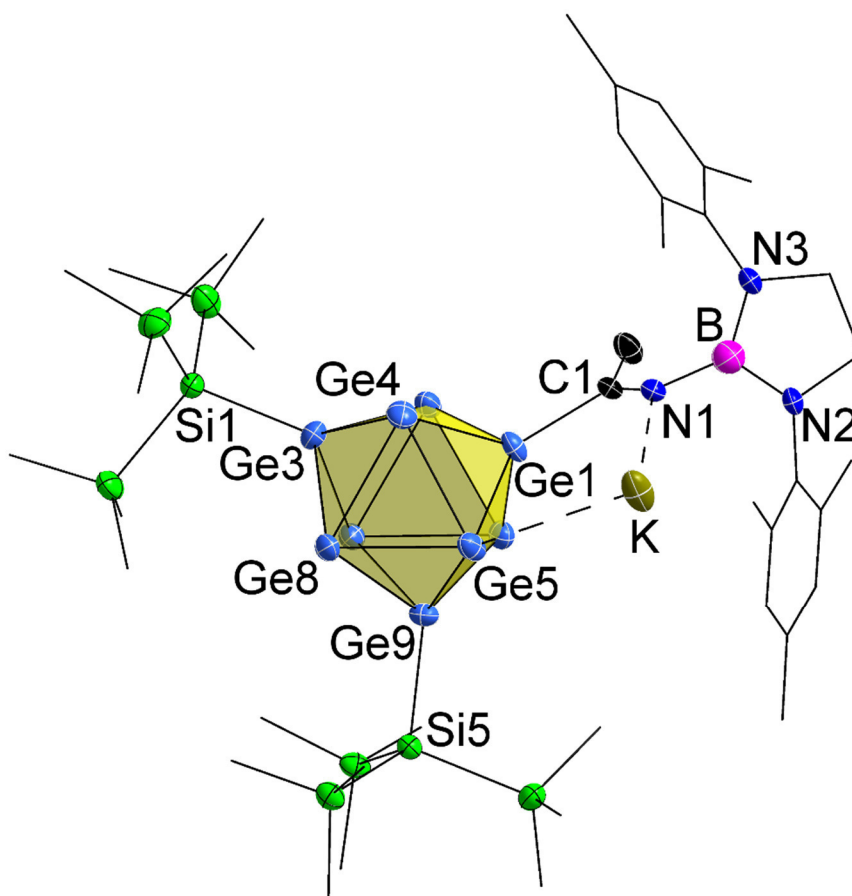


Figure S4. Molecular structure of compound **6**. All ellipsoids are shown at a 50 % probability level. For clarity, protons and co-crystallized solvent molecules are omitted. Carbon atoms of silyl groups and the DAB^{Mes} moiety are presented as black wire sticks. For crystallographic data and selected bond lengths of **6** see Tables S3 and S7.

Table S7. Selected bond lengths in compound **6**.

bond	distance [Å]
Ge1-Ge2	2.5332(7)
Ge1-Ge4	2.5360(7)
Ge1-Ge5	2.5573(7)
Ge2-Ge3	2.5232(7)
Ge2-Ge6	2.6599(7)
Ge2-Ge7	2.7213(7)
Ge3-Ge4	2.5267(7)
Ge3-Ge7	2.5128(7)
Ge3-Ge8	2.5532(7)
Ge4-Ge5	2.6679(7)
Ge4-Ge8	2.7396(7)
Ge5-Ge8	2.6347(7)
Ge5-Ge9	2.5308(7)
Ge6-Ge7	2.6637(7)
Ge6-Ge9	2.5300(7)
Ge7-Ge9	2.5541(7)
Ge8-Ge9	2.5619(7)
Ge1-C1	1.997(4)
Ge3-Si1	2.369(1)
Ge9-Si5	2.381(1)
Ge2-Ge4	3.370(1)
Ge5-Ge6	3.663(1)
Ge7-Ge8	3.201(1)

NMR spectra

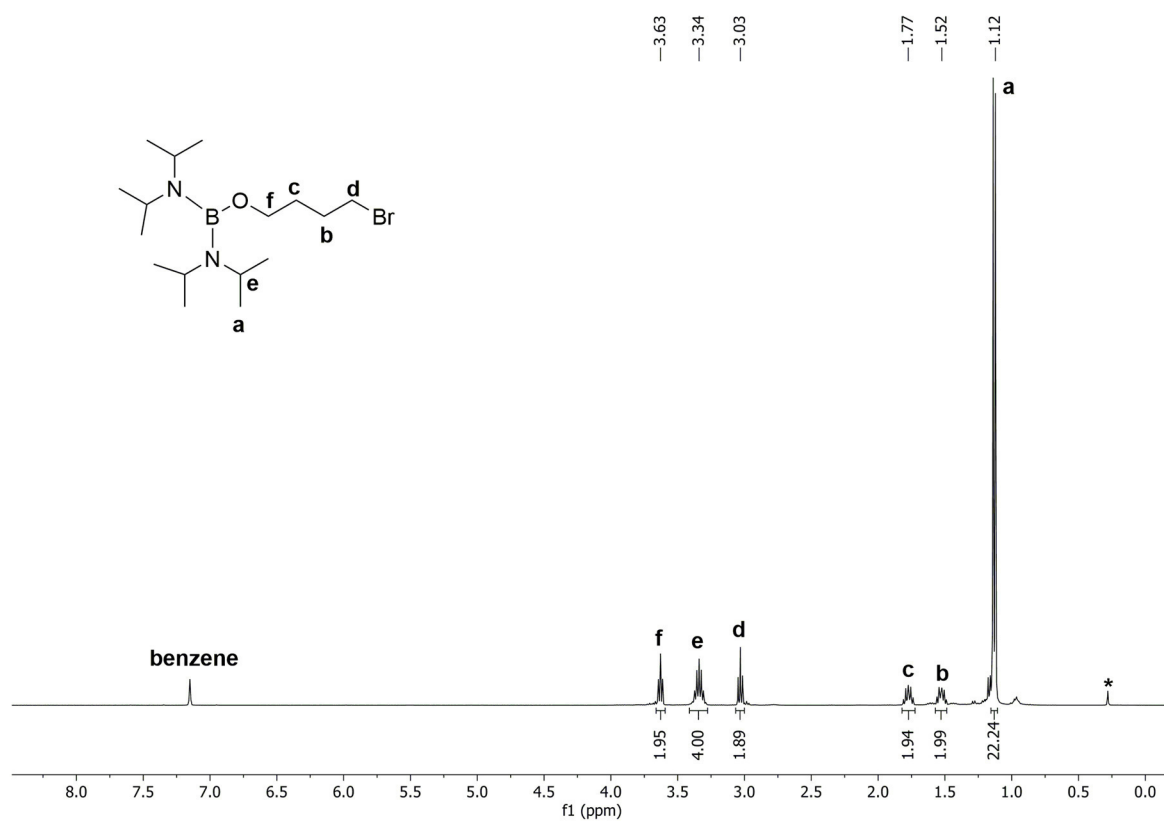


Figure S5. ^1H NMR spectrum of $(i\text{Pr}_2\text{N})_2\text{B}-(\text{CH}_2)_4\text{-Br}$ acquired in C_6D_6 . * silicon grease.

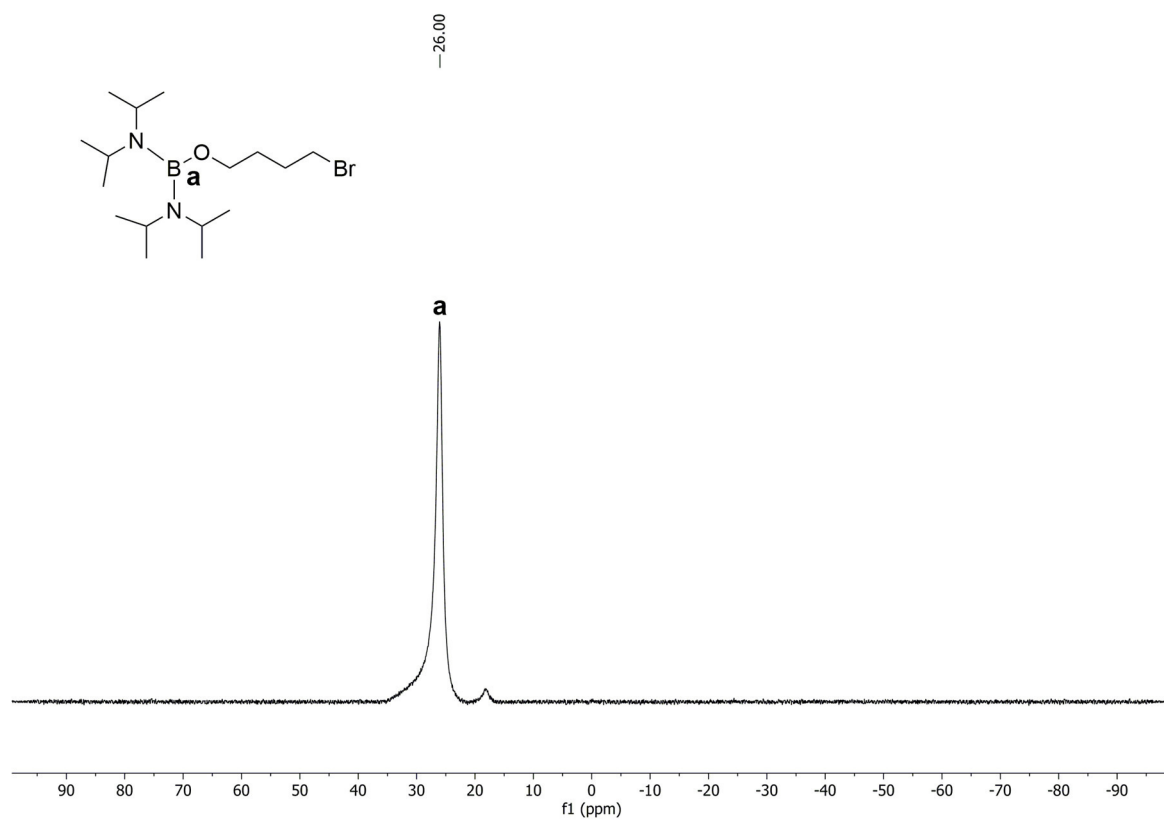


Figure S6. ^{11}B NMR spectrum of $(i\text{Pr}_2\text{N})_2\text{B}-\text{O}-(\text{CH}_2)_4\text{-Br}$ acquired in C_6D_6 .

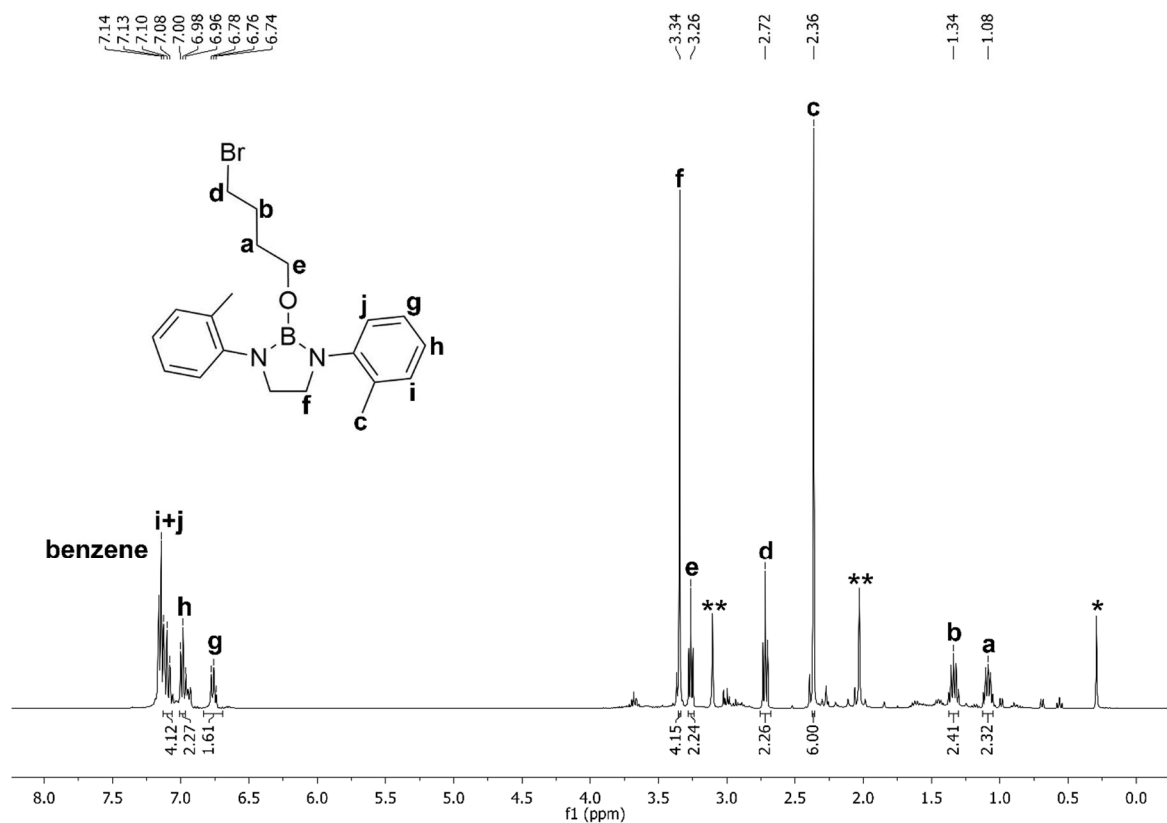


Figure S7. ^1H NMR spectrum of $\text{DAB}^{\text{o-tol}}\text{-O}-(\text{CH}_2)_4\text{-Br}$ acquired in C_6D_6 . * silicon grease; ** unknown side product(s).

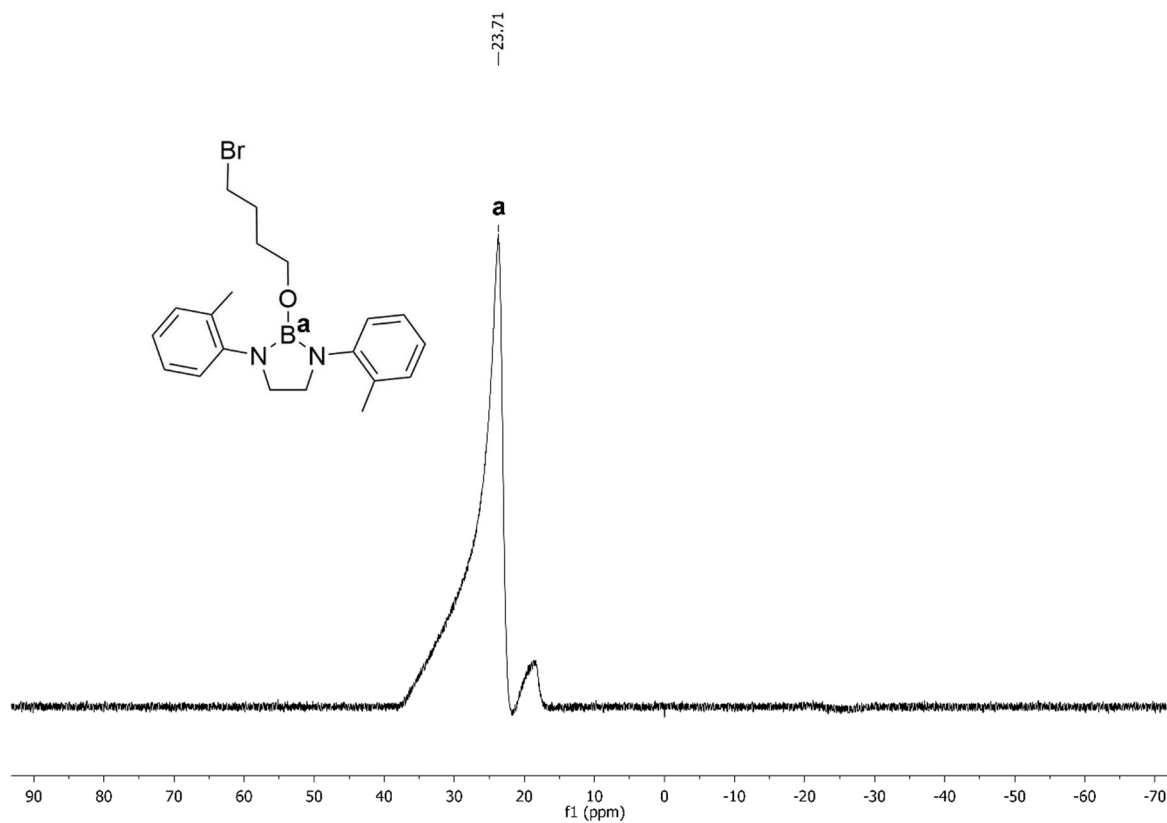


Figure S8. ^{11}B NMR spectrum of $\text{DAB}^{\text{o-tol}}\text{-O}-(\text{CH}_2)_4\text{-Br}$ acquired in C_6D_6 . Impurity is caused by unidentified species.

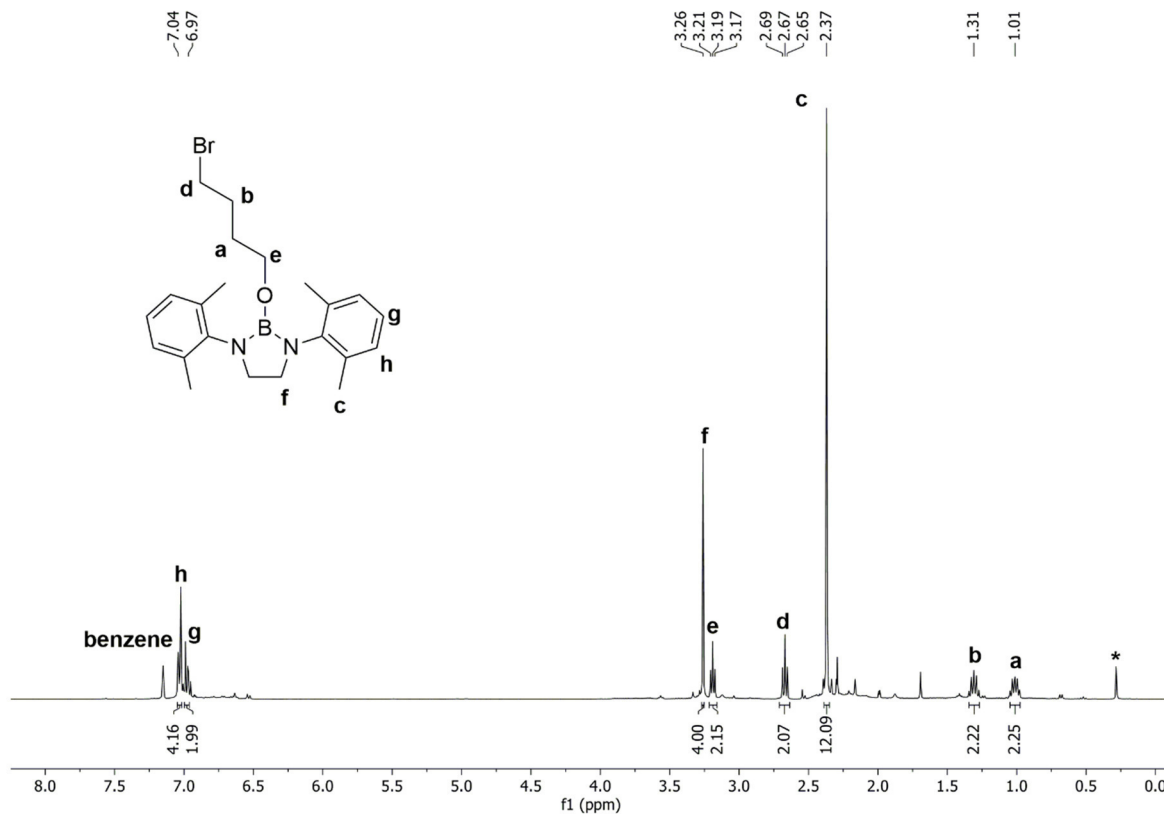


Figure S9. ¹H NMR spectrum of $\text{DAB}^{\text{o-xyL}}\text{-O}-(\text{CH}_2)_4\text{-Br}$ acquired in C_6D_6 . * silicon grease.

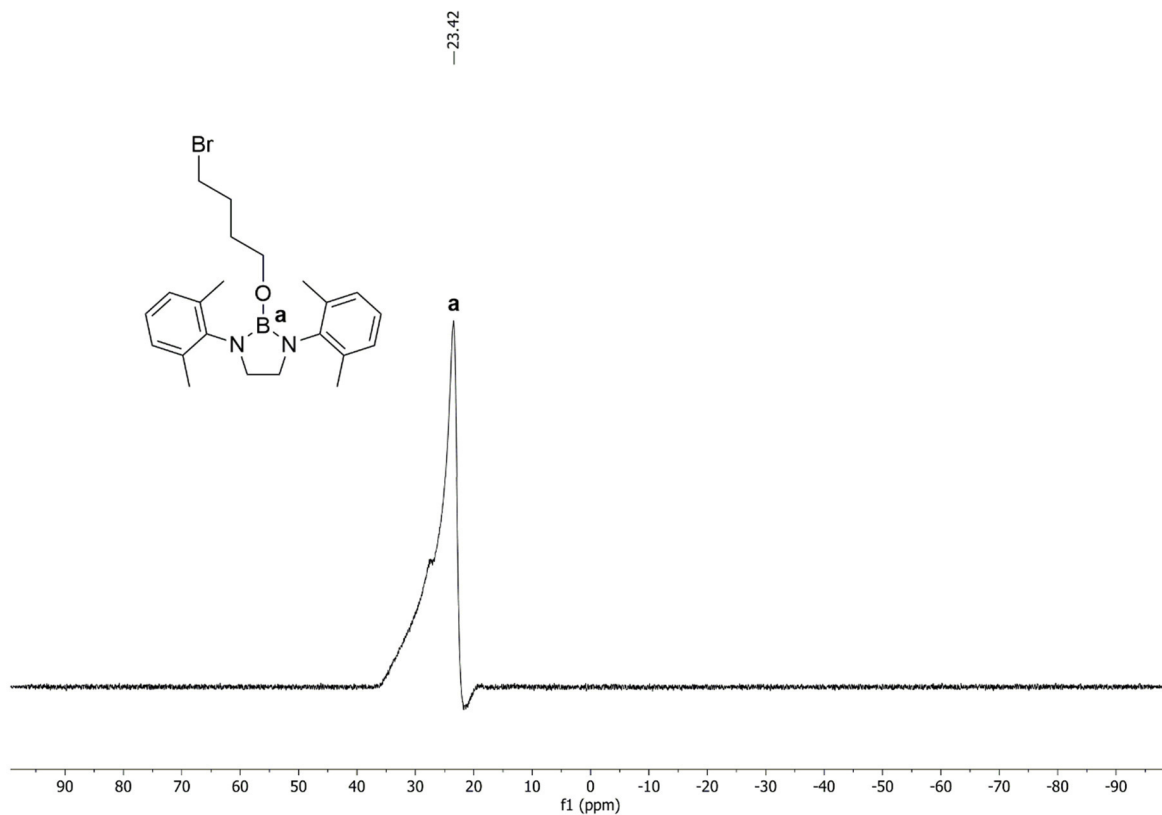


Figure S10. ¹¹B NMR spectrum of $\text{DAB}^{\text{o-xyL}}\text{-O}-(\text{CH}_2)_4\text{-Br}$ acquired in C_6D_6 . Impurity is caused by an unidentified species.

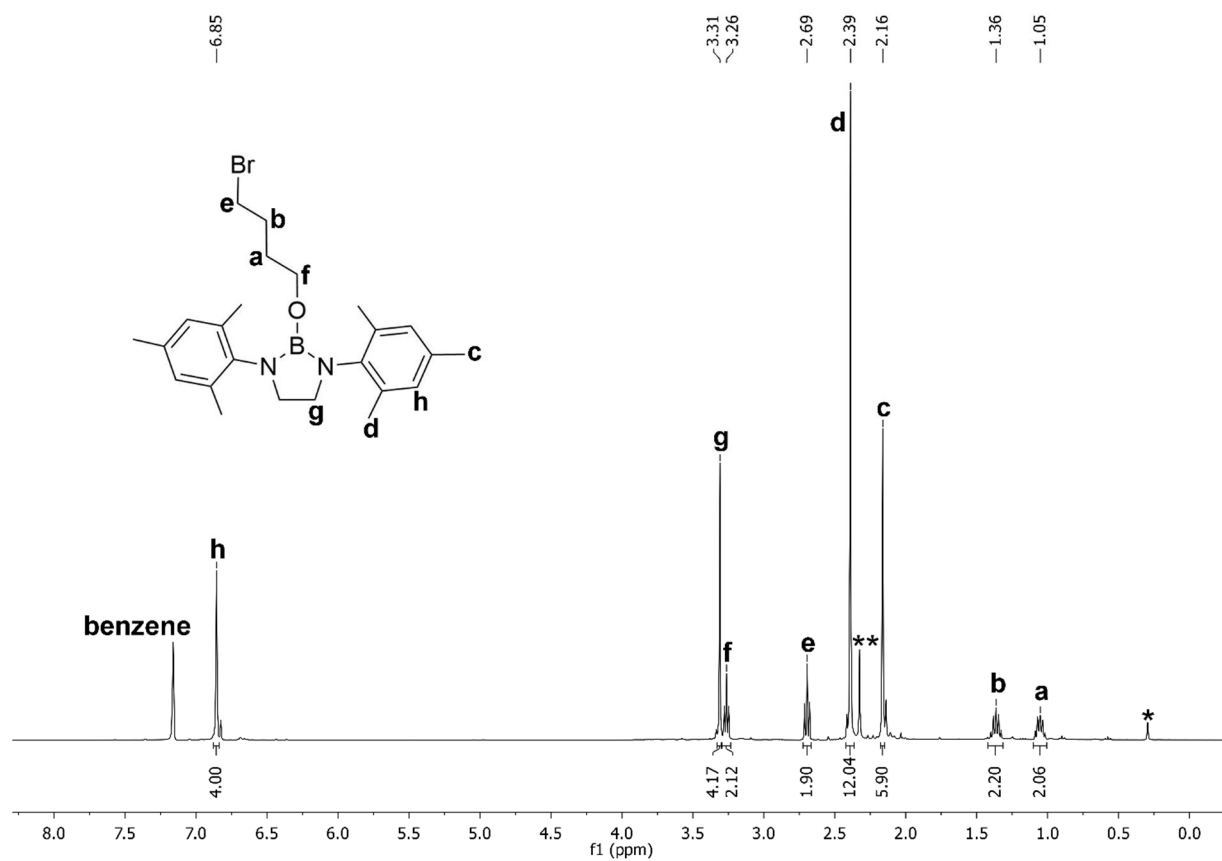


Figure S11. ¹H NMR spectrum of DAB^{Mes}-O-(CH₂)₄-Br acquired in C₆D₆. * silicon grease; ** unknown side product(s).

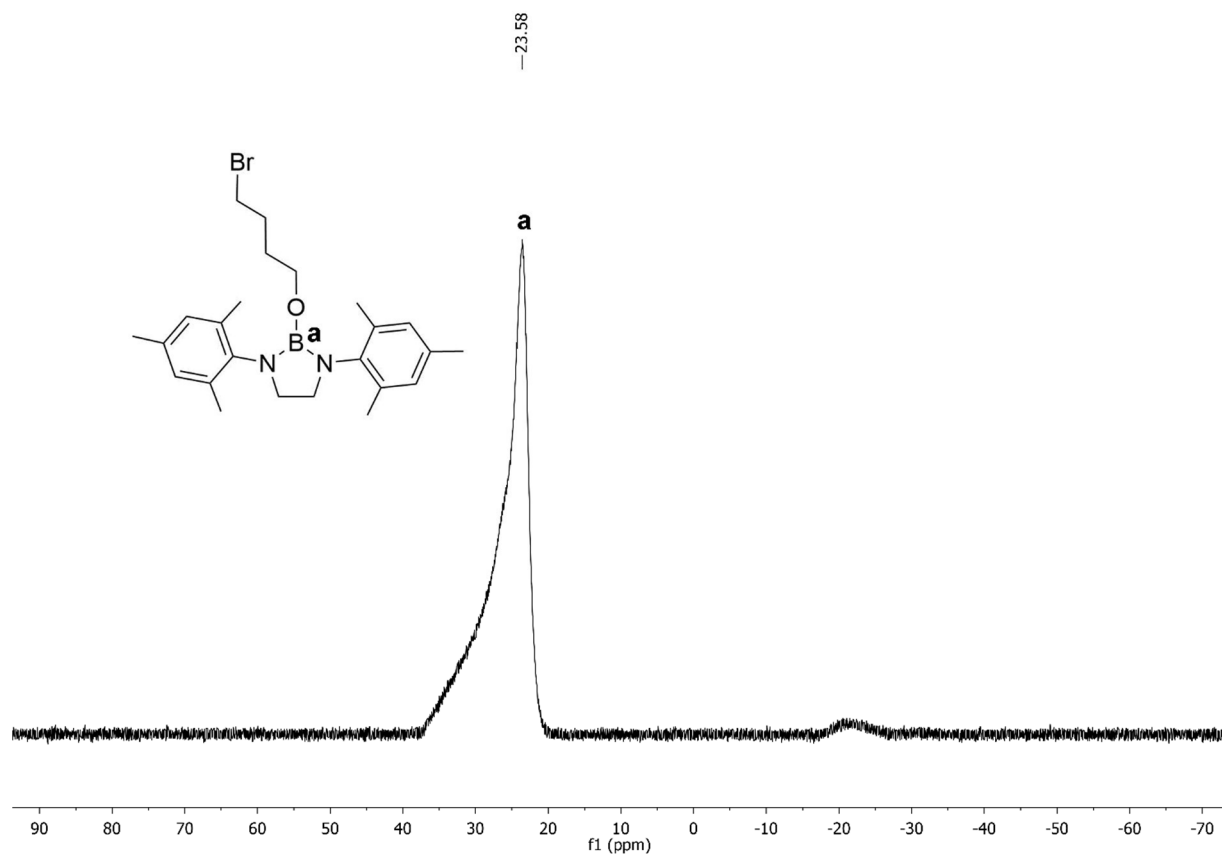


Figure S12. ¹¹B NMR spectrum of DAB^{Mes}-O-(CH₂)₄-Br acquired in C₆D₆. Impurity is caused by an unidentified species.

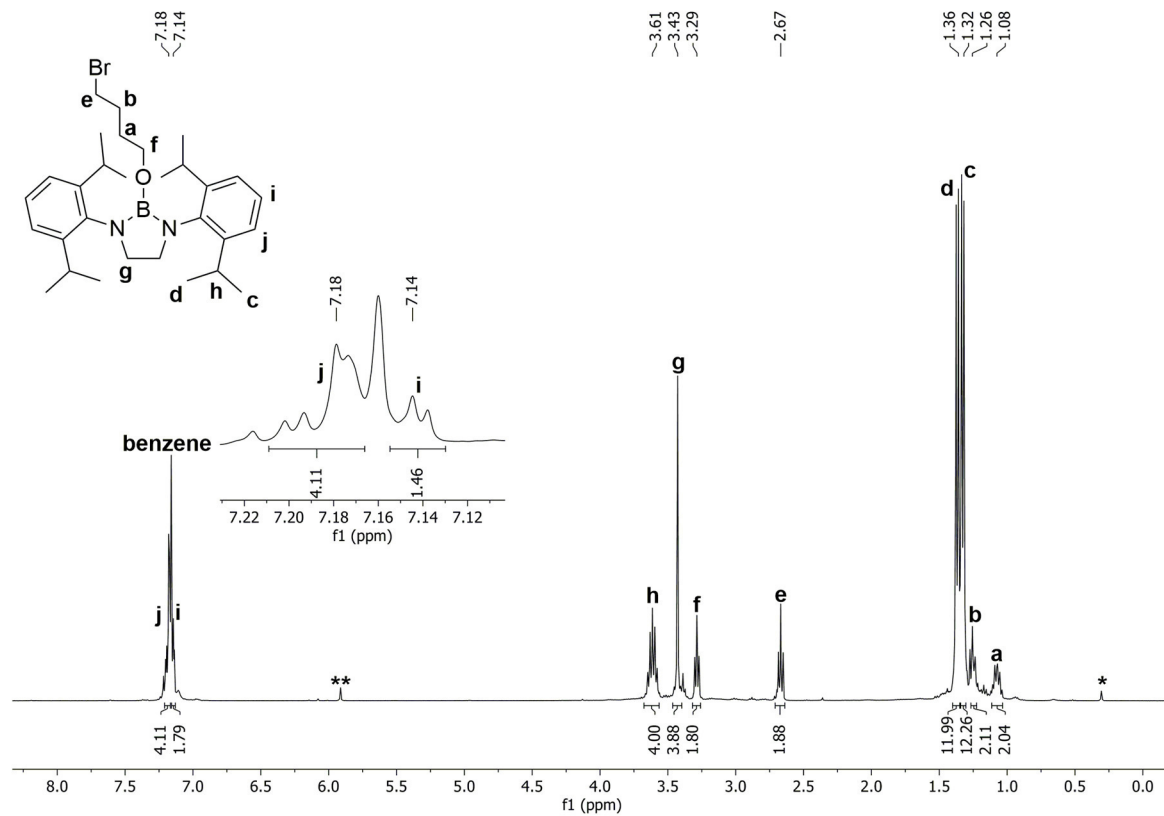


Figure S13. ¹H NMR spectrum of DAB^{Dipp}-O-(CH₂)₄-Br acquired in C₆D₆. * silicon grease; ** unknown side product.

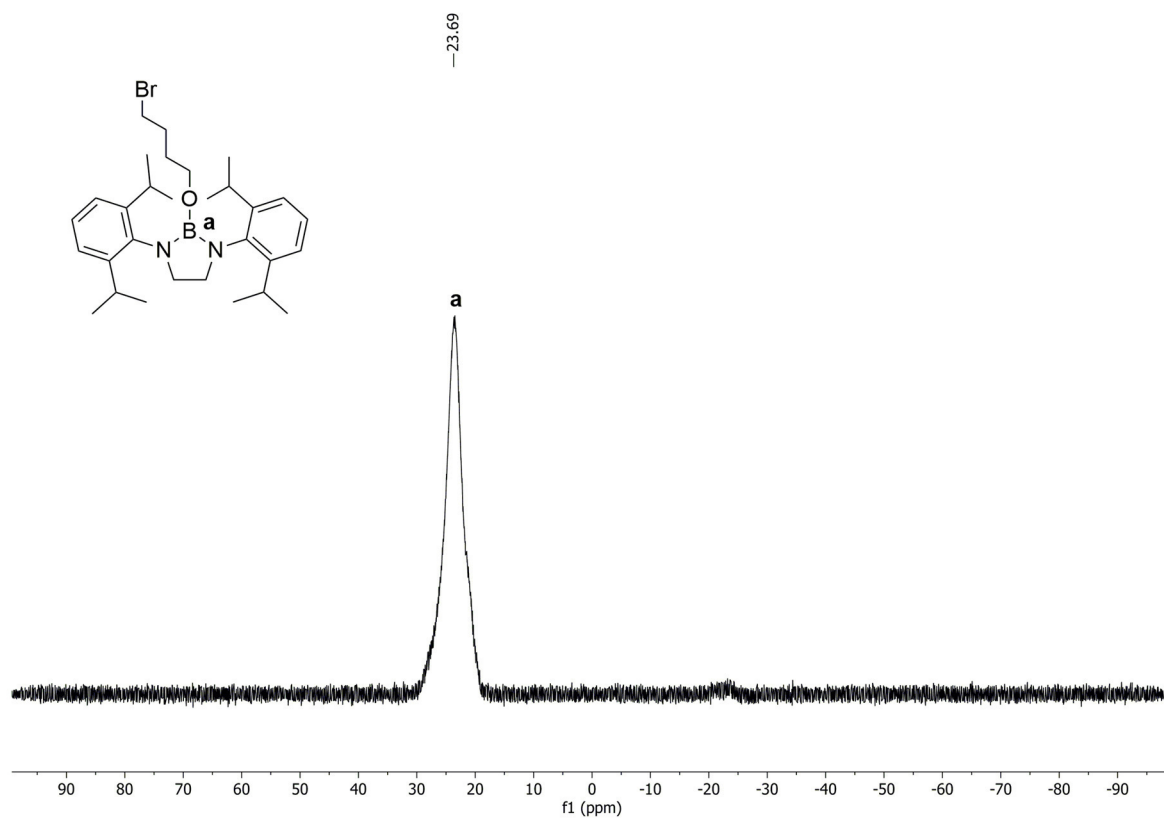


Figure S14. ¹¹B NMR spectrum of DAB^{Dipp}-O-(CH₂)₄-Br acquired in C₆D₆.

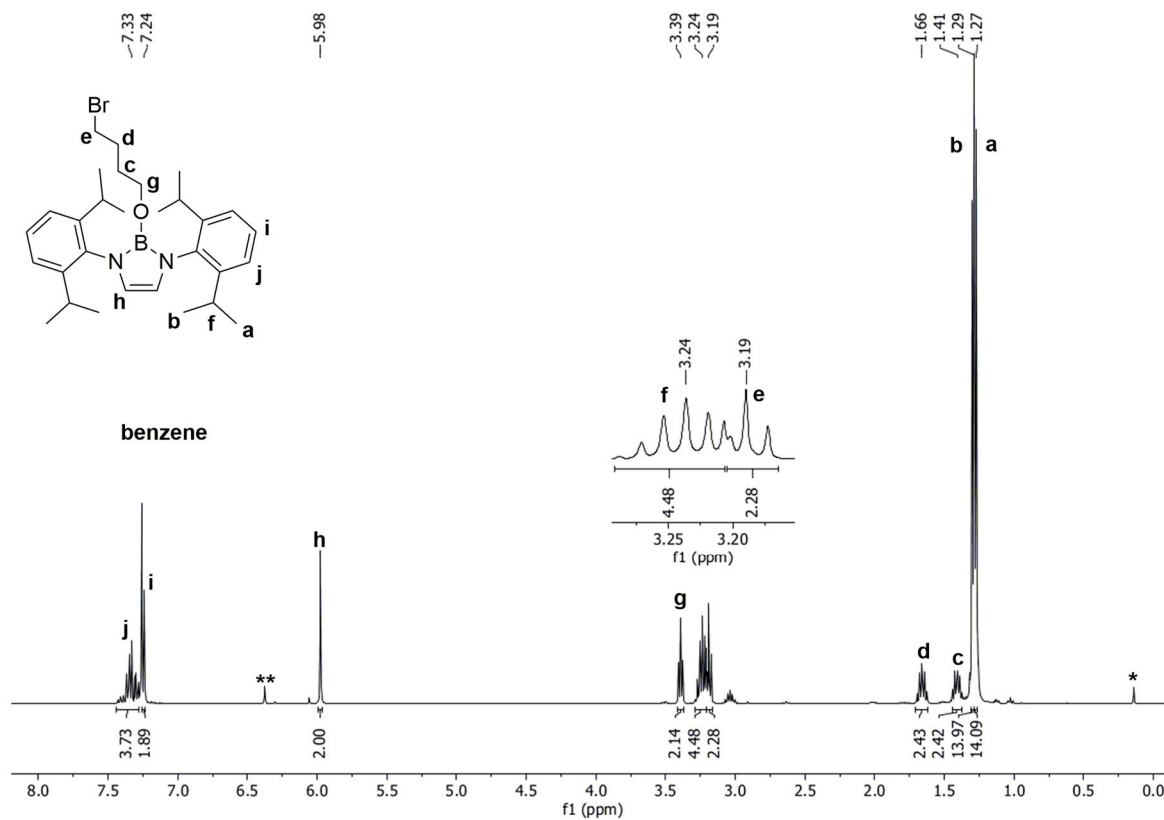


Figure S15. ¹H NMR spectrum of DAB(II)^{Dipp}-O-(CH₂)₄-Br acquired in C₆D₆. * silicon grease; ** unknown side product.

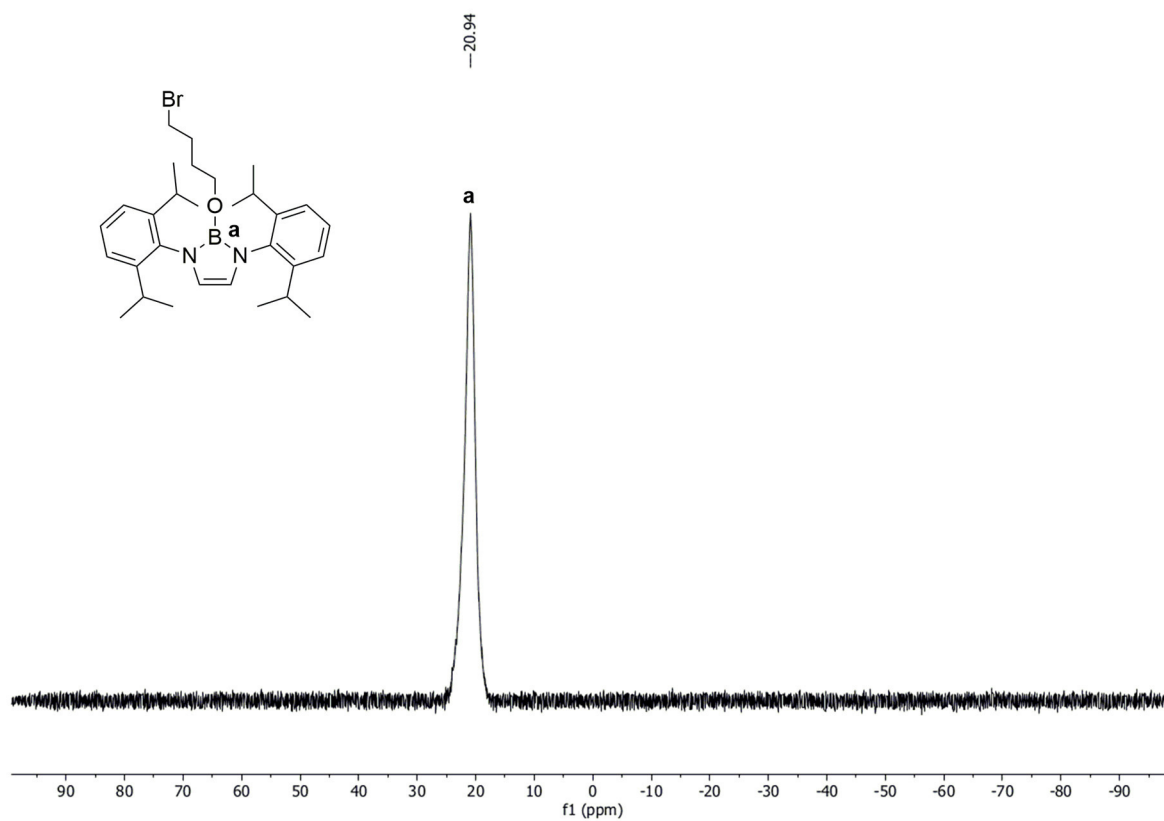


Figure S16. ¹¹B NMR spectrum of DAB(II)^{Dipp}-O-(CH₂)₄-Br acquired in C₆D₆.

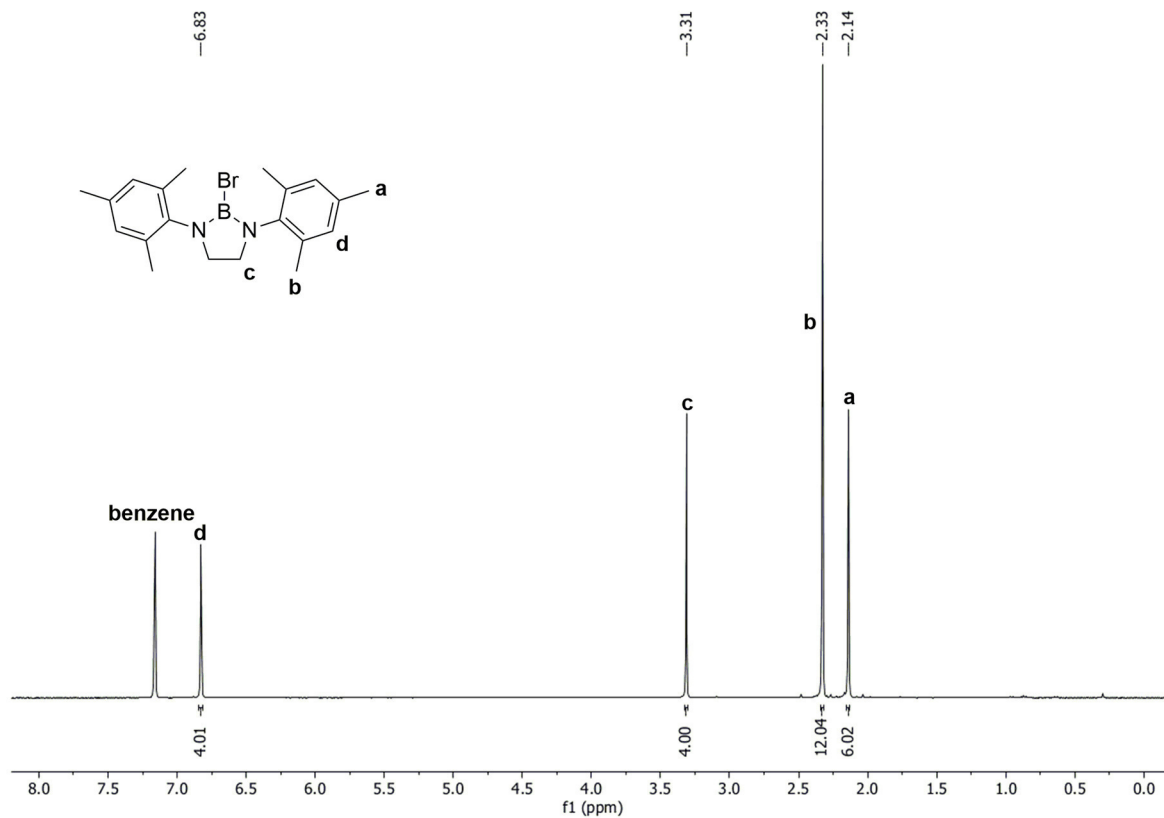


Figure S17. ¹H NMR spectrum of DAB^{Mes}-Br acquired in C₆D₆ (before MeCN application).

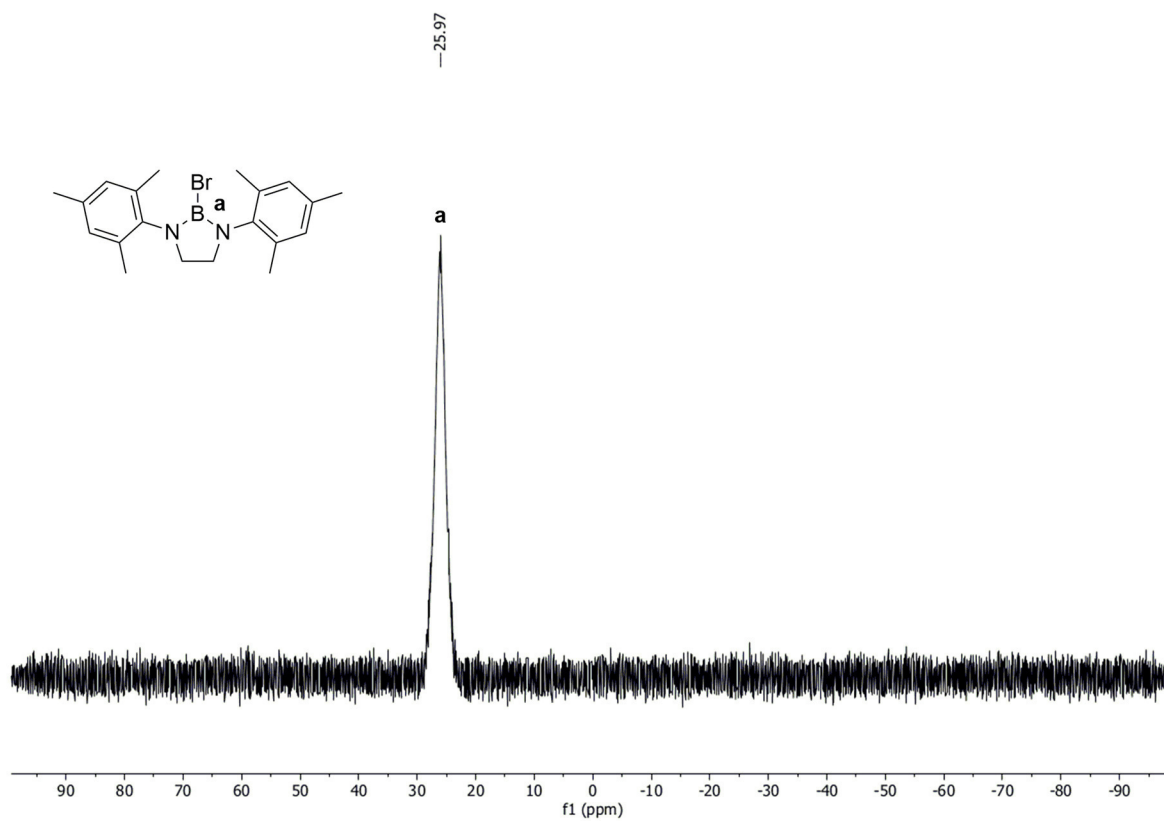


Figure S18. ¹¹B NMR spectrum of DAB^{Mes}-Br acquired in C₆D₆ (before MeCN application).

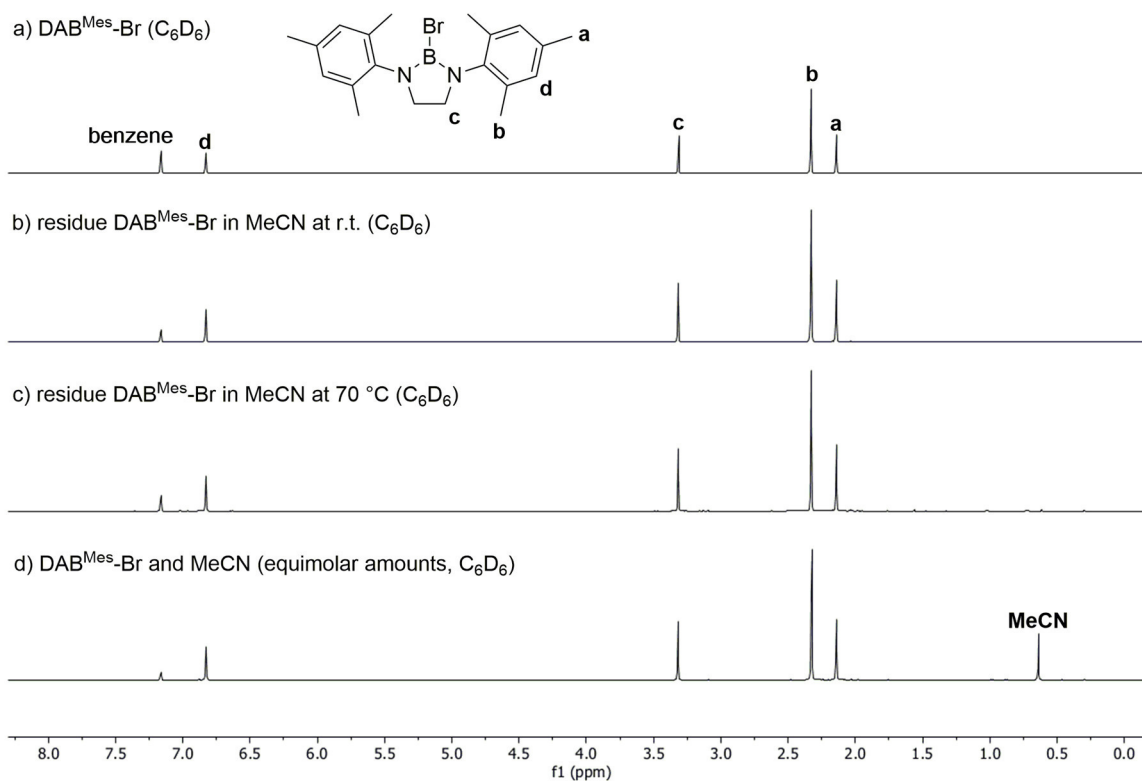


Figure S19. ^1H NMR spectra of $\text{DAB}^{\text{Mes}}\text{-Br}$ acquired in C_6D_6 : a) pure reactant $\text{DAB}^{\text{Mes}}\text{-Br}$; b) residue of the reaction of $\text{DAB}^{\text{Mes}}\text{-Br}$ and MeCN at r.t. for 16 h; c) residue of the reaction of $\text{DAB}^{\text{Mes}}\text{-Br}$ and MeCN at 70 °C for 16 h; d) *in situ* monitoring of a combination of $\text{DAB}^{\text{Mes}}\text{-Br}$ and MeCN (equimolar amounts). Signal integration according to Figure S17.

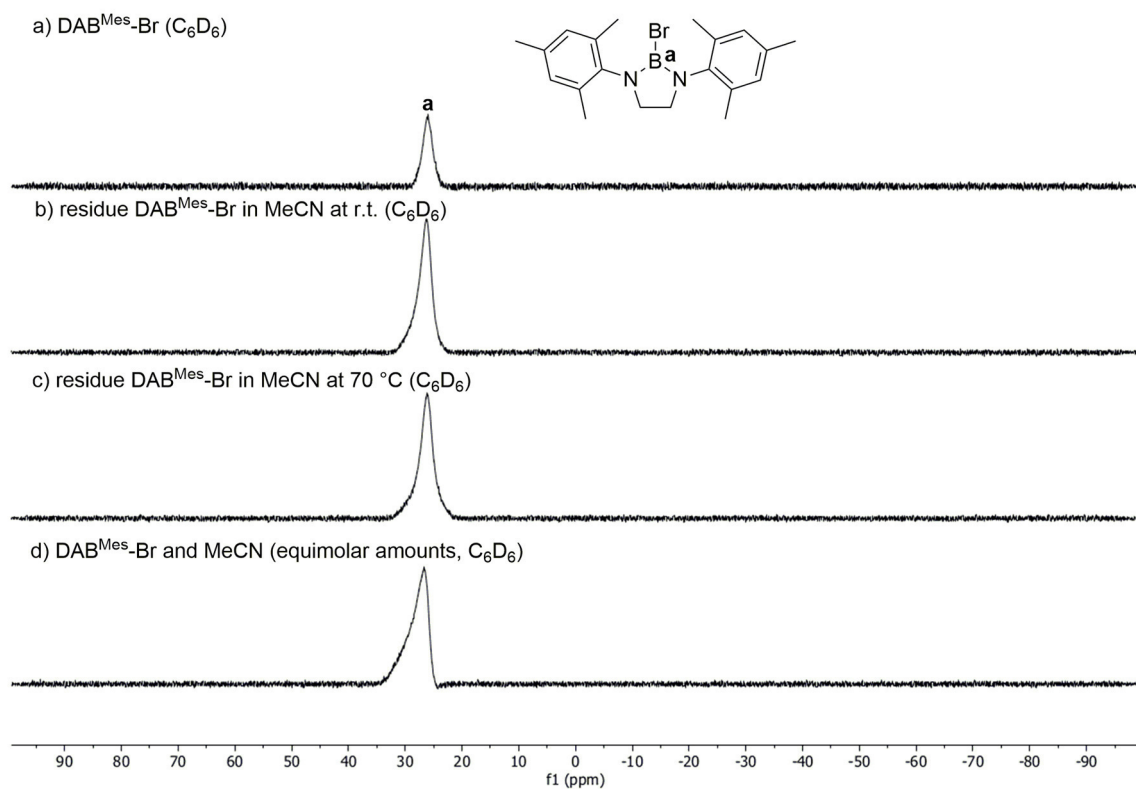


Figure S20. ^{11}B NMR spectra of $\text{DAB}^{\text{Mes}}\text{-Br}$ acquired in C_6D_6 : a) pure reactant $\text{DAB}^{\text{Mes}}\text{-Br}$; b) residue of the reaction of $\text{DAB}^{\text{Mes}}\text{-Br}$ and MeCN at r.t. for 16 h; c) residue of the reaction of $\text{DAB}^{\text{Mes}}\text{-Br}$ and MeCN at 70 °C for 16 h; d) *in situ* monitoring of a combination of $\text{DAB}^{\text{Mes}}\text{-Br}$ and MeCN (equimolar amounts).

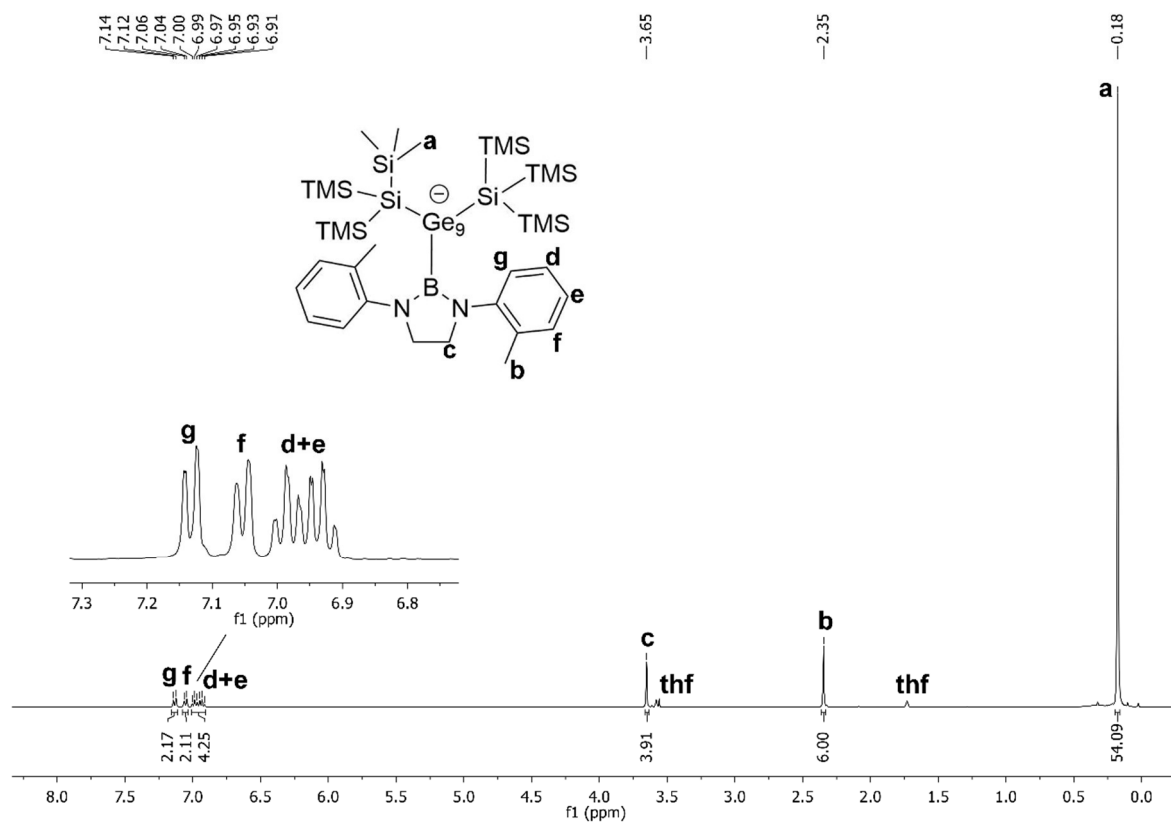


Figure S21. ¹H NMR spectrum of compound **1** acquired in thf-*d*₈.

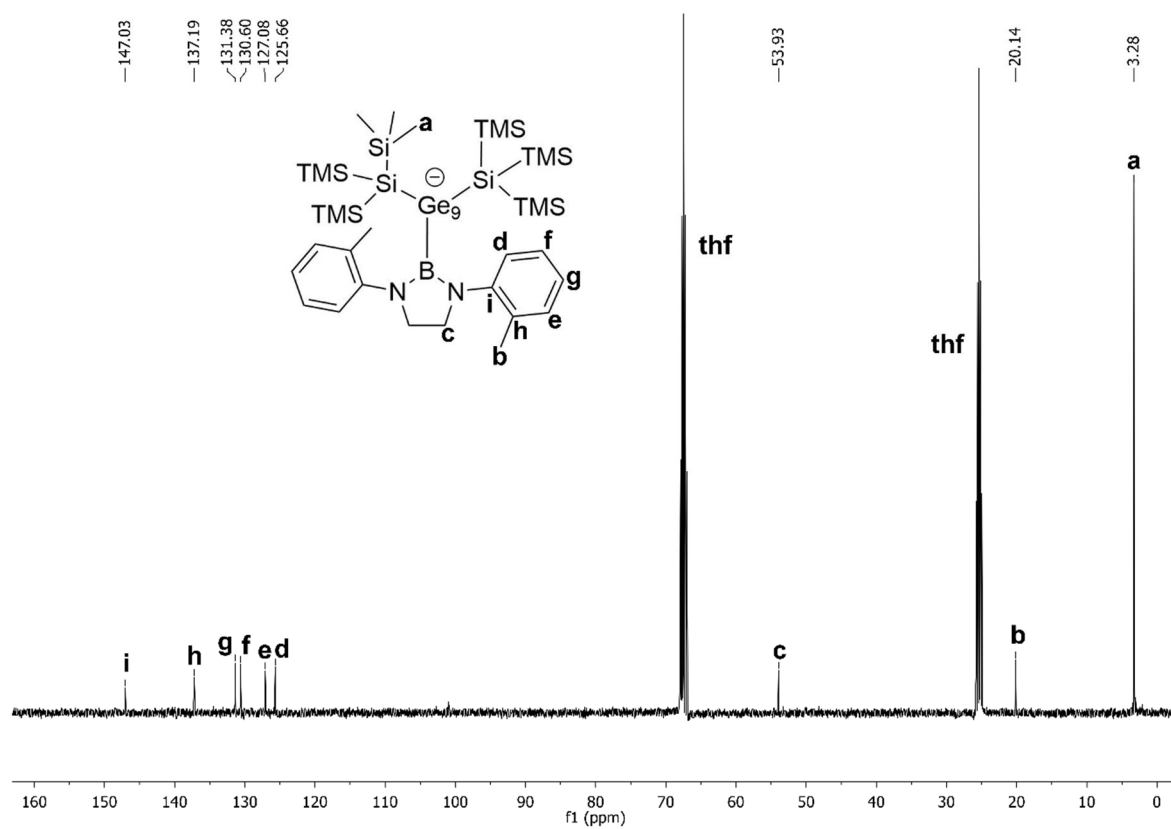


Figure S22. ¹³C NMR spectrum of compound **1** acquired in thf-*d*₈.

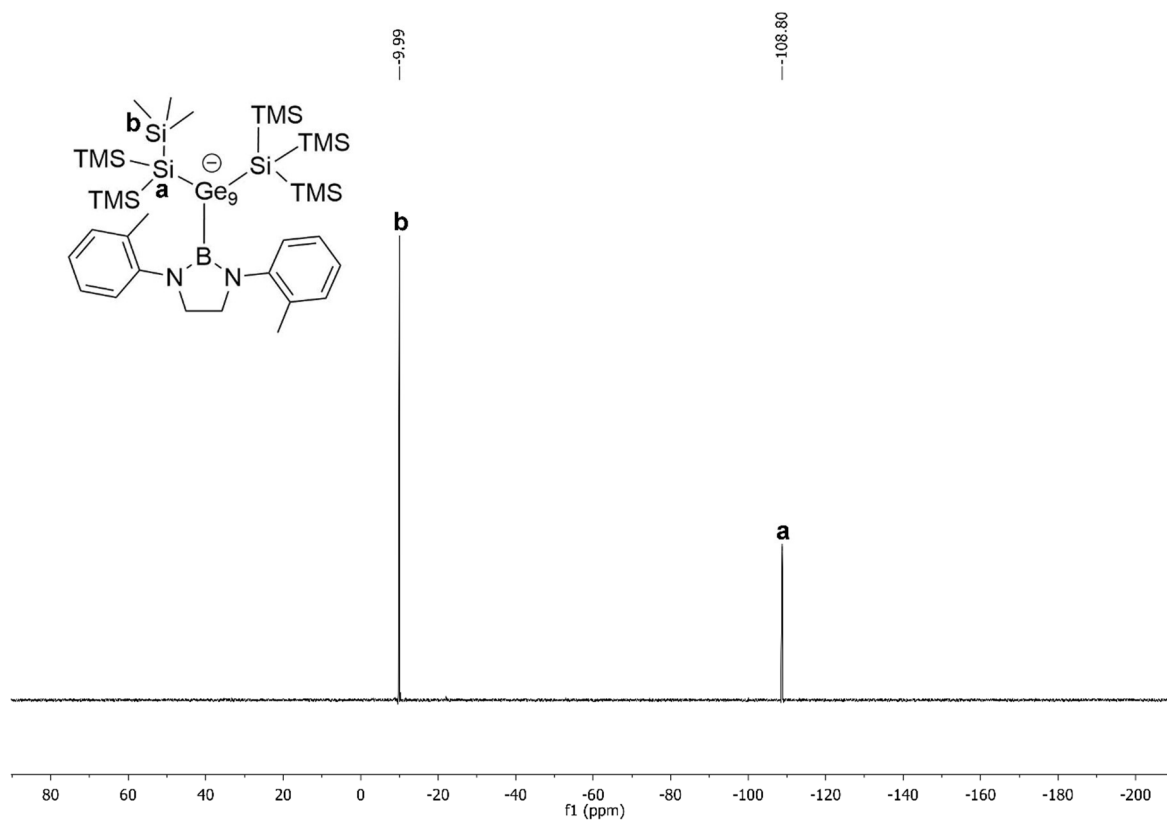


Figure S23. ^{29}Si -INEPT NMR spectrum of compound 1 acquired in thf-d_6 .

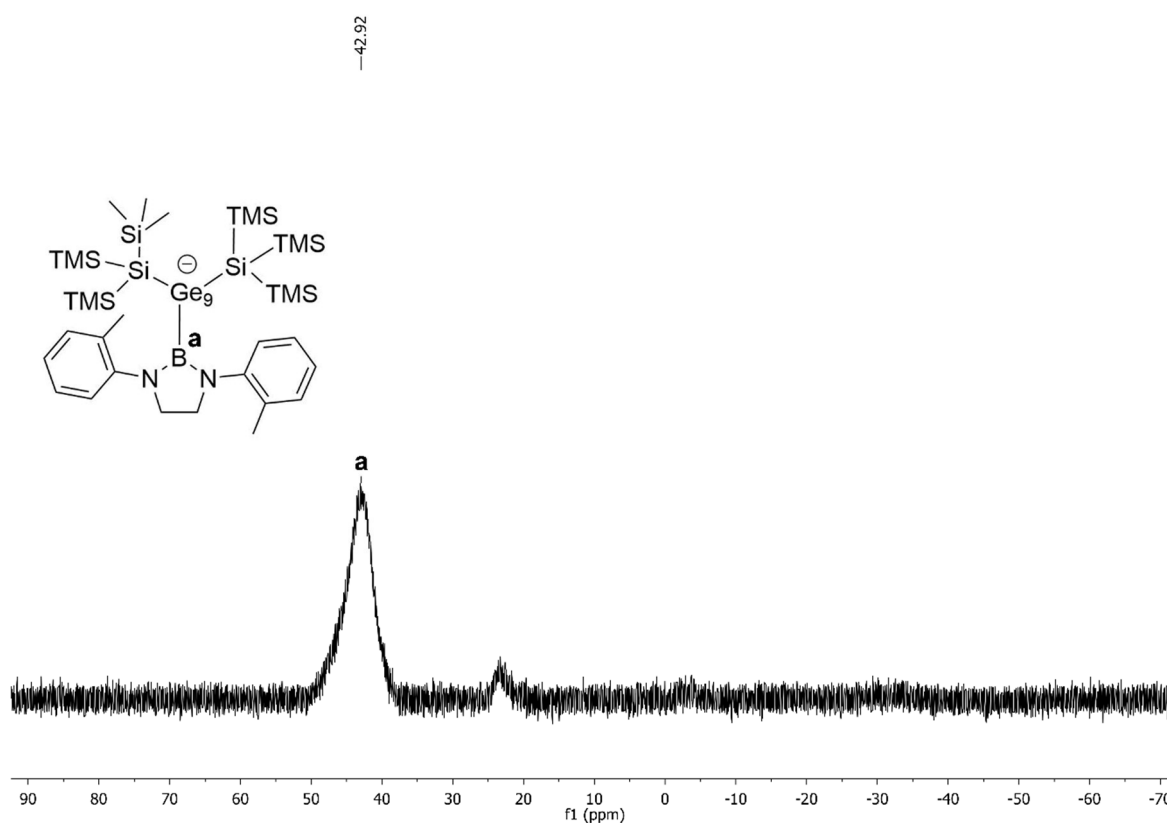


Figure S24. ^{11}B NMR spectrum of compound 1 acquired in thf-d_6 . Impurity is caused by an unidentified species.

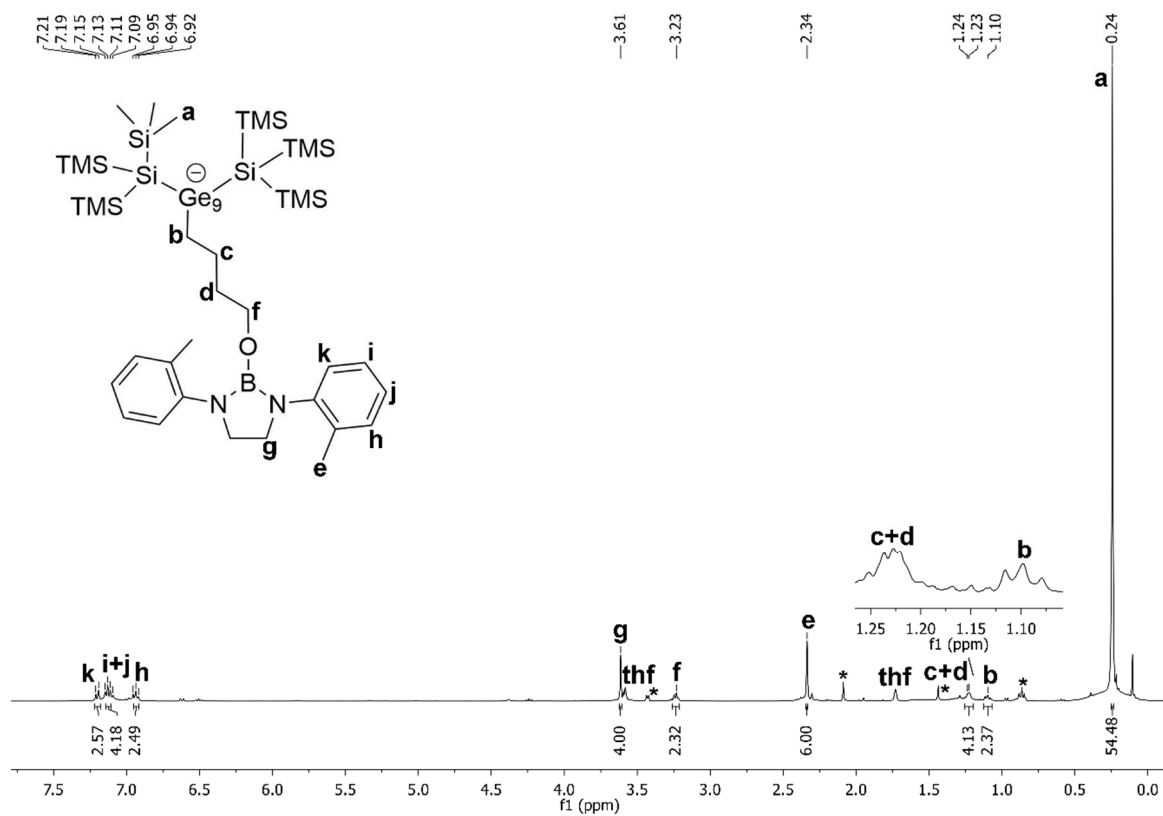


Figure S25. ¹H NMR spectrum of compound **2** acquired in thf-*d*₈. Asterisked signals are caused by unknown impurities.

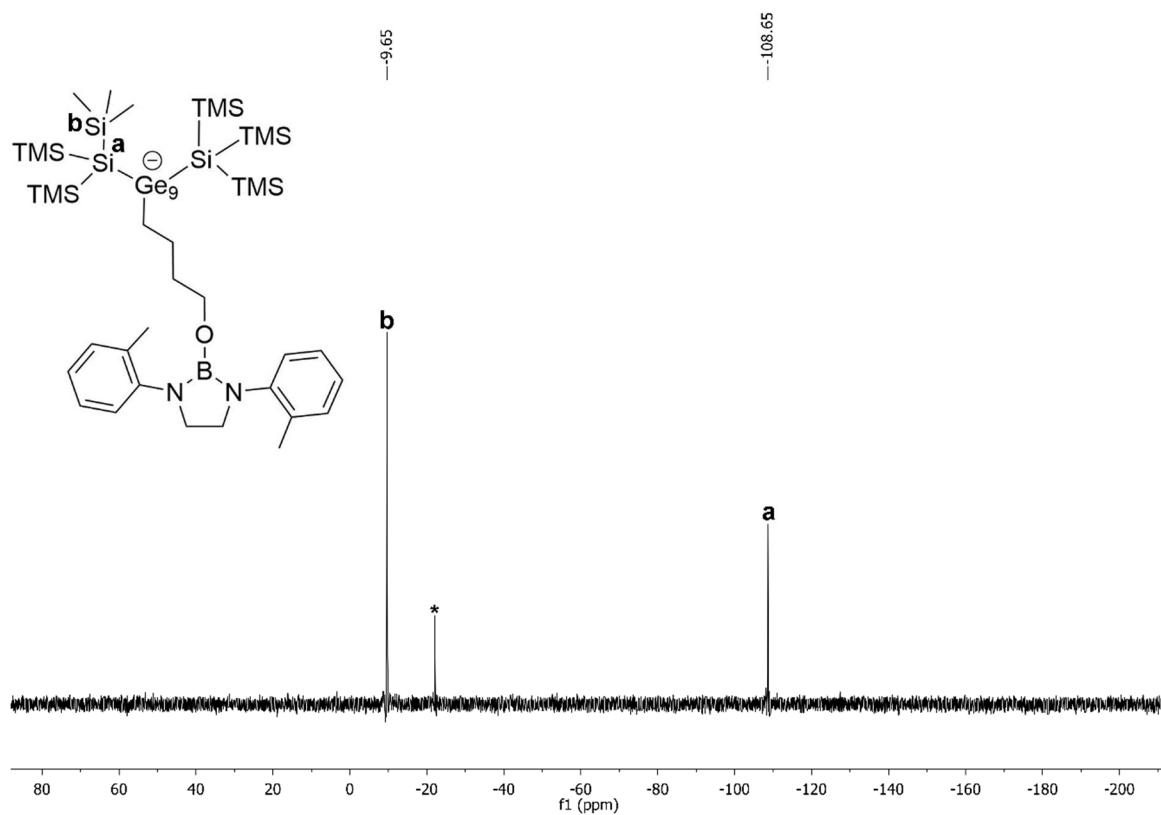


Figure S26. ²⁹Si-INEPT NMR spectrum of compound **2** acquired in thf-*d*₈. Asterisked signal caused by silicon grease.

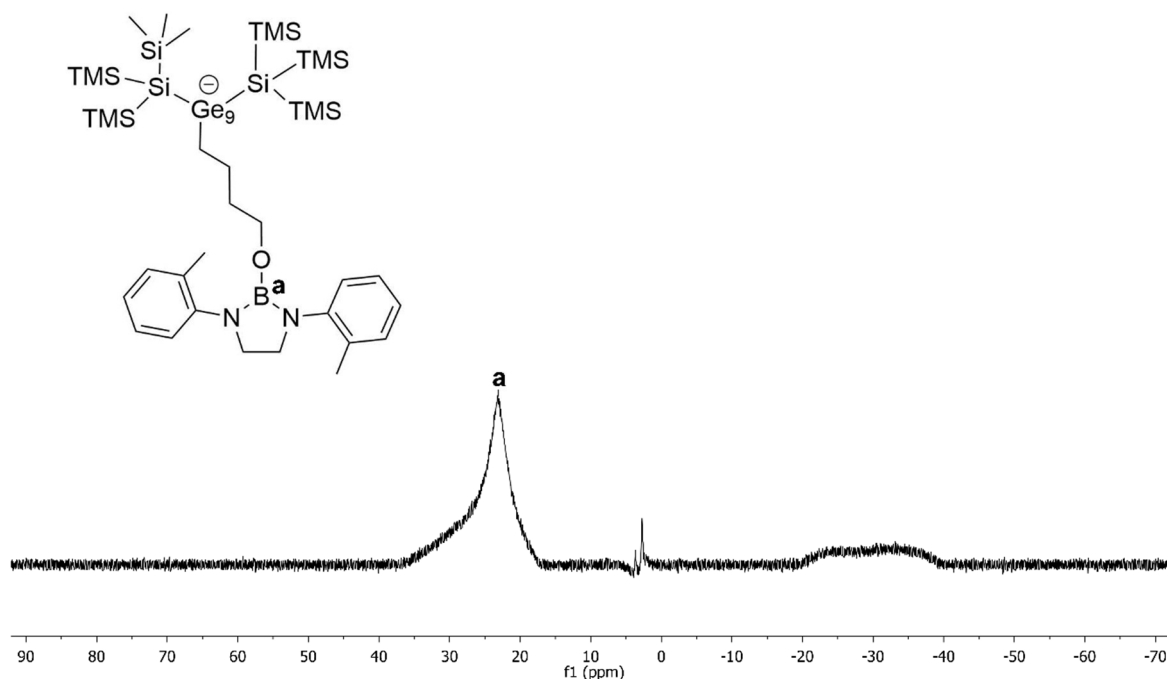


Figure S27. ^{11}B NMR spectrum of compound **2** acquired in $\text{thf-}d_6$. Impurity is caused by unidentified species.

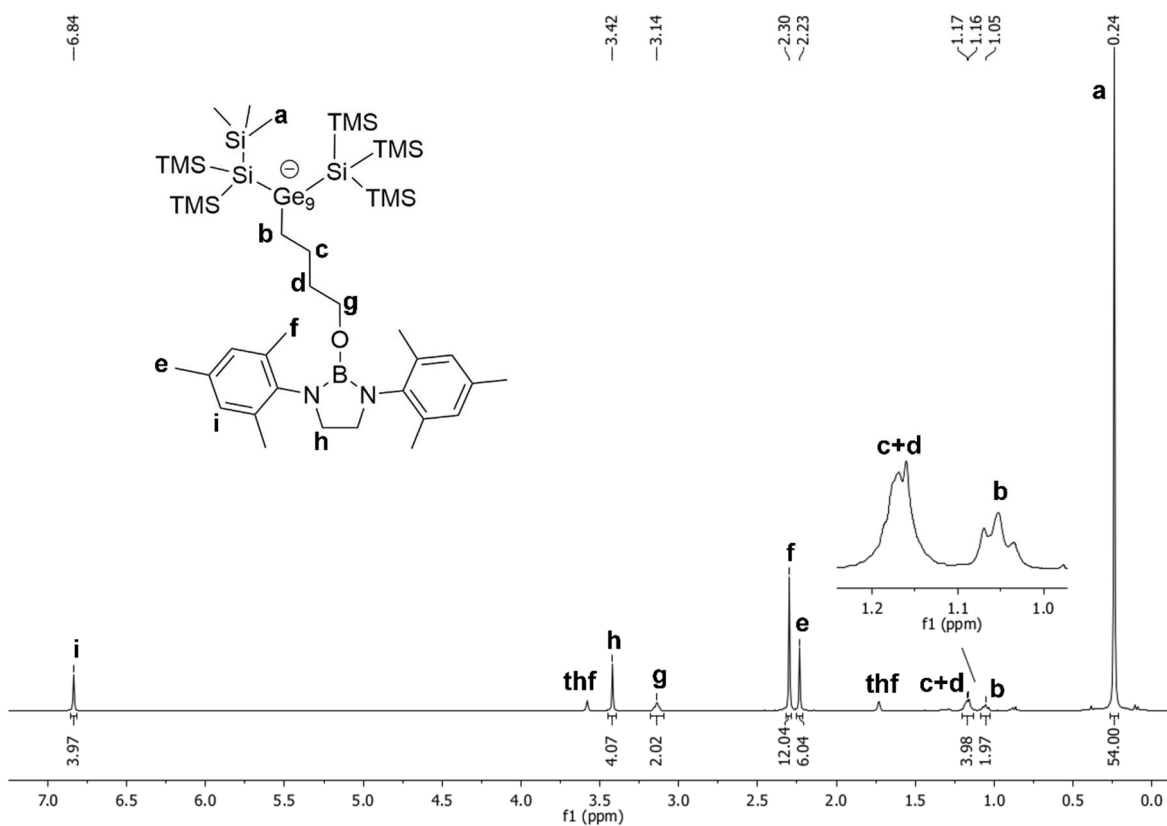


Figure S28. ^1H NMR spectrum of compound **3** acquired in $\text{thf-}d_6$.

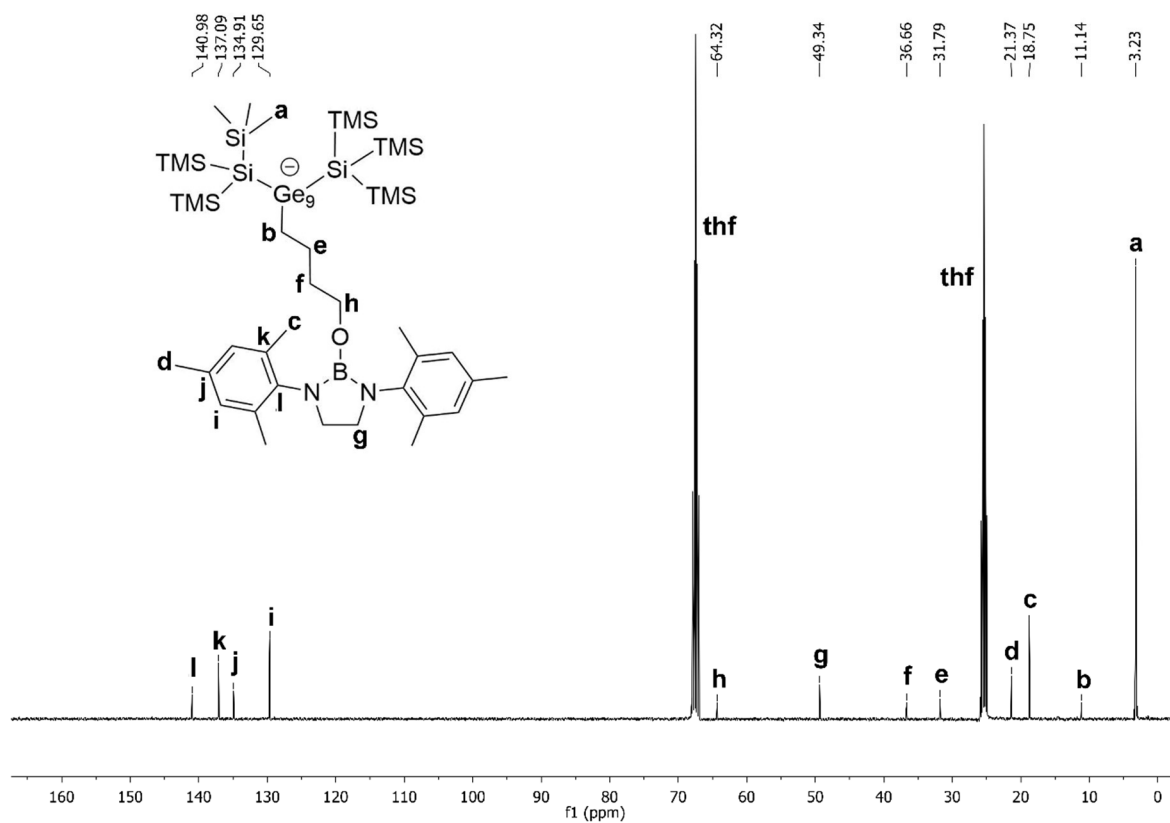


Figure S29. ^{13}C NMR spectrum of compound 3 acquired in $\text{thf-}d_8$.

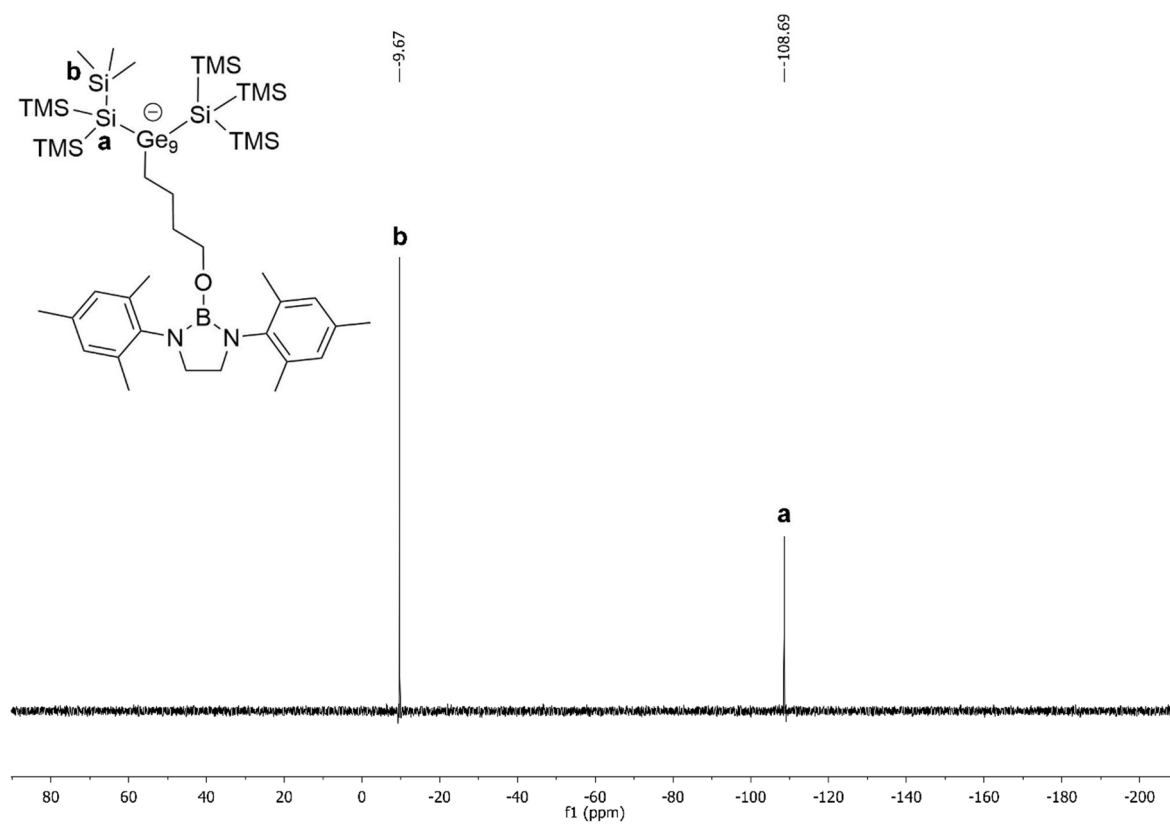


Figure S30. ^{29}Si -INEPT NMR spectrum of compound 3 acquired in $\text{thf-}d_8$.

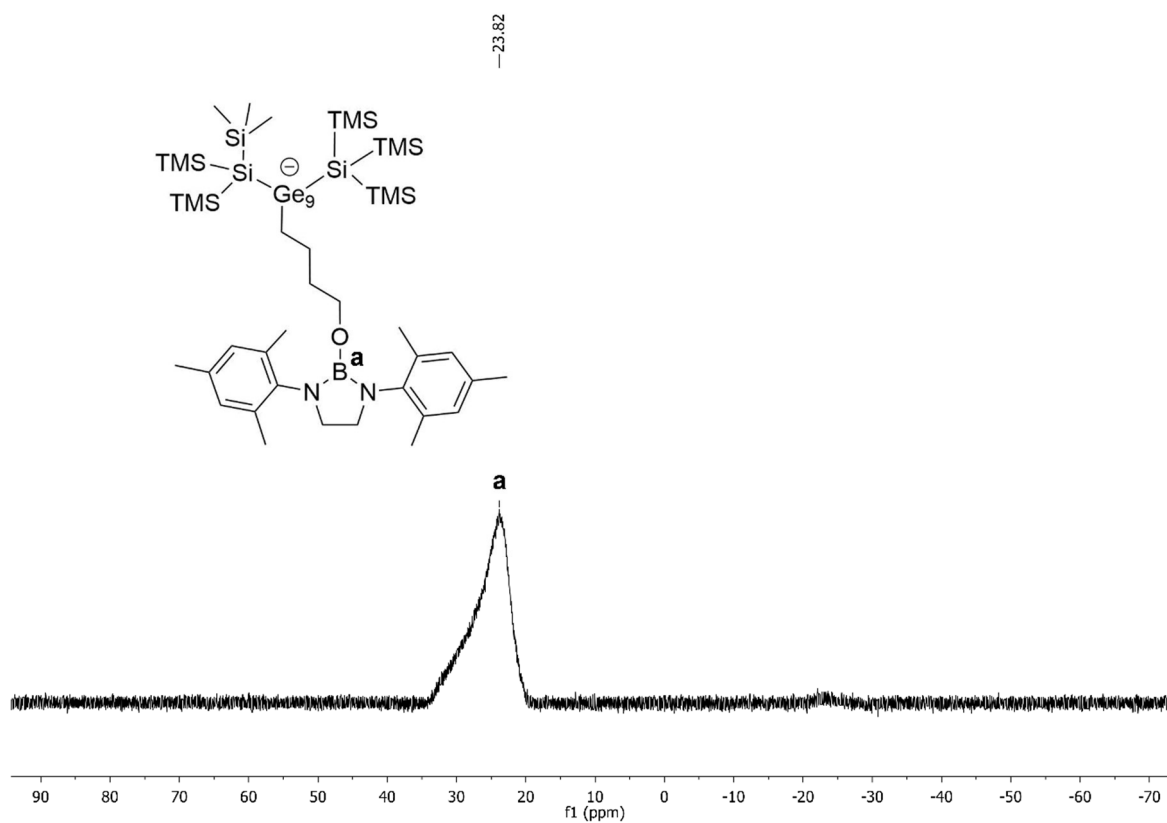


Figure S31. ^{11}B NMR spectrum of compound **3** acquired in $\text{thf-}d_6$. Impurity is caused by an unidentified species.

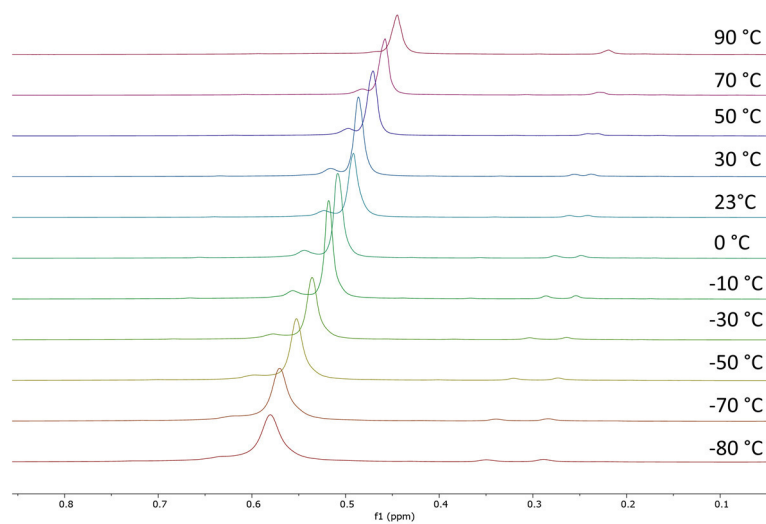


Figure S32. Selected area of VT (variable temperature) ^1H NMR spectra of compound **3** acquired in $\text{tol-}d_8$.

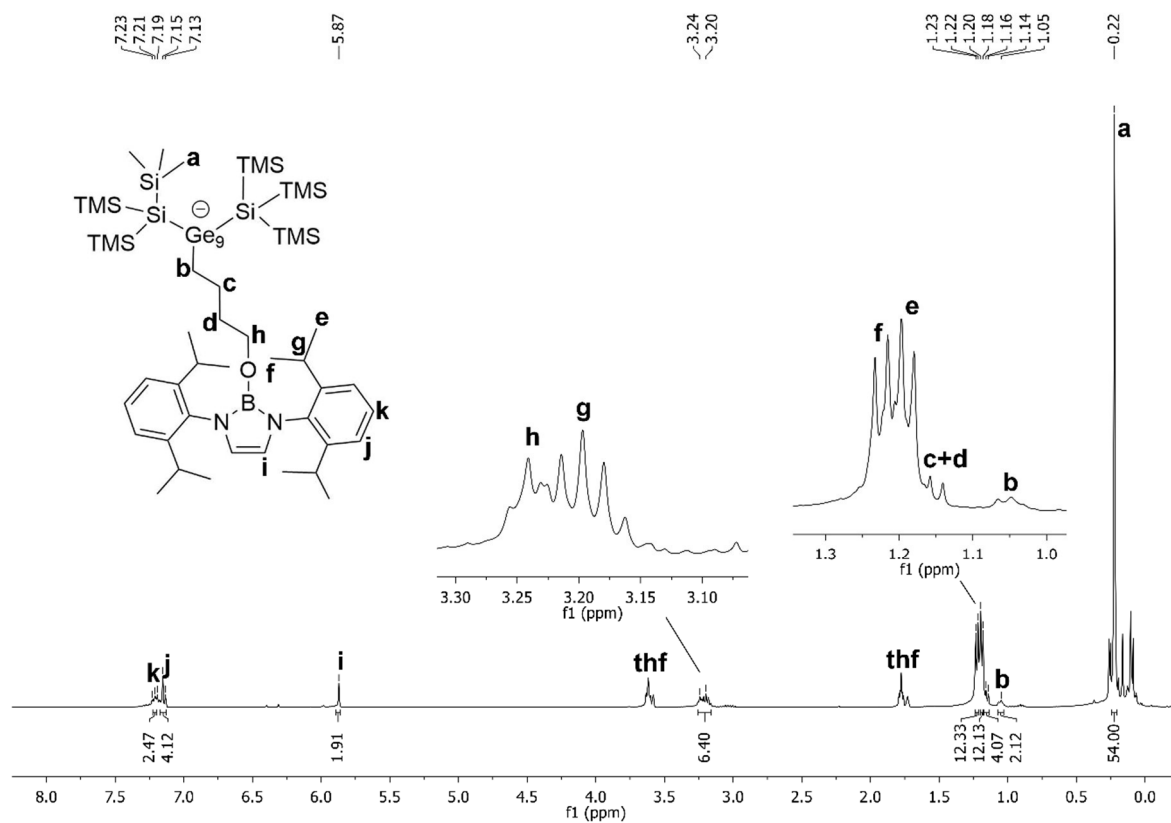


Figure S33. ^1H NMR spectrum of compound **4** acquired in $\text{thf-}d_6$.

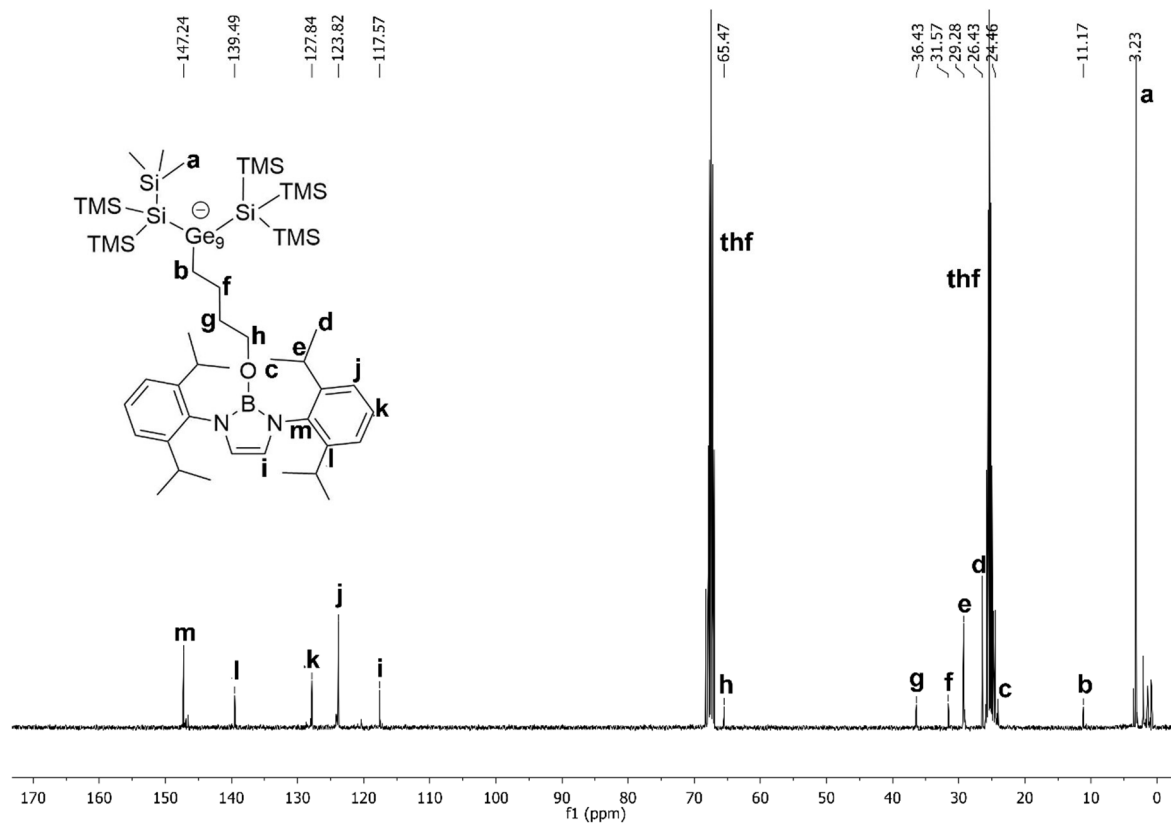


Figure S34. ^{13}C NMR spectrum of compound **4** acquired in $\text{thf-}d_6$.

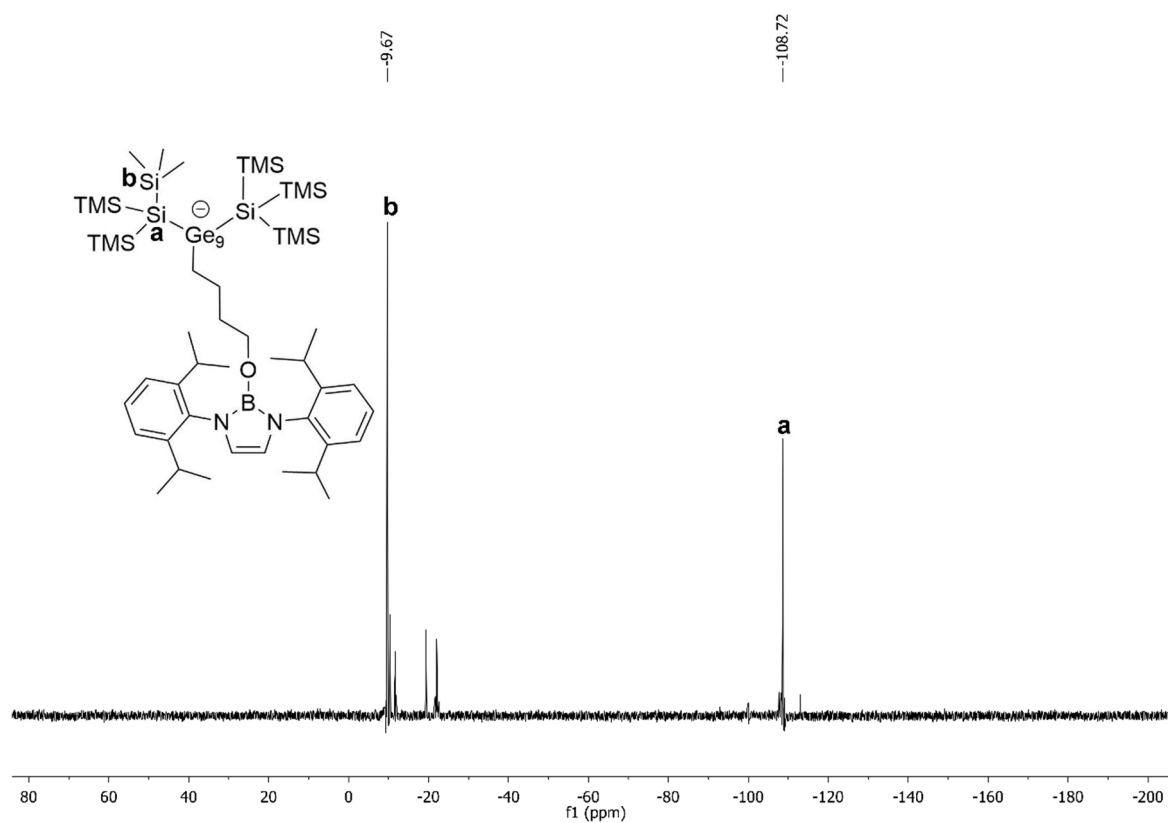


Figure S35. ^{29}Si -INEPT NMR spectrum of compound **4** acquired in $\text{thf-}d_6$. Impurity is caused by unidentified species.

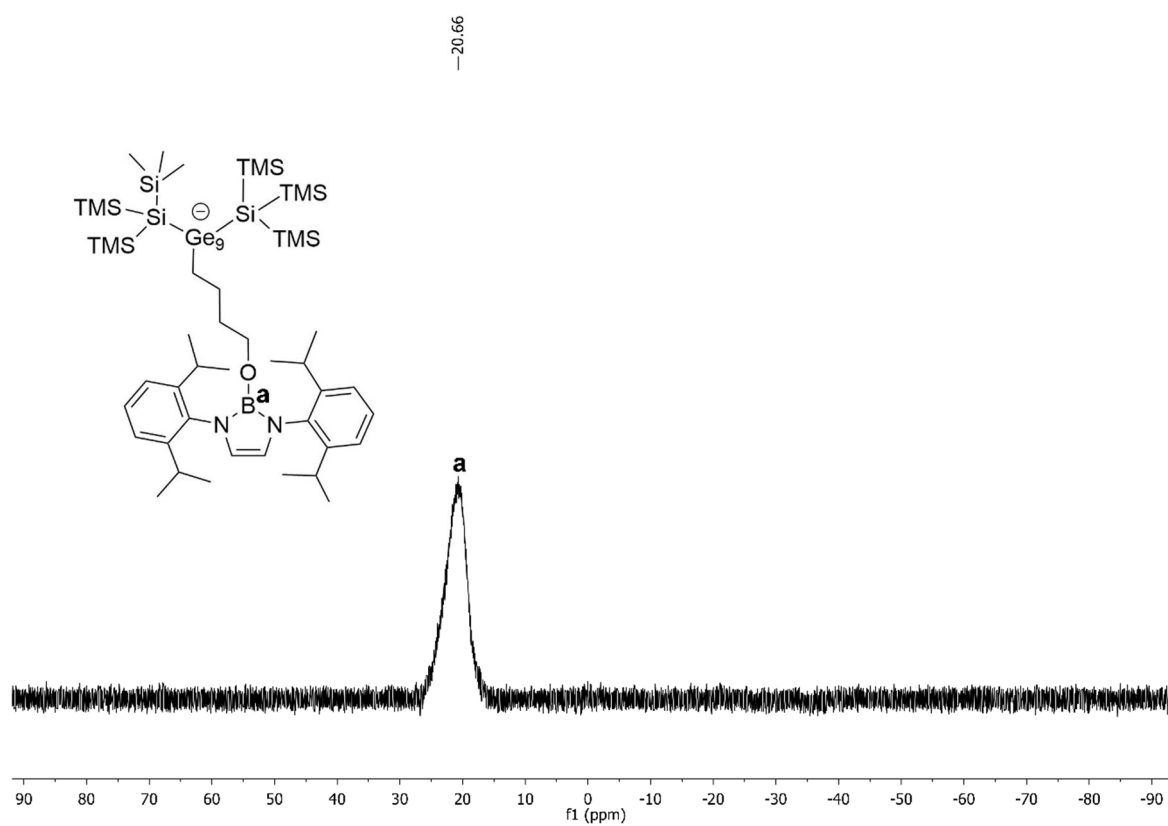


Figure S36. ^{11}B NMR spectrum of compound **4** acquired in $\text{thf-}d_6$.

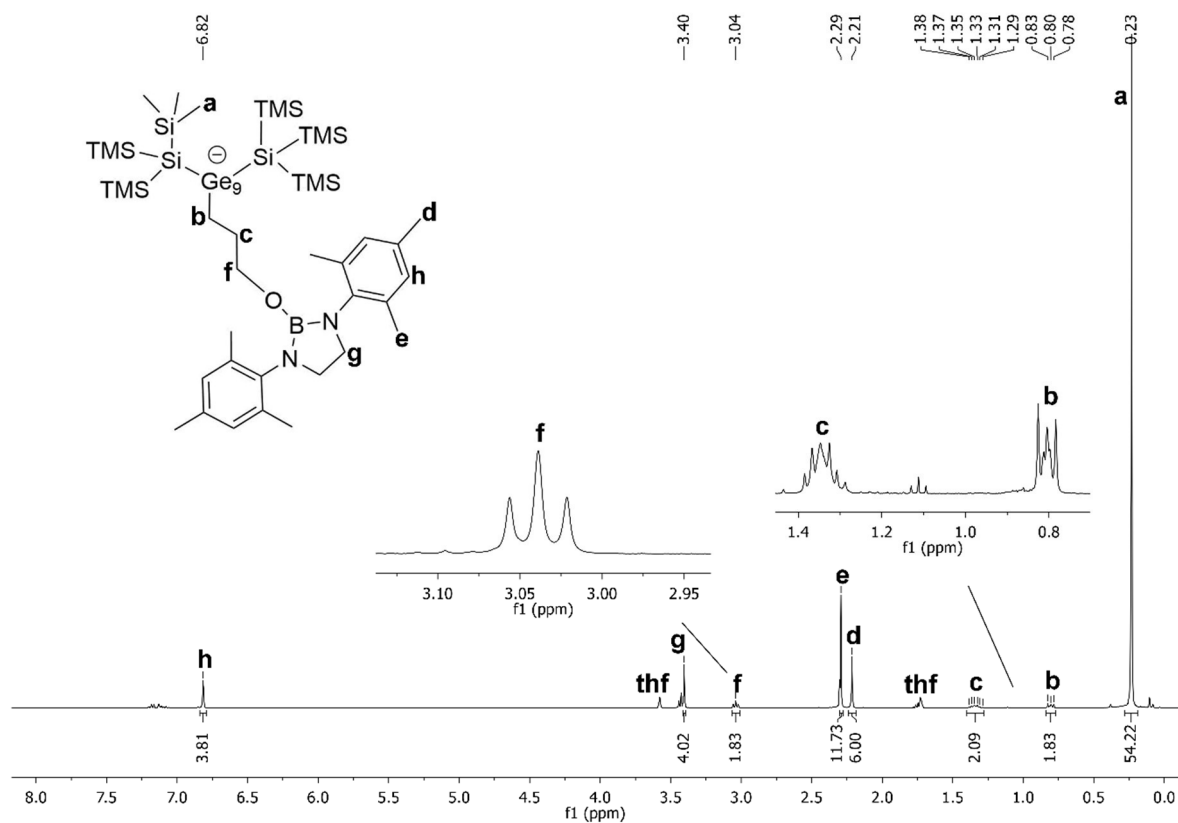


Figure S37. ¹H NMR spectrum of compound **5** acquired in thf-*d*₈.

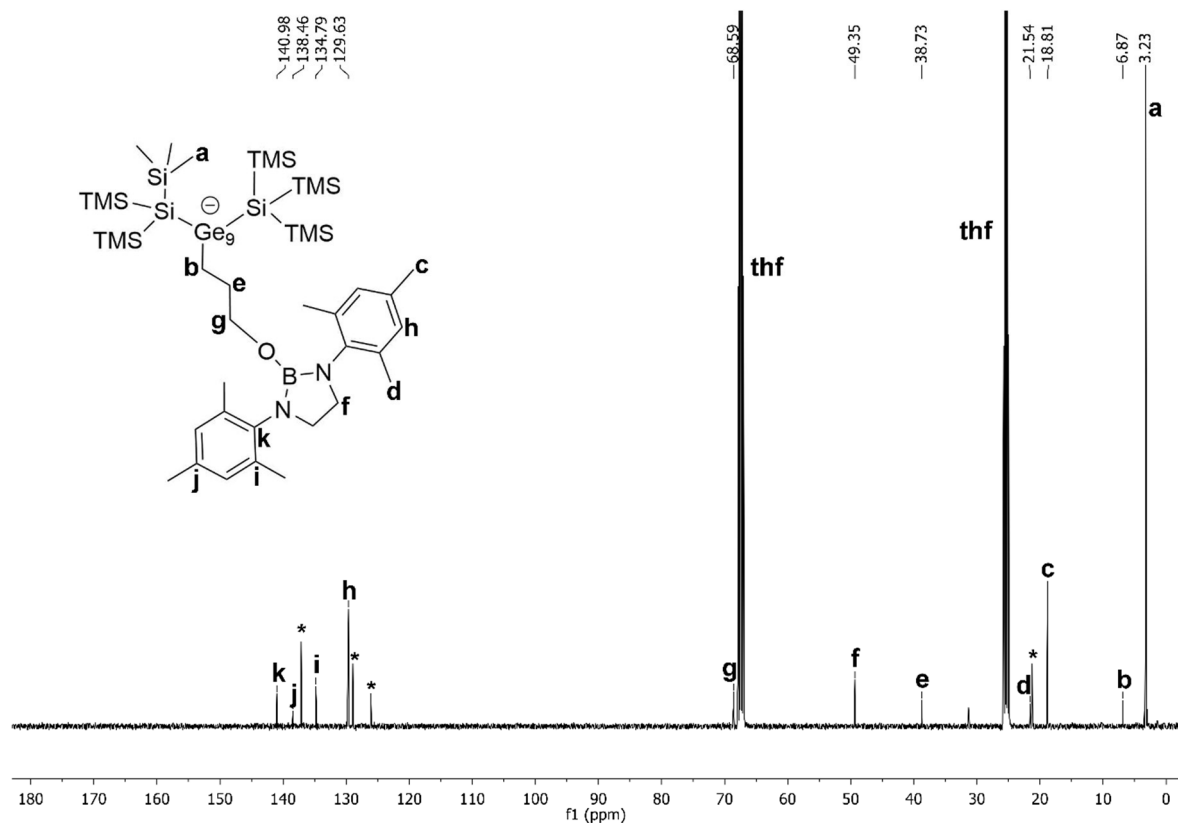


Figure S38. ¹³C NMR spectrum of compound **5** acquired in thf-*d*₈. Asterisk signal is caused by unknown impurity.

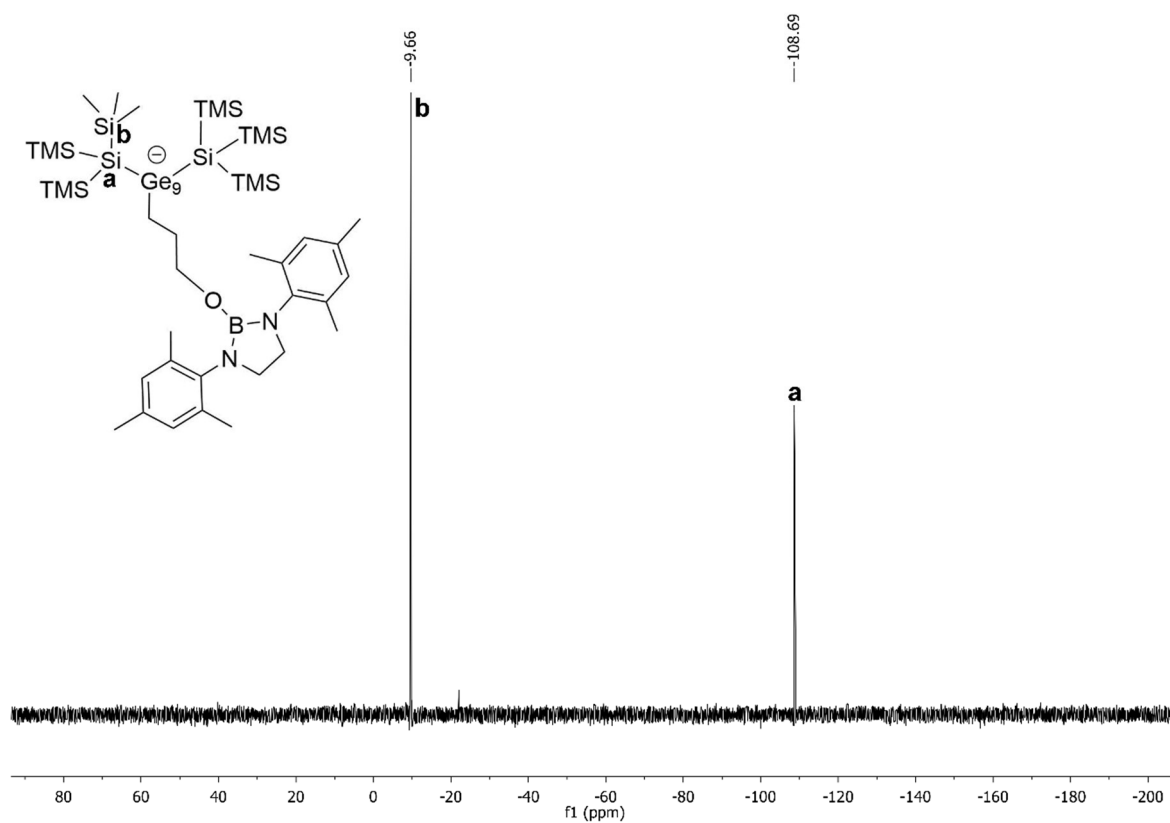


Figure S39. ^{29}Si -INEPT NMR spectrum of compound 5 acquired in thf-d_6 .

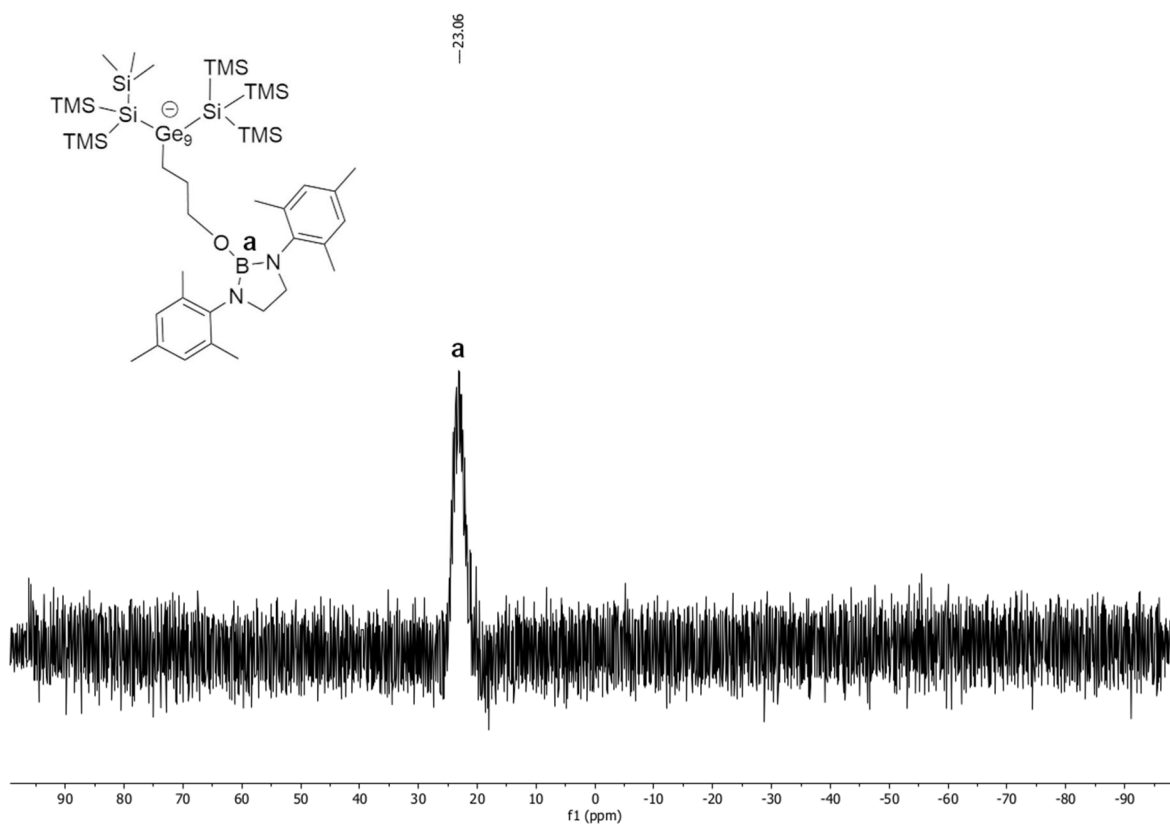


Figure S40. ^{11}B - NMR spectrum of compound 5 acquired in thf .

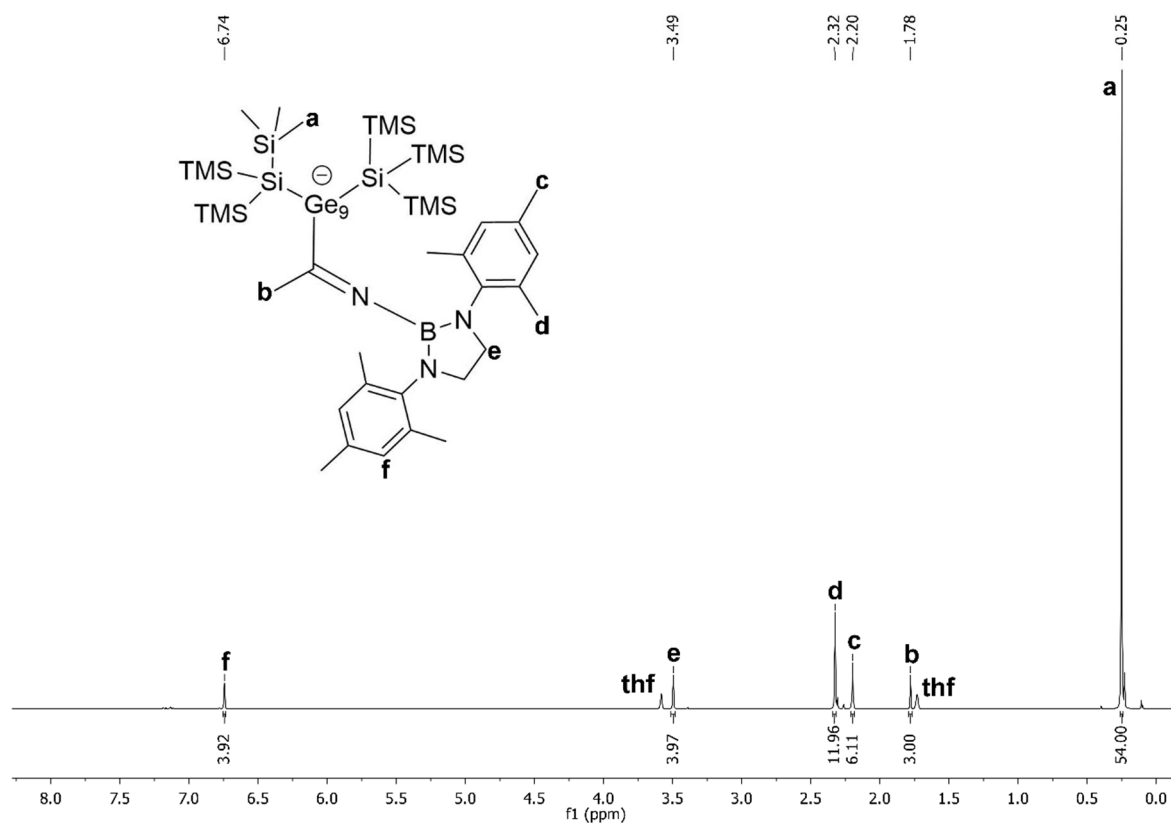


Figure S41. ¹H NMR spectrum of compound **6** acquired in thf-*d*₈.

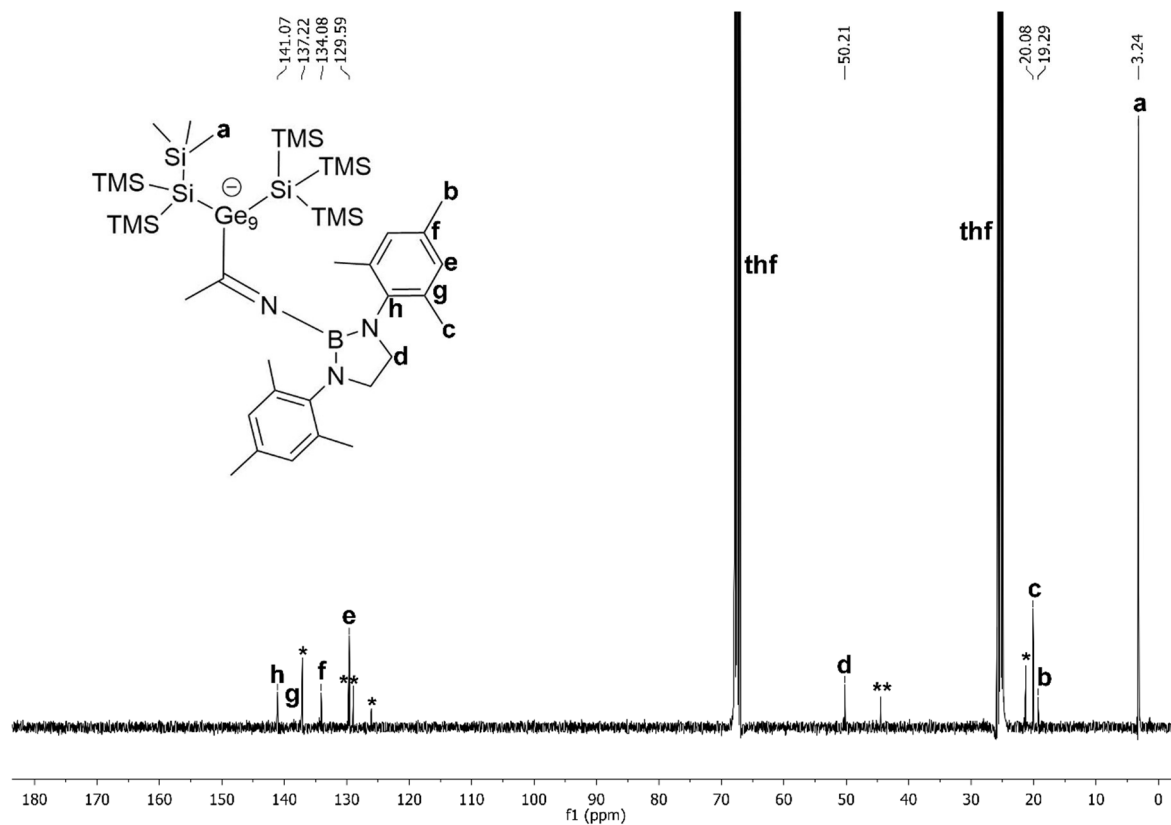


Figure S42. ¹³C NMR spectrum of compound **6** acquired in thf-*d*₈. * toluene; ** unknown impurity.

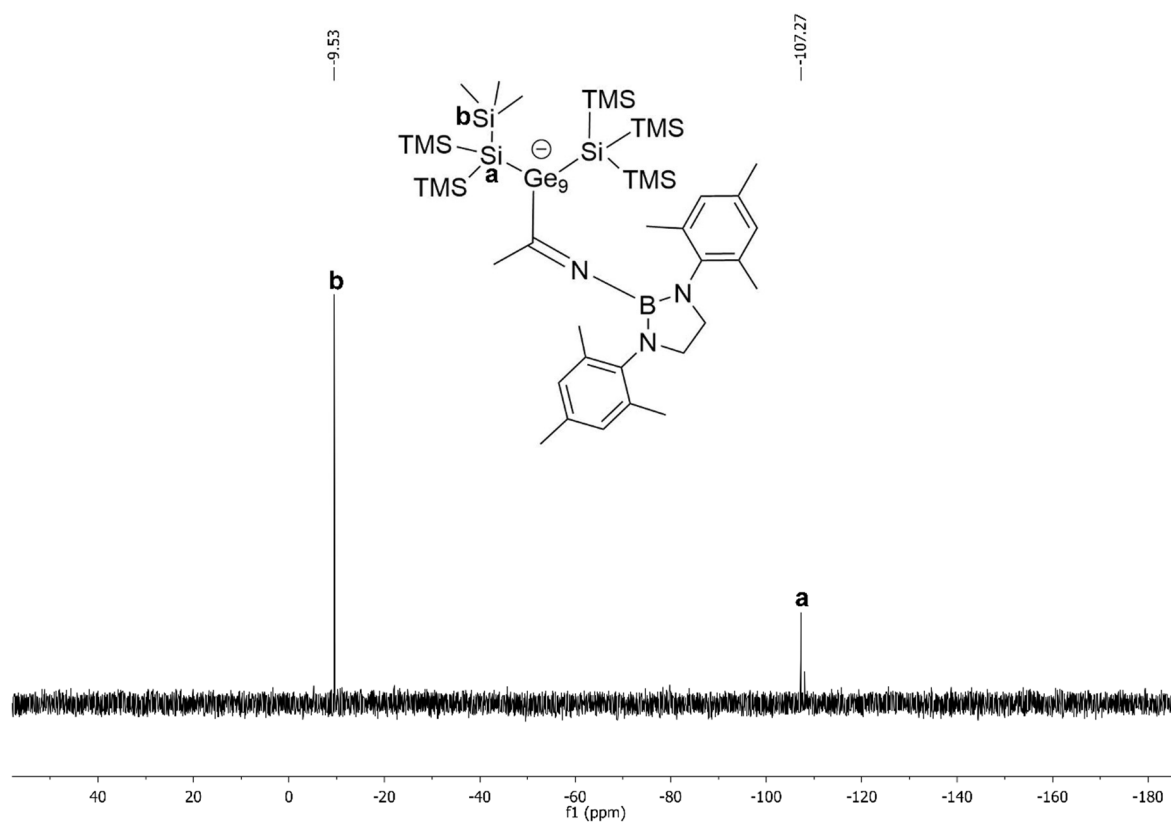


Figure S43. ^{29}Si -INEPT NMR spectrum of compound **6** acquired in thf-d_6 .

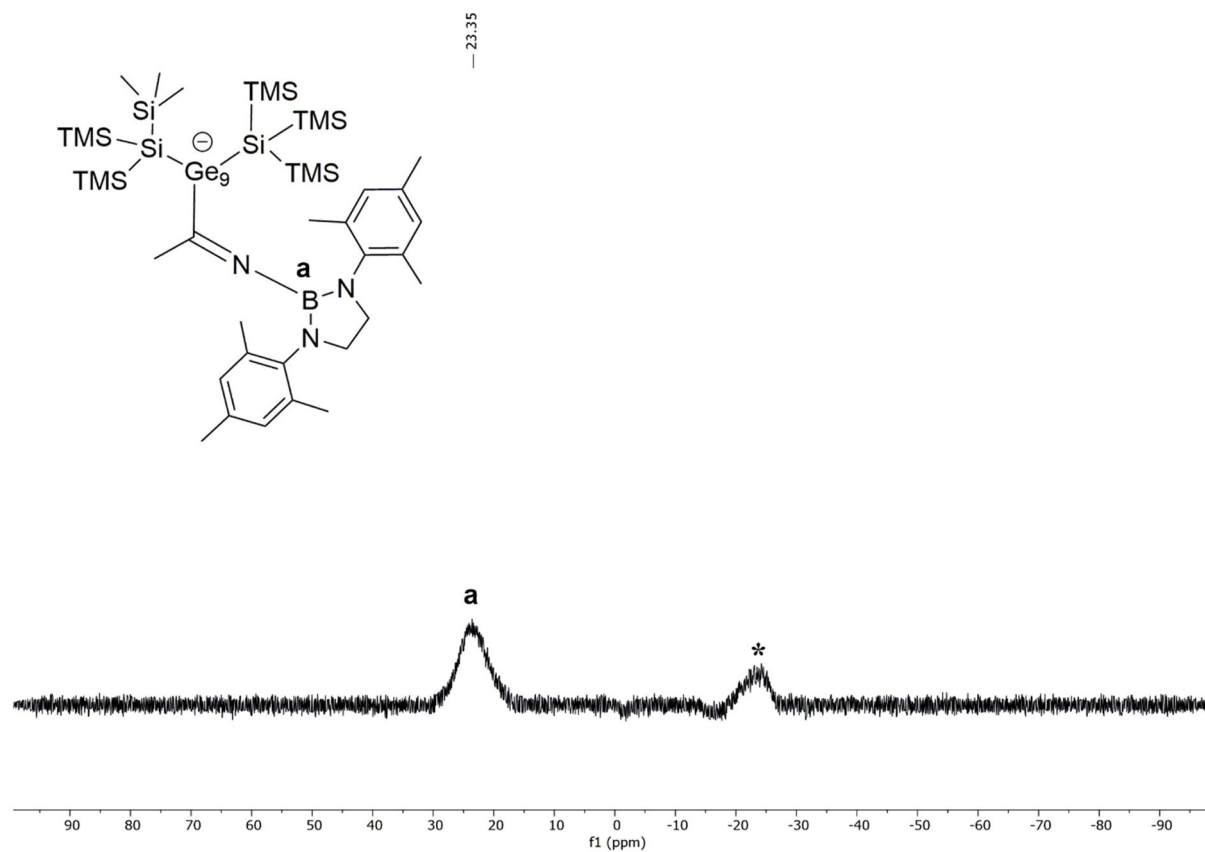


Figure S44. ^{11}B NMR spectrum of compound **6** acquired in thf-d_6 . Asterisk signal is caused by glass of NMR tube.

ESI MS spectra

Table S8. Overview of performed ESI MS investigations of reactions of the cluster $[\text{Ge}_9\{\text{Si}(\text{TMS})_3\}_2]^{2-}$ with different boranes in thf (deuterated, non-deuterated), tmo and MeCN (deuterated, non-deuterated).

	thf	tmo	MeCN
DAB^{o-tol}-Br	deuterated and non-deuterated	-	-
DAB^{Mes}-Br	deuterated and non-deuterated	non-deuterated	deuterated and non-deuterated
DAB(II)^{Dipp}-Br	deuterated and non-deuterated	non-deuterated	deuterated and non-deuterated
DAB^{Dipp}-Br	deuterated and non-deuterated	non-deuterated	deuterated and non-deuterated
DAB^{o-xyI}-Br	non-deuterated	non-deuterated	non-deuterated
(ⁱPr₂N)₂B-Br	deuterated and non-deuterated	no insertion of tmo between cluster and borane observed	deuterated and non-deuterated

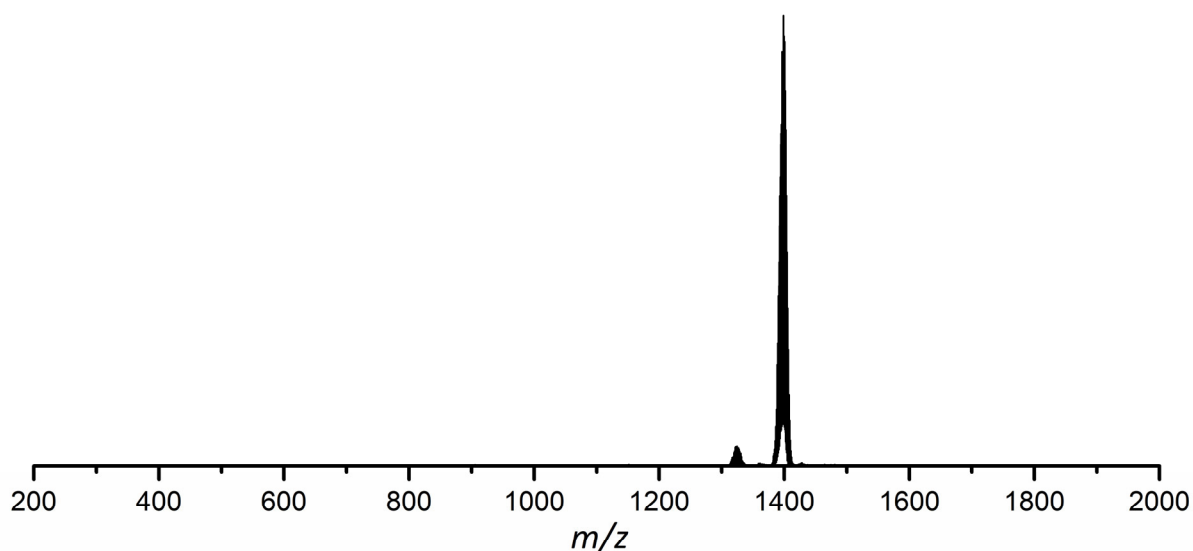


Figure S45. ESI MS spectrum (negative-ion mode, 3500 V, 300 °C) of a thf solution of $[\text{Ge}_9\{\text{Si}(\text{TMS})_3\}_2\text{DAB}^{\text{o-tol}}]^-$ (**1a**). The molecule peak of **1a** is detected at m/z 1398.7. A detailed view of the signal of anion **1a** is provided in Figure S46.

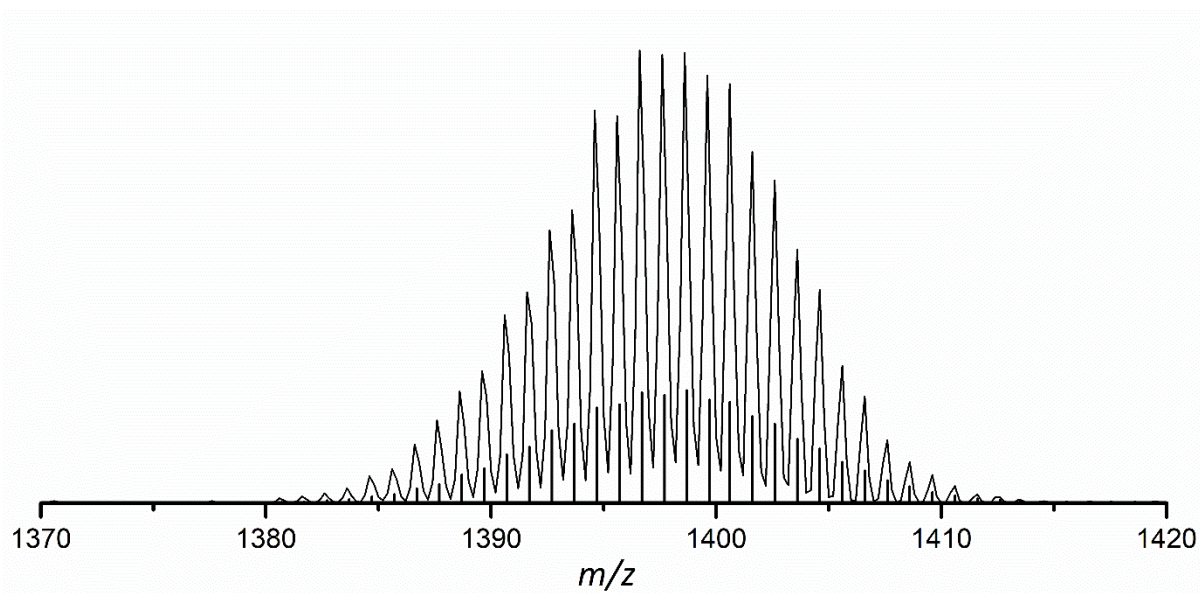


Figure S46. Detailed view on ESI MS signal of $[\text{Ge}_9\{\text{Si}(\text{TMS})_3\}_2\text{DAB}^{\text{o-tol}}]^-$ (**1a**) at m/z 1398.7.

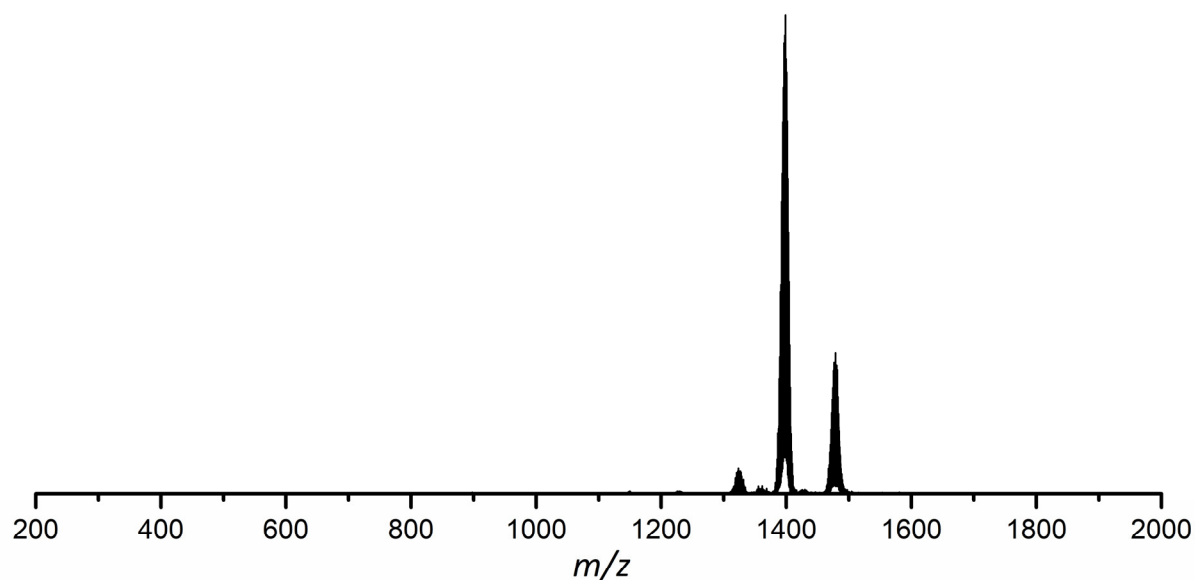


Figure S47. ESI MS spectrum (negative-ion mode, 3500 V, 300 °C) of thf diluted reaction mixture of $[\text{Ge}_9\{\text{Si}(\text{TMS})_3\}_2]^{2-}$ and $\text{DAB}^{\text{o-tol}}\text{Br}$ in thf- d_8 . Thf- d_8 was added to a mixture of the reactants. The detected signals can be assigned to $[\text{Ge}_9\{\text{Si}(\text{TMS})_3\}_2\text{DAB}^{\text{o-tol}}]^-$ (**1a**; m/z 1398.7) and $[\text{Ge}_9\{\text{Si}(\text{TMS})_3\}_2(\text{CD}_2)_4\text{O-DAB}^{\text{o-tol}}]^-$ (**2a-d₈**; m/z 1478.8).

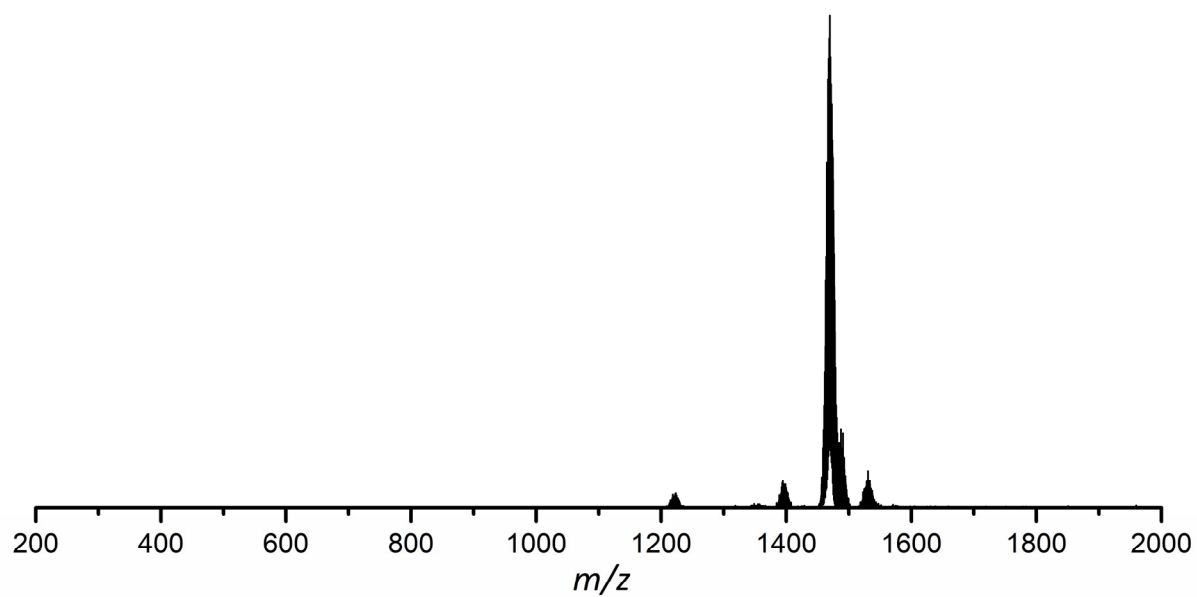


Figure S48. ESI MS spectrum (negative-ion mode, 3500 V, 300 °C) of a thf solution of $[\text{Ge}_9\{\text{Si}(\text{TMS})_3\}_2(\text{CH}_2)_4\text{O-DAB}^{0-10}]^-$ (**2a**). The molecule peak of **2a** is detected at m/z 1470.8. A detailed view of the signal of anion **2a** is provided in Figure S49.

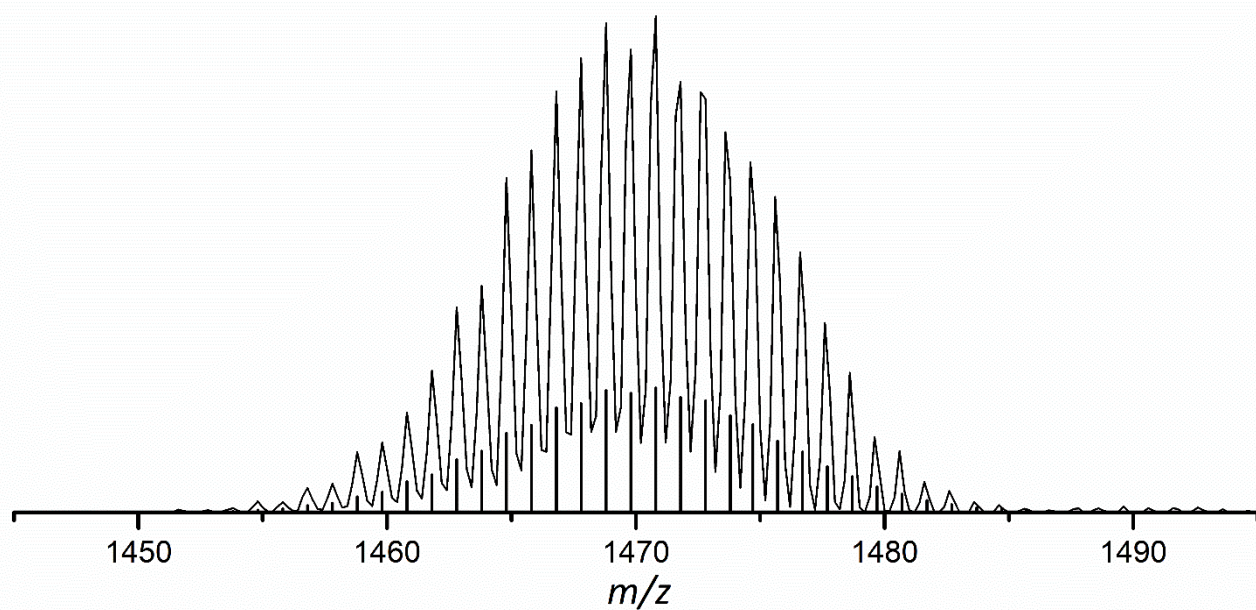


Figure S49. Detailed view on ESI MS signal of $[\text{Ge}_9\{\text{Si}(\text{TMS})_3\}_2(\text{CH}_2)_4\text{O-DAB}^{0-10}]^-$ (**2a**) at m/z 1470.8.

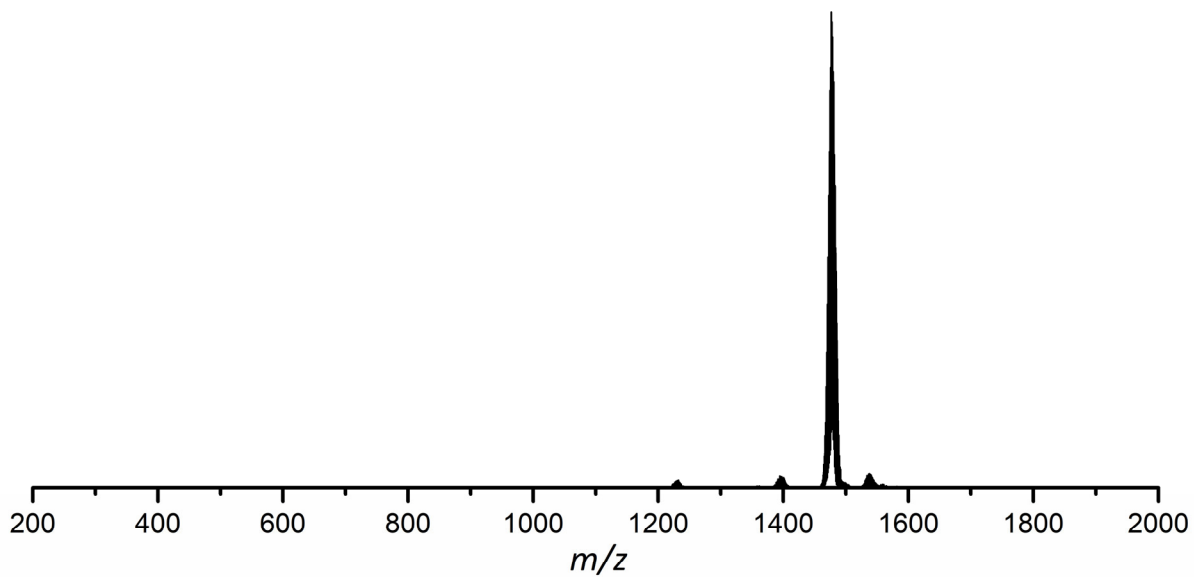


Figure S50. ESI MS spectrum (negative-ion mode, 3500 V, 300 °C) of a thf solution of $[\text{Ge}_9\{\text{Si}(\text{TMS})_3\}_2(\text{CD}_2)_4\text{O-DAB}^{9-10j-}]^-$ (**2a-d₈**). The molecule peak of **2a-d₈** is detected at m/z 1478.8. A detailed view of the signal of anion **2a-d₈** is provided in Figure S51.

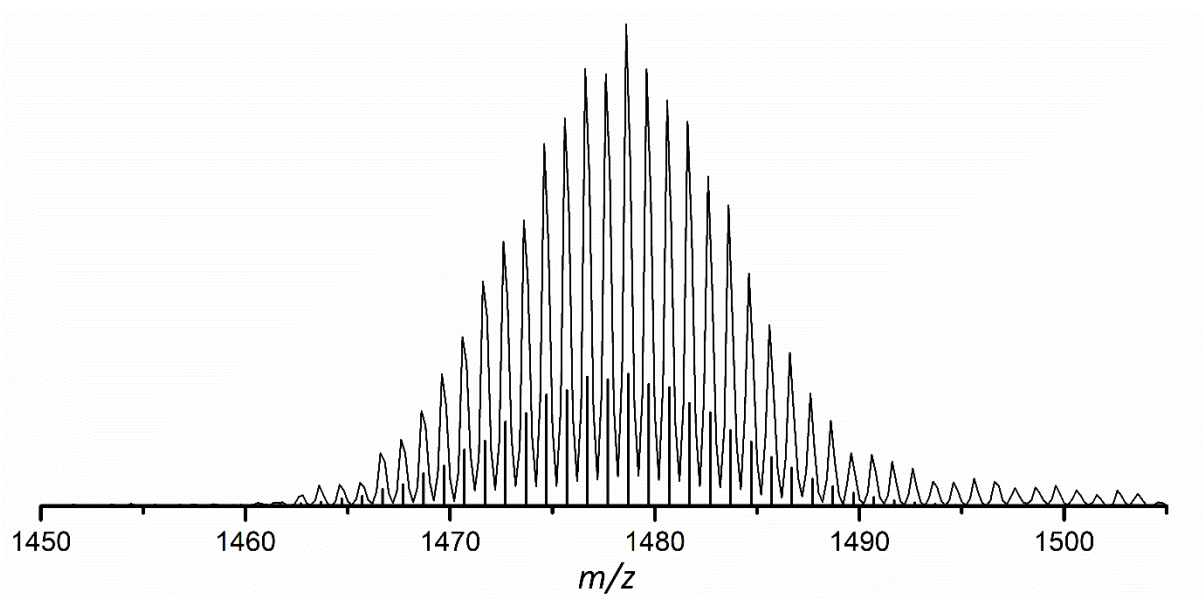


Figure S51. Detailed view on ESI MS signal of $[\text{Ge}_9\{\text{Si}(\text{TMS})_3\}_2(\text{CD}_2)_4\text{O-DAB}^{9-10j-}]^-$ (**2a-d₈**) at m/z 1478.8.

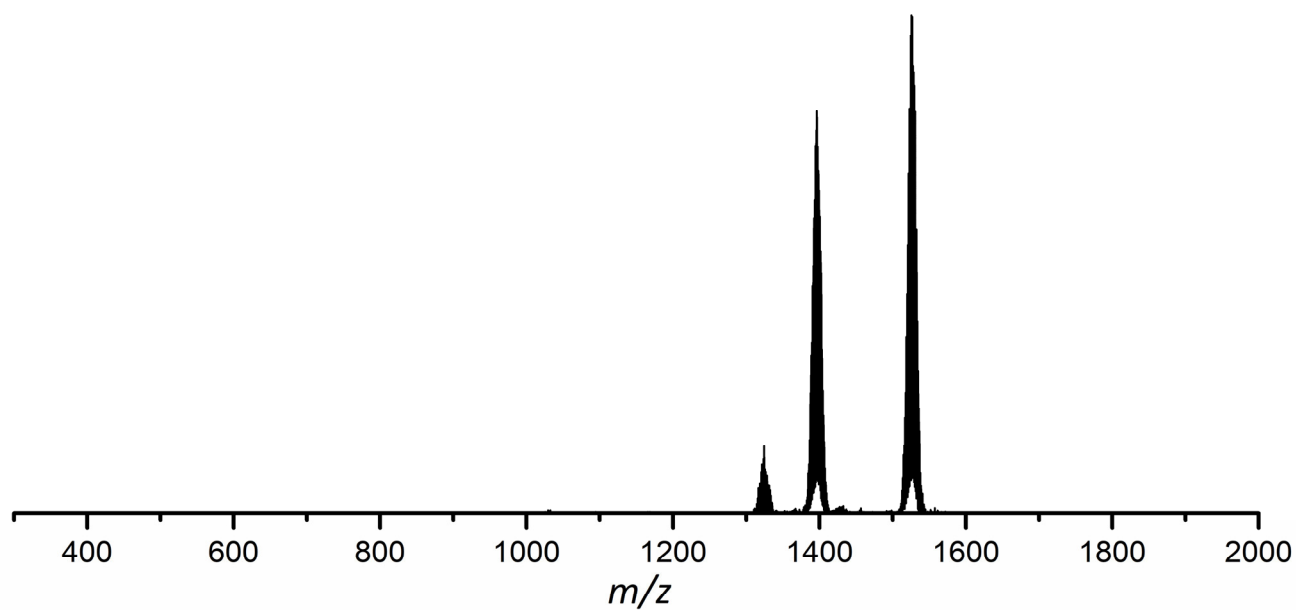


Figure S52. ESI MS spectrum (negative-ion mode, 3500 V, 300 °C) of a thf solution of $[\text{Ge}_9\{\text{Si}(\text{TMS})_3\}_2(\text{CH}_2)_4\text{O-DAB}^{\text{Mes}}]^-$ (**3a**). The molecule peak of **3a** is detected at m/z 1526.8. A detailed view of the signal of anion **3a** is provided in Figure S53. The signal detected at m/z 1396 can be assigned to $[\text{Ge}_9\{\text{Si}(\text{TMS})_3\}_3]^-$, which is formed during the ionization process in the mass spectrometer.

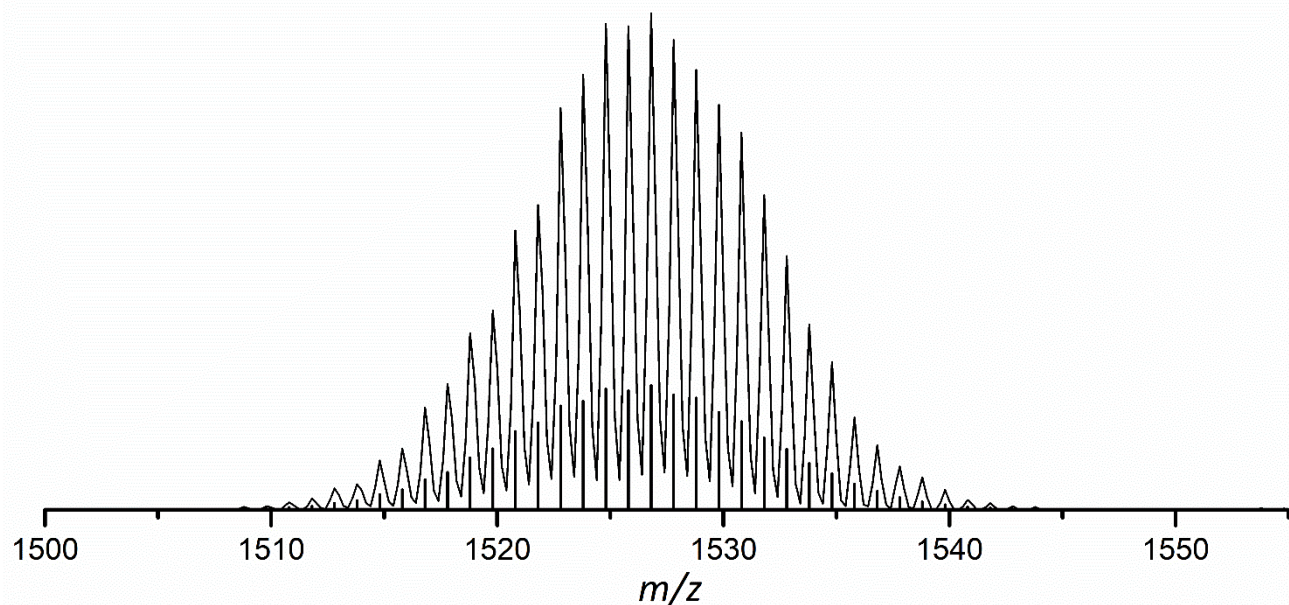


Figure S53. Detailed view on ESI MS signal of $[\text{Ge}_9\{\text{Si}(\text{TMS})_3\}_2(\text{CH}_2)_4\text{O-DAB}^{\text{Mes}}]^-$ (**3a**) at m/z 1526.8.

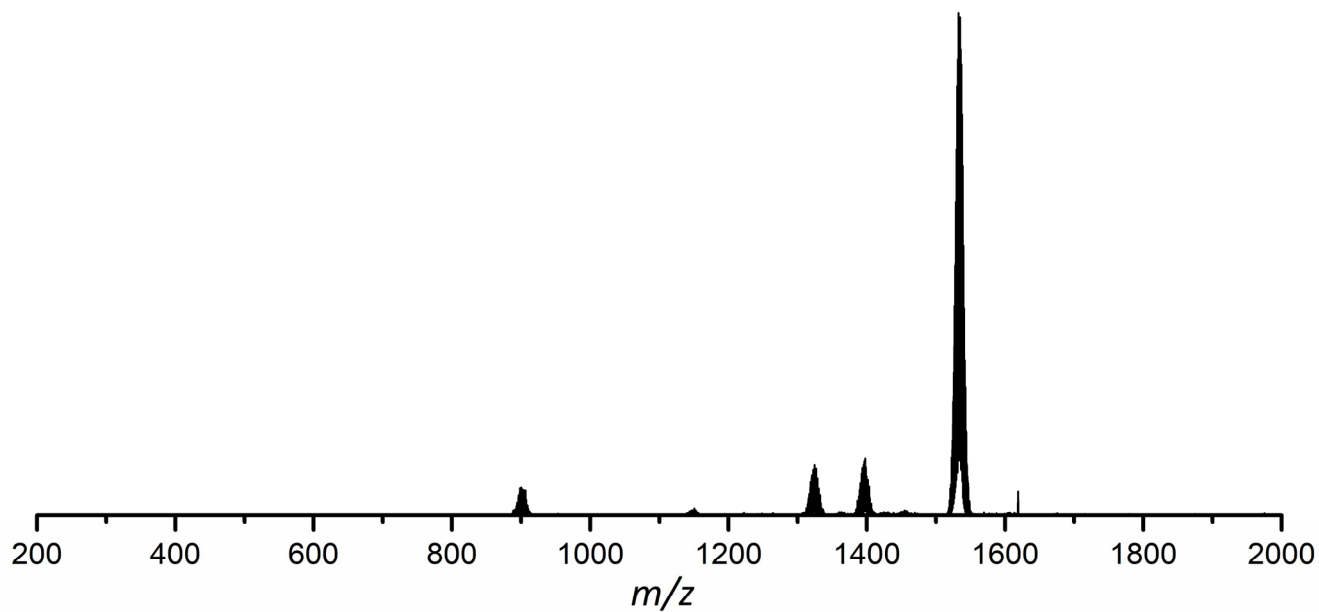


Figure S54. ESI MS spectrum (negative-ion mode, 3500 V, 300 °C) of a thf solution of $[\text{Ge}_9\{\text{Si}(\text{TMS})_3\}_2(\text{CD}_2)_4\text{O-DAB}^{\text{Mes}}]^-$ ($3a-d_8$). The molecule peak of $3a-d_8$ is detected at m/z 1534.8. A detailed view of the signal of anion $3a-d_8$ is provided in Figure S55.

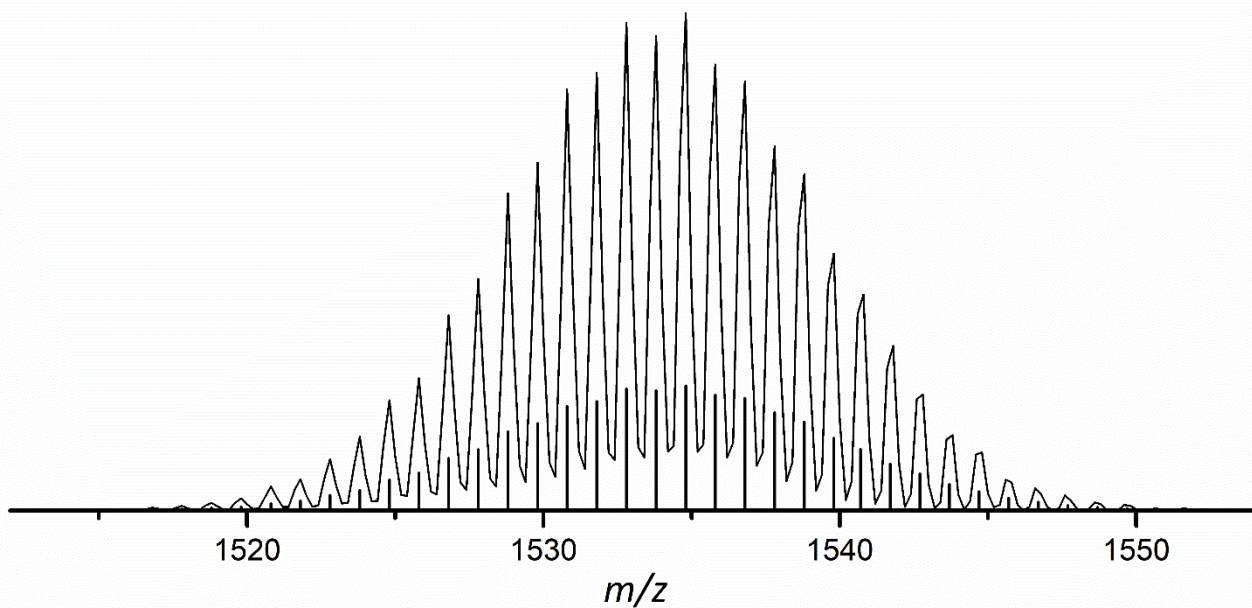


Figure S55. Detailed view on ESI MS signal of $[\text{Ge}_9\{\text{Si}(\text{TMS})_3\}_2(\text{CD}_2)_4\text{O-DAB}^{\text{Mes}}]^-$ ($3a-d_8$) at m/z 1534.8.

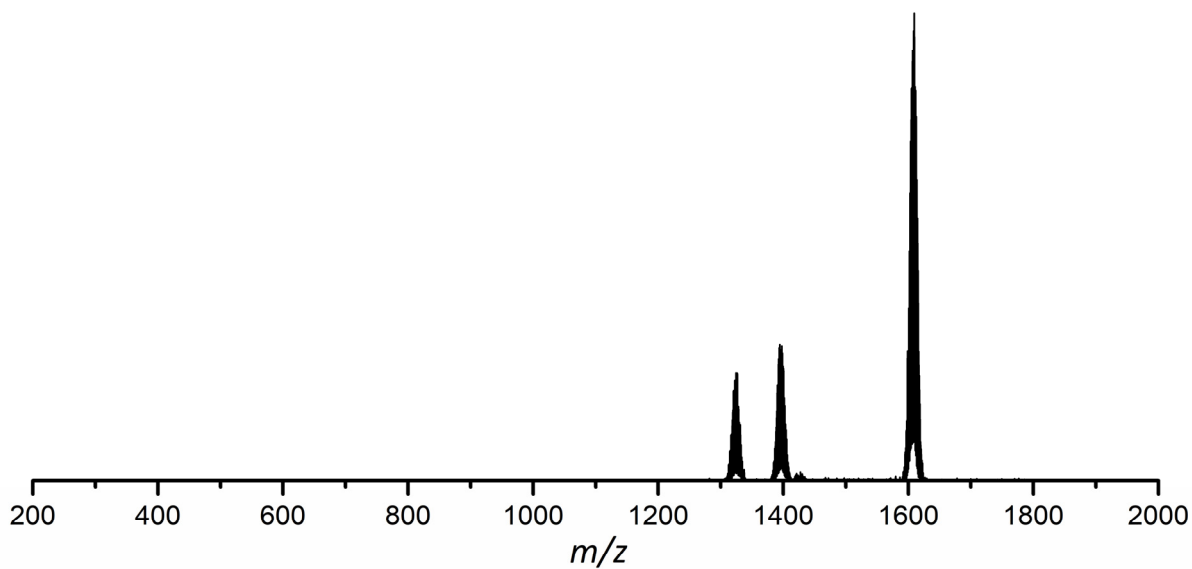


Figure S56. ESI MS spectrum (negative-ion mode, 3500 V, 300 °C) of a thf solution of $[\text{Ge}_9\{\text{Si}(\text{TMS})_3\}_2(\text{CH}_2)_4\text{O-DAB(II)}^{\text{Dipp}}]^-$ (**4a**). The molecule peak of **4a** is detected at m/z 1608.8. A detailed view of the signal of anion **4a** is provided in Figure S57. The signal detected at m/z 1396 can be assigned to $[\text{Ge}_9\{\text{Si}(\text{TMS})_3\}_3]^-$, which is formed during the ionization process in the mass spectrometer.

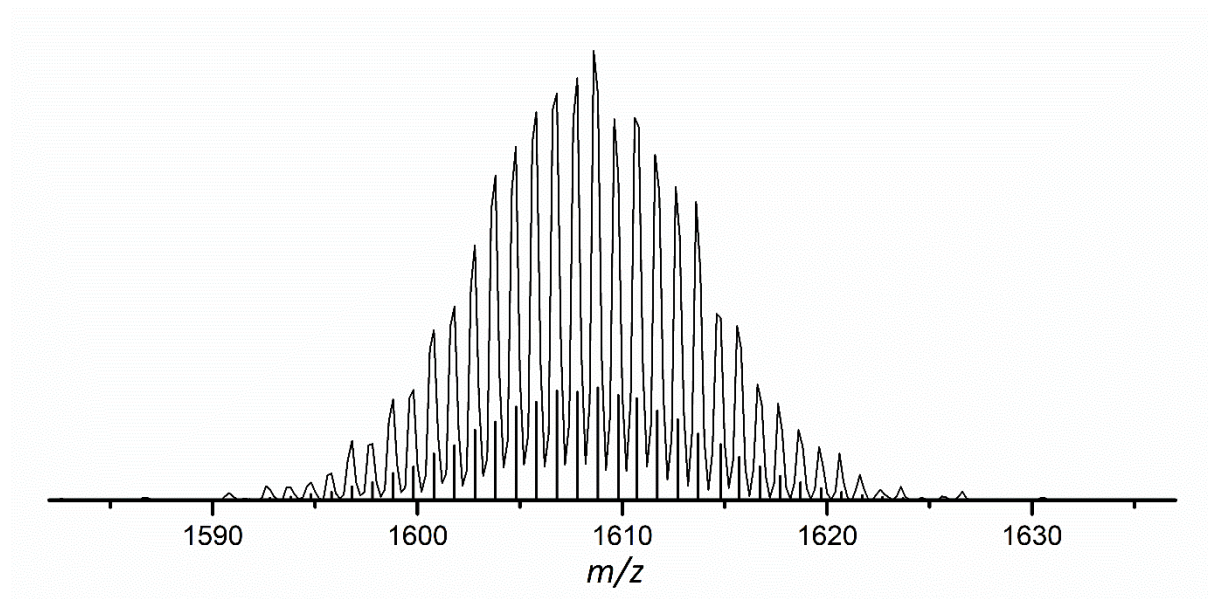


Figure S57. Detailed view on ESI MS signal of $[\text{Ge}_9\{\text{Si}(\text{TMS})_3\}_2(\text{CH}_2)_4\text{O-DAB(II)}^{\text{Dipp}}]^-$ (**4a**) at m/z 1608.8.

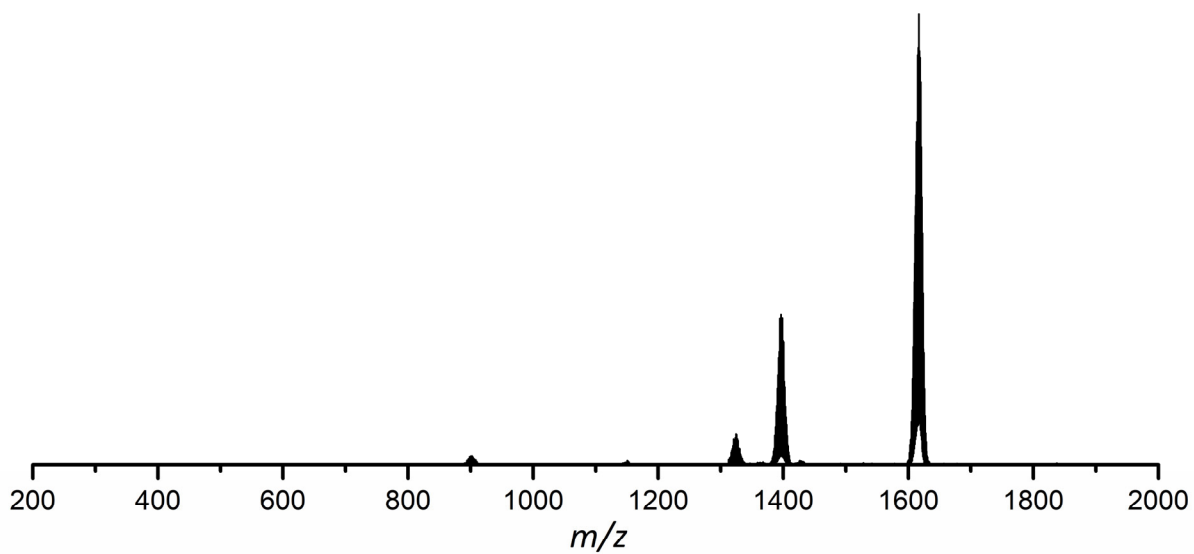


Figure S58. ESI MS spectrum (negative-ion mode, 3500 V, 300 °C) of a thf solution of $[\text{Ge}_9\{\text{Si}(\text{TMS})_3\}_2(\text{CD}_2)_4\text{O-DAB}(\text{II})^{\text{Dipp}}]^-$ (**4a-d₈**). The molecule peak of **4a-d₈** is detected at m/z 1616.8. A detailed view of the signal of anion **4a-d₈** is provided in Figure S59. The signal detected at m/z 1396 can be assigned to $[\text{Ge}_9\{\text{Si}(\text{TMS})_3\}_3]^-$, which is formed during the ionization process in the mass spectrometer.

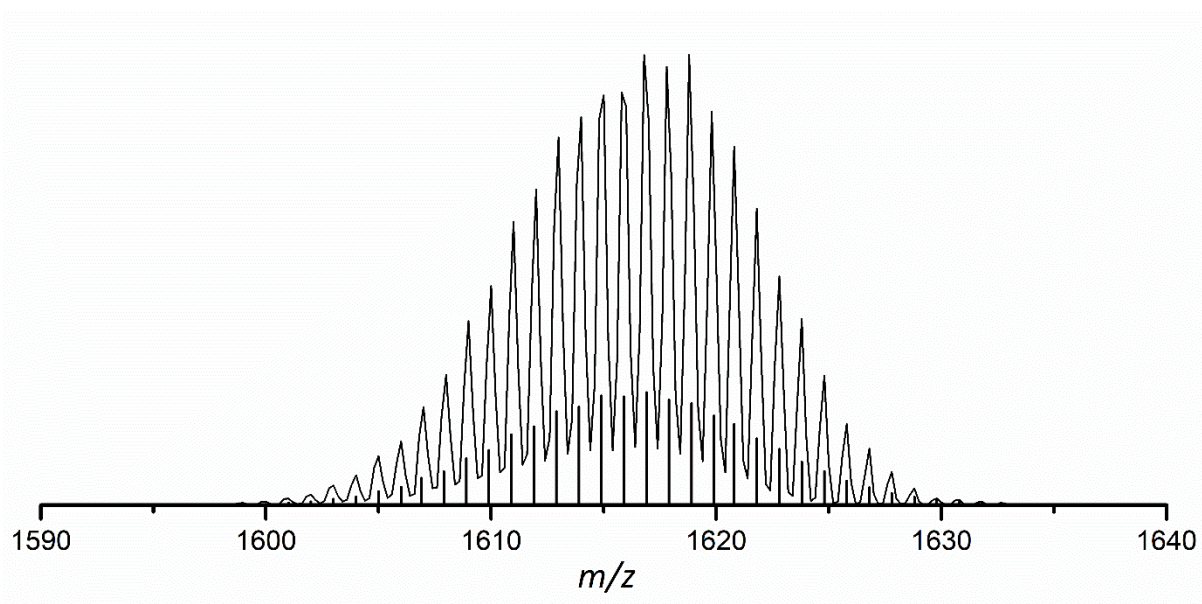


Figure S59. Detailed view on ESI MS signal of $[\text{Ge}_9\{\text{Si}(\text{TMS})_3\}_2(\text{CD}_2)_4\text{O-DAB}(\text{II})^{\text{Dipp}}]^-$ (**4a-d₈**) at m/z 1616.8.

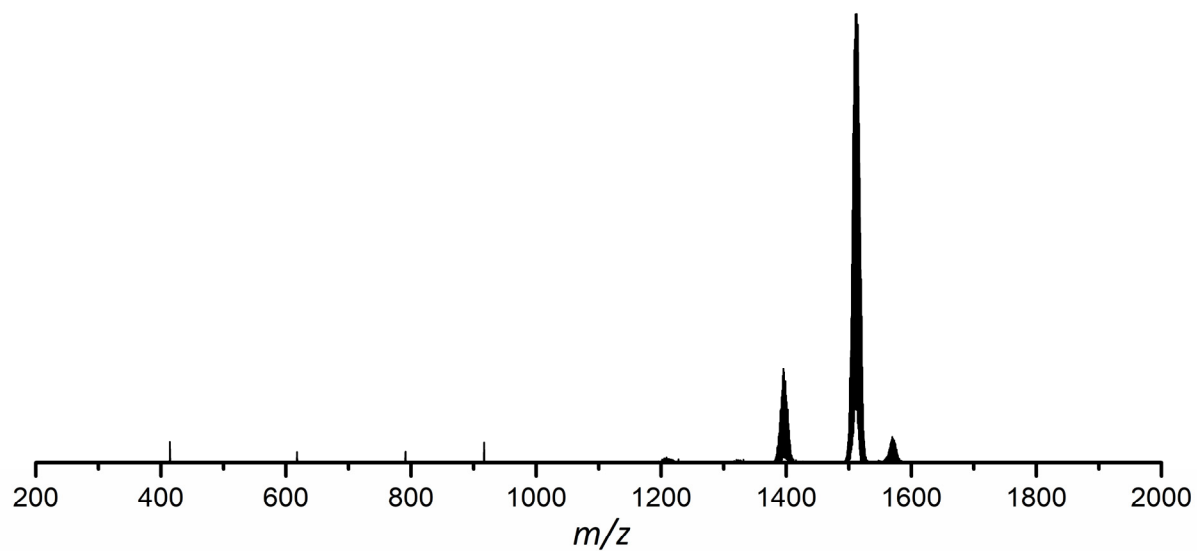


Figure S60. ESI MS spectrum (negative-ion mode, 3500 V, 300 °C) of a thf solution of $[\text{Ge}_9\{\text{Si}(\text{TMS})_3\}_2(\text{CH}_2)_3\text{O-DAB}^{\text{Mes}}]^-$ (**5a**). The molecule peak of **5a** is detected at m/z 1512.8. A detailed view of the signal of anion **5a** is provided in Figure S61. The signal detected at m/z 1396 can be assigned to $[\text{Ge}_9\{\text{Si}(\text{TMS})_3\}_3]^-$, which is formed during the ionization process in the mass spectrometer.

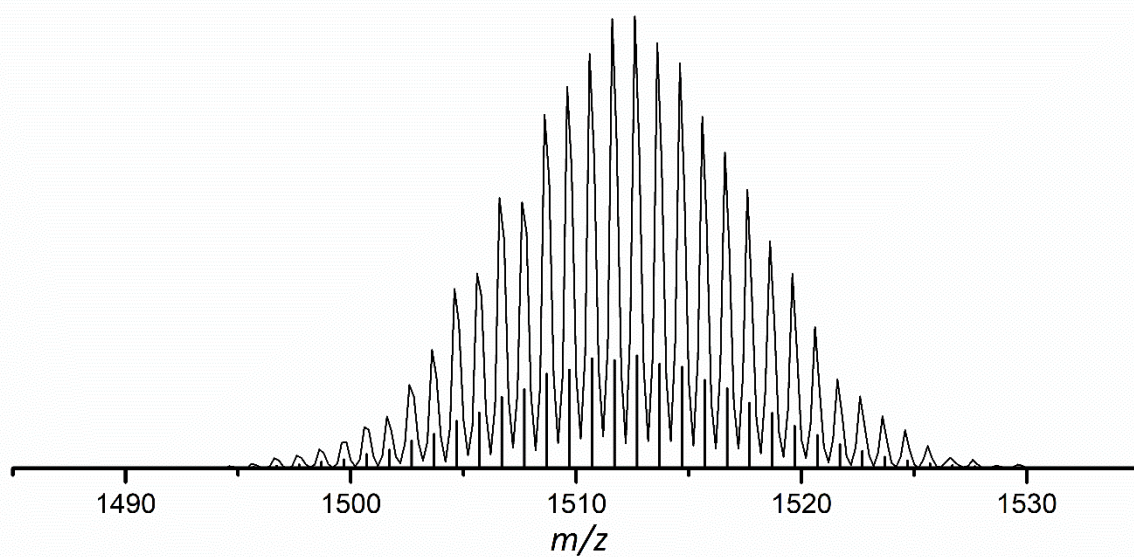


Figure S61. Detailed view on ESI MS signal of $[\text{Ge}_9\{\text{Si}(\text{TMS})_3\}_2(\text{CH}_2)_3\text{O-DAB}^{\text{Mes}}]^-$ (**5a**) at m/z 1512.8.

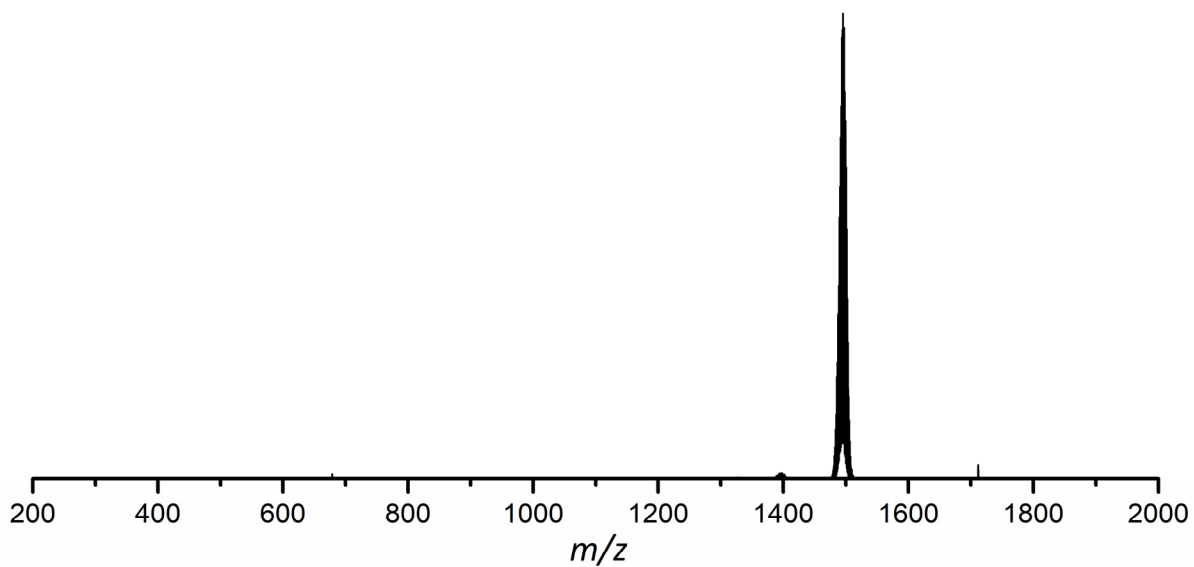


Figure S62. ESI MS spectrum (negative-ion mode, 3500 V, 300 °C) of a MeCN solution of $[\text{Ge}_9\{\text{Si}(\text{TMS})_3\}_2\text{CH}_3\text{C}=\text{N-DAB}^{\text{Mes}^-}]^-$ (**6a**). The molecule peak of **6a** is detected at m/z 1495.8. A detailed view of the signal of anion **6a** is provided in Figure S63.

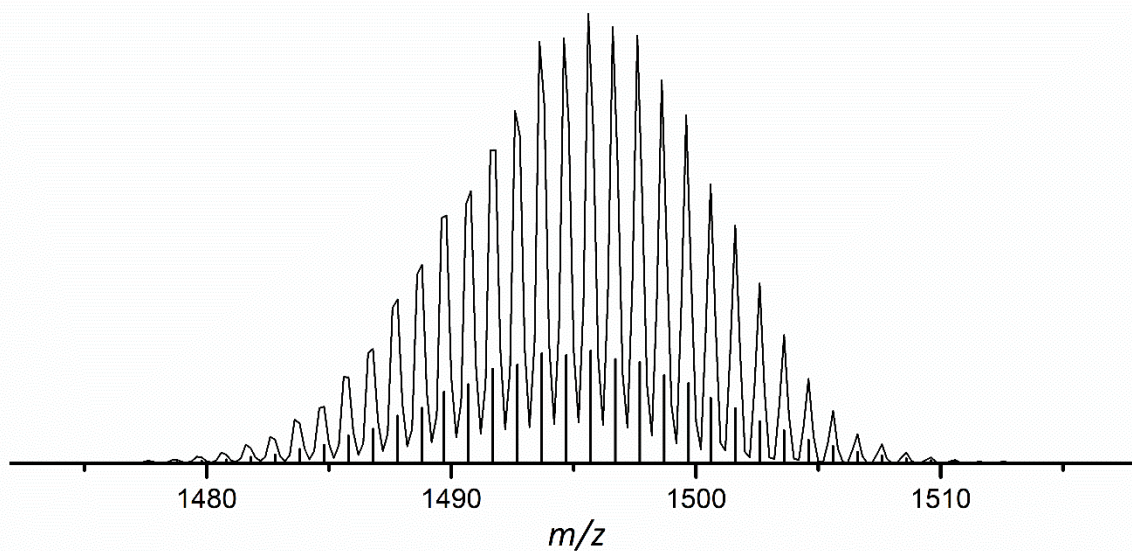


Figure S63. Detailed view on ESI MS signal of $[\text{Ge}_9\{\text{Si}(\text{TMS})_3\}_2\text{CH}_3\text{C}=\text{N-DAB}^{\text{Mes}^-}]^-$ (**6a**) at m/z 1495.8.

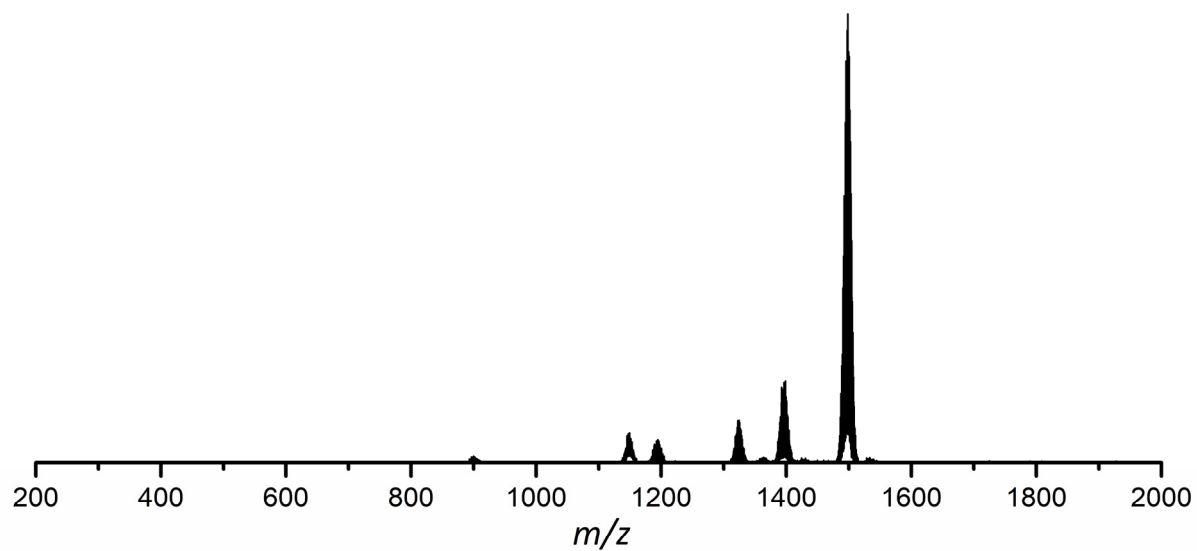


Figure S64. ESI MS spectrum (negative-ion mode, 3500 V, 300 °C) of a MeCN solution of $[\text{Ge}_9\{\text{Si}(\text{TMS})_3\}_2\text{CD}_3\text{C}=\text{N-DAB}^{\text{Mes}}]^-$ (**6a-d₃**). The molecule peak of **6a-d₃** is detected at m/z 1498.8. A detailed view of the signal of anion **6a-d₃** is provided in Figure S65.

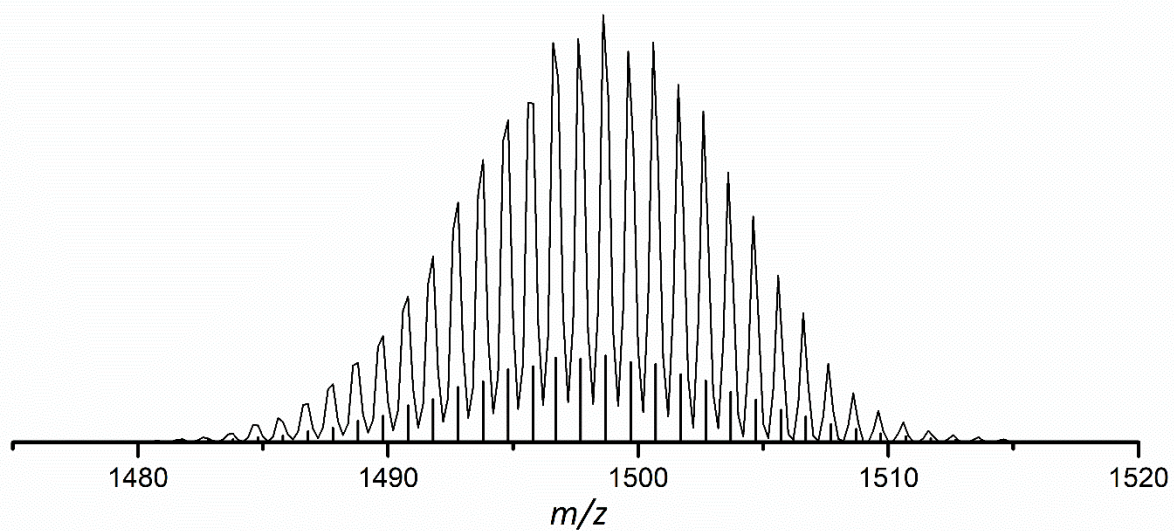


Figure S65. Detailed view on ESI MS signal of $[\text{Ge}_9\{\text{Si}(\text{TMS})_3\}_2\text{CD}_3\text{C}=\text{N-DAB}^{\text{Mes}}]^-$ (**6a-d₃**) at m/z 1498.8.

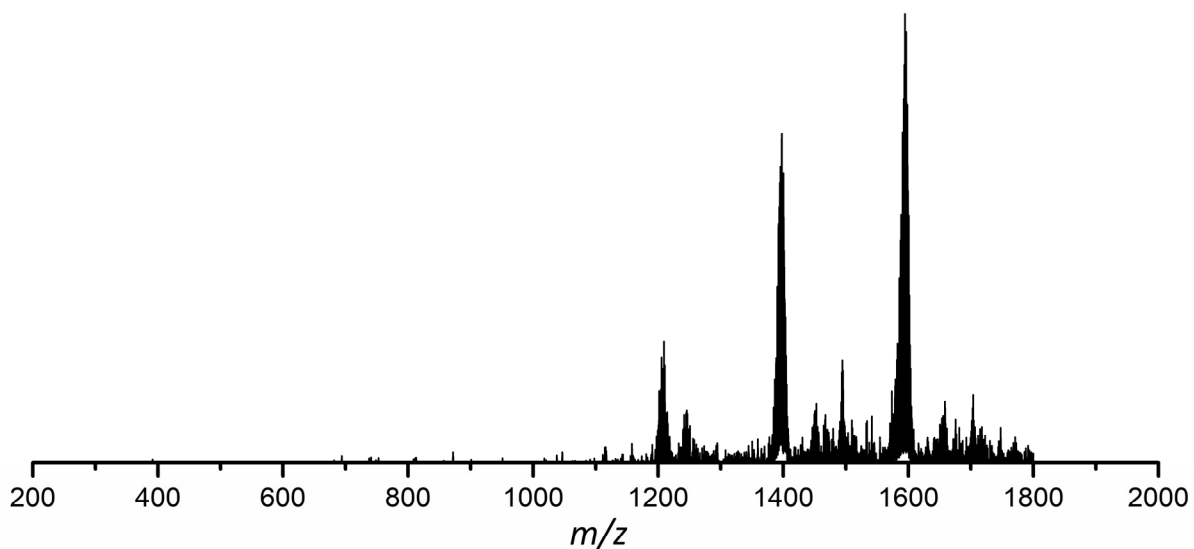


Figure S66. ESI MS spectrum (negative-ion mode, 3500 V, 300 °C) of a thf solution of $[\text{Ge}_9\{\text{Si}(\text{TMS})_3\}_2(\text{CH}_2)_3\text{O-DAB}(\text{II})^{\text{Dipp}}]$. The molecule peak is detected at m/z 1594.8. A detailed view of the signal is provided in Figure S67. The signal detected at m/z 1396 can be assigned to $[\text{Ge}_9\{\text{Si}(\text{TMS})_3\}_3]^-$, which is formed during the ionization process in the mass spectrometer.

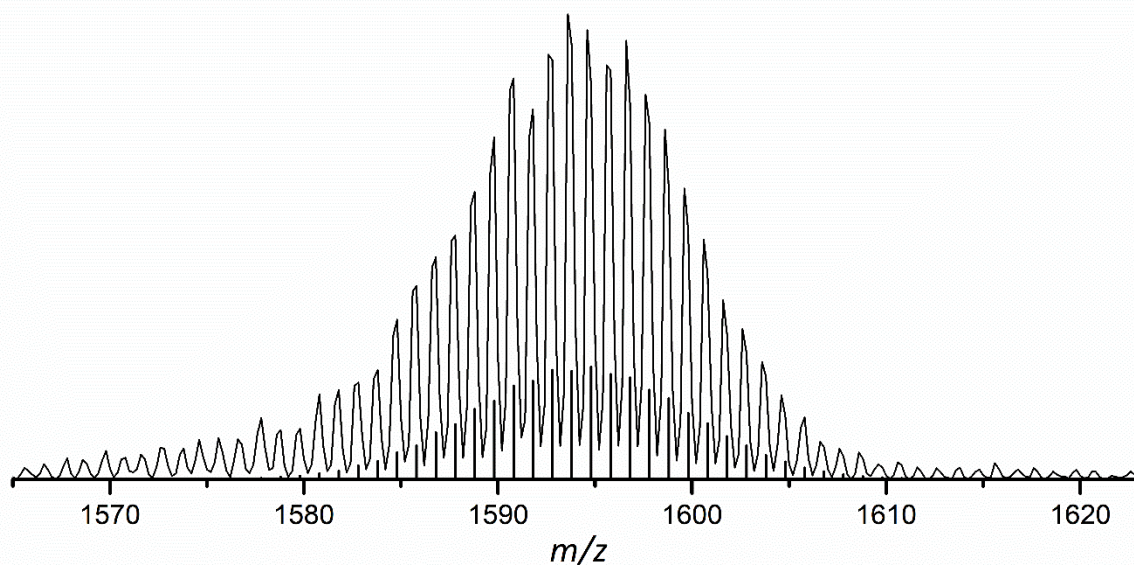


Figure S67. Detailed view on ESI MS signal of $[\text{Ge}_9\{\text{Si}(\text{TMS})_3\}_2(\text{CH}_2)_3\text{O-DAB}(\text{II})^{\text{Dipp}}]$ at m/z 1594.8.

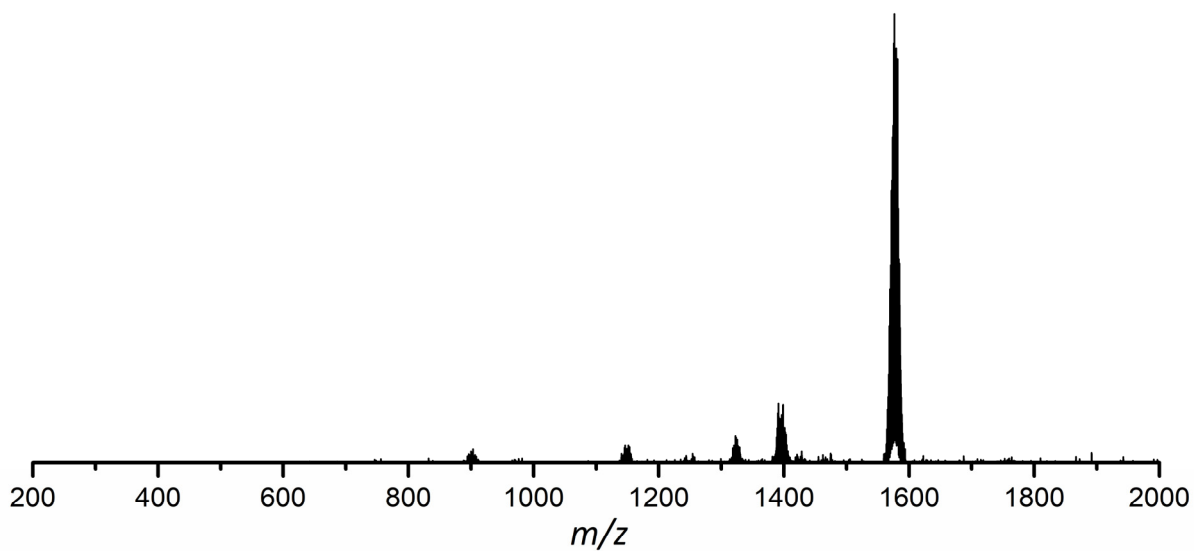


Figure S68. ESI MS spectrum (negative-ion mode, 3500 V, 300 °C) of a MeCN solution of $[\text{Ge}_9\{\text{Si}(\text{TMS})_3\}_2\text{CH}_3\text{C}=\text{N-DAB}(\text{II})^{\text{Dipp}}]$. The molecule peak is detected at m/z 1577.8. A detailed view of the signal is provided in Figure S69.

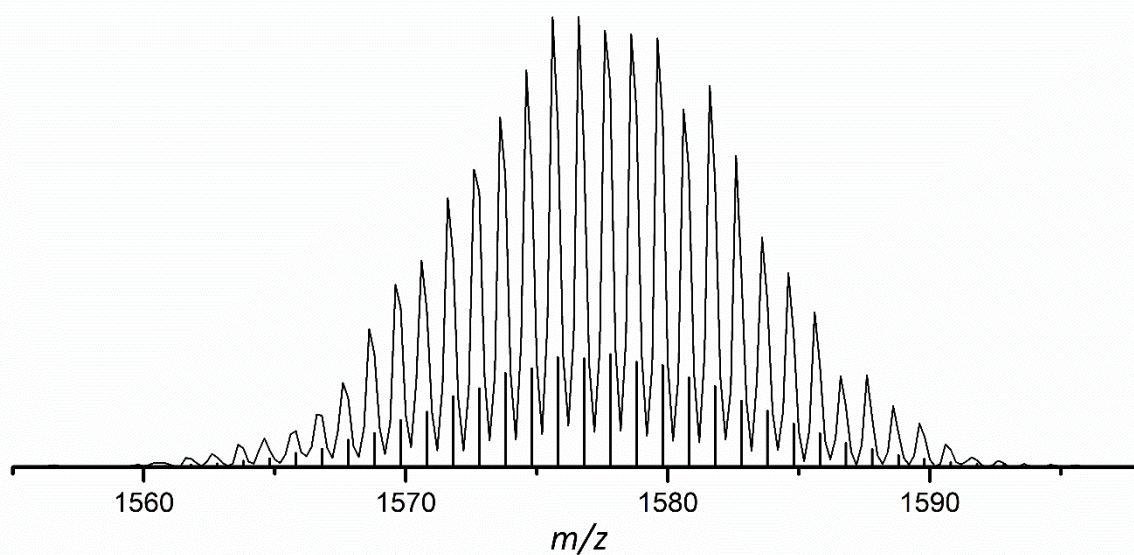


Figure S69. Detailed view on ESI MS signal of $[\text{Ge}_9\{\text{Si}(\text{TMS})_3\}_2\text{CH}_3\text{C}=\text{N-DAB}(\text{II})^{\text{Dipp}}]$ at m/z 1577.8.

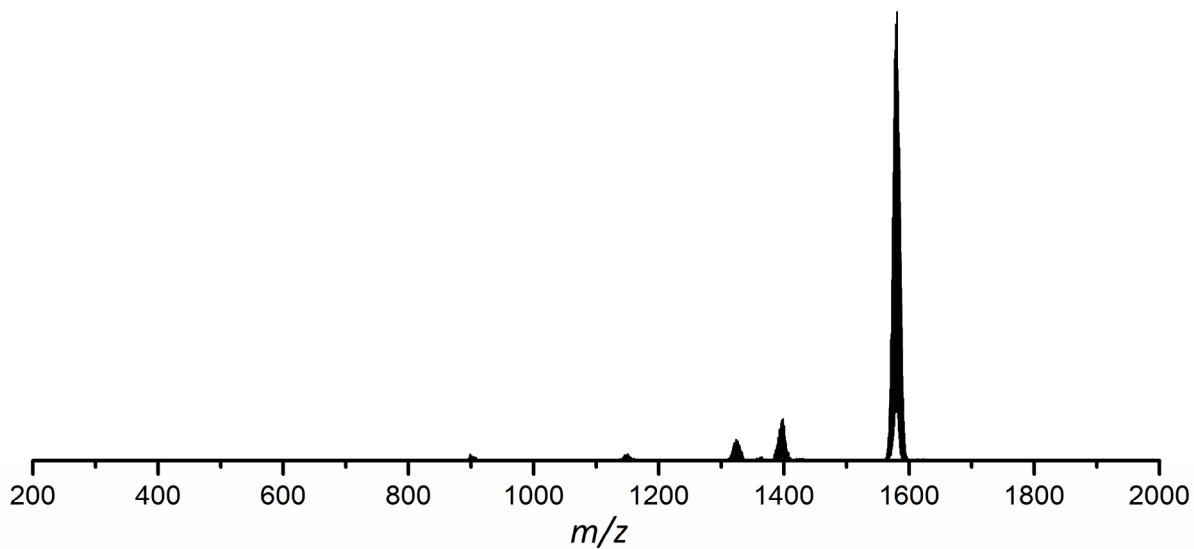


Figure S70. ESI MS spectrum (negative-ion mode, 3500 V, 300 °C) of a MeCN solution of $[\text{Ge}_9\{\text{Si}(\text{TMS})_3\}_2\text{CD}_3\text{C}=\text{N-DAB}(\text{II})^{\text{Dipp}}]$. The molecule peak is detected at m/z 1580.8. A detailed view of the signal is provided in Figure S71.

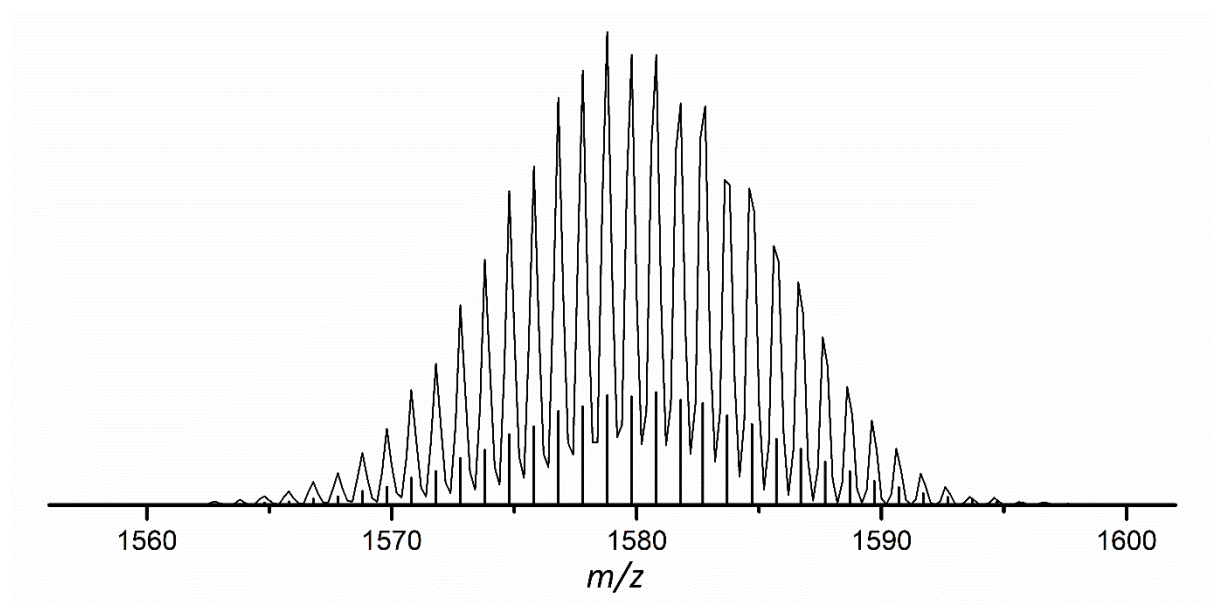


Figure S71. Detailed view on ESI MS signal of $[\text{Ge}_9\{\text{Si}(\text{TMS})_3\}_2\text{CD}_3\text{C}=\text{N-DAB}(\text{II})^{\text{Dipp}}]$ at m/z 1580.8.

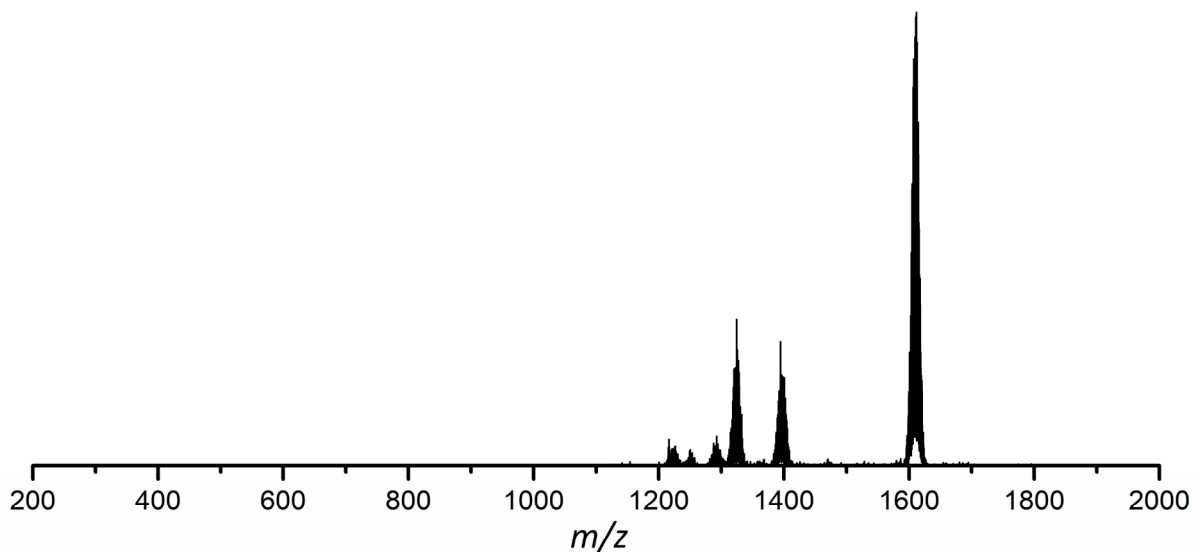


Figure S72. ESI MS spectrum (negative-ion mode, 3500 V, 300 °C) of a thf solution of $[\text{Ge}_9\{\text{Si}(\text{TMS})_3\}_2(\text{CH}_2)_4\text{O-DAB}^{\text{Dipp}}]^-$. The molecule peak is detected at m/z 1610.8. A detailed view of the signal is provided in Figure S73. The signal detected at m/z 1396 can be assigned to $[\text{Ge}_9\{\text{Si}(\text{TMS})_3\}_3]^-$, which is formed during the ionization process in the mass spectrometer.

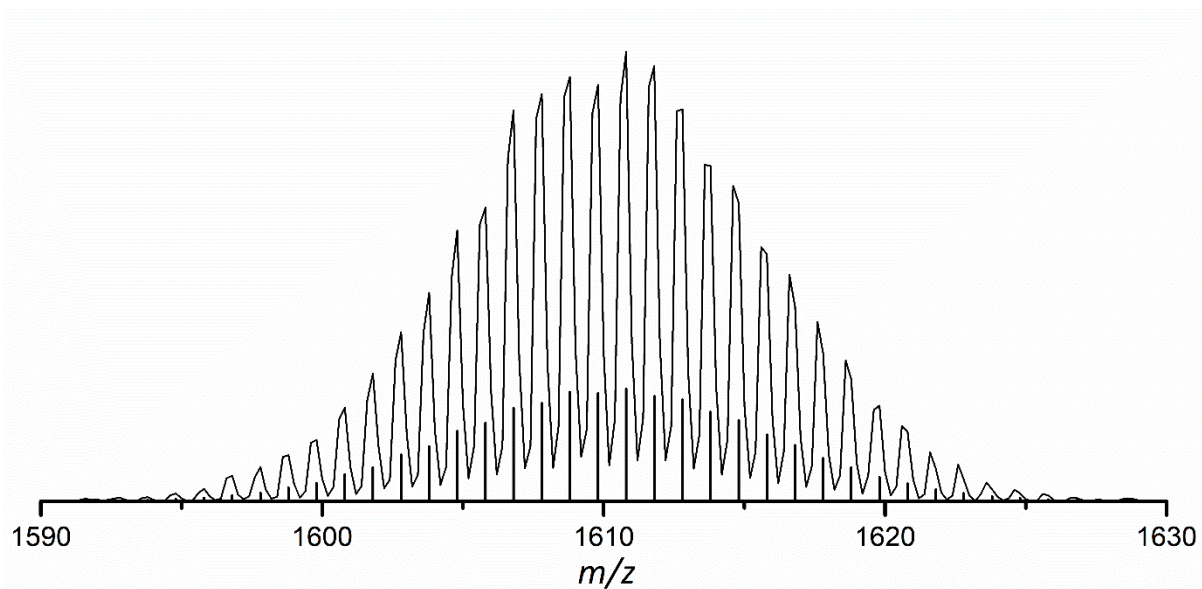


Figure S73. Detailed view on ESI MS signal of $[\text{Ge}_9\{\text{Si}(\text{TMS})_3\}_2(\text{CH}_2)_4\text{O-DAB}^{\text{Dipp}}]^-$ at m/z 1610.8.

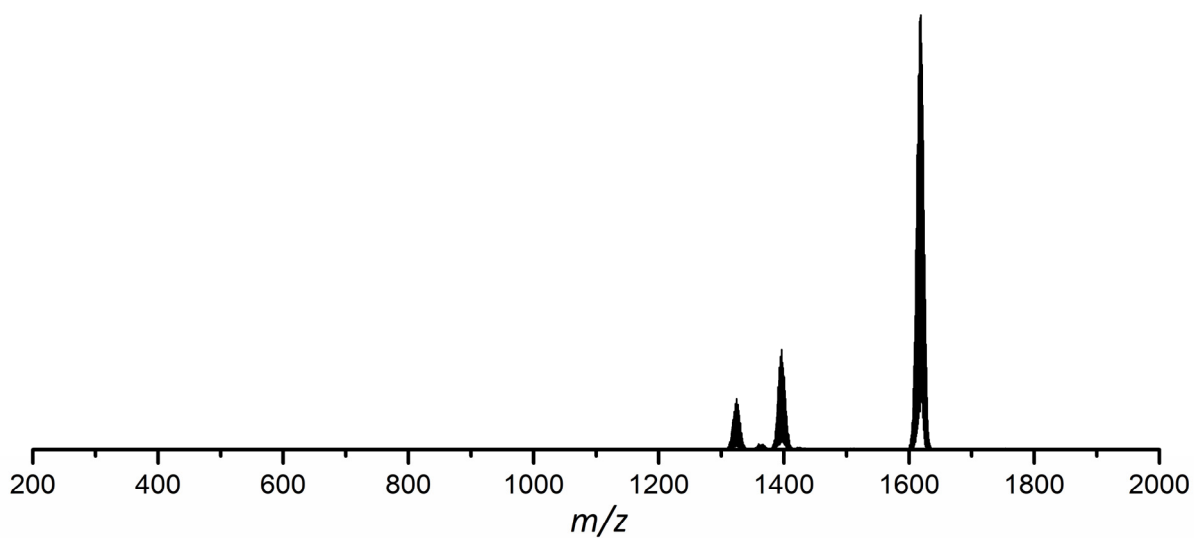


Figure S74. ESI MS spectrum (negative-ion mode, 3500 V, 300 °C) of a thf solution of $[\text{Ge}_9\{\text{Si}(\text{TMS})_3\}_2(\text{CD}_2)_4\text{O-DAB}^{\text{DipP}}]^-$. The molecule peak is detected at m/z 1618.8. A detailed view of the signal is provided in Figure S75. The signal detected at m/z 1396 can be assigned to $[\text{Ge}_9\{\text{Si}(\text{TMS})_3\}_3]^-$, which is formed during the ionization process in the mass spectrometer.

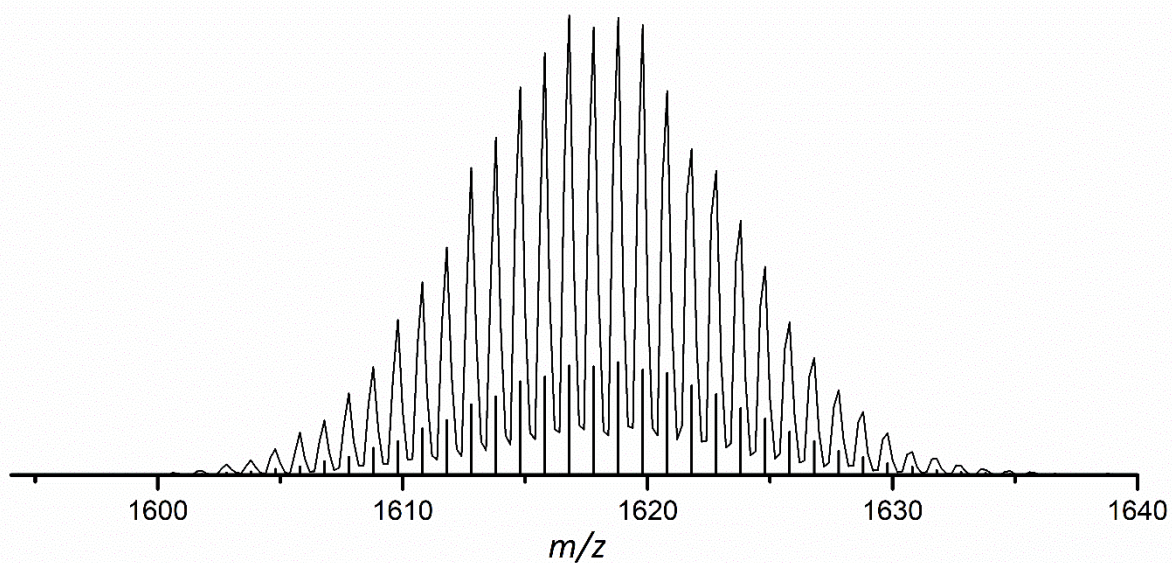


Figure S75. Detailed view on ESI MS signal of $[\text{Ge}_9\{\text{Si}(\text{TMS})_3\}_2(\text{CD}_2)_4\text{O-DAB}^{\text{DipP}}]^-$ at m/z 1618.8.

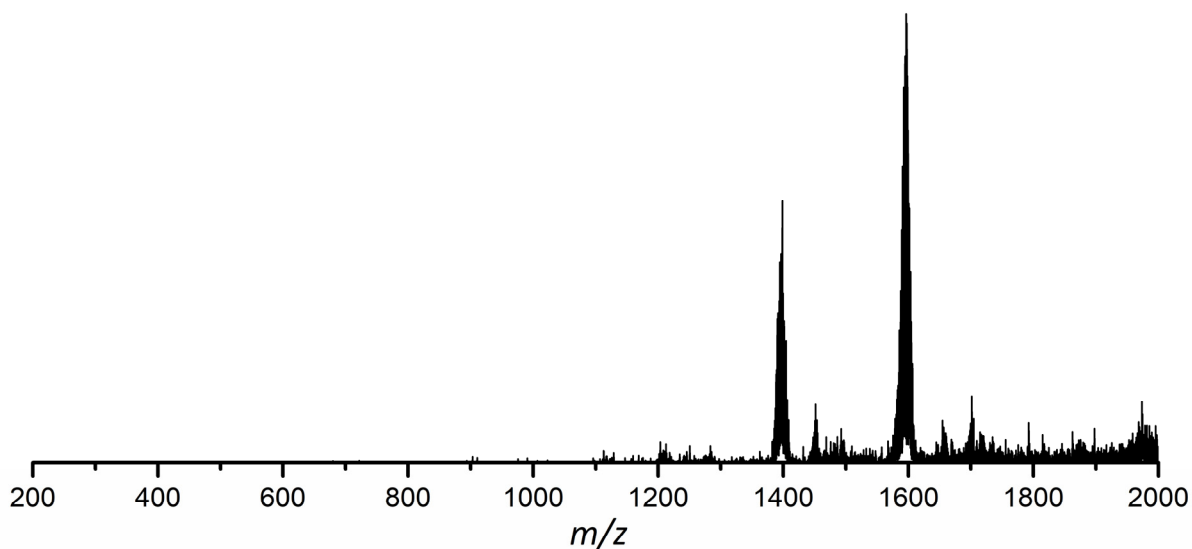


Figure S76. ESI MS spectrum (negative-ion mode, 3500 V, 300 °C) of a thf solution of $[\text{Ge}_9\{\text{Si}(\text{TMS})_3\}_2(\text{CH}_2)_3\text{O-DAB}^{\text{DipP}}]^-$. The molecule peak is detected at m/z 1596.8. A detailed view of the signal is provided in Figure S77. The signal detected at m/z 1396 can be assigned to $[\text{Ge}_9\{\text{Si}(\text{TMS})_3\}_3]^-$, which is formed during the ionization process in the mass spectrometer.

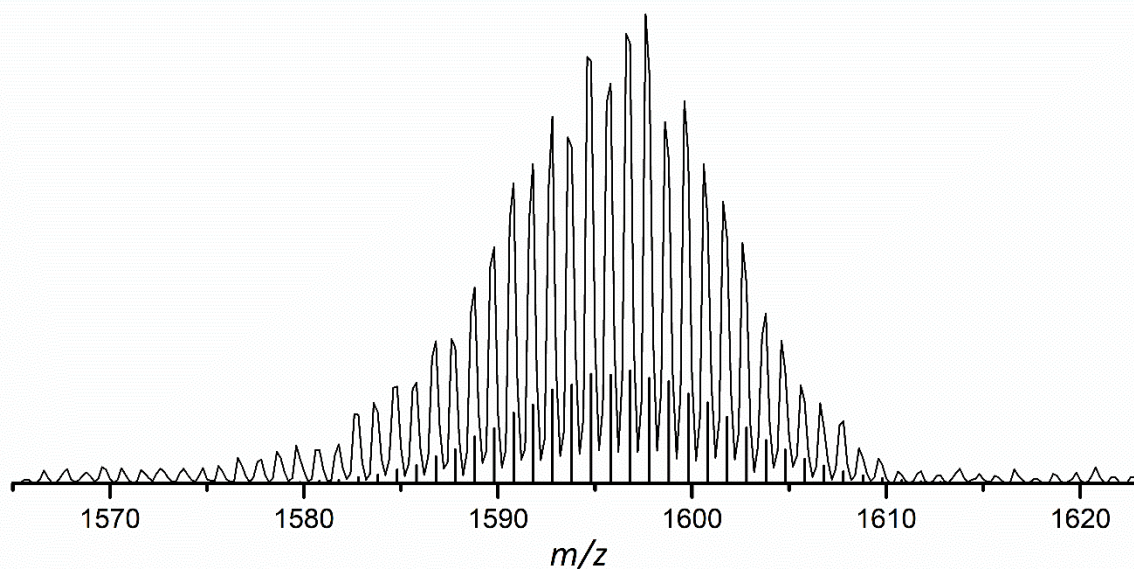


Figure S77. Detailed view on ESI MS signal of $[\text{Ge}_9\{\text{Si}(\text{TMS})_3\}_2(\text{CH}_2)_3\text{O-DAB}^{\text{DipP}}]^-$ at m/z 1596.8.

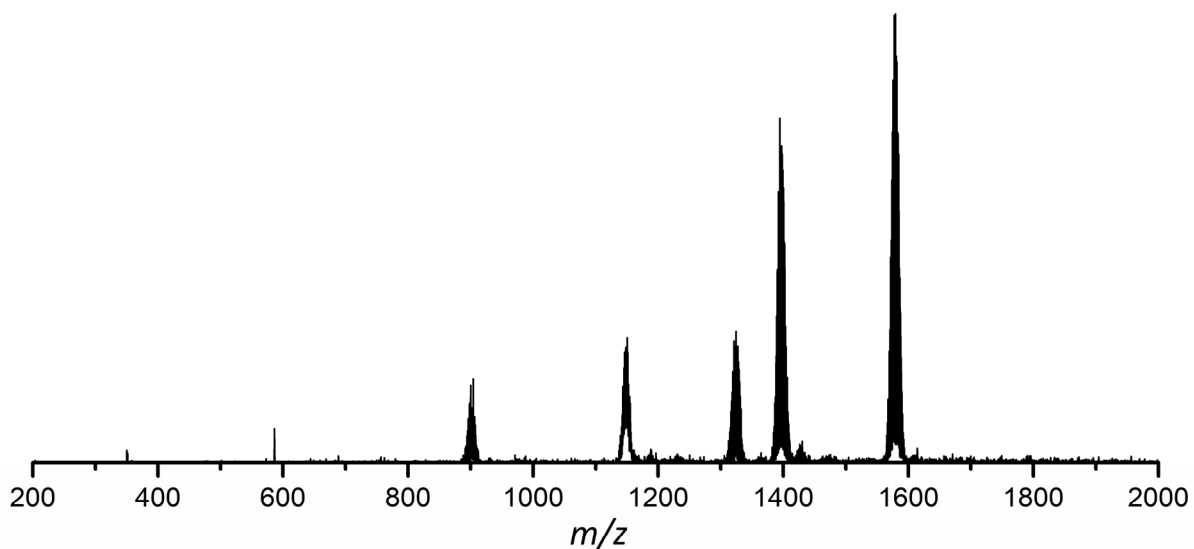


Figure S78. ESI MS spectrum (negative-ion mode, 3500 V, 300 °C) of a thf solution of $[\text{Ge}_9\{\text{Si}(\text{TMS})_3\}_2\text{CH}_3\text{C}=\text{N-DAB}^{\text{Dipp}}]^-$. The molecule peak is detected at m/z 1579.8. A detailed view of the signal is provided in Figure S79. The signal detected at m/z 1396 can be assigned to $[\text{Ge}_9\{\text{Si}(\text{TMS})_3\}_3]^-$, which is formed during the ionization process in the mass spectrometer.

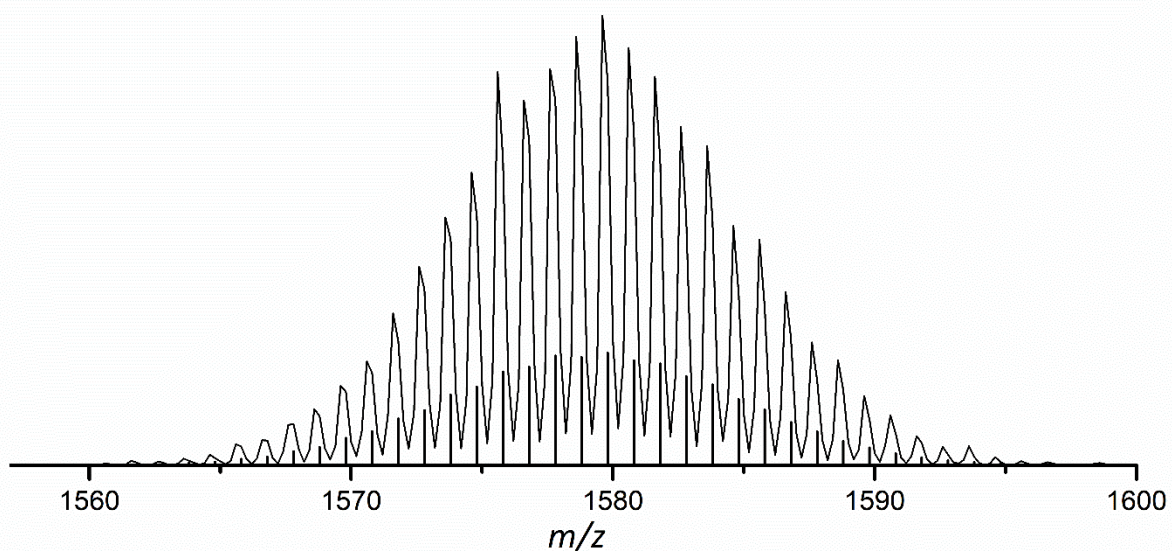


Figure S79. Detailed view on ESI MS signal of $[\text{Ge}_9\{\text{Si}(\text{TMS})_3\}_2\text{CH}_3\text{C}=\text{N-DAB}^{\text{Dipp}}]^-$ at m/z 1579.8.

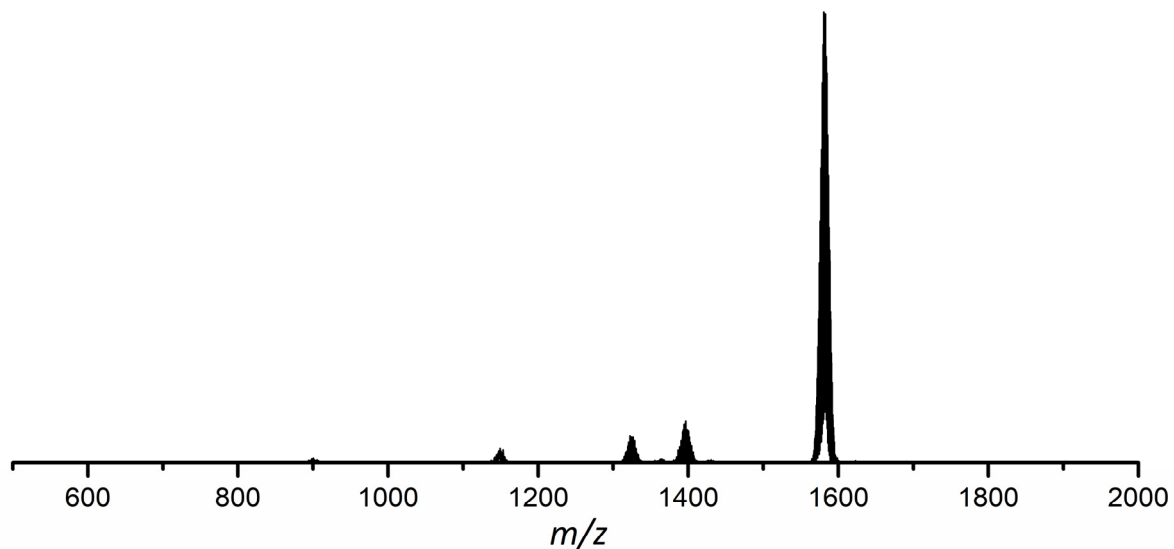


Figure S80. ESI MS spectrum (negative-ion mode, 3500 V, 300 °C) of a thf solution of $[\text{Ge}_9\{\text{Si}(\text{TMS})_3\}_2\text{CD}_3\text{C}=\text{N-DAB}^{\text{Dipp}}]$. The molecule peak is detected at m/z 1582.8. A detailed view of the signal is provided in Figure S81. The signal detected at m/z 1396 can be assigned to $[\text{Ge}_9\{\text{Si}(\text{TMS})_3\}_3]^-$, which is formed during the ionization process in the mass spectrometer.

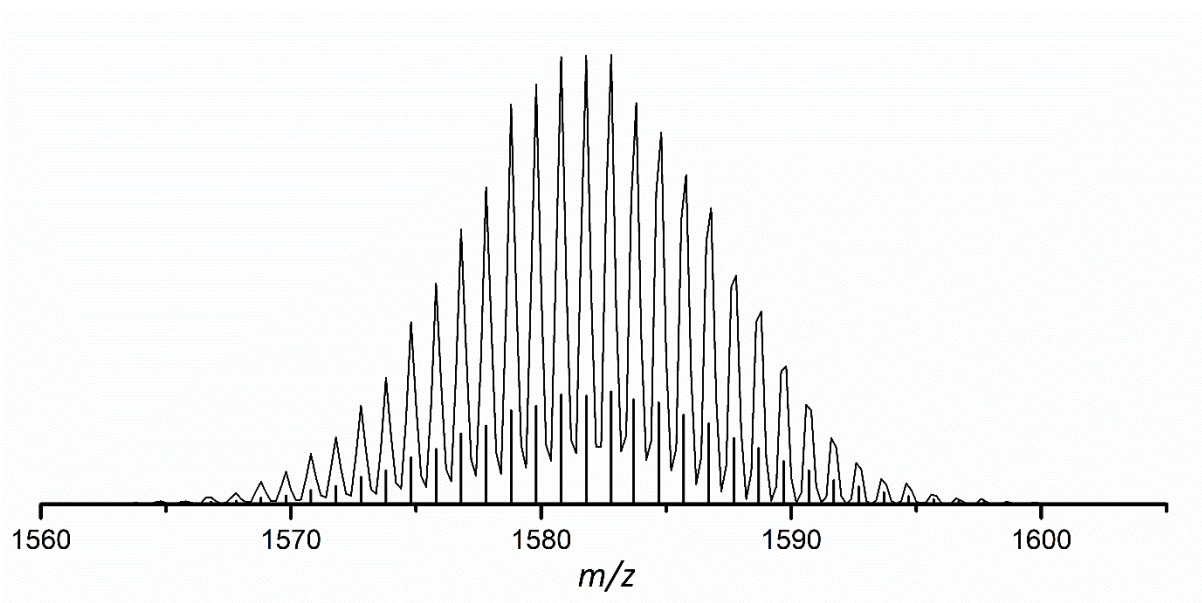


Figure S81. Detailed view on ESI MS signal of $[\text{Ge}_9\{\text{Si}(\text{TMS})_3\}_2\text{CD}_3\text{C}=\text{N-DAB}^{\text{Dipp}}]$ at m/z 1582.8.

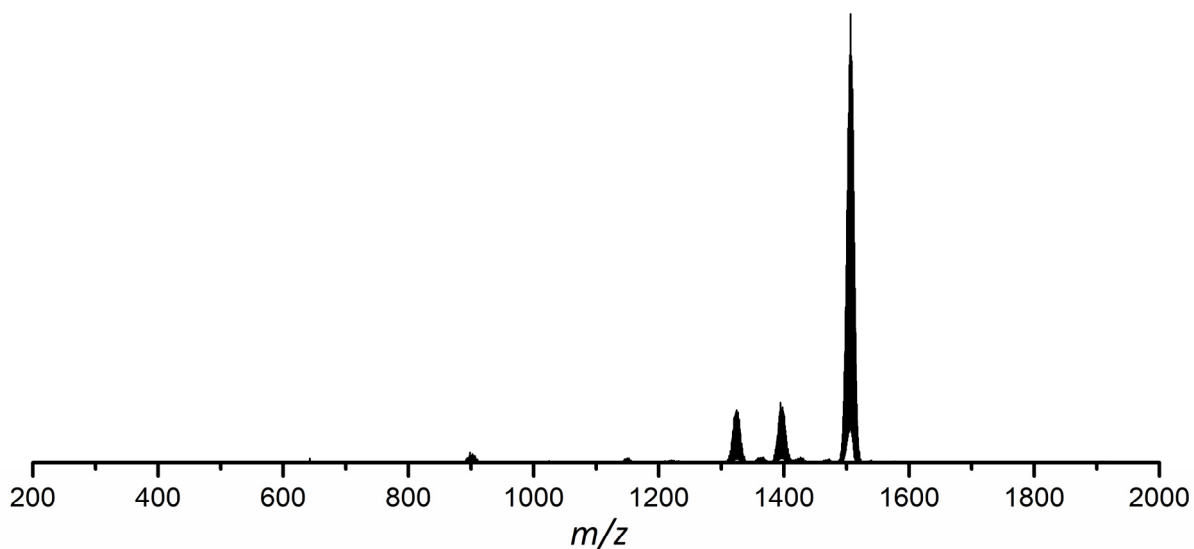


Figure S82. ESI MS spectrum (negative mode, 3500 V, 300 °C) of a thf solution of $[\text{Ge}_9\{\text{Si}(\text{TMS})_3\}_2(\text{CH}_2)_4\text{O-DAB}^{9-\text{xy}}]$. The molecule peak is detected at m/z 1506.8. A detailed view of the signal is provided in Figure S83. The signal detected at m/z 1396 can be assigned to $[\text{Ge}_9\{\text{Si}(\text{TMS})_3\}_3]^-$, which is formed during the ionization process in the mass spectrometer.

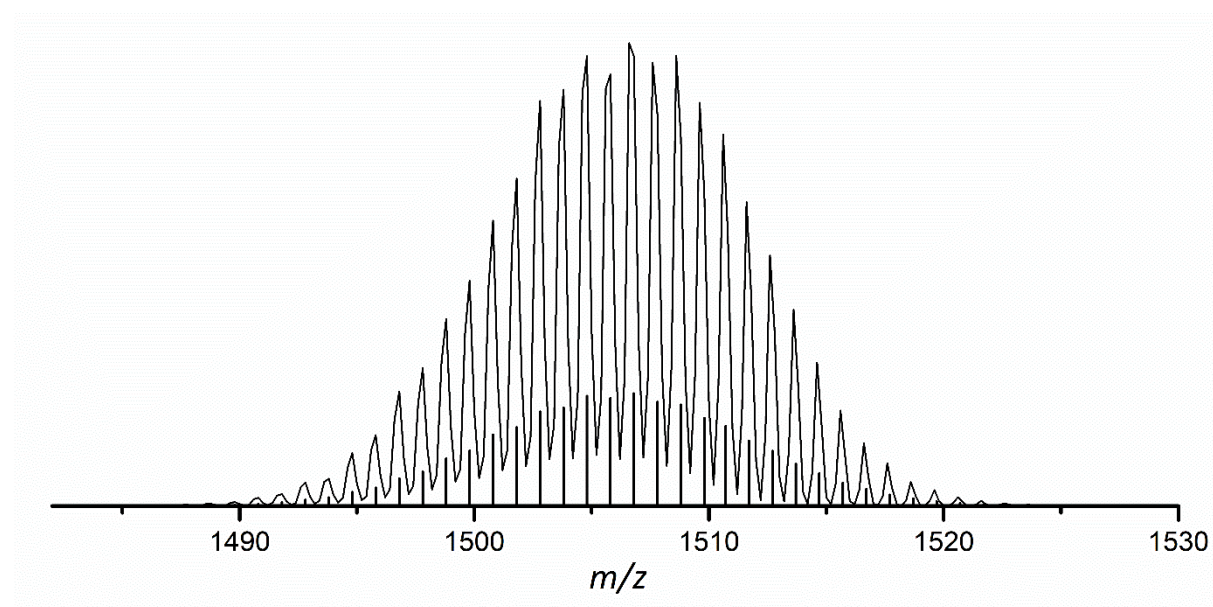


Figure S83. Detailed view on ESI MS signal of $[\text{Ge}_9\{\text{Si}(\text{TMS})_3\}_2(\text{CH}_2)_4\text{O-DAB}^{9-\text{xy}}]$ at m/z 1506.8.

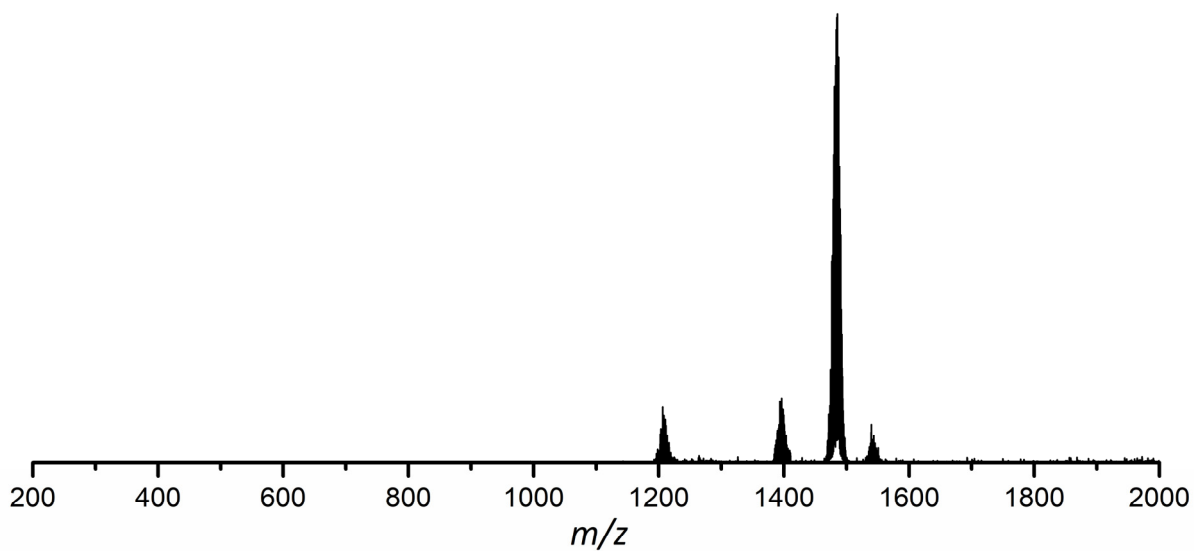


Figure S84. ESI MS spectrum (negative-ion mode, 3500 V, 300 °C) of a thf solution of $[\text{Ge}_9\{\text{Si}(\text{TMS})_3\}_2(\text{CH}_2)_3\text{O-DAB}^{2-\text{xy}}]^-$. The molecule peak is detected at m/z 1484.8. A detailed view of the signal is provided in Figure S85. The signal detected at m/z 1396 can be assigned to $[\text{Ge}_9\{\text{Si}(\text{TMS})_3\}_3]^-$, which is formed during the ionization process in the mass spectrometer.

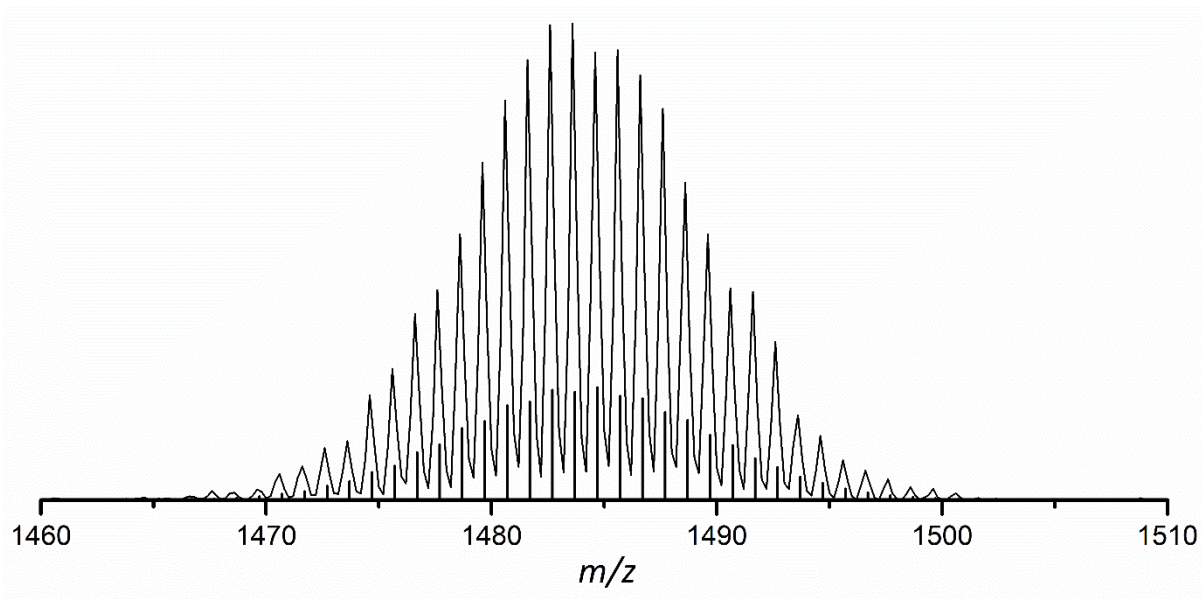


Figure S85. Detailed view on ESI MS signal of $[\text{Ge}_9\{\text{Si}(\text{TMS})_3\}_2(\text{CH}_2)_3\text{O-DAB}^{2-\text{xy}}]^-$ at m/z 1484.8.

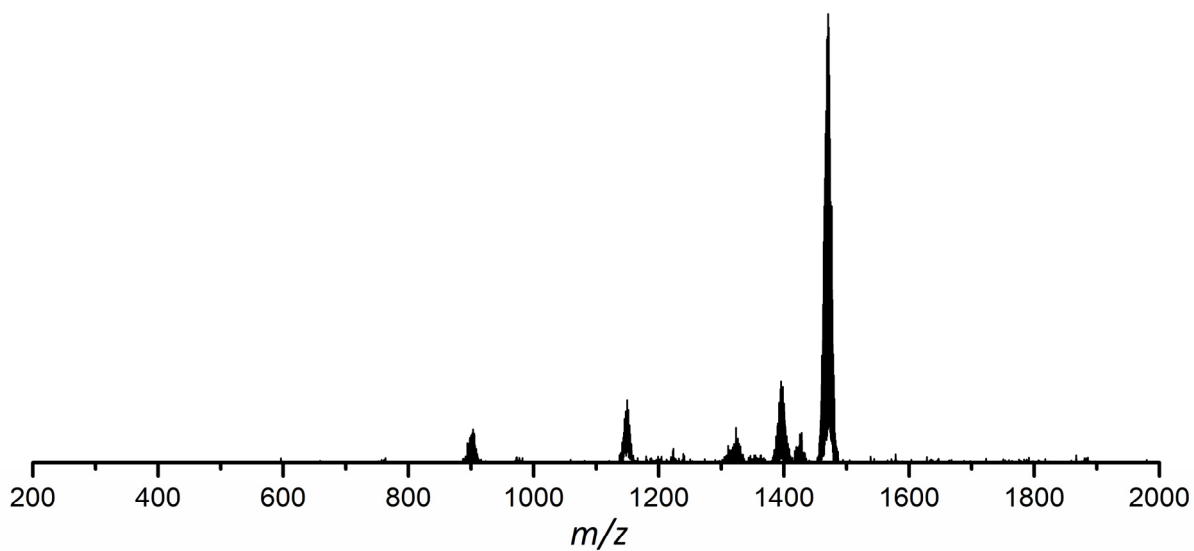


Figure S86. ESI MS spectrum (negative-ion mode, 3500 V, 300 °C) of a thf solution of $[\text{Ge}_9\{\text{Si}(\text{TMS})_3\}_2\text{CD}_3\text{C}=\text{N-DAB}^{\text{o-xy}}]^-$. The molecule peak is detected at m/z 1470.8. A detailed view of the signal is provided in Figure S87. The signal detected at m/z 1396 can be assigned to $[\text{Ge}_9\{\text{Si}(\text{TMS})_3\}_3]^-$, which is formed during the ionization process in the mass spectrometer.

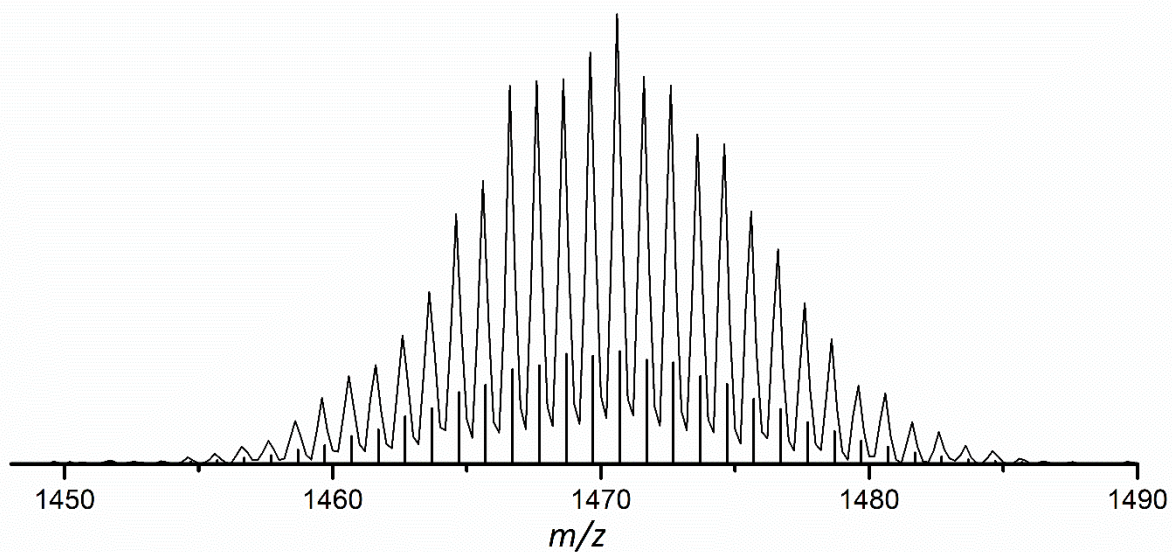


Figure S87. Detailed view on ESI MS signal of $[\text{Ge}_9\{\text{Si}(\text{TMS})_3\}_2\text{CD}_3\text{C}=\text{N-DAB}^{\text{o-xy}}]^-$ at m/z 1470.8.

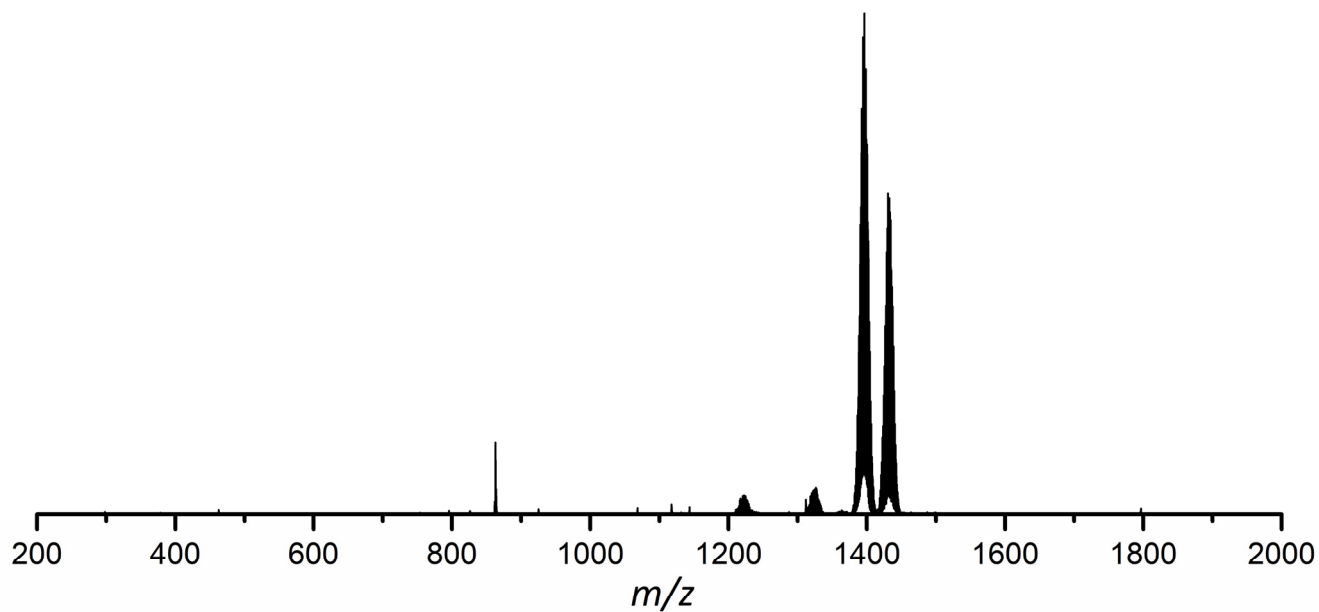


Figure S88. ESI MS spectrum (negative-ion mode, 3500 V, 300 °C) of a thf solution of $[\text{Ge}_9\{\text{Si}(\text{TMS})_3\}_2(\text{CH}_2)_4\text{O-B}(\text{N}^i\text{Pr}_2)_2]^-$. The molecule peak is detected at m/z 1432.8. A detailed view of the signal is provided in Figure S89. The signal detected at m/z 1396 can be assigned to $[\text{Ge}_9\{\text{Si}(\text{TMS})_3\}_3]^-$, which is formed during the ionization process in the mass spectrometer.

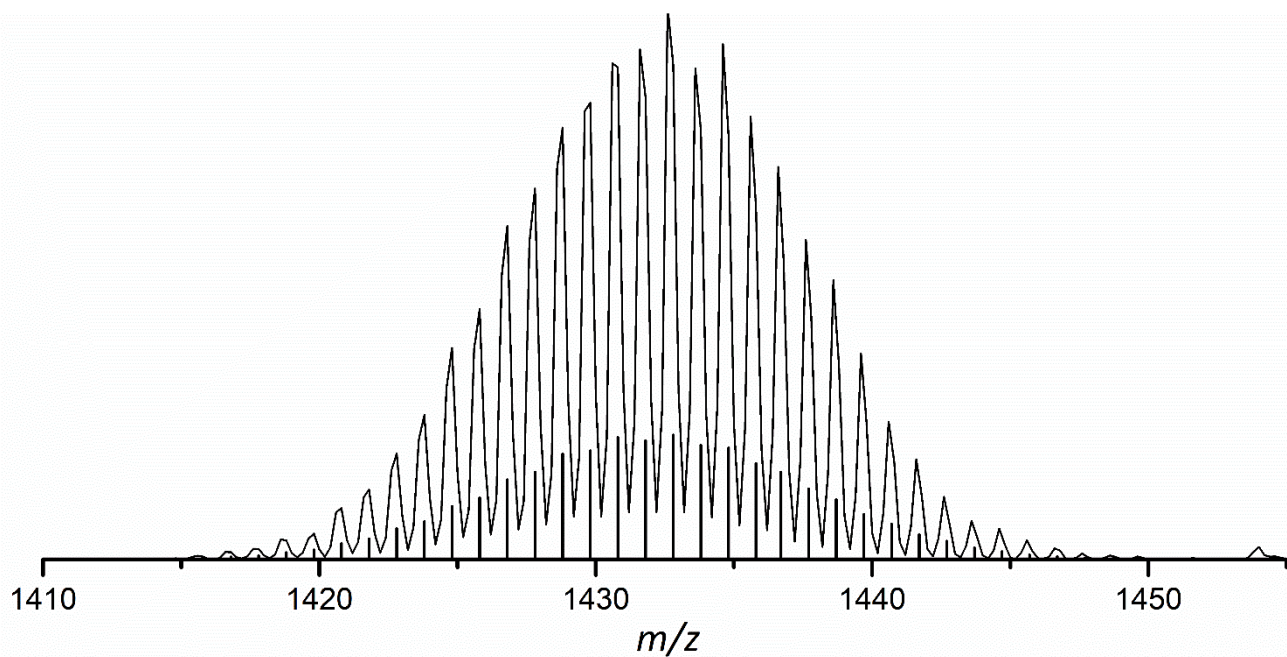


Figure S89. Detailed view on ESI MS signal of $[\text{Ge}_9\{\text{Si}(\text{TMS})_3\}_2(\text{CH}_2)_4\text{O-B}(\text{N}^i\text{Pr}_2)_2]^-$ at m/z 1432.8.

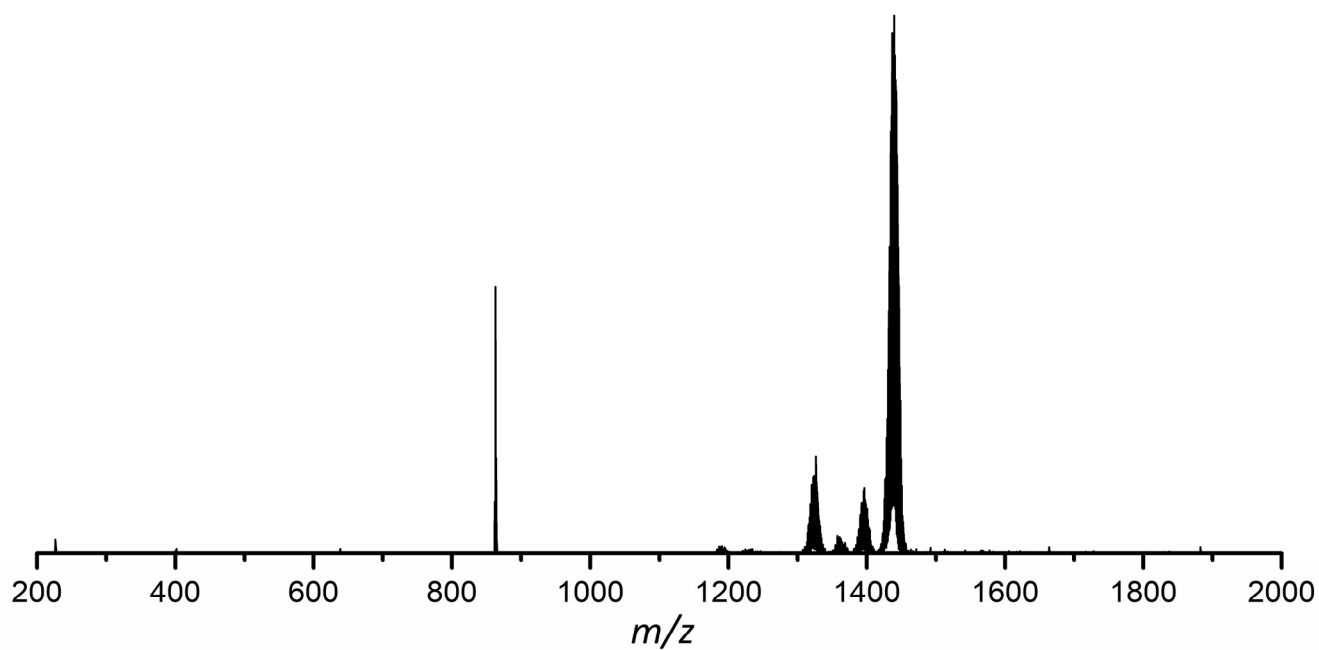


Figure S90. ESI MS spectrum (negative-ion mode, 3500 V, 300 °C) of a thf solution of $[\text{Ge}_9\{\text{Si}(\text{TMS})_3\}_2(\text{CD}_2)_4\text{O-B}(\text{N}^i\text{Pr}_2)_2]^-$. The molecule peak is detected at m/z 1440.8. A detailed view of the signal is provided in Figure S91. The signal detected at m/z 1396 can be assigned to $[\text{Ge}_9\{\text{Si}(\text{TMS})_3\}_3]^-$, which is formed during the ionization process in the mass spectrometer.

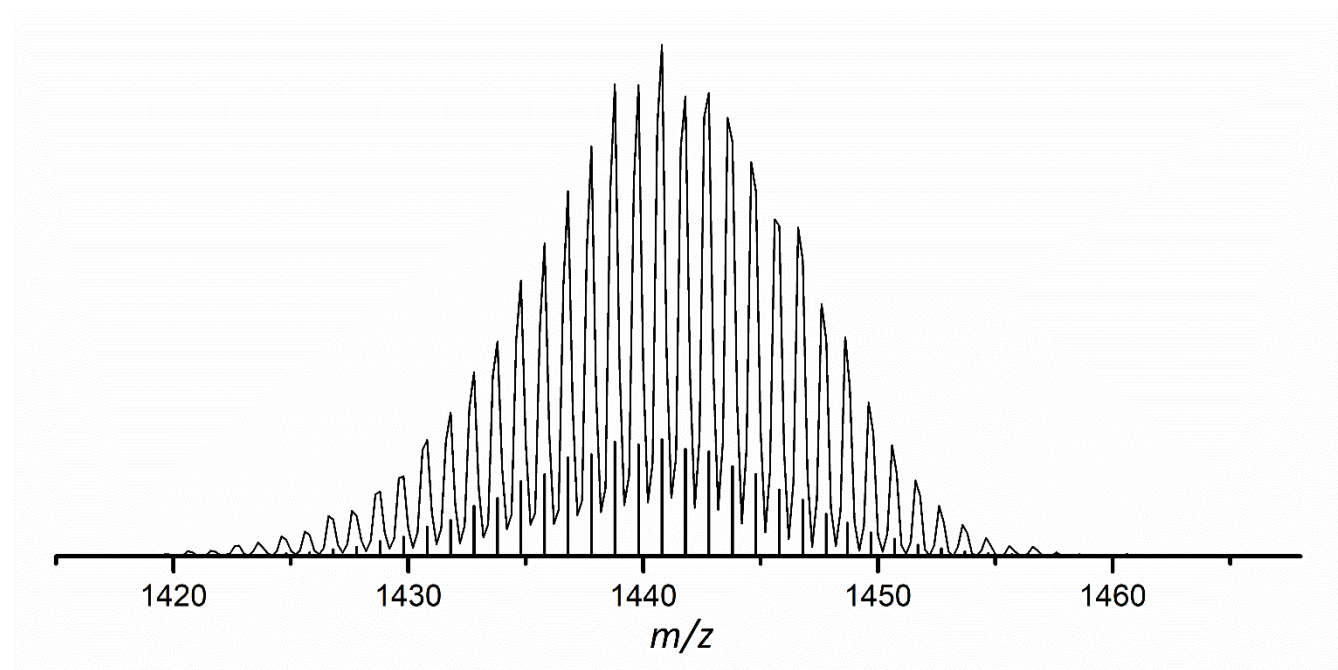


Figure S91. Detailed view on ESI MS signal of $[\text{Ge}_9\{\text{Si}(\text{TMS})_3\}_2(\text{CD}_2)_4\text{O-B}(\text{N}^i\text{Pr}_2)_2]^-$ at m/z 1440.8.

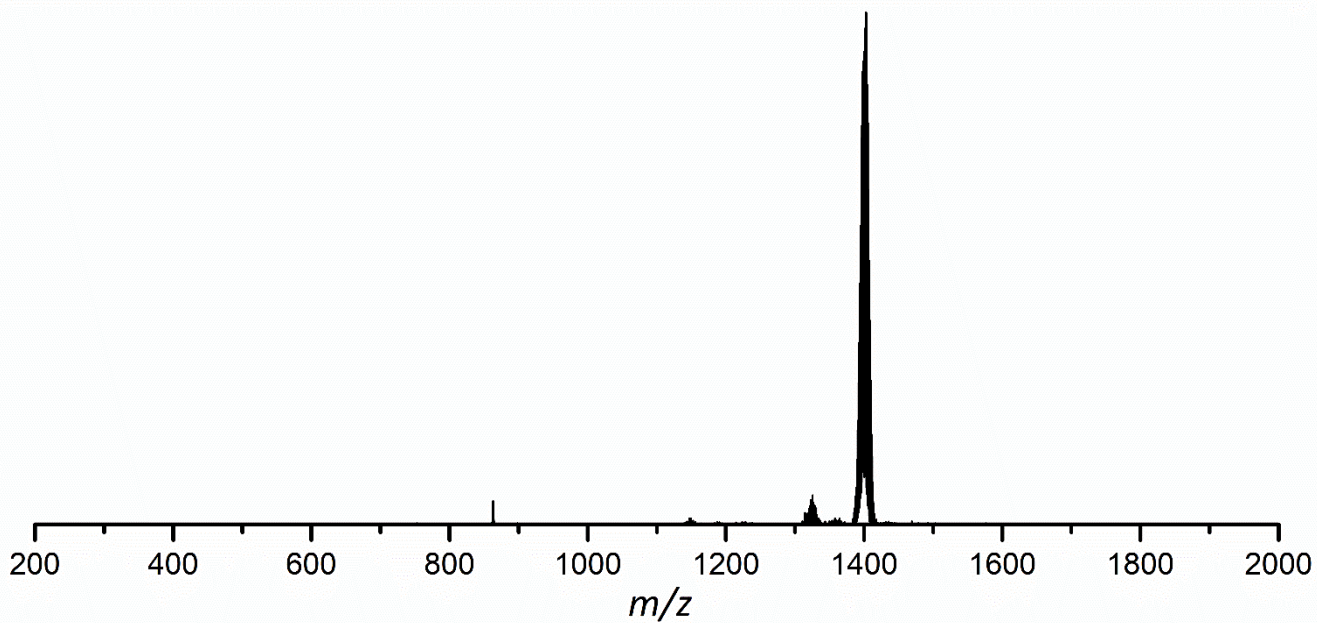


Figure S92. ESI MS spectrum (negative-ion mode, 3500 V, 300 °C) of a thf solution of $[\text{Ge}_9\{\text{Si}(\text{TMS})_3\}_2\text{CH}_3\text{C}=\text{N}-\text{B}(\text{N}^i\text{Pr}_2)_2]^-$. The molecule peak is detected at m/z 1401.8. A detailed view of the signal is provided in Figure S93.

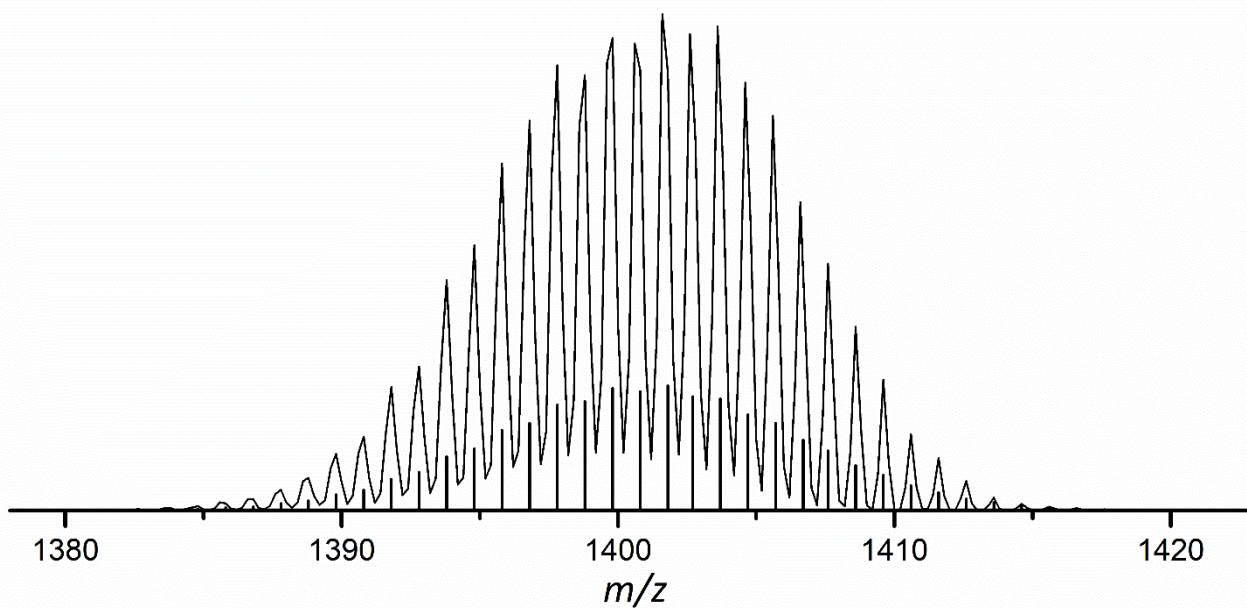


Figure S93. Detailed view on ESI MS signal of $[\text{Ge}_9\{\text{Si}(\text{TMS})_3\}_2\text{CH}_3\text{C}=\text{N}-\text{B}(\text{N}^i\text{Pr}_2)_2]^-$ at m/z 1401.8.

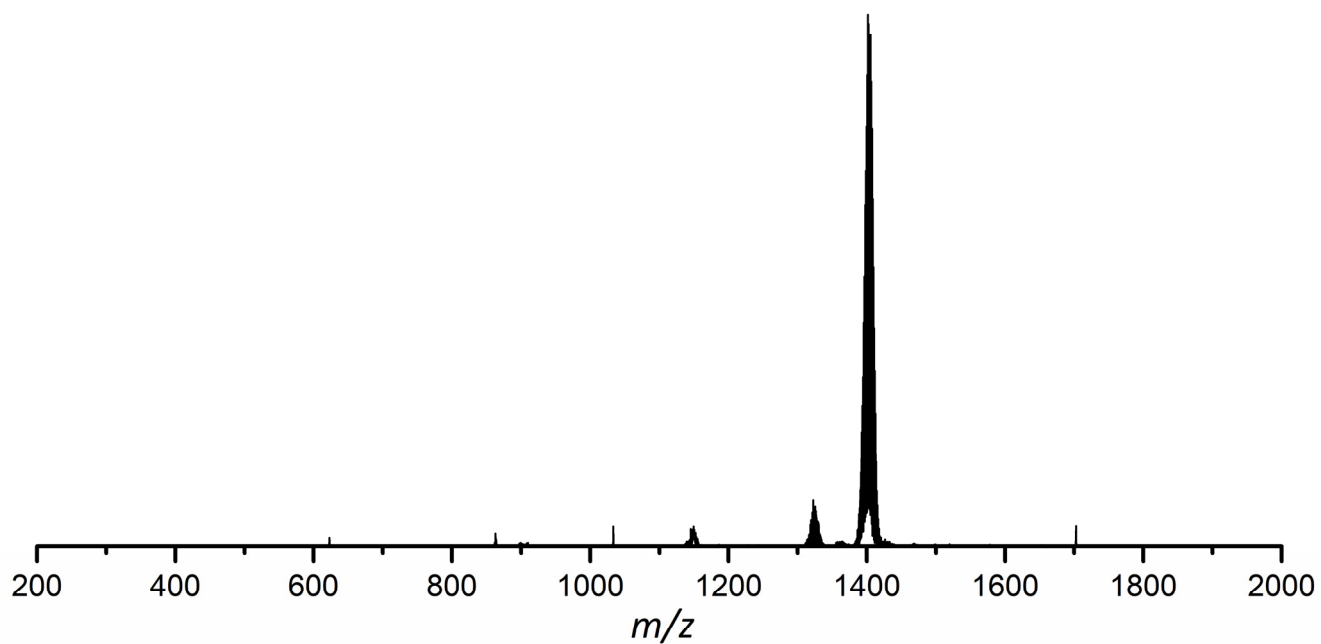


Figure S94. ESI MS spectrum (negative-ion mode, 3500 V, 300 °C) of a thf solution of $[\text{Ge}_9\{\text{Si}(\text{TMS})_3\}_2\text{CD}_3\text{C}=\text{N}-\text{B}(\text{N}^i\text{Pr}_2)_2]^-$. The molecule peak is detected at m/z 1404.8. A detailed view of the signal is provided in Figure S95.

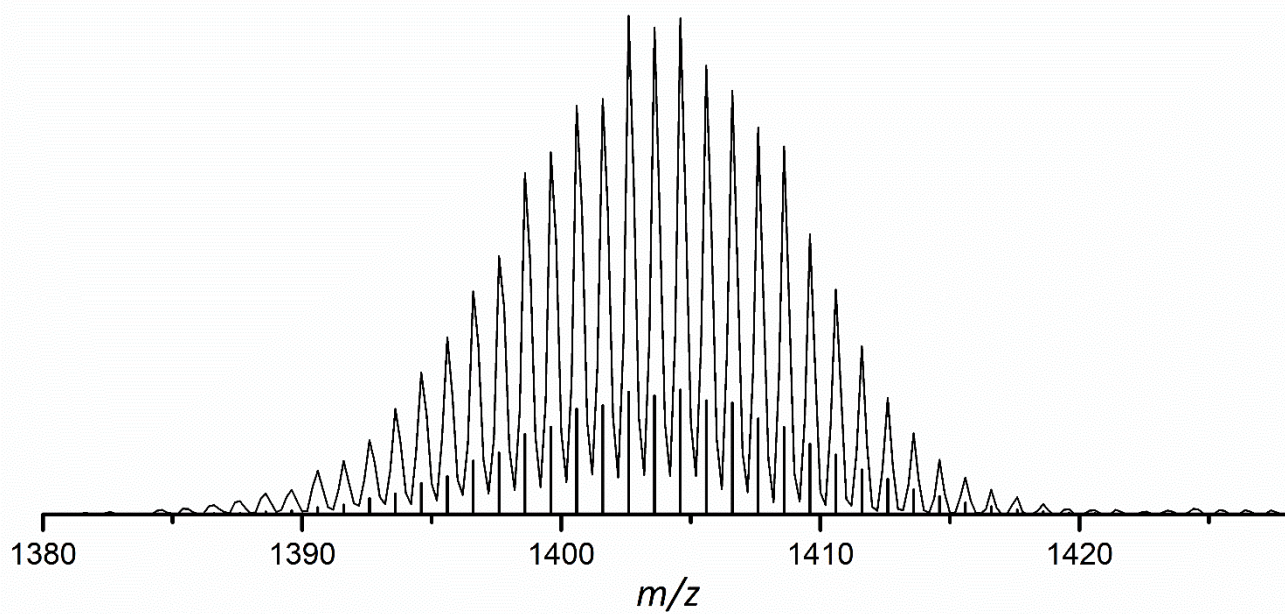


Figure S95. Detailed view on ESI MS signal of $[\text{Ge}_9\{\text{Si}(\text{TMS})_3\}_2\text{CD}_3\text{C}=\text{N}-\text{B}(\text{N}^i\text{Pr}_2)_2]^-$ at m/z 1404.8.

References

- 1 O. Kysliak and A. Schnepf, *Dalton Trans.*, 2016, **45**, 2404.
- 2 Y. Segawa, Y. Suzuki, M. Yamashita and K. Nozaki, *J. Am. Chem. Soc.*, 2008, **130**, 16069.
- 3 P. Chavant and M. Vaultier, *J. Organomet. Chem.*, 1993, **455**, 37.
- 4 G. M. Sheldrick, *Acta Crystallogr. Sec. C. Struct. Chem.*, 2015, **71**, 3.
- 5 A. L. Spek, *Acta Crystallogr. Sect. D. Biol. Crystallogr.*, 2009, **65**, 148.
- 6 G. R. Fulmer, A. J. Miller, N. H. Sherden, H. E. Gottlieb, A. Nudelman, B. M. Stoltz, J. E. Bercaw and K. I. Goldberg, *Organometallics*, 2010, **29**, 2176.

6.6 Counterion Related Structural Isomerism in the Nonagermanide Clusters $A[\text{Ge}_9\{\text{Si}(\text{TMS})_3\}_2(\text{CH}_2)_4\text{O-DAB}^{\text{Mes}}]$ ($A = \text{K}, \text{Cs}$)

C. Wallach,[‡] D. M. Dankert[‡] and T. F. Fässler

[‡]: authors contributed equally to this work.

Manuscript for publication.

Contents and Contributions

The reaction of the twofold silylated cluster $[\text{Ge}_9\{\text{Si}(\text{TMS})_3\}_2]^{2-}$ with the bromo-1,3,2-diazaborolidine $\text{DAB}^{\text{Mes}}\text{-Br}$ in thf yields the mono-anion $[\text{Ge}_9\{\text{Si}(\text{TMS})_3\}_2(\text{CH}_2)_4\text{O-DAB}^{\text{Mes}}]^-$ (**1a**). Within this species a ring-opened ether moiety is contained. In a previous study we observed an asymmetric ligand arrangement at the $[\text{Ge}_9]$ core for the potassium salt $\text{K}[\text{Ge}_9\{\text{Si}(\text{TMS})_3\}_2(\text{CH}_2)_4\text{O-DAB}^{\text{Mes}}]$ (**1-K**). Within this manuscript the influence of the counterion on the substitution pattern is evaluated by preparing the cesium analogue **1-Cs**. Indeed, in the latter species a symmetric substitution of the nine-atom Ge cluster is observed, and the crystal structures of **1-K** and **1-Cs** are discussed comparatively. Furthermore, the species **1-Li** and **1-Rb** are prepared, however no single crystalline material is obtained. In additional experiments it is shown that the application of sequestering agents to the reaction solution of the cluster and the diazaborolidine does not have any influence on the formation of the aforementioned compounds containing **1a**.

The experimental work leading to the isolation of the compounds **1-Li**, **1-Rb**, and **1-Cs** was performed by M. Sc. Dominik M. Dankert as a part of his Master's thesis, which I supervised. Furthermore, he collected the NMR spectroscopic data. ESI-MS measurements were performed by me. Additionally, I selected a suitable single crystal of **1-Cs**, measured it, and conducted the refinement of the single crystal structure data. The manuscript was written by me, including the processing of the acquired spectra. EDX analysis was performed by Maria Müller (Prof. Fässler, TUM). Elemental analysis data were acquired by Ulrike Ammari and Bircan Dilki in the micro-analytical laboratory of the Technical University of Munich. Temperature-dependent NMR spectra were recorded by M. Sc. Nicole Willeit and M. Sc. Kevin Frankiewicz.

Counterion Related Structural Isomerism in the Nonagermanide Clusters $A[\text{Ge}_9\{\text{Si}(\text{TMS})_3\}_2(\text{CH}_2)_4\text{O-DAB}^{\text{Mes}}]$ ($A = \text{K}, \text{Cs}$)

C. Wallach,^a D. M. Dankert^a and T. F. Fässler*

M. Sc. Christoph Wallach, M. Sc. Dominik Dankert, Prof. Dr. Thomas F. Fässler
Department Chemie, Technische Universität München
Lichtenbergstraße 4, 85747 Garching, Germany
*e-mail: thomas.faessler@lrz.tum.de
^a: authors contributed equally to this work

Abstract

The majority of known structures of threefold functionalized $[\text{Ge}_9]$ clusters corresponds to slightly distorted tricapped trigonal prisms, with substituents binding to the capping Ge atoms. However, few exemptions exist deviating from this rule, yet the reasons why are not fully understood. Herein we report the synthesis and structure determination from single crystals of the compound $\text{Cs}[\text{Ge}_9\{\text{Si}(\text{TMS})_3\}_2(\text{CH}_2)_4\text{O-DAB}^{\text{Mes}}]$ (**1-Cs**, TMS = trimethylsilyl, DAB = 1,3,2-diazaborolidine, Mes = 2,4,6-trimethylphenyl). The compound contains the anion **1a**, $[\text{Ge}_9\{\text{Si}(\text{TMS})_3\}_2(\text{CH}_2)_4\text{O-DAB}^{\text{Mes}}]^-$, in which the arrangement of ligands at the $[\text{Ge}_9]$ cluster significantly differs to the one in the same anion observed in the previously reported potassium-species (**1-K**). Thus, we report on the first isomer pair of the anion **1a**. Variable temperature NMR studies for **1-K** and **1-Cs** account for a reversible isomerization upon crystallization. According to further NMR spectroscopic investigations, sequestering the alkali metal counterions during the reaction does not affect the formation of the anion **1a**.

Introduction

The *Zintl* phase K_4Ge_9 is readily obtained from the reaction of the elements at elevated temperature and contains bare $[\text{Ge}_9]^{4-}$ clusters.^[1] Thus, the solid-state precursor offers access to defined molecular building blocks, which show a variable reactivity due to their high negative charge. In recent years, many investigations focused on reactions of the clusters towards transition metal complexes, and the attachment of main group element fragments has been reported.^[2-4] One major achievement was the silylation of $[\text{Ge}_9]^{4-}$ clusters, yielding the twofold and threefold silylated clusters $[\text{Ge}_9\{\text{Si}(\text{TMS})_3\}_2]^{2-}$ and $[\text{Ge}_9\{\text{Si}(\text{TMS})_3\}_3]^-$, respectively.^[5-8] The silylated species show an enhanced solubility as well as a decreased reductive potential, enabling targeted reactions. Furthermore, the stabilization *via* silylation was recently transferred to elusive $[\text{Si}_9]^{4-}$ clusters.^[9-10] Starting from silylated $[\text{Ge}_9]$ clusters, mixed-functionalized species such as phosphanyl-^[11-14] and boranyl-decorated clusters were prepared.^[15] These functionalizations account for the introduction of reactive sites comprising

Lewis basic and Lewis acidic functions, respectively. Intriguingly, the nine-atom clusters show a broad variety of reactive sites. Exemplarily, transition metals can either be encapsulated into the cluster core after cleaving their organic ligands,^[2] or organometallic fragments decorate the cluster in various coordination modes (η^1 - η^5).^[3-4] Due to the lack of valence d orbitals, the bonding of main group element fragments to the cluster core is usually limited to the formation of 2-centre-2-electron bonds, with few exceptions existing for triel element based substituents^[16-18] and Sn organyls,^[18-19] exhibiting partial multi-centered bonds.

The (distorted) symmetry of substituted nine-atom germanium clusters is usually best described as a mono-capped square antiprism or as a tricapped trigonal prism. The former case results in a C_{4v} -symmetric cluster ($d_1/d_2 = 1.00$), while a D_{3h} symmetry of the nine-atom cluster is adopted in the ideal latter case ($h_1 = h_2 = h_3$).^[20] As soon as ligands bind to the $[Ge_9]$ cluster, the vertex atoms are deflected from their original positions and the symmetry is distorted, which can be quantified by the description of the ratio of the diagonals d_1/d_2 and the heights h_1 - h_3 of the trigonal prism (Figure 1a and b, Table 1).

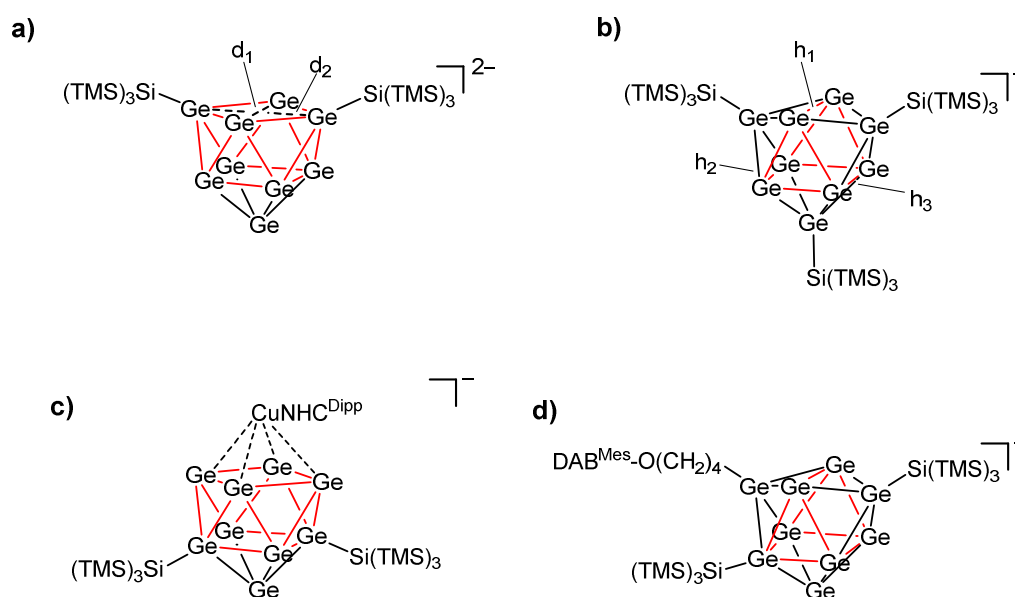


Figure 1. Different substitution patterns of the $[Ge_9]$ core. a) Two ligands binding to the free pseudo-square face of the $[Ge_9]$ cluster;^[6] b) three ligands binding to Ge vertex atoms capping the trigonal prism;^[5] c) two ligands binding to the capped square face of the $[Ge_9]$ cluster;^[21] d) asymmetric substitution of the trigonal prism with one silyl ligand binding to the trigonal prism base.^[22] The square antiprism in a) and b) as well as the trigonal prism in b) and d) are indicated by red lines.

In case of the twofold silylated cluster, two ligands are attached at Ge atoms of the pseudo-square plane, causing an elongation of one diagonal, and the $[Ge_9]$ cage becomes approximately C_{2v} -symmetric (Figure 1a, Table 1).^[6, 23] In the threefold silylated cluster, a distorted C_{2v} -symmetry is observed due to the shortening of one prism height in comparison

to the two others (Figure 1b, Table 1).^[5, 7, 23-24] The two latter described substitution patterns are the most common ones in [Ge₉] cluster chemistry. Deviations from the typically observed substitution patterns are observed exemplarily in the ion NHC^{Dipp}Cu[Ge₉{Si(TMS)₃}₂]⁻ [NHC^{Dipp} = 1,3-bis(2,6-di-*iso*-propylphenyl)imidazoleylidene], in which the two hypersilyl groups bind to Ge atoms of the capped square plane of the antiprism. Most likely, this feature is induced by the high steric demand of the Dipp wingtip substituents of the Cu-carbene (Figure 1c).^[21] The cluster core features a slightly distorted C_{4v} symmetry.

In case of the cluster featuring three substituents, either all substituents are of one kind, or two groups are identical while the third group is different. Table 1 provides an overview on the trigonal prism heights h₁ to h₃ and the ratio of the diagonals d₁/d₂ (determined at the site of the longest prism height) in several published, mixed-substituted anions. In the table h₃ refers to the prism height which is opposed to the different third ligand. In some cases the prism heights significantly differ from each other, and the cluster is best described as C_s-symmetric. As key example, the functionalized clusters [Ge₉{Si(TMS)₃}₂{SiPh₂CH=CH₂}]⁻ and [Ge₉{Si(TMS)₃}₂{SiPh₂{(CH₃)₃CH=CH₂}]⁻ can be quoted, in which the ligands are attached at Ge vertices capping the trigonal prism.^[7]

Table 1. Overview of trigonal prism heights and the ratio of the diagonals in several published, mixed-substituted anionic clusters and anion **1a**. As reference the data for the twofold and threefold silylated clusters are included. h₃ refers to the prism height opposed to the third introduced ligand. The approximate symmetry of the [Ge₉] core is given. ^a: values for each [Ge₉] core are presented; ^b: values for a second possible orientation of the trigonal prisms in the cluster are given.

anion	h ₁ [Å]	h ₂ [Å]	h ₃ [Å]	d ₁ /d ₂	sym	ref
[Ge ₉ {Si(TMS) ₃ } ₂] ²⁻	2.881	2.884	3.987	1.26	~C _{2v}	[6]
[Ge ₉ {Si(TMS) ₃ } ₃] ⁻	3.138	3.517	3.529	1.00	~C _{2v}	[5]
[Ge ₉ {Si(TMS) ₃ } ₂ {Si(TMS) ₂ (SiPh ₃) ₂ }] ⁻	3.296	3.411	3.349	1.07	~D _{3h}	[23]
[Ge ₉ {Si(TMS) ₃ } ₂ {SiPh ₂ CH=CH ₂ }] ⁻	3.337	3.780	3.036	1.12	C _s	[7]
[Ge ₉ {Si(TMS) ₃ } ₂ {SiPh ₂ {(CH ₃) ₃ CH=CH ₂ }] ⁻	3.146	3.733	3.249	1.20	C _s	[7]
[Ge ₉ {Si(TMS) ₃ } ₂ -SiMe ₂ -C ₆ H ₄ -SiMe ₂ Ge ₉ {Si(TMS) ₃ } ₂] ²⁻ ^a	3.341	3.663	3.144	1.06	~C _{2v}	[24]
	3.302	3.606	3.176	1.05	~C _{2v}	[22]
[Ge ₉ {Si(TMS) ₃ } ₂ P ^t Bu ₂] ⁻	3.620	3.658	3.070	1.06	~C _{2v}	[11]
[Ge ₉ {Si(TMS) ₃ } ₂ MeC=N-DAB ^{Mes}] ⁻	3.370	3.663	3.201	1.07	~C _{2v}	[22]
[Ge ₉ {Si(TMS) ₃ } ₂ (CH ₂) ₃ O-DAB ^{Mes}] ⁻	3.429	3.525	3.295	1.01	~D _{3h}	[22]
[Ge ₉ {Si(TMS) ₃ } ₂ (CH ₂) ₄ O-DAB(II) ^{Dipp}] ⁻ ^b	2.814	3.916	2.932	1.22	~C _{2v}	[22]
	2.605	2.688	3.210	1.22	~C _{2v}	
[Ge ₉ {Si(TMS) ₃ } ₂ (CH ₂) ₄ O-DAB ^{Mes}] ⁻ (1a in 1-K) ^b	2.759(1)	3.976(1)	2.932(1)	1.26	~C _{2v}	[22]
	2.606(1)	2.693(1)	3.163(1)	1.26	~C _{2v}	
[Ge ₉ {Si(TMS) ₃ } ₂ (CH ₂) ₄ O-DAB ^{Mes}] ⁻ (1a in 1-Cs)	3.386(1)	3.691(1)	3.183(1)	1.09	~C _{2v}	

In a recent study we investigated the Lewis acid-base-like incorporation of solvent molecule fragments between the silylated cluster $[\text{Ge}_9\{\text{Si}(\text{TMS})_3\}_2]^{2-}$ and the bromo-1,3,2-diazaborole $\text{DAB}(\text{II})^{\text{Dipp}}\text{-Br}$ as well as the bromo-1,3,2-diazaborolidine $\text{DAB}^{\text{Mes}}\text{-Br}$. As reaction products the compounds $\text{K}[\text{Ge}_9\{\text{Si}(\text{TMS})_3\}_2(\text{CH}_2)_4\text{O-DAB}(\text{II})^{\text{Dipp}}]$ and $\text{K}[\text{Ge}_9\{\text{Si}(\text{TMS})_3\}_2(\text{CH}_2)_4\text{O-DAB}^{\text{Mes}}]$ (**1-K**) were obtained, respectively, comprising the ring-opened thf fragment $-(\text{CH}_2)_4\text{O}$.^[22] A schematic structure of the anion **1a**, $[\text{Ge}_9\{\text{Si}(\text{TMS})_3\}_2(\text{CH}_2)_4\text{O-DAB}^{\text{Mes}}]^-$, is depicted in Figure 1d. The single crystal structure determination of **1-K** revealed an asymmetric substitution of the cluster, with one hypersilyl group binding to a Ge atom of the trigonal prism base (Figure 2a). The same observation applies for the utilization of the borane $\text{DAB}(\text{II})^{\text{Dipp}}\text{-Br}$. The observed asymmetric substitution of the cluster results in a heavily distorted C_{2v} -symmetric cluster core (Table 1). The reasons for the asymmetric substitution of the $[\text{Ge}_9]$ core remained unclear. A potential influence might be ascribed to the counterion K^+ , as it coordinates to the cluster as well as to the oxygen atom of the ring-opened ether fragment, thus potentially inducing a preferential substitution pattern.

In order to investigate the role of the cation in more detail, we intended to synthesize the ion-exchanged cluster series $\text{A}[\text{Ge}_9\{\text{Si}(\text{TMS})_3\}_2(\text{CH}_2)_4\text{O-DAB}^{\text{Mes}}]$ for $\text{A} = \text{Li}, \text{K}, \text{Rb},$ and Cs (**1-Li** to **1-Cs**). For **1-Cs** we obtained single crystals that allowed for the structure determination of the anion **1a** in the Cs-congener. Within **1-Cs** the cluster ion forms a structural isomer concerning the ligand arrangement observed for the cluster moiety in compound **1-K**.

Results and discussion

Two distinct reaction protocols were used for the synthesis of compounds **1-Li** to **1-Cs**. Whereas for K-Cs the corresponding A_4Ge_9 phases were used as precursors, the corresponding Li_4Ge_9 phase is not accessible, demanding for an alternative synthesis route. As an initial step, the synthesis of **1-Li** comprises the production of compound **1-K**, which is readily obtained by stirring the twofold silylated cluster $\text{K}_2[\text{Ge}_9\{\text{Si}(\text{TMS})_3\}_2]$ and $\text{DAB}^{\text{Mes}}\text{-Br}$ in thf for three hours.^[22] The formed compound **1-K** comprises a ring-opened thf-moiety, which is incorporated between the cluster and the borane in a reaction comprising two steps. In a first step, the bromoborane $\text{DAB}^{\text{Mes}}\text{-Br}$ initiates a ring-opening reaction with thf, yielding the intermediate species $\text{DAB}^{\text{Mes}}\text{-O}(\text{CH}_2)_4\text{-Br}$. Subsequently, the silylated cluster attacks the electrophilic C atom adjacent to the Br atom in a $\text{S}_{\text{N}}2$ -like reaction. Under formation of KBr the respective cluster is formed.^[22] For the synthesis of **1-Li**, 2.5 equivalents of LiCl are added to a thf solution of **1-K** to alter the counterions. The exchange is driven by the approximately 150-times higher solubility of LiCl in thf compared to KCl (49.58 mg/mL *versus* 0.30 mg/mL, respectively).^[25] Qualitative EDX-analysis data (Figure S20) account for a successful substitution of K^+ by Li^+ , while ^1H NMR spectroscopic investigations reveal that the anion **1a**

remained intact during the ion-exchange. Unfortunately, solutions of **1-Li** are not stable over time and decompose under the formation of unidentified, insoluble materials, prohibiting single crystal growth. In principle the reaction protocol could be transferred to yield the species **1a-Na**, however no suitable Na salt featuring a much higher solubility than the corresponding K-salt in thf was found. An incomplete ion-exchange would result in a cluster featuring a mixed-alkali metal counterion sphere, thus no further investigations in this direction were performed. In analogy to Li the 4:9 phase of Na and Ge is not accessible via solid-state reactions, prohibiting the reaction protocol applied for **1-K** to **1-Cs**.

In contrast, the solids $A_4\text{Ge}_9$ are readily obtained for $A = \text{K}, \text{Rb},$ and Cs by fusing the elements at $650\text{ }^\circ\text{C}$, and the contained $[\text{Ge}_9]^{4-}$ clusters can be transferred into the silylated species $A_2[\text{Ge}_9\{\text{Si}(\text{TMS})_3\}_2]$ by the heterogeneous reaction with two equivalents of $(\text{TMS})_3\text{SiCl}$ in MeCN.^[6] However, the heavier the alkali metal is, the longer reaction times are required to achieve a stoichiometric silylation of the $[\text{Ge}_9]$ cage (K: 6d, Rb: 10d, Cs: 14d). The compounds $A[\text{Ge}_9\{\text{Si}(\text{TMS})_3\}_2(\text{CH}_2)_4\text{O-DAB}^{\text{Mes}}]$ (**1-K** to **1-Cs**) were prepared in analogy to the protocol reported before.^[22] Regardless of the respective counterions, all acquired ^1H NMR spectra showed the same set of signals, revealing one characteristic sharp singlet of the TMS group protons, indicating a D_{3h} -symmetric cluster in solution ($\delta = 0.24$ ppm, thf- d_8). Furthermore, elemental analyses, EDX spectroscopy, as well as ESI-MS measurements corroborate the syntheses of the respective species (see Supporting Information). While the single crystal structure of **1-K** has already been reported,^[22] reasonable amounts of red needles formed from a concentrated toluene solution of **1-Cs**. However, for **1-Rb** this procedure was not successful.

Compound **1-Cs** crystallizes in the triclinic space group $P\bar{1}$ with two formula units per unit cell (Table S2). The structure of the cluster is best described as a distorted trigonal prism with three Ge atoms capping the rectangular prism faces. The capping Ge atoms (Ge1, Ge3, Ge9) form *exo*-bonds to the Si and C atoms of the hypersilyl and $-(\text{CH}_2)_4\text{O-DAB}^{\text{Mes}}$ ligands, respectively. The distortion of the prism is expressed by the three different prism heights $h_1 = 3.386(1)$ Å, $h_2 = 3.691(1)$ Å, and $h_3 = 3.183(1)$ Å (Table 1). Due to the strong elongation of h_2 (Ge5-Ge6), the cluster can also be regarded as a distorted mono-capped square antiprism with the ratio of the diagonals $\text{Ge5-Ge6/G1-Ge9} = 1.09$, resulting in a distorted C_{2v} -symmetric cluster core. One mesityl group of the scorio-like ligand DAB^{Mes} shows a η^6 -coordination to the Cs atom. The coordination sphere of Cs is completed by a η^3 -coordination to the Ge1-Ge2-Ge4 triangular face of the cluster, with Cs-Ge distances of approximately 4.0 Å, and a coordination to the O atom of the ring-opened ether fragment (Cs-O = 3.168(3) Å, Table 2).

Assuming a related underlying trigonal prism for the ligand arrangement at **1-K**, a different substitution pattern results (Figure 2a).^[22] One of the hypersilyl ligands and the $-(\text{CH}_2)_4\text{O-DAB}^{\text{Mes}}$ fragment are attached at Ge vertices capping the trigonal prism as in **1-Cs**.

However, the second hypersilyl ligand binds to a Ge vertex atom of the trigonal prism base. The asymmetric substitution is expressed in a highly distorted C_{2v} -symmetry, derived from the prism heights $h_1 = 3.976(1)$ Å and $h_2 = 2.759(2)$ Å. The ratio of the diagonals is $Ge_2-Ge_4/Ge_1-Ge_3 = 1.26$, thus the cluster should not be described as C_{4v} -symmetric. Due to the strongly elongated prism height Ge_2-Ge_4 , an alternative trigonal prism could be chosen, with prism heights $Ge_1-Ge_3 = 3.163(1)$ Å, $Ge_5-Ge_8 = 2.606(1)$ Å, and $Ge_6-Ge_7 = 2.693(1)$ Å, resulting in a less distorted C_{2v} -symmetry. However, for a more convenient comparison of the species **1-K** and **1-Cs** the analogous prisms are indicated in Figure 2. Other Ge-Ge, Ge-Si, and Ge-C bond lengths in are in accordance with the ones reported for compound **1-Cs** (Table 2 and S3). In analogy to **1-Cs**, the K^+ cation coordinates to the oxygen atom of the ring-opened thf fragment and to one aromatic mesityl ring of the boranyl ligand. The number of Ge vertices in proximity to the alkali metal cation differs with two and three for **1-K** and **1-Cs**, respectively (Figure 2).

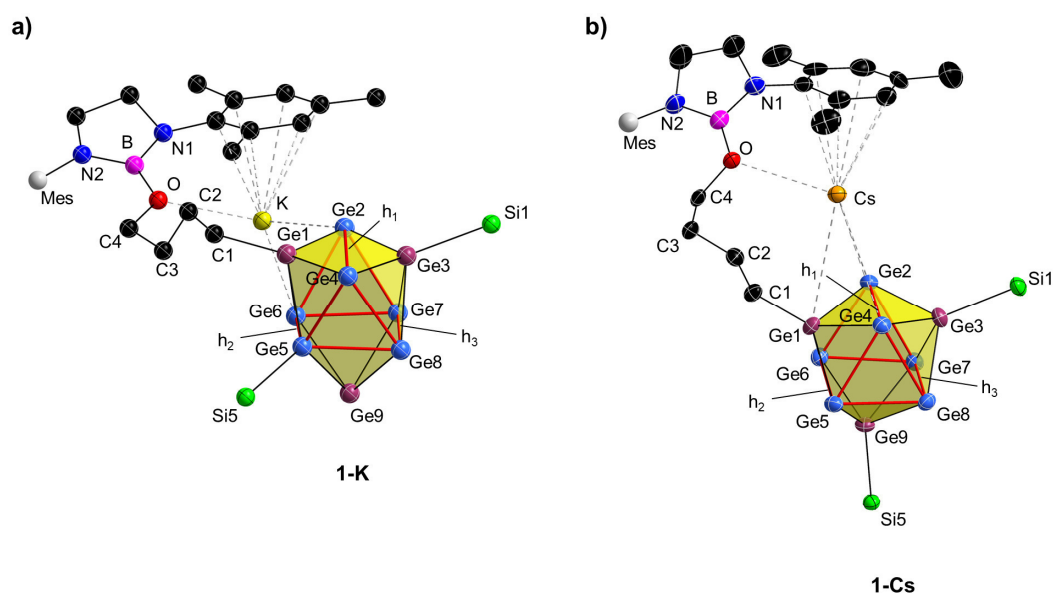


Figure 2. a) Molecular structure of compound **1-K** (literature)^[22] in a standard ball and stick illustration; b) molecular structure of **1-Cs**. In b) all ellipsoids are presented at a 50 % probability level. In a) and b) hydrogen atoms and co-crystallizing solvent molecules are omitted for clarity. In both molecules the mesityl group which is not coordinating to the alkali metal cation is indicated as a grey sphere. The coordination spheres of the alkali metal counterions are indicated by dashed grey lines. Prism heights are labelled h_1 to h_3 and corresponding distances are included in Table 1 and 2. The Ge atoms capping the trigonal prisms are indicated in purple for a better visibility, and the trigonal prisms are indicated by red lines. A full ellipsoid plot of **1-Cs** is presented in Figure S1.

Table 2. Selected interatomic distances in compounds **1-K** (literature)^[22] and **1-Cs**.

atoms	distance [Å] (1-K)	distance [Å] (1-Cs)
Ge1-C1	1.995(5)	1.976(4)
Ge3-Si1	2.396(2)	2.380(1)
Ge5-Six	2.395(2) (Si5)	2.383(1) (Si9)
Ge-Ge _{short}	2.504(1) (Ge3-Ge4)	2.521(1) (Ge3-Ge4)
Ge-Ge _{long}	2.761(1) (Ge2-Ge7)	2.728(1) (Ge4-Ge8)
Ge2-Ge4 (h ₁)	3.976(1)	3.386(1)
Ge5-Ge6 (h ₂)	2.759(2)	3.691(1)
Ge7-Ge8 (h ₃)	2.932(1)	3.183(1)
A-O	2.855(4)	3.168(3)
A-Ge1	4.631(1)	4.057(1)
A-Ge _x	3.536(1) (Ge6)	4.001(1) (Ge2)
A-Ge _x	3.540(1) (Ge7)	3.913(1) (Ge4)
A-C _{mesityl} (mean)	3.280	3.544

In our previous article we anticipated the chain lengths of the ring-opened ether molecule as a possible reason for the alteration of the substitution pattern, since the chemical similar species $[\text{Ge}_3\{\text{Si}(\text{TMS})_3\}_2(\text{CH}_2)_3\text{O-DAB}^{\text{Mes}}]^-$, which comprises a shorter hydrocarbon chain of solely three CH_2 units, showed a symmetrical substitution pattern contrasting **1-K**. Taking the new observations into consideration, this assumption might not describe the entire truth. Indeed, also the character of the counter cation seems to play a role. However, besides the varying number of Ge vertices nearby the alkali metal cation in **1-Cs** no significant differences are observed in comparison to **1-K**. Even upon taking the orientation of the unit formulas in the unit cell into consideration, no explanation for an alternating substitution pattern can be derived (Figure S3). Thus, it is assumed that the isomerization indeed is a process occurring during the crystallization, comprising either a migration of Ge vertex atoms or a scrambling of the substituents across the cluster surface.

Although an asymmetric substitution is observed for **1-K** in the solid-state, the silyl group protons do not show any splitting in the ^1H NMR spectrum over a temperature range from $-90\text{ }^\circ\text{C}$ to $60\text{ }^\circ\text{C}$ in $\text{thf-}d_8$.^[22] In order to investigate whether the ligand rearrangement is a reversible process, compound **1-K** was reproduced in good quantities. According to a complete single crystal structure analysis, the crystals were identical to the ones reported before.^[22] Subsequently, the supernatant toluene solution was removed from the crystals *via* a syringe, and the still slightly toluene-wet crystals were dissolved in $\text{thf-}d_8$ (no drying of the residue was performed to avoid any possible rearrangement upon removal of toluene from the crystal structure). However, the isomerization seems to be a reversible process, which is only observable in the solid-state, as again no splitting of the TMS group protons was observed in the ^1H NMR spectra of crystalline material ($-90\text{ }^\circ\text{C}$ to $60\text{ }^\circ\text{C}$, Figure S18). The same observations hold true for the symmetrically substituted compound **1-Cs**, whose TMS proton signal does not change upon lowering the temperature (Figure S19). Based on these observations one must assume the cluster rearrangement or the exchange of ligands at $-90\text{ }^\circ\text{C}$

is still faster than the time-resolution of the NMR device. Quantum chemical calculations might reveal insights into the reasons for the observed preferential ligand arrangements by comparison of the energy differences between certain optimized geometries.

In order to investigate whether the alkali metal counterion influences the formation of the species **1-K** to **1-Cs**, studies using the sequestering agents 18-crown-6 and [2.2.2]cryptand as complexation agents for the cations were conducted. Hereby, either the precursors $A_2[Ge_9\{Si(TMS)_3\}_2]$ ($A = K, Rb, Cs$) were stirred with sequestering agents in thf for one hour before the bromo-borane was added, or all solid compounds were weighed into a Schlenk tube, and subsequently dissolved in thf. For **1-Rb** [2.2.2]cryptand was used as sequestering agent, while 18-crown-6 was used in case of **1-Cs**, since Cs forms “exclusive” complexes with [2.2.2]cryptand in which the Cs^+ ions partially remain solvated.^[26-28] The recorded 1H NMR spectra reveal that the formation of the products **1-K** to **1-Cs** is independent of the reaction path, and the soluble products comprising the anions **1a** are identical to the ones formed in absence of complexation agents. This is especially indicated by the unaltered shift of the silyl group protons, which are observed at a chemical shift of $\delta = 0.24$ ppm in $thf-d_8$, irrespective to the application of any sequestering agent. The successful complexation of the alkali metal cations by the sequestering ethers is corroborated by the shift of their initial signals. In conclusion, the experiments account for a minor role of the alkali metal cations regarding the formation of compounds **1-K** to **1-Cs**. Figure 3 gives an overview of the acquired 1H NMR spectra ($thf-d_8$) of sequestered and non-sequestered cluster species.

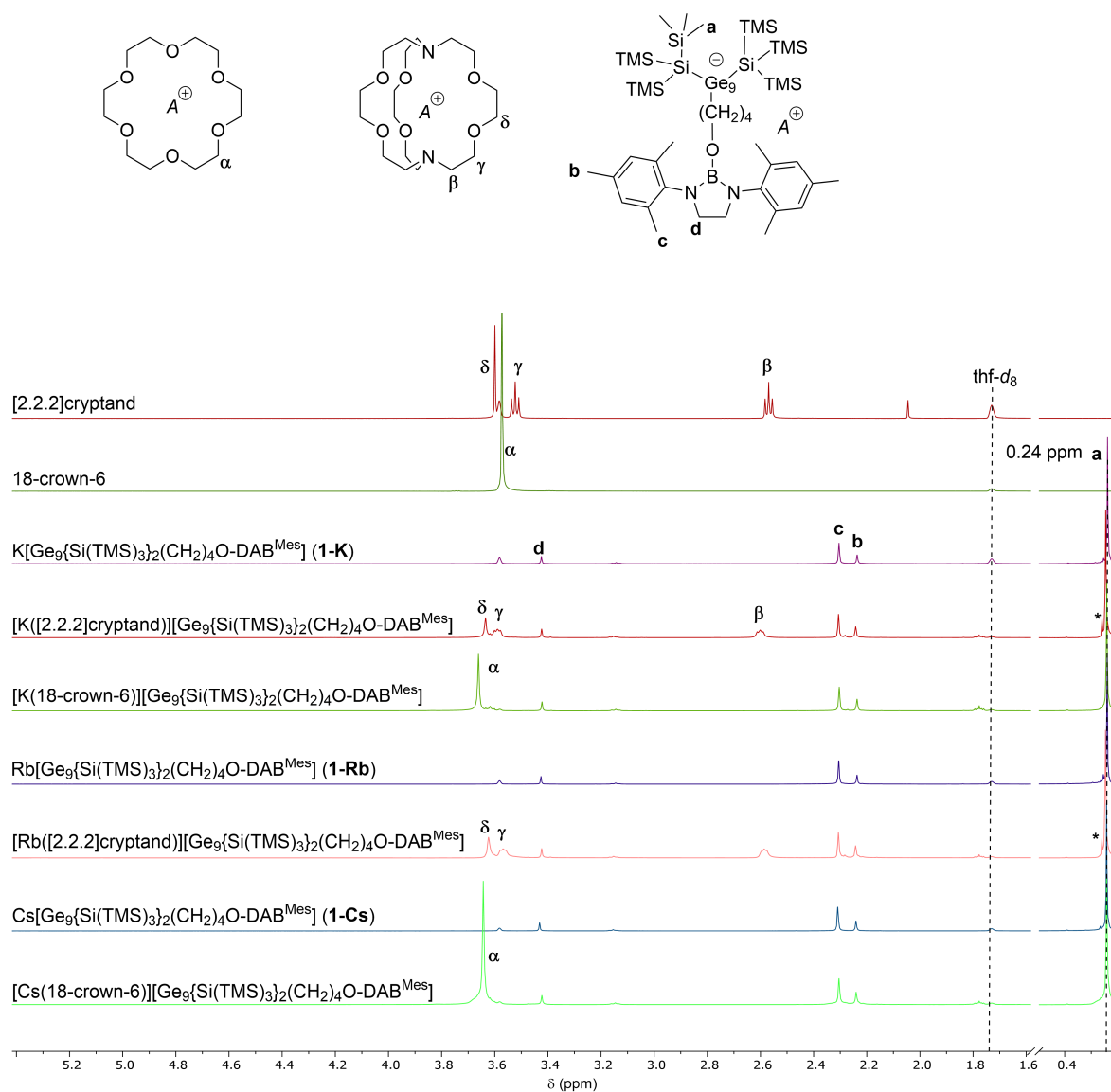


Figure 3. ^1H NMR spectra ($\text{thf-}d_8$) of [2.2.2]cryptand, 18-crown-6, **1-K** to **1-Cs**, and the respective species featuring sequestered alkali metal cations in the region from $\delta = 5.4$ ppm to 0.2 ppm. The asterisked signal belongs to an unidentified impurity.

Conclusion

The comparison of the single crystal structures of the compounds $A[\text{Ge}_9\{\text{Si}(\text{TMS})_3\}_2(\text{CH}_2)_4\text{O-DAB}^{\text{Mes}}]$ [$A = \text{K}$ (**1-K**), Cs (**1-Cs**)] revealed a decisive role of the alkali metal counterion on the ligand arrangement at the $[\text{Ge}_9]$ cluster in the solid-state. However, the formed reaction product **1a** generally is irrespective from the applied alkali metal cations. Temperature dependent ^1H NMR investigations account for a symmetrical substitution of anion **1a** in solution for both compounds. Thus, the asymmetric substitution pattern in the K-species is most probably a characteristic limited to the solid-state. Hence, the isomerization

can be described as a reversible process. However, the exact reason and mechanism for the rearrangement is still not fully understood and is subject to ongoing studies in our laboratories.

Contributions

CW authored the manuscript, refined the single crystal structure data, and ministered the experimental work, which was performed by DMD. TFF supervised the project.

Conflicts of interest

There are no conflicts to declare.

Acknowledgements

C. W. and D. D. thank the Deutsche Forschungsgemeinschaft (DFG, German Research Foundation) for funding (project number 245845833) within International Research Training Group IRTG 2022 – Alberta Technical University of Munich School for Functional Hybrid Materials (ATUMS). C. W. also thanks the Studienstiftung des Deutschen Volkes for granting a PhD scholarship. M. Sc. Kevin Frankiewicz and M. Sc. Nicole Willeit are acknowledged for the acquisition of variable-temperature NMR data.

References

- [1] V. Queneau and S. C. Sevov, *Angew. Chem. Int. Ed.* **1997**, *36*, 1754.
- [2] W. Klein, A. Schier and T. F. Fässler, *Molecules Meet Solids: From Wade–Mingos Clusters to Intermetalloid Clusters*; in: *Structure and Bonding*, vol. 188, Springer, Berlin, Heidelberg, **2021**, DOI 10.1007/430_2021_82.
- [3] C. Liu and Z.-M. Sun, *Coord. Chem. Rev.* **2019**, *382*, 32.
- [4] R. J. Wilson, N. Lichtenberger, B. Weinert and S. Dehnen, *Chem. Rev.* **2019**, *119*, 8506.
- [5] F. Li and S. C. Sevov, *Inorg. Chem.* **2012**, *51*, 2706.
- [6] O. Kysliak and A. Schnepf, *Dalton Trans.* **2016**, *45*, 2404.
- [7] K. Mayer, L. J. Schiegerl, T. Kratky, S. Günther and T. F. Fässler, *Chem. Commun.* **2017**, *53*, 11798.
- [8] L. J. Schiegerl, F. S. Geitner, C. Fischer, W. Klein and T. F. Fässler, *Z. Anorg. Allg. Chem.* **2016**, *642*, 1419.
- [9] L. J. Schiegerl, A. J. Karttunen, W. Klein and T. F. Fässler, *Chem. Eur. J.* **2018**, *24*, 19171.
- [10] L. J. Schiegerl, A. J. Karttunen, W. Klein and T. F. Fässler, *Chem. Sci.* **2019**, *10*, 9130.
- [11] F. S. Geitner, J. V. Dums and T. F. Fässler, *J. Am. Chem. Soc.* **2017**, *139*, 11933.
- [12] F. S. Geitner, C. Wallach and T. F. Fässler, *Chem. Eur. J.* **2018**, *24*, 4103.
- [13] F. S. Geitner, W. Klein and T. F. Fässler, *Angew. Chem. Int. Ed.* **2018**, *57*, 14509.
- [14] C. Wallach, F. S. Geitner, W. Klein and T. F. Fässler, *Chem. Eur. J.* **2019**, *25*, 12349.
- [15] C. Wallach, F. S. Geitner, A. J. Karttunen and T. F. Fässler, *Angew. Chem. Int. Ed.* **2021**, *60*, 2648.
- [16] D. F. Hansen, B. Zhou and J. M. Goicoechea, *J. Organomet. Chem.* **2012**, *721*, 53.
- [17] D. Rios, M. M. Gillett-Kunnath, J. D. Taylor, A. G. Oliver and S. C. Sevov, *Inorg. Chem.* **2011**, *50*, 2373.
- [18] F. Li and S. C. Sevov, *J. Am. Chem. Soc.* **2014**, *136*, 12056.
- [19] F. Li, A. Muñoz-Castro and S. C. Sevov, *Angew. Chem. Int. Ed.* **2012**, *51*, 8581.
- [20] S. Scharfe, F. Kraus, S. Stegmaier, A. Schier and T. F. Fässler, *Angew. Chem. Int. Ed.* **2011**, *50*, 3630.
- [21] F. S. Geitner and T. F. Fässler, *Inorg. Chem.* **2020**, *59*, 15218.
- [22] C. Wallach, F. S. Geitner and T. F. Fässler, *Chem. Sci.* **2021**, *12*, 6969.
- [23] O. Kysliak, T. Kunz and A. Schnepf, *Eur. J. Inorg. Chem.* **2017**, *2017*, 805.
- [24] O. Kysliak, C. Schrenk and A. Schnepf, *Inorg. Chem.* **2017**, *56*, 9693.
- [25] G. J. Lovinger, M. D. Aparece and J. P. Morken, *J. Am. Chem. Soc.* **2017**, *139*, 3153.
- [26] C. M. Goff, M. A. Matchette, N. Shabestary and S. Khazaeli, *Polyhedron* **1996**, *15*, 3897.
- [27] E. Kauffmann, J. L. Dye, J. M. Lehn and A. I. Popov, *J. Am. Chem. Soc.* **1980**, *102*, 2274.
- [28] E. Mei, L. Liu, J. L. Dye and A. I. Popov, *J. Solution Chem.* **1977**, *6*, 771.

Supporting Information

Counterion Related Structural Isomerism in the Nonagermanide Clusters $A[\text{Ge}_9\{\text{Si}(\text{TMS})_3\}_2(\text{CH}_2)_4\text{O-DAB}^{\text{Mes}}]$ ($A = \text{K}, \text{Cs}$)

C. Wallach, D. M. Dankert and T. F. Fässler

	page
1. Experimental details	327
2. Crystallographic details	331
3. NMR spectra	335
4. EDX spectra	345
5. ESI-MS spectrum of 1a	346
6. References	347

1. Experimental details

General

All manipulations were performed under the exclusion of moisture and oxygen by utilizing standard Schlenk and glove box techniques under Argon atmosphere. All used solvents were obtained from a MBraun Grubbs solvent purification system. Glassware was dried at 650 °C under dynamic vacuum prior to usage. [2.2.2]cryptand (*Acros Organics*) was dried over night by applying a dynamic vacuum. 18-crown-6 (*Merck*) was sublimated before usage. The solid-state precursors A_4Ge_9 ($A = K, Rb, Cs$) were prepared by fusion of the elements at 650 °C in stainless-steel autoclaves. The preparation of the respective silylated compounds $A_2[Ge_9\{Si(TMS)_3\}_2]$ followed the route for the preparation of the K-species with adjusted reaction times (K: 6d, Rb: 10d, Cs: 14d).^[1] The bromo-1,3,2-diazaborolidine $DAB^{Mes}-Br$ was prepared according to literature procedures.^[2] All other chemicals were used without further purification.

Single crystal structure determination

A concentrated toluene solution of **1-Cs** was stored at r.t. for three days until the growth of crystals was detected. The flask was transferred into a glovebox and the moisture- and air-sensitive crystals were transferred into perfluoralkyl ether oil. Suitable single crystals were isolated under a microscope and fixed on glass capillaries. The data collection was performed using a STOE StadiVari diffractometer ($MoK\alpha$ radiation) equipped with a DECTRIS PILATUS 300K detector, with the crystal positioned in a 150 K cold N_2 gas stream. Direct methods (SHELXS-97)^[3] were used to solve the structure, and the structure refinement was performed by full-matrix least-squares calculations against F^2 (SHELXL-2018).^[4] Anisotropic displacement parameters were set for all non-hydrogen atoms. The positions of hydrogen atoms were modelled using a riding model.

NMR spectroscopy

All spectra were acquired on a Bruker Avance Ultrashield 400 MHz spectrometer. The calibration of the 1H NMR and ^{13}C NMR spectra was performed by using the residual proton and carbon signals of the respective deuterated solvents. The solvent peaks serve as internal reference and the chemical shifts are reported in parts per million (ppm) relative to TMS.^[5] Signal multiplicities are reported as followed: singlet (s), triplet (t), multiplet (m), broad signal (br).

ESI-MS spectrometry

A Bruker Daltronic HCT mass spectrometer (dry gas temperature: 300 °C; injection speed: 300 μ L/h) was used for the data acquisition. The collected data were evaluated using the Bruker Compass Data Analysis 4.0 SP 5 program (Bruker), and spectra were plotted using OriginPro2021 (Origin Lab) and Excel (Microsoft 365).

Elemental analysis

The analyses were performed by the microanalytical laboratory of the Chemistry Department of the Technical University of Munich. The C, H, and N content was analyzed using a combustion analyzer (EURO EA, HEKA tech).

EDX spectroscopy

For the data collection a Hitachi TM-1000 tabletop scanning electron microscope device was used. The respective samples were stuck on a carbon sticky tape under Ar atmosphere, and the samples were transferred to the EDX device in a closed glass.

Syntheses

Li[Ge₉{Si(TMS)₃}₂(CH₂)₄O-DAB^{Mes}] (1-Li)

In a first step the K-compound **1-K** (99.6 mg, 63.6 μmol, 1 equiv.) is prepared in analogy to the literature.^[6] Afterwards, compound **1-K** is dissolved in toluene and filtered to remove trace amounts of the bis-silylated cluster as well as other insoluble salts. Subsequently, a flask is loaded with LiCl (6.7 mg, 159 μmol, 2.5 equiv.) and a thf solution of compound **1-K** is added. The suspension is stirred for 3 h at r.t. and afterwards filtered. The solvent is removed from the reaction solution under dynamic vacuum, the residue is re-dissolved in toluene (2 mL), and the solution is filtered to remove any remaining inorganic salts. NMR spectroscopy and elemental analysis were performed from the dried filtrate since no crystalline material was obtained. However, NMR sample solutions of the cluster species featuring Li⁺ counter ions are not stable and decompose within few hours, thus only the data of the ¹H NMR spectrum are reported here. Yield: 49 mg, 32 μmol, 45 %.

¹H NMR (400 MHz, 298 K, thf-*d*₃): δ [ppm] = 6.84 (s, 4H, CH_{Mes}), 3.42 (s, 4H, CH₂_{DAB}), 3.14 (t, 2H, ³J_{H-H} = 5.9 Hz, CH₂_{thf}), 2.30 (s, 12H, CH₃_{Mes(o)}), 2.23 (s, 6H, CH₃_{Mes(p)}), 1.21-1.15 (m, 4H, CH₂_{thf}), 1.09-1.03 (m, 2H, CH₂_{thf}), 0.24 (s, 54H, CH₃_{TMS}). **ESI-MS**: *m/z* 1526.08 (**1a**).

Elemental analysis: anal. calcd. for LiC₄₂H₈₈BGe₉N₂OSi₈: C, 32.90; H, 5.79; N, 1.83; found: C, 33.66; H, 6.16; N, 1.71.

K[Ge₉{Si(TMS)₃}₂(CH₂)₄O-DAB^{Mes}] (1-K)

The synthesis is performed in analogy to the literature procedure. The acquired NMR spectra are in accordance to the ones reported.^[6] Crystals were grown at r.t. from a concentrated toluene solution, and the single crystal structure determination revealed the same substitution pattern and lattice parameters as described before.^[6]

Rb[Ge₉{Si(TMS)₃}₂(CH₂)₄O-DAB^{Mes}] (1-Rb)

The procedure closely follows the synthesis of **1-K**.^[6] Rb₂[Ge₉{Si(TMS)₃}₂] (98.9 mg, 75 μmol, 1 equiv.) is used as precursor substituting the K-species. NMR spectroscopy and elemental analysis were performed from the dried reaction residue since no crystalline material was

obtained. Yield: 37 mg, 23 μmol , 30 %. Due to the lack of crystalline material, the elemental analysis data deviate from the ideal values.

^1H NMR (400 MHz, 298 K, $\text{thf-}d_8$): δ [ppm] = 6.84 (s, 4H, CH_{Mes}), 3.43 (s, 4H, CH_2_{DAB}), 3.15 (t, 2H, $^3J_{\text{H-H}} = 6.1$ Hz, CH_2_{thf}), 2.31 (s, 12H, $\text{CH}_3_{\text{Mes(o)}}$), 2.24 (s, 6H, $\text{CH}_3_{\text{Mes(p)}}$), 1.21-1.15 (m, 4H, CH_2_{thf}), 1.09-1.03 (m, 2H, CH_2_{thf}), 0.24 (s, 54H, CH_3_{TMS}). **^{13}C NMR** (101 MHz, 298 K, $\text{thf-}d_8$): δ [ppm] = 141.00 (s, $\text{C}_{\text{Mes(N)}}$), 137.13 (s, $\text{C}_{\text{Mes(o)}}$), 134.96 (s, $\text{C}_{\text{Mes(p)}}$), 129.71 (s, CH_{Mes}), 64.35 (s, $\text{CH}_2\text{-O}$), 49.36 (s, CH_2_{DAB}), 36.66 (s, CH_2), 31.78 (s, CH_2), 21.36 (s, $\text{CH}_3_{\text{Mes(p)}}$), 18.75 (s, $\text{CH}_3_{\text{Mes(o)}}$), 11.11 (s, CH_2_{Ge}), 3.24 (s, CH_3_{TMS}). **$^{29}\text{Si-INEPT}$ NMR** (79 MHz, 298 K, $\text{thf-}d_8$): δ [ppm] = -9.65 (s, Si_{TMS}), -108.62 (s, Si_{Ge9}). **^{11}B NMR** (128 MHz, 298 K, $\text{thf-}d_8$): δ [ppm] = 23.22 (br, B_{DAB}). **ESI-MS**: m/z 1526.8 (**1a**). **Elemental analysis**: anal. calcd. for $\text{RbC}_{42}\text{H}_{88}\text{BGe}_9\text{N}_2\text{OSi}_8$: C, 31.30; H, 5.50; N, 1.74; found: C, 32.84; H, 5.69; N, 2.21.

Cs[Ge₉{Si(TMS)₃}₂(CH₂)₄O-DAB^{Mes}] (1-Cs)

The procedure closely follows the synthesis of **1-K**.^[6] $\text{Cs}_2[\text{Ge}_9\{\text{Si}(\text{TMS})_3\}_2]$ (106.1 mg, 75 μmol , 1 equiv.) is used as precursor substituting the K-species. NMR spectroscopy and elemental analysis were performed from the dried crystalline material. Yield: 56 mg, 34 μmol , 45 %.

^1H NMR (400 MHz, 298 K, $\text{thf-}d_8$): δ [ppm] = 6.86 (s, 4H, CH_{Mes}), 3.43 (s, 4H, CH_2_{DAB}), 3.15 (t, 2H, $^3J_{\text{H-H}} = 6.0$ Hz, CH_2_{thf}), 2.31 (s, 12H, $\text{CH}_3_{\text{Mes(o)}}$), 2.24 (s, 6H, $\text{CH}_3_{\text{Mes(p)}}$), 1.21-1.16 (m, 4H, CH_2_{thf}), 1.10-1.04 (m, 2H, CH_2_{thf}), 0.24 (s, 54H, CH_3_{TMS}). **^{13}C NMR** (101 MHz, 298 K, $\text{thf-}d_8$): δ [ppm] = 141.00 (s, $\text{C}_{\text{Mes(N)}}$), 137.20 (s, $\text{C}_{\text{Mes(o)}}$), 135.08 (s, $\text{C}_{\text{Mes(p)}}$), 129.74 (s, CH_{Mes}), 64.38 (s, $\text{CH}_2\text{-O}$), 49.36 (s, CH_2_{DAB}), 36.61 (s, CH_2), 31.80 (s, CH_2), 21.33 (s, $\text{CH}_3_{\text{Mes(p)}}$), 18.74 (s, $\text{CH}_3_{\text{Mes(o)}}$), 11.08 (s, CH_2_{Ge}), 3.23 (s, CH_3_{TMS}). **$^{29}\text{Si-INEPT}$ NMR** (79 MHz, 298 K, $\text{thf-}d_8$): δ [ppm] = -9.60 (s, Si_{TMS}), -108.49 (s, Si_{Ge9}). **^{11}B NMR** (128 MHz, 298 K, $\text{thf-}d_8$): δ [ppm] = 23.32 (br, B_{DAB}). **ESI MS**: m/z 1526.8 (**1a**). **Elemental analysis**: anal. calcd. for $\text{CsC}_{42}\text{H}_{88}\text{BGe}_9\text{N}_2\text{OSi}_8$: C, 30.40; H, 5.35; N, 1.69; found: C, 30.08; H, 5.06; N, 1.44.

Reactions with sequestered counter ions A⁺ (A = K, Rb, Cs)

To further investigate the influence of the counter ion on the reaction, sequestering agents were used to mask the alkaline metal ions during the formation of the products **1-K** to **1-Cs**. Two different reaction protocols were applied: a) the bis-silylated cluster was stirred for 1 h with the sequestering reactant before the addition of $\text{DAB}^{\text{Mes}}\text{-Br}$, and b) the silylated cluster, the sequestering agent and the bromo-borane were dissolved simultaneously in thf . Indeed, the product species formed are independent from the protocol. Due to the varying sizes of the alkali metal ions, different sequestering agents are used, which are [2.2.2]cryptand for Rb^+ and 18-crown-6 for Cs^+ (Cs^+ is not fully encapsulated in the free sphere of the cryptand molecule).^[7] K^+ forms stable coordination complexes with both organic molecules, and thus was tested twice as a reference.

Protocol a)

In a typical reaction $\text{A}_2[\text{Ge}_9\{\text{Si}(\text{TMS})_3\}_2]$ (50 μmol , 1 equiv.) is stirred with the sequestering agent (100 μmol , 2 equiv.) for 1 h in thf (2 mL). Afterwards, the borane $\text{DAB}^{\text{Mes}}\text{-Br}$ (19.3 mg, 50 μmol , 1 equiv.) is added to the reaction flask, and the solution is stirred overnight.

Subsequently, the reaction solution is filtered, and the solvent is removed under vacuum. The obtained solid residue is dissolved in thf- d_8 and a ^1H NMR spectrum is recorded.

Protocol b)

In a typical reaction $\text{A}_2[\text{Ge}_9\{\text{Si}(\text{TMS})_3\}_2]$ (50 μmol , 1 equiv.), the sequestering agent (100 μmol , 2 equiv.), and the borane $\text{DAB}^{\text{Mes}}\text{-Br}$ (19.3 mg, 50 μmol , 1 equiv.) are dissolved in thf (2 mL), and the solution is stirred overnight. Subsequently, the reaction solution is filtered, and the solvent is removed under vacuum. The obtained solid residue is dissolved in thf- d_8 and a ^1H NMR spectrum is recorded.

Table S1. Weighed samples for the reactions with sequestering agents.

compound	<i>m</i> [mg]	<i>n</i> [μmol]	equiv.
$\text{K}_2[\text{Ge}_9\{\text{Si}(\text{TMS})_3\}_2]$	61.4 mg	50	1
$\text{Rb}_2[\text{Ge}_9\{\text{Si}(\text{TMS})_3\}_2]$	66.0 mg	50	1
$\text{Cs}_2[\text{Ge}_9\{\text{Si}(\text{TMS})_3\}_2]$	70.7 mg	50	1
$\text{DAB}^{\text{Mes}}\text{-Br}$	19.3 mg	50	1
18-crown-6	26.4 mg	100	2
[2.2.2]cryptand	37.6 mg	100	2

[K(18-crown-6)][$\text{Ge}_9\{\text{Si}(\text{TMS})_3\}_2(\text{CH}_2)_4\text{O-DAB}^{\text{Mes}}$]

^1H NMR (400 MHz, 298 K, thf- d_8): δ [ppm] = 6.84 (s, 4H, CH_{Mes}), 3.66 (s, 24H, $\text{CH}_2_{\text{crown}}$), 3.42 (s, 4H, CH_2_{DAB}), 3.14 (t, 2H, $^3J_{\text{H-H}} = 6.0$ Hz, CH_2_{thf}), 2.30 (s, 12H, CH_3_{Mes}), 2.24 (s, 6H, CH_3_{Mes}), 1.20-1.15 (m, 4H, CH_2_{thf}), 1.10-1.04 (m, 2H, CH_2_{thf}), 0.24 (s, 54H, CH_3_{TMS}).

[K([2.2.2]cryptand)][$\text{Ge}_9\{\text{Si}(\text{TMS})_3\}_2(\text{CH}_2)_4\text{O-DAB}^{\text{Mes}}$]

^1H NMR (400 MHz, 298 K, thf- d_8): δ [ppm] = 6.85 (s, 4H, CH_{Mes}), 3.63 (s, 12H, $\text{CH}_2_{\text{crypt}}$), 3.61-3.55 (m, 12H, $\text{CH}_2_{\text{crypt}}$), 3.42 (s, 4H, CH_2_{DAB}), 3.15 (t, 2H, $^3J_{\text{H-H}} = 5.8$ Hz, CH_2_{thf}), 2.62-2.59 (m, 12H, $\text{CH}_2_{\text{crypt}}$), 2.31 (s, 12H, CH_3_{Mes}), 2.24 (s, 6H, CH_3_{Mes}), 1.21-1.16 (m, 4H, CH_2_{thf}), 1.11-1.07 (m, 2H, CH_2_{thf}), 0.25 (s, 54H, CH_3_{TMS}).

[Rb([2.2.2]cryptand)][$\text{Ge}_9\{\text{Si}(\text{TMS})_3\}_2(\text{CH}_2)_4\text{O-DAB}^{\text{Mes}}$]

^1H NMR (400 MHz, 298 K, thf- d_8): δ [ppm] = 6.85 (s, 4H, CH_{Mes}), 3.62 (s, 12H, $\text{CH}_2_{\text{crypt}}$), 3.58-3.55 (m, 12H, $\text{CH}_2_{\text{crypt}}$), 3.42 (s, 4H, CH_2_{DAB}), 3.15 (t, 2H, $^3J_{\text{H-H}} = 5.8$ Hz, CH_2_{thf}), 2.60-2.57 (m, 12H, $\text{CH}_2_{\text{crypt}}$), 2.31 (s, 12H, CH_3_{Mes}), 2.24 (s, 6H, CH_3_{Mes}), 1.21-1.15 (m, 4H, CH_2_{thf}), 1.11-1.05 (m, 2H, CH_2_{thf}), 0.25 (s, 54H, CH_3_{TMS}).

[Cs(18-crown-6)][$\text{Ge}_9\{\text{Si}(\text{TMS})_3\}_2(\text{CH}_2)_4\text{O-DAB}^{\text{Mes}}$]

^1H NMR (400 MHz, 298 K, thf- d_8): δ [ppm] = 6.85 (s, 4H, CH_{Mes}), 3.64 (s, 24H, $\text{CH}_2_{\text{crown}}$), 3.42 (s, 4H, CH_2_{DAB}), 3.15 (t, 2H, $^3J_{\text{H-H}} = 5.7$ Hz, CH_2_{thf}), 2.30 (s, 12H, CH_3_{Mes}), 2.24 (s, 6H, CH_3_{Mes}), 1.21-1.15 (m, 4H, CH_2_{thf}), 1.10-1.05 (m, 2H, CH_2_{thf}), 0.24 (s, 54H, CH_3_{TMS}).

2. Crystallographic details

Table S2. Crystallographic data of compound **1-Cs**.

Compound	1-Cs
formula	CsC ₄₂ H ₈₈ BGe ₉ N ₂ OSi ₈ ·tol
fw [g·mol ⁻¹]	1751.02
space group	<i>P</i> $\bar{1}$
<i>a</i> [Å]	14.797(3)
<i>b</i> [Å]	15.777(3)
<i>c</i> [Å]	19.386(4)
α [deg]	113.10(3)
β [deg]	95.10(3)
γ [deg]	109.90(3)
<i>V</i> [Å ³]	3782.6(9)
<i>Z</i>	2
<i>T</i> [K]	150
λ [Å]	0.71073
ρ_{calcd} [g·cm ⁻³]	1.537
μ [mm ⁻¹]	4.155
collected reflections	38451
indep. reflections	14030
$R_{\text{int}} / R_{\sigma}$	0.0464/0.0566
parameters / restraints	669/0
R_1 [$I > 2 \sigma(I)$ / all data]	0.0355/0.0711
wR_2 [$I > 2 \sigma(I)$ / all data]	0.0602/0.0676
goodness of fit	0.978
max./min. diff. el. density [e · Å ⁻³]	1.267/-0.578
CCDC	not yet assigned

Table S3. Selected bond lengths and torsion angles in compound **1-Cs** in comparison to compound **1-K** (literature).^[6]

bond	distance [Å] (1-K)	distance [Å] (1-Cs)
Ge1-Ge2	2.5038(8)	2.5565(8)
Ge1-Ge4	2.5675(7)	2.543(1)
Ge1-Ge5	2.5339(8)	2.526(1)
Ge1-Ge6	2.7612(8)	2.5269(9)
Ge2-Ge3	2.5503(8)	2.540(2)
Ge2-Ge6	2.6985(9)	2.6544(9)
Ge2-Ge7	2.6740(8)	2.728(1)
Ge3-Ge4	2.5460(8)	2.5213(9)
Ge3-Ge7	2.6127(8)	2.526(1)
Ge3-Ge8	2.5899(8)	2.5573(9)
Ge4-Ge5	2.6750(8)	2.6502(8)
Ge4-Ge8	2.7432(8)	2.704(1)
Ge5-Ge6	2.7587(8)	2.704(1)
Ge5-Ge8	2.6063(8)	2.667(1)
Ge5-Ge9	2.5437(8)	2.5301(8)
Ge6-Ge7	2.6926(8)	2.677(1)
Ge6-Ge9	2.6077(8)	2.548(2)
Ge7-Ge8	2.9322(8)	3.183(1)
Ge7-Ge9	2.5900(9)	2.5381(8)
Ge8-Ge9	2.6804(9)	2.577(1)
Ge1-C1	1.995(5)	1.976(4)
Ge3-Si1	2.396(2)	2.380(1)
Ge5-Six	2.395(2) (Si5)	2.383 (1) (Si9)
Ge2-Ge4 (h1)	3.976(1)	3.386(1)
Ge5-Ge6 (h2)	2.759(2)	3.691(1)
Ge7-Ge8 (h3)	2.932(1)	3.183(1)
A-O	2.855(4)	3.168(3)
A-Ge1	4.631(1)	4.057(1)
A-Gex	3.536(1) (Ge6)	4.001(1) (Ge2)
A-Gex	3.540(1) (Ge7)	3.913(1) (Ge4)
A-C _{mesityl} (mean)	3.280	3.544
torsion angle	angle [°] (1-K)	angle [°] (1-Cs)
Ge1-Ge2-Ge4-Ge3	173.5	146.9

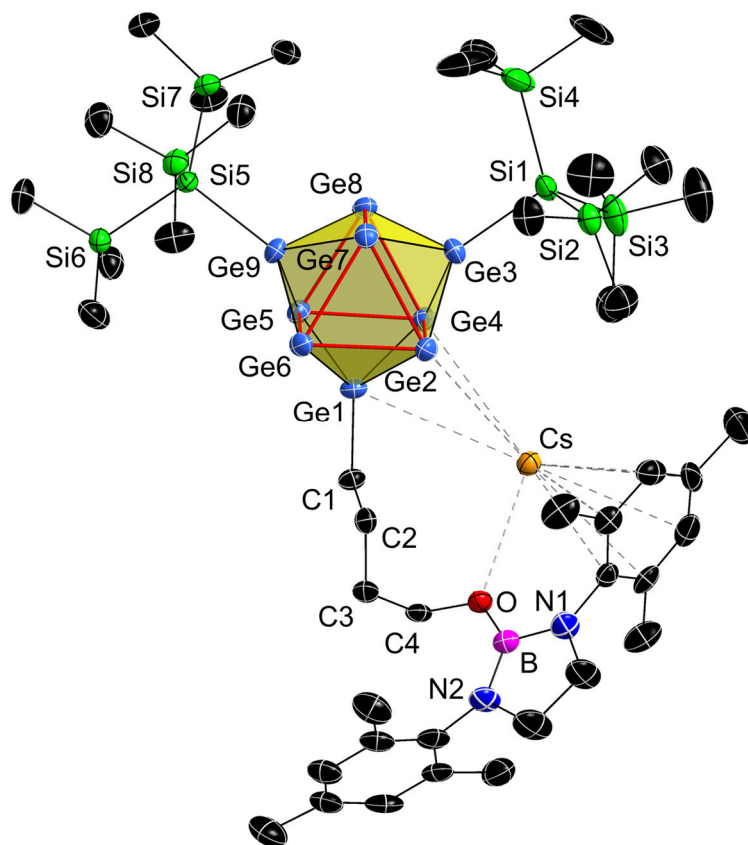


Figure S1. Full ellipsoid plot of the molecular structure of compound **1-Cs**. All ellipsoids are presented at a 50 % probability level. Hydrogen atoms as well as the co-crystallizing toluene molecule are omitted. The trigonal prism is indicated by thick red lines, and the coordination sphere of the Cs⁺ ion is indicated by dashed grey lines.

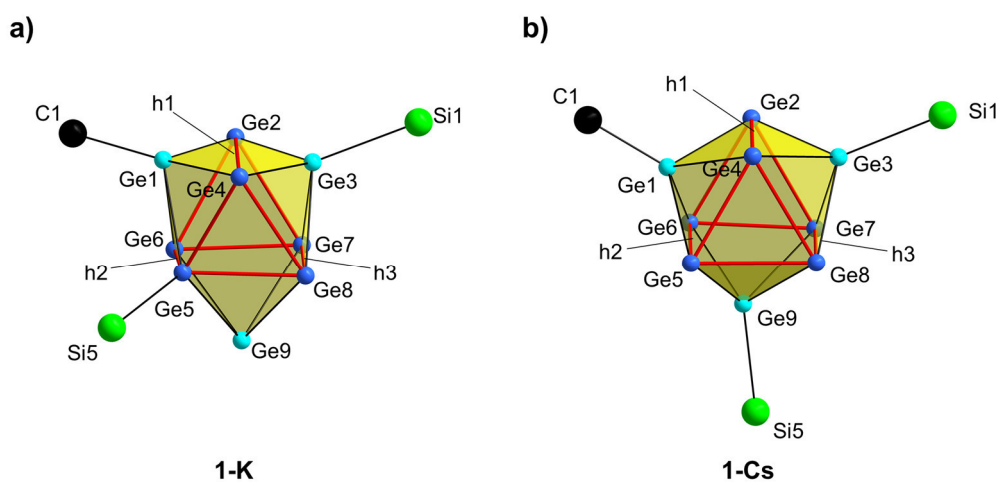


Figure S2. Schematic comparison of the substitution pattern of the [Ge₉] cluster in compounds a) **1-K** (literature)^[6] and b) **1-Cs**. Atoms are presented as standard balls. In a) the asymmetric substitution pattern is caused by Si5 binding to Ge5 which is part of a trigonal prism base. In b) all ligands bind to Ge vertex atoms capping the trigonal prism. Ge atoms capping the trigonal prism are indicated in turquoise for clarity and the trigonal prisms are indicated by red lines. The prism heights h1 – h3 are summarized in Table S3.

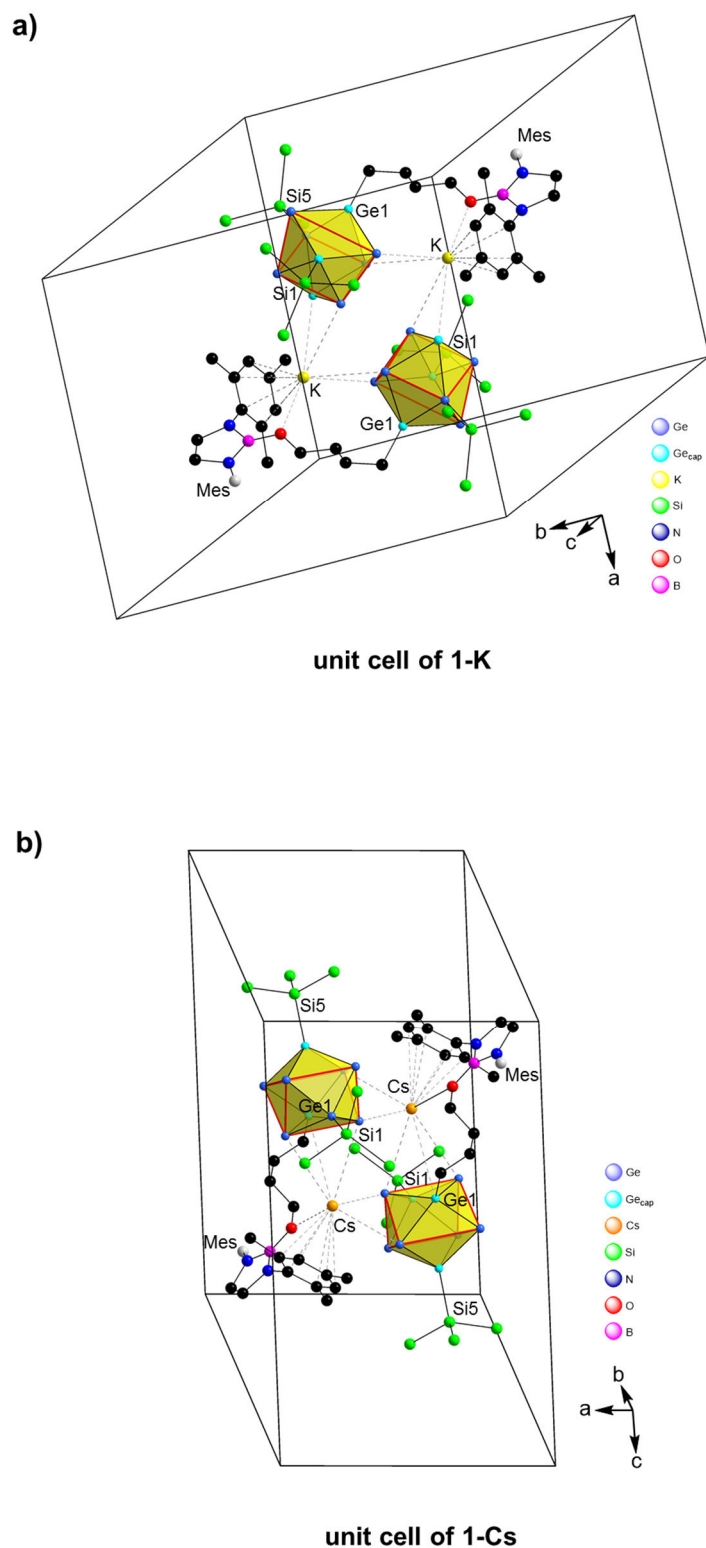


Figure S3. Arrangement of the unit formulas in the unit cells of a) **1-K** (literature)^[6] and b) **1-Cs**. Atoms are represented as standard balls. The co-crystallizing toluene molecules were neglected for clarity, as they do not exhibit a coordination to any other groups or atoms. The Mes groups not taking part in any coordination are indicated by grey spheres, while the coordination spheres of the alkali metal cations are indicated by dashed grey lines.

3. NMR spectra

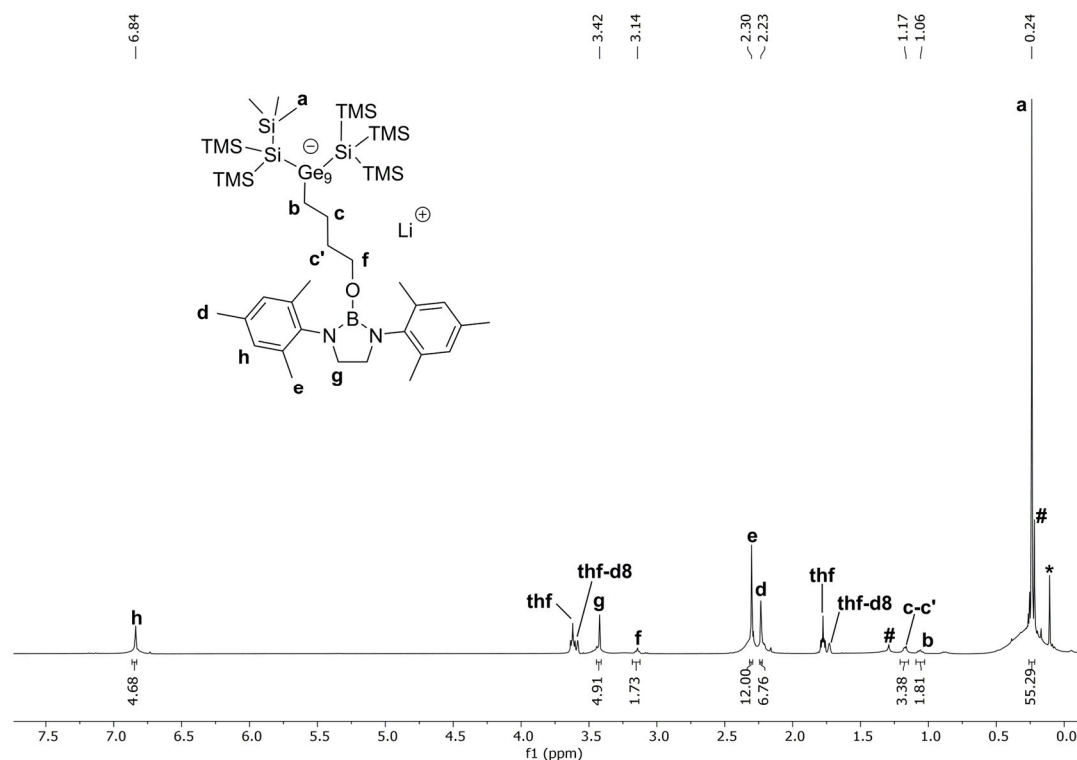
NMR spectra of compounds **1-Li**, **1-Rb** and **1-Cs**

Figure S4. ^1H NMR spectrum of $\text{Li}[\text{Ge}_9\{\text{Si}(\text{TMS})_3\}_2(\text{CH}_2)_4\text{O-DAB}^{\text{Mes}}]$ (**1-Li**) acquired in thf-d_8 . The asterisked signal is assigned to silicon grease. Signals indexed with # belong to an unidentified impurity.

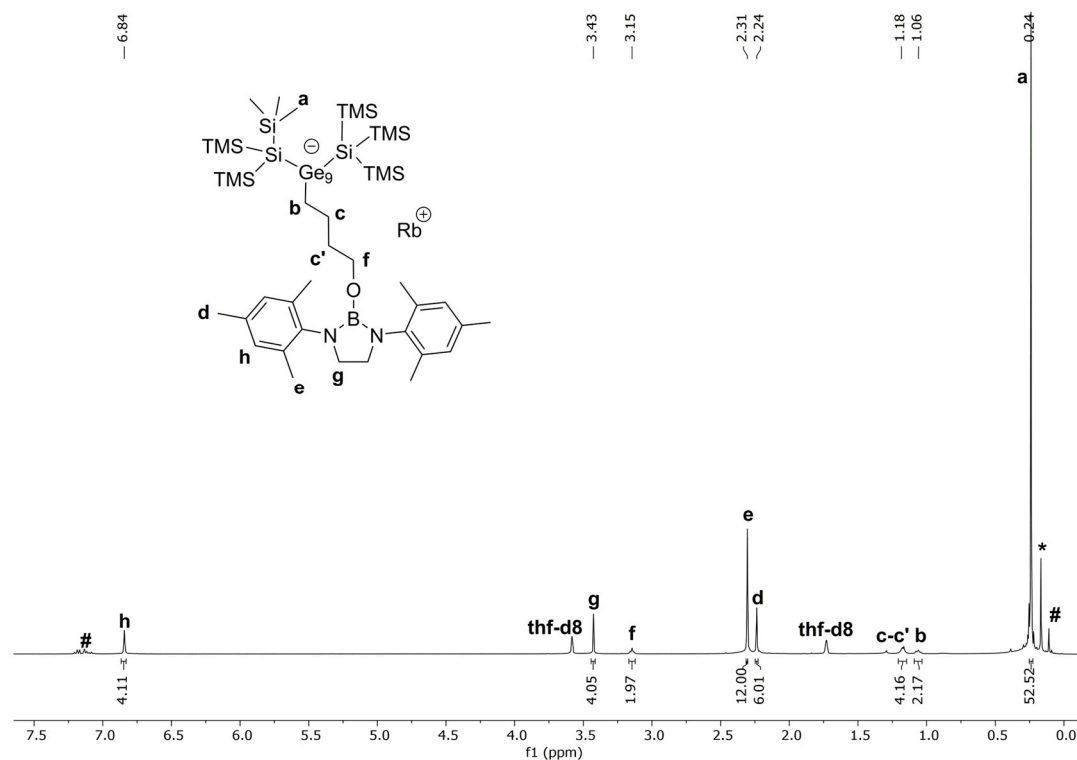


Figure S5. ^1H NMR spectrum of $\text{Rb}[\text{Ge}_9\{\text{Si}(\text{TMS})_3\}_2(\text{CH}_2)_4\text{O-DAB}^{\text{Mes}}]$ (**1-Rb**) acquired in thf-d_8 . The asterisked signal is assigned to $\text{Rb}_2[\text{Ge}_9\{\text{Si}(\text{TMS})_3\}_2]$. Signals indexed with # belong to an unidentified impurity.

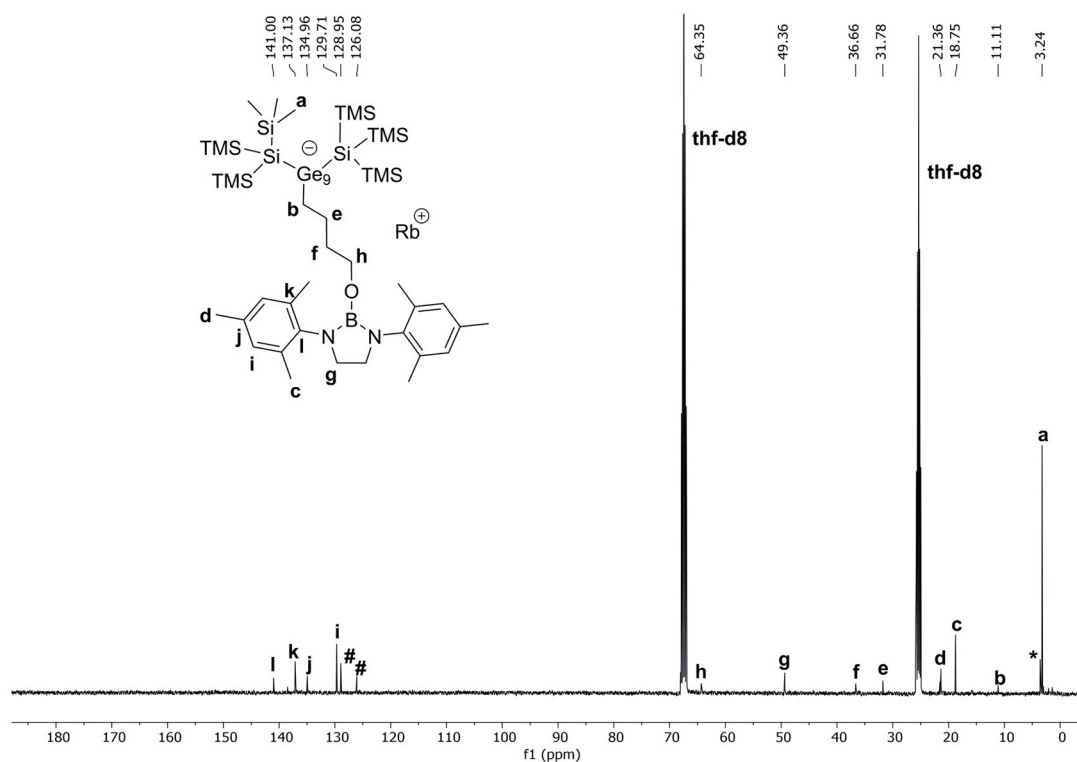


Figure S6. ^{13}C NMR spectrum of $\text{Rb}[\text{Ge}_9\{\text{Si}(\text{TMS})_3\}_2(\text{CH}_2)_4\text{O-DAB}^{\text{Mes}}]$ (**1-Rb**) acquired in thf-d_8 . The asterisked signal is assigned to $\text{Rb}_2[\text{Ge}_9\{\text{Si}(\text{TMS})_3\}_2]$. Signals indexed with # belong to an unidentified impurity.

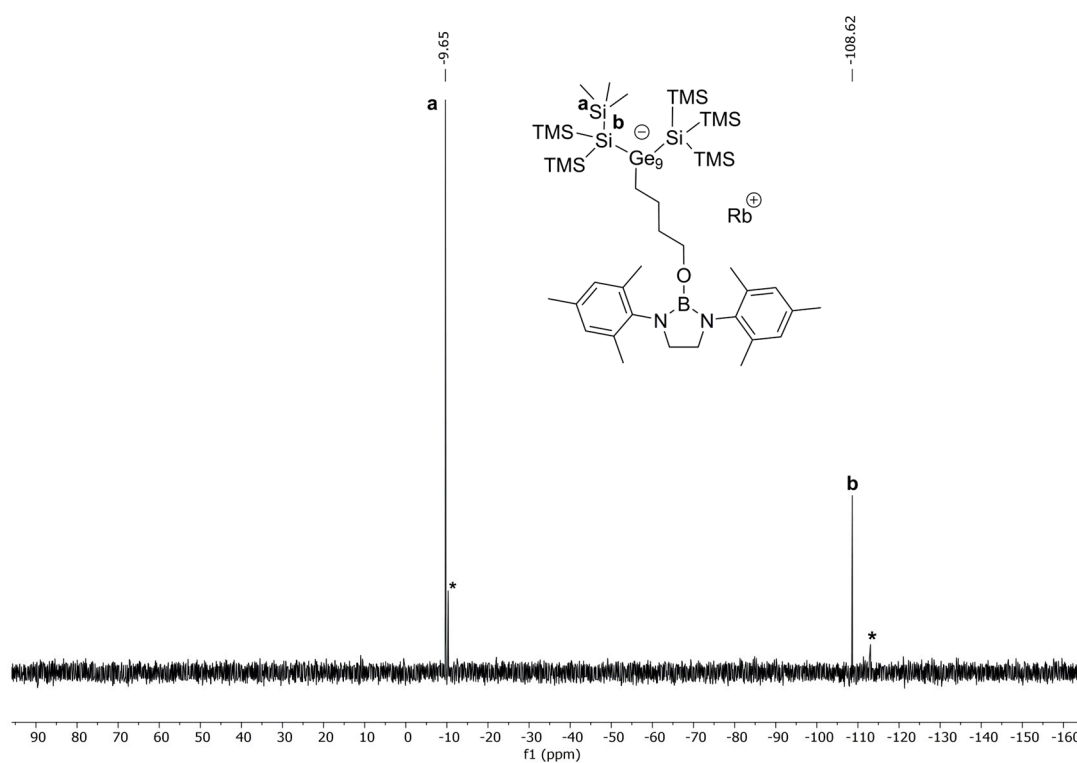


Figure S7. ^{29}Si INEPT spectrum of $\text{Rb}[\text{Ge}_9\{\text{Si}(\text{TMS})_3\}_2(\text{CH}_2)_4\text{O-DAB}^{\text{Mes}}]$ (**1-Rb**) acquired in thf-d_8 . The asterisked signals are assigned to $\text{Rb}_2[\text{Ge}_9\{\text{Si}(\text{TMS})_3\}_2]$.

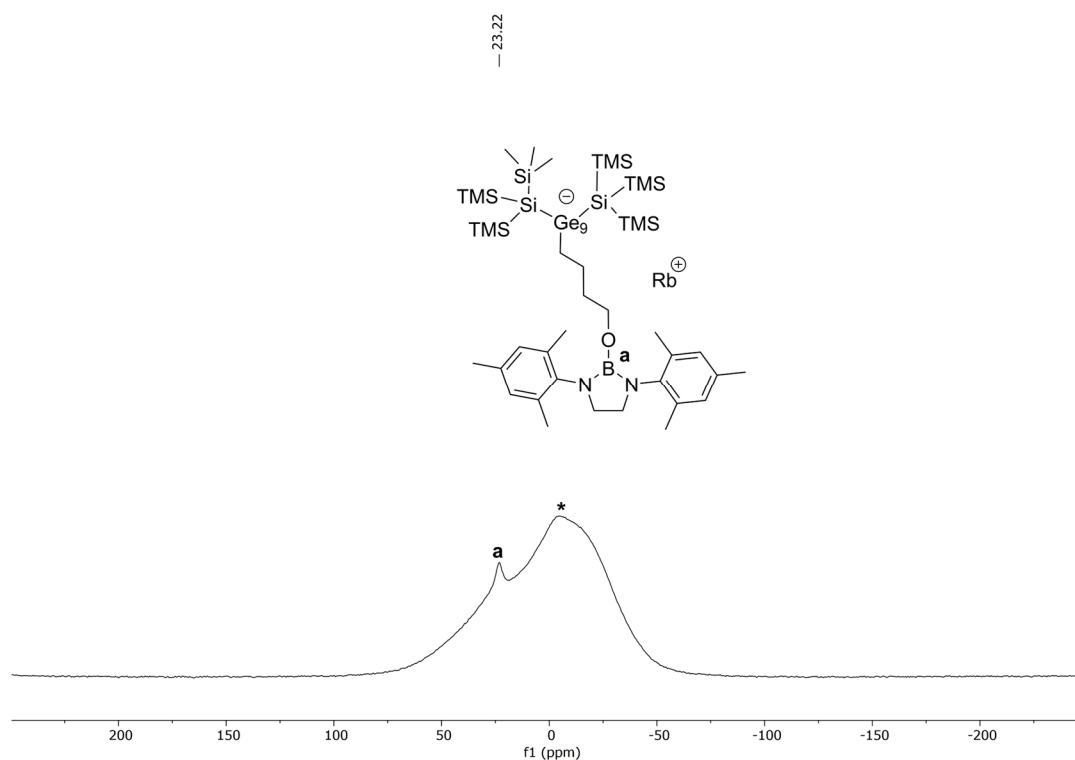


Figure S8. ^{11}B NMR spectrum of $\text{Rb}[\text{Ge}_9\{\text{Si}(\text{TMS})_3\}_2(\text{CH}_2)_4\text{O-DAB}^{\text{Mes}}]$ (**1-Rb**) acquired in thf-d_8 . The broad, asterisked signal is caused by the glass of the NMR tube.

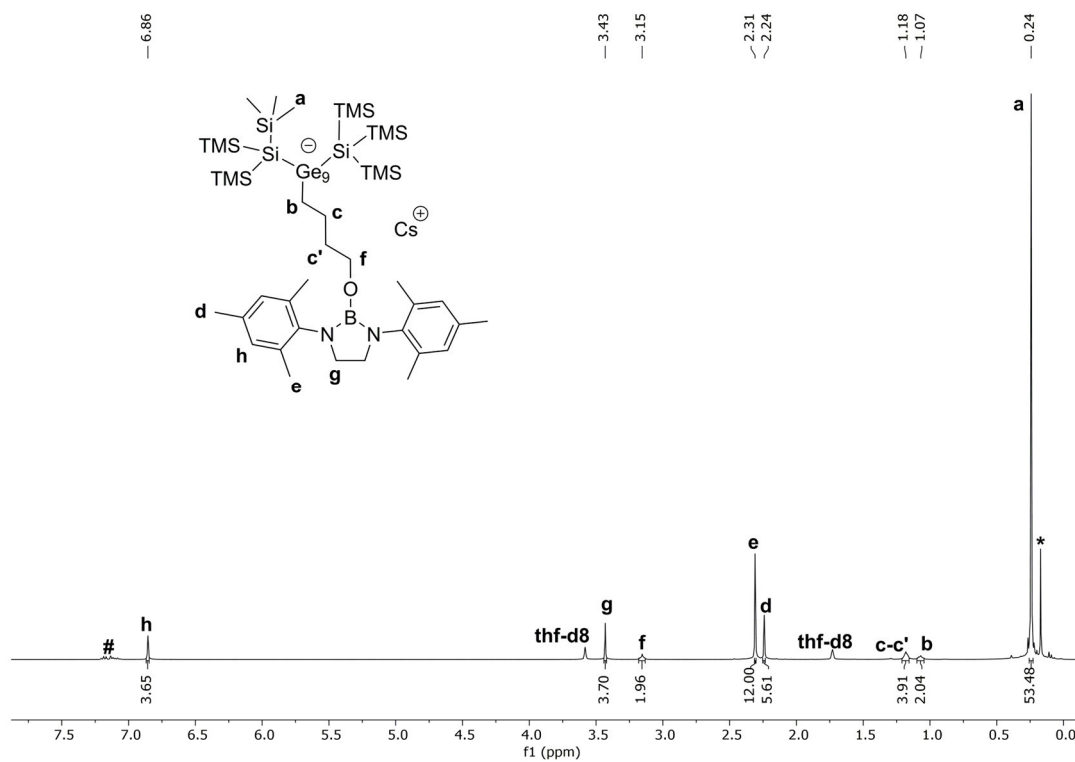


Figure S9. ^1H NMR spectrum of $\text{Cs}[\text{Ge}_9\{\text{Si}(\text{TMS})_3\}_2(\text{CH}_2)_4\text{O-DAB}^{\text{Mes}}]$ (**1-Cs**) acquired in thf-d_8 . The asterisked signal is assigned to $\text{Cs}_2[\text{Ge}_9\{\text{Si}(\text{TMS})_3\}_2]$. The signal indexed with # belongs to an unidentified impurity.

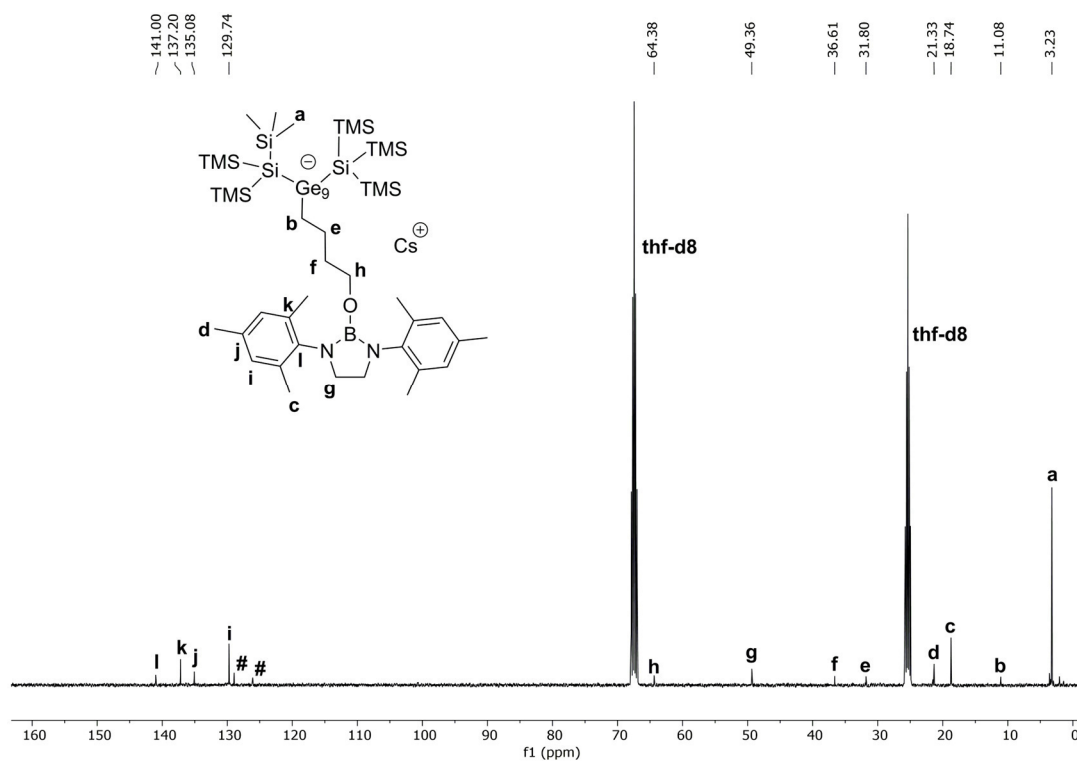


Figure S10. ^{13}C NMR spectrum of $\text{Cs}[\text{Ge}_9\{\text{Si}(\text{TMS})_3\}_2(\text{CH}_2)_4\text{O-DAB}^{\text{Mes}}]$ (**1-Cs**) acquired in thf-d_8 . Signals indexed with # belong to an unidentified impurity.

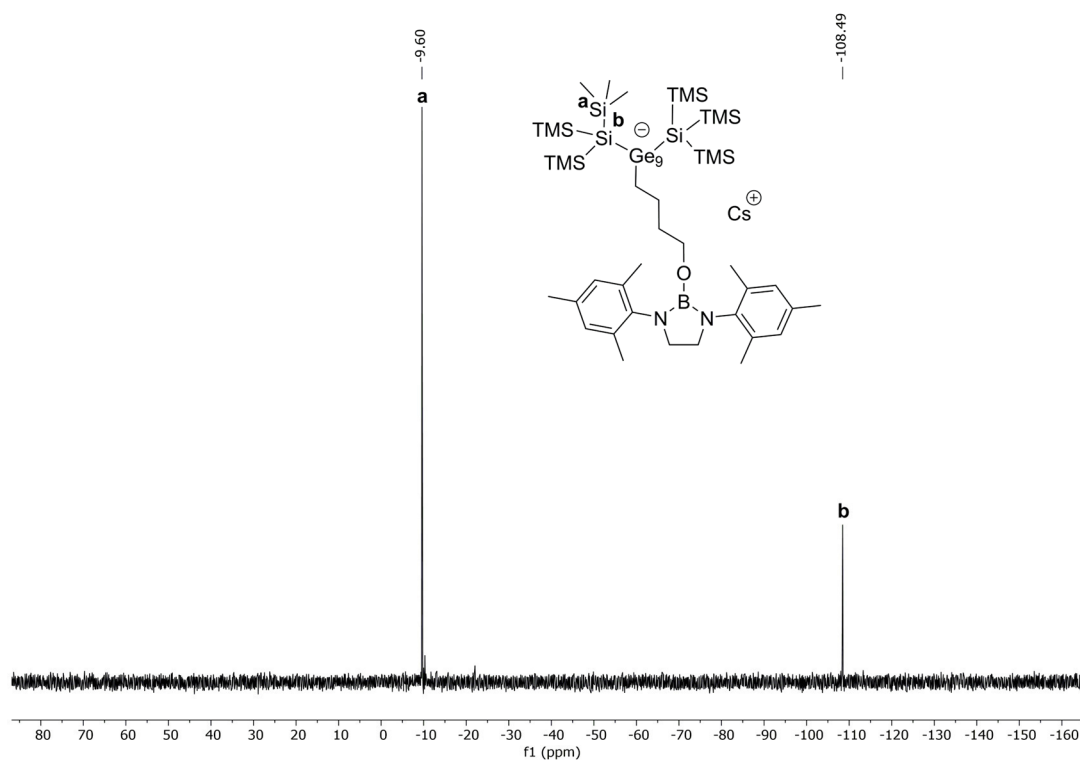


Figure S11. ^{29}Si INEPT spectrum of $\text{Cs}[\text{Ge}_9\{\text{Si}(\text{TMS})_3\}_2(\text{CH}_2)_4\text{O-DAB}^{\text{Mes}}]$ (**1-Cs**) acquired in thf-d_8 .

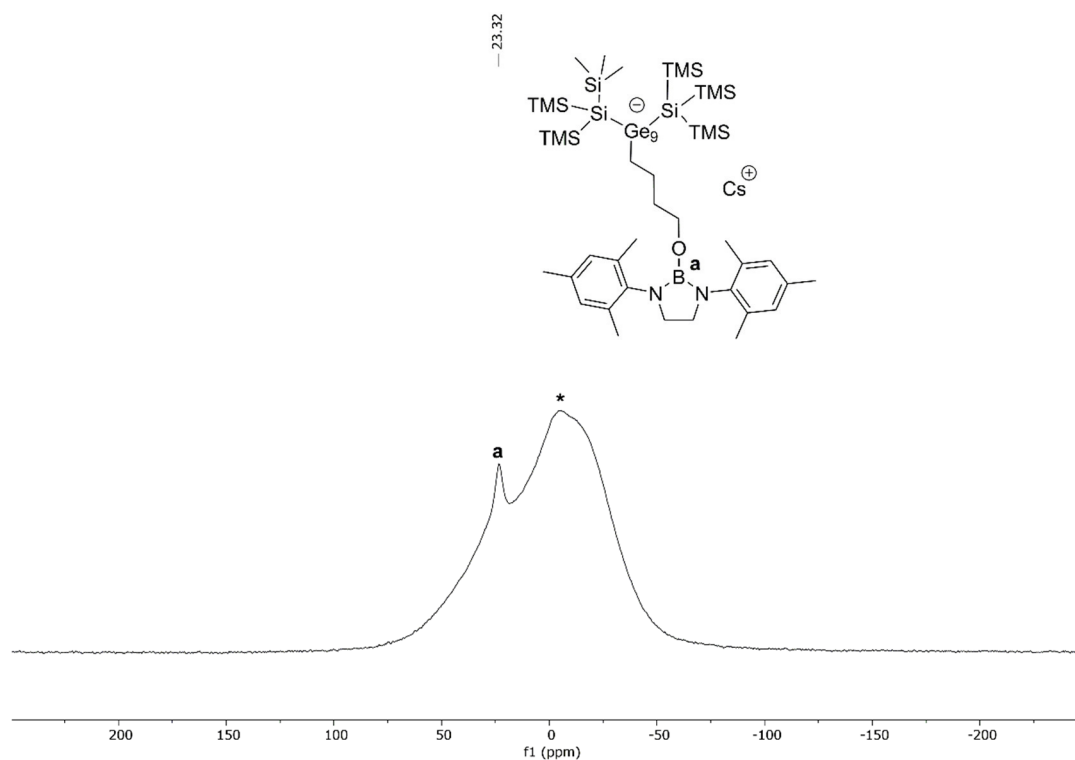


Figure S12. ^{11}B NMR spectrum of $\text{Cs}[\text{Ge}_9\{\text{Si}(\text{TMS})_3\}_2(\text{CH}_2)_4\text{O-DAB}^{\text{Mes}}]$ (**1-Cs**) acquired in thf-d_8 . The broad, asterisked signal is caused by the glass of the NMR tube.

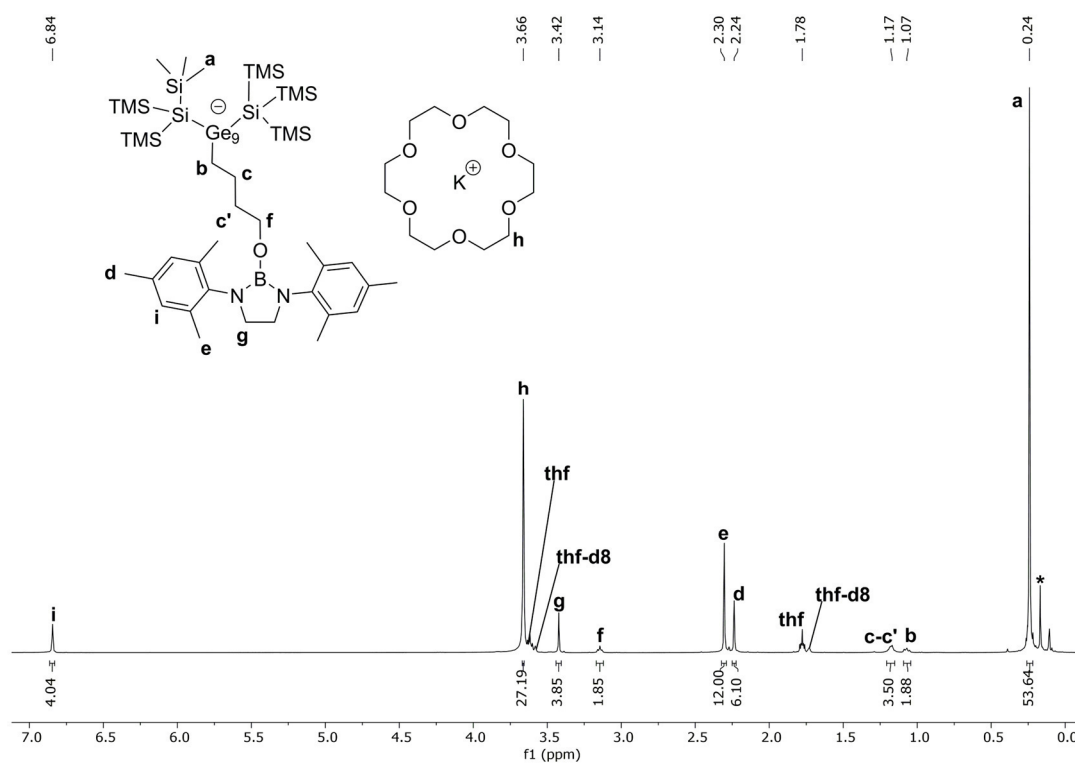
Reactions with sequestered counter ions A^+ ($A = K, Rb, Cs$)

Figure S13. ^1H NMR spectrum of $[\text{K}(18\text{-crown-6})][\text{Ge}_9(\text{Si}(\text{TMS})_3)_2(\text{CH}_2)_4\text{O-DAB}^{\text{Mes}}]$ acquired in thf-d_8 . The asterisked signal is assigned to $\text{K}_2[\text{Ge}_9(\text{Si}(\text{TMS})_3)_2]$. Excessive solvent from the reaction is indexed as thf. The signal intensity of the crown ether's CH_2 groups might be influenced by an interference with signals arising from remaining thf.

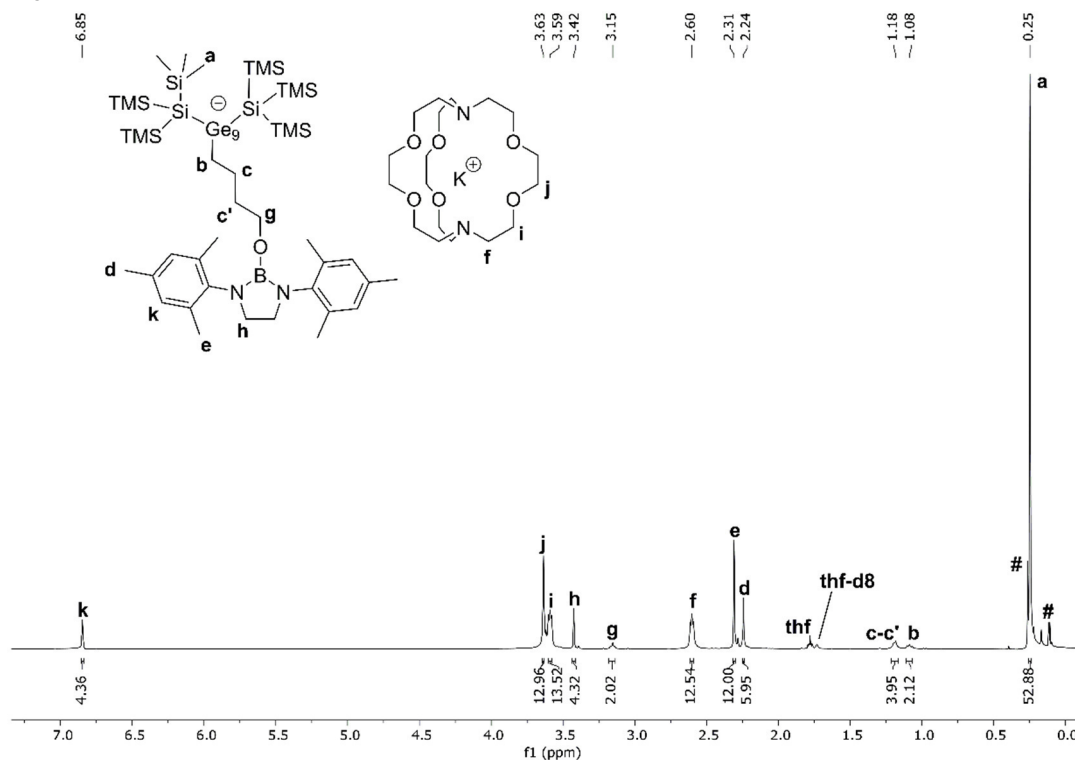


Figure S14. ^1H NMR spectrum of $[\text{K}([2.2.2]\text{cryptand})][\text{Ge}_9(\text{Si}(\text{TMS})_3)_2(\text{CH}_2)_4\text{O-DAB}^{\text{Mes}}]$ acquired in thf-d_8 . The signals marked with # are caused by unidentified impurities. Excessive solvent from the reaction is indexed as thf. The second signal of thf-d_8 at $\delta = 3.58$ ppm overlaps with the cryptand's signal i.

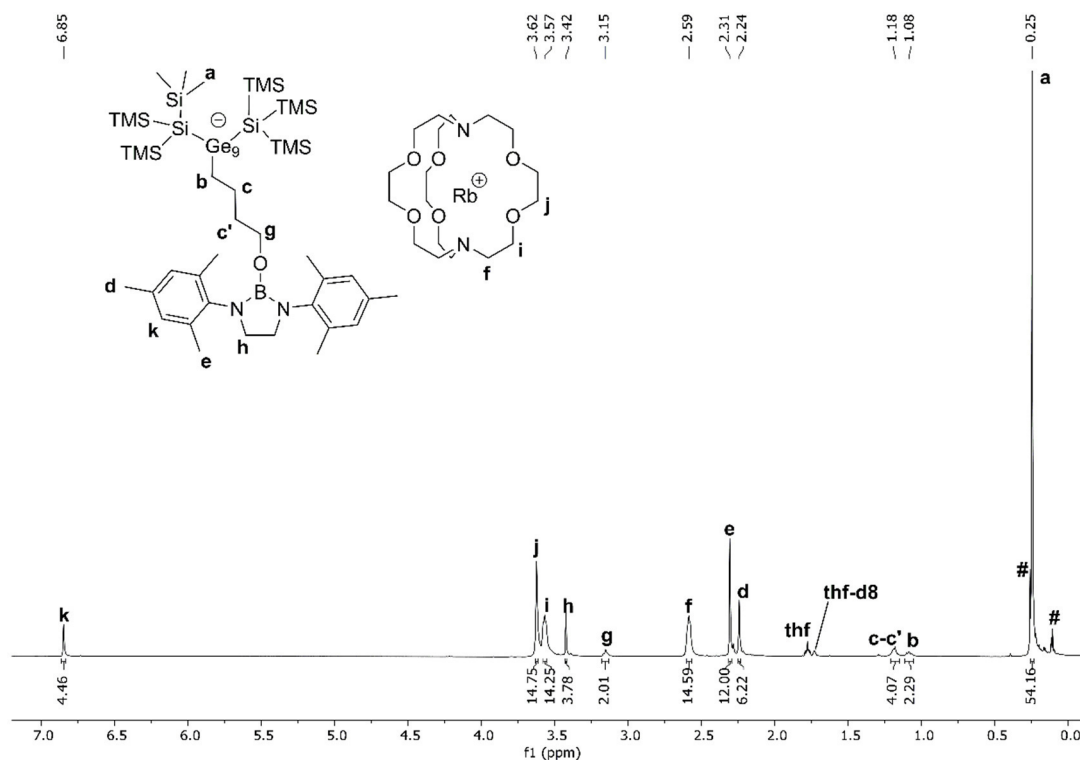


Figure S15. ^1H NMR spectrum of $[\text{Rb}([2.2.2]\text{cryptand})][\text{Ge}_9(\text{Si}(\text{TMS})_3)_2(\text{CH}_2)_4\text{O-DAB}^{\text{Mes}}]$ acquired in thf-d_8 . The signals marked with # are caused by unidentified impurities. Excessive solvent from the reaction is indexed as thf. The second signal of thf-d_8 at $\delta = 3.58$ ppm overlaps with the cryptand's signal i.

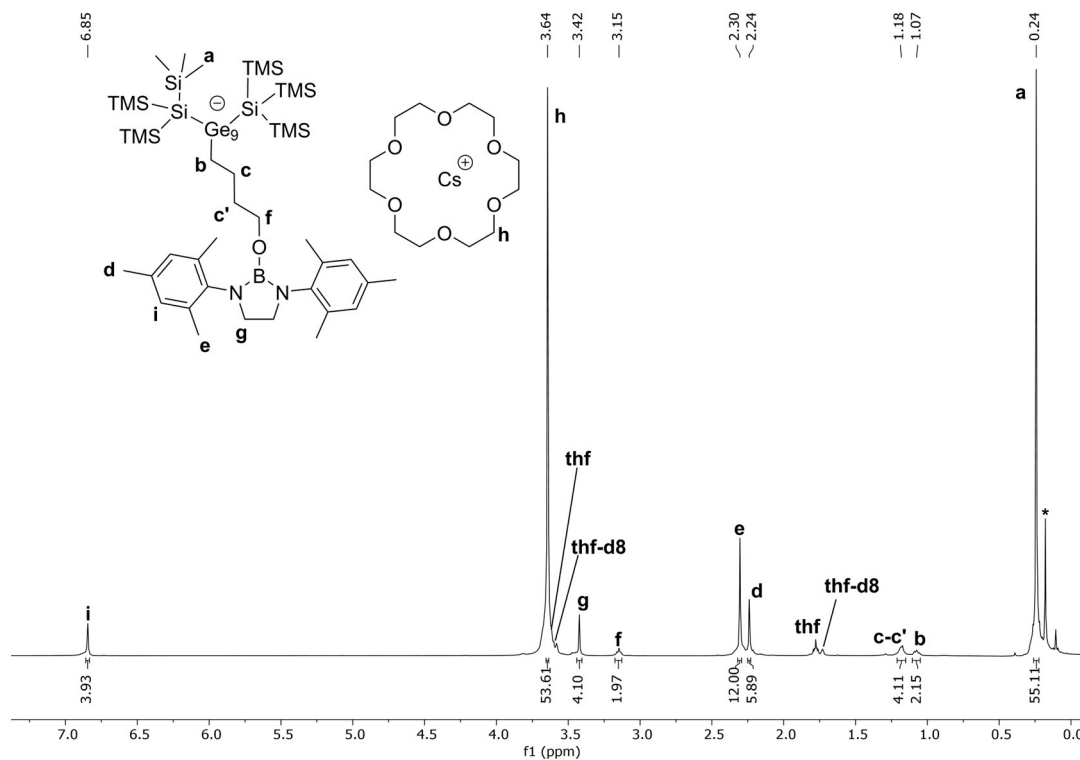


Figure S16. ^1H NMR spectrum of $[\text{Cs}(18\text{-crown-6})][\text{Ge}_9(\text{Si}(\text{TMS})_3)_2(\text{CH}_2)_4\text{O-DAB}^{\text{Mes}}]$ acquired in thf-d_8 . The asterisked signal is assigned to $\text{Cs}_2[\text{Ge}_9(\text{Si}(\text{TMS})_3)_2]$. Excessive solvent from the reaction is indexed as thf. The signal intensity of the crown ether's CH_2 groups might be influenced by an interference with signals arising from remaining thf.

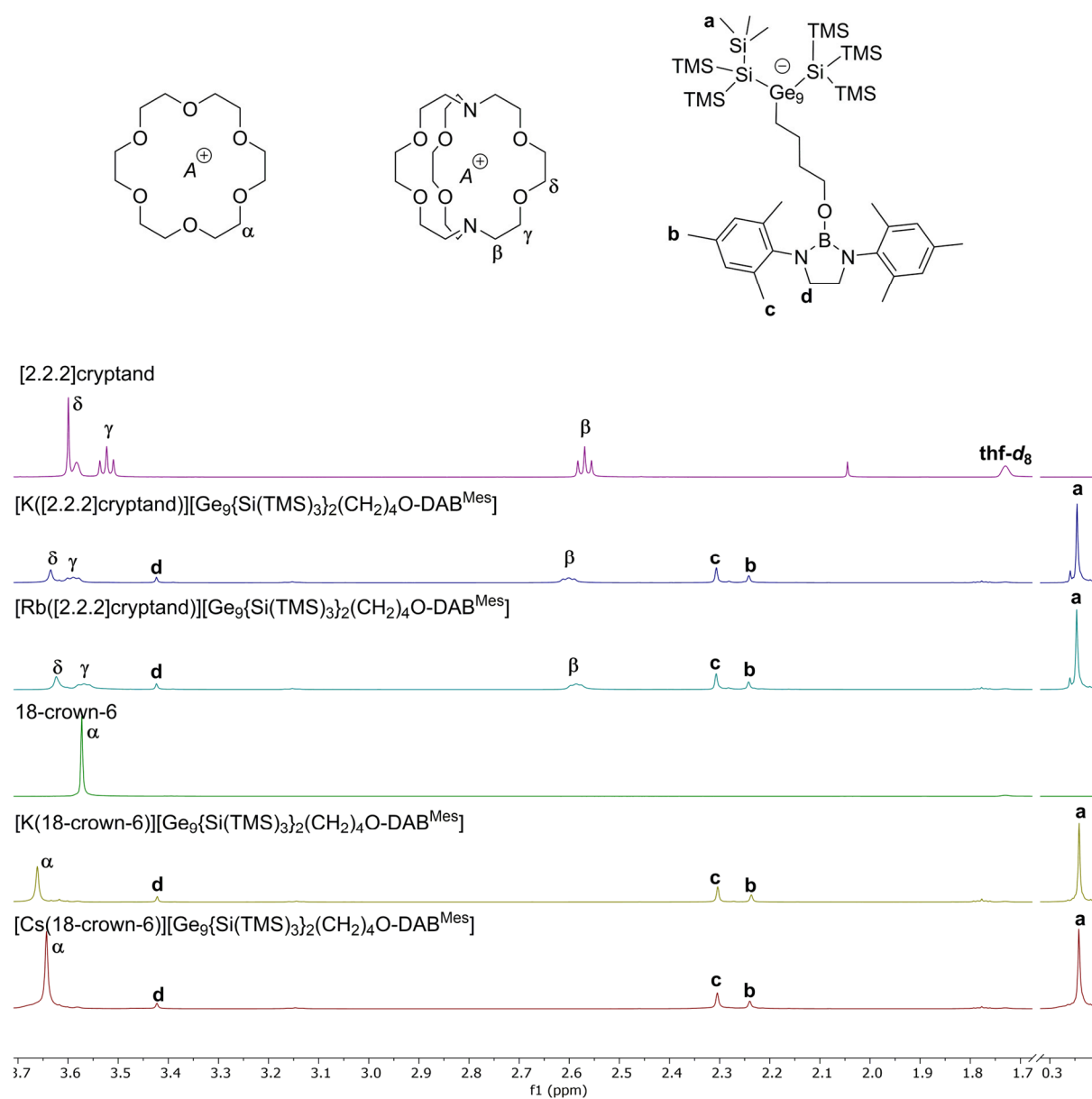


Figure S17. Stacked ^1H NMR spectra of the sequestering agents [2.2.2]cryptand and 18-crown-6, and the cluster species **1-K** to **1-Cs** featuring sequestered alkali metal ions. All spectra were acquired in thf-d_8 . Only the most intense signals were assigned to the cluster species.

Variable temperature NMR data of 1-K

For the sample preparation compound **1-K** was synthesized, and crystallized from toluene at r.t. The single crystal structure and the correlated asymmetric substitution pattern was verified by a complete single crystal structure determination, and is in accordance to the structure reported before.^[6] For the sample preparation single crystalline material of **1-K** was collected directly from the mother liquor (without removing any remaining toluene traces under vacuum) and dissolved in thf-*d*₈. The temperature-dependent ¹H NMR spectra reported in the previous manuscript were acquired from non-single crystalline material (solid residue of the reaction), consequently the substitution pattern was not verified before the data acquisition.

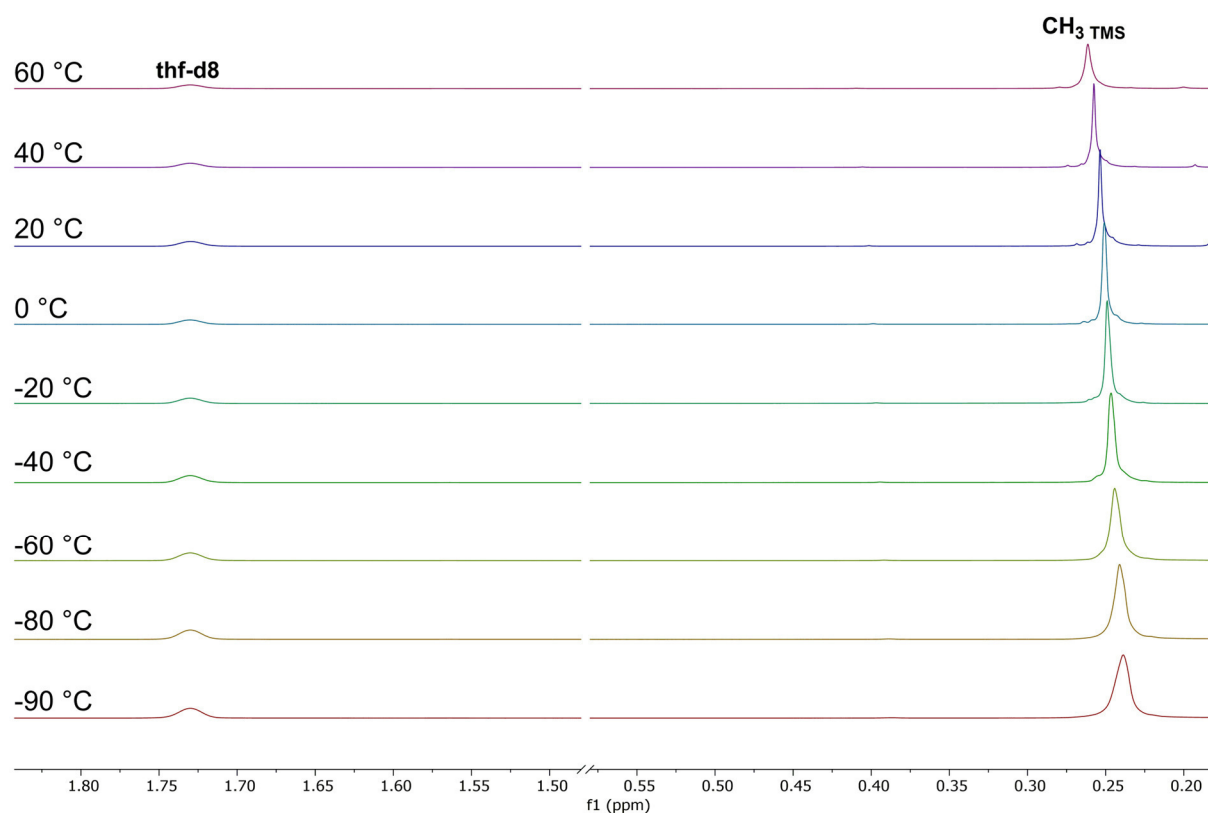


Figure S18. Temperature-dependent, stacked ¹H NMR spectra of compound **1-K** acquired from single crystalline material in thf-*d*₈. No signal splitting of the protons of the hypersilyl groups is detected.

Variable temperature NMR data of **1-Cs**

For the sample preparation dried, single crystalline material of compound **1-Cs** was dissolved in thf- d_8 .

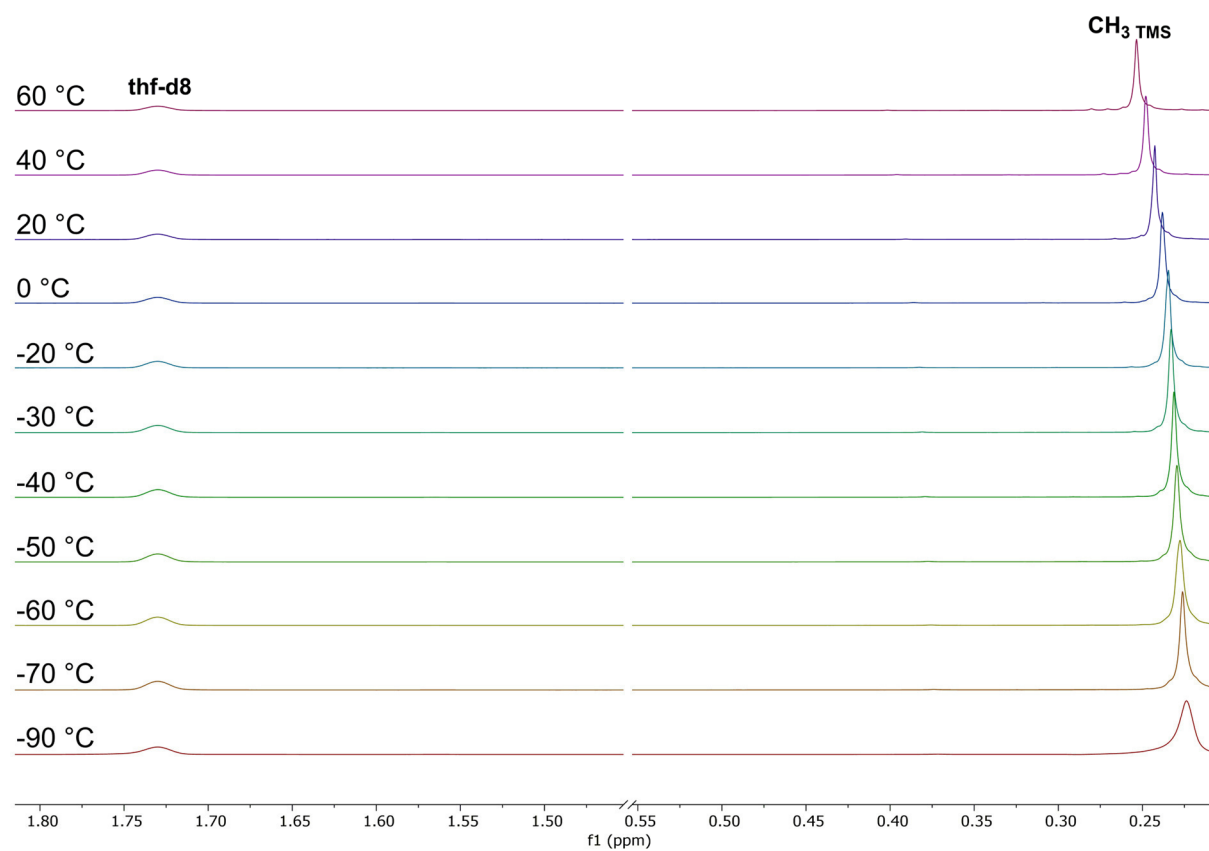


Figure S19. Temperature-dependent, stacked ^1H NMR spectra of compound **1-Cs** acquired from single crystalline material in thf- d_8 . No signal splitting of the protons of the hypersilyl groups is detected.

4. EDX spectra

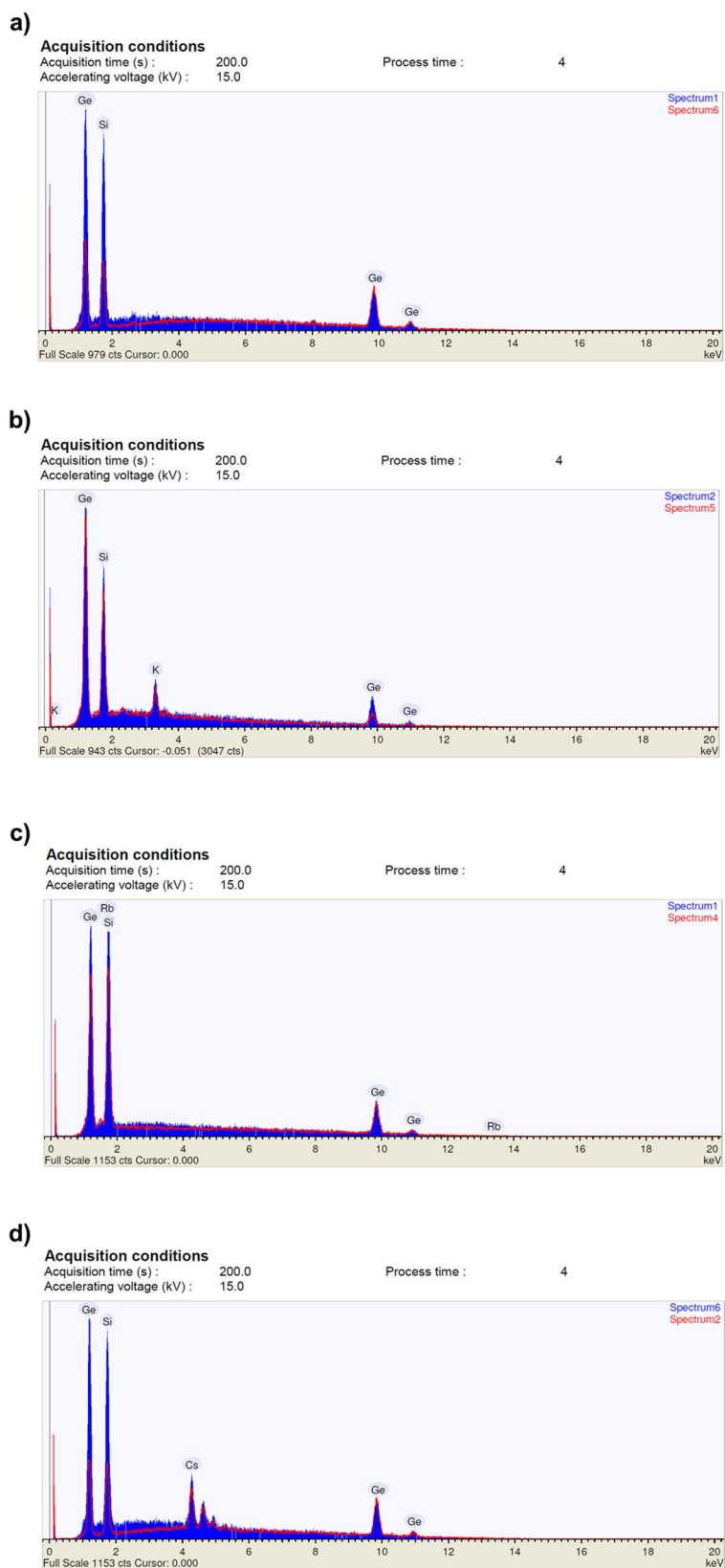


Figure S20. Qualitative EDX spectra of the compounds a) **1-Li**; b) **1-K**; c) **1-Rb** and d) **1-Cs**. In a) the Li atoms cannot be detected due to the measurement setup and spectrometer. However, the absence of K atoms accounts for a successful synthesis of **1-Li**. In c) signals of Rb and Si overlap.

5. ESI-MS spectrum of 1a

The ESI-MS spectra of **1a** in **1-Li** to **1-Cs** equal each other, thus here only the spectrum acquired from a thf solution of **1-Cs** is presented exemplarily.

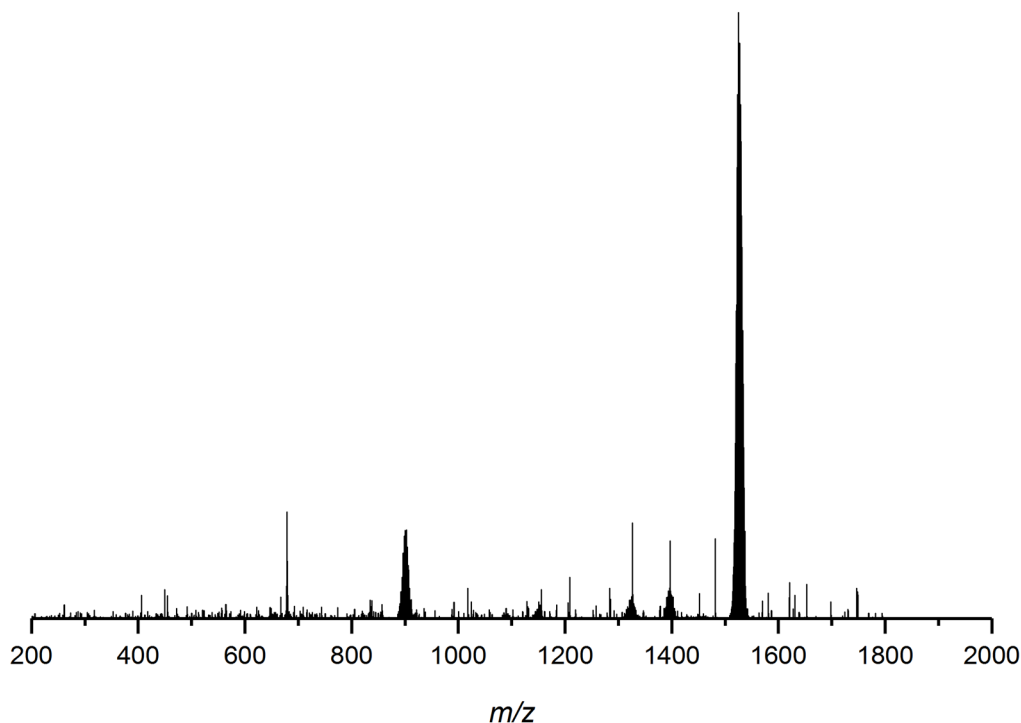


Figure S21. ESI-MS spectrum (negative-ion mode, 3500 V, 300 °C) of a thf solution of Cs[Ge₉{Si(TMS)₃}₂(CH₂)₄O-DAB^{Mes}]⁻ (**1-Cs**). The molecule peak of [Ge₉{Si(TMS)₃}₂(CH₂)₄O-DAB^{Mes}]⁻ (**1a**) is detected at *m/z* 1526.8. A detailed view of the signal is provided in Figure S22. The signal at *m/z* 902.2 belongs to [Ge₉{Si(TMS)₃}], the signal at *m/z* 1396.6 is assigned to [Ge₉{Si(TMS)₃}₃]. The signal at *m/z* 1326.2 is caused by an unidentified species.

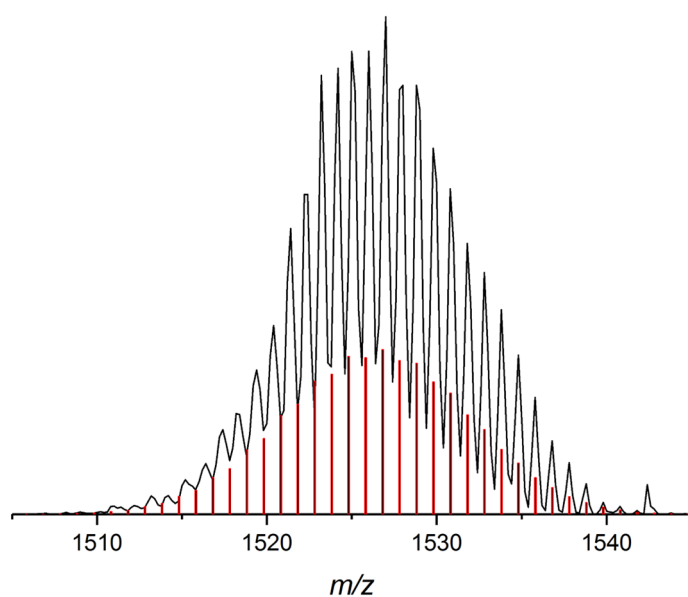


Figure S22. Detailed view of the ESI-MS signal of [Ge₉{Si(TMS)₃}₂(CH₂)₄O-DAB^{Mes}]⁻ (**1a**) at *m/z* 1526.8.

6. References

- [1] O. Kysliak and A. Schnepf, *Dalton Trans.* **2016**, 45, 2404.
- [2] Y. Segawa, Y. Suzuki, M. Yamashita and K. Nozaki, *J. Am. Chem. Soc.* **2008**, 130, 16069.
- [3] G. M. Sheldrick, *Acta Crystallogr. Sect. A: Found. Crystallogr.* **2008**, 64, 112.
- [4] G. M. Sheldrick, *Acta Crystallogr. Sect. C: Struct. Chem.* **2015**, 71, 3.
- [5] G. R. Fulmer, A. J. Miller, N. H. Sherden, H. E. Gottlieb, A. Nudelman, B. M. Stoltz, J. E. Bercaw and K. I. Goldberg, *Organometallics* **2010**, 29, 2176.
- [6] C. Wallach, F. S. Geitner and T. F. Fässler, *Chem. Sci.* **2021**, 12, 6969.
- [7] E. Mei, L. Liu, J. L. Dye and A. I. Popov, *J. Solution Chem.* **1977**, 6, 771.

6.7 Charge-Transfer Processes in Functionalized [Ge₉] Clusters Based on the Reversible Formation of a Zwitterion

C. Wallach, Y. Selic, F. S. Geitner, W. Klein, A. J. Karttunen and T. F. Fässler

Manuscript for publication.

Contents and Contributions

The reaction of the twofold silylated cluster $K_2[Ge_9\{Si(TMS)_3\}_2]$ with the bromo-1,3,2-diazaborole $DAB(II)^{Dipp}-Br$ in acetonitrile yielded the red species $K[Ge_9\{Si(TMS)_3\}_2\{MeC=N\}-DAB(II)^{Dipp}]$ (**1-K**). The incorporated imine moiety could readily be protonated by the application of stoichiometric amounts of the acid $NEt_3 \cdot HCl$, and the deep green zwitterionic compound $[Ge_9\{Si(TMS)_3\}_2\{MeC=N(H)\}-DAB(II)^{Dipp}]$ (**1-H**) was obtained. The intensely colored cluster species both were investigated by UV-Vis absorption spectroscopy, and in a combined UV-Vis and NMR spectroscopic study the reversible formation (deprotonation) of the compound **1-H** was investigated by the application of the base KO^tBu . Quantum chemical calculations revealed that charge-transfer processes between the cluster and the antibonding π^* -orbital of the attached imine moiety occur, most probably causing the intense green color. In further studies the solvent acetonitrile was substituted by a row of various nitriles, leading to the incorporation of different imine moieties between the cluster core and the boranyl moiety. The resulting species were investigated using ESI-MS spectroscopy. A special focus was set on the introduction of the long-chain imines bearing a hexyl and hexenyl chain. The monoanionic species were crystallized in combination with the MeCN-incorporated congener as the Cu-carbene salts $NHC^{Dipp}Cu[Ge_9\{Si(TMS)_3\}_2\{R^lCN\}-DAB^R]$ [$DAB(II)^{Dipp}$, $R^l = Me$ (**1b-Cu**); $R = Mes$, $R^l = (CH_2)_4CH_3$ (**2a-Cu**); $(CH_2)_3CH=CH_2$ (**3b-Cu**)]. The corresponding species feature an imine-enamine tautomerism and were characterized by single crystal X-ray diffraction analysis and LIFDI-MS measurements. The developed reaction protocol allows for the variable introduction of two functional groups in close proximity to the $[Ge_9]$ cluster, which are the imine moiety and an alkenyl moiety, respectively.

The experimental work leading to the isolation of compounds **1-K**, **1-H**, as well as **1b-Cu**, **2a-Cu**, and **3b-Cu** was performed by me, including the acquisition and evaluation of spectroscopic data and the selection of single crystals. I measured the single crystals and performed the initial structure refinement. Dr. Wilhelm Klein finalized the single crystal structure refinement for publication. The crystallization of compounds **1-K** and **1-H** was technically supported by Dr. Felix S. Geitner. LIFDI-MS measurements were performed by Dr. Max Schütz and M. Sc. Maximilian Muhr (Prof. Fischer, TUM), I evaluated and plotted the acquired data.

The UV-Vis absorption spectra and kinetic data were collected by me, M. Sc. Lukas Niederegger (Prof. Hess, TUM) provided support regarding the technical setup for the measurements. Variable temperature NMR data were acquired by M. Sc. Philip Keil (Dr. Hadlington, TUM). Elemental analysis data were acquired by Ulrike Ammari and Bircan Dilki in the microanalytical laboratory of the Chemistry Department of the Technical University of Munich. M. Sc. Yasmin Selic and Prof. Dr. Antti J. Karttunen (Aalto University, Finland) did the quantum chemical calculations. The molecular orbital figures and electron density difference plots were created by me. The manuscript was authored by me, including the creation of figures, tables, and schemes. M. Sc. Yasmin Selic, Dr. Wilhelm Klein, and Prof. Dr. Antti J. Karttunen proof-read the final version of the manuscript.

Charge-Transfer Processes in Functionalized [Ge₉] Clusters Based on the Reversible Formation of a Zwitterion

Christoph Wallach,^a Yasmin Selic,^a Felix S. Geitner,^a Wilhelm Klein,^a Antti J. Karttunen^b and Thomas F. Fässler^{a*}

^[a] M. Sc. C. Wallach, M. Sc. Y. Selic, Dr. F. S. Geitner, Dr. W. Klein, Prof. Dr. T. F. Fässler

Department Chemie

Technische Universität München

Lichtenbergstraße 4, 85747 Garching, Germany

*e-mail: thomas.faessler@lrz.tum.de

^[b] Prof. Dr. A. J. Karttunen

Department of Chemistry and Materials Science

Aalto University

00076 Aalto (Finland)

Abstract

Deltahedral tetrel element *Zintl* clusters form intensively colored solutions. Few information on the underlying coloring-effects is provided and usually the color of the clusters cannot be tailored in a straightforward way. Herein, we report the synthesis of the red cluster ion [Ge₉{Si(TMS)₃}₂{CH₃C=N}-DAB(II)^{Dipp}]⁻ (**1**⁻; TMS = trimethylsilyl; DAB(II) = 1,3,2-diazaborole; (II) = unsaturated backbone; Dipp = 2,6-di-*iso*-propylphenyl) comprising an incorporated imine fragment. The imine entity in **1**⁻ is readily protonated by stoichiometric amounts of NEt₃·HCl yielding the deep green, zwitterionic cluster [Ge₉{Si(TMS)₃}₂{CH₃C=N(H)}-DAB(II)^{Dipp}] (**1**-H). UV-Vis investigations combined with time-dependent density functional theory calculations account for a charge-transfer process causing the observed bathochromic shift. Further investigations reveal that the iminium entity can be deprotonated, implying a reversible formation of the zwitterion **1**-H. In addition, the imine moiety acts as a carrier for organic fragments such as alkyl, alkenyl, and aryl groups, thus enabling the attachment of various functional groups at the nine-atom cluster. Three of the resulting species were transferred into the Cu-carbene adducts NHC^{Dipp}Cu[Ge₉{Si(TMS)₃}₂{RⁱCN}-DAB^{Rⁱ}] [DAB(II)^{Dipp}, Rⁱ = CH₃ (**1b**-Cu); DAB^{Mes}, Rⁱ = CH₃(CH₂)₄ (**2a**-Cu), CH₂=CH(CH₂)₃ (**3b**-Cu); NHC^{Dipp} = 1,3-bis(2,6-di-*iso*-propylphenyl)imidazolyldine; DAB = 1,3,2-diazaborolidine; Mes = 2,4,6-trimethylphenyl]. In the obtained Cu-coordinated clusters, an imine-enamine tautomerism is observed in the solid-state.

Introduction

The chemistry of main group element clusters has been subject to intensive investigations within recent years, aiming for the synthesis of novel materials at the border of solid-state-like structures and isolated molecules.^[1-7] Reactions of the tetrel element clusters [E₉]⁴⁻, which are extracted from the binary phases A₄E₉ or A₁₂E₁₇ (A = alkali metal, E = Si-Pb),^[8] form one major

pillar in this field. The nine-atom clusters can be transferred into solution without changes in their inherent structure,^[9-10] and serve as molecular three-dimensional precursors in subsequent reactions. Besides the isolation of intermetaloid clusters, which form in reactions of $[E_9]^{4-}$ clusters with transition metal complexes,^[1-3] investigations mainly focus on the reactivity of $[E_9]^{4-}$ ($E = \text{Si}, \text{Ge}$) clusters towards main group element compounds. Due to their fourfold negative charge, the nine-atom clusters feature a highly reducing potential and a low solubility in many solvents. Just recently, the isolation of several protonated nine-atom clusters has been reported, bearing the smallest possible ligand for a charge reduction.^[11-15] Another strategy to overcome the mentioned limitations was found in the silylation of the silicide and germanide clusters using chlorosilanes, yielding species such as $[E_9R_2]^{2-}$ and $[E_9R_3]^-$ ($E = \text{Si}$,^[16-17] Ge ;^[18-20] $R = \text{Si}(\text{TMS})_3, \text{Si}^i\text{Bu}_2\text{H}$). Due to the straightforward production of the twofold silylated $[\text{Ge}_9]$ cluster, its mediocre steric shielding, and the remaining negative charge of -2, a prosperous chemistry evolved using the dianion $[\text{Ge}_9\{\text{Si}(\text{TMS})_3\}_2]^{2-}$ as a precursor. Thus, mixed-functionalized clusters bearing covalently bound group 13,^[21] 14,^[20, 22-23] or 15^[24-26] element-based fragments became accessible, leading for example to a coupling of two cluster entities via a rigid silane.^[27] The decoration of the twofold silylated cluster with phosphanyl fragments accounts for the introduction of Lewis basic groups to the cluster,^[24-26] and also the threefold phosphanylated species $[\text{Ge}_9\{\text{P}(\text{N}^i\text{Pr}_2)\}_3]^-$ has been reported.^[28] In addition, the bare $[\text{Ge}_9]$ cages can be functionalized with organic ligands, leading to the formation of vinylated cluster species such as $[\text{Ge}_9(\text{CH}=\text{CH}_2)]_2^{4-}$,^[29] or so called *Zintl* triads form.^[30-32] The latter clusters consist out of two $[\text{Ge}_9]$ clusters interconnected by a conjugated hydrocarbon chain, exemplarily found in the ion $[\text{R-Ge}_9-(\text{CH}=\text{CH}-\text{CH}=\text{CH})-\text{Ge}_9-\text{R}]^{4-}$ ($R = \text{CH}=\text{CH}_2$).^[31]

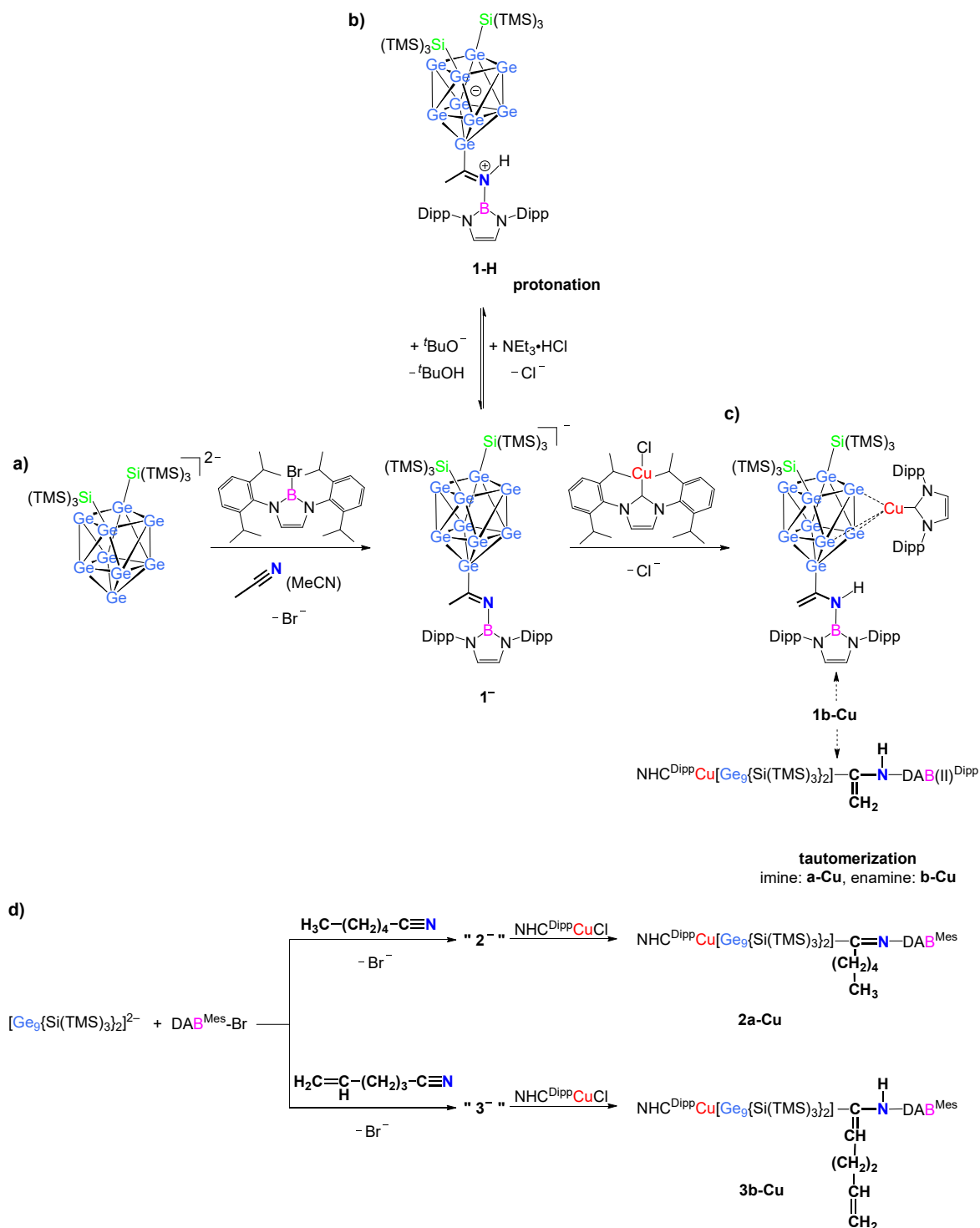
Upon dissolving the aforementioned cluster species usually red to brown solutions are obtained, which color is indicative for *Zintl* clusters in solution. In rare cases the formation of green species was reported, caused by the oxidation of bare germanide clusters to species of higher nuclearity, such as the polyanionic tetramer $[\text{Ge}_9=\text{Ge}_9=\text{Ge}_9=\text{Ge}_9]^{8-}$.^[33-35] Furthermore, a correlation between the optical properties of deltahedral germanides and fullerenes was drawn.^[36] However, a targeted synthesis of oxidized bare $[\text{Ge}_9]$ species is oftentimes hampered by the formation of by-products and low yields. Consequently, investigating the optical properties of silylated clusters accounts for an alternative. Indeed, femto-second pump probe absorption spectroscopy of the cluster $[\text{Ge}_9\{\text{Si}(\text{TMS})_3\}_3]^-$ revealed a photoexcitation-induced transfer of one cluster electron to the solvent or ligand environment, thereby generating a transient $[\text{Ge}_9]^0$ species.^[37-38] Similar findings were reported for the transition metal decorated species $[\text{Ge}_9\{\text{Si}(\text{TMS})_3\}_3\text{FeCp}(\text{CO})_2]$, which formally can be described as a combination of a $[\text{Ge}_9]^0$ and an Fe(I) entity, formed by a reversible electron transfer between the cluster core and the Fe(II) ligand.^[39] Furthermore, the absorption maximum of a transition metal decorated

silylated $[\text{Ge}_9]$ cluster depends on the number of coordinated metal atoms, as shown for the cluster $[\text{PtZn}_2\text{Ge}_{18}\{\text{Si}(\text{TMS})_3\}_8]$ forming violet solutions.^[40]

Due to the observed interesting physical properties of silylated $[\text{Ge}_9]$ clusters we aimed for the introduction of a π -system near the cluster core, thus potentially allowing charge transfer processes between the negatively charged cluster and the ligand sphere. Only recently, we have reported the attachment of imine moieties at the twofold silylated cluster, accounting for the introduction of such an unsaturated organic moiety.^[41] Upon taking the imine-comprising anion $[\text{Ge}_9\{\text{Si}(\text{TMS})_3\}_2\{\text{CH}_3\text{C}=\text{N}\}\text{-DAB}(\text{II})^{\text{Dipp}}]^-$ (**1**⁻) as basis for further reactions, the protonation of the imine function did not only lead to the generation of a new zwitterionic cluster $[\text{Ge}_9\{\text{Si}(\text{TMS})_3\}_2\{\text{CH}_3\text{C}=\text{N}(\text{H})\}\text{-DAB}(\text{II})^{\text{Dipp}}]$ (**1-H**), but also to a simultaneous color change from initially deep red to fir green, respectively. **1-H** was investigated by a combined UV-Vis spectroscopic/quantum chemical calculations study, accounting for charge-transfer processes between the $[\text{Ge}_9]$ cluster and the iminium entity. In further experiments we introduced imine moieties bearing various organic ligands to the cluster by exchanging the applied nitrile used as solvent. Several of the resulting species were isolated as Cu-carbene adducts $\text{NHC}^{\text{Dipp}}\text{Cu}[\text{Ge}_9\{\text{Si}(\text{TMS})_3\}_2\{\text{R}'\text{CN}\}\text{-DAB}^{\text{R}'}]$ (**1b-Cu**, **2a-Cu**, **3b-Cu**).

Results and discussion

The following Scheme 1 provides an overview of the performed reactions and the obtained reaction products, which will be discussed in the following sections.



Scheme 1. Overview of the performed reactions and resulting products. a) Synthesis of anion **1⁻** starting from $[\text{Ge}_9(\text{Si}(\text{TMS})_3)_2]^{2-}$ and the bromo-diazaborole $\text{DAB(II)}^{\text{Dipp}}\text{-Br}$; b) protonation of anion **1⁻** by $\text{NEt}_3\cdot\text{HCl}$ yielding **1-H**; c) reaction of anion **1⁻** with the Cu-carbene $\text{NHC}^{\text{Dipp}}\text{CuCl}$ forming the adduct **1b-Cu**; d) variation of the incorporated imine moiety by applying different nitriles yielding the non-isolable ions "**2⁻**" and "**3⁻**", which were transferred into the Cu-carbene adducts **2a-Cu** and **2b-Cu**. The Cu-comprising species show an imine-enamine tautomerism in the solid-state resulting in the tautomers **a-Cu** (imine) and **b-Cu** (enamine).

Synthesis of **1⁻** and **1-H**

The reaction of the twofold silylated cluster $[\text{Ge}_9\{\text{Si}(\text{TMS})_3\}_2]^{2-}$ with equimolar amounts of the sterically hindered bromo-1,3,2-diazaborole $\text{DAB}(\text{II})^{\text{Dipp}}\text{-Br}$ [(II) = unsaturated backbone] in MeCN yielded the compound $[\text{Ge}_9\{\text{Si}(\text{TMS})_3\}_2\{\text{CH}_3\text{C}=\text{N}\}\text{-DAB}(\text{II})^{\text{Dipp}}]^-$ (**1⁻**), bearing an incorporated imine fragment between the cluster and the boranyl moiety (Scheme 1a).^[41] The proposed reaction mechanism follows a frustrated Lewis acid-base-like reaction, in which the nitrile's N atom coordinates to the empty p_z orbital of the borane in a first step, forming a non-isolable transition state. In a second step, the cluster attacks the electrophilic C atom adjacent to the N atom, causing a Ge-C and a N-B bond formation under cleavage of Br^- .^[41] The mass peak of **1⁻** was monitored in ESI-MS measurements at m/z 1577.9 (Figure S28). In the ^1H NMR spectrum a shift of the singlet of the hypersilyl group protons from $\delta = 0.16$ ppm ($[\text{Ge}_9\{\text{Si}(\text{TMS})_3\}_2]^{2-}$) to 0.22 ppm (thf- d_8) was observed, with the protons of the cluster, the boranyl entity, and the incorporated imine fragment showing a 1:1:1 ratio (Figure S6).

Interestingly, solutions containing anion **1⁻** instantly turn green when exposed to moisture. Consequently, we reacted a toluene solution of **1⁻** with equimolar amounts of the soft acid $\text{NEt}_3\cdot\text{HCl}$, yielding a green reaction solution over night (Scheme 1b). In ^1H NMR investigations a shift of the signal from $\delta = 0.22$ ppm (**1⁻**) to 0.28 ppm (thf- d_8 , **1-H**) was observed, and the ^{11}B NMR signal shifted from $\delta = 22.3$ ppm to 18.6 ppm, indicating the formation of a new species (Figures S6 to S13). Furthermore, an iminium proton was detected in the ^1H NMR spectrum at $\delta = 9.82$ ppm, hinting for the species $[\text{Ge}_9\{\text{Si}(\text{TMS})_3\}_2\{\text{CH}_3\text{C}=\text{N}(\text{H})\}\text{-DAB}(\text{II})^{\text{Dipp}}]$, **1-H**. The protonation of the imine moiety, which shows the structural feature of a Schiff base is a suitable way to prove the functionality of the respective group in anion **1⁻**.^[42]

The potassium salt of **1⁻** (**1-K**) and compound **1-H** were obtained as red and green crystals from diethyl ether and hexane solutions, respectively, with the unit formula comprising two diethyl ether molecules and one hexane molecule. Both compounds crystallize in the monoclinic space group $P\bar{1}$ with two formula units per unit cell, and the single crystal structure determination corroborated the anticipated molecular formula of **1⁻** and **1-H** (Figure 1, Table S1). In compound **1-H**, the iminium hydrogen atom was derived from the difference Fourier electron density map and was refined freely. The shape of the $[\text{Ge}_9]$ cores in **1-K** and **1-H** is best described as distorted tricapped trigonal prisms, with one prism height Ge7-Ge8 being shortened compared to the two others (Ge2-Ge4 and Ge5-Ge6), resulting in slightly distorted C_{2v} -symmetric cluster cores (Tables 1 and S3). The two hypersilyl groups and the imine fragment bind to the Ge atoms capping the trigonal prism. In each compound one of the hypersilyl groups is disordered, which is illustrated in detail in the Supporting Information together with full ellipsoid plots of the molecules (Figures S1 and S2). All Ge-Ge and Ge-Si bond lengths are in accordance with previously reported data.^[18-19, 41]

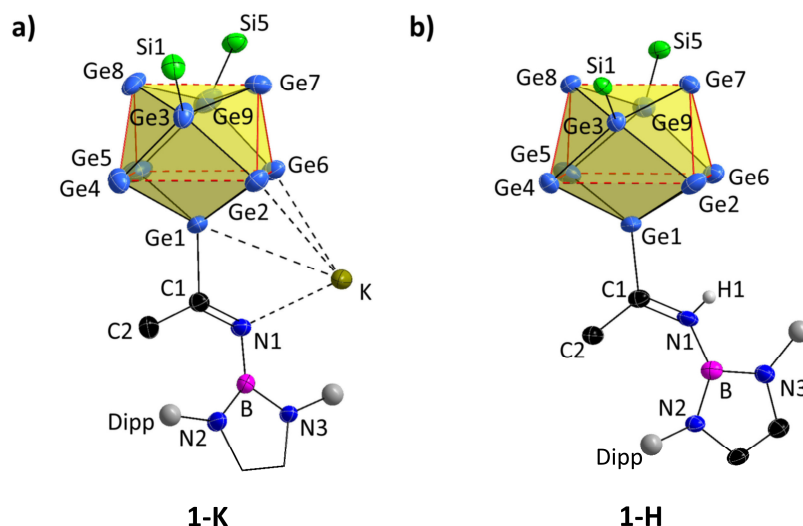


Figure 1. Molecular structure of a) **1-K** and b) **1-H**. All ellipsoids are shown at a 50 % probability level. For clarity the TMS groups of the hypersilyl ligands, hydrogen atoms, and co-crystallizing solvent molecules are omitted. The Dipp wingtips are illustrated as grey spheres. In a) and b) only the major occupied hypersilyl group Si5 is presented. Trigonal prismatic bases are indicated by red lines. Full ellipsoid plots of the structures are provided in the Supporting information (Figures S1 and S2).

In **1-H** the bond Ge1-C1 is 1.912(3) Å long which is shorter than in **1-K** [Ge1-C1 = 1.985(5) Å]. A comparison of the Ge-C bond length in **1-H** with previously reported [Ge₉] cluster species comprising Ge-C *exo*-bonds reveals the bond in **1-H** is the shortest one occurring in such clusters. The Ge-C contact coming closest to this value is 1.918(9) Å in a minor conformer within the crystal structure of the *Zintl* triad [Ge₉-CH=CH-CH=CH-Ge₉]⁶⁻.^[30] However, the Ge-C bond in **1-H** is significantly longer than a Ge=C double bond, usually adapting values of around 1.8 Å, and is in range with various reported Ge-C single bonds.^[43-46] The bond C1=N1 in **1-H** is elongated if compared to **1-K** (Table 1), but still in the range of a formal C=N double bond.^[47] Slightly elongated C=N bonds have previously been reported for molecules comprising cationic iminium moieties.^[48] The C=N double bond character in **1-K** and **1-H** is confirmed by the only slightly distorted trigonal planar coordination of C1 by Ge1, N1, and C2, featuring a dihedral angle $\omega_{C2-C1-Ge1-N1}$ of approximately 180° (Table 1).

Table 1. Selected distances and angles in compounds **1-K**, **1-H**, **1b-Cu**, **2a-Cu**, and **3b-Cu**. *R* = organic ligand at imine-side chain. **: H atom refined with a restrained distance (HFIX command).

distance [Å]	1-K	1-H	1b-Cu	2a-Cu	3b-Cu
Ge1-C1	1.985(5)	1.912(3)	1.947(9)	2.03(1)	1.97(1)
C1-N1	1.280(6)	1.325(4)	1.38(1)	1.25(1)	1.39(1)
C1-C2	1.501(7)	1.487(4)	1.33(1)	1.50(1)	1.35(1)
B1-N1	1.448(6)	1.464(4)	1.45(1)	1.42(2)	1.46(1)
angle [°]					
N1-C1-Ge1	120.3(3)	118.6(2)	116.1(7)	123.9(9)	114.8(8)
C2-C1-Ge1	115.1(3)	122.3(2)	119.6(8)	114.6(9)	122.5(8)
C2-C1-N1	124.6(4)	119.1(3)	124.4(9)	121.4(1)	122.6(1)
C1-N1-B1	126.0(4)	137.2(3)	135.8(8)	137.7(1)	130.9(1)
C1-C2- <i>R</i>	109.5(4)	109.5(3)	120.1(4)**	113.6(9)	128.5(1)
$\omega_{C2-C1-Ge1-N1}$	180	179.8	180	177.1	179.4

Formally, compound **1-H** can be described as a zwitterion with the negative charge delocalized over the $[\text{Ge}_9]$ cluster core and the positive charge localized at the nitrogen atom of the iminium moiety. Furthermore, it is the first transition metal-free, charge neutral $[\text{Ge}_9]$ cluster bearing only three substituents. The mass peak of the charge neutral compound **1-H** was detected in LIFDI-MS measurements at m/z 1578.9 (Figure S41), revealing a mass difference of exactly one hydrogen atom in comparison to anion **1**⁻.^[49]

UV-Vis Investigations and Quantum Chemical Calculations

To obtain more information about the bathochromic shift induced by protonating the imine functionality, UV-Vis studies of **1**⁻ and **1-H** in solution were carried out. For anion **1**⁻ a broad absorption band is observed at a wavelength of $\lambda = 248$ nm (5.0 eV, thf, Figure 2a). Compound **1-H** features broad absorption bands at $\lambda = 387$ nm and 437 nm (3.2 eV and 2.8 eV), and a maximum absorption peak at $\lambda = 671$ nm (1.85 eV, toluene, Figure 2b). The respective extinction coefficients were determined to $40,286.2 \text{ l}\cdot\text{mol}^{-1}\cdot\text{cm}^{-1}$ (**1**⁻) and $14,237.0 \text{ l}\cdot\text{mol}^{-1}\cdot\text{cm}^{-1}$ (**1-H**) ($\lambda = 671$ nm) for compound **1-H** (Figures S45 and S46). The absorption maximum of compound **1-H** at $\lambda = 671$ nm in the red area of the electromagnetic spectrum causes its visible green complementary color.

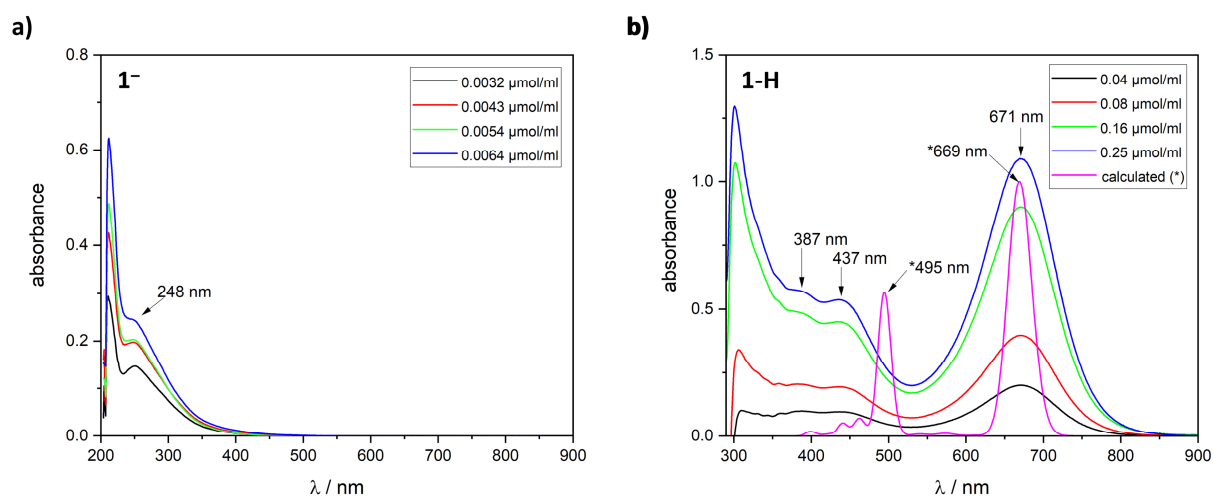


Figure 2. a) UV-Vis absorption spectra of red solutions of anion **1**⁻ in thf showing a shoulder at $\lambda = 248$ nm (5.0 eV); b) UV-Vis absorption spectra of green solutions of compound **1-H** in toluene showing signals at $\lambda = 387$ nm (3.2 eV), $\lambda = 437$ nm (2.8 eV), and $\lambda = 671$ nm (1.85 eV). The calculated absorption spectrum of **1-H**, obtained at DFT-BP86/TZVP level of theory,^[50-54] is presented as pink graph and shows maxima at $\lambda = 495$ nm (2.14 eV, transition $S_0 \rightarrow S_8$) and $\lambda = 669$ nm (1.85 eV, transition $S_0 \rightarrow S_2$). The calculated spectrum is based on the vertical excitation energies of the 30 lowest-energy singlet excited states (the shortest calculated wavelength was 396 nm).

It is noteworthy, that the absorption maximum of anion **1**⁻ does not significantly differ from the maxima observed for the pure precursor $\text{DAB}(\text{II})^{\text{Dipp-Br}}$, the reactant $[\text{Ge}_9\{\text{Si}(\text{TMS})_3\}_2]^{2-}$, or species with incorporated ether molecules (Figures S48-S53). Thus, the observed absorption bands cannot be assigned to any distinct excited state of the monoanionic cluster. In Figure 2,

peaks at approximately $\lambda = 210$ nm (thf) and $\lambda = 310$ nm (toluene) are artefacts caused by the absorption of the solvent.

To investigate the electronic properties of **1-H**, we optimized the geometry of the compound starting from the single crystal structure data and calculated the 30 lowest-energy vertical excitations using density functional theory (DFT-BP86/TZVP level of theory and time-dependent DFT, TD-DFT).^[50-54] The most intense signals in the calculated absorption spectrum are observed at $\lambda = 669.0$ nm (1.85 eV, transition $S_0 \rightarrow S_2$; Figure 2b, pink graph) and $\lambda = 495$ nm (2.14 eV, transition $S_0 \rightarrow S_8$). The longer-wavelength absorption band matches well with the experimentally observed maximum at $\lambda = 671$ nm. The shorter-wavelength absorption at $\lambda = 495$ nm is red-shifted by approximately 0.3 eV in comparison to the experimentally observed shoulder at $\lambda = 437$ nm. The $S_0 \rightarrow S_8$ excitation is more delocalized compared to the $S_0 \rightarrow S_2$ excitation (Figures S59 and S60), and TD-DFT typically shows larger errors when the extent of charge-transfer increases.^[55] The red species **1⁻** absorbs light of wavelengths below 350 nm, and a detailed TD-DFT investigation of the high-energy excited states was not carried out.

The molecular orbital analysis revealed that the HOMO of compound **1-H** is based at the $[\text{Ge}_9]$ core and extends to the atom C1, which is covalently bound to the cluster (Figure 3a). The LUMO is mostly located at the atoms C1 and N1, thus forming the anti-bonding π^* orbital of the C=N double bond (Figure 3b). The HOMO-LUMO gap was calculated to 1.40 eV ($\lambda = 886$ nm).

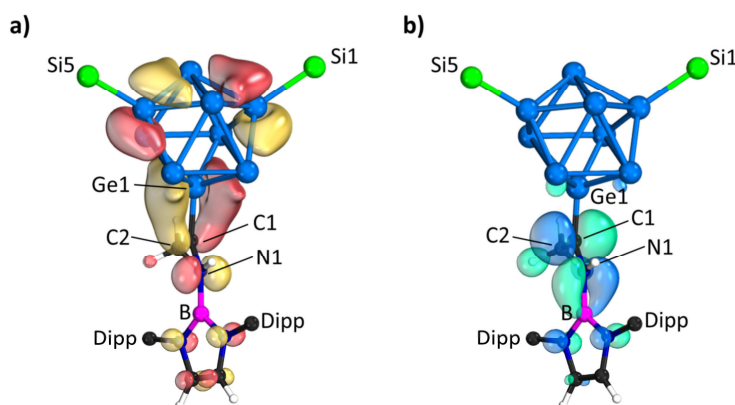


Figure 3. Molecular orbitals of **1-H** calculated at the DFT-BP86/TZVP level of theory. a) Representation of the HOMO distributed over $[\text{Ge}_9]$ and C1; b) representation of the LUMO forming the antibonding π^* orbital of the C=N double bond. Molecular orbital plots are drawn in such way that 50 % of the density is enclosed within the isosurface, corresponding approximately to an isovalue of 0.04 a.u. Additional illustrations with ligands drawn in full are provided in Figure S61.

According to the molecular orbital analysis a charge transfer from the formally negatively charged cluster into the antibonding π^* orbital of the imine moiety is theoretically feasible.

Indeed, TD-DFT calculations reveal that the electron density at the $[\text{Ge}_9]$ moiety is reduced during the $S_0 \rightarrow S_2$ excitation ($\lambda = 669 \text{ nm}$), while the electron density at the C1 atom increases. The electron density change during the excitation is presented in Figure 4a and b, in which yellow and red color indicate decreasing and increasing electron density, respectively. Figure 4c shows a schematic Lewis formula and a postulated mesomeric structure of compound **1-H**. Via the formulation of a proposed resonance structure (non-isolable) the electron density transfer during the $S_0 \rightarrow S_2$ excitation can be estimated. According to the scheme, the electron density is transferred from the cluster and the adjacent N atom to the electrophilic central C1 atom, which features a formal positive charge in the border structure. During the calculated $S_0 \rightarrow S_8$ transition ($\lambda = 495 \text{ nm}$) a similar change in the electron density at the atom C1 is observed, however here also the boranyl ligand, which is a spectator ligand in the $S_0 \rightarrow S_2$ excitation, is participating by donating electron density into the system. Further graphical illustrations of the excitations can be found in the Supporting Information (Figure S59 and S60). In conclusion, the absorption maximum of **1-H** in the red region of the electromagnetic spectrum and the corresponding lowest-energy excited state at $\lambda = 669 \text{ nm}$ make the compound an interesting starting point for further investigations targeting the design of light-harvesting cluster compounds.

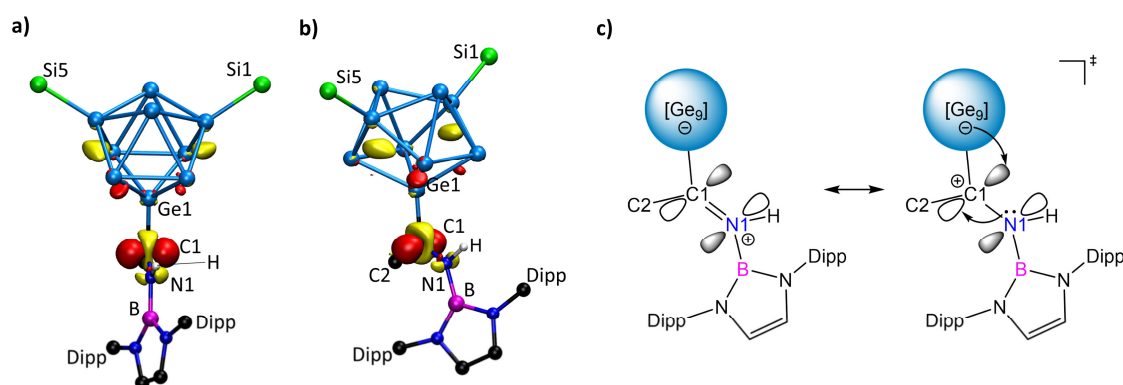


Figure 4. Electron density difference plots for the $S_0 \rightarrow S_2$ excitation of compound **1-H** (calculated $\lambda = 669 \text{ nm}$). a) and b) represent the same electronic transition from a different perspective (rotated by approximately 45°). During the electronic transition, red color corresponds to increasing electron density and yellow color corresponds to decreasing electron density. The isovalue of the electron density isosurfaces is 0.002 a.u. and hydrogen atoms are omitted for clarity. c) represents perspective b) as a schematic Lewis formula revealing a potential mesomeric structure, which is used to illustrate the change in electron density during the excitation.

Reversible Zwitterion Formation

As depicted in Scheme 1b the formation of the zwitterionic species **1-H** by protonation of anion **1⁻** is a reversible process. The reaction of a green toluene solution of **1-H** with equimolar amounts of the base KO^tBu led to a color change from formerly green to red within few minutes. ^1H NMR spectroscopic investigations in C_6D_6 corroborated the reformation of the monoanionic cluster **1⁻** upon adding a $\text{thf-}d_8$ solution of the base to the green complex in a NMR tube.

Indicative for the reversibility of the protonation are the decay of the NH signal intensity at $\delta = 9.95$ ppm, and the unambiguous shift of the hypersilyl group protons from $\delta = 0.47$ ppm (**1-H**) to 0.51 ppm (**1⁻**) (Figure S54). Furthermore, the degradation of the green color was measured in time-resolved UV-Vis absorption experiments. Here, the decay of the absorption at a continuous excitation with light of $\lambda = 671$ nm was monitored upon the injection of a KO^tBu solution to a stirred toluene solution of **1-H** (Figure 5a).

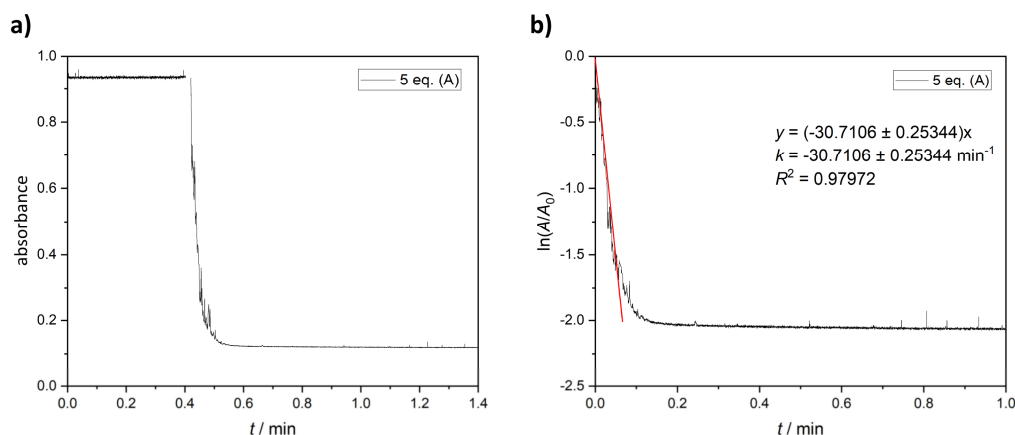


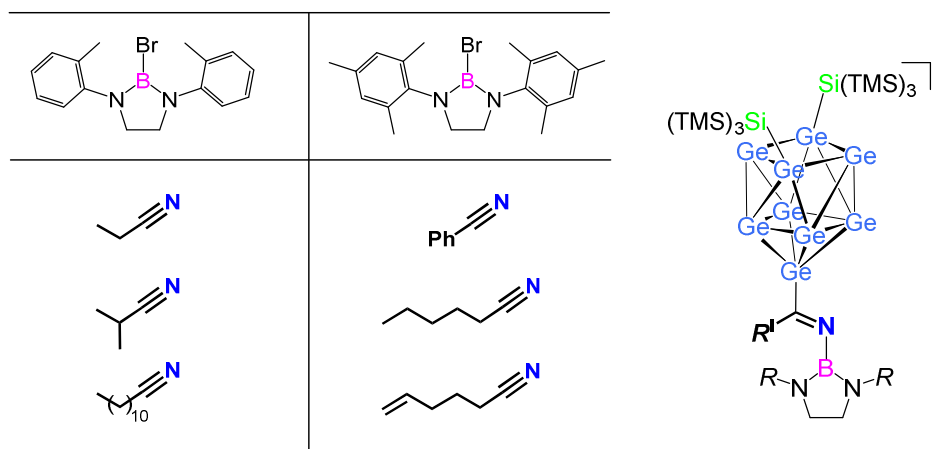
Figure 5. a) Time-dependent absorption spectrum of **1-H** recorded at a constant excitation wavelength of 671 nm. At $t = 0.4$ min 5 equivalents KO^tBu are added to the stirred solution. b) Plot for the determination of the rate constant k (-30.7 min^{-1}). Recorded data is presented in black, the linear regression is indicated by a red line.

The initial absorption was measured for approximately half a minute to assure no self-degradation occurred, before the base-containing solution was added, leading almost instantaneously to a drop in the absorption intensity. The addition of 5 and 10 equivalents of KO^tBu yielded almost identical time-dependent degradation curves (Figure S56). Thus, it is assumed that the reaction for the addition of 5 equivalents approximately follows a kinetic of pseudo-first order. Consequently, the rate constants k were derived from the equation $A = A_0 e^{-kt}$ by plotting $\ln(A/A_0)$ over t , and performing a linear regression ($A = \text{absorption}$, $k = \text{rate constant}$, $t = \text{time}$; Figures 5b and S57).^[56] The rate constant adopts values of -26.5 min^{-1} (mean value of three measurements) and -30.6 min^{-1} (single measurement), for the application of 5 and 10 equivalents of KO^tBu respectively. The respective approximate half-lives are $\ln(2)/k = 1.6$ s and 1.3 s, respectively. In conclusion, the basicity of the O^tBu⁻ anion is larger than the basicity of the imine moiety in **1-H**. For comparison, bare [Sn₉]⁴⁻ clusters show a larger basicity than O^tBu⁻, since the species [Sn₉-H]³⁻ is not deprotonated by the same base.^[11]

Variation of the Imine Moieties

The incorporation of an imine moiety between the cluster and the boranyl ligand offers the possibility for a variable introduction of organic ligands to the $[\text{Ge}_9]$ cluster core. As a proof of concept, the insertion of different imine fragments was achieved in reactions of the bromo-diazaborolidines $\text{DAB}^R\text{-Br}$ ($R = o\text{-tol}$, Mes) with the precursor $[\text{Ge}_9\{\text{Si}(\text{TMS})_3\}_2]^{2-}$ in various nitriles. An overview of the tested combinations is provided in Table 2.

Table 2. Overview of the tested nitriles for the incorporation of imine groups featuring various organic ligands between the twofold silylated cluster and the boranyl fragment. A schematic representation of the resulting monoanionic species is provided.



The successful incorporation of propionitrile, *iso*-butyronitrile, dodecanenitrile, benzonitrile, hexanenitrile, and hexenenitrile was proven by ESI-MS investigations monitoring the mass peaks of the resulting monoanionic species (Figures S27-S40). Thus, a reliable reaction protocol for the attachment of different functional groups at the $[\text{Ge}_9]$ cluster was introduced. Interestingly, the application of acrylonitrile did not lead to an incorporation of the nitrile between the cluster and the borane, but to the formation of colorless fumes and an entirely solid, so far unidentified reaction product.

The reaction with hexanenitrile and hexenenitrile was investigated in more detail. Due to the high boiling point of the nitriles it was not possible to isolate the corresponding monoanions $[\text{Ge}_9\{\text{Si}(\text{TMS})_3\}_2\{\text{R}^i\text{C}=\text{N}\}\text{-DAB}^{\text{Mes}}]^-$ [$R^i = \text{CH}_3(\text{CH}_2)_4$, “**2**”; $\text{CH}_2=\text{CH}(\text{CH}_2)_3$, “**3**”; Scheme 1d] in analogy to anion **1**⁻. Instead, oily residues were obtained after removal of the solvents under vacuum. Purifying these residues by washing was prevented through the high solubility of the ions in solvents of different polarity (MeCN to hexane). In previous studies, we have shown that the addition of Cu-carbenes $\text{NHC}^{\text{Dipp}}\text{CuCl}$ to anionic cluster species leads to the formation of neutral Cu-carbene adducts, which crystallize more readily.^[21, 28, 57-58] To prove that the ligand arrangement at the $[\text{Ge}_9]$ core is not altered upon the coordination of a Cu-carbene

fragment, a MeCN solution of **1**⁻ was reacted with NHC^{Dipp}CuCl, forming the adduct NHC^{Dipp}Cu[Ge₉{Si(TMS)₃}₂{CH₂=C–N(H)}–DAB(II)^{Dipp}] (**1b-Cu**, Figure 6a). In analogous reactions the adducts **2a-Cu**, NHC^{Dipp}Cu[Ge₉{Si(TMS)₃}₂{CH₃(CH₂)₄–C=N}–DAB^{Mes}] (Figure 6b), and **3b-Cu**, NHC^{Dipp}Cu[Ge₉{Si(TMS)₃}₂{CH₂=CH(CH₂)₂CH=CH–N(H)}–DAB^{Mes}] (Figure 6c), were isolated. For the synthesis of the compounds, the respective nitrile was removed from the reaction mixture of the diazaborolidine and the twofold silylated cluster under vacuum. Subsequently, the residues were dissolved in MeCN and the neutral Cu-adducts were crushed out as brown precipitates by the addition of a MeCN solution of NHC^{Dipp}CuCl.

Single crystals of all three Cu-containing compounds grew from concentrated solutions of the complexes, with the crystallographic data presented in the Supporting Information (Tables S2 and S3). In the compounds **1b-Cu**, **2a-Cu**, and **3b-Cu** an imine-enamine tautomerism is observed (tautomers **a** and **b**), resulting in enamines comprising shortened C1-C2 bonds and elongated C1-N1 bonds in **1b-Cu** and **3b-Cu**, while in **2a-Cu** typical bond lengths of an imine entity are observed (Table 1). According to ¹H NMR spectroscopic investigations, the enamine character of **1b-Cu** and **3b-Cu** is most probably limited to the solid-state. However, the exact reasons for the deviation between the compounds **1b-Cu** and **3b-Cu** to **2a-Cu** are not fully understood, yet. **1b-Cu** and **2a-Cu** crystallize in the triclinic space group *P* $\bar{1}$, while **3b-Cu** adopts the monoclinic space group *C2/c*. In all Cu-carbenes the [Ge₉] cores are best described as distorted tricapped trigonal prisms with approximate *C*_{2v} symmetry. Similar to the ligand arrangement in compounds **1-K** and **1-H** the ligands are bound to the three Ge atoms capping the trigonal prism. Ge-Ge and Ge-Si bond lengths are in accordance with the two latter compounds. The coinage metal coordinates to the triangular plane Ge4-Ge5-Ge8 in a η³-coordination as typically observed, revealing Ge-Cu distances in agreement with published data.^[21, 28, 57-58] Furthermore, the approximately trigonal planar arrangement of the atoms C2-C1-Ge1-N1 observed in **1-K** and **1-H** is maintained in the Cu adducts (Table 1). The terminating C=C double bond in **3b-Cu** was refined on a split position (site occupation C5A/C6A: 0.62; C5B/C6B: 0.38). The double bond character of the alkene functionality is manifested by the bond lengths C5A=C6A = 1.27(9) Å, which is shortened compared to the aliphatic bond C5-C6 in **2a-Cu** [1.44(2) Å]. However, due to severe disorder, the minor species B shows a non-reliable bond length of C5B=C6B = 1.4(2) Å.

The formation of the compounds **1b-Cu**, **2a-Cu**, and **3b-Cu** was further corroborated by ¹H NMR spectroscopic investigations showing a 1:1:1 ratio of the cluster in relation to the boranyl and NHC^{Dipp} ligands. It is noteworthy, that a splitting of the NMR signals of the hypersilyl groups and the boranyl ligand in **3b-Cu** is observed, accounting either for a dynamic exchange of cluster substituents over the cluster surface or a scrambling of vertex atoms, which processes have been described before.^[11, 13, 59-62] Variable temperature ¹H NMR data show a coalescence

of the signals at approximately 60°C (Figure S26). However, the solid-state structure of **3b-Cu** contrasts an asymmetrical substitution pattern in analogy to **1b-Cu** and **2a-Cu**. LIFDI-MS measurements (Figures S42 to S44) revealed the molecular mass peaks at m/z 2029.1 (**1b-Cu**), m/z 2003.1 (**2a-Cu**), and m/z 2001.1 (**3b-Cu**).

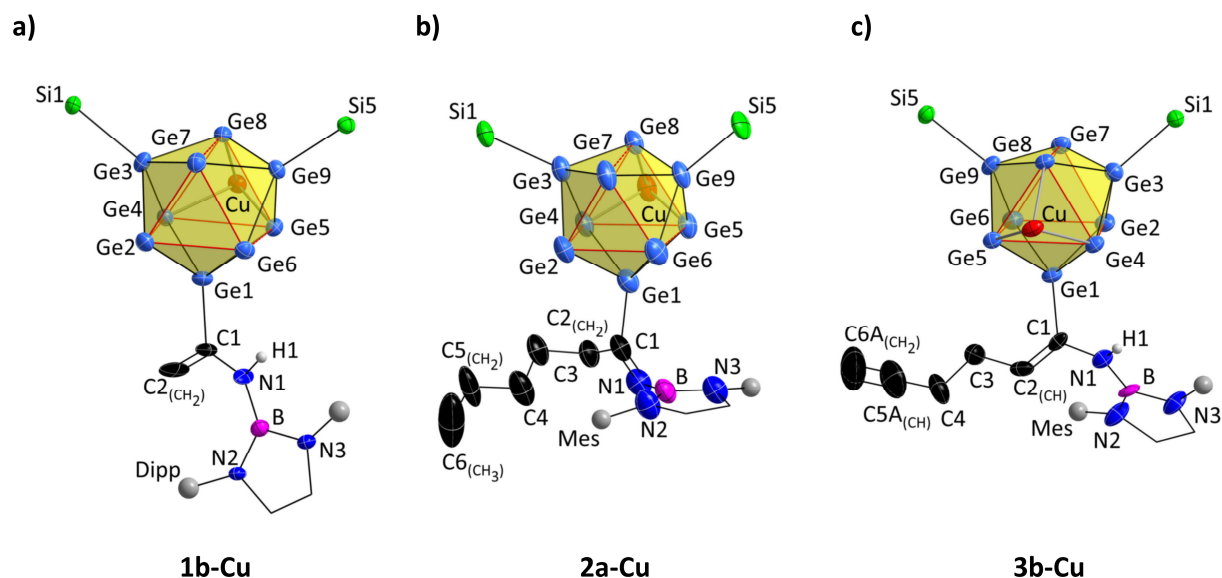


Figure 6. Molecular structures of a) **1b-Cu**, b) **2a-Cu**, and c) **3b-Cu** representing solely the major occupation of C5 and C6 (site occupation factor 0.62). All ellipsoids are shown at a 50 % probability level. For clarity reasons the TMS groups of the hypersilyl ligands as well as hydrogen atoms and co-crystallizing solvent molecules (**1b-Cu**: two toluene; **2a-Cu**: one hexane; **3b-Cu**: two C_6D_6) are omitted. The wingtip substituents Dipp and Mes are represented as grey spheres. The NHC ligands are omitted for clarity. Trigonal prismatic bases are indicated by red lines. Full ellipsoid plots of the structures are provided in the Supporting information (Figures S3-S5).

Conclusions

Herein we describe the reversible formation of the metal-free *Zintl* cluster zwitterion **1-H** by protonation of the imine functionality in anion **1⁻**. The intense green color of **1-H** is most probably caused by charge-transfer processes between the cluster and the antibonding π^* orbital of the imine moiety as corroborated by quantum chemical calculations. Furthermore, the isolation of **1b-Cu**, **2a-Cu**, and **3b-Cu** accounts for a variable introduction of organic moieties to the $[Ge_9]$ cluster core in a one-pot synthesis strategy, starting from the respective nitriles, the twofold silylated cluster and a bromo-diazaborolidine. The Cu-carbene adducts exhibit an imine-enamine tautomerism in the solid-state, leading to two tautomers **a** and **b**, which is not fully understood yet, and subject to ongoing investigations in our laboratory. The presented reactions allow for the introduction of up to two functional groups at the $[Ge_9]$ cluster, which are the enamine/imine entity as well as an olefin group. Tailoring the electronic situation at the imine fragment is subject of forthcoming studies, aiming for a targeted control of the light-absorbing properties of the cluster compound, which can be seen as a first step on the way to the design of cluster-based light harvesting molecules.

Author contributions

CW performed the experimental work and authored the manuscript. YS and AJK performed the quantum chemical calculations. FSG supported the crystallization of compounds **1-K** and **1-H**. WK refined the crystal structure data. TFF supervised the project.

Conflict of interest

There are no conflicts to declare.

Acknowledgements

The authors thank the Deutsche Forschungsgemeinschaft (DFG, German Research Foundation, project number 245845833) within International Research Training Group IRTG 2022 (ATUMS) for funding. CW thanks the Studienstiftung des Deutschen Volkes for granting a PhD scholarship. A. J. K thanks Academy of Finland for funding (grant 340584) and CSC, the Finnish IT Center for Science for computational resources. The authors thank Dr. Max Schütz and M. Sc. Maximilian Muhr (Chair of Inorganic and Metal-Organic Chemistry, Prof. Fischer, TUM) for the acquisition of LIFDI-MS data. Furthermore, the authors thank M. Sc. Lukas Niederegger (Chair of Bioinorganic Chemistry, Prof. Hess, TUM) for his help concerning all technical aspects of the UV-Vis measurements. M. Sc. Philipp Keil (Dr. Terrance Hadlington, TUM) is acknowledged for the acquisition of variable temperature NMR data.

References

- [1] C. Liu and Z.-M. Sun, *Coord. Chem. Rev.* **2019**, *382*, 32.
- [2] R. J. Wilson, N. Lichtenberger, B. Weinert and S. Dehnen, *Chem. Rev.* **2019**, *119*, 8506.
- [3] W. Klein, A. Schier and T. F. Fässler, *Molecules Meet Solids: From Wade–Mingos Clusters to Intermetallic Clusters; in: Structure and Bonding*, vol. 188, Springer, Berlin, Heidelberg, **2021**, DOI 10.1007/430_2021_82.
- [4] Y. Wang, J. E. McGrady and Z.-M. Sun, *Acc. Chem. Res.* **2021**, *54*, 1506.
- [5] A. Schnepf, *Chem. Soc. Rev.* **2007**, *36*, 745.
- [6] A. Schnepf, *New J. Chem.* **2010**, *34*, 2079.
- [7] Y. Heider and D. Scheschkewitz, *Chem. Rev.* **2021**, *121*, 9674.
- [8] S. Scharfe, F. Kraus, S. Stegmaier, A. Schier and T. F. Fässler, *Angew. Chem. Int. Ed.* **2011**, *50*, 3630.
- [9] C. Suchentrunk, J. Daniels, M. Somer, W. Carrillo-Cabrera and N. Korber, *Z. Naturforsch. B* **2005**, *60*, 277.
- [10] S. Ponou and T. F. Fässler, *Z. Anorg. Allg. Chem.* **2007**, *633*, 393.
- [11] F. S. Kocak, D. O. Downing, P. Zavalij, Y.-F. Lam, A. N. Vedernikov and B. Eichhorn, *J. Am. Chem. Soc.* **2012**, *134*, 9733.
- [12] T. Henneberger, W. Klein and T. F. Fässler, *Z. Anorg. Allg. Chem.* **2018**, *644*, 1018.
- [13] C. Lorenz, F. Hastreiter, J. Hioe, N. Lokesh, S. Gärtner, N. Korber and R. M. Gschwind, *Angew. Chem. Int. Ed.* **2018**, *57*, 12956.
- [14] C. Lorenz and N. Korber, *Crystals* **2018**, *8*, 374.
- [15] L. J. Schiegerl, A. J. Karttunen, J. Tillmann, S. Geier, G. Raudaschl-Sieber, M. Waibel and T. F. Fässler, *Angew. Chem. Int. Ed.* **2018**, *57*, 12950.
- [16] L. J. Schiegerl, A. J. Karttunen, W. Klein and T. F. Fässler, *Chem. Eur. J.* **2018**, *24*, 19171.
- [17] L. J. Schiegerl, A. J. Karttunen, W. Klein and T. F. Fässler, *Chem. Sci.* **2019**, *10*, 9130.
- [18] F. Li and S. C. Sevov, *Inorg. Chem.* **2012**, *51*, 2706.
- [19] O. Kysliak and A. Schnepf, *Dalton Trans.* **2016**, *45*, 2404.
- [20] O. Kysliak, T. Kunz and A. Schnepf, *Eur. J. Inorg. Chem.* **2017**, *2017*, 805.
- [21] C. Wallach, F. S. Geitner, A. J. Karttunen and T. F. Fässler, *Angew. Chem. Int. Ed.* **2021**, *60*, 2648.
- [22] K. Mayer, L. J. Schiegerl, T. Kratky, S. Günther and T. F. Fässler, *Chem. Commun.* **2017**, *53*, 11798.
- [23] O. Kysliak and A. Schnepf, *Z. Anorg. Allg. Chem.* **2019**, *645*, 335.
- [24] F. S. Geitner, J. V. Dums and T. F. Fässler, *J. Am. Chem. Soc.* **2017**, *139*, 11933.
- [25] F. S. Geitner, C. Wallach and T. F. Fässler, *Chem. Eur. J.* **2018**, *24*, 4103.
- [26] C. Wallach, F. S. Geitner, W. Klein and T. F. Fässler, *Chem. Eur. J.* **2019**, *25*, 12349.
- [27] O. Kysliak, C. Schrenk and A. Schnepf, *Inorg. Chem.* **2017**, *56*, 9693.
- [28] F. S. Geitner, W. Klein and T. F. Fässler, *Angew. Chem. Int. Ed.* **2018**, *57*, 14509.
- [29] C. B. Benda, H. He, W. Klein, M. Somer and T. F. Fässler, *Z. Anorg. Allg. Chem.* **2015**, *641*, 1080.
- [30] M. M. Bentlohner, S. Frischhut and T. F. Fässler, *Chem. Eur. J.* **2017**, *23*, 17089.
- [31] S. Frischhut, M. M. Bentlohner, W. Klein and T. F. Fässler, *Inorg. Chem.* **2017**, *56*, 10691.
- [32] M. M. Bentlohner, W. Klein, Z. H. Fard, L. A. Jantke and T. F. Fässler, *Angew. Chem. Int. Ed.* **2015**, *54*, 3748.
- [33] L. Yong, S. D. Hoffmann and T. F. Fässler, *Z. Anorg. Allg. Chem.* **2004**, *630*, 1977.
- [34] L. Xu and S. C. Sevov, *J. Am. Chem. Soc.* **1999**, *121*, 9245.
- [35] K. Mayer, W. Klein, S. Geier and T. F. Fässler, *Z. Anorg. Allg. Chem.* **2021**, *647*, 377.
- [36] S. Frischhut, J. G. Machado de Carvalho, A. J. Karttunen and T. F. Fässler, *Z. Anorg. Allg. Chem.* **2018**, *644*, 1337.
- [37] M. Klinger, C. Schenk, F. Henke, A. Clayborne, A. Schnepf and A.-N. Unterreiner, *Chem. Commun.* **2015**, *51*, 12278.
- [38] N. C. Michenfelder, C. Gienger, M. Dilanas, A. Schnepf and A.-N. Unterreiner, *Molecules* **2020**, *25*, 2639.
- [39] N. C. Michenfelder, C. Gienger, A. Schnepf and A.-N. Unterreiner, *Dalton Trans.* **2019**, *48*, 15577.

- [40] O. Kysliak, D. D. Nguyen, A. Z. Clayborne and A. Schnepf, *Inorg. Chem.* **2018**, *57*, 12603.
- [41] C. Wallach, F. S. Geitner and T. F. Fässler, *Chem. Sci.* **2021**, *12*, 6969.
- [42] G. P. Moss, P. A. S. Smith and D. Tavernier, *Pure Appl. Chem.* **1995**, *67*, 1307.
- [43] J. Barrau, J. Escudie and J. Satge, *Chem. Rev.* **1990**, *90*, 283.
- [44] F. Meiners, W. Saak and M. Weidenbruch, *Organometallics* **2000**, *19*, 2835.
- [45] T. L. Windus and M. S. Gordon, *J. Am. Chem. Soc.* **1992**, *114*, 9559.
- [46] M. W. Hull, A. Ugrinov, I. Petrov and S. C. Sevov, *Inorg. Chem.* **2007**, *46*, 2704.
- [47] F. H. Allen, O. Kennard, D. G. Watson, L. Brammer, A. G. Orpen and R. Taylor, *J. Chem. Soc., Perkin Trans. 2* **1987**, S1.
- [48] L. Szi-Ferenc, Z. Csaszar, G. r. Lendvay, A. Benyei, S. Balogh, B. Nanasi, G. Farkas and J. Bakos, *Organometallics* **2018**, *37*, 2203.
- [49] M. Muhr, P. Heiß, M. Schütz, R. Bühler, C. Gemel, M. H. Linden, H. B. Linden and R. A. Fischer, *Dalton Trans.* **2021**, *50*, 9031.
- [50] A. D. Becke, *Phys. Rev. A* **1988**, *38*, 3098.
- [51] F. Furche and R. Ahlrichs, *J. Phys. Chem.* **2002**, *117*, 7433.
- [52] F. Furche and D. Rappoport, *Density Functional Methods for Excited States: Equilibrium Structure and Electronic Spectra*; in: *Computational Photochemistry*, vol. 16, Elsevier: Amsterdam, The Netherlands, **2005**, ISBN: 9780080455198.
- [53] J. P. Perdew, *Phys. Rev. B* **1986**, *33*, 8822.
- [54] F. Weigend and R. Ahlrichs, *Phys. Chem. Chem. Phys.* **2005**, *7*, 3297.
- [55] A. Dreuw and M. Head-Gordon, *Chem. Rev.* **2005**, *105*, 4009.
- [56] E. V. Anslyn, D. A. Dougherty and E. V. Dougherty, *Modern Physical Organic Chemistry*, University Science Books, Sausalito, California, **2006**, ISBN 9781891389313.
- [57] F. S. Geitner and T. F. Fässler, *Eur. J. Inorg. Chem.* **2016**, *2016*, 2688.
- [58] F. S. Geitner, M. A. Giebel, A. Pöthig and T. F. Fässler, *Molecules* **2017**, *22*, 1204.
- [59] F. Li, A. Muñoz-Castro and S. C. Sevov, *Angew. Chem. Int. Ed.* **2016**, *55*, 8630.
- [60] F. Li and S. C. Sevov, *J. Am. Chem. Soc.* **2014**, *136*, 12056.
- [61] S. Frischhut, F. Kaiser, W. Klein, M. Drees, F. E. Kühn and T. F. Fässler, *Organometallics* **2018**, *37*, 4560.
- [62] F. S. Geitner and T. F. Fässler, *Inorg. Chem.* **2020**, *59*, 15218.

Charge-Transfer Processes in Functionalized [Ge₉] Clusters Based on the Reversible Formation of a Zwitterion

Christoph Wallach, Yasmin Selic, Felix S. Geitner, Wilhelm Klein, Antti J. Karttunen and Thomas F. Fässler

Supporting Information

Content	page
1. Experimental details.....	367
2. Syntheses of compounds 1 to 3.....	369
3. Crystallographic details.....	372
4. NMR spectra.....	378
5. Mass spectra.....	389
6. UV-Vis spectra.....	400
7. Kinetic studies.....	407
7. Computational details.....	412
8. References.....	421

1. Experimental details

General

All manipulations were performed under dry, oxygen-free conditions under argon atmosphere using standard Schlenk or glove box techniques. Glassware was dried prior to use by heating it *in vacuo*. The solvents were obtained from an MBraun Grubbs apparatus. [2.2.2]cryptand (Merck) and $\text{NEt}_3 \cdot \text{HCl}$ (Sigma Aldrich) were dried overnight in vacuo prior to usage. Et_2O and thf were dried over Na/benzophenone and distilled prior to usage. All other commercially available chemicals were used without further purification. K_4Ge_9 was prepared by fusion of stoichiometric amounts of the elements in stainless-steel tubes at 650 °C. The twofold silylated cluster $\text{K}_2[\text{Ge}_9\{\text{Si}(\text{TMS})_3\}_2]$,^[1] the bromo-1,3,2-diazaborole $\text{DAB}(\text{II})^{\text{Dipp}}\text{-Br}$ and bromo-1,3,2-diazaborolodine $\text{DAB}^{\text{R}}\text{-Br}$ ($\text{R} = \text{o-tol}, \text{Mes}$),^[2-3] the imidazolium salt $\text{NHC}^{\text{Dipp}} \cdot \text{HCl}$, as well as the respective NHC complex $\text{NHC}^{\text{Dipp}}\text{CuCl}$ ^[4-5] were prepared according to modified literature procedures.

Single crystal structure determination

The air- and moisture-sensitive crystals of **1** to **3** were transferred from the mother liquor into perfluoroalkyl ether oil in an argon filled glove box. For diffraction data collection, the single crystals were fixed on a glass capillary and positioned in a 150 K cold N_2 gas stream.^[6] Data collection was performed with a STOE StadiVari diffractometer ($\text{MoK}\alpha$ radiation) equipped with a DECTRIS PILATUS 300K detector. Structures were solved by Direct Methods (SHELXS-97) and refined by full-matrix least-squares calculations against F^2 (SHELXL-2018).^[7] The positions of the hydrogen atoms were calculated and refined using a riding model. Unless stated otherwise, all non-hydrogen atoms were treated with anisotropic displacement parameters. The supplementary crystallographic data for this paper have been deposited with the Cambridge Structural database and are available free of charge via www.ccdc.cam.ac.uk/data_request/cif by quoting the deposition numbers CCDC 2161506 (**1-K**), CCDC 2161507 (**1-H**), CCDC 2161508 (**1b-Cu**), CCDC 2161509 (**2a-Cu**), and CCDC 2161510 (**3b-Cu**). The crystallographic data of compounds **1** to **3** are summarized in Table S1 and S2.

In compound **1-K** the atoms of one hypersilyl ligand were refined at two split positions each with site occupation factors of 57.7 % and 42.3 %, respectively. Another SiMe_3 group of the second hypersilyl ligand and one CH_3 unit of an $i\text{Pr}$ group also show some disorder and were refined including ISOR and DFIX restraints. One diethyl ether molecule, coordinating the K^+ ion, was located from the electron density map and could be refined including ISOR restraints. A second ether molecule could not be stabilized during the refinement and, thus, its electron density was treated with the Platon Squeeze function.^[8] In **1-H** again one hypersilyl group is disordered and was refined at split positions (s.o.f.: 83.5 %/16.5 %) including ISOR restraints for three C atoms. One hexane solvent molecule was treated with Platon Squeeze. In **1b-Cu** one $i\text{Pr}$ group is refined at split positions (s.o.f.: 64.5 %/35.5 %) and one of their methyl groups as well as several atoms of the toluene solvent molecules had to be restrained with ISOR commands. In **3b-Cu** the two terminal C atoms of the alkyl chain are refined at split positions (s.o.f.: 62.0 %/38.0 %) and were fixed including one DFIX restraint. Additional ISOR restraints were applied for two methyl-C atoms of different $i\text{Pr}$ groups and some atoms of the co-crystallizing benzene molecules.

NMR spectroscopy

NMR spectra were measured on a Bruker Avance Ultrashield 400 MHz spectrometer. The ^1H NMR and ^{13}C NMR spectra were calibrated using the residual signals of the used deuterated solvents.^[9] Chemical shifts are reported in parts per million (ppm) relative to TMS, with the solvent peaks serving as internal reference. Abbreviations for signal multiplicities are: singlet (s), doublet (d), triplet (t), heptet (hept), broad signal (br).

Ultraviolet-visible spectroscopy

UV-Vis spectra were recorded on an Agilent Cary 60 UV-Visible spectrophotometer at the Chair of Bioinorganic Chemistry (Prof. Hess, TUM). The absorption spectra were recorded with a step size of 1 nm. Before the measurements, the absorption spectra of the respective solvents were recorded and used for the automated baseline correction in the measuring program Cary WinUV Scan Application (Agilent Technologies).

For kinetic studies the solutions were stirred with a magnetic stirring bar inside the cuvette at approximately 2500 rpm. The solutions were excited with a wavelength of 671 nm and the absorption was recorded every 0.0125 s, while the base KO^tBu was injected. Data evaluation was performed using the Cary WinUV Kinetics Application (Agilent Technologies) and spectra were plotted using the programs OriginPro2021 (Origin Lab) and Excel (Microsoft 365).

Electrospray ionization mass spectrometry

ESI-MS analyses were performed on a Bruker Daltonic HCT mass spectrometer (injection speed: 240 $\mu\text{L}/\text{h}$, negative-ion mode, 300 °C dry gas temperature) in thf. The data evaluation and the calculation of the theoretical isotope distribution was carried out using the Bruker Compass Data Analysis 4.0 SP 5 program (Bruker). Spectra were plotted using OriginPro2021 (Origin Lab) and Excel (Microsoft 365).

Liquid injection field desorption ionization (LIFDI) mass spectrometry

LIFDI-MS measurements were performed using an ExactiveTM PlusOrbitrap system from the Thermo Fisher Scientific company equipped with an ion source from Linden CMS at the Chair of Inorganic and Metal-Organic Chemistry (Prof. Fischer, TUM).^[10] The samples were dissolved in toluene in an Ar filled glovebox and applied on a graphite dendrite-coated tungsten wire. As ionization voltage 10 kV were adjusted. Spectra were acquired in the positive ion mode (radical cations). The theoretical isotope distribution was calculated using enviPat Web 2.4 on <https://www.envipat.eawag.ch/>.

Elemental analysis

Elemental analyses were carried out in the microanalytical laboratory of the Chemistry Department of the Technische Universität München. Analyses of C, H and N were performed in a combustion analyzer (EURO EA, HEKA tech).

2. Syntheses of compounds 1 to 3

Synthesis of $\text{K}[\text{Ge}_9\{\text{Si}(\text{TMS})_3\}_2\{\text{CH}_3\text{C}=\text{N}\}\text{-DAB(II)}^{\text{Dipp}}] \cdot 2 \text{Et}_2\text{O}$ (**1-K**)

In a typical experiment equimolar amounts of $\text{K}_2[\text{Ge}_9\{\text{Si}(\text{TMS})_3\}_2]$ (92.0 mg, 0.075 mmol, 1 eq.) and $\text{DAB(II)}^{\text{Dipp}}\text{-Br}$ (35.0 mg, 0.075 mmol, 1 eq.) were weighed into a Schlenk tube in the glove box, and MeCN (2 mL) was added. After stirring for 4 d at 40 °C, the solvent was removed in vacuo yielding a brown oil. The residue was treated with diethyl ether (3 · 3 mL, addition and removal under vacuum), yielding a brown solid. Subsequently, the solid was dissolved in diethyl ether (3 mL) giving a dark red solution. Upon slow evaporation of the solvent at room temperature, orange block-shaped crystals of the product **1-K** were formed (62 mg, 38 μmol , 51 %).

^1H NMR (400 MHz, 298 K, $\text{thf-}d_8$): δ [ppm] = 7.13-7.08 (m, 2H, $\text{CH}_{\text{DAB(p)}}$), 7.06-7.03 (m, 4H, $\text{CH}_{\text{DAB(m)}}$), 5.99 (s, 2H, $\text{CH}_{\text{DAB-N}}$), 3.21 (hept, $^3J_{\text{HH}} = 6.8$ Hz, 4H, CH_{iPr}), 1.83 (s, 3H, Me_{MeCN}), 1.21 (d, $^3J_{\text{HH}} = 6.8$ Hz, 12H, Me_{DAB}), 1.11 (d, $^3J_{\text{HH}} = 6.8$ Hz, 12H, Me_{DAB}), 0.22 (s, Me_{TMS}). **^{13}C NMR** (101 MHz, 298 K, $\text{thf-}d_8$): δ [ppm] = 146.97 (s, $\text{C}_{\text{DAB-N}}$), 139.83 (s, $\text{C}_{\text{DAB(o)}}$), 127.16 (s, $\text{CH}_{\text{DAB(m)}}$), 123.76 (s, $\text{CH}_{\text{DAB(p)}}$), 118.63 (s, $\text{CH}_{\text{DAB-N}}$), 66.37 (s, C_{MeCN}), 43.42 (s, Me_{MeCN}), 28.89 (s, Me_{DAB}), 15.75 (s, CH_{iPr}), 3.22 (s, Me_{TMS}). **$^{29}\text{Si-INEPT}$ NMR** (79 MHz, 298 K, $\text{thf-}d_8$): δ [ppm] = -9.65 (s, Si_{TMS}), -107.64 (s, Si_{Ge9}). **^{11}B NMR** (128 MHz, 298 K, $\text{thf-}d_8$): δ [ppm] = 22.29 (br). **Elemental analysis** (filtered over hexane): anal. calcd. for $\text{Ge}_9\text{Si}_8\text{BC}_{46}\text{H}_{93}\text{N}_3\text{K} \cdot 0.25$ hex: C, 34.83; H, 5.94; N, 2.57; found: C, 34.83; H, 6.18; N, 2.53. **ESI-MS**: m/z 1577.8 (**1⁻**).

Synthesis of $[\text{Ge}_9\{\text{Si}(\text{TMS})_3\}_2\{\text{CH}_3\text{C}=\text{N(H)}\}\text{-DAB(II)}^{\text{Dipp}}] \cdot \text{hex}$ (**1-H**)

In a typical experiment equimolar amounts of $\text{K}_2[\text{Ge}_9\{\text{Si}(\text{TMS})_3\}_2]$ (92.0 mg, 0.075 mmol, 1 eq.) and $\text{DAB(II)}^{\text{Dipp}}\text{-Br}$ (35.0 mg, 0.075 mmol, 1 eq.) were weighed into a Schlenk tube in the glove box and MeCN (2 mL) was added. After stirring for 4 d at 40 °C, the solvent was removed in vacuo yielding a brown oil (crude product **1-K**). The residue was redissolved in toluene (2 mL) and added via a syringe filter to solid $\text{NEt}_3 \cdot \text{HCl}$ (10.3 mg, 0.075 mmol, 1 eq.). Stirring at room temperature overnight resulted in a deep green solution, which was filtered to remove remaining solids, before the solvent was removed in vacuo. The obtained green residue was treated with hexane (2 · 5 mL, addition and removal under vacuum) yielding a green solid. Dissolution in hexane (3 mL) and storage in a freezer at -40 °C gave dark green crystals of the product (36 mg, 24 μmol , 32 %).

^1H NMR (400 MHz, 298 K, $\text{thf-}d_8$): δ [ppm] = 9.82 (s, 1H, NH), 7.42-7.37 (m, 2H, $\text{CH}_{\text{DAB(p)}}$), 7.32-7.28 (m, 4H, $\text{CH}_{\text{DAB(m)}}$), 6.37 (s, 2H, $\text{CH}_{\text{DAB-N}}$), 2.78 (hept, $^3J_{\text{HH}} = 6.8$ Hz, 4H, CH_{iPr}), 1.27 (s, 3H, Me_{MeCN}), 1.16 (d, $^3J_{\text{HH}} = 6.8$ Hz, 24H, Me_{DAB}), 0.28 (s, Me_{TMS}). **^{13}C NMR** (101 MHz, 298 K, $\text{thf-}d_8$): δ [ppm] = 146.42 (s, $\text{C}_{\text{DAB-N}}$), 136.58 (s, $\text{C}_{\text{DAB(o)}}$), 129.71 (s, $\text{CH}_{\text{DAB(p)}}$), 125.19 (s, $\text{CH}_{\text{DAB(m)}}$), 120.44 (s, $\text{CH}_{\text{DAB-N}}$), 34.85 (s, Me_{MeCN}), 29.48 (s, CH_{iPr}), 24.53 (s, Me_{DAB}), 3.02 (s, Me_{TMS}). **$^{29}\text{Si-INEPT}$ NMR** (79 MHz, 298 K, $\text{thf-}d_8$): δ [ppm] = -8.56 (s, Si_{TMS}), -98.24 (s, Si_{Ge9}). **^{11}B NMR** (128 MHz, 298 K, $\text{thf-}d_8$): δ [ppm] = 18.58 (br). **Elemental analysis**: anal. calcd. for $\text{Ge}_9\text{Si}_8\text{BC}_{46}\text{H}_{94}\text{N}_3$: C, 35.00; H, 6.00; N, 2.66; found: C, 35.38; H, 6.06; N, 2.78. **LIFDI-MS**: m/z 1578.9.

Synthesis of NHC^{Dipp}Cu[Ge₉{Si(TMS)₃}₂{CH₂=C–N(H)}–DAB(II)^{Dipp}] · 2 tol (1b-Cu)

In a typical experiment MeCN solutions (2 mL each) of **1-K** (81 mg, 0.050 mmol, 1 eq.) and CuNHC^{Dipp}Cl (24.3 mg, 0.050 mmol, 1 eq.) were prepared. The latter solution was added dropwise to the red MeCN solution containing **1-K** under permanent shaking of the flask. Immediately, the formation of a light brown precipitate was observed. The precipitate was allowed to settle for 15 minutes, and subsequently the remaining orange supernatant solution was filtered off. The residue was washed with MeCN (3 · 3 mL), and afterwards remaining trace amounts of MeCN were removed under dynamic vacuum. The residue was redissolved in toluene (3 mL), the deep red solution was filtered, concentrated to half of its original volume, and stored in a freezer at -40 °C for crystallization. Dark red single crystals of the product **1b-Cu** were obtained after three weeks (58 mg, 29 μmol, 39 %).

¹H NMR (400 MHz, 298 K, thf-*d*₈): δ [ppm] = 7.35 (s, 2H, CH_{DAB(p)}), 7.32-7.29 (m, 2H, CH_{CuDipp(p)}), 7.27-7.23 (m, 4H, CH_{DAB(m)}), 7.22 (s, 2H, CH_{CuDipp-N}), 7.18-7.16 (m, 4H, CH_{CuDipp(m)}), 5.99 (s, 2H, CH_{DAB-N}), 3.19 (hept, ³J_{HH} = 6.9 Hz, 4H, CH_{DAB-iPr}), 2.82 (hept, ³J_{HH} = 6.9 Hz, 4H, CH_{Cu-Dipp-iPr}), 2.31 (s, 3H, Me_{MeCN}), 1.42 (d, ³J_{HH} = 6.9 Hz, 12H, Me_{CuDipp}), 1.28 (d, ³J_{HH} = 6.9 Hz, 12H, Me_{DAB}), 1.19 (d, ³J_{HH} = 6.9 Hz, 12H, Me_{DAB}), 1.14 (d, ³J_{HH} = 6.9 Hz, 12H, Me_{CuDipp}), 0.15 (s, 54H, Me_{TMS}). **¹³C NMR** (101 MHz, 298 K, thf-*d*₈): δ [ppm] = 147.04 (s, C_{CuDipp-N}), 146.30 (s, C_{DAB-N}), 139.52 (s, C_{DAB(o)}), 136.34 (s, CH_{CuDipp(m)}), 131.00 (s, CH_{DAB(m)}), 127.72 (s, CH_{CuDipp-N}), 125.19 (s, CH_{CuDipp(p)}), 124.06 (s, CH_{DAB(p)}), 119.13 (s, CH_{DAB-N}), 43.30 (s, Me_{MeCN}), 29.65 (s, Me_{CuDipp-iPr}), 29.05 (s, Me_{DAB-iPr}), 3.22 (s, Me_{TMS}). **²⁹Si-INEPT NMR** (79 MHz, 298 K, thf-*d*₈): δ [ppm] = -9.53 (s, Si_{TMS}), -104.60 (s, Si_{Ge9}). **¹¹B NMR** (128 MHz, 298 K, thf-*d*₈): δ [ppm] = 20.31 (br). **Elemental analysis**: anal. calcd. for Ge₉Si₈BC₇₃H₁₂₉CuN₅ · 2 tol: C, 43.16; H, 6.50; N, 3.45; found: C, 43.69; H, 6.47; N, 3.63. **LIFDI-MS**: *m/z* 2029.1.

Synthesis of NHC^{Dipp}Cu[Ge₉{Si(TMS)₃}₂{CH₃(CH₂)₄–C=N}–DAB^{Mes}] · hex (2a-Cu)

In a typical experiment equimolar amounts of K₂[Ge₉{Si(TMS)₃}₂] (92.0 mg, 0.075 mmol, 1 eq.) and DAB^{Mes}-Br (37.3 mg, 0.097 mmol, 1.3 eq.) were weighed into a Schlenk tube in the glove box, and hexanenitrile (2 mL) was added. After stirring over night, the solvent was removed in vacuo yielding a brown oil. The residue was redissolved in MeCN (2 mL) and filtered. To the filtrate a MeCN solution (1 mL) of CuNHC^{Dipp}Cl (36.5 mg, 0.075 mmol, 1 eq.) was added, leading to the formation of a light brown precipitate. The obtained solid was washed with MeCN (3 · 3 mL), and subsequently dried under reduced pressure. The light brown powder was dissolved in hexane (2 mL) leading to a red solution, which was filtered, concentrated, and kept for crystallization at r.t. After two days, single crystals of **2a-Cu** suitable for single crystal diffraction were obtained (55 mg, 27 μmol, 37 %).

¹H NMR (400 MHz, 298 K, thf-*d*₈): δ [ppm] = 7.78 – 7.65 (m, 4H, CH_{CuDipp(m)}), 7.31 (s, 2H, CH_{CuDipp-N}), 7.24-7.22 (m, 4H, CH_{DAB(m)}), 7.21 (s, 2H, CH_{CuDipp(p)}), 6.81 (s, 2H, CH_{2 DAB-N}), 2.80 (hept, ³J_{HH} = 6.9 Hz, 12H, CH_{iPr}), 2.38 (s, 12H, Me_{DAB}), 2.24 (s, 6H, Me_{DAB}), 1.33 (d, ³J_{HH} = 6.9 Hz, 12H, Me_{CuDipp}), 1.12 (d, ³J_{HH} = 6.9 Hz, 12H, Me_{CuDipp}), 0.90 – 0.84 (m, 8H, CH_{2 hexanenitrile}), 0.76 (t, ³J_{HH} = 7.3 Hz, 3H, Me_{hexanenitrile}), 0.17 (s, 54H, Me_{TMS}). **¹³C NMR** (101 MHz, 298 K, thf-*d*₈): δ [ppm] = 146.26 (s, C_{CuDipp-N}), 141.10 (s, C_{DAB-N}), 137.29 (s, C_{CuDipp(o)}), 136.33 (s, C_{DAB(o)}), 134.32 (s, C_{DAB(p)}), 131.01 (s, CH_{CuDipp-N}), 129.79 (s, CH_{CuDipp(p)}), 125.25 (s, CH_{DAB(o)/CuDipp(o)}), 124.01 (s, CH_{2 DAB-N}), 50.54 (s, C_{hexanenitrile}), 32.09 (s, CH_{iPr}), 29.99 (s, Me_{iPr}), 23.76 (s, CH₂

hexanenitrile), 23.00 (s, CH₂ hexanenitrile), 21.26 (s, Me_{DAB}), 20.43 (s, CH₂ hexanenitrile), 19.83 (s, Me_{DAB}), 14.53 (s, CH₂ hexanenitrile), 11.79 (s, Me_{hexanenitrile}), 3.28 (s, Me_{TMS}). **²⁹Si-INEPT NMR** (79 MHz, 298 K, thf-*d*₈): δ [ppm] = -9.56 (s, Si_{TMS}), -104.81 (s, Si_{Ge9}). **¹¹B NMR** (128 MHz, 298 K, thf-*d*₈): δ [ppm] = 23.32 (br). **Elemental analysis:** anal. calcd. for Ge₉Si₈BC₇₁H₁₂₇CuN₅: C, 42.56; H, 6.39; N, 3.50; found: C, 42.79; H, 6.59; N, 3.38. **LIFDI-MS:** *m/z* 2003.1. **ESI-MS:** *m/z* 1551.8 [Ge₉{Si(TMS)₃}₂{CH₃(CH₂)₄C=N}-DAB^{Mes}]^(2⁻).

Synthesis of NHC^{Dipp}Cu[Ge₉{Si(TMS)₃}₂{CH₂=CH(CH₂)₂CH=CH-N(H)}-DAB^{Mes}] · 2 C₆D₆ (3b-Cu)

In a typical experiment equimolar amounts of K₂[Ge₉{Si(TMS)₃}₂] (92.0 mg, 0.075 mmol, 1 eq.) and DAB^{Mes}-Br (37.3 mg, 0.097 mmol, 1.3 eq.) were weighted into a Schlenk tube in the glove box, and hexanenitrile (2 mL) was added. After stirring over night, the solvent was removed in vacuo yielding a brown oil. The residue was redissolved in MeCN (2 mL) and filtered. To the filtrate a MeCN solution (1 mL) of CuNHC^{Dipp}Cl (36.5 mg, 0.075 mmol, 1 eq.) was added, leading to the formation of a dark brown precipitate. The obtained solid was washed with MeCN (3 · 3 mL), and subsequently dried under reduced pressure. The light brown powder was redissolved in deuterated benzene (1 mL) forming a red solution, which was filtered, concentrated, and kept for crystallization at r.t. After four days, single crystals of **3b-Cu** suitable for single crystal diffraction were obtained (49 mg, 24 μmol, 32 %).

In the ¹H NMR spectrum the signal intensity of the aromatic protons is slightly too low, the reason why is not fully understood. However, all other signal intensities are congruent with the results of the single crystal structure determination and LIFDI-MS measurements. Two CH₂ groups of the imine hydrocarbon chain are hidden by the methyl groups of the [NHC^{Dipp}Cu]⁺ fragment. In the ¹³C NMR spectrum not all C atoms of the imine hydrocarbon chain could be identified, and the signal assignment was partially hampered by a signal splitting of the DAB^{Mes} moiety.

¹H NMR (400 MHz, 298 K, thf-*d*₈): δ [ppm] = 7.41-7.31 (m, 4H, CH_{CuDipp(m)}), 7.29 (s, 1H, CH_{CuDipp(N)}), 7.26 (s, 1H, CH_{CuDipp(N)}), 7.24-7.21 (m, 2H, CH_{CuDipp(p)}), 7.17-7.08 (m, 4H, CH_{DAB(m)}), 6.89 (s, 2H, CH_{2 DAB-N}), 6.76 (s, 2H, CH_{2 DAB-N}), 5.69-5.44 (m, 1H, CH_{hexanenitrile}), 4.84-4.68 (m, 2H, CH_{2 hexanenitrile}), 2.76 (hept, ³J_{HH} = 6.9 Hz, 4H, CH_{CuDipp}), 2.37 (d, ³J_{HH} = 7.1 Hz, 12H, Me_{DAB}), 2.28 (s, 3H, Me_{DAB}), 2.23 (s, 3H, Me_{DAB}), 1.71-1.67 (m, 2H, CH_{2 hexanenitrile}), 1.36 (d, ³J_{HH} = 6.9 Hz, 6H, Me_{CuDipp}), 1.27 (d, ³J_{HH} = 6.9 Hz, 6H, Me_{CuDipp}), 1.11 (d, ³J_{HH} = 6.9 Hz, 12H, Me_{CuDipp}), 0.18 (s, 27H, Me_{TMS}), 0.16 (s, 27H, Me_{TMS}). **¹³C NMR** (101 MHz, 298 K, thf-*d*₈): δ [ppm] = 146.19 (C_{CuDipp-N}), 141.52 (C_{DAB-N}), 140.81 (C_{CuDipp(o)}), 140.35 (s, CH_{hexanenitrile}), 137.58 (C_{DAB(o)}), 137.41 (C_{DAB(o)}), 136.32 (C_{DAB(p)}), 136.19 (C_{DAB(p)}), 131.26 (CH_{CuDipp(m)}), 130.96 (CH_{CuDipp(m)}), 129.97 (CH_{2 DAB-N}), 125.28 (CH_{DAB(m)}), 125.05 (CH_{DAB(m)}), 124.16 (CH_{CuDipp-N}), 123.75 (CH_{Dipp(p)}), 113.79 (s, CH_{2 hexanenitrile}), 51.24 (s, C_{hexanenitrile}), 34.75 (s, CH_{2 hexanenitrile}), 32.52 (s, CH_{iPr}), 29.65 (s, Me_{iPr}), 21.32 (s, Me_{DAB}), 21.18 (Me_{DAB}), 19.82 (Me_{DAB}), 3.37 (s, Me_{TMS}), 3.23 (s, Me_{TMS}). **²⁹Si-INEPT NMR** (79 MHz, 298 K, thf-*d*₈): δ [ppm] = -9.54 (s, Si_{TMS}), -9.69 (s, Si_{TMS}), -104.53 (s, Si_{Ge9}), -105.16 (s, Si_{Ge9}). **¹¹B NMR** (128 MHz, 298 K, thf-*d*₈): δ [ppm] = 14.63 (br). **Elemental analysis:** anal. calcd. for Ge₉Si₈BC₇₁H₁₂₅CuN₅: C, 42.61; H, 6.30; N, 3.50; found: C, 41.97; H, 6.10; N, 3.40. **LIFDI-MS:** *m/z* 2001.1. **ESI-MS:** *m/z* 1549.8 [Ge₉{Si(TMS)₃}₂{CH₂=CH(CH₂)₃C=N}-DAB^{Mes}]^(3⁻).

3. Crystallographic details

Table S1. Crystallographic data of 1-K and 1-H.

compound	1-K	1-H
formula	C ₄₆ H ₉₃ BGe ₉ KN ₃ Si ₈ · 2 Et ₂ O	C ₄₆ H ₉₄ BGe ₉ N ₃ Si ₈ · hex
fw [g·mol ⁻¹]	1690.29	1578.08
space group	<i>P</i> $\bar{1}$	<i>P</i> $\bar{1}$
<i>a</i> [Å]	13.0188(5)	9.7366(3)
<i>b</i> [Å]	13.3953(6)	16.2389(5)
<i>c</i> [Å]	24.370(1)	25.2269(7)
α [°]	100.647(4)	91.344(2)
β [°]	95.564(3)	96.901(2)
γ [°]	96.878(3)	98.417(3)
<i>V</i> [Å ³]	4115.6(3)	3913.7(2)
<i>Z</i>	2	2
<i>T</i> [K]	150(2)	150(2)
λ [Å]	Mo <i>K</i> α	Mo <i>K</i> α
ρ_{calcd} [g·cm ⁻³]	1.424	1.412
μ [mm ⁻¹]	3.439	3.558
collected reflections	82563	72763
indep. reflections	16169	15330
<i>R</i> _{int} / <i>R</i> _σ	0.0548/0.0379	0.0477/0.0307
parameters / restraints	771/167	720/117
<i>R</i> ₁ [<i>I</i> > 2 σ (<i>I</i>) / all data]	0.0485/0.0769	0.0301/0.0440
w <i>R</i> ₂ [<i>I</i> > 2 σ (<i>I</i>) / all data]	0.1054/0.1199	0.0656/0.0726
goodness of fit	1.015	1.045
max./min. diff. el. density [e·Å ⁻³]	1.52/-1.40	0.58/-0.66
depository no.	CCDC 2161506	CCDC 2161507

Table S2. Crystallographic data of **1b-Cu**, **2a-Cu**, and **3b-Cu**.

compound	1b-Cu	2a-Cu	3b-Cu
formula	C ₇₃ H ₁₂₉ BCuGe ₉ N ₅ Si ₈ · 2 tol	C ₇₁ H ₁₂₇ BCuGe ₉ N ₅ Si ₈ · hex	C ₇₁ H ₁₂₅ BCuGe ₉ N ₅ Si ₈ · 2 C ₆ D ₆
fw [g·mol ⁻¹]	2213.45	2089.32	2168.41
space group	<i>P</i> $\bar{1}$	<i>P</i> $\bar{1}$	<i>C2/c</i>
a [Å]	13.3505(7)	13.7268(3)	56.227(1)
b [Å]	15.350(1)	14.6165(4)	13.2997(3)
c [Å]	29.600(2)	27.3953(8)	28.5604(6)
α [°]	79.344(5)	75.936(2)	90
β [°]	88.017(5)	84.735(2)	103.903(2)
γ [°]	66.280(4)	73.107(2)	90
V [Å ³]	5452.5(6)	5100.4(2)	20731.9(8)
Z	2	2	2
T [K]	150(2)	150(2)	150(2)
λ [Å]	Mo <i>K</i> α	Mo <i>K</i> α	Mo <i>K</i> α
ρ_{calcd} [g·cm ⁻³]	1.348	1.360	1.390
μ [mm ⁻¹]	2.761	2.947	2.903
collected reflections	107634	86840	189918
indep. reflections	21410	19902	19584
$R_{\text{int}} / R_{\sigma}$	0.2091/0.1775	0.1795/0.1403	0.2077/0.1260
parameters / restraints	1045/60	916/0	1003/43
R_1 [$I > 2 \sigma(I)$ / all data]	0.0739/0.1837	0.0878/0.1681	0.0810/0.1680
wR_2 [$I > 2 \sigma(I)$ / all data]	0.1324/0.1685	0.2009/0.2425	0.1707/0.2055
goodness of fit	1.015	1.019	1.057
max./min. diff. el. density [e·Å ⁻³]	0.78/-0.81	1.93/-1.10	0.99/-0.70
depository no.	CCDC 2161508	CCDC 2161509	CCDC 2161510

Table S3. Selected distances and angles in compounds **1** to **3**. *: H atom refined without restraints; **: H atom refined with a restrained distance (HFIX command). *R* = organic ligands at the imine side-chain. H2 = hydrogen atom at C2.

Compound	1-K	1-H	1b-Cu	2a-Cu	3b-Cu
bond	distance [Å]	distance [Å]	distance [Å]	distance [Å]	distance [Å]
Ge1-Ge2	2.5278(8)	2.5570(6)	2.541(2)	2.554(2)	2.554(2)
Ge1-Ge4	2.5312(8)	2.5292(5)	2.487(2)	2.512(2)	2.499(2)
Ge1-Ge5	2.5365(8)	2.5533(6)	2.516(2)	2.501(2)	2.504(2)
Ge1-Ge6	2.5340(8)	2.5567(5)	2.558(2)	2.529(2)	2.561(2)
Ge2-Ge3	2.5217(7)	2.5342(4)	2.571(2)	2.583(2)	2.563(2)
Ge2-Ge6	2.6633(8)	2.5724(5)	2.695(2)	2.730 (2)	2.692(2)
Ge2-Ge7	2.6714(8)	2.7253(5)	2.613(2)	2.642(2)	2.598(2)
Ge3-Ge4	2.5398(8)	2.5496(4)	2.512(2)	2.503(2)	2.507(2)
Ge3-Ge7	2.5508(8)	2.5670(4)	2.568(2)	2.549(2)	2.562(2)
Ge3-Ge8	2.5436(8)	2.5486(4)	2.538(2)	2.511(1)	2.520(2)
Ge4-Ge5	2.6491(9)	2.5861(4)	2.991(2)	2.991(1)	3.012(2)
Ge4-Ge8	2.6989(9)	2.7192(4)	2.813(2)	2.806(2)	2.812(2)
Ge5-Ge8	2.540(1)	2.7337(5)	2.828(2)	2.823(2)	2.837(2)
Ge5-Ge9	2.4986(8)	2.5481(5)	2.505(2)	2.509(2)	2.506(2)
Ge6-Ge7	2.6654(8)	2.7134(4)	2.673(2)	2.620(2)	2.644(2)
Ge6-Ge9	2.4986(8)	2.5464(5)	2.563(2)	2.571(2)	2.570(2)
Ge7-Ge9	2.5587(8)	2.5623(5)	2.556(2)	2.560(2)	2.560(2)
Ge8-Ge9	2.5392(9)	2.5563(4)	2.535(2)	2.530(2)	2.517(2)
Ge1-C1	1.985(5)	1.912(3)	1.947(9)	2.03(1)	1.97(1)
Ge3-Si1	2.369(1)	2.3790(8)	2.385(3)	2.388(3)	2.381(3)
Ge9-Si5(A/B)	2.472(4) (A) 2.283(5) (B)	2.370(3) (A) 2.43(2) (B)	2.387(3)	2.380(3)	2.391(3)
Ge2-Ge4	3.562(1)	3.732(1)	3.483(2)	3.133(2)	3.398(2)
Ge5-Ge6	3.515(1)	3.760(1)	3.227(2)	3.363(2)	3.247(2)
Ge7-Ge8	3.212(1)	3.052(1)	3.430(2)	3.575(2)	3.463(2)
C1-C2	1.501(7)	1.487(4)	1.33(1)	1.50(1)	1.35(1)
C1-N1	1.280(6)	1.325(4)	1.38(1)	1.25(1)	1.39(1)
B1-N1	1.448(6)	1.464(4)	1.45(1)	1.42(2)	1.46(1)
B1-N2	1.447(6)	1.421(4)	1.42(1)	1.41(2)	1.39(2)
B1-N3	1.436(6)	1.422(4)	1.44(1)	1.42(2)	1.44(2)
Cu-Ge4	-	-	2.508(2)	2.517(2)	2.547(2)
Cu-Ge5	-	-	2.549(2)	2.534(2)	2.530(2)
Cu-Ge8	-	-	2.535(2)	2.475(2)	2.475(2)
atoms	angle [°]	angle [°]	angle [°]	angle [°]	angle [°]
C1-C2-R	109.5	109.5	120.1(4) **	113.6(9)	128.5(1)
C1-C2-H2	109.5	109.5	119.3(5) **	108.9	115.0(4) **
C2-C1-N1	124.6(4)	119.1(3)	124.4(9)	121.4(1)	122.6(1)
C2-C1-Ge1	115.1(3)	122.3(2)	119.6(8)	114.6(9)	122.5(8)
N1-C1-Ge1	120.3(3)	118.6(2)	116.1(7)	123.9(9)	114.8(8)
C1-N1-B1	126.0(4)	137.2(3)	135.8(8)	137.7(1)	130.9(10)
C1-N1-H1	-	113(2) *	112.1(4) **	-	113.9(4) **
B1-N1-H1	-	110(2) *	112.0(4) **	-	114.0(6) **

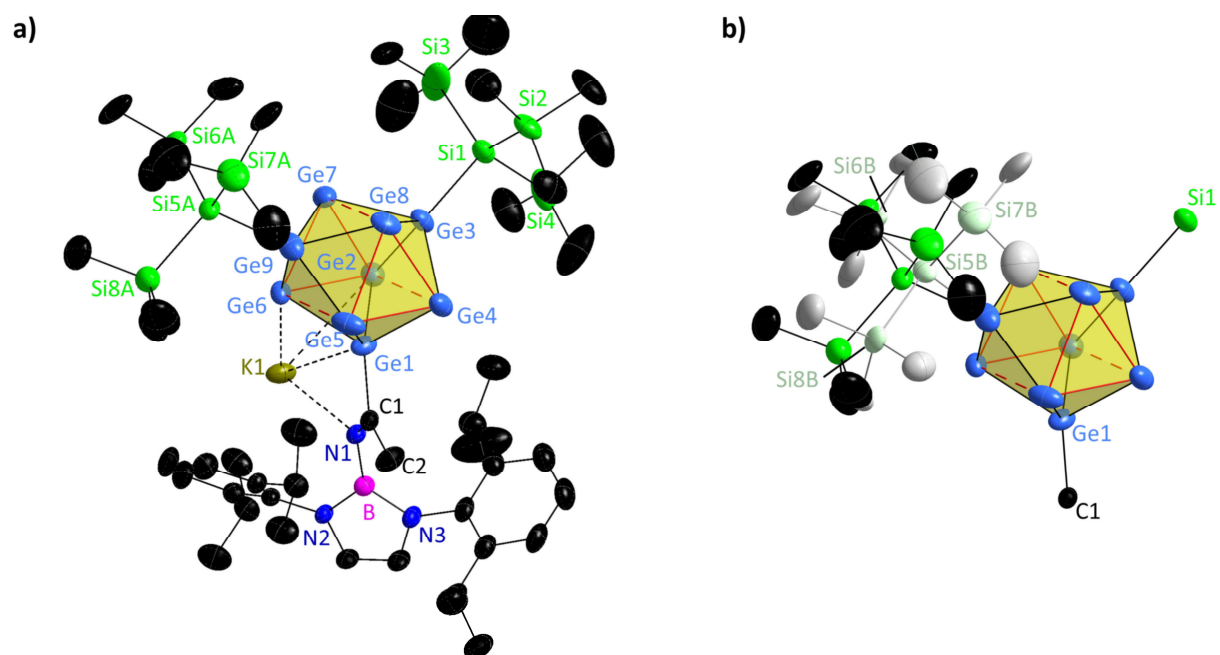


Figure S1. a) Full ellipsoid plot of compound **1-K**; b) representation of the split position in **1-K** (site occupation factor of species A: 0.577, B: 0.423). All ellipsoids are presented at a 50 % probability level. Hydrogen atoms and co-crystallizing ether molecules are omitted for clarity. In b) the imine moiety, the boranyl ligand as well as the TMS groups at Si1 are omitted for clarity. Trigonal prismatic bases are indicated by dashed red lines.

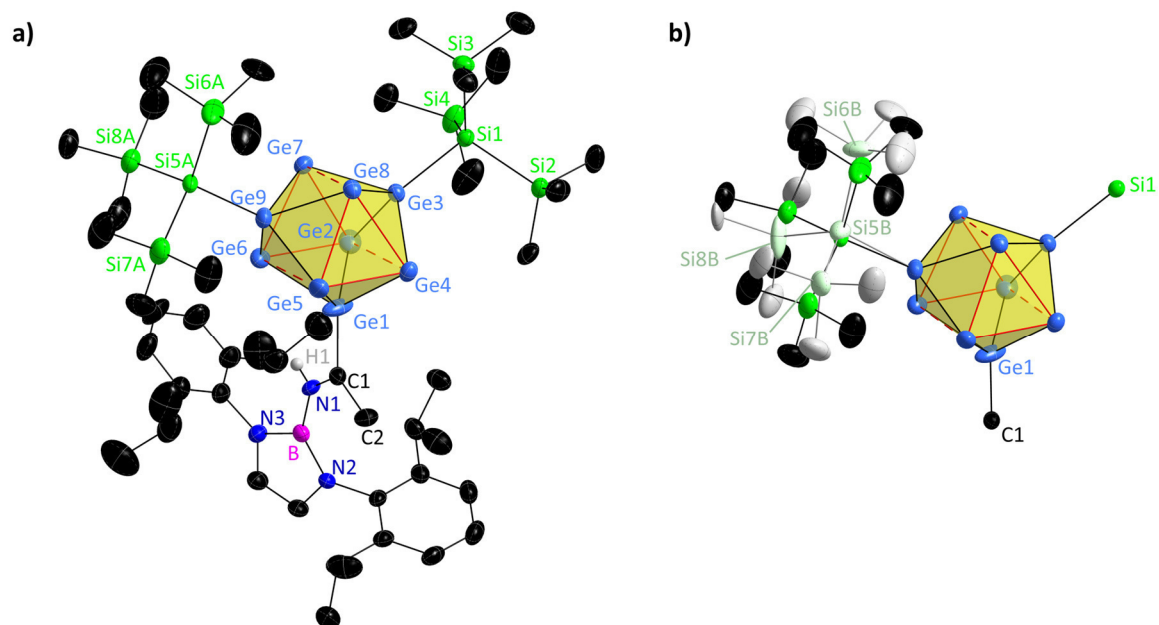


Figure S2. a) Full ellipsoid plot of compound **1-H**; b) representation of the split position in **1-H** (site occupation factor of species A: 0.835, B: 0.165). All ellipsoids are presented at a 50 % probability level. Hydrogen atoms are omitted for clarity. In b) the imine moiety, the boranyl ligand as well as the TMS groups at Si1 are omitted for clarity. Trigonal prismatic bases are indicated by dashed red lines.

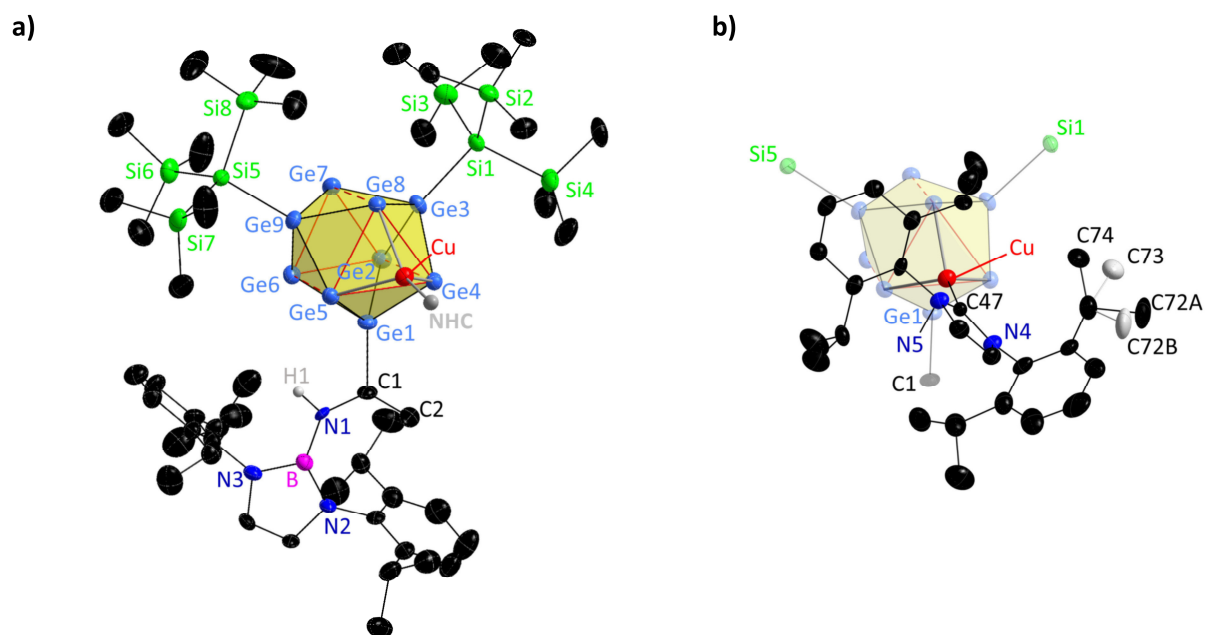


Figure S3. a) Ellipsoid plot of compound **1b-Cu** with emphasis on the boranyl ligand (neglect of NHC ligand); b) ellipsoid plot of compound **1b-Cu** with emphasis on the NHC ligand (neglect of TMS groups, the boranyl ligand and the incorporated imine), and representation of the split position of one *i*Pr group (site occupation factors of 0.355 in grey and 0.645 in black). All ellipsoids are presented at a 50 % probability level. Hydrogen atoms and co-crystallizing toluene molecules are omitted for clarity. Trigonal prismatic bases are indicated by dashed red lines.

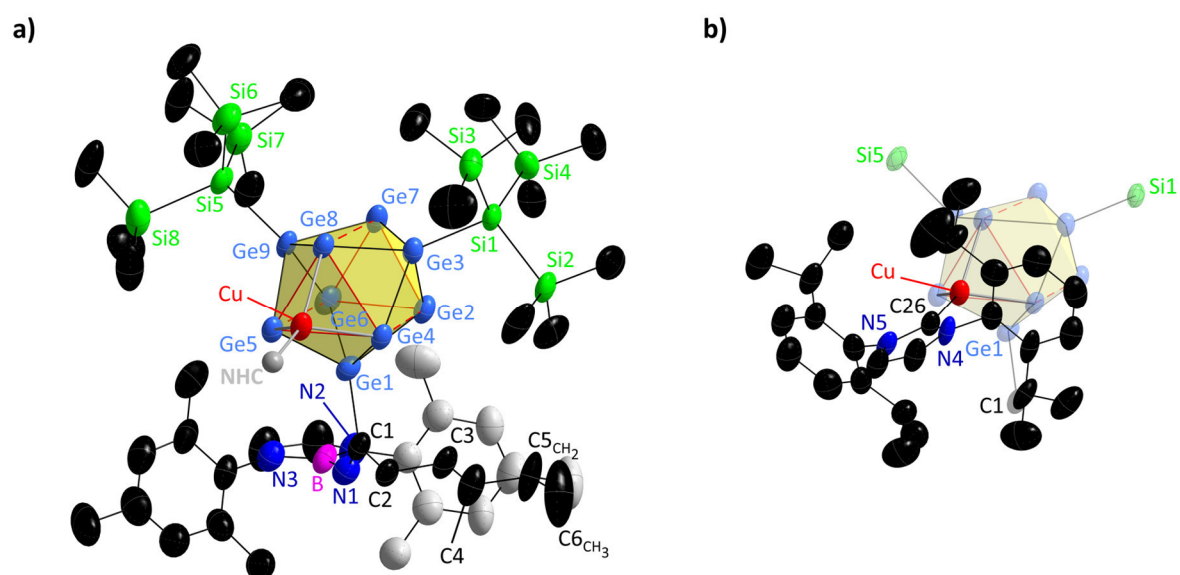


Figure S4. a) Ellipsoid plot of compound **2a-Cu** with emphasis on the boranyl ligand (neglect of NHC ligand). One Mes wingtip is shown in grey for a better visibility of the hydrocarbon chain; b) ellipsoid plot of compound **2a-Cu** with emphasis on the NHC ligand (neglect of TMS groups, the boranyl ligand and the incorporated imine). All ellipsoids are presented at a 50 % probability level. Hydrogen atoms and the co-crystallizing hexane molecule are omitted for clarity. Trigonal prismatic bases are indicated by dashed red lines.

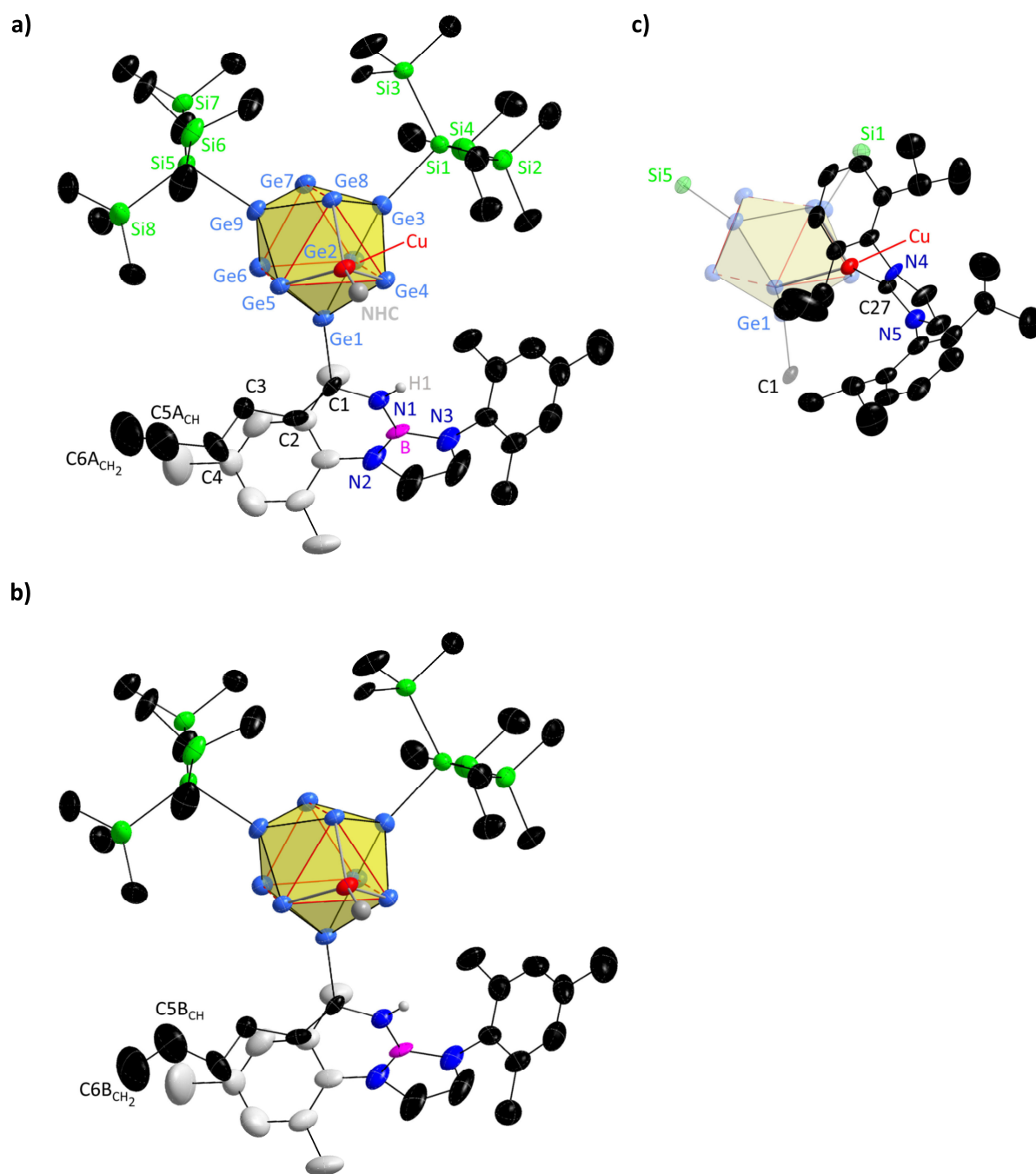


Figure S5. a) Ellipsoid plot of compound **3b-Cu** with emphasis on the boranyl ligand (neglect of NHC ligand). One Mes wingtip is shown in grey for a better visibility of the hydrocarbon chain; the majority species of C5 and C6 is shown (A: site occupation factor of 0.62); b) ellipsoid plot for the minor species of Ge5 and Ge6 (B: site occupation factor of 0.38); c) ellipsoid plot of compound **3b-Cu** with emphasis on the NHC ligand (neglect of TMS groups, the boranyl ligand and the incorporated imine). All ellipsoids are presented at a 50 % probability level. Hydrogen atoms and co-crystallizing benzene molecules are omitted for clarity. Trigonal prismatic bases are indicated by dashed red lines.

4. NMR spectra

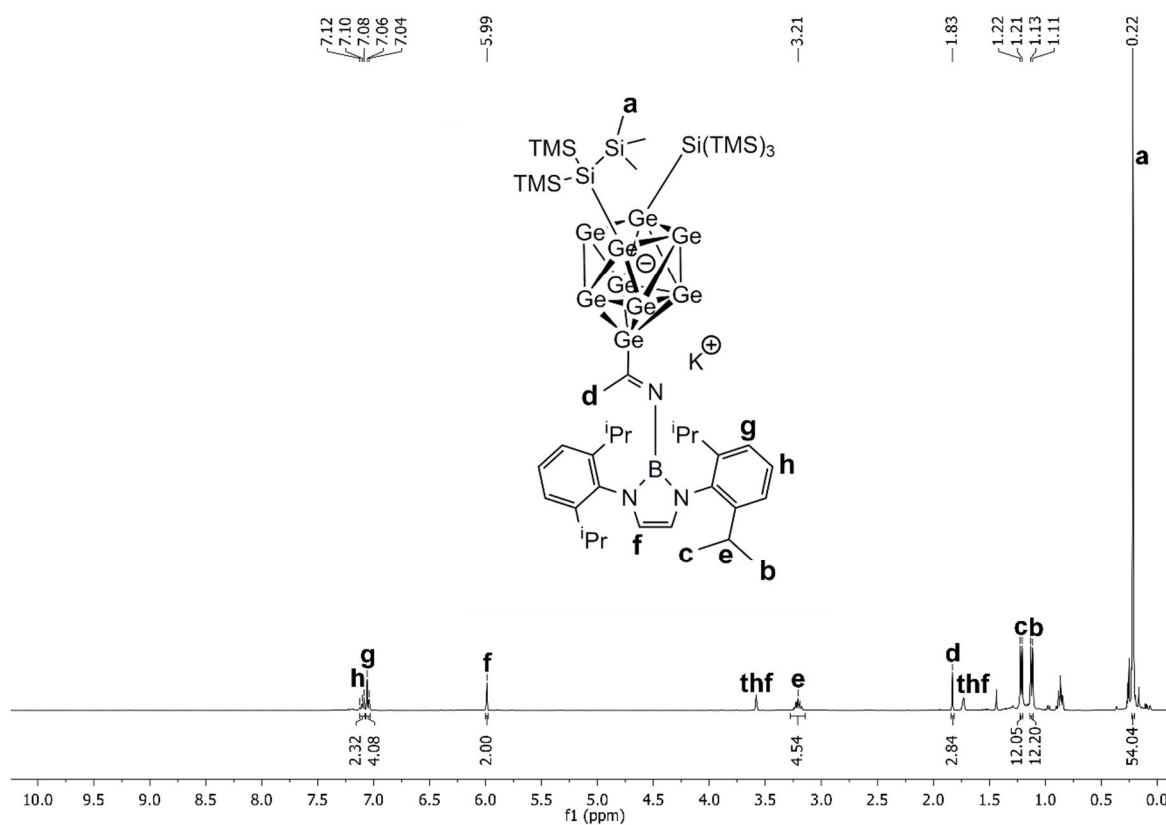


Figure S6. ^1H NMR spectrum of 1^- in $\text{thf-}d_8$.

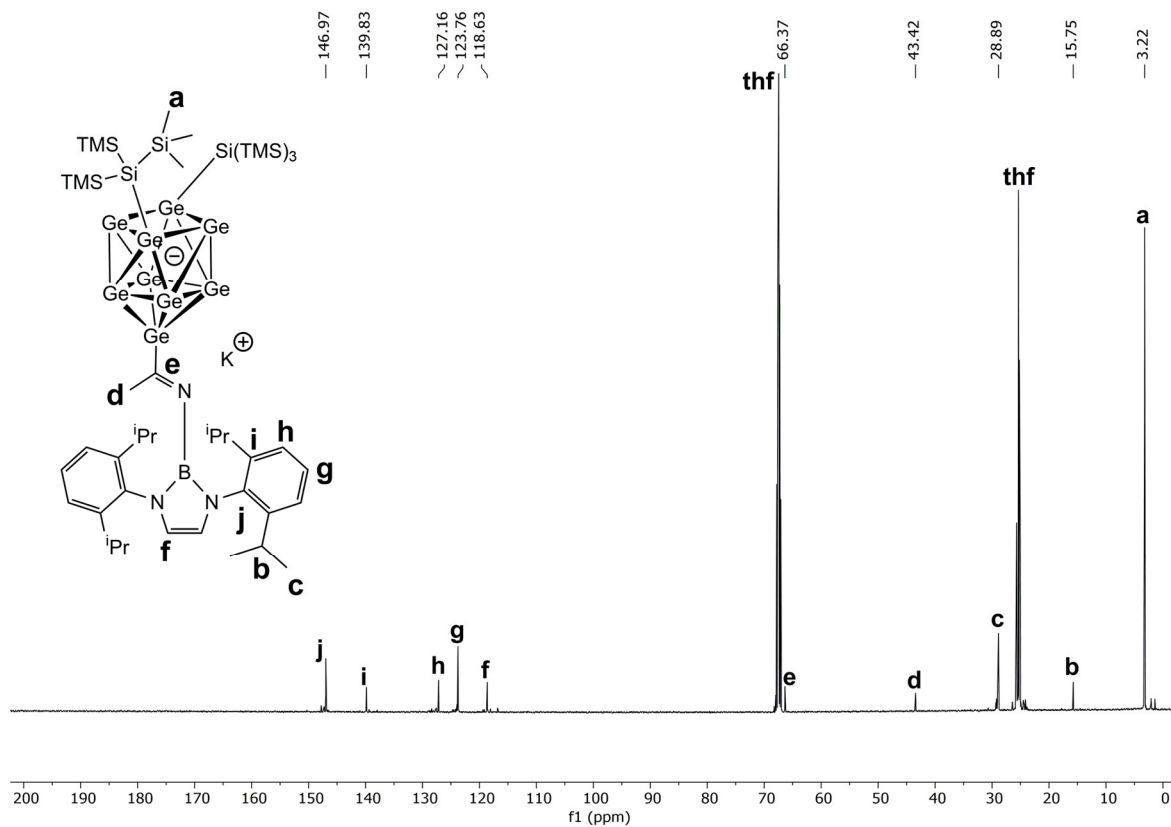


Figure S7. ^{13}C NMR spectrum of compound 1^- in $\text{thf-}d_8$.

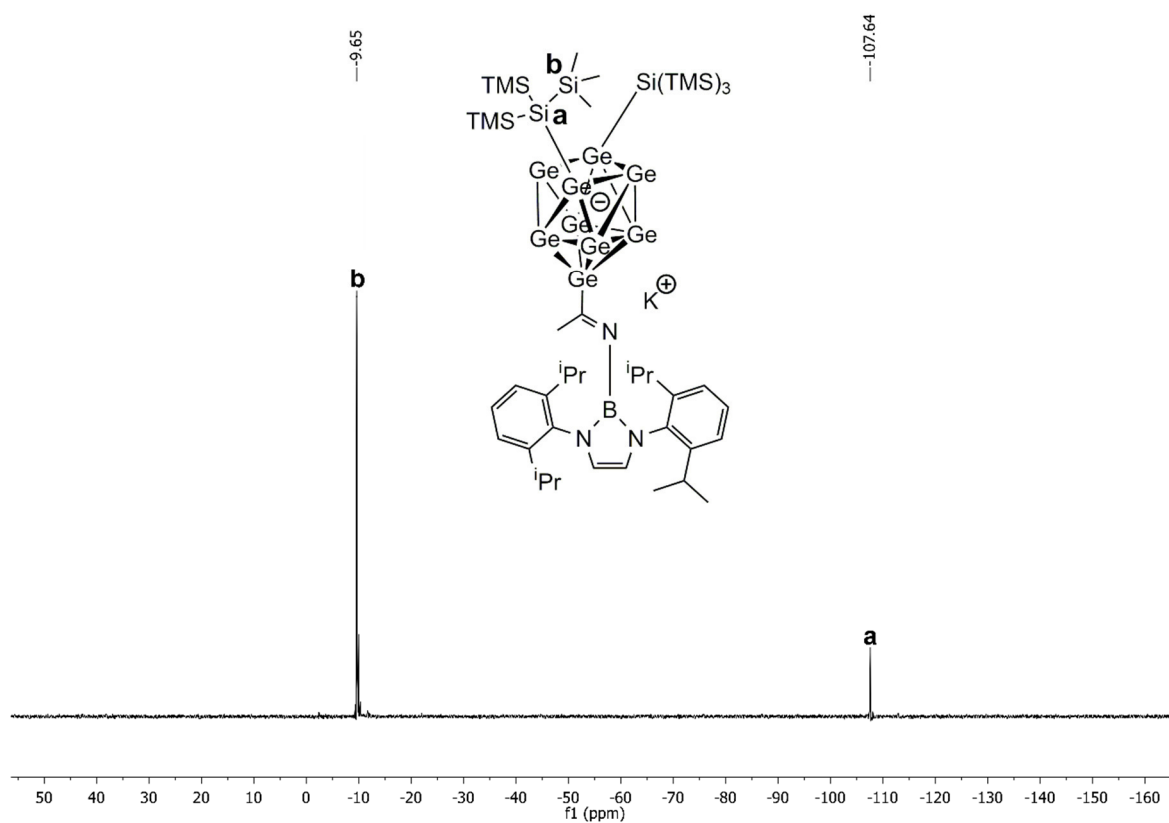


Figure S8. ^{29}Si INEPT NMR spectrum of compound **1**⁻ in thf-d_8 .

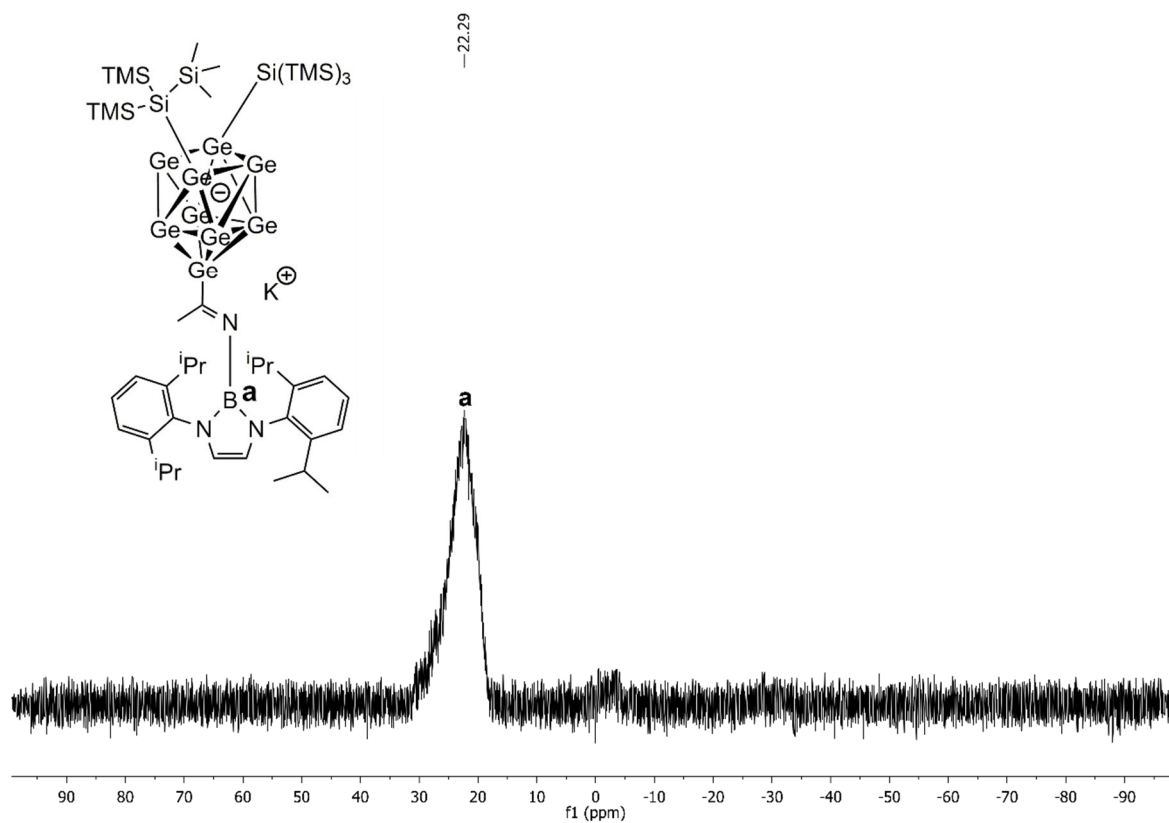


Figure S9. ^{11}B NMR spectrum of compound **1**⁻ in thf-d_8 .

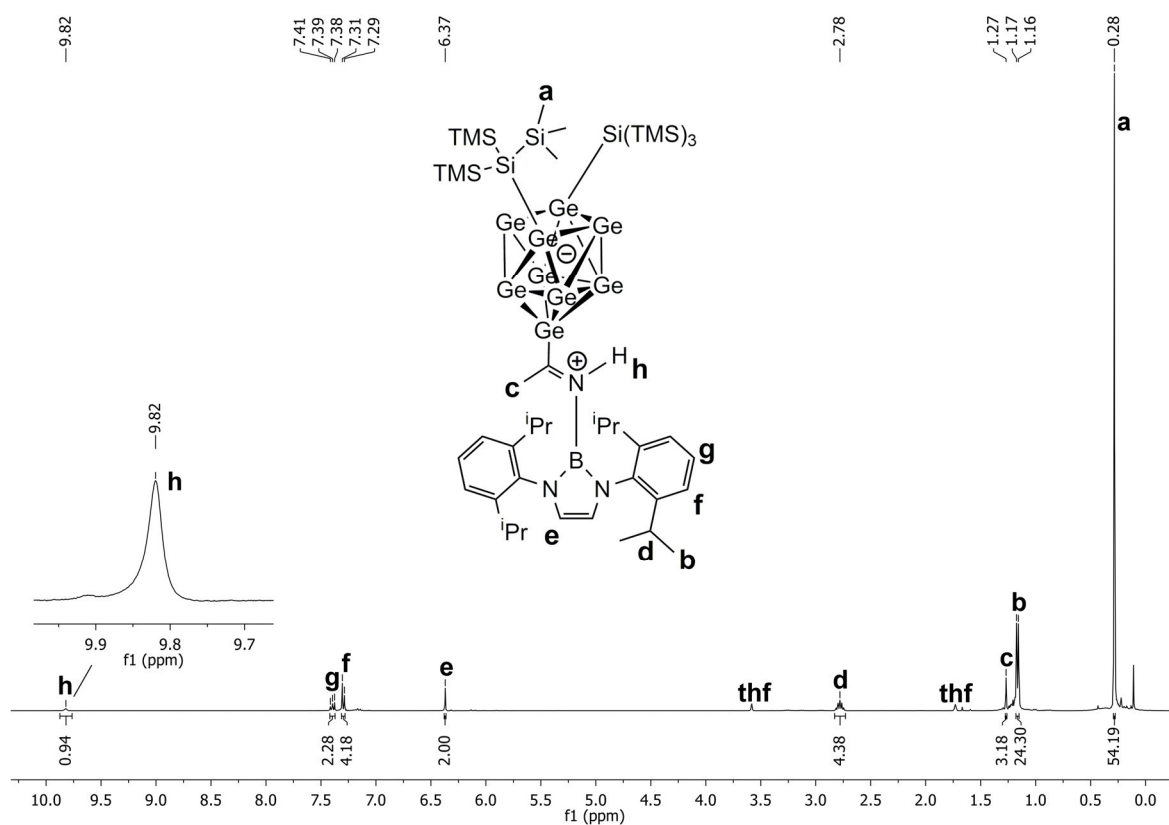


Figure S10. ^1H NMR spectrum of compound **1-H** in $\text{thf-}d_8$.

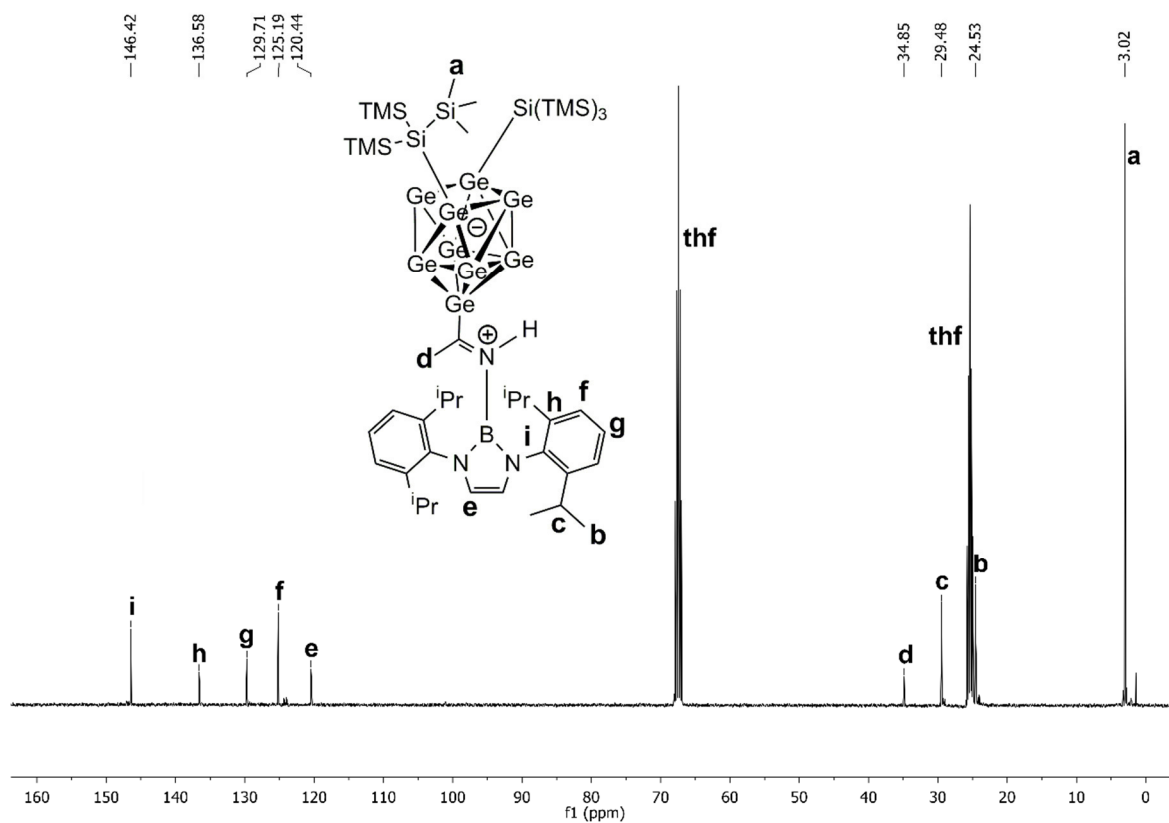


Figure S11. ^{13}C NMR spectrum of compound **1-H** in $\text{thf-}d_8$.

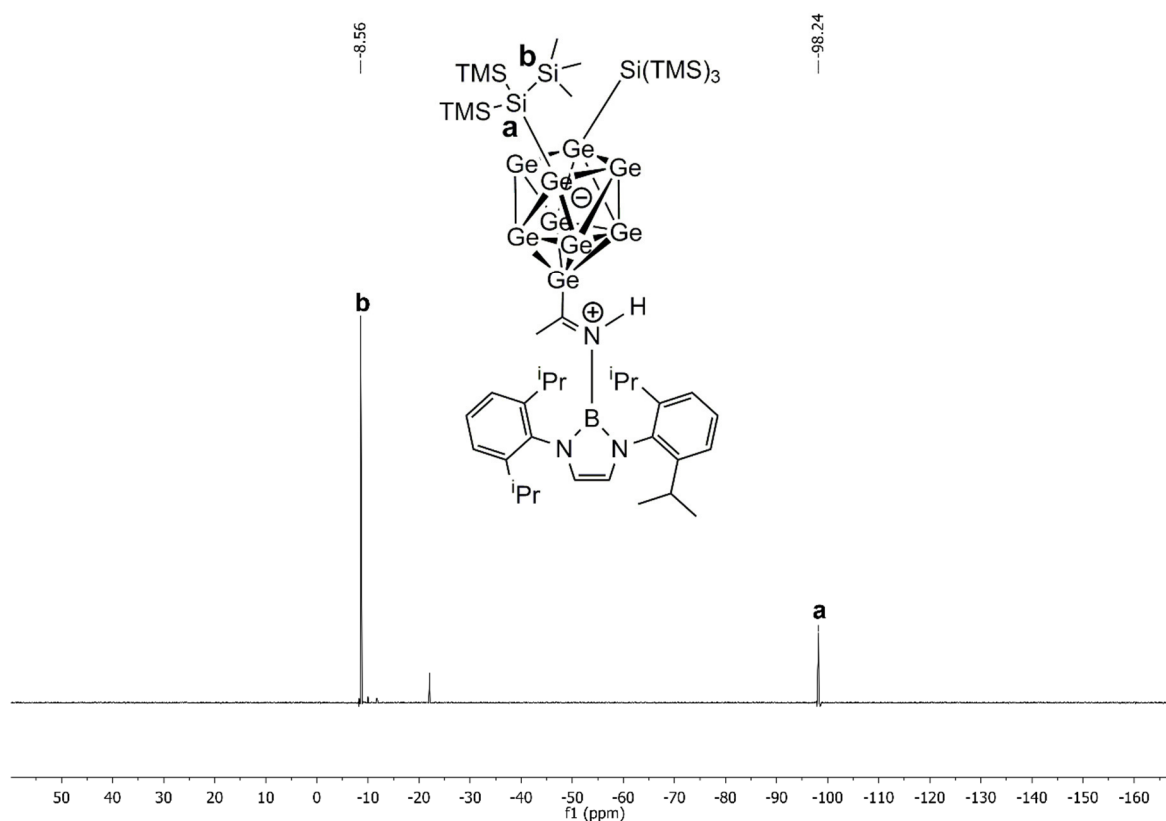


Figure S12. ^{29}Si INEPT NMR spectrum of compound **1-H** in $\text{thf-}d_8$. The impurity is caused by silicon grease.

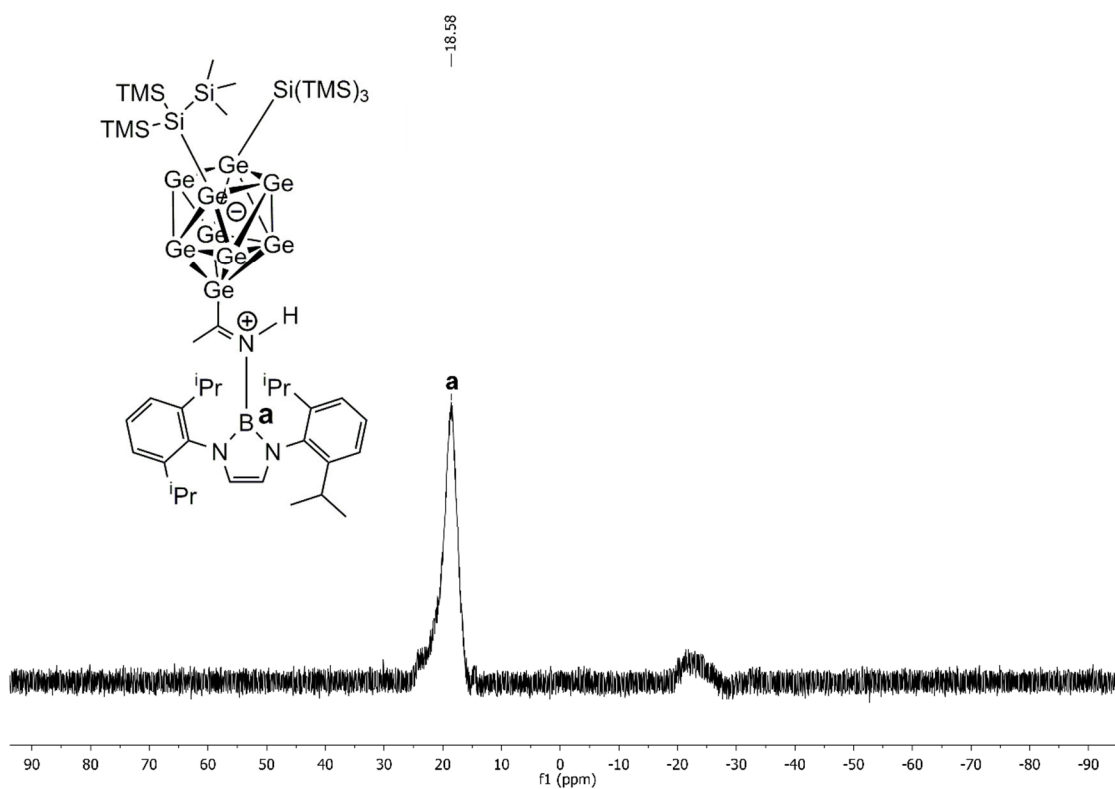


Figure S13. ^{11}B NMR spectrum of compound **1-H** in $\text{thf-}d_8$. The impurity is caused by the glass of the NMR tube.

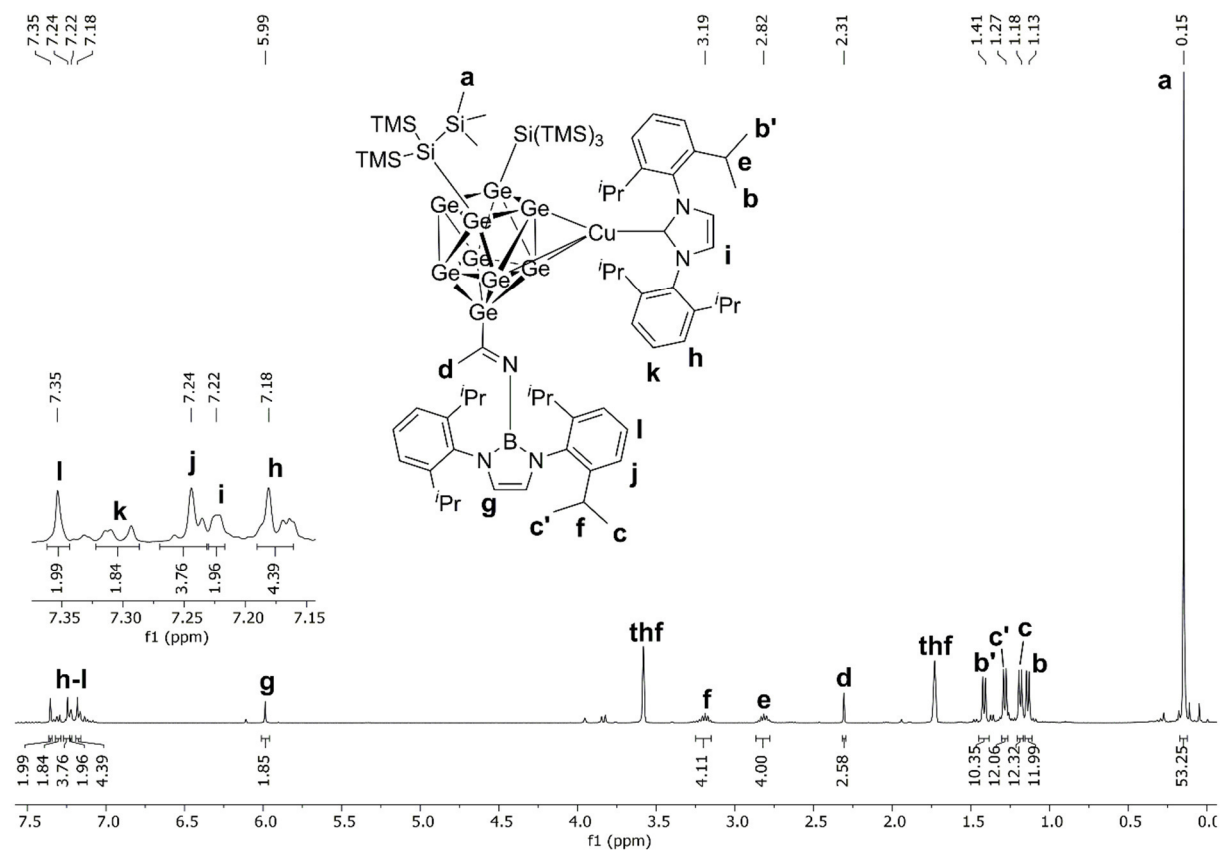


Figure S14. ^1H NMR spectrum of compound **1b-Cu** in thf-d_8 .

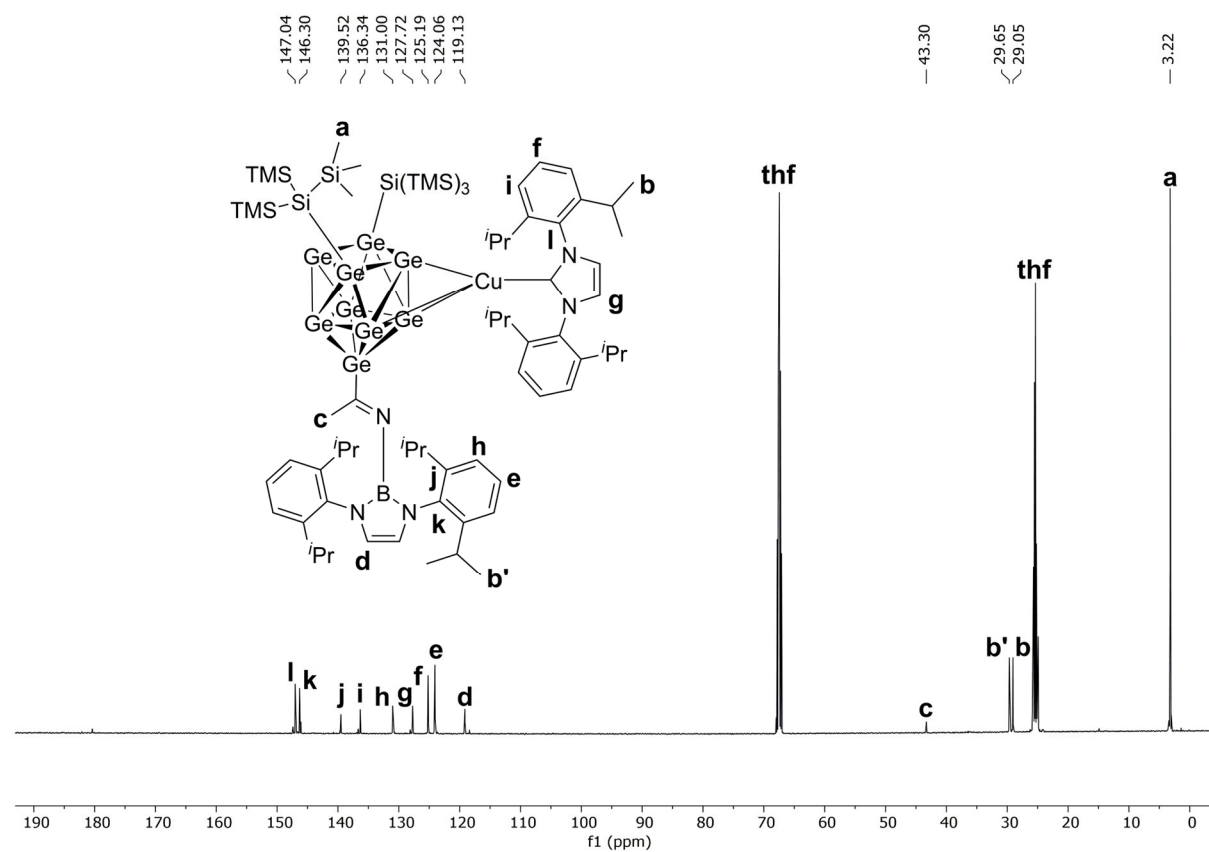


Figure S15. ^{13}C NMR spectrum of compound **1b-Cu** in thf-d_8 .

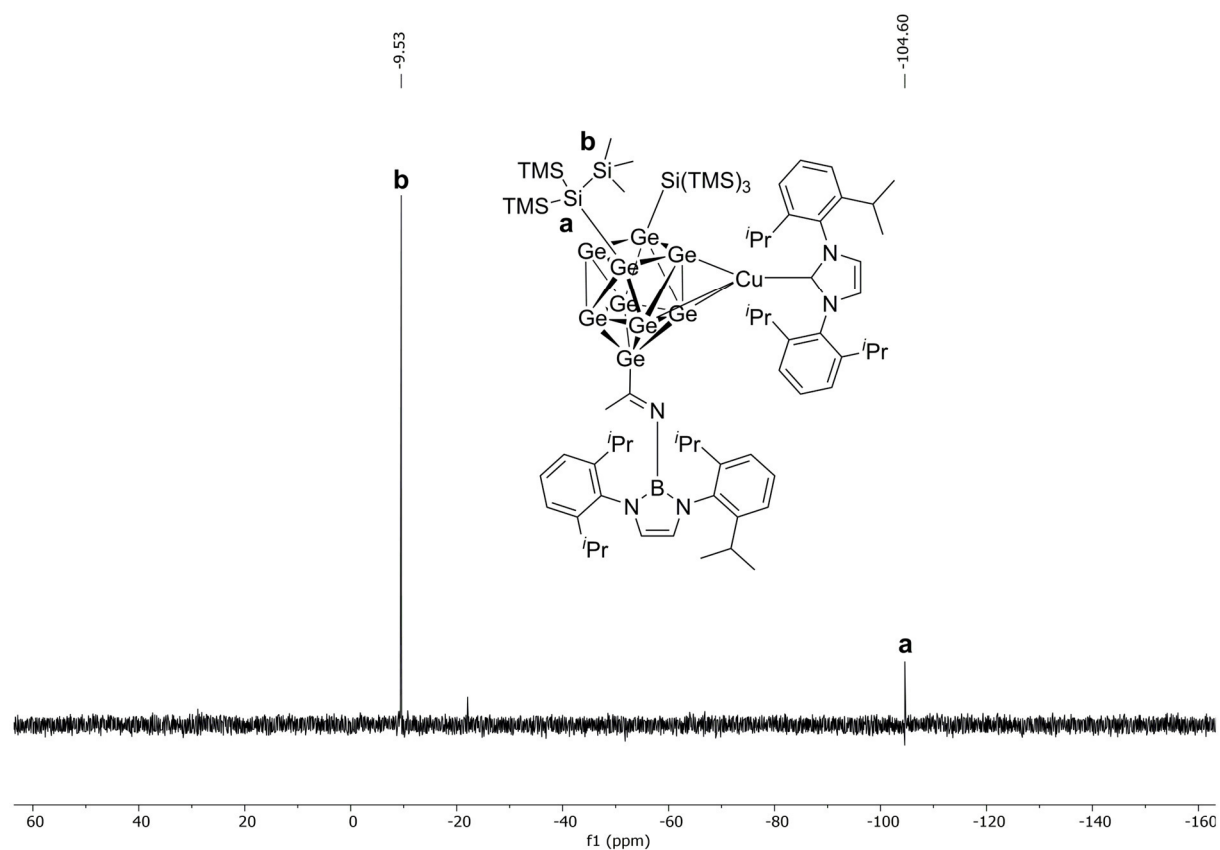


Figure S16. ^{29}Si INEPT NMR spectrum of compound **1b-Cu** in $\text{thf-}d_8$. The impurity is caused by silicon grease.

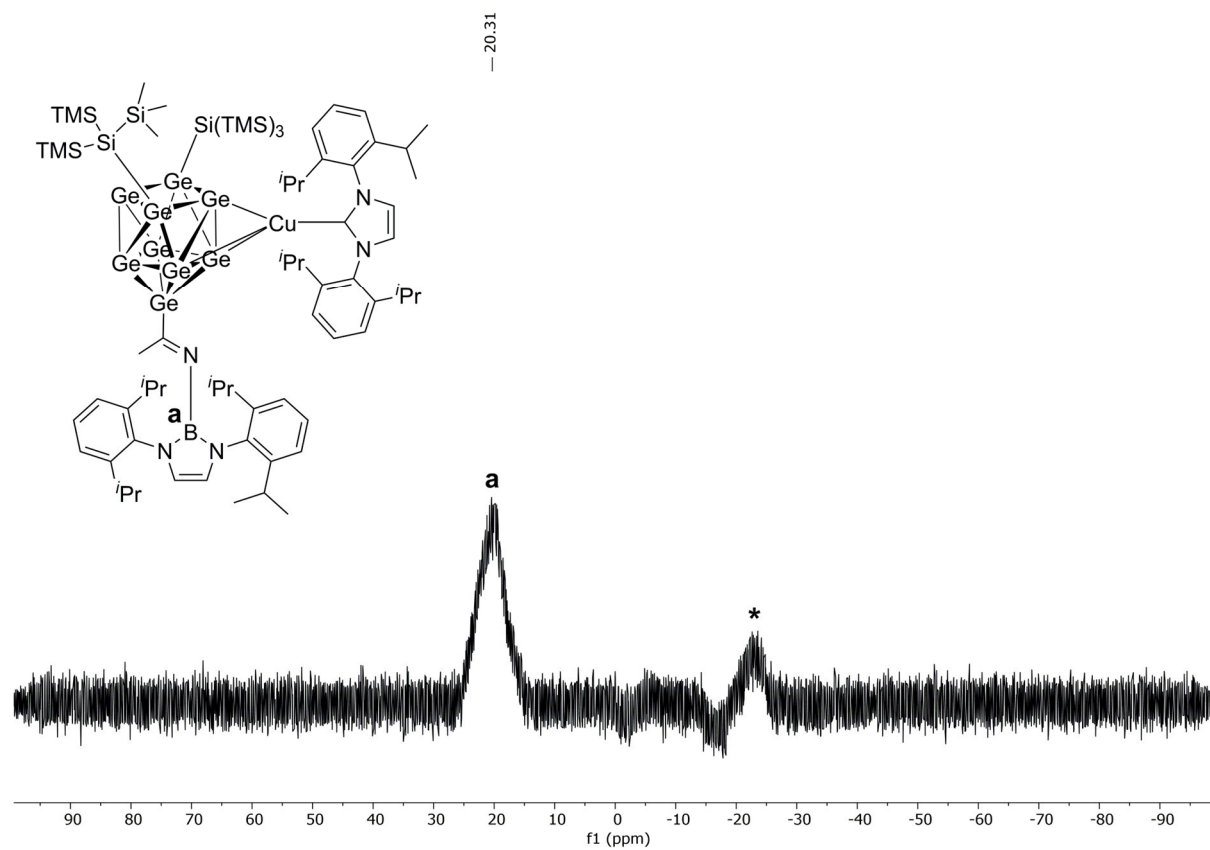


Figure S17. ^{11}B NMR spectrum of compound **1b-Cu** in $\text{thf-}d_8$. The asterisked signal is caused by the glass of the NMR tube.

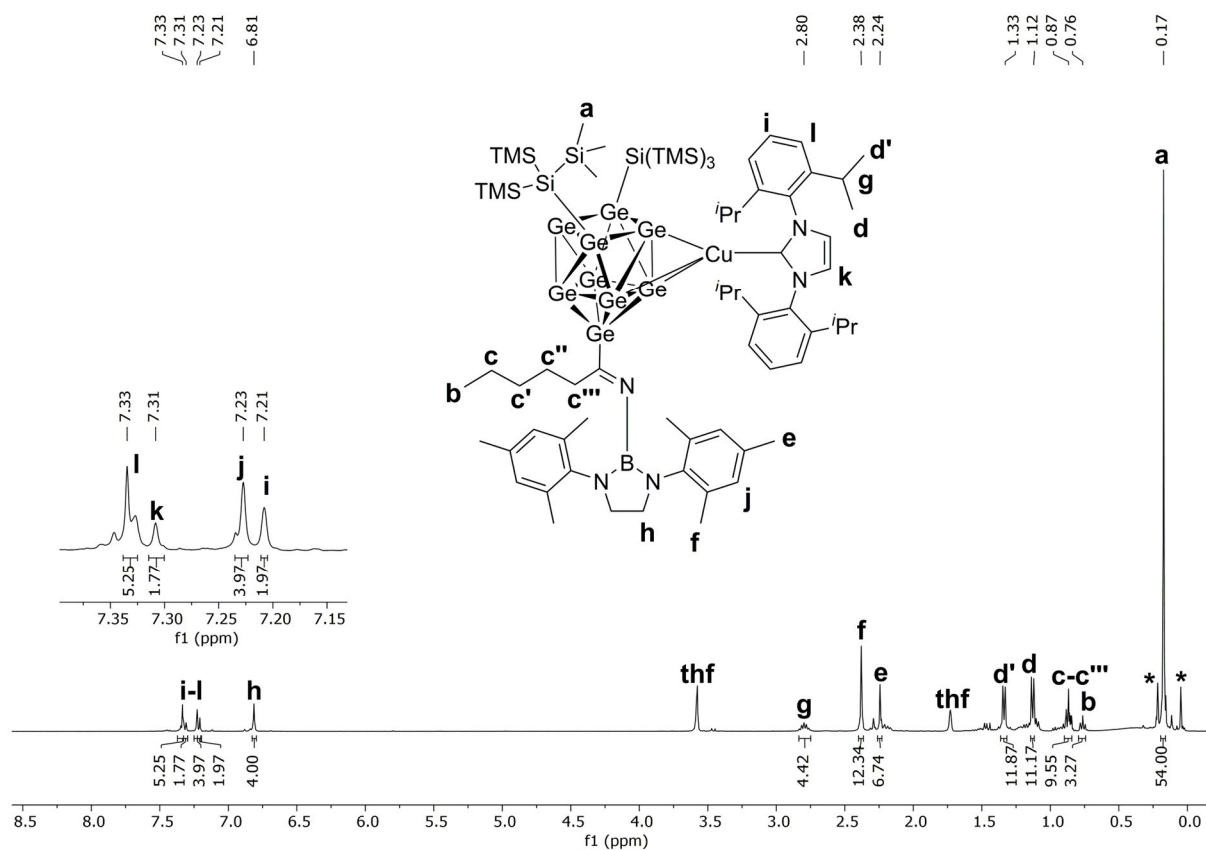


Figure S18. ¹H NMR spectrum of compound **2a-Cu** in thf-*d*₈. The asterisked signals are caused by unidentified impurities.

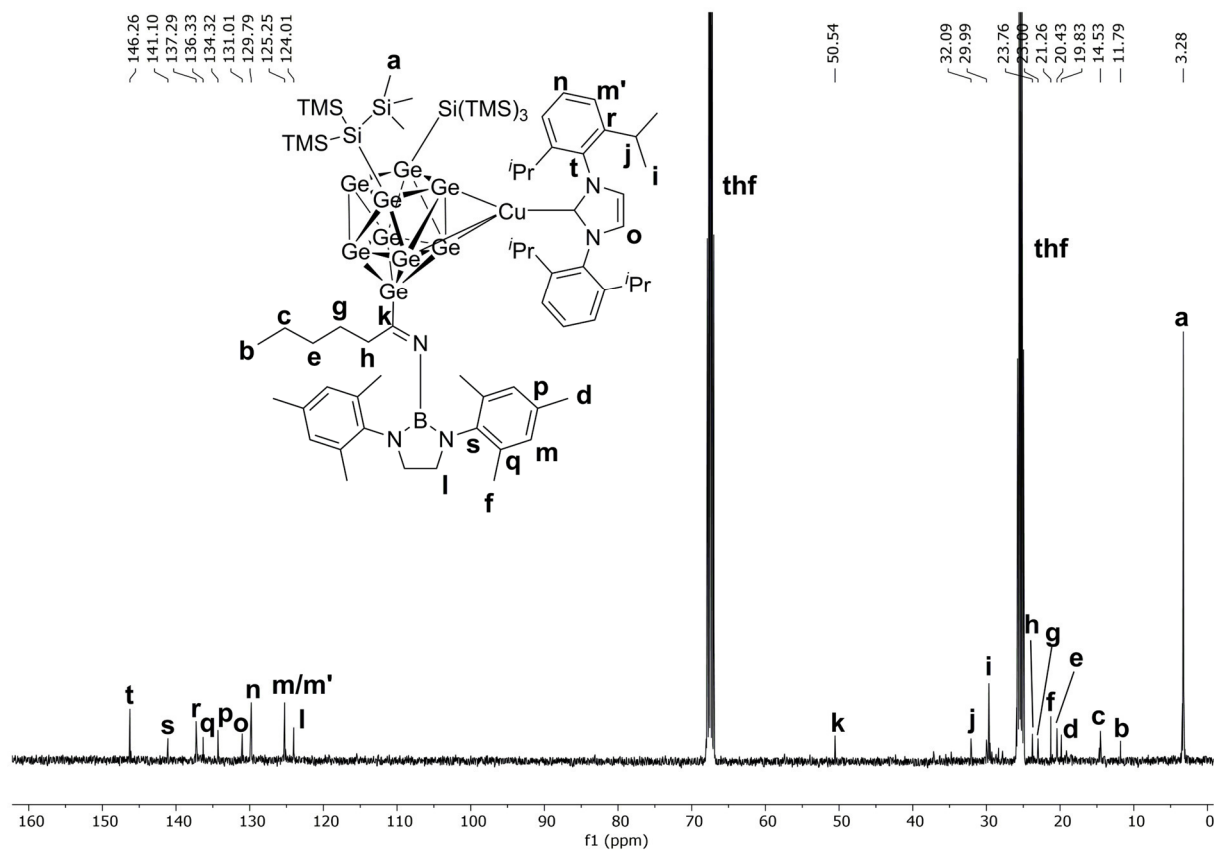
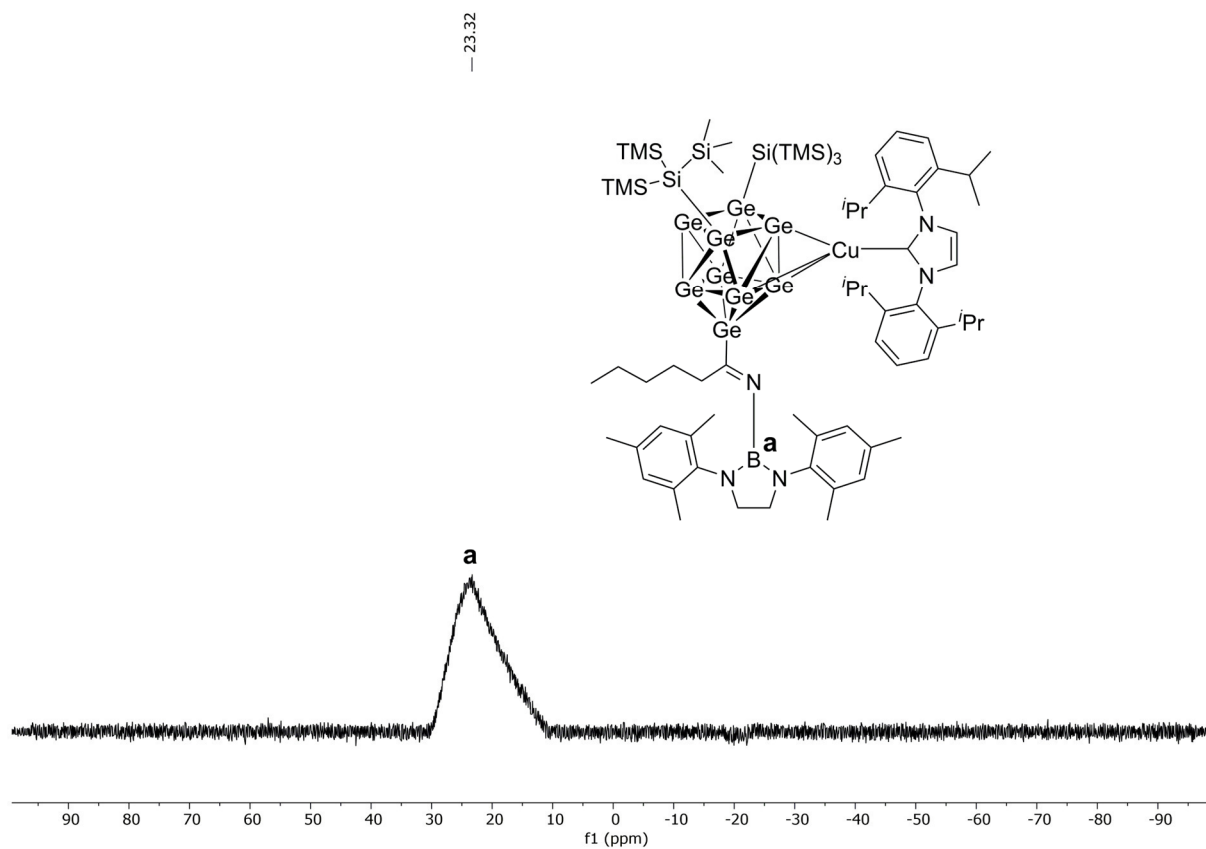
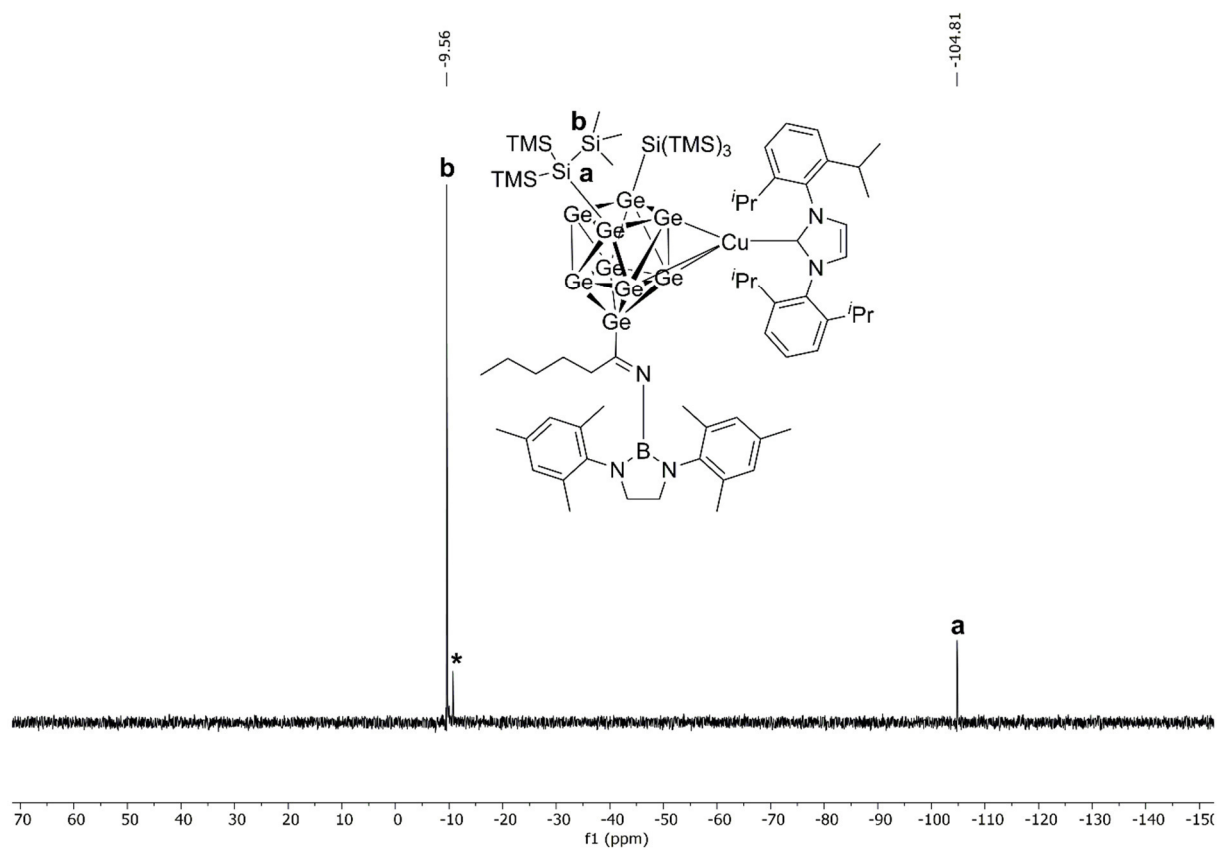


Figure S19. ¹³C NMR spectrum of compound **2a-Cu** in thf-*d*₈.



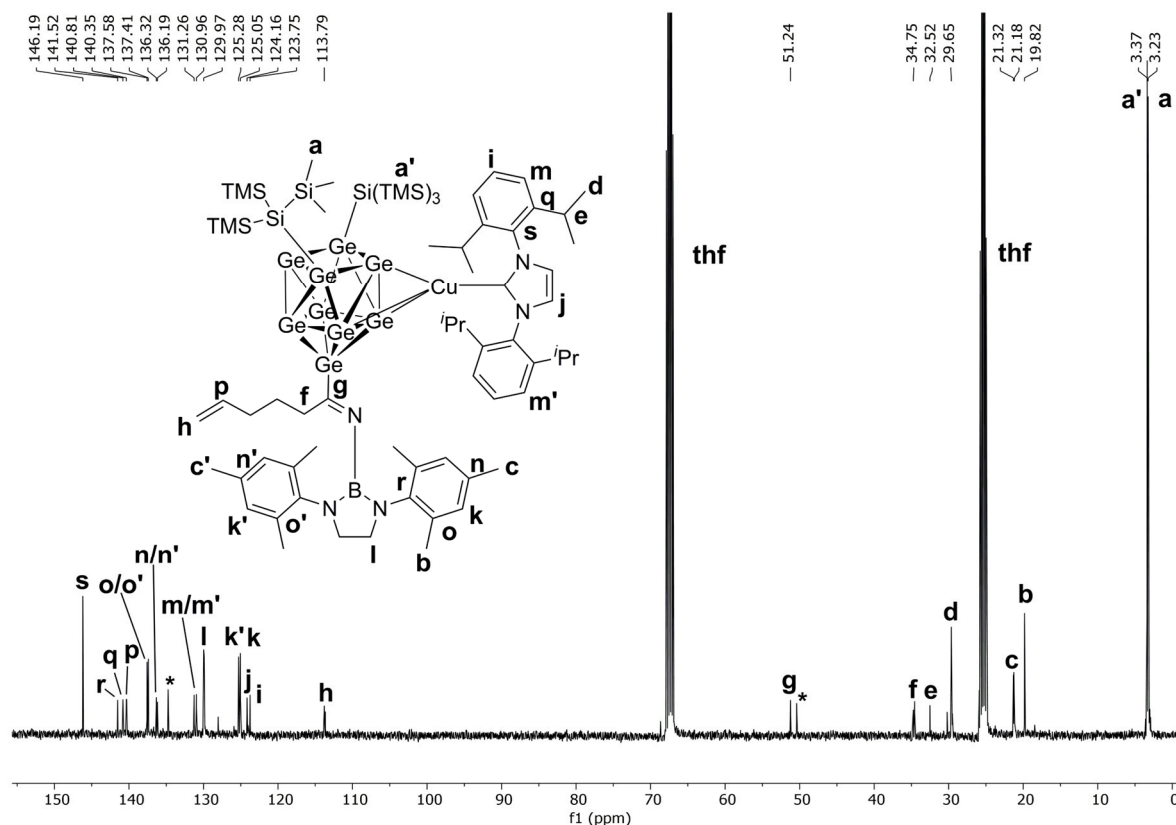
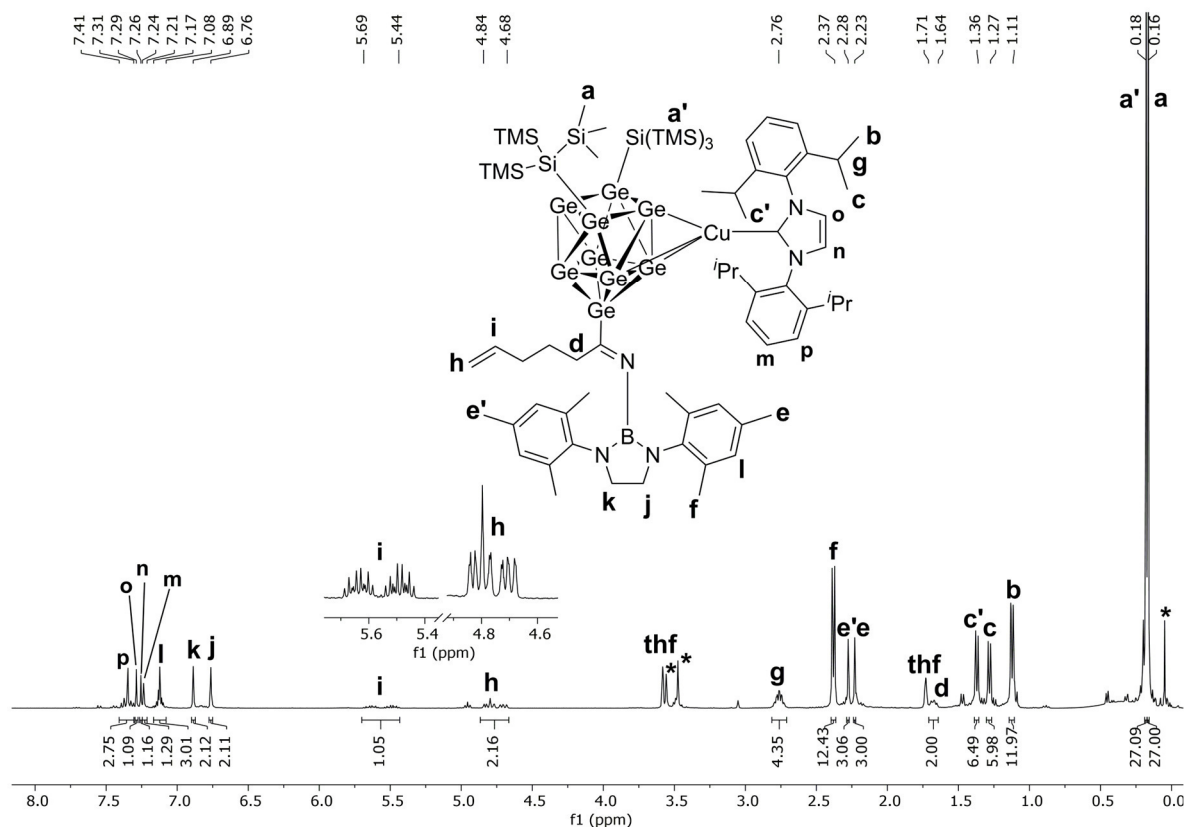
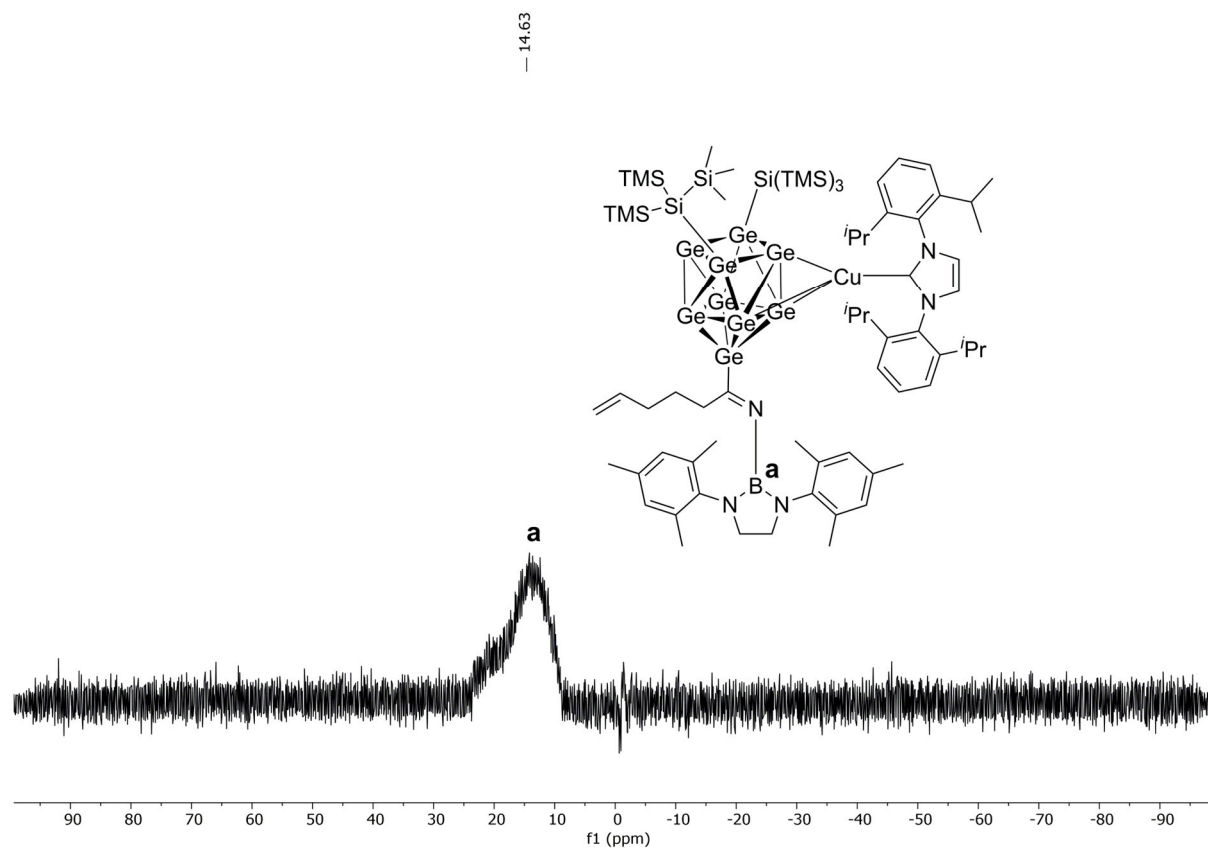
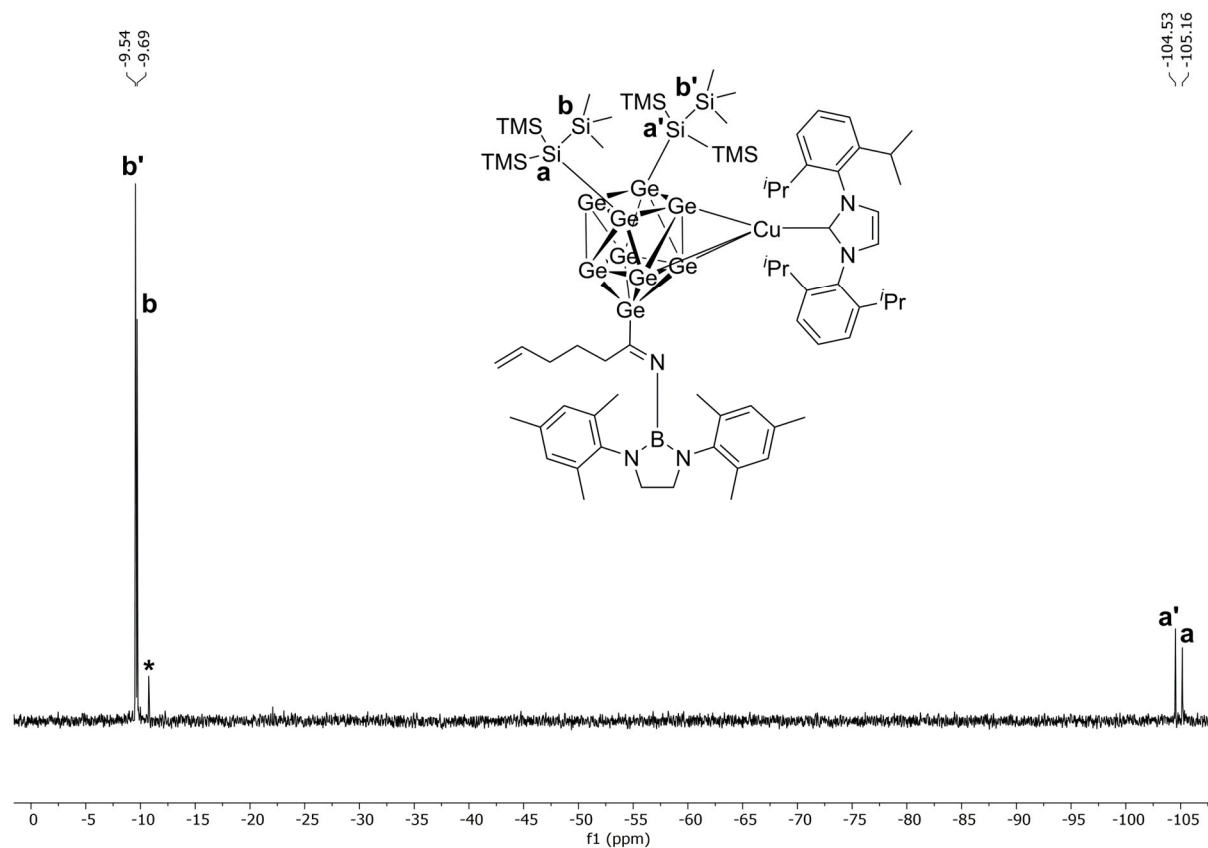


Figure S23. ^{13}C NMR spectrum of compound **3b-Cu** in thf-d_8 . The asterisked signals are caused by unidentified C atoms. Not all C atoms of the imine hydrocarbon chain could be unequivocally identified.



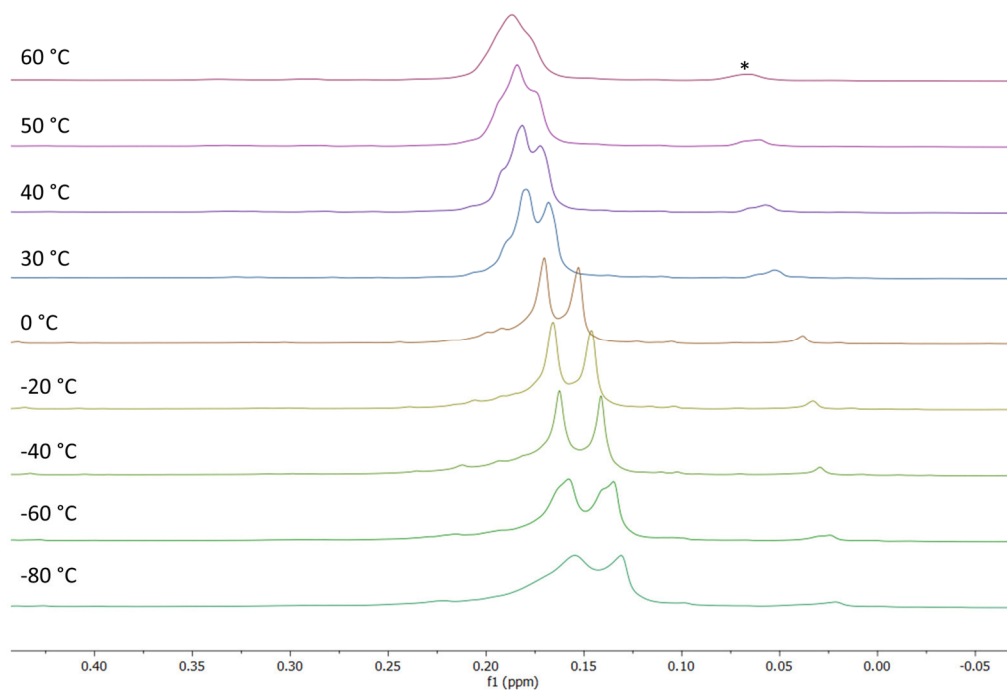
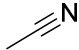
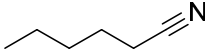
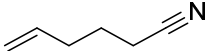
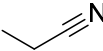
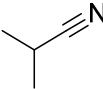
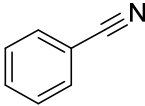
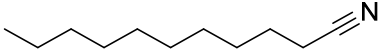


Figure S26. Variable temperature ¹H NMR spectra of compound **3b-Cu** in thf-*d*₈ from -80 °C to 60 °C. The signal set at approximately $\delta = 0.15$ ppm is caused by the split hypersilyl group protons. The asterisked signal belongs to an unidentified impurity.

5. Mass spectra

The following figures contain the overview ESI-MS mass spectra, as well as the selected areas with the mass peaks of the nitrile incorporated cluster species. Additional signals are caused by the ionization of the cluster anions, and ionization products were identified using the ESI-MS software. All spectra were acquired in the negative-ion mode in diluted thf solution (injection speed: 240 $\mu\text{L/h}$, 300 $^{\circ}\text{C}$ dry gas temperature). The theoretical isotope distribution was simulated with the Bruker Compass Data Analysis 4.0 SP 5 program.

Table S4. Overview on tested nitriles for the successful incorporation between the cluster $[\text{Ge}_9\{\text{Si}(\text{TMS})_3\}_2]^{2-}$ and the respective bromo-diazaborolidine, summarizing the corresponding ESI-MS mass peaks.

anion	nitrile	diazaborolidine	ESI-MS mass peak m/z
1 ⁻		DAB(II) ^{Dipp} -Br	1577.9
2 ⁻		DAB ^{Mes} -Br	1551.8
3 ⁻		DAB ^{Mes} -Br	1549.8
-		DAB ^{o-tol} -Br	1454.0
-		DAB ^{o-tol} -Br	1467.3
-		DAB ^{Mes} -Br	1557.8
-		DAB ^{o-tol} -Br	1580.1

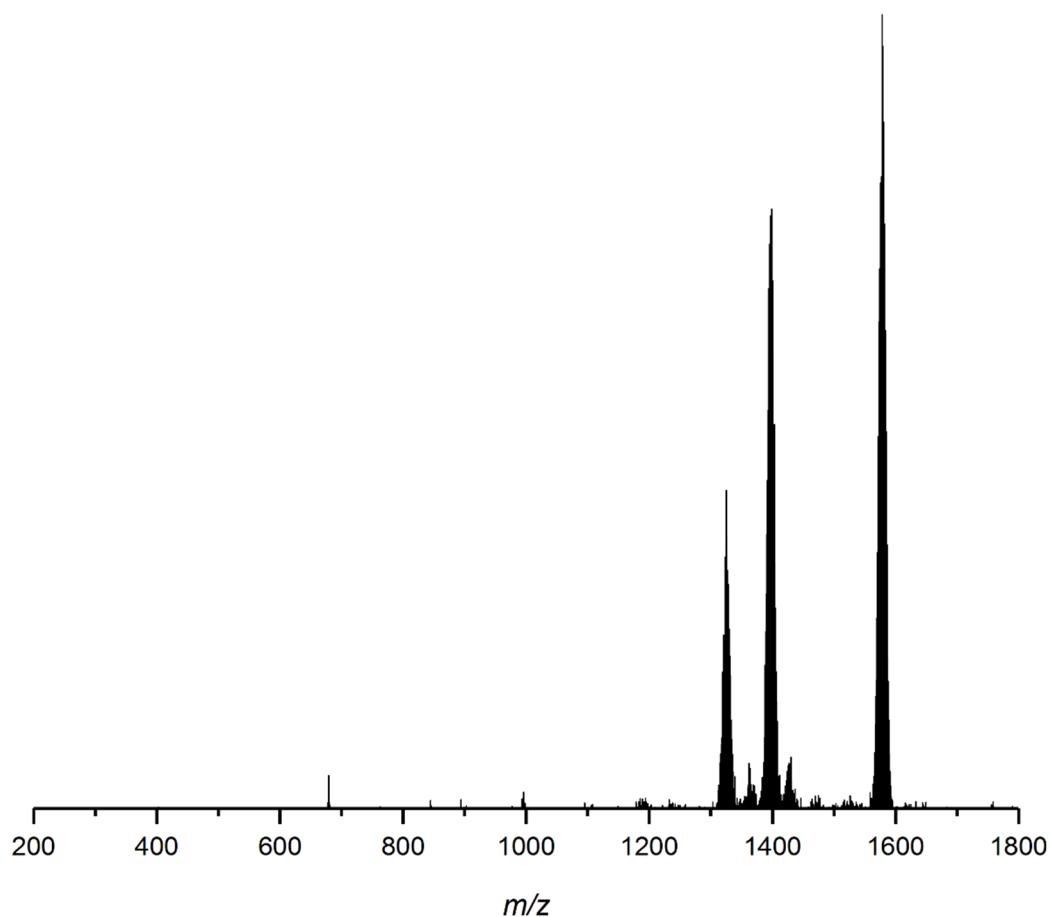


Figure S27. ESI-MS overview spectrum of the solution containing the anion $[\text{Ge}_9\{\text{Si}(\text{TMS})_3\}_2\{\text{CH}_3\text{C}=\text{N}\}\text{-DAB}(\text{II})^{\text{Dipp}}]^-$ (**1a**) at m/z 1577.9. Ionization products: $[\text{Ge}_9\{\text{Si}(\text{TMS})_3\}_2\{\text{Si}(\text{TMS})_2\}]^-$ at m/z 1323.6; $[\text{Ge}_9\{\text{Si}(\text{TMS})_3\}_3]^-$ at m/z 1396.5.

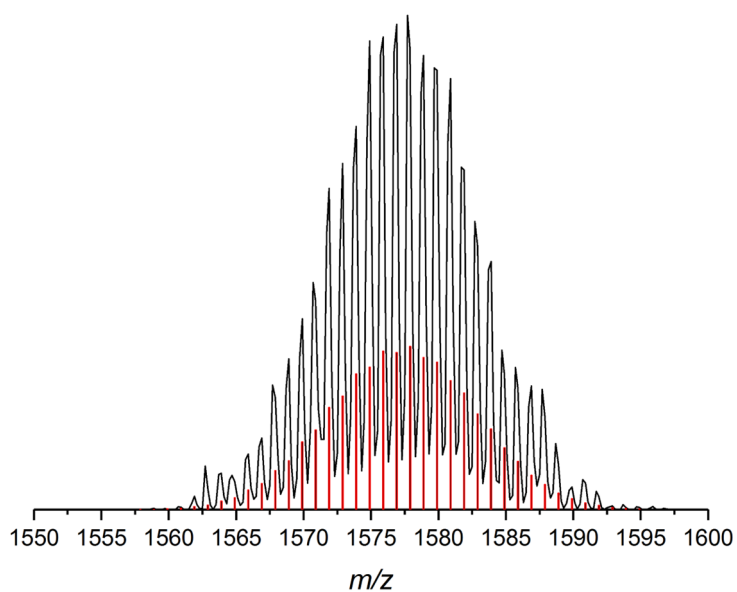


Figure S28. ESI-MS signal of $[\text{Ge}_9\{\text{Si}(\text{TMS})_3\}_2\{\text{CH}_3\text{C}=\text{N}\}\text{-DAB}(\text{II})^{\text{Dipp}}]^-$ (**1⁻**) at m/z 1577.9. Calculated isotope pattern is presented as red bars.

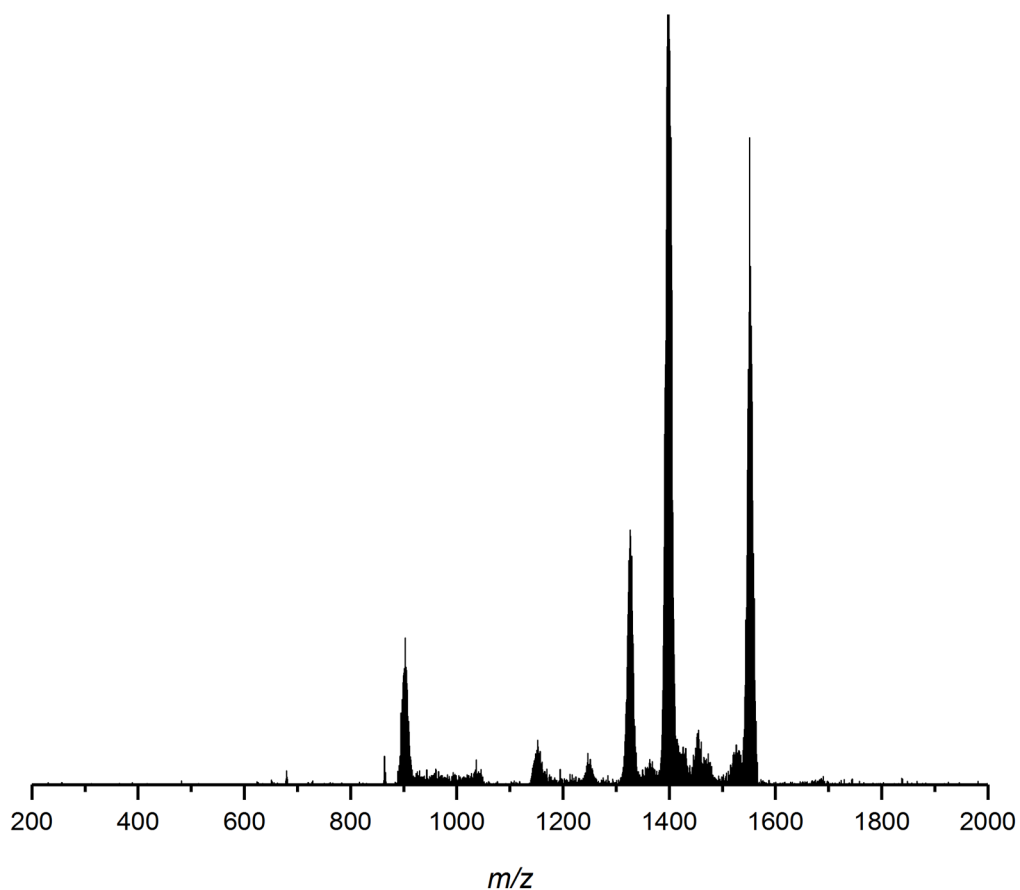


Figure S29. ESI-MS overview spectrum of the solution containing the anion $[\text{Ge}_9\{\text{Si}(\text{TMS})_3\}_2\{\text{CH}_3(\text{CH}_2)_4\text{C}=\text{N}\}\text{-DAB}^{\text{Mes}}]^-$ (**2**⁻) at m/z 1551.8. Ionization products: $[\text{Ge}_9\{\text{Si}(\text{TMS})_3\}]^-$ at m/z 901.2; $[\text{Ge}_9\{\text{Si}(\text{TMS})_3\}_2\{\text{Si}(\text{TMS})_2\}]^-$ at m/z 1323.6; $[\text{Ge}_9\{\text{Si}(\text{TMS})_3\}_3]^-$ at m/z 1396.5.

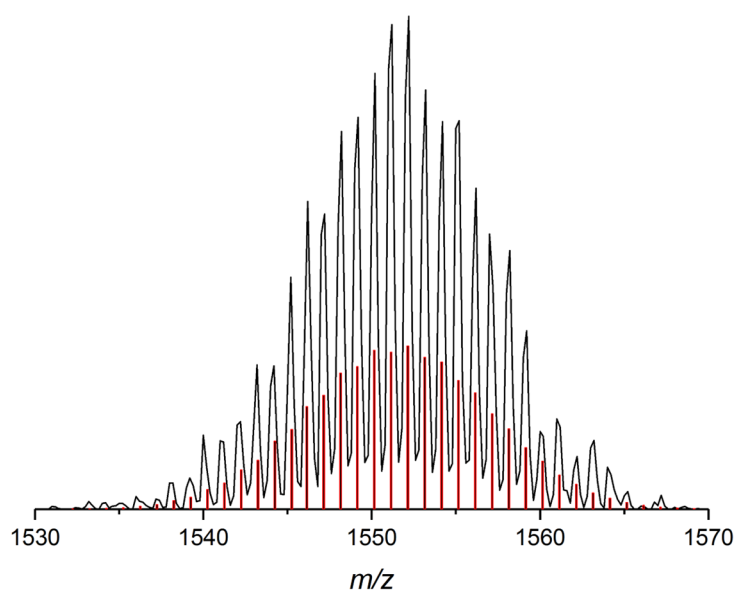


Figure S30. ESI-MS signal of $[\text{Ge}_9\{\text{Si}(\text{TMS})_3\}_2\{\text{CH}_3(\text{CH}_2)_4\text{C}=\text{N}\}\text{-DAB}^{\text{Mes}}]^-$ (**2**⁻) at m/z 1551.8. Calculated isotope pattern is presented as red bars.

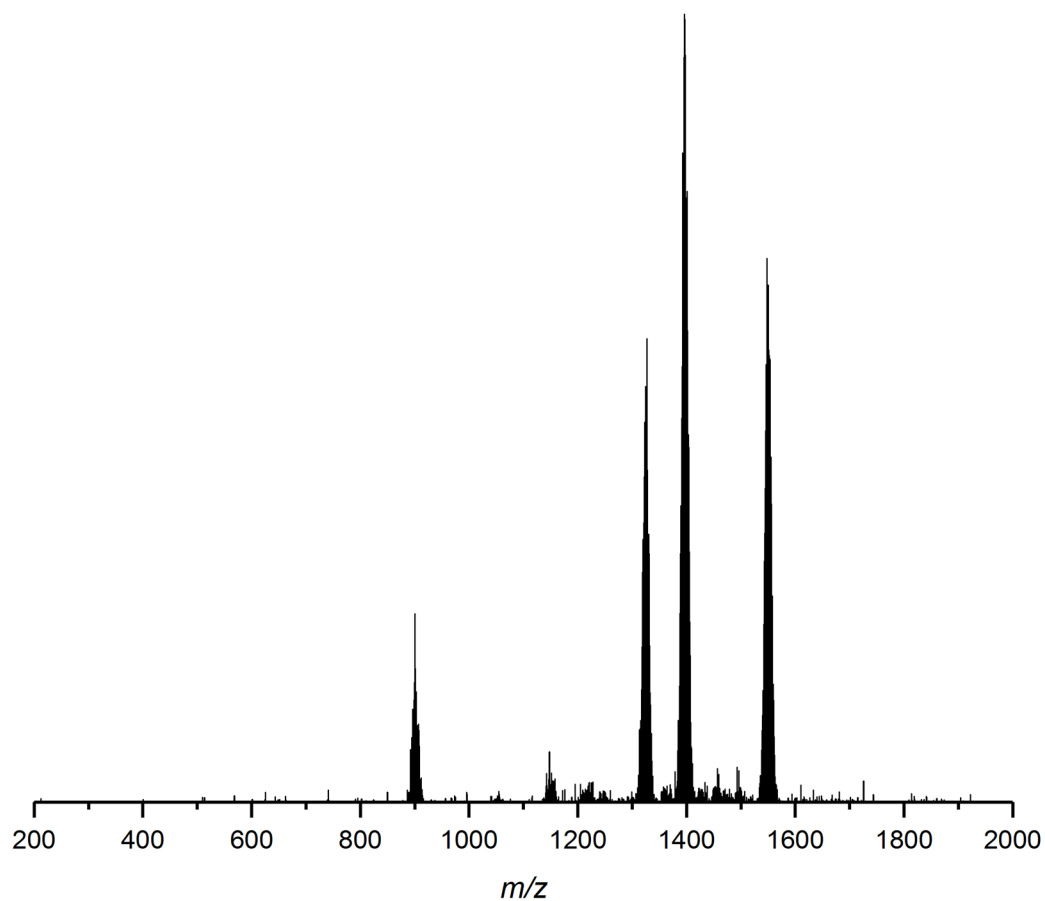


Figure S31. ESI-MS overview spectrum of the solution containing the anion $[\text{Ge}_9\{\text{Si}(\text{TMS})_3\}_2\{\text{CH}_2=\text{CH}(\text{CH}_2)_3\text{C}=\text{N}\}-\text{DAB}^{\text{Mes}}]^-$ (**3**⁻) at m/z 1549.8. Ionization products: $[\text{Ge}_9\{\text{Si}(\text{TMS})_3\}]^-$ at m/z 901.2; $[\text{Ge}_9\{\text{Si}(\text{TMS})_3\}_2\{\text{Si}(\text{TMS})_2\}]^-$ at m/z 1323.6; $[\text{Ge}_9\{\text{Si}(\text{TMS})_3\}_3]^-$ at m/z 1396.5.

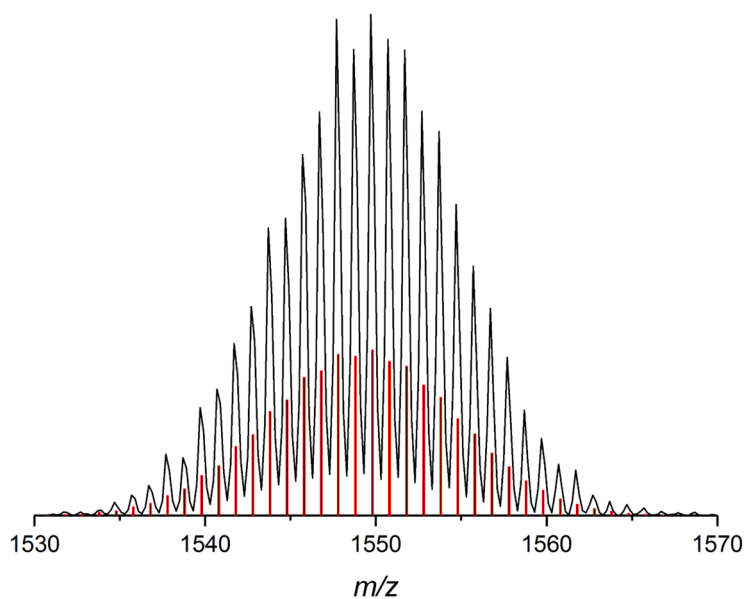


Figure S32. ESI-MS signal of $[\text{Ge}_9\{\text{Si}(\text{TMS})_3\}_2\{\text{CH}_2=\text{CH}(\text{CH}_2)_3\text{C}=\text{N}\}-\text{DAB}^{\text{Mes}}]^-$ (**3**⁻) at m/z 1549.8. Calculated isotope pattern is presented as red bars.

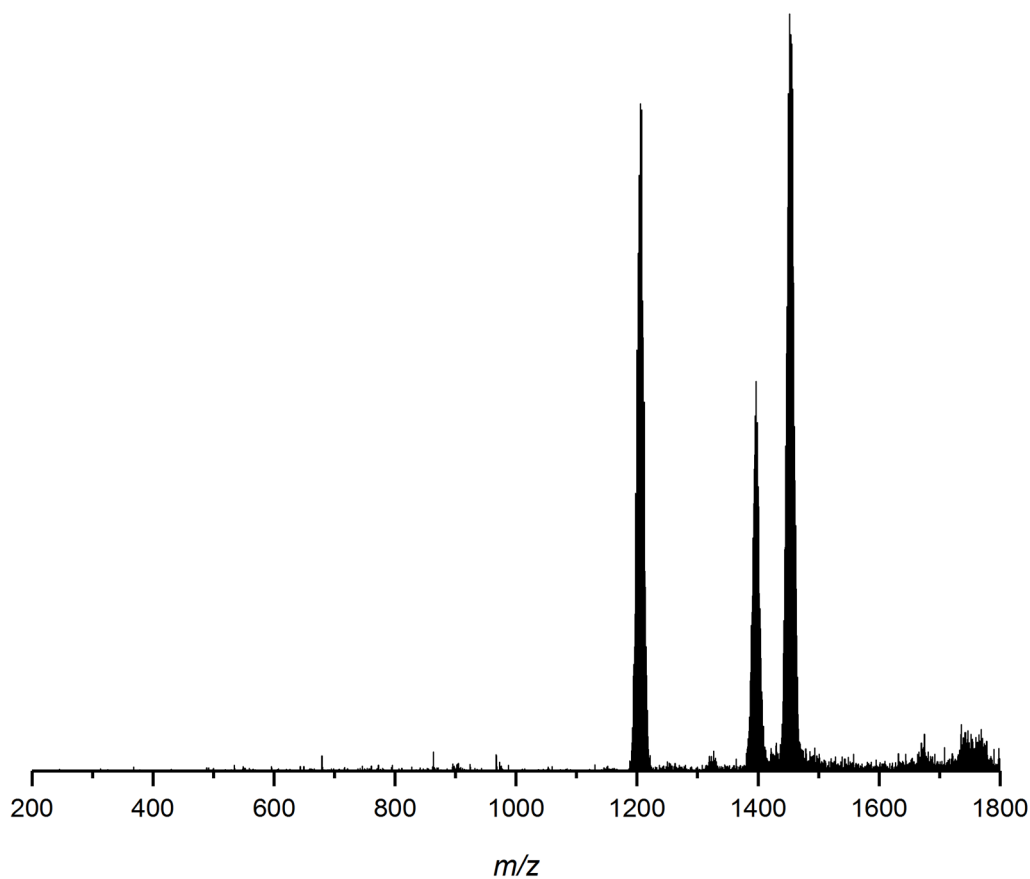


Figure S33. ESI-MS overview spectrum of the solution containing the anion $[\text{Ge}_9\{\text{Si}(\text{TMS})_3\}_2\{\text{CH}_3\text{CH}_2\text{C}=\text{N}\}\text{-DAB}^{\text{o-tol}}\text{-}]^-$ at m/z 1454.0. Ionization products: $[\text{Ge}_9\{\text{Si}(\text{TMS})_3\}_2\{\text{CH}_3\text{CH}_2\text{C}=\text{N}\}\text{-}]^-$ at m/z 1204.4; $[\text{Ge}_9\{\text{Si}(\text{TMS})_3\}_3\text{-}]^-$ at m/z 1396.5.

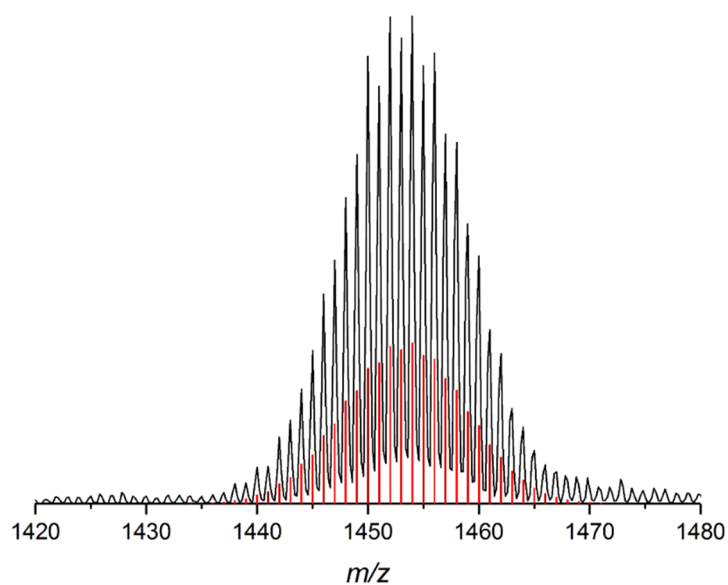


Figure S34. ESI-MS signal of $[\text{Ge}_9\{\text{Si}(\text{TMS})_3\}_2\{\text{CH}_3\text{CH}_2\text{C}=\text{N}\}\text{-DAB}^{\text{o-tol}}\text{-}]^-$ at m/z 1454.0. Calculated isotope pattern is presented as red bars.

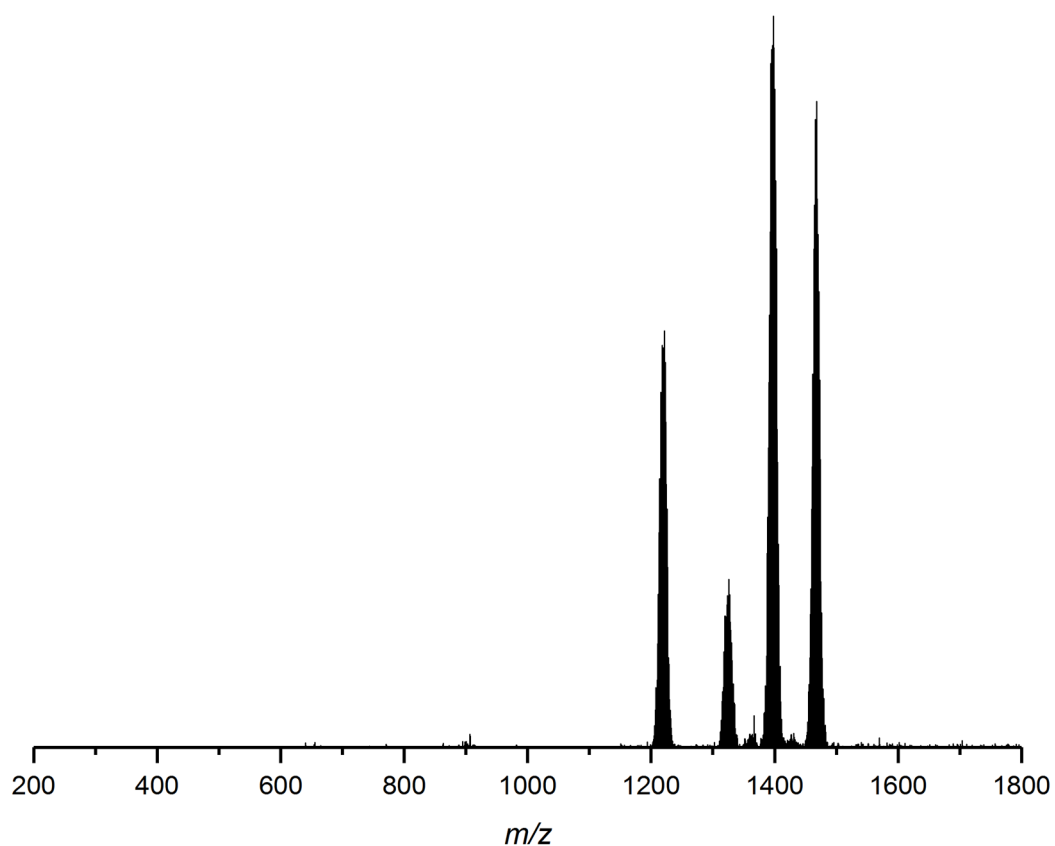


Figure S35. ESI-MS overview spectrum of the solution containing the anion $[\text{Ge}_9\{\text{Si}(\text{TMS})_3\}_2\{(\text{CH}_3)_2\text{CHC}=\text{N}\}\text{-DAB}^{\text{o-tol}}]^-$ at m/z 1467.3. Ionization products: $[\text{Ge}_9\{\text{Si}(\text{TMS})_3\}_2\{\text{C}_4\text{H}_8\text{O}\}]^-$ at m/z 1220.9; $[\text{Ge}_9\{\text{Si}(\text{TMS})_3\}_2\{\text{Si}(\text{TMS})_2\}]^-$ at m/z 1323.6; $[\text{Ge}_9\{\text{Si}(\text{TMS})_3\}_3]^-$ at m/z 1396.5.

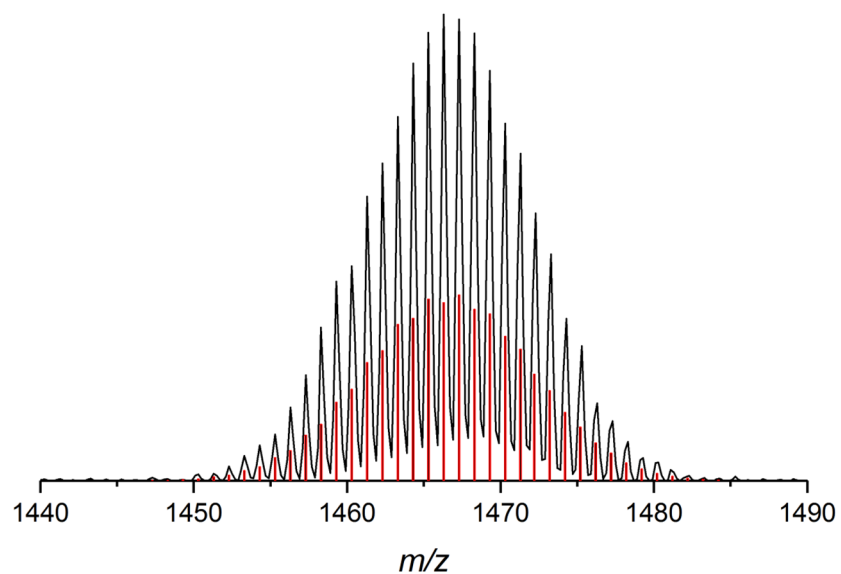


Figure S36. ESI-MS signal of $[\text{Ge}_9\{\text{Si}(\text{TMS})_3\}_2\{(\text{CH}_3)_2\text{CHC}=\text{N}\}\text{-DAB}^{\text{o-tol}}]^-$ at m/z 1467.3. Calculated isotopic pattern is presented as red bars.

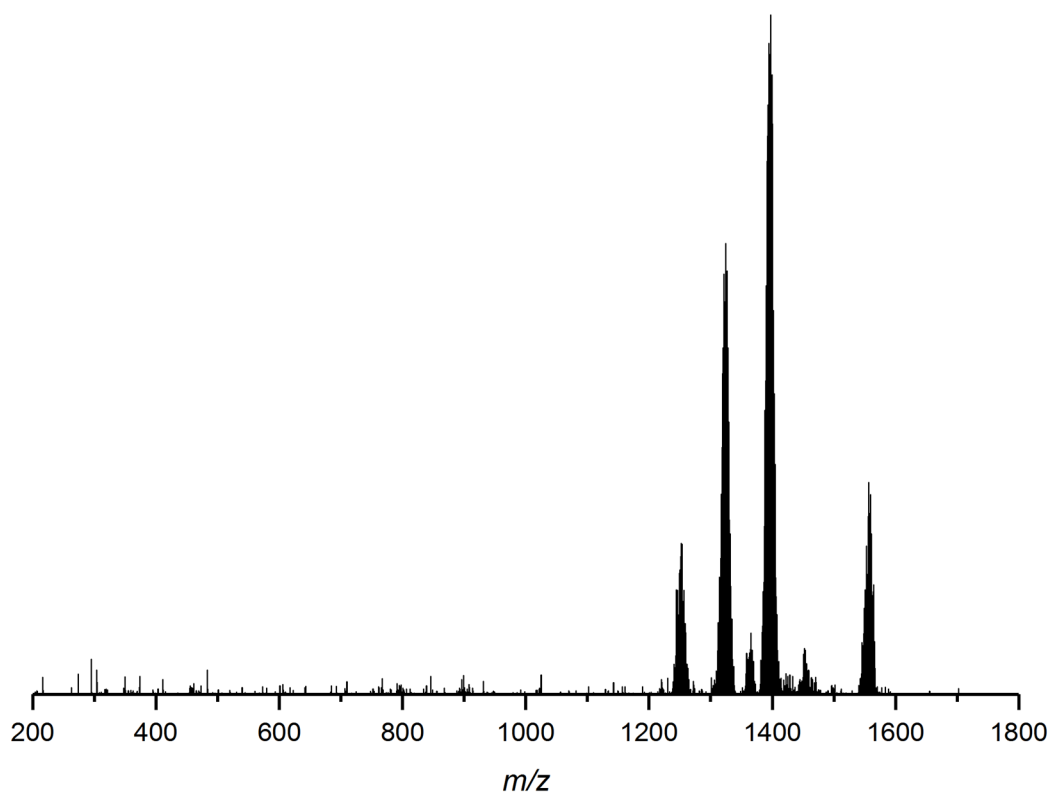


Figure S37. ESI-MS overview spectrum of the solution containing the anion $[\text{Ge}_9\{\text{Si}(\text{TMS})_3\}_2\{\text{PhC}=\text{N}\}\text{-DAB}^{\text{Mes}}]^-$ at m/z 1557.8. Ionization products: $[\text{Ge}_9\{\text{Si}(\text{TMS})_3\}_2\{\text{PhC}=\text{N}\}]^-$ at m/z 1252.3; $[\text{Ge}_9\{\text{Si}(\text{TMS})_3\}_2\{\text{Si}(\text{TMS})_2\}]^-$ at m/z 1323.6; $[\text{Ge}_9\{\text{Si}(\text{TMS})_3\}_3]^-$ at m/z 1396.5.

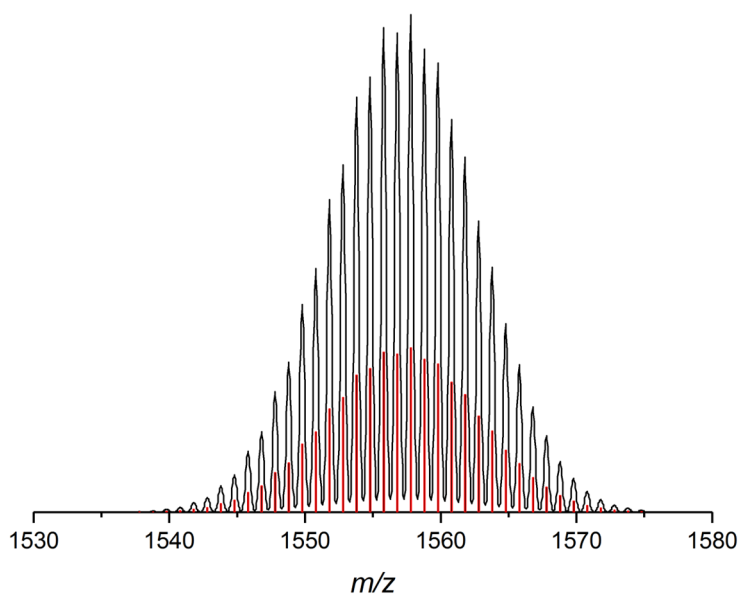


Figure S38. ESI-MS signal of $[\text{Ge}_9\{\text{Si}(\text{TMS})_3\}_2\{\text{PhC}=\text{N}\}\text{-DAB}^{\text{Mes}}]^-$ at m/z 1557.8. Calculated isotope pattern is presented as red bars.

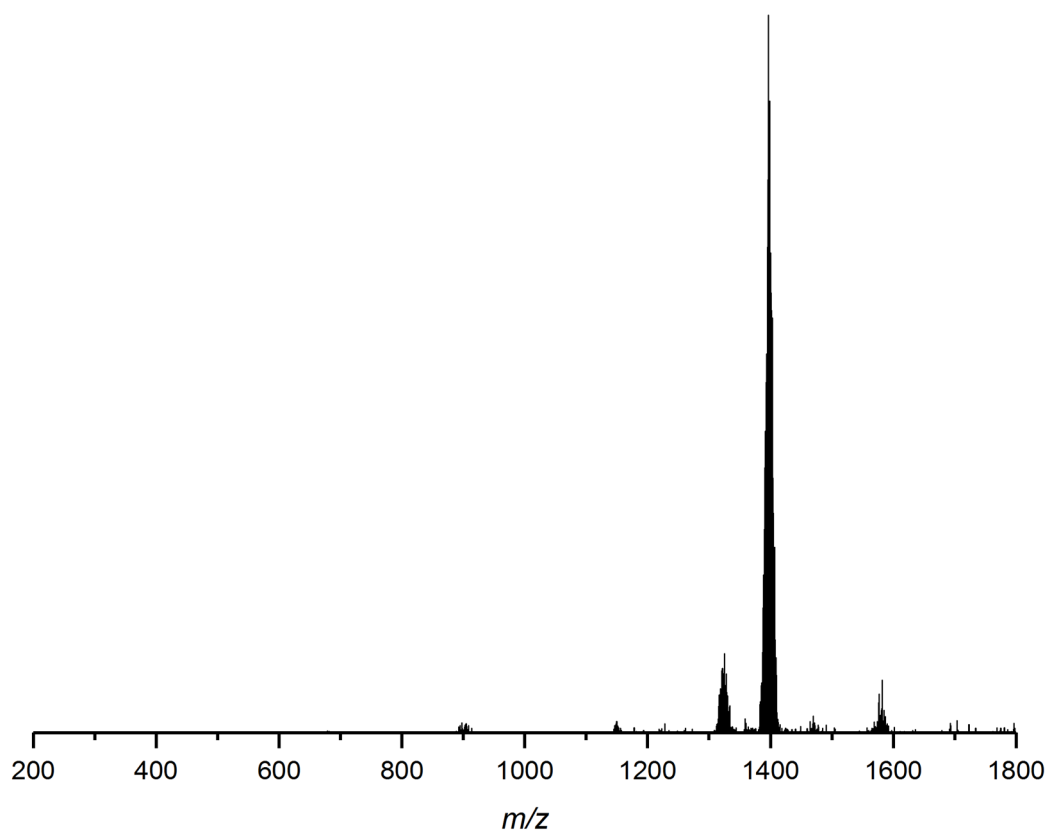


Figure S39. ESI-MS overview spectrum of the solution containing the anion $[\text{Ge}_9\{\text{Si}(\text{TMS})_3\}_2\{\text{CH}_3(\text{CH}_2)_9\text{C}=\text{N}\}\text{-DAB}^{\text{o-tol}}]^-$ at m/z 1580.1. Ionization products: $[\text{Ge}_9\{\text{Si}(\text{TMS})_3\}_2\{\text{Si}(\text{TMS})_2\}]^-$ at m/z 1323.6; $[\text{Ge}_9\{\text{Si}(\text{TMS})_3\}_3]^-$ at m/z 1396.5.

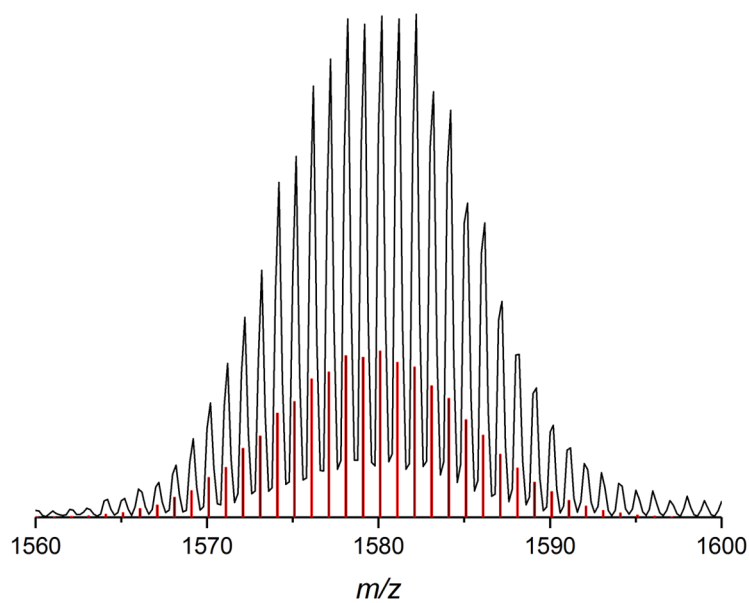
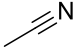
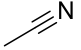
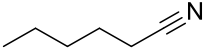
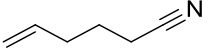
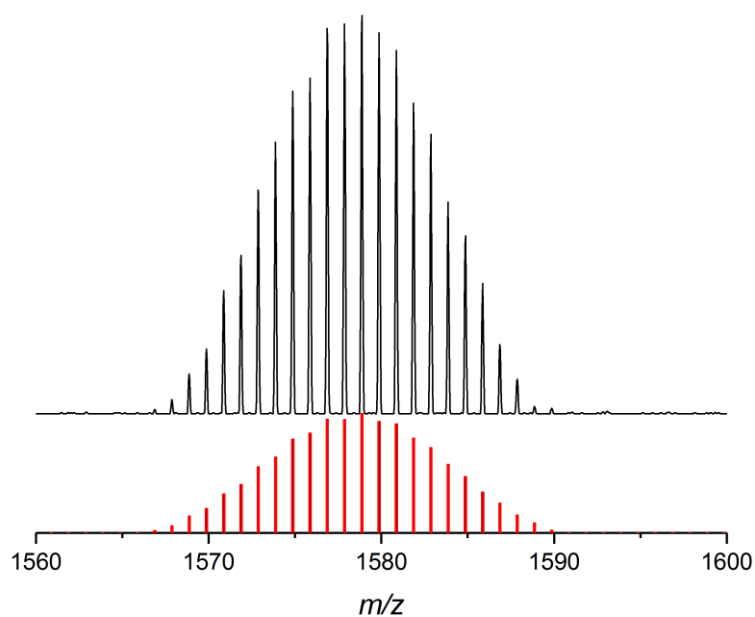


Figure S40. ESI-MS signal of $[\text{Ge}_9\{\text{Si}(\text{TMS})_3\}_2\{\text{CH}_3(\text{CH}_2)_9\text{C}=\text{N}\}\text{-DAB}^{\text{o-tol}}]^-$ at m/z 1580.1. Calculated isotope pattern is presented as red bars.

Table S5. Overview on LIFDI-MS mass peaks of neutral cluster compounds with incorporated imine moiety.

compound	nitrile	diazaborolidine	LIFDI-MS mass peak m/z
1-H		DAB(II) ^{Dipp} -Br	1578.9
1b-Cu		DAB(II) ^{Dipp} -Br	2029.1
2a-Cu		DAB ^{Mes} -Br	2003.1
3b-Cu		DAB ^{Mes} -Br	2001.1

**Figure S41.** LIFDI-MS signal of $[\text{Ge}_9\{\text{Si}(\text{TMS})_3\}_2\{\text{CH}_3\text{C}=\text{N}(\text{H})\}\text{-DAB}(\text{II})^{\text{Dipp}}]$ (**1-H**) at m/z 1578.9. Calculated isotope pattern is presented as red bars.

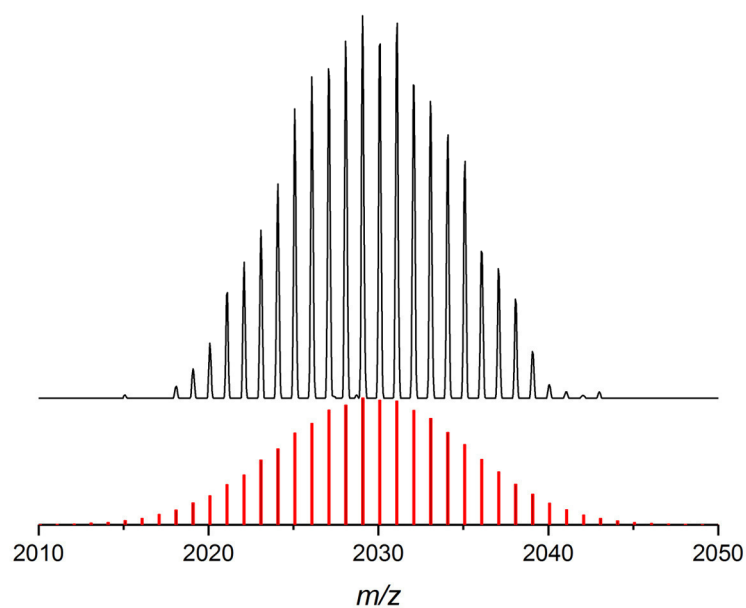


Figure S42. LIFDI-MS signal of $\text{CuNHC}^{\text{Dipp}}[\text{Ge}_9\{\text{Si}(\text{TMS})_3\}_2\{\text{CH}_3\text{C}=\text{N}\}\text{-DAB}(\text{II})^{\text{Dipp}}]$ (**1b-Cu**) at m/z 2029.1. Calculated isotope pattern is presented as red bars.

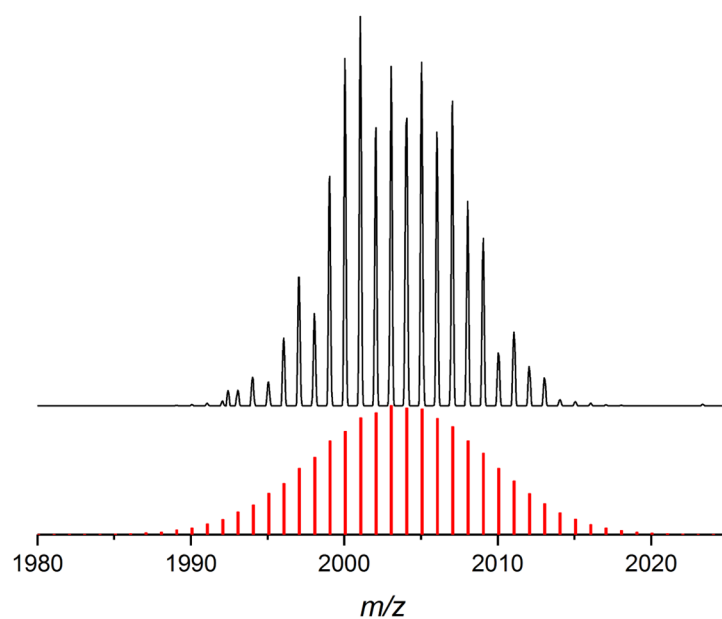


Figure S43. LIFDI-MS signal of $\text{CuNHC}^{\text{Dipp}}[\text{Ge}_9\{\text{Si}(\text{TMS})_3\}_2\{\text{CH}_3(\text{CH}_2)_4\text{C}=\text{N}\}\text{-DAB}^{\text{Mes}}]$ (**2a-Cu**) at m/z 2003.1. Calculated isotope pattern is presented as red bars.

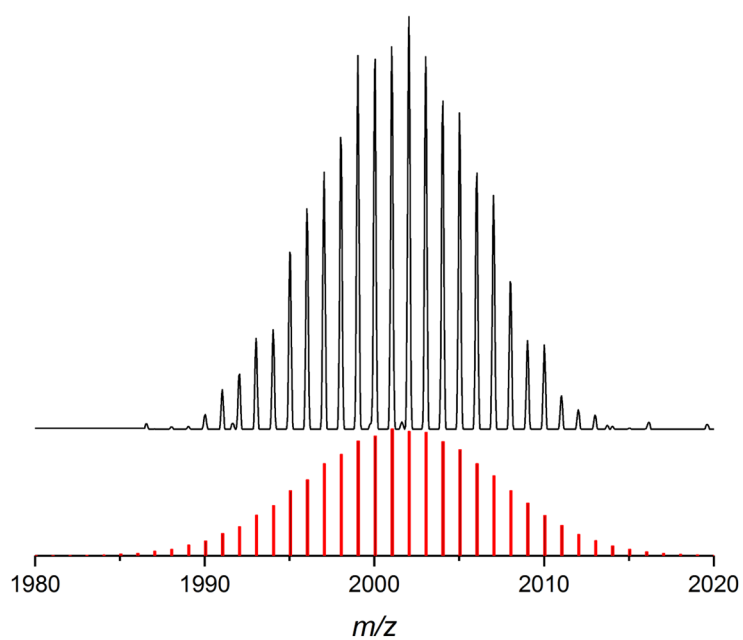


Figure S44. LIFDI-MS signal of $\text{CuNHC}^{\text{Dipp}}[\text{Ge}_9\{\text{Si}(\text{TMS})_3\}_2\{\text{CH}_2=\text{CH}(\text{CH}_2)_3\text{C}=\text{N}\}-\text{DAB}^{\text{Mes}}]$ (**3b-Cu**) at m/z 2001.1. Calculated isotope pattern is presented as red bars.

6. UV-Vis spectra

Absorption spectra

For the measurements an Eppendorf pipette was used to measure the volume of the standard solution and to fill up the cuvette to a total volume of exactly 3 ml. The standard solutions were prepared according to the following table. The syntheses of $K[Ge_9\{Si(TMS)_3\}_3]$ and of the compounds containing ring-opened ether fragments is described elsewhere.^[11-12] Note that the signals at $\lambda = 211$ to 221 nm (thf) and $\lambda = 301$ nm (toluene) are artefacts caused by the absorption of the solvent.

Table S6. Overview on the preparation of standard solutions for UV-Vis measurements and corresponding maximum absorption wavelength λ of the respective compounds.

Compound	mass [mg]	thf [ml]	toluene [ml]	λ [nm]
$K[Ge_9\{Si(TMS)_3\}_2\{CH_3C=N\}-DAB(II)^{Dipp}]$ (1-K)	1.3	5		248
$[Ge_9\{Si(TMS)_3\}_2\{CH_3C=N(H)\}-DAB(II)^{Dipp}]$ (1-H)	1.3		1	387, 437, 671
$[Ge_9\{Si(TMS)_3\}_2\{CH_3C=N(H)\}-DAB(II)^{Dipp}]$ (1-H)	4.2	1		433, 656
DAB ^{Mes} -Br	1.5	1		246, 328
DAB(II) ^{Dipp} -Br	1.5	1		247, 327
$K_2[Ge_9\{Si(TMS)_3\}_2]$	2.3	5		236
$K[Ge_9\{Si(TMS)_3\}_3]$	2.3	5		259
$K[Ge_9\{Si(TMS)_3\}_2\{(CH_2)_4-O\}-DAB(II)^{Dipp}]$	1.9	5		258
$K[Ge_9\{Si(TMS)_3\}_2\{(CH_2)_4-O\}-DAB^{Mes}]$	1.8	5		238
$K[Ge_9\{Si(TMS)_3\}_2\{(CH_2)_3-O\}-DAB^{Mes}]$	1.3	5		240

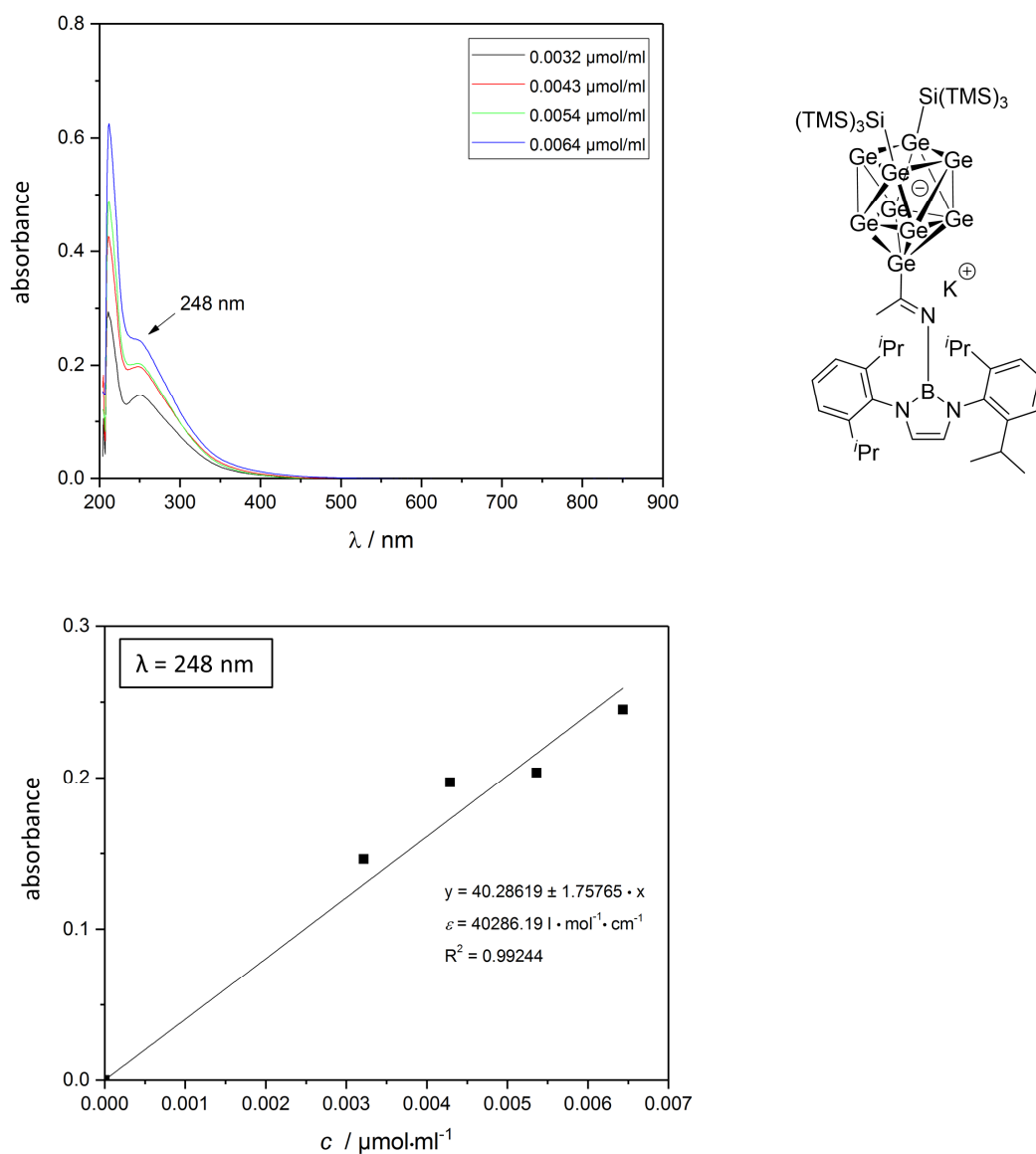
$[\text{Ge}_9\{\text{Si}(\text{TMS})_3\}_2\{\text{CH}_3\text{C}=\text{N}\}\text{-DAB}(\text{II})^{\text{Dipp}}]^- (1^-)$ 

Figure S45. UV-Vis absorption spectra (recorded in thf) and determination of the extinction coefficient at $\lambda = 248 \text{ nm}$ of $[\text{Ge}_9\{\text{Si}(\text{TMS})_3\}_2\{\text{CH}_3\text{C}=\text{N}\}\text{-DAB}(\text{II})^{\text{Dipp}}]^- (1^-)$.

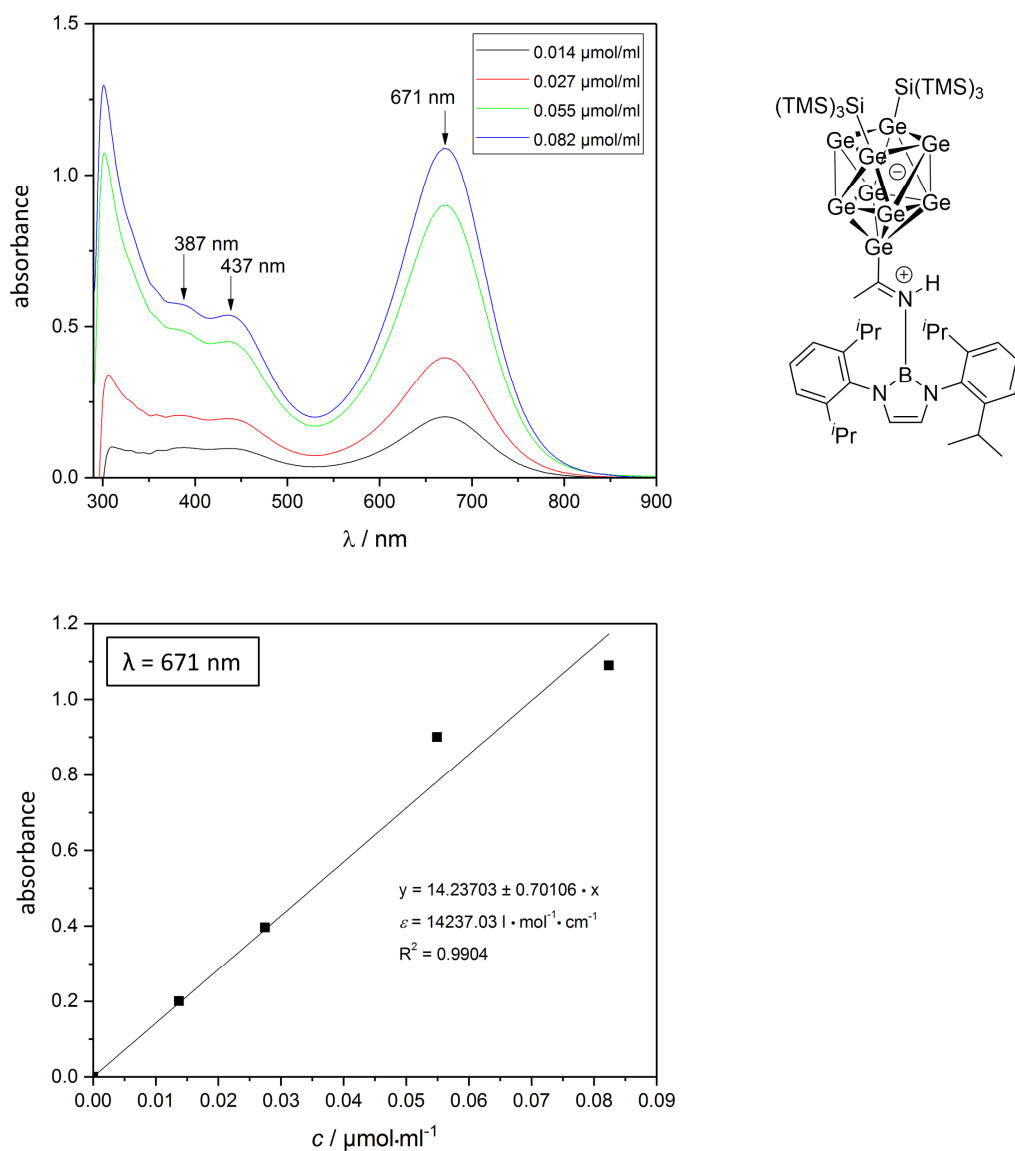
[Ge₉{Si(TMS)₃}₂{CH₃C=N(H)}-DAB(II)^{Dipp}] (1-H, toluene)

Figure S46. UV-Vis absorption spectra (recorded in toluene) and determination of the extinction coefficient at λ = 671 nm of [Ge₉{Si(TMS)₃}₂{CH₃C=N(H)}-DAB(II)^{Dipp}] (1-H).

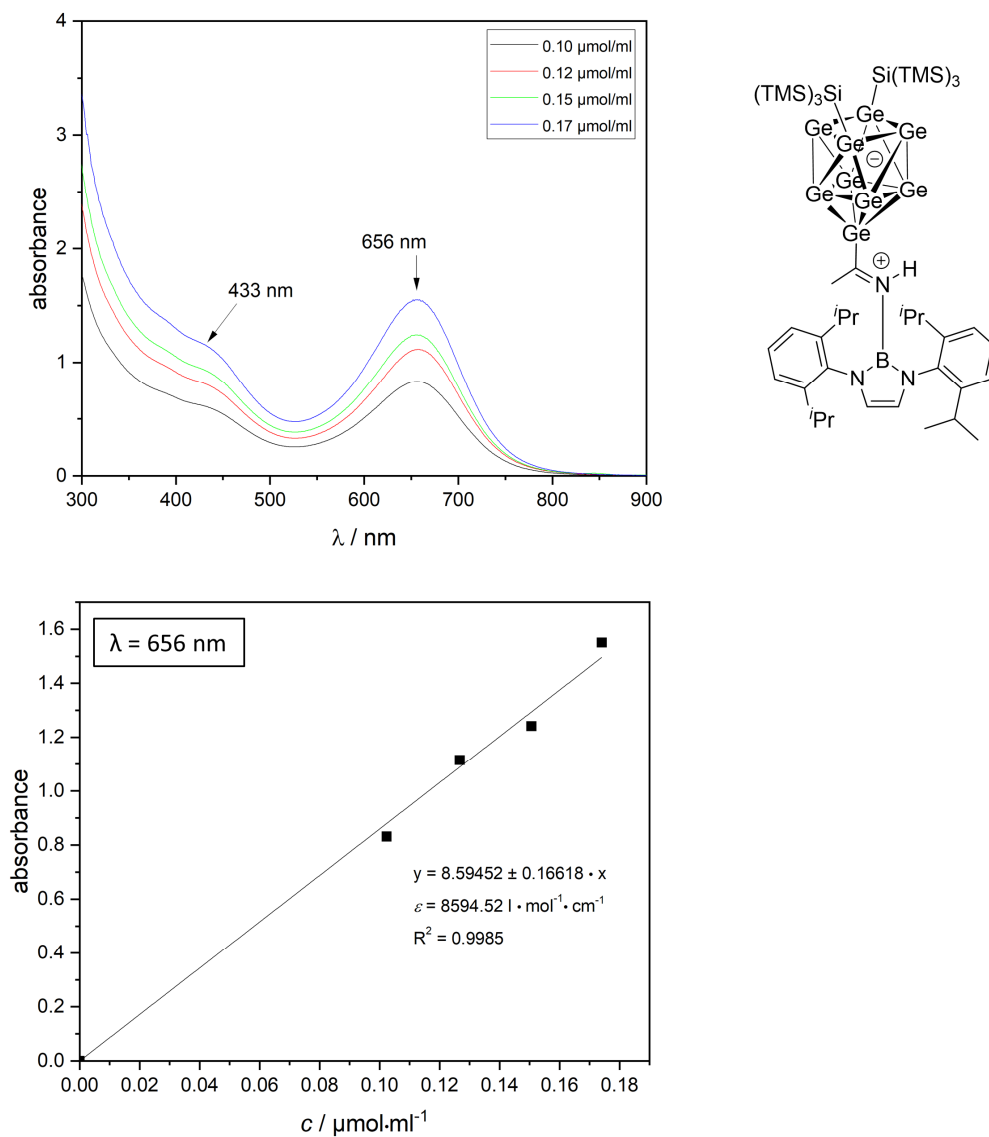
[Ge₉{Si(TMS)₃}₂{CH₃C=N(H)}-DAB(II)^{Dipp}] (1-H, thf)

Figure S47. UV-Vis absorption spectra (recorded in thf) and determination of the extinction coefficient at $\lambda = 656 \text{ nm}$ of $[\text{Ge}_9\{\text{Si}(\text{TMS})_3\}_2\{\text{CH}_3\text{C}=\text{N}(\text{H})\}\text{-DAB}(\text{II})^{\text{Dipp}}]$ (**1-H**).

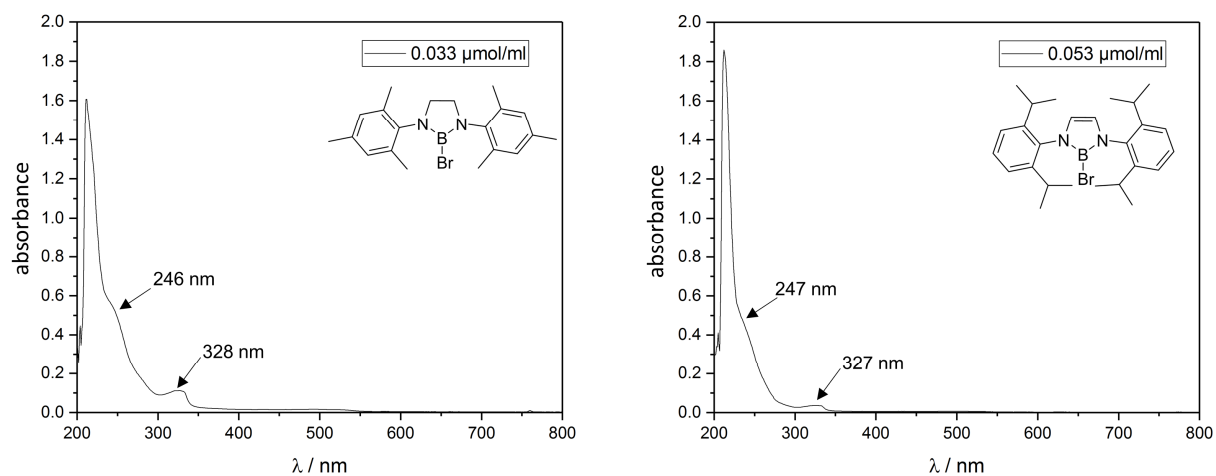
DAB^{Mes}-Br and DAB(II)^{Dipp}-Br

Figure S48. UV-Vis absorption spectra (recorded in thf) of DAB^{Mes}-Br (left) and DAB(II)^{Dipp}-Br (right).

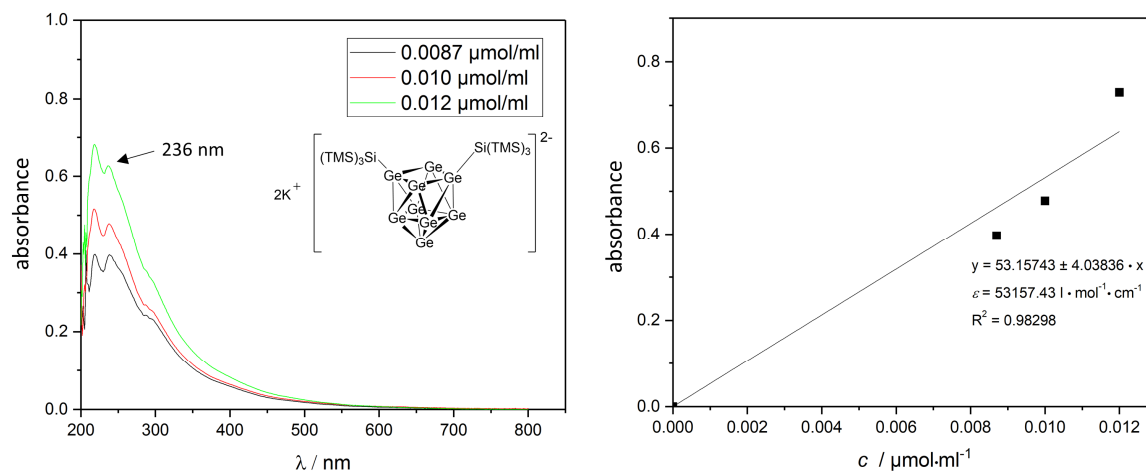
K₂[Ge₉{Si(TMS)₃}₂]

Figure S49. UV-Vis absorption spectra (recorded in thf) and determination of the extinction coefficient at λ = 236 nm of K₂[Ge₉{Si(TMS)₃}₂].

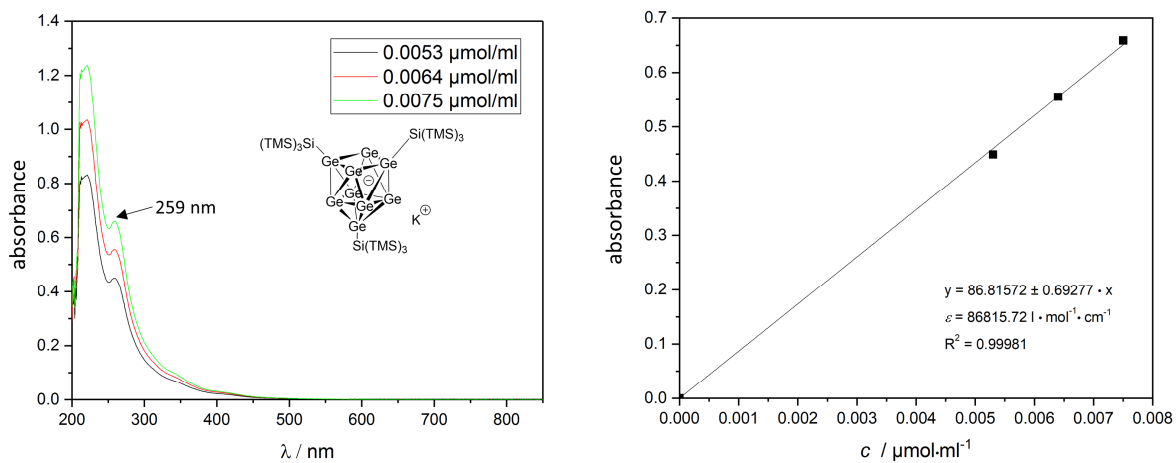
K[Ge₉{Si(TMS)₃}₃]

Figure S50. UV-Vis absorption spectra (recorded in thf) and determination of the extinction coefficient at $\lambda = 259 \text{ nm}$ of K[Ge₉{Si(TMS)₃}₃].

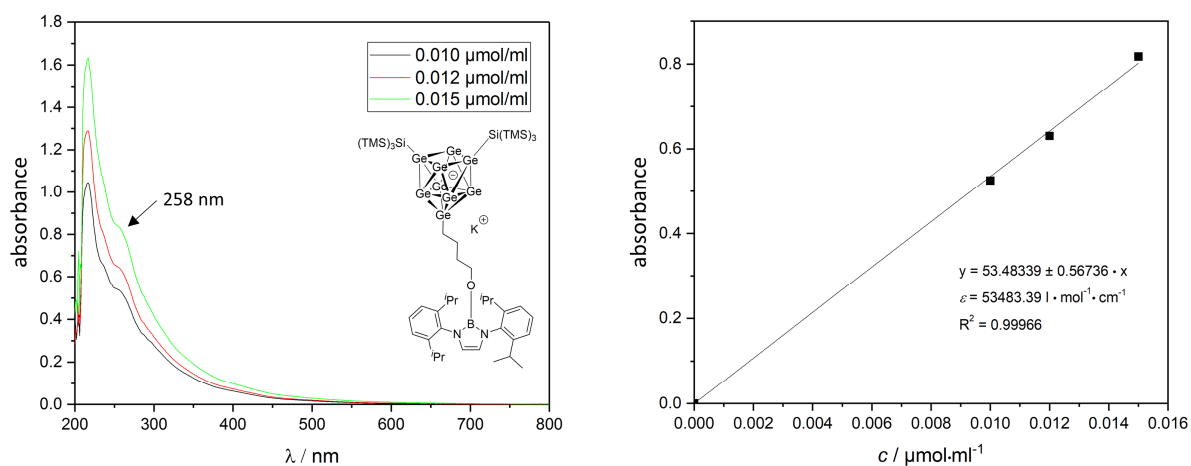
K[Ge₉{Si(TMS)₃}₂{(CH₂)₄-O}-DAB(II)^{Dipp}]

Figure S51. UV-Vis absorption spectra (recorded in thf) and determination of the extinction coefficient at $\lambda = 258 \text{ nm}$ of K[Ge₉{Si(TMS)₃}₂{(CH₂)₄-O}-DAB(II)^{Dipp}].

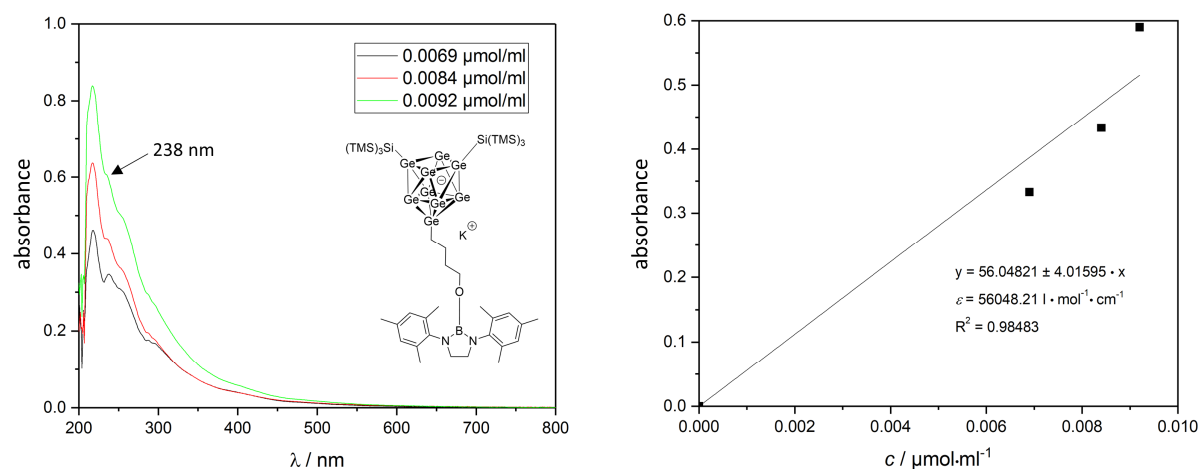
K[Ge₉{Si(TMS)₃}₂{(CH₂)₄-O}-DAB^{Mes}]

Figure S52. UV-Vis absorption spectra (recorded in thf) and determination of the extinction coefficient at $\lambda = 238$ nm of K[Ge₉{Si(TMS)₃}₂{(CH₂)₄-O}-DAB^{Mes}].

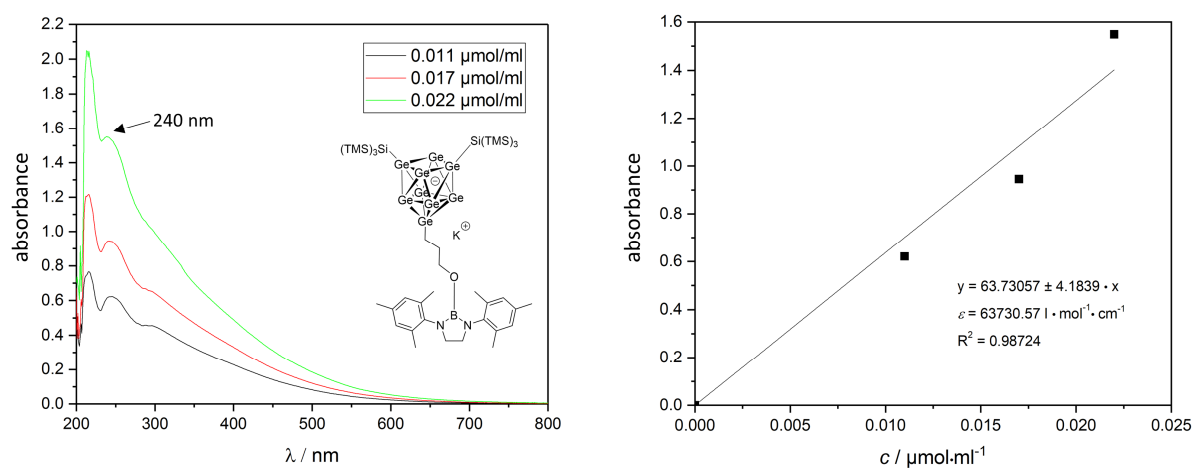
K[Ge₉{Si(TMS)₃}₂{(CH₂)₃-O}-DAB^{Mes}]

Figure S53. UV-Vis absorption spectra (recorded in thf) and determination of the extinction coefficient at $\lambda = 240$ nm of K[Ge₉{Si(TMS)₃}₂{(CH₂)₃-O}-DAB^{Mes}].

7. Kinetic studies

The protonation of the red species **1⁻** to yield **1-H** (deep green, Figure 53b) is reversible. The stepwise addition of defined amounts of KO^tBu leads to decreasing amounts of the protonated species **1-H** until solely **1⁻** remains in solution (C₆D₆).

For the reaction set-up **1-H** (13 mg, 8.3 μmol) was weighed in a J-Young tube and 0.4 ml C₆D₆ was added. A standard solution of KO^tBu (1 mg, 9.0 μmol) in 0.1 ml of C₆D₆ and 10 μl thf-*d*₈ was prepared. 20 μl of the KO^tBu solution was added to the green solution in the NMR tube and a ¹H NMR spectrum was recorded (Figure 53c). The ratio of **1-H**:**1⁻** can be determined by integrating the silyl group protons (**1⁻**: δ = 0.51 ppm; **1-H**: δ = 0.47 ppm). The rest of the standard solution was added to the NMR tube, and the ¹H NMR spectrum shows a full deprotonation of **1-H** yielding **1⁻** (Figure S53d).

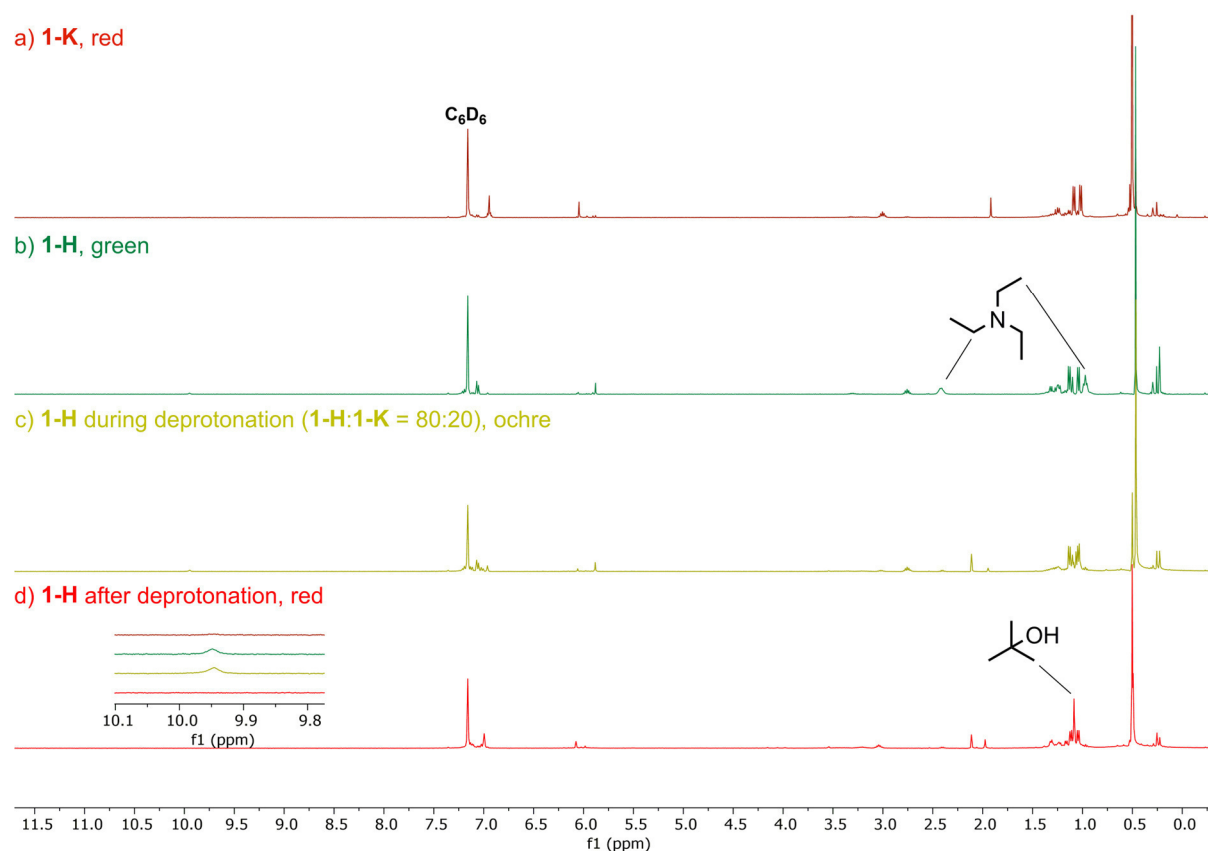
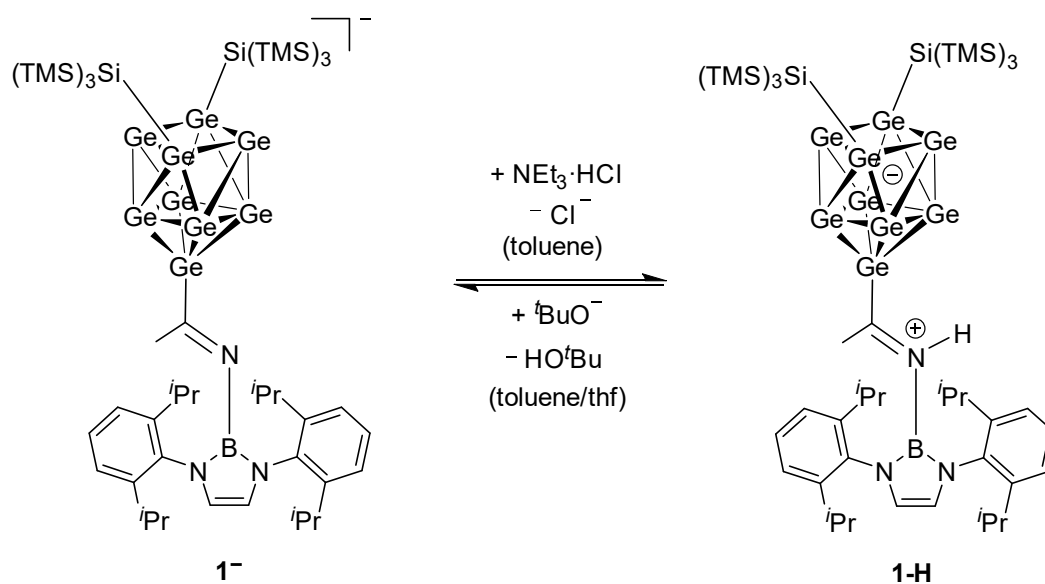


Figure S54. Reversible protonation of **1⁻** in C₆D₆. a) ¹H NMR spectrum of anion **1⁻** in C₆D₆; b) formation of **1-H** by addition of 1 eq. NEt₃·HCl to the reaction solution; c) addition of 0.2 eq. KO^tBu to a solution of **1-H** in C₆D₆; d) full conversion of **1-H** into **1⁻** upon addition of 1 eq. KO^tBu.



Scheme 1. Reversible formation of the zwitterion **1-H** by addition of $\text{NEt}_3 \cdot \text{HCl}$ to **1⁻**, and subsequent deprotonation by KO^tBu .



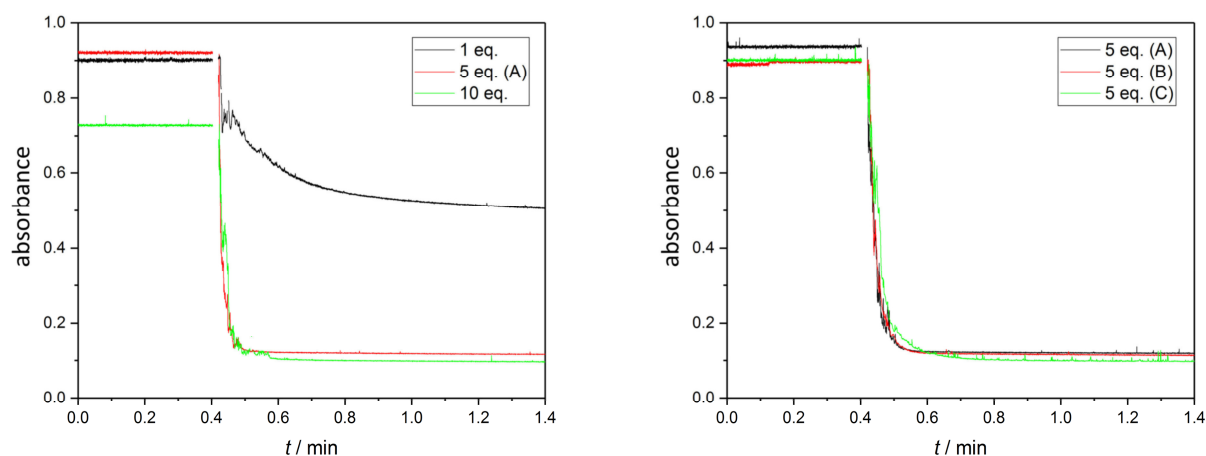
Figure S55. UV-Vis cuvettes with a solution of **1⁻** after the deprotonation using KO^tBu (left), and before the deprotonation (**1-H**, right). The yellowish color of **1⁻** is a concentration effect, in higher concentrations **1⁻** is deep red.

The deprotonation of **1-H** can also be monitored in the UV-Vis spectrometer. A standard solution of **1-H** (2.6 mg, 1.6 μmol) in 2 ml toluene was prepared. For each measurement 300 μl of the standard solution was transferred in the cuvette, 2.7 ml of toluene was added, and the cuvette was sealed with a rubber septum. A second standard solution of KO^tBu (2.7 mg, 24 μmol) in 1 ml thf was prepared. For the measurements the following volumes of the KO^tBu standard solution were used.

Table S7. Summary of the used volumes of the standard KO^tBu solution for the deprotonation of **1-H** in UV-Vis studies.

equivalents	volume KO ^t Bu standard [μ l]
1	10
5	50
10	100

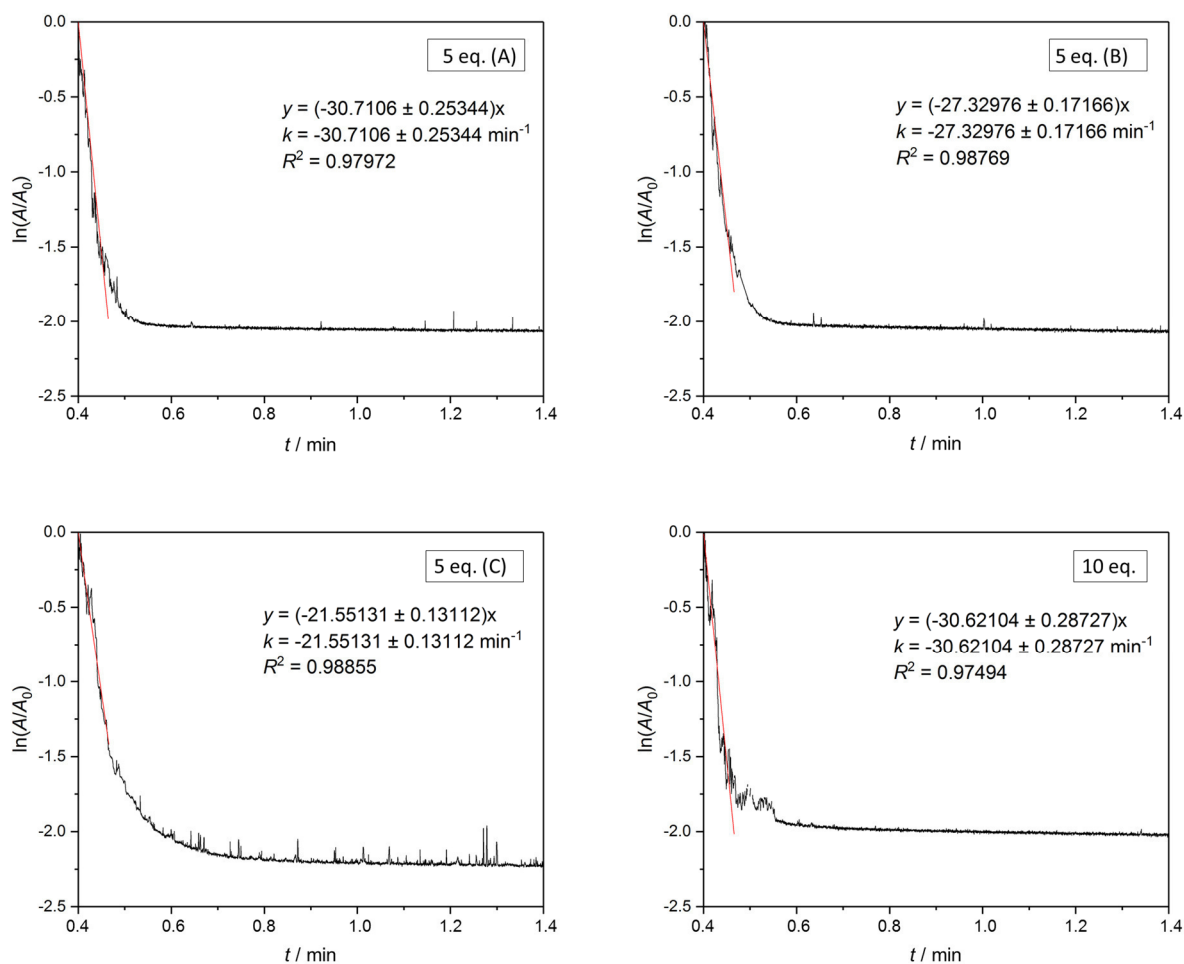
For the measurements the absorption at a 671 nm excitation wavelength was continuously recorded. The respective amount of KO^tBu solution was taken up in a Hamilton syringe and added via the septum in one single shot directly into the stirred green solution of **1-H**. The injection led to strong absorption bands at approximately $t = 0.4$ min caused by the needle of the syringe disturbing the beam path. The corresponding spike-signals were deleted for plotting the data. A time-dependent decrease of the absorption was observed (Figure S55). The measurement for 5 eq. was repeated three times (A-C).

**Figure S56.** Time-dependent absorption spectra of **1-H** recorded at an excitation wavelength of 671 nm and addition of 1, 5, or 10 eq. of KO^tBu. Small spikes are caused by the jumping stirring bar.

A reaction of pseudo-first order is assumed for the addition of 5 and 10 eq. of KO^tBu as the slopes of the curves are almost identically. By applying the equation $A = A_0 e^{-kt}$ the rate constant k is determined from the plot of $\ln(A/A_0)$ over t and performing a linear regression (A : absorption, k : rate constant, t : time, Figure S56).^[13]

Table S8. Summary of the calculated rate constants for the deprotonation of **1-H** for different equivalents of KO^tBu investigated by UV-Vis measurements.

equivalents	rate constant k [min ⁻¹]
5 (A)	-30.7
5 (B)	-27.3
5 (C)	-21.5
10	-30.6

**Figure S57.** Plots for the determination of the rate constant k . Recorded data is presented in black, linear regression is indicated by red lines.

The addition of a mixture of equimolar amounts of KO^tBu and [2.2.2]cryptand to a green solution of **1-H** led to an instant colour change to red. The rate constant was determined to approximately -500 min^{-1} . However, the collected data should only be seen as approximate values as the data collection was limited by the time resolution of the UV-Vis spectrometer.

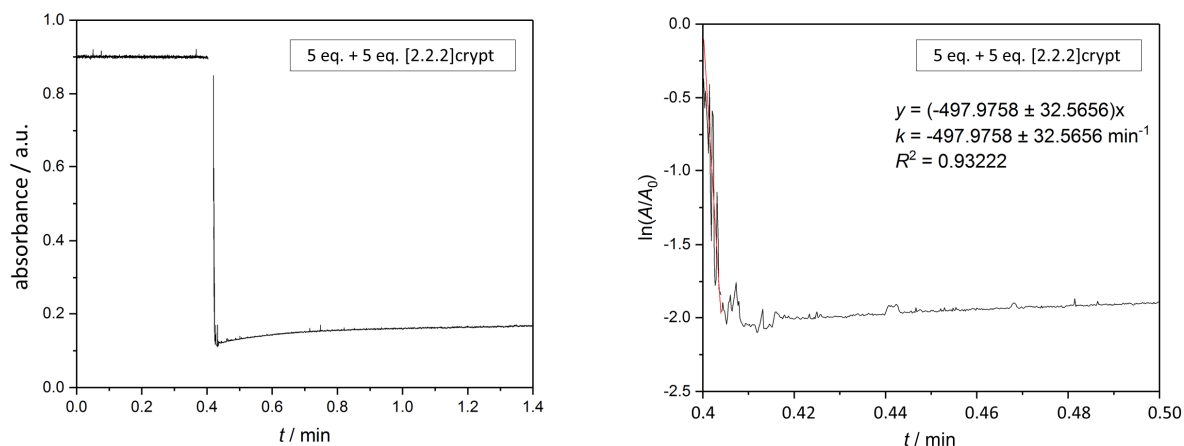


Figure S58. Absorption spectrum and linear regression for the deprotonation of **1-H** by addition of a mixture of KO^tBu and [2.2.2]cryptand (5 eq. each). Recorded data is presented in black, linear regression is indicated by the red line. Small spikes are caused by the jumping stirring bar.

8. Computational details

Quantum chemical calculations were carried out for compound **1-H** with the TURBOMOLE program package,^[14] using the PB86 hybrid density functional method (DFT-BP86),^[15-16] and polarized triple- ζ -valence Karlsruhe basis sets (def2-TZVP for Ge, Si, B, and N and def-TZVP for C and H).^[17] Multipole-accelerated resolution-of-the-identity technique was used to speed up the calculations.^[18-20] *m4* integration grid was applied for the numerical integration of the exchange-correlation functional. The initial geometry of the compound **1-H** was taken from the crystal structure. Concerning the split position of the hypersilyl group, only the group with the larger site occupancy factor of 0.835 was considered. The geometry of the compound was fully optimized at the DFT-BP86/TZVP level of theory without any symmetry constraints. Ge-Ge distances vary between 2.59 Å and 2.74 Å in the optimized structure. The Ge-C1 and C1-N distances are 1.94 Å and 1.35 Å, respectively. The HOMO-LUMO gap at the optimized geometry is 1.40 eV.

The first vertical excitation energies of the 30 lowest-energy singlet excited states of **1-H** were calculated at the optimized S_0 geometry using time-dependent DFT (TD-DFT).^[21-22] The most intense excitations in the calculated absorption spectrum were observed at $\lambda = 495$ nm (2.14 eV, transition $S_0 \rightarrow S_8$) and $\lambda = 669.0$ nm (1.85 eV, transition $S_0 \rightarrow S_2$). The VMD program was used to visualize the electron density difference plots of the singlet excitations.^[23] The molecular orbitals of compound **1-H** were illustrated using IboView.^[24] We also carried out TD-DFT calculations on the anion **1⁻** (experimental absorption maxima at $\lambda = 211$ nm and $\lambda = 248$ nm) to confirm that the calculations did not provide similar excited states as in **1-H**.

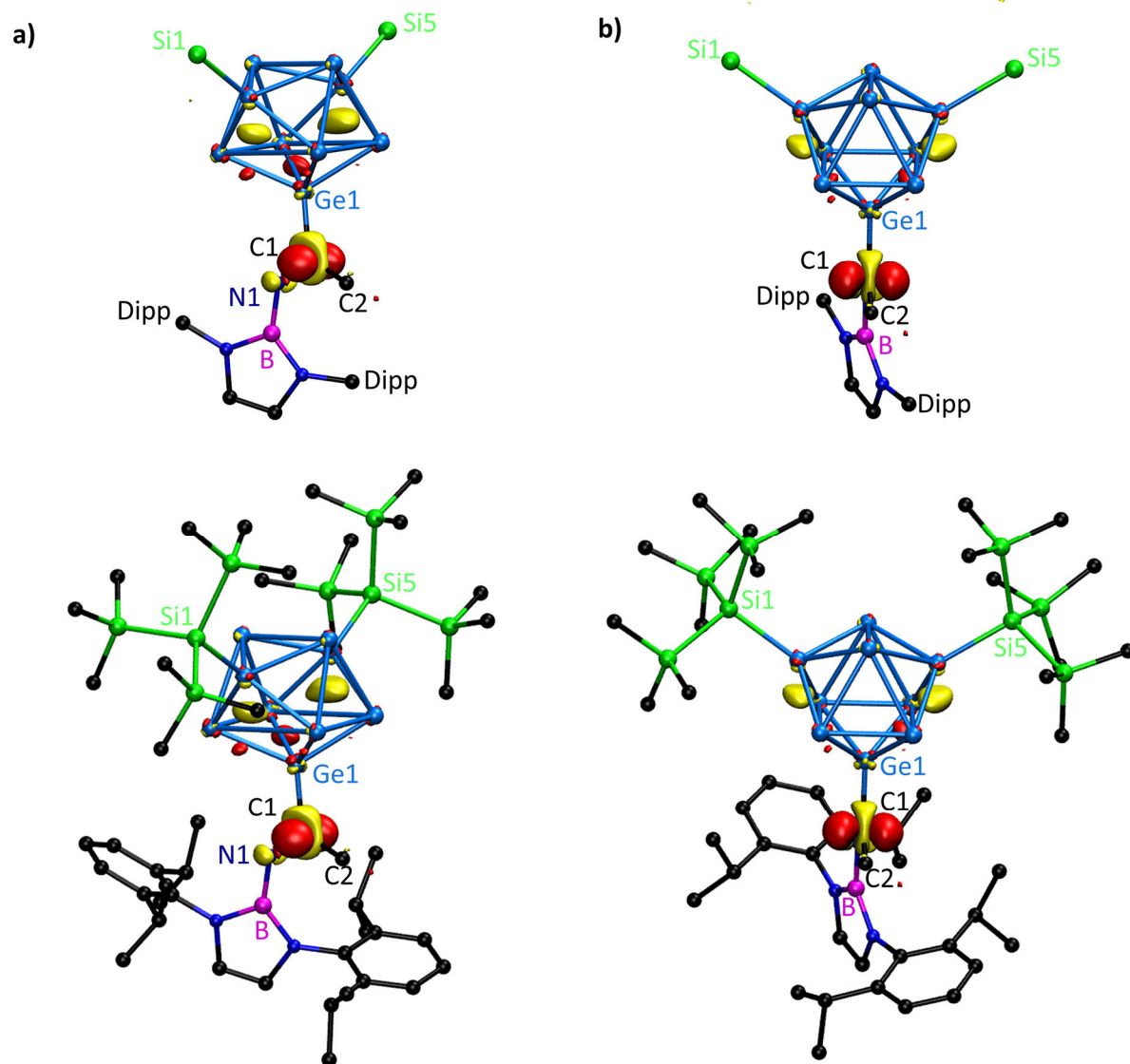


Figure S59. Electron density difference plots for the $S_0 \rightarrow S_2$ excitation of compound **1-H** (calculated $\lambda = 669$ nm). a) and b) show the same molecule from different perspectives with neglected TMS groups and Dipp-ligands (above) or the full molecule (below). During the electronic transition, the red color corresponds to increasing electron density and yellow color corresponds to decreasing electron density. The isovalue of the electron density isosurfaces is 0.002 a.u. and hydrogen atoms are omitted for clarity.

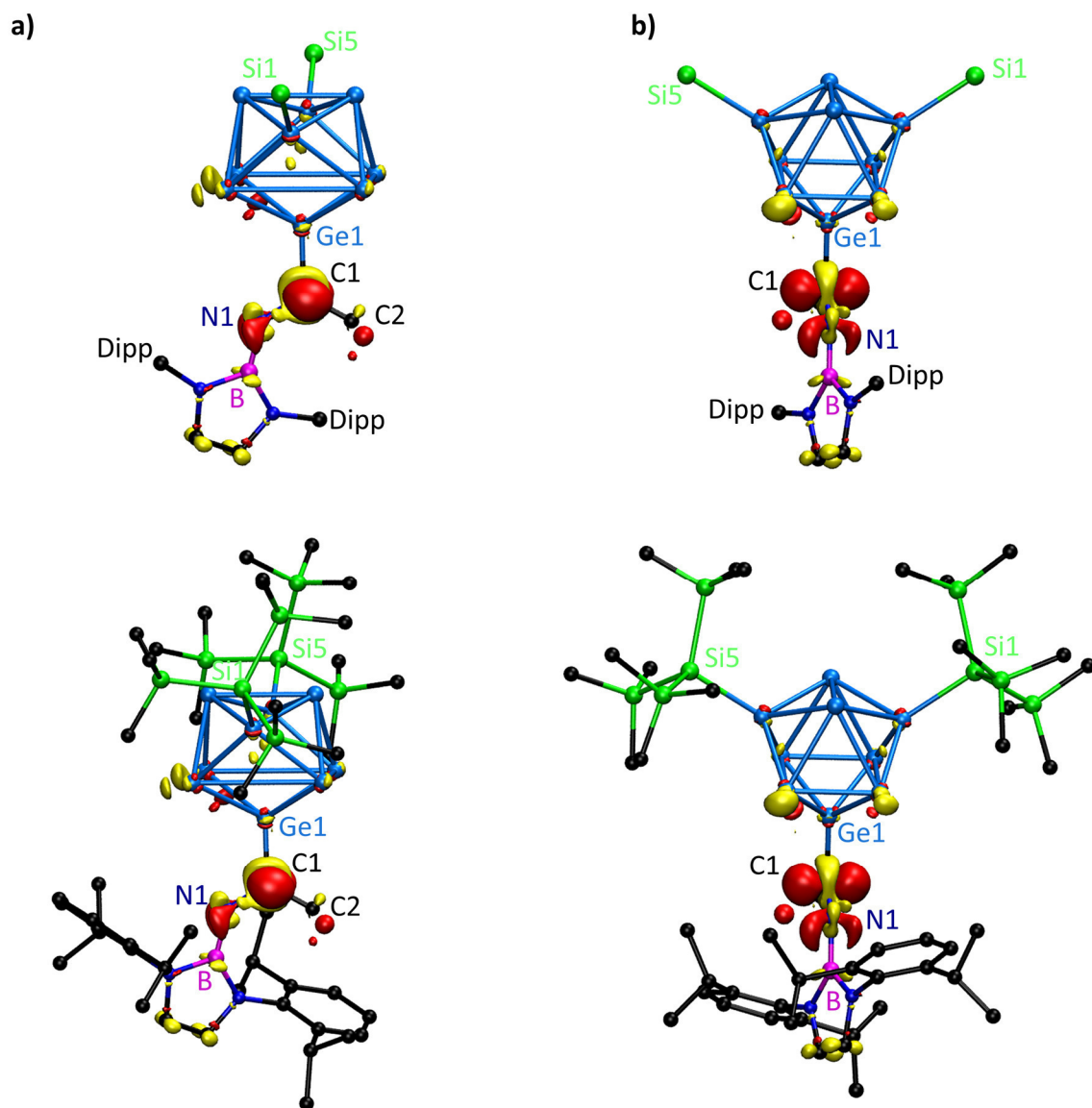


Figure S60. Electron density difference plots for the $S_0 \rightarrow S_8$ excitation of compound **1-H** (calculated $\lambda = 495$ nm). a) and b) show the same molecule from different perspectives with neglected TMS groups and Dipp-ligands (above) or the full molecule (below). During the electronic transition, the red color corresponds to increasing electron density and yellow color corresponds to decreasing electron density. The isovalue of the electron density isosurfaces is 0.002 a.u. and hydrogen atoms are omitted for clarity.

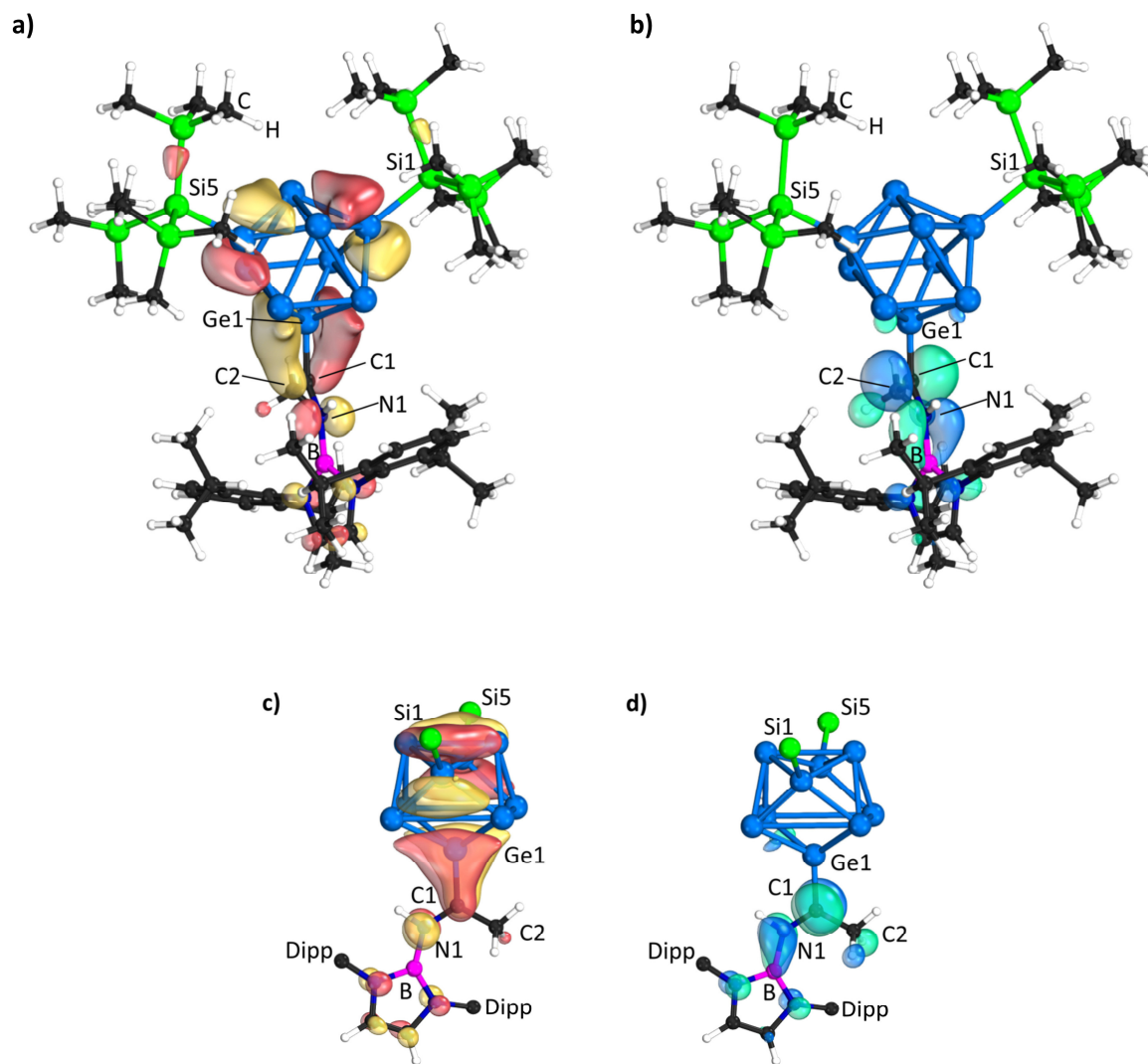


Figure S61. Full plot of a) the HOMO and b) the LUMO of **1-H**. Furthermore, alternative orientations of c) the HOMO and d) the LUMO of **1-H** are presented. Orbital figures are drawn in such way that 50 % of the density is enclosed within the surface, corresponding approximately to an isovalue of 0.04 a.u.

To exclude that the imine ligand causes the intensive absorption band at $\lambda = 671$ nm for **1-H**, we optimized the structure of the ligand fragment $[\text{DAB}^{\text{Dipp}}\text{N}(\text{H})=\text{CHCH}_3]^+$ at the DFT-BP86/TZVP level of theory and calculated its lowest-energy singlet excited states. Within the cation, the $[\text{Ge}_9]$ cluster moiety was replaced with a hydrogen atom.

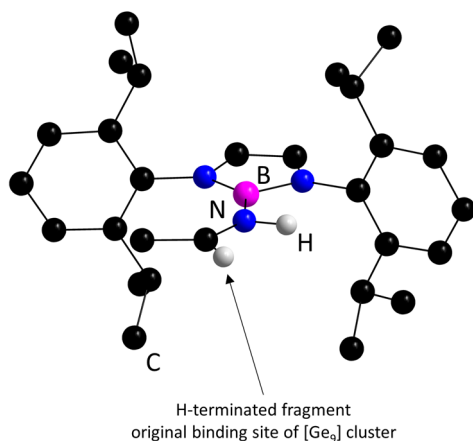


Figure S62. Optimized structure of the H-terminated ligand fragment $[\text{DAB}^{\text{Dipp}}\text{N}(\text{H})=\text{CHCH}_3]^+$.

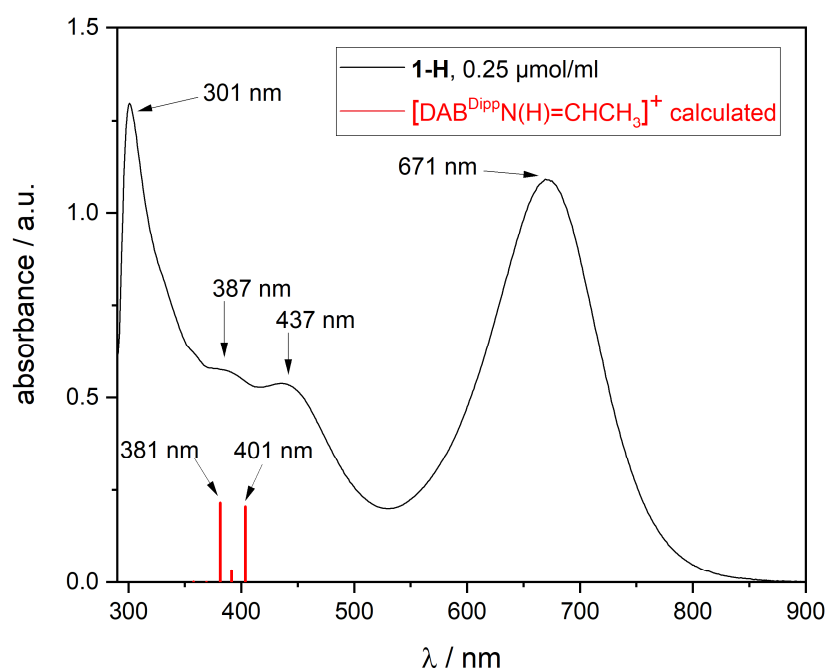


Figure S63. UV-Vis absorption spectra (recorded in toluene) of compound **1-H** and the calculated lowest-energy singlet vertical excitations for the H-terminated ligand fragment $[\text{DAB}^{\text{Dipp}}\text{N}(\text{H})=\text{CHCH}_3]^+$.

Optimized Cartesian coordinates of 1-H in XYZ format.

161

Compound 1-H, DFT-BP86/TZVP

H	21898788	-819671	74986750
C	53759330	7798351	76424216
H	59259355	12025603	84968713
H	43399366	11415751	77008657
H	58242399	11800748	67207557
C	21682227	-10529304	70170493
N	28555168	-21481411	75719343
C	15182580	-14345334	58851296
B	26058040	-32904015	67152460
C	35166067	-19949140	88414310
H	9087937	-8414402	52118553
N	17513671	-27935749	56581014
N	29499199	-47167237	67553338
C	47665401	-13311409	88947300
C	28803262	-24727961	100115960
C	12077084	-34985599	45281842
Ge	39079844	-74030840	71172727
C	39109433	-54783878	73226976
H	23136935	-52635198	61643017
C	53823440	-11876029	101462763
C	54441155	-7614712	76513970
C	35481498	-23128630	112355406
C	14962366	-31132306	99937580
C	19941152	-36391951	33596482
C	-1004648	-40339507	46133248
Ge	16204130	-86484093	71831670
Ge	49514167	-88243605	90288181
Ge	62126516	-85554542	67555501
Ge	28911932	-83760937	49219891
C	49962290	-48123145	81025150
H	63487249	-6844586	102118145
C	47874496	-16801596	113070005
H	48873112	-11240036	67747050
C	69044667	-12287330	75040111
H	30809728	-26834929	121499382
H	11688229	-31729143	89456848
C	4756590	-22318861	107419760
C	15069378	-45447002	105606215
C	14431568	-43399666	22771274
C	33936848	-30465634	32422295

C	-6028940	-47216085	34988394
C	-9692753	-38680935	58555947
Ge	29784597	-104239407	84885642
Ge	25736579	-108997646	59498987
Ge	52923409	-110381494	74585149
Ge	48791061	-100312161	50880429
H	58012359	-55198305	83334521
H	46176610	-44056503	90540192
H	54160704	-39626429	75391548
H	52886576	-15653045	122697834
H	69869800	-23245866	75122568
H	75393932	-8408909	83142950
H	73246155	-8643925	65549296
H	7306266	-21442829	118088937
H	-5312152	-26700776	106736281
H	4366591	-12170560	103211009
H	18087511	-45575279	116185095
H	21949052	-51984881	100065018
H	5020535	-49870510	104978077
H	20328675	-44677446	13674759
C	1588120	-48770181	23422814
H	36299608	-25625057	42011314
C	34503323	-19585651	21516883
C	44560146	-41337430	29939542
H	-16070697	-51472745	35416687
H	-3475682	-34038405	66355189
C	-21502848	-29152417	55807713
C	-14710941	-52185147	63998595
Si	19434084	-118958316	101273352
Si	58428745	-112335043	32011176
H	-2486142	-54226864	14893943
H	44507075	-15015928	21173497
H	27168112	-11615696	23401269
H	32410153	-23792189	11566222
H	44344212	-49054684	37763952
H	54624412	-36892757	29778323
H	42993035	-46355022	20276263
H	-27436603	-27637454	64948719
H	-28188486	-33265822	48093993
H	-18027837	-19319457	52328608
H	-20310636	-50674836	73346732
H	-6415394	-59097895	66077976
H	-21467656	-57160767	56883477
Si	25362754	-109992902	122573359
Si	27203290	-141352884	98592827
Si	-4146325	-117550299	97796467
Si	65574266	-133896153	39325894

Si	76760981	-99180102	24271506
Si	41601808	-114306739	15177896
C	14830370	-117945006	136237568
C	22561370	-91267737	123084581
C	43615142	-113363088	126406745
C	21073033	-152089847	113020463
C	46104269	-142248947	98393326
C	20568681	-148654714	82420601
C	-13025350	-130676900	108272451
C	-8763997	-120502706	79673905
C	-10678498	-100498970	102898934
C	70122808	-144658784	24341591
C	51839055	-142678119	48933257
C	80820185	-132555917	50495144
C	86434539	-108568885	10891117
C	88791797	-95056454	38299632
C	70507048	-82888186	16854698
C	49404965	-120357614	-1054004
C	33146291	-97734963	11635454
C	28332101	-126789656	20383057
H	42772487	-144023019	42868075
H	17962557	-114115155	146084633
H	15870075	-128889526	136417549
H	4154141	-115608274	135006162
H	25368559	-87336596	132989887
H	12053022	-88628397	121238199
H	28697244	-86136645	115532853
H	45698209	-124129262	127227801
H	46383260	-108672221	135985963
H	50189583	-109227862	118618386
H	25269313	-148733438	122617100
H	24244040	-162532230	111481799
H	10118955	-152010467	113928653
H	50465026	-138619147	107810622
H	50372314	-136245790	90220562
H	49318934	-152696152	96985550
H	9606598	-149526521	82562869
H	24715008	-158737791	80828504
H	23340421	-142459361	73766033
H	-10609431	-129808038	118961904
H	-10421340	-140864486	105050772
H	-23932729	-129536797	107184465
H	-19714613	-120068192	78504634
H	-5365764	-130333278	76118423
H	-4360926	-112888018	73069816
H	-9297638	-98646586	113650202
H	-21460604	-99809538	100730527

H	-5604440	-92452595	97374678
H	73928027	-154411062	27787424
H	77916386	-140037739	18112764
H	61393002	-146581760	17934349
H	49055888	-136978012	57922608
H	55285340	-152633193	52166279
H	83621787	-142542585	54216385
H	78856386	-126150628	59217626
H	89485757	-128440631	45118449
H	90957705	-117762937	14889501
H	94605591	-102244544	7058647
H	80089897	-111386129	2368132
H	93039979	-104105549	42871297
H	83874443	-89282871	46271823
H	97136553	-89010139	34389932
H	64417754	-77282161	24093785
H	64382084	-84580100	7880417
H	79030936	-76537036	13952264
H	54799040	-129853221	197452
H	56471380	-112990159	-5144718
H	41518257	-121937738	-8588213
H	40305269	-90133867	8199082
H	28096423	-93745171	20558092
H	25557406	-99059211	3753054
H	23782031	-124069026	30024553
H	32445663	-136944611	21336537
H	20316557	-127121375	12827669

9. References

- [1] O. Kysliak and A. Schnepf, *Dalton Trans.* **2016**, 45, 2404.
- [2] P. Chavant and M. Vaultier, *J. Organomet. Chem.* **1993**, 455, 37.
- [3] Y. Segawa, Y. Suzuki, M. Yamashita and K. Nozaki, *J. Am. Chem. Soc.* **2008**, 130, 16069.
- [4] L. Hintermann, *Beilstein J. Org. Chem.* **2007**, 3, 22.
- [5] O. Santoro, A. Collado, A. M. Slawin, S. P. Nolan and C. S. Cazin, *Chem. Commun.* **2013**, 49, 10483.
- [6] T. Kottke and D. Stalke, *J. Appl. Crystallogr.* **1993**, 26, 615.
- [7] G. M. Sheldrick, *Acta Crystallogr. Sect. C: Struct. Chem.* **2015**, 71, 3.
- [8] A. L. Spek, *Acta Crystallogr. Sect. D: Biol. Crystallogr.* **2009**, 65, 148.
- [9] G. R. Fulmer, A. J. Miller, N. H. Sherden, H. E. Gottlieb, A. Nudelman, B. M. Stoltz, J. E. Bercaw and K. I. Goldberg, *Organometallics* **2010**, 29, 2176.
- [10] M. Muhr, P. Heiß, M. Schütz, R. Bühler, C. Gemel, M. H. Linden, H. B. Linden and R. A. Fischer, *Dalton Trans.* **2021**, 50, 9031.
- [11] C. Wallach, F. S. Geitner and T. F. Fässler, *Chem. Sci.* **2021**, 12, 6969.
- [12] F. Li and S. C. Sevov, *Inorg. Chem.* **2012**, 51, 2706.
- [13] E. V. Anslyn, D. A. Dougherty and E. V. Dougherty, *Modern Physical Organic Chemistry*, University Science Books, Sausalito, California, **2006**, ISBN 9781891389313.
- [14] TURBOMOLE V7.3 2018, a development of University of Karlsruhe and Forschungszentrum Karlsruhe GmbH, 1989-2007; TURBOMOLE GmbH, since 2007; available from www.turbomole.com, accessed 3rd March 2022.
- [15] A. D. Becke, *Phys. Rev. A* **1988**, 38, 3098.
- [16] J. P. Perdew, *Phys. Rev. B* **1986**, 33, 8822.
- [17] F. Weigend and R. Ahlrichs, *Phys. Chem. Chem. Phys.* **2005**, 7, 3297.
- [18] K. Eichkorn, O. Treutler, H. Öhm, M. Häser and R. Ahlrichs, *Chem. Phys. Lett.* **1995**, 240, 283.
- [19] F. Weigend, *Phys. Chem. Chem. Phys.* **2006**, 8, 1057.
- [20] M. Sierka, A. Hogeckamp and R. Ahlrichs, *J. Phys. Chem.* **2003**, 118, 9136.
- [21] F. Furche and R. Ahlrichs, *J. Phys. Chem.* **2002**, 117, 7433.
- [22] F. Furche and D. Rappoport, *Density Functional Methods for Excited States: Equilibrium Structure and Electronic Spectra*; in: *Computational Photochemistry*, vol. 16, Elsevier: Amsterdam, The Netherlands, **2005**, ISBN: 9780080455198.
- [23] W. Humphrey, A. Dalke and K. Schulten, *J. Mol. Graph.* **1996**, 14, 33.
- [24] G. Knizia and J. E. Klein, *Angew. Chem. Int. Ed.* **2015**, 54, 5518.

6.8 Intermediates and Products of the Reaction of Zn(II) Organyls with Tetrel Element *Zintl* Ions: Cluster Extension Versus Complexation

C. Wallach,[‡] K. Mayer,[‡] T. Henneberger, W. Klein and T. F. Fässler

[‡]: authors contributed equally to this work.

Published in: *Dalton Transactions* **2020**, 49, 6191.

© The Royal Society of Chemistry 2020. Reproduced with permission from the Royal Society of Chemistry.

Access online via: <https://pubs.rsc.org/en/content/articlelanding/2020/dt/d0dt01096k/unauth>.

Contents and Contributions

Reaction products of the *Zintl* phases K_4Ge_9 and $A_{12}E_{17}$ ($A = K, Rb$; $E = Si-Sn$) with zinc organyls ZnR_2 ($R = Et, Cp^*, Ph, Mes$) obtained from liquid ammonia are described. In a series of experiments, the Zn-coordinated cluster species $[(\eta^3\text{-}\eta^3\text{-}Ge_4)(ZnEt)_2]^{2-}$ (**1a**), $[(\eta^2\text{-}Sn_4)Zn(\eta^2\text{-}Sn_4)]^{6-}$ (**2a**), and $[(\eta^4\text{-}Ge_9)(ZnEt)]^{3-}$ (**3a**) were isolated. Furthermore, the amides $[(ZnPh_2)_2(\mu_2\text{-}NH_2)_2]^{2-}$ (**4a**) and $\{[Zn(\mu_2\text{-}NH_2)_4][ZnEt)_2(\mu_2\text{-}NH_2)_2]_2\}^{2-}$ (**5a**) were characterized, in combination with cleaved organic ligands R^- in the anions $[ZnR_3]^-$ [$R = Ph$ (**6a**), Mes (**7a**)] and $[Cp^*]^-$ (**8a**). While the characterized cluster species extend the number of known four- and nine-atom polyanions coordinating to Zn(II), the crystallization of various cluster-free by-products accounts for the detection of intermediates on the way to intermetaloid tetrel element-Zn clusters. By comparing the structure motifs in the isolated species, a potential reaction sequence was derived. Most probably, in liquid ammonia amides form, which coordinate to the ZnR_2 precursors. This coordination weakens the Zn- R bonds, which subsequently are cleaved, allowing for the addition of the $[ZnR]^+$ fragment to tetrel element cluster anions. Generally, an *in-situ* monitoring of reactions taking place in liquid ammonia is difficult, thus this study provides indirect insights into potential reaction paths via the characterization of several single crystal structures.

The single crystals containing the discussed structure motifs were prepared by Dr. Kerstin Mayer (**1a**, **2a**, **3a**, **5a**), Dr. Thomas Henneberger (**4a**, **6a**, **7a**), and me (**8a**). Single crystals were selected accordingly, while I selected the crystal comprising **1a**, additionally. The initial structure refinements were performed by the respective person. Dr. Wilhelm Klein finalized the single crystal structure refinements for publication. The samples for the ESI-MS measurements

were prepared by me, including the subsequent data acquisition and evaluation. The manuscript was authored by me, including the creation of figures, tables, and schemes. Dr. Kerstin Mayer and Dr. Annette Schier proof-read the manuscript. The publication of the manuscript was managed by Prof. Dr. Thomas F. Fässler, the peer-review process including corrections was a joined task accomplished by Prof. Dr. Thomas F. Fässler, Dr. Wilhelm Klein and me.

A graphical illustration of the results was published as an inside front cover: DOI 10.1039/D0DT90093A. The illustration was designed by me; Dr. Kerstin Mayer provided help with the portrayal of Triton.

Dalton Transactions

An international journal of inorganic chemistry

rsc.li/dalton



ISSN 1477-9226

PAPER

C. Wallach *et al.*

Intermediates and products of the reaction of Zn(II) organyls
with tetrel element *Zintl* ions: cluster extension *versus*
complexation

Cite this: *Dalton Trans.*, 2020, **49**, 6191Intermediates and products of the reaction of Zn(II) organyls with tetrel element *Zintl* ions: cluster extension versus complexation†C. Wallach,[‡] K. Mayer,[‡] T. Henneberger, W. Klein and T. F. Fässler[†] 

The discovery of low-valent Zn compounds resulted in the renaissance of organometallic Zn complexes. Polyhedral clusters of tetrel elements can interact with Zn atoms either as Lewis donors or by incorporation of the Zn atoms as additional cluster vertices. Herein we report the reactions of ZnR₂ (R = ethyl (Et), pentamethylcyclopentadiene (Cp*), phenyl (Ph) and 1,3,5-trimethylbenzene (Mes)) with *Zintl* ions of the types [E₄]⁴⁻ (E = Ge, Sn) and [Ge₉]⁴⁻ in liquid ammonia. Besides the desired *Zintl* ion complexes, intermediates were isolated that give insight into the reaction of organo Zn compounds in liquid ammonia. Three ions, [(η³-η³-Ge₄)(ZnEt)₂]²⁻ (**1a**), [(η²-Sn₄)Zn(η²-Sn₄)]⁶⁻ (**2a**) and [(η⁴-Ge₉)(ZnEt)₃]³⁻ (**3a**), were obtained and characterized by means of single crystal X-ray diffraction analysis. Furthermore, amides [(ZnPh₂)₂(μ₂-NH₂)₂]²⁻ (**4a**) and {[Zn(μ₂-NH₂)₄][(ZnEt)₂(μ₂-NH₂)₂]²⁻ (**5a**) were formed during the reactions, together with the addition products [ZnPh₃]⁻ (**6a**) and [ZnMes₃]⁻ (**7a**) and an anion [Cp*]⁻ (**8a**), suggesting the following reaction sequence: in liquid ammonia the *Zintl* anions form amides, which then serve as ligands for ZnR₂ molecules. The NH₂⁻ ligands weaken the corresponding Zn–R bonds, and thus bond cleavage and the addition of the *Zintl* anion to the Zn ion can take place, additionally promoted by the trapping of the leaving group R⁻ by unreacted Zn organyls with the formation of [ZnR₃]⁻.

Received 17th February 2020,
Accepted 2nd April 2020

DOI: 10.1039/d0dt01096k

rsc.li/dalton

Introduction

Regarding the syntheses of novel materials, *Zintl* phases have become a steadily growing field of interest over the last few decades. Compounds that contain well-defined small atomic clusters are especially suitable for a bottom-up approach to obtain well-defined mixed atomic clusters.^{1–6} A series of reactions are known to build up larger structures by atom-wise cluster extension.^{1,7} For Ge-containing species, a prosperous chemistry has been established, covering the whole field from organo-substituted clusters^{8–11} over cage compounds carrying main group element fragments,^{12–19} to transition metal-substituted cluster species.³ The decoration of anionic element clusters with organic ligands or main group element fragments usually results in species with 2e–2e *exo* cluster bonds, whereas the substitution with transition metal fragments more often leads to coordination complexes with delocalized multicen-

tered bonds (although some exceptions like covalently bonded Fe and Cr units in silylated clusters, have been reported).^{20,21}

Manifold reactions of pre-formed *Zintl* clusters in ethylenediamine or NH₃(l) with main group element compounds and with transition metal complexes, which might lead to a cluster extension, have been reported. The extension of mono-capped square-antiprismatic [E₉] clusters mainly occurs on the easily accessible square plane of the cage, leading to heteroatomic ten-atomic *closo* clusters as favored products. The examples are [(η⁴-E₉)M]ⁿ⁻ (E = Si, M = Zn;²² E = Ge, M = Tl,²³ Sn,²⁴ Cu,²⁵ Zn;^{22,24,26} Ni;²⁷ Pd;²⁸ E = Sn, M = Cd,²⁹ Ir,³⁰ Cu, Ag, Au,³¹ Zn,^{22,26} Cr,^{32,33} Mo,^{33,34} W;^{33,34} E = Pb, M = Cd,²⁹ Ir,³⁵ Zn,^{22,26} Cr,³⁶ Mo,³⁴ W³⁴). Subsequently, the *closo* fragments can form dimers *via* heteroatoms, which are prone to stabilize the unusual formal oxidation states of the M atoms, as *e.g.* in [(η⁴-E₉)M–M(η⁴-E₉)]⁶⁻ (E = Ge, M = Zn(l);³⁷ E = Pb, M = Cd(l)³⁸). Alternatively, the coordination sphere of the transition metal atom can become saturated by a second cluster unit, resulting in dimers such as [(η⁴-Ge₉)Cu(η¹-Ge₉)]⁷⁻ (ref. 25) and [(η⁴-Sn₉)Ag(η¹-Sn₉)]⁷⁻.³¹ In comparison with [E₉]⁴⁻ clusters, [E₄]⁴⁻ tetrahedra exhibit an even higher reductive potential, and they are less soluble due to an increased charge-to-atom ratio. To date, solution-based reactions of preformed four-atomic clusters have therefore been limited to liquid ammonia, and so far only derivatives with coordinative bonds to transition metals have been observed. In a standard procedure the corresponding

Department Chemie, Technische Universität München, Lichtenbergstraße 4, 85747 Garching b. München, Germany. E-mail: thomas.faessler@lrz.tum.de

† Electronic supplementary information (ESI) available: Crystallographic details and structures of compounds 1–8, mass spectrum of 3a. CCDC 1982121–1982128. For ESI and crystallographic data in CIF or other electronic format see DOI: 10.1039/D0DT01096K

‡ Authors contributed equally to this work

$A_{12}E_{17}$ phase with the pre-formed *Zintl* cluster units is dissolved in liquid ammonia in the presence of a sequestering agent and a transition metal complex. The resulting products contain either isolated tetrahedra carrying a transition metal fragment, or transition metal-bridged tetrahedra. The examples for the former species are $[(\eta^3:\eta^3-E_4)(CuMes)_2]^{4-}$ ($E = Si;^{39} Ge^{40}$) as well as a mixed tetrel element cluster $[(\eta^3:\eta^3-(Si_{4-x}Ge_x))(CuMes)_2]^{4-}$ (ref. 41) and a protonated species $[(\mu_2-H)(\eta^2-Ge_4)ZnPh_2]^{3-}$,⁴² in which the proton bridges an edge of the $[Ge_4]$ tetrahedron. Transition metal-bridged tetrahedra are found *e.g.* in polyanions $[(\eta^2-Sn_4)Au(\eta^2-Sn_4)]^{6-}$ (ref. 43) and $[(\eta^2-Sn_4)Zn(\eta^3-Sn_4)]^{6-}$.⁴⁴ In the latter anions the ligands of the organo Zn species are replaced with tetrahedral clusters, and the original formal oxidation number of Zn remains unchanged. Organo Zn compounds have played an important role as reactants in *Zintl* cluster chemistry for many years now. Besides the beforehand mentioned clusters $[(\eta^4-E_9)Zn]^{3-}$ and $[(\eta^4-Ge_9)Zn-Zn(\eta^4-Ge_9)]^{6-}$, dimeric $[(\eta^4-Ge_9)Zn(\eta^3-Ge_9)]^{6-}$ and its structural isomer $[(\eta^3-Ge_9)Zn(\eta^3-Ge_9)]^{6-}$, trimeric $[(\eta^4-Ge_9)Zn(\eta^1:\eta^1-Ge_9)Zn(\eta^4-Ge_9)]^{8-}$ and polymeric $[\infty[Zn\{\mu_2(\eta^1:\eta^4-Ge_9)\}]]^{2-}$ anions are also formed upon the reaction with various organo Zn reagents.^{24,37} Even though there are numerous reports on the isolation of novel products, information on how the organo metal compounds react in liquid ammonia is rare. Due to its high polarity and its ability to dissolve *Zintl* phases, liquid NH_3 is an often applied solvent in *Zintl* cluster chemistry. However, monitoring such reactions is difficult and thus information on the reaction pathways and mechanisms is limited. Reactions have been monitored directly by solution-based NMR spectroscopy, which is still far away from being a routine method.^{45–48} We now study the reaction of ZnR_2 for $R = Et, Cp^*, Ph$ and Mes with the *Zintl* ions $[E_4]^{4-}$ ($E = Ge, Sn$) and $[Ge_9]^{4-}$ in liquid ammonia and report the anion $[(\eta^3:\eta^3-Ge_4)(ZnEt)_2]^{2-}$ (**1a**), which represents the first tetrel atom tetrahedron connected to two organo Zn fragments. In addition, we present the anion $[(\eta^2-Sn_4)Zn(\eta^2-Sn_4)]^{6-}$ (**2a**) together with the Zn-expanded nine-atomic cluster anion $[(\eta^4-Ge_9)(ZnEt)]^{3-}$ (**3a**), all of which are formed upon the reaction of *Zintl* phases with Zn(II) compounds in liquid ammonia. Furthermore, we describe two Zn amides (**4a** and **5a**) which, together with the anionic species $[ZnPh_3]^-$ (**6a**), $[ZnMes_3]^-$ (**7a**) and $[Cp^*]^-$ (**8a**), are formed upon the reaction of Zn(II) complexes in liquid ammonia. They represent suitable intermediates and by-products allowing a better understanding of possible reaction paths in liquid ammonia as a solvent.

Results and discussion

Synthesis of compounds 1–8

All compounds have been synthesized by the dissolution of the corresponding powdered *Zintl* phase together with either [2.2.2]crypt or 18-crown-6 as sequestering agents and a Zn(II) source in liquid ammonia. Single crystals were obtained after several months of storage of the reaction mixtures at $-70^\circ C$.

[2.2.2]crypt: 4,13,16,21,24-hexaoxa-1,10-diazabicyclo[8.8.8]hexacosane;
18-crown-6: 1,4,7,10,13,16-hexaoxacyclooctadecane.

Crystal structure of

$[K([2.2.2]crypt)]_2[(\eta^3:\eta^3-Ge_4)(ZnEt)_2] \cdot 2 NH_3$ (**1**)

Single crystals of compound **1** were obtained from a reaction of $K_{12}Ge_{17}$ with $ZnEt_2$. **1** crystallizes with the space group $P\bar{1}$. The single crystal structure determination reveals two organo-metallic ZnEt fragments that coordinate in an η^3 -mode to two triangular faces of the $[Ge_4]$ tetrahedron. Apart from Zn, only Cu and Cd units are known to form this coordination mode with tetrahedral anions, *e.g.* in $[(\eta^3:\eta^3-Si_4)(CuMes)_2]^{4-}$ and $[Cd_3(\eta^2:\eta^3-Ge_3P)_3]^{3-}$.^{39,49} In $[(\eta^3:\eta^3-Ge_4)(ZnEt)_2]^{2-}$ (**1a**) the two Zn atoms are sharing a Ge–Ge edge of the tetrahedron, leading to a strongly elongated edge with a Ge1–Ge2 distance of 2.9279(4) Å (Fig. 1), which is much longer than the other Ge–Ge distances between 2.4714(4) Å (Ge3–Ge4) and 2.6046(4) Å (Ge2–Ge4). The anion **1a** can be described as three face-sharing tetrahedra, Ge1–Ge2–Ge3–Ge4, Ge1–Ge2–Ge3–Zn1 and Ge1–Ge2–Ge4–Zn2, with the two Zn-containing ones being strongly distorted. This distortion is mainly caused by the elongation of the edges Ge3–Zn1 (2.7096(5) Å) and Ge4–Zn2 (2.6822(5) Å), whereas the other Ge–Zn distances are much shorter and range from 2.5134(4) Å (Ge2–Zn2) to 2.5267(4) Å (Ge1–Zn2). Overall the Ge–Ge and the Ge–Zn distances are in accordance with previously reported ones.^{37,50} A seesaw-like structural motif of Ge1–Zn1–Ge2–Zn2 with a torsion angle of $\omega_{Ge1-Zn1-Ge2-Zn2} = 129.667(4)^\circ$ is also found in the analogous MesCu derivative $[(\eta^3:\eta^3-Ge_4)(CuMes)_2]^{4-}$, although with a, in this case, much larger angle $\omega_{Ge1-Cu1-Ge2'-Cu2} = 150.35^\circ$ (Fig. 1b and c). Due to the tilt of the Zn atoms towards the

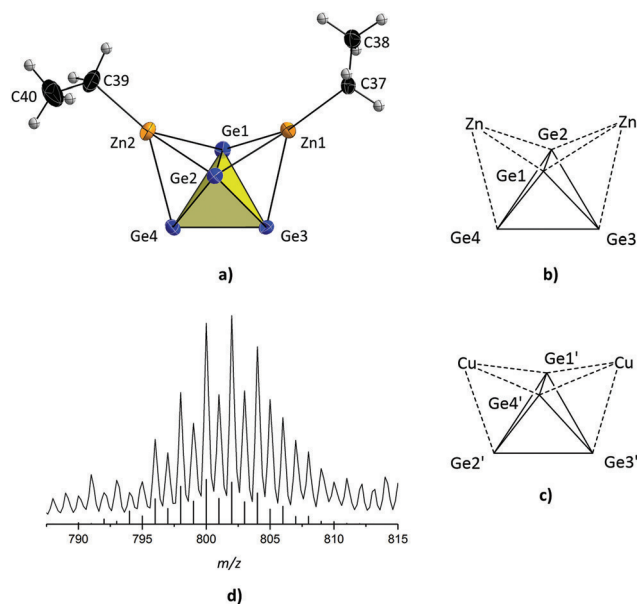


Fig. 1 (a) Structure of **1a**, showing the η^3 -coordination mode of the organo Zn ligands to the $[Ge_4]$ cluster core. All ellipsoids (except H) are shown at a 50% probability level. Color code: Ge: blue; Zn: orange; C: black; H: grey; (b) and (c): schematic representation of the structural relationship of **1a** (b) and $[(\eta^3:\eta^3-Ge_4)(CuMes)_2]^{4-}$ (c).⁴⁰ (d) ESI-MS spectrum of $[K([2.2.2]crypt)][Ge_4(ZnEt)]^-$ in MeCN (negative ion mode, 2500 V, $300^\circ C$). The calculated pattern is shown as black bars.

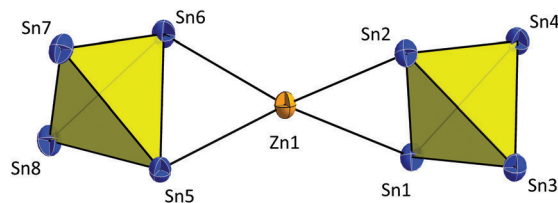


Fig. 2 Structure of **2a**, showing the two-fold coordination mode of the Zn atom to both $[\text{Sn}_4]$ clusters. All ellipsoids are shown at a 50% probability level. Color code: Sn: blue; Zn: orange.

Ge1–Ge2 edge the coordination is more η^2 in character, whereas an η^3 -character is observed in the case of the Cu complex (the Ge–Cu distances are between 2.457(1) and 2.520(1) Å). In solution a mono-substituted cluster is observed. After the removal of liquid ammonia from the reaction mixture of K_4Ge_4 , ZnEt_2 and [2.2.2]crypt and extraction of the residue with MeCN, ESI-MS investigations showed signals corresponding to the anion $\{[\text{K}([2.2.2]\text{crypt})][\text{Ge}_4(\text{ZnEt})]\}^-$ at m/z 802.0 (Fig. 1d).

Crystal structure of $[\text{K}]_6[(\eta^2\text{-Sn}_4)\text{Zn}(\eta^2\text{-Sn}_4)] \cdot 16 \text{NH}_3$ (**2**)

The reaction of $\text{K}_{12}\text{Sn}_{17}$ with ZnCp^*_2 leads to the formation of crystals of **2**. Compound **2** crystallizes in the space group $P\bar{1}$ and contains a dimer of two $[\text{Sn}_4]$ clusters that are bridged by a Zn atom. The Sn–Zn distances in the anion $[(\eta^2\text{-Sn}_4)\text{Zn}(\eta^2\text{-Sn}_4)]^{6-}$ (**2a**, Fig. 2) range from 2.7258(8) Å (Zn1–Sn6) to 2.7611(8) Å (Zn1–Sn2); the Sn–Sn bond distances vary from 2.8827(6) Å (Sn6–Sn8) to 3.0785(6) Å (Sn1–Sn2). These values are in agreement with previously reported ones, e.g. in the anions $[(\eta^4\text{-Sn}_6)\text{ZnR}]^{3-}$ (R = C_6H_5 ,²² Mes, ^iPr).²⁶ Transition metal-bridged clusters are not exclusively formed in solution, but can also be observed after direct fusion of the elements, as shown in $[(\eta^3\text{-Ge}_4)\text{Zn}(\eta^3\text{-Ge}_4)]^{6-}$ of the phase Cs_6ZnGe_8 ⁵¹ and in its structural isomer $[(\eta^2\text{-Ge}_4)\text{Zn}(\eta^3\text{-Ge}_4)]^{6-}$ found in $\text{K}_{14}\text{ZnGe}_{16}$.⁴⁰ A η^2 – η^2 -coordination mode has been found in the corresponding Au complexes and in the mixed tetrel element cluster $[(\eta^2\text{-(Si/Ge)}_4)\text{Zn}(\eta^2\text{-(Si/Ge)}_4)]^{6-}$ obtained from liquid ammonia.^{43,52} Even though all Zn–Sn and Sn–Sn distances are in the same range (deviation <0.08 Å), the structural isomer $[(\eta^3\text{-Sn}_4)\text{Zn}(\eta^2\text{-Sn}_4)]$ (**2b**)⁴⁴ reveals another type of coordination mode. The Zn atom in **2a** coordinates to two edges, which are almost perpendicular to each other ($\omega_{\text{Sn1-Sn2-Sn6-Sn5}} = 82.231(1)^\circ$), and the tetrahedral $[\text{Sn}_4]$ units coordinate in an almost linear manner to the Zn atom, with angles to the center of gravity of the tetrahedra (ct) of $174.832(3)^\circ$ ($\angle(\text{ct}_{\text{Sn1-to-Sn4-Zn-ct}_{\text{Sn5-to-Sn8}}})$) and 173.651° ($\angle(\text{ct}_{\text{Sn1-Sn1-Sn2-Sn3-Zn-ct}_{\text{Sn4-Sn5-Sn5-Sn6}}})$) for **2a** and **2b**, respectively. Due to the high instability of the acetonitrile extract, ESI-MS measurements could not be carried out, unfortunately. Instead, a Sn mirror was formed in the injection needle almost immediately.

Crystal structure of $[\text{K}([2.2.2]\text{crypt})]_3[(\eta^4\text{-Ge}_9)(\text{ZnEt})] \cdot 7.4 \text{NH}_3$ (**3**)

Crystals of compound **3** were isolated from the reaction mixture of K_4Ge_9 and ZnEt_2 in liquid ammonia. **3** contains the anion $[(\eta^4\text{-Ge}_9)(\text{ZnEt})]^{3-}$ (**3a**) with the $[\text{ZnEt}]^+$ moiety capping

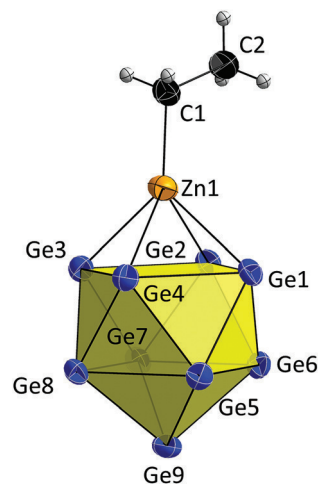


Fig. 3 Structure of **3a** showing the only slightly distorted C_{4v} -symmetric shape of the $[\text{Ge}_9]$ cluster core. All ellipsoids (except H) are shown at a 50% probability level. Color code: Ge: blue; Zn: orange; C: black; H: grey.

the pseudo square plane of the Ge cage (Fig. 3). The formation of **3a** corresponds to the substitution of one ethyl group of the organo Zn compound with the $[\text{Ge}_9]$ cluster. As in similar compounds such as $[(\eta^4\text{-E}_9)\text{ZnR}]^{3-}$ (E = Si–Pb, R = Ph; E = Ge, R = Mes, *iso*-propyl),^{22,26} **3a** exhibits only a slightly distorted C_{4v} -symmetric cage with almost equal diagonal lengths of the open square ($d_{\text{Ge1-Ge3}}/d_{\text{Ge2-Ge4}} = 1.01$).⁵³ The Zn atom coordinates to the almost planar open square Ge1–Ge4 ($\omega_{\text{Ge1-Ge4}} = 0.4^\circ$) with Zn–Ge distances in the range between 2.5922(1) Å (Ge3–Zn1) and 2.6436(1) Å (Ge1–Zn1), and Ge–Ge distances between 2.5470(1) Å (Ge2–Ge7) and 2.7961(1) Å (Ge2–Ge3), which agree with the corresponding values of previously reported Ge–Zn clusters such as $[(\eta^4\text{-Ge}_9)\text{Zn-Zn}(\eta^4\text{-Ge}_9)]^{6-}$.^{24,37,50} The cluster can be described either as a ten vertex *closo* cluster or as a species, in which the square plane of **3a** acts as a 6-electron-donor, resulting in 18 valence electrons for Zn. Such ten-atomic $[(\eta^4\text{-E}_9)\text{M}]^{n-}$ (E = tetrel element, M = metal) *closo* clusters are well known.^{24,25,32} After the removal of liquid ammonia from the reaction mixture of K_4Ge_9 , ZnEt_2 and [2.2.2]crypt, ESI-MS spectra were recorded in MeCN, which showed signals at $m/z = 746.2$, corresponding to the mass of **3a** (Fig. S11†).

Fragmentation of the Zn organyls in $\text{NH}_3(l)$

Reactions in liquid ammonia require long times due to the low temperatures. NMR investigations of the reactions of *Zintl* ions in this solvent were carried out by the group of Korber, but organometallic intermediates have not been described as yet.^{44,47,48} However, the detection or even isolation and characterization of such intermediates and/or by-products may shed some light on the reaction mechanisms. Recently, the characterization of a series of anions found upon the formation of transition metal complexes of homoatomic tin clusters in solution suggested that the transition metal complex might step-

wise release ligands in liquid ammonia solution. In the reaction mixtures of Cp_2TiCl_2 and K_4Sn_9 the species $[\text{TiCp}_2(\eta^1\text{-Sn}_9)(\text{NH}_3)]^{3-}$, $[\text{TiCp}(\eta^4\text{-Sn}_8)]^{4-}$ and $[\text{Ti}(\text{TiCp})(\text{TiCp}_2)\text{Sn}_{15}]^{n-}$ ($n = 4$ or 5) were observed, and they - with Cp_2Ti , CpTi and the bare Ti - contain all possible fragments of Cp_2TiCl_2 .⁵⁴

From the reaction of $\text{K}_{12}\text{Ge}_{17}$ with ZnPh_2 in the presence of 18-crown-6 crystals of the Zn amide complex, $[\text{K}(18\text{-crown-6})_2\mathbf{4a}\cdot 8\text{NH}_3]$ (**4a**) containing the anion $[(\text{ZnPh}_2)_2(\mu_2\text{-NH}_2)_2]^{2-}$ (**4a**) (Fig. 4) has been isolated. **4a** is an amide adduct of an uncharged ZnPh_2 molecule which corresponds to a dimer, in which two ZnPh_2 molecules are bridged by two NH_2^- ligands. The Zn and N atoms build up a square plane ($\omega_{\text{Zn1-N1-N1'-Zn1'}} = 180.00(4)^\circ$) with an almost ideal angle of 90° ($\angle(\text{Zn1-N1-Zn1}') = 91.36(3)^\circ$) and with Zn-N distances of 2.104(4) Å (Zn-N) and 2.045(4) Å (Zn-N'). Both Zn atoms still carry two phenyl ligands with significantly elongated Zn-C distances of 2.046(4) Å (Zn-C13) and 2.034(4) Å (Zn-C19) when compared to 1.94 and 1.95 Å in ZnPh_2 , respectively.⁵⁵ From a similar reaction of $\text{K}_{12}\text{Ge}_{17}$ with ZnEt_2 in liquid ammonia, which led to the formation of **1a** and **3a**, we were able to also isolate the dark column-shaped crystals containing the amide complex $[(\text{Zn}(\mu_2\text{-NH}_2)_4)[(\text{ZnEt})_2(\mu_2\text{-NH}_2)_2]^{2-}$ (**5a**) which crystallizes as the corresponding $\text{K}(18\text{-crown-6})$ salt (Fig. 5). The compound crystallizes in the space group $P\bar{1}$, and the anion contains four $[\text{ZnEt}]^+$ fragments (Zn2 to Zn5) and one bare Zn^{2+} ion (Zn1) in which both Et ligands are stripped off. The five Zn atoms are linked by bridging N atoms of eight amide ligands. Thus all Zn-containing units of the ion arise from the release of one or two ethyl ligands, respectively. The structure can also be described as a linear arrangement of three edge-sharing $[(\text{NH}_2)_4]^{4-}$ tetrahedra, with the central one encompassing a Zn^{2+} ion (tetrahedral angles between $106.10(3)^\circ$ and $112.39(1)^\circ$). Two faces of the two outer tetrahedra (tetrahedral angles $105.54(3)^\circ$ to $114.25(4)^\circ$) are bridged by two ZnEt fragments each. The Zn-N distances range from 2.038(2) Å (Zn1-N2) to 2.089(2) Å (Zn2-N6), and the Zn-C distances range from 2.031(2) Å (Zn4-C29) to 2.052(3) Å (Zn2-C25) and are thus elongated with respect to the ones in ZnEt_2 (Zn-C: 1.948(5)

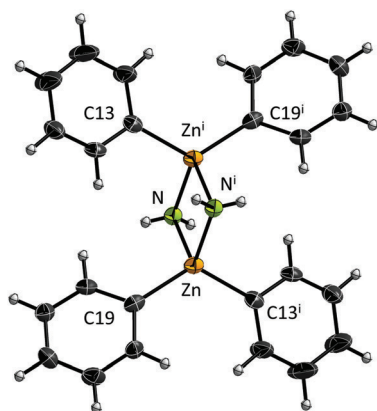


Fig. 4 Structure of the Zn amide **4a**. All ellipsoids (except H) are shown at a 50% probability level. Color code: Zn: orange; N: green; C: black; H: grey. Symmetry operation: $i: -(1-x), (1-y),$ and $(1-z)$.

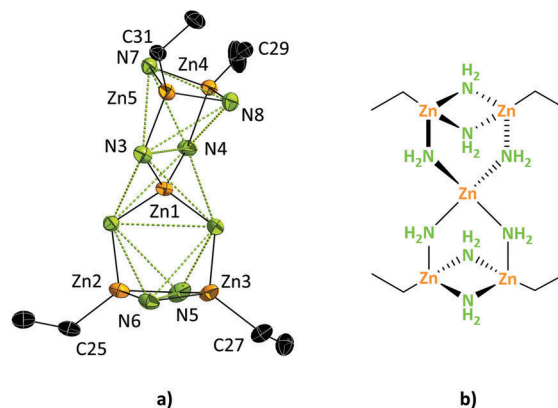


Fig. 5 (a) Structure of the Zn amide **5a**. All ellipsoids are shown at a 50% probability level. Color code: Zn: orange; N: green; C: black. Protons are omitted for clarity. Tetrahedra built by NH_2^- fragments are indicated by the dashed lines. (b) Schematic representation of the anion **5a**.

Å).⁵⁶ The formation of amides from liquid ammonia is not yet fully understood. It may occur through the deprotonation of NH_3 by cluster anions acting as the corresponding base,^{47,48,57} or the clusters may act as reducing reagents. However, the formation of amides in liquid ammonia solution may be important for the release of the organic substituents on the Zn atom, which are then replaced with the amides. This can be seen as an initial step before a nucleophilic attack of the Zintl cluster occurs. Thus, **5a** is a potential intermediate towards the formation of **1a** and **3a** allowing the formation and transfer of Zn-R units to the clusters. Assuming comparable reactivities of other Zn(II) compounds like ZnCp^*_2 , the formation of transition metal-bridged ions like $[(\eta^2\text{-Sn}_4)\text{Zn}(\eta^2\text{-Sn}_4)]^{6-}$ (**2a**) also becomes reasonable. From similar reactions of organo Zn compounds in liquid ammonia two further compounds were isolated, which give evidence that the Zn organyls can also act as a trap for the leaving group R^- , thereby giving $[\text{ZnPh}_3]^-$ (**6a**) and $[\text{ZnMes}_3]^-$ (**7a**). These anions were found in the salt $[\text{K}_{0.8}\text{Rb}_{0.2}(18\text{-crown-6})][\text{ZnPh}_3]$ (**6**) with sequestered alkali metal cations, and in $[\text{K}(18\text{-crown-6})][\text{ZnMes}_3]\cdot\text{NH}_3\cdot 2\text{thf}$ (**7**) (Fig. 6).

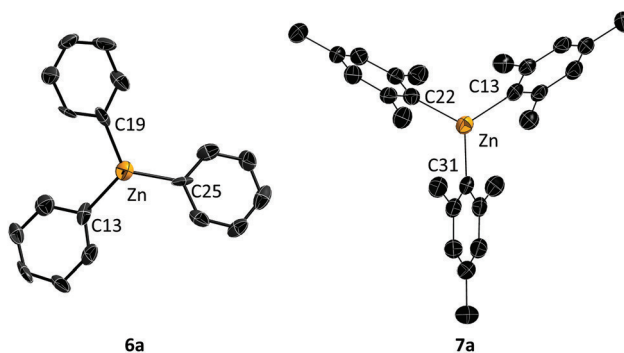


Fig. 6 Structures of the Zn adducts $[\text{ZnR}_3]^-$ **6a** and **7a**. All ellipsoids are shown at a 50% probability level. Color code: Zn: orange; C: black. Protons are omitted for clarity.

The Zn–C bonds range from 2.013(1) Å (Zn–C13) to 2.030(8) Å (Zn–C25) in **6a** and from 2.041(3) Å (Zn–C13) to 2.047(3) Å (Zn–C31) in **7a**. The bonds are elongated with respect to the ones in the beforehand mentioned ZnPh₂ and ZnMes₂ (Zn–C: 1.9422(2) Å).⁵⁸ The Zn–C bonds are slightly tilted out of the ideal plane [**6a**: $\omega_{\text{C25-Zn-C19-C13}} = 172.345(2)^\circ$; **7a**: $\omega_{\text{C13-Zn-C22-C31}} = 179.363(3)^\circ$]. Furthermore, upon the reaction of the *Zintl* phase with the nominal composition “K₅Co_{1.2}Ge₉” with ZnCp*₂ in liquid ammonia, single crystals of [K(18-crown-6)][Cp*]₂·2 NH₃ (**8**) were isolated. Compound **8** contains the ion [Cp*][−], which originates from the Zn organyl and was stabilized by a [K(18-crown-6)]⁺ counter ion. These findings indicate that the Zn(II) reactants dissociate in liquid ammonia and then become available for further reactions like complexation (**1a–3a**) and amide and adduct formation (**4a–7a**). The structure of **8** together with crystallographic details for compounds **1–8** is shown in the ESI.†

Experimental section

All manipulations were carried out under oxygen-free, dry conditions in an argon atmosphere using standard Schlenk or glove box techniques. Glassware was dried prior to use by heating it *in vacuo*. Liquid ammonia was dried over sodium metal and subsequently condensed onto the reactants. ZnEt₂ (Aldrich, 1 m in hexane) and ZnPh₂ (ABCR, 99%) were used without further purification. [2.2.2]Crypt (Acros, 98%) was dried *in vacuo* for 8 h prior to use. 18-Crown-6 (Merck) was sublimated *in vacuo* prior to use. ZnCp*₂⁵⁹ and ZnMes₂⁶⁰ were prepared according to the literature. The preparation of the solid phase precursors K₄Ge₉ and K₁₂E₁₇ (E = Ge, Sn) was done by fusion of the stoichiometric amounts of the elements in stainless-steel tubes at 650 and 800 °C, respectively. Mixed phases K₆Rb₆Si₁₇ and K₁₂Si₈Ge₉ were prepared by fusion of the elements in sealed tantalum ampules at 800 °C. The *Zintl* phase with the nominal composition “K₅Co_{1.2}Ge₉” was prepared according to the literature.⁶¹

Single crystal structure determination

All air-, moisture- and temperature-sensitive crystals were transferred from the reaction vessel to cooled perfluoroalkyl ether oil (<−30 °C) under a cold stream of N₂ gas. For data collection, the single crystals were mounted on loops and positioned under a cooled N₂ gas stream. Data collection was performed using an STOE StadiVari diffractometer with a DECTRIS PILATUS 300 K detector or an Oxford Diffraction Xcalibur3 diffractometer equipped with a Sapphire 3 detector (both instruments operating with Mo K α radiation). The structures were solved by direct methods (SHELXS-2014) and refined by full-matrix least-squares calculations against *F*² (SHELXL-2014).⁶² For the determination and refinement of the positions of the hydrogen atoms a riding model was applied. All non-hydrogen atoms were refined with anisotropic displacement parameters. Crystallographic data for **1–8** are given in the ESI.†

General procedure for the syntheses of compounds **1–8**

In a glove box the solid phase was weighed into a dried Schlenk tube together with the sequestering agent and the Zn(II) reagent. Afterwards, the tube was connected to the Schlenk line, and 2–3 mL pre-dried ammonia was condensed into the reaction vessel using an isopropanol/dry ice bath. The reaction mixtures were stored at −70 °C for crystallization. Due to the thermal sensitivity of the crystals owing to the rapid loss of ammonia, the yields are only approximate values.

[K([2.2.2]crypt)]₂[(η^3 - η^3 -Ge₄)(ZnEt)₂]₂·2 NH₃ (**1**). K₁₂Ge₁₇ (128 mg, 75 μ mol, 1 eq.), ZnEt₂ (12 mg, 100 μ mol, 1.3 eq.) and [2.2.2]crypt (51 mg, 135 μ mol, 1.8 eq.). One block-shaped, orange crystal of **1** could be isolated from the red reaction solution after 16 months. **ESI-MS**: (negative ion mode, 2500 V, 300 °C): *m/z* 802.0 {[K([2.2.2]crypt)][Ge₄(ZnEt)][−].

K₆[(η^2 -Sn₄)Zn(η^2 -Sn₄)]·16 NH₃ (**2**). K₁₂Sn₁₇ (373 mg, 150 μ mol, 1 eq.), ZnCp*₂ (25 mg, 75 μ mol, 0.5 eq.) and [2.2.2]crypt (51 mg, 135 μ mol, 0.9 eq.). Dark-red needles of **2** could be isolated from the red reaction solution after 16 months (yield approx. 60%).

[K([2.2.2]crypt)]₃[(η^4 -Ge₉)(ZnEt)]·7.4 NH₃ (**3**). K₄Ge₉ (61 mg, 75 μ mol, 1 eq.), ZnEt₂ (12 mg, 100 μ mol, 1.3 eq.) and [2.2.2]crypt (51 mg, 135 μ mol, 1.8 eq.). Block-shaped, orange-brown crystals of **3** could be isolated from the red reaction solution after 4 months (yield approx. 10–20%). **ESI-MS**: (negative ion mode, 2500 V, 300 °C): *m/z* 746.2 [Ge₉(ZnEt)][−].

[K(18-crown-6)]₂[(ZnPh₂)₂(μ_2 -NH₂)₂]₂·4 NH₃ (**4**). Route 1: K₁₂Ge₁₇ (128 mg, 75 μ mol, 1 eq.), ZnPh₂ (49 mg, 225 μ mol, 3 eq.) and 18-crown-6 (36 mg, 135 μ mol, 1.8 eq.). One orange crystal of **4** could be isolated from the red reaction solution after 7 weeks.

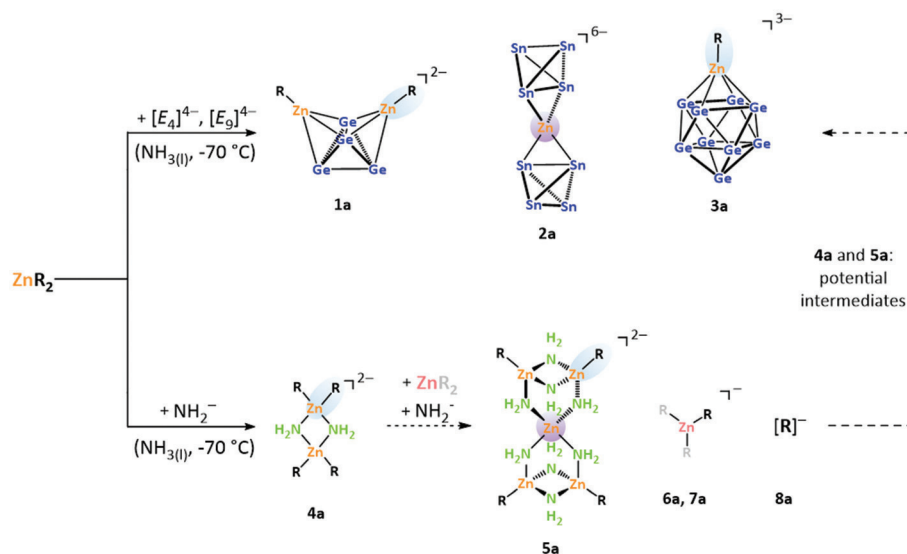
Route 2: K₁₂Si₁₇ (71 mg, 75 μ mol, 1 eq.), ZnPh₂ (49 mg, 225 μ mol, 3 eq.) and 18-crown-6 (36 mg, 135 μ mol, 1.8 eq.). One orange crystal of **4** could be isolated from the red reaction solution after 8 months.

[K(18-crown-6)]₂[(Zn(μ_2 -NH₂)₄)]₂[(ZnEt)₂(μ_2 -NH₂)₂]₂·5 NH₃ (**5**). K₁₂Ge₁₇ (128 mg, 75 μ mol, 1 eq.), ZnEt₂ (12 mg, 100 μ mol, 1.3 eq.) and 18-crown-6 (36 mg, 135 μ mol, 1.8 eq.). Dark column-shaped crystals of **5** could be isolated from the red reaction solution after 23 months (yield approx. 10%).

[K_{0.8}Rb_{0.2}(18-crown-6)][ZnPh₃] (**6**). K₆Rb₆Si₁₇ (92 mg, 75 μ mol, 1 eq.), ZnPh₂ (99 mg, 450 μ mol, 6 eq.) and 18-crown-6 (71 mg, 270 μ mol, 3.6 eq.). One red crystal of **6** could be isolated from the red reaction solution after 13 months.

[K(18-crown-6)][ZnMes₃]₂·NH₃·2thf (**7**). K₁₂Si₈Ge₉ (101 mg, 75 μ mol, 1 eq.), ZnMes₂ (23 mg, 75 μ mol, 1 eq.) and 18-crown-6 (36 mg, 135 μ mol, 1.8 eq.). The reaction solution was stored overnight at −40 °C, stirred for 3 h and then layered with 1 mL of thf. One yellow crystal of **7** could be isolated from the red reaction solution after 3 weeks.

[K(18-crown-6)][Cp*]₂·2NH₃ (**8**). “K₅Co_{1.2}Ge₉” (50 mg, 55 μ mol, 1 eq.), ZnCp*₂ (18.5 mg, 55 μ mol, 1 eq.) and 18-crown-6 (26.1 mg, 99 μ mol, 1.8 eq.). One spherical yellow crystal was isolated from the red reaction solution after



Scheme 1 Possible scheme for the reactions of Zn(II) compounds and *Zintl* ions in liquid ammonia: formation of Zn-*Zintl* clusters **1a–3a** upon the reaction of Zn(II) organyls with anions $[E_4]^{4-}$ and $[E_9]^{4-}$ in $NH_3(l)$; formation of Zn amides **4a** and **5a**, addition products **6a** and **7a** and ligand splitting (**8a**) upon the reaction of Zn(II) reagents with amide anions; **4a** and **5a** might serve as potential intermediates in Zn-*Zintl* cluster formation (derived from structural similarities within the different anions **1a–3a** as well as **4a** and **5a** as emphasized by the blue ellipses and purple cycles).

11 months. The crystal was found to be isostructural with $[K_{0.3}Rb_{0.7}(18\text{-crown-6})][Cp^*] \cdot 2NH_3$.⁶³

Discussion and conclusions

We report the synthesis and characterization of a series of Zn(II)-containing *Zintl* anions, $[(\eta^3\text{-}Ge_4)(ZnEt)_2]^{2-}$ (**1a**), $[(\eta^2\text{-}Sn_4)Zn(\eta^2\text{-}Sn_4)]^{6-}$ (**2a**) and $[(\eta^4\text{-}Ge_9)(ZnEt)]^{3-}$ (**3a**). Furthermore, two Zn amides, $[(ZnPh_2)_2(\mu_2\text{-}NH_2)_2]^{2-}$ (**4a**) and $[[Zn(\mu_2\text{-}NH_2)_4][[(ZnEt)_2(\mu_2\text{-}NH_2)_2]_2]^{2-}$ (**5a**), and simple adducts $[ZnPh_3]^-$ (**6a**) and $[ZnMes_3]^-$ (**7a**) are found in the course of the reactions, which allow a deeper insight into the formation of Zn *Zintl* cluster complexes. Even though not all products were isolated with the same Zn derivatives, the assembly of all these different species and fragments in the reaction mixtures together with their structural similarities emphasized in Scheme 1 gives evidence for the following potential reaction sequence: the organo Zn compounds ZnR_2 give the NH_2^- complex **4a** in which the Zn–C bond is weakened. Upon reaction with other ZnR_2 molecules and NH_2^- units **5a–7a** can be formed with the release of ligands $[R]^-$ (**8a**). Thus, the addition of a *Zintl* anion to the Zn atom and complex formation as in **2a** and **1a** as well as **3a**, respectively, can occur, accompanied by the release of the NH_2^- units and the R^- ligands. The trapping of the leaving group R^- by a Zn atom of an intact Zn organyl or a sequestered ion as in **6a**, **7a** and **8**, respectively, supports this reaction path. Therefore, the formation of amide complexes might promote the ligand exchange on the Zn atom. During the formation of **1a** to **3a**, however, no intermediate Zn amide complexes were isolated according to Scheme 1. Thus, further investigations are needed to find out whether

the intermediate ions **4a** and **5a** can be prepared in good yields from liquid ammonia also in the absence of a *Zintl* phase. Preliminary results have shown that adding an excess of Zn organyls to the reaction mixtures seems to enhance the reactivity of the organo Zn compounds. This will be the subject of forthcoming investigations.

Conflicts of interest

There are no conflicts to declare.

Acknowledgements

C. W. thanks the Deutsche Forschungsgemeinschaft (DFG, German Research Foundation) for funding (project number 245845833) within the International Research Training Group IRTG 2022 – Alberta Technical University of Munich School for Functional Hybrid Materials (ATUMS). Support from TUM IGSSE is greatly appreciated. C. W. also thanks the Studienstiftung des Deutschen Volkes for granting a PhD scholarship. We acknowledge Dr A. Schier for proof-reading the manuscript.

Notes and references

- 1 K. Mayer, J. Weßing, T. F. Fässler and R. A. Fischer, *Angew. Chem., Int. Ed.*, 2018, **57**, 14372.
- 2 C. Liu and Z.-M. Sun, *Coord. Chem. Rev.*, 2019, **382**, 32.
- 3 R. J. Wilson, N. Lichtenberger, B. Weinert and S. Dehnen, *Chem. Rev.*, 2019, **119**, 8506.

- 4 B. Weinert, S. Mitzinger and S. Dehnen, *Chem. – Eur. J.*, 2018, **24**, 8470.
- 5 S. C. Sevov and J. M. Goicoechea, *Organometallics*, 2006, **25**, 5678.
- 6 S. Scharfe, F. Kraus, S. Stegmaier, A. Schier and T. F. Fässler, *Angew. Chem., Int. Ed.*, 2011, **50**, 3630.
- 7 S. Mitzinger, L. Broeckaert, W. Massa, F. Weigend and S. Dehnen, *Nat. Commun.*, 2016, **7**, 10480.
- 8 A. Ugrinov and S. C. Sevov, *J. Am. Chem. Soc.*, 2003, **125**, 14059.
- 9 M. W. Hull, A. Ugrinov, I. Petrov and S. C. Sevov, *Inorg. Chem.*, 2007, **46**, 2704.
- 10 C. B. Benda, J. Q. Wang, B. Wahl and T. F. Fässler, *Eur. J. Inorg. Chem.*, 2011, 4262.
- 11 M. M. Bentlohner, W. Klein, Z. H. Fard, L. A. Jantke and T. F. Fässler, *Angew. Chem., Int. Ed.*, 2015, **54**, 3748.
- 12 A. Schnepf, *Angew. Chem., Int. Ed.*, 2003, **42**, 2624.
- 13 F. Li and S. C. Sevov, *Inorg. Chem.*, 2012, **51**, 2706.
- 14 O. Kysliak and A. Schnepf, *Dalton Trans.*, 2016, **45**, 2404.
- 15 F. Li, A. Muñoz-Castro and S. C. Sevov, *Angew. Chem., Int. Ed.*, 2012, **51**, 8581.
- 16 L. G. Perla and S. C. Sevov, *J. Am. Chem. Soc.*, 2016, **138**, 9795.
- 17 L. G. Perla, A. Muñoz-Castro and S. C. Sevov, *J. Am. Chem. Soc.*, 2017, **139**, 15176.
- 18 F. S. Geitner, J. V. Dums and T. F. Fässler, *J. Am. Chem. Soc.*, 2017, **139**, 11933.
- 19 F. S. Geitner, W. Klein and T. F. Fässler, *Angew. Chem., Int. Ed.*, 2018, **57**, 14509.
- 20 C. Schenk and A. Schnepf, *Chem. Commun.*, 2009, 3208.
- 21 N. C. Michenfelder, C. Gienger, A. Schnepf and A.-N. Unterreiner, *Dalton Trans.*, 2019, **48**, 15577.
- 22 J. M. Goicoechea and S. C. Sevov, *Organometallics*, 2006, **25**, 4530.
- 23 D. Rios, M. M. Gillett-Kunnath, J. D. Taylor, A. G. Oliver and S. C. Sevov, *Inorg. Chem.*, 2011, **50**, 2373.
- 24 M. M. Bentlohner, L. A. Jantke, T. Henneberger, C. Fischer, K. Mayer, W. Klein and T. F. Fässler, *Chem. – Eur. J.*, 2016, **22**, 13946.
- 25 S. Scharfe and T. F. Fässler, *Eur. J. Inorg. Chem.*, 2010, 1207.
- 26 B. Zhou, M. S. Denning, C. Jones and J. M. Goicoechea, *Dalton Trans.*, 2009, 1571.
- 27 J. M. Goicoechea and S. C. Sevov, *J. Am. Chem. Soc.*, 2006, **128**, 4155.
- 28 Z.-M. Sun, Y.-F. Zhao, J. Li and L.-S. Wang, *J. Cluster Sci.*, 2009, **20**, 601.
- 29 B. Zhou, M. S. Denning, T. A. Chapman and J. M. Goicoechea, *Inorg. Chem.*, 2009, **48**, 2899.
- 30 J. Q. Wang, S. Stegmaier, B. Wahl and T. F. Fässler, *Chem. – Eur. J.*, 2010, **16**, 1793.
- 31 F. Geitner, W. Klein and T. Fässler, *Dalton Trans.*, 2017, **46**, 5796.
- 32 B. W. Eichhorn, R. C. Haushalter and W. T. Pennington, *J. Am. Chem. Soc.*, 1988, **110**, 8704.
- 33 B. Kesanli, J. Fettinger and B. Eichhorn, *Chem. – Eur. J.*, 2001, **7**, 5277.
- 34 J. Campbell, H. P. Mercier, H. Franke, D. P. Santry, D. A. Dixon and G. J. Schrobilgen, *Inorg. Chem.*, 2002, **41**, 86.
- 35 D. O. Downing, P. Zavalij and B. W. Eichhorn, *Eur. J. Inorg. Chem.*, 2010, 890.
- 36 B. W. Eichhorn and R. C. Haushalter, *J. Chem. Soc., Chem. Commun.*, 1990, 937.
- 37 K. Mayer, L. A. Jantke, S. Schulz and T. F. Fässler, *Angew. Chem., Int. Ed.*, 2017, **56**, 2350.
- 38 B. Zhou, M. S. Denning, T. A. Chapman, J. E. McGrady and J. M. Goicoechea, *Chem. Commun.*, 2009, 7221.
- 39 M. Waibel, F. Kraus, S. Scharfe, B. Wahl and T. F. Fässler, *Angew. Chem., Int. Ed.*, 2010, **49**, 6611.
- 40 S. Stegmaier, M. Waibel, A. Henze, L.-A. Jantke, A. J. Karttunen and T. F. Fässler, *J. Am. Chem. Soc.*, 2012, **134**, 14450.
- 41 M. Waibel, G. Raudaschl-Sieber and T. F. Fässler, *Chem. – Eur. J.*, 2011, **17**, 13391.
- 42 T. Henneberger, W. Klein, J. V. Dums and T. F. Fässler, *Chem. Commun.*, 2018, **54**, 12381.
- 43 C. B. Benda, M. Waibel, T. Köchner and T. F. Fässler, *Chem. – Eur. J.*, 2014, **20**, 16738.
- 44 F. Fendt, C. Koch, S. Gärtner and N. Korber, *Dalton Trans.*, 2013, **42**, 15548.
- 45 M. Neumeier, F. Fendt, S. Gärtner, C. Koch, T. Gärtner, N. Korber and R. M. Gschwind, *Angew. Chem., Int. Ed.*, 2013, **52**, 4483.
- 46 F. Fendt, C. Koch, M. Neumeier, S. Gärtner, R. M. Gschwind and N. Korber, *Chem. – Eur. J.*, 2015, **21**, 14539.
- 47 C. Lorenz, F. Hastreiter, J. Hioe, N. Lokesh, S. Gärtner, N. Korber and R. M. Gschwind, *Angew. Chem., Int. Ed.*, 2018, **57**, 12956.
- 48 F. Hastreiter, C. Lorenz, J. Hioe, S. Gärtner, N. Lokesh, N. Korber and R. M. Gschwind, *Angew. Chem., Int. Ed.*, 2019, **58**, 3133.
- 49 S. Mitzinger, J. Bandemehr, K. Reiter, J. S. McIndoe, X. Xie, F. Weigend, J. F. Corrigan and S. Dehnen, *Chem. Commun.*, 2018, **54**, 1421.
- 50 C. B. Benda, R. Schäper, S. Schulz and T. F. Fässler, *Eur. J. Inorg. Chem.*, 2013, 5964.
- 51 V. Queneau and S. C. Sevov, *J. Am. Chem. Soc.*, 1997, **119**, 8109.
- 52 M. Waibel, T. Henneberger, L.-A. Jantke and T. F. Fässler, *Chem. Commun.*, 2012, **48**, 8676.
- 53 T. F. Fässler, *Coord. Chem. Rev.*, 2001, **215**, 347.
- 54 C. B. Benda, M. Waibel and T. F. Fässler, *Angew. Chem., Int. Ed.*, 2015, **54**, 522.
- 55 P. R. Markies, G. Schat, O. S. Akkerman, F. Bickelhaupt, W. J. Smeets and A. L. Spek, *Organometallics*, 1990, **9**, 2243.
- 56 J. Bacsá, F. Hanke, S. Hindley, R. Odedra, G. R. Darling, A. C. Jones and A. Steiner, *Angew. Chem., Int. Ed.*, 2011, **50**, 11685.
- 57 C. Lorenz and N. Korber, *Crystals*, 2018, **8**, 374.
- 58 S. C. Cole, M. P. Coles and P. B. Hitchcock, *Dalton Trans.*, 2003, 3663.

- 59 R. Blom, J. Boersma, P. Budzelaar, B. Fischer, A. Haaland, H. Volden and J. Weidlein, *ActaChem.Scand., Ser.A*, 1986, **40**, 113.
- 60 W. Seidel and I. Bürger, *Z. Anorg. Allg. Chem.*, 1981, **473**, 166.
- 61 B. J. Witzel, W. Klein, J. V. Dums, M. Boyko and T. F. Fässler, *Angew. Chem., Int. Ed.*, 2019, **58**, 12908.
- 62 G. Sheldrick, *Acta Crystallogr., Sect. C: Struct. Chem.*, 2015, **71**, 3.
- 63 T. Henneberger, W. Klein and T. F. Fässler, *Z. Kristallogr. – New Cryst. Struct.*, 2019, **234**, 1241.

Intermediates and Products of the Reaction of Zn(II) Organyls with Tetrel Element *Zintl* Ions: Cluster Extension *versus* Complexation

C. Wallach, K. Mayer, T. Henneberger, W. Klein, T.F. Fässler

Technische Universität München, Department Chemie,
Lichtenbergstraße 4, 85747 Garching, Germany

Supporting Information

Crystallographic details for compounds 1 – 8	2
Crystal structures of 1 – 8 and selected bond lengths of 1a – 8a	3
ESI-MS spectra	13

Table S1: Crystallographic details for compounds **1** – **8**.

Compound	1	2	3	4
formula unit	C ₄₀ H ₈₈ N ₆ O ₁₂ K ₂ Ge ₄ Zn ₂	H ₁₈ N ₆ K ₆ Sn ₈ Zn	C ₅₆ H _{135.2} N _{13.4} O ₁₈ K ₃ Ge ₉ Zn	C ₃₂ H ₉₉ N ₁₃ O ₁₂ K ₂ Zn ₅
fw [g·mol ⁻¹]	1344.46	1522.03	2120.64	1263.29
space group	<i>P</i> $\bar{1}$	<i>P</i> $\bar{1}$	<i>P</i> $\bar{1}$	<i>P</i> $\bar{1}$
<i>a</i> [Å]	11.8577(4)	9.6916(6)	14.6139(7)	11.554(2)
<i>b</i> [Å]	14.5738(5)	12.2418(7)	14.9181(6)	14.140(3)
<i>c</i> [Å]	18.8964(7)	18.6684(8)	23.6002(8)	18.988(4)
α [°]	80.349(3)	99.120(4)	97.552(3)	89.02(3)
β [°]	74.590(3)	90.067(4)	91.645(3)	77.37(3)
γ [°]	69.598(3)	94.894(5)	117.312(3)	87.11(3)
<i>V</i> [Å ³]	2940.45(2)	2178.7(2)	4508.7(3)	3023.2(1)
<i>Z</i>	2	2	2	2
<i>T</i> [K]	150(2)	120(2)	150(2)	150(2)
λ [Å]	0.71073	0.71073	0.71073	0.71073
ρ_{calcd} [g·cm ⁻³]	1.518	2.320	1.562	1.388
μ [mm ⁻¹]	3.017	5.635	3.416	2.148
collected reflections	80187	50041	93046	69261
independent reflections	11534	8378	17700	11852
<i>R</i> _{int} / <i>R</i> _s	0.0515/0.247	0.0912/0.0626	0.0891/0.0574	0.0192/0.114
parameters / restraints	597/12	289/0	913/0	611/12
<i>R</i> ₁ [<i>I</i> > 2 σ (<i>I</i>) / all data]	0.0304/0.0396	0.0322/0.0494	0.0509/0.0793	0.0267/0.0340
w <i>R</i> ₂ [<i>I</i> > 2 σ (<i>I</i>) / all data]	0.0704/0.0761	0.0667/0.0694	0.1210/0.1374	0.0613/0.0668
goodness of fit	1.062	0.919	1.022	1.104
max./min. diff. el. density [e·Å ⁻³]	2.262/-1.382	1.311/-0.935	1.012/-0.880	0.768/-0.572
depository no.	CCDC 1982121	CSD 1982122	CCDC 1982123	CCDC 1982124

Compound	5	6	7	8
formula unit	C ₄₈ H ₉₆ N ₁₀ O ₁₂ K ₂ Zn ₂	C ₃₀ H ₃₉ O ₆ K _{0.84} Rb _{0.16} Zn	C ₄₇ H ₇₆ NO ₈ KZn	C ₂₂ H ₄₅ N ₂ O ₆ K
fw [g·mol ⁻¹]	1214.28	607.38	887.55	472.70
space group	<i>P</i> $\bar{1}$	<i>Pca</i> 2 ₁	<i>P</i> 2 ₁ / <i>c</i>	<i>Pbca</i>
<i>a</i> [Å]	11.963(5)	21.842(2)	15.7570(5)	10.1910(2)
<i>b</i> [Å]	12.328(5)	7.2588(15)	13.1722(5)	16.1458(3)
<i>c</i> [Å]	12.683(6)	18.322(3)	23.6712(8)	32.8773(9)
α [°]	107.43(4)	90	90	90
β [°]	106.66(4)	90	94.486(3)	90
γ [°]	104.16(3)	90	90	90
<i>V</i> [Å ³]	1594.0(1)	2904.9(8)	4898.0(3)	5409.7(2)
<i>Z</i>	1	4	4	8
<i>T</i> [K]	120(2)	120(2)	120(2)	150(2)
λ [Å]	0.71073	0.71073	0.71073	0.71073
ρ_{calcd} [g·cm ⁻³]	1.265	1.389	1.204	1.161
μ [mm ⁻¹]	0.942	1.269	0.635	0.231
collected reflections	16857	30260	55312	148069
independent reflections	6272	5705	9472	5311
<i>R</i> _{int} / <i>R</i> _s	0.0828/0.1765	0.1990/0.3101	0.0706/0.1068	0.0382/0.0115
parameters / restraints	344/0	343/72	552/0	295/0
<i>R</i> ₁ [<i>I</i> > 2 σ (<i>I</i>) / all data]	0.0510/0.1097	0.0540/ 0.1647	0.0455/0.0950	0.0353/0.0422
w <i>R</i> ₂ [<i>I</i> > 2 σ (<i>I</i>) / all data]	0.1003/0.1106	0.0902/ 0.1059	0.1018/0.1107	0.0939/0.0987
goodness of fit	0.768	0.655	0.840	1.021
max./min. diff. el. density [e·Å ⁻³]	0.913/-0.608	0.826/-0.486	0.659/-0.489	0.354/-0.313
CCDC	CCDC 1982125	CCDC 1982126	CCDC 1982127	CCDC 1982128

Crystal structures of 1 – 8 and selected bond lengths of 1a – 8a

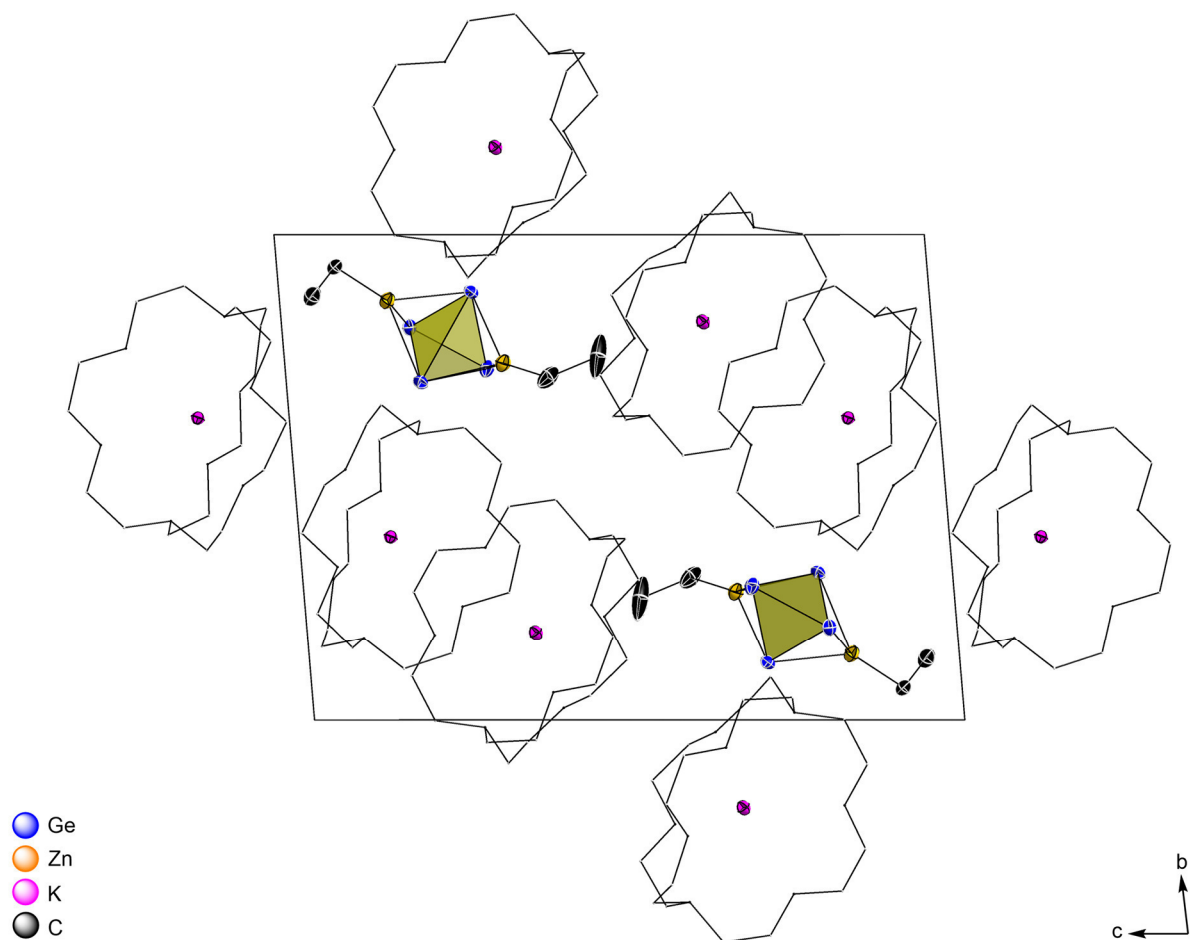
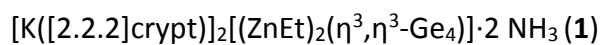


Figure S1: Crystal structure of compound **1**, view along $[\bar{1}00]$. All ellipsoids are shown at a 50 % probability level as octants. Color code: Ge: blue; Zn: orange; K: purple; C: black. The clusters are shown as polyhedra. Ammonia molecules as well as protons are omitted. Cryptand molecules are presented as wire/stick for clarity.

Table S2: Selected bond lengths in **1**.

Atoms	Bond lengths [Å]	Atoms	Bond lengths [Å]
Ge1 – Ge2	2.9279(4)	Ge3 – Ge4	2.4714(4)
Ge1 – Ge3	2.5859(4)	Ge1 – Ge4	2.5970(4)
Ge2 – Ge3	2.5976(4)	Ge2 – Ge4	2.6046(4)
Ge1 – Zn1	2.5159(4)	Ge1 – Zn2	2.5267(4)
Ge2 – Zn1	2.5177(4)	Ge2 – Zn2	2.5134(4)
Ge3 – Zn1	2.7096(5)	Ge4 – Zn2	2.6822(5)
Zn1 – C37	2.009(3)	Zn2 – C39	2.004(3)
C37 – C38	1.534(4)	C39 – C40	1.523(6)

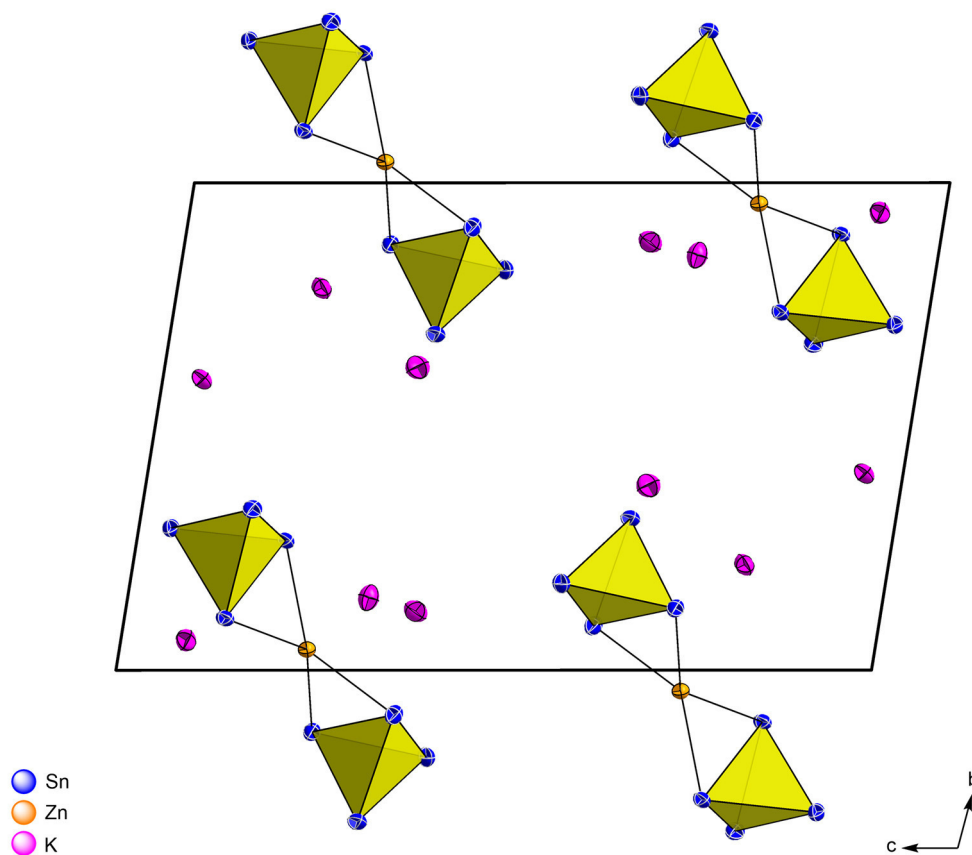
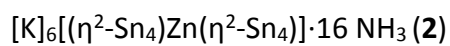


Figure S2: Crystal structure of compound **2**, view along $\bar{1}00$. All ellipsoids are shown at a 50 % probability level. Color code: Sn: blue; Zn: orange; K: purple. The clusters are shown as polyhedra. Ammonia molecules are omitted for clarity.

Table S3: Selected bond lengths in **2**.

Atoms	Bond lengths [Å]	Atoms	Bond lengths [Å]
Zn1 – Sn1	2.7450(8)	Zn1 – Sn5	2.7512(8)
Zn1 – Sn2	2.7611(8)	Zn1 – Sn6	2.7258(8)
Sn1 – Sn2	3.0785(6)	Sn5 – Sn6	3.0723(6)
Sn1 – Sn3	2.9038(6)	Sn5 – Sn7	2.8964(6)
Sn1 – Sn4	2.9071(6)	Sn5 – Sn8	2.9033(6)
Sn2 – Sn3	2.9100(6)	Sn6 – Sn7	2.8998(6)
Sn2 – Sn4	2.8904(6)	Sn6 – Sn8	2.8827(6)
Sn3 – Sn4	2.9492(6)	Sn7 – Sn8	2.9402(6)

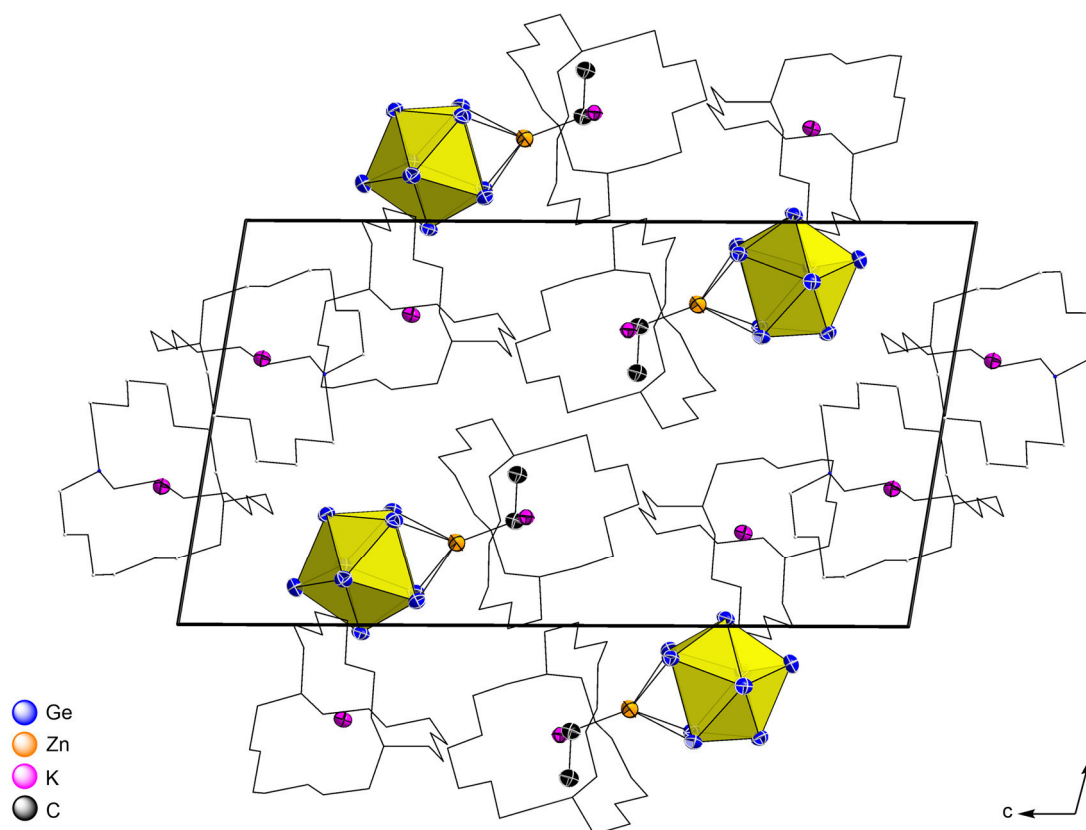
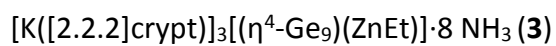


Figure S3: Crystal structure of compound **3**, view along $\bar{1}00$. All ellipsoids are shown at a 50 % probability level. Color code: Ge: blue; Zn: orange; K: purple; C: black. The clusters are shown as polyhedra. Ammonia molecules as well as protons are omitted, cryptand molecules are presented as wire/stick for clarity.

Table S4: Selected bond lengths in **3**.

Atoms	Bond lengths [Å]	Atoms	Bond lengths [Å]
Ge1–Zn	2.6437(9)	Ge5–Ge9	2.5813(8)
Ge2–Zn	2.6001(8)	Ge6–Ge9	2.6001(8)
Ge3–Zn	2.5921(9)	Ge7–Ge9	2.5645(8)
Ge4–Zn	2.6105(8)	Ge8–Ge9	2.5733(8)
Ge1–Ge2	2.7643(8)	Ge5–Ge6	2.8036(8)
Ge2–Ge3	2.7962(8)	Ge6–Ge7	2.8131(8)
Ge3–Ge4	2.7868(8)	Ge7–Ge8	2.8612(8)
Ge4–Ge1	2.7493(8)	Ge8–Ge5	2.8465(8)
Ge1–Ge5	2.5590(7)	Ge3–Ge7	2.5591(7)
Ge1–Ge6	2.5717(7)	Ge3–Ge8	2.5494(7)
Ge2–Ge6	2.5692(7)	Ge4–Ge5	2.5742(7)
Ge2–Ge7	2.5478(7)	Ge4–Ge8	2.5590(8)
Zn–C1	2.015(5)	C1–C2	1.515(7)

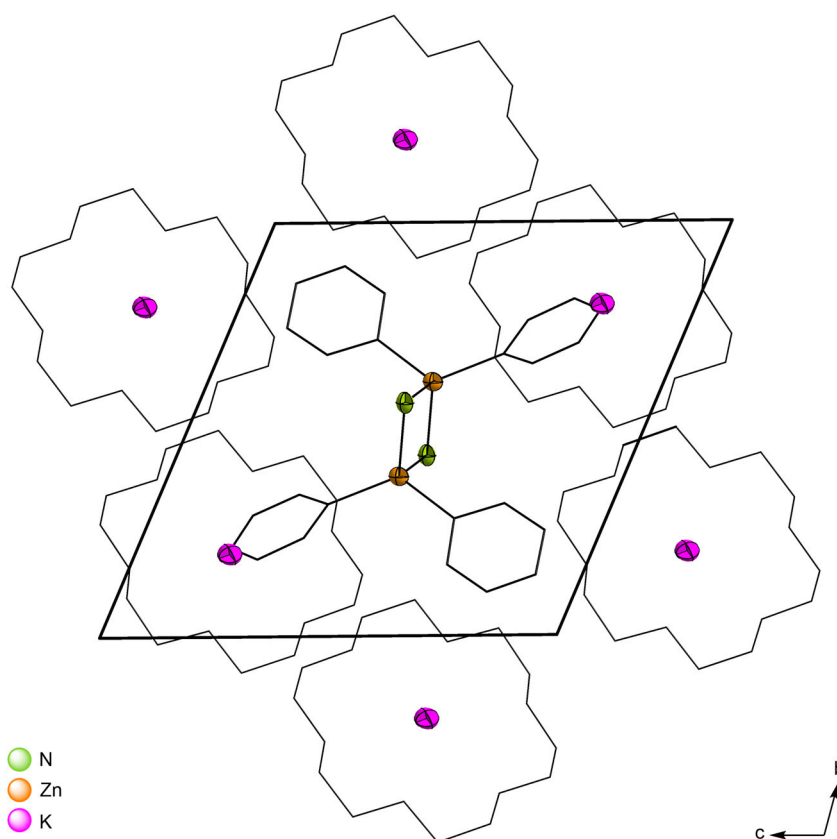
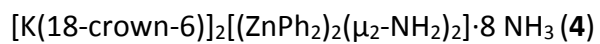


Figure S4: Crystal structure of compound **4**, view along $[\bar{1}00]$. All ellipsoids are shown at a 50 % probability level. Color code: N: green; Zn: orange; K: purple. Ammonia molecules as well as protons are omitted, crown ether molecules as well as phenyl groups are presented as wire/stick for clarity.

Table S5: Selected bond lengths in **4** (Symmetry operation: i: $-(1-x), (1-y), (1-z)$).

Atoms	Bond lengths [\AA]
Zn–N	2.104(4)
Zn–N ⁱ	2.045(4)
Zn–C13	2.046(4)
Zn–C19	2.034(4)

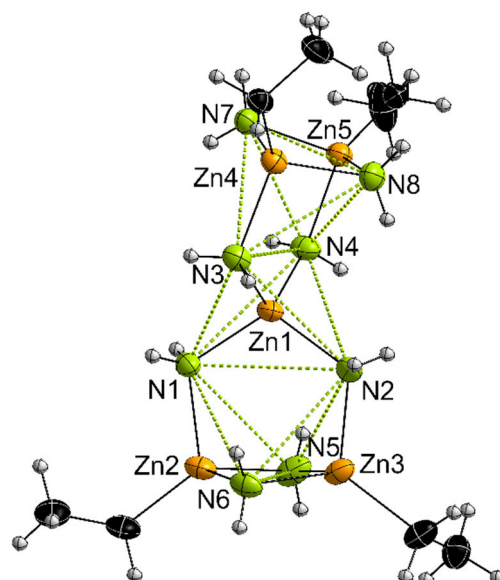
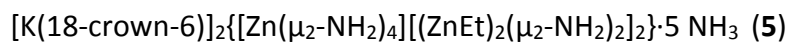


Figure S5: Molecular structure of the pentanuclear Zn complex **5a**. All ellipsoids are shown at a 50 % probability level. Color code: Zn: orange; N: light blue; C: black; H: grey.

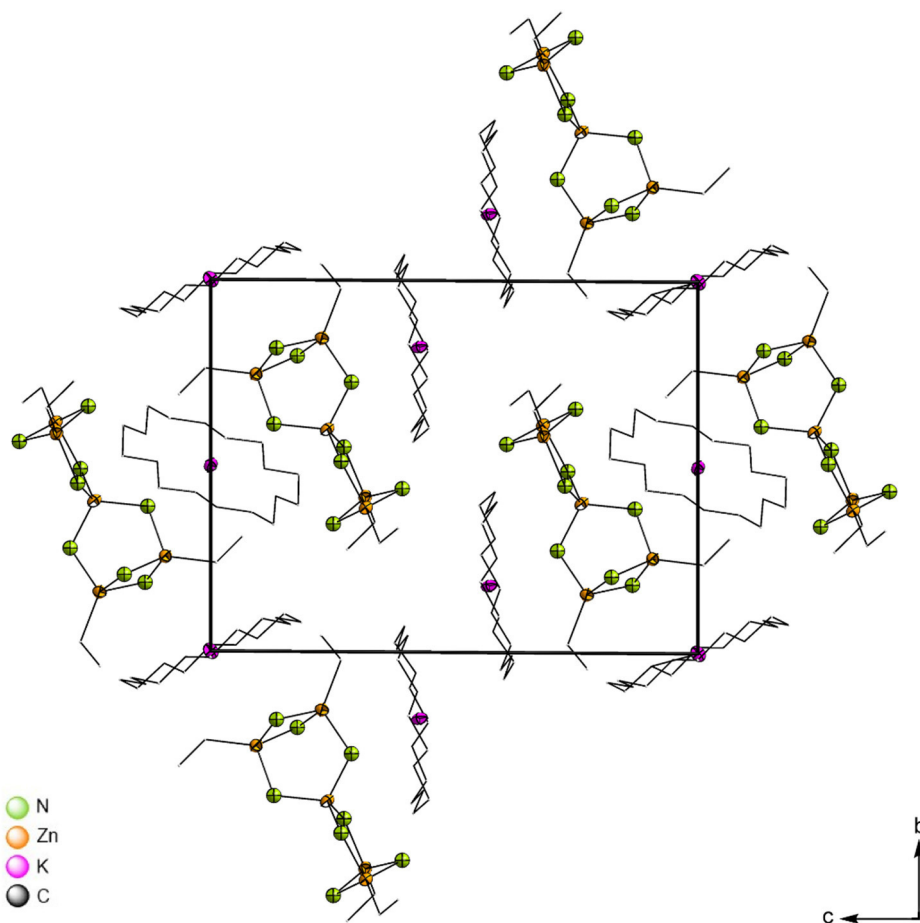


Figure S6: Crystal structure of compound **5**, view along $[100]$. All ellipsoids are shown at a 50 % probability level. Color code: N: green; Zn: orange; K: purple. Ammonia molecules as well as protons are omitted, crown ether molecules as well as ethyl groups are presented as wire/stick for clarity.

Table S6: Selected bond lengths in **5**.

Atoms	Bond lengths [Å]	Atoms	Bond lengths [Å]
Zn1 – N1	2.0550(2)	Zn1 – N3	2.042(2)
Zn1 – N2	2.038(2)	Zn1 – N4	2.052(2)
Zn2 – N1	2.0649(2)	Zn4 – N3	2.081(2)
Zn2 – N5	2.060(2)	Zn4 – N7	2.080(2)
Zn2 – N6	2.089(2)	Zn4 – N8	2.075(2)
Zn3 – N2	2.077(2)	Zn5 – N4	2.063(2)
Zn3 – N5	2.075(2)	Zn5 – N7	2.0778(2)
Zn3 – N6	2.080(2)	Zn5 – N8	2.084(2)
Zn2 – C25	2.052(3)	C25 – C26	1.534(4)
Zn3 – C27	2.047(2)	C27 – C28	1.580(3)
Zn4 – C29	2.031(2)	C29 – C30	1.515(4)
Zn5 – C31	2.039(2)	C31 – C32	1.534(3)

[K_{0.8}Rb_{0.2}(18-crown-6)][ZnPh₃] (**6**)

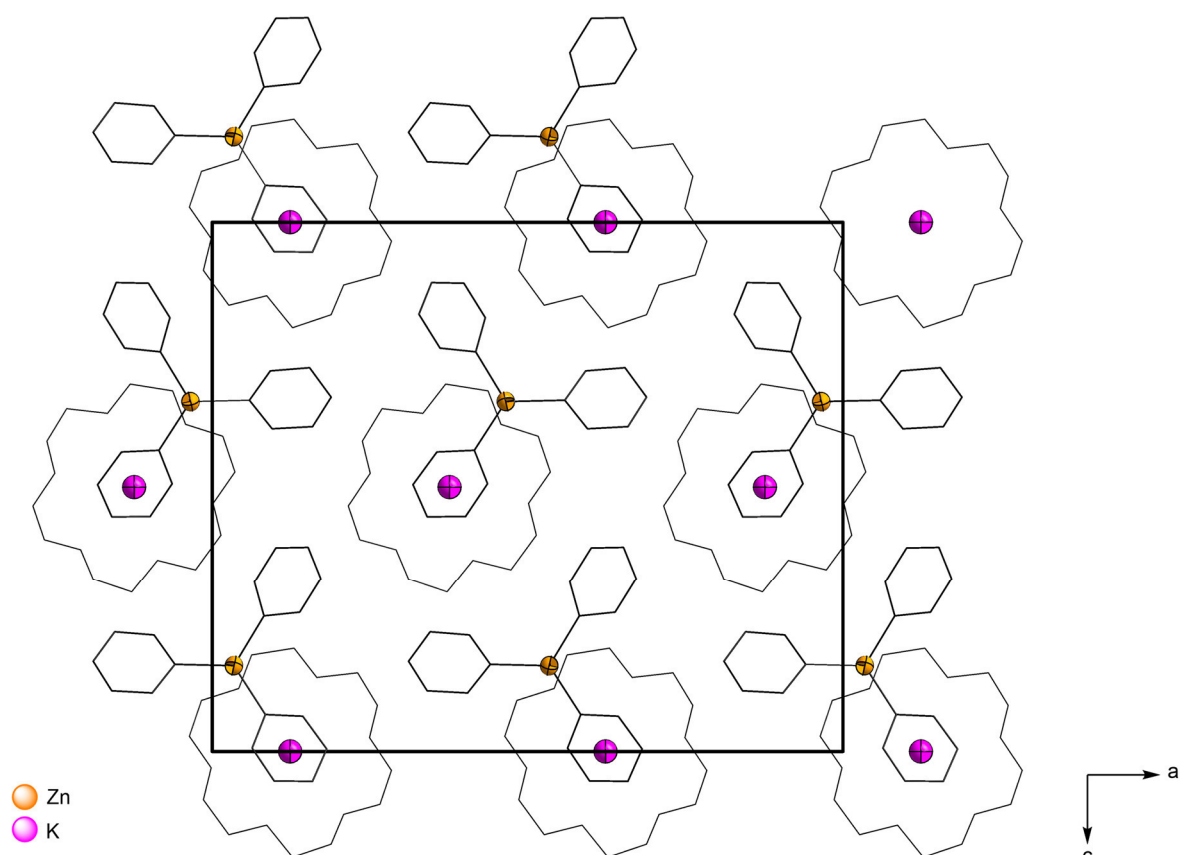


Figure S7: Crystal structure of compound **6**, view along $[0\bar{1}0]$. All ellipsoids are shown at a 50 % probability level. Color code: Zn: orange; K/Rb: purple; C: black. Protons are omitted, crown ether molecules as well as phenyl groups are presented as wire/stick for clarity.

Table S7: Selected bond lengths in **6**.

Atoms	Bond lengths [Å]
Zn–C13	2.013(1)
Zn–C19	2.018(2)
Zn–C25	2.030(8)
C16–C17	1.343(2) (shortest C–C)
C13–C14	1.420(2) (longest C–C)

[K(18-crown-6)][ZnMes₃] \cdot NH₃ \cdot 2 thf (**7**)

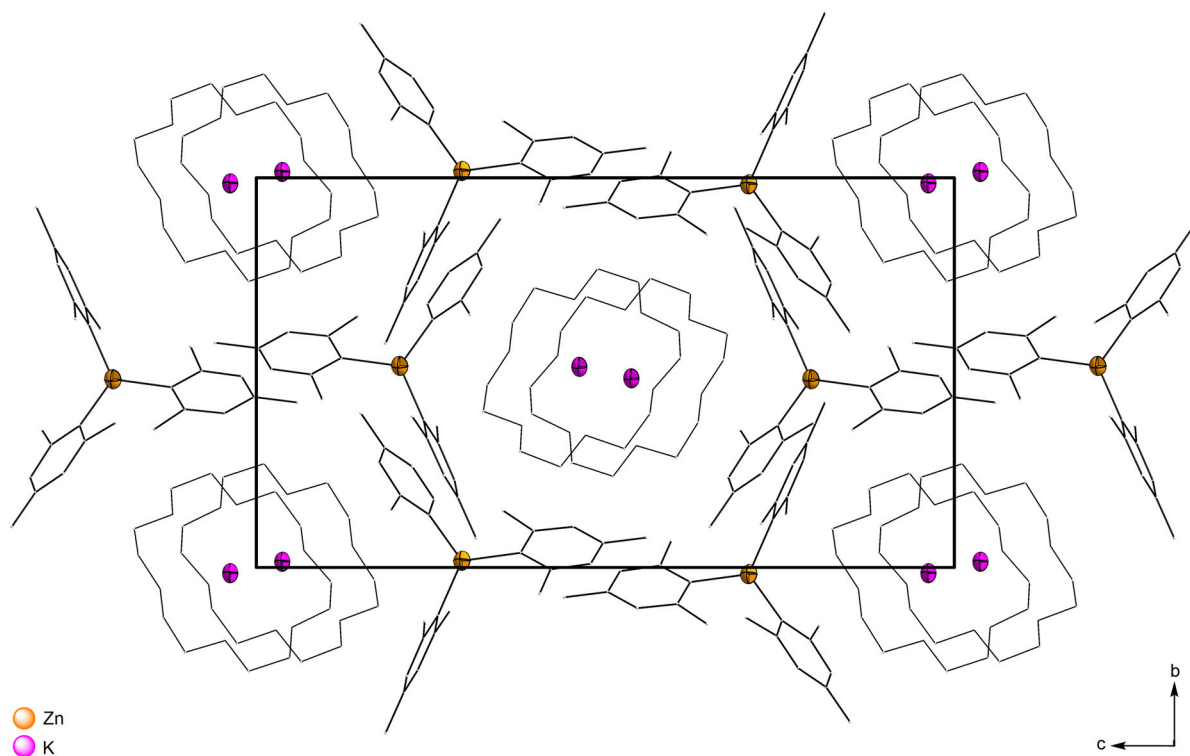


Figure S8: Crystal structure of compound **7**, view along $[100]$. All ellipsoids are shown at a 50 % probability level. Color code: Zn: orange; K: purple; C: black. Protons, NH₃ as well as thf molecules are omitted, crown ether molecules as well as mesityl groups are presented as wire/stick for clarity.

Table S8: Selected bond lengths in **7**.

Atoms	Bond lengths [Å]
Zn–C13	2.041(3)
Zn–C22	2.042(3)
Zn–C31	2.047(3)
C33–C34	1.382(4) (shortest C–C)
C25–C29	1.521(4) (longest C–C)

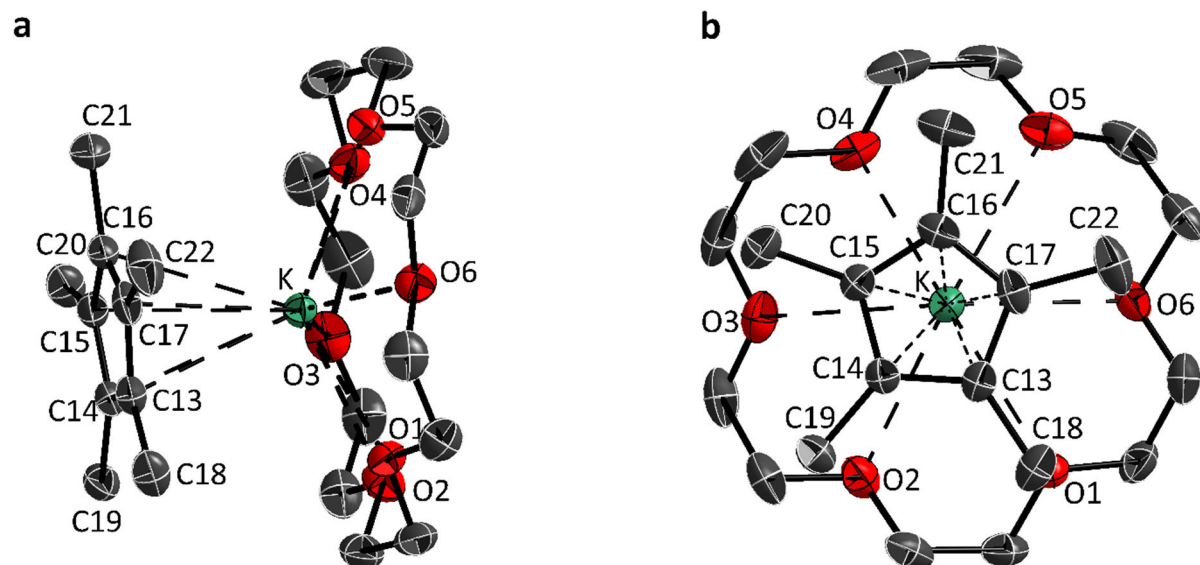
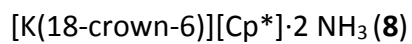


Figure S9: Molecular structure of **8a** in a) side view and b) top view. All ellipsoids are shown at a 50 % probability level. C: black; K: purple; O: red. Ammonia molecules as well as protons are omitted.

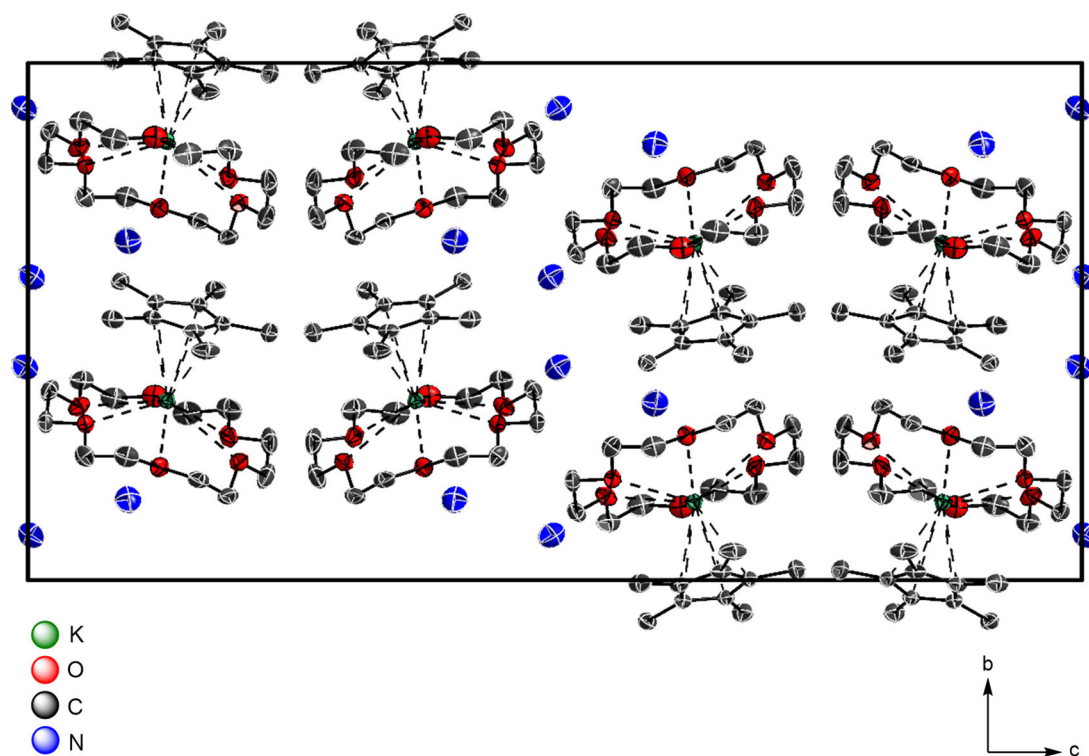


Figure S10: Crystal structure of compound **8**, view along [100]. All ellipsoids are shown at a 50 % probability level. Color code: K: green; C: black; O: red; N blue. Protons are omitted for clarity.

Table S9: Selected bond lengths in **8**.

Atoms	Bond lengths [Å]	Atoms	Bond lengths [Å]
K-O1	2.9647(10)	C13-C14	1.415(2)
K-O2	3.1146(11)	C14-C15	1.415(2)
K-O3	2.9132(12)	C15-C16	1.407(2)
K-O4	2.8872(11)	C16-C17	1.413(2)
K-O5	3.0673(11)	C17-C13	1.412(2)
K-O6	2.9768(11)	C13-C18	1.505(2)
K-C13	3.0278(13)	C14-C19	1.506(2)
K-C14	3.1194(13)	C15-C20	1.507(2)
K-C15	3.1531(13)	C16-C21	1.506(2)
K-C16	3.0744(14)	C17-C22	1.504(2)
K-C17	2.9941(14)		

ESI-MS spectra

ESI-MS analyses were performed on a Bruker Daltonic HCT mass spectrometer (dry gas temperature: 300 °C; injection speed: 240 $\mu\text{L}/\text{h}$), and the data evaluation was carried out using the Bruker Compass Data Analysis 4.0 SP 5 program (Bruker). Data evaluation was performed using OriginPro2016G (Origin Lab) and Excel 2016 (Microsoft). The sample preparation was as follows:

Reaction for anion **1a**: Onto a mixture of K_4Ge_4 (35 mg, 80 μmol , 1 eq.), ZnEt_2 (160 μL , 160 μmol , 2 eq.) and [2.2.2]crypt (53.1 mg, 140 μmol , 1.8 eq.) 2 mL of liquid ammonia are condensed.

Reaction for anion **3a**: Onto a mixture of K_4Ge_9 (40 mg, 50 μmol , 1 eq.), ZnEt_2 (100 μL , 100 μmol , 2 eq.) and [2.2.2]crypt (33.5 mg, 90 μmol , 1.8 eq.) 2 mL of liquid ammonia are condensed.

After the addition of ammonia, the obtained dark red solutions were stirred at -78 °C for 4 h using a glass stirring bar and subsequently stored in a freezer at -40 °C for 2 weeks. Afterwards, the solvent was evaporated, the residue extracted with acetonitrile (1 mL), and the obtained solution was injected into the measuring device after filtration. Due to slow molecular dynamics at -40 °C product formation is a long lasting process and signal-to-noise ratios of such ESI-MS measurements are usually low. However, signals at m/z 802.0 $\{[\text{K}([\text{2.2.2}]\text{crypt})][\text{Ge}_4(\text{ZnEt})]\}^-$ (ionization product of **1a**, negative-ion mode, 2500 V, 300 °C) and m/z 746.2 for $[\text{Ge}_9(\text{ZnEt})]^-$ (**3a**, negative-ion mode, 2500 V, 300 °C) could be detected and are in good accordance to the theoretical isotope distribution (black bars in Figures 1 and S11). Sn-containing samples could not be measured due to their high instability which led to an immediate metal mirror formation in the injection needle.

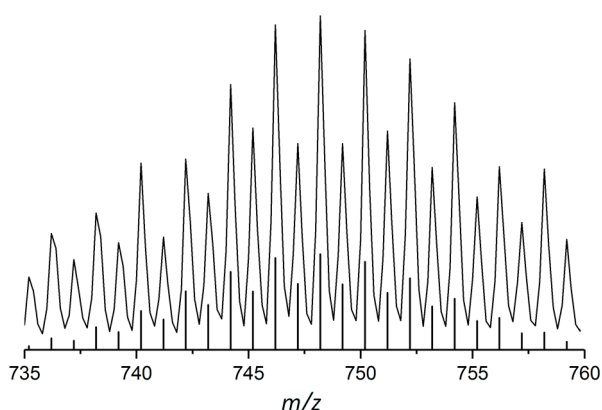


Figure S11: ESI-MS spectrum of $[\text{Ge}_9(\text{ZnEt})]^-$ (**3a**) in MeCN (negative-ion mode, 2500 V, 300 °C) monitoring the molecule peak at m/z 746.2. The calculated pattern is presented as red bars. Due to the low concentration of **3a** in the injected solution, the signal to noise ratio was low.

6.9 Filled Trivacant Icosahedra as Building Fragments in 17-atom Endohedral Germanides $[TM_2@Ge_{17}]^{n-}$ ($TM = Co, Ni$)

C. Wallach, Y. Selic, B. J. L. Witzel, W. Klein and T. F. Fässler

Published in: *Dalton Transactions* **2021**, 50, 13671.

© The Royal Society of Chemistry 2021. Reproduced with permission from the Royal Society of Chemistry.

Access online *via*: <https://pubs.rsc.org/en/content/articlelanding/2021/dt/d1dt03078g/unauth>.

Contents and Contributions

The two 17-atom endohedral germanium clusters $[Co_2@Ge_{17}]^{6-}$ (**1a**) and $[Ni_2@Ge_{17}]^{4-}$ (**2a**) are synthesized and structurally characterized. The clusters bridge the gap between known 16- and 18-atom doubly filled germanium clusters and resemble the lighter congeners to the respective tin-based clusters. Two different synthesis strategies were chosen yielding the respective clusters: anion **1a** formed in liquid ammonia by reacting a pre-formed phase of nominal composition “ $K_5Co_{1.2}Ge_9$ ” with a titanium organyl; anion **2a** was synthesized starting from pristine $[Ge_9]^{4-}$ clusters by reactions with biscyclooctadiene nickel. The shell of vertex atoms in which the transition metals are encapsulated resembles an icosahedral atom arrangement, which is discussed in more detail including quantum chemical calculations. On a side note, the known filled ten-atom cluster $[Co@Ge_{10}]^{3-}$ (**3a**) was isolated from liquid ammonia.


The experiments leading to the single crystals containing the filled polyanions were performed by Dr. Benedikt J. L. Witzel (**1a**, **3a**) and me (**2a**). The single crystals were selected and measured by the respective person, including the initial structure refinement. Dr. Wilhelm Klein finalized the single crystal structure refinements for publication. The samples for the ESI-MS measurements were prepared by me, including the subsequent data acquisition and evaluation. EDX analysis was performed by Maria Müller (Prof. Fässler, TUM). The optimization of the cluster geometries and correlated quantum chemical calculations were done by M. Sc. Yasmin Selic. The manuscript was authored by me, including the creation of figures, tables, and schemes. M. Sc. Yasmin Selic and Dr. Annette Schier proof-read the manuscript. The publication of the manuscript was managed by Prof. Dr. Thomas F. Fässler, the peer-review process including corrections was a joined task accomplished by Prof. Dr. Thomas F. Fässler, Dr. Wilhelm Klein and me.

Cite this: *Dalton Trans.*, 2021, **50**, 13671Received 10th September 2021,
Accepted 13th September 2021

DOI: 10.1039/d1dt03078g

rsc.li/dalton

Filled trivacant icosahedra as building fragments in 17-atom endohedral germanides $[TM_2@Ge_{17}]^{n-}$ ($TM = Co, Ni$)[†]

Christoph Wallach, Yasmin Selic, Benedikt J. L. Witzel, Wilhelm Klein and Thomas F. Fässler 

The syntheses and the characterization of two 17-atom endohedral Ge clusters, $[Co_2@Ge_{17}]^{6-}$ (**1a**) and $[Ni_2@Ge_{17}]^{4-}$ (**2a**), are reported. The anions **1a** and **2a**, which close the gap between the known 16- and 18-atom Ge clusters, are investigated by single crystal X-ray diffraction and by quantum chemical calculations. The structures mark a new example on the pathway for cluster growth towards larger clusters with icosahedral symmetry. Furthermore, the $[Co@Ge_{10}]^{3-}$ anion (**3a**) is obtained from liquid ammonia.

Bare tetrel element clusters endohedrally filled with transition metals prompted the definition of intermetallic clusters.¹ Such clusters resemble atom arrangements occurring in intermetallic compounds and lie at the borderline of molecules and solid state structures.^{1–5} In recent years several examples of tetrel element-based structures have been reported, most often obtained from homoatomic nine-atom clusters as starting units. Even though endohedrally filled, nine-atom clusters are scarcely known in the solid such as in K_5CoSn_9 ,^{6,7} $K_{13}CoSn_{17}$, $Na_{12}Ni_{1-x}Sn_{17}$,⁸ $K_{12}Pd_{1-x}Sn_{17}$, and K_4RhPb_9 ,⁹ they are generally obtained from solution by reacting bare tetrel element clusters $[E_9]^{4-}$ ($E = Ge, Sn, Pb$) with transition metal complexes. The smallest so prepared $[TM@E_9]^{x-}$ clusters comprise Ru,^{10,11} Co,¹¹ Ni,¹² or Cu¹³ atoms in a d^{10} electron configuration with cluster charges between 6- and 3-. Impressive examples of larger clusters such as $[Rh_3@Sn_{24}]^{5-}$,¹⁴ $[Au_8Pb_{33}]^{6-}$, $[Au_{12}Pb_{44}]^{8-}$,¹⁵ and $[Au_3Ge_{45}]^{8-}$ (ref. 16) demonstrate the possibility for a bottom-up synthesis.^{2,4,17} The mechanism of cluster growth is still under debate, however, a stepwise synthesis, in which a transition metal complex is added to the *Zintl* cluster and the ligand is cleaved subsequently, seems reasonable. This possible reaction path is corroborated by the isolation of intermediates on the way

to binary Au–Pb clusters¹⁵ or to larger Ti–Sn clusters such as $[(\eta^5-C_5H_5)_2Ti(\eta^1-Sn_9)]^{2-}$, $[(\eta^5-C_5H_5)Ti(\eta^4-Sn_8)]^{3-}$ and $\{[(\eta^5-C_5H_5)_2Ti]_2\{(\eta^5-C_5H_5)Ti\}Sn_{15}\}^{n-}$.¹⁸ Furthermore, a cluster growth through fragmentation is frequently observed resulting in anions of the types $[TM@E_n]^{x-}$ ($n = 10, 11, 12$) and $[TM_2@E_m]^{x-}$ ($m = 16, 17, 18$)^{2,4} with the known examples $[Co_2@Ge_{16}]^{4-}$,^{19,20} $[Fe_2@Ge_{16}]^{4-}$,²¹ $[Pd_2@Ge_{18}]^{4-}$,²² and the 17-atom Sn cages containing Co,^{6,7} Ni,²³ Rh,¹⁴ and Pt.²⁴ Whereas many structures of dimeric 17-atom endohedral Sn cluster have been reported, that support the step-wise cluster growth mechanism, no Ge species comprising 17 Ge atoms has been described. We carried out experiments from two different starting points to achieve its synthesis. On the one hand we followed the established procedure of the reaction of $[Ge_9]^{4-}$ with $Ni(cod)_2$ in ethylenediamine,^{12,25,26} on the other hand we induced the fusion of pre-formed filled $[Co@Ge_9]^{5-}$ clusters¹¹ in liquid ammonia. The two approaches resulted in the first endohedrally filled $[TM_2@Ge_{17}]^{n-}$ anions [$TM = Co$ (**1a**) and Ni (**2a**) with $n = 6$ and 4 , respectively]. Quantum chemical calculations corroborate the experimentally obtained structures as energetic minima.

A finely ground alloy of nominal composition “ $K_5Co_{1.2}Ge_9$ ”, that according to Raman spectroscopy comprises filled clusters,¹¹ was dissolved in liquid ammonia in the presence of $[Cp_2Ti(NH_3)_2]Cl(NH_3)$. After several months black crystals of $[K([2.2.2]crypt)_2K_4[Co_2@Ge_{17}]\cdot 15NH_3$ (**1**) were isolated from the reaction mixture. Compound **1** crystallizes in the monoclinic space group $P2_1/c$ and contains the doubly filled 17-vertex atom polyanion $[Co_2@Ge_{17}]^{6-}$ (**1a**). The structure of anion **1a** can be described as two fused distorted $[CoGe_9]$ entities sharing one vertex atom (Ge9). The nine atom clusters correspond to tri-capped trigonal prisms with two strongly elongated prism heights (Ge5–Ge8, Ge6–Ge7 and Ge10–Ge13, Ge11–Ge12) forming two rectangular faces (Ge5–Ge8 and Ge10–Ge13) with a dihedral angle of 14.0° between the planes, that are merged by the shared face-capping atom Ge9. Alternatively, the anion can be viewed as two $[Ge_8]$ tubs (Ge1–Ge8 and Ge10–Ge17) that align around a central Co–Ge–Co strand (Fig. 1a).

Department Chemie, Technische Universität München, Lichtenbergstraße 4, 85748 Garching b. München, Germany. E-mail: thomas.faessler@lrz.tum.de

[†]Electronic supplementary information (ESI) available: Experimental details, crystallographic data, ESI MS spectra, computational details. CCDC 2081217–2081219. For ESI and crystallographic data in CIF or other electronic format see DOI: 10.1039/d1dt03078g

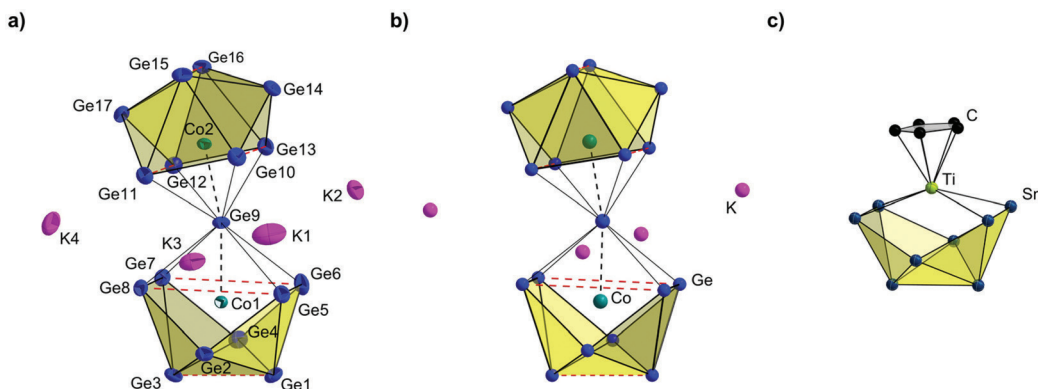


Fig. 1 (a) Structure of the $[\text{Co}_2@Ge_{17}]^{6-}$ anion (**1a**) including coordinating non-sequestered K^+ cations with emphasis on the arrangement of the two $[Ge_9]$ tubs around a central, bent Co–Ge–Co strand; all ellipsoids are presented at a 50% probability level; (b) DFT-optimized structure of the $\{K_4[Co_2@Ge_{17}]\}^{2-}$ anion based on the single crystal structure data; trigonal prismatic bases are indicated as red dashed lines. (c) Structure of $[\eta^5\text{-C}_5\text{H}_5]\text{Ti}(\eta^4\text{-Sn}_8)^{3-}$ containing a corresponding $[Sn_8]$ tub coordinated to a $\text{Ti}(\text{C}_5\text{H}_5)$ moiety.¹⁸

A similar coordination has been observed before for a $[Sn_8]$ unit in $[\eta^5\text{-C}_5\text{H}_5]\text{Ti}(\eta^4\text{-Sn}_8)^{3-}$ (Fig. 1c), and for isoelectronic 17-atom stannides with the incorporated transition metals Ni²³ and Rh.¹⁴ Furthermore, $[Ge_8]$ tubs are found in the β -structure isomer of $[Co_2@Ge_{16}]^{4-}$,²⁰ however, in this anion the tubs are fused *via* a shared square plane instead of an interconnecting vertex atom. In all $[E_{17}]$ units the $[E_8]$ tubs are rotated with respect to each other by approximately 90°. Similar to the interatomic distances between the tetrel atom and the transition metal in the known $[TM_2@Sn_{17}]^{n-}$ entities, in **1a** the Co–Ge distances of the Co–Ge–Co strand are the shortest with 2.1924(9) Å (Co1) and 2.1998(9) Å (Co2). Other Ge–Co bond lengths range from 2.393(1) Å (Ge10–Co2) to 2.4618(9) Å (Ge3–Co1) and are slightly larger than those in $[Co@Ge_9]^{5-}$ (ref. 11) and also than the sum of the covalent radii of Ge and Co of 2.32 Å.²⁷ Ge–Ge distances in **1a** and the volumes of the cluster halves are in accordance with the recently reported Co-filled $[Ge_9]$ cage $[Co@Ge_9]^{5-}$ (Tables S2 and S4†).¹¹

To verify the structure of anion **1a** as the energetic minimum (Table S7†), we performed quantum chemical calculations on a PBE0/def2-TZVP level of theory by using a Conductor-like Screening Model (COSMO) with default parameters.^{28–32} For the bare $[Co_2@Ge_{17}]^{6-}$ anion the calculated structure shows S_4 symmetry with a linear arrangement of the Co–Ge–Co strand (Fig. S7†). However, when the non-sequestered potassium ions are included with fixed positions, an optimized structure with a Co–Ge–Co angle of 168.9° in $\{K_4[Co_2@Ge_{17}]\}^{2-}$ is found, which is in good accordance with the experimental data of 166.9° (Fig. 1b, Tables 1 and S4†). The effect of the counter ions on the structure, and especially the bending of the $TM\text{--}E\text{--}TM$ dumbbell was recently examined by Liu *et al.* for the $[Rh_2@Sn_{17}]^{6-}$ anion (Rh–Sn–Rh = 163.9°).¹⁴

Unfortunately, no Ti-containing product could be identified yet, thus leaving the mechanism of the formation of **1a** unclear. However, if just the precursor “ $K_5Co_{1.2}Ge_9$ ” is dissolved in liquid ammonia solely crystals containing the anion

Table 1 Comparison of angles $TM\text{--}E\text{--}TM$, interatomic distances and dihedral angles between the rectangular planes in the anions **1a** and **2a** and in other 17-atom filled cages reported in the literature. The initial structures used for the optimization are given in brackets

	$\angle (TM\text{--}E\text{--}TM)/^\circ$	Distance of central cage-connecting atom to atoms of the rectangular plane/Å	Dihedral angle between rectangular planes/ $^\circ$
1a $[Co_2@Ge_{17}]^{6-}$	166.9(1)	2.8983(9)–2.9763(9)	14.0
1a optimized ($[Co_2@Ge_{17}]^{6-}$)	180	2.804–2.812	0.0
1a optimized ($\{K_4[Co_2@Ge_{17}]\}^{2-}$)	168.9	2.8885–2.9150	11.7
2a $[Ni_2@Ge_{17}]^{4-}$	148.8(2)	2.484(5)–3.422(2)	0.0
2a optimized ($[Ni_2@Ge_{17}]^{4-}$)	146.5	2.7018–3.8457	14.7
$[Ni_2@Sn_{17}]^{4-}$ (ref. 23)	180	3.1177(3)–3.1364(3)	0.0
$[Rh_2@Sn_{17}]^{6-}$ (ref. 14)	163.9	2.9333(5)–3.2486(5)	13.9

$[Co@Ge_9]^{5-}$ are obtained.¹¹ The reaction mixture from which compound **1** was isolated also contained the ammoniate $[K(2.2.2\text{-crypt})]_3[Co@Ge_{10}]\cdot 9NH_3$ (**3**) with the $[Co@Ge_{10}]^{3-}$ anion (**3a**), which has been obtained before from ethylenediamine solutions.^{33,34} Further details on compound **3** are included in the ESI.†

The $[Ni_2@Ge_{17}]^{4-}$ anion (**2a**, Fig. 2a) in $[K(2.2.2\text{-crypt})]_4[Ni_2@Ge_{17}]\cdot en$ (**2**) is formed upon the reaction of K_4Ge_9 with $Ni(\text{cod})_2$ in *en*. Compound **2** crystallizes in the monoclinic space group $C2/c$. The structure of the anion **2a** deviates from that of anion **1a** because of a different position of the shared Ge vertex atom (Ge5). In **2a** it is located next to a twofold symmetry axis through the Ni atoms, thus causing a split into Ge5 and Ge5ⁱ (50% site occupation each). This feature was manifested in repeated single crystal structure determinations of crystals isolated from different experiments and persisted even

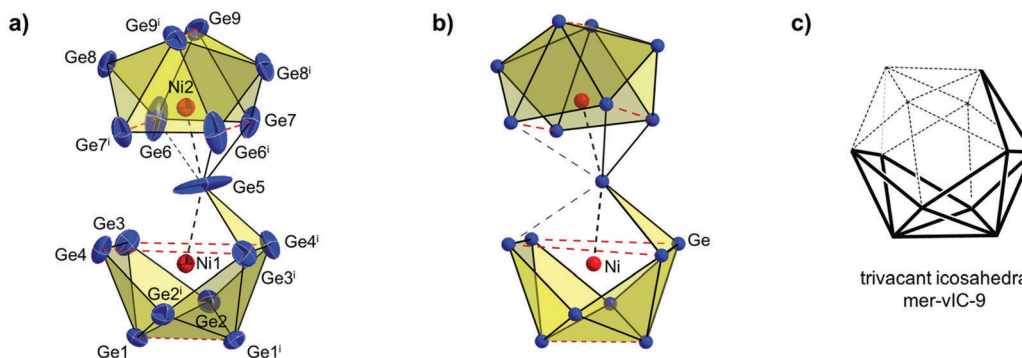


Fig. 2 (a) Structure of the $[\text{Ni}_2@Ge_{17}]^{4-}$ anion (**2a**) showing the trivalent icosahedron (Ge1–Ge5) as well as the coordinating $[Ge_8]$ tub (Ge6–Ge9); symmetry operation (i): $1 - x, y, 0.5 - z$; all ellipsoids are presented at a 50% probability level; (b) DFT-optimized structure of the $[\text{Ni}_2@Ge_{17}]^{4-}$ anion based on the single crystal structure data; trigonal prismatic bases are indicated as dashed red lines; (c) schematic representation of a trivalent icosahedron mer-vIC-9 resembling the orientation of the vertices Ge1–Ge5 in the anion **2a**. The vacant positions of the icosahedron are indicated by dashed lines.³⁵

upon varying the temperature during data collection (120 K and 150 K). The split position, which persists also when the structure is refined in the non-centrosymmetric space group Cc , leads to two different coordination polyhedra of the Ni atoms. Two sets of symmetry equivalent Ge6 to Ge9 atoms together with Ge5 form a polyhedron that derives from a tri-capped trigonal prismatic Ge9 cluster in which one capping atom Ge5 has longer distances to two of the Ge atoms [2.993 (1) Å (Ge5–Ge6) and 3.224(2) Å (Ge5–Ge7ⁱ)]. Furthermore, Ge5 completes the atoms Ge1 to Ge4 forming a $[Ge_8]$ tub (as observed in **1a**) to a trivalent icosahedron mer-vIC-9 corresponding to a *hypho*-icosahedron according to the nomenclature of Alvarez (Fig. 2c).³⁵

The single crystal data of **2** were used for the optimization of the structure of the anion. For the initial structure the split position was deleted, and Ge5 was set in an ideal center forming a linear Ni–Ge–Ni unit. However, in the optimized structure Ge5 is deflected from its initial position featuring a comparable orientation as observed in the experiment (Fig. 2b). The calculated interatomic distances Ge–Ge and Ni–Ge range from 2.567 Å to 2.938 Å and 2.205 Å to 2.461 Å, respectively, and are in accordance with those in the experimentally determined structure (Table S4†). The Ni–Ge5–Ni angle of 148.8° (calculated: 146.5°) deviates significantly from the linear Ni–Sn–Ni arrangement in the isoelectronic $[\text{Ni}_2@Sn_{17}]^{4-}$ anion (Table 1).²³ The volumes of the two cluster halves are almost identical and comparable to the volumes in anion **1a** (Table S4†). However, in the calculated structure the formerly coplanar surfaces Ge3–Ge4 and Ge6–Ge7 are tilted towards each other with a dihedral angle of 14.7°. To verify Ge as the element connecting the $[Ge_8]$ tubs, we also optimized the theoretical structure of $[\text{Ni}_3@Ge_{16}]^{4-}$ using the crystal structure data of **2a** and replacing Ge5 by Ni. The so obtained optimized structure shows no similarity to anion **2a**, thus indicating Ge (rather than Ni) at the respective position in the anion structure (Fig. S8†), which is in congruence with ESI MS measurements.

Anion **2a** was detected in the solid precipitate as well as in the filtered reaction solution in ESI MS measurements at m/z 1352.5 ($[\text{Ni}_2@Ge_{17}]^-$) and m/z 1767.8 ($[\text{K}([2.2.2] \text{crypt})][\text{Ni}_2@Ge_{17}]^-$), as shown in Fig. 3. Further signals at m/z 1410.5, m/z 1482.4, m/z 1825.7, and m/z 1899.6 were observed, which fit the masses of the anions $[\text{Ni}_3@Ge_{17}]^-$, $[\text{Ni}_3@Ge_{18}]^-$ (known species),³⁶ $[\text{K}([2.2.2] \text{crypt})][\text{Ni}_3@Ge_{17}]^-$, and $[\text{K}([2.2.2] \text{crypt})][\text{Ni}_3@Ge_{18}]^-$, respectively (Fig. S4†).

Although the appearance of various anions in the ESI MS experiment could result from the ionization process, it might also account for the presence of an equilibrium in the reaction solution. Furthermore, at m/z 843.1 a signal is observed which might originate from a reaction of a nine-atom cluster with a single Ge atom after its split from another $[Ge_9]$ cluster during

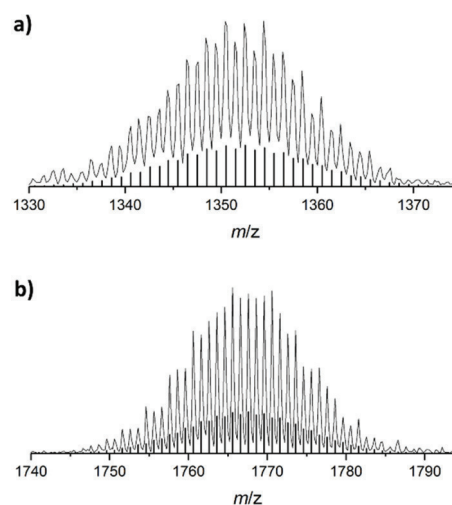


Fig. 3 Selected areas of ESI MS spectra of the anion **2a** (dimethylformamide, negative-ion mode, 2000 V, 300 °C); (a) molecule peak of $[\text{Ni}_2@Ge_{17}]^-$ (**2a**) at m/z 1352.5; (b) molecule peak of $[\text{K}([2.2.2] \text{crypt})][\text{Ni}_2@Ge_{17}]^-$ at m/z 1767.8. Calculated isotope patterns are presented as black bars.

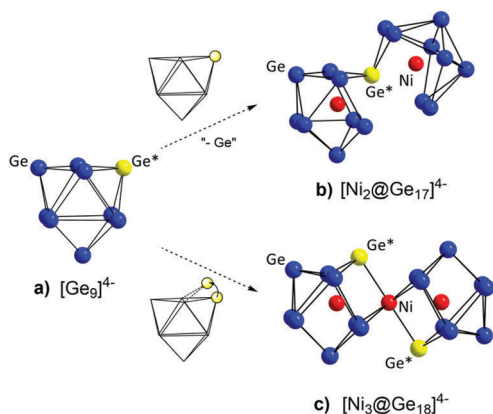


Fig. 4 Structural comparison of (a) $[\text{Ge}_9]^{4-}$,³⁷ (b) the novel cluster **2a** $[\text{Ni}_2@Ge_{17}]^{4-}$, and (c) the $[\text{Ni}_3@Ge_{18}]^{4-}$ anion³⁶ with respect to the position of one vertex atom Ge^* of the pseudo square plane in $[\text{Ge}_9]$.

the formation of $[\text{Ni}_2@Ge_{17}]^{4-}$ (Fig. 4 and S5†). It was described earlier, that a larger $\text{Ni}(\text{cod})_2$ excess leads to high yields of $[\text{Ni}_3@Ge_{18}]^{4-}$ ions with significant structural differences compared to the anion **2a** (Fig. 4 and S2†).³⁶ However, since the former anion was also detected in the precipitate of the reaction yielding **2a** by ESI MS measurements, the exact impact of the stoichiometry is not yet clear (Fig. S4†).

Within this work we describe the synthesis and characterization of two 17-atom Co- and Ni-filled Ge cluster dimers, thereby closing the gap between the 16- and 18-atom endohedral Ge clusters. Quantum chemical calculations confirm the experimentally determined structures as true local minima. Furthermore, the choice of the transition metal seems to be a decisive factor for the formation of either more spherical $[\text{TM}@Ge_n]^{n-}$ clusters as observed in **1a** or of a less symmetrical arrangement of Ge atoms as observed in **2a**, which is the basis for ongoing experiments in our laboratories.

Author contributions

Compounds **1** and **3** were synthesized by BJLW, compound **2** by CW, who also authored the manuscript. YS performed the quantum chemical calculations. WK refined the crystal structure data. TFF supervised the project.

Conflicts of interest

There are no conflicts to declare.

Acknowledgements

The authors thank the Deutsche Forschungsgemeinschaft (DFG, German Research Foundation, project number 245845833) within IRTG 2022 (ATUMS) for funding. CW thanks the Studienstiftung des Deutschen Volkes for granting a PhD scholarship.

Notes and references

- 1 T. F. Fässler and S. D. Hoffmann, *Angew. Chem., Int. Ed.*, 2004, **43**, 6242.
- 2 C. Liu and Z.-M. Sun, *Coord. Chem. Rev.*, 2019, **382**, 32.
- 3 R. J. Wilson, N. Lichtenberger, B. Weinert and S. Dehnen, *Chem. Rev.*, 2019, **119**, 8506.
- 4 W. Klein, A. Schier and T. F. Fässler, *Structure and Bonding*, Springer, Berlin, Heidelberg, 2021, DOI: 10.1007/430_2021_82.
- 5 Y. Wang, J. E. McGrady and Z.-M. Sun, *Acc. Chem. Res.*, 2021, **54**, 1506.
- 6 V. Hlukhyy, H. He, L. A. Jantke and T. F. Fässler, *Chem. – Eur. J.*, 2012, **18**, 12000.
- 7 H. He, W. Klein, L. A. Jantke and T. F. Fässler, *Z. Anorg. Allg. Chem.*, 2014, **640**, 2864.
- 8 V. Hlukhyy, S. Stegmaier, L. van Wüllen and T. F. Fässler, *Chem. – Eur. J.*, 2014, **20**, 12157.
- 9 M. Boyko, V. Hlukhyy, H. Jin, J. Dums and T. F. Fässler, *Z. Anorg. Allg. Chem.*, 2020, **646**, 1575.
- 10 Y. Wang, C. Zhang, X. Wang, J. Guo, Z.-M. Sun and H. Zhang, *ACS Catal.*, 2020, **10**, 7808.
- 11 B. J. Witzel, W. Klein, J. V. Dums, M. Boyko and T. F. Fässler, *Angew. Chem., Int. Ed.*, 2019, **58**, 12908.
- 12 J. M. Goicoechea and S. C. Sevov, *J. Am. Chem. Soc.*, 2006, **128**, 4155.
- 13 S. Scharfe, T. F. Fässler, S. Stegmaier, S. D. Hoffmann and K. Ruhland, *Chem. – Eur. J.*, 2008, **14**, 4479.
- 14 C. Liu, X. Jin, L. Li, J. Xu, J. E. McGrady and Z.-M. Sun, *Chem. Sci.*, 2019, **10**, 4394.
- 15 C.-C. Shu, H. W. Morgan, L. Qiao, J. E. McGrady and Z.-M. Sun, *Nat. Commun.*, 2020, **11**, 3477.
- 16 A. Spiekermann, S. D. Hoffmann, T. F. Fässler, I. Krossing and U. Preiss, *Angew. Chem., Int. Ed.*, 2007, **46**, 5310.
- 17 S. Scharfe, F. Kraus, S. Stegmaier, A. Schier and T. F. Fässler, *Angew. Chem., Int. Ed.*, 2011, **50**, 3630.
- 18 C. B. Benda, M. Waibel and T. F. Fässler, *Angew. Chem., Int. Ed.*, 2015, **54**, 522.
- 19 X. Jin, G. Espinoza-Quintero, B. Below, V. Arcisauskaite, J. M. Goicoechea and J. E. McGrady, *J. Organomet. Chem.*, 2015, **792**, 149.
- 20 C. Liu, I. A. Popov, L. J. Li, N. Li, A. I. Boldyrev and Z. M. Sun, *Chem. – Eur. J.*, 2018, **24**, 699.
- 21 H. W. Morgan, K.-S. Csizi, Y.-S. Huang, Z.-M. Sun and J. E. McGrady, *J. Phys. Chem. A*, 2021, **125**, 4578.
- 22 J. M. Goicoechea and S. C. Sevov, *J. Am. Chem. Soc.*, 2005, **127**, 7676.
- 23 E. N. Esenturk, J. C. Fettinger and B. W. Eichhorn, *J. Am. Chem. Soc.*, 2006, **128**, 12.
- 24 B. Kesanli, J. E. Halsig, P. Zavalij, J. C. Fettinger, Y.-F. Lam and B. W. Eichhorn, *J. Am. Chem. Soc.*, 2007, **129**, 4567.
- 25 C. Zhang, H. W. Morgan, Z.-C. Wang, C. Liu, Z.-M. Sun and J. E. McGrady, *Dalton Trans.*, 2019, **48**, 15888.
- 26 M. M. Gillett-Kunnath, J. I. Paik, S. M. Jensen, J. D. Taylor and S. C. Sevov, *Inorg. Chem.*, 2011, **50**, 116955.

- 27 P. Pyykkö and M. Atsumi, *Chem. – Eur. J.*, 2009, **15**, 186.
- 28 C. Adamo and V. Barone, *J. Chem. Phys.*, 1999, **110**, 6158.
- 29 J. P. Perdew, M. Ernzerhof and K. Burke, *J. Chem. Phys.*, 1996, **105**, 9982.
- 30 F. Weigend and R. Ahlrichs, *Phys. Chem. Chem. Phys.*, 2005, **7**, 3297.
- 31 F. Weigend, *Phys. Chem. Chem. Phys.*, 2006, **8**, 1057.
- 32 A. Klamt and G. Schüürmann, *J. Chem. Soc., Perkin Trans. 2*, 1993, 799.
- 33 J. Q. Wang, S. Stegmaier and T. F. Fässler, *Angew. Chem., Int. Ed.*, 2009, **48**, 1998.
- 34 C. Liu, L. J. Li, I. A. Popov, R. J. Wilson, C. Q. Xu, J. Li, A. I. Boldyrev and Z. M. Sun, *Chin. J. Chem.*, 2018, **36**, 1165.
- 35 A. Ruiz-Martínez, D. Casanova and S. Alvarez, *Dalton Trans.*, 2008, 2583.
- 36 J. M. Goicoechea and S. C. Sevov, *Angew. Chem., Int. Ed.*, 2005, **44**, 4026.
- 37 S. Ponou and T. F. Fässler, *Z. Anorg. Allg. Chem.*, 2007, **633**, 393.

Filled Trivacant Icosahedra as Building Fragments in 17-atomic Endohedral Germanides $[TM_2@Ge_{17}]^{n-}$ ($TM = Co, Ni$)

Christoph Wallach, Yasmin Selic, Dr. Benedikt J. L. Witzel, Dr. Wilhelm Klein, Prof. Dr. Thomas F. Fässler

e-mail: thomas.faessler@lrz.tum.de

Supporting information

1. Experimental details	1
2. Crystallographic details	3
3. ESI MS sample preparation and spectra of 2a	11
4. EDX analysis	13
5. Computational details.....	14
6. References	23

1. Experimental details

General

All experiments were carried out under oxygen-free, dry conditions using standard glove box and Schlenk line techniques. Glassware was dried prior to use by heating it *in vacuo*. The solid-state phase K_4Ge_9 is prepared by fusion of stoichiometric amounts of the elements in a stainless-steel autoclave at 650 °C. The phase of nominal composition " $K_5Co_{1.2}Ge_9$ "¹ and the titanyl complex $[Cp_2Ti(NH_3)_2]Cl(NH_3)_2$ are prepared according to the literature. $Ni(cod)_2$ (*Sigma Aldrich*, stored at -30 °C under Ar) is used without further purification. Liquid ammonia was dried over sodium metal, and [2.2.2]crypt (*Merck*) was dried overnight applying dynamic vacuum before usage. Ethylenediamine (en) was dried over CaH_2 at 120 °C for two days prior to distillation, toluene was obtained from an MBraun Grubbs apparatus and stored over molecular sieve.

ESI MS analysis

ESI MS analyses were performed on a Bruker Daltonic HCT mass spectrometer (dry gas temperature: 300 °C; injection speed: 300 μ L/h), and the data evaluation was carried out using the Bruker Compass Data Analysis 4.0 SP 5 program (Bruker). Spectra were plotted using OriginPro2016G (Origin Lab) and Excel 2016 (Microsoft).

EDX analysis

EDX measurements were performed using a Hitachi TM-1000 tabletop spectroscopy. Data evaluation was performed using the SWIFT-ED-TM program (Oxford Instruments).

Single crystal structure determination

Air- and moisture-sensitive crystals of **1** and **3** were transferred from the mother liquor into cooled perfluoroalkyl ether oil and isolated from polycrystalline material under a cooled stream of nitrogen.³ Crystals of **2** were selected under a microscope in the glove box. For diffraction data collection, the single crystals were mounted on a glass capillary and positioned in a 150 K cold N_2 gas stream. Data collection was performed with a STOE StadiVari diffractometer (Mo $K\alpha$ radiation) equipped with a DECTRIS PILATUS 300K detector. Structures were solved by Direct Methods (SHELXS-97) and refined by full-matrix least-squares calculations against F^2 (SHELXL-2014 or SHELXL-2018).⁴ The hydrogen atoms were positioned in calculated positions and refined using a riding model. Unless stated otherwise, all non-hydrogen atoms were treated with anisotropic displacement parameters. Cluster volumes were calculated using VESTA.⁵ Further details of the crystal structure investigations may be obtained from the joint CCDC/FIZ Karlsruhe online deposition service: <https://www.ccdc.cam.ac.uk/structures/?> by quoting the depository numbers CCDC-2081217 (**1**), CCDC-2081218 (**2**), and CCDC-2081219 (**3**). The crystallographic data for compounds **1** - **3** are summarized in Table S1.

Quantum chemical calculations

Quantum chemical calculations were performed with the TURBOMOLE program package,⁶ using the PBE0 hybrid density functional method^{7, 8} and polarized triple- ζ -valence Karlsruhe basis sets (DFT-PBE0/TZVP with def2-TZVP on Ge and Ni/Co).⁹ Multipole-accelerated resolution-of-the-identity technique was used to speed up the calculations.¹⁰⁻¹² $m4$ integration grid was applied for the numerical integration of the exchange-correlation functional. As initial structures the data of the crystal structure determinations of compounds **1a** and **2a** were used. The structures were optimized without any symmetry constraints. A COSMO solvent field was applied to counter the anionic charge.¹³

Synthesis of compounds 1 – 3

[K([2.2.2]crypt)]₂K₄[Co₂@Ge₁₇] · 15 NH₃ (1)

"K₅Co_{1.2}Ge₉" (100 mg, 0.113 mmol, 1 equiv.), [Cp₂Ti(NH₃)₂]Cl(NH₃) (28 mg, 0.113 mmol, 1 equiv.) and [2.2.2]crypt (76.8 mg, 0.204 mmol, 1.8 equiv.) were weighed into a Schlenk tube. Subsequently liquid ammonia (5 mL) was condensed onto the solid mixture leading to the formation of a deep red solution. A black crystal suitable for single crystal X-ray diffraction could be isolated after 6 months.

[K([2.2.2]crypt)]₄[Ni₂@Ge₁₇] · en (2)

The synthesis generally followed the method applied by Sevov and co-workers for the synthesis of the cluster unit [Ni₃@Ge₁₈]⁴⁻.¹⁴

K₄Ge₉ (121.6 mg, 150.1 μ mol, 1 equiv.), Ni(cod)₂ (90.8 mg, 330.1 μ mol 2.2 equiv.) and [2.2.2]crypt (169.4 mg, 450.0 μ mol, 3 equiv.) were weighted into a Schlenk tube, and en (2.5 mL) was added via a syringe. After stirring the reaction for 2 h, the dark suspension was filtered over a glass filter-packed pipette, and the resulting filtrate was carefully layered with toluene (2 mL). After two month of crystallization time, small amounts of brown, block-shaped single crystals were collected (crystalline yield approximately 5 % based on the [Ge₉] precursor).

ESI MS: m/z 1352.5 for [Ni₂@Ge₁₇]⁻ and m/z 1767.8 for [K([2.2.2]crypt)][Ni₂@Ge₁₇]⁻. **EDX:** K, Ni, Ge (qualitative).

[K(2.2.2-crypt)]₃[Co@Ge₁₀] · 9 NH₃ (3)

A black crystal of **3** suitable for single crystal X-ray diffraction was isolated after 5 months from the same reaction solution from which [K([2.2.2]crypt)]₂K₄[Co₂@Ge₁₇] · 15 NH₃ (**1**) was isolated one month later. Since crystals can only be isolated from liquid ammonia one after another it is not entirely clear if the 10-atom cluster formed simultaneously with anion **1a** or if **1a** formed due to opening the reaction flask.

2. Crystallographic details

Table S1. Crystallographic data of compounds **1** – **3**.

Compound	1	2	3
formula	$\text{K}_6\text{N}_{19}\text{O}_{12}\text{C}_{36}\text{H}_{117}\text{Co}_2\text{Ge}_{17}$	$\text{K}_4\text{N}_{10}\text{O}_{24}\text{C}_{74}\text{H}_{152}\text{Ni}_2\text{Ge}_{17}$	$\text{K}_3\text{N}_{15}\text{O}_{18}\text{C}_{54}\text{H}_{134}\text{CoGe}_{10}$
fw / g·mol ⁻¹	2594.97	3073.9	2184.89
space group	<i>P</i> 2 ₁ / <i>c</i>	<i>C</i> 2/ <i>c</i>	<i>P</i> $\bar{1}$
<i>a</i> / Å	19.6865(6)	27.8606(5)	12.414(2)
<i>b</i> / Å	32.1696(10)	16.5164(2)	16.140(2)
<i>c</i> / Å	15.3982(4)	27.9518(4)	25.212(3)
α / deg	90	90	72.851(9)
β / deg	110.634(2)	117.468(1)	89.887(9)
γ / deg	90	90	70.505(9)
<i>V</i> / Å ³	9126.2(5)	11412.2(3)	4524.1(9)
<i>Z</i>	4	4	2
<i>T</i> / K	150	150(2)	150(2)
λ / Å	0.71073	0.71073	0.71073
ρ_{calcd} / g·cm ⁻³	1.889	1.789	1.604
μ / mm ⁻¹	6.181	4.932	3.649
collected reflections	277912	155284	15796
indep. reflections	17914	11191	13148
<i>R</i> _{int} / <i>R</i> _σ	0.1763/0.0555	0.0487/0.0183	0.0965/0.1500
parameters / restraints	834/6	614/19	910/104
<i>R</i> ₁ [<i>I</i> > 2 σ(<i>I</i>) / all data]	0.0472/0.0683	0.0714/0.0873	0.0757/ 0.1618
<i>wR</i> ₂ [<i>I</i> > 2 σ(<i>I</i>) / all data]	0.1053/0.1142	0.1525/0.1648	0.1682/0.2110
goodness of fit	1.028	1.071	0.902
max./min. diff. el. density / e·Å ⁻³	1.553/-1.455	4.568/-3.875	1.280/-1.651
CCDC	2081217	2081218	2081219

[K([2.2.2]crypt)]₂K₄[Co₂@Ge₁₇] · 15 NH₃ (1)**Table S2.** Selected interatomic distances and angles in anion **1a**.

Atoms	distance / Å	atoms	distance / Å
Ge1-Ge2	2.6374(9)	Ge1-Co1	2.4317(9)
Ge1-Ge3	2.8083(9)	Ge2-Co1	2.4421(9)
Ge1-Ge4	2.6244(9)	Ge3-Co1	2.4618(9)
Ge1-Ge5	2.9199(9)	Ge4-Co1	2.4484(9)
Ge1-Ge6	2.8851(9)	Ge5-Co1	2.4021(10)
Ge2-Ge3	2.6682(9)	Ge6-Co1	2.3940(9)
Ge2-Ge6	2.7221(9)	Ge7-Co1	2.4167(10)
Ge2-Ge7	2.6768(9)	Ge8-Co1	2.3934(9)
Ge3-Ge4	2.6963(10)	Ge9-Co1	2.1924(9)
Ge3-Ge7	2.7359(9)	Ge9-Co2	2.1998(9)
Ge3-Ge8	2.7664(10)	Ge10-Co2	2.3927(10)
Ge4-Ge5	2.7229(9)	Ge11-Co2	2.4041(9)
Ge4-Ge8	2.6719(10)	Ge12-Co2	2.4184(10)
Ge5-Ge6	2.6099(9)	Ge13-Co2	2.3932(9)
Ge5-Ge9	2.9316(9)	Ge14-Co2	2.4528(10)
Ge6-Ge9	2.8983(9)	Ge15-Co2	2.4481(9)
Ge7-Ge8	2.6264(9)	Ge16-Co2	2.4412(9)
Ge7-Ge9	2.9589(9)	Ge17-Co2	2.4385(10)
Ge8-Ge9	2.9763(9)		
Ge9-Ge10	2.9301(9)		
Ge9-Ge11	2.9376(9)		
Ge9-Ge12	2.9303(9)		
Ge9-Ge13	2.9056(9)		
Ge10-Ge11	2.6510(9)		
Ge10-Ge14	2.7027(9)		
Ge10-Ge15	2.7903(9)		
Ge11-Ge17	2.6637(9)		
Ge12-Ge13	2.6061(9)	atoms	angle / deg
Ge12-Ge17	2.6638(9)	Co1-Ge9-Co2	166.9(1)
Ge13-Ge14	2.7351(10)		
Ge13-Ge16	2.8129(9)		
Ge14-Ge15	2.6567(10)		
Ge14-Ge16	2.6609(10)		
Ge15-Ge16	2.7542(9)		
Ge15-Ge17	2.7170(10)		
Ge16-Ge17	2.6751(9)		

[K([2.2.2]crypt)]₄[Ni₂@Ge₁₇] · en (2)

Atoms Ge5, C38 and N6 were refined using an ISOR (0.01) command; the distance between C38 and N6 was restrained with a DFIX (1.5) command.

The high maximum and minimum difference electron density is mainly located in close distance around Ge5 indicating a more complex disorder than described by the present refinement. However, a refinement with the Ge5 atom at more than the given split positions was not successful. A refinement with other elements than Ge (e.g. Ni) on position Ge5 resulted in worse reliability factors.

Table S3. Selected interatomic distances and angles in **2a**. Symmetry operation (i): 1-x, y, 0.5-z.

atoms	distance / Å	atoms	distance / Å
Ge1-Ge2	2.683(1)	Ge1-Ni1	2.433(1)
Ge1-Ge2 ⁱ	2.676(1)	Ge2-Ni1	2.462(1)
Ge1-Ge3	2.869(1)	Ge3-Ni1	2.411(1)
Ge1-Ge4	2.825(1)	Ge4-Ni1	2.422(1)
Ge1-Ge1 ⁱ	2.713 (2)	Ge5-Ni1	2.236(3)
Ge1-Ge2 ⁱ	2.676(1)	Ge5-Ni2	2.144(3)
Ge1 ⁱ -Ge2	2.676(1)	Ge6-Ni2	2.390(1)
Ge1 ⁱ -Ge2 ⁱ	2.683(1)	Ge7-Ni2	2.390(1)
Ge1 ⁱ -Ge3 ⁱ	2.869(1)	Ge8-Ni2	2.435(1)
Ge1 ⁱ -Ge4 ⁱ	2.825(1)	Ge9-Ni2	2.394(1)
Ge2-Ge3	2.667(1)	Ni1-Ni2	4.215(2)
Ge2-Ge4 ⁱ	2.725(1)		
Ge2 ⁱ -Ge4	2.725(1)		
Ge2 ⁱ -Ge3 ⁱ	2.667(1)		
Ge3-Ge4	2.622(1)		
Ge3-Ge5 ⁱ	2.735(5)		
Ge3 ⁱ -Ge5	2.735(5)		
Ge3 ⁱ -Ge4 ⁱ	2.622(1)		
Ge4-Ge5 ⁱ	2.501(4)		
Ge4 ⁱ -Ge5	2.501(4)		
Ge5-Ge7	2.415(4)		
Ge5-Ge6 ⁱ	2.799(6)		
Ge5 ⁱ -Ge6	2.903(6)		
Ge5 ⁱ -Ge7 ⁱ	2.411(4)		
Ge6-Ge7	2.589(1)		
Ge6-Ge8	2.657(1)		
Ge6-Ge9	2.896(1)		
Ge6 ⁱ -Ge7 ⁱ	2.589(1)		
Ge6 ⁱ -Ge8 ⁱ	2.657(1)		
Ge6 ⁱ -Ge9 ⁱ	2.896(1)		
Ge7-Ge8 ⁱ	2.706(2)		
Ge7 ⁱ -Ge8	2.706(2)		
Ge7 ⁱ -Ge9 ⁱ	2.833(2)		
Ge8-Ge9	2.696(2)		
Ge8-Ge9 ⁱ	2.681(1)		
Ge8 ⁱ -Ge9	2.681(1)		
Ge8 ⁱ -Ge9 ⁱ	2.696(2)		
Ge9-Ge9 ⁱ	2.704(2)		

atoms	angle / deg
Ni1-Ge5-Ni2	148.4(1)
Ni1-Ge5 ⁱ -Ni2	148.4(1)

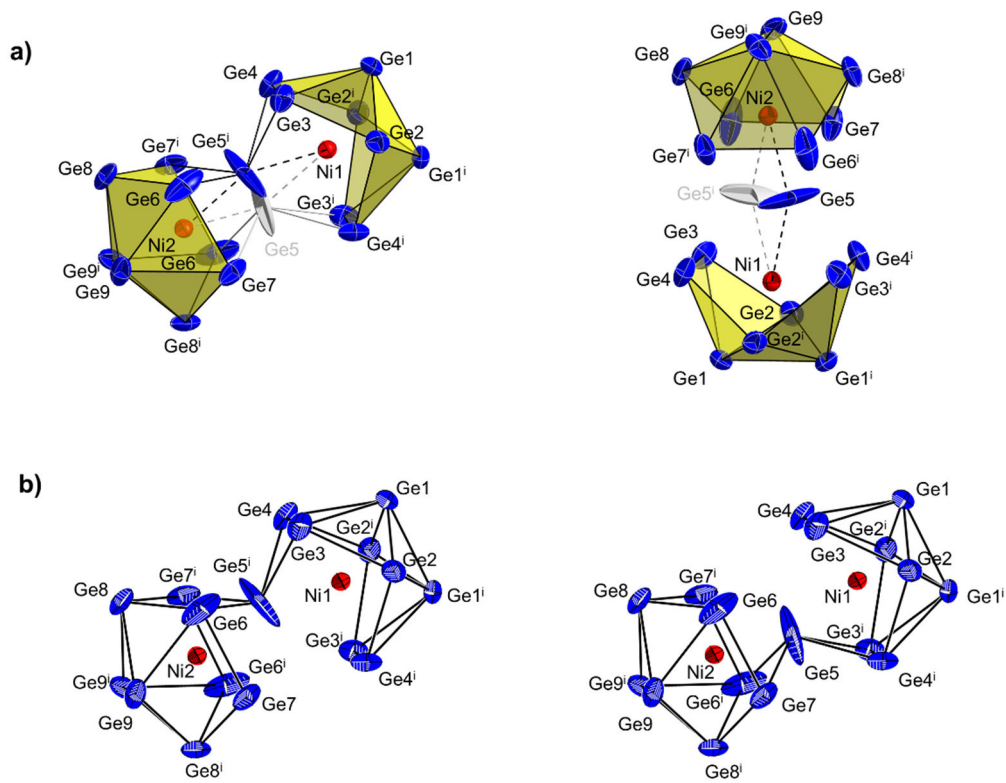


Figure S1. Different views of anion **2a**. a) Emphasis on the [Ge₈] tubs forming the cluster and representation of the split position of Ge5 (site occupation factor of 0.5 each). b) Structure of anion **2a** emphasizing the single split positions. All atoms are represented with anisotropic displacement parameters at a 50 % probability level. Symmetry operation (i): 1-x, y, 0.5-z.

The novel cluster **2a** and the reported anion $[\text{Ni}_3@\text{Ge}_{18}]^{4-}$ ¹⁴ show building principles similar to a C_{4v} symmetric $[\text{Ge}_9]$ cluster (Figure S2).¹⁵ However, the vertex atoms are dislocated from their original positions, which is caused by the incorporated Ni atoms resulting in elongated Ge-Ge distances. The longest distance between Ge atoms in the bare $[\text{Ge}_9]$ cage (characterized from solid state) can be found between $\text{Ge}5^{\text{A}}-\text{Ge}6^{\text{A}}$ with 2.88 Å¹⁵ which is significantly shorter than the distances $\text{Ge}6^{\text{i}}-\text{Ge}7$ (3.89 Å) in $[\text{Ni}_2@\text{Ge}_{17}]^{4-}$ or $\text{Ge}5^{\text{B}}-\text{Ge}6^{\text{B}}$ (3.66 Å) in $[\text{Ni}_3@\text{Ge}_{18}]^{4-}$.¹⁵ Figure S2 gives a comparison of the different structural motifs. The most prominent difference between $[\text{Ge}_9]^{4-}$, **2a** and $[\text{Ni}_3@\text{Ge}_{18}]^{4-}$ is that in the latter ion one Ge atom (drawn in yellow) is tilted out of the former pseudo square plane. This observation can be evaluated by measuring the dihedral angles of the plane which are $\omega_{\text{Ge}1\text{A}-\text{Ge}2\text{A}-\text{Ge}3\text{A}-\text{Ge}4\text{A}} = 1.8^\circ$ ($[\text{Ge}_9]^{4-}$); $\omega_{\text{Ge}5^{\text{i}}-\text{Ge}7^{\text{i}}-\text{Ge}6-\text{Ge}8} = 1.7^\circ$ (**2a**); $\omega_{\text{Ge}1\text{B}-\text{Ge}2\text{B}-\text{Ge}3\text{B}-\text{Ge}4\text{B}} = 44.0^\circ$ ($[\text{Ni}_3@\text{Ge}_{18}]^{4-}$).

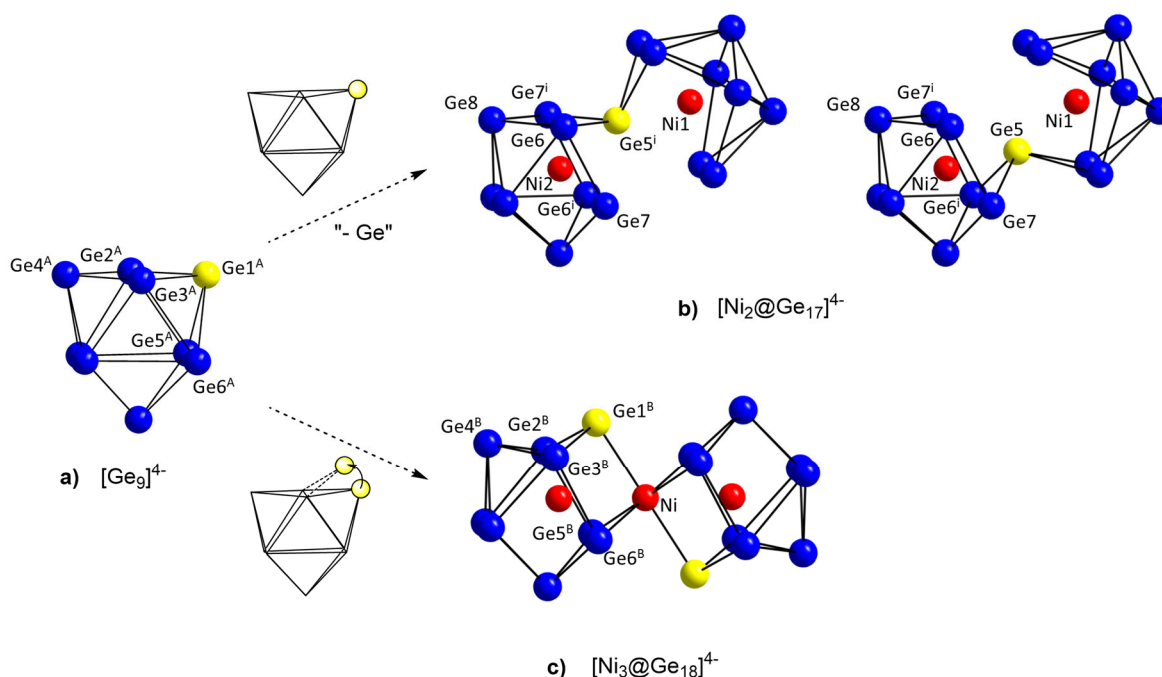


Figure S2. Representation of structural similarities and differences between a) $[\text{Ge}_9]^{4-}$,^[15] b) the novel cluster **2a** ($[\text{Ni}_2@\text{Ge}_{17}]^{4-}$) and c) the known anion $[\text{Ni}_3@\text{Ge}_{18}]^{4-}$ ^[14] with respect to the position of one vertex atom (with yellow color) of the pseudo square plane in $[\text{Ge}_9]$. Symmetry operation (i): $1-x, y, 0.5-z$.

Table S4. Summary of interatomic distances, angles and cluster volumes in the anions **1a** and **2a** in comparison to literature data.

	$d(E-E) / \text{\AA}$	$d(TM-E) / \text{\AA}$	$\sphericalangle (TM-E-TM) / \text{deg}$	dihedral angle of rectangular planes / deg	volume / \AA^3
1a [Co ₂ @Ge ₁₇] ⁶⁻	2.606(1) – 2.938(1)	2.192(1) – 2.462(1)	166.9(1)	14.0	26.68/ 26.82
1a optimized (K ₄ [Co ₂ @Ge ₁₇] ²⁻)	2.631 – 2.938	2.184 – 2.446	168.9	11.7	26.35/ 26.34
2a [Ni ₂ @Ge ₁₇] ⁴⁻	2.415(4) – 2.903(6)	2.144(3) – 2.462(1)	148.4(1)	0.0	26.71/ 25.86
2a optimized ([Ni ₂ @Ge ₁₇] ⁴⁻)	2.567 – 2.938	2.205 – 2.461	146.5	14.7	26.75/ 26.69
[Co@Ge ₉] ^{5- 1}	2.683 – 2.811	2.331 – 2.374	–	–	26.40
[Ni@Ge ₉] ^{3- 16}	2.558 – 2.876	2.254 – 2.410	–	–	25.17/ 25.67
[Ni ₂ @Sn ₁₇] ^{4- 17}	2.971 – 3.209	2.382 – 2.740	180	0.0	–
[Rh ₂ @Sn ₁₇] ^{6- 18}	2.933 – 3.247	2.498 – 2.761	163.9	13.9	–

[K(2.2.2-crypt)]₃[Co@Ge₁₀] · 9 NH₃ (**3**)

Compound **3**, [K(2.2.2-crypt)]₃[Co@Ge₁₀] · 9 NH₃, was isolated from the same reaction solution anion **1a** has been obtained from before. The anion features the pentagonal prismatic ion [Co@Ge₁₀]³⁻ (**3a**) which has been obtained previously from reactions in en solutions.^{19, 20}

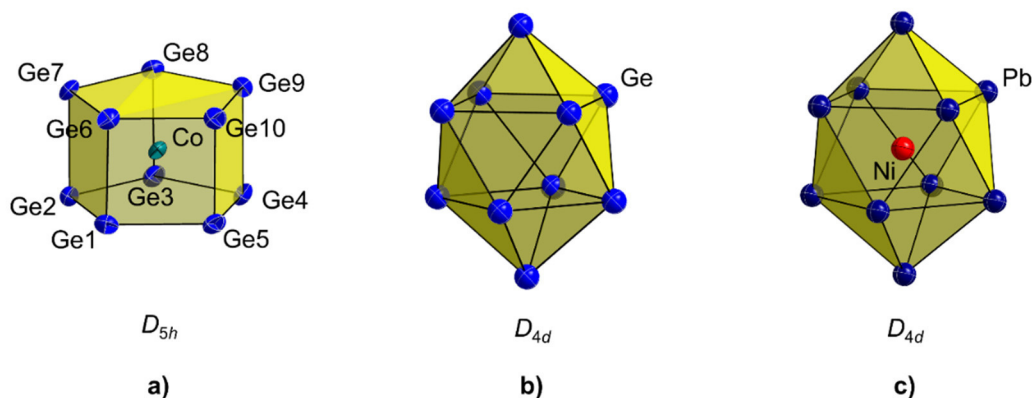


Figure S1. Structure of anion **3a** featuring D_{5h} symmetry. All ellipsoids are presented at a 50 % probability level. b) Structure of the anion [Ge₁₀]²⁻ with D_{4d} symmetry.^[21,22] c) Structure of the anion [Ni@Pb₁₀]²⁻ with D_{4d} symmetry.^[23]

The formation of a pentagonal prism for the Co-filled anion is rather unexpected, as both the empty [Ge₁₀]²⁻^{21, 22} as well as the corresponding Ni-filled Pb²³ cluster feature deltahedral *closo*-clusters, i.e. doubly capped square antiprisms with D_{4d} symmetry (Figures S3b and c). Theoretical considerations revealed that a size effect has to be taken into account as a possible reason for the formation of the pentagonal prism around the larger Co⁻ anion as compared to the smaller Ni⁰ atoms or even unoccupied voids.²⁴ As the h/e ratio (h : height of prism; e : lengths of edges of the pentagonal surfaces) is close to 1, a polyhedron with D_{5h} symmetry results.

Table S5. Summary of interatomic distances in **3a**, the previously published [Co@Ge₁₀]³⁻ anions^[21] and the empty anion [Ge₁₀]²⁻.^[19,20]

	$d(\text{Ge}-\text{Ge})_{\text{edge}} /$ Å	$d(\text{Ge}-\text{Ge})_{\text{height}} /$ Å	$d(\text{Co}-\text{Ge}) /$ Å	volume / Å ³	$h_{\text{max}}/e_{\text{min}}$	symmetry
3a [Co@Ge ₁₀] ³⁻	2.501(2) – 2.538(2)	2.583(2) – 2.621(2)	2.494(2) – 2.516(2)	28.58	1.05	D_{5h}
[Co@Ge ₁₀] ³⁻ ¹⁹	2.502 – 2.527	2.600 – 2.622	2.479 – 2.525	28.55	1.05	D_{5h}
[Co@Ge ₁₀] ³⁻ ²⁰	2.508 – 2.530	2.596 – 2.609	2.488 – 2.514	28.45	1.04	D_{5h}
[Ge ₁₀] ²⁻ ²¹	2.543 – 2.822	–	–	26.95	–	D_{4d}

Table S6. Selected interatomic distances in **3a**.

atoms	distance / Å	atoms	distance / Å
Ge1-Ge2	2.511(2)	Ge1-Co	2.511(2)
Ge1-Ge5	2.538(2)	Ge2-Co	2.503(2)
Ge1-Ge6	2.593(2)	Ge3-Co	2.494(2)
Ge2-Ge3	2.536(2)	Ge4-Co	2.501(2)
Ge2-Ge7	2.605(2)	Ge5-Co	2.512(2)
Ge3-Ge4	2.518(2)	Ge6-Co	2.509(2)
Ge3-Ge8	2.611(2)	Ge7-Co	2.516(2)
Ge4-Ge5	2.523(2)	Ge8-Co	2.512(2)
Ge4-Ge9	2.621(2)	Ge9-Co	2.507(2)
Ge5-Ge10	2.583(2)	Ge10-Co	2.512(2)
Ge6-Ge7	2.513(2)		
Ge6-Ge10	2.516(2)		
Ge7-Ge8	2.520(2)		
Ge8-Ge9	2.523(2)		
Ge9-Ge10	2.501(2)		

3. ESI MS sample preparation and spectra of 2a

ESI MS spectra of the reaction mixture were performed from (A) the solid precipitate and (B) the reaction solution after two months (Figure S4).

A: The supernatant solution was removed using a syringe, and the remaining dark precipitate was subsequently dissolved in dmf, filtered through a syringe filter and injected into the ESI MS.

B: An aliquot of the reaction solution (en) was diluted with dmf, filtered through a syringe filter and injected into the ESI MS.

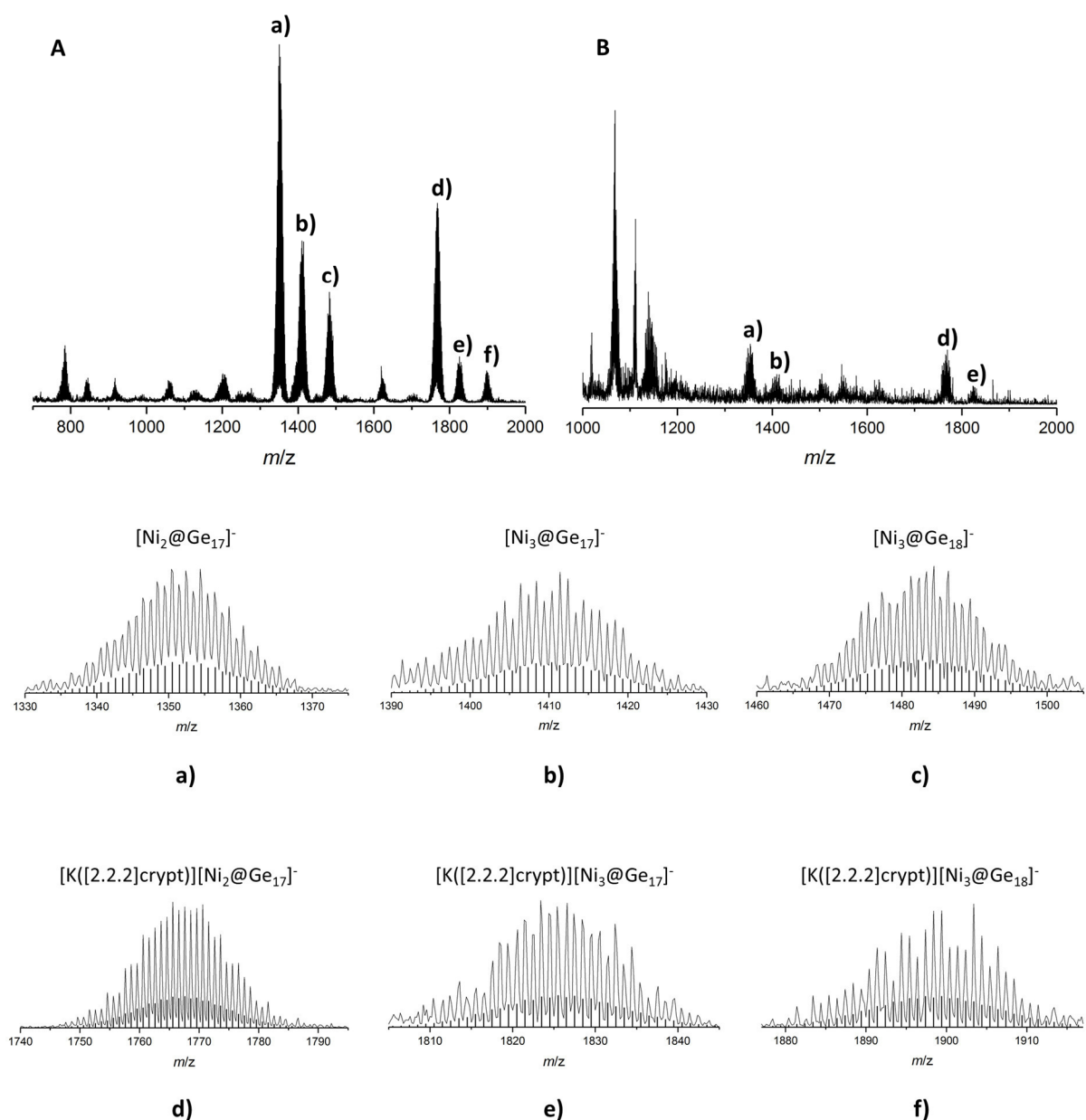


Figure S2. A: ESI MS spectrum of the precipitate of the reaction of K_4Ge_9 , $\text{Ni}(\text{cod})_2$ and $[2.2.2]\text{crypt}$ recorded in dmf (negative ion mode, 2000V, 300 °C); B: ESI MS spectrum of the reaction solution of the reaction of K_4Ge_9 , $\text{Ni}(\text{cod})_2$ and $[2.2.2]\text{crypt}$ recorded in dmf (negative ion mode, 2000V, 300 °C). The following molecule peaks are monitored: a) $[\text{Ni}_2@\text{Ge}_{17}]^-$ (m/z 1352.5), b) $[\text{Ni}_3@\text{Ge}_{17}]^-$ (m/z 1410.3), c) $[\text{Ni}_3@\text{Ge}_{18}]^-$ (m/z 1482.4), d) $[\text{K}([2.2.2]\text{crypt})][\text{Ni}_2@\text{Ge}_{17}]^-$ (m/z 1767.8), e) $[\text{K}([2.2.2]\text{crypt})][\text{Ni}_3@\text{Ge}_{17}]^-$ (m/z 1825.5), and f) $[\text{K}([2.2.2]\text{crypt})][\text{Ni}_3@\text{Ge}_{18}]^-$ (m/z 1899.4). Calculated isotope patterns are presented as black bars.

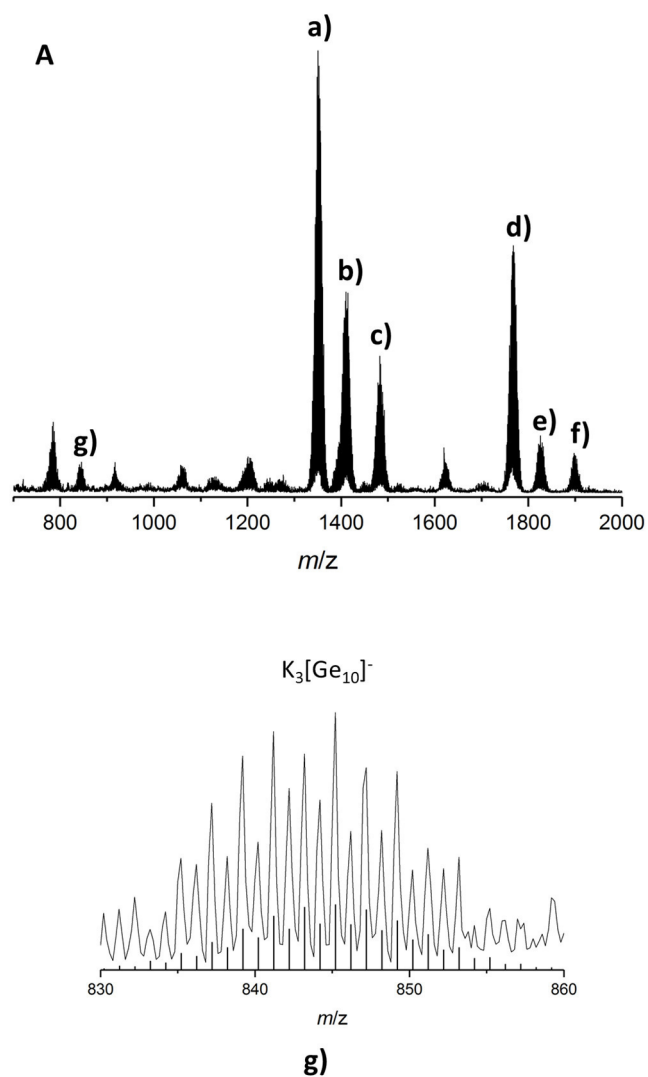


Figure S5. A: ESI MS spectrum of the precipitate of the reaction of K_4Ge_9 , $Ni(cod)_2$ and [2.2.2]crypt recorded in dmf (negative ion mode, 2000V, 300 °C); a) - f) see Figure S4; g) $K_3[Ge_{10}]^-$ (m/z 843.1). Calculated isotope pattern is presented as black bars.

4. EDX analysis

Spectrum details

Project: CW-112.ipj
Spectrum name: Spectrum4

Acquisition conditions

Acquisition time (s) : 200.0
Accelerating voltage (kV) : 15.0

Process time : 4

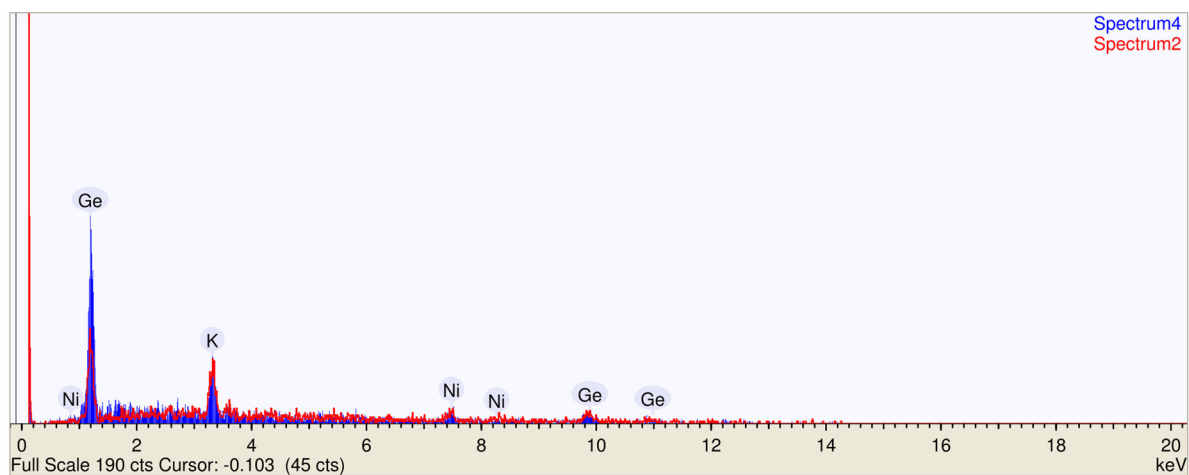


Figure S6. Qualitative EDX spectra of compound **2**. The red and blue lines resemble two point measurements at different crystal sites.

Single crystals of **2** were isolated from a heterogeneous/amorphous precipitate, thus hampering a quantitative EDX analysis. For compounds **1** and **3**, which were obtained from reactions in liquid ammonia, EDX measurements were not possible.

5. Computational details

Table S7. Summarized results of the structure optimization based on the single crystal diffraction data.

initial structure	optimized symmetry	total molecular energy / eV	HOMO-LUMO gap / eV	TM-Ge-TM (optimized) / deg	TM-Ge-TM (experimental) / deg	MO number	electrons (total)	lowest vibration frequency / cm^{-1}
$[\text{Co}_2@\text{Ge}_{17}]^{6-}$	s4	-1035966.5	2.95770	180.00	166.79	906	604	15.60
$\text{K}_4[\text{Co}_2@\text{Ge}_{17}]^{2-}$	d2d	-1101243.8	2.83937	168.86	166.79	1038	676	21.00
$[\text{Ni}_2@\text{Ge}_{17}]^{4-}$	c1	-1042795.9	2.85455	146.51	148.34	906	604	19.99

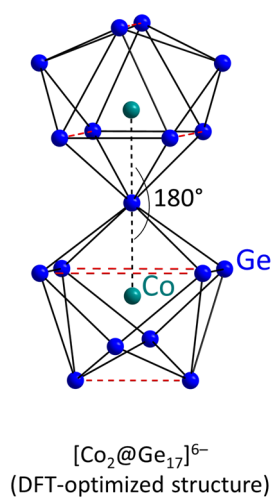


Figure S7. DFT-optimized structure of the anion $[\text{Co}_2@\text{Ge}_{17}]^{6-}$ with a linear arrangement of the strand Co-Ge-Co caused by the neglect of K^+ cations.

Additional DFT calculations were carried out to investigate the character of the element connecting the $[\text{Ge}_8]$ tubs in **2a**. Based on the results of the single crystal structure data of anion **2a**, the atom Ge5 was substituted by Ni, and the fourfold negative charge was kept. The structure refinement revealed a fused structure not congruent to the initial crystal structure data corroborating the interconnecting atom to be Ge (rather than Ni).

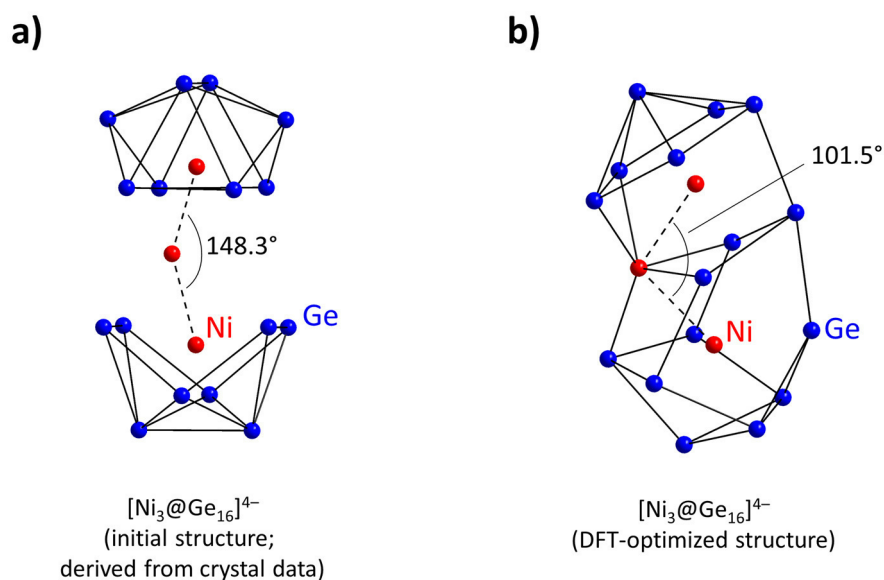


Figure S8. DFT-optimization for the theoretical anion $[\text{Ni}_3@\text{Ge}_{16}]^{4-}$. a) Initial structure with substitution of the cage-connecting atom Ge5 by Ni (derived from the single crystal structure data of anion **2a**); b) optimized structure of the theoretical anion $[\text{Ni}_3@\text{Ge}_{16}]^{4-}$.

Atomic coordinates and vibrational data

[Co₂@Ge₁₇]⁶⁻

atomic coordinates

Ge	1.3560329	-0.0065502	4.1144867
Ge	-0.0033006	2.1565276	3.2407876
Ge	-1.3560329	0.0065502	4.1144867
Ge	0.0033006	-2.1565276	3.2407876
Ge	1.9151593	-1.3239414	1.5770737
Ge	1.9311641	1.2776155	1.5819224
Ge	-1.9151593	1.3239414	1.5770737
Ge	-1.9311641	-1.2776155	1.5819224
Ge	-0.0000000	0.0000000	0.0000000
Ge	-1.2776155	1.9311641	-1.5819224
Ge	1.3239414	1.9151593	-1.5770737
Ge	1.2776155	-1.9311641	-1.5819224
Ge	-1.3239414	-1.9151593	-1.5770737
Ge	-2.1565276	-0.0033006	-3.2407876
Ge	0.0065502	1.3560329	-4.1144867
Ge	-0.0065502	-1.3560329	-4.1144867
Ge	2.1565276	0.0033006	-3.2407876
Co	0.0000000	0.0000000	2.1571425
Co	0.0000000	-0.0000000	-2.1571425

Vibrational spectrum

mode	symmetry	wave number cm ⁻¹	IR intensity kJ/mol	selection rules	
				IR	RAMAN
1		-0.00	0.00000	-	-
2		-0.00	0.00000	-	-
3		0.00	0.00000	-	-
4		0.00	0.00000	-	-
5		0.00	0.00000	-	-
6		0.00	0.00000	-	-
7	e	15.60	0.09165	YES	YES
8	e	15.60	0.09165	YES	YES
9	b	39.38	0.07528	YES	YES
10	e	46.44	0.10409	YES	YES
11	e	46.44	0.10409	YES	YES
12	a	69.87	0.00000	NO	YES
13	e	74.44	0.52083	YES	YES
14	e	74.44	0.52083	YES	YES

15	a	79.90	0.00000	NO	YES
16	b	89.72	0.04484	YES	YES
17	b	92.77	0.55718	YES	YES
18	e	94.13	0.03654	YES	YES
19	e	94.13	0.03654	YES	YES
20	a	103.01	0.00000	NO	YES
21	a	106.89	0.00000	NO	YES
22	e	108.44	0.62780	YES	YES
23	e	108.44	0.62780	YES	YES
24	b	116.51	0.20393	YES	YES
25	a	117.16	0.00000	NO	YES
26	b	120.38	2.89831	YES	YES
27	a	130.90	0.00000	NO	YES
28	b	132.78	0.60244	YES	YES
29	e	134.53	0.00145	YES	YES
30	e	134.53	0.00145	YES	YES
31	a	140.08	0.00000	NO	YES
32	b	140.53	0.19622	YES	YES
33	e	146.45	1.52459	YES	YES
34	e	146.45	1.52459	YES	YES
35	e	156.64	11.52067	YES	YES
36	e	156.64	11.52067	YES	YES
37	b	169.46	38.75330	YES	YES
38	e	172.09	14.52318	YES	YES
39	e	172.09	14.52318	YES	YES
40	b	196.97	0.16824	YES	YES
41	a	197.63	0.00000	NO	YES
42	e	200.39	2.23392	YES	YES
43	e	200.39	2.23392	YES	YES
44	a	201.79	0.00000	NO	YES
45	b	208.70	2.26865	YES	YES
46	e	213.54	1.84934	YES	YES
47	e	213.54	1.84934	YES	YES
48	a	215.36	0.00000	NO	YES
49	b	227.57	1.99460	YES	YES
50	a	230.09	0.00000	NO	YES
51	b	270.72	2.54305	YES	YES
52	e	314.98	18.18693	YES	YES
53	e	314.98	18.18693	YES	YES
54	e	361.12	47.18061	YES	YES
55	e	361.12	47.18061	YES	YES

56	a	385.67	0.00000	NO	YES
57	b	469.37	210.07783	YES	YES

K₄[Co₂@Ge₁₇]²⁻

atomic coordinates

Ge	-4.1476467	1.1478481	-1.1047862
Ge	-3.7933833	-1.3499229	-0.3649102
Ge	-3.3706738	-0.7446066	-2.9360878
Ge	-2.3011043	1.7170288	-2.8905459
Ge	-1.5589924	2.3185322	-0.3637549
Ge	-2.4855640	0.4455914	1.1855808
Ge	-1.5362855	-2.2340971	-1.4746022
Ge	-0.6224152	-0.3491917	-3.0323931
Ge	-0.0047280	-0.1101668	-0.1938808
Ge	1.3016870	-2.2939703	1.1859579
Ge	0.2367783	-0.4346780	2.6843332
Ge	1.5038194	2.3070523	0.3570030
Ge	2.6301866	0.5446762	-1.2077902
Ge	3.6890702	-1.4367933	0.2901374
Ge	3.0992784	-0.9319332	2.8163964
Ge	4.0327310	1.0369305	1.1481984
Ge	2.0452610	1.5252809	2.8538726
Co	-1.9760046	0.0887625	-1.1120958
Co	1.8402390	0.0141906	0.9680420
K	-1.9491870	-3.2011548	1.9705887
K	1.0426230	2.7972752	-3.2719113
K	1.8398530	-2.7809648	-2.4087313
K	-1.1038570	3.0171852	3.1623387

Vibrational spectrum

mode	symmetry	wave number	IR intensity	selection rules	
		cm ⁻¹	kJ/mol	IR	RAMAN
1		-0.00	0.00000	-	-
2		-0.00	0.00000	-	-
3		-0.00	0.00000	-	-
4		-0.00	0.00000	-	-
5		0.00	0.00000	-	-
6		0.00	0.00000	-	-
7	a	21.00	0.48817	YES	YES
8	a	27.20	0.42934	YES	YES
9	a	33.89	3.39896	YES	YES

10	a	36.18	0.52749	YES	YES
11	a	38.27	11.77906	YES	YES
12	a	44.94	10.66707	YES	YES
13	a	47.18	2.76524	YES	YES
14	a	51.44	0.23684	YES	YES
15	a	53.29	1.42739	YES	YES
16	a	54.16	0.12685	YES	YES
17	a	65.50	1.69950	YES	YES
18	a	67.94	6.39345	YES	YES
19	a	72.03	5.16110	YES	YES
20	a	72.84	10.82004	YES	YES
21	a	74.51	7.77268	YES	YES
22	a	75.33	7.09274	YES	YES
23	a	79.74	0.86834	YES	YES
24	a	81.17	11.84953	YES	YES
25	a	86.26	25.55502	YES	YES
26	a	87.40	15.42050	YES	YES
27	a	89.79	5.92656	YES	YES
28	a	90.46	26.98226	YES	YES
29	a	95.13	3.06232	YES	YES
30	a	97.80	21.21377	YES	YES
31	a	99.74	17.01889	YES	YES
32	a	101.29	1.20026	YES	YES
33	a	105.50	2.25921	YES	YES
34	a	108.51	2.68477	YES	YES
35	a	112.47	1.86096	YES	YES
36	a	116.77	0.08316	YES	YES
37	a	118.13	0.42756	YES	YES
38	a	121.24	1.37018	YES	YES
39	a	135.75	0.13492	YES	YES
40	a	139.97	0.06879	YES	YES
41	a	143.89	1.82066	YES	YES
42	a	146.70	2.77360	YES	YES
43	a	147.00	3.68836	YES	YES
44	a	150.73	4.87695	YES	YES
45	a	152.13	1.65690	YES	YES
46	a	154.96	4.10554	YES	YES
47	a	155.86	8.30558	YES	YES
48	a	157.74	7.38886	YES	YES
49	a	166.07	20.57558	YES	YES
50	a	173.51	11.11562	YES	YES

51	a	176.58	12.21596	YES	YES
52	a	192.63	0.59006	YES	YES
53	a	199.41	0.64662	YES	YES
54	a	200.61	2.23459	YES	YES
55	a	200.89	2.41250	YES	YES
56	a	202.73	3.42174	YES	YES
57	a	202.92	4.72449	YES	YES
58	a	205.49	0.64645	YES	YES
59	a	205.73	0.69155	YES	YES
60	a	212.36	0.06783	YES	YES
61	a	225.70	1.78546	YES	YES
62	a	231.98	0.12192	YES	YES
63	a	257.33	2.05690	YES	YES
64	a	306.44	14.69350	YES	YES
65	a	307.60	16.05865	YES	YES
66	a	357.09	30.51728	YES	YES
67	a	360.51	44.07716	YES	YES
68	a	364.50	14.13907	YES	YES
69	a	439.63	206.04614	YES	YES

[Ni₂@Ge₁₇]⁴⁻

atomic coordinates

Ge	-0.0904626	-4.1806707	-1.2621903
Ge	1.3164729	-1.9778556	-2.0699121
Ge	2.0740268	-3.4016310	0.1189707
Ge	-2.2431026	-3.1242658	0.0219819
Ge	-0.1132455	-4.0208440	1.4541951
Ni	-0.0140932	-2.1074819	-0.0234505
Ge	0.5300271	-0.0048490	-0.4000329
Ge	-1.3106530	-1.6574565	-1.9998425
Ge	1.2160596	-1.5190146	1.9508433
Ge	-1.3511541	-1.3833792	1.8200824
Ge	1.8396178	1.7179305	1.5537735
Ge	2.2296747	1.9970337	-1.0588110
Ni	0.0309564	2.1033835	0.0080404
Ge	-1.7555836	1.4723244	-1.4566859
Ge	-1.9635036	1.3717833	1.0997029
Ge	1.2370543	4.1888995	0.2276000
Ge	-0.3135678	3.1451307	2.2033691
Ge	0.1401941	3.3726097	-2.0938694
Ge	-1.4587175	4.0083528	-0.093764

Vibrational spectrum

mode	symmetry	wave number cm ⁻¹	IR intensity kJ/mol	selecti on rules	
				IR	RAMAN
1		-0.00	0.00000	-	-
2		0.00	0.00000	-	-
3		0.00	0.00000	-	-
4		0.00	0.00000	-	-
5		0.00	0.00000	-	-
6		0.00	0.00000	-	-
7	a	19.99	0.44780	YES	YES
8	a	27.30	0.01066	YES	YES
9	a	35.75	0.07010	YES	YES
10	a	39.89	0.11450	YES	YES
11	a	47.34	0.02792	YES	YES
12	a	63.65	0.34392	YES	YES
13	a	65.57	0.01710	YES	YES
14	a	75.35	0.46010	YES	YES
15	a	81.34	0.15045	YES	YES
16	a	87.39	0.03589	YES	YES
17	a	91.02	0.53639	YES	YES
18	a	92.53	0.42975	YES	YES
19	a	98.96	1.10198	YES	YES
20	a	99.47	1.36175	YES	YES
21	a	102.84	0.28583	YES	YES
22	a	103.35	0.60777	YES	YES
23	a	109.13	1.94384	YES	YES
24	a	112.94	0.07222	YES	YES
25	a	122.76	3.14962	YES	YES
26	a	129.37	0.02850	YES	YES
27	a	130.73	0.89868	YES	YES
28	a	132.42	0.01696	YES	YES
29	a	138.98	0.47940	YES	YES
30	a	141.25	3.54189	YES	YES
31	a	141.92	1.42124	YES	YES
32	a	142.52	0.15646	YES	YES
33	a	143.86	0.16772	YES	YES
34	a	146.19	0.36600	YES	YES
35	a	148.16	0.56555	YES	YES
36	a	152.52	3.70365	YES	YES
37	a	153.35	3.79684	YES	YES

38	a	167.58	6.42386	YES	YES
39	a	169.25	5.89241	YES	YES
40	a	192.79	0.77813	YES	YES
41	a	193.01	0.61960	YES	YES
42	a	196.53	0.19297	YES	YES
43	a	198.99	2.97817	YES	YES
44	a	200.80	0.55939	YES	YES
45	a	202.78	2.25243	YES	YES
46	a	204.32	0.40238	YES	YES
47	a	205.81	0.26254	YES	YES
48	a	211.82	0.01377	YES	YES
49	a	221.79	2.80620	YES	YES
50	a	227.18	0.09801	YES	YES
51	a	251.85	0.00653	YES	YES
52	a	286.04	7.41579	YES	YES
53	a	287.14	11.01077	YES	YES
54	a	330.32	21.64704	YES	YES
55	a	330.91	28.75105	YES	YES
56	a	337.96	0.68157	YES	YES
57	a	405.96	82.97496	YES	YES

6. References

1. B. J. Witzel, W. Klein, J. V. Dums, M. Boyko and T. F. Fässler, *Angew. Chem. Int. Ed.*, **2019**, *58*, 12908.
2. C. B. Benda, M. Waibel and T. F. Fässler, *Angew. Chem. Int. Ed.*, **2015**, *54*, 522.
3. T. Kottke and D. Stalke, *J. Appl. Crystallogr.*, **1993**, *26*, 615.
4. G. M. Sheldrick, *Acta Crystallogr., Sect. C: Struct. Chem.*, **2015**, *71*, 3.
5. K. Momma and F. Izumi, *J. Appl. Crystallogr.*, **2011**, *44*, 1272.
6. TURBOMOLE V7.3 2018, a development of University of Karlsruhe and Forschungszentrum Karlsruhe GmbH, 1989-2007, TURBOMOLE GmbH, since 2007; available from www.turbomole.com.
7. J. P. Perdew, K. Burke and M. Ernzerhof, *Phys. Rev. Lett.*, **1996**, *77*, 3865.
8. C. Adamo and V. Barone, *J. Chem. Phys.*, **1999**, *110*, 6158.
9. F. Weigend and R. Ahlrichs, *Phys. Chem. Chem. Phys.*, **2005**, *7*, 3297.
10. K. Eichkorn, O. Treutler, H. Öhm, M. Häser and R. Ahlrichs, *Chem. Phys. Lett.*, **1995**, *240*, 283.
11. F. Weigend, *Phys. Chem. Chem. Phys.*, **2006**, *8*, 1057.
12. M. Sierka, A. Hogekamp and R. Ahlrichs, *J. Chem. Phys.*, **2003**, *118*, 9136.
13. A. Klamt and G. Schüürmann, *J. Chem. Soc. Perkin Trans. 2*, **1993**, 799.
14. J. M. Goicoechea and S. C. Sevov, *Angew. Chem. Int. Ed.*, **2005**, *44*, 4026.
15. S. Ponou and T. F. Faessler, *Z. Anorg. Allg. Chem.*, **2007**, *633*, 393.
16. J. M. Goicoechea and S. C. Sevov, *J. Am. Chem. Soc.*, **2006**, *128*, 4155.
17. E. N. Esenturk, J. C. Fettinger and B. W. Eichhorn, *J. Am. Chem. Soc.*, **2006**, *128*, 12.
18. C. Liu, X. Jin, L. Li, J. Xu, J. E. McGrady and Z.-M. Sun, *Chem. Sci.*, **2019**, *10*, 4394.
19. J. Q. Wang, S. Stegmaier and T. F. Fässler, *Angew. Chem. Int. Ed.*, **2009**, *48*, 1998.
20. C. Liu, L. J. Li, I. A. Popov, R. J. Wilson, C. Q. Xu, J. Li, A. I. Boldyrev and Z. M. Sun, *Chin. J. Chem.*, **2018**, *36*, 1165.
21. M. M. Bentlohner, C. Fischer and T. F. Fässler, *Chem. Commun.*, **2016**, *52*, 9841.
22. D. Rios and S. C. Sevov, *Inorg. Chem.*, **2010**, *49*, 6396.
23. E. N. Esenturk, J. Fettinger and B. Eichhorn, *Chem. Commun.*, **2005**, 247.
24. M. Uta, D. Cioloboc and R. King, *Inorg. Chem.*, **2012**, *51*, 3498.

6.10 Nonagermanide *Zintl* Clusters with Mg²⁺ Counter Ions

C. Wallach, W. Klein and T. F. Fässler

Published in: *Zeitschrift für Anorganische und Allgemeine Chemie* **2022**, advance article, DOI: 10.1002/zaac.202200065.

© Wiley-VCH GmbH, Weinheim, 2022, no reprint license ID applicable, open-access article, unchanged reprinted version licensed under the terms of a Creative Commons Attribution 4.0 International License.

Access online *via*: <https://onlinelibrary.wiley.com/doi/full/10.1002/zaac.202200065>.

Contents and Contributions

Ion-exchange processes at germanide clusters bearing potassium counterions are described upon the application of organomagnesium compounds. The reaction of the silylated cluster $K[Ge_9\{Si(TMS)_3\}_3]$ with the Mg(II) complex $Mg(NacNac^{Mes})_2$ in acetonitrile yields the counterion-exchanged compound $[Mg(NacNac^{Mes})(MeCN)_4][Ge_9\{Si(TMS)_3\}_3] \cdot MeCN$ (**1a-Mg**), while reactions of the solid-state phase K_4Ge_9 with the same organometallic precursor lead to the isolation of crystals of $[K[2.2.2]crypt]_4[Mg(NacNac^{Mes})(NH_3)_4]_2[Ge_9-Ge_9] \cdot 32.58 NH_3$ (**2a-KMg**). The latter species comprises a dimeric $[Ge_9-Ge_9]^{6-}$ unit, which is a common oxidation product of $[Ge_9]^{4-}$ clusters in liquid ammonia. From reactions of the precursors K_4Ge_9 and $K_{12}Ge_{17}$ with the Mg(I) species $[Mg(NacNac^{Mes})]_2$ in liquid ammonia the compounds $[K[2.2.2]crypt][NacNac^{Mes}] \cdot NH_3$ (**3**) and $[K(18-crown-6)][NacNac^{Mes}] \cdot 3 NH_3$ (**4**), respectively, were obtained.

The experimental work leading to the isolation of the compounds **1** to **4**, including their characterization, was performed by me. The initial structure refinements were performed by me. Dr. Wilhelm Klein finalized the single crystal structure refinements for publication. A first sample of the Mg(I) compound $[Mg(NacNac^{Mes})]_2$ was generously donated by Prof. Dr. Cameron Jones, Monash University, Australia. Elemental analysis data were acquired by Ulrike Ammari and Bircan Dilki in the microanalytical laboratory of the Chemistry Department of the Technical University of Munich. EDX analysis was performed by Maria Müller (Prof. Fässler, TUM). The manuscript was authored by me, including the creation of figures, tables, and schemes. Dr. Wilhelm Klein and Dr. Annette Schier proof-read the manuscript. The publication of the manuscript was managed by Prof. Dr. Thomas F. Fässler, the peer-review process including corrections was a joined task accomplished by Prof. Dr. Thomas F. Fässler and me.

DOI: 10.1002/zaac.202200065

Nonagermanide *Zintl* Clusters with Mg^{2+} Counter Ions

Christoph Wallach,^[a] Wilhelm Klein,^[a] and Thomas F. Fässler^{*[a]}Dedicated to Professor Cameron Jones on the Occasion of his 60th Birthday.

Ion exchange processes are rarely investigated with respect to tetrel element *Zintl* clusters. We now discovered that the addition of Mg complexes to nonagermanide anions comprising K^+ counter cations results in an exchange of the alkali ions by alkaline earth cations. Upon stirring $\text{K}[\text{Ge}_9\{\text{Si}(\text{TMS})_3\}_3]$ (TMS = trimethylsilyl) and $\text{Mg}(\text{NacNac}^{\text{Mes}})\text{I}$ ($\text{NacNac}^{\text{Mes}} = N,N'$ -bis(2,4,6-trimethylphenyl)- β -diketiminato) in MeCN the product $[\text{Mg}(\text{NacNac}^{\text{Mes}})(\text{MeCN})_4][\text{Ge}_9\{\text{Si}(\text{TMS})_3\}_3]\cdot\text{MeCN}$ is formed. Reactions of $\text{Mg}(\text{NacNac}^{\text{Mes}})\text{I}$ with K_4Ge_9 in liquid ammonia as a

solvent yielded $[\text{K}[2.2.2]\text{crypt}]_4[\text{Mg}(\text{NacNac}^{\text{Mes}})(\text{NH}_3)_4]_2[\text{Ge}_9\text{---}\text{Ge}_9]\cdot 32.58 \text{ NH}_3$ featuring a mixed alkali/alkaline earth metal cationic sphere and an oxidative coupling of the $[\text{Ge}_9]^{4-}$ clusters. From comparable reactions of $[\text{Mg}(\text{NacNac}^{\text{Mes}})]_2$ with K_4Ge_9 or $\text{K}_{12}\text{Ge}_{17}$ in liquid ammonia crystals of $[\text{K}[2.2.2]\text{crypt}][\text{NacNac}^{\text{Mes}}]\cdot\text{NH}_3$ and $[\text{K}(18\text{-crown-6})][\text{NacNac}^{\text{Mes}}]\cdot 3 \text{ NH}_3$, respectively, were isolated. All compounds were characterized by means of single crystal structure determination.

Introduction

The usage of main group element clusters obtained from *Zintl* phases in solution has developed to an attractive synthetic strategy for the generation of extended atom-precise metalloid and intermetalloid clusters.^[1] *Zintl* phases that contain alkali metals as the electropositive component serve as precursors, and the clusters can be isolated from solution with the help of alkali metal sequestering agents. In case of the tetrel element clusters the phases A_4E_9 and $A_{12}E_{17}$ comprising an alkali metal (A) matrix with embedded tetrel element clusters $[\text{E}_9]^{4-}$ ($E = \text{Ge}, \text{Sn}, \text{Pb}$) and a combination of $[\text{E}_4]^{4-}$ and $[\text{E}_3]^{4-}$ ($E = \text{Si}, \text{Ge}, \text{Sn}, \text{Pb}$) clusters, respectively, are especially suitable starting materials for further reactions due to the good solubility of the nine-atom clusters.^[1a,2]

For the nine-atom clusters a prosperous chemistry has evolved, and the discrete polyanions have been used as cornerstones in the synthesis of filled, substituted, and extended cage compounds.^[1-3] The $[\text{E}_9]^{4-}$ clusters are transferred into solution without changes concerning their inherent structure.^[4] In recent years, the protonation of such clusters has been described in species like $[\text{HE}_9]^{3-}$ ($E = \text{Si},^{[5]} \text{Ge},^{[6]} \text{Sn}^{[7]}$), $[\text{H}_2\text{Si}_9]^{2-}$ ^[8] and $[\text{H}_2(\text{Si}/\text{Ge})_9]^{2-}$ ^[5a] bearing the smallest possible ligand. However, the cage compounds also form covalent 2-centre-2-electron bonds to main group element compounds

resulting in multi-decorated species such as $[\text{Ge}_9\{\text{Si}(\text{TMS})_3\}_2]^{2-}$,^[9] $[\text{Ge}_9\{R\}_3]^-$ ($R = \text{Si}(\text{TMS})_3$,^[10] SiH^tBu_2)^[11] and $[\text{Ge}_9\{PRR'\}_3]^-$ ($R = N'\text{Pr}_2$; $R' = ^t\text{Bu}, N'\text{Pr}_2$).^[12] Particularly the twofold silylated $[\text{Ge}_9]$ cluster has served as a precursor for the generation of mixed-substituted cluster species, exemplarily enabling the linking of two cluster entities by a bridging silyl ligand,^[13] and only recently the introduction of Lewis basic phosphanyl^[14] and Lewis acidic boranyl groups^[15] to the respective dianion has been reported. Apart from the described reactions, extended cluster species might arise from a partial oxidation of the nine-atom polyanions in solution yielding interconnected cages with covalent $E\text{---}E$ bonds. The simplest example is the dimeric germanide $[\text{Ge}_9\text{---}\text{Ge}_9]^{6-}$, which consists of two bridged $[\text{Ge}_9]^{3-}$ units.^[4a,16] A similar connectivity is found in polymeric $[\text{Ge}_9]^{2-}$.^[17] Further oligomeric anions show multi-interconnected cages like $[\text{Ge}_9\text{---}\text{Ge}_9\text{---}\text{Ge}_9]^{6-}$ ^[18] or $[\text{Ge}_9\text{---}\text{Ge}_9\text{---}\text{Ge}_9\text{---}\text{Ge}_9]^{8-}$.^[19] Despite the many isolated representatives the mechanism of cluster oxidation is not fully understood yet. However, it is postulated that the solutions contain various species $[\text{Ge}_9]^{n-}$ ($n = 2\text{---}4$) together with solvated electrons, which could account for redox reactions and the formation of the described Ge oligomers.^[2]

Over the last decades a huge number of solid-state phases containing group 14 element polyanions other than $[\text{E}_4]^{4-}$ and $[\text{E}_9]^{4-}$ has been reported. Thus, dumbbells of Si or Ge are described in phases like Li_7Si_2 ^[20] or Li_3NaGe_2 ^[21] and structure motifs like five-^[22] or six-membered^[23] tetrel element rings, as well as a butterfly-like atom arrangement of $[\text{E}_4]^{6-}$ moieties ($E = \text{Si},^{[24]} \text{Ge}^{[25]}$) in the solids Ba_3E_4 have been found. Furthermore, planar polyanionic Si_{12} units are observed in the solid state in $\text{Ca}_7\text{Mg}_{7.5\pm\delta}\text{Si}_{14}$.^[26] All of these tetrel element building blocks of the solid-state phases could in principle be used as precursors for subsequent reactions, but reactions with *Zintl* phases comprising alkaline earth metals are rare. As a scarce example, Si and Ge nano-sheets are obtained upon deintercalation of the alkaline earth ions from the phases CaE_2 ($E = \text{Si}, \text{Ge}$),^[27] that

[a] M. Sc. C. Wallach, Dr. W. Klein, Prof. Dr. T. F. Fässler
Department Chemie, Technische Universität München
Lichtenbergstraße 4, 85747 Garching, Germany
E-mail: thomas.faessler@lrz.tum.de

Supporting information for this article is available on the WWW under <https://doi.org/10.1002/zaac.202200065>

© 2022 The Authors. Zeitschrift für anorganische und allgemeine Chemie published by Wiley-VCH GmbH. This is an open access article under the terms of the Creative Commons Attribution License, which permits use, distribution and reproduction in any medium, provided the original work is properly cited.

comprise a layer structure, and serve as substrate in following reactions.^[28]

Even though numerous compounds with negatively charged nine-atom tetrel element clusters have been isolated from solution, they all contain to the best of our knowledge alkali metal counter ions. Due to the lack of solid-state precursors with $[E_9]^{4-}$ anions in combination with alkaline earth metals, we investigated ion exchange reactions starting from the potassium germanides K_4Ge_9 and $K_{12}Ge_{17}$ and organic Mg salts as ion exchanging reactants.

Results and discussion

Reactivity of Mg(II) organyls towards $[Ge_9]$ Zintl clusters

The reaction of $K[Ge_9\{Si(TMS)_3\}_3]$ (**1 a-K**) with a three-fold excess of the Mg(II) species $Mg(NacNac^{Mes})I$ in MeCN yields a milky deep orange suspension. After filtration and storage of the concentrated filtrate overnight, crystals of compound **1 a-Mg**, $[Mg(NacNac^{Mes})(MeCN)_4][Ge_9\{Si(TMS)_3\}_3] \cdot MeCN$, suitable for single crystal diffraction were obtained. Compound **1 a-Mg** (Figure 1) is the ion-exchanged analogue of the K-containing silylated $[Ge_9]$ precursor. A full ellipsoid plot of compound **1 a-Mg** can be found in Figure S1.

The structure of the anion $[Ge_9\{Si(TMS)_3\}_3]^-$ (**1a**) is best described as a C_{2v} -symmetric tricapped trigonal prism (Figure 1, dashed red lines) with prism heights $Ge2-Ge4$, $Ge5-Ge6$ and $Ge7-Ge8$ of 3.485(1) Å, 3.344(1) Å and 3.415(1) Å, respectively. All Ge-Ge and Ge-Si distances are in agreement with the

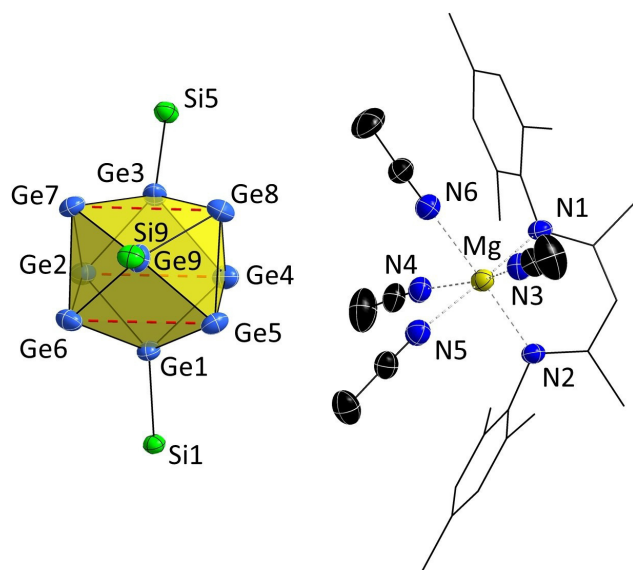


Figure 1. Structure of the formula unit of **1 a-Mg**. All ellipsoids are shown at a 50% probability level. The tricapped trigonal prism is indicated by dashed red lines. TMS groups, hydrogen atoms and the co-crystallized MeCN molecule are omitted, and the carbon atoms of the $[NacNac^{Mes}]^-$ ligand are shown as wire-sticks for clarity. A plot showing all atoms as ellipsoids can be found in the Supporting Information (Figure S1).

reported ones in compound **1 a-K**.^[10] The Mg^{2+} ion is embedded in an octahedral matrix of N atoms provided by the $[NacNac^{Mes}]^-$ ligand and the solvent molecules [2.114(3) Å ($Mg-N2$) to 2.223(3) Å ($Mg-N6$)]. The $Mg-N$ distances are in accordance with those in the octahedral complex $[Mg(NH_3)_6]^{2+}$ [2.1969(1) Å].^[29] The octahedral coordination of the Mg^{2+} cation by polar groups is very common, and also present e.g. in $[Mg(H_2O)_6]^{2+}$ and in protein chemistry.^[30] Ge atoms are not located in the first coordination sphere of the Mg^{2+} ion, and, regarding the shortest distance of 6.305(1) Å between Mg and Ge atoms ($Mg-Ge4$), any direct interactions can be excluded. Compound **1 a-Mg** was further investigated by NMR spectroscopy (1H , ^{13}C , ^{29}Si) and by elemental analysis. The 1H NMR spectrum (Figure S2) unambiguously shows the presence of the $[NacNac^{Mes}]^-$ ligand and the silylated cluster in a 1:1 ratio, while Mg was monitored in qualitative EDX measurements (Figure S6). The elemental analysis is in accordance with the formula $C_{56}H_{119}Ge_9MgN_5Si_{12}$, matching the sum of the single units $[Ge_9\{Si(TMS)_3\}_3]^-$, $[Mg(NacNac^{Mes})]^+$, and three MeCN molecules. The different number of solvent molecules is most probably due to excessive drying of the solid in vacuo prior to the analysis.

The reactivity of **1 a-Mg** was tested by dissolving the compound in $thf-d_8$ and the addition of a $thf-d_8$ solution of the N-heterocyclic carbene $NHC^{Dipp}Cu-Cl$ [$NHC^{Dipp} = 1,3$ -di(2,6-diisopropylphenyl)imidazolyliidene]. The 1H NMR spectrum revealed the same signals as reported for the reaction of **1 a-K** and $NHC^{Dipp}Cu-Cl$, indicating the analogous formation of $(NHC^{Dipp}Cu)[Ge_9\{Si(TMS)_3\}_3]$.^[31] Hence, the counter ion seems to play a minor role in the tested reaction. Despite the straightforward formation of **1 a-Mg**, no clean ion exchange reaction with the closely related dianionic species $[Ge_9\{Si(TMS)_3\}_3]^{2-}$ could be observed, and the 1H NMR spectra of the reaction outcome showed a vast, so far unidentified mixture of products.

Further investigations focused on the reactivity of the Mg(II) organyl towards bare $[Ge_9]^{4-}$ clusters in liquid ammonia. Block-shaped dark brown crystals of $[K[2.2.2]crypt]_4[Mg(NacNac^{Mes})(NH_3)_4]_2[Ge_9-Ge_9] \cdot 32.58 NH_3$ (**2 a-KMg**) were isolated after several months. Compound **2 a-KMg** crystallizes in the triclinic space group $P\bar{1}$ with two formula units per unit cell and contains a dimeric $[Ge_9-Ge_9]^{6-}$ unit (**2a**, Figure 2a), four cationic $[K[2.2.2]crypt]^+$ moieties, and two $[Mg(NacNac^{Mes})(NH_3)_4]^+$ molecules (Figure 2d). Four of the 34 co-crystallizing ammonia molecules are only partially occupied ($N26: 0.79$ and $N27: 0.50$), resulting in an overall number of 32.58 NH_3 molecules per unit cell. The 18-atom $[Ge_9-Ge_9]^{6-}$ cluster consists of two $[Ge_9]$ moieties which are interconnected by a Ge-Ge exo-bond between two vertices of the pseudo square planes of the cages [$d(Ge1-Ge1^i) = 2.531(1)$ Å]. The symmetry of the $[Ge_9]$ moieties is best described as capped square antiprisms with a slightly distorted C_{4v} symmetry. The deviation is best expressed by the ratio of the diagonal length of the open square face $Ge1-Ge2-Ge3-Ge4$ given by $d_{Ge2-Ge4} : d_{Ge1-Ge3} = 1.09$ and the dihedral angle $\omega_{Ge1-Ge2-Ge4-Ge3} = 0.5^\circ$. The exo-bond $Ge1-Ge1^i$ is almost collinear to the shorter diagonal of the square planes (Figure 2b). Analogous $[Ge_9]$ dimers have previously been reported in anions isolated from ethylenedi-

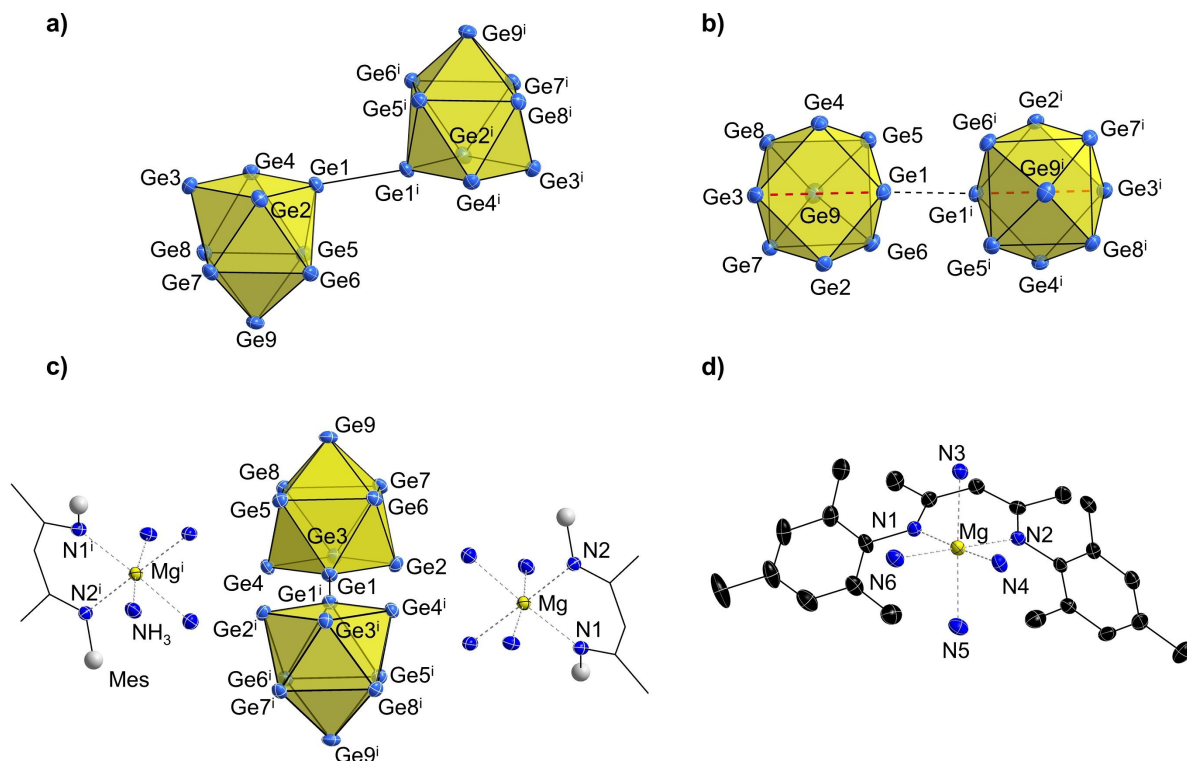


Figure 2. a) Molecular structure of anion **2a**; b) top view of the molecular structure of **2a** with indication of the collinear arrangement of the cluster-connecting exo-bond (Ge1–Ge1'; dashed black line) and the diagonals of the square planes (indicated by dashed red lines); c) arrangement of **2a** and the counter ions $[\text{Mg}(\text{NacNac}^{\text{Mes}})(\text{NH}_3)_4]^+$; d) molecular structure of the cationic fragment $[\text{Mg}(\text{NacNac}^{\text{Mes}})(\text{NH}_3)_4]^+$ emphasizing the octahedral coordination of Mg(II). All ellipsoids are shown at a 50% probability level. In c) the backbone of the $[\text{NacNac}^{\text{Mes}}]^-$ ligand is shown as wire-sticks, and Mes groups as grey spheres for clarity. Hydrogen atoms are omitted in c) and d). Symmetry operation (i): 1–x, 1–y, 1–z.

amine, N,N-dimethylformamide, or liquid ammonia.^[16b,c,e,f] Ge–Ge distances are in accordance with those in the latter dimeric species.

Compound **2a-KMg** comprises a mixed alkali/alkaline earth metal cationic sphere with four [2.2.2]crypt-sequestered K^+ ions and two $[\text{Mg}(\text{NacNac}^{\text{Mes}})(\text{NH}_3)_4]^+$ units balancing the negative charge of the germanide dimer. The Mg^{2+} cations are found in distances above 4.839(2) Å (Mg–Ge2) to the nearest Ge atoms (Figure 2c), which is approximately double the sum of the covalent radii.^[32] The Mg^{2+} cation is coordinated by two N atoms of the bidentate ligand $[\text{NacNac}^{\text{Mes}}]^-$, and the octahedral ligand environment is completed by four additional NH_3 molecules (Figure 2d). The Mg–N distances range from 2.200(5) Å (Mg–N2) to 2.241(5) Å (Mg–N5) with the shortest bonds between Mg and N atoms of the β -diketiminato ligand. With an almost planar torsion angle of the equatorial plane of the octahedron of coordinating N atoms $\omega_{\text{N2-N1-N4-N6}} = 175.4^\circ$, approximate rectangular angles $\text{N}_x\text{–Mg–N}_y$, and an almost linear arrangement of N3–Mg–N5 ($\angle_{\text{N3–Mg–N5}} = 171.4^\circ$), the symmetry deviates only slightly from a perfect octahedron (Supporting information Table S2). However, the reason for the dimerization of the $[\text{Ge}_9]$ clusters in solution still remains unclear.

Reactivity of Mg(I) organyls towards $[\text{Ge}_9]$ Zintl clusters

Due to their steric shielding β -diketiminates are often applied as ligands for the stabilization of unusual oxidation states such as in $[\text{Mg}(\text{NacNac}^{\text{Dipp}})]_2$ (Dipp = 2,6-diisopropylphenyl)^[33] or $[\text{Zn}(\text{NacNac}^{\text{Mes}})]_2$ ^[34] and the reaction of the Zn(I) organyl with K_4Ge_9 in ethylenediamine yielded the polymeric anion $[\text{Zn}\{\text{trans-}\mu_2(\eta^3\text{-}\eta^3\text{-Ge}_9)\}]_2^{2-}$.^[35] Since $[\text{Mg}(\text{NacNac}^{\text{Mes}})]_2$ immediately leads to an unidentified, insoluble species when exposed to ethylenediamine, we studied its reactivity towards liquid ammonia. The Mg(I) compound was weighed into a Schenk tube, and two milliliters of ammonia were condensed on top of it. Even though the reactant does not dissolve in liquid ammonia, a color change from initially bright yellow to orange-red was observed, which might be caused by the coordination of NH_3 molecules to Mg. After storing the suspension for one day at -40°C the solvent was evaporated, thereby restoring the former yellow color. The ^1H NMR spectrum of the product does not significantly differ from that of the initial reactant (Figure S5), thus corroborating the stability of the organo-metallic compound in NH_3 (l). Subsequently, we investigated the reactivity of $[\text{Mg}(\text{NacNac}^{\text{Mes}})]_2$ towards Zintl phases in liquid ammonia. After several months the formation of solids was observed. However, attempts to isolate crystals from the

reddish precipitate were hampered by a rapid degradation of the solid material upon opening the reaction flask, indicated by a color change to brown-green. Nevertheless, we were able to isolate the side-products $[K[2.2.2]crypt][NaCNac^{Mes}] \cdot NH_3$ (**3**) as well as $[K(18-crown-6)][NaCNac^{Mes}] \cdot 3 NH_3$ (**4**) as yellow or colorless crystals, respectively (Figure 3). Both compounds crystallize in the space group $P\bar{1}$ with two formula units per unit cell. The C–N distances in the $[NaCNac^{Mes}]^-$ moieties as well as the K–O distances in the cryptand and crown ether are in agreement with previously reported data.^[36] The experiment which resulted in the formation of **3** also contained crystals of the known ammoniate $[K[2.2.2]crypt]_3[Ge_9] \cdot 8 NH_3$ as a by-product, which comprises $[Ge_9]^{3-}$ anions – the paramagnetic monomer of **2a**.^[37]

Conclusion

The two anionic *Zintl* clusters $[Mg(NaCNac^{Mes})(MeCN)_4][Ge_9\{Si(TMS)_3\}_3] \cdot MeCN$ (**1a-Mg**) and $[K[2.2.2]crypt]_4[Mg(NaCNac^{Mes})(NH_3)_4]_2[Ge_9-Ge_9] \cdot 32.58 NH_3$ (**2a-KMg**) with either pure alkaline earth metal or mixed alkali/alkaline earth metal counterions were obtained via counter ion exchange starting from potassium germanide precursors by offering a Mg(II) source. In both cases the alkaline earth metal does not directly coordinate to the Ge cluster, which contrasts observations made for analogous Zn compounds. When a Mg(I) compound is used, oxidized $[Ge_9]^{3-}$ clusters and the side products $[K[2.2.2]crypt][NaCNac^{Mes}] \cdot NH_3$ (**3**) and $[K(18-crown-6)][NaCNac^{Mes}] \cdot 3 NH_3$ (**4**) were isolated. The transfer of the herein presented reactions to analogous Si- and Sn-based *Zintl* clusters and the influence of the counter ion on the solubility of the clusters is under current investigation in our laboratories.

Experimental details

General considerations

All experiments were carried out under a dry, oxygen-free atmosphere using standard glove box and Schlenk-line techniques. Glassware was dried by heating it at 650 °C *in vacuo*. MeCN (VWR) was purified in a MBraun solvent purification system and stored over molecular sieves. The solid phases K_4Ge_9 and $K_{12}Ge_{17}$ were prepared by fusion of stoichiometric amounts of the elements at elevated temperatures in a stainless-steel autoclave and a tantalum ampule, respectively. $K[Ge_9\{Si(TMS)_3\}_3]$ and $NHC^{Dipp}Cu-Cl$ were prepared according to literature procedures.^[10,38] Liquid ammonia was dried over sodium metal, and $[2.2.2]crypt$ (Merck) was dried overnight applying dynamic vacuum before usage. 18-Crown-6 (Merck) was purified by sublimation before usage. $Mg(NaCNac^{Mes})I$ was prepared according to modified literature procedures, and $[Mg(NaCNac^{Mes})]_2$ was generously donated by Prof. C. Jones, Monash University, Australia.^[33,39]

Single crystal structure determination

The air- and moisture-sensitive crystals of **2–4** were transferred from the mother liquor into cooled perfluoroalkyl ether oil and isolated from polycrystalline material under a cooled stream of nitrogen.^[40] Crystals of **1a-Mg** were transferred in and isolated under perfluoroalkyl ether oil at room temperature in a glove box. For diffraction data collection, the single crystals were mounted on a glass capillary and positioned in a 150 K cold N_2 gas stream. Data collection was performed with a STOE StadiVari diffractometer ($MoK\alpha$ radiation) equipped with a DECTRIS PILATUS 300 K detector. Structures were solved by Direct Methods (SHELXS-97)^[41] and refined by full-matrix least-squares calculations against F^2 (SHELXL-2014 or SHELXL-2018).^[42] The positions of the hydrogen atoms were calculated and refined using a riding model. Unless stated otherwise, all non-hydrogen atoms were treated with anisotropic displacement parameters. The supplementary crystallographic data for this paper have been deposited with the Cambridge Structural database and are available free of charge via www.ccdc.cam.ac.uk/data_request/cif. The crystallographic data for compounds **1–4** are summarized in Table 1.

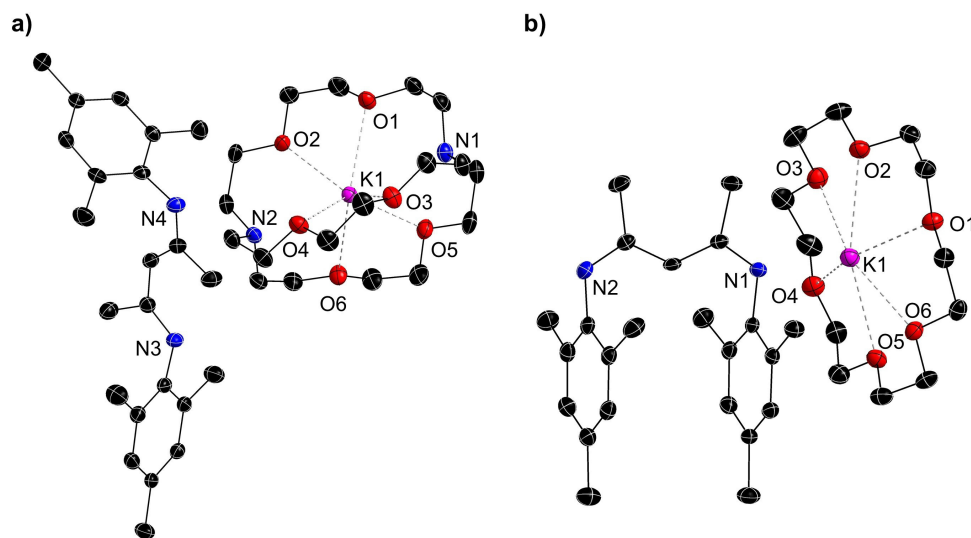


Figure 3. Structure of the formula unit of a) compound **3** and b) compound **4**. All ellipsoids are shown at a 50% probability level. The co-crystallizing NH_3 molecules and hydrogen atoms are omitted for clarity.

Table 1. Crystallographic data of compounds 1–4.

compound	1 a-Mg	2 a-KMg	3	4
formula	C ₆₀ H ₁₂₅ Ge ₉ MgN ₇ Si ₁₂	C ₁₁₈ H _{323.74} Ge ₁₈ K ₄ Mg ₂ N _{52.58} O ₂₄	C ₄₁ H ₆₈ KN ₅ O ₆	C ₃₅ H ₆₂ KN ₅ O ₆
fw [g·mol ⁻¹]	1959.70	4376.44	766.10	687.99
space group	<i>P</i> $\bar{1}$	<i>P</i> $\bar{1}$	<i>P</i> $\bar{1}$	<i>P</i> $\bar{1}$
<i>a</i> [Å]	15.5673(6)	15.8617(3)	12.6685(5)	11.5238(9)
<i>b</i> [Å]	16.2296(7)	17.2066(4)	13.3496(6)	12.7793(9)
<i>c</i> [Å]	20.6144(9)	20.2740(4)	27.8011(13)	13.9201(11)
α [deg]	90.658(3)	89.173(2)	80.259(3)	95.485(6)
β [deg]	94.783(3)	70.622(2)	86.359(3)	104.540(6)
γ [deg]	108.461(3)	80.298(2)	71.456(3)	92.242(6)
<i>V</i> [Å ³]	4919.1(4)	5140.1(2)	4393.1(3)	1971.0(3)
<i>Z</i>	2	2	2	2
<i>T</i> [K]	150(2)	150(2)	150(2)	150(2)
λ [Å]	0.71073	0.71073	0.71073	0.71073
ρ_{calcd} [g·cm ⁻³]	1.323	1.414	1.158	1.159
μ [mm ⁻¹]	2.895	2.738	0.169	0.181
collected reflections	93691	122523	81650	37380
indep. reflections	19301	20152	17271	7735
<i>R</i> _{int} / <i>R</i> _{σ}	0.0613/0.0433	0.1248/0.0560	0.0539/0.0458	0.0605/0.0479
parameters/restraints	842/0	978/0	989/0	432/0
<i>R</i> ₁ [<i>I</i> > 2 σ (<i>I</i>)/all data]	0.0376/0.0633	0.0604/0.0846	0.0382/0.0673	0.0423/0.0765
<i>wR</i> ₂ [<i>I</i> > 2 σ (<i>I</i>)/all data]	0.0778/0.0893	0.1365/0.1543	0.0876/0.0982	0.0960/0.1108
goodness of fit	1.032	1.150	1.016	1.017
max./min. diff. el. density [e·Å ⁻³]	0.562/-0.413	1.431/-1.003	0.248/-0.219	0.257/-0.280
deposition no.	CCDC-2117110	CCDC-2117111	CCDC-2117112	CCDC-2117113

NMR spectroscopy

¹H and ²⁹Si INEPT NMR spectra were measured on a Bruker Avance Ultrashield 400 MHz spectrometer; the ¹³C NMR spectrum was measured on a Bruker Avance HD 400 MHz spectrometer. The ¹H NMR and ¹³C NMR spectra were calibrated using the residual signals of the used deuterated solvent. Chemical shifts are reported in parts per million (ppm) relative to TMS, with the solvent peaks serving as internal reference.^[43] Singlets are abbreviated with (s).

Elemental analysis

The elemental analysis was carried out in the microanalytical laboratory of the Chemistry Department of the Technical University of Munich. Analyses of C, H and N were performed in a combustion analyzer (EURO EA, HEKA tech).

Syntheses

[Mg(NacNac^{Mes})(MeCN)₄][Ge₉{Si(TMS)₃]₃]·MeCN (1 a-Mg)

Solid K[Ge₉{Si(TMS)₃]₃] (28.7 mg, 20.0 μ mol, 1 equiv.) and Mg(NacNac^{Mes})I (29.1 mg, 60 μ mol, 3 equiv.) were weighed into a Schlenk tube, and MeCN (1 mL) was added. The orange suspension was stirred for three days, filtered, and after reduction of the volume of the filtrate stored for crystallization at r.t. Overnight, orange needle-shaped crystals suitable for single crystal diffraction were obtained (23.9 mg, 12.2 μ mol, 61 %).

¹H NMR (400 MHz, 298 K, C₆D₆): δ [ppm] = 6.83 (s, 4H, CH_{Mes(m)}), 4.93 (s, 1H, CH_{NacNac}), 2.18 (s, 12H, CH_{3 Mes}), 1.66 (s, 6H, CH_{3 Mes}), 1.45 (s, 6H, CH_{3 NacNac}), 0.51 (s, 81H, CH_{3 TMS}). ¹³C NMR (101 MHz, 298 K, C₆D₆): δ [ppm] = 147.30 (s, C_{Mes-N}), 133.34 (s, C_{Mes(p)}), 132.14 (s, C_{Mes(o)}), 129.21 (s, CH_{Mes(m)}), 118.07 (s, C_{NacNac}), 95.03 (s, CH_{NacNac}), 24.29 (s, CH_{3 Mes}),

20.89 (s, CH_{3 NacNac}), 18.90 (s, CH_{3 Mes}), 3.26 (s, CH_{3 TMS}). ²⁹Si-INEPT NMR (79 MHz, 298 K, C₆D₆): δ [ppm] = -9.46 (s, Si_{TMS}), -107.01 (s, Si_{Ge9}). **Elemental analysis:** anal. calcd. for C₅₆H₁₁₉Ge₉MgN₅Si₁₂: C, 35.82; H, 6.39; N, 3.73; found: C, 35.11; H, 6.44; N, 3.51.

[K{2.2.2}crypt]₄[Mg(NacNac^{Mes})(NH₃)₄]₂[Ge₉-Ge₉]·32.58 NH₃ (2 a-KMg)

Equimolar amounts of K₄Ge₉ (80.0 mg, 99.0 μ mol, 1 equiv.) and Mg(NacNac^{Mes})I (55.2 mg, 99.0 μ mol, 1 equiv.) were weighed in into a Schlenk tube. After the addition of [2.2.2]crypt (66.9 mg, 178.2 μ mol, 1.8 equiv.) liquid ammonia (2 mL) was condensed onto the solid mixture, instantly causing the formation of a red solution. The flask was stored at -70 °C. One dark brown, block-shaped single crystal of 2 a-KMg was obtained after 8 months.

[K{2.2.2}crypt][NacNac^{Mes}]-NH₃ (3)

K₄Ge₉ (70.0 mg, 90.0 μ mol, 1 equiv.) and [Mg(NacNac^{Mes})₂] (32.1 mg, 45.0 μ mol, 0.5 equiv.) were weighed in into a Schlenk tube. After the addition of [2.2.2]crypt (58.6 mg, 160.0 μ mol, 1.8 equiv.) liquid ammonia (2 mL) was condensed onto the solid mixture, instantly causing the formation of a red solution with remaining yellow solids. The flask was stored at -40 °C. Several colorless spherical crystals of 3 were obtained after 18 months. Due to the experimental setup an exact yield could not be determined.

[K(18-crown-6)][NacNac^{Mes}]-3 NH₃ (4)

K₁₂Ge₁₇ (100.0 mg, 59.0 μ mol, 1 equiv.), 18-crown-6 (31.0 mg, 117.0 μ mol, 2 equiv.) and [Mg(NacNac^{Mes})₂] (25.2 mg, 35.0 μ mol, 0.6 equiv.) were weighed in into a Schlenk tube. Subsequently, liquid ammonia (2 mL) was condensed onto the solid mixture,

instantly causing the formation of a red solution with remaining yellow solids. The flask was stored at -70°C . Several colorless spherical crystals of **4** were obtained after 24 months. Due to the experimental setup an exact yield could not be determined.

Author contributions

C. W. performed experiments and authored the manuscript. W. K. refined the single crystal structure data. T. F. F. supervised the project.

Acknowledgements

C. W. thanks the Deutsche Forschungsgemeinschaft (DFG, German Research Foundation) for funding (project number 245845833) within International Research Training Group IRTG 2022 – Alberta Technical University of Munich School for Functional Hybrid Materials (ATUMS). C. W. also thanks the Studienstiftung des Deutschen Volkes for granting a PhD scholarship and special thanks to Prof. C. Jones (Monash University, Australia) for providing the Mg(I) precursor. Open Access funding enabled and organized by Projekt DEAL.

Conflict of Interest

The authors declare no conflict of interest.

Data Availability Statement

The data that support the findings of this study are available in the supplementary material of this article.

Keywords: magnesium · germanium · Zintl cluster · ion exchange · liquid ammonia

- [1] a) S. Scharfe, F. Kraus, S. Stegmaier, A. Schier, T. F. Fässler, *Angew. Chem. Int. Ed.* **2011**, *50*, 3630; b) C. Liu, Z.-M. Sun, *Coord. Chem. Rev.* **2019**, *382*, 32; c) R. J. Wilson, N. Lichtenberger, B. Weinert, S. Dehnen, *Chem. Rev.* **2019**, *119*, 8506; d) W. Klein, A. Schier, T. F. Fässler, *Molecules Meet Solids: From Wade-Mingos Clusters to Intermetalloid Clusters; in: Structure and Bonding*, vol. 188, Springer, Berlin, Heidelberg, **2021**, DOI 10.1007/430_2021_82.
- [2] S. C. Sevov, J. M. Goicoechea, *Organometallics* **2006**, *25*, 5678.
- [3] Y. Wang, J. E. McGrady, Z.-M. Sun, *Acc. Chem. Res.* **2021**, *54*, 1506.
- [4] a) C. Suchentrunk, J. Daniels, M. Somer, W. Carrillo-Cabrera, N. Korber, *Z. Naturforsch. B* **2005**, *60*, 277; b) M. Somer, W. Carrillo-Cabrera, E. M. Peters, K. Peters, H. G. v Schnering, *Z. Anorg. Allg. Chem.* **1998**, *624*, 1915; c) S. Joseph, C. Suchentrunk, F. Kraus, N. Korber, *Eur. J. Inorg. Chem.* **2009**, *2009*, 4579.
- [5] a) T. Henneberger, W. Klein, T. F. Fässler, *Z. Anorg. Allg. Chem.* **2018**, *644*, 1018; b) C. Lorenz, F. Hastreiter, J. Hioe, N. Lokesh, S. Gärtner, N. Korber, R. M. Gschwind, *Angew. Chem. Int. Ed.* **2018**, *57*, 12956.
- [6] C. Lorenz, N. Korber, *Crystals* **2018**, *8*, 374.
- [7] F. S. Kocak, D. O. Downing, P. Zavalij, Y.-F. Lam, A. N. Vedernikov, B. Eichhorn, *J. Am. Chem. Soc.* **2012**, *134*, 9733.
- [8] L. J. Schiegerl, A. J. Karttunen, J. Tillmann, S. Geier, G. Raudaschl-Sieber, M. Waibel, T. F. Fässler, *Angew. Chem. Int. Ed.* **2018**, *57*, 12950.
- [9] O. Kysliak, A. Schnepf, *Dalton Trans.* **2016**, *45*, 2404.
- [10] F. Li, S. C. Sevov, *Inorg. Chem.* **2012**, *51*, 2706.
- [11] O. Kysliak, T. Kunz, A. Schnepf, *Eur. J. Inorg. Chem.* **2017**, *2017*, 805.
- [12] F. S. Geitner, W. Klein, T. F. Fässler, *Angew. Chem. Int. Ed.* **2018**, *57*, 14509.
- [13] O. Kysliak, C. Schrenk, A. Schnepf, *Inorg. Chem.* **2017**, *56*, 9693.
- [14] a) F. S. Geitner, J. V. Dums, T. F. Fässler, *J. Am. Chem. Soc.* **2017**, *139*, 11933; b) F. S. Geitner, C. Wallach, T. F. Fässler, *Chem. Eur. J.* **2018**, *24*, 4103; c) C. Wallach, F. S. Geitner, W. Klein, T. F. Fässler, *Chem. Eur. J.* **2019**, *25*, 12349.
- [15] C. Wallach, F. S. Geitner, A. J. Karttunen, T. F. Fässler, *Angew. Chem. Int. Ed.* **2021**, *60*, 2648.
- [16] a) T. F. Fässler, U. Schütz, *Inorg. Chem.* **1999**, *38*, 1866; b) L. Xu, S. C. Sevov, *J. Am. Chem. Soc.* **1999**, *121*, 9245; c) R. Hauptmann, T. F. Fässler, *Z. Anorg. Allg. Chem.* **2003**, *629*, 2266; d) R. Hauptmann, T. F. Fässler, *Z. Kristallogr. New Cryst. Struct.* **2003**, *218*, 461; e) A. Nienhaus, S. D. Hoffmann, T. F. Fässler, *Z. Anorg. Allg. Chem.* **2006**, *632*, 1752; f) S. Scharfe, T. F. Fässler, *Z. Anorg. Allg. Chem.* **2011**, *637*, 901; g) K. Mayer, M. Giebel, M. M. Bentlohner, W. Klein, T. F. Fässler, *Z. Kristallogr. New Cryst. Struct.* **2015**, *230*, 286.
- [17] a) C. Downie, Z. Tang, A. M. Guloy, *Angew. Chem. Int. Ed.* **2000**, *39*, 337; b) C. Downie, J.-G. Mao, H. Parmar, A. M. Guloy, *Inorg. Chem.* **2004**, *43*, 1992.
- [18] A. Ugrinov, S. C. Sevov, *J. Am. Chem. Soc.* **2002**, *124*, 10990.
- [19] a) L. Yong, S. D. Hoffmann, T. F. Fässler, *Z. Anorg. Allg. Chem.* **2004**, *630*, 1977; b) K. Mayer, W. Klein, S. Geier, T. F. Fässler, *Z. Anorg. Allg. Chem.* **2021**, *647*, 377.
- [20] H. Schäfer, H. Axel, A. Weiss, *Z. Naturforsch. B* **1965**, *20*, 1010.
- [21] L. M. Scherf, A. J. Karttunen, O. Pecher, P. C. Magusin, C. P. Grey, T. F. Fässler, *Angew. Chem. Int. Ed.* **2016**, *55*, 1075.
- [22] a) O. Yañez, V. Garcia, J. Garza, W. Orellana, A. Vásquez-Espinal, W. Tiznado, *Chem. Eur. J.* **2019**, *25*, 2467; b) S. Dupke, T. Langer, R. Pöttgen, M. Winter, H. Eckert, *Solid State Nucl. Magn. Reson.* **2012**, *42*, 17; c) R. Nesper, J. Curda, H. G. v Schnering, *J. Solid State Chem.* **1986**, *62*, 199; d) A. Kuhn, P. Sreeraj, R. Poettgen, H. D. Wiemhoefer, M. Wilkening, P. Heitjans, *Angew. Chem. Int. Ed.* **2011**, *50*, 12099; e) I. Todorov, S. C. Sevov, *Inorg. Chem.* **2004**, *43*, 6490; f) H. Eickhoff, W. Klein, L. Toffoletti, G. Raudaschl-Sieber, T. F. Fässler, *Z. Anorg. Allg. Chem.* **2022**, DOI 10.1002/zaac.202100376.
- [23] a) R. C. Gil, W. Carrillo-Cabrera, M. Schultheiss, K. Peters, H. G. v Schnering, Y. Grin, *Z. Anorg. Allg. Chem.* **1999**, *625*, 285; b) I. Todorov, S. C. Sevov, *Inorg. Chem.* **2006**, *45*, 4478; c) H. G. v Schnering, U. Bolle, J. Curda, K. Peters, W. Carrillo-Cabrera, M. Somer, M. Schultheiss, U. Wedig, *Angew. Chem. Int. Ed.* **1996**, *35*, 984.
- [24] U. Aydemir, A. Ormeci, H. Borrmann, B. Böhme, F. Zürcher, B. Uslu, T. Goebel, W. Schnelle, P. Simon, W. Carrillo-Cabrera, *Z. Anorg. Allg. Chem.* **2008**, *634*, 1651.
- [25] F. Zürcher, R. Nesper, *Angew. Chem. Int. Ed.* **1998**, *37*, 3314.
- [26] R. Nesper, A. Currao, S. Wengert, *Chem. Eur. J.* **1998**, *4*, 2251.
- [27] a) S. Yamanaka, H. Matsu-ura, M. Ishikawa, *Mater. Res. Bull.* **1996**, *31*, 307; b) G. Vogt, M. S. Brandt, M. Stutzmann, *Adv. Mater.* **2000**, *12*, 1278.
- [28] a) T. Helbich, A. Lyuleeva, I. M. Höhle, P. Marx, L. M. Scherf, J. Kehrlé, T. F. Fässler, P. Lugli, B. Rieger, *Chem. Eur. J.* **2016**, *22*,

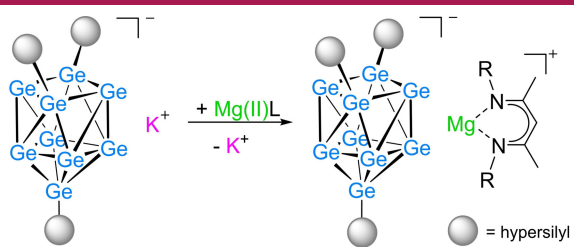
- 6194; b) T. Helbich, A. Lyuleeva, T. Ludwig, L. M. Scherf, T. F. Fässler, P. Lugli, B. Rieger, *Adv. Funct. Mater.* **2016**, *26*, 6711; c) H. Yu, T. Helbich, L. M. Scherf, J. Chen, K. Cui, T. F. Fässler, B. Rieger, J. G. Veinot, *Chem. Mater.* **2018**, *30*, 2274; d) M. J. Kloberg, H. Yu, E. Groß, F. Eckmann, T. M. Restle, T. F. Fässler, J. G. Veinot, B. Rieger, *Adv. Mater.* **2021**, *33*, 2100288.
- [29] K. Cenzual, S. Iwata, *PAULING FILE Multinaries Edition - 2012*, Springer, Heidelberg, $\text{Mg}(\text{NH}_3)_6\text{Cl}_2$ ($\text{MgCl}_2[\text{NH}_3]_6$, $T=130\text{ K}$) Crystal Structure **2016**, https://materials.springer.com/isp/crystallographic/docs/sd_1002929, accessed 21st February 2022.
- [30] a) F. A. Mautner, H. Krischner, C. Kratky, *Z. Naturforsch. B* **1986**, *41*, 935; b) M. S. Cates, M. L. Teodoro, G. N. Phillips Jr, *Biophys. J.* **2002**, *82*, 1133; c) I. Tiritiris, T. Schleid, *Z. Anorg. Allg. Chem.* **2004**, *630*, 541; d) F. T. Senguen, Z. Grabarek, *Biochemistry* **2012**, *51*, 6182; e) K. R. Andress, J. Gundermann, *Z. Kristallogr., Kristallgeom., Kristallphys., Kristallchem.* **1934**, *87*, 345.
- [31] F. S. Geitner, T. F. Fässler, *Eur. J. Inorg. Chem.* **2016**, *2016*, 2688.
- [32] P. Pyykkö, M. Atsumi, *Chem. Eur. J.* **2009**, *15*, 186.
- [33] S. P. Green, C. Jones, A. Stasch, *Science* **2007**, *318*, 1754.
- [34] S. Schulz, D. Schuchmann, U. Westphal, M. Bolte, *Organometallics* **2009**, *28*, 1590.
- [35] C. B. Benda, R. Schäper, S. Schulz, T. F. Fässler, *Eur. J. Inorg. Chem.* **2013**, *2013*, 5964.
- [36] a) W. Clegg, E. K. Cope, A. J. Edwards, F. S. Mair, *Inorg. Chem.* **1998**, *37*, 2317; b) A. V. Jentzsch, D. Emery, J. Mareda, S. K. Nayak, P. Metrangolo, G. Resnati, N. Sakai, S. Matile, *Nat. Commun.* **2012**, *3*, 1; c) A. Chekhlov, *Russ. J. Inorg. Chem.* **2009**, *54*, 280.
- [37] C. B. Benda, PhD Thesis, Technical University of Munich, **2013**.
- [38] a) L. Hintermann, *Beilstein J. Org. Chem.* **2007**, *3*, 22; b) O. Santoro, A. Collado, A. M. Slawin, S. P. Nolan, C. S. Cazin, *Chem. Commun.* **2013**, *49*, 10483.
- [39] J. Prust, K. Most, I. Müller, E. Alexopoulos, A. Stasch, I. Usón, H. W. Roesky, *Z. Anorg. Allg. Chem.* **2001**, *627*, 2032.
- [40] T. Kottke, D. Stalke, *J. Appl. Crystallogr.* **1993**, *26*, 615.
- [41] G. M. Sheldrick, *Acta Crystallogr. Sect. A* **2008**, *64*, 112.
- [42] G. M. Sheldrick, *Acta Crystallogr. Sect. C* **2015**, *71*, 3.
- [43] G. R. Fulmer, A. J. Miller, N. H. Sherden, H. E. Gottlieb, A. Nudelman, B. M. Stoltz, J. E. Bercaw, K. I. Goldberg, *Organometallics* **2010**, *29*, 2176.

Manuscript received: February 14, 2022

Revised manuscript received: March 9, 2022

Accepted manuscript online: March 17, 2022

RESEARCH ARTICLE



*M. Sc. C. Wallach, Dr. W. Klein,
Prof. Dr. T. F. Fässler**

1 – 8

**Nonagermanide Zintl Clusters
with Mg²⁺ Counter Ions**



Zeitschrift für anorganische und allgemeine Chemie

Supporting Information

Nonagermanide *Zintl* Clusters with Mg^{2+} Counter Ions

Christoph Wallach, Wilhelm Klein, and Thomas F. Fässler*

Supporting Information

Nonagermanide *Zintl* Clusters with Mg²⁺ Counter Ions

Christoph Wallach, Wilhelm Klein and Thomas F. Fässler

1. Crystallographic details	S1
2. NMR spectra of compound 1a-Mg	S5
3. NMR spectrum of [Mg(NacNac ^{Me5})] ₂ after treatment with NH ₃ (l)	S6
4. EDX spectra of compounds 1 – 4	S7

1. Crystallographic details

Table S1. Selected interatomic distances and angles in **1a-Mg**.

atoms	distance [Å]	atoms	angle [deg]
Ge1-Ge2	2.5475(6)	N1-Mg-N3	94.9(1)
Ge1-Ge4	2.5297(6)	N1-Mg-N4	97.8(1)
Ge1-Ge5	2.5355(6)	N1-Mg-N5	175.4(1)
Ge1-Ge6	2.5347(5)	N1-Mg-N6	92.2(1)
Ge2-Ge3	2.5258(5)	N2-Mg-N1	88.8(1)
Ge2-Ge6	2.6924(6)	N2-Mg-N3	99.1(1)
Ge2-Ge7	2.7016(5)	N2-Mg-N4	94.4(1)
Ge3-Ge4	2.5328(5)	N2-Mg-N5	94.0(1)
Ge3-Ge7	2.5352(5)	N2-Mg-N6	176.3(1)
Ge3-Ge8	2.5345(6)	N4-Mg-N3	161.5(1)
Ge4-Ge5	2.6723(6)	N4-Mg-N5	84.3(1)
Ge4-Ge8	2.6758(5)	N4-Mg-N6	81.9(1)
Ge5-Ge8	2.6421(5)	N5-Mg-N3	82.1(1)
Ge5-Ge9	2.5379(5)	N5-Mg-N6	84.1(1)
Ge6-Ge7	2.6602(5)		
Ge6-Ge9	2.5353(6)	N1-N3-N4-N5	170.6(1)
Ge7-Ge9	2.5429(6)	N1-N2-N6-N5	173.9(1)
Ge8-Ge9	2.5309(5)		
Ge2-Ge4	3.485(1)		
Ge5-Ge6	3.344(1)		
Ge7-Ge8	3.415(1)		
Ge1-Si1	2.3745(9)		
Ge3-Si5	2.3701(9)		
Ge9-Si9	2.369 (1)		
Ge4-Mg	6.305(1)		
Ge5-Mg	6.323(1)		
Ge8-Mg	6.346(1)		
Mg-N1	2.121(3)		
Mg-N2	2.114(3)		
Mg-N3	2.220(4)		
Mg-N4	2.210(4)		
Mg-N5	2.219(3)		
Mg-N6	2.223(3)		

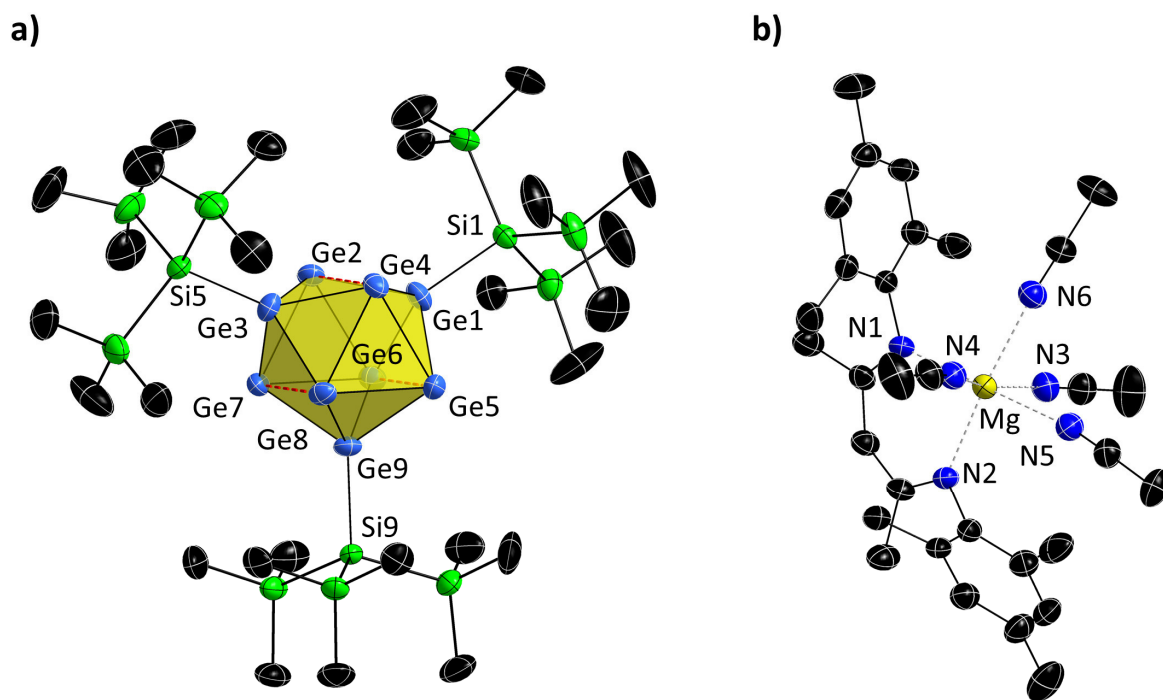


Figure S1. Full ellipsoid plot of compound **1a-Mg**. a) Structure of monoanionic $[\text{Ge}_9\{\text{Si}(\text{TMS})_3\}_3]^-$ (**1a**); b) structure of the cationic fragment $[\text{Mg}(\text{NacNac}^{\text{Mes}})(\text{MeCN})_4]^+$. Co-crystallizing MeCN molecules and hydrogen atoms are omitted for clarity. Trigonal prism bases are indicated by dashed red lines.

Table S2. Selected interatomic distances and angles in **2a-KMg**. Symmetry operation (i): 1-x, 1-y, 1-z.

atoms	distance [Å]	atoms	angle [deg]
Ge1-Ge1 ⁱ	2.531(1)	N1-Mg-N3	87.7(2)
Ge1-Ge2	2.5470(9)	N1-Mg-N4	176.1(2)
Ge1-Ge4	2.5251(9)	N1-Mg-N5	100.4(2)
Ge1-Ge5	2.6205(9)	N2-Mg-N1	85.2(2)
Ge1-Ge6	2.6341(9)	N2-Mg-N3	90.0(2)
Ge2-Ge3	2.6123(9)	N2-Mg-N4	96.9(2)
Ge2-Ge6	2.6761(9)	N2-Mg-N5	93.7(2)
Ge2-Ge7	2.5624(9)	N2-Mg-N6	177.2(2)
Ge3-Ge4	2.6397(9)	N3-Mg-N4	89.1(2)
Ge3-Ge7	2.6162(9)	N3-Mg-N5	171.4(2)
Ge3-Ge8	2.6319(9)	N4-Mg-N5	82.8(2)
Ge4-Ge5	2.6871(9)	N6-Mg-N1	92.3(2)
Ge4-Ge8	2.5653(9)	N6-Mg-N3	91.3(2)
Ge5-Ge6	2.788(1)		
Ge5-Ge8	2.7750(9)	Ge1-Ge2-Ge4-Ge3	179.5(1)
Ge5-Ge9	2.5798(9)	N1-N2-N6-N4	175.4(1)
Ge6-Ge7	2.7463(9)	N1-N3-N5-N4	179.3(1)
Ge6-Ge9	2.5794(9)		
Ge7-Ge8	2.8436(9)		
Ge7-Ge9	2.5779(9)		
Ge8-Ge9	2.585(1)		
Ge1-Ge3	3.489(1)		
Ge2-Ge4	3.804(1)		
Ge2-Mg	4.839(2)		
Ge4-Mg	4.866(2)		
Ge5-Mg	5.504(2)		
Ge6-Mg	4.915(2)		
Mg-N1	2.207(5)		
Mg-N2	2.200(5)		
Mg-N3	2.222(5)		
Mg-N4	2.236(5)		
Mg-N5	2.241(5)		
Mg-N6	2.206(6)		

Table S3. Selected interatomic distances in **3**.

atoms	distance [Å]
K1-O1	2.878(1)
K1-O2	2.783(1)
K1-O3	2.817(1)
K1-O4	2.856(2)
K1-O5	2.833(1)
K1-O6	2.827(1)
K1-N1	3.047(1)
K1-N2	3.022(1)

Table S4. Selected interatomic distances in **4**.

atoms	distance [Å]
K1-O1	2.918(1)
K1-O2	2.823(1)
K1-O3	2.855(1)
K1-O4	2.868(1)
K1-O5	2.888(1)
K1-O6	2.857(1)
K1-N1	2.837(1)
K1-N3	3.134(2)

2. NMR spectra of compound **1a-Mg**

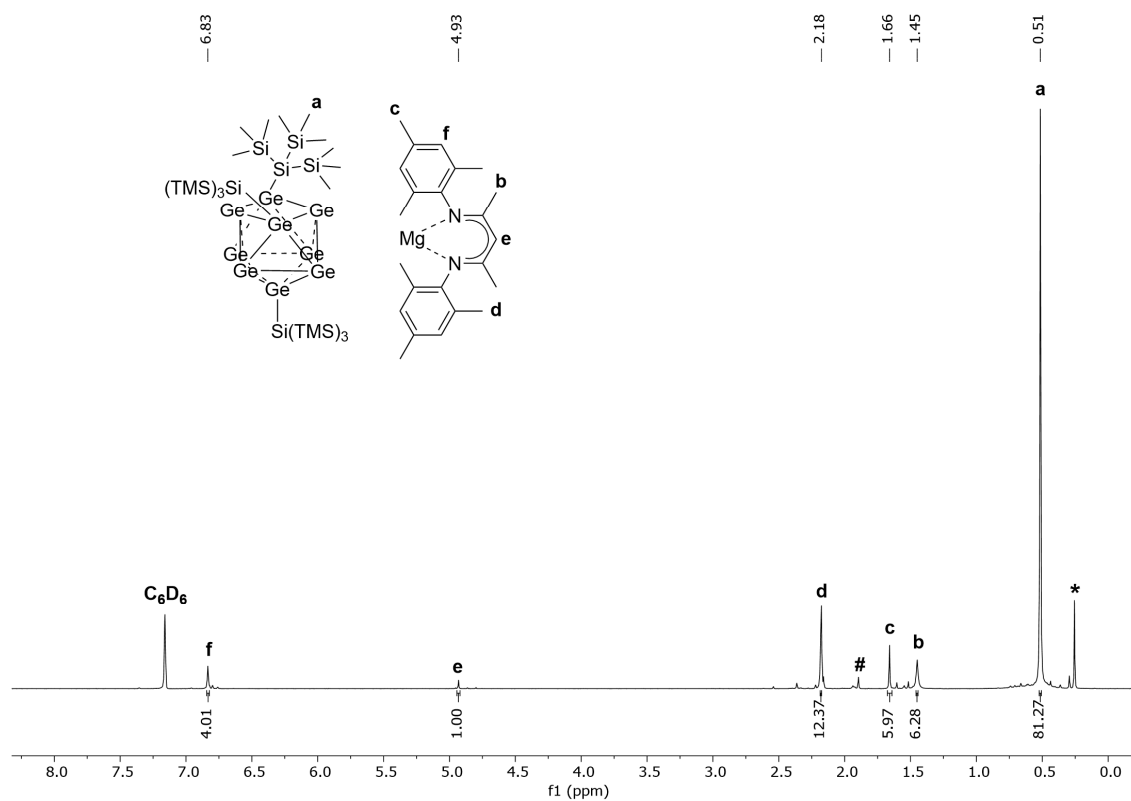


Figure S2. ^1H NMR spectrum of **1a-Mg** acquired in C_6D_6 . Asterisk signal is assigned to silicon grease; signal marked with # belongs to an unidentified impurity.

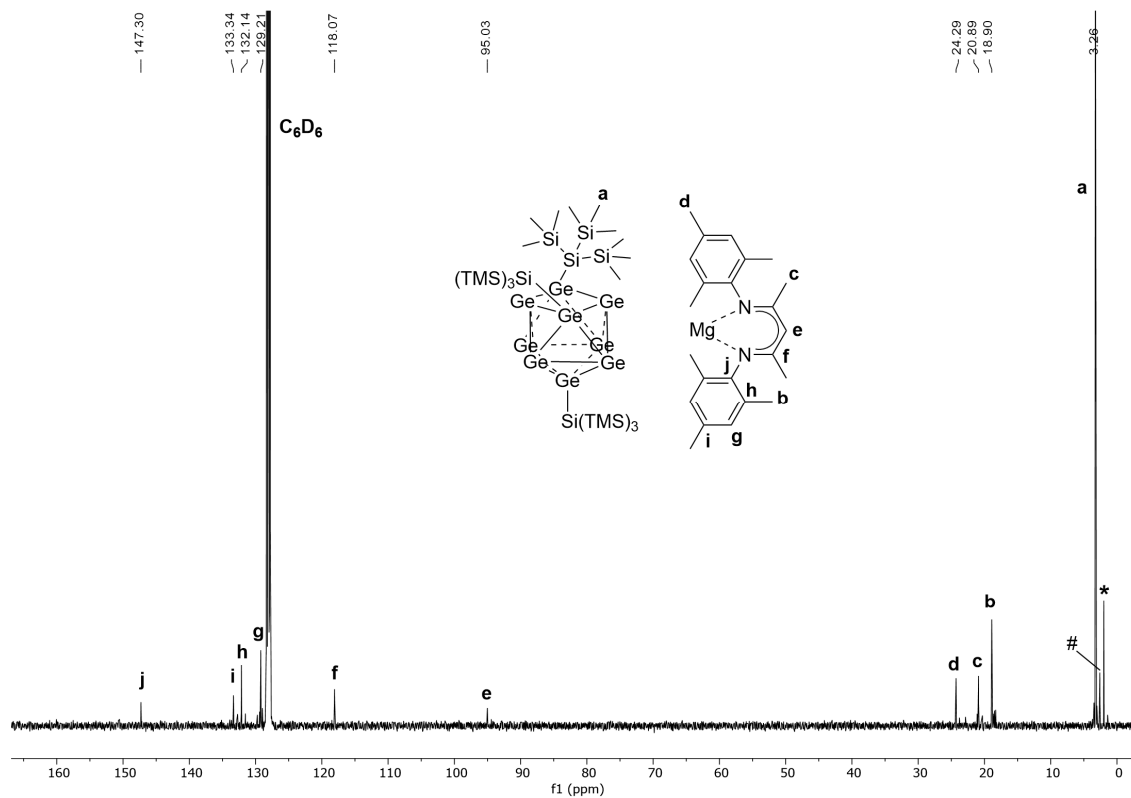


Figure S3. ^{13}C NMR spectrum of **1a-Mg** acquired in C_6D_6 . Asterisk signal is assigned to silicon grease; signal marked with # belongs to an unidentified impurity.

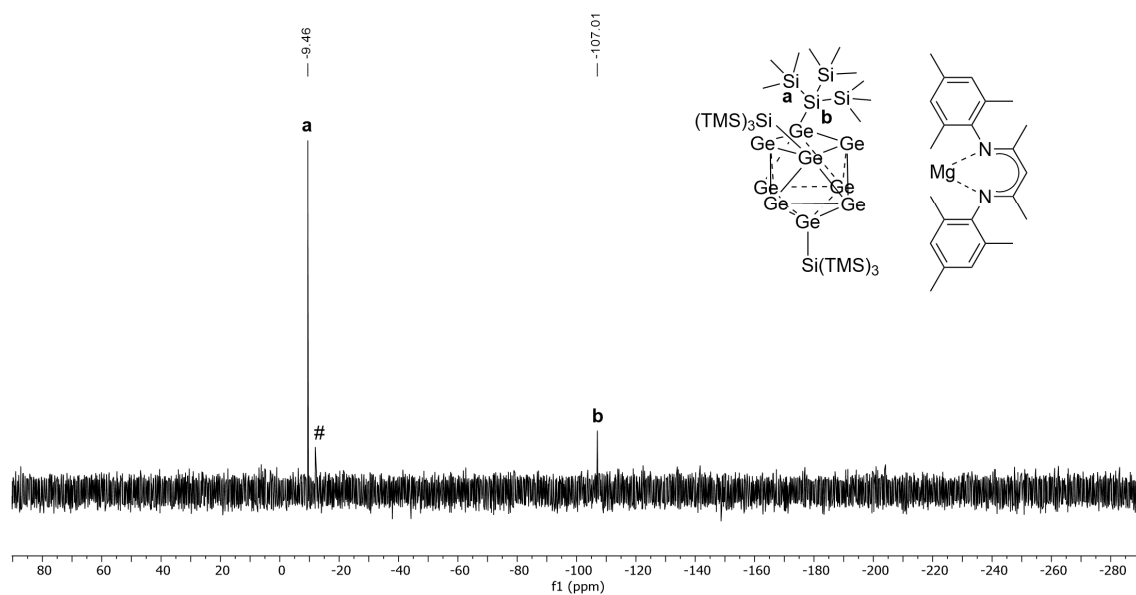


Figure S4. ^{29}Si INEPT spectrum of **1a-Mg** acquired in C_6D_6 . The signal marked with # belongs to an unidentified impurity.

3. NMR spectrum of $[\text{Mg}(\text{NacNac}^{\text{Mes}})]_2$ after treatment with NH_3 (I)

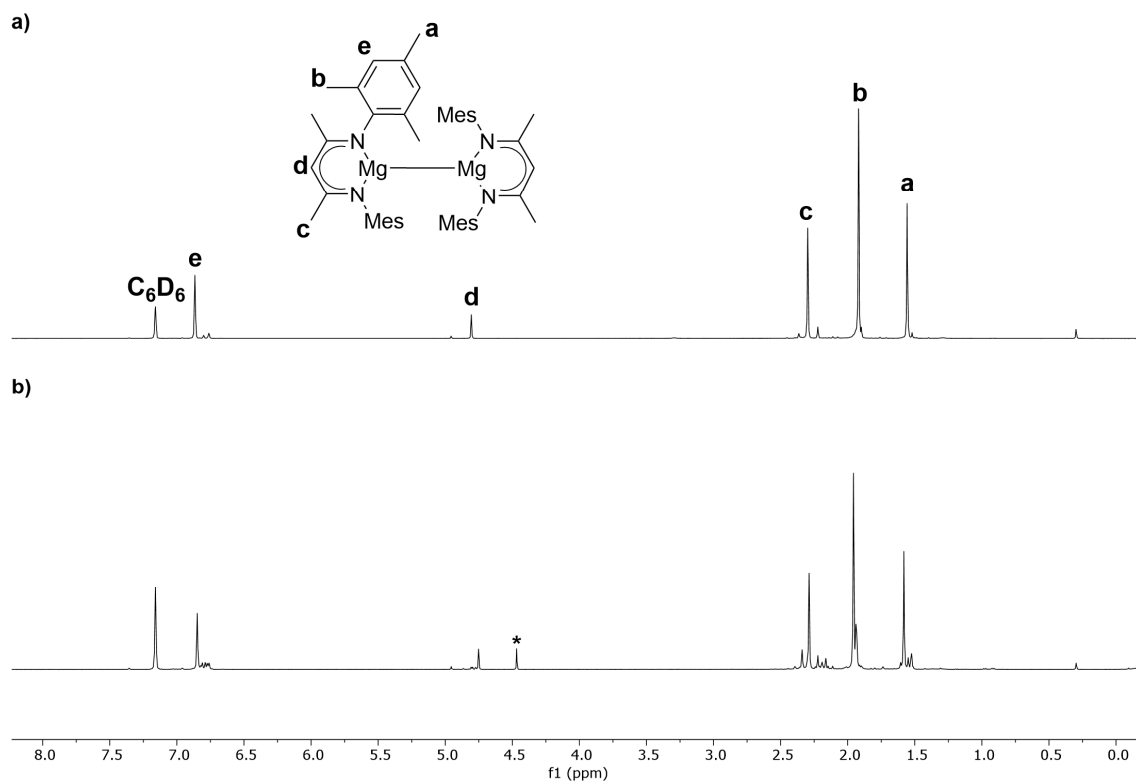


Figure S5. ^1H NMR spectra acquired in C_6D_6 of a) $[\text{Mg}(\text{NacNac}^{\text{Mes}})]_2$ and b) $[\text{Mg}(\text{NacNac}^{\text{Mes}})]_2$ after treatment with NH_3 (I). The asterisked signal in b) marks an unidentified impurity.

4. EDX spectra of compounds 1 – 4

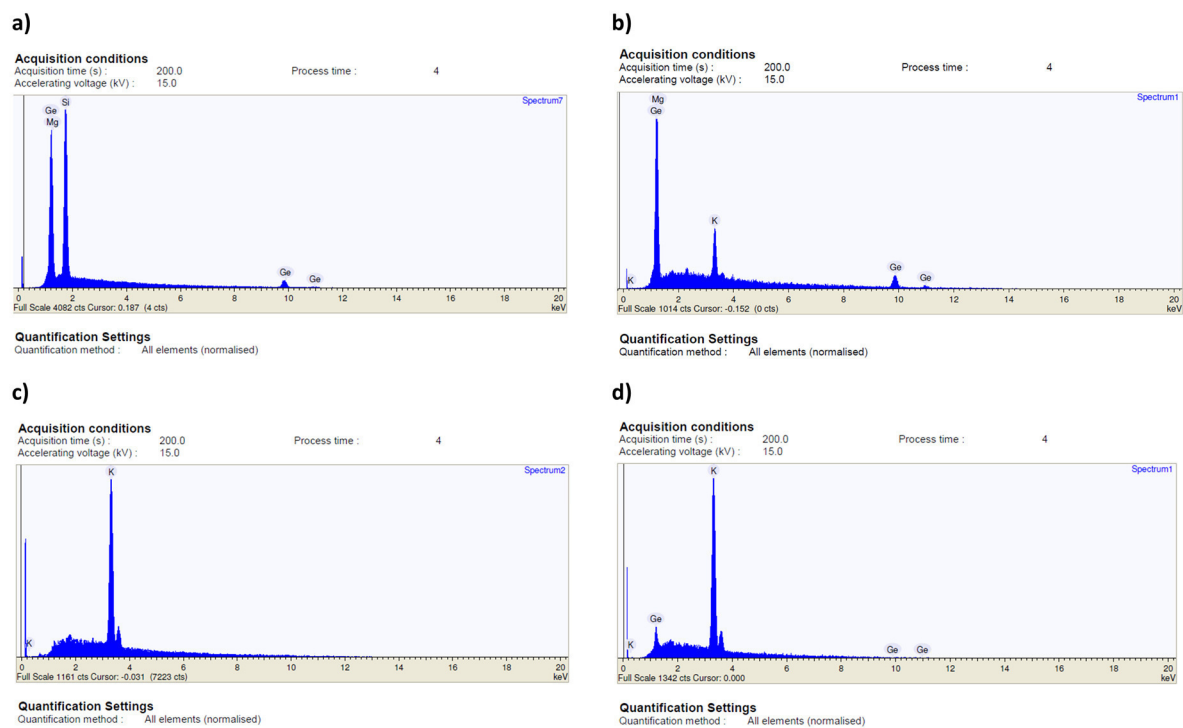


Figure S6. Qualitative EDX spectra of single crystalline material of a) **1a-Mg**; b) **2a-KMg**; c) **3** and d) **4**. In d) signals of Ge are observed which are assigned to remaining impurities on the crystal's surface.

6.11 Crystal Structure of N^2,N^4 -dimesitylpentane-2,4-diamine, $C_{23}H_{34}N_2$

Christoph Wallach, Wilhelm Klein and Thomas F. Fässler

Crystal structure communication submitted for publication in: *Z. Kristallogr., New Cryst. Struct.*

Contents and Contributions

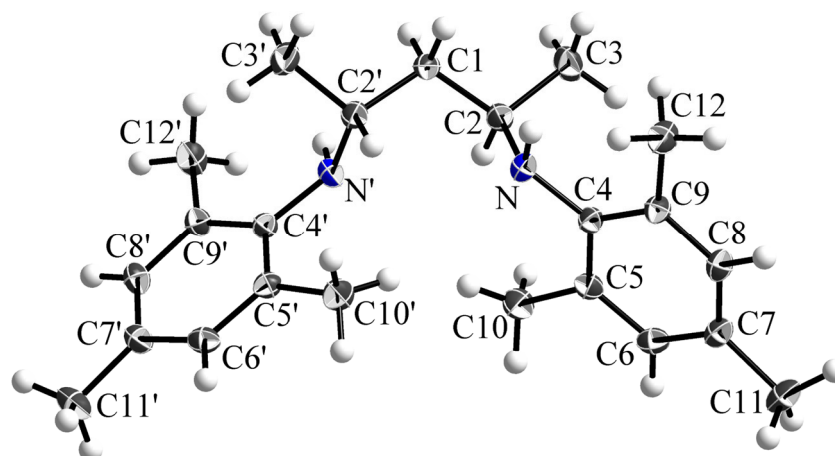
The single crystal structure of the organic compound N^2,N^4 -dimesitylpentane-2,4-diamine is reported. The compound was obtained as a by-product during the synthesis of the reactant $NacNac^{Mes}H$. The synthesis and single crystal selection was performed by me. Dr. Wilhelm Klein refined the single crystal structure data. The manuscript for publication was written by me and submitted for publication by Dr. Wilhelm Klein.

Crystal Structure of N^2,N^4 -dimesitylpentane-2,4-diamine, $C_{23}H_{34}N_2$

Christoph Wallach, Wilhelm Klein and Thomas F. Fässler

Technische Universität München
Department Chemie, Lichtenbergstr. 4
85747 Garching, Germany

e-mail: thomas.faessler@lrz.tum.de

**Abstract**

$C_{23}H_{34}N_2$, monoclinic, $C2/c$ (no. 15), $a = 15.2448(11)$ Å, $b = 8.2189(5)$ Å, $c = 16.7350(16)$ Å, $\alpha = 90^\circ$, $\beta = 103.133(7)^\circ$, $\gamma = 90^\circ$, $V = 2042.0(3)$ Å³, $Z = 4$, $R_{gt}(F) = 0.0438$, $wR_{ref}(F^2) = 0.1277$, $T = 150$ K.

Table 1. Data collection and handling.

Crystal:	Colorless block, 0.2 × 0.2 × 0.1 mm
Wavelength:	Mo K α radiation (0.71073 Å)
μ :	0.064 mm ⁻¹
Diffractometer, scan mode:	STOE StadiVari, ω
$2\theta_{\max}$:	60°
$N(hkl)_{\text{measured}}$, $N(hkl)_{\text{unique}}$	34500, 2983
Criterion for I_{obs} , $N(hkl)_{\text{gt}}$:	$I_{\text{obs}} > 2 \sigma(I_{\text{obs}})$, 2179
$N(\text{param})_{\text{refined}}$:	122
Programs:	X-Area, ^[1] SHELXS, ^[2] SHELXL-2014, ^[3] Diamond ^[4]

Source of material

All reactions were performed under ambient conditions. Few single crystals of N^2, N^4 -dimesitylpentane-2,4-diamine (**1**, mesityl = 2,4,6-trimethylphenyl) were obtained as a by-product during the preparation and crystallization of $\text{NaCNac}^{\text{MesH}}$ [N, N' -di(2,4,6-trimethylphenyl)- β -diketiminate].^[5] The ligand $\text{NaCNac}^{\text{MesH}}$ was prepared according to a modified literature procedure.^[6] Acetylacetone (*Merck*), 2,4,6-trimethylaniline (*Alfa Aesar*), and *p*-toluenesulfonic acid (*Merck*) were used without further purification. Acetylacetone (5 g, 50 mmol, 1 equiv.) and 2,4,6-trimethylaniline (13.5 g, 100 mmol, 2 equiv.) were dissolved in toluene (200 mL) and cooled in an ice bath. Subsequently, *p*-toluenesulfonic acid (8.6 g, 50 mmol, 1 equiv.) was added to the flask. After stirring the reaction mixture for 15 h at 110 °C, the solvent was removed under reduced pressure. The solid precipitate was dissolved in dichloromethane (100 mL) and the organic phase was extracted with a saturated potassium carbonate solution. The aqueous phase was re-extracted twice with dichloromethane and the solvent was removed from the combined organic phases under vacuum. The crude product was recrystallized from methanol. Few colorless crystals of **1** were obtained as a by-product besides the main product $\text{NaCNac}^{\text{MesH}}$.

Experimental details

The single crystal of **1** was selected under a microscope equipped with a light source in an Ar-filled glove box. Subsequently, the crystal was transferred under Ar to the diffractometer (*STOE StadiVari*) equipped with a *PILATUS 300K* detector (*DECTRIS*) and a Mo K α radiation source ($\lambda = 0.71073$ Å). For the data collection the crystal was cooled in a 150 K cold stream of dry nitrogen. The single crystal structure was solved by direct methods using the program *SHELXS-97*.^[2] Structure refinements were performed by full-matrix least-squares calculations against F^2 (*SHELXL-2014*).^[3] A riding model was used to calculate and refine the positions of hydrogen atoms, except for the hydrogen atom bound to nitrogen which was located from the difference Fourier map and was refined with free positional and isotropic displacement

parameters. Other elements than hydrogen were refined with anisotropic displacement parameters.

Discussion

*N*²,*N*⁴-dimesitylpentane-2,4-diamine **1** crystallizes in the monoclinic space group *C2/c* with four molecules per unit cell and all atoms at general *8f* Wyckoff positions except for C1 at a *4e* site which lies on a twofold axis, defining one molecule half as asymmetric unit. It represents the fully reduced congener to the organic compound *NacNac*^{Mes}H (**2**), which serves as a ligand in e.g. magnesium organyls.^[7-8] However, due to the absence of any reducing agent in the reaction mixture the formation of compound **1** cannot be explained in a straightforward way. Structurally similar compounds like *N*²,*N*⁴-di(*iso*-propylphenyl)-3,3-dimethylpentane-2,4-diamine (**3**) have been reported before,^[9-10] some of which were prepared by the reduction of the corresponding aryl-diimines with LiAlH₄.^[11] Diamines obtained via this route have been applied as ligands for the generation of nickel complexes, which are used as catalytic species in the polymerization of polyethylene.^[11]

The presence of amine moieties was corroborated not only by evaluating the difference Fourier electron density map, revealing hydrogen atoms adjacent to the nitrogen atoms, but also by comparing the C-C and C-N bond lengths of **1** to the compounds **2** and **3**.^[8-9] The backbone of compound **1** comprises solely C-C and N-C single bonds [C1-C2 = 1.5364(13) Å, N-C2 = 1.4749(14) Å, N-C4 = 1.4237(13) Å] in analogy to molecule **3**. In contrast, the backbone of the unsaturated compound **2** reveals shortened C=C and N=C double bonds of 1.397 Å and 1.324 Å (mean values), respectively.^[8] The NH groups form neither intramolecular nor intermolecular hydrogen bonds of relevant strength, also no π - π interactions between the mesityl residues indicated by the parallel orientation of the aryl rings are present.

Table 2. Fractional atomic coordinates and isotropic or equivalent isotropic displacement parameters (Å²).

	<i>x</i>	<i>y</i>	<i>z</i>	<i>U</i> _{iso} [*] / <i>U</i> _{eq}
C1	0.5000	0.64420(18)	0.2500	0.0228(3)
H1A	0.4481	0.7154	0.2266	0.027*
H1B	0.5519	0.7154	0.2734	0.027*
C2	0.52311(7)	0.54381(13)	0.18010(7)	0.0238(2)
H2	0.4696	0.4754	0.1552	0.029*
C3	0.54380(9)	0.65475(16)	0.11294(8)	0.0356(3)
H3A	0.5923	0.7302	0.1372	0.053*
H3B	0.4897	0.7167	0.0875	0.053*
H3C	0.5626	0.5883	0.0711	0.053*
N	0.59849(6)	0.43451(11)	0.21606(6)	0.0235(2)

Table 2 continued

H1	0.6455(11)	0.499(2)	0.2479(11)	0.044(4)*
C4	0.63402(7)	0.32711(12)	0.16458(6)	0.0202(2)
C5	0.58201(7)	0.19841(13)	0.12242(7)	0.0223(2)
C6	0.62219(8)	0.08763(13)	0.07811(7)	0.0246(2)
H6	0.5864	0.0026	0.0490	0.030*
C7	0.71248(8)	0.09742(13)	0.07514(7)	0.0251(2)
C8	0.76200(7)	0.22660(14)	0.11607(7)	0.0253(2)
H8	0.8235	0.2370	0.1139	0.030*
C9	0.72504(7)	0.34183(13)	0.16031(7)	0.0223(2)
C10	0.48513(8)	0.17106(15)	0.12607(8)	0.0311(3)
H10A	0.4457	0.2356	0.0833	0.047*
H10B	0.4765	0.2044	0.1800	0.047*
H10C	0.4703	0.0554	0.1173	0.047*
C11	0.75574(10)	-0.03149(16)	0.03248(8)	0.0360(3)
H11A	0.8068	0.0158	0.0141	0.054*
H11B	0.7115	-0.0729	-0.0151	0.054*
H11C	0.7770	-0.1210	0.0707	0.054*
C12	0.78280(8)	0.47986(16)	0.20280(8)	0.0322(3)
H12A	0.8428	0.4731	0.1910	0.048*
H12B	0.7882	0.4721	0.2621	0.048*
H12C	0.7549	0.5840	0.1828	0.048*

Table 3. Anisotropic atomic displacement parameters (\AA^2).

	U^{11}	U^{22}	U^{33}	U^{12}	U^{13}	U^{23}
C1	0.0213(6)	0.0190(6)	0.0292(8)	0.000	0.0082(6)	0.000
C2	0.0229(5)	0.0237(5)	0.0261(5)	0.0013(4)	0.0079(4)	0.0033(4)
C3	0.0401(7)	0.0353(6)	0.0361(7)	0.0072(5)	0.0181(6)	0.0141(5)
N	0.0239(4)	0.0248(4)	0.0224(5)	0.0042(3)	0.0063(4)	-0.0015(3)
C4	0.0221(5)	0.0201(5)	0.0189(5)	0.0018(4)	0.0054(4)	0.0009(4)
C5	0.0226(5)	0.0213(5)	0.0220(5)	0.0000(4)	0.0033(4)	0.0023(4)
C6	0.0286(5)	0.0208(5)	0.0225(5)	-0.0001(4)	0.0018(4)	-0.0012(4)
C7	0.0295(5)	0.0245(5)	0.0209(5)	0.0072(4)	0.0049(4)	-0.0003(4)
C8	0.0224(5)	0.0291(5)	0.0247(5)	0.0039(4)	0.0062(4)	-0.0007(4)
C9	0.0223(5)	0.0238(5)	0.0206(5)	-0.0001(4)	0.0044(4)	-0.0015(4)
C10	0.0255(5)	0.0301(6)	0.0385(7)	-0.0067(4)	0.0089(5)	-0.0048(5)
C11	0.0421(7)	0.0322(6)	0.0336(7)	0.0123(5)	0.0084(6)	-0.0070(5)
C12	0.0239(5)	0.0359(6)	0.0375(7)	-0.0057(5)	0.0086(5)	-0.0117(5)

Table 4. Geometric parameters (Å, °). Symmetry code: (i) $-x+1, y, -z+1/2$.

Atoms	Distances	Atoms	Distances
C1—C2	1.5364(13)	C6—C7	1.3909(15)
C1—C2 ⁱ	1.5364(13)	C6—H6	0.9500
C1—H1A	0.9900	C7—C8	1.3897(16)
C1—H1B	0.9900	C7—C11	1.5104(15)
C2—N	1.4749(14)	C8—C9	1.3972(14)
C2—C3	1.5348(15)	C8—H8	0.9500
C2—H2	1.0000	C9—C12	1.5111(16)
C3—H3A	0.9800	C10—H10A	0.9800
C3—H3B	0.9800	C10—H10B	0.9800
C3—H3C	0.9800	C10—H10C	0.9800
N—C4	1.4237(13)	C11—H11A	0.9800
N—H1	0.953(17)	C11—H11B	0.9800
C4—C9	1.4108(14)	C11—H11C	0.9800
C4—C5	1.4110(14)	C12—H12A	0.9800
C5—C6	1.4001(15)	C12—H12B	0.9800
C5—C10	1.5088(15)	C12—H12C	0.9800

Atoms	Angles [°]	Atoms	Angles [°]
C2—C1—C2 ⁱ	115.03(12)	C5—C6—H6	118.8
C2—C1—H1A	108.5	C8—C7—C6	117.25(10)
C2 ⁱ —C1—H1A	108.5	C8—C7—C11	121.48(11)
C2—C1—H1B	108.5	C6—C7—C11	121.21(11)
C2 ⁱ —C1—H1B	108.5	C7—C8—C9	122.66(10)
H1A—C1—H1B	107.5	C7—C8—H8	118.7
N—C2—C3	112.95(9)	C9—C8—H8	118.7
N—C2—C1	107.98(8)	C8—C9—C4	119.24(10)
C3—C2—C1	111.06(10)	C8—C9—C12	119.75(9)
N—C2—H2	108.2	C4—C9—C12	121.02(9)
C3—C2—H2	108.2	C5—C10—H10A	109.5
C1—C2—H2	108.2	C5—C10—H10B	109.5
C2—C3—H3A	109.5	H10A—C10—H10B	109.5
C2—C3—H3B	109.5	C5—C10—H10C	109.5
H3A—C3—H3B	109.5	H10A—C10—H10C	109.5
C2—C3—H3C	109.5	H10B—C10—H10C	109.5
H3A—C3—H3C	109.5	C7—C11—H11A	109.5
H3B—C3—H3C	109.5	C7—C11—H11B	109.5
C4—N—C2	119.94(9)	H11A—C11—H11B	109.5
C4—N—H1	110.1(10)	C7—C11—H11C	109.5
C2—N—H1	107.7(10)	H11A—C11—H11C	109.5
C9—C4—C5	119.10(9)	H11B—C11—H11C	109.5
C9—C4—N	119.43(9)	C9—C12—H12A	109.5
C5—C4—N	121.30(9)	C9—C12—H12B	109.5
C6—C5—C4	119.25(9)	H12A—C12—H12B	109.5

Table 4 continued			
C6—C5—C10	118.33(10)	C9—C12—H12C	109.5
C4—C5—C10	122.37(10)	H12A—C12—H12C	109.5
C7—C6—C5	122.47(10)	H12B—C12—H12C	109.5
C7—C6—H6	118.8		

Acknowledgements

CW thanks the Deutsche Forschungsgemeinschaft (DFG, German Research Foundation, project number 245845833) within the International Research Training Group IRTG 2022 (ATUMS) for funding. Furthermore, CW thanks the Studienstiftung des Deutschen Volkes for granting a PhD scholarship.

References

- [1] Stoe & Cie GmbH: X-Area, Version 1.76. Stoe & Cie GmbH, Darmstadt, Germany **2017**.
- [2] G. M. Sheldrick, *A short history of SHELX*, *Acta Crystallogr. Sect. A: Found. Crystallogr.* **2008**, *64*, 112.
- [3] G. M. Sheldrick, *Crystal structure refinement with SHELXL*, *Acta Crystallogr. Sect. C: Struct. Chem.* **2015**, *71*, 3.
- [4] K. Brandenburg, Diamond Version 3.2k, Crystal Impact GbR, Bonn, 2014.
- [5] C. Wallach, W. Klein, T. F. Fässler, *Nonagermanide Zintl Clusters with Mg²⁺ Counter Ions*, *Z. Anorg. Allg. Chem.*, **2022**, DOI 10.1002/zaac.202200065.
- [6] E. Rossetto, M. Caovilla, D. Thiele, R. F. de Souza and K. Bernardo-Gusmão, *Ethylene oligomerization using nickel- β -diimine hybrid xerogels produced by the sol-gel process*, *Appl. Catal. A: Gen.* **2013**, *454*, 152.
- [7] S. P. Green, C. Jones and A. Stasch, *Stable magnesium (I) compounds with Mg-Mg bonds*, *Science* **2007**, *318*, 1754.
- [8] J. Prust, K. Most, I. Müller, E. Alexopoulos, A. Stasch, I. Usón and H. W. Roesky, *Synthesis and Structures of β -Diketoiminate Complexes of Magnesium*, *Z. Anorg. Allg. Chem.* **2001**, *627*, 2032.
- [9] D. T. Carey, F. S. Mair, R. G. Pritchard, J. E. Warren and R. J. Woods, *Borane and alane reductions of bulky N,N'-diaryl-1,3-diimines: structural characterization of products and intermediates in the diastereoselective synthesis of 1,3-diamines*, *Dalton Trans.* **2003**, 3792.
- [10] J. Magull and A. Simon, *Zur Reaktion von Makrozyklen mit Lanthanoiden. II. Die Strukturen von $[K(thf)_3]_2[(C_{22}H_{28}N_4)_2Sm_2] \cdot 4THF$ und $[(C_{22}H_{22}N_4)Co] \cdot DME$* , *Z. Anorg. Allg. Chem.* **1992**, *615*, 81.
- [11] G. Rong, G. Zifang, Z. Junling, L. Dongbing, L. Yan, Z. Xiaofan, F. Jie, Z. Junhui and L. Jingjing, Beijing Research Institute of Chemical Industry, China Petroleum & Chemical Corporation, patent no. CN111116787, 8th May **2020**, https://scifinder-n.cas.org/searchDetail/reference/622cbae55709576d8_a282d95/referenceDetails, accessed 12th March 2022.

7 COMPLETE LIST OF PUBLICATIONS

‡: authors contributed equally to this work.

Peer-reviewed manuscripts in order of appearance:

1. C. Wallach,‡ F. S. Geitner,‡ W. Klein and T. F. Fässler, *Enhancing the Variability of [Ge₉] Cluster Chemistry through Phosphine Functionalization*, *Chem. Eur. J.* **2019**, *25*, 12349.
2. C. Wallach,‡ K. Mayer,‡ T. Henneberger, W. Klein and T. F. Fässler, *Intermediates and Products of the Reaction of Zn(II) Organyls with Tetrel Element Zintl Ions: Cluster Extension Versus Complexation*, *Dalton Trans.* **2020**, *49*, 6191.

A graphical illustration of the results was published as an inside front cover: DOI 10.1039/D0DT90093A.
3. C. Wallach,‡ F. S. Geitner,‡ A. J. Karttunen and T. F. Fässler, *Boranyl-Functionalized [Ge₉] Clusters: Providing the Idea of Intramolecular Ge/B Frustrated Lewis Pairs*, *Angew. Chem. Int. Ed.* **2021**, *60*, 2648.
4. C. Wallach,‡ F. S. Geitner ‡ and T. F. Fässler, *FLP-type Nitrile Activation and Cyclic Ether Ring-Opening by Halo Borane Nonagermanide-Cluster Lewis Acid–Base Pairs*, *Chem. Sci.* **2021**, *12*, 6969.
5. C. Wallach, Y. Selic, B. J. L. Witzel, W. Klein and T. F. Fässler, *Filled Trivacant Icosahedra as Building Fragments in 17-atom Endohedral Germanides [TM₂@Ge₁₇]ⁿ⁻ (TM = Co, Ni)*, *Dalton Trans.* **2021**, *50*, 13671.
6. C. Wallach, W. Klein and T. F. Fässler, *Nonagermanide Zintl Clusters with Mg²⁺ Counter Ions*, *Z. Anorg. Allg. Chem.* **2022**, accepted manuscript, DOI: 10.1002/zaac.202200065.
7. C. Wallach, W. Klein and T. F. Fässler, *Oxidative Coupling of Silylated Nonagermanide Clusters*, *Chem. Commun.* **2022**, *58*, 5486.
8. C. Wallach, W. Klein and T. F. Fässler, *Crystal Structure of (1,4,7,10,13,16-hexaoxacyclooctadecane-κ⁶O₆) potassium (2-methylphenylamino)ethyl-2-methylphenylamide ammoniate (1/3.5), [K(18-crown-6)](o-CH₃C₆H₄)NH(CH₂)₂N(o-CH₃C₆H₄) · 3.5 NH₃, C₂₈H_{53.5}KN_{5.5}O₆*, single crystal structure communication submitted for publication in *Z. Kristallogr., New Cryst. Struct.*
9. C. Wallach, W. Klein and T. F. Fässler, *Crystal Structure of N²,N⁴-dimesitylpentane-2,4-diamine, C₂₃H₃₄N₂*, single crystal structure communication submitted for publication in *Z. Kristallogr., New Cryst. Struct.*

List of manuscripts prepared for publication:

10. C. Wallach, Y. Selic, F. S. Geitner, W. Klein, A. J. Karttunen and T. F. Fässler, *Charge-Transfer Processes in Functionalized [Ge₉] Clusters Based on the Reversible Formation of a Zwitterion*, manuscript for publication.
11. C. Wallach, D. M. Dankert ‡ and T. F. Fässler, *Counterion Related Structural Isomerism in the Nonagermanide Clusters A[Ge₉{Si(TMS)₃]₂(CH₂)₄O-DAB^{Mes}] (A = K, Cs)*, manuscript for publication.

Conference contribution

1. Synthesis and Isolation of 17-atomic Endohedral Germanides [TM₂@Ge₁₇]ⁿ⁻ (TM = Co, Ni) Comprising Filled Trivacant Icosahedral Building Fragments
Christoph Wallach, Yasmin Selic, Benedikt Witzel, Wilhelm Klein and Thomas F. Fässler
Poster, GDCh Wissenschaftsforum Chemie 2021, online-conference.